

**Department of Imaging and Applied Physics
School of Physical Sciences**

**Improving Hyperspectral Image Consistency for Vegetation
Classification over the Port Hedland Coastal Region**

Shawn Henson Bos

**This thesis is presented for the Degree of
Doctor of Philosophy
of
Curtin University**

July 2020

Statement of Originality

To the best of my knowledge and belief this thesis contains no material previously published by any other person except where due acknowledgment has been made.

This thesis contains no material which has been accepted for the award of any other degree or diploma in any university.

Signature:

Date: 26-07-2020

Statement of Contribution by Others

The contents of all chapters and appendices in this thesis are my own work.

(signature of Candidate)

(signature of Supervisor)

Abstract

Mangrove forests are ecologically significant systems, providing a habitat to numerous species of animals. They also perform other important functions such as providing coastal areas with protection from cyclones, erosion and tsunami events. Around the world, there are approximately 70 mangrove species of which 47 reside in Australia and just 7 in the Port Hedland coastal region. These forests are in decline around the world, many due to man's activities. From 1950 to 2000, about a third of all mangroves have been lost, with 25% between 1980 and 2000 alone.

The Port Hedland harbour (Western Australia) is the largest bulk export harbour in the world. Since 1963, some 12.8% cumulative losses in mangroves have occurred, with another 1.5% mangrove removal approved for additional harbour expansion as part of the South West Creek Dredging and Reclamation Project (2012 – 2016). Although these additional losses were minimised through careful planning, re-propagation is an approach to mitigate these losses. Re-propagation refers to not only replacing these mangroves but also to replicating the habitat, vegetation structure and composition in addition to the ecological composition of mangrove communities. A map, showing both the extent and composition of existing mangrove species, would provide invaluable insights in supporting the planning of re-propagation and associated activities.

Remote sensing offers the ability to map and monitor mangrove environments for management and conservation. The use of an airborne sensor allows large regions to be spectrally recorded in short periods at high spatial resolution. Hyperspectral data has the potential to provide not only additional but also more detailed environmental parameters (e.g. biochemical and biophysical) over those derived using multispectral data.

The focus in this work is the classification of mangroves, for which the overall accuracy is generally higher for processing techniques based on hyperspectral data compared to those using multispectral data or photointerpretation. In particular, the thematic map produced in this work adopted the unsupervised classifier (primarily k-means) with feature reduction performed using principal component analysis (PCA).

In this study, an airborne-based survey collected hyperspectral data with an AISA EAGLE sensor over the Port Hedland coastal region in September 2010. A total of 137 flight line image segments were recorded, representing covering a total areal coverage of approximately 214 km². Each image pixel covers a spatial area of 1 m² with spectra recorded using 246 spectral bands, covering the spectral range 0.40 – 0.98 μm.

Initially we examined the feasibility of spectrally distinguishing mangrove species, using field data collected during September 2013. Reflectance spectra for each species were recorded using a hand-held ASD field spectrometer. Between-species comparisons using spectral angles showed high similarity in many cases. Using a tally based system to count the number of spectral angles exceeding specific threshold values, the results showed that, on average, *Bruguiera exaristata* was the most similar to all other mangrove species, followed closely by both (equally) *Rhizophora stylosa* and *Aegialitis annulata*. The most spectrally distinct mangrove species was, on average, *Osbornia octodonta*. The highest level of spectral similarity between mangrove species existed between *Rhizophora stylosa* and *Bruguiera exaristata* where the spectral angle was 0.02 ± 0.08 rad (therefore being spectrally indistinguishable). The highest spectral difference existed between *Bruguiera exaristata* and *Avicennia marina* where the spectral angle was 0.17 ± 0.08 rad. *Bruguiera exaristata* and *Osbornia octodonta* were also highly dissimilar (0.16 ± 0.04 rad) as were *Avicennia marina* and *Ceriops australis* (0.15 ± 0.08 rad). However, these larger spectral angles were uncommon.

The 137 flight line segments were radiometrically corrected using the Tafkaa atmospheric model then “stitched” together to produce a full-scene reflectance and radiance data sets. Attempts to apply supervised classification methods to the airborne reflectance data, using the ASD field data for training, highlighted significant inconsistencies. The mean spectral angle between image mangrove spectra and ASD spectra for *Avicennia marina* was 0.09 rad, exceeding all spectral angles between mangrove species. In addition, significant scene brightness inconsistencies between flight line segments were identified. These inconsistencies could not be resolved by adjusting Tafkaa model parameters, thus the inconsistencies are assumed to be inherent in the raw flight-recorded data.

Spectral and brightness inconsistencies were identified at three major levels. These included: 1) spectral brightness changes within a flight line, 2) jumps in brightness between adjacent flight lines, and 3) an overall change in brightness across the whole scene in a north-south direction. A normalisation process was developed to improve the spectral consistency over the image. The spectral normalisation process was applied to pre-classified images, whereby each image was masked to remove either water, leaving just land pixels or non-vegetative pixels, leaving just vegetative pixels. The normalisation process did not adjust airborne spectra to be more similar to the ASD spectra; rather, it was designed to produce spectra that are more consistent over the full extent of the scene.

The vegetative mask was developed to identify vegetation pixels within the scene. It was developed based on a mean-gradient (MG) method, which employed several wavelength bands on either side of the vegetative “red-edge” position, a spectral reflectance feature. The use of MG threshold values allowed for an appropriate vegetative density to be selected, with particular emphasis to retain the dense mangrove forested regions.

Normalised reflectance and radiance images were classified using unsupervised classification applied to vegetated pixels following feature reduction using the PC transform. Class-pair spectral separabilities were assessed using Jeffries-Matusita (JM) distances with class-pairs merged (as required) according to probabilities.

The best thematic map was selected on the basis of having the highest number of mangrove classes at moderate and low probabilities, meaning a JM distance ≥ 1.8 and ≥ 1.7 , respectively. The normalised vegetative map, using radiance data, produced the best results. Mangrove classes from the normalised image were spatially sound and unaffected by flight line boundaries. In addition, the separability between classes was also increased compared to results of the non-normalised data, leading to more detailed classification structures.

The similarity in spectral angles from the ASD field data suggested that the mangrove species were likely indistinguishable in the airborne data, so the identified spectral regions in the airborne vegetation class map at $JM \geq 1.8$ were categorised into broad “mangrove type” regions. The mean spectral differences between these thematic classes were interpreted according to vegetative densities.

Field work data showed the existence of different heights for mangroves composed of communities with identical species.

At a lower degree of confidence, $JM \geq 1.7$, an attempt was made to identify the actual mangrove species based on probability arguments using field work observations. As *Avicennia marina* is the most dominant species, classes were interpreted in terms of this species but for different canopy heights. In addition, the mean class spectra that were dark were interpreted in terms of *Rhizophora stylosa*, being the second most abundant mangrove. They were also decomposed according to canopy heights.

The validity of the thematic spatial patterns and interpretations were verified to a commercially produced map, which was based on an airborne photographic survey combined with field classification. The airborne hyperspectral map has six mangrove-related spatial structures, with gross distributions comparing favourably to the results of the commercial survey consisting of five mangrove classes.

Acknowledgements

First and foremost, I wish to thank the Pilbara Ports Authority (PPA) for making their airborne-based Port Hedland hyperspectral data available in addition to offering a generous scholarship, without which I would have been unable to commence a PhD thesis. In particular I thank their Sustainability Coordinator, Nicole Wylie, whose assistance throughout the years has been graciously appreciated. Her site knowledge led to sound recommendations in choosing the most appropriate field collection sites, which together with her botanic knowledge ensured that ASD spectral samples were recorded from a diverse range of species.

I am indebted to my supervisor, Dr. Peter Fearn, whose support ensured a great deal of learning and progress was made. I also give special thanks to Professor Mervyn Lynch who (together with Dr. Peter Fearn) provided the opportunity for myself to undertake this thesis in the first place. Both supervisors went to enormous lengths to secure the scholarship on offer from the Port Hedland Ports Authority (PHPA) (now known as PPA). Curtin University also deserves to be mentioned in their collaboration with PHPA. I also give thanks to Dr. Brendan McGann, who became my supervisor when Dr. Fearn was made redundant.

My gratitude also goes out to the members of the Remote Sensing and Satellite Research Group at Curtin University (RSSRG) for providing useful assistance throughout the period. This gratitude extends in particular to Dr. Mark Broomhall with whom I have collaborated several times, especially during field trips.

Curtin University library must also be acknowledged in making available a free version of Endnote for PhD students, which has made the task of referencing so much more manageable. On the subject of software, Dr. Peter Fearn has always fulfilled my request in purchasing software in order to facilitate the thesis. In particular, this includes both ENVI (Environment for Visualising Images by Harris Geospatial Solutions, Inc.) and MATLAB (Matrix Laboratory by MathWorks).

I give particular thanks to my parents for their support - not only emotional but also financial - such as providing assistance toward a new (much faster!) computer, without which data processing would have taken a lot longer.

Emotionally, the moods experienced throughout the thesis are appropriately captured by Mahler's 9th symphony; in particular the Adagio which captures moments of tension and dramatic climaxes, while fading away into nothingness at the end (reflecting peace and the completion of the thesis). The funeral march in the first movement has also (unfortunately) been reminiscent of my experiences, when both my parents passed away in quick succession during the course of this thesis. I am deeply saddened that their absence denies them the opportunity to be present at my graduation and to read my completed thesis, thereby gaining a better understanding of the work their son had undertaken.

Finally, last but certainly not least, a special gratitude is extended to my dear wife for her love, patience, support and encouragement. She has made numerous sacrifices to support this research, and whose financial help ensured that bills could be paid.

Table of Contents

Statement of Originality	i
Statement of Contribution by Others	ii
Abstract	iii
Acknowledgements.....	vii
1 Introduction	1
1.1 The Significance of Mangrove Ecosystems	3
1.2 Overview of Hyperspectral Remote Sensing.....	4
1.3 Thesis Objectives	5
1.4 Thesis Outline	6
2 Review of Literature	9
2.1 Introduction.....	11
2.2 Sensors in Remote Sensing.....	13
2.2.1 Non-Hyperspectral Remote Sensing Sensors.....	13
2.2.2 Hyperspectral Remote Sensing Sensors.....	22
2.3 Spectral Characteristics of Vegetation	25
2.3.1 Spectral Properties of Vegetation.....	25
2.3.2 Factors Influencing Vegetation Spectra	28
2.3.3 Atmospheric Effects on Spectra.....	41
2.3.4 Summary to this point.....	44
2.4 Preprocessing	45
2.4.1 Atmospheric Scattering.....	45
2.4.2 Radiometric Correction	48
2.4.3 Geometric Effects.....	51
2.5 Feature Reduction	51
2.5.1 Characteristics of Hyperspace.....	53
2.5.2 Hughes Effect	55
2.5.3 Principal Component Analysis (PCA).....	63
2.5.4 Maximum Noise Fraction (MNF).....	70
2.5.5 Separability Measures.....	71
2.5.6 Summary and Discussion	78
2.6 Classification Techniques	80
2.6.1 Overview	81
2.6.2 Vegetation Indices (VI).....	85

2.6.2.1	Normalised Difference Vegetation Index (NDVI).....	88
2.6.3	Unsupervised Classification	90
2.6.3.1	The k-means Classifier	92
2.6.3.2	ISODATA.....	95
2.6.4	Supervised Classification.....	96
2.6.4.1	Maximum Likelihood (ML).....	98
2.6.4.2	Support Vector Machine (SVM).....	101
2.6.4.3	Spectral Angle Mapper (SAM)	103
2.6.5	Summary to this point.....	105
2.7	Accuracy Assessment	106
2.8	Classification in Practice	108
2.8.1	Mangrove Forests	108
2.8.2	Non-Mangrove Forests	121
2.8.3	Savannahs	122
2.8.4	Unmanned Aerial Vehicles	123
2.8.5	Summary and Discussion	125
2.9	Hyperspectral Data Mining Paradigm	126
2.10	Main Point Summary.....	128
3	Study Region and Image Acquisition	129
3.1	Introduction.....	129
3.2	Study Region.....	129
3.3	Image Acquisition	136
4	Research Methods and Results	146
4.1	Introduction.....	146
4.2	Methods and Discussion	146
4.3	Objective 1: Generation of a Hyperspectral Library.....	152
4.3.1	ASD Background	152
4.3.2	Field Trip Planning.....	157
4.3.3	Spectral Library Log.....	161
4.4	Objective 2: Ability to Discriminate between Mangroves	165
4.4.1	Spectral Angle Interpretation	165
4.4.2	Mangrove Spectra and Distinguishability.	175
4.4.3	Mangrove Spectral Differentiability.....	180
4.4.4	Spectral Similarity Assessment using Separability Measures	184
4.4.5	Summary and Discussion	185

4.5	Objective 3a: Production of a Vegetation Map.....	188
4.5.1	Image Classification using the NDVI.....	189
4.5.2	Image Classification using a Mean Gradient.....	195
4.5.3	Image and Spectral Issues	213
4.5.3.1	Missing Data	214
4.5.3.2	Spectral Changes across Flight Lines	214
4.5.3.3	Spectral Artefacts.....	215
4.5.4	Summary and Discussion	223
4.5.5	Classification Paradigm	225
4.5.6	Development of a Vegetation-Mask.....	233
4.5.7	Classification of the PHPA_Ref_VI image.....	235
4.5.8	Atmospheric Correction Analysis.....	251
4.5.9	Image Normalisation	254
4.5.9.1	Line-averaging Process and Spectral Effects	255
4.5.9.2	Normalisation Process	267
4.5.9.3	Image Comparisons	276
4.5.9.4	Normalisation Mean Spectral Effect on Images	283
4.5.9.5	Normalised Images Nomenclature	288
4.5.9.6	Spectral Comparison between ASD and Hyperspectral Datasets 292	
4.5.10	Summary and Discussion	297
4.5.11	Thematic Maps.....	300
4.5.11.1	Classifying the N_Rad_VI_VI image	301
4.5.11.2	Analysis of Thematic Map.....	318
4.5.11.3	Summary and Discussion	325
4.6	Objective 3b: Thematic Map Interpretation and Validity.....	332
4.6.1	Field Trip Planning.....	332
4.6.2	Field Work Results.....	337
4.6.3	Field Interpretation of Thematic Classes	340
4.6.4	Validation with Published Maps and Discussion.....	357
4.6.5	Summary and Discussion	375
4.6.6	Mangrove Distribution Maps for the Port Hedland Coastal Region..	376
5	Conclusion and Recommendations	382
6	References	389
Appendix A	Vegetation Indices.....	410
A.1	Relative Vegetation Index (RVI).....	410

A.2	Soil Adjusted Vegetation Index (SAVI).....	410
A.3	Mangrove Specific Vegetation Indices	412
A.3.1	The Mangrove Recognition Index (MRI)	412
A.3.2	The Mangrove Vegetation Index (MVI).....	413
A.4	Other Vegetation Indices.....	413
Appendix B	Atmospheric Models – a basic review.....	414
Appendix C	Feature Reduction – mathematical details	420
C.1	Characteristics of Hyperspace	420
C.2	Principal Component Analysis (PCA)	424
C.3	Separability Measures	426
Appendix D	Error Matrices and Accuracy Assessment	428
D.1	Error Matrix	428
D.2	Khat Statistic.....	438
Appendix E	Supervised Classification.....	441
E.1	Maximum Likelihood (ML).....	441
E.2	Support Vector Machine (SVM)	443
E.3	Spectral Angle Mapper (SAM)	445
Appendix F	PCA – A Detailed Numerical Example	448
Appendix G	Field Trip 1 Results.....	455
G.1	Field Trip Logs.....	455
G.2	ASD Spectral Plots	460
G.3	Spectral Angles between Spectra.....	493
G.4	Full Spectral plots and Spectral Angles	519
Appendix H	Gradient Red-Edge Method	525
H.1	Method 1	525
H.1.1	Special Case on Method 1	526
H.2	Method 2	527
Appendix I	GPS Locational Uncertainties	529
I.1	GPS Coordinates and ENVI Pixel Space	529
I.2	Integrity of GPS Coordinates in ASD Measurements	532
Appendix J	Supervised SAM Classification	543
J.1	Image SAM Classification using ASD Spectra	543
J.2	SAM using Image Reference Data	548
Appendix K	Technical details behind Normalisation	556
K.1	Steps	556

K.2	Further Background.....	556
K.3	Technical Elaboration of Steps	557
K.4	Flight Line Behaviour and Georectification	568
Appendix L	Additional Normalised Hyperspectral Images	573
L.1	N_Ref_NoMask image construction	573
L.2	Development of a Land-mask.....	581
L.3	N_Ref_Land image construction	595
L.4	Development of a vegetation-mask	601
L.5	N_Ref_VI image construction.....	601
L.6	N_Rad_Land image construction	605
L.7	N_Ref_Res_VI image construction	611
L.8	N_Rad_Res_VI image construction	616
Appendix M	Artificial Spectral Artefacts.....	621
Appendix N	Spectral Analysis of Normalised images.....	625
N.1	Image ROI Selection Strategy	625
N.2	Reflectance-based images.....	630
N.3	Radiance-based images	646
N.4	Conclusion	659
Appendix O	Normalisation Spectral Artefacts	661
Appendix P	Thematic Maps	672
P.1	Classification based on the N_Ref_NoMask_VI image	672
P.2	Classification based on the N_Ref_Land_VI image	677
P.3	Classification based on the N_Ref_VI_VI image.....	682
P.4	Classification based on the N_Rad_Land_VI image	685
P.5	Classification based on the N_Ref_Res_VI_VI image	690
P.6	Classification based on the N_Rad_Res_VI_VI image	693
P.7	Classification based on a spectral subset for N_Rad_VI_VI	695
Appendix Q	Tafkaa Model Details.....	699
Q.1	Target Surface Reflectance and the Tafkaa Model	699
Q.2	Flight Line Segment Parameters.....	703
Q.3	Tafkaa Computational Details	711
Appendix R	SAM Interpolation Mathematical Details.....	712
Appendix S	Classification Technicalities.....	714
S.1	JM Distance Pair Combinations	714
S.2	MNF Transform Band Selections	714

Appendix T	Mangrove Botanic Classification.....	717
Appendix U	Displaying image using ENVI	722
Appendix V	Unsupervised Classification in Practice	727
Appendix W	Mask File Behaviour in ENVI.....	730
W.1	Mask building for a region in a test image	730
W.2	Unsupervised classification	731
W.3	PC Transform	733
W.4	ROI Statistics Complications	735
Appendix X	Meteorological Data.....	744

List of Figures

Figure 1: Representation of a mixed and pure pixel.....	21
Figure 2: Contrast between Landsat bands and AVIRIS contiguous bands	23
Figure 3: An example of an ASD recorded spectrum for <i>Bruguiera exaristata</i>	26
Figure 4: Spectral examples for 3 different cover types	27
Figure 5: Spectral example highlighting the red-edge position.....	27
Figure 6: Effect of leaf layers on reflectance	29
Figure 7: The reflectance of wheat under control and nitrogen-deficiency.....	32
Figure 8: Metal-induced stress on sorghum causing a blue-shift.....	33
Figure 9: Spectral reflectance differences in wheat leaves during senescence	34
Figure 10: Effect of wheat senescence on canopy spectral reflectance.....	34
Figure 11: Red-edge inflexion point position for maize leaves of various ages	35
Figure 12: Reflectance spectra for mature peace lily with varyious degrees of leaf dehydration	36
Figure 13: Example spectra for the same corn species exhibiting significant differences	39
Figure 14: Example spectra for three different species having similar spectra	39
Figure 15: Spectral reflectance characteristics for mangroves and terrestrial vegetation	40
Figure 16: Spectral effects caused by atmospheric water absorption on a typical vegetation spectrum	42
Figure 17: Atmospheric transmittance effect of solar radiation on wavelengths.....	43
Figure 18: Atmospheric path radiance effects on a pixel by solar radiation.....	47
Figure 19: A linear surface is used to classify testing data from training data.....	56
Figure 20: Mean recognition accuracy with measurement complexity n for an infinite dataset.	60
Figure 21: Mean recognition accuracy with measurement complexity for different numbers of training samples.	61
Figure 22: Mean recognition accuracy with measurement complexity for different numbers of training samples and where the two class probabilities are different.	63

Figure 23: Upper and lower bounds for the probability of correct class classification with JM distance.....	74
Figure 24: The effect of the transformed divergence on the pairwise probability for correct class identification	77
Figure 25: Illustration of the relationship between spectra and classification	83
Figure 26: Common classification schemes covered	85
Figure 27: Spectral examples for three different types of cover types	86
Figure 28: Illustrating the steps in the k-means clustering algorithm	93
Figure 29: Merging or splitting of clusters in ISODATA	95
Figure 30: Normal distribution functions are used in ML for classification	99
Figure 31: Representation of two classes in 2D spectral space.	101
Figure 32: The region between the dashed hyperplanes is termed a margin.....	102
Figure 33: Spectral angles partition spectral space for classification	105
Figure 34: A map showing the location of Port Hedland in Western Australia.....	130
Figure 35: The five key regions for spectral data sampling in the Port Hedland coastal region.	131
Figure 36: Location of ore and salt stockpiles	131
Figure 37: Map showing the South West Creek region	132
Figure 38: Climate graph for Port Hedland	134
Figure 39: Plot showing the wind speed on the day of the airborne survey.....	135
Figure 40: Plot showing the wind direction on the day of the airborne survey	136
Figure 41: True colour image showing the extent of the aerial survey.....	140
Figure 42: True colour image showing flight lines of the aerial survey	141
Figure 43: True colour image illustrating different flight line segment widths.....	143
Figure 44: True colour image illustrating the relationship between different flight line segment widths and the final stitched image.....	143
Figure 45: Measuring reflectance spectra using the ASD field spectrometer.....	153
Figure 46: Example of an ASD spectrum for one single measurement of [FM] <i>Bruguiera exaristata1</i> located on Finucane Island.	154
Figure 47: Final averaged ASD spectrum for a single species of <i>Bruguiera exaristata1</i> [FM] on Finucane Island.	156

Figure 48: Image showing the region of interest to collect samples at Redbank ...	159
Figure 49: Redbank classification map	159
Figure 50: Spectral comparison between [RB] Shallow water soil and [FM] <i>Aegialitis annulata</i> 2	168
Figure 51: Spectral comparison between [FU] Red soil and [FR] <i>Acaria sp.</i>	169
Figure 52: Spectral comparison between [FU] <i>Aegiceras corniculatum</i> 2 and [FM] <i>Ceriops australis</i>	170
Figure 53: Spectral comparison between [FM] <i>Ceriops australis</i> and [FM] <i>Avicennia marina</i> 2	171
Figure 54: Spectral comparison between [FM] <i>Avicennia marina</i> 1 and [FM] <i>Rhizophora stylosa</i>	172
Figure 55: Spectral comparison between [FM] <i>Avicennia marina</i> 1 and [FM] <i>Aegialitis annulata</i> 1	173
Figure 56: Spectral comparison between [FM] <i>Bruguiera exaristata</i> 1 and [FM] <i>Rhizophora stylosa</i>	174
Figure 57: ASD mean spectra for the 7 mangrove species found on Finucane Island.	175
Figure 58: A magnified view of Figure 57 for mangrove ASD mean spectra.	176
Figure 59: Comparison between ASD and PHPA_Ref spectra for [FR] <i>Avicennia marina</i> on Finucane Island	180
Figure 60: Finucane Island selected to study the effect of NDVI.....	190
Figure 61: NDVI result as an image for Finucane Island	191
Figure 62: NDVI ranges using colours	191
Figure 63: Sample spectra for two pixels.....	193
Figure 64: Three mean cover type spectra explaining mean gradient method	196
Figure 65: Mean-gradient map	198
Figure 66: Frequency histogram for all mean gradients in the Utah region.	199
Figure 67: Frequency histogram for the MG over the Utah region.....	200
Figure 68: Plot of ideal case for cover types	200
Figure 69: Smoothing the gradient by a 51-point moving average	202
Figure 70: Classification result using mean gradients for 3 classes.....	203
Figure 71: Classification result using mean gradients for 7 classes.....	204

Figure 72: Grey MG map showing bright regions containing vegetation.....	206
Figure 73: Grey vegetation map using a MG threshold less than 5000.....	207
Figure 74: True colour vegetation map using a MG of at least 5000	208
Figure 75: Vegetation map using a MG threshold of at least 10,000.....	208
Figure 76: True colour vegetation map using a MG of at least 10,000	209
Figure 77: Grey vegetation map using a MG threshold of at least 30,000.....	210
Figure 78: True colour vegetation map using a MG of at least 30,000	210
Figure 79: The effect of class densities on spatial map resolution	212
Figure 80: MG classificaiton map for 3 cover types	213
Figure 81: True colour image showing water brightness changes within individual flight lines	215
Figure 82: True colour image showing distortion	216
Figure 83: Example of distorted pixel spectrum	216
Figure 84: Magnified view of image distortion.....	217
Figure 85: True colour image showing the location of five defined ROI's on Finucane Island.....	218
Figure 86: Vegetative spectral means corresponding to each of the five ROI's.....	219
Figure 87: True colour image showing locations of negative reflectance spectra ...	220
Figure 88: True colour image showing the location of four defined ROI's.....	221
Figure 89: Vegetative spectral means corresponding to each of the four ROI's.....	222
Figure 90: Photo showing different mangrove species on Finucane Island	231
Figure 91: Map showing the extent of 'strong' vegetation as a mask.....	234
Figure 92: Image showing the relationship between a true colour image and the associated vegetative-mask.....	235
Figure 93: A true colour image for the result of applying the vegetation-mask to the PHPA_Ref image	237
Figure 94: Plot of eigenvalues with 15 PC bands	238
Figure 95: Plot for the cumulative variance (%) with 15 PC bands.....	238
Figure 96: The thematic map from k-means classifying a 9 PC band PHPA_Ref_VI dataset using 10 clusters and 50 iterations.....	240

Figure 97: Image showing the effect of horizontal striping causing class membership changes across flight lines	241
Figure 98: Thematic map as obtained by merging classes from the 10 class k-means PHPA_Ref_VI map, leaving 5 classes separable at $JM \geq 1.7$	246
Figure 99: Magnified view of Figure 98 over Finucane Island.	247
Figure 100: Thematic map as obtained by merging classes from the 10 class k-means PHPA_Ref_VI map, leaving a total of 4 classes at $JM \geq 1.9$	248
Figure 101: The thematic map from ISODATA classifying a 9 PC band PHPA_Ref_VI dataset using 5 to 10 clusters and 50 iterations.....	250
Figure 102: Pixel orientation in relation to flight line number.	256
Figure 103: Line-averaged reflectance plot for the PHPA_Ref image (unmasked) .	258
Figure 104: Illustration showing that flight lines 1 and 2 are composed of multiple flight line segments.....	259
Figure 105: Flight line and pixel orientation in relation to flight line number.	260
Figure 106: Line-averaging plot, showing the mean result over each flight line for the PHPA reflectance image.	261
Figure 107: Line-averaging plot, showing the mean result over each flight line of the radiance image (i.e. PHPA_Rad).	263
Figure 108: Mean flight line radiance plot by masking radiance flight lines	264
Figure 109: Line-averaging plot after vegetatively masking individual reflectance lines	266
Figure 110: Plot showing the result of rotating each individual flight line of Figure 108.....	268
Figure 111: Plot showing the effect of joining adjacent flight line edges after global linear detrending	270
Figure 112: The N_Rad_VI true colour image	272
Figure 113: The N_Rad_VI_VI image.....	275
Figure 114: The white boxed regions indicate the magnified locations for Figure 115 to Figure 118.	278
Figure 115: Magnified view of the northernmost region of Figure 114.....	279
Figure 116: Magnified view of the centre region of Figure 114.	280
Figure 117: Magnified view of the eastern region of Figure 114.	281

Figure 118: Magnified view of the western region of Figure 114.	282
Figure 119: Annotated line-averaging plot for N_Rad_VI.....	283
Figure 120: The yellow and blue transects represent a vertical line of pixels located at rows 6500 and 7000, respectively.	284
Figure 121: N_Rad_VI_VI image transect at pixel row 6500	285
Figure 122: Plot showing vertical line spectra for the PHPA_Rad_VI image	286
Figure 123: Plot showing vertical line spectra for the PHPA_Rad_VI image	287
Figure 124: Flow chart containing an overview of the processes used to generate stitched reflectance-based images.....	290
Figure 125: Flow chart containing an overview of the processes used to generate stitched radiance-based images	291
Figure 126: Plot showing spectral reflectance of [FR] <i>Avicennia marina</i> for all images and the ASD.....	294
Figure 127: Plot showing spectral reflectance of [FR] <i>Acarica sp.</i> for all images and the ASD	296
Figure 128: Thematic map using 50 iterations for a 10 class k-means classifier of the 15 PC band N_Rad_VI_VI dataset.....	303
Figure 129: Thematic map by merging classes from the 10 class k-means classifier of the 15 PC band N_Rad_VI_VI dataset to $JM \geq 1.8$	304
Figure 130: Thematic map by merging classes from the 10 class k-means classifier of the 15 PC band N_Rad_VI_VI dataset to $JM \geq 1.9$	305
Figure 131: Thematic map using 50 iterations for a 15 class k-means classifier of the 15 PC band N_Rad_VI_VI dataset.....	307
Figure 132: Thematic map by merging classes from the 15 class k-means classifier of the 15 PC band N_Rad_VI_VI dataset to $JM \geq 1.7$	309
Figure 133: Thematic map by merging classes from the 15 class k-means classifier of the 15 PC band N_Rad_VI_VI dataset to $JM \geq 1.8$	310
Figure 134: Thematic map by merging classes from the 15 class k-means classifier of the 15 PC band N_Rad_VI_VI dataset to $JM \geq 1.9$	311
Figure 135: Map showing a distinct class amongst the mangrove forests.....	317
Figure 136: Normalised radiance mean spectra for classes 1, 2, 8 and 15	318
Figure 137: The red-edge in the reflectance spectrum	320
Figure 138: The red-edge in the radiance spectrum.....	320

Figure 139: True colour image showing the magenta coloured class lying amongst the salt pond regions.....	321
Figure 140: Thematic classes 1, 2 and 8 superimposed onto a true colour image (corresponding to the $JM \geq 1.8$ N_Rad_VI_VI thematic map) ..	321
Figure 141: Thematic class 1 superimposed onto a true colour image (corresponding to the $JM \geq 1.8$ N_Rad_VI_VI thematic map)	322
Figure 142: Normalised radiance mean spectra for classes 4, 12, 13 and 14 (corresponding to the $JM \geq 1.8$ N_Rad_VI_VI thematic map)	323
Figure 143: Mixed pixels	333
Figure 144: Field sites selected on Finucane Island	334
Figure 145: Field sites selected on Redbank.....	335
Figure 146: Photo carefully identifying and spectrally recording a mangrove.....	335
Figure 147: Field sites selected in the Port Hedland coastal region	336
Figure 148: Photo showing field site 3.....	341
Figure 149: Photo showing field site 4.....	342
Figure 150: Photo showing field site 2.....	346
Figure 151: Photo showing field site 3.....	346
Figure 152: Photo showing field site 4.....	347
Figure 153: Photo showing field site 34.....	348
Figure 154: Photo showing field site 14.....	349
Figure 155: Photo showing field site 24.....	349
Figure 156: Comparison between thematic map and true colour image.....	350
Figure 157: Photographic evidence of sparsely populated dwarf shrubs of <i>Avicennia marina</i>	350
Figure 158: Photo showing field site 21.....	352
Figure 159: Comparison between thematic map and true colour image.....	356
Figure 160: Vegetative classification map as produced by WorleyParsons	358
Figure 161: Comparison between WorleyParsons and JM18 map (left half).....	361
Figure 162: Comparison between WorleyParsons and JM17 map (left half).....	362
Figure 163: Comparison between WorleyParsons and JM18 map (right half).....	363
Figure 164: Comparison between WorleyParsons and JM17 map (right half).....	364

Figure 165: Comparison between WorleyParsons and true colour image.....	365
Figure 166: Normalised mean radiance spectra for classes 3, 4, 11, 12 and 14 of the JM17 map	366
Figure 167: True colour image over Pretty Pool	367
Figure 168: True colour image over Pretty Pool (magnified) and compared to the N_Rad_VI_VI image	368
Figure 169: Classes superimposed onto the N_Rad_VI_VI image at Pretty Pool....	369
Figure 170: Mangrove classification map as produced by Paling.....	373
Figure 171: Final mangrove map with legend based on JM18 thematic classes (left half).....	378
Figure 172: Final mangrove map with legend based on JM18 thematic classes (right half).....	379
Figure 173: Final mangrove map with legend based on JM17 thematic classes (left half).....	380
Figure 174: Final mangrove map with legend based on JM17 thematic classes (right half).....	381
Figure 175: Fractional volume of a hypersphere inscribed in a hypercube	422
Figure 176: Fractional volume relationship with number of dimensions.....	423
Figure 177: Physical location for the three field regions on Finucane Island as defined in Table 67	461
Figure 178: <i>Aegialitis annulata</i> spectra from different trees (1 & 2). [FM].....	462
Figure 179: <i>Aegialitis annulata</i> 3 (left) and <i>Avicennia marina</i> 1 (right). [FM].....	463
Figure 180: <i>Avicennia marina</i> 2 & 3 (left and right image, respectively). [FM].....	464
Figure 181: <i>Bruguiera exaristata</i> 1 & 2 (left and right image, respectively) [FM]...	465
Figure 182: <i>Ceriops australis</i> (left) & <i>Osbornia octodonta</i> (right). [FM].....	466
Figure 183: <i>Rhizophora stylosa</i> . [FM]	467
Figure 184: <i>Acaria</i> sp. (left) & <i>Avicennia marina</i> (right). [FR].....	468
Figure 185: <i>Frankenia ambita</i> (left) & <i>Trianthema turgidifolia</i> (right). [FR].....	469
Figure 186: <i>Tecticornia</i> sp. 1 (left) & <i>Tecticornia</i> sp. 2 (right). [FR]	470
Figure 187: <i>Tecticornia</i> sp. 3 (left) & <i>Tecticornia</i> sp. 4 (right). [FR]	471
Figure 188: <i>Sporobolus virginicus</i> 1 (left) & <i>Sporobolus virginicus</i> 2 (right). [FR]....	472

Figure 189: <i>Triodia pungens</i> . [FR]	473
Figure 190: Sandy salty crusty soil. [FR]	474
Figure 191: <i>Aegiceras corniculatum</i> 1 (left) & <i>Aegiceras corniculatum</i> 2 (right). [FU]	475
Figure 192: <i>Avicennia marina</i> (left) & <i>Salsola kali</i> (right). [FU]	476
Figure 193: Red soil. [FU]	477
Figure 194: <i>Avicennia marina</i> (left) & <i>Bruguiera exaristata</i> (right). [RB]	478
Figure 195: <i>Ceriops australis</i> (left) & <i>Rhizophora stylosa</i> (right). [RB]	479
Figure 196: Dry soil (left) & Wet soil (right). [RB]	480
Figure 197: Shallow water soil. [RB]	481
Figure 198: <i>Avicennia marina</i> (left) & <i>Limonium</i> (right). [LP]	482
Figure 199: <i>Tecticornia</i> sp. (left). [LP]	483
Figure 200: Dredge dam on top (left) & Dredge dam road (right). [LP]	484
Figure 201: Hard packed dirt road (left) & Salty reddish crust (right). [LP]	485
Figure 202: <i>Acacia translucens</i> (left) & <i>Aerva javanica</i> (right). [PP]	486
Figure 203: <i>Cenchrus ciliaris</i> (left) & <i>Corchorus parviflorus</i> (right). [PP]	487
Figure 204: <i>Tecticornia</i> sp. 1 (left) & <i>Tecticornia</i> sp. 2 (right). [PP]	488
Figure 205: <i>Trianthema turgidifolia</i> (left) & <i>Triodia pungens</i> (right). [PP]	489
Figure 206: Interstitial salt crusted sand (left) & Road (sandy hard packed) (right). [PP]	490
Figure 207: Old bitumen (left) & Salt flat plain (right). [PP]	491
Figure 208: Shell laden sand. [PP]	492
Figure 209: Full spectral plots for <i>Aegialitis annulata</i> 1 (left) and <i>Avicennia</i> <i>marina</i> 1 (right). [FM]	521
Figure 210: Full spectral plots for <i>Bruguiera exaristata</i> 1 (left) and <i>Ceriops</i> <i>australis</i> (right). [FM]	522
Figure 211: Full spectral plots for <i>Osbornia octodonta</i> (left) and <i>Rhizophora</i> <i>stylosa</i> (right). [FM]	523
Figure 212: Full spectral plots for <i>Aegiceras corniculatum</i> 1 [FU] (left) and the 7 mangrove species found at Finucane Island.	524

Figure 213: ENVI's Pixel Locator tool (left) and the pixel location as displayed on the true colour image (right).....	529
Figure 214: The GPS coordinates are stored in the photographed image file.	535
Figure 215: Photo of [FR] <i>Acaria sp.</i> on Finucane Island	536
Figure 216: Close-up photo taken of the [FR] <i>Acaria sp.</i> from Figure 215.	536
Figure 217: Photograph's GPS location for [FR] <i>Acaria Sp.</i> shown in image.	537
Figure 218: ASD GPS location for [FR] <i>Acaria sp.</i>	538
Figure 219: Measuring the distance from the ASD GPS coordinates for [FR] <i>Acaria sp.</i> to the edge of the feature (i.e. minimum distance).....	539
Figure 220: [FR] <i>Avicennia marina</i> on Finucane Island.....	540
Figure 221: Photographic GPS location for [FR] <i>Avicennia marina</i> on Finucane Island.	541
Figure 222: Probable correct photo location for [FR] <i>Avicennia marina</i>	541
Figure 223: SAM classification map for [FM] <i>Ceriops australis</i> (left) and [FM] <i>Rhizophora stylosa</i> (right).....	544
Figure 224: Occurrence between [FM] <i>Ceriops australis</i> and [FM] <i>Rhizophora stylosa</i> and the SAM classification map for [FM] <i>Avicennia marina 1</i>	545
Figure 225: Plot showing ASD and airborne (PHPA_Ref data) spectra for [FR] <i>Avicennia marina</i> on Finucane Island.	547
Figure 226: Plot showing ASD and airborne (PHPA_Ref data) spectra for [FR] <i>Acaria sp.</i> on Finucane Island.	547
Figure 227: Three regions used superimposed onto a true colour image.....	550
Figure 228: Example pixel spectra collected for training.....	551
Figure 229: Classification result using default spectral angles	552
Figure 230: Classification result using the default angle for deep water and overlap between shallow water and deep water classification	553
Figure 231: Classification result using the default angle for deep water and shallow water	553
Figure 232: Classification result using the default angle for the beach only.....	554
Figure 233: Classification result using a SA of 0.5 rad	554
Figure 234: Classified results for various spectral angles	555
Figure 235: Simplistic representation of the first step of normalisation.....	559

Figure 236: Simplistic representation for the effect of rotating all flight lines.	560
Figure 237: Simplistic representation of the second step of normalisation.	561
Figure 238: Simplistic representation for the effect of rotating the global linear line	562
Figure 239: A simplistic representation of the third (and last) step of normalisation.	563
Figure 240: True colour images showing the effect of incorrectly and correctly stitching an image	567
Figure 241: Image of an uncorrected georectified flight line segment 1b	568
Figure 242: Image for the corrected georectified flight line segment 1b.....	569
Figure 243: Image of an uncorrected georectified flight line segment 2a	570
Figure 244: Image for the corrected georectified flight line segment 2a.....	570
Figure 245: Images for flight line segment 1b in two orientations	571
Figure 246: Line-averaging plot, showing the mean result over each flight line for the reflectance image (PHPA_Ref).	574
Figure 247: Plot showing the effect of rotating each individual flight line	575
Figure 248: Plot showing the effect of global linear detrending in addition to the joining up of adjacent flight line edges.....	576
Figure 249: The true colour N_Ref_NoMask image as constructed using the normalisation process	578
Figure 250: True colour stitched PHPA_Ref image	579
Figure 251: N_Ref_NoMask_VI image after vegetatively masking N_Ref_NoMask.....	580
Figure 252: k-means classification result using three classes.....	583
Figure 253: Spectral sample plot for water from flight line segment 29a.....	586
Figure 254: Spectral sample plot for soil from flight line segment 29a.....	587
Figure 255: Spectral sample plot for vegetation from flight line segment 29a.....	588
Figure 256: Spectral sample plot for soil, water and vegetation from flight line segment 29a	588
Figure 257: Gradient maps for a) method 1 (left), b) method 2 (middle).	590
Figure 258: Gradient threshold map for method 2 (left).....	591

Figure 259: True colour, inverted and gradient images for flight line segment 5e	592
Figure 260: True colour, inverted and gradient images for flight line segment 6b	593
Figure 261: A magnified view of the red 'boxed' region of Figure 260	594
Figure 262: Buildings exhibit negative gradients	595
Figure 263: Line-averaging plot for land-masked individual reflectance flight line segments.	596
Figure 264: Plot showing the effect of rotating each individual flight line	598
Figure 265: Plot showing the effect of global linear detrending and the joining of adjacent flight line edges	599
Figure 266: The true colour N_Ref_Land stitched image.	600
Figure 267: N_Ref_Land_VI image after vegetatively masking N_Ref_Land	600
Figure 268: Line-averaging plot for vegetatively-masked individual reflectance flight lines.	602
Figure 269: Plot shows the effect of rotating each individual flight line	603
Figure 270: Plot showing the effect of global linear detrending in addition to the joining up of adjacent flight line edges.....	604
Figure 271: True colour stitched N_Ref_VI image	604
Figure 272: N_Ref_VI_VI image after vegetatively masking N_Ref_VI.....	605
Figure 273: Line-averaging plot after land-masking the individual radiance flight lines	606
Figure 274: Plot showing the effect of rotating each individual flight line	607
Figure 275: Plot showing the effect of global linear detrending and the joining of adjacent flight line edges	608
Figure 276: Plot showing the result of connecting the adjacent flight line edges ..	609
Figure 277: The true colour N_Rad_Land stitched image	610
Figure 278: N_Rad_Land_VI image after vegetatively masking N_Rad_Land.....	610
Figure 279: Image showing the effect of removing urban residential regions.....	612
Figure 280: Line-averaging plot after vegetatively-masking individual reflectance flight lines	613
Figure 281: Plot showing the effect of rotating each individual flight line	613

Figure 282: Plot showing the effect of global linear detrending and the joining of adjacent flight line edges	614
Figure 283: The true colour N_Ref_Res_VI stitched image	615
Figure 284: N_Ref_Res_VI_VI image after vegetatively masking N_Ref_Res_VI	616
Figure 285: Line-averaging plot after vegetatively-masking individual radiance flight lines	617
Figure 286: Plot showing the effect of rotating each individual flight line	618
Figure 287: Plot showing the effect of global linear detrending and the joining of adjacent flight line edges	619
Figure 288: The true colour N_Rad_Res_VI stitched image	620
Figure 289: N_Rad_Res_VI_VI image after vegetatively masking N_Rad_Res_VI ..	620
Figure 290: Example spectrum corresponding to a pixel in the pink coloured (salt pond) region of the true colour image map.....	623
Figure 291: Example spectrum corresponding to a pixel in the light blue coloured region	624
Figure 292: Example spectrum corresponding to a pixel in the blue coloured region	624
Figure 293: Locations of ROI 23b and ROI 28c defined on Finucane Island	627
Figure 294: Locations of ROI 22d N and ROI 22d S defined on Finucane Island.....	627
Figure 295: Locations of ROI's NW, SW, 2b and 3b	628
Figure 296: Mean spectra plot for the five reflectance-based images for ROI 2b ..	631
Figure 297: Mean spectra plot for the five reflectance-based images for ROI 3a ..	633
Figure 298: Mean reflectance spectra for ROI's 22d N and 22d S.....	635
Figure 299: True colour image of flight line edges for the PHPA_Ref and N_Ref_VI.....	638
Figure 300: Mean spectra plot for five reflectance-based images for ROI 23b.....	639
Figure 301: ROI's superimposed onto the N_Ref_VI_VI image	641
Figure 302: ROI averages for PHPA_Ref_VI and N_Ref_VI_VI.....	641
Figure 303: Mean reflectance spectra for ROI 28c	643
Figure 304: Mean reflectance spectra for ROI NW and ROI SW.....	644
Figure 305: Mean spectra plot for the four radiance-based images for ROI 2b.....	647

Figure 306: Mean spectra plot for the four radiance-based images for ROI 3a.....	647
Figure 307: Mean radiance spectra for ROI's 22d N and 22d S	650
Figure 308: Mean radiance spectra for ROI 23b	652
Figure 309: ROI averages for PHPA_Rad_VI and N_Rad_VI_VI	654
Figure 310: Mean radiance spectra for ROI 28c	655
Figure 311: Mean radiance spectra for ROI NW and ROI SW	658
Figure 312: Magnified view over the blue spectral region of ROI 22d N	662
Figure 313: PHPA_Rad_VI flight line-average plot for flight lines 23 and 22	663
Figure 314: N_Rad_VI_VI flight line-averaged plot for flight lines 23 and 22	664
Figure 315: The effect of flight line rotation for PHPA_Rad_VI.....	666
Figure 316: The effect of removing large brightnesses in PHPA_Rad_VI.....	667
Figure 317: Fully normalised result after removal of extreme radiances	668
Figure 318: Mean spectra over a group of pixels of flight line 22d in the northern region for the full normalisation process	669
Figure 319: Mean spectra over a group of pixels of flight line 22d in the southern region for the full normalisation process	670
Figure 320: Thematic map obtained using 50 iterations for a 10 class k-means classifier of the 8 PC band N_Ref_NoMask_VI dataset	674
Figure 321: Thematic map obtained using 50 iterations using ISODATA classification on the 8 PC band N_Ref_NoMask_VI dataset.....	675
Figure 322: Thematic map as obtained by merging classes from the 10 class k-means N_Ref_NoMask_VI map of the 8 PC band dataset.....	676
Figure 323: The thematic map from k-means classifying a 9 PC band PHPA_Ref_Land_VI dataset using 10 clusters and 50 iterations	679
Figure 324: The thematic map from ISODATA classifying a 9 PC band PHPA_Ref_Land_VI dataset using 5 to 10 clusters and 50 iterations	680
Figure 325: Thematic map as obtained by merging classes from the 10 class k- means PHPA_Ref_Land_VI map, leaving 5 classes separable at JM ≥ 1.8	681
Figure 326: Thematic map obtained using 50 iterations for a 10 class k-means classifier of the 10 PC band N_Ref_VI_VI dataset.....	684

Figure 327: Thematic map as obtained by merging classes from the 10 class k-means N_Ref_VI_VI map, leaving 5 classes separable at $JM \geq 1.7$	685
Figure 328: Thematic map obtained using 50 iterations for a 10 class k-means classifier of the 11 PC band N_Rad_Land_VI dataset	687
Figure 329: Thematic map as obtained by merging classes from the 10 class k-means N_Rad_Land_VI map of the 11 PC band dataset	688
Figure 330: Yellow class structure as present in the PHPA_Ref_VI and N_Rad_VI_VI thematic maps	689
Figure 331: Thematic map as obtained by merging classes from the 10 class k-means N_Ref_Res_VI map, leaving 5 classes separable at $JM \geq 1.7$...	691
Figure 332: Thematic map as obtained by merging classes from the 10 class k-means N_Rad_Res_VI map, leaving 6 classes separable at $JM \geq 1.7$..	696
Figure 333: Thematic map as obtained by merging classes from the 15 class k-means N_Rad_VI_VI_subset map, leaving 7 classes separable at $JM \geq 1.7$	698
Figure 334: Atmospheric scattering effects on a pixel by solar radiation.	699
Figure 335: Sun-sensor geometry, showing the solar and viewing zenith and azimuth angles.	701
Figure 336: Automatic histogram stretching in ENVI effect on images	724
Figure 337: An example of interactively adjusting the histogram in ENVI.	725
Figure 338: Manual adjustment of the histogram allows for natural colours.....	726
Figure 339: Image showing the region on Finucane Island used in this study	730
Figure 340: Image of classification result both with and without a mask.....	732
Figure 341: Image of PC transform result both with and without a mask	734
Figure 342: The ROI Tool in ENVI	735
Figure 343: Test image used for the study in this section.	736
Figure 344: Small and large ROI's results.....	736
Figure 345: Image showing ENVI's "Output ROI Values to ASCII" dialog box	741
Figure 346: The ENVI dialog box used to import the a ROI text file.	743

List of Tables

Table 1: Sensors as used on Landsat 1 and 2	15
Table 2: Radiometric resolution for various satellite-based sensors.	17
Table 3: Comparison of photointerpretation versus quantitative analysis.....	18
Table 4: Representative image interpretation formats for various Land use/Land cover classification levels.....	19
Table 5: Optimal measurement complexities.....	62
Table 6: Example of retaining the first p bands	69
Table 7: Class separation probabilities as a function of distance.....	78
Table 8: Relationship between slope and reflectance for vegetation, soil and water.....	86
Table 9: A summary for the overall classification accuracies	109
Table 10: PHPA image characteristics.....	138
Table 11: Number of flight line segments corresponding to each flight line.	142
Table 12: Estimated proportions of vegetation in each region at Redbank.....	160
Table 13: Quantitative estimation for the proportion of vegetation classes in each region defined at Redbank	160
Table 14: List of all mangrove species and soils sampled.....	162
Table 15: List of all non-mangrove species sampled.	162
Table 16: Spectral angles for the 7 mangroves at Finucane Island.	177
Table 17: The SAs for all species of <i>Bruguiera exaristata</i> with 'typical' mangroves.....	183
Table 18: Final mean tally totals for small and large spectral angles corresponding to mangrove species.....	183
Table 19: Defined red-edge wavelengths for each of the two intervals.	198
Table 20: Areas corresponding to each of the three cover types.....	203
Table 21: Effective red-edge gradients for 7 classes.	204
Table 22: Areas corresponding to each of the seven cover types.....	205
Table 23: Cumulative variance for the PC transform of the PHPA_Ref_VI image...	239

Table 24: Separability report for the k-means 10 class (50 iterations) classifier of the 9 PC band N_Ref_VI_VI dataset.	242
Table 25: Separability report for the k-means 10 class (50 iterations) classifier of the 9 PC band N_Ref_VI_VI dataset after class 4 is merged into class 5 (leaving 9 separable classes)	244
Table 26: Separability report for the k-means 10 class (50 iterations) classifier of the 9 PC band N_Ref_VI_VI dataset after class 5 is merged into class 9 (leaving 8 separable classes).	244
Table 27: Separability report for the k-means 10 class (50 iterations) classifier of the 9 PC band N_Ref_VI_VI dataset after class 7 is merged into class 8 and class 3 into class 9 (leaving 6 separable classes).	245
Table 28: Complete separability report for the k-means 10 class (50 iterations) classifier of the 9 PC band N_Ref_VI_VI dataset after class 8 is merged into class 10 (leaving 5 separable classes).	245
Table 29: Separability report leaving 4 highly separable classes at $JM \geq 1.9$	248
Table 30: A list of significant Tafkaa parameters	251
Table 31: Example for the contents of a Tafkaa input file.	252
Table 32: SA between reflectance-based image pairs for [FR] <i>Avicennia marina</i> ...	295
Table 33: SA between reflectance-based dataset pairs for [FR] <i>Acaria sp.</i>	297
Table 34: Cumulative variance of the PC transform for the N_Rad_VI_VI image ...	301
Table 35: Separability report for the k-means 10 class (50 iterations) classifier of the 15 PC band N_Rad_VI_VI dataset.	302
Table 36: Separability report for the k-means 10 class (50 iterations) classifier where $JM \geq 1.7$ of the 15 PC band N_Rad_VI_VI dataset.....	306
Table 37: Separability report for the k-means 15 class (50 iterations) classifier where $JM \geq 1.7$ for the 15 PC band N_Rad_VI_VI dataset.	308
Table 38: Separability report for the k-means 15 class (50 iterations) classifier where $JM \geq 1.8$ for the 15 PC band N_Rad_VI_VI dataset.	312
Table 39: Separability report for the k-means 15 class (50 iterations) classifier where $JM \geq 1.9$ for the 15 PC band N_Rad_VI_VI dataset.	313
Table 40: Proportions of each class (in %) occupying the final thematic maps of JM17, JM18 and JM19.....	314
Table 41: Comparison between N_Rad_VI_VI and N_Rad_VI_VI_subset	315

Table 42: Both JM and SAs between class pairs corresponding to the $JM \geq 1.8$ N_Rad_VI_VI thematic map.....	323
Table 43: All SA pairs are shown for classes 1, 12, 13 and 14	324
Table 44: Summary table characterising all k-means classification results.....	330
Table 45: Summary table characterising all ISODATA classification results.....	331
Table 46: Mangrove abbreviations used in-field.	337
Table 47: Example of recording field trip results.....	339
Table 48: Summary of interpretation for the classes of the $JM \geq 1.8$ N_Rad_VI_VI thematic map.....	340
Table 49: A two way JM distance table for classes of 3, 4, 11 and 12 in the JM17 map.....	371
Table 50: Mangrove communities and their populations.	374
Table 51: Example for the structure of a simple error matrix.	429
Table 52: Example of an accuracy assessment table.	430
Table 53: Corresponding error matrix using the data	430
Table 54: The Producer's and User's accuracy	432
Table 55: Number of training pixels related to thematic map accuracy	434
Table 56: Number of testing pixels required for a single class category with 95% confidence and 10% error	436
Table 57: Numeric interpretation of the Kappa coefficient in relation to the degree of classification agreement.....	440
Table 58: ENVI PCA statistics file content	451
Table 59: MATLAB program used to link ENVI's PC coordinates to theory.....	451
Table 60: Program output for the MATLAB program	452
Table 61: Example of retaining the first p bands	454
Table 62: Log of mangrove samples taken at Finucane Island	455
Table 63: Log of samples taken at Utah.....	456
Table 64: Log of samples taken at Finucane Island.....	457
Table 65: Log of samples taken at Redbank and Lumsden Point	458
Table 66: Log of samples taken arranged by date	459
Table 67: Region codes to identify ASD spectral sample locations	460

Table 68: Spectral angles of FM with other FM land cover types	497
Table 69: Spectral angles of FM with other FM and FR land cover types	498
Table 70: Spectral angles of FM with FR and FU land cover types	499
Table 71: Spectral angles of FM with FU and RB land cover types.....	500
Table 72: Spectral angles of FM with RB and LP land cover types	501
Table 73: Spectral angles of FM with LP and PP land cover types.....	502
Table 74: Spectral angles of FM with PP land cover types	503
Table 75: Spectral angles of FR with other FR land cover types.....	504
Table 76: Spectral angles of FR with other FR and FU land cover types.....	505
Table 77: Spectral angles of FR with FU and RB land cover types.....	506
Table 78: Spectral angles of FR with LP and PP land cover types.....	507
Table 79: Spectral angles of FR with PP land cover types.....	508
Table 80: Spectral angles of FR with PP land cover types.....	509
Table 81: Spectral angles of FU and RB with other FU and RB land cover types.....	510
Table 82: Spectral angles of FU and RB with other RB and LP land cover types.....	511
Table 83: Spectral angles of FU and RB with LP and PP land cover types	512
Table 84: Spectral angles of FU and RB with PP land cover types.....	513
Table 85: Spectral angles of LP with other LP and PP land cover types	514
Table 86: Spectral angles of LP with PP land cover types.....	515
Table 87: Spectral angles of LP with PP land cover types.....	516
Table 88: Spectral angles of PP with other PP land cover types.....	517
Table 89: Spectral angles of PP with other PP land cover types.....	518
Table 90: Full spectral angles of selected mangrove species on Finucane Island ...	520
Table 91: Pixel values as displayed by the Pixel Locator tool	529
Table 92: Pixel values as entered into the Pixel Locator tool	530
Table 93: Comparing actual Pixel values to those entered into the Pixel Locator tool	532
Table 94: A small excerpt from the GPS log file entries.....	533
Table 95: A list of flight line segments containing land and water	583
Table 96: Plot colours associated with reflectance-based images	629

Table 97: Plot colours associated with radiance-based images	629
Table 98: Spectral angles between the image mean ROI spectra	632
Table 99: Spectral angles between the image mean ROI spectra	634
Table 100: Spectral angles between mean spectra	636
Table 101: Spectral angles between the mean spectra.....	636
Table 102: Reflectance values corresponding to default RGB wavelengths	640
Table 103: Reflectance values corresponding to default RGB wavelengths	642
Table 104: Spectral angles between the image mean ROI spectra	642
Table 105: Spectral angles between the image mean ROI spectra	643
Table 106: Spectral angles between the image mean ROI spectra	645
Table 107: Spectral angles between the image mean ROI spectra	645
Table 108: Spectral angles between the image mean ROI spectra	648
Table 109: Spectral angles between the image mean ROI spectra	649
Table 110: Spectral angles between the image mean ROI spectra	653
Table 111: Spectral angles between the image mean ROI spectra	653
Table 112: Spectral angles between the image mean ROI spectra	653
Table 113: Spectral angles between the image mean ROI spectra	655
Table 114: Spectral angles between the mean spectra	657
Table 115: Spectral angles between the mean spectra.....	657
Table 116: Cumulative variance for the PC transformed N_Ref_NoMask_VI	673
Table 117: Separability report for the k-means 10 class (50 iterations) classifier of the 8 PC band N_Ref_NoMask_VI dataset	673
Table 118: Separability report for the k-means 10 class (50 iterations) classifier where $JM \geq 1.9$ of the 8 PC band N_Ref_NoMask_VI dataset.....	676
Table 119: Separability report for the k-means 10 class (50 iterations) classifier where $JM \geq 1.8$ of the 8 PC band N_Ref_NoMask_VI dataset.....	677
Table 120: Cumulative variance for the PC transformed N_Ref_Land_VI.....	678
Table 121: Separability report for the k-means 10 class (50 iterations) classifier of the 9 PC band N_Ref_Land_VI dataset	678
Table 122: Separability report for the k-means 10 class (50 iterations) classifier of the 9 PC band N_Ref_Land_VI dataset	681

Table 123: Cumulative variance of the PC transformed N_Ref_NoMask_VI	682
Table 124: Separability report for the k-means 10 class (50 iterations) classifier of the 10 PC band N_Ref_VI_VI dataset	683
Table 125: Cumulative variance of the PC transformed N_Rad_Land_VI image	685
Table 126: Separability report for the k-means 10 class (50 iterations) classifier of the 11 PC band N_Rad_Land_VI dataset	686
Table 127: Separability report for the k-means 10 class (50 iterations) classifier where $JM \geq 1.9$ of the 11 PC band N_Rad_Land_VI dataset	690
Table 128: Cumulative variance of the PC transformed N_Ref_Res_VI_VI.....	691
Table 129: Separability report for the k-means 10 class (50 iterations) classifier where $JM \geq 1.65$ of the 9 PC band N_Ref_Res_VI_VI dataset.....	692
Table 130: Separability report for the k-means 10 class (50 iterations) classifier where $JM \geq 1.9$ of the 9 PC band N_Ref_Res_VI_VI dataset.....	692
Table 131: Cumulative variance of the PC transformed N_Rad_Res_VI_VI.....	693
Table 132: Separability report for the k-means 10 class (50 iterations) classifier where $JM \geq 1.7$ of the 7 PC band N_Rad_Res_VI_VI dataset	694
Table 133: Separability report for the k-means 10 class (50 iterations) classifier where $JM \geq 1.9$ of the 7 PC band N_Rad_Res_VI_VI dataset	694
Table 134: Time and navigation parameters for the central pixel in each flight line segment, obtained from each flight line segment header file.....	710
Table 135: The cumulative variance for each MNF transformed band for the N_Ref_NoMask image.....	715
Table 136: Abbreviations to identify mangrove species in field work.....	717
Table 137: Image storage data types used by ENVI.....	722
Table 138: k-means 50 and 100 iteration thematic map class populations, where classes are separable at $JM \geq 1.7$	728
Table 139: k-means 50 and 100 iteration thematic map class populations, where classes are separable to $JM \geq 1.8$ (left table) and $JM \geq 1.9$	728
Table 140: Pixel counts for each class.....	732
Table 141: The eigenvalues for the PC transform.....	734
Table 142: Statistics as returned by the ENVI ROI Tool for the small ROI	737
Table 143: Statistics as returned by the ENVI ROI Tool for the large ROI	737

Table 144: Meteorological data leading up to the PHPA aerial survey day 745

1 Introduction

Remote sensing involves the recording by a sensor of electromagnetic radiation interacting with physical objects from which useful products may be derived. If the data are collected over an extended gridded region, the recorded information manifests itself as a spectral image. The type of product that may be derived is dependent upon the application sought. For example, maps of various types of minerals are of particular interest to a geologist, while an ecologist may harbour an interest in a vegetative map.

Using a computer, patterns in image spectra are grouped using classification processes, thereby leading to a thematic map. Similar groupings define thematic class structures, which relate to cover types (e.g. vegetation, water, soil, urban structures). Remote sensing offers the ability to construct a thematic map detailing the distribution of these physical objects in a timely manner.

Our particular interest lies in the characterisation of vegetation located on the coastal region of Port Hedland in Western Australia. Large regions of mangrove forests are situated not only directly adjacent to the sea but also along estuaries and even further inland.

The ecological significance of mangrove ecosystems are evident from numerous studies (Cashion, 2013). Remote sensing has the ability to monitor mangrove ecosystems over time, extending over periods covering decades, for the purpose of management and conservation (Alongi (2002), Wilkie and Fortuna (2003)).

Traditional approaches in remote sensing record data using aerial photography and multispectral sensing (Newton et al., 2009). Improvements in both sensor and computer technologies (Goetz, 2009) has led to the development of hyperspectral remote sensing. The spectral resolution of a hyperspectral sensor is far superior over non-hyperspectral sensors, which refers to both the number of bands and the bandwidth of a sensor (Campbell and Wynne (2011), p. 286). To elaborate on this vital point, the number of bands for hyperspectral images tend to run into the hundreds compared to traditional based images, which are limited to about three (for photographic) or ten (for multispectral) bands (further details are given in

Section 2.2.1). The increase in spectral resolution allows for the recording of highly detailed spectral information over a scene. Spectrally identifying cover types in an image requires comparisons with accurate field data (e.g. a species of mangrove or soil type).

The process of extracting image information is called data mining and is required for the spectral content to be used for classification purposes. Both hyperspectral and multispectral data mining are performed by computers whose algorithms are based on solid mathematical and physical principles. Photographic aerial surveys, on the other hand, remain popular but rely on human analysts. Some studies suggest computer-based approaches to be more accurate (E. P. Green, Clark, Mumby, Edwards, & Ellis, 1998) but it is likely to depend on the particular product being derived and the experience of the (human) analyst.

Traditional (i.e. non hyperspectral) approaches have highlighted difficulties in spectrally discriminating between different species types, or indeed even between the broader cover types (e.g. mangrove versus non-mangrove) [E. P. Green, C. D. Clark, et al. (1998), Bhattarai and Giri (2011)]. Encouragingly, recent advances using hyperspectral field data have demonstrated the potential to spectrally separate different species of mangroves (Vaiphasa, Ongsomwang, Vaiphasa, and Skidmore (2005), Wang and Sousa (2009)). However, spectral separation between a few of the examined species continues to remain elusive, despite the use of high quality spectral data under ideal (laboratory) conditions. This problem is still under active research (Vaiphasa et al. (2005), Koedsin and Vaiphasa (2013), Prasad and Gnanappazham (2014)).

Classes found on a thematic map may not necessarily be spectrally separable. In reality, a particular class may represent groupings of spectrally indistinguishable features (e.g. two closely related species of vegetation). Separability statistics (discussed in detail in Section 2.5.5) provides a quantitative approach to assess the extent to which classes are spectrally similar.

This thesis is ultimately concerned with the classification of vegetation using hyperspectral remote sensing over the Port Hedland coastal region, with particular emphasis to coastal mangrove forests. Along the way, several spectral inconsistencies were discovered in the Port Hedland hyperspectral image which led

to the development of the normalisation process. The application of this process led to a more consistent thematic map for vegetation.

This introduction outlines the significance of mangrove forests (Section 1.1), and a general overview of hyperspectral remote sensing (Section 1.2). The objectives for this thesis are stated and discussed in detail under Section 1.3, before concluding with an outline for the overall thesis structure in Section 1.4.

1.1 The Significance of Mangrove Ecosystems

Coastal mangrove ecosystems are crucial ecological systems where habitats are used as nurseries by fish and crustacean species (Manson, Loneragan, Harch, Skilleter, & Williams, 2005). These habitats also provide important breeding grounds for birds, mammals and reptiles (Alongi, 2002). In fact, according to the Australian Institute of Marine Science *“Biologists estimate 75% of the commercially caught fish and prawns in Queensland spend at least some part of their life cycle living in the mangroves”* (Australian Institute of Marine Science, n.d.).

Mangroves also perform functions not directly related to biological systems. For instance, mangroves keep coastal erosion in check (Thampanya, Vermaat, Sinsakul, & Panapitukkul, 2006) and form a significant defence against tsunami events (Alongi, 2008). Furthermore, coastal mangroves protect wetland regions behind them from hurricanes, even up to category 5 in strength (K. Zhang et al., 2012). According to Emery (2009), mangrove forests protected villages from the storm surge that resulted from the 1999 super cyclone in India and that the death toll would have been three times higher in the absence of mangroves. These types of events do impact the mangrove forests which may take decades to recover (Smith, Robblee, Wanless, & Doyle, 1994). Mangroves are also negatively affected by pests; for example, tree fruit production of *Rhizophora* are inhibited by caterpillars in northern Australia (Robertson & Blaber, 1992). Areas depleted of mangroves tend to result in higher algal biomass (Granek & Ruttenberg, 2008).

These studies demonstrate the benefits of conserving mangrove forests. However, over the last 50 years cumulative losses have been estimated to be a third

(Alongi, 2002) with more than 25% of the loss occurring between 1980 and 2000 (Wilkie & Fortuna, 2003). Although the reasons for these losses are many, human-induced losses are mainly due to timber, food and medicines. Fortunately, recognition of the important roles served by mangrove forests has led to rehabilitation and restoration projects around the world (Alongi, 2002).

World-wide there are approximately 70 mangrove species, of which about 47 reside in the Australasia region (Australia, New-Zealand, Papua New Guinea) (Alongi, 2002). The Port-Hedland coastal region contains 7 species.

Remote sensing offers the ability to accurately map and monitor mangrove forests for management and conservation. Data may be recorded by a variety of different sensor types (e.g. photographic, multispectral, hyperspectral, Light Detection and Ranging (LiDAR), radar, microwave) carried aboard various platforms (e.g. aeroplanes or satellites). These approaches are surely advantageous to on-foot approaches where areas may be practically inaccessible. In addition, remote sensing covers large regions in an efficient and timely manner with results that are reproducible due to computer processing using sound physical models and mathematical methods.

1.2 Overview of Hyperspectral Remote Sensing

A key difference between traditional remote sensing (i.e. using aerial photographs or multispectral images) and hyperspectral remote sensing lies in both the number of spectral bands available and their narrow bandwidth.

These hyperspectral sensors have enabled the recording of detailed image spectra. This has opened the door to providing better and even new products across many disciplines. For example, in forestry, hyperspectral remote sensing has allowed the means to assess Kyoto Protocol information such as the state of forest carbon content, afforestation, reforestation and deforestation (ARD) (Goodenough et al., 2004). Disease detection has also been improved with the use of narrowband sensing, leading to early detection of stress due to insect attack. The subtle changes in tree canopies were not detectable using broadband sensing. Hyperspectral

remote sensing allows infestations to be fought much earlier for improved forest disease control (Goodenough, Hao, Gordon, Niemann, and Quinn (2012), Kharuk, Ranson, Kozuhovskaya, Kondakov, and Pestunov (2004)). Other researchers have used hyperspectral data to estimate the fuel content of forests for burn severity assessment (Jia et al., 2006). Hyperspectral data has also improved the ability to assess forest health and stress (Goodenough et al., 2006). Several Geological applications may be found in F. D. Van der Meer et al. (2012), where hyperspectral remote sensing has been able to identify more surface mineral detail than previous methods. Other applications include (but are not limited to) defence (e.g. detection of land mines (Winter, 2003)), soil mapping and classification (Ben-Dor et al., 2009), oil spill detection (Leifer et al., 2012). Hyperspectral data has even been used for the evaluation and design of Panda conservation policies (Y. Li et al., 2013).

The number of studies specifically applied to remote sensing of mangrove classification is currently limited. However, a number of laboratory studies using hyperspectral field data have demonstrated encouraging results for the discrimination between species of mangroves (e.g. Vaiphasa et al. (2005), Prasad and Gnanappazham (2014)). In the real world, only a few studies exist to demonstrate the effectiveness of airborne hyperspectral mangrove classification. This includes the successful discrimination between different species of mangrove vegetation (Held, Ticehurst, Lymburner, and Williams (2003), Hirano, Madden, and Welch (2003)) and distinguishing mangrove from non-mangroves (Yang, Everitt, Fletcher, Jensen, & Mausel, 2009).

Compared to multispectral data, hyperspectral data offers improved discrimination (Treitz & Howarth, 1999) to allow classification at species level (e.g. Hirano et al. (2003), Held et al. (2003), Koedsin and Vaiphasa (2013))

1.3 Thesis Objectives

There are three main objectives for this thesis, as listed next in detail.

Objective 1:

Development of a hyperspectral library of vegetative species for the Port Hedland coastal region.

Objective 2:

To investigate the ability to discriminate between and classify different types of vegetative matter, with particular emphasis on mangroves.

Objective 3:

To produce and interpret a vegetation map and assess its validity to those produced by other parties.

Objective 3 consists of two parts and for clarification purposes is subdivided into two sub-objectives:

Sub-objective 3a:

To produce a vegetation map

Sub-objective 3b:

To interpret and validate the thematic map against those produced by other parties

1.4 Thesis Outline

Chapter 2 provides an overview of the literature. In particular, some background given in Section 2.1 to give a basic insight into the factors faced when classifying an image for vegetation. Section 2.2 discusses various sensors and platforms used for remote sensing. Specifications for the various sensors, allow the abilities and limitations to be appreciated, especially in relation to classification (considered in Section 2.8).

Vegetative spectra are uniquely shaped and spectrally distinguishable from non-vegetative spectra; the key characteristic being the red-edge. A detailed discussion along with examples of vegetative spectra are detailed in Section 2.3.1.

There are several influences which determines the shape of a vegetative spectrum, with examples and details given in Section 2.3.2 (non-atmospheric influences) and Section 2.3.3 (atmospheric effects).

To elaborate on the influence the atmosphere has on a recorded spectrum, Section 2.4.1 describes various mechanisms the atmosphere plays in distorting a spectrum. Section 2.4.2 is concerned with eliminating atmospheric influences while Section 2.4.3 briefly discusses other (non-atmospheric) effects on spectra.

Although it appears an image may be classified after the removal of atmospheric influences, there are further factors which must be considered for hyperspectral images. These ramifications stem arise due to fundamental mathematical properties of hyperspectral space. Section 2.5 provides these details along with common resolutions used in the remote sensing community.

A review of common classification methods is presented in Section 2.6, which leads to the production of a thematic map; the main aim of this thesis. However, the accuracy of the thematic map also needs to be assessed. Standard approaches are discussed in Section 2.7, while Section 2.8 discusses classification methodology, results and accuracy assessment as used in other vegetative fields of study.

Finally, as a result of the literature review, a classification paradigm is developed (Section 2.9) to produce a thematic mangrove map for the Port Hedland coastal region using hyperspectral data.

Chapter 3 provides background information concerning the sensor used in the Port Hedland (airborne) hyperspectral survey along with climatic and geographic information.

Chapter 4 outlines the actual research component to meet the thesis objectives. Generation of the hyperspectral library (i.e. Objective 1) is addressed in Section 4.3, while spectral discrimination analysis (i.e. Objective 2) is addressed in Section 4.4. Section 4.5 forms the bulk of the thesis research, whereby a thematic map is produced (Objective 3 – part 1) and validated against maps produced by other researchers Section 4.6 (Objective 3 – part 2).

Chapter 5 presents an overall summary and includes recommendations for future work.

Finally, additional support material is found in the Appendices, covering additional literature reviewed documentation, technical elaborations, extended examples and further results.

2 Review of Literature

A literature review provides the scope necessary to address the objectives. The first section (2.2) provides detailed information regarding the type of sensors used in remote sensing. The background puts into perspective the advantages and disadvantages for the various sensors used with particular emphasis on the recent historical period. The kinds of sensors used by researchers for vegetative-based classification influences the quality of their result. It is therefore important to briefly cover the types of sensors used by researchers as identified further in the literature review. Traditional (non-hyperspectral) sensors are reviewed in Section 2.2.1, followed by the relatively-new hyperspectral sensors in Section 2.2.2.

As our interest lies in vegetative characterisation (Section 2.3), spectral properties of vegetation (Section 2.3.1) needs to be understood. However, vegetative spectra themselves are influenced by the immediate physical environment, which forms the discussion in Section 2.3.2. Atmospheric interactions of radiative energy also have a significant effect on the spectral shape, forming the basis of the discussion in Section 2.3.3. A summary of key aspects concerning vegetative spectra are listed in bullet point form in Section 2.3.4. These key points are of special significance, particularly when interpreting thematic map class spectra in Section 4.6.3.

A detailed discussion of atmospheric scattering effects is covered in Section 2.4.1. Spectra distorted by atmospheric scattering are further affected by atmospheric gasses. Section 2.4.2 details effects of gasses and briefly describes several models used in the remote sensing community to remove atmospheric influences from spectra. Section 2.4.3 briefly describes geometric effects in forming an image.

Section 2.5 introduces feature reduction, which is concerned with selecting optimal bands for further processing (in our case, classification). As this thesis is concerned with using a hyperspectral dataset, we need to appreciate the mathematical characteristics of hyperspace (Section 2.5.1), which have real physical consequences (Section 2.5.2). Two popular transforms – the Principal Component (PC) Transform (Section 2.5.3) and the Maximum Noise Fraction (MNF) (Section

2.5.4) – are discussed for feature reduction. In a basic sense, both of these transforms optimise spectral information by maximising variance (the PC Transform) or by minimising noise (the MNF). The significance is that a subset of bands are selected, thereby mitigating the Hughes effect (Hughes, 1968). Feature reduction using separability statistics (Section 2.5.5) is another popular choice in remote sensing (hence the inclusion under Section 2.5) but tends to be more popular when applied to multispectral data compared to hyperspectral data. In fact, the analysis becomes particularly difficult for hyperspectral data due to the vast quantity of bands. The statistics may also be used for separability analysis of classes as a result of classification, which forms the interest in this thesis. Section 2.5.6 ties together the findings in the form of a brief summary.

Following feature reduction, various common remote sensing classification approaches are discussed in Section 2.6. Although Vegetation Indices (VI's) do not rely on feature reduction, they still form part of vegetative classification (Section 2.6.2). Many different VI's have been developed over the past few decades (Haboudane, Miller, Pattey, Zarco-Tejada, and Strachan (2004), Jones (2010, p. 169) Box 7.1). Beyond simple VI's lay clustering techniques, utilising the whole spectrum instead of a limited number of bands (e.g. the basic NDVI uses two - the Normalised Difference Vegetation Index (NDVI) is discussed in detail in Section 2.6.2.1).

Two particularly common unsupervised classification methods are k-means and the Interactive Self-Organising Data Analysis Techniques (ISODATA), which are reviewed in detail in Sections 2.6.3.1 and 2.6.3.2, respectively. Three popular supervised methods are also covered, starting with Maximum Likelihood (ML) (Section 2.6.4.1), Support Vector Machine (SVM) (Section 2.6.4.2) and the Spectral Angle Mapper (SAM) (Section 2.6.4.3).

Classification accuracies tend to be assessed using two common approaches; the error matrix (Appendix D.1) and the Khat statistic (Appendix D.2).

Practical case studies of vegetative classification (Section 2.8), along with accuracies and classification methods used, are considered for different types of regions. These range from mangrove forests (Section 2.8.1) to non-mangrove forests (Section 2.8.2) and savannahs (Section 2.8.3). A summary of key points are presented in Section 2.8.5.

From all the literature reviewed, a hyperspectral classification paradigm is detailed in Section 2.9. This provides a guide for the key steps used by researchers in the field of hyperspectral remote sensing data to classify vegetation.

Finally, a summary of the literature review is presented in Section 2.10 to highlight key points which need to be carried further into the thesis.

2.1 Introduction

A method based on a vegetative index allows vegetation to be discriminated from non-vegetation matter. However, it is based upon a very limited number of wavelengths. For example, the NDVI relies on just 2 wavelengths. Hyperspectral data extends over hundreds of wavelengths, thereby potentially allowing for a more detailed level of classification – for example, being able to distinguish between different types of vegetation, including at species level.

Spectral reference samples for a given land cover type (e.g. vegetation or soil type) may be recorded in-field using an Analytical Spectral Devices (ASD) field spectrometer (see Section 4.3.3). Comparisons between these spectral reference samples with target image spectra (i.e. as obtained by the AISA EAGLE airborne hyperspectral sensor in the current thesis) allows image pixels to be physically identified according to field-data.

However, there are complications in directly comparing image and ASD spectra. Recorded image spectra are in units of radiance while ASD spectra are of reflectance-type. Furthermore, ASD spectral quality is always higher than spectra recorded by airborne surveys, owing to atmospheric distortion and instrument noise. Fortunately, an atmospheric correction model is based on physical atmospheric processes and removes effects due to water vapour, ozone, wind, sun-sensor geometry, and so on. When applied to the image data, it attempts to eliminate atmospheric effects, thereby making airborne spectra look like ground spectra, so they can be compared on an equal basis. An additional benefit is the conversion of image radiance-based units to the unitless reflectance type, which makes direct comparisons with ASD recorded spectra possible.

There are additional complications in matching ground to image spectra, besides atmospheric effects. For instance, vegetation under stress causes spectral changes (L. Li, Ustin, and Lay (2005), Ustin, Roberts, Gamon, Asner, and Green (2004)). These stresses are caused by lack of water, lack or excess of minerals, disease and so on (Seelig et al. (2008), Chang and Collins (1983)). Even the growth stage of a plant affects the spectral shape; hence the creation of an ASD spectral library is ideally conducted simultaneously with the time of the airborne survey to reduce spectral differences. It is possible that ASD spectral field samples were recorded at sites where healthy vegetation exists but as the airborne survey extends over a wide area, a portion those spectra may be affected by stress. Therefore, the unhealthy spectra remain unmatched as they were not recorded. It is unlikely for ASD spectral samples to cover all variations of vegetative states. It is also impossible to know *a priori* where to collect these samples. A number of sites may also be inaccessible due to a number of reasons (e.g. physical or legal), thereby restricting the number of ASD spectral samples that may be recorded. Expert local knowledge helps in these situations to target important field collection sites. Further complications arise when the spectral variability is larger within a particular species than between different species (Price, 1994).

The port of Port Hedland exports some 98.3% of iron-ore by tonnage (Pilbara Ports Authority, 2019). The highly dusty environment leads to vegetation being covered in a layer of iron-oxide dust, thereby changing the spectral nature of the vegetative leaves as iron dust spectral signatures are mixed with pure vegetative spectral signatures. It is thought that the mangrove *Avicennia marina* is particularly sensitive to iron dust effects as dust is trapped (and retained) in the hairy leaf structure. The proximity to dust sources by mangroves is expected to cause an increase in leaf temperature, further causing an increase in the rate of both photosynthesis and transpiration. It is probable that these effects lead to water stress (E. Paling, Humphries, McCardle, & Thomson, 2001).

In practice, spectral signatures may contain spectral mixtures from nearby cover types. This is both true for on-ground measurements and for those recorded by an airborne sensor. However, for an airborne sensor the spatial resolution is an additional factor. As the spatial resolution of the airborne sensor is rather limited,

image pixels contain spectral mixtures of neighbouring spectra. For example, a shrub covering an area of 0.5 m x 0.5 m and surrounded by soil, will result in the pixel spectrum being composed of a proportion of both the soil and the shrub spectra. Large areas (i.e. greater than the spatial resolution) of uniform and dense vegetation will diminish this problem, allowing pixels to contain spectrally 'pure' (i.e. purer) vegetation spectra. It should be noted that even soil spectra are non-uniform and are affected by albedo, soil particle size and water content (Price, 1994), further complicating the spectral mixture.

2.2 Sensors in Remote Sensing

Aerial imagery using photography has been used for several decades (E. P. Green, C. D. Clark, et al., 1998) and was the principal means to conduct remote sensing. Initially, Earth observing satellites carried systems comprising of red (R), green (G), blue (B) (RGB) and near-infrared (NIR) sensors along with an experimental multispectral sensor. However, technical problems with the RGB and NIR sensors facilitated the popularity of data being collected using the experimental multispectral sensor (Campbell & Wynne, 2011, p. 165). This opened up new ways of processing for the production of new products. More recently, the detailed information captured by hyperspectral sensors has taken the quality of products to levels not previously attainable.

The purpose for this Chapter is to provide an overview of both non-hyperspectral sensors (Sections 2.2.1) and hyperspectral sensors (Section 2.2.2). The review is concerned with sensor history, applications and technical information. This background aids in understanding the advantages as well as any limitations of the various sensors.

2.2.1 Non-Hyperspectral Remote Sensing Sensors

Most studies in remote sensing have made use of data collected from either aerial photography or multispectral sensors (Newton et al., 2009). Due to the high costs

associated with satellite systems, aircraft based cameras have been used to map more than 80% of the earth's surface (Sandau (2010), p. 15). Costs for hyperspectral systems may amount to a factor of 10 price difference compared to digital photographic systems (Escobar, Everitt, Noriega, Cavazos, & Davis, 1998), although with improved technologies (e.g. cheaper storage space) this is expected to decrease.

Aerial imagery has been used for several decades which uses a human analyst for photointerpretation. It is a very accurate but labour-intensive process (Hirano et al., 2003), using scene information typically captured with 4 bands; RGB and NIR (near-infrared) (Chandelier & Martinoty, 2009). The NIR band is necessary to monitor vegetation (discussed in detail in Section 2.3.1). Aerial photographic images are commonly colour enhanced prior to photointerpretation (Richards, 2013, p. 81). To improve the quality of remotely sensed images, computer processing removes effects caused by atmospheric haze variations, topology and Bidirectional Reflectance Distribution Function (BRDF) effects between images (Chandelier & Martinoty, 2009). BRDF is discussed in more detail in Section 2.3.3 but it is basically a function which describes the view angle effects of reflected radiation from a surface.

The spatial resolution attainable by aerial photographic imagery is remarkable; down to 2.5 cm, although 10-15 cm suits most demand. A resolution of 90 cm is considered to be coarse (Holmes, 2012).

Compared with aerial surveys, satellites vastly increase the coverage available. The first satellite designed to remotely monitor Earth's natural resources was Landsat 1 (NASA Landsat Science (2019d) and Lillesand (2008, p. 399)). It was launched in 1972 and passed the same point on the Earth every 18 days. The design maintained compatibility with existing aerial photographic methods, as a Return Beam Vidicon (RBV) sensor was utilised (effectively a camera). To replicate the information found on colour infrared film, this system also made use of four bands (RGB and NIR) and recorded scenes at high spatial resolution. In addition, the satellite carried an experimental Multispectral Scanner System (MSS) sensor. This sensor consisted of four spectral bands at equivalent spatial resolution but higher radiometric resolution, which represents the number of brightness values (e.g.

2 values represents just black and white). The MSS sensor was therefore able to record more brightness levels than the RBV sensor and had a spectral resolution of approximately 100 nm (Schowengerdt, 2007, p. 3).

Actual transmission of data back to earth was performed digitally for MSS data, while analogue was used for RBV based images (thereby resulting in more noise) (Cohen & Goward, 2004).

The spectral bands along with their resolutions for both the Landsat 1 and 2 sensors are summarised in Table 1.

Sensor	Spectral range (nm)	Spatial resolution (m)
RBV	475 - 575	80
	580 - 680	80
	690 – 830	80
MSS	500 – 600	79
	600 – 700	79
	700 - 800	79
	800 - 1100	79

Table 1: Sensors as used on Landsat 1 and 2 (Lillesand, 2008, p. 401).

For both the Landsat 1 and 2 (launched in 1975), the MSS sensor proved more reliable and recorded more data than the RBV sensor. Due to the technical difficulties with the RBV sensor, remote sensing scientists concentrated on utilising MSS data (Campbell & Wynne, 2011, p. 165). As a result, the methodology developed now forms part of standard remote sensing imaging practice (Campbell & Wynne, 2011, p. 167).

Further satellites were deployed with the addition of an extra RBV and MSS channel for Landsat 3, while Landsat 4 and 5 both gained a TM sensor (consisting of 7 bands). The TM sensor provided for a maximum spatial resolution of 30 m. With particular emphasis on vegetation, these were designed to provide improved discrimination between vegetation species (Lillesand (2008, p. 411) and Campbell and Wynne (2011, p. 173)).

There is no data available for Landsat 6 as it failed to launch in 1993 (Lillesand (2008), p. 414). Landsat 7 gained the ETM+ sensor, which basically adds an additional band at higher spatial resolution to the previous ETM sensor (NASA Landsat Science, 2019e) and a Scan Line Corrector (SLC) to help compensate for the forward motion of the satellite. More information concerning the difference between ETM and ETM+ may be found at Kramer (2002b), NASA Landsat Science (2019e) and Boccia (2019).

The most recent mission is that of Landsat 8, launched in early 2013 (NASA Landsat Science, 2019b). An improvement over earlier designs is the collection of data by a pushbroom sensor, which has less moving parts and is therefore less likely to break (which it did in Landsat 7). One disadvantage of the pushbroom sensor is increased complexity in calibration (NASA Landsat Science, 2019c). The pushbroom sensor has been designed for the Landsat 9 satellite, due for launch in late 2020 (NASA Landsat Science, 2019a).

While Landsat satellites are US based systems, the Le Système pour l'Observation de la Terre (SPOT) (Earth Observation System) - based satellites are designed in France (Campbell and Wynne (2011) p. 180). SPOT 1 was launched in 1986 while SPOT 7 (2014) is the latest. SPOT 1 -3 contain the same High Resolution Visible (HRV) sensors and are designed to operate in either panchromatic (which covers red, blue and green wavelengths) mode at 10 m spatial resolution, or multispectral mode at 20 m spatial resolution (SPOT Image, 2010). The spectral range (for SPOT 1 – 3) in panchromatic mode (XP mode) is 510 – 730 nm while in multispectral mode (XS mode) the band ranges are 500 – 590 nm, 610 – 680 nm and 780 – 890 nm. A mid-IR range of 1580 – 1750 nm at 20 m spatial resolution was added to SPOT 4 to improve vegetative monitoring (Lillesand, 2008, p. 441). Further improvements were made to SPOT 5, with the addition of two HRG (high resolution geometric) instruments that provided for an increased resolution up to 2.5 m for panchromatic images. Furthermore, a VEGETATION instrument was placed on SPOT 4 & 5 with a 1 km spatial resolution. SPOT 6 & 7 again increases spatial resolution; a resolution of 6 m is achieved using the multispectral bands while 1.5 m is attained for panchromatic images (Airbus Defence & Space, 2015). SPOT 7 is the latest in the series, which was launched in 2014.

High resolution satellite systems achieve even higher spatial resolution. The IKONOS satellite has a spatial resolution of 1 m for the panchromatic sensor and a 4 m resolution for the multispectral (4 band) sensor. The QuickBird has one of the highest spatial resolutions available of all satellites with a 0.61 m panchromatic sensor. The GeoEye-1 performs at 0.41 m (panchromatic) and 1.64 m (multispectral) which is the highest resolution satellite currently available (Lillesand, 2008, p. 459).

It should be noted that not all Landsat and SPOT satellites are still operational (e.g. Landsat 1 – 5 and SPOT 1 – 5 have been decommissioned).

The Sentinel series of satellites began operation with Sentinel-1A in 2014, with the most recent (Sentinel-5P) launched in 2017. Sentinel-2 carries a multispectral sensor consisting of 13 bands with 12 bit radiometric resolution (European Space Agency, 2020).

The radiometric resolutions of various sensors are shown in Table 2.

Sensor	Radiometric resolution (bits)	Reference
Landsat 1 - 3	6 or 7 ^a	http://www.oneonta.edu/faculty/baumanpr/geosat2/RS%20Landsat/RS-Landsat.htm
Landsat 4, 5 & 7 ^b	8	http://www.geoimage.com.au/satellite/landsat7 http://geomatica.como.polimi.it/corsi/remote_sensing/C03Satellites.pdf
Landsat 8	12	http://www.geoimage.com.au/satellite/landsat-8
SPOT 1 - 3	8	Lillesand (2008) p. 436.
SPOT 4 - 5	8 ^c 10 ^d	http://www.geo-airbusds.com/en/192-the-spot-satellites/r329_9_spotsatellitetechnicaldata_en_sept2010.pdf
SPOT 6 & 7	12	http://www.geo-airbusds.com/en/147-spot-6-7-satellite-imagery/r12317_9_spot6-7_technical_sheet.pdf
IKONOS	11	Lillesand (2008) p. 456.
QuickBird	11	Lillesand (2008) p. 456.
GeoEye-1	11	http://www.geoimage.com.au/satellite/geoeeye-1

a = 7 for the first 3 MSS bands but 6 bits for the 4th MSS band; b = Landsat 6 never went operational as it was lost; c = using high resolution instruments; d = for the VEGETATION instrument.

Table 2: Radiometric resolution for various satellite-based sensors.

The higher the radiometric resolution, the greater the possibility to discriminate between small variations in brightness values between neighbouring pixels which may be significant in differentiating between different species of vegetation.

The number of brightness (i.e. intensity) levels (L) may be represented mathematically as:

$$L = 2^k$$

where k is the number of bits (Gonzalez & Woods, 2008, p. 57). A value of 1 bit represents a black and white image (2^1) as there are two brightness levels (black and white). The human eye is able to 'see' about 16 levels, corresponding to 4 bits. This is rather limited compared to the detail recorded in multispectral (and hyperspectral) images – e.g. 12 bits for Landsat 8 gives 4096 discrete intensities (compared to just 16 levels in humans).

Whereas digital aerial photographs are analysed by experienced human analysts (termed a photointerpreter), multispectral data rely on computers with algorithms to process the data instead. Advantages and disadvantages of both processes may be found in Richards (2013) and are listed in Table 3.

Photointerpretation (human analyst)	Quantitative analysis (computer)
On a scale large compared with pixel size	Can work at the individual pixel level
Less accurate area estimates	Accurate area estimates are possible
Limited ability to handle many bands	Full multi band analysis is possible
Can use only a limited number of brightness values in each band (about 16)	Can use the full radiometric resolution available (256, 1024, 4096, etc.)
Shape determination is easy	Shape determination is complex
Spatial information is easy to use in general	Spatial decision making in general is limited

Table 3: Comparison of photointerpretation versus quantitative analysis (taken from Richards (2013) Table 3.1).

While it is true that the spatial resolution of photographic-based images are superior to those produced by satellite-based sensors, the need for such high resolution is dependent upon the application required. Special classification levels have been developed as early as the mid 1970's by the United States Geological Survey (USGS) (J. R. Anderson, Hardy, Roach, & Witmer, 1976). Land use (i.e. how an region of land is used by humans) and land cover (i.e. surface feature present) classification level I forms the broadest category (e.g. urban or built-up land, agricultural land, wetland). Level II breaks down a level I category into more detail; e.g. wetland into either forested wetland or non-forested wetland. Higher levels relate to more specific categorisation and require higher resolution imagery.

The classification scheme as shown in Table 4 suggests that (generally) as the spatial resolution of recorded data increases, the level of classification detail increases.

Land use/Land cover classification level	Representative format for image interpretation
I	<ul style="list-style-type: none"> • Satellite data: low to moderate resolution (e.g. Landsat MSS).
II	<ul style="list-style-type: none"> • Aerial photographs: small scale. • Satellite data: moderate resolution (e.g. Landsat TM).
III	<ul style="list-style-type: none"> • Aerial photographs: medium scale. • Satellite data: moderate to high resolution (e.g. IKONOS).
IV	<ul style="list-style-type: none"> • Aerial photographs: large scale. • Satellite data: high resolution (e.g. QuickBird).

Table 4: Representative image interpretation formats for various Land use/Land cover classification levels. (taken from Lillesand (2008, p. 218)).

High resolution aerial photographs are often used for forest characterisation, including species identification. The increased spatial resolution allows pixels to contain individual tree crowns (Wulder, Hall, Coops, & Franklin, 2004).

However, the number of bands in aerial photographs are rather limited. By using more bands, more information is recorded allowing more detailed products to be derived (further discussed in Section 2.2.2).

Radiometric resolution is also important. If we only record in black and white (i.e. 2 levels meaning 1 bit of storage) then the number of brightness levels between different types of vegetation (for example) is very limited. This complicates the vegetative discrimination process. In fact, it is the brightness that allows for the differentiation between coniferous and deciduous trees (Lillesand, 2008, p. 14).

Clearly, there are advantages in using appropriate combinations of high spatial, radiometric resolution and recording scenes over many wavelengths at low spectral resolution. The word 'appropriate' relates to the application required. For example, the identification of electrical transmission lines would be rather limited (if not impossible) using large spatial resolutions. Similarly, using a high spatial resolution sensor to record spectral data for large homogenous regions of grassland is also inappropriate and requires more computational processing and large storage requirements.

The significance of using appropriate resolutions is not lost by J. Gao (1999) where the accuracy for mapping mangroves increased with spectral rather than spatial resolution (further detail is provided under Section 2.8.1). This does not imply that spatial resolution is insignificant; it is the basic unit upon which classification is performed on remote sensing data (Lechner, Langford, Bekessy, & Jones, 2012) with a higher spatial resolution being required to classifying smaller targets (Piiroinen, Heiskanen, Mõttus, & Pellikka, 2015). Consider the effect of spatial resolution on classification for a 20 m x 20 m pixel. By referring to the left image of Figure 1, the spectral signature of a mixed pixel (one that contains spectral signatures from multiple sources in a pixel) may mask out finer details of interest.

If the scene were homogeneous, then a spatial resolution of 20 m might suffice as the whole pixel is covered with one type of spectrum (the red mangrove - the right image of Figure 1). Nevertheless, this amount of detail is less discernible when spectra are a mixture of other cover types (i.e. red mangrove forest, red mangrove scrub and water). The mixed pixel (left image of Figure 1) is composed of an overall distorted spectrum made up of a mixture of three individual spectra each

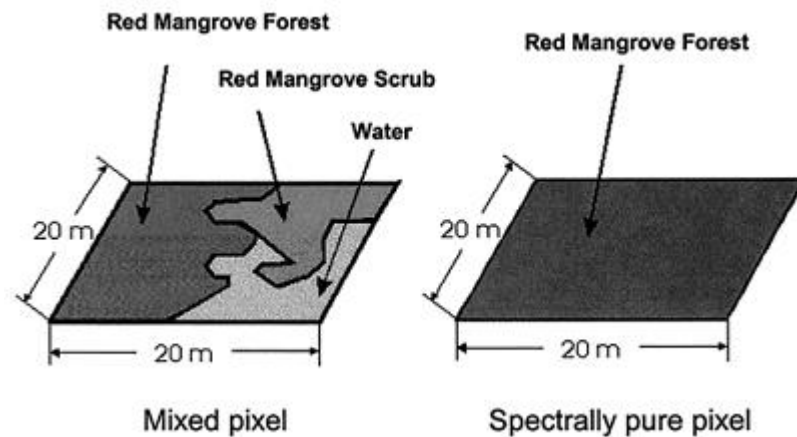


Figure 1: Representation of a mixed (left) versus pure pixel (right) (Hirano et al., 2003).

contributing their own proportions. If the spatial resolution were increased indefinitely, pure spectra would remain within each pixel. In practice, the spatial resolution is limited and mixed pixels always exist. For vegetative mapping, fractions of soil spectra are commonly mixed with vegetative pure spectra. However, for regions containing dense vegetation (i.e. no soil), spectra corresponding to different vegetative species may form a mixture; i.e. mixtures of adjacent species will influence the pixel spectrum sensed.

At Landsat sensor spatial resolutions, the larger pixel sizes lead to pixels having mixtures of soil spectra, combinations of vegetative types (e.g. tree and grass) and even shadows (Wulder et al., 2004). With increased spatial resolutions, features become more separable thereby improving classification at pixel level (Wulder et al., 2004).

It is appropriate at this point to introduce a formal definition of a feature. One such definition is given by Dougherty (2012, p. 11) as:

“features are characteristic properties of objects whose value should be similar for objects in a particular class, and different from the values for objects in another class (or from the background)”.

The aim of classification is to categorise features together into classes representative of particular land use and land-cover types (J. B. Anderson (1971) as detailed in Section 2.6 below).

2.2.2 Hyperspectral Remote Sensing Sensors

A key difference between hyperspectral and non-hyperspectral sensors lies in the number of bands by which scenes are recorded. Multispectral sensors generally utilise more bands ($\approx 3 - 10$) than photographic images (typically 3). On the other hand, hyperspectral sensors contain 100's of bands. Sensors in excess of 100 bands are considered hyperspectral (Wong & Fung, 2014).

The spectral resolution for hyperspectral sensors are also far superior to multispectral sensors. Whereas the bands of multispectral sensors are defined in ranges (e.g. Landsat TM mapper band 1 ranges from 0.45 – 0.52 μm), hyperspectral bands are much more highly resolved; for example, the Airborne Visible/Infrared Imaging Spectrometer (AVIRIS) bands have a bandwidth of only about 0.01 μm (FWHM) (Kramer, 2002a). As a result, bands are very narrow and form a contiguous range. The narrow bandwidth of hyperspectral sensors allow much more detailed reflectance spectra to be recorded, with more subtle variations compared to the coarser bandwidths found in multispectral sensors (R. Jensen et al., 2007).

The effect is highlighted at the top of Figure 2, showing the 224 AVIRIS contiguous bands. In comparison, the 6 multispectral bands of Landsat 6 span wide ranges of wavelengths (illustrated at the bottom of Figure 2).

Whereas the wavelengths for pixel spectra from a hyperspectral sensor are contiguous, those for a multispectral sensor contain discrete bands thus forming a histogram. For the first time in remote sensing, spectra recorded of objects approach those attainable under laboratory conditions using imaging spectroscopy. Due to this link, hyperspectral imaging is also called imaging spectroscopy. As a result, hyperspectral libraries now contain object spectra allowing spectral comparisons with field-measured spectra for identification. Object samples may be brought into the laboratory and spectroscopically analysed. Outside a laboratory based environment, an ASD field spectrometer (see Section 4.3.1) is often used to record sample spectra for particular land-cover types. The basic approach is clear;

matching ground spectra with airborne collected spectra for cover type identification.

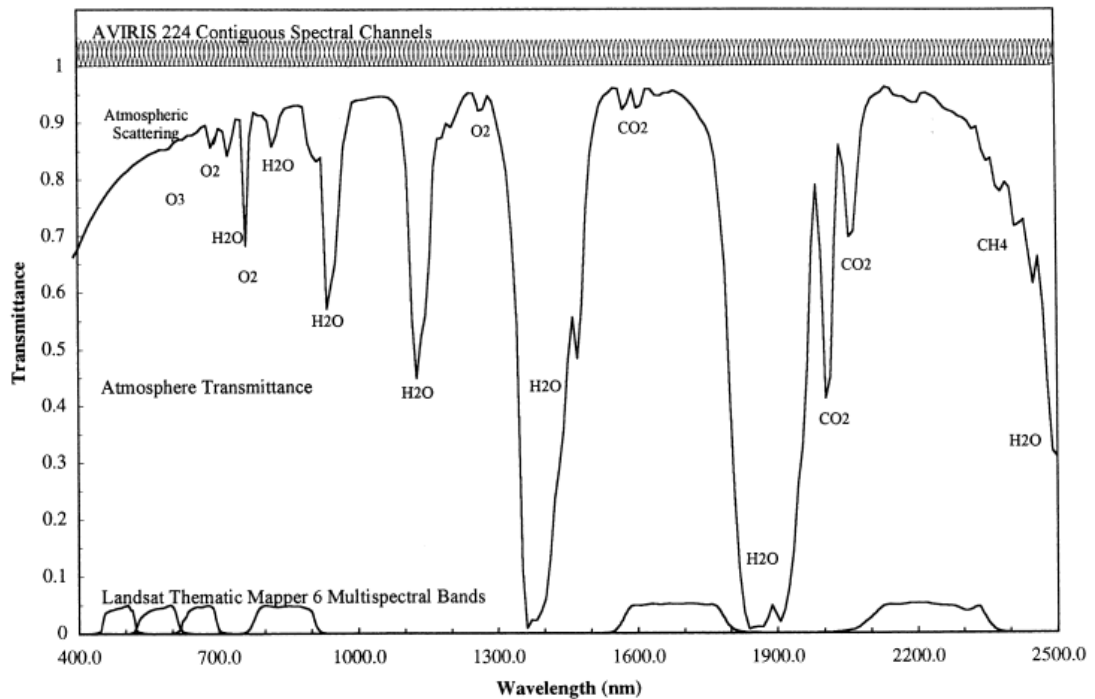


Figure 2: Contrast between Landsat bands and AVIRIS contiguous bands (R. O. Green et al., 1998).

It is important to realise that Figure 2 also illustrates the effects of atmospheric scattering on solar irradiance (i.e. solar radiation transmitted to the earth). Further details concerning atmospheric effects on spectra is considered in Section 2.3.

Currently, there are two satellites carrying a hyperspectral sensor; the EO-1 (carrying the Hyperion sensor (Goetz, 2009)) and the PRISM (ESA, 2019). When comparing Hyperion (hyperspectral) data to Landsat TM (a multispectral sensor), the storage space requirements increases by a factor of about 73, amounting to many gigabytes of data (P. S. Thenkabail, Enclona, Ashton, & Van Der Meer, 2004). However, comparison to earlier remote sensing instruments (e.g. LANDSAT) - having spectral band widths of about $0.27 \mu\text{m}$ -(Lillesand, 2008, p. 381) hyperspectral sensors offer a (nearly) continuous spectrum with spectral resolution in the order of $0.01 \mu\text{m}$. The higher spectral resolution allows much more detailed (spectral) information to be recorded concerning targets, which impacts thematic classification accuracy.

It is understandable why satellite sensors have limited bands and spatial resolution; due to limited storage capabilities. This data must also be sent to Earth under a limited transfer rate for timely signal transmission. For an airborne-based survey, the storage data is immediate and available to the analyst as it is stored locally.

The first airborne (i.e. not spaceborne) hyperspectral sensor in operation was the AVIRIS (Airborne Visible/Infrared Imaging Spectrometer) which took its first spectral images in 1987. It covers a contiguous range from 400 – 2500 nm consisting of 224 bands at 10 nm spectral resolution and 20 m spatial resolution (R. O. Green et al., 1998). Compared to Landsat, the increase in the number of spectral bands allows for much higher quality spectra (see Figure 2).

Many studies (e.g. E. P. Green, C. D. Clark, et al. (1998), Held et al. (2003)) use the Compact Airborne Spectrographic Imager (CASI) spectrometer. It is commonly carried aboard a light aeroplane and consists of a maximum of 288 bands with a bandwidth (FWHM) of 2.9 nm covering a spectral range of 385-905 nm (Treitz & Howarth, 1999). The radiometric resolution of CASI is 12 bits (CASI, n.d.) and has a spatial resolution of 1 m (Clark, Ripley, Green, Edwards, & Mumby, 1997) (although this depends on the height and speed of the platform (CASI, n.d.)).

Airborne remote sensing (i.e. using an aeroplane) offers advantages over satellite remote sensing, including:

- Lower geometric distortion
- Instant coverage when needed
- Choice of sensor suitable for the task and budget
- Sensor calibration prior to flight
- Smaller spatial resolution

In practice complications arise when analysing hyperspectral data; it has been found to be highly sensitive to atmospheric effects (R. Jensen et al. (2007) and Section 2.4.2). Not only do spectra exhibit natural variations (Section 2.3.2) but to correlate them against a hyperspectral library, airborne spectra require atmospheric correction (Section 2.4.2).

Apart from spectral considerations, the very nature of using such a high number of bands leads to problems which are mathematically integral to high dimensional

space. This is referred to as a high-dimensional problem and occurs when the number of features is over 100 (Wong & Fung, 2014). The theory is explored in Section 2.5.1 leading to practical consequences discussed in Section 2.5.2 and current solutions in Sections 2.5.3 and 2.5.4.

The primary interest in this thesis lays in the production of a vegetative thematic map, in particular the distribution of mangroves across the Port Hedland coastal region. The highly detailed spectra, as recorded by a hyperspectral sensor, offers the best opportunity to produce such a detailed thematic map.

2.3 Spectral Characteristics of Vegetation

The rather unique properties of vegetative spectra are outlined in Section 2.3.1 and supported by spectral examples. The actual shape of vegetative spectra is influenced by factors directly affecting the immediate vegetative environment (e.g. amount of water or soil nutrients) and forms the discussion in Section 2.3.2. Interactions caused by atmospheric radiative transfer processes also have a significant impact on the spectral shape. These atmospheric effects are explained in Section 2.3.3.

2.3.1 Spectral Properties of Vegetation

A unique characteristic of vegetative spectra allow it to be distinguished from non-vegetative spectra. An example of a vegetative spectrum is presented in Figure 3. The horizontal scale denotes the wavelength (in nm) while the vertical axis is the reflectance. A high reflectance indicates a high reflection of light (at a particular wavelength) and is perceived as 'bright', while a low reflectance is 'dull'.

In approximate terms, the human eye perceives the 400 - 500 nm wavelengths as blue, 500 - 600 nm as green and 600 – 700 nm as red (Campbell and Wynne (2011), p. 35). With reference to Figure 3, the leaves for this species of mangrove (*Bruguiera exaristata*) relatively reflect highly at ≈ 550 nm in the wavelength region perceived by the eye. This bright reflection corresponds to the green region, low

reflectances are observed over both the blue and red regions of the spectrum; hence the leaves appear green to our eyes. The sharp increase in reflectance near

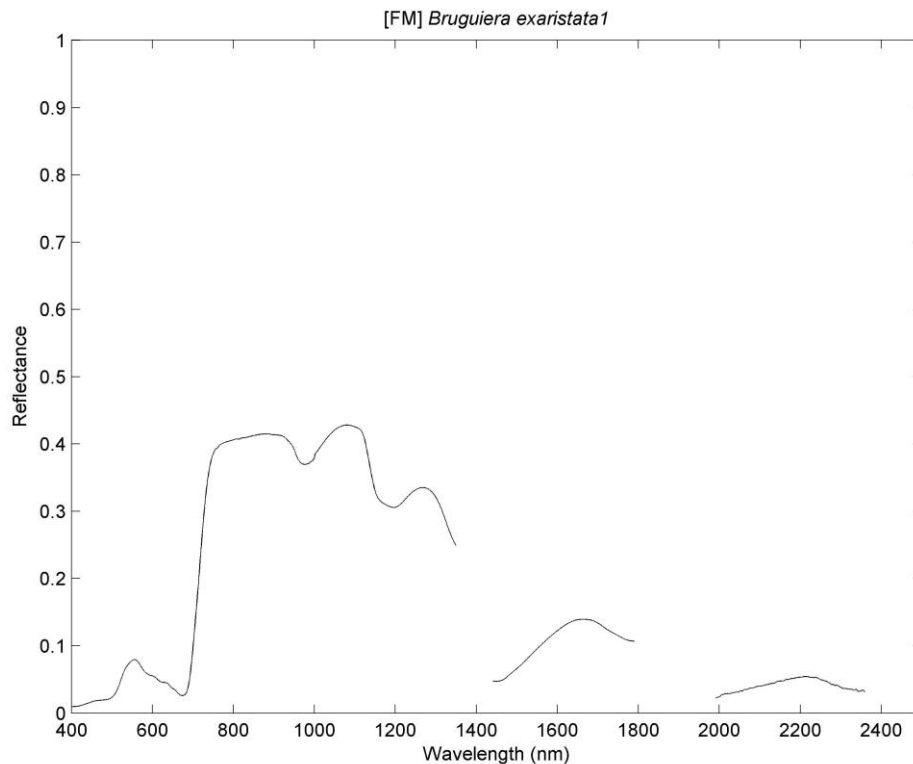


Figure 3: An example of an ASD¹ recorded spectrum for *Bruguiera exaristata*. A value of 1 represents total reflection, whereas 0 represents no reflection. The [FM] code identifies the site of the spectral sample, while a numbered suffix attached to a species name (e.g. *Bruguiera exaristata1*) identifies the spectral sample that was recorded (the nomenclature is explained in detail in Section 4.3.3).

700 nm is known as the red-edge, and is not perceived by human vision. If we could perceive wavelengths at the red-edge, then vegetation would appear exceptionally bright red compared to the (relatively) dull green colour we do perceive (further spectral features are withheld until Section 4.3.1).

The key spectral differences between vegetative and non-vegetative spectra are illustrated by example for three different cover types (see Figure 4). The vertical axis represents the reflectance (effectively brightness), while the horizontal axis represents the wavelength (in μm).

¹ While the ASD field spectrometer is discussed in detail in Section 4.3.1, it is a hand-held sensor that allows the recording of ground spectra from 350 to 2400 nm.

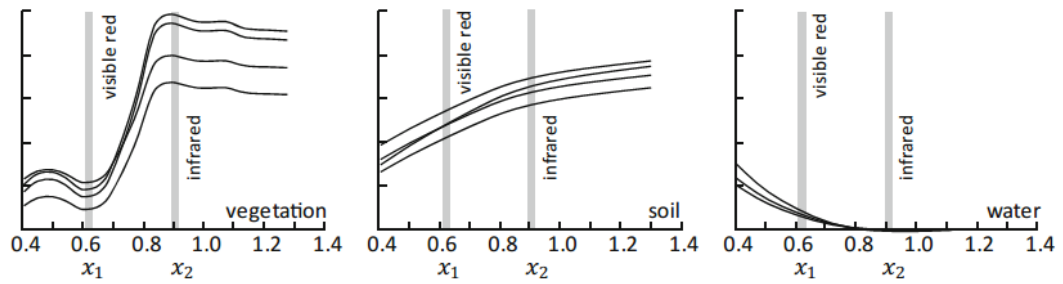


Figure 4: Spectral examples for 3 different types of cover: vegetation, soil and water (left to right) (Richards, 2013, p. 89).

Vegetation-based spectra have a characteristic sharp gradient located at approximately $0.7 \mu\text{m}$. This characteristic is unique to vegetation (Horler, Dockray, & Barber, 1983). The steep positive gradient is due to the sharp increase in reflectance at around $690 - 750 \text{ nm}$ (Zarco-Tejada, Miller, Noland, Mohammed, & Sampson, 2001). This special property in the spectrum is known as the red-edge and distinguishes vegetative spectra from non-vegetative spectra. In an image, as each pixel contains one spectrum, it is therefore possible to identify pixels containing vegetation.

The length (or size) of the red-edge is related to confidence in having vegetative spectra, and discussed more fully in Section 4.5.1.

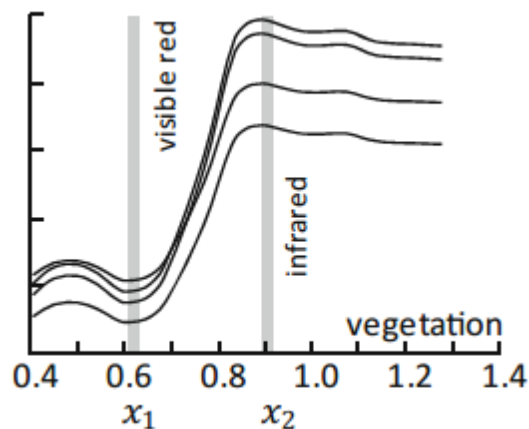


Figure 5: The high slope in the $690 - 750 \text{ nm}$ range is called the red-edge. It is a characteristic of vegetative spectra (Richards, 2013, p. 89).

The red-edge terminology is appropriate as the reflectances in the red wavelength region are low (i.e. at the edge of the red end of the visible spectrum, around 650 nm) but is very high at the NIR (roughly 800 nm) region.

The red-edge positive slope arises from the biochemistry of the leaves themselves. The internal structure of leaves strongly reflect in the NIR region of the spectrum (Silleos, Alexandridis, Gitas, & Perakis, 2006), while the upper surface of (healthy) leaves strongly absorb red light (Gilabert, González-Piqueras, García-Haro, & Meliá, 2002). These characteristics allow vegetation to be spectrally detected; vegetative based indices (discussed in detail in Section 2.6.2) are defined in terms of NIR (high reflectance) and (red) R (low reflectance) wavelengths. The low reflection in the visible part of the spectrum is due to absorption by the leaf chemistry (in particular, chlorophyll).

The red-edge property of vegetation has influenced satellite sensor design. For example, even the early Landsat 1 covers the R and NIR wavelengths (Table 1, p. 15 of Section 2.2.1).

2.3.2 Factors Influencing Vegetation Spectra

The shape of a vegetative spectrum is influenced by numerous factors. Those related directly to the vegetation itself include the type of vegetation, canopy density, leaf orientation, health, water content, phenology (seasonal influence on vegetation) and senescence (aging in vegetation). Non-direct vegetative influences include effects due to atmospheric scattering (discussed in Section 2.3.3). Even soil influences the spectrum, which are due to; type, particle size, density, nutrient content and water content (Ben-Dor, 2002).

Spectra of vegetation situated in shadows may appear bluer and darker than under full illumination conditions different, causing misclassification (Lillesand, 2008, p. 23).

A vegetative spectral shape is also influenced by the number of leaf layers (Horler et al., 1983), as illustrated in Figure 6; as the number of leaf layers (or leaf area index (Sandmeier, Müller, Hosgood, & Andreoli, 1998)) of cotton increases, so

too does the reflectance. The Leaf Area Index (LAI) may be defined as “the one-sided leaf area per unit projected ground area” (Jones, 2010, p. 175).

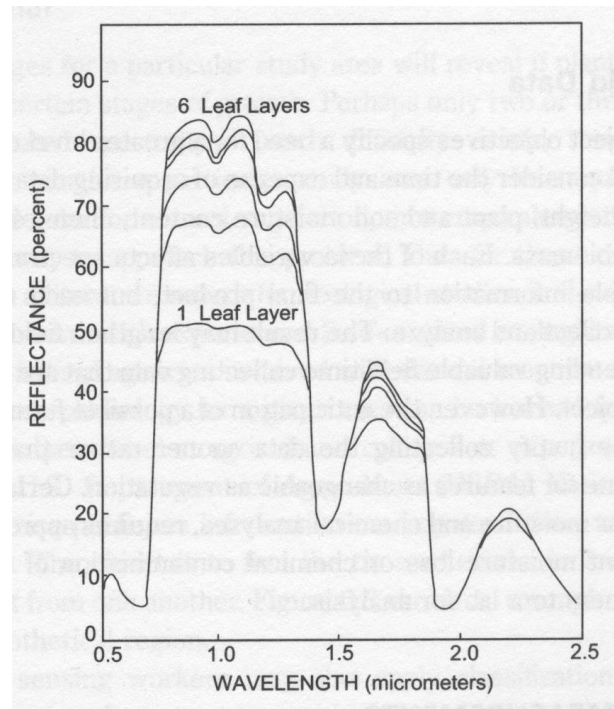


Figure 6: The reflectance increases for additional cotton leaf layers (Myers, 1970). (figure taken from McCoy (2005, p. 77)).

Figure 6 shows that the addition of subsequent layers of leaves adds a diminishing effect to the reflectance. For example, after four layers, the effects of adding another one or two layers has a relatively small effect to the reflectance when compared to adding a single leaf layer to the very first one. This observation also applies to other plants, such as barley leaves (Horler et al., 1983).

The maximum NIR reflectance occurs when the number of leaf layers are approximately eight (Bauer, Craig S. T. Daughtry, Larry L. Biehl, Edward T. Kanemasu, & Hall, 1986). An explanation is offered by considering that the sensor for one leaf layer records a limited reflectance of the cotton plant itself; the signal being reflected by adjacent soil (depending on the constituents of the immediate surroundings of the plant). As the number of leaves increase, the density of the leaves increases and reflects more signal, hence a higher reflectance is measured.

Interestingly, the effect of adding additional leaf layers does not increase the reflectance proportionally across all wavelengths. For instance, at the 500 nm

wavelength, there appears little affect caused by the additional leaf layers, while large differences are apparent at the 1000 nm wavelength; the reflectance in the NIR region appears considerably enhanced. This was also found to be the case when multiple leaf layers of eucalypt leaves were examined (L. Kumar, Skidmore, & Mutanga, 2010).

In practice, vegetation consists not of single stacked leaves but of canopy structures. Inside a canopy, multiple scattering fill in shadows resulting in a decrease in contrast inside the canopy (Sandmeier et al., 1998). The non-Lambertian nature of vegetation results in a decrease in apparent reflectance with increasing solar zenith (a Lambertian surface is one where the reflected brightness is constant, independent of viewing angle). This decrease in reflectance is due to increasing shadowing (Roberts, Green, & Adams, 1997). Furthermore, the green and NIR wavelengths are reflected and thereby undergo multiple scattering. The reflectance anisotropy (i.e. scattering directional dependence) is small. In contrast, the blue and red wavelengths are absorbed resulting in high anisotropy (Sandmeier et al., 1998). As a result of multiple scattering of NIR in canopies, the NIR to red contrast of canopy spectra is greater than for leaf spectra (Roberts et al., 1997). For sparse vegetation, the effects of multiple scattering is negligible in vegetation (Hu, Lucht, Li, & H. Strahler, 1997).

For dense erectophile canopies (where leaves are vertically orientated), the lowest reflectance values would be expected to occur at nadir position. In practice, it is observed to be slightly in the forward scatter direction (Sandmeier et al., 1998) and is due to the sensor being orientated slightly forward toward the illumination direction, thereby viewing shadowed leaf surfaces. Planophile canopies (leaves horizontally orientated) are expected to scatter more strongly in the forward direction than erectophile canopies with a more isotropic (i.e. scatters equally in all directions) distribution (Sandmeier et al., 1998). Geographically, erect leaves occur more frequently around the equatorial regions, while horizontal leaves occur more frequently towards the poles (Jones, 2010, p. 55).

For many species, the orientation of the leaves may follow the sun's movement (heliotropic movement). For well-watered plants, the leaf blade is perpendicular to the sun (diaheliotropic movement) while for water stressed leaves the blade's

orientation is parallel (paraheliotropic) (Jones, 2010, p. 57). Therefore, the reflectance is influenced by the time of day (i.e. sun's zenith angle).

Scattering not only occurs within a canopy but also by the immediate surroundings – e.g. soil. To complicate any analysis in vegetative – soil scattering effects, soil spectra itself is affected by soil slope, particle size, viewing geometry (Ben-Dor, 2002) as well as topography (Asner & Martin, 2009). In one study, rough soil (created by ploughing) caused more scattering in the antisolar direction (backscatter toward the sun) than the smoother surface (Irons, Campbell, Norman, Graham, & Kovalick, 1992). However, the directional anisotropy was unaffected by soil roughness and bare soil gave maximum reflectance in the direction of the sun (Irons et al., 1992), which highlights the non-Lambertian character of soil scattering. Furthermore, for sparse homogeneous canopies, the soil's anisotropic backscattering (antisolar direction) heavily influences the reflectance in the visible bands (Kimes, 1983). Some of the reflected radiation is actually due to fluorescence, although only 1 – 5% of NIR reaches the remote sensor. Researchers have found vegetative stress detection to be one application of fluorescent radiation (Meroni et al., 2009).

It is useful to define the Red-Edge Inflection Point (REIP) for the work that follows, as it defines the position of the red-edge and is used as an indicator of stress and senescence in vegetation. There are two main approaches in determining this REIP. The first is based on curve fitting. There are various types of curve fitting techniques, with each approaching the problem differently. The second approach is based on the derivative. Again, there are different approaches exploited in finding the REIP. Further details are described in L. Li et al. (2005), with the particular mechanics beyond the scope of this thesis. However, all methods aim to determine the wavelength of the REIP.

The effect on spectral reflectances caused by nutrient deficiencies on wheat leaves is documented by Ayala-Silva and Beyl (2005). Both nitrogen (N) and magnesium (Mg) are essential nutrients in the formation of chlorophyll - a green pigment which allows photosynthesis to occur. Deficiencies in either N or Mg results in severe chlorosis (yellowing of leaves). Figure 7 shows two reflectance spectra for wheat, under both control and nitrogen-deficient conditions.

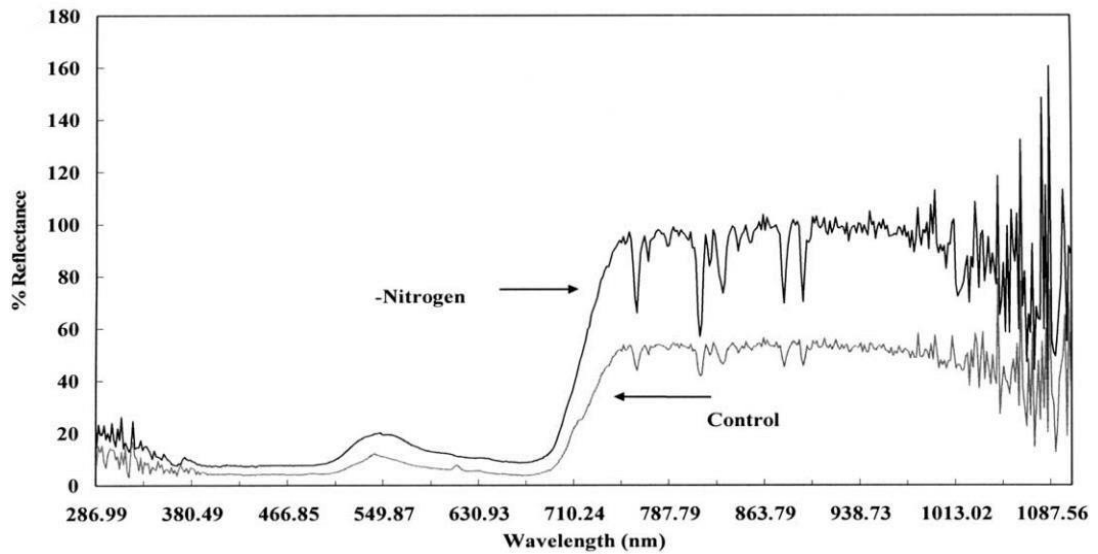


Figure 7: The reflectance of wheat (in %) under control and nitrogen-deficient conditions (Ayala-Silva & Beyl, 2005).

The reflectance for nitrogen-deficient wheat shows an increase in reflectance over both the visible and NIR spectral regions. Similar results were obtained for the other nutrient deficient samples tested (magnesium, phosphorus, potassium and calcium). The change is due to a decrease in photosynthetic pigments (chlorosis), resulting in an increased reflectance in the visible region (as less light is absorbed) (L. Li et al., 2005) and the NIR region (Ustin et al., 2004). Significantly, the REIP moved toward the shorter wavelengths (713 nm for the control and 708 nm for the N deficient specimen). The red-edge slopes for both the N and Mg deficient samples were the steepest slopes compared to the other nutrient samples tested. However, all nutrient-deficient spectra exhibited a red-edge shift toward shorter wavelengths (termed a blue-shift) (Ustin et al., 2004). Biologically, all nutrient deficient wheat samples were significantly reduced compared to the control samples, particularly for those deficient in N (Ayala-Silva & Beyl, 2005).

A red-shift also occurs for vegetation affected by an oil spill, where the REIP shifted from 703.08 nm (for the unaffected vegetation) to 721.05 nm (for those affected by oil) (L. Li et al., 2005). However, not all red-edge shifts are red. An example for metal induced stress on vegetation (e.g. by toxic metals in soil) resulting in a blue-shift is shown by Chang and Collins (1983). Figure 8 shows a blue-shift in the red-edge position for sorghum under the influence of CuSO_4 .

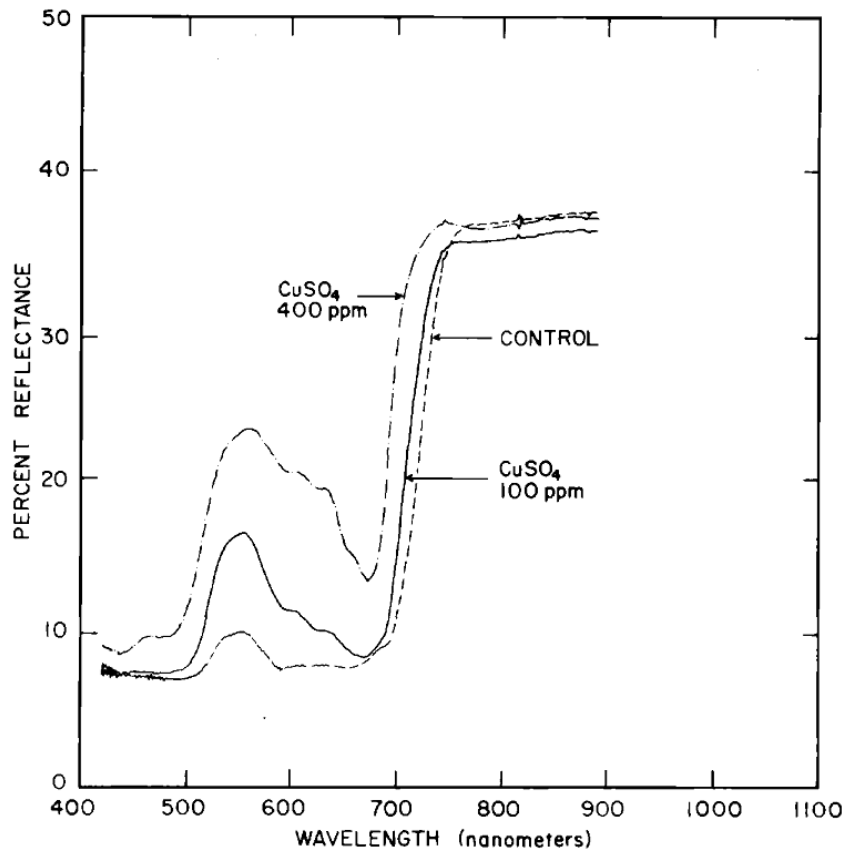


Figure 8: Metal-induced stress on sorghum causing a blue-shift (Chang & Collins, 1983).

Chang and Collins (1983) point out that a similar blue-shift occurs for excessive amounts of copper, zinc and nickel.

The reflectance of a particular type of vegetation is also affected by senescence. An example is given in Figure 9 and Figure 10 for both wheat leaf and wheat canopy, respectively (Xiaoping, Ni, Jing, Jie, & Jingsong, 2008). Both figures show different reflectances according to the senescence stage of the plant.

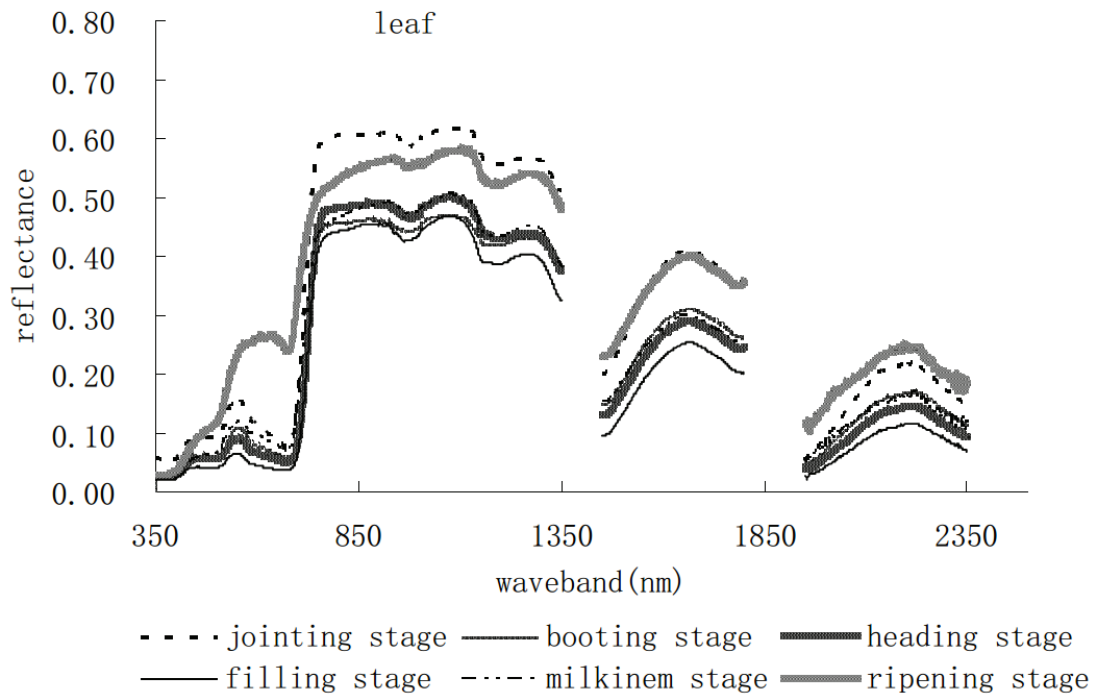


Figure 9: Spectral reflectance differences in wheat leaves during senescence (Xiaoping et al., 2008).

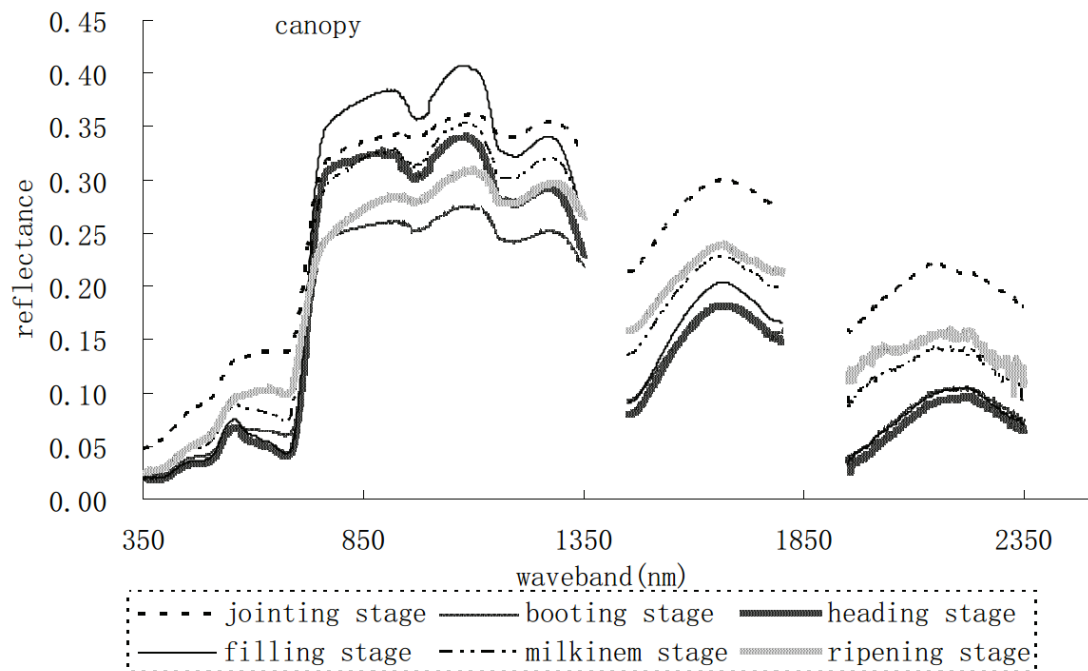


Figure 10: Effect of wheat senescence on canopy spectral reflectance (Xiaoping et al., 2008). (Details about wheat growth stages are readily on the internet. Basically the sequence is: tillering, jointing, boot, heading, flowering, milk, dough).

From the joining stage to the heading stage, there is a red-shift in reflectance, while from the heading stage to the ripening stage there is a blue-shift. In addition to wheat, Collins (1978) also observed a red-shift for sorghum throughout the growing season, until the onset of senescence where the red-edge undergoes a blue-shift.

The influence of leaf age on the red-edge reflectance of maize is shown in Figure 11 (using the first derivative) (Moses Azong Cho & Skidmore, 2006).

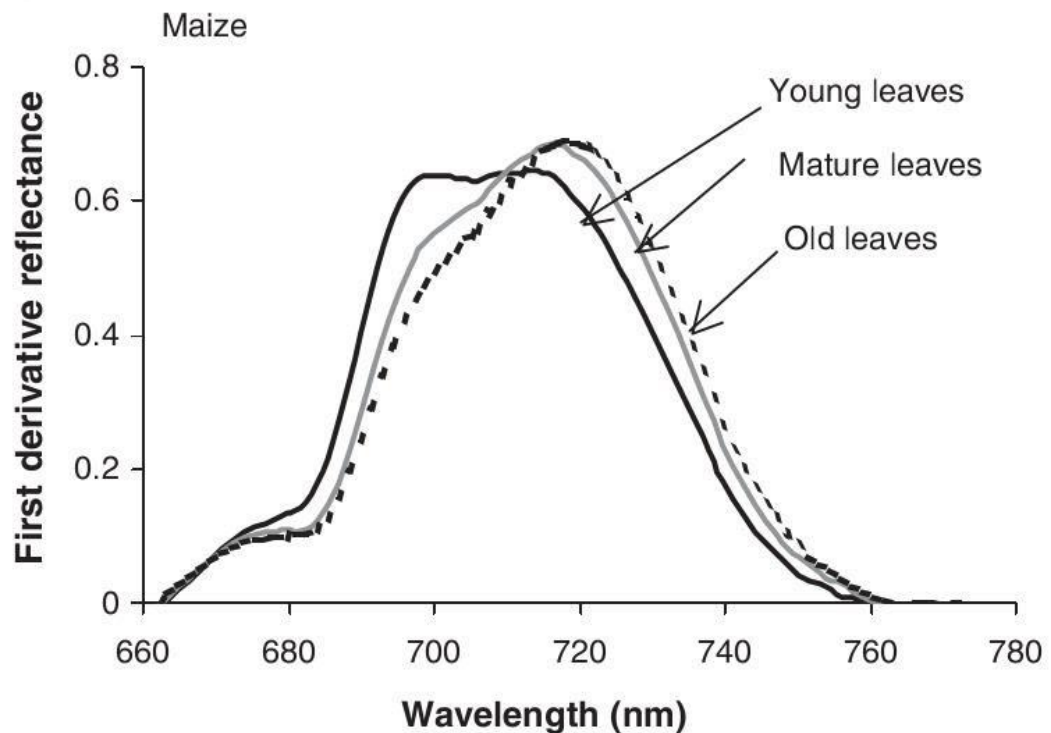


Figure 11: This illustration shows the variation in the red-edge inflexion point for maize leaves of various ages (Moses Azong Cho & Skidmore, 2006).

The figure shows that as the leaf ages, the REIP moves toward longer wavelengths – a red-shift.

Phenological changes in vegetation are particularly powerful as a means of discriminating between crop or even natural vegetation and allows a vegetation index to be used to separate broad vegetative types (Jones, 2010, p. 284), as the NDVI differs according to season and vegetative type.

The amount of water present in an actual leaf also affects the reflectance spectrum and is commonly quantified using the Relative Water Content (RWC). Mathematically, this is defined according to the sample weight (W) of each leaf.

$$RWC = \frac{W_{\text{fresh}} - W_{\text{dried}}}{W_{\text{saturated}} - W_{\text{dried}}}$$

The weight of a fresh leaf (W_{fresh}) represents that of the sample being investigated. The saturated weight ($W_{\text{saturated}}$) of a leaf is that obtained by leaving it in water for 24 hours. The dried weight (W_{dried}) is prepared by drying the leaf for 24 hours at 80°C in an oven. A small RWC value represents a dry leaf as the numerator approaches zero. Using similar reasoning, for a wet sample, the RWC would approach 1. The effect of RWC on reflectance is shown in Figure 12 for a mature peace lily (*Spathiphyllum lynnise*).

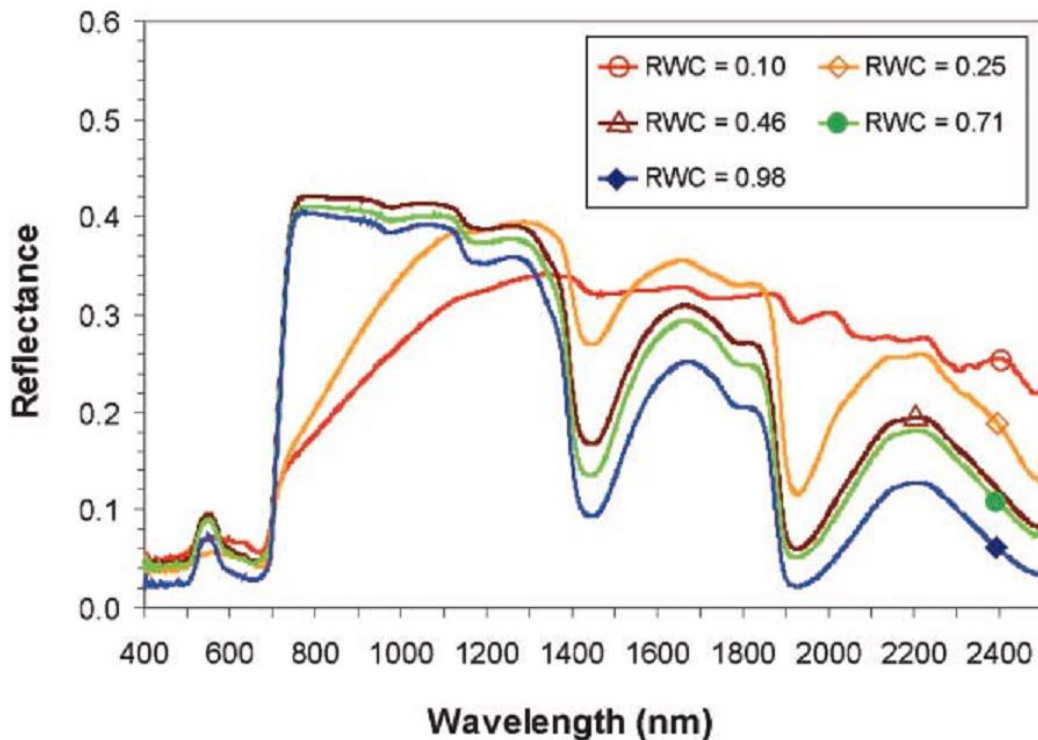


Figure 12: Variation in reflectance spectra for a mature peace lily in varying degrees of leaf dehydration (Seelig et al., 2008).

Water absorbs light and hence the higher the water content, the lower the reflectance (and the higher the RWC). When the RWC drops too low, the leaf chemistry changes, causing subsequent changes in the spectrum.

It is important to realise that when using remotely sensed hyperspectral data to assess whether or not vegetation is under stress, a stress-free spectral sample is required along with a stressed spectral sample (to compare it against). An expert in plant physiology directs an ASD field specialist to collect the necessary data. Only then can comparisons be made and a red-edge shift be determined. If the reference spectrum is obtained from the field, then specialised equipment must be manned by experts to conduct the measurements to ensure the vegetative sample (e.g. a particular species of mangrove) grows in a stress-free environment. Therefore, appropriately selected reference spectra are required relevant to the desired application. For example, if the desire is to determine a young mangrove against an old mangrove, then suitable samples are required of each type of mangrove. Both old and young mangroves would (ideally) have (for example) similar soil nutrients (and quantities), to eliminate nutrient effects on the red-edge position. By eliminating all other factors (apart from senescence), a change in red-edge position can be used to detect changes due to senescence.

The extent to which vegetative spectra are distinguishable from each other is considered by Asner and Martin (2009). For trees in the Hawaiian rainforest, it was found that the chemistry of several canopies were similar in leaf nitrogen (N) and phosphorus (P) concentrations. However, differences were apparent by the inclusion of additional constituents, such as; water, chlorophyll-a content, chlorophyll-b content, carotenoid pigments, specific leaf area. As a result, spectral signatures were often unique for the three dozen-odd canopy rainforest species studied in Hawaii. This shows the importance of obtaining spectra at high spectral resolution, thereby allowing for finer targeting of the biochemical parameters in vegetation (Ustin et al., 2004), leading to better determination of chemical content of vegetation.

The effect of N concentrations on two species of mangrove has also been studied by C. Zhang, Kovacs, Wachowiak, and Flores-Verdugo (2013). These mangroves were *Avicennia germinans* and *Rhizophora mangle*. Leaves were collected from both species and stored in plastic bags, before an ASD FieldSpec 3 JR spectroradiometer measured their reflectances under laboratory conditions. The mangroves are physically located in an area directly south of Mazatlán in Mexico.

The results shows significant leaf size differences exist between the two different mangrove species and their conditions. The leaf area for *Rhizophora mangle* were double in size (35.17 cm²) compared to *Avicennia germinans* (16.93 cm²). Healthy leaves were generally larger, compared to those in poor condition; approximately double for both species. Nitrogen concentration for *Avicennia germinans* were also significantly higher than that for *Rhizophora mangle*. Therefore, the leaf area sizes of different species of mangroves may vary significantly, as do their N concentrations. Furthermore, healthy mangroves exhibit a higher reflectance in the NIR and a lower reflectance in the visible. This applied to both mangroves. These observations explain the yellowish leaf colour in unhealthy mangroves, as the reflectance is higher in the visible region of the spectrum.

The increase in higher resolution data recorded by narrowband sensors compared to broadband sensing, does not necessarily guarantee that vegetative species are distinguishable. As early as 1994, Price (1994) made a number of conclusions based on agricultural crop studies:

- several samples of a particular species show significant variability (refer to Figure 13);
- spectra from multiple species may be too similar to distinguishable (see Figure 14);
- the mixture of spectra from several species corresponds closely to the spectrum of a single species.

Figure 13 shows major differences in spectra for the same species, while Figure 14 shows a higher degree of similarity between spectra of three different species. Therefore, the spectral variation within a (single) species may exceed the variation between species. This has significant ramifications, potentially causing false classification for species. Several reasons are apparent for discriminating between spectra. Canopies containing highly random needle orientation scatter radiation in random directions (Price, 1994). Other variables include; dust, humidity, contributions from branches, bark, soil, the age of the leaf (Ghiyamat & Shafri, 2010) and even leaf hairs (Jones, 2010).

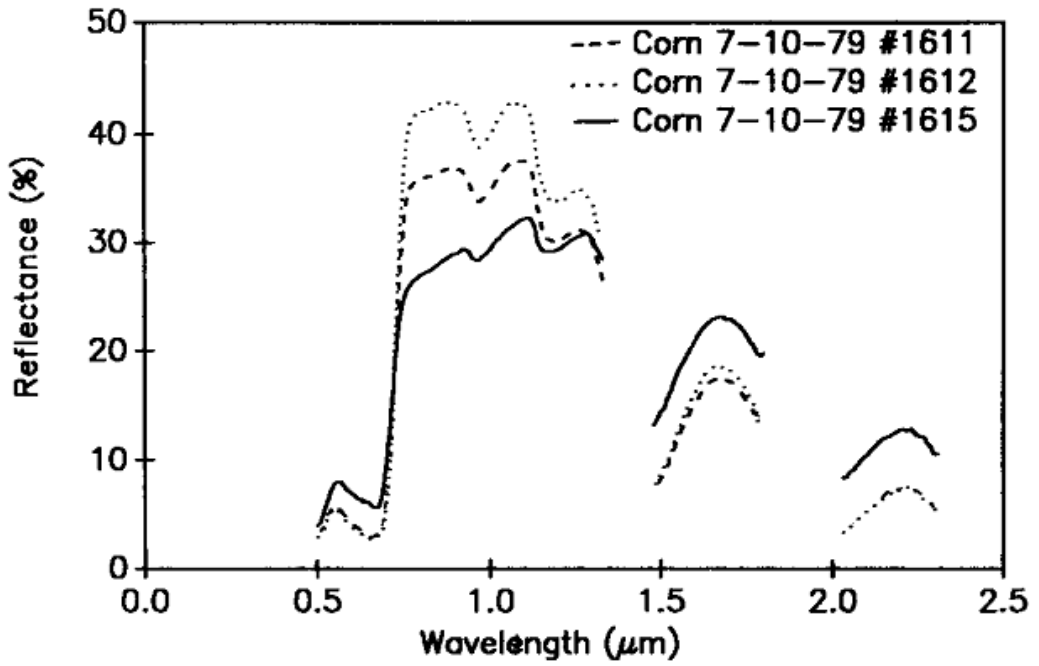


Figure 13: This illustration shows that spectra for the same species exhibits significant differences (Price, 1994).

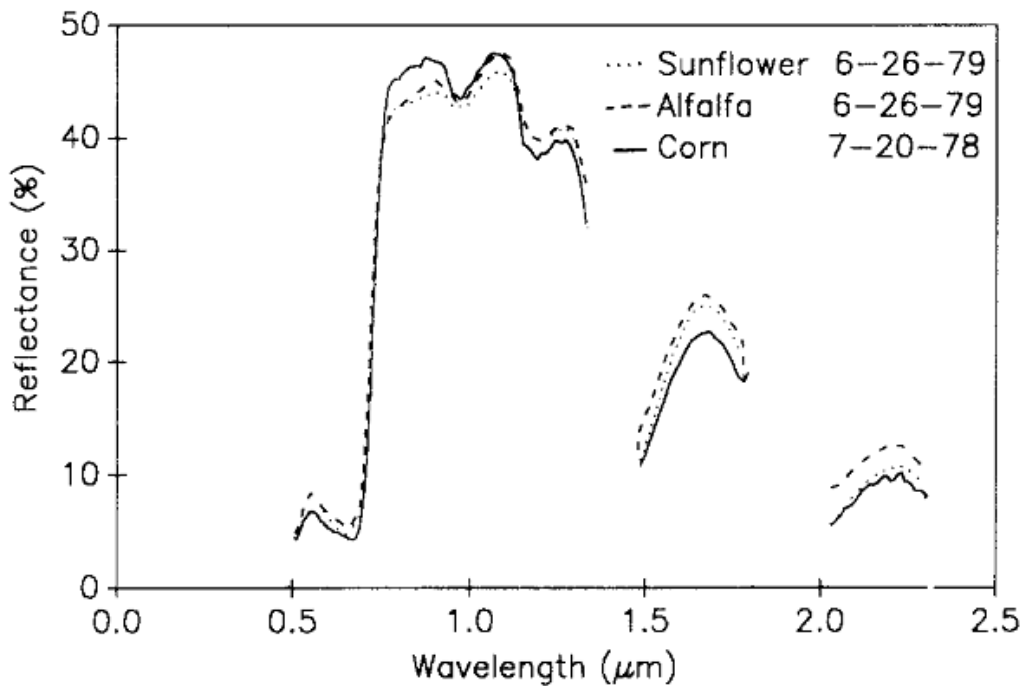


Figure 14: This illustration shows similar spectra for three different species (Price, 1994).

In fact, even in 'simple' vegetative mapping, a number of these factors have been known for some time, leading to the development of various types of VI's. The most popular VI is the NDVI - discussed in Section 2.6.2.1. Other VI's also exist, mainly to

overcome shortcomings with the behaviour of the NDVI - e.g. the Soil Adjusted Vegetation Index (SAVI) (Huete, 1988). The SAVI is discussed in more detail in Appendix A.2.

Ultimately, the goal of this research lies in classifying mangroves, mangrove-specific vegetation indices have been specifically designed to distinguish between the wetland mangrove forests, terrestrial forests and other land cover. The NDVI is unable to distinguish between mangrove and terrestrial vegetation (Winarso, 2014).

Anatomically, the structure of mangrove leaves is uniquely defined by their achlorophyllous water storage tissue (Das, 1996). This has the effect of increasing both leaf and canopy moisture content, compared to terrestrial vegetation (Tomlinson, 2016). Therefore, researches have exploited this unique property to develop new mangrove-specific vegetation indices.

Spectrally, Figure 15 illustrates the differences between mangroves and non-mangroves in a spectral sense.

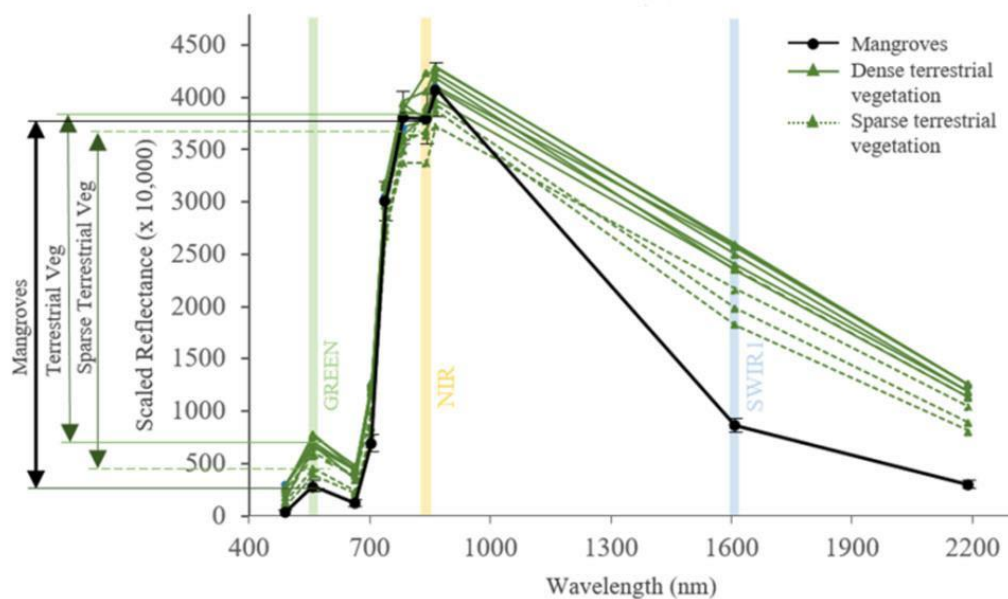


Figure 15: This figure shows the scaled spectral reflectance characteristics for mangroves and terrestrial vegetation, which is consistently lower for mangroves in the green (560 nm) and SWIR1 (1610 nm) sentinel-2 bands. The reflectance in the NIR varies (being higher or lower than mangroves), dependent on the health of the leaf. (The figure is a direct copy of figure 2 in Baloloy, Blanco, Sta. Ana, and Nadaoka (2020)).

The higher reflectance in the green band is indicative of higher chlorophyll content, while the NIR band relates to canopy density. The higher the canopy density, the greater the NIR reflectance. The SWIR is affected by leaf water content; a lower reflectance indicative of higher moisture (T. Kumar, Mandal, Dutta, Nagaraja, & Dadhwal, 2019).

The Mangrove Recognition Index (MRI) differentiates between mangroves and non-mangroves, and defined mathematically in Appendix A.3.1. Unfortunately, the MRI requires both low and high tidal data. The larger the difference, the higher the accuracy of the index. The index was designed using Landsat TM data, thereby incorporating SWIR bands.

To overcome the requirement of multiple tidal data, the Mangrove Vegetation Index (MVI) was developed by Baloloy et al. (2020). It is defined in Appendix A.3.2. The larger the MRI of a pixel, the higher the probability that the pixel belongs to a mangrove forest. The Mangrove Vegetation Index (MVI) uses the NIR, SWIR1 and green bands of the sentinel-2 satellite, and does not require tidal information.

2.3.3 Atmospheric Effects on Spectra

The atmosphere itself affects the spectral shape of all types of spectra, not just vegetation. As Section 2.3 is concerned with the factors influencing vegetative spectra, a detailed discussion of atmospheric effects (e.g. scattering) is withheld until Section 2.4.1.

Atmospheric water vapour, in particular absorbs the most significant proportion of solar radiation over several wavelengths. This is illustrated in Figure 16 specifically for a typical vegetation spectrum.

Solar radiation is absorbed by various gasses in the atmosphere, where the influence affects wavelengths differently. Although water vapour forms a significant effect on transmission, other gasses cannot be discounted. The key gases to produce observable effects in the 0.4 - 2.5 μm region are; water vapour (H_2O), carbon dioxide (CO_2), ozone (O_3), nitrous oxide (N_2O), carbon monoxide (CO), methane (CH_4) and oxygen (O_2) (B.-C. Gao, Heidebrecht, & Goetz, 1993). When retrieving surface reflectances over dark targets (such as vegetation) near the 0.4

μm region, nitrogen dioxide (NO_2) introduces errors on the order of 10-20 % (B.-C. Gao, Montes, Davis, & Goetz, 2009).

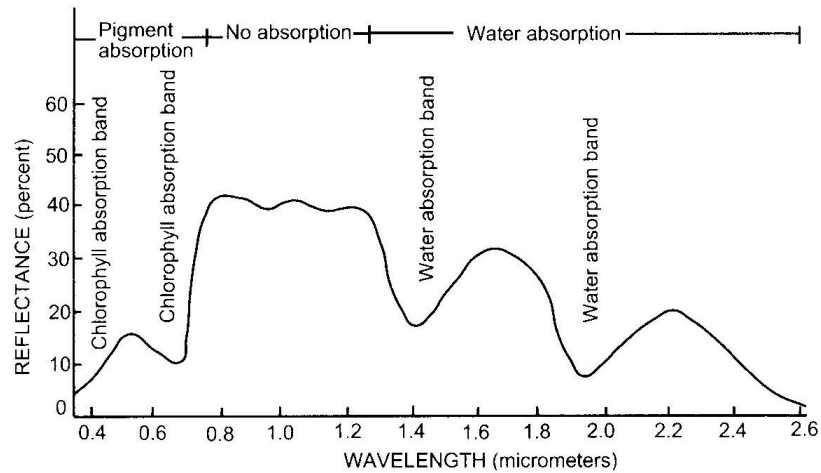


Figure 16: Spectral effects caused by atmospheric water absorption on a typical vegetation spectrum (Hoffer, 1968). (The image was taken from McCoy (2005, p. 72)).

The amount of aerosol scattering decays over the range 0.4 to 0.8 μm . Ozone absorption occurs near the 0.6 μm band centre, while water vapour occurs at 0.73, 0.82, 0.94, 1.14, 1.38 and 1.88 μm . Oxygen absorption occurs at 0.76 μm and carbon dioxides at approximately 1.56, 2.01 and 2.08 μm . Methane absorption occurs at 2.25 μm (Ben-Dor, 2002). Figure 17 illustrates the strength of absorption due to various atmospheric gasses.

The lowest transmittance value is zero, which means that all solar radiation transmitted through the earth's atmosphere is absorbed (i.e. no radiation is transmitted). The maximum transmittance value is one, indicating that all radiation is transmitted (i.e. no radiation is absorbed).

At the 400 nm wavelength (corresponding to blue), between 65% and 70% of irradiance is transmitted through the atmosphere. As some 30 - 35% is not transmitted, it is scattered and turns the sky blue. Water vapour has the greatest effect on absorption. Regions where little (or no) absorption occurs are termed atmospheric windows (B.-C. Gao et al., 1993).

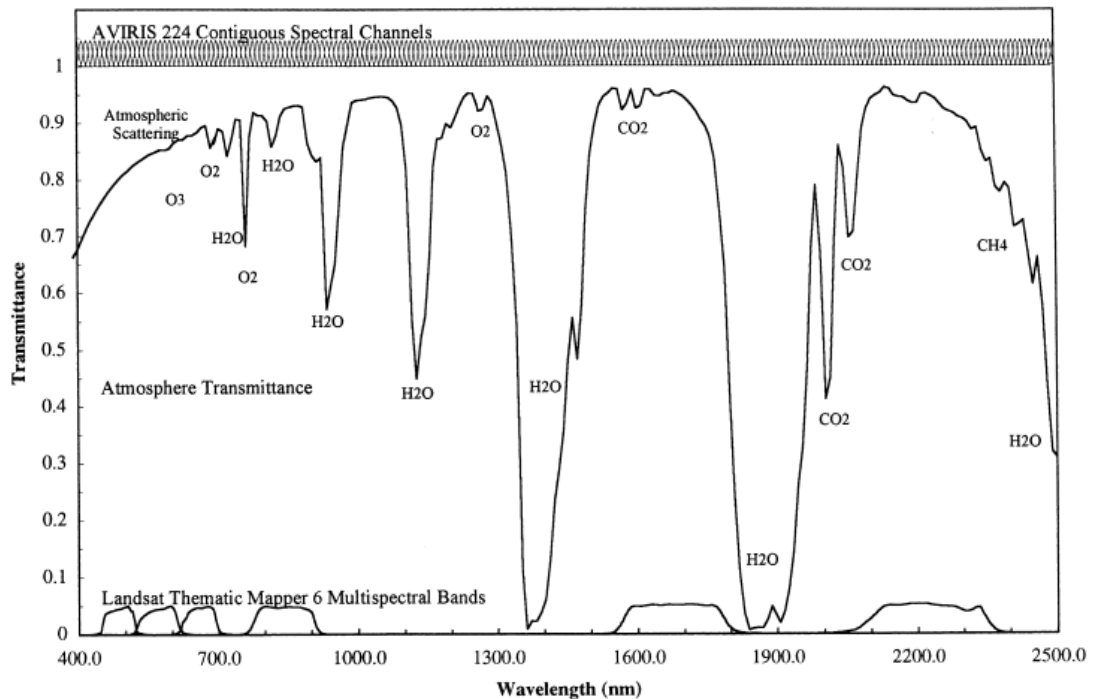


Figure 17: Atmospheric transmittance effect of solar radiation on wavelengths (R. O. Green et al., 1998).
[Figure 2 of Section 2.2.2 has been reproduced here to aid discussion].

It is appropriate to formally define a number of terms used briefly in the preceding work and further terms for subsequent work. The majority of these definitions were taken from Section 2.2.5 of Jones (2010). Electromagnetic radiation contains energy, measured in the unit of Joule (J). Power is the rate of transfer of energy, expressed in the unit Watt (W). The rate of radiant energy from the sun to the earth is called the radiant flux (**F**) also with units of W. The radiant flux incident upon or emitted from a unit area is the radiant flux density (**R**) (Wm^{-2}). For a radiant flux incident upon a horizontal surface, the common term becomes irradiance (**I**) (with the same unit of Wm^{-2}). If the radiant flux leaves a surface, it is termed the radiant exitance. The radiant flux density emitted from a unit area into a solid angle is termed the radiance (**L**) with units of $\text{Wm}^{-2}\text{sr}^{-1}$ (sr = steradian). The radiance thereby contains a direction, which is significant to describe the energy distribution from a reflected surface. That is, the intensity of the energy reflected from a surface is dependent upon the incident and viewing angles (in addition to wavelength), unless the surface is an ideal Lambertian surface (reflecting the same radiance in all

directions). This ideal surface is uncommon in the real world. For instance, the backscatter direction of a vegetative canopy tends to be brighter than other directions (Jones, 2010, p. 200). The reflective property of a surface is described by the BRDF (bidirectional reflectance distribution function). Both the spectral radiance ($\text{Wm}^{-2} \text{sr}^{-1} \mu\text{m}^{-1}$) and spectral irradiance ($\text{Wm}^{-2} \mu\text{m}^{-1}$) cater for the wavelength dependence of radiance and irradiance.

2.3.4 Summary to this point

Key points to be brought forward in this thesis are:

- Hyperspectral data for vegetation contains a red-edge.
- The red-edge is unique to vegetative spectra.
- The length of the red-edge relates vegetative density. The longer it is, the more vegetation present in the spectrum.
- The addition of leaf layers increases the NIR reflectance but leaves the visible (i.e. RGB) spectral region unaffected.
- Nutrient-deficient vegetative spectra have an increased reflectance extending over both RGB and NIR regions compared to healthy vegetative spectra.
- A blue or red-shift in the REIP (red-edge position) occurs, depending on the stress induced on vegetation.
- Senescence and phenology affects the spectral shape of vegetation, as does water content.
- Vegetative spectra belonging to different species (interspecies) may differ less than spectra belonging to the same species (intraspecies). This means that spectra for like species can vary more than between species.
- The atmosphere changes the solar reflected energy as recorded by the sensor.

2.4 Preprocessing

Preprocessing is concerned with enhancing the image data prior to data analysis or information extraction (Landgrebe, 2003, p. 443).

Typical scenarios include:

- geometric preprocessing (e.g. geometric distortions due to the actual flight, registration correction)
- radiometric preprocessing (e.g. atmospheric radiance effects (P. M. Mather, and Koch, M., 2011, p. 112))
- data transformation (e.g. feature reduction)

In this thesis, geometric preprocessing is discussed only briefly in Section 2.4.3, whereas radiometric preprocessing forms the basis for discussion in Sections 2.4.1 and 2.4.2. For data transformation details are covered in a new section (i.e. Section 2.5) rather than a single sub-section of preprocessing (i.e. under Section 2.4), as the number of considerations are too numerous.

2.4.1 Atmospheric Scattering

Remote sensing in the solar spectrum is concerned with the reflection of solar radiation from an object. Solar energy must traverse the Earth's atmosphere before the spectrum of the reflected object is recorded at the sensor. The radiation which ultimately reaches the sensor is affected by the atmosphere in three ways: transmittance, sky irradiance and path radiance (Richards, 2013, p. 35).

Transmittance is the factor by which irradiance is diminished due to passage through a specific distance of a scattering and/or absorbing medium (often the full column of the Earth's atmosphere as it impacts the solar irradiance that impinged the Top Of the Atmosphere (TOA) (covered in Section 2.3.3). In the absence of absorption and scattering, the solar irradiance and transmittance are equal – i.e. 100% of solar irradiance arrives at the ground.

There are three types of scattering events; Rayleigh, Mie and non-selective (Jones, 2010, p. 19). Rayleigh scattering is caused by gas molecules, as they are much smaller than the wavelengths of light. Mie scattering is caused by particles of about the same size, such as smoke, dust particles (Chavez, 1988), haze and fumes (Richards, 2013). Blue wavelengths in particular are affected more by haze than longer wavelengths (Cohen & Goward, 2004). Rayleigh scattering effects are strongest in the 0.4 - 0.7 μm range but are negligible above 1 μm and decreases rapidly ($\sim\lambda^{-4}$) in comparison to aerosol scattering ($\sim\lambda^{-2}$ to $\sim\lambda^{-1}$). As a result, near 1 μm (for typical atmospheric conditions), the aerosol scattering contributes to $\sim 10\%$ of the total radiance as measured by a downward looking satellite over land areas (B.-C. Gao et al., 1993). Non-selective scattering is due to particle sizes being much larger than the wavelengths (e.g. clouds and fog).

Some 18% of incoming radiation is diffuse; i.e. sky irradiance that's scattered into the lower atmosphere. The incoming radiation scattered into the upper atmosphere is caused by aerosols and air molecules (Sandau, 2010, p. 134).

The influences due to sky irradiance and path radiance are best served with the aid of a diagram (Figure 18). The definitions for the terms used in the following descriptions were defined in Section 2.3.3.

Solar irradiance arriving at the top of the atmosphere undergoes atmospheric scattering (due to gases and aerosols). The radiation is reflected from a pixel but there is a directional effect (for a non-Lambertian surface – typically found in the real world). This means that the amount of reflected radiation varies according to the sensed angle of the pixel, so the term radiance is used to describe this angular dependence. Moreover, spectral radiance also describes an additional wavelength dependence.

Sky irradiance is due to radiation scattering from the atmospheric constituents itself onto a pixel (sky irradiance 1 in Figure 18) or reflected by neighbouring pixels, then scattered onto the pixel being sensed (sky irradiance 2 in Figure 18) (Richards, 2013, p. 34).

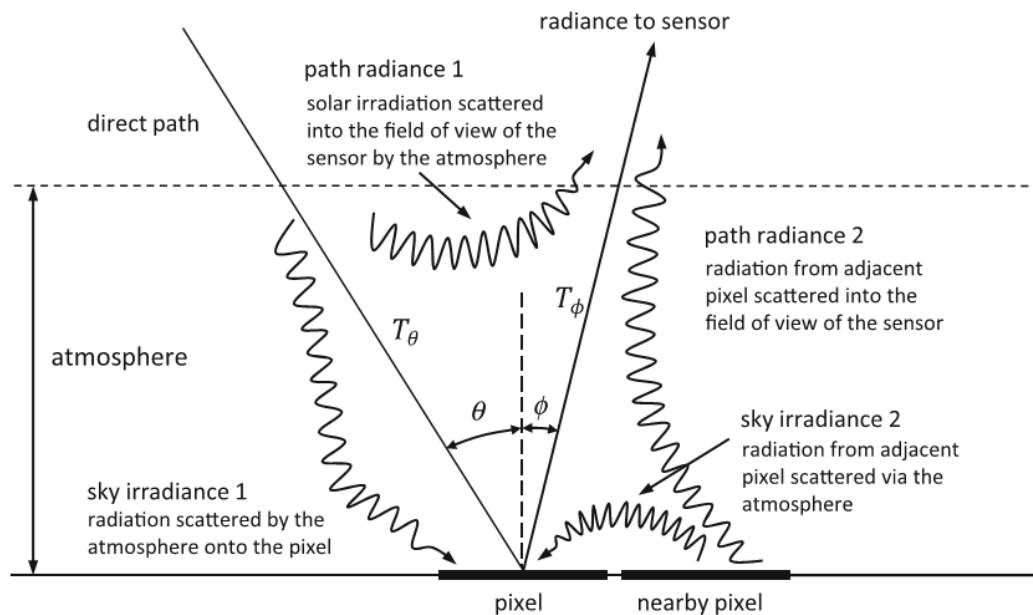


Figure 18: Atmospheric path radiance effects on a pixel by solar radiation.
 (Figure taken from Richards (2013, p. 34), Figure 2.5).

Path radiance is due to radiance from adjacent pixels (called the adjacency effect (Campbell & Wynne, 2011) or the environment influence (Milovich, Frulla, & Gaguardini, 1995)) as well as due to atmospheric scattering toward the sensor. The sensor therefore views radiation from a scene not directly under view (Landgrebe, 2003, p. 43). The adjacency effect decreases with increasing wavelength and is caused by both Rayleigh and aerosol scattering (Richter, Bachmann, Dorigo, & Muller, 2006).

In practical terms, the vegetative reflectance spectrum obtained from leaves will contain spectral contributions from dry leaves, branches, the actual tree trunk in addition to soil (L. Kumar et al., 2010).

Besides scattering events, the atmosphere is also in a constant state of flux. Aerosols may be turbulent and water vapour may be highly variable in both space and time (Sandau, 2010).

The theory discussed in this section highlights the difficulty of obtaining a pure spectral signal for a particular cover type (e.g. vegetation). Atmospheric models attempt to derive surface reflectances of targets spectra by eliminating atmospheric effects.

2.4.2 Radiometric Correction

Radiometric atmospheric correction (also termed atmospheric correction) decreases (or, ideally, eliminates) the effects on sensor radiance measurements caused by the atmospheric effects (i.e. absorption and scattering).

As atmospheric effects occur over all recorded wavelengths (but not equally), photographic recording methods are also affected and need correction (e.g. removal of haze). With multispectral sensors, correction is even more important. Whereas multispectral data is recorded in atmospheric windows, this is no longer the case for hyperspectral data (Goetz, 2009). Consequently, atmospheric correction for hyperspectral based data is harder than non-hyperspectral data (P. S. Thenkabail et al., 2004). Figure 17 (p. 43 of Section 2.3.3) illustrated this difference; multispectral bands form an average over the transmitted wavelengths, while the high radiometric resolution of hyperspectral sensors causes recorded data to be affected by absorption to a much finer degree.

The atmospheric correction process converts radiance values to surface reflectances, removing sun and view angle effects (Ustin et al., 2004), thereby eliminating illumination changes across the scene (R. Jensen et al., 2007). This allows field measured reflectance data (described in detail in Section 4.3.1) to be directly compared with spectra obtained from airborne sensors. Together with a hyperspectral library, land-cover types may be identified. In practice, however, limitations exist; for example, the effects of mixed spectra within pixels (Section 2.2.1) obscure the pure spectra.

The reflectance (r) is mathematically defined as:

$$r = \frac{\text{target radiance}}{\text{solar irradiance}} \quad (2.4.2.1)$$

(Richards, 2013, p. 40)

Different approaches have been developed to remove atmospheric effects from spectra. Atmospheric correction using models are based on physical processes,

although non-physical processes (i.e. empirical methods) have also been employed. Overall, the physics-based approaches are more effective and more popular (Jones, 2010, p. 139). In practice, the physics-based approaches are modelled using computer code based on mathematical equations describing atmospheric radiative processes.

Two widely used products are MODerate resolution atmospheric TRANsmission (MODTRAN) and Second Simulation of a Satellite Signal in the Solar Spectrum (6S). Other radiative transfer models are tweaked to cater for specific scenarios (e.g. the Spectral reflectance Image Extraction from Radiance with Relief and Atmospheric correction (SIERRA) model for mountainous regions) but are still using MODTRAN or 6S computer code.

Appendix B contains more detail about the MODTRAN or 6S models, but in this section, only Tafkaa is elaborated upon as it is used in this thesis.

Tafkaa is an acronym for “The Algorithm Formerly Known As ATREM” (B.-C. Gao and Goetz (1990)). It was originally developed to retrieve water-leaving reflectance spectra using hyperspectral remote sensing over deep ocean areas (B.-C. Gao, Montes, Ahmad, & Davis, 2000). Tafkaa is based on ATREM 4.0 and uses 6S code for scattering calculations (more details are given in Appendix B) but Tafkaa is really defined by the addition of the special “Tafkaa_tabular” module (explained below).

The ATREM algorithm model extends over the 0.4 – 2.5 μm region (B.-C. Gao et al., 1993), thereby being suitable for hyperspectral data (Zheng, Kindel, & Goetz, 2003). ATREM incorporates 6S radiative transfer code, allowing it to model atmospheric scattering (Kruse, 2004). The 6S code models gas absorption and incorporates BRDF effects while also incorporating a canopy model for vegetation (Eismann, 2012, p. 209). Shortcomings of ATREM include the overestimation of water vapour over vegetative regions (Goetz, Kindel, Ferri, & Zheng, 2003) as well as neglecting topographic and adjacency effects (B.-C. Gao et al., 2009).

The incorporation of a vegetative canopy model into 6S is desirable from a vegetative classification viewpoint (thesis objective 3). The incorporation by Tafkaa to include the 6S code as well as covering the 0.4 – 2.5 μm region makes it a candidate model to use for atmospheric correction. Alternative models (see Appendix B), such as the High-Accuracy Atmospheric Correction for Hyperspectral

data (HATCH) and Atmospheric and Topographic Correction (ATCOR) are based on MODTRAN rather than 6S, but these do not incorporate a vegetative canopy model.

An advantage of Fast Line-of-Sight Atmospheric Analysis of Spectral Hypercubes (FLAASH) is that it accounts for the adjacency effect. However, FLAASH tends to be slow, compared to ATREM and produces large temporary files (Kruse (2004)).

The SIERRA model has been optimised for use over mountainous regions, which is not necessary for the Port Hedland coastal region - there are no mountains in Port Hedland.

While water vapour is estimated using the 0.94 and 1.14 μm wavelengths (HATCH) or 0.94 and 1.13 μm wavelengths (ATCOR), Tafkaa uses 0.914 and 1.14 μm . The 1.14 μm wavelength lies beyond the range wavelengths recorded in the Port-Hedland hyperspectral data. However, Tafkaa does allow for the retrieval of water vapour using the 0.820 μm wavelength (Montes, Gao, and Davis (2004), p. 17) - which is ideal, as the PHPA airborne hyperspectral data incorporates this wavelength.

The "Tafkaa_tabular" module takes into account specular reflections over an air-water interface, thereby making it suitable for use in airborne hyperspectral remote sensing in situations that include water targets. Montes et al. (2004) states that NO_2 gas is taken into account by the model but mainly for the stratospheric region of the atmosphere. Airborne data sensed over polluted areas will not be accurate and further refinements are necessary for the Tafkaa code to take into account tropospheric NO_2 gas. However, according to the Port Hedland Port Authority (n.d.), NO_2 port emissions are within the standards of acceptable air quality.

It should be noted that the Tafkaa User's Guide (Montes et al., 2004) dates back to 2004 and may be out-of-date. For instance, according to B.-C. Gao et al. (2009) the S6 code models atmospheric absorption effects due to NO_2 in the 0.4 – 0.8 μm region but it is unclear if this refers to the tropospheric layer. This range does not cover the full hyperspectral range; it is therefore unclear if the wavelengths outside of the 0.4 – 0.8 μm range are insignificant.

Although each model have their pros and cons, the characteristics of Tafkaa makes the model well suited to fulfil the needs as a correction-based model for this thesis, especially as it incorporates vegetation and hyperspectral data- it is the model of choice in this thesis.

2.4.3 Geometric Effects

For sensors mounted on aeroplanes, changes in platform attitude (i.e. yaw, roll and pitch) have a direct influence on sensed data by causing an image to be warped (Appendix K.4 contains examples of affected images). Fortunately, attitude parameters are kept track of by the Internal Navigation System (INS) for each flight line (Lee, Theiss, Bethel, & Mikhail, 2000). In addition, the INS also maintains a record of velocity changes (The Editors of Encyclopaedia Britannica, 2019). The AISA sensor itself stores information relating to INS and Global Positioning System (GPS) locational data, allowing the hyperspectral image to be geocorrected (R. Jensen et al., 2007).

Fortunately for the PhD candidate, the Port-Hedland hyperspectral data required only two types of preprocessing – radiometric and georectification. Radiometric correction is performed using Tafkaa (as discussed previously). Georectification is conducted using the ENvironment for Visualising Images (ENVI) by Harris Geospatial Solutions, Inc.)² by processing .GLT files (geographic lookup table files), to remove the warping effect. The resulting image is geometrically correct and contains UTM coordinates.

2.5 Feature Reduction

Feature reduction is concerned with the selection of an appropriate subset of bands (e.g. in an image) without loss of information (Richards, 2013, p. 343).

² Homepage: <https://www.harrisgeospatial.com/>

There are good reasons for doing this, as shall be discussed further on. However, it is important to give some background concerning the characteristics of hyperspace, which have properties well beyond our common 3D experiences.

Mathematical equations, developed for 3D need to be re-written to make them appropriate for space containing a large number of dimensions. Hyperspectral data contains hundreds of bands thereby requiring high-dimensionality equations for the purpose of processing. Some of these high-dimensional properties lead to the Hughes effect (Hughes, 1968), which shows that the accuracy of classification actually decreases with increased dimension. This means that by incorporating the large number of hyperspectral bands, classification accuracy decreases (after reaching a maximum), which is contrary to what might be expected. Section 2.5.1 outlines the peculiar properties of hyperspace, while Section 2.5.2 identifies issues when related more specifically to hyperspectral remote sensing. The two most common remedies are covered in both Section 2.5.3 and 2.5.4. These solutions make use of spectral data transforms, which basically optimises the information content in a hyperspectral image in terms of significance (either based on variance or noise). After selecting a subset of transformed bands, the (transformed) image which is favoured by accounting for the Hughes effect and may be further used for classification purposes.

Although feature selection using separability measures (Section 2.5.5) has been used in multispectral data, where the (small) number of bands have allowed feature reduction to be attainable (Landgrebe (2003), p. 279), the large number of bands in hyperspectral data makes the system unmanageable. Although there are ways around this (e.g. search algorithms (P. M. Mather, and Koch, M. (2011), p. 278)), it is more common to perform feature reduction using Principal Component Analysis (PCA) or MNF for hyperspectral datasets. It might appear that separability measures is a topic out of place but still serves a purpose in assessing how spectrally different classes are on a thematic map.

Our journey begins by examining the behaviour of hyperspace which forms the background for data mining techniques developed for hyperspectral remote sensing.

2.5.1 Characteristics of Hyperspace

The properties of hyperspectral space exceed our common experiences of three dimensional space. It is important to gain an appreciation of these as they have real implications in remote sensing and need to be considered for the development of techniques for classification using hyperspectral data. The hyperspectral airborne data for the Port Hedland coastal region contains 246 bands, placing it well into the realms of hyperspace.

Although the mathematical arguments are given in some detail in Appendix C.1, for the purposes of discussion, it is sufficient here to simply state the main points:

- Most of hyperspace is empty and becomes more so as the dimension increases.
- In hyperspace, most of the data tends to be located toward the edges.
- The use of low dimensionality equations (e.g. Gaussian distribution function, Euclidean distance) is inadequate for hyperspectral space.

(most of this section is a summarised form taken from Landgrebe (2003) (chapter 5), with further details given in Appendix C.1).

The counter-intuitive results of hyperspace are often referred to as the “curse of dimensionality” in the literature.

The first point implies that hyperspectral space is mostly empty and by using appropriate mathematical techniques, most information can be ‘rearranged’ to reduce the number of features. Using appropriate separability measures, the high dimensional space may be projected to a lower dimensional space. In practical terms, this leads to a reduced number of (transformed) bands to process. Computationally, the new (reduced) transformed dataset leads to dramatic improvements in processing speeds.

The main point here, however, is that these high dimensional spaces have direct consequences for classification in remote sensing. For example, parametric classification methods assume classes to be normally distributed (to be elaborated

in Section 2.6.4.1). The familiar low-dimensional Gaussian distribution function needs to be modified before it can be implemented in a high-dimensional space (discussed further in Section 2.6.4.1, with the equation given in Appendix E.1 – i.e. Equation (E.1.2)).

In addition, the rather simple Euclidean distance (D_E)

$$D_E = \left\{ (\boldsymbol{\mu}_i - \boldsymbol{\mu}_j)^T (\boldsymbol{\mu}_i - \boldsymbol{\mu}_j) \right\}^{1/2} \quad (2.5.1.1)$$

(Schowengerdt, 2007, p. 398)

takes on a more complicated structure

$$D_M = \left\{ (\boldsymbol{\mu}_i - \boldsymbol{\mu}_j)^T \left\{ \frac{\mathbf{C}_i + \mathbf{C}_j}{2} \right\}^{-1} (\boldsymbol{\mu}_i - \boldsymbol{\mu}_j) \right\}^{1/2} \quad (2.5.1.2)$$

and is now called the Mahalanobis distance (D_M).

In both Equations 2.5.1.1 and 2.5.1.2 subscript i and j refers to class i and j respectively. The mean column vector is denoted by $\boldsymbol{\mu}$ while the covariance matrix is denoted by \mathbf{C} . In terms of feature space, the mean vector defines the location of the class distribution, whereas the shape of the distribution is described by the covariance matrix (Landgrebe, 2003, p. 140).

The Mahalanobis distance is a generalised Euclidean distance applicable for higher dimensional space and is required in the maximum likelihood (ML) classifier.

The Mahalanobis distance allows for a quadratic surface (e.g. hyperellipsoids) (Richards, 2013, p. 203), while a classifier based on Equation 2.5.1.1 (termed a minimum distance classifier) only allows for a hyperplane decision boundary (Richards, 2013, p. 267), which may be unsatisfactory (Chulhee & Landgrebe, 1993).

The covariance matrix is a second order statistic (because it relies on two variables), thereby allowing correlations between classes to be taken into account (Richards, 2013, p. 481). This is particularly significant when dealing with high-dimensional data (Chulhee & Landgrebe, 1993). A first order classifier (e.g. the

minimum distance) is unable to take into account the very high correlation which exists between adjacent bands, thereby limiting the performance as a classifier (Chulhee & Landgrebe, 1993). Geometrically, the covariance matrix determines the shape of the clusters by taking into account their variances (Borgelt, Timm, & Kruse, 2000). The actual cluster location is determined by the mean (P. M. Mather, and Koch, M., 2011, p. 249).

The high-dimensional form for distance measures (e.g. the Mahalanobis distance) allow separability measures to be formulated correctly for use with multispectral, and especially hyperspectral data. Moreover, the multi-dimensional Gaussian distribution function is required for supervised classification schemes, such as the ML method (Section 2.6.4.1).

2.5.2 Hughes Effect

When classifying an image in remote sensing using supervised classification, the actual class statistics are estimated using training data. For the ML classifier (described in detail in Section 2.6.4.1), these statistics are used to calculate the normal distributions for each class of which class membership is determined according to the highest probability. For unsupervised classification, training data is not required, as there are no parameters to estimate.

It is not difficult to envisage a scenario where the accuracy of the statistics is related to the number (and quality) of training samples obtained and to the number of spectral bands. For example, consider a situation where pixel spectra consist of 10 spectral bands but where class statistics are estimated using two samples. The resulting statistics (mean and covariance) are likely to be poor representations of the estimated normal distribution. Conversely, consider 100 samples instead; surely, the estimated statistics from these larger numbers of samples represent the 'true' statistics more accurately. It may appear reasonable that as the number of training samples increases, the accuracy of the classifier increases. However, this is not so and was first proposed in a landmark paper by Hughes (1968). In low dimensional multispectral space, the Hughes effect (as it became known) is fairly

insignificant but with the advent of hyperspectral data, the effect can no longer be ignored (Richards, 2013, p. 256).

The Hughes effect may be understood by considering a practical example. As discussed by Richards (2013) (Section 8.3.7, p. 256), consider having two dimensional data (i.e. two bands) and one training pixel per class. This is visually illustrated in the left image of Figure 19. The two classes are represented each with a square and a circle.

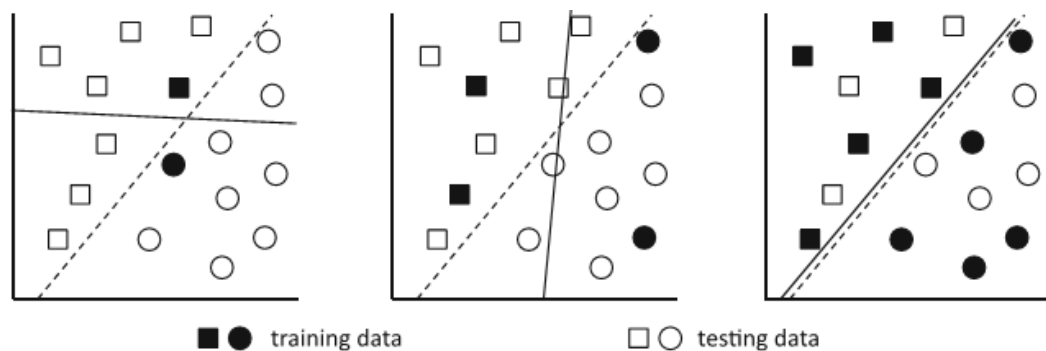


Figure 19: A linear surface is used to classify testing data from training data. The dashed line represents the optimal solution.

The use of only one training sample per class (each consisting of 2 bands) allows a line (separating the two classes) to be drawn in a non-unique manner consisting of many degrees of freedom; i.e. the position of the line is inaccurate and not uniquely determined. Now, consider the effect of doubling the number of samples to two (each containing 2 bands) – as shown in the centre plot (Figure 19). This time, the (solid) line provides a better discriminating solution between the two classes. However, there are still many possibilities for the position of the line. When considering five samples, the discriminating line is much better defined, as shown in the right plot. Essentially, by increasing the number of samples, the accuracy of the classifier is improved. Later in this section, it will be shown that the accuracy reaches an optimal point, after which the accuracy decreases as the number of training samples increases.

Although not discussed by Richards (2013), let us turn our investigation back to Figure 19, in particular the left image and imagine the effect of adding another band. Our image now becomes three dimensional. It is not hard to envisage the

solid line becoming a plane. However, with the addition of a third axis the degree of freedom of the plane must increase, for we are able to move the discriminating plane about more freely as a result of this new axis, thereby decreasing the location of the desired position to separate the classes. In other words, by increasing the number of bands, we are decreasing the classification accuracy. Although we need to be careful oversimplifying the example, this section will show that there is actually an optimal number of bands to produce the best classification result, after which classification accuracy decreases with any further increase in bands. This result is a consequence of the Hughes effect and shown graphically in Figure 21 (page 61).

Whereas the preceding results were intuitively derived, Hughes (1968) went much further by tackling the classification problem from a mathematical viewpoint, offering more insight into the limitations posed by the number of bands and number of training samples on classification accuracy.

Mathematically, a classification problem may be stated as follows, and is known as Bayes theorem:

$$p(\omega_i | \mathbf{x}) = p(\mathbf{x} | \omega_i) p(\omega_i) / p(\mathbf{x}) \quad (2.5.2.1)$$

(taken from Richards (2013, p. 251))

ω_i defines the individual class from M total classes (i.e. $\omega_1, \omega_2, \dots, \omega_M$). The vector \mathbf{x} defines an N band pixel measurement vector, as defined by $\mathbf{x} = [x_1, x_2, \dots, x_N]^T$.

Each component (i.e. x_1, x_2, \dots, x_N) represents a grey level.

The term $p(\omega_i | \mathbf{x})$ defines the posterior probabilities; the probability of finding class ω_i at a pixel with location \mathbf{x} in spectral space. The class conditional probabilities $p(\mathbf{x} | \omega_i)$ are estimated from training data, which describe the probability of finding a pixel at position \mathbf{x} in spectral space from each of the classes. For a parametric classifier (e.g. Maximum Likelihood), $p(\mathbf{x} | \omega_i)$ is modelled using a Gaussian function. The $p(\omega_i)$ term defines the prior probabilities. The terminology

“prior” refers to the fact that $p(\omega_i)$ are estimated from previous results. For example, the class probabilities may be estimated using historical data (e.g. an agricultural field) but are difficult to obtain in practice (Schowengerdt, 2007, p. 417).

Given a pixel \mathbf{x} , there is the possibility that multiple classes exist at that location. Clearly it is desirable to label the pixel as belonging to the class with the highest probability:

$$\mathbf{x} \in \omega_i \text{ if } p(\omega_i | \mathbf{x}) > p(\omega_j | \mathbf{x}) \text{ for all } j \neq i$$

(taken from Richards (2013, p. 250))

Hughes (1968) expresses the maximum probability of a class (i.e. choosing the most likely class) in terms of a measurement complexity which Landgrebe (2003, p. 132) expresses in terms of the number of brightness values for each band. This may be understood by considering a simple example where a one band sensor records just one bit. The data recorded takes on two possibilities: 0 and 1. If the one band sensor is able to record two bits, the possibilities are 00, 01, 10 and 11. For a two band sensor, the possibilities are 0000, 0001, 0010, 0011, 0100, etc. (16 in all). In general, the measurement complexity (n) is given by:

$$n = \left(2^{\text{number of bits}} \right)^{\text{no of bands}}$$

Practically, the Landsat TM comprises 7 bands with 8 bits each. The measurement complexity is 7.2×10^{16} bins (the unit is expressed in terms of bins). Hyperspectral data (with 256 bands) clearly contain a much higher order of complexity than the previous multispectral sensors. This has real consequences in relation to selecting the number of training samples, as will be shown later in this section.

Hughes (1968) described the pattern recognition problem in terms of n (i.e. the measurement complexity) possible measurement values x_i :

$$P(c_1 | x_i) > P(c_2 | x_i)$$

which is effectively Equation (2.5.2.1). It should be noted that, for simplicity, Hughes (1968) only considered two classes from which the key results were obtained.

The recognition probability (i.e. accuracy) may be stated:³

$$\begin{aligned} P_{cr}(n, p_{c1}) &= \sum_{i=1}^n \left[\max_{j=1,2} P(c_j | x_i) \right] P(x_i) \\ &= \sum_i \max_j P(c_j, x_i) \\ &= \sum_i \left[\max_j P(x_i | c_j) \right] p_{c_j} \end{aligned}$$

In the language of Hughes, the $p(\mathbf{x} | \omega_i)$ terms (from Richards) are now $P(x_i | c_j)$ which must be estimated from training data. Hughes goes further and derives an expression for the mean correct recognition probability – i.e. over all possible pattern classifiers (in remote sensing terms (Landgrebe, 2003, p. 132)) – which is denoted by $\bar{P}_{cr}(n, p_{c1})$.

The essence of the Hughes effect regards the behaviour of $\bar{P}_{cr}(n, p_{c1})$. For an infinite dataset for two classes, where each class has an equal probability (i.e. $p_{c1} = p_{c2} = 0.5$):

$$\bar{P}_{cr}\left(n, \frac{1}{2}\right) = \frac{3n-2}{4n-2}$$

For a single measurement, $\bar{P}_{cr}\left(1, \frac{1}{2}\right) = 0.5$ while for five measurements $\bar{P}_{cr}\left(5, \frac{1}{2}\right) = 0.72$. In the limit as $n \rightarrow \infty$ the above equation reduces to:

$$\bar{P}_{cr}(n = \infty, p_{c1}) = 1 - p_{c1}p_{c2}$$

³ The PhD candidate believes the “cr” subscripts on P is short for “correct recognition”.

Therefore, for the case of an infinite dataset, the maximum mean recognition accuracy for $p_{c1} = p_{c2} = 0.5$ is 75%. In general, the Figure 20 shows the behaviour for the mean recognition probability with the measurement complexity n (related to the number of features, or bands in remote sensing (Fu, Landgrebe, and Phillips (1969), Richards (2013, p. 257))).

When $p_{c1} = p_{c2} = 0.5$, the asymptote of 75% continues to 91% where $p_{c1} = 0.9$. The results for $p_{c1} = 0.9$ and $p_{c1} = 0.1$ are equivalent, as are the curves for $p_{c1} = 0.6$ and $p_{c1} = 0.4$ and so on.

The measurement complexity for hyperspectral data exceeds that of multispectral, due to the vast increase in the number of bands used by the recording instrument. The plot suggests that by increasing the number of bands, the mean recognition accuracy increases (as the most accurate result is obtained when $n \rightarrow \infty$).

The preceding results were obtained using an infinite dataset. Hughes goes on to consider the effect on a limited dataset (i.e. limited training data). The results are shown graphically in Figure 21.

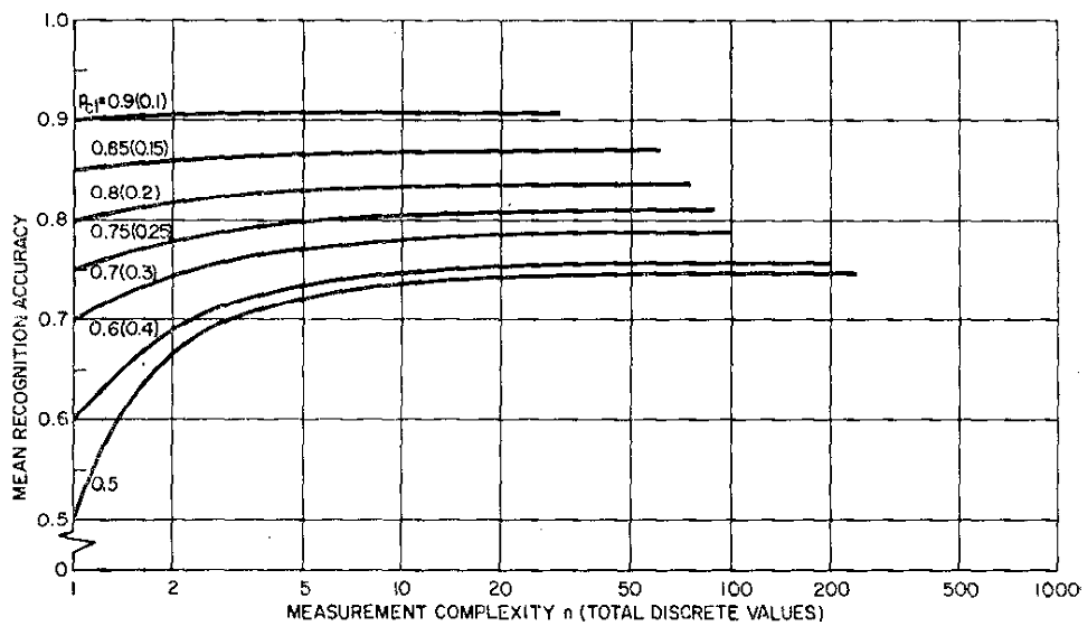


Figure 20: Mean recognition accuracy with measurement complexity n for an infinite dataset.

The numbers inside the vertical axis refer to p_{c1} . The curves are equivalent for $p_{c1} = 0.9$ and 0.1 , so Hughes simply indicated this by writing 0.9 (0.1). The same applies to the rest of the numbers.

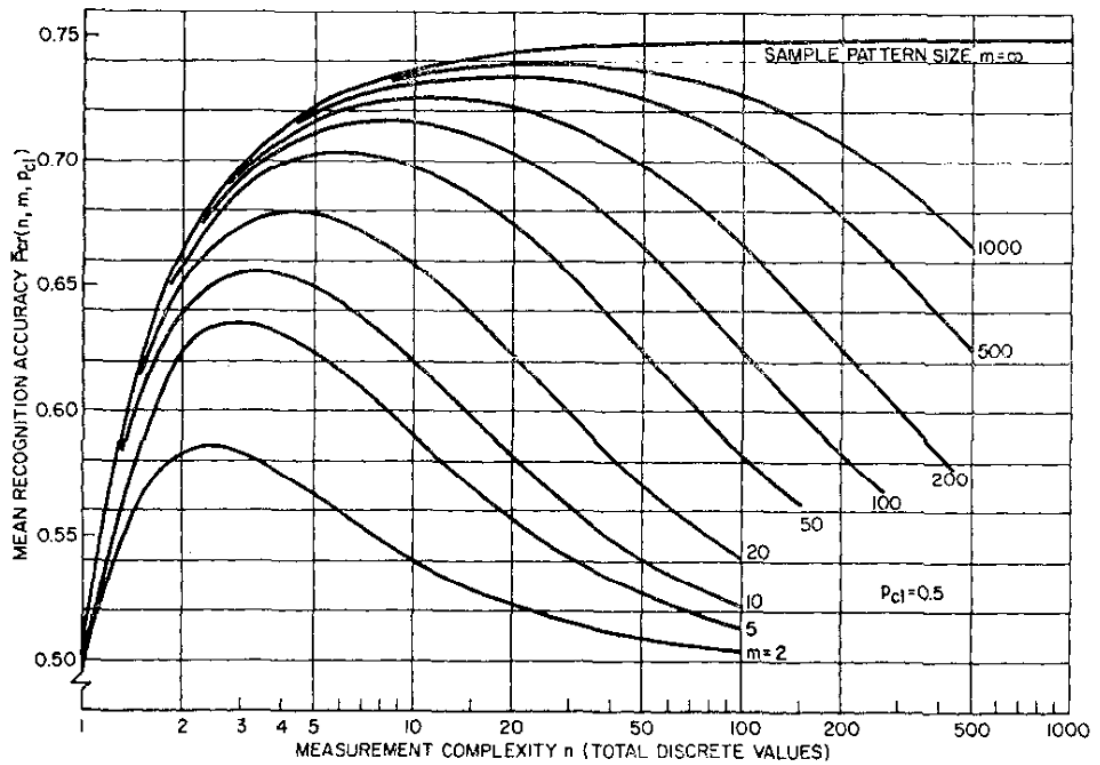


Figure 21: Mean recognition accuracy with measurement complexity for different numbers of training samples (m). ($p_{c1} = p_{c2} = 0.5$).

The letter m represents the number of measurement samples (i.e. training samples in remote sensing terms). Compared to the earlier result, for an infinite dataset, the measurement complexity influences the classification accuracy. In fact, there is an optimal measurement complexity n_{opt} for maximum accuracy. For example, when $m = 2$, the $n_{opt} = 2$ (note: n are discrete values). As n increases, there is no longer an asymptote toward a maximum mean recognition accuracy – that has already occurred at $n_{opt} = 2$. As the number of training samples (m) increases, n_{opt} also increases. The optimal measurement values for n_{opt} are summarised in Table 5.

The results have direct consequences for remote sensing; a multispectral classification result may indeed be more accurate than a hyperspectral result owing to the increased complexity due to the large number of bands. However, the converse is also true, depending on the number of training data available. By increasing the number of training samples, a hyperspectral result may be more accurate (compared to the equivalent multispectral) as the measurement

complexity has increased. For example, by having 1000 training samples (i.e. $m = 1000$), a hyperspectral result with 23 bands (i.e. $n_{opt} = 23$) will produce a more accurate result (73.9% - see Table 5) compared to a 5 band multispectral dataset (from Figure 21, at $n = 5$, the accuracy is about 72% for $m = 1000$ samples).

Hughes also considered the case where the two class probabilities differ, resulting in a complicated pattern for the set of curves (as shown in Figure 22).

In this case, $p_{c1} = 0.2$ (which, according to Figure 20 means the curve to $p_{c1} = 0.8$ is the same). According to Hughes, when the probability of the two classes is markedly different, then there is a maximum acceptable measurement complexity n_{max} which increases in value with m . The maximum values $n_{max}(m) \sim m/2$ and are located where the curves fall below the level $\bar{P}_{cr} = 0.8$. The curve for $m = \infty$ is the same as that for $p_{c1} = 0.2 = 0.8$ of Figure 20.

The consideration of just 2 classes already leads to complicated mathematics and graphs. It is unusual in remote sensing to only consider 2 classes and even more unusual for the probabilities of classes to be equal. Despite this, the fundamental conclusions by Hughes must be considered in classification work, especially when dealing with hyperspectral data, where the measurement complexity is high.

m	n_{opt}	$\bar{P}_{cr}(m, n_{opt}, \frac{1}{2})$
2	2	0.5833
5	3	0.6350
10	3	0.6548
20	4	0.6791
50	6	0.7031
100	8	0.7161
200	11	0.7257
500	17	0.7345
1000	23	0.7390
∞	∞	0.7500

Table 5: Optimal measurement complexities corresponding to the curves in Figure 21.

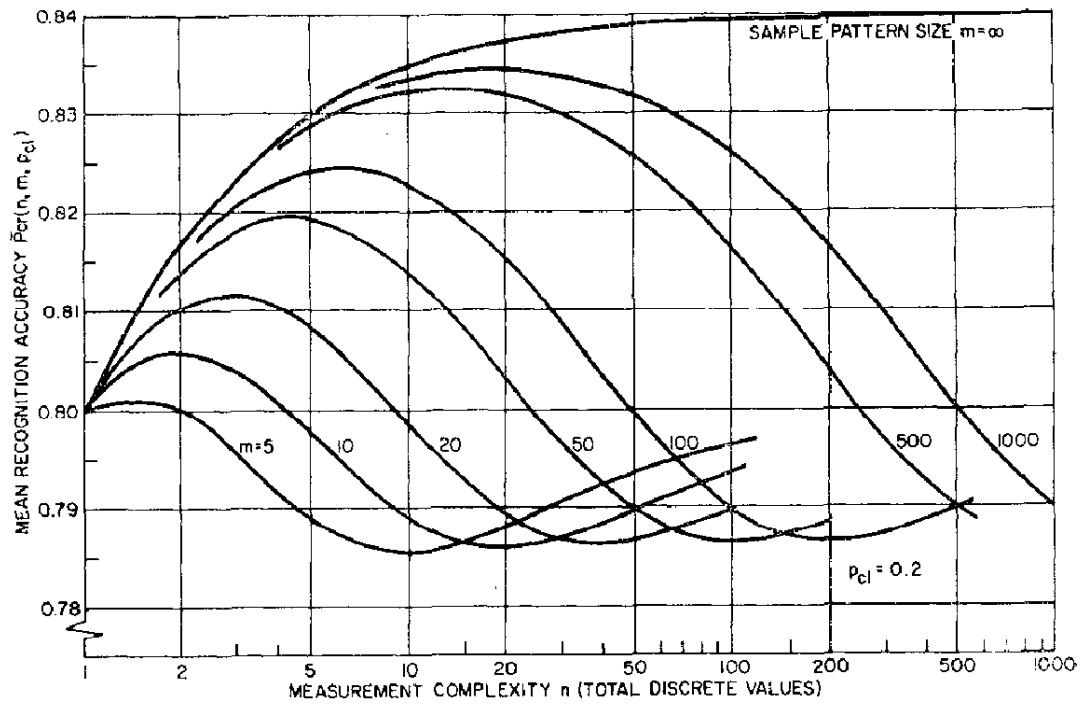


Figure 22: Mean recognition accuracy with measurement complexity (n) for different numbers of training samples (m) and where the two class probabilities are different ($p_{c1} = 0.2$).

2.5.3 Principal Component Analysis (PCA)

Principal Component Analysis (PCA) is one of the most popular methods for feature reduction. It is also referred to as a Hotelling transform or a Karhunen-Loève transform in the literature (Kaewpijit, Le Moigne, & El-Ghazawi, 2002).

The equations stated in this section have mostly been taken from Richards (2013) (in particular Section 6.3.1), with minor symbol alterations.

Quantitatively, a pixel containing N bands may be represented by a vector \mathbf{x} as follows:

$$\mathbf{x} = \begin{bmatrix} x_1 \\ x_2 \\ \vdots \\ x_N \end{bmatrix} \quad (2.5.3.1)$$

Each component (i.e. x_1, x_2, \dots, x_N) represents a grey level.

If there are K such vectors, then each individual vector may be written as \mathbf{x}_k . The mean value for pixel vector \mathbf{x} is given by the expectation value:

$$\boldsymbol{\mu} = \mathcal{E}\{\mathbf{x}\} \quad (2.5.3.2)$$

Explicitly, the mean $\boldsymbol{\mu}$ is calculated from K individual vectors \mathbf{x}_i :

$$\boldsymbol{\mu} = \frac{1}{K} \sum_{i=1}^K \mathbf{x}_i$$

Similarly, the covariance matrix is given by

$$\mathbf{C} = \mathcal{E}\{(\mathbf{x} - \boldsymbol{\mu})(\mathbf{x} - \boldsymbol{\mu})^T\} \quad (2.5.3.3)$$

For an unbiased population of K vectors \mathbf{x}_i :

$$\mathbf{C} = \frac{1}{K-1} \sum_{i=1}^K (\mathbf{x}_i - \boldsymbol{\mu})(\mathbf{x}_i - \boldsymbol{\mu})^T$$

It is clear that the matrix \mathbf{C} must be symmetric.

A principal component transformation is a linear transformation, defined by:

$$\mathbf{y} = \mathbf{G}\mathbf{x} \quad (2.5.3.4)$$

The transformation matrix \mathbf{G} is termed the principal transformation matrix.

In order to distinguish between the \mathbf{x} and \mathbf{y} spaces (\mathbf{y} being the transformed space and \mathbf{x} the original space), subscripts will be introduced. For example,

Equation (2.5.3.2) is written as $\boldsymbol{\mu}_x = \mathcal{E}\{\mathbf{x}\}$ to refer to \mathbf{x} space, while $\boldsymbol{\mu}_y = \mathcal{E}\{\mathbf{y}\}$

refers to \mathbf{y} space. Similar changes are made to Equation (2.5.3.3):

$$\mathbf{C}_x = \varepsilon \left\{ (\mathbf{x} - \boldsymbol{\mu}_x)(\mathbf{x} - \boldsymbol{\mu}_x)^T \right\} \quad (2.5.3.5)$$

and

$$\mathbf{C}_y = \varepsilon \left\{ (\mathbf{y} - \boldsymbol{\mu}_y)(\mathbf{y} - \boldsymbol{\mu}_y)^T \right\} \quad (2.5.3.6)$$

The PC transformation proceeds by substituting Equation (2.5.3.4) into Equation (2.5.3.6):

$$\begin{aligned} \mathbf{C}_y &= \varepsilon \left\{ (\mathbf{G}\mathbf{x} - \mathbf{G}\boldsymbol{\mu}_x)(\mathbf{G}\mathbf{x} - \mathbf{G}\boldsymbol{\mu}_x)^T \right\} \\ &= \varepsilon \left\{ \mathbf{G}(\mathbf{x} - \boldsymbol{\mu}_x)(\mathbf{G}(\mathbf{x} - \boldsymbol{\mu}_x))^T \right\} \\ &= \varepsilon \left\{ \mathbf{G}(\mathbf{x} - \boldsymbol{\mu}_x)(\mathbf{x} - \boldsymbol{\mu}_x)^T \mathbf{G}^T \right\} \\ &= \mathbf{G} \varepsilon \left\{ (\mathbf{x} - \boldsymbol{\mu}_x)(\mathbf{x} - \boldsymbol{\mu}_x)^T \right\} \mathbf{G}^T \\ &= \mathbf{G}\mathbf{C}_x\mathbf{G}^T \end{aligned}$$

The eigenvalues of \mathbf{C}_x forms the diagonal matrix \mathbf{C}_y , while \mathbf{G}^T contains the eigenvectors of \mathbf{C}_x .

$$\mathbf{C}_y = \begin{bmatrix} \lambda_1 & & \mathbf{0} \\ & \ddots & \\ \mathbf{0} & & \lambda_N \end{bmatrix}$$

The eigenvalues are calculated by solving the secular (or characteristic) equation $|\mathbf{C}_x - \lambda\mathbf{I}| = 0$. Note also that $\mathbf{C} = \mathbf{C}^T$. The eigenvalues are arranged such that $\lambda_1 > \lambda_2 > \dots > \lambda_N$ (for convenience). A numerical example for the principal component transformation is given in explicit detail in Appendix C.2.

The components of \mathbf{C}_x may be written as:

$$C_{mn} = \varepsilon \left\{ (x_m - \mu_m)(x_n - \mu_n)^T \right\}$$

For the diagonal components $m = n$:

$$C_{nn} = \varepsilon \left\{ (x_n - \mu_n)^2 \right\}$$

This form makes it clear that the diagonal components represent the variance (Landgrebe (2003, p. 283). As the eigenvalues are arranged in decreasing order, this means that the variances are also arranged in decreasing order as indeed are the eigenvectors. In practice, as the first eigenvector accounts for most of the variation in an image, so too does the first PC (principal component) (i.e. PC1). The variation decreases with increasing component number; \therefore PC1 > PC2 > PC3

The correlation matrix \mathbf{R} is related to the elements of the covariance matrix. If the elements of the correlation matrix and covariance matrix are given by r_{ij} and c_{ij} respectively, then the elements of the correlation matrix are given by:

$$r_{ij} = \frac{c_{ij}}{\sqrt{c_{ii}c_{jj}}}$$

For the diagonal elements $j = i$ we find $r_{ii} = 1$. If a (non-diagonal) element is zero, it means that there is no correlation between the elements (i.e. bands) in the \mathbf{y} vector; we have successfully eliminated all correlation between bands in the original vector \mathbf{x} . This is the essence of the principal component transformation.

The correlation matrix measures the degree of correlation between spectral bands. For instance, consider an image comprised of four pixels and each pixel having two bands (in spectral space). The band data represents a grey level in an image pixel. Next, plot each pixel vector onto 2D spectral space, where the first and second bands lay along the x and y axes respectively. If the four pixel vectors lie in a perfect straight line, then the two bands are perfectly correlated. This means that band two data can be constructed from band one data (and vice-versa) and that the

data of one band (either one) is redundant. This means that if band one of a pixel is bright (or dark), the second band is also bright (or dark). If, graphically, the pixel vectors do not line in a straight line, then a portion of band 1 data will be uncorrelated with band 2 data. Therefore, a bright band 1 pixel may not necessarily have a bright band 2 pixel. If the pixel vectors form a perfect circle, then there is no correlation between band 1 and band 2 data. This means, zero correlation and therefore no relationship exists between band 1 and band 2 data. This means that no relationship exists between the pixels - each are uniquely defined. This means that, if one pixel is bright, it is not possible to predict whether the next pixel is bright or dark (Richards, 2013, p. 165).

In the case where the correlation is high, a population of vectors can be predicted from one vector, so that the number of pixels may be reduced (due to redundant information) in a calculation (e.g. classification).

An interpretation relating to correlations and principal components may be found by studying the sets of PC images shown in Richards (2013, p. 175). For a set of four bands which exhibit low correlation to each other, the PC components show a high degree of variance. When a highly correlated set of four bands were used, the PC components indicate a higher drop off in variance. In other words, the first PC component contains most of the contrast and most of the information. Subsequent components reveal very little additional information (and contrast, therefore appearing quite dark). The eigenvalues (which represent variance and hence contrast) would show a very rapid drop off in this situation, with PC1 containing most of the variance. In the former case, for low correlation between the four bands, the eigenvalue drop-off would be much slower as most PC components contain important information. According to Silleos et al. (2006), PC1 tends to represent albedo (i.e. soil background) and PC2 variations in vegetative cover. However, it is likely to be dependent on the particular dataset being analysed; for example, consider an image of an urban area against a forested area.

Another physical example is presented by Varshney and Arora (2004, p. 128). They used an AVIRIS-based classified image, whose land cover characteristics are well known from ground truth data. A corresponding colour map is found on p. 312 of their book. The cover types include alfalfa, corn, grass, hay, oats, soybeans,

wheat, woods, buildings, roads as well as stone or steel towers. Varshney and Arora (2004, p. 211) displays the first 10 principal components as a set of images. The first image (thereby containing the highest variance) contains large areas of dark and light regions. In fact, the first 4 PC components clearly show boundaries of a number of different cover types. Even the latter PC components 5th to 7th show trees, grass and grass pastures. The last 3 components are noisy, especially the last which contains barely any information.

The rate at which the eigenvalues drop off is an important factor; if most of the variance is contained in PC1 then it could very well be that PC4 contains a lot of noise instead of a latter PC. Therefore, care must be taken when attaching too much physical meaning to the transformed images, as “each band is a linear combination of the original bands” (this also applies to MNF in Section 2.5.4) (Han, Goodenough, Dyk, & Chen, 2004).

For feature reduction, the interest is in using a selected subset of bands from the original spectral dataset. For the PCA transform, there are different choices available to select an ‘appropriate’ number of PC components. One method uses a cumulative variance threshold. As most of the variance is contained in the first few PC bands, a suitable subset of PC bands may be selected for further processing. The approach involves calculating the total cumulative contribution (i.e. variance) for each band and displaying the result in descending order using a table. The number of bands to retain may be selected according to a threshold value. Two commonly selected thresholds for the total cumulative variance are 95% (e.g. E. P. Green, C. D. Clark, et al. (1998), Siljestrom, Moreno, Vikgren, and Caceres (1997), P. S. Thenkabail et al. (2004)) and 99% (Varshney and Arora, 2004, p. 210 & 225, Xiuping, Bor-Chen, and Crawford (2013)).

Table 6 illustrates the process of selecting bands based on the 99% cumulative variance method. The results shown in this table come from Appendix F where a detailed numerical example is given. In this particular case, for a dataset containing 10 spectral bands, 2 PC bands are retained meeting a 95% total cumulative variance threshold and 6 PC bands for a 99% total cumulative variance threshold. The bold highlighted entries in the table correspond to the number of required PC bands (i.e. 2 and 6).

		eigenvalue	cumulative variance	cumulative variance (%)
Band	1	17753.85	17753.85	91.93
Band	2	911.92	18665.77	96.66
Band	3	240.11	18905.88	97.90
Band	4	115.86	19021.75	98.50
Band	5	86.88	19108.63	98.95
Band	6	69.61	19178.24	99.31
Band	7	44.86	19223.10	99.54
Band	8	37.03	19260.13	99.73
Band	9	27.47	19287.60	99.88
Band	10	23.79	19311.39	100.00
	Total	19311.39	189716.35	100.00

Table 6: Example of retaining the first p bands, depending on the threshold value set for the total cumulative variance (%). In this case, 2 or 6 PCA bands would be retained for a 95% or 99% threshold, respectively.

Another method for selecting a subset of PC bands uses a scree test. In this case, the eigenvalues are plotted onto a graph and (visually) examined for any natural breaks where the curve begins to flatten. As discussed earlier in this section, the first eigenvalue contains most of the variance, and so on. Therefore, in a plot the first eigenvalue has the greatest value, followed by the second and so on. The drop off is non-linear. To determine the scree position, Cattell (1966) imagines a ball rolling down from the first eigenvalue position. The point where the ball enters a straight end portion represents the ‘foot of a mountain’ and is called the scree position. The number of factors (i.e. eigenvalues) retained is determined by the scree position – all eigenvalues prior to the scree position are retained (Costello & Osborne, 2005). This method appears to be a popular choice and is often used as a default in statistical packages (along with the Kaiser-Guttman method (discussed next) -(Wilson & Cooper, 2008)). The scree position may be well-defined for strong factors but this may not be the case in practice. As such, there have been critics of the method ((Wilson and Cooper (2008), Costello and Osborne (2005)). In one case, the actual scree position could not be agreed upon when a scree plot was presented to six experienced researchers (Ledesma, Valero-Mora, & Macbeth, 2015). This illustrates that the definition for the scree position given by Cattell (1966) is rather vague.

The third and final method (discussed below) retains eigenvalues > 1.0 . This rule is known as the Kaiser-Guttman rule (Henry F. Kaiser, 1991) and amounts to retaining a sixth to a third of the total number of variables (H. F. Kaiser, 1960). According to the online notes from Harris Geospatial Solutions “*eigenvalues close to 1 are mostly noise*” (Harris Geospatial Solutions, 2019d).

It appears that the makers of ENVI endorse this method for selecting an appropriate number of eigenvalues (further evidence may be found in the next section on MNF). The endorsement by Harris Geospatial Solutions of retaining eigenvalues > 1.0 is somewhat understandable, as it has become the default setting in most statistical software packages (Costello and Osborne (2005), H. F. Kaiser (1986)) and claimed to be mathematically justifiable (H. F. Kaiser (1986), Henry F. Kaiser (1991)); others beg to differ. One such critic (Velicer & Jackson, 1990) found the method to be poorly justified and to be one of the least accurate. Other critics make similar remarks and do not recommend its use (a list of references may be found in Wilson and Cooper (2008)). The continued use is due to ease of implementation. In addition, there is a very high probability that it will lead to incorrect results (Velicer & Jackson, 1990) with consistent overestimation (Wilson & Cooper, 2008).

2.5.4 Maximum Noise Fraction (MNF)

Originally defined as the maximum noise fraction (MNF) by A. A. Green, Berman, Switzer, and Craig (1988), it is also referred to as the minimum noise fraction (Eismann, 2012, p. 518) or indeed even as noise-adjusted principal components in the literature (Richards, 2013, p. 186).

The MNF transforms image data into components which maximises the signal-to-noise ratio. Equivalently, it minimises the noise fraction (Imani & Ghassemian, 2015). The concept is similar to the PC transform but instead of transforming bands into PC components based on maximising variance, the MNF transforms bands with respect to maximising the signal to noise ratio (i.e. minimising noise). As noted by P. Mather, and Brandt, T. (2009, p. 52) “*the MNFs produce components that*

successively maximize the signal-to-noise ratio, just as PCA generates components that successively maximize the variance”.

As with PCA, MNF bands are ordered and the methods of MNF band selections are equivalent. Therefore, the cumulative variance method (Table 6) is applicable here also, as is the Kaiser-Guttman rule and scree test (both described in detail in Section 2.5.3). Again, (as for the PCA) the Harris Geospatial Solutions documentation states that *“bands with large eigenvalues (greater than 1) contain data, and bands with eigenvalues near 1 contain noise”* (Harris Geospatial Harris Geospatial Solutions, 2019c). Therefore, eigenvalues near 1 may be discarded.

The MNF transform of an image results in components that are based on noise quality and is often more suited to airborne data compared to PCA (A. A. Green et al. (1988)). Both transforms (i.e. PCA and MNF) become identical when the noise variance within each band are equal for all bands (A. A. Green et al., 1988).

As with PCA, MNF images may be used directly for classification. The study by Mundt et al. (2005) was concerned with discriminating invasive species using hyperspectral data, and found the producer’s/overall accuracy to be 23%/17% higher when classifying an MNF-reduced image compared to one reduced by PCA. Both images were classified using SAM (Section 2.6.4.3). The producer’s accuracy is the probability that the features in reality (i.e. on the ground) are correctly identified on the classified map, which is produced by the analyst. The overall accuracy expresses the proportion of pixels that were correctly classified (more details are provided in Section 2.7). The study by Mundt et al. (2005) identified mesic hoary cress to a producer’s/overall accuracy of 54%/63% for MNF reduced data together with the SAM classifier.

2.5.5 Separability Measures

The extent to which spectral classes overlap is quantified using separability statistics. Two particularly useful measures commonly used in remote sensing are both the Jeffries-Matusita (JM) distance and the transformed divergence distance measures.

It was found early on in feature selection that both the Bhattacharyya distance and transformed divergence gave superior results over the divergence for average pairwise distances (P. H. Swain, A.G. Wacker, 1971); however, this study neglected any mention of the JM distance. Subsequent work revealed that both the JM distance and the transformed divergence measures were better indicators of classification accuracy than either of the Bhattacharyya and divergence measures (Mausel, Kramber, & Lee, 1990). In addition, both the JM distance and the transformed divergence separability measures yielded similar results (Mausel et al., 1990). However, according to P. H. Swain, R.C. King (1973), the JM distance has a slight edge in predicting the most suitable pairs of classes over the transformed divergence.

Mathematically, the JM distance is defined as

$$J_{ij} = 2\left(1 - e^{-B_{ij}}\right) \quad (2.5.5.1)$$

(Richards, 2013, p. 350)

The JM distance represents an average distance between pairs of normally distributed classes (class i and class j). The JM distance makes use of the Bhattacharyya distance (B_{ij}), given by:

$$B_{ij} = (\boldsymbol{\mu}_i - \boldsymbol{\mu}_j)^T \left\{ \frac{\mathbf{C}_i + \mathbf{C}_j}{2} \right\}^{-1} (\boldsymbol{\mu}_i - \boldsymbol{\mu}_j) + \frac{1}{2} \ln \left\{ \frac{|(\mathbf{C}_i + \mathbf{C}_j)/2|}{|\mathbf{C}_i \mathbf{C}_j|^{1/2}} \right\} \quad (2.5.5.2)$$

(Richards, 2013, p. 350)

The variables of this equation were first defined in Section 2.5.1 and given in more detail in Section 2.5.3.

This relationship between B_{ij} and J_{ij} holds as long as the classes are normally distributed (Landgrebe, 2003, p. 159) – a common assumption made in the context of remote sensing.

It is evident that the first term is connected to the familiar Mahalanobis distance (D_M)- Equation 2.5.1.2 (Section 2.5.1). In fact, Schowengerdt (2007, p. 398) mentions that the first term is (D_M). However, this is not consistent with the definition for both D_M and B_{ij} . The PhD candidate believes the first term to actually be D_M^2 . Nevertheless, the first term contains the Mahalanobis distance. Richards (2013, p. 350) states that “*the first term ... is like the square of the normalised distance between the class means*”. This matches the D_M^2 argument. The second term counteracts the exponential growth in increasing distances between class means (Richards, 2013, p. 350). Canty (2009) gives a more mathematical interpretation for the second term, in that it “*measures the difference between covariance matrices of the two classes*”.

The fact that the Bhattacharyya is linked to the Mahalanobis distance is significant as it incorporates the properties of high dimensional space, as discussed in Section 2.5.1. In addition, both distances are based on multivariate normality (P. M. Mather, and Koch, M., 2011, p. 278).

It is interesting to highlight some of the important properties concerning the Bhattacharyya distance. When $\mathbf{C}_i = \mathbf{C}_j$, the second term reduces to $\ln(1) = 0$.

Therefore, the second term vanishes and $B_{ij} = D_M^2$. Furthermore, if $\mu_1 = \mu_2$ then the first term vanishes. This means that if the mean of both classes are identical (but not necessarily the covariance matrices) then the first term vanishes (i.e. $D_M = 0$). This weakness of the Mahalanobis distance is overcome by the Bhattacharyya distance.

A particularly important property for remote sensing is that as $B_{ij} \rightarrow \infty$ then $J_{ij} \rightarrow 2$ (using Equation (2.5.5.1)). This means that if the distance between spectral class distributions is large, a (maximum) separability of 2 is approached (asymptotic). This implies that the two classes are separable (i.e. the probability of placing a pixel into a class is 100% accurate).

Landgrebe (2003, p. 158) relates the JM distance to the probability of correct classification. In particular, the lower and upper probability bounds for correct classification are represented by the following inequality equation:

$$\frac{1}{16}(2 - J_{ij})^2 \leq P_E \leq \frac{1}{4}(2 - J_{ij}) \quad (2.5.5.3)$$

where P_E is the probability of a classification error ($\therefore 1 - P_E = P_C$ is the probability for a correct classification).⁴ A graphical representation for Equation (2.5.5.3) is displayed in Figure 23.

In practice, the JM distance allows the extent of separability between two classes to be assessed. For a two class density function, a JM distance > 1.9 indicates good separability, while values from 1.0 to 1.9 suggest the two classes are separable to some extent (Treitz & Howarth, 2000). Indeed, Vaiphasa et al. (2005) used the 1.9 separability threshold for mangrove species separability (more details about their work will be given in Section 2.8.1).

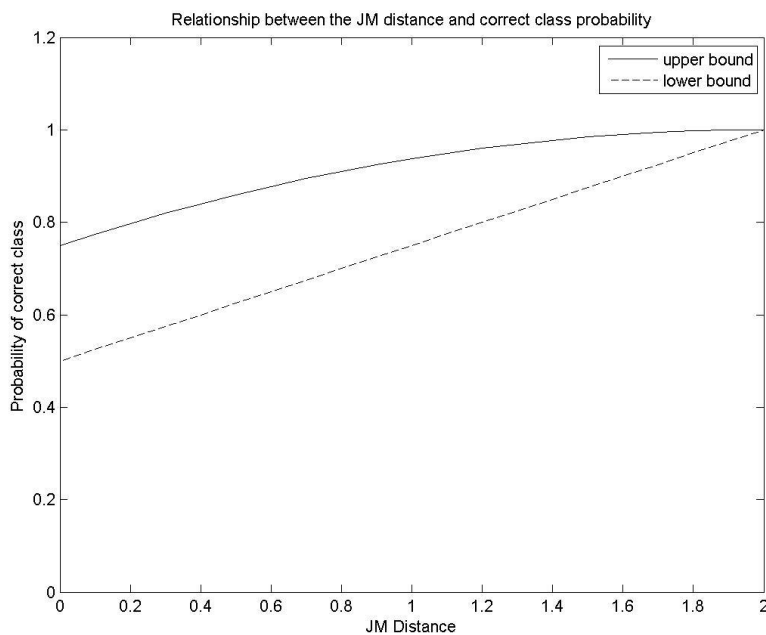


Figure 23: Upper and lower bounds for the probability of correct class classification with JM distance.
(The figure was generated by the PhD candidate and matches Landgrebe (2003, p. 158) Figure 3-33).

⁴ The probability for a correct classification is actually a misnomer. Technically, it is related to the probability of obtaining a correct class. The final classification result may be sound mathematically (i.e. JM distance > 1.9) but it relies on the data given rather than making judgements concerning the real world. Accuracy assessment (Section 2.7) is concerned with assessing the accuracy of the final classification product.

The other common separability distance measure is the transformed divergence distance (d_{ij}^T) and is given by:

$$d_{ij}^T = 2\left(1 - e^{-d_{ij}/8}\right) \quad (2.5.5.4)$$

(Richards, 2013, p. 352)

where,

$$d_{ij} = \frac{1}{2} \text{tr} \left\{ (\mathbf{C}_i - \mathbf{C}_j)(\mathbf{C}_i^{-1} - \mathbf{C}_j^{-1}) \right\} + \frac{1}{2} \text{tr} \left\{ (\mathbf{C}_i^{-1} + \mathbf{C}_j^{-1})(\boldsymbol{\mu}_i - \boldsymbol{\mu}_j)(\boldsymbol{\mu}_i - \boldsymbol{\mu}_j)^T \right\}$$

(the above expression was taken from P. M. Mather, and Koch, M. (2011, p. 277) rather than Richards (2013, p. 348), which is incorrect).

In this form, the transformed divergence is based on the distance between two normal distributions (P. H. Swain, R.C. King, 1973) - a derivation which is given in Richards (2013, p. 347). For our purpose, it highlights the fact that pairs of classes are assumed to be normally distributed for this relationship to hold. It is interesting to note that $d_{ij} = 0$ if both $\boldsymbol{\mu}_i = \boldsymbol{\mu}_j$ and $\mathbf{C}_i = \mathbf{C}_j$. Consequently, $d_{ij}^T = 0$ also (i.e. the classes are assumed to be identical).

In the literature, the value of d_{ij}^T may be scaled by a factor of 1000, giving:⁵

$$d_{ij}^T = 2000\left(1 - e^{-d_{ij}/8}\right) \quad (2.5.5.5)$$

(Yelena M. Gambarova (2010), P. Mather, and Brandt, T. (2009, p. 53), John R. Jensen (1996, p. 220), Mausel et al. (1990)).

Unless otherwise specified, any reference to the transformed divergence distance in this thesis takes the form as specified by Equation (2.5.5.4).

Numerical values given in John R. Jensen (1996, p. 225) provide for an interpretation between the transformed divergence distance and the separability between two classes. It is suggested:⁶

⁵ Interestingly, the PhD candidate was unable to find a similarly scaled JM distance in the literature!

- $d_{ij}^T = 2$ gives excellent separability
- $d_{ij}^T > 1.9$ gives good separability
- $d_{ij}^T < 1.7$ gives poor separability

Wang, Sousa, and Gong (2004) give a similar interpretation for the Bhattacharyya distance, where values > 1.9 give good spectral separability between two classes. A value < 1 indicates poor separability and a value > 1 means that the classes are separable to some extent.

Richards (2013, p. 352) goes further and give actual mathematical equations for the probability of correct classification (P_c), in a similar manner to Equation (2.5.5.3) for the JM distance:

$$P_c < 1 - \frac{1}{8} \left[1 - \frac{1}{2} d_{ij}^T \right]^4 \quad (2.5.5.6)$$

However, the PhD candidate believes this is erroneous and should in fact be:

$$P_c < 1 - \frac{1}{4} \left[1 - \frac{1}{2} d_{ij}^T \right]^4 \quad (2.5.5.7)$$

The reasons are given in Appendix C.3.

A visual representation of Equation (2.5.5.7) is displayed in Figure 24 and gives the “theoretical upper bound”.

The empirical result was obtained using computer-based simulations whereby 2790 sets of second order statistics data were generated from real remote sensing data (P. H. Swain, R.C. King, 1973).

⁶ Note: John R. Jensen (1996) actually states that $d_{ij}^T = 2000$ gives excellent separability, but as stated in this thesis report, we will consider d_{ij}^T in the form of Equation (2.5.5.4) rather than Equation (2.5.5.5), so these values have been scaled accordingly.

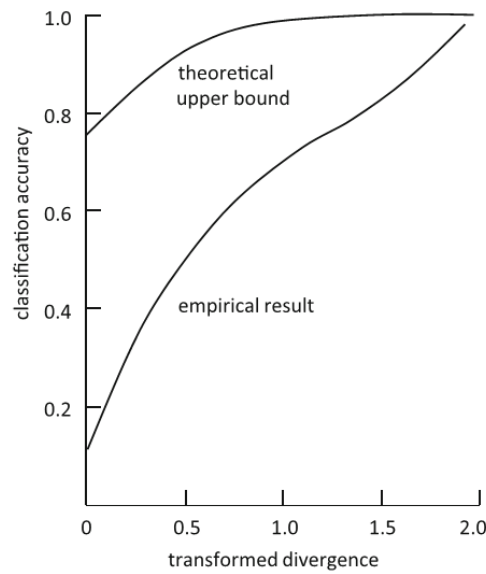


Figure 24: The effect of the transformed divergence on the pairwise probability for correct class identification (taken from Richards (2013, p. 353) figure 10.5).⁷

For a transformed divergence distance approaching 2 for a pair of classes, the probability of those classes being separable approaches 1 (i.e. highly probable). Interestingly, a value of 1.7 is considered poor even though Equation (2.5.5.7) gives a (highly probable) result of 0.9999. Table 7 summarises some of these results.

With the appropriate background completed, some remarks must be made. The divergence measure gives a misleading result for classification probabilities. The introduction of the exponential term overcomes this limitation (i.e. leading to the transformed divergence) (Richards, 2013, p. 351). The transformed divergence and JM distances are very similar (Mausel et al., 1990) but from a computational viewpoint, the transformed divergence is less complex (therefore faster) as there is one less matrix inversion involved (P. H. Swain, R.C. King, 1973).

⁷ Note: Although Richards (2013) used the uncorrected Equation (2.5.5.6) instead of Equation (2.5.5.7), the figure was demonstrated (by the PhD candidate) to be correct. As the empirical result was also shown simultaneously with the theoretical upper bound, it was decided to utilise Richards (2013, p. 353) figure 10.5 for Figure 24 above).

d_{ij}^T	P_c
1.5	0.9990
1.6	0.9996
1.7	0.9999
1.8	1.0000
1.9	1.0000
2.0	1

Table 7: Class separation probabilities as a function of distance.

Both the JM distance and the Transformed Divergence measures are better than Bhattacharyya distance and divergence measures for selecting features relevant for classification (Mausel et al., 1990). The JM distance has the additional advantage over the transformed divergence by having a lower classification accuracy bound as a function of the distance (P. H. Swain, R.C. King, 1973).

Furthermore, for normally distributed data (Thomas *et al.* 2003), the JM distance is more effective than the transformed divergence (Richards, 2013, p. 352) and offers a similar interpretation to the transformed divergence – i.e. > 1.9 indicates good spectral separability between classes, while < 1.0 indicates poor separation (Thomas et al., 2003). This interpretation, as extended to the JM distance, has been used by other researchers (e.g. Schmidt and Skidmore (2003)). Therefore, the class separation probability interpretations of Table 7 for the transformed divergence is applicable to JM distance statistics.

2.5.6 Summary and Discussion

Hyperspace exhibits mathematical properties that exceed our common experiences based on 3 dimensional space. Low dimensionality equations had to be modified in order to be suitable for the analysis of hyperspectral data.

Hughes (1968) showed that there is a limit to classification accuracy, even in the absence of a limit for the number of training data available to the classifier. It has

been further shown that there is an optimal measurement complexity in order to reach a maximum classifier accuracy, which increases as the number of training samples increases. In remote sensing terms, for a set number of training samples, the use of either too few or too much data may not optimally produce the maximum classification accuracy. For instance, in certain situations, multispectral data could result in a higher classification accuracy compared to hyperspectral data. Indeed, the use of too much data is not desired for a classifier. Feature reduction allows data to be optimised (e.g. according to maximum variance), and redundant – highly correlated - data to be eliminated. The selection of a limited set of transformed bands, allows for a more optimal complexity to be reached to increase classification accuracy. If the number of training data were not an issue (but not infinite), then hyperspectral data (containing more bands) will produce an optimal measurement complexity greater than multispectral data is able to produce. Therefore, in theory hyperspectral data is able to produce more accurate classification results providing there is sufficient training data available.

Feature reduction is concerned with reducing redundant (correlated) data and is typically a step taken prior to further processing. In fact, Kaewpijit, Le Moigne, and El-Ghazawi (2003) state that “*conventional classification methods may not be used without dimension reduction pre-processing*” and that “*PCA has been the technique of choice for dimension reduction*”. Whereas PC transforms data based on variance, MNF does so on the basis of noise. Both transforms provide the ability to reduce the quantity of data to be processed (prior to classification) by optimising data to a new transformed domain. Selection of these transformed bands are made on the basis of selecting a subset of eigenvalues. One popular selection method retains the number of transformed bands based on a cumulative variance calculation (e.g. 95% or 99%). The transformation is required to improve classification accuracies in hyperspectral data as it mitigates the Hughes effect. The smaller transformed image has the additional benefit of (vastly) decreasing the amount of computer processing time required during the classification process.

2.6 Classification Techniques

The classification process uses the spectral content of an image for the purpose of categorising pixels into various land cover classes. The land use and land cover classification system is defined by 10 classification criteria, as outlined in J. B. Anderson (1971) (and summarised in J. R. Anderson et al. (1976)):

1. An accuracy of at least 85 - 90% (or more) where the image is used for interpretation.
2. The accuracy of several categories should be similar (subcategories are allowed to be merged into larger categories to meet this condition).
3. The results should be repeatable and time independent (i.e. remote sensing surveys conducted at different times should give comparable results).
4. The classification scheme may introduce more categories as land areas increase, so to make it applicable to extensive regions.
5. Activity-based categories (e.g. grazing of short grass rangeland) should be replaced with vegetative and other cover types (e.g. short grass).
6. Imagery should be taken at a suitable time for classification purposes. For example, remote sensing imagery should be taken under cloud-free conditions. As another example, remote sensing of a snow-covered region is inappropriate when categories of vegetation and/or soil are the target of the classification process.
7. Subcategories need to be effectively used and may be obtained from ground surveys, enhanced remote sensing data or by using a larger scale.
8. The recognition that classification categories (i.e. classes) may be collapsed into a smaller number of categories as needed.
9. It should be possible to compare land use information at future times.
10. The way land is used needs to be recognised in the classification scheme.

The actual process of classification may be performed using the human eye (Section 2.2.1) or by computer, where the classification process relies on algorithms that fall into two broad approaches - supervised and unsupervised (although strictly

there is a third - the hybrid classifier (Campbell & Wynne, 2011, p. 337), which is a combination of each but lies beyond the scope of this thesis).

In broad terms, the classification process is as follows. For both multispectral and (especially) hyperspectral data, feature reduction is often performed prior to classification and is considered a pre-processing technique. It is especially significant to mitigate the Hughes effect; *“using too many bands, too high a dimensional space, can be just as bad as not using enough”* (Landgrebe, 2003, p. 23). Both the PC (Section 2.5.3) and MNF (Section 2.5.4) transform spectral bands into a transformed dataset that is optimised in terms of variance (i.e. PCA) or noise (i.e. MNF). However, the total number of transformed bands remains equal in number to the original image and is (effectively) ordered sequentially in terms of significance. By selecting an appropriate number of (significant) transformed bands, the transformed image is smaller than the original image. This reduction is performed primarily because of the Hughes effect (Section 2.5.2), although additional benefits include a reduction in data storage requirements and faster computer processing speeds. Classification proceeds on this reduced (and transformed) data rather than the original spectral image data.

By means of a simple example, Section 2.6.1 introduces the basic concepts behind using spectral bands for classification. From this, a somewhat simplistic approach leads to the development a VI (Section 2.6.2). It should be noted that VI's make use of a rather limited set of bands and tends to be applied directly to a dataset rather than a transformed dataset. More advanced classifiers (discussed in Sections 2.6.3 and 2.6.4) utilise all wavelengths for classification, potentially leading to the ability to distinguish between more cover types.

2.6.1 Overview

The process of classification aims to produce a map containing different cover types of interest to the analyst. The classification process itself uses algorithms to produce a map whereby each pixel is categorised according to a class. This final classified map is termed a thematic map. The mathematical process is unaware about the meaning of the classes present on a thematic map. It is the analyst who interprets

the classes and assigns cover types on the basis of hyperspectral libraries and/or by using field data.

In this thesis, we are interested in categorising different types of vegetation. Using ground-truth data, classes may be labelled appropriately at low level (e.g. mangrove versus grass) or even at species level (e.g. different species of mangroves).

Using feature-reduced data (e.g. as obtained by PCA), various classification algorithms exist to produce a thematic map. Some of the most common algorithms are discussed in this section.

Figure 25 illustrates how spectra are used to construct a very simple classifier, based upon the work from Richards (2013, p. 89); the figure is copied here for convenience. The top image of Figure 25 defines three regions - water, vegetation and soil. The middle graphs show three spectra, each one corresponding to each cover type (identical to those of Figure 4, p. 27 of Section 2.3.1). Each one of these plots defines a spectral space, corresponding to the spectral samples in the image. Two of the wavelengths (x_1 and x_2) are represented in 2D space (the bottom graph). A suitable selection of x_1 and x_2 allows for sufficient spectral discrimination between the three classes. The bottom graph represents data in feature space, where each point is called a feature. Each grouping of features (represented by the dashed boundary) represents a class (further details are given in Section 2.6.3.1). The position of the boundary is therefore essential in separating classes; the boundary effectively 'decides' the outcome of classes and is termed the decision boundary. In this case, the decision boundary is linear, although other shapes also exist (discussed further in Sections 2.6.4.1 and 2.6.4.2).

For pixels representing vegetation, the ratio of x_2 to x_1 is particularly high (as $x_2 \gg x_1$) and therefore is positioned in the upper left of feature space (the bottom image). For water, the band values are both low, while for soil both values are higher. Hence, by selecting suitable band combinations, the points tend to cluster into different regions in feature space (i.e. classes are separable between different regions). For this reason, classification is also called clustering.

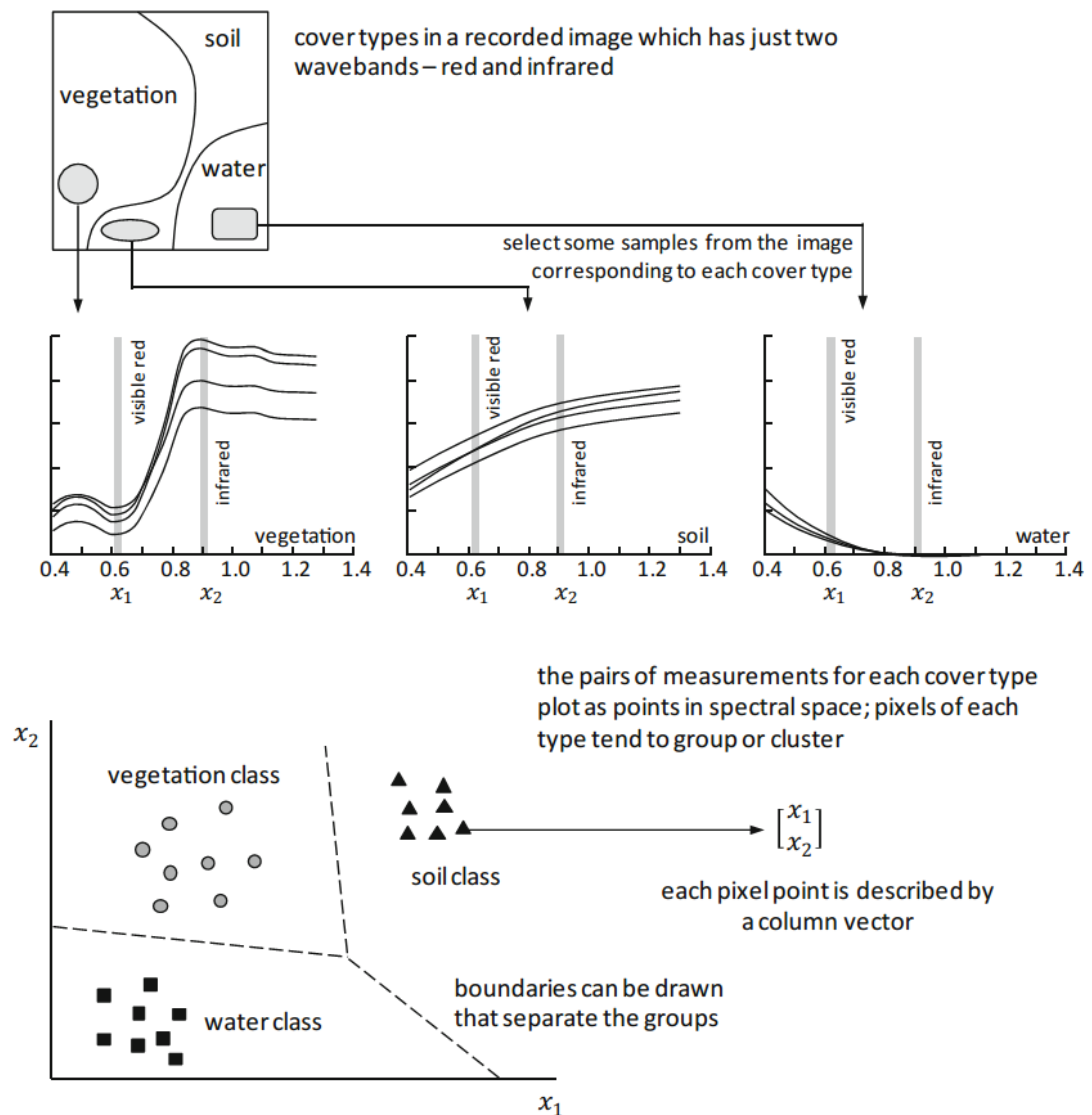


Figure 25: Illustrating the relationship between spectra and classification (Richards, 2013, p. 89).

This simple example separated three different cover types using only two bands – it does not take much imagination to realise the possibilities when more bands are used. Hyperspectral data uses hundreds of bands, thereby allowing for much higher discriminating possibilities in spectral data. This is the motivation behind using hyperspectral imaging. However, we notice that not many bands are actually required in the simple example (above) for feature separation. This is the essence behind feature reduction, as many bands are not required due to data redundancy.

Indeed, before the advent of hyperspectral images, sensors were rather limited and restricted to only sensing a small number of bands. Only two bands are required to identify vegetative land cover and defines a VI (Section 2.6.2).

The classification algorithms are themselves either parametric or non-parametric (although semi-parametric (Canty, 2009, p. 187) is an additional type, which is not discussed here). Parametric models are based on spatial statistics where algorithms assume that classes are normally distributed. Both mean and covariance matrices are estimated using training pixels (Hubert-Moy, Cotonnec, Le Du, Chardin, & Perez, 2001). The number of independent training samples for each class must be at least $n + 1$ for n features, otherwise the covariance matrix will be singular. In practice, these singular situations may arise when using very-high-dimensional data (Benediktsson, Sveinsson, & Amason, 1995). These limitations are overcome using nonparametric approaches, where the model makes no assumption about the distribution of the data (P. M. Mather, and Koch, M., 2011, p. 279).

Figure 26 presents an overview of the classification methods discussed in the remainder of this section and how they are categorised. For example, ML is a parametric (i.e. assumes normally distributed data) supervised (i.e. required training samples) classifier. Details for the ML classifier are found in Section 2.6.4.1.

Prior to hyperspectral remote sensing, the limited number of bands available meant that limited information was available to develop useful products. With the advent of hyperspectral remote sensing, specific wavelengths could be targeted to characterise even more features of interest to the analyst (e.g. biochemical or biophysical (Ustin et al., 2004)).

Despite the many classifiers available to remote sensing, it is not possible to select a 'best' classifier, as it depends on the particular dataset being analysed (Schowengerdt, 2007, p. 427).

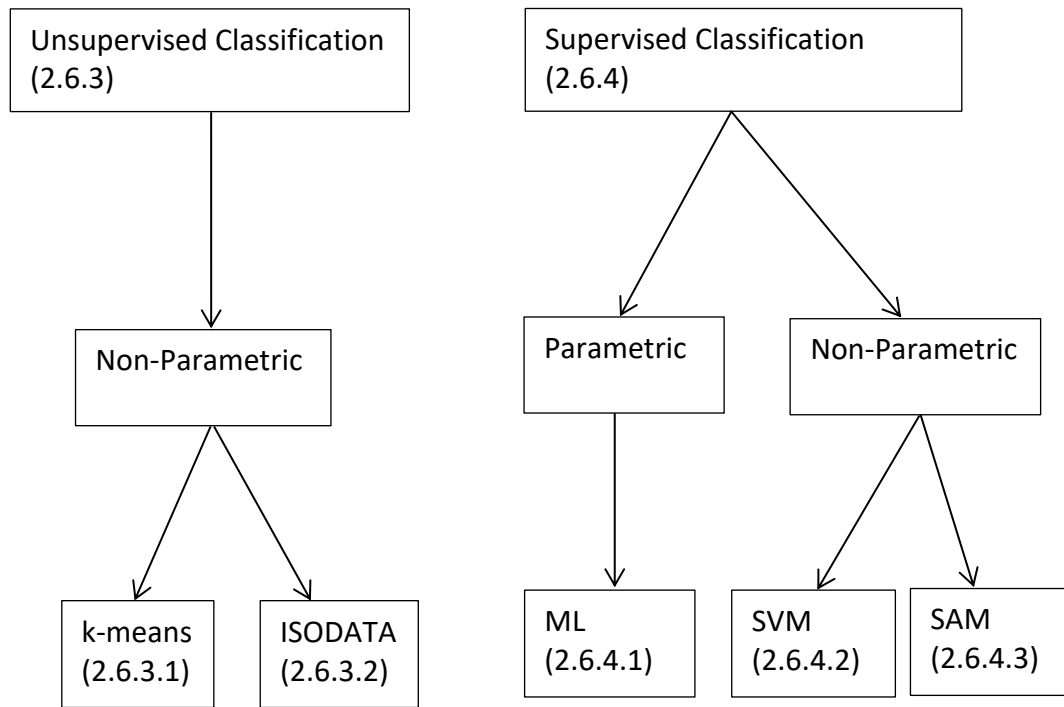


Figure 26: Upcoming classification schemes covered under this section (i.e. Section 2.6). The numbering inside the boxes refer to the Section number containing detailed information.

(Figure 26 was produced using several sources: Xiuping et al. (2013), Moses Azong Cho et al. (2012), Jones (2010, p. 185)).

2.6.2 Vegetation Indices (VI)

The proceeding section discussed a method to differentiate between spectra of three cover types. In this section, a more formal approach is taken in order to develop a quantitative approach to spectrally identify vegetation – a vegetation index (VI). Characteristics of sensors are also discussed in relation to a VI.

To facilitate the discussion, Figure 4 is copied here for convenience (i.e. Figure 27).

To develop a mathematical approach to distinguishing these three spectra, it is useful to introduce the following terminology. The reflectance at wavelengths x_1 and x_2 will be denoted by $R(x_1)$ and $R(x_2)$, respectively. Using a linear function, the gradient (m) between these reflectances is:

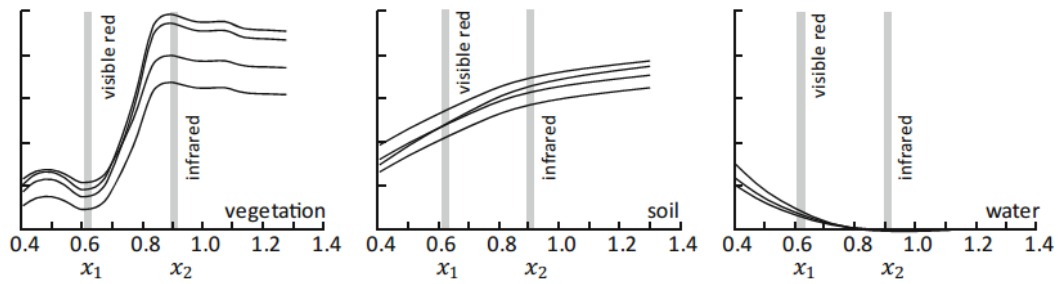


Figure 27: Spectral examples for three different types of cover types: vegetation, soil and water (left to right) (Richards, 2013).

$$m = \frac{R(x_2) - R(x_1)}{x_2 - x_1} \quad (2.6.2.1)$$

The following observations regarding the spectra shown in Figure 27 are summarised in table form.

Cover type	$R(x_1)$	$R(x_2)$	m
Vegetation	small	large	positive (large)
Soil	medium	medium	positive (small)
Water	small	zero	negative

Table 8: Relationship between slope and reflectance for vegetation, soil and water.

By calculating the gradient for each pixel using the process described, pixels having negative gradient values must relate to water spectra. In addition, water may be distinguished from soil and vegetation with high confidence by selecting appropriate (large positive gradient) threshold values. Spectrally, the gradient for water is expected to be always negative, while gradients for soil range from zero to (small) positive values and vegetation from (small positive) gradients onwards.

In practice, for sparsely distributed vegetation, vegetative spectra are strongly affected by soil background (Huete, Jackson, & Post, 1985) and effectively increases the difficulty in separating vegetation from soil background. In addition, the

selection of suitable gradient threshold values are also not transparent (as discussed in more detail in Section 4.5.2).

The wavelengths x_1 and x_2 form just two single points in Equation (2.6.2.1). In the hyperspectral scheme, these correspond to two distinct wavelengths. However, in multispectral sensors, bands cover a range of wavelengths. For example, for the Landsat 1 satellite, the single point $x_1 \approx 0.6 \mu\text{m}$ would be captured by RBV channel 2 while $x_2 \approx 0.9 \mu\text{m}$ would be captured by the 3rd MSS channel (referring back to Table 1, p. 15 of Section 2.2.1). For this reason, the low radiometric resolution of non-hyperspectral sensors lead to VI's that refers to channels rather than individual wavelengths (example: Table 1 in J. R. Jensen et al. (1991)). Therefore, for hyperspectral data, two individual wavelengths are used for Equation (2.6.2.1). In multispectral data, the channel extends over ranges of wavelengths, effectively representing averages when viewed from a continuous (hyperspectral) viewpoint. Therefore, the functions $R(x_1)$ and $R(x_2)$ effectively represent average reflectances. In the hyperspectral scheme, the selection of two wavelengths is sensitive to noise; a small change in one single wavelength can have a large effect on the gradient. By covering numerous wavelengths, an averaging-based approach reduces noise. This approach is developed in Section 4.5.2.

Spectral vegetation indices are affected by factors such as the bidirectional reflectance function (BRDFs) at two or more wavelengths, soil, atmosphere and background litter (Myneni & Asrar, 1994). In addition, the geometry of the remote sensor influences the amount of radiation recorded - *"a nadir-pointing sensor can receive 20 - 30% more reflected radiation from a planophile canopy than from an erectophile canopy"* (Jackson & Huete, 1991). View-angle effects are also considered by Galvão, Roberts, Formaggio, Numata, and Breunig (2009); compared to backscattering, forward scattering increased the overall classification accuracy of soy-bean variety by approximately 20%.

2.6.2.1 Normalised Difference Vegetation Index (NDVI)

Equation Chapter 2 Section 6

The Normalised Difference Vegetation Index (NDVI) is the most popular VI used in remote sensing to characterise vegetation (Prasad S. Thenkabail, Smith, & De Pauw, 2000). It is a transform based on a simple ratio:

$$\text{NDVI} = \frac{\text{NIR} - \text{R}}{\text{NIR} + \text{R}} \quad (2.6.2.1.1)$$

(taken from Satyanarayana, Mohamad, Idris, Mohd-Lokman, and Dahdouh-Geubas (2011)).

Due to this simple form, it is a computationally fast and efficient to produce a vegetative-based map. An even simpler form of a VI is the RVI (Relative Vegetation Index) or SR (Simple Ratio), discussed in Appendix A.1. The NDVI is more popular as it overcomes shortcomings with the RVI.

With reference to Equations (2.6.2.1) and Equation (2.6.2.1.1), $R(x_1) = \text{R}$ and $R(x_2) = \text{NIR}$. The NIR (i.e. x_2) is defined in the near infrared (760 - 900 nm) band and R (i.e. x_1) in the red (630 - 690 nm) bands. Variations exist in the literature for these ranges. For example, Bartholy and Pongracz (2005) state that NIR and R wavelengths cover ranges of 580 - 680 nm and 730 - 1100 nm, respectively. It is (therefore) likely to be defined in accordance to the channel range defined by the (non-hyperspectral) sensor.

Mathematically, the NDVI varies between -1 and 1, as easily demonstrated:

- if $\text{NIR} \gg \text{R}$ then $\text{NDVI} \rightarrow \frac{\text{NIR}}{\text{NIR}} = 1$
- if $\text{R} \gg \text{NIR}$ then $\text{NDVI} \rightarrow \frac{-\text{R}}{\text{R}} = -1$

Therefore: $-1 \leq \text{NDVI} \leq 1$

In addition, the $\text{NDVI} = 0$ when $\text{NIR} = \text{R}$.

Physically, a value of -1 relates to non-vegetative surfaces while 1 represents highly vegetated surfaces (Silleos et al., 2006). This is not hard to understand; for water $(NIR - R) < 0$ and $(NIR + R)$ is always positive. Therefore, $NDVI < 0$. For the soil spectrum, a small positive value results. This is in line with the conclusions summarised in Table 8. A key difference to a 'pure gradient' definition (i.e. Equation (2.6.2.1)) is that the $NIR + R$ term (in the denominator) effectively scales the NDVI to lie between -1 and 1.

In view of these details, the following results are self-explanatory; a value of zero indicates the absence of vegetation while positive values represent a high density of green leaves (Satyanarayana et al., 2011).

For multispectral data, the reflectances amount to being averaged results over wavelengths being defined in the 0.5 – 0.7 μm and 0.7 – 0.9 μm ranges (Carlson & Ripley, 1997). However, the narrowband nature of hyperspectral sensors enables specific wavelengths to be targeted instead, thereby allowing more specific detail to be extracted (Ustin et al., 2004). For example, Haboudane et al. (2004), has defined the NDVI as:

$$NDVI = \frac{(R_{800} - R_{670})}{(R_{800} + R_{670})} \quad (2.6.2.1.2)$$

This means that 800 nm is used for the NIR and 670 nm for R.

Haboudane et al. (2004) applied the work to agricultural crops, while Zarco-Tejada et al. (2001) were interested in chlorophyll content estimation in closed forest forests, and used the following form:

$$NDVI = \frac{(R_{774} - R_{677})}{(R_{774} + R_{677})} \quad (2.6.2.1.3)$$

The choice of wavelengths are dependent on the maximum absorption in the red (due to chlorophyll pigments) and maximum reflection in the infrared (caused by leaf cellular structure) (Haboudane et al., 2004). The fundamental concept behind

the NDVI is unchanged though and the use of these narrowband indices are now termed spectral (vegetation) indices.

In practical terms, the calculation of the NDVI allows for the generation of a vegetative map. The limited number of wavelengths exploited does not, however allow vegetation to be categorised to any great extent. For example, the intensity of NIR reflectances have been used to differentiate deciduous trees (maple) from coniferous trees (pine), as the reflectance from deciduous trees is higher in the NIR compared to coniferous (Lillesand, 2008, p. 14). Therefore, the appropriate selection of wavelengths allows for cover type differentiation simply due to their differences in reflectance intensities.

One of the advantages of the NDVI is that it is relatively insensitive to topological effects (i.e. variation in illumination) (Silleos et al., 2006). However, the NDVI also has a number of well-known shortcomings. For example, the NDVI saturates when the leaf area index (LAI) > 2 (Haboudane et al., 2004) (the LAI was defined in Section 2.3.2, p. 28). This means that the NDVI reaches a maximum value and does not increase with increasing LAI. In effect, the NDVI is unable to yield any more useful information when it is saturated. The NDVI has also been found to be sensitive to; soil effects (Huete, 1988), atmospheric effects (Kaufman & Tanre, 1992) and sun/sensor geometry (Epiphonio & Huete, 1995).

Although the preceding discussion defines the variables R and NIR in terms of reflectances (i.e. Equation (2.6.2.1.1)), the NDVI may also be expressed in terms of radiances, digital number or output voltages of detectors. The flexibility offered by the various units allows the NDVI to be used for satellite, airborne as well as ground-based radiometer data (Jackson & Huete, 1991).

2.6.3 Unsupervised Classification

Unsupervised based-classifiers do not require training data, thereby allowing features to be classified directly from the image. This generally leads to lower classification accuracies compared to supervised methods, particularly when led by experienced human operators with good training data. However, one particular advantage of the unsupervised approach is that it is independent of any human

operator and does not require field data, which thereby reduces the amount of time needed for analysis. A typical strategy uses unsupervised classification on an image to gain an insight into the class distributions present in the data (Richards, 2013, p. 94). It allows a human operator to identify regions requiring closer scrutiny and to plan for field data collection. The spectral data collected is then used to train a supervised classifier, prior to image classification.

As both unsupervised and supervised classification techniques are commonly used, it is of interest to understand the advantages and disadvantages of each. These are listed below in relation to unsupervised classification:

Advantages

- No extensive prior knowledge of the region is required.
- Opportunity for human error is minimized.
- Unique classes are recognized as distinct units.

Disadvantages

- Unsupervised classification identifies spectrally homogeneous classes within the data that do not necessarily correspond to the informational categories that are of interest to the analyst.
- The analyst has limited control over the menu of classes and their specific identities.
- Spectral properties of specific informational classes will change over time.

Campbell and Wynne (2011, p. 340)

The final bullet-point is concerned with vegetative senescence, which was discussed in Section 2.3.2.

In a similar manner, the advantages and disadvantages for supervised classification are given in Section 2.6.4.

The following two sections are concerned with introducing the key concepts behind the two most popular unsupervised classifiers; k-means and ISODATA.

2.6.3.1 The k-means Classifier

At a fundamental level, the basic concept behind this classification technique is the generation of cluster centres (in feature space) and the reassigning of pixel vectors to these cluster centres based on mean and distances.

In a nutshell, the process assigns pixel vectors to a (user) specified number of cluster centres. This number is somewhat arbitrary but 35 iterations was suggested by P. M. Mather, and Koch, M. (2011) in their work. Initially, the position of each cluster centre is arbitrary, although their location must be distinct. Some choices also lead to a faster convergence (Richards, 2013, p. 325). Pixel vectors are the assigned (based on minimum distance) to each cluster centre, and a new cluster centre mean is calculated. The process repeats, in an iterative manner, whereby pixel vectors are reassigned to these new clusters (based on minimum distance). The process stops when the cluster centre means remain unchanged, meaning that no change in position has occurred.

A step-by-step algorithm is found in Richards (2013, p. 322), Landgrebe (2003, p. 165) or indeed just about any remote sensing book. The book by Hartigan (1975) contains an actual FORTRAN program.

A visual representation of the process is useful in gaining an insight into the steps involved. For simplicity, only 2 bands are considered in Figure 28 (i.e. labelled as the x and y coordinates). For hyperspectral data with n bands, clustering takes place in n dimensional space. The space in which clustering takes place is termed feature space (Jones, 2010, p. 86). Each point in feature space is described by a pixel vector, where each component represents a grey level for each spectral band (Equation (2.5.3.1), p. 63 of Section 2.5.3). In the present case (for 2 dimensions)

the vector $\mathbf{x} = \begin{bmatrix} x_1 \\ x_2 \end{bmatrix}$.

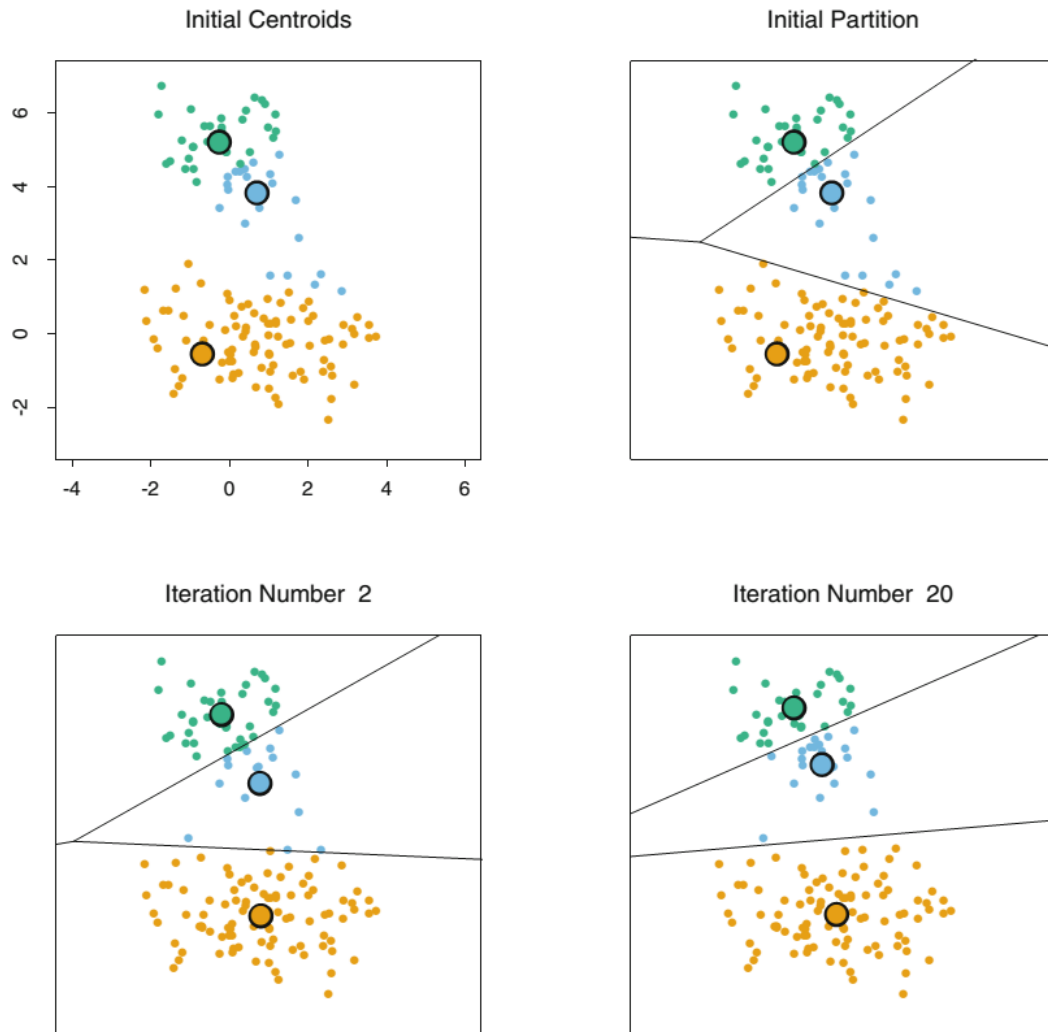


Figure 28: Illustrating the steps involved in the k-means clustering algorithm (source: Hastie, Tibshirani, and Friedman (2009, p. 511)).

The top left illustration in Figure 28 shows the initial calculated cluster centres (three have been specified). They may be assigned randomly, although different methods exist (Richards, 2013, p. 325). Next (top right image), pixels are assigned to the initial cluster centres based on minimising the SSE (sum of squared error distance - Equation (2.6.3.1.1) below). Since these pixels have relocated, a new cluster mean is calculated (bottom left image). Pixels are again assigned to their nearest (new) cluster centre. The process repeats until the SSE is a minimum. In practice, a reasonable maximum number of iterations is specified for an acceptable solution, as the computational process may otherwise exceed a reasonable time frame for convergence.

The distance measure commonly used is the SSE (sum of squared error), defined as:

$$\text{SSE} = \sum_{C_i} \sum_{\mathbf{x} \in C_i} (\mathbf{x} - \boldsymbol{\mu}_i)^T (\mathbf{x} - \boldsymbol{\mu}_i) \quad (2.6.3.1.1)$$

(Richards, 2013, p. 321)

Here, $\mathbf{x} \in C_i$ (i.e. pixel vector \mathbf{x} is assigned to a cluster belonging to class i) and $\boldsymbol{\mu}_i$ the mean vector corresponding to the cluster i .

The inner sum represents the sum of all pixels in the cluster while the outer sum then sums up the result over every cluster. Clustering is considered complete when a small sum is achieved (P. Mather, and Brandt, T., 2009, p. 165).

The SSE distance measure is based on the Euclidean distance:

$$D_E^2 = (\mathbf{x}_i - \boldsymbol{\mu}_j)^2$$

(P. Mather, and Brandt, T., 2009, p. 54)

where \mathbf{x}_i corresponds to the i th pixel vector and $\boldsymbol{\mu}_j$ the mean vector of the j th cluster.

A Euclidean-based distance measure results in clusters which are circular in shape (in 2D or spheroidal in hyperspace P. M. Mather, and Koch, M. (2011, p. 235)) but is the more common measure used in k -means classification. The popularity of the Euclidean distance is due to the simpler mathematical form, thereby increasing processing speed. Despite this, k -means classification remains a very intense computational process. Considering P pixels and C clusters results in a need to calculate $P \times C$ distances. For a really tiny square image of 100 by 100 pixels with 5 classes, this amounts to 50,000 calculations. A 100 x 100 image storing integers (each 2 bytes in size) results in a file size of 20 k bytes. Considering that the PHPA airborne hyperspectral image is 100 GB in size (see Section 3.3), it is no surprise that the classification process takes days to complete.

Although other distance measures exist, the SSE distance measure limits the number of calculations involved compared to (for example) the Mahalanobis distance, which requires the calculation of covariance matrices.

2.6.3.2 ISODATA

ISODATA (Interactive Self-Organising Data Analysis Techniques) builds upon the k -means clustering technique to overcome some of its limitations.

In the k -means method, the user specifies the number of clusters to be used in the process. This number remains constant during the iterative clustering process. In ISODATA clustering, the process extends the k -means method by allowing the number of clusters to change; the user specifies a range instead (a minimum and a maximum). The merging or splitting of clusters is 'decided' by the cluster's standard deviation and distance between cluster centres (P. M. Mather, and Koch, M., 2011, p. 235). The concept is illustrated using Figure 29.

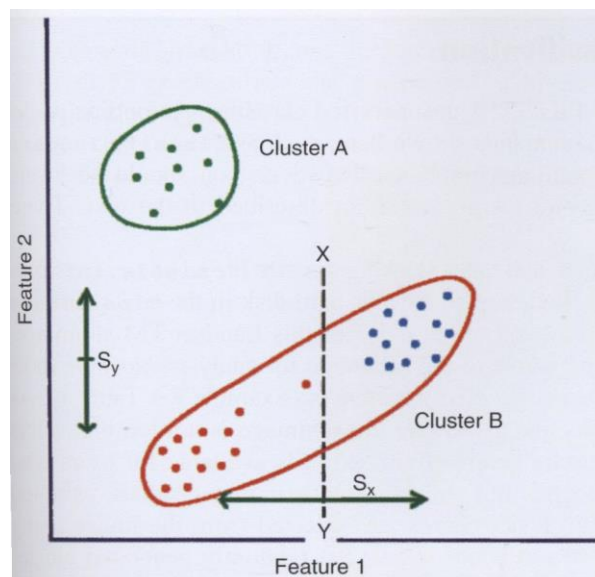


Figure 29: For ISODATA, clusters may be merged or split in feature space according to user defined parameters.
(figure taken from P. M. Mather, and Koch, M. (2011, p. 235), figure 8.7).

If the standard deviation (denoted by S_y and S_x) of a cluster is larger than a user specified value, then clusters are split. If the intercentre distance between clusters

are smaller than a user specified value, then the clusters are merged. The line XY shows a possible position where the large cluster B may be split using a well-defined user value. As for the k -means approach, the process repeats until the interclass mean distances fall below a threshold (P. M. Mather, and Koch, M., 2011, p. 235).

Specific algorithmic steps may be found in Eismann (2012, p. 584) but are not repeated here.

2.6.4 Supervised Classification

The accuracy of a supervised classifier relies on the careful selection of training data, which must be a good representation for each class. Typically, an analyst interacts with a software package to label class training pixels. The computer then uses a supervised classification algorithm to spectrally match the data contained in each pixel with the known training input. For example, in an image containing only vegetation and water, an analyst trains the classifier by selecting a group of pixels representative of water (class 1) and selects another group of pixels for vegetation (class 2). After classification, the final map would (ideally) contain 2 classes, where all pixels are categorised as either water or vegetation.

The selection of training regions, along with the number of pixels in each, must be carefully considered to obtain the best spectral samples to achieve the best possible classification accuracy. The process may therefore introduce a bias by the analyst. For example, selecting training pixels of type 'forest' neglects any difference between forest-types and their state (e.g. health). The analyst, in effect causes a bias in the classification outcome by imposing a structure on the data. There are further complications, as detailed in Campbell and Wynne (2011, p. 350). For instance, by leaving out particular cover types from the classifier, the algorithm may not be able to represent the unknown types, leading to unclassified pixels (Jones, 2010, p. 191).

The actual task of selecting training data is therefore non-trivial and rather time-consuming. There is also the question of how much training data to collect (for each class), as the answer is influenced by the Hughes effect (Section 2.5.2). For

hyperspectral data in particular, there is no simple answer to this question, with a detailed discussion presented in Appendix D.1.

With the many complications introduced by supervised classification, it is perhaps worth pondering if the extra effort is worthwhile, as the actual accuracy for supervised classification is not necessarily higher than unsupervised classification (e.g. E. P. Green, C. D. Clark, et al. (1998), D'Iorio, Jupiter, Cochran, and Potts (2007)). However, one particular advantage gained by using the supervised classifier is that the class identities in a thematic map are known immediately, due to knowing the identities of input training data (Campbell & Wynne, 2011, p. 349). For the thematic map produced by an unsupervised classifier, the class identifies are unknown. However, it could be argued that in both cases, class information had to be established in some manner, whether by field work, photointerpretation or otherwise. The only difference is that the class identities are obtained before (supervised) or after classification (unsupervised).

The accuracy of a classifier is influenced by the actual dataset being mined (Schowengerdt, 2007, p. 427); therefore, it is not known beforehand which classifier will produce the best results.

Of the types of supervised classifiers available, the Spectral Angle Mapper (SAM) and Support Vector Machine (SVM) are very popular choices among remote sensing researchers. However, the reason for choosing a classifier is non-trivial, as the performance is dependent on the data (Schowengerdt, 2007, p. 427). Historically, the Maximum Likelihood (ML) classifier has been particularly popular for use with multispectral data as the number of training samples are manageable (M. A. Cho et al., 2010). However, for hyperspectral data, the large number of training samples required makes the ML classifier unattractive but with feature reduction the problem is somewhat alleviated.

The following three sections outline the key concepts behind the three popular supervised classifiers; maximum likelihood, support vector machine and spectral angle mapper.

2.6.4.1 Maximum Likelihood (ML)

The classification example provided in Figure 25 (p. 83 of Section 2.6.1) explained the relationship between spectral space, feature space and class membership of features. In that particular case, the classes were separated by a linear boundary which worked well for a two band system. However, the addition of another band results in a three dimensional feature space and lines are replaced by planes. For higher dimensional space (in particular for hyperspectral data), planes become hyperplanes.

The maximum likelihood (ML) classifier uses a discriminant function to separate the clusters in feature space using a number of trained spectra representative for each class. The discriminant function allows decision surfaces to take on non-linear shapes; for example, parabolas, ellipses and circles in two dimensions and hypersurfaces in three dimensions (e.g. hyperspheres). The advantage gained by using higher degrees of freedom allows for the construction of actual boundaries, thereby potentially improving classification accuracy.

The actual class samples are selected from the image itself. This process is termed training and involves selecting pixels that are a good representation for the class. The identity of the selected pixels may be based on ground surveys, aerial photography or other reference data (Richards, 2013, p. 92).

The ML classifier assumes that class distributions are normally distributed (thereby making the ML classifier parametric) (Mahesh Pal & Mather, 2006). This allows the Gaussian function to be used as a basis for class discrimination, whose mathematical properties are well understood, even in high dimensional space. Mathematically, the training data is used to estimate both the mean and covariance for each class. Unknown pixels are then assigned to a particular class membership based on maximum likelihood (i.e. probability). Figure 30 illustrates the concept graphically.

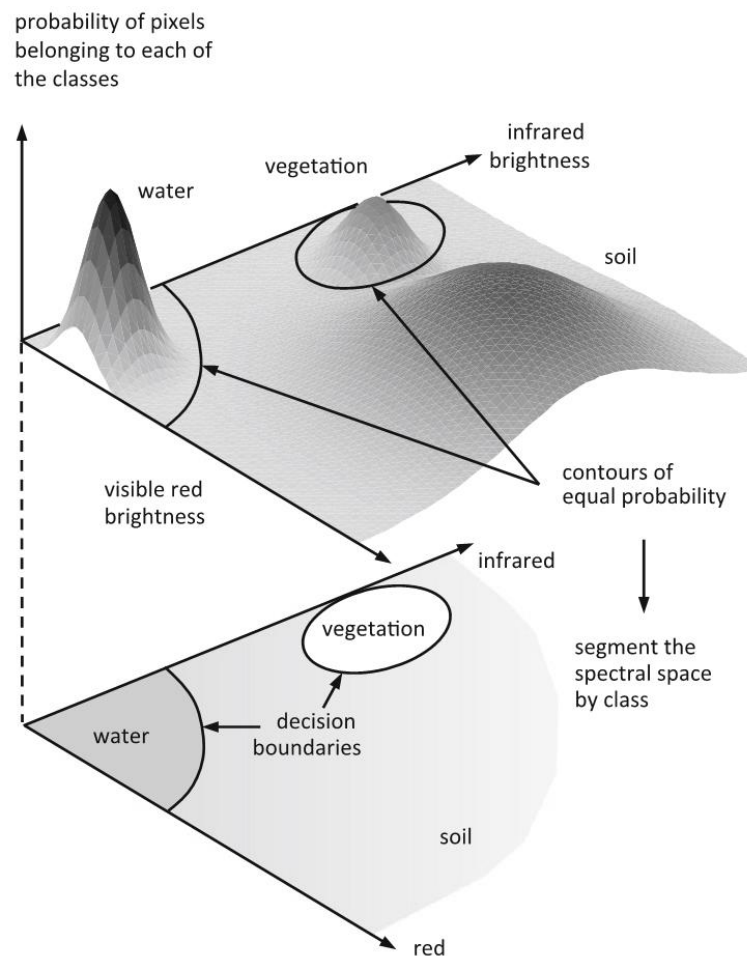


Figure 30: Normal distribution functions are used to determine the probabilities for class identification (taken from Richards (2013, p. 91) Fig 3.6).

In reality, the end-product (i.e. a thematic map) appears not to be overly sensitive to any violations to this assumption (Richards, 2013, p. 90). If the classes are not normally distributed, then the classification results are invalid (Wang, Silván-Cárdenas, & Sousa, 2008).

As discussed in Section 2.5.1, the multidimensional Gaussian function (Equation (E.1.2) of Appendix E.1) must be implemented in this work. The actual mathematical details for the ML classifier are covered in Appendix E.1.

In practice, the ML classifier requires a large number of training samples in order to (accurately) estimate the mean and covariance matrix for each class (P. M. Mather, and Koch, M., 2011, p. 240). Otherwise, the matrix elements are inaccurate, leading to poor classification results. If the number of training samples for each class is less than the dimension of the feature space, then the covariance

matrix does not contain enough entries to be invertible. The ML method of classification is therefore directly linked to the training size to ensure the covariance matrix is not singular.

Hyperspectral data in particular requires a high number of training data. To gain an appreciation of this relationship, consider a hyperspectral dataset with N bands. For hyperspectral data, N is particularly large leading to large covariance matrices (each consisting of $N \times N$ elements). To invert this matrix, at least $N(N+1)$ training samples are required (Richards (2013), p. 255). In practice, the number is higher as pixels are spatially correlated – i.e. pixels are generally not random in their spatial distribution. For example, pixels of a forest are spatially correlated to some extent. The lack of variability between spectral bands between pixels results in a low variance (i.e. covariance matrix). For identical pixels, the covariance matrix must be zero. The correlation between neighbouring pixels is termed spatial autocorrelation (P. M. Mather, and Koch, M., 2011, p. 241). The dependency of the ML classifier on the covariance matrix (Equation (E.1.4) of Appendix E.1) suggests that high spatial autocorrelation leads directly to low classification accuracies. In fact, in general all classifiers are affected; high spatial autocorrelation gives rise to low classification accuracies (P. M. Mather, and Koch, M., 2011, p. 242). One way to reduce the effects of autocorrelation is to randomly select the training data, which increases classification accuracy (Mahesh Pal & Mather, 2006).

Not all classifiers are as sensitive to the requirement of large numbers of training classes. The SVM (Support Vector Machine - the next section) is particularly effective for small training sizes. In addition, compared to SVM, the ML is particularly vulnerable to the Hughes phenomenon (Dalponte, Bruzzone, Vescovo, & Gianelle, 2009).

This section has stated the need of training samples but has not provided an answer to the number required. There is no easy answer to this; further considerations are withheld until Appendix D.1.

2.6.4.2 Support Vector Machine (SVM)

Another popular supervised classification scheme used in remote sensing is the support vector machine (SVM). It has the advantage over ML of requiring a relatively small training set – those being located near the decision boundary (G. M. Foody & Mathur, 2004). In addition, the SVM does not assume classes to be normally distributed (as ML does); in fact, SVM makes no assumptions at all about class distributions (Jones, 2010, p. 191). SVM is particularly effective in separating classes whereby their means are close together (P. S. Thenkabail, Lyon, J. G., and Huete, A., 2011, p. 113).

The theory behind this method is summarised using the treatment of Richards (2013). Let us first simplify the example of Figure 25 (p. 83 of Section 2.6.1) by considering just two classes instead of three. This allows the support vectors to be written in terms of two equations (to illustrate the concept in 2 dimensions).

Some slack is built into the position of the separating hyperplane, thereby allowing classes close to the separating hyperplane to be placed into either class. Hereby, the two additional hyperplanes (shown by dashed lines in Figure 32) run parallel and on either side of the separating hyperplane displayed in Figure 31.

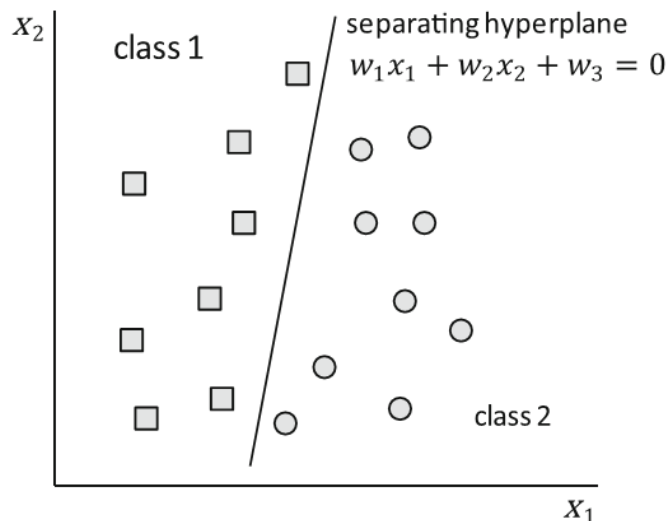


Figure 31: Representation of two classes in 2D spectral space. A line separates the two classes (called a decision boundary). (taken from Richards (2013, p. 275), Fig 8.12).

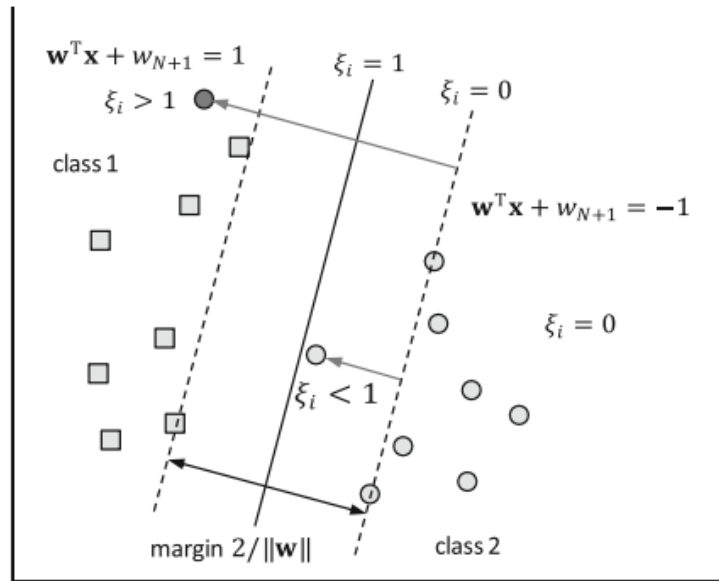


Figure 32: The region between the dashed hyperplanes is termed a margin. (taken from Richards (2013, p. 277), Fig 8.13).

The region between these two hyperplanes (to either side of the separating hyperplane) is termed a margin and training samples defined on the margin are called support vectors).

The aim in this method is to find the position of this line. The mathematical treatment is given in detail in Appendix E.2 but the essence is that it leads to a decision boundary which is able to take on different shapes and is mathematically described by a kernel function. The kernel function then defines the classification surface to use. The ENVI software package defines four kernel functions; linear, polynomial, Gaussian radial function and the sigmoidal function (Canty, 2009, p. 232).

In practice, the SVM is computationally intensive. However, an advantage of this approach is that it only requires training data that are located near the interclass boundaries, thereby potentially greatly reducing the amount of field samples required. This means that the training data needs to be accurate. In addition, the choice of selecting a particular mapping function (i.e. kernel function) is not a trivial one. In fact, it is rather unclear as to which kernel is to be used in the classification scheme. In practice, the Gaussian radial function tends to be used more frequently (P. M. Mather, and Koch, M., 2011, p. 268).

There has been some debate in the remote sensing community about whether the Hughes effect affects SVM. Dalponte et al. (2009) showed that neither SVM nor ML classifiers were significantly affected by the Hughes effect but that the classification accuracy for SVM were superior to ML. However, M. Pal and Foody (2010) found evidence that the SVM was affected by the Hughes effect. In their study, the classification accuracy was assessed for an agricultural site where both DAIS and AVIRIS data were analysed in terms of the number of training set sizes per class (the DAIS is a Digital Airborne Imaging Spectrometer consisting of 79 channels). Combinations of 8, 15, 25, 50, 75 and 100 pixels were used for training. The results suggested that larger training sets are required for larger amounts of features and that 100 pixels per class be selected to obtain good classification accuracy. The work also recommended that feature selection be applied prior to classification.

2.6.4.3 Spectral Angle Mapper (SAM)

The spectral angle mapper (SAM) (or spectral angle mapping) allows spectral similarity to be quantified. It was developed for hyperspectral remote sensing (P. S. Thenkabail, Lyon, J. G., and Huete, A., 2011, p. 110) and is a widely used approach.

Of specific interest in this thesis is the use of SAM to quantitatively assess the spectral similarity of different spectral samples. These include ground reference spectra recorded by the ASD field spectrometer in addition to airborne spectra. The ASD is discussed in detail in Section 4.3.1.

An advantage of SAM is that it accounts for different illumination conditions, a result proven in Appendix E.3. For example, a spectrum obtained in overcast conditions produce the same angular spectral value as for those recorded under sunlit conditions (notwithstanding the spectral effects of shading and illumination on the spectra). It is also insensitive to topographical variations.

Reference spectra may be sourced from laboratory measurements, field spectra or even from the image itself. Typically, they are sourced from a library which is built from field or laboratory measurements. In classification, target pixels are directly compared to reference spectra in the library. A small spectral angle between a target and reference spectrum suggests they are highly similar (or the

same). As the identity of the reference spectrum is known, the (matched) target spectrum identity is therefore also known. However, in practice there are additional complications. For example, in vegetation, the phenology, senescence and health-state of a plant affects the spectral shape (the factors were discussed in Section 2.3.2). It is therefore important to understand the environmental conditions of the vegetation in both reference and target spectra to minimise the spectral differences. For example, minimising differences due to phenology by recording field spectra at the same time as an airborne survey.

Mathematically, the spectral angle is defined in terms of angle θ (in units of radians):

$$\theta = \cos^{-1} \left(\frac{\sum_{i=1}^n r_i t_i}{\left[\sum_{i=1}^n r_i^2 \right]^{1/2} \left[\sum_{i=1}^n t_i^2 \right]^{1/2}} \right) \quad (2.6.4.3.1)$$

Here, r_i is the reference pixel vector and t_i the target (image) pixel vector. The summation extends over n bands.

Two classes are shown in Figure 33 to explain the relationship between the spectral angle and the classification of a pixel vectors. Individual pixel vectors are shown in squares and circles. Although the angle γ changes for each pixel vector (as shown in the left image), a clear boundary exists between each group of vectors. The angle of all vectors represented by squares are larger than the threshold γ^* and less for the circled vectors. Therefore, all vectors where $\gamma > \gamma^*$ are grouped together as class 1, while those where $\gamma < \gamma^*$ are categorised as class 2.

In practice, mean target and reference spectra are used to calculate spectral angles. A maximum angle may also be specified as a threshold value, above the calculated angle to allow for some degree of variability. Angles larger than this maximum leaves unclassified pixels – indeed, ENVI uses this approach (Harris Geospatial Solutions, 2019e).

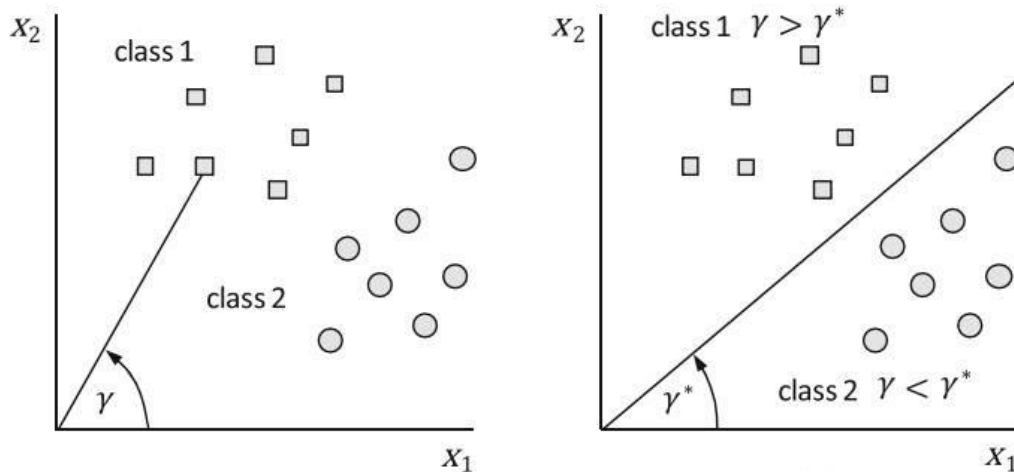


Figure 33: The calculation of spectral angles for pixel vectors positioned in spectral space (left image) are used to partition spectral space into class regions using a threshold (right figure). (both figures were taken from Richards (2013, p. 274), Fig 8.11).

The spectral angle itself is expressed in units of radians and an interpretation is required to appreciate the significance of the equation. Clearly, an angle of 0 rad indicates two identical vectors (i.e. spectra), whereas an angle of $\frac{\pi}{2} \approx 1.57$ rad (i.e. 90°) represents total dissimilarity between the reference and target spectra.

Section 4.4.1 gives several spectral plots to gain an appreciation for spectral angle magnitudes along with their visual counterpart.

2.6.5 Summary to this point

Vegetative indices are effectively basic ratios of two bands, which allows for limited discrimination between vegetative types. They are commonly used in the production of vegetative versus non-vegetative land cover maps.

Recording remote sensing data using more spectral bands and more sophisticated classification methods allows for the production of more detailed maps, consisting of numerous classes. In obtaining such a product, it is not unusual to initially perform unsupervised classification on an image to gain an understanding for the number of classes which may be reasonably discernible in addition to their spatial distribution. The map is called a thematic map.

Two particularly common types of unsupervised classifiers are k-means clustering and ISODATA. A key advantage of ISODATA over k-means is that it allows the analyst to specify a range of classes prior to proceeding with the classification attempt, while k-means allows for just one specific number of classes.

Another classification approach uses training samples, to train the classifier. This form of classification, called supervised classification, uses a library (e.g. hyperspectral library) to match individual pixels to known cover type spectra. Training may also be performed using image data itself. Guidelines provide recommendations as to what constitutes an appropriate number of samples (per class) for training data. Commonly used classifiers are the ML, SVM and SAM. Several studies demonstrate that SVM is particularly effective in classifying hyperspectral data, as it is less sensitive to the Hughes effect and requires a much smaller training set. However, selecting the best kernel function for the classification process is not always clear, nor is the selection of sound training data (i.e. located near the classification boundary).

2.7 Accuracy Assessment

Although mathematically the classification results may appear sound, the real test is in assessing the integrity of the thematic map in practical terms. Practically, this often involves recording class information by ground truthing or photointerpretation (Congalton and Green (1999), Stehman (2001)). However, this assumes that photointerpretation is 100% correct, which is rarely the case (Congalton, 1991). It is also possible to perform the comparisons using existing reputable maps.

In remote sensing, accuracy assessment is commonly performed using an error matrix approach. On a basic level, an error matrix is a square array containing class populations determined from a thematic map and from reference data (e.g. ground truth data). The column entries represent correct (reference) data. The rows contain entries from class populations from a thematic map. As the populations are neatly summarised, it is possible to readily assess the accuracy of a thematic map.

In practice, there are typically discrepancies between thematic class data and reference data.

Whereas off-diagonal entries represent misclassified entries, diagonal entries in an error matrix represent correctly classified classes. The sum of all diagonal matrix entries and dividing by the total number of pixels checked, defines the overall accuracy (OA); the most commonly cited measure in the literature.

When a pixel is misclassified, the error is termed an omission error as the true class (with respect to reference data) has been omitted from the thematic map. For example, a thematic map may show a pixel as belonging to class X when it should be labelled as class Y (according to reference data). In an error matrix, omissions errors (for each class) are calculated by tallying up the column entries (except diagonal entries) and divided by the column totals.

Where an error of omission is viewed with respect to the reference data, an error of commission is from the viewpoint of the thematic map. An error of commission is due to an error caused by the classifier (i.e. incorrectly classified pixels with respect to reference data). In an error matrix, commissions errors (for each class) are calculated by tallying up the row entries (except diagonal entries) and divided by the row totals.

The probability that a selected pixel is classified according to the cover type of interest is called the producer's accuracy, which is the complement of the omission error – i.e. producer's accuracy = (100% - omission error).

The probability of a selected class on a map being present on the ground is called the user's accuracy. It is the complement of commission error – i.e. user's accuracy = 100% - commission error.

The kappa statistic is also derived from the error matrix and measures the performance of true agreement in a classified map in relation to one produced at random.

Further details, along with explicit examples, are covered in Appendix D, which also raises considerations in relation to finding optimal training sample sizes for supervised classifiers.

2.8 Classification in Practice

Remote sensing has been used in many disciplines for land use/cover assessment. The interest in the current thesis lies with the ability to classify vegetation with particular emphasis on mangrove forests.

Classification not only encompasses the mapping of land-cover types at broad categories (e.g. grass versus mangrove) but also at species level and even their state (e.g. health or stressed).

The Port Hedland coastal region contains not only mangrove forests but also grassland regions consisting of sparse vegetation. It is not uncommon to find small shrubs or a tree amongst grass, especially further in from the coast. Therefore, it is necessary to review the literature to examine techniques of classification for forests (both mangrove and non-mangrove) in addition to grasslands (e.g. the African savannah).

2.8.1 Mangrove Forests

The effect on classification accuracy by various methodologies and sources of data were reviewed by E. P. Green, C. D. Clark, et al. (1998). In their study, SPOT XS, Landsat TM and CASI datasets were analysed. A total of five different processing methods were used among the datasets, all situated over the Turks and Caicos Islands. The five methods were:

1. Visual interpretation
2. Vegetation index; in particular the NDVI.
3. Unsupervised classification; using ISODATA (classes merged using field reference data)
4. Supervised classification; where field data or aerial photographs were used as a basis for selecting training data for the ML classifier.
5. PCA and band ratios.

For the fifth method, band ratios were selected according to the actual canopy spectra and physical properties of mangroves. The PC transform was then performed on both bands and band ratios.

The following table summarises the overall classification accuracies for discriminating between mangrove and non-mangroves land covers.

Method	Data source		
	SPOT XP	Landsat TM	CASI
1	35%	42%	71%
2	~50%	57%	~55%
3	57%	~70%	~89%
4	57%	~70%	~94%
5	57%	92%	96%

Table 9: A summary for the overall classification accuracies as obtained from various journal sources for the discrimination between mangroves and non-mangroves (E. P. Green, C. D. Clark, et al., 1998). Note that numbers preceded with an approximation sign (i.e. “~”) were estimated from the graphs in Fig. 3 of E. P. Green, C. D. Clark, et al. (1998).

The low accuracies displayed in Table 9 for SPOT XP data show that no discrimination was possible, likely due to the limited spatial resolution of the sensor. For the Landsat TM data, no significant difference exists between the unsupervised and supervised classification results (methods 3 & 4). Method five (PCA and band ratios) produces the best result, where discrimination between mangroves and non-mangroves were attainable. However, accurate discrimination was not possible for method 1, even by using CASI data. Overall, method 1 (photo-interpretation) produced poor results. Method two (using NDVI) also performed poorly overall. CASI produced impressive accuracies for methods 3 – 5, with method five in particular (96%).

Species level mangrove discrimination was met with limited success using the Landsat TM data. Although it could not accurately classify all nine classes of mangroves (accuracy of 31%), the *Rhizophora* species could be accurately mapped

(77%). However, by defining three classes (*Rhizophora*, 'other' mangrove and non-mangrove), classification accuracies significantly increased (~90% as estimated from Fig. 5 in E. P. Green, C. D. Clark, et al. (1998)). The reason was put down as possibly due to spatial resolution. It was found that CASI could classify nine classes accurately, with method five attaining an overall accuracy of 85%. No significant difference was found for the accuracy between supervised and unsupervised classification, although the user accuracy was higher for supervised classification. Method five produced the highest accuracies (overall and user).

A reduction in the number of classification categories also improved classification accuracy for SPOT (multispectral) data over Waitemata Harbour (New Zealand). Initially, Jay Gao (1998) produced a thematic map comprising of eight categories using the three bands of SPOT multispectral data. These categories were defined as: forest, pasture, mangroves, urban residential, urban industrial, shallow estuary, deep water and mudflats. Although the satellite (i.e. SPOT) data were acquired in May 1988, aerial photographs (taken in June 1994) were used for classification accuracy assessment and for guidance in the selection of training samples. Spectral similarities were found to exist between urban residential regions and sparse mangroves containing mudflats as background. Dense mangroves were also spectrally similar to forest and pasture. As a result, misclassifications arose. Both the ML and minimum distance classifiers were found to realistically represent mangrove distributions. However, the ML was found to more accurately represent dense mangroves and ended up as the classifier of choice. The parallelepiped method was also investigated but the results proved unsatisfactory. In all, it was found that mangroves were classified at 76% accuracy. After defining two categories for mangroves (based on density) and then merging these back together after classification, an accuracy of 81.4% was attained.

More recently, Bhattarai and Giri (2011) examined the distribution of mangrove forests over numerous regions in the western Pacific. The data were comprised of 128 Landsat (ETM+) scenes between 1999 and 2004. As the atmospheric conditions were not available, the data were not atmospherically corrected prior to classification. Three cover types were defined; mangrove, non-mangrove and water. Using the ERDAS image processing software package (Hexagon, 2019), 50 to 150

spectral clusters were defined for ISODATA clustering. The water bodies themselves were classified using supervised classification. To obtain greater accuracy, water bodies and barren lands were removed from regions within mangroves. Classification accuracies were assessed using high resolution satellite data (QuickBird and IKONOS) in addition to existing classified maps, aerial photographs and Google Earth. The overall classification accuracy was 92.5% with producer's and user's accuracies being 93% and 93.9% respectively for mangroves. The Kappa coefficient was 0.90.

A study over southwest Florida by Ramsey and Jensen (1996) concluded that mean leaf reflectances for black and red mangrove were less variable than within each species. The result suggests that species composition would be difficult using satellite data from the Advanced Very High Resolution Radiometer (AVHRR) (a 4 band multispectral satellite (P. S. Thenkabail, Lyon, J. G., and Huete, A., 2011, p. 5)), Landsat TM and SPOT. The conclusion was based on analysing the correlation between satellite channels and field data. The field work collected leaf samples at 19 sites and measuring the reflectances in a laboratory environment within 10 hours of collection. A helicopter was also used to measure upwelling radiance to determine canopy spectra. In total, four mangrove species were of interest; black (*Avicennia germinans L.*), red (*Rhizophora mangle L.*), white (*Laguncularia racemosa*) and buttonwood (*Conocarpus erectus*) – although it was remarked that buttonwood is not strictly a mangrove. At one site, it was found that leaf reflectances between red, black and white mangroves were indistinguishable. Overall, the results suggest that there were no significant spectral differences between the mangrove species studied.

It is the spatial resolution of multispectral satellite-based sensors that are likely to be the limiting factor in the ability to discriminate mangrove species from each other (E. P. Green, C. D. Clark, et al., 1998). By contrast, the 8 band CASI sensor (having a spatial resolution of 1 m) was found to be successful in separating species of mangroves. The limiting success of satellite data were also borne out by the work by Ramsey and Jensen (1996), where two mangrove species were determined to be inseparable. By reducing the number of land cover types, the broader categories

were likely to lead to more successful classification (E. P. Green, C. D. Clark, et al. (1998), Ramsey and Jensen (1996), Bhattarai and Giri (2011)).

Compared to multispectral data, hyperspectral data has the ability to achieve much higher levels of discrimination between mangrove species. For example, red mangroves (*Rhizophora mangle*) were found to be poorly separable from black mangroves (*Avicennia germinans*) by Wang et al. (2004) using IKONOS imagery (IKONOS is a multispectral satellite). The Bhattacharya distance was only 0.66. The mangroves included in their study were the two as indicated in addition to white mangrove (*Laguncularia racemosa*). The study site was located at Punta Galeta (near Panama). However, by using hyperspectral data collected using a Field Spec Pro FR spectrometer, Wang and Sousa (2009) found these mangroves were separable. Spectral means were calculated from 20 sample leaves collected at each mangrove tree (10 each from the upper and lower tree canopies). In all, 30 mangrove trees (for each species) were sampled. Due to the small number of training samples, dependent on the number of bands in the data, ANOVA was used to identify key spectral features, allowing mangrove species to be distinguished. The highly correlated spectral bands were then reduced using LDA (Linear Discriminant Analysis) feature selection and used for classification. ANOVA (Analysis of Variance) is a statistical test, which examines the variation between group means and basically identifies spectral positions where maximum separations exist between mangrove spectra. Like PCA, it is a method commonly used for feature selection. The Mahalanobis distance was used for classification. A total of 6 wavelengths provided the best means to separate between the mangrove species.

Further evidence for the advantages posed by hyperspectral data for species separability comes from Vaiphasa et al. (2005), again under laboratory conditions. In this case, spectra were collected using a FieldSpec Pro FR spectrometer for 16 Thai mangrove species. Some 20 - 30 crown canopy leaves were collected for each species. A one-way ANOVA was used to examine the spectral response for each of the 16 mangroves for spectral differences over all wavelengths. The process identified four essential spectral bands for which the JM distance metric was used to calculate the separability between all 16 mangrove pair combinations. Of the 120 pairs, only 10 had a separability below 1.90 (using JM distance). In particular, the

most spectrally similar members belonged to the *Rhizophoraceae* family, especially *Rhizophora mucronata*.

Koedsin and Vaiphasa (2013) also found difficulties separating species in the *Rhizophoraceae* family. In particular, both species *Rhizophora apiculata* and *Rhizophora mucronata* could not be clearly spectrally separated, either by using laboratory measurements or by using Hyperion data. In total, five different mangrove species were classified in a region over Southern Thailand resulting in accuracies of 92%. Field work samples were selected in accordance with the stratified random sampling method – the stratification achieved by using 15 clusters in the k-mean classifier.⁸ Feature reduction of the 2010 Hyperion (satellite) data were achieved using a genetic search algorithm. Atmospheric correction was performed using ENVI's FLAASH module while classification itself used the SAM classifier.

The difficulty in separating species of *Rhizophoraceae* family (including genera comprising of *Bruguiera*, *Ceriops*, *Kandelia* and *Rhizophora*) have also been documented by others (e.g. Vaiphasa et al. (2005), Koedsin and Vaiphasa (2013) and Prasad and Gnanappazham (2014)). Prasad and Gnanappazham (2014) used 20 piles of freshly picked leaves, with spectra recorded using an ASD FieldSpec 3 spectroradiometer under laboratory conditions for mangroves located in India. According to Prasad and Gnanappazham (2014), the species were separable using statistical parametric methods, in particular the one-way ANOVA. Interestingly, as part of pre-processing, collected spectra were smoothed using a 2nd order Savitzky-Golay filter (filter size 15). However, according to Vaiphasa (2006), the JM distance decreases by applying filters (even of this kind). Both studies covered *Rhizophora apiculata* and *Rhizophora mucronata*, although they were sampled in different regions (Thailand and India). These species are also found in Malaysia. Beh Boon Chun, Jafri, and San (2011) obtained in-field spectra of 4 mangroves species in Malaysia; *Rhizophora apiculata*, *Rhizophora mucronata*, *Acrostichum speciosum* and *Acrostichum aureum*. Again, an ASD spectrometer was used to obtain 10 spectral samples for each species. However, no quantitative analysis was undertaken in

⁸ Stratified random sampling is briefly discussed in Appendix D.1, which contains a comprehensive discussion regarding accuracy assessment.

detailing how these could be spectrally separated – the task was left for further study.

Still in Malaysia, five mangrove species spectra were also recorded using an ASD spectrometer by Kamaruzaman and Kasawani (2007). Once again, 10 spectral readings were taken for each species; *Rhizophora apiculata*, *Bruguiera cylindrical*, *Avicennia alba*, *Heritiera littoralis* and *Hibiscus tiliaceus*. Canonical stepwise discriminant statistical analysis was able to separate between the five species using narrow contiguous bands in the NIR region. However, the spectral reflectances of the species were not (statistically) significantly different.

Tanumi Kumar, Panigrahy, Kumar, and Parihar (2013) found that the NIR bands represented the highest percentage of uncorrelated bands in their mangrove study in the Bhitarkanika coastal region. Using 1998 Hyperion data for Indian mangroves, a total of five mangrove classes were obtained representing pure or mixed spectra of different mangrove species (with one containing a mixture of mangrove and grass). The PC transform was used as a basis to calculate correlations between bands. In all, an image consisting of 56 uncorrelated bands was formed from the original 196 bands and deemed optimal for the purpose of classification. Classes were considered to be spectrally distinct if the JM distance ≥ 1.90 . Using three classification methods, it was found that SVM produced the best result with an overall accuracy of 96.85% and kappa of 0.96. The MD (Maximum Distance) method produced an overall accuracy of 72.81% (and kappa of 0.66), while the SAM classifier gave the poorest result of 70.11% (kappa of 0.64).

In a more recent study by T. Kumar et al. (2019), Hyperion image data were used to classify the mangrove habitats of Henry Island and Lothian Island. Out of the 242 bands, 91 bands were eliminated due to a variety of reasons; overlapping bands between two spectrometers in the VNIR and SWIR regions, uncalibrated bands, high noise level bands, and those affected by water vapour absorption. The FLAASH atmospheric module was used for atmospheric correction. Data dimensionality reduction used the MNF transform, and bands selected on the basis of the cumulative percentage of variance. However, as all MNF bands contained information, all 151 bands were used for classification. The SVM classifier produced seven mangrove classes and had the highest overall classification accuracy at

99.08%. For the other two classifiers, MD (minimum distance) had an overall accuracy of 95.63%, while SAM gave 88.51%. T. Kumar et al. (2019) also found *Avicennia marina* and *Avicennia alba* distinguishable, because their communities formed large homogenous patches. The key aspects to distinguishing these two mangroves relate to *Avicennia alba* having a higher reflectance in the green and NIR bands.

Another study, by Basheer, El Kafrawy, and Mekawy (2019) also demonstrated that the NIR region is key in discriminating mangroves from each other, although differences were also experienced in the blue and red regions. No significant differences were apparent in the green and SWIR regions. Spectral differences were assessed using ANOVA. The data were collected using the ASD spectrometer over ten sites, along the Red Sea region in Egypt. Just two mangroves exist in that region; *Avicennia marina* (black or grey mangrove) and *Rhizophora mucronata* (red mangrove). To obtain a spectral reflectance for each site, an average was taken over five ASD measurements.

Manna and Raychaudhuri (2018) used Sentinel-2 multispectral data over Lothian Island, a region also covered by T. Kumar et al. (2019). The Sentinel-2 has 13 bands with spatial resolutions of 10, 20 and 60 m. The blue, green, red and NIR bands have a resolution of 10 m. A total of 16 land cover types were identified, which also include non-vegetation; sand, bare soil, mudflat and saline blanks⁹. A total of 10 cover types consisted of mangrove assemblage categories. The mangrove forests themselves contain only mangroves, although different species exist within the mangrove assemblages. Therefore, the 10 mangrove classes represent pure species in addition to mangrove assemblages. It is acknowledged that discrimination between mangroves in the NIR region is superior using AVIRIS (hyperspectral) data. Using Sentinel-2 data, the overall accuracy of the SVM classifier was 93.9 %. Although some of the classes represented pure species, the mixed classes consists of three or more mangrove species. Two classes were categorised according to the age of *Avicennia alba*; young and mature. Their work showed that highly resolved

⁹ Saline blanks are formations where vegetated surfaces are transformed into highly saline land areas, and are due to changes in salinity with elevation (Manna & Raychaudhuri, 2018).

spatial Sentinel-2 data is able to distinguish mangroves up to assemblage and species level.

Spectral angle mapping using AVIRIS hyperspectral data demonstrated the feasibility of mangrove forest classification (Hirano et al., 2003). The region under consideration was the Everglades National Park, Florida, USA. Although the results were mixed, the producer's accuracies for mangrove forests (black, red, white) ranged from 73.5 - 95.7%. However, the results were worse for mangrove scrub types ranging from 40 - 48%. The overall producer's accuracy was 65.7 %. ATREM was the atmospheric model of choice. The classification map contained mangroves (black, red, white), three other forest classes, mangrove scrub (black, white, red and a mixture), classes of prairies and marshes, exotics (lather leaf) and non-vegetation including water, beach and mud. The ENVI image processing software package was used for the actual MNF transform in addition to producing a PPI (pixel purity index) image. Noise in the 224 band AVIRIS image was reduced using the MNF transform, which was classified using spectral library for the SAM classification. Accuracy assessment was conducted against a reputable database (the Everglades Vegetation Database) by using 537 stratified random sample points. The Everglades Vegetation Database itself was judged to be approximately 90% correct and was the product of field work and extensive helicopter surveys. Discrepancies between the AVIRIS classified image and the Everglades Vegetation Database were put down to a limitation in spatial resolution, resulting in mixed spectra. It was also suggested that regions having discrepancies require further investigation in the form of field work.

An airborne survey using the AISA+ hyperspectral sensor showed that black mangroves (*Avicennia germinans*) were distinguishable from other plant species (e.g. mixed herbaceous plants) and other cover types (e.g. soil, water), according to a study by Yang et al. (2009). Two separate sites on South Padre Island, Texas, USA were selected for study. The empirical line correction method was used to convert the recorded radiance data to reflectance data. Analysis showed that the blue spectral region appeared rather noisy, which resulted in the elimination of the first 16 bands. In addition, reflectance values for wavelengths greater than 924 nm were removed as they were considered unreliable, leaving a total of 214 of the original 248 bands. The MNF transform further reduced the dataset, leaving 20 bands. The

choice for this selection was based on both the eigenvalue plot and actual visual inspection of the MNF band images in addition to the realisation that eigenvalues near one contain noise. The performance of four classifiers was tested: minimum distance, Mahalanobis distance, ML and SAM. To clarify, in all, four classifiers were used for two sites using both the 214 hyperspectral reflectance image in addition to the 20 MNF band data. Training data were obtained using the actual image itself, with the number of pixels ranging from 540 – 1391 across both sites. Regions of interest defined known cover types. A 10 class and 14 class map were derived for site 1 and 2, respectively. Some cover types were broadly defined, such as “mixed vegetation 1” up to “mixed vegetation 4” and the end product resulted in class merging. This led to a 5 class map for site 1 and 5 classes for site 2. The number of classes remained unchanged whether the map was produced using the 214 band hyperspectral image or the 20 band MNF image. Accuracy assessment was based on assigning 150 points to the classes in a stratified random pattern to each site. For site 1, the SAM classifier produced the lowest accuracy of 84% but ML (and Mahalanobis distance) produced 95% for the classification based on the 214 band hyperspectral image. For the 20 band MNF image, the accuracy of SAM increased to 91% while ML remained unchanged at 95%. For site 2 using the 214 band hyperspectral dataset, the overall accuracy of the SAM, ML and Mahalanobis distance classifiers were 85%, 86% and 91% respectively. For the MNF 20 band image, SAM produced an accuracy of 87% while the ML classifier gave the highest accuracy of 91%. Overall, the ML classifier performed better than the SAM classifier and the MNF 20 band image also produced higher accuracies compared to using the 214 band hyperspectral image. The higher accuracy result for the reduced MNF image (compared to the full image) is in line with the Hughes effect.

Held et al. (2003) classified mangroves using hyperspectral data located at the mouth of the Daintree River in far north Queensland, Australia. Some 25 mangrove species are known to live together in clusters of single species or as ‘mixed complexes’. A 14 band CASI sensor was used at 2.5 m spatial resolution covering a spectral range of 400 – 1000 nm. Field data were collected coincidentally with the CASI overflight using two hand-held spectroradiometers, using an identical spectral range to the CASI. Classification proceeded by masking out all areas of rainforest,

water and sugarcane areas. An overall accuracy of 60.8% was attained using SAM classification. This accuracy was assessed by comparing 930 classification pixels with a map produced by another researcher. It is speculated that sand-dune and mixed *Bruguiera* stands were largely responsible for the low accuracy obtained. Mangrove communities such as those located at the water's edge were clearly distinguishable (e.g. *Rhizophora sp.* and *Ceriops sp.* (being more salt-tolerant)). Radar based data were also used in the study – AIRSAR (National Aeronautics & Space Administration's polarimetric radar) with 10 m spatial resolution. Both CASI and AIRSAR bands were transformed using band ratios and band differences, respectively. The 5 band transformed CASI data were able to correctly classify 57.9% of the mangrove types, while the AIRSAR (also 5 bands) produced an improved result of 71.0%. Data fusion of both data gave the best result of 76.5%. The ML classifier was used in all of these cases.

D'Iorio et al. (2007) compared classification results using three different sources over the island of Molokai, Hawaii. The first source came from an aerial photographic image (1 band at 0.25 m resolution over 400 – 700 nm spectral range), the second was an ASTER multispectral satellite image (14 bands at 15 – 30 m over 520 – 12000 nm range), while the last image was hyperspectral - AVIRIS (224 bands at 17 m over 400 – 2450 nm range). All data were collected in the year 2000. Atmospheric corrections were performed using ACORN v3.12 for the ASTER data, while ATREM was used for the AVIRIS dataset. Pre-processing involved removing wavebands where overcompensation in water absorption occurred, which applies to both ACORN and ATREM. Other wavebands (e.g. CO₂ absorption features) were also removed. The interest in this work was in the identification of the invasive red mangrove *Rhizophora mangle L.*, having been introduced from Florida to Hawaii in 1902. Classification was performed on each of the three datasets using three different approaches: 1) visual interpretation, 2) unsupervised classification using ISODATA, and 3) using SAM. Visual interpretation was performed by two analysts; one who was familiar with the site and the other who wasn't. Both ENVI v3.5 and PCI Geomatics' APEX photogrammetric software were utilised to aid processing. For ISODATA classification, they used 100 iterations with a convergence threshold of 99% in addition to specifying a maximum of 25 classes and a minimum

of 10 pixels per class. For SAM classification, known zones of mangroves were defined using Regions of Interest (ROI's). The mean spectra were then used for SAM training. Classification accuracies were assessed using at least 50 sites per habitat class with points selected using stratified random sampling. The classes were grouped into "mangrove" and "non-mangrove". Accuracies for visual classification ranged from 83.3 - 98.0% and ISODATA from 79.6 - 89.6%. The poorest results were produced by SAM, with accuracies ranging from 65.5 - 72.2%. Therefore, classification using aerial photography gave the best results. However, they suggested that this might be due to the low spatial resolution used. Indeed, the analysis of hyperspectral data with limited spatial resolution led Hirano et al. (2003) to the same conclusion regarding accuracy.

Interestingly, according to J. Gao (1999), it is the spectral resolution that is key to mapping mangroves rather than the spatial resolution. Accuracies of 87.5 - 95% from Landsat TM data were attained compared to 67.5 - 77.5% using SPOT XS data over Waitemata harbour, Auckland, New Zealand. Classification was concerned with separating broad classes (i.e. not at mangrove species level) and was achieved using the ML classifier. Although J. Gao (1999) found the spectral resolution to be the key to mapping mangroves, both D'Iorio et al. (2007) and Wang and Sousa (2009) argue that both high spatial and spectral resolution are important. E. P. Green, C. D. Clark, et al. (1998) drew the same conclusion by highlighting that the airborne CASI sensor allowed for superior spatial and spectra resolution over satellite sensors, thereby increasing classification accuracy.

The NDVI also plays an important role in monitoring mangrove populations. This index is based on band ratios and therefore is affected by the red-edge position. As the state of health of vegetation influences the red-edge position (see Section 2.3.2), the NDVI has the ability to monitor the health of mangrove forests. Furthermore, the NDVI may also be used to monitor canopy density (J. R. Jensen et al., 1991), which is the amount of light able to get through the canopy to the ground. The following paragraphs highlight some of the case studies involving the NDVI.

Mangrove forests on the East Coast Peninsula of Malaysia were environmentally assessed by Satyanarayana et al. (2011). For healthy mangroves (i.e. young, growing

and mature trees), the NDVI ranged from 0.40 - 0.68. On the other hand, the NDVI for environmentally stressed mature forests resulted in lower values with a range of 0.38 - 0.47. The stress was due to sand deposition and or/poor tidal inundation. In their analysis, they used very high resolution (2.4 m) multispectral satellite data (QuickBird). An overall accuracy of 88.3% was achieved using ML supervised classification for land-use/cover classes.

Kovacs, Flores-Verdugo, Wang, and Aspden (2004) confirmed that VI's could successfully monitor degraded mangrove forests - highly disturbed sand resulted in low LAI's. It was found that the SR (simple ratio) was well correlated with the LAI (with the NDVI varying slightly less). The study region was over the Agua Brava Lagoon System of Nayarit (Mexico) using IKONOS satellite data (with 1 m pixel resolution).

Jean-Baptiste and Jensen (2006) used ASTER (Advanced Spaceborne Thermal Emission and Reflection Radiometer) data for predicting mangrove biophysical variables for coastal mangrove vegetation in Haiti and compared their results with the SR, NDVI and SAVI. They found the percentage canopy closure to have a correlation of 0.908 with both NDVI and SAVI and 0.897 with SR. The LAI was most strongly correlated with SR (0.870) but marginally less than both NDVI and SAVI (both having 0.851).

Multispectral studies (e.g. Jay Gao (1998), E. P. Green, C. D. Clark, et al. (1998)) highlight limitations in using multispectral-based data. Although broad category land cover types (e.g. forest versus urban) are achievable at good accuracies, species level classification is unattainable. However, laboratory studies using hyperspectral data (Kamaruzaman and Kasawani (2007), Prasad and Gnanappazham (2014), Vaiphasa et al. (2005)) suggests otherwise. In practice, few studies have been considered for mangrove classification (Held et al. (2003), Hirano et al. (2003), Ramsey and Jensen (1996)). In addition, whereas the ML classifier may be the most effective method for multispectral data (Wang et al. (2008)), the same is not true for hyperspectral data. Mahesh Pal and Mather (2006) have shown the SVM classifier to outperform the ML classifier in their study, but more importantly, the SVM classifier is less sensitive to the Hughes effect. As with multispectral data, hyperspectral data may also be reduced using feature reduction techniques (e.g.

PCA). In fact, for hyperspectral data this is much more justifiable as the Hughes effect shows that the actual classification accuracy may be increased in this manner.

2.8.2 Non-Mangrove Forests

During the past few decades, most studies have tended towards studying coniferous (needle-bearing trees) and deciduous (broad-leaved trees) forests due to the low spatial resolution of satellite data (e.g. Landsat TM) (Ghiyamat & Shafri, 2010). The limited spectral resolution of the sensor limits the ability to discriminate species. For example, Coleman, Gudapati, and Derrington (1990) found that by using Landsat TM data, different pine species (a type of conifer) had similar reflectances and were not separable. The higher spectral resolution of hyperspectral remote sensing offers the potential of discriminating forest vegetation at species level (Ghiyamat & Shafri, 2010) but success is not guaranteed. For instance, although some species of eucalypt were separable using hyperspectral data, not all could be discriminated. The reasons were put down to differences in illumination due to reflected radiation interacting with wet and dry leaves, branches, tree trunks and soil (L. Kumar et al., 2010).

An early investigation into the feasibility of classifying forest species using AVIRIS (hyperspectral data) was conducted by Martin, Newman, Aber, and Congalton (1998). The study site was taken at Harvard Forest in central Massachusetts (USA). Atmospheric effects were removed using ATREM and the 224 hyperspectral bands subsetted into 11 bands using the transformed divergence for feature selection. An ML classifier was used to assign 11 forest categories. An error matrix showed that 123 out of 164 samples were correctly classified (75%) with a Kappa statistic of 0.68. Higher accuracy could be obtained by including more training sites.

Classification accuracies using hyperspectral data does appear to offer improved results compared to multispectral. Goodenough et al. (2003) showed that Hyperion data were able to achieve an overall accuracy of 90.0% in classifying 10 different land cover types - an accuracy of over 80% would exceed most forest inventory systems. In comparison, the overall accuracies for the ALI (Advanced Land Imager - a multispectral sensor) and Landsat ETM+ were 84.8% and 75.0%, respectively. The

study region was conducted over Vancouver Island (Canada). Classification was performed using the MNF transform (for feature reduction) together with the ML classifier.

The classification process for mangrove forests use similar techniques to non-mangrove forests, as expected. According to Dinuls, Erins, Lorencs, Mednieks, and Sinica-Sinavskis (2012), tree species classification is usually performed using semiautomatic methods based on approaches such as maximum likelihood, Bayes, support vector machines and spectral angle mapping.

2.8.3 Savannahs

Savannah ecosystems are characterized by highly varied canopies with different crown shape and heights. Furthermore, the vegetation may consist of different structures that may be open grassland or consisting of dense woody thicket. The open canopy structure in particular exposes soil which scatters radiance (Naidoo *et al.* 2012). Further complications, with respect to spectral characterisation, arise due to the various phenological stages of trees as well as the spectral confusion of trees caused by the grass background. As a result, classification of trees and shrub in these kinds of environments have been particularly challenging (Moses Azong Cho *et al.*, 2012).

However, the feasibility of mapping savanna tree species has been successfully demonstrated for airborne hyperspectral data by Moses Azong Cho *et al.* (2012). Seven common tree species were mapped over the Sabi Sands Reserve and communal lands adjacent to the Kruger National Park, South Africa. As may be expected, trees with larger crowns were classified to a higher accuracy than those with smaller crowns. The ML classifier was used, although the SAM classifier was also considered but rejected as the ML classifier offers the advantage of being able to account for both first and second-order variations in spectral data. Practically, this suggests an improvement quantitatively by accounting for vegetative spectral variability more freely. The 72 band hyperspectral image was classified to an overall accuracy of 65%, arising due to the high spectral confusion between two species. It

was suggested that a non-parametric classifier might perform better for cases of high within-species variability.

Just as for forests, it is both the spectral and spatial resolution of the sensor that is important. In particular, the spatial resolution needs to be able to capture the scale of the lateral variability of a tree canopy (Naidoo *et al.* 2012).

2.8.4 Unmanned Aerial Vehicles

In recent times, the utilisation of Unmanned Aerial Vehicles (UAV's) has grown in popularity. Lu and He (2018) have classified grassland species in a heterogeneous grassland ecosystem using images acquired by a UAV. The data were recorded over the Koffler Scientific Reserve in Southern Ontario, Canada. The UAV operated at an altitude of about 70 m Above Ground Level (AGL) and carried a modified camera consisting of 3 spectral channels, centred in the green, blue and NIR wavelengths. Their results showed that spatial resolutions of 5 and 15 cm allowed for overall classification accuracies around 80%, while at a smaller resolution of 20 cm, the overall accuracy dropped to 73%. Classification was attained using the random forest method in addition to Object-Based Image Analysis (OBIA).

While pixel-based classification methods spectrally analyse each pixel, OBIA segments an image into spectral and spatially homogenous objects (Mahdavi *et al.*, 2018). These objects incorporate geometric features as well as spectral features into the classification process, thereby increasing the accuracy compared to pixel-based classification methods. Kamal and Phinn (2011) also showed higher overall classification accuracies in classifying mangroves in the Brisbane (Australia) region - 76% using OBIA versus 69% using SAM. However, this is disputed by Duro, Franklin, and Dubé (2012), as many comparisons are made using simple classification algorithms (e.g. K-NN). For instance, the study by Kamal and Phinn (2011) used SAM as their supervised classification method and compared the result against OBIA. When modern supervised algorithms are used to compare between object-based and pixel-based classifications, Duro *et al.* (2012) demonstrates no significant difference in overall classification accuracy. While pixel-based classifications are quicker to produce, object-based classifications offer a generalised visual

appearance closer in perception to those of human analysts. However, by using additional processing of pixel-based imagery, either pre or post classification, similar generalised land cover patterns can be produced to the object-based classification result.

One characteristic of OBIA is that classification rule sets are transferrable to similar sites with minimal impact to training data (Laliberte, Goforth, Steele, & Rango, 2011).

Data acquired from UAV's have demonstrated the ability to derive canopy heights. Zarco-Tejada, Diaz-Varela, Angileri, and Loudjani (2014) used track overlaps (over 80%) to derive a digital surface model (DSM) with accuracies comparable to LiDAR-based systems. Data were recorded at 4.5 cm pixel⁻¹ spatial resolution using a modified Panasonic Lumix DMC-GF1 camera, with the sensor operating at 200 m AGL. The UAV operated completely autonomously along pre-defined flight plans over an olive orchard in Alcolea, Cordoba, southern Spain. Field data were also obtained for tree height validation. A 5 cm pixel⁻¹ resolution surface model was generated and compared to those at 20, 25, 30, 35, 40 and 50 cm pixel⁻¹ image resolutions. The Digital Elevation Map (DEM) data obtained using 5 cm resolution data had errors comparable to LiDAR, while degradation was particularly evident at image resolutions smaller than 35 cm pixel⁻¹. A different approach, compared to terrain mapping, uses stereo vision and is capable of attaining higher accuracies than LiDAR (Stefanik, Gassaway, Kochersberger, & Abbott, 2011).

Cao et al. (2018) recorded image data at 2 cm spatial resolution from a UAV carrying a hyperspectral UHD 185 sensor consisting of 138 bands, although only 125 of these were utilised, covering a spectral range of 450 – 998 nm at 4 nm resolution. Tree heights were obtained using UAV-derived DSM data. The purpose was to classify mangroves at the Qi'ao Island mangrove nature reserve, in Guangdong Province, China. The UAV was flown at 80 m AGL and recorded spectra at a spatial resolution of 2 cm. The overall mean spectral profiles of the mangroves proved highly similar, with considerable spectral overlap between different species, although notable differences exist in the 550 nm and NIR regions. Classification incorporated OBIA, while feature reduction was performed using the classification and regression tree (CART) method. The UAV hyperspectral image was resampled

into 15 cm, 30 cm and 50 cm spatial resolutions, with classification results compared. The 15 cm resolution produced the best result, with an overall classification accuracy of 89.55%, attained using the SVM classifier with the incorporation of tree height information. Their work demonstrated that the UAV hyperspectral image improves classification accuracy, while the DSM data increases the capability for mangrove species to be differentiated. The use of DEM data also improves classification accuracy in other studies (e.g. Q. S. Li, Wong, and Fung (2017)).

It is important to note that UAV acquired images require radiometric and geometric correction (Hruska, Mitchell, Anderson, & Glenn, 2012). Furthermore, there are a number of operational difficulties concerned with UAV, as outlined in Hardin and Jensen (2011). These include: limited flight times; typically extending over a few hours, thereby limiting flight ranges. There are additional considerations; such as atmospheric thermals and wind buffeting causing platform instabilities, thereby introducing complex angular and georeferencing problems, potentially rendering multiple images worthless. For this reason, flight sorties are often conducted during the early morning when air is expected to be more stable; however, early mornings leads to long shadows, potentially introducing further problems.

2.8.5 Summary and Discussion

Similar techniques have been used in multispectral-based remote sensing for classifying vegetation in general. These fundamental processes also apply to hyperspectral remote sensing, including accuracy assessment.

For mangrove forests in particular, higher levels of discrimination is possible for hyperspectral data, compared to multispectral. In particular, laboratory work suggest that classification at species level is attainable using hyperspectral data. One approach found several mangrove species separable, using ANOVA to identify key spectral differences between mangrove species and LDA for feature reduction and classification.

With the advent of modern computer systems, high spatial and spectral information are able to be recorded (e.g. by an airborne sensor) and processed in a timely manner to produce useful products (e.g. thematic maps). Standard remote sensing approaches for data extraction include feature reduction (e.g. PCA, MNF), unsupervised classification (e.g. k-means, ISODATA), supervised classification (e.g. ML, SVM, SAM) and are applicable to classifying vegetation, ranging from dense forests (e.g. mangrove and non-mangrove) to savannahs.

The many successful classification studies by researchers, using remotely sensed data, provides encouragement that the airborne Port Hedland data may be classified using similar approaches.

2.9 Hyperspectral Data Mining Paradigm

One paradigm for hyperspectral data mining is outlined by P. S. Thenkabail, Lyon, J. G., and Huete, A. (2011, p. 96). The involved steps are:

1. Feature selection/extraction
2. Information extraction
3. Estimated information (map, table).

Step 1 was further split into two streams: unsupervised and supervised approaches. Unsupervised methods of feature selection/extraction included PCA, MNF and ICA (independent component analysis – not discussed in this thesis) to reduce the dimensionality of the data. Divergence measures such as JM distances are commonly used for cluster analysis (unsupervised) or selecting the best discrimination of features in training data (supervised). Similarity measures include correlations to measure similarity between spectral bands. Spatial autocorrelation is also used as a criterion for band selection as it measures the information content of a band.

Step 2 includes unsupervised classification methods, such as clustering (e.g. k-means, ISODATA) and supervised methods such as SAM and SVM (although there are more).

Step 3 involves accuracy assessment of the product (i.e. thematic map). The error matrix approach and Kappa coefficient are commonly used approaches.

A similar paradigm may be found on page 223 of Varshney and Arora (2004). Water absorption and noisy bands were first removed from the hyperspectral data, after which feature extraction takes place (e.g. PCA). This is followed by a "Ranking Criterion". For PCA, this relates to ranking the variance of the bands, followed by "Feature Selection", where the first M transformed bands are selected (M being based on the cut-off criteria, e.g. 99% cumulative variance threshold). Classification then proceeds using this reduced dataset (e.g. using k-means; although the paper details an ICAMM algorithm which also involves k-means - ICAMM is an ICA mixture model).

Belluco et al. (2006) used a number of methods in mapping salt-marsh vegetation using multi and hyper spectral data:

- K-means classifier with 50 classes (then merged classes depending on site knowledge or spectral separation)
- SAM with pixels that were averaged spectra within training sets.
- SAM applied to full number of bands.
- ML classification on the reduced dataset (using first 4 MNF bands), because of the Hughes effect.
- PCA was also used prior to ML classification (first 4 bands).
- The Bhattacharyya distance was also for feature reduction prior to ML classification (again using 4 bands).
- Atmospheric correction was performed using ATCOR.
- Classification proceeded on several different sources of data over the same region, with the results subsequently compared.

2.10 Main Point Summary

The high number of bands recorded by hyperspectral sensors allow for more detailed environmental assessment compared to previous approaches. Processing techniques used in multispectral remote sensing also apply to hyperspectral remote sensing, although there are additional considerations such as the Hughes effect and the increased sensitivity to atmospheric effects.

The characteristic red-edge in spectra is what identifies vegetation. A shift in position can be used to monitor stress. The NIR spectral region is particularly significant in vegetation, and is affected by the density of leaf layers, nutrient content, senescence, and water content. Even with the high fidelity of hyperspectral data vegetative spectra may appear very similar to each other. A study showed that the variation in spectra belonging to different species may exhibit a higher degree of similarity compared to the spectra belonging to the same species.

To mitigate the Hughes effect, feature reduction is required. The commonly used approaches are the PCA and MNF. The reduced transformed image, is classified using unsupervised classification to gain an understanding of the spatial class structures present. These classes are then statistically assessed to determine the extent of spectral separation, using separability statistics (e.g. the JM distance).

A supervised classification approach usually follows the preliminary unsupervised result and generally produces higher accuracies.

Accuracy assessment is typically performed as a post-classification process, whereby an error matrix is used to record comparison statistics between image classes and known results (e.g. from previous map data, or a field survey). If the overall accuracy is over 85% (with no class less than 70%), then the map is considered to be of practical use. The details are covered in further detail in Appendix D.1.

A range of different classification techniques are available but similar approaches exist between different types of forests and rangelands.

3 Study Region and Image Acquisition

3.1 Introduction

A map is introduced in Section 3.2 which shows the location of Port Hedland in relation to Western Australia. This sets the scene for a discussion of the climatic conditions vegetation, in particular mangrove forests, must endure. The final section (Section 3.3) contains a technical discussion related to the hyperspectral image acquisition.

3.2 Study Region

The town of Port Hedland is located in the Pilbara region of Western Australia at approximately $20^{\circ}18'42''\text{S}$ and $118^{\circ}34'52''\text{E}$ (see Figure 34).

The Port Hedland coastal region contains five zones of particular interest for PhD field-related work, as defined on the following map (Figure 35). These regions are located on either PHPA or public land and physically accessible.

The zone directly to the north of Lumsden Point belongs to BHP and is (effectively) inaccessible without the necessary paperwork and inductions. Finucane Island actually encompasses Utah and connects to the mainland by means of a causeway (labelled in Figure 35). The Utah region contains stockpiles of ore, along with berthing facilities to load ships with ore products. To the north of Utah are additional stockpile areas (as clearly indicated in Figure 36 (left image)). Lumsden Point contains a large dredge-dam and an urban industrial area directly to the south. Redbank contains a light industrial area in addition to a small urban residential region. Both Lumsden Point and Redbank are directly accessible due to the road network already in place. Pretty Pool lies north of the salt stockpiles (shown in Figure 36 (right image)) and to the east of urban residential settlement.



Figure 34: Location of Port Hedland in Western Australia (as indicated by the large black arrow). (the map was obtained from the image “Western Australia” (RealAustraliaTravel, 2014)).

From a global perspective, the mangrove forests lie adjacent to the sea and surround the river estuaries. A total of seven mangrove species are known to exist in the Port Hedland coastal region; *Aegialitis annulata*, *Aegiceras corniculatum*, *Avicennia marina*, *Bruguiera exaristata*, *Ceriops australis*, *Osbornia octodonta*, and *Rhizophora stylosa*. Finucane Island is unique in having all seven species.

The Port Hedland harbour is currently managed by the Pilbara Ports Authority (PPA) but prior to amalgamating with the Dampier Port Authority (on the 1st of July 2014), it was managed by the Port Hedland Port Authority (PHPA). The amalgamation occurred while this thesis was well underway.

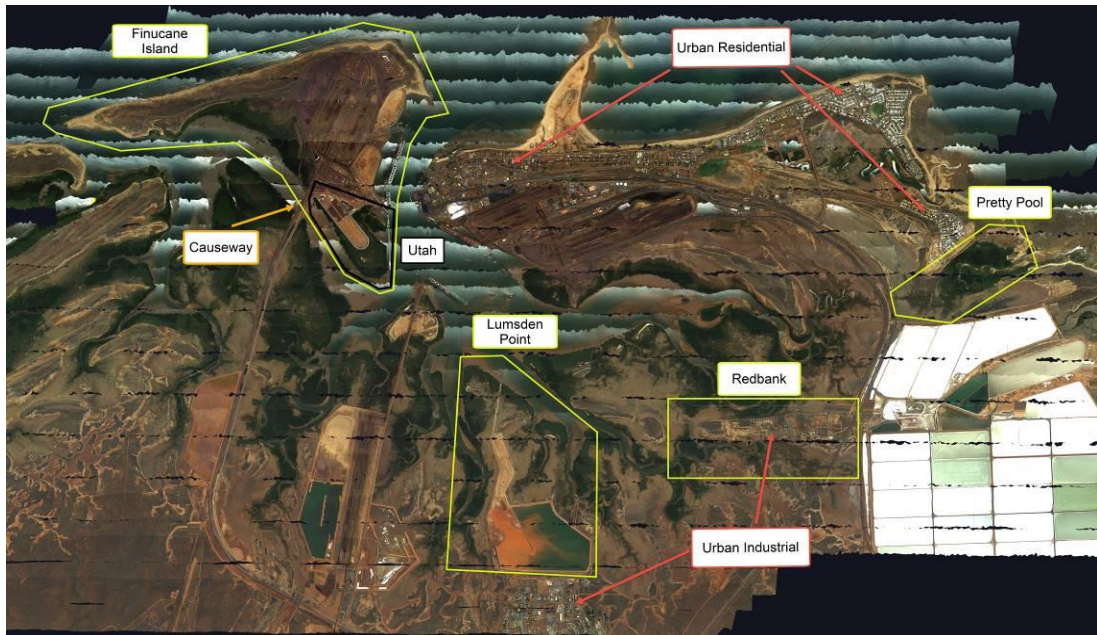


Figure 35: The five key regions for spectral data sampling in the Port Hedland coastal region.

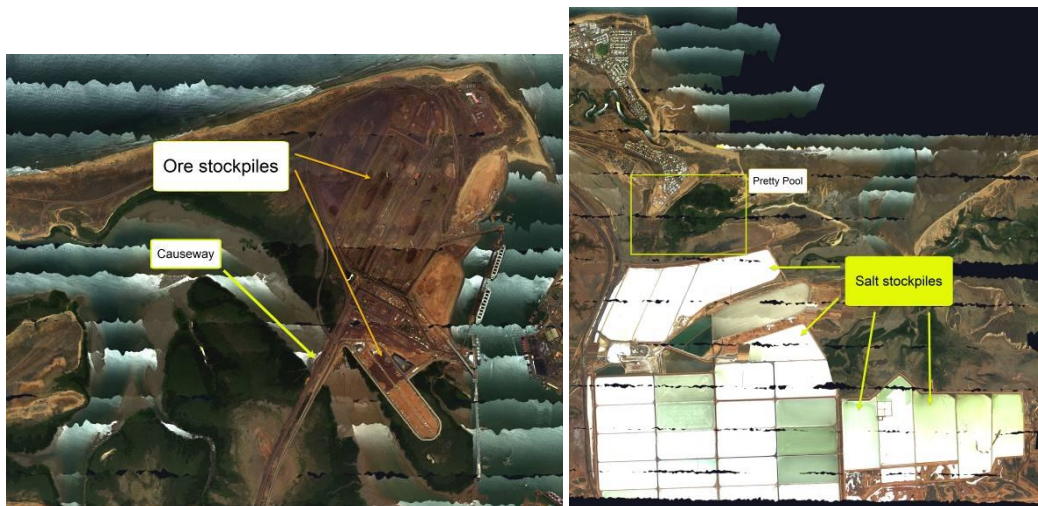


Figure 36: Location of ore stockpiles on Finucane Island (left image) and salt stockpiles in the eastern region of Port Hedland (right image).

As the PPA is responsible for other sites besides Port Hedland, the acronym PPHA is maintained to emphasise the role of the PPA Port Hedland division in this thesis. For instance, the image recorded during the Port Hedland hyperspectral survey is referred to as the PPHA image, rather than the PPA image.

The Port Hedland harbour is the largest in the world by bulk export tonnage, exporting significant quantities of iron-ore, comprising some 98.3% of all tonnage (Pilbara Ports Authority, 2019).

The economic success of the resources industry in Western Australia led to port expansions but at a cost to native mangrove populations. some 302.1 ha of 2676 ha having been disturbed (i.e. 11.3%) since 1963 (Port Hedland Port Authority, n.d., p. 66).

The recent expansion of the South West Creek region (Figure 37) has resulted in the addition of eight shipping berths, conducted in two phases.

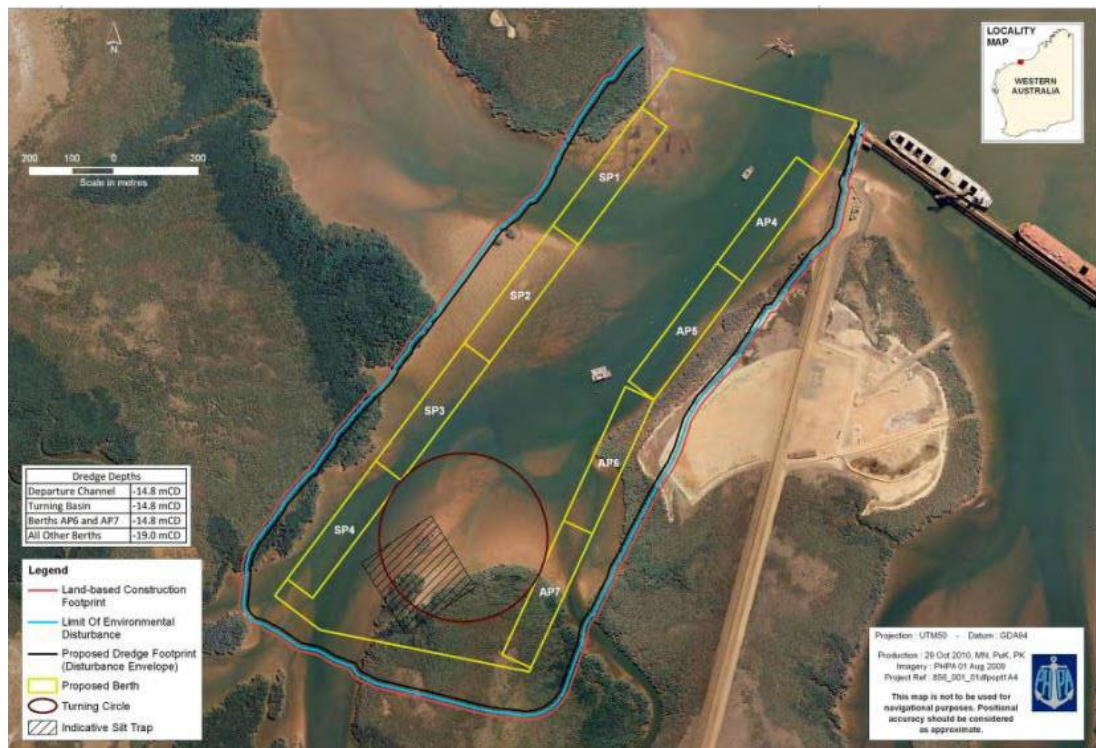


Figure 37: South West Creek region - Utah is located at the top-centre. (Port Hedland Port Authority, 2011, p. 9).

Dredging occurred over two phases. The first phase from 17 May 2011 to 28 May 2012, with the second dredging phase from 11 Feb 2014 to 2 April 2014 (Pilbara Ports Authority, 2016, p. 3). The impact to the health of mangroves were mandated by a Ministerial Statement 859, resulting in WorleyParsons (<https://www.worleyparsons.com>) conducting health surveys in a series over eight impact sites along with three reference sites (Pilbara Ports Authority, 2016, p. 4). Some 12 months after the completion of the dredging project, a study concluded that dredging activities caused no significant impact to mangrove health in the study areas (Pilbara Ports Authority, 2016, p. 24).

Careful planning also resulted in minimising mangrove impacts; for example, using suitable berth layouts. However, despite the best of intentions, the loss of 40 ha could not be avoided. This brings the total loss of mangroves, since 1963, to 342 ha or a cumulative loss of 12.8%. The 40 ha loss represents only 1.5% “highly unlikely to represent a significant loss in terms of overall contribution to primary productivity and ecological function of the area in the context of the local assessment unit, or the region as a whole” (Port Hedland Port Authority, 2011, p. 13).

The acceptance of further loss of mangroves (since 1963) in future harbour expansions is unlikely without re-propagation, which involves replicating “the habitat, vegetation structure, vegetation composition and ecological composition of mangrove communities” (Port Hedland Port Authority, n.d., p. 66).

Man’s harbour activities also lead to the emission of dust particulates. These affect not only mangroves but also the health of people where particle sizes of diameter 10 µm or smaller cause respiratory problems (Pilbara Ports Authority, n.d., p. 7). In particular, iron oxide particles make up 93% of total dust. As mentioned in Section 2.1, iron-ore dust affects mangroves to different degrees, with *Avicennia marina* being particularly sensitive. These mangroves are in poorer health but extend over a small spatial scale (< 50 m) (E. Paling et al., 2001).

Port Hedland experiences very hot summers from December to March with a mean maximum temperature of approximately 36°C (long term average). Temperatures over 35°C are common during summer and even exceed 40°C some of the time. The winter season runs from June to September with a mean temperature of 29°C. Rainfall occurs mostly during summer, with the highest mean of 96.5 mm occurring in February. Winters tend to be dry, with August, September and October having mean rainfall of 4.7 mm, 1.2 mm and 0.9 mm, respectively (Weatherzone, 2017).

The following climate graph (Figure 38) highlights the extreme conditions experienced at Port Hedland.

Apart from extremely hot summers, Port Hedland may also experience cyclones over the summer period (Bureau of Meteorology, 2015). These have a direct impact on coastal mangrove populations, with *Rhizophora* being much more affected by

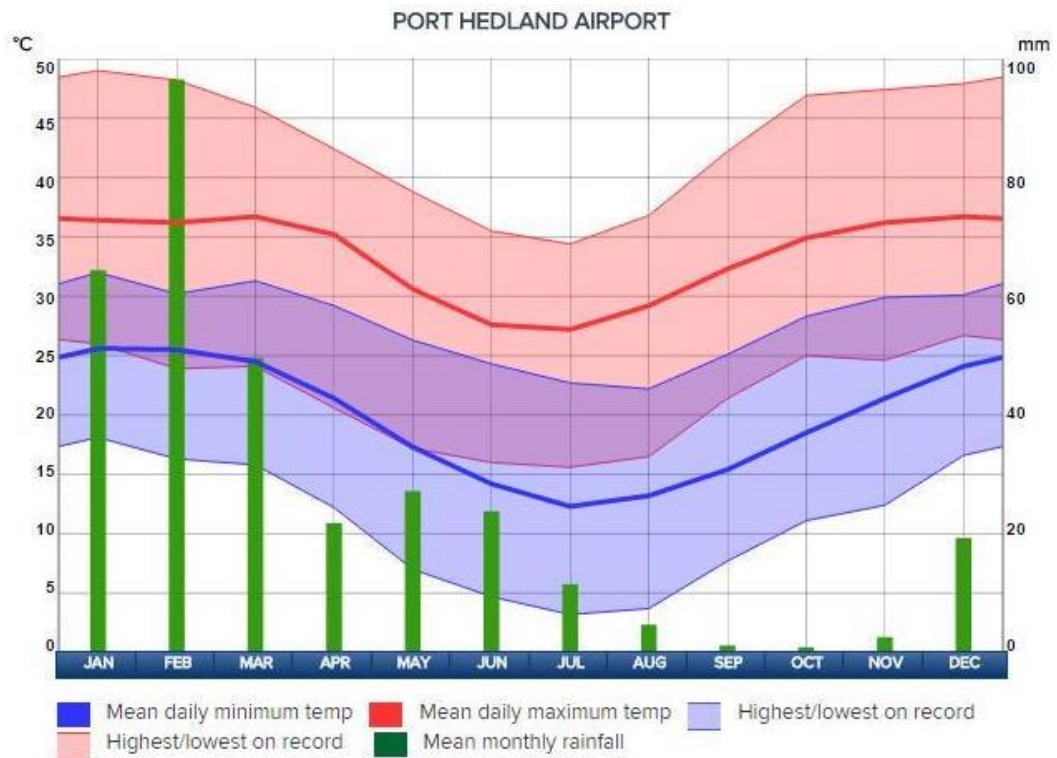


Figure 38: Climate graph for Port Hedland (Weatherzone, 2017).

winds than *Avicennia* - a conclusion based on an impact study by E. I. Paling, Kobryn, and Humphreys (2008) on mangrove populations due to cyclone Vance in 1999 (a particularly strong cyclone).

The Port Hedland aerial survey was conducted on the 17th September of 2010, between 8:44 am – 12:56 pm. According to historical meteorological data acquired for from the Bureau of Meteorology (<http://www.bom.gov.au>), the minimum and maximum temperatures were 16.2°C and 31.5°C, respectively over the time period. The records also show windy conditions throughout the time of the survey, as represented in Figure 39. The wind speeds are given in km/h during the data collection period.

The mode wind speed was 28 km/h, with a mean of 29.61 km/h during the time of the survey. It should be noted that the data shown in Figure 39 is the “Highest wind speed in last 1 minutes in km/h”. The highest speed is important in terms of the impact on causing more dust to become airborne. When using the “Average wind speed in last 1 minutes in km/h”, the mode and mean were 24 km/h and 24.89 km/h respectively.

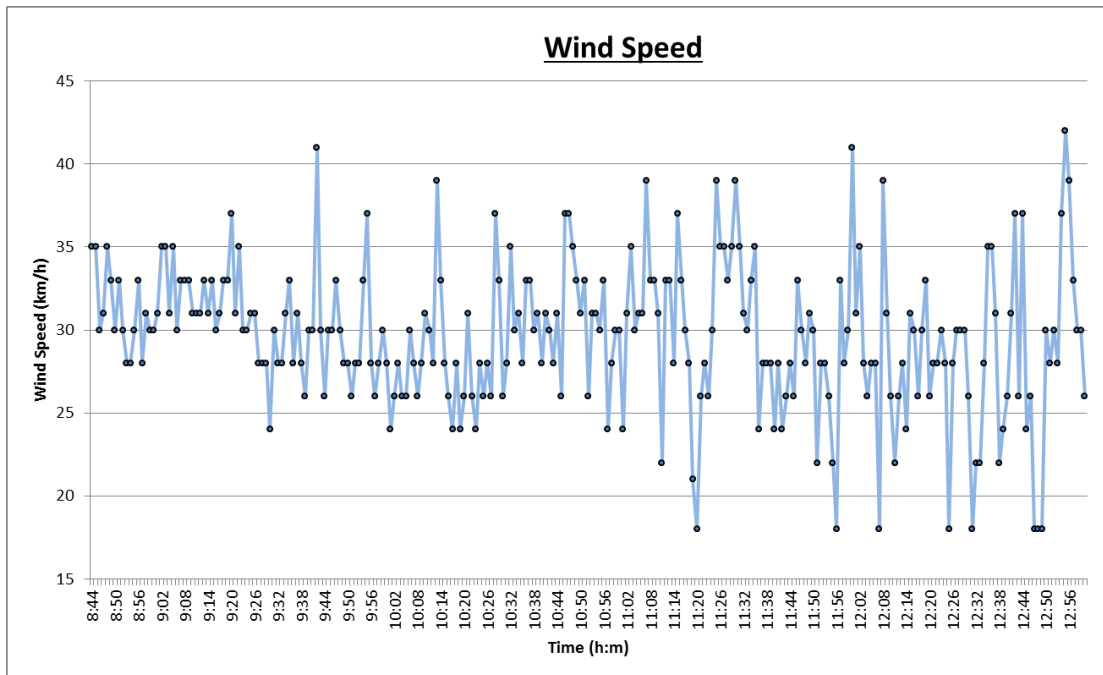


Figure 39: Wind Speed (km/h) on the day of the PHPA aerial hyperspectral survey. Time is shown in 24-hour format, covering the time of the aerial survey.

According to the Beaufort scale (Royal Meteorological Society, 2018), a wind speed of between 20 – 28 km/h is considered a moderate breeze, which is enough to raise dust and loose paper. Small tree branches also begin to move. Figure 39 shows this wind range was exceeded numerous times. A fresh breeze covers the range 29 – 38 km/h, which causes small tree leaves to sway, while moderate sized branches also move. Three wind speeds were in excess of 40 km/h, considered a strong breeze, where large tree branches are set in motion.

Wind direction is quoted in the direction the wind is coming from (i.e. average direction of wind in last 1 minutes in degrees true).

The wind graph shows varying wind directions, although generally the wind is mostly from the southeast.

Meteorological data mid-September period shows that 8.6 mm of rain fell must prior to the PHPA airborne hyperspectral survey, with 4 mm and 4.6 mm falling on the 13th and 15th of September, respectively. No rain fell on the 17th of September (the day of the survey), nor were there any clouds.

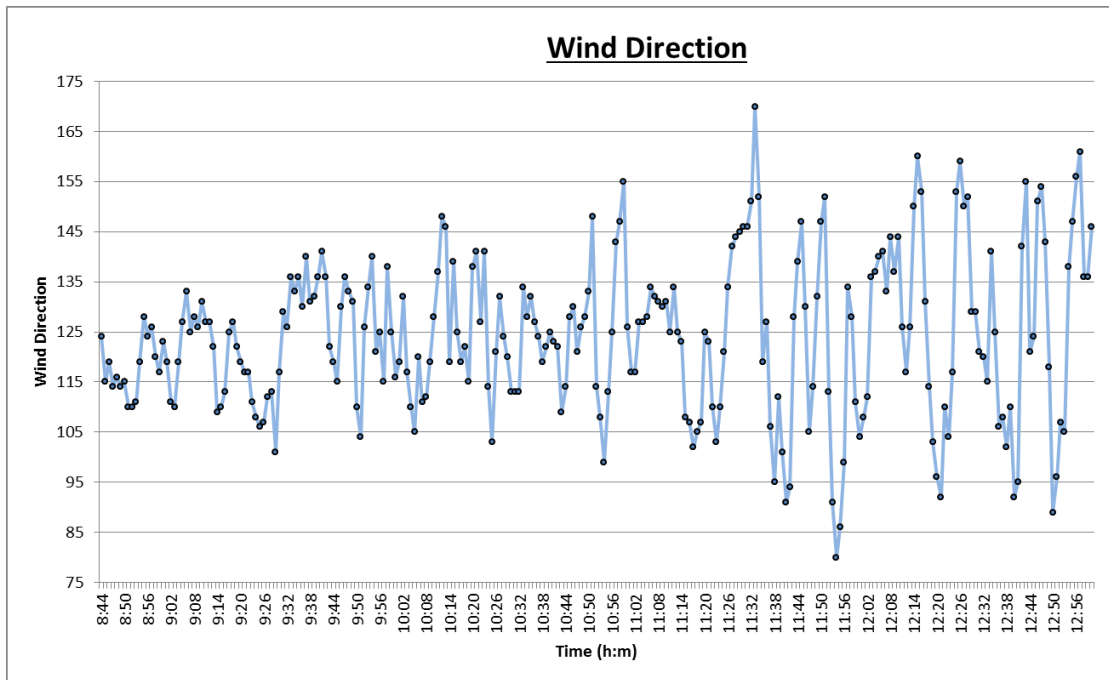


Figure 40: Wind Direction (in degrees true) on the day of the PHPA aerial hyperspectral survey. Time is shown in 24-hour format, covering the time of the aerial survey.

It is possible to form a picture of the weather conditions on the day of the survey, by referring to Figure 42 (p. 141 of Section 3.3), Table 134 (p. 710 of Appendix Q.2) and the meteorological data (Table 144, p. 745 of Appendix X). The rain, which fell on the 13th of September 2010, is likely to have evaporated, due to the low humidity and high temperature experienced after 9am (the maximum temperature was 34°C). The rain, which fell on the 15th, may have remained longer in the soil, as the humidity was higher during the day and in view of the rather low maximum temperature of just 21°C. There was no rain on the actual day of the survey, nor any clouds.

3.3 Image Acquisition

The PHPA aerial survey was conducted on the 17th September 2010 using the AISA EAGLE hyperspectral sensor for data collection (Specim, 2012). The project was a collaboration between the Airborne Research Australia, Flinders University (Adelaide, South Australia) and Curtin University (Bentley, Western Australia).

This linear array pushbroom sensor recorded hyperspectral scenic data using 247 bands with a spectral range covering 400.7 – 987.0 nm at 2.9 nm spectral resolution (Specim, 2012). However, the 247th band was deemed bad, leaving 246 bands available for analysis (i.e. 400.7 - 984.5 nm). The spatial resolution of the collected data is 1 m.

In addition, data were recorded using a full waveform LiDAR sensor, allowing for detailed topographical and vegetative canopy structure mapping. Unfortunately, due to time constraints the analysis of this data is outside the scope of this thesis.

In all, the PhD candidate was supplied with the following data:

- A total of 137 radiance-based data files in ENVI BSQ file format, each file being approximately 1.5 GB in size (the total size of all files amounting to 165 GB). These files were not georectified (further details are found in Appendix K.4 but is not preliminary for the work that follows).
- A total of 137 reflectance-based data files also stored in ENVI BSQ file format. The radiometric correction was performed using Tafkaa and accompanied by Tafkaa input and history files, thereby allowing the integrity of the model parameters to be assessed. Each of the 137 reflectance file were identical in file size to the radiance files. These files were not georectified.
- A total of 136 geographic lookup table files (format: GLT (actually the binary format is of .BIL type)). These files allow for the georectification of each of the radiance files (discussed in further detail in Appendix K.4 but may optionally may be left out without loss of continuity). One file was missing – that of flight line segment 22a. However, the information to be gained would have been insignificant as the physical location is over the sea (refer to Figure 42).
- One large 100 GB stitched ENVI .BSQ reflectance file, covering the complete PHPA region (the stitched image is smaller than the sum of individual files due to overlap between image flight lines).

The PHPA reflectance-based 100 GB hyperspectral image was originally constructed by In-Situ Marine Optics (IMO) (<http://www.insitumarineoptics.com>), specifically by

Dr. Wojciech Klonowski. However, no further processing was performed by IMO and their image is hereforth referred to as IMO_Ref (i.e. produced by IMO with reflectance type data).

The PhD candidate also produced a reflectance-based image, from the supplied radiance data. The purpose was to examine the reasonableness of the Tafkaa input parameters (discussed in Section 4.5.8) in addition to gaining experience with both the atmospheric model and the stitching process in ENVI. This image is referred to as PHPA_Ref (i.e. PHPA region, Reflectance data). Spectrally, both IMO_Ref and PHPA_Ref were identical.

The following table summarises the characteristics for the recorded hyperspectral data over the Port Hedland coastal region:

Date image was acquired	17 Sept 2010
Time period of acquisition	8:44 am – 1:00 pm
Spectral coverage	400.7 – 984.5 nm
Spectral Resolution	~ 2.2 nm ¹⁰
Spatial Resolution	1 m
Number of Bands	246 ¹¹
Number of Lines in image	9005
Number of Samples in image	23768
North-West Image coordinates	20°17'27.41"S and 118°29'10.00"E
South-West Image coordinates	20°22'20.22"S and 118°29'12.79"E
North-East Image coordinates	20°17'19.93"S and 118°42'49.13"E
South-East Image coordinates	20°22'12.70"S and 118°42'52.36"E

Table 10: PHPA image characteristics

The surveyed area is depicted in Figure 41 and covers a distance of 9.005 km in the north-south direction and 23.768 km in the west-east direction, giving a total area

¹⁰ The mean spectral resolution is 2.23̄ as every 3rd spectral difference was 2.3 nm rather than 2.2 nm.

¹¹ The actual number of bands recorded was 247 but the last band was marked bad (possibly due to instrumental issues), leaving 246 bands.

of 214 km² (excluding any regions not sensed – displayed as black pixels). Figure 41 is referred to as the PHPA_Ref image (as is Figure 42). Note that the two figures are not strictly identical, as Figure 42 has been image-enhanced but only for the purpose of display. The enhanced image data is not used (Figure 42) to produce any results. For this reason, both Figure 41 and Figure 42 are given the same name – PHPA_Ref.

The survey began in the south-west (flight line 1) at 8.44 am and concluded in the north-east at 1.00 pm (flight line 29). Sunrise and sunset occurred at 6:01 am and 6:01 pm, respectively. Each odd-numbered flight line was flown in an easterly direction. Therefore, flight line 1 was flown eastwards, 2 westwards, 3 eastwards and so on until flight line 23 where flight lines were no longer flown adjacent. Despite this, all the odd-numbered flight lines were flown eastwards while even-numbered flight lines were flown westwards.

The direction in which the sensor was flown, thereby affects the ordering of the recorded data. Image examples are given in Appendix K.4. The details may be omitted here, but the important point is that the effects have been taken into account for the normalisation work covered in Section 4.5.9.

Figure 42 shows the final stitched image with labels to portray important information concerning flight lines. Each (white) label contains two numbers; the top number refers to the flight segment number (e.g. 1A refers to flight line 1 but segment “A”), while the number immediately underneath refers to the total numbered flight line segment. For example, the final number is 137, which corresponds to flight line segment 29D. The direction of travel by the airborne sensor is indicated by the arrow next to each label.

The location and size of each label indicates the location and width of each flight line image file. A yellow label over salt pond regions improves the contrast to the white background. The black regions correspond to regions where no data were recorded (referred to as masked pixels in the image).

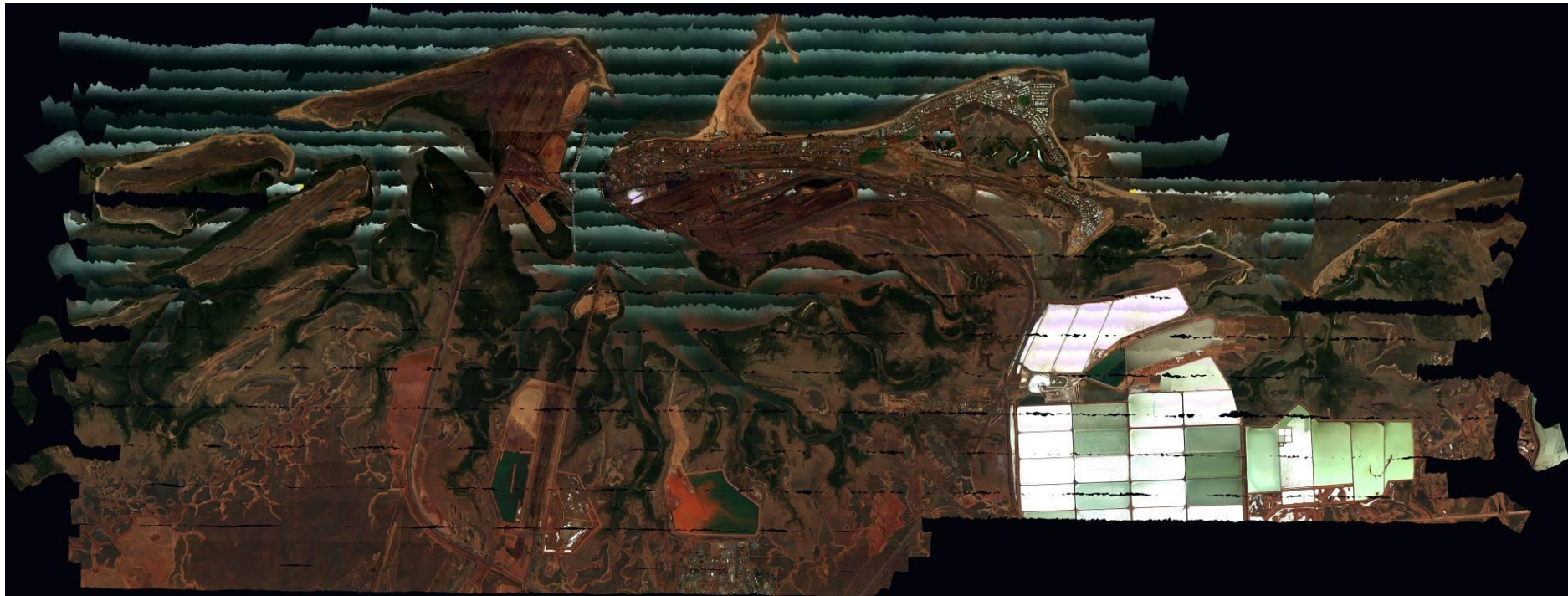


Figure 41: True colour image of the PHPA airborne hyperspectral survey. The image is referred to as the PHPA_Ref image.

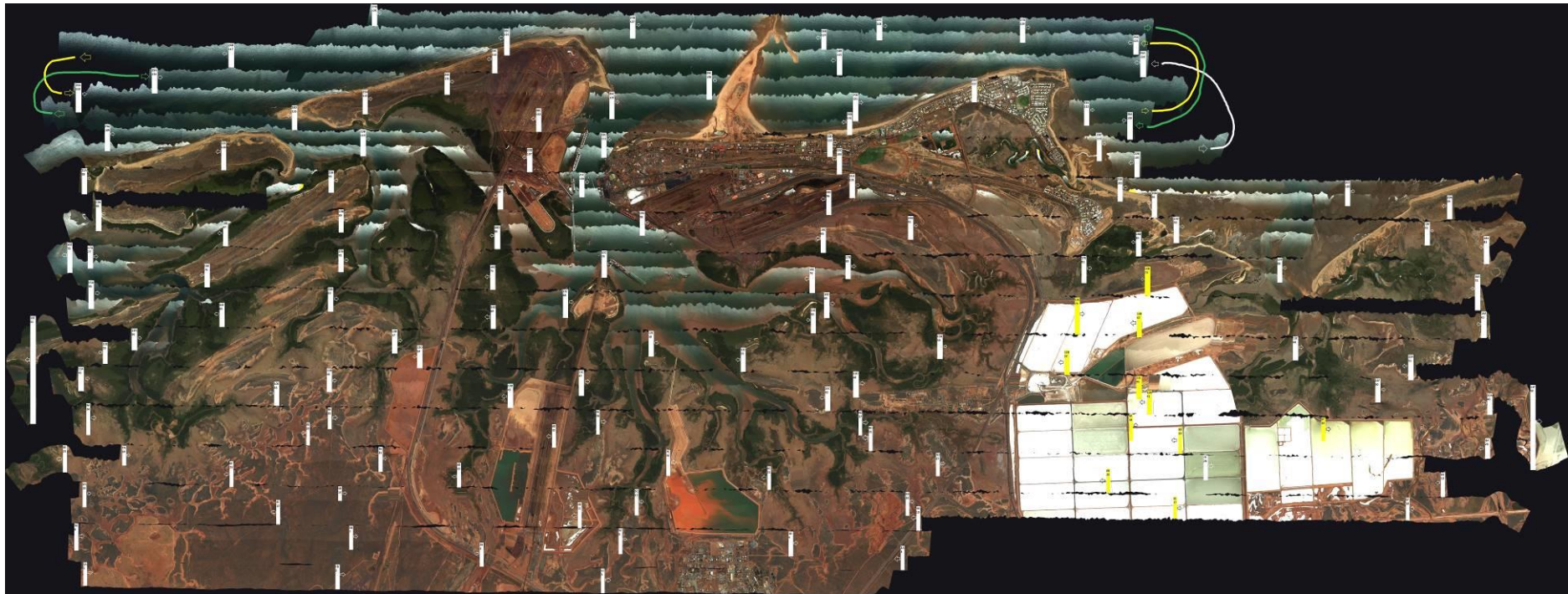


Figure 42: True colour image of the aerial survey conducted over the Port Hedland coastal region in September 2010.

All 29 flight lines are shown (full extent left to right) in addition to the 137 flight line segments (the start of each segment is indicated by vertical white markers). Both the brightness and contrast of Figure 41 has been enhanced to visually allow various cover types to be more readily distinguished. Like Figure 41, this figure is also referred to as the PHPA_Ref image.

(The RGB used for image display are bands 18 (B), 66 (G) and 116 (R), corresponding to 0.4388, 0.5494 and 0.6687 μm respectively).

The flight order is mostly sequential but with some changes in the northern section of the image. The sequence from 1 to 23 are in sequential order, but then changes to 28, 25, 29, 24, 26 and 27. Why the pilot changed the path sequence is unknown to the PhD candidate. The northern-most flight line is 27 (top of the image) and illustrates that the airborne sensor was flown in a west-east direction, as this flight number is an odd number.

The following table shows the number of flight segments for each flight line. For example, flight line 1 consists of 3 separate segments. Computationally, this means that flight line 1 consists of 3 separate files (hereby referred to as) 1a, 1b, 1c while flight line 5 (for example) consists of 6 segmented files: 5a, 5b, 5c, 5d, 5e, 5f.¹²

Number of flight line segments	Flight line
2	2
3	1, 4, 26
4	3, 20, 24, 27, 28, 29
5	6, 7, 8, 10, 12, 13, 14, 16, 18, 22, 23, 25
6	5, 9, 11, 15, 17, 19, 21

Table 11: Number of flight line segments corresponding to each flight line.

The process of joining up all these individual 137 flight line segments, to form one complete image (i.e. Figure 42), is termed stitching.

For the stitched image, it is not possible to specify exactly the number of pixels contained in a particular flight line, due to overlap with adjacent flight lines. Each entire flight line is made of flight line segments. For example, less pixels were used from flight line segment 5B compared to flight line segment 4C to form the stitched image (see Figure 43).

Figure 44 shows another example, where more of flight line segment 22D is used in the stitched image than flight line segment 23B. Although though the number of pixels used in the stitched image varies, each individual flight line segment is exactly 965 pixels 'wide'. Although the 'width' of the 4C label is larger than that for 5B, both

¹² It should be noted that although uppercase letters were used in Figure 42 for flight line segments, they may also be referred to in lowercase. Therefore, flight line segment 5A may identically be referred to as flight line segment 5a.



Figure 43: The stitched image uses varying amounts of pixels from different flight line segments to form the final complete image. This image is a magnified view of Figure 42.

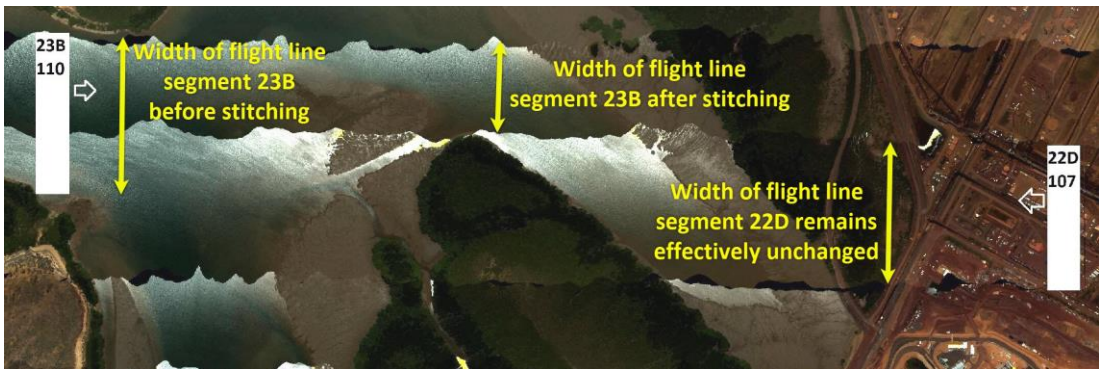


Figure 44: To form a stitched image, some pixels are discarded from particular flight line segments. While the ‘width’ of flight line segment 22d remains unchanged, the stitching process uses only a portion of those from flight line segment 23b.

flight line segments are 965 pixels ‘wide’. The label on the image (i.e. in Figure 43) shows (roughly) the extent each flight line segment forms in the final image. In this case, the stitched image used many more pixels belonging to flight line segment 4C compared to 5B.

Specific details concerning the actual height, flight line segment time of acquisition, and so on provided in Table 134 (p. 710 of Appendix Q.2). Other parameters include, the centre longitude or latitude coordinates corresponding to each image flight segment, altitude of sensor, solar zenith angle and azimuth angles. The table shows (for example) that the sensor to ground height varied, but was generally around 600 m.

As the Port Hedland aerial survey was sensed using hyperspectral data, an RGB true colour image is formed by using the three bands defined below. In this thesis, the following combinations are consistently used to represent a visual image (e.g. Figure 42).

**NOTE: All true colour images produced in this thesis are displayed
using the following default RGB bands:**

Band 18 (B): 0.4388 μm

Band 66 (G): 0.5494 μm

Band 116 (R): 0.6687 μm

A comment needs to be made in regard to the use of terminology when referring to hyperspectral ‘images’. The data collected by the remote sensor records spectra over 246 bands (which are effectively wavelengths). The particular RGB bands selected to form an image (Figure 42) is somewhat arbitrary, for it depends on the application as to which bands would be suited for the task at hand. For example, when mapping for vegetation, it is usually more appropriate to incorporate at least one NIR band.

The collection of hyperspectral data that is spatially arranged to give physical meaning (e.g. a map), may be referred to as an image (even though a very small subset of bands are selected for display – typically RGB). However, the recording of hyperspectral quality spectra of different cover types is referred to as data. It is understood that when hyperspectral image data is processed to form a new dataset, the data still has a spatial component to it. In other words, it is possible to form a new image based on hyperspectral processing (i.e. covering all 246 bands) of an existing (e.g. unprocessed) image. In this context, deriving a new image is understood to indicate that each pixel contains 246 bands – not 3 RGB bands.

Furthermore, it is important to establish the nomenclature when referring to new images, several which are formed in Section 4.5.9 and Appendix L. To reduce the somewhat tedious (and rather monotonous) wording associated with image

comparisons, grammatical rules are somewhat relaxed to instead allow the use of statements such as:

In comparing the PHPA_Ref image with the N_Ref_VI image, ...

it is preferable to shorten this to:

In comparing PHPA_Ref with N_Ref_VI, ...

or even further to:

Comparing PHPA_Ref with N_Ref_VI, ...

There is no ambiguity as the image nomenclature follows strict rules and are precisely defined, so the monotonous extra words can be avoided. The removal of repeated-words actually allows for easier reading, particularly so in Appendix N.

4 Research Methods and Results

4.1 Introduction

Section 4.3 addresses objective 1, whereby a hyperspectral library is created for the Port Hedland coastal region. It contains spectral information of various land cover types with ASD spectral quality.

Spectral similarity between cover types is assessed in Section 4.4 using the hyperspectral library.

The major objective of this thesis is concerned with producing a thematic map. The objective is referred to as sub-objective 3a. The whole of Section 4.5 encompasses the main portion of this thesis and consists of several pieces of work.

Section 4.6 is devoted to validating the accuracy of the thematic map, which defines sub-objective 3b.

4.2 Methods and Discussion

This section outlines the methods and factors involved to address each of the three thesis objectives, as stated in Section 1.3.

Objective 1:

Development of a hyperspectral library of vegetative species for the Port Hedland coastal region.

An ASD field spectrometer recorded 10 – 15 individual spectral measurements for each cover type at various geometrical positions to capture BRDF effects. The average spectrum of these measurements was then stored into the hyperspectral library, one for each cover type. In practice however, prior to calculating an average spectrum for each cover type, each individual measurement was plotted to visually identify erroneous spectra, such as those caused by accidental recording during

transition in the field. This occurred a few times, as manoeuvring the bulky ASD spectrometer along with the connected laptop resulted in accidental recordings - made as a result of hitting the spacebar. These invalid spectra (outliers) were removed prior to calculating the mean spectrum. The measurement variability within the 10 - 15 samples was calculated using the standard deviation and represents the spectral uncertainty. This uncertainty is due not only to the natural variability within each cover type but also encompasses variability due to BRDF in addition to instrumental uncertainty (e.g. temperature changes caused by changes in dark current - more details are given in Section 4.3.1). The spectral plot for each cover type therefore represents a mean measurement spectrum along an uncertainty represented by one standard deviation from the mean - a common approach adopted in remote sensing (e.g. Asner and Martin (2009), Wang and Sousa (2009), Ramsey and Jensen (1996)).

Steps for objective 1:

- Familiarisation with the ASD Field Spectrometer, both practical and theoretical (Section 4.3.1).
- Planning which cover types to record spectral samples of, with consideration to physical accessibility (Section 4.3.2).
- Collecting field spectra over several sites (Section 4.3.3 and Appendix G.1). Both these sections discuss the nomenclature used in this thesis for spectral plots. This identifies not only the spectral sample (e.g. a mangrove species) but their physical location.
- Plotting every single measured spectra with those in clear error dismissed (visual inspection). Combining valid measurement data statistically using the mean, with the standard deviation (SD) representing spectral uncertainty (Section 4.3.1).
- The final plots are given in Appendix G.2.

Objective 2:

To investigate the ability to discriminate between and classify different types of vegetative matter, with particular emphasis on mangroves.

The ability to discriminate between cover types relies on the nature of similarity between spectral samples in the hyperspectral library. Two approaches were adopted to assess spectral similarity; SAM and separability statistics (using the JM distance). The SAM method calculates an angle between pairs of spectra, thereby providing an indication of the limits in spectral differentiability. Smaller angles are synonymous with a low probability of separability, while larger angles suggest a high degree of distinguishable spectra. If mangroves are spectrally highly separable, then there is a good chance that advanced classifiers can distinguish between the different species. For the JM distance, the calculated values lend themselves to well-defined interpretations for the probability of spectral distinguishability. These values were defined in Section 2.5.5 and are useful in interpreting spectral separability for vegetation (mangrove species in particular).

Steps for objective 2:

- Assessing spectral similarities by calculating spectral angles between each pair of cover types. These spectra are defined in the hyperspectral library. The results of the spectral angles are given in Appendix G.3.
- Gaining an appreciation for Spectral Angle (SA) magnitudes by plotting pairs of spectra. Section 4.4.1 provides numerous graphical examples.
- Section 4.4.2 examines the difficulties in spectrally identifying mangroves at species level.
- Section 4.4.3 introduces an approach to assess how different mangrove species are to each other using spectra.
- Section 4.4.4 discusses why JM distances are not used for spectral separability assessment in field samples.

Objective 3:

To produce and interpret a vegetation map and assess its validity to those produced by other parties.

This objective contains two parts, which may be clarified as multiple sub-objectives:

Sub-objective 3a:

To produce a vegetation map

Sub-objective 3b:

To interpret and validate the thematic map against those produced by other parties

The first part of objective 3a is concerned with initially generating a simple map; consisting of vegetation and non-vegetation for the Port Hedland coastal region. This was accomplished by using an approach based on the vegetative index (covered in Section 4.5.2).

More sophisticated algorithms allow for the generation of a detailed thematic map, which formed the next step. A supervised classifier compares image pixel spectra to those stored in a hyperspectral library. An advantage of the supervised SAM classifier is that the actual difference in brightness between the ASD and image spectra is neglected, as SAM is not sensitive to these changes (as discussed in Appendix E.3). However, the spectral characteristics of vegetation itself (i.e. ignoring atmospheric absorption, etc.) is known to be influenced by state of health, environmental conditions (e.g. lack of water), senescence and phenology (Section 2.3.2). Therefore, ideally a field trip would coincide with the time of the aerial survey. Alas, this did not occur leading the ASD spectra to possibly contain undesirable differences compared to spectra measured by the airborne sensor. As a result, to mimic the phenology and climatic influences on the vegetation, the field

trip was conducted in the same month as that of the airborne survey (but 3 years later).

Beside these factors, Section 4.4.2 and Appendix J.1 (in particular) shows that supervised classifiers (including SAM) cannot be used to classify mangroves at species level because of the inferior quality of airborne-based spectra compared to ASD spectra. Due to the issues faced for a supervised classifier, an unsupervised classifier was selected instead. Both the ISODATA and k-means classifiers are not reliant on ground-truth data. Instead, both methods group together features related to spectral similarity, thereby allowing for the production of a thematic map with classes. However, the number of classes is an input parameter and is an unknown. Therefore, the initial approach selected a small number of classes for classification, and assessed for spectral similarity using the JM distance. Class pairs were merged if the spectral similarity between class pairs were too high, resulting in a decrease in a total number of thematic classes. Conversely, for class pairs exhibiting a high spectral difference, the number of classes for the classifier was increased, as the separability statistics suggest a high difference between the class spectra. In this case, it is entirely possible that classes may be subdivided spectrally into more classes, potentially capturing more detail in the scene for an existing cover type (e.g. subdividing a broad mangrove class further into separate species) or even creating new types of cover types entirely (e.g. subdividing into grass or soil).

Feature selection of hyperspectral data can lead to an increase in classification accuracy. The PC transform was selected to reduce the number of features, thereby increasing classification accuracy but to a point (due to the Hughes effect). Although not appropriate for the SAM classifier - as the transformed bands no longer contain a direct one-to-one link to those in the hyperspectral library - it is appropriate for the unsupervised classifiers.

During the course of the thesis work, several spectral inconsistencies became apparent in the original airborne data (Section 4.5.3). Reducing these brightness inconsistencies became a major focus in this thesis, forming the bulk of the work under Section 4.5.9. An empirical mathematical correction termed normalisation,

aims to improve spectral inconsistencies using three steps. The efforts of this work came to fruition by leading to a higher quality thematic map.

Sub-objective 3b is concerned with interpreting the classification classes identified by the classifier on the thematic map. In remote sensing, it is common for accuracy assessment to be conducted on the thematic map. In particular, an error matrix approach (discussed in Appendix D) is commonly performed but requires random sampling over the scene. In the current work, this was not possible due to time constraint factors and numerous inaccessible field sites, either physically or due to health and safety regulations. The relatively small number of field samples, non-random samples, locational uncertainties also disallowed the effective use of supervised classifiers, including ML and SVM in the current thesis. Instead of a quantitative error matrix approach, validation was based on visually assessing spatial class structures against maps as obtained by third parties.

Steps for sub-objective 3a – The production of a vegetation map:

- Production of a vegetation versus non-vegetation map (Section 4.5.2).
- Development of a vegetative mask to eliminate non-vegetative spectra from an image prior to classification (Section 4.5.6).
- Feature reduction using PCA prior to unsupervised classification (Section 4.5.7).
- Unsupervised classification of the PHPA_Ref image (Section 4.5.7). Separabilities of classes assessed using JM distances.
- Production of a spectrally more-consistent hyperspectral image using normalisation (Section 4.5.9) (forming the bulk of the thesis work).
- Classification of the normalised image, using PCA and unsupervised classification. Class separability assessment using JM distances. All this work is found under Section 4.5.11.

Steps for sub-objective 3b – thematic map interpretation and validation with other parties:

- Field work planning (Section 4.6.1) and data collection (Section 4.6.2) to physically identify and interpret the spectral classes present in the best thematic map product (Section 4.6.3).
- Validating the thematic maps with third party image products. (Section 4.6.4).

4.3 Objective 1: Generation of a Hyperspectral Library

An ASD field spectrometer collected spectra for 55 ground cover types during a field trip in September 2013 for the Port Hedland coastal region. The calculation of mean spectra for each cover type allowed the building of a hyperspectral library (objective 1) for the Port Hedland coastal region.

Section 4.3.1 discusses the technical details of an ASD field spectrometer, while Section 4.3.2 is concerned with field trip planning. A list of sampled cover types are presented in tabular form in Section 4.3.3, while each of the numerous spectral plots are given in Appendix G.

4.3.1 ASD Background

Analytical Spectral Devices, Inc., originally developed the ASD field spectrometer but is now part of Malvern Panalytical (<http://www.malvernpanalytical.com>). This instrument collects various land cover spectra (e.g. different soils and plants) through an optical sensor. A 2-metre optical fibre cable allows the sensor access to taller vegetation. Connected to the ASD Spectrometer (located in the backpack; see Figure 45) is a notebook computer and GPS. This allows spectral samples to be stored in digital files, along with GPS coordinates for each measurement. Figure 45

shows the field-operator (PhD candidate!) collecting a vegetative spectrum of a mangrove.

A total of 10 - 15 samples per land cover type was recorded, consistent with the approach adopted by other researchers (e.g. Schmidt and Skidmore (2003), P. S. Thenkabail et al. (2004), Kamaruzaman and Kasawani (2007)), thereby allowing for the timely sampling of cover types. Given that both the ASD and notebook operate on batteries, sampling occurred in the 2 - 3 hour period prior to and after solar noon.



Figure 45: Measuring reflectance spectra using the ASD field spectrometer.

This timing also minimises sun angle effects (the ideal timing, according to McCoy (2005, p. 55)). However, the recharging of batteries for both devices necessitated a one-hour lunch break, timed to coincide close to the solar noon. Of the 10 - 15 samples taken for each land cover type, about half of the spectral samples were initially recorded at close range (at about 10 cm) with the second half further away (1 – 2 m). The initial samples tended to be closer (e.g. near an individual leaf), while latter samples took a more global perspective (measuring further away, resulting in less ‘pure’ samples, but more akin to airborne-sensed data). Each measurement was taken between nadir and 25°.

The ASD spectrometer is directed at a small spatial area, typically a few tens of square centimetres. The reflectance spectrum collected typically represents a ‘pure’ sample of a particular cover type (e.g. tree). In contrast, an airborne instrument samples the ground reflectance over an area of approximately 1 square metre or more, depending on the sensor architecture and altitude of the aircraft. As such, the reflectance spectrum measured for each image pixel is often a mixture of spectra from a number of different plant species, as well as the underlying soil if the

plant canopy is open and the soil is visible. In cases of mixed spectra, the ability to distinguish and classify vegetation is more difficult.

The ASD spectrometer covers a spectral range from 350 – 2500 nm at 1 nm resolution. An example of a single measured spectrum is shown in Figure 46. An overall mean reflectance spectrum was taken as the representative spectrum from the 10 - 15 spectral samples (except any erroneous ones which were deleted). The standard deviation (SD) of these spectral samples is shown as a dashed magenta line in the plot and represents the uncertainty. Assuming variation in samples follows a Gaussian distribution, 68% of the population are contained within the 1 SD limit from the mean.

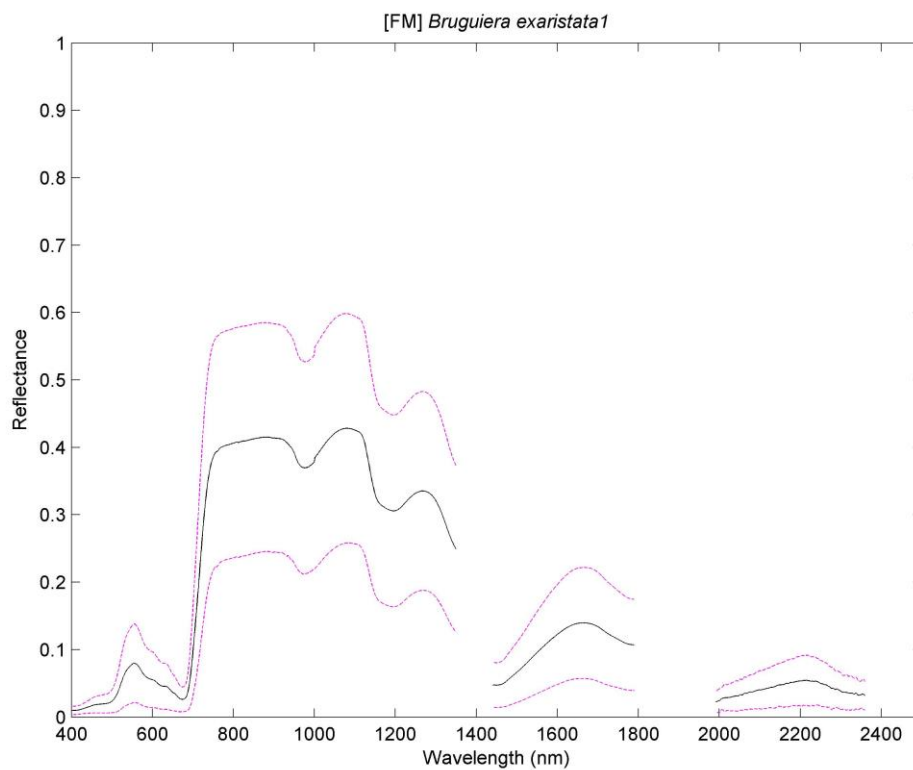


Figure 46: Example of an ASD spectrum for one single measurement of [FM] *Bruguiera exaristata1* located on Finucane Island.

A value of 1 represents total reflection, whereas 0 represents no reflection.

Note: The code [FM] refers to the recorded location of the ASD spectral sample. Section 4.3.3 provides further details on the nomenclature used in this thesis.

A rough calculation estimated that about 10 - 15 cover types could be collected per day. Given that field work was to be conducted over a 5 day period, 5 regions were chosen for analysis. Field data were processed and plots produced each evening in order to assess the integrity of the collected results. This allowed problems to be identified prior to departure from Port Hedland and sample collection to be repeated, if necessary. Indeed, a few of the 10 - 15 measurement plots clearly contained invalid results and were deleted prior to calculating the final (averaged) spectrum. The cause for at least some of the faulty measurements were due to accidentally pressing the spacebar on the notebook while manoeuvring around on uneven ground between field cover types, resulting in a recorded spectral measurement of whatever the sensor was pointing to at that instant.

The ASD measures the reflected energy from the sun's radiation. As the sun's radiation traverses the Earth's atmosphere, it is preferentially absorbed by various gases in the atmosphere. For example, the 940 nm 'dip' is likely to be due to water vapour absorption (Richards (2013), p. 41). Atmospheric correction models attempt to remove these kinds of effects.

The ASD field spectrometer contains three different sensors to span the wavelength range displayed in Figure 46. The transitions from sensor to sensor cause discontinuities in the spectrum near the 1400 and 1900 nm wavelengths. In addition, atmospheric absorption occurs in regions of 1350 – 1440 nm, 1790 – 1990 nm and 2360 - 2500 nm (P. S. Thenkabail et al., 2004). As a result, these spectral regions were 'blanked out' (which is a common approach taken in remote sensing), leaving clear spaces in any plot.

Although the ASD records the reflectance over the full spectral range (350 – 2500 nm), the airborne data covered a relatively narrow range (400 – 985 nm). The spectral plots of the PHPA hyperspectral library (see Appendix G.2, page 460) also deliberately cover the range from 400 – 990 nm, as an extended spectral range adds no value for a SAM classifier. An example of a final averaged ASD spectrum is shown in Figure 47, for the mangrove species *Bruguiera exaristata*¹ located on Finucane Island. The wavelength increment for the ASD is 1 nm, the airborne data were taken over (approximately) every 2.2 nm. The suffix "1" attached to the species name (*Bruguiera exaristata*) follows the nomenclature introduced in Section 4.3.3.

Basically, the “1” refers to the first species of *Bruguiera exaristata* for which spectral samples were recorded using the ASD. A suffix of “2” used for *Bruguiera exaristata* identifies a separate mangrove but of the same species. Section 4.3.3 provides further details on the nomenclature used in this thesis.

At each site, the ASD required calibration prior to any recording of spectral samples, which involved the recording of a white reference to give the incident energy. Physically this translates to measuring the reflected energy from a ‘pure’ white reference panel using the ASD sensor. This panel contains a coating of BaSO₄, to give it Lambertian properties; although this appears to be dependent on the manufacturer (Jackson, Clarke, & Susan Moran, 1992).

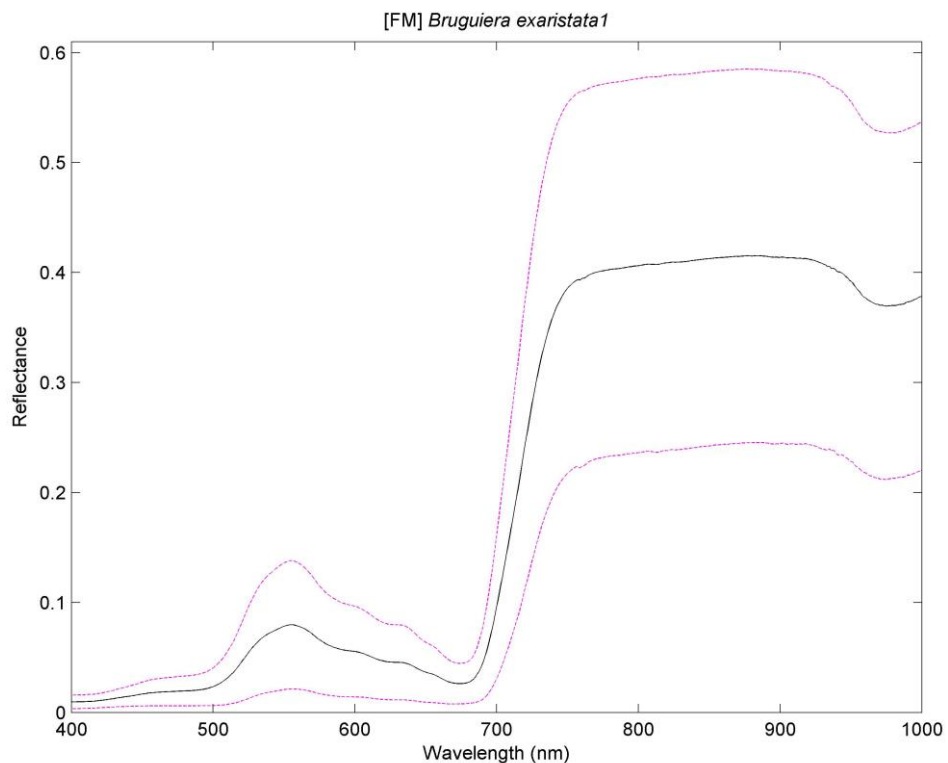


Figure 47: Final averaged ASD spectrum for a single species of *Bruguiera exaristata*1 [FM] on Finucane Island.

The black line in Figure 47 represents the mean of all measurements. The dashed line indicates 1 SD (a widely taken approach e.g. Ramsey and Jensen (1996)).

Whereas the aerial hyperspectral data is recorded in units of radiance and converted to reflectance through an atmospheric correction process, the ASD gives the reflectance directly:

$$\text{Reflectance} = \frac{\text{target energy}}{\text{incident energy}} = \frac{(\text{target} - \text{dark current})}{(\text{reference} - \text{dark current})} \times 100\% \quad (4.3.1.0)$$

(P. S. Thenkabail et al., 2004)

The target refers to the measurement of the surface to record the spectrum of.

As the dark current drifts with time and temperature (P. S. Thenkabail et al., 2004), the ASD was warmed up (i.e. switched on) for about 30 minutes prior to use. The dark current is the signal measured in the absence of radiation. It is caused by electronic noise and is always present at temperatures other than absolute zero (Richards (2013), p. 28). The process is called optimisation and is required prior to obtaining a white reference. A white reference was obtained approximately every 30 minutes, and more frequently in changing light conditions (e.g. caused by moving clouds).

Equation (4.3.1.0) may be written in terms of a correction factor k .

$$r = \frac{\text{target radiance}}{\text{panel radiance}} \times k \quad (4.3.1.1)$$

(McCoy (2005), p. 45)

Under ideal conditions, $k = 1$ so that Equation (4.3.1.0) is essentially Equation (2.4.2.1) (of Section 2.4.2). The panel radiance is that as measured by the white reference, which is assumed to be Lambertian.

4.3.2 Field Trip Planning

Planning for the field trip relied on identifying key sites for sampling. Initially, unsupervised classification of the PHPA airborne data allowed spectrally similar classes to be grouped together. Although the method is unable to assign a physical

identity to each class, the distribution and location of spectrally similar classes identifies useful sites to record spectra using the ASD.

However, not every region was accessible, due to physical or political reasons (e.g. special permission is required to access mining leased land). Thankfully, the PHPA Sustainability Coordinator (Nicole Wylie) provided assistance in identifying accessible regions. Furthermore, it became apparent that several regions of interest identified in the 2010 PHPA airborne image were no longer in existence due to man's regional development. As a result, the sites agreed upon for ASD spectral sampling were primarily located within the 5 key regions, as shown in Figure 35 (p. 131).

Nicole Wylie's local knowledge also allowed the PhD candidate to specifically collect ASD spectral samples for all seven species of mangrove trees on Finucane Island – the only place where all seven species is found. Her botanic knowledge allowed for the identification of vegetation at species level (not only mangroves).

The unsupervised classification k-means method was applied to the 5 regions, to help identify spectral targets of interest. Prior to the actual field trip, these thematic maps were sent to Nicole Wylie for feedback. An example is shown in Figure 48, for a region of interest (ROI) at Redbank. The region covered by the red square in Figure 48 is magnified (four times) to produce a suitably-sized study area as shown in Figure 49 (left image). The classification result is shown in the right image (Figure 49) where the k-means method produced 3 classes. The site was visited during the first field trip to investigate the physical composition for each spectral class in addition to identifying vegetative species present (in particular mangroves).

Nicole Wylie visually identified the mangrove species present in this study region, and attempted to estimate their proportions (roughly) in the three coloured regions drawn in Figure 49 (left image). These estimated proportions are given in Table 12.

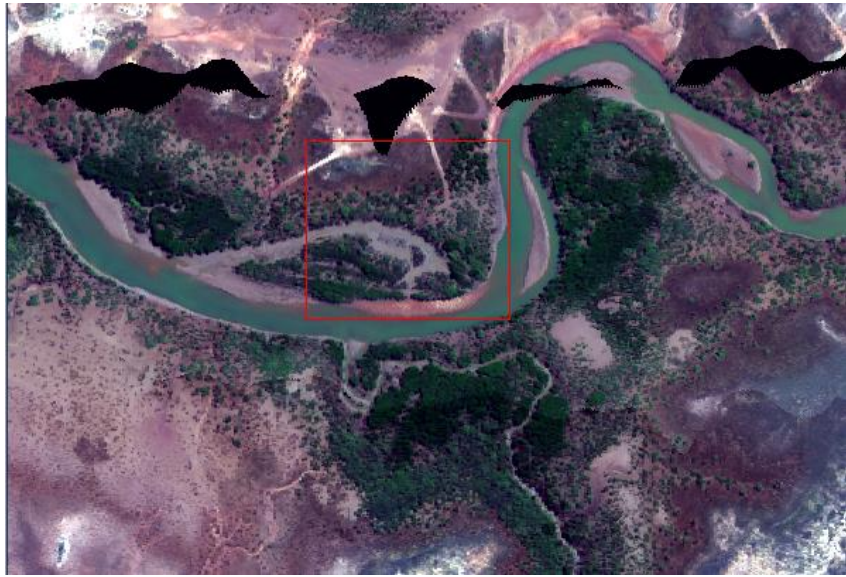


Figure 48: The red square covers the region of interest for sampling at Redbank

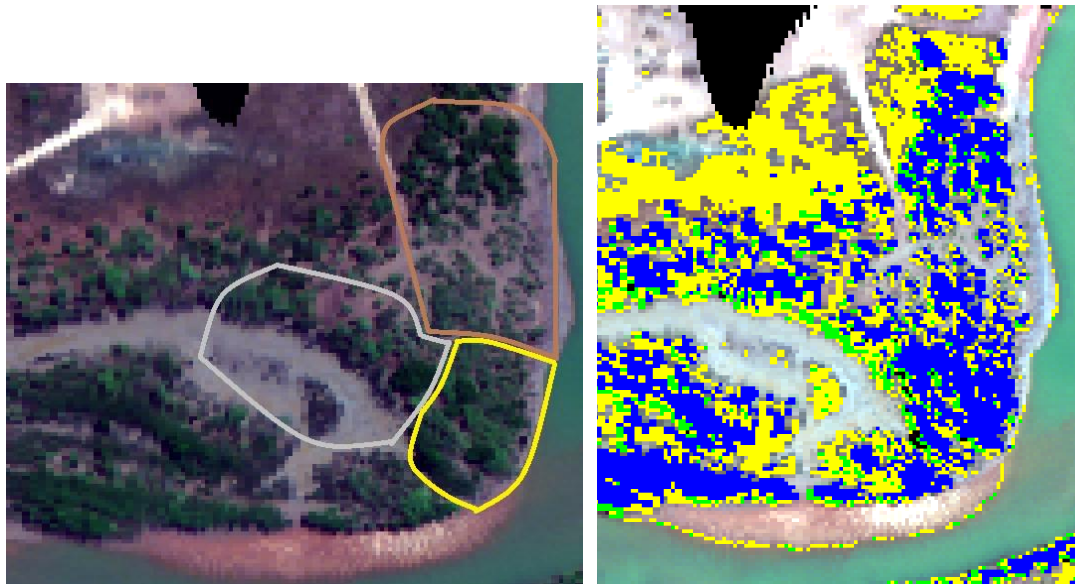


Figure 49: Region at Redbank magnified four times (left image) and the classification map overlaid onto the magnified image (right image).

Region	Species present	Estimated Proportions (%)
Yellow	<i>Avicennia marina</i>	45
	<i>Rhizophora stylosa</i>	50
	<i>Ceriops australis</i>	5
Brown	<i>Avicennia marina</i>	50
	<i>Ceriops australis</i>	45
	<i>Bruguiera exaristata</i>	5
Cream	<i>Avicennia marina</i>	50
	<i>Ceriops australis</i>	50

Table 12: Estimated proportions of vegetation in each region defined at Redbank (i.e. Figure 49 (left image)) by visual means.

The proportions of class pixels for these three-coloured regions are shown in Table 13.

Region	Blue Class (%)	Yellow Class (%)	Green Class (%)
Yellow	70	20	10
Brown	55	35	10
Cream	40	45	15

Table 13: Quantitative estimation for the proportion of vegetation classes in each region defined at Redbank (i.e. Figure 49 (left image)).

There is clearly a discrepancy between the results of the thematic map results and those obtained by field work. For example, Nicole estimated roughly 50% for each of two mangrove species located in the yellow region (when counting *Ceriops australis* toward *Avicennia marina*), while the two most dominant classes come to 70% and 20%. However, the proportions as estimated in the brown and cream regions are more closely matched. For the cream region in particular, Nicole estimated 50% for each of two mangrove species. The k-means method roughly provided similar estimates; the yellow class comprising 45% and the blue class 40%.

There are a number of points to be raised. The boundaries hand-drawn by Nicole Wylie on a physical map were not meant for detailed quantitative analysis. Furthermore, the mangrove populations were visually estimated. Although care was

taken to accurately transfer these hand-drawn regions onto an image (i.e. Figure 49, left image), the boundary positions are still approximations. Small positional changes introduces different class populations. In fact, by making a relatively small change to the boundary of the brown region, the proportions of k-means classes changes by around 10%.

There may be other reasons for the discrepancy. Classes may actually represent spectral mixtures. For example, the coloured class (Figure 49, right image) corresponding to the brown coloured region of Figure 49, left image, might represent a spectral mixture of soil and vegetation (e.g. mangrove). It is possible that soil dominates the pixel spectrum, thereby masking the spectral signature of any vegetative species in the vicinity. If the green coloured classes were counted toward the yellow coloured class instead, then the proportions for each mangrove species become similar to Nicole's estimate for the brown coloured region (of Figure 49, left image). It is also possible for the green coloured class to represent mixtures of both blue and yellow coloured spectral classes.

The k-means method categorises spectrally similar features. The three resulting classes do not necessarily represent three species of mangroves. In fact, in hindsight this is unlikely, given the high spectral similarity between many of them (as discussed in Section 4.4.2). The classes may also represent states of vegetation, as stress affects the position of the red-edge. However, it is encouraging that the k-means method identified 3 classes, as Nicole also identified primarily 3 species of mangrove.

4.3.3 Spectral Library Log

It was imperative to record spectra of all the mangrove species present in the Port Hedland coastal region. The local knowledge provided by Nicole Wylie led the PhD candidate to Finucane Island - the only site where all seven mangrove species are found.

The following three tables show the spectrally sampled land cover types, using the ASD field spectrometer.

All mangrove species sampled:

All non-vegetation sampled (mostly soil):

All Mangroves Sampled	All Non-Vegetation Sampled
<i>Aegialitis annulata</i>	dredge dam on top
<i>Aegiceras corniculatum</i>	dredge dam road
<i>Avicennia marina</i>	dry soil
<i>Bruguiera exaristata</i>	hard packed dirt road
<i>Ceriops australis</i>	interstitial salt crusted sand
<i>Osbornia octodonta</i>	old bitumen
<i>Rhizophora stylosa</i>	red soil
	road (sandy hard packed)
	salt flat plain
	salty reddish crust
	shallow water soil
	shell laden sand
	salty reddish crust
	wet soil

Table 14: List of all mangrove species sampled (left) and soils (right)

All non-mangrove vegetation sampled:

All Non-Mangrove Vegetation Sampled	
<i>Acaria sp.</i>	<i>Limonium</i>
<i>Acacia translucens</i>	<i>Sporobolus virginicus</i> ¹³
<i>Aerva javanica</i>	<i>Salsola kali</i>
<i>Cenchrus ciliaris</i>	<i>Tecticornia sp.</i>
<i>Corchorus parviflorus</i>	<i>Trianthema turgidifolia</i>
<i>Frankenia ambita</i>	<i>Triodia pungens</i> ¹⁴

Table 15: List of all non-mangrove species sampled.

Full daily field logs as well as spectral results are given in Appendix G.

Mean spectral plots for each cover type are given in Appendix G.2 (p. 460). Each plot represents the ASD spectrum of one cover type (i.e. an individual plant species or soil type). The mean spectrum is represented by a black solid line, while a dashed

¹³ The common name for *Sporobolus virginicus* is marine couch

¹⁴ The common name for *Triodia pungens* is spinifex.

magenta line represents the spectral uncertainty, as calculated by the SD. The straightforward process of calculating both the spectral mean and uncertainty were described briefly in Section 4.3.1.

The title for each plot follows a standard format, comprising of two components:

[region code] "*name of cover type*"

The first component is the **[region code]** field, which identifies where the spectral sample was recorded while the second component "*name of the cover type*" identifies the kind of cover type. For vegetative species cover types, the names are given in italics (by convention). Cover type samples are identified using numbered suffixes attached to cover type names. The absence of a numbered suffix indicates that only one spectral sample was recorded for the cover type (each consisting of 10-15 individual measurements). For example, for the mangrove *Rhizophora stylosa* indicates that only one mangrove tree was used to record the spectra (i.e. consisting of 10-15 individual measurements of the tree). However, *Avicennia marina1* and *Avicennia marina2* indicate two individual trees for sampling. The nomenclature uses a [region code] in addition to numbering, thereby allowing the spectral samples to be distinguished and related back to physical sampling locations (each measurement was accompanied by a GPS location).

The region codes given in Appendix G.2 (p. 460) identifies the physical location where spectral ASD samples were recorded; when the first letter is "F", it indicates the cover type was sampled on Finucane Island. As many samples were recorded on Finucane Island, a second letter is introduced to identify one of three 'subregions'. The other codes used are: "RB" for Redbank, "LP" for Lumsden Point and "PP" for Pretty Pool.

ASD spectral angles between pairs of cover types are displayed in Table 68 to Table 89 of Appendix G.3 (p. 493). The angles are given in the form of mean \pm uncertainty. Mathematical details concerning both the calculation of the mean and uncertainty is explored further in Appendix G.3 (p. 493).

Note: Throughout this thesis, some minor inconsistencies occur in the use of spaces between species names and their sample numbers. At times, these spaces are missing - especially true in tables (e.g. Table 16, p. 177 of Section 4.4.2) and some plots (e.g. Figure 57, p. 175 of Section 4.4.2). However, the plots in Appendix G.4 do contain spaces. It is important to note that the samples are identical; for example, *Avicennia marina 2* and *Avicennia marina2* both represent exactly the same spectral samples.

4.4 Objective 2: Ability to Discriminate between Mangroves

The ASD hyperspectral library together with spectral angles are used to assess spectral similarity between cover types (objective 2).

There does not appear to be a clear cut interpretation for spectral angles in the literature as there is for the JM distance (Section 2.5.5, p. 71). Section 4.4.1 places a context on interpreting the spectral angle (SA), by comparing spectral differences both graphically and quantitatively between various cover types. Factors influencing spectral matching between ASD and airborne hyperspectral spectra are discussed in Section 4.4.2. The spectra separability of mangroves are considered in Section 4.4.3 using ASD data. Ideally, separabilities are assessed quantitatively using JM based separability statistics instead of spectral angles (SAs). The reasons for using SAs are made clear in Section 4.4.4, before drawing conclusions in Section 4.4.5.

4.4.1 Spectral Angle Interpretation

To appreciate the effect of spectra on SA magnitudes, a small selection of spectral plots are considered in this section. The complete list of SAs between all pairs of cover types are given in Table 68 to Table 89 of Appendix G.3 (p. 493), where SAs are stated in the form: mean \pm SD. These were calculated using ASD field trip data. All cover type plots are found in Appendix G.2 (p. 460), with a selection of these copied to this section to highlight spectral differences between pairs of plots and their effect on SAs. Note that it is the mean SAs, not the uncertainty, which is of interest in this section.

Later in this section, Figure 50 to Figure 56 are arranged on consecutive pages, beginning with Figure 50 on p. 168. These figures contain spectra corresponding to pairs of cover types, arranged in decreasing order of mean SA. Each figure makes use of a standardised thesis nomenclature, where site codes (e.g. [FM]) apply to ASD data collection sites – further details were given in Section 4.3.3. The use of identical scales for each plot makes intercomparisons an easier task. The SA in each figure is also roughly half that of the preceding figure (e.g. 0.88 rad in Figure 50 and 0.38 rad in Figure 51).

Figure 50 displays two spectra, corresponding to two vastly different cover types – shallow water soil and mangrove *Aegialitis annulata*. The red-edge that is characteristic of vegetation (as discussed in Section 2.3.1) is clearly absent in soil (as expected), contributing to large spectral differences and manifested in the large SA of 0.88 rad. The two spectra are clearly very different to each other; for instance, in the NIR spectral region (at wavelengths in excess of 700 nm), the reflectance for soil is much smaller than that corresponding to mangrove. The sharp rise at 700 nm is reminiscent of a vegetative spectrum (as discussed at length in Section 2.3.1). The vastly different spectra leads to the large mean SA of 0.88 rad.

The SA is calculated between pairs of spectra and is invariant with respect to either one or both spectra being multiplied by a constant (as demonstrated in Appendix E.3). This is only true if every reflectance value is multiplied by one and the same constant factor. If even one reflectance is modified by a different factor, then the SA will change; effectively the spectrum corresponds to a different cover type.

The soil spectrum of Figure 51 follows the mangrove (*Acaria sp.*) curve a little more closely. There is (overall) a higher degree of similarity between both the vegetative and soil spectra overall. In particular, the reflectances in excess of 800 nm between soil and the mangrove are more closely matched, as are those under 500 nm. The key differences lie on the red-edge (around 700 and 750 nm) where the reflectance changes abruptly for the mangrove. Between 750 – 900 nm, both spectra appear similar, with a very gentle parabolic shape for the soil and virtually no slope for the mangrove. At around 980 nm and onwards, both spectra are positive in slope. Compared to Figure 50, the closer spectral similarity leads to a smaller SA of 0.38 rad.

As the spectral similarity increases, the SA decreases as borne out by the rest of the figures. For example, comparing spectra between two types of the same cover type (e.g. vegetation), it is expected that broad patterns become more alike – both are green plants and both contain the red-edge characteristic. Therefore, large spectral regions are expected to follow similar patterns.

This is indeed the case, as shown in Figure 52, for *Aegiceras corniculatum* and *Ceriops australis*. Multiplying each reflectance for *Aegiceras corniculatum* will never

produce a match with *Ceriops australis* - if they did, the SA becomes zero, indicating identical spectra. Although a scale factor could lead to reflectances matching up those in the 400 – 500 nm reflectances more closely, differences still exist in slope (and reflectances) between (particularly) the 550 - 700 nm range. There is an addition slope change at around the 950 to 1000 nm range. However, overall, there are some structural similarities.

The next figure (Figure 53) roughly halves the preceding SA leads to 0.13 rad between *Ceriops australis* and *Avicennia marina*. At this point, the slopes appear very similar throughout for both species. These small changes result in a small SA, indicating higher spectral similarity.

As the spectral similarity of mangroves species increases (Figure 54 to Figure 56,), the SA decreases. In fact, the spectral plotted differences appear (visually) rather small at a SA of 0.08 rad (Figure 54) and almost identical at a SA of 0.02 rad (Figure 56) (as expected).

In general, large spectral differences between pairs of cover types (e.g. vegetation and soil) result in large SAs. Comparing two species of vegetation against each other increases the spectral similarity due to the spectral characteristics (e.g. red-edge) of vegetation, thereby decreasing the SA. For highly similar pairs of spectra (e.g. between mangroves *Bruguiera exaristata* and *Rhizophora stylosa*), the SA becomes so small that the spectra are almost indistinguishable. A SA of zero indicates the spectra are equivalent, as argued mathematically in Section 2.6.4.3.

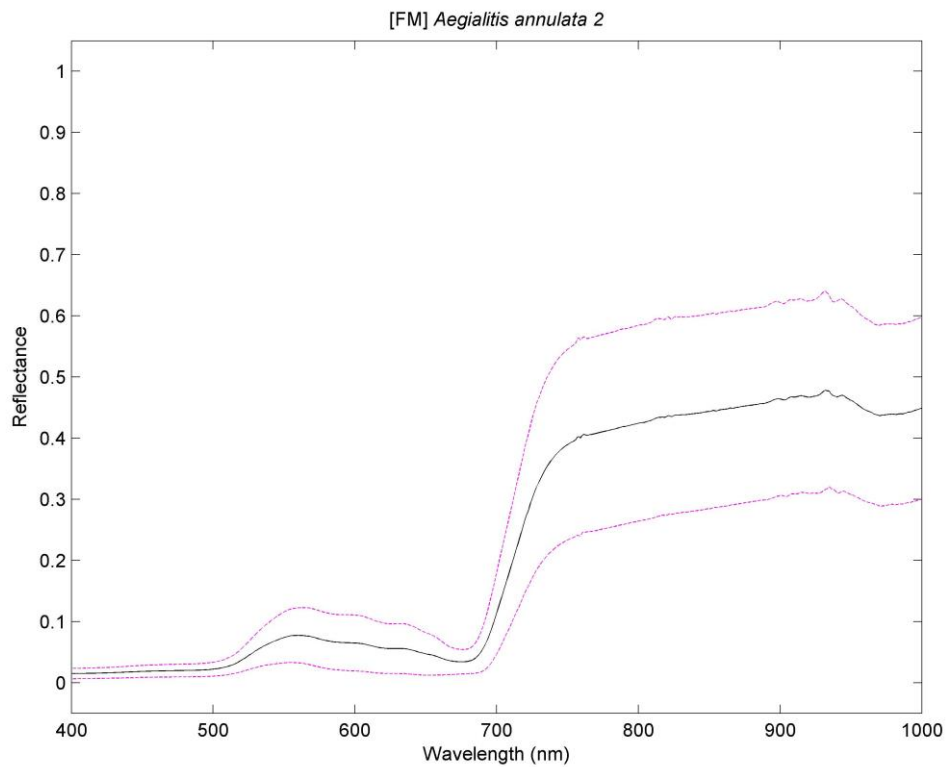
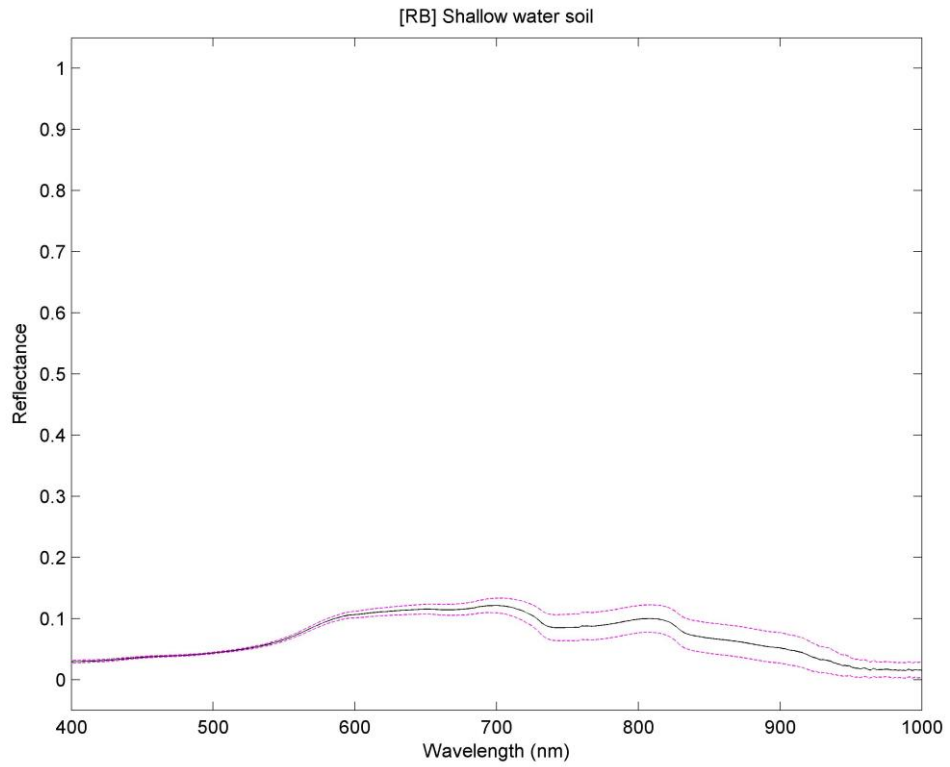


Figure 50: Spectral comparison between [RB] Shallow water soil and [FM] *Aegialitis annulata* 2 where $SA = 0.88 \pm 0.11$ rad.

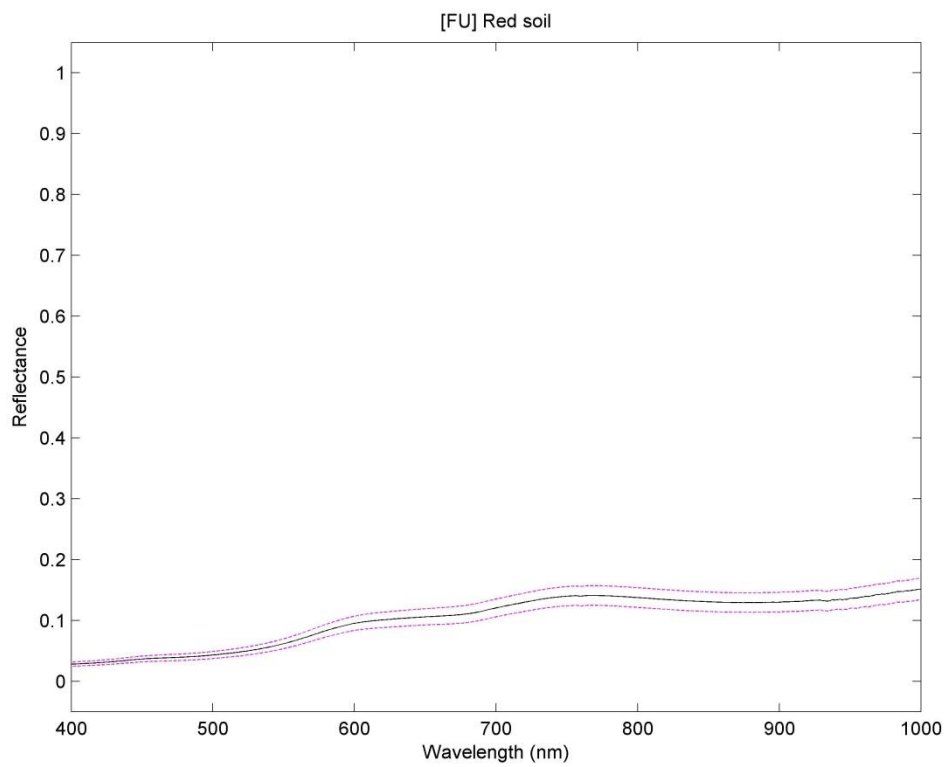
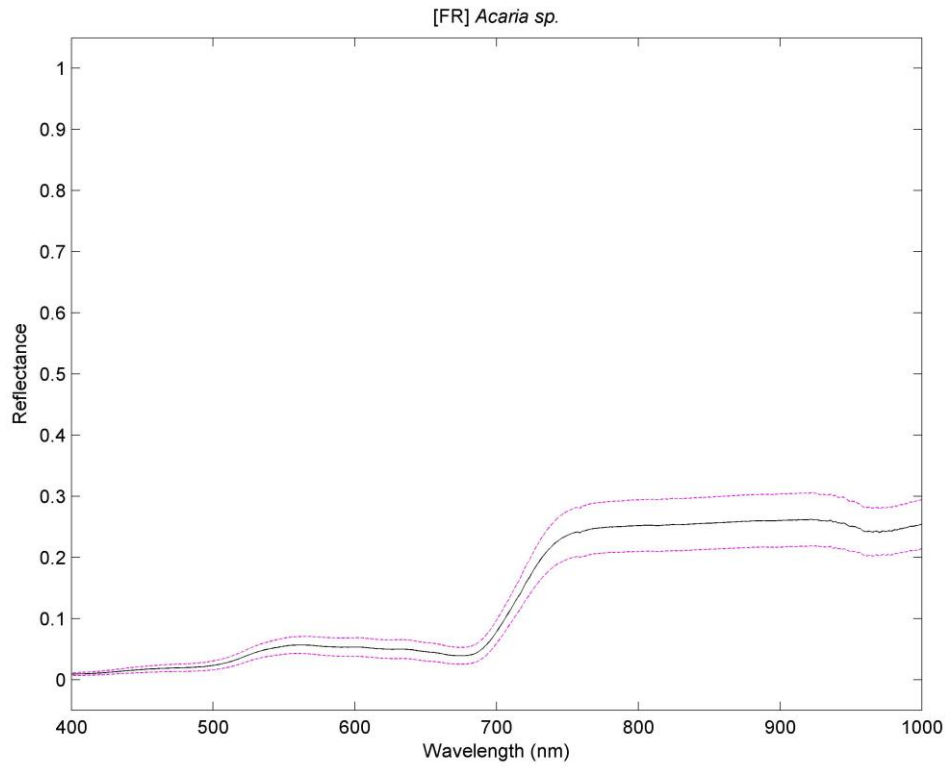


Figure 51: Spectral comparison between [FU] Red soil and [FR] *Acaria sp.*
 where $SA = 0.38 \pm 0.03$ rad.

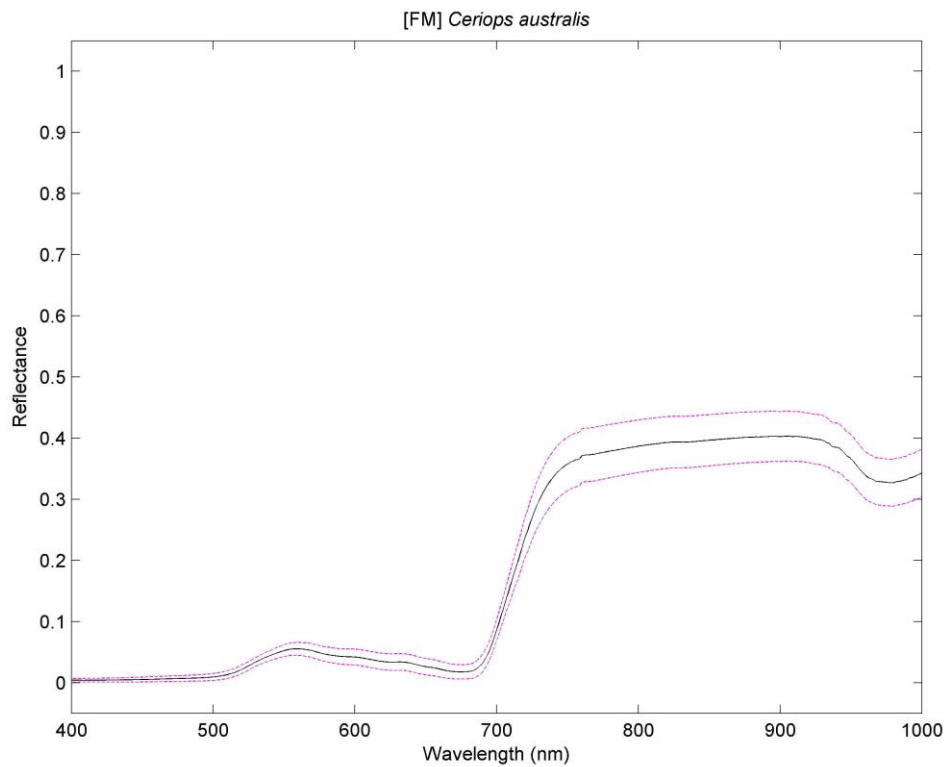
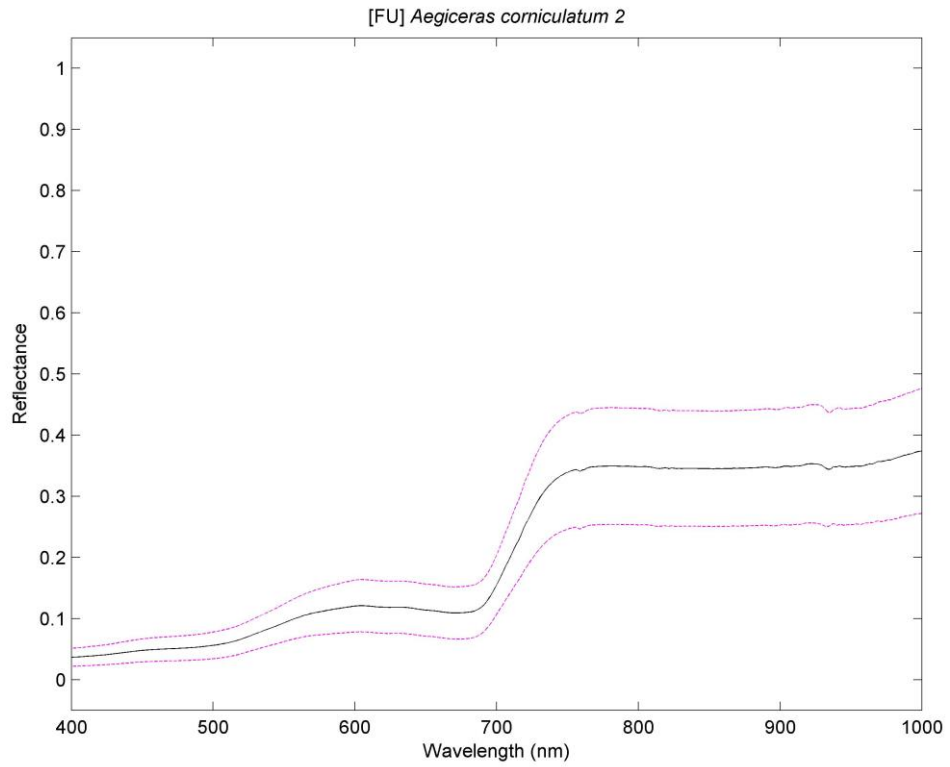


Figure 52: Spectral comparison between [FU] *Aegiceras corniculatum* 2 and [FM] *Ceriops australis* where $SA = 0.21 \pm 0.04$ rad.

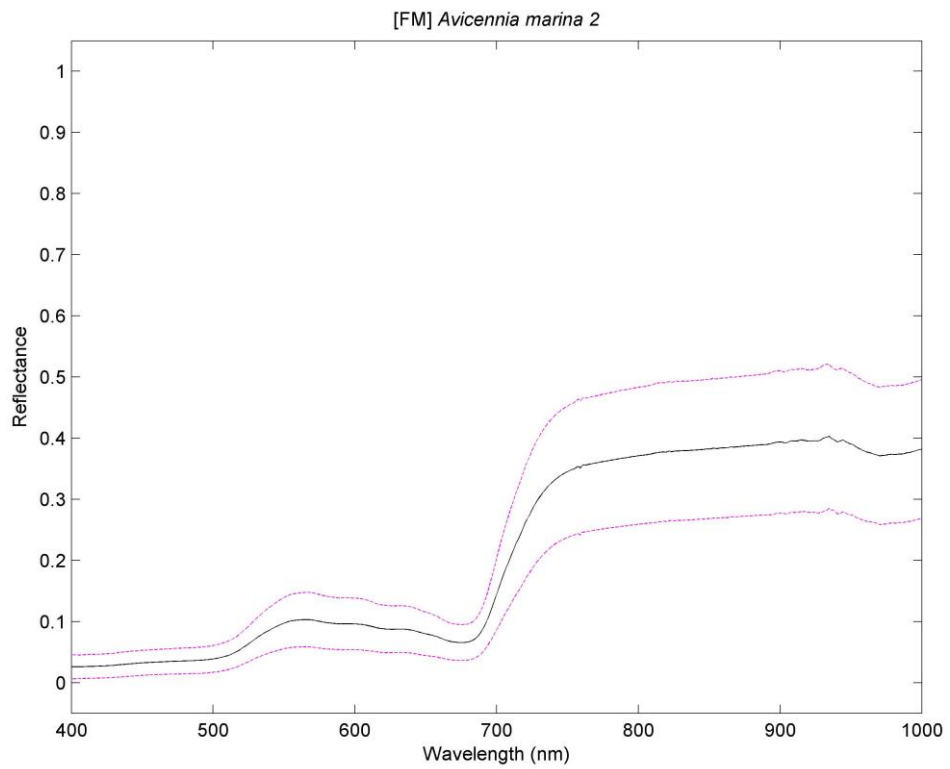
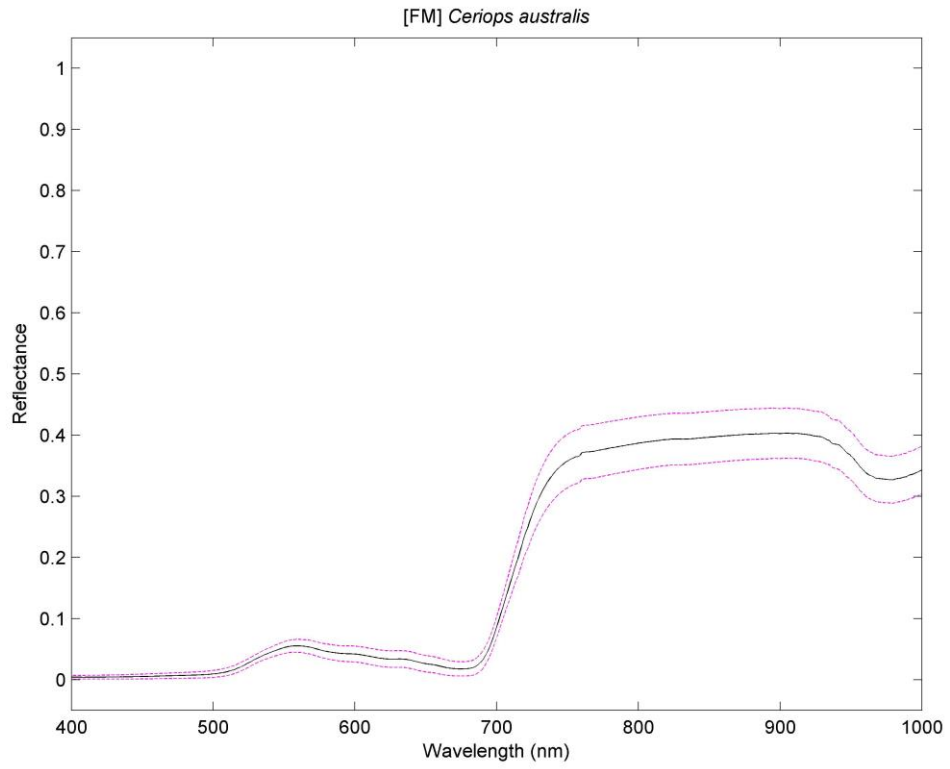


Figure 53: Spectral comparison between [FM] *Ceriops australis* and [FM] *Avicennia marina 2* where $SA = 0.13 \pm 0.04$ rad.

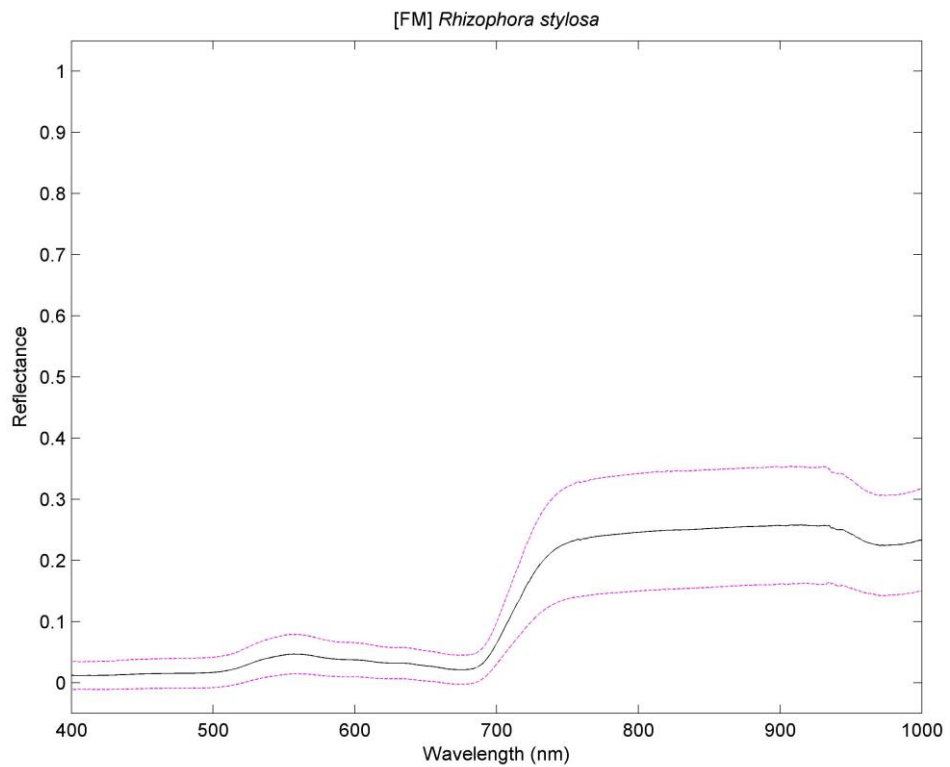
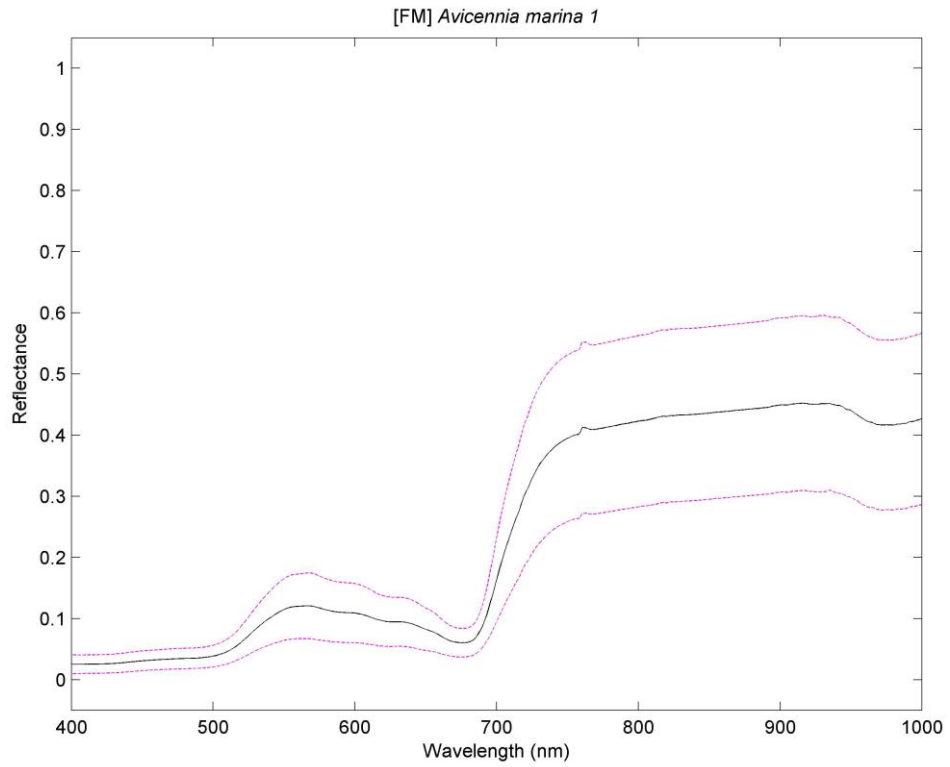


Figure 54: Spectral comparison between [FM] *Avicennia marina* 1 and [FM] *Rhizophora stylosa* where $SA = 0.08 \pm 0.04$ rad.

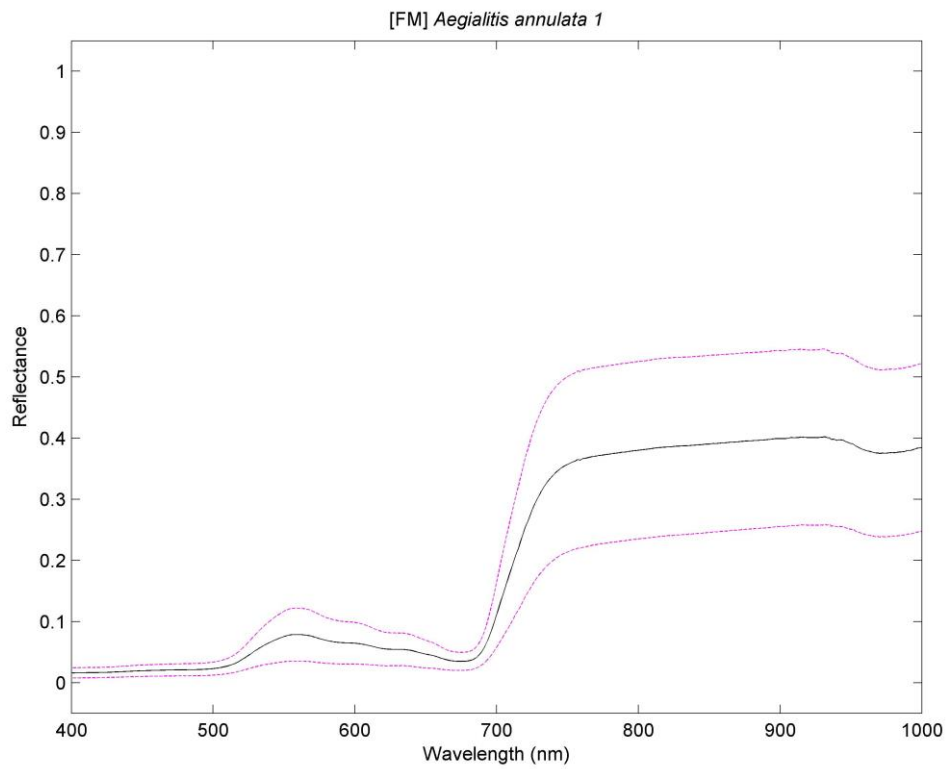
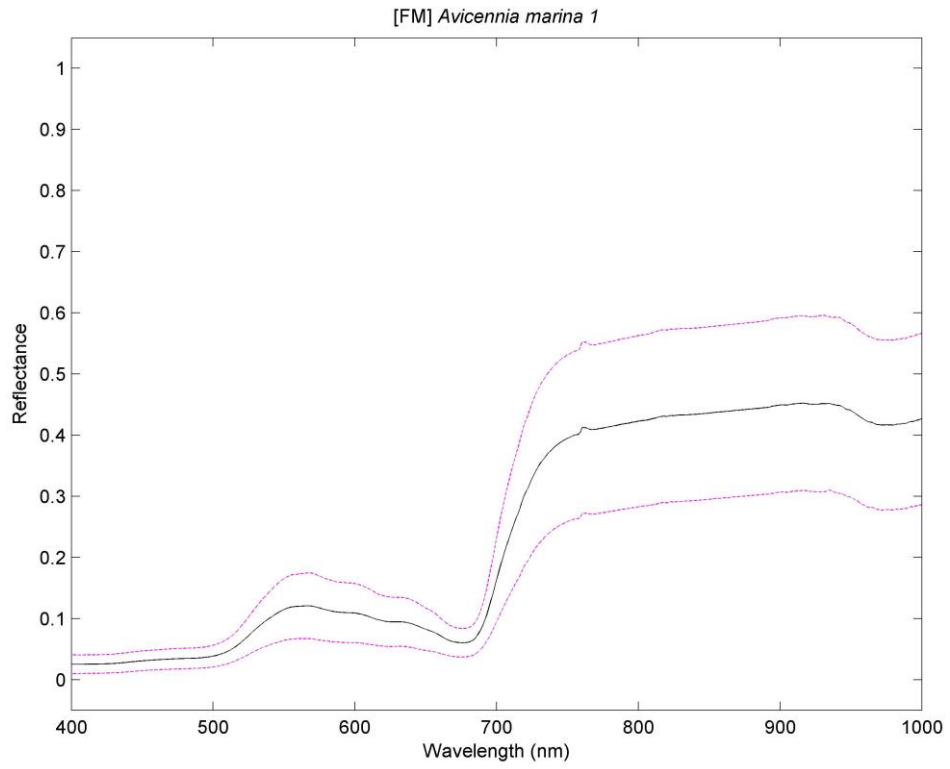


Figure 55: Spectral comparison between [FM] *Avicennia marina* 1 and [FM] *Aegialitis annulata* 1 where $SA = 0.06 \pm 0.03$ rad.

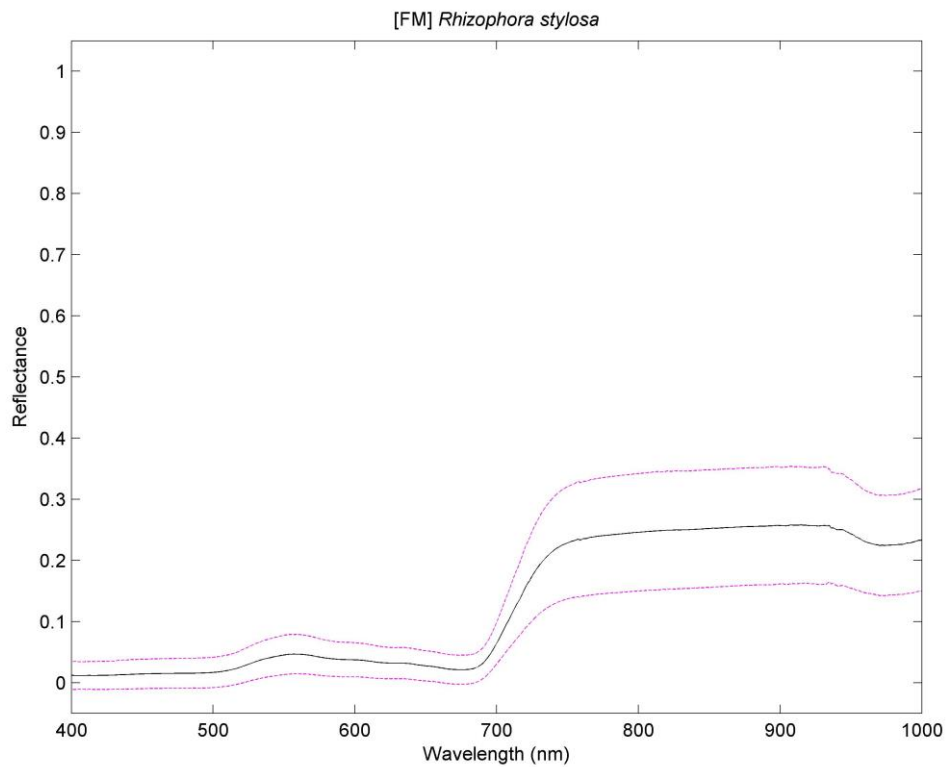
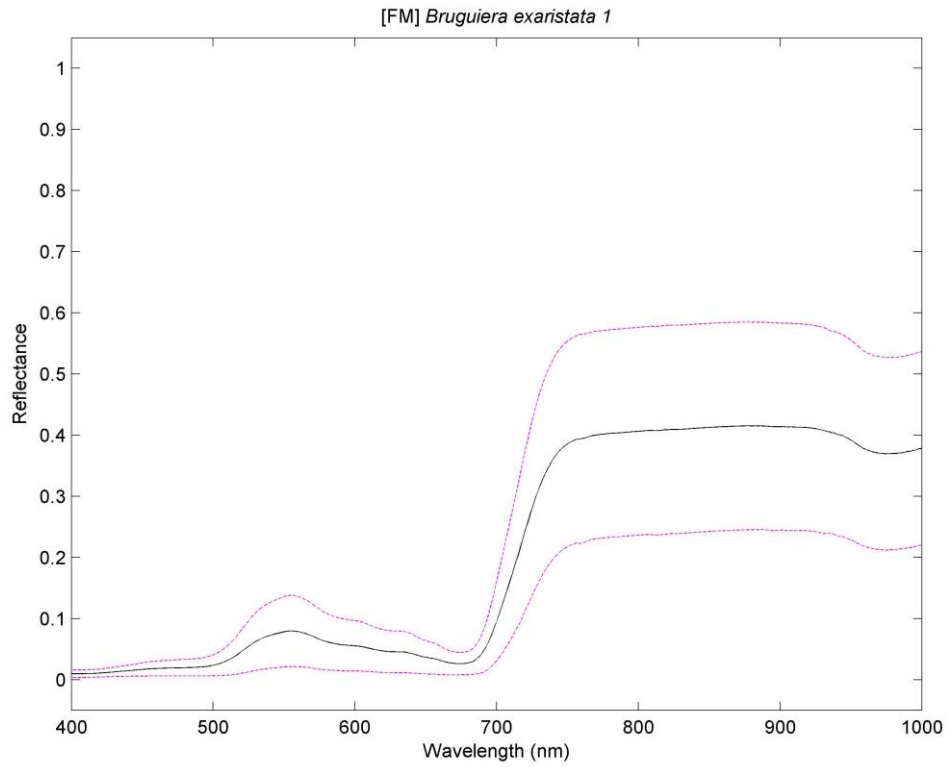


Figure 56: Spectral comparison between [FM] *Bruguiera exaristata* 1 and [FM] *Rhizophora stylosa* where $SA = 0.02 \pm 0.07$ rad.

4.4.2 Mangrove Spectra and Distinguishability.

It is useful to plot the mean ASD spectra for all 7 species of mangroves, to provide a visual overview of the differences and similarities between the spectra. Figure 57 shows the mean spectra for mangroves located at Finucane Island.

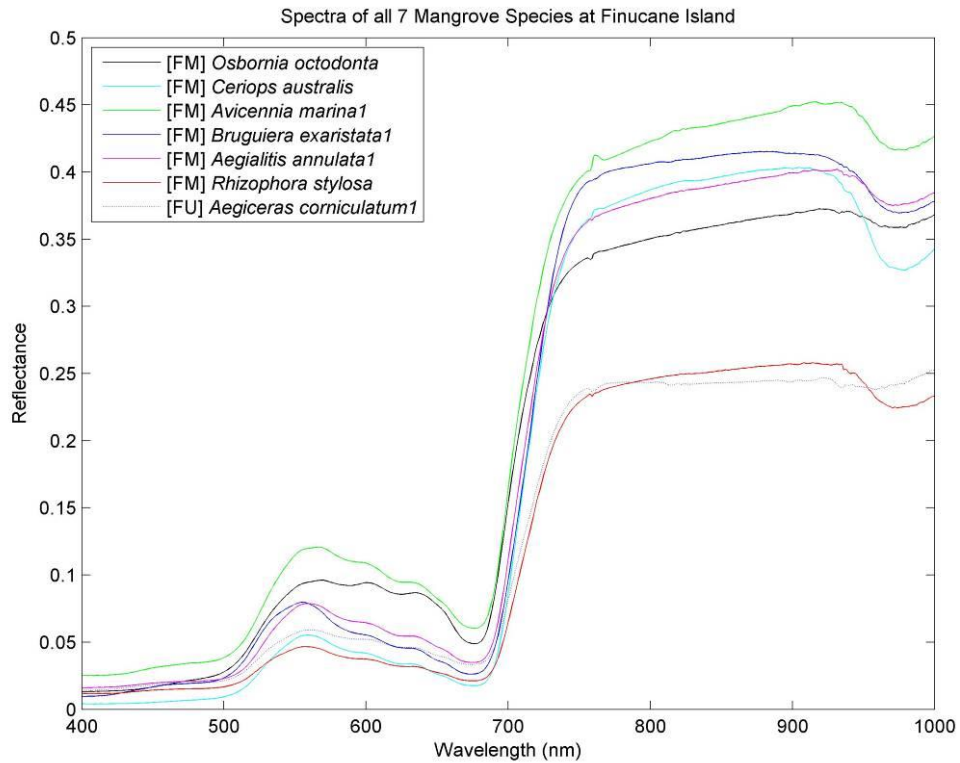


Figure 57: ASD mean spectra for the 7 mangrove species found on Finucane Island.

The plot shows minor positional differences for the red-edge between species. The most obvious difference between spectra occur between 500 nm and 700 nm, where curve gradients vary.

Other notable differences in Figure 57 relate to brightness differences. For example, in the RGB (i.e. 400 – 700 nm) region, *Avicennia marina* is particularly bright compared to the dark *Rhizophora stylosa* mangrove and is discernible to the human eye. However, in the NIR region, the human eye is not able to perceive the difference in brightness between these two species.

Figure 58 gives a magnified plot of Figure 57 for the same spectra but restricted in range (500 – 700 nm instead of 400 – 1000 nm).

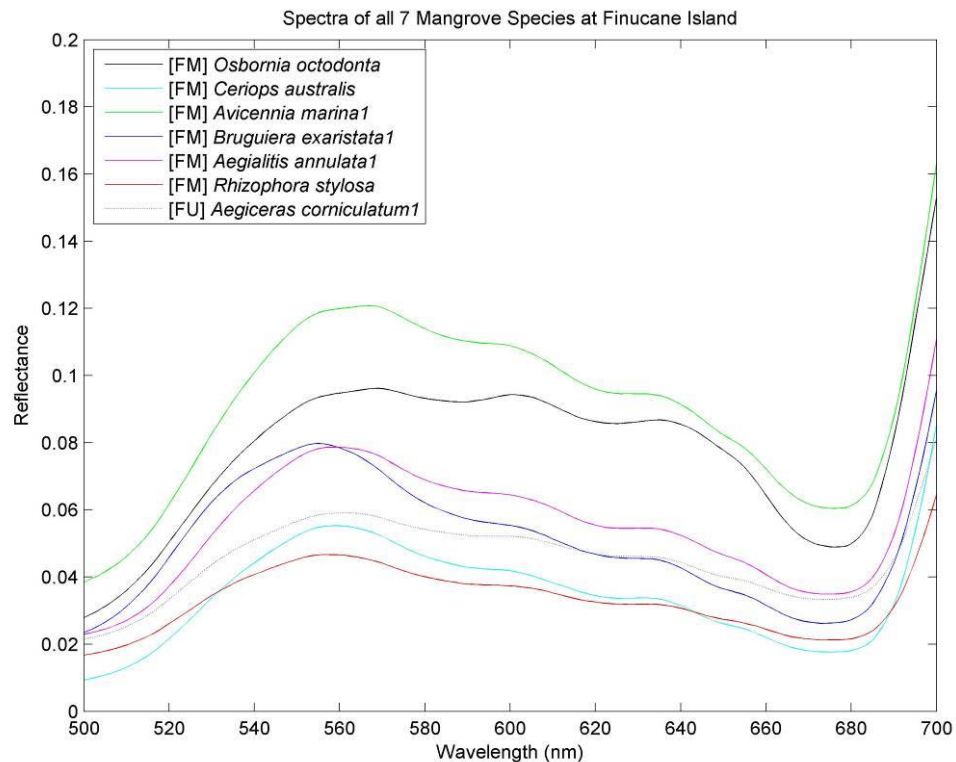


Figure 58: A magnified view of Figure 57 for mangrove ASD mean spectra. The same colour scheme as Figure 57 is used but restricted in range covering 500 - 700 nm.

The spectral similarities for *Bruguiera exaristata 1* and *Rhizophora stylosa* are particularly high, and reflected by the small SA of 0.02 ± 0.07 rad between these two species (see Table 16 (over the page) or the complete Table 69 (p. 498 of Appendix G.3) - Table 16 contains a summary of Table 69 and restricted to the Finucane Island mangroves). Details concerning how the SA uncertainty is calculated is given in Appendix G.3.

The SA between *Aegialitis annulata1* and *Rhizophora stylosa* of 0.03 ± 0.06 rad also infers a high degree of spectral similarity. The largest SA is 0.13 ± 0.04 rad, between *Osbornia octodonta* and *Ceriops australis*. However, the visual difference is not immediately discernible even for a SA at this level (see Figure 53). Taking account of the associated measurement uncertainty attached to each mean SA, the degree of similarity is even higher.

It needs to be highlighted that the observations described above pertain only to the mangrove species represented in Figure 58. In reality, more than one sample of

Region		FM	FM	FM	FM	FM	FM	FR	FU
Region	Cover Type	<i>Aegialitis annulata</i> 1	<i>Avicennia marina</i> 1	<i>Bruguiera exaristata</i> 1	<i>Ceriops australis</i>	<i>Osbornia octodonta</i>	<i>Rhizophora stylosa</i>	<i>Avicennia marina</i>	<i>Aegiceras corniculatum</i> 1
FM	<i>Aegialitis annulata</i> 1		0.06 ± 0.03	0.04 ± 0.04	0.07 ± 0.02	0.08 ± 0.04	0.03 ± 0.06	0.08 ± 0.04	0.05 ± 0.04
FM	<i>Avicennia marina</i> 1			0.09 ± 0.04	0.12 ± 0.04	0.03 ± 0.04	0.08 ± 0.04	0.03 ± 0.03	0.04 ± 0.04
FM	<i>Bruguiera exaristata</i> 1				0.04 ± 0.03	0.11 ± 0.04	0.02 ± 0.07	0.10 ± 0.05	0.07 ± 0.05
FM	<i>Ceriops australis</i>					0.13 ± 0.04	0.05 ± 0.06	0.13 ± 0.04	0.11 ± 0.03
FM	<i>Osbornia octodonta</i>						0.09 ± 0.04	0.04 ± 0.03	0.05 ± 0.04
FM	<i>Rhizophora stylosa</i>							0.09 ± 0.05	0.06 ± 0.05
FR	<i>Avicennia marina</i>								0.04 ± 0.04
FU	<i>Aegiceras corniculatum</i> 1								

Table 16: Spectral angles for the 7 mangroves at Finucane Island.

a single species may have been recorded. However, some of these samples are not considered 'true' representative mangrove samples. For instance, the spectrum for *Aegialitis annulata3* is unlike the two other samples for the same species, as it contained yellow leaves (a sign of chlorosis). The relatively large SA between *Aegialitis annulata3* and the other two samples (i.e. *Aegialitis annulata1* and *Aegialitis annulata2*) highlight an untypical spectrum. *Aegialitis annulata3* is therefore termed a 'non-typical' vegetative (spectral) sample. Further details are provided in Appendix G.3.

From Table 16, the SA between like-species located at two different sites ([FM] *Avicennia marina1* and [FR] *Avicennia marina*) is 0.03 ± 0.03 rad. This shows a very high spectral similarity between the species, where the SA varies between 0.00 rad (i.e. identical spectra) and 0.06 rad. However, the SA between [FR] *Avicennia marina* and [FM] *Osbornia octodonta* is only 0.04 ± 0.03 rad. Therefore, the SA varies between 0.01 rad and 0.07 rad. The 0.01 rad SA is much less than the upper SA of 0.06 rad for the same (*Avicennia marina*) species and is reminiscent of the conclusion reached by Price (1994) of Section 2.3.2, where interspecies spectra may vary more than intraspecies spectra. The situation is made worse when including mangroves from all sites (the full table of SAs of Table 69, p. 498 of Appendix G.3 – but dismissing 'non-typical' samples). For example, the SA between like species *Ceriops australis* at both [FM] and [RB] sites is 0.07 ± 0.06 rad, while the interspecies SA between *Ceriops australis* and several other species exceed this SA; e.g. [FM] *Aegialitis annulata1* at 0.07 ± 0.02 rad, [FM] *Bruguiera exaristata1* at 0.04 ± 0.03 rad and [RB] *Rhizophora stylosa* at 0.03 ± 0.03 rad.

Even by dismissing the measurement uncertainty, the subtle spectral differences between species demands very high quality airborne spectra for any chance at species differentiation. Even for ASD quality-like spectra, species differentiation at spectral level is a considerable challenge, especially when taking into account the measurement uncertainties. For instance, Table 16 shows the SA between [FM] *Osbornia octodonta* and [FM] *Rhizophora stylosa* as 0.09 ± 0.04 rad while between [FM] *Osbornia octodonta* and [FM] *Aegialitis annulata1* the SA is 0.08 ± 0.04 rad. A large overlap exists between these two SAs when taking into account the

uncertainty. The individual plots to these three species are found in Appendix G.2, highlighting large measurement uncertainties:

[FM] *Osbornia octodonta* (Figure 182, p.466)

[FM] *Rhizophora* (Figure 183, p.467)

[FM] *Aegialitis annulata*1 (Figure 178, p.462)

The hyperspectral library contains ASD quality spectra. When training a supervised classifier, these high quality spectra are compared to airborne recorded spectra, which are noisy. In Figure 59, the SA between the ASD and image (i.e. obtained from PHPA_Ref) spectra is 0.11 rad. This exceeds the majority of the mean SAs in Table 16, and all entries when incorporating the measurement uncertainties.

The above discussion considered spectra in a purely mathematical sense – numbers with measurement uncertainties. In reality, spectra differ according to physical processes; for instance, vegetation under stress causing a shift in the red-edge (as highlighted in Section 2.3.2). The airborne spectrum may therefore be different (e.g. stressed) compared to seemingly healthy vegetation recorded with the ASD (or vice-versa) at the same physical location. Consequently, it is possible for a vegetative species to be spectrally mismatched (even by ignoring ASD measurement uncertainty). In fact, it is possible for the spectral changes attributed to nutrient and/or water content, senescence, phenology or disease to cause a higher spectral match between ASD and airborne spectra, leading to misclassification.

Simultaneous recording of ASD ground spectra with airborne spectra decreases the possibility of such spectral mismatches, where spectra are recorded of vegetation having the same state as the airborne recorded spectra. Unfortunately, the ASD data were recorded some 3 years after the conclusion of the airborne survey. However, it is supposed that the mangrove forest distributions themselves changed little during the time period, as they live for many decades – in excess of 100 years (Cutler, 2014). As mentioned previously, seasonal effects (e.g. due to flowering) were minimised by deliberately recording ASD samples during the same month as the original PHPA hyperspectral airborne survey.

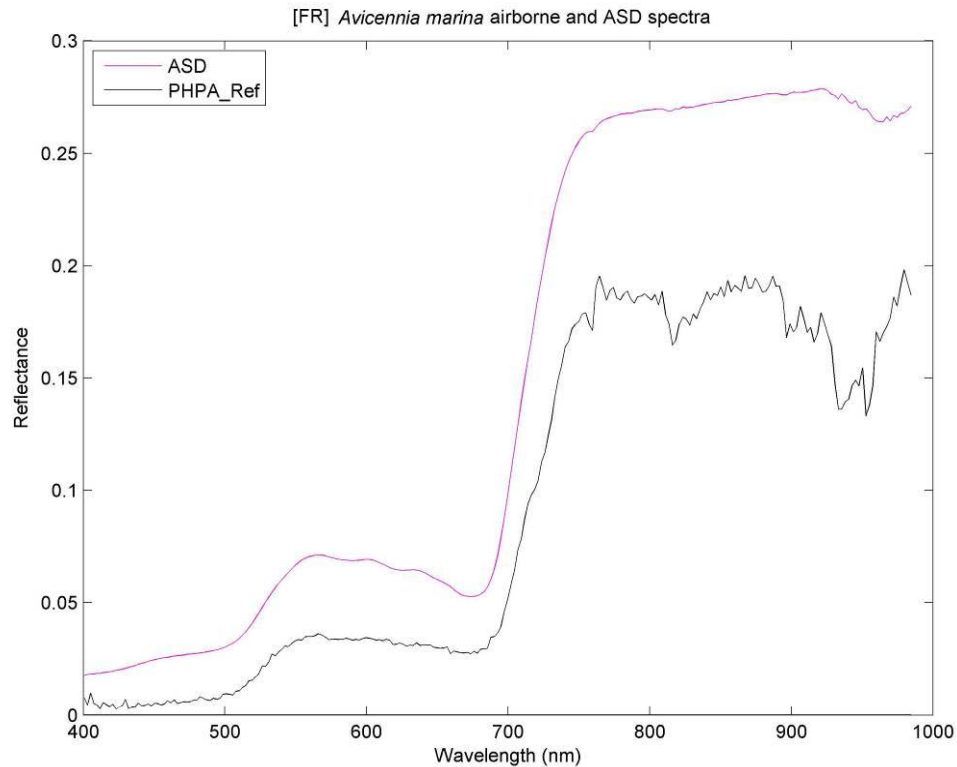


Figure 59: Comparison between ASD and PHPA_Ref (i.e. airborne-based image) reflectance spectra for [FR] *Avicennia marina* on Finucane Island. Section 4.5.9.6 contains a more detailed comparison between ASD and airborne spectra.

4.4.3 Mangrove Spectral Differentiability

The previous section discussed several factors involved in spectrally distinguishing the seven mangrove species on Finucane Island. Only one spectral sample from each mangrove was used in the analysis (but composed of 10 – 15 individual measurements). In reality, the first field trip took more samples at different sites.

This section identifies the spectrally most similar and dissimilar mangroves from each other. However, this task is made more difficult due to the large number of wide ranging SAs for each mangrove, as given in Table 68 to Table 89 of Appendix G.3.

The following conditions reduce the complexity in analysing the data:

- Only mean angles are considered (i.e. the uncertainties are ignored)

- Only ‘typical’ mangrove spectra are considered – therefore, [FU] *Avicennia marina*, [FU] *Aegiceras corniculatum*², [FU] *Aegialitis annulata*³ and [FR] *Avicennia marina* are dismissed (Reasons are given in Appendix G.3).
- Only mean SAs over (but not including) 0.10 rad and under (but not including) 0.05 rad are tallied up (i.e. counted). Those over 0.10 rad are considered ‘large’ and those under 0.05 rad considered ‘small’.
- The tally does not consider ‘like’ species (e.g. a SA between *Avicennia marina*¹ and *Avicennia marina*² of 0.11 rad is not tallied up against the ‘large’ SA).
- The tally counts only one mean SA if there are multiple specimens. For instance, *Avicennia marina* has a mean SA with *Aegialitis annulata*¹ of 0.11 rad and a mean SA of 0.12 rad with *Aegialitis annulata*² - the ‘large’ SA tally is counted only once.
- The tally uses a mean number for the ‘small’ and ‘large’ SA. For example, *Bruguiera exaristata*¹ contains 3 small SAs and 3 large SAs while *Bruguiera exaristata*² contains 2 small SAs and 3 large SAs. In this case, the tally for *Avicennia marina* is considered to have 2.5 small SAs and 3 large SAs.

The reasoning behind the last condition stems from an observation that a mangrove species in one location may behave (spectrally) different to the same mangrove species at another location. For example, the SA between [FM] *Osbornia octodonta* and [FM] *Rhizophora stylosa* is 0.09 ± 0.04 rad, while the SA between [FM] *Osbornia octodonta* and [RB] *Rhizophora stylosa* is 0.12 ± 0.03 rad. The SA of 0.09 rad is not counted toward the ‘large’ angle, while the 0.12 rad is. Therefore, for this single species of *Rhizophora stylosa*, a ‘large’ angle does exist and must be counted. For this reason, the maximum number is tallied up when considering a single species.

Table 17 contains the SAs for all species of *Bruguiera exaristata* with all other ‘typical’ mangrove species. The ‘nontypical’ mangroves are crossed out, thereby not counted toward the tallies corresponding to the ‘large’ and ‘small’ SAs (which make up the last two rows in the table).

The mechanics behind this table is similar to that of Table 16. For example, the SA between [FM] *Bruguiera exaristata*¹ and [FM] *Aegialitis annulata*¹ is 0.04 ± 0.04 rad.

To illustrate how the tally system works in practice, consider the second column for [FM] *Bruguiera exaristata*². Mangroves with which it forms a small SA (i.e. less than 0.05 rad) are: [FM] *Aegialitis annulata*¹, [FM] *Aegialitis annulata*², [FM] *Ceriops australis*, [FM] *Rhizophora stylosa* and [RB] *Rhizophora stylosa*. The tally is five, but as both the single mangrove species *Aegialitis annulata* and *Rhizophora stylosa* are listed twice (in the rows – thereby tallied twice), the tally reduces by two. Therefore, the final count is three.

In this manner, the final tally is summarised in Table 18 and encompassing all 7 mangrove species.

From Table 18, on average, the mangrove species *Osbornia octodonta* is the most different to other mangrove species (due to the highest number of large SAs). In fact, a large spectral difference to 3 of the 7 mangrove species. Spectrally, the most similar (i.e. smallest SA) mangrove species with all other mangrove species are *Bruguiera exaristata*, followed closely by both *Rhizophora stylosa* and *Aegialitis annulata*.

	Region	FM	FM	RB
Region	Cover Type	<i>Bruguiera exaristata</i> 1	<i>Bruguiera exaristata</i> 2	<i>Bruguiera exaristata</i>
FM	<i>Aegialitis annulata</i> 1	0.04 ± 0.04	0.04 ± 0.05	0.09 ± 0.03
FM	<i>Aegialitis annulata</i> 2	0.05 ± 0.05	0.04 ± 0.06	0.09 ± 0.04
FM	<i>Aegialitis annulata</i>3	-0.27 ± 0.04	-0.27 ± 0.05	-0.31 ± 0.03
FM	<i>Avicennia marina</i> 1	0.09 ± 0.04	0.09 ± 0.05	0.14 ± 0.04
FM	<i>Avicennia marina</i> 2	0.10 ± 0.04	0.10 ± 0.05	0.15 ± 0.04
FM	<i>Avicennia marina</i> 3	0.12 ± 0.08	0.12 ± 0.08	0.17 ± 0.08
FM	<i>Bruguiera exaristata</i> 1	-	-0.02 ± 0.07	0.06 ± 0.03
FM	<i>Bruguiera exaristata</i> 2	-0.02 ± 0.07	-	0.06 ± 0.05
FM	<i>Ceriops australis</i>	0.04 ± 0.03	0.04 ± 0.05	0.03 ± 0.03
FM	<i>Osbornia octodonta</i>	0.11 ± 0.04	0.11 ± 0.04	0.16 ± 0.04
FM	<i>Rhizophora stylosa</i>	0.02 ± 0.07	0.02 ± 0.08	0.07 ± 0.06
FR	<i>Avicennia marina</i>	-0.10 ± 0.05	-0.10 ± 0.05	-0.15 ± 0.04
FU	<i>Aegiceras corniculatum</i> 1	0.07 ± 0.05	0.08 ± 0.05	0.13 ± 0.04
FU	<i>Aegiceras corniculatum</i>2	-0.17 ± 0.05	-0.17 ± 0.06	-0.22 ± 0.04
FU	<i>Avicennia marina</i>	-0.19 ± 0.05	-0.19 ± 0.06	-0.24 ± 0.04
RB	<i>Avicennia marina</i>	0.06 ± 0.05	0.06 ± 0.06	0.11 ± 0.04
RB	<i>Bruguiera exaristata</i>	-0.06 ± 0.03	-0.06 ± 0.05	-
RB	<i>Ceriops australis</i>	0.05 ± 0.07	0.05 ± 0.07	0.09 ± 0.06
RB	<i>Rhizophora stylosa</i>	0.04 ± 0.04	0.03 ± 0.05	0.04 ± 0.03
LP	<i>Avicennia marina</i>	0.07 ± 0.04	0.07 ± 0.04	0.12 ± 0.02
	tally: small SA (< 0.05 rad)	3	3	2
	tally: large SA (> 0.10 rad)	2	2	3

Table 17: The spectral angles for all species of *Bruguiera exaristata* with 'typical' mangroves. The 'nontypical' mangroves are crossed out and not counted toward the tally.

Mangrove species	Small SA (< 0.05 rad)	Large SA (> 0.10 rad)
<i>Avicennia marina</i>	1.4	2.2
<i>Ceriops australis</i>	1.5	1.5
<i>Rhizophora stylosa</i>	2.5	1
<i>Bruguiera exaristata</i>	2.7	2.3
<i>Osbornia octodonta</i>	1	3
<i>Aegialitis annulata</i>	2.5	0.5
<i>Aegiceras corniculatum</i>	1	2

Table 18: Final mean tally totals for small and large spectral angles corresponding to mangrove species.

4.4.4 Spectral Similarity Assessment using Separability Measures

Spectral separabilities were calculated using SAs. Ideally, the statistics would be expressed in terms of the JM distance, as it relates directly to the thematic map and takes into account spectral variability; the JM distance uses 2nd order statistics SAs do not.

The advantage of the JM distance is realised when considering a thematic map whereby classes have been merged to a JM distance of 1.8, indicates a sound degree of spectral separability. If JM distance for ASD spectra between pairs of cover types (e.g. mangroves) were less than 1.8, it suggests a low probability of class separability on a thematic map. A direct link therefore exists between class separability on a thematic map and ASD recorded cover types.

The JM distance relies on a covariance matrix (see Equation (2.5.5.1) of Section 2.5.5) to express variability between bands. It also relies on a mean vector corresponding to a class. There needs to be enough variability (with respect to the number of bands) for the covariance matrix to be invertible. The problem of covariance matrix inversion is known to hyperspectral remote sensing and is the result of having an excess number of bands in relation to the number of samples. The PC transform is one method used to reduce the number of bands by reducing their correlation.

For the ASD data, only 10 - 15 spectral measurements were taken for each sample (e.g. a mangrove tree). Samples were also taken at other sites, consisting of the same cover type. In all, *Avicennia marina* was the most widely found mangrove, located over the whole Port Hedland coastal region and resulted in a total of 60 measurements across all sites (i.e. for 5 individual mangrove trees). Compared to the 591 ASD spectral bands (400 – 990 nm), even this number pales in relation to the number of samples required to calculate an invertible matrix. For example, Congalton and Green (1999) suggest a number of at least 75 per category (as discussed in detail under Section D.1). This number is not 75 measurements of a single mangrove but rather 75 mangrove trees of a single type. Considering that 10 - 15 ASD measurements are reasonable for a single tree, it amounts to at least 750 ASD measurements just for one cover type!

As a result, it is unfortunately not mathematically possible to obtain the mangrove separability for all species in terms of the JM distance with the ASD data currently at hand.

4.4.5 Summary and Discussion

Using ASD field recorded spectra, spectral similarities between pairs of cover types were assessed quantitatively using SAs, whose magnitudes were interpreted in Section 4.4.1. This work suggests that large angular differences (in excess of about 0.4 rad) allows for the confident differentiation between vegetative and non-vegetative cover types (e.g. soil and vegetation). The NDVI (for example) is able to confidently identify vegetation from non-vegetation. Smaller SAs are evident between like cover types, such as between two vegetative types. Higher level classifiers (both unsupervised and supervised) are needed to help distinguish between spectra which are more alike. Instead of using two values (e.g. the NDVI), higher level classifiers use the whole spectrum for pattern matching. Visually, the spectral differences are evident from the plots for SAs of 0.21 rad (Figure 52) but are harder to discern at 0.13 rad (Figure 53). Two spectra are particularly difficult to differentiate for SAs of around 0.10 rad (and less). As the angle of separation decreases, the probability of spectrally separating two cover types decreases. A zero angle indicates complete similarity between pairs of spectra (i.e. identical spectra). Two spectra may appear different graphically, but still produce a zero SA. This arises when one spectrum is multiplied by a constant (i.e. multiplying all reflectances over all wavelengths), thereby appearing to produce a new spectrum. However, it is actually unchanged as the spectral angle mapper is invariant with respect to brightness.

Spectrally distinguishing different species of mangroves requires SAs having mean values of (roughly) 0.02 – 0.08 rad, as shown in Table 68 to Table 89 (Appendix G.3). This does not even take into account the uncertainty caused by the natural variability of vegetation. Such small angles suggest that most mangroves spectrally indistinguishable from each other. In practical terms, *Osbornia octodonta* is the easiest (in general) to distinguish from other mangrove species, with

Bruguiera exaristata the hardest, followed closely by *Rhizophora stylosa* and *Aegialitis annulata* (equally on average).

There are also situations where interspecies spectral variability exceeds intra-species variability demonstrating that different species may appear more similar than like species.

In an ideal sense, the ASD hyperspectral library for the Port Hedland coastal region is used to train a supervised classifier (e.g. SAM), thereby allowing spectra in pixel spectra to be matched with identified cover types from field work. However, Section 4.4.2 showed that the difference between airborne reflectance spectral quality and the ASD spectra is too large to confidently classify mangroves at species level. The uncertainty is compounded as ground spectra were recorded some three years after the airborne survey, as the state of the mangrove may differ.

There is also the possibility of having unknown cover types (i.e. not sampled in the field work) present in pixel data but whose identity is unknown. For instance, if an unknown cover type has a pixel spectrum very similar to another pixel spectrum, which has been identified in field work. This leads to misidentification and potentially overstating the population of a particular cover type.

Despite these factors, an attempt was made using the PHPA ASD hyperspectral library for training the supervised SAM classifier over the Finucane Island region. The results are shown in Appendix J, which proved unsatisfactory (as expected!), with the noisy airborne spectra being a real impediment.

Another attempt used a very limited set of pixel spectra to train the SAM classifier over an even smaller region. The work is found in Appendix J.2 and demonstrates the effectiveness of the SAM classifier when selecting suitable SAs, leaving behind only vegetation regions. Instead of using vegetative pixels for training, a different approach was taken by training the classifier using only non-vegetative samples. Removing non-vegetative pixels from the scene successfully left behind vegetation pixels.

There is, however a caveat to this work on supervised classification. As demonstrated in Section 4.5.9.1, image spectral inconsistencies became apparent during the course of this research. Spectra were shown to change within flight lines, across flight lines and even over the whole image. When selecting training image

spectra for one cover type, the image spectra change according to the location where they are collected. This means that a supervised classifier could produce different classes depending on where the training pixels were collected, even though they belong to the same cover type. This undesirable effect reduces the confidence associated with the supervised result.

4.5 Objective 3a: Production of a Vegetation Map

Equation Chapter 4 Section 5

At the lowest-detail, a vegetation map shows regions where vegetation exists (i.e. vegetation versus non-vegetation). It is not concerned with the type of vegetation; such a simple map can be obtained using VI's. The NDVI in particular has been extensively utilised for a number of decades, making its properties well understood. Section 4.5.1 examines the behaviour of the NDVI in the context of Finucane Island.

A different approach to VI's is considered in Section 4.5.2, which overcomes NDVI shortcomings as a result of negative reflectances contained in the PHPA hyperspectral image. It also exploits more wavelengths than the typical NDVI, which uses just two, thereby providing a smoothing effect on the noisy data. This work led to the production of vegetative versus non-vegetative maps.

The basic vegetation map as produced using the NDVI in Section 4.5.1 revealed inconsistent data patterns across flight line boundaries, resulting in an investigation of the image. The findings are presented in Section 4.5.3.

The important findings for this work (i.e. Section 4.5 thus far) are summarised and discussed in Section 4.5.4 before proceeding to unsupervised classification. A hyperspectral based classification paradigm is developed in Section 4.5.5, which leads to the production of a thematic map.

As our interest lies in producing a vegetative-based thematic map, non-vegetative cover types were eliminated using a mask (the technical details are discussion in Section 4.5.6). This helps reduce the number of classes in the thematic map and improves the performance of the classifier (as there is less data).

The resulting image thereby contains only vegetative regions, and is classified using the classification paradigm of Section 4.5.5. The result is a thematic map discussed in detail in Section 4.5.7 for the PHPA reflectance-based image (i.e. PHPA_Ref – viz. Figure 42, p. 141 of Section 3.3). However, the thematic map clearly contains a number of spatially inconsistent class regions, undermining the confidence in the integrity of the result.

As the reflectance image is produced from airborne radiance data, Section 4.5.8 examines the integrity of the Tafkaa input parameters in an attempt to account for the inconsistent spatial nature of classes in the thematic map. However, these

parameters appear sound, thereby forming the basis of a whole new approach to study the spectral behaviour over the whole image. The result identified brightness inconsistencies in the reflectance data leading to a correction-process termed normalisation. This empirical-based approach improves the spectral brightness consistency over the whole image. Section 4.5.9 introduces and discusses normalisation at length before using the spectrally-improved image (i.e. the normalised image) to produce a new thematic map.

The effect of several different image masks (e.g. like that of Section 4.5.6) on normalisation were also investigated. The 'best' thematic result is presented in Section 4.5.11, thereby fulfilling the requirements for thesis sub-objective 3a. The other normalisation attempts are found in the Appendices (*viz.* image construction in Appendix L and their associated thematic maps in Appendix O).

4.5.1 Image Classification using the NDVI

The region of Finucane Island (see Figure 35, p. 131 of Section 3.2) is suitable to investigate the behaviour of the NDVI as it contains a mixture of cover types, including vegetation, soil, iron-ore stockpiles and water. The results of this preliminary analysis were used to guide subsequent approaches for vegetative classification. Figure 60 shows a true colour image of the region used in this study.

The bands in the PHPA airborne hyperspectral image do not contain the exact 670 nm and 800 nm wavelengths in accordance with the NDVI definition of Haboudane et al. (2004) (i.e. Equation (2.6.2.1.2) of Section 2.6.2.1). The closest wavelength to 670 nm are 668.7 and 671.1 nm in the PHPA dataset. The same applies to the 800 nm; only 798.8 nm and 801.3 nm are defined in the hyperspectral dataset.

One way to resolve of this problem is by using cubic spline interpolation; to find the reflectances corresponding to the 670 nm and 800 nm wavelengths. Appendix R provides further details regarding cubic spline interpolation.

The actual NDVI value was calculated pixel-by-pixel and stored as a new image

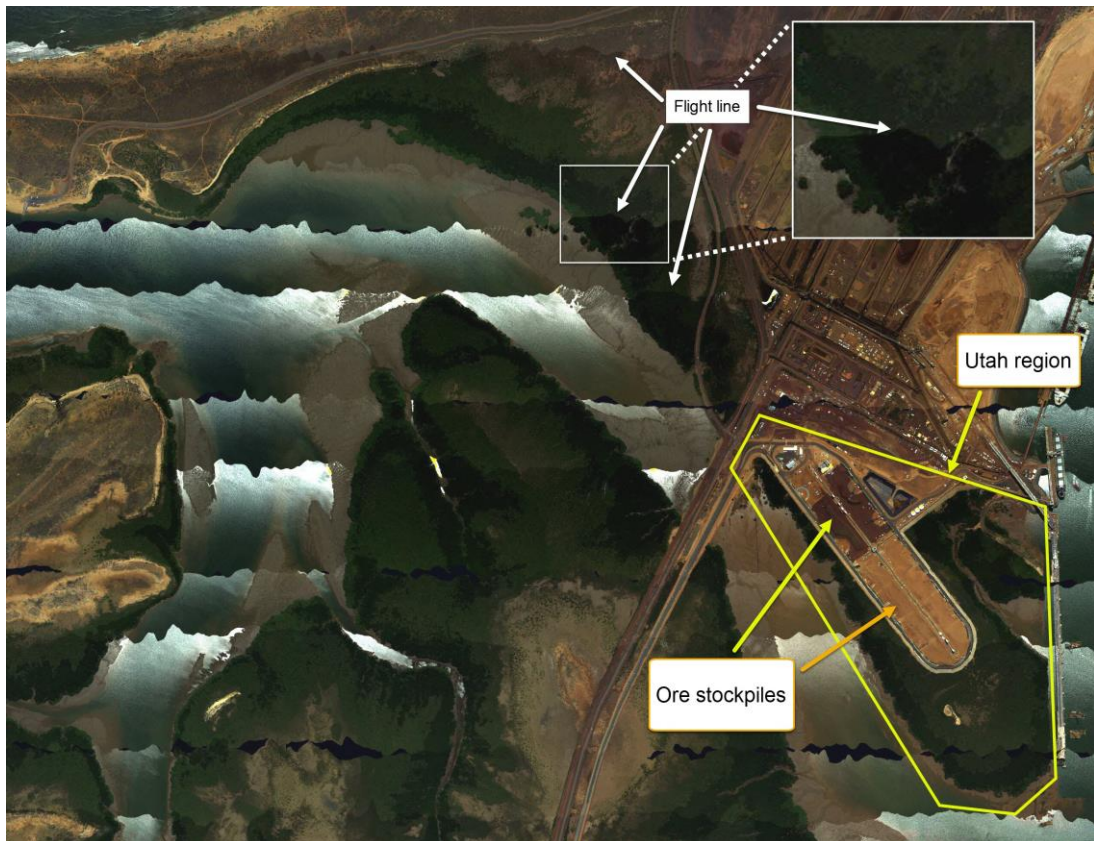


Figure 60: Finucane Island selected to study the effect of NDVI.
 The smaller white boxed region is magnified and used later in Figure 62.
 White arrows point toward flight line boundaries. The Utah region is defined within the yellow boundaries and contains ore stock piles.

using a C++ program. Each pixel therefore contains a single NDVI value. The result is shown in Figure 61, showing numerous bright pixels, representing vegetation while darker shades occur over soil and water. The brighter the pixel, the higher the NDVI. However, individual NDVI values can be inspected on a pixel basis using ENVI. However, it is difficult to discern any gross patterns – the pixels all appear equally white to the analyst. Instead of inspecting each pixel value manually for spatial patterns, a classification-type map may be constructed using colours defined by ranges of NDVI values. The concept is similar to that used in classification schemes, where classes instead define patterns of spectral similarity, but in this case, groups of similar NDVI values.

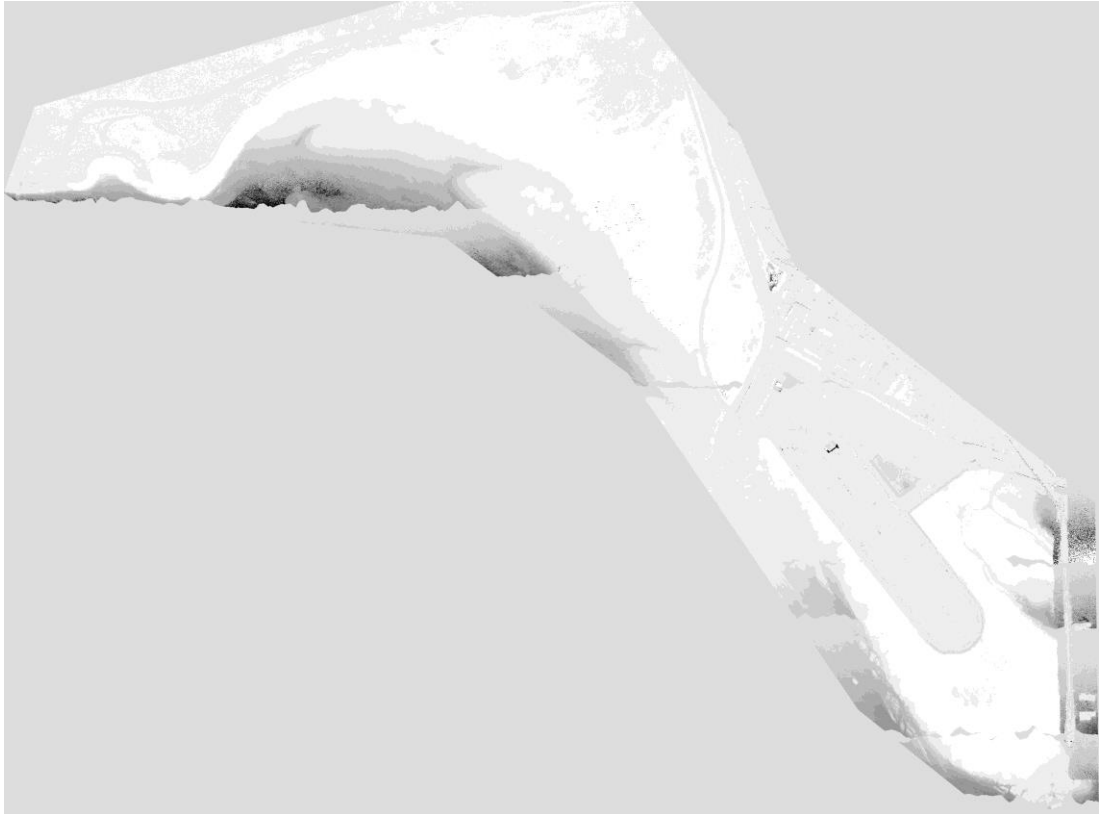


Figure 61: NDVI result as an image for Finucane Island using the definition of Haboudane et al. (2004) for PHPA_Ref data. High positive NDVI values relate to bright white regions while dark areas relate to large negative values.

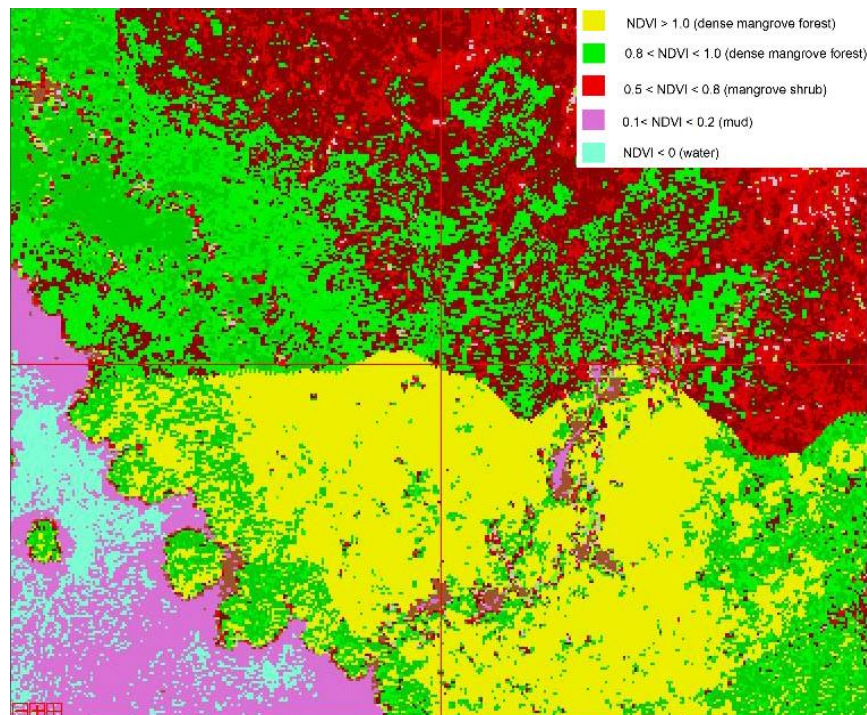


Figure 62: The colours cover different NDVI ranges, as shown in the legend.

This figure is a magnified view of the white-boxed region in Figure 60. The physical features present are shown in brackets beside the NDVI values in the legend.

A total of 20 colours, each one defining a 0.1 range of NDVI values, allows the analyst to discern broad patterns without being overwhelmed. Figure 62 shows part of this work and corresponds to the white-boxed region of Figure 60.

Although dense mangroves cover the green and yellow coloured regions, there appears to be a distinct boundary. The boundary is also defined by a flight line boundary in the stitched image.

The green colour (both light and dark) contain NDVI values between 0.8 and 1.0, while for the red (all shades) the NDVI values lie between 0.5 and 0.8. Rather surprisingly, the NDVI values in the yellow region range are over the allowed NDVI limit of exceeding 1.0. As discussed further down, it is bad image data which causes negative NDVI values, rather than a limitation of the NDVI itself.

It is useful to introduce the concept of a red-edge length to aid discussion. Vegetation has a clearly defined red-edge spectral feature distinct from non-vegetation (see for example Figure 4 (p. of Section 2.3.1)). The red-edge length refers to the size of the red-edge and can be defined according to the difference in brightness (e.g. reflectance) at the NIR and R wavelengths. With reference to Equation (2.6.2.1) (Section 2.6.2.1), the red-edge length is simply: $NIR - R$. For example, the red-edge length of [FM] *Aegialitis annulata* 2 is clearly more distinct than that for [RB] "Shallow water soil" Figure 50 (p. 168 of Section 4.4.1), and is therefore longer. The red-edge length of [FM] *Avicennia marina* 1 is also longer than [FM] *Rhizophora stylosa* (see Figure 57, p. 175 of Section 4.4.2).

High NDVI values result from spectra containing large red-edges, and relates to a high probability of finding vegetation (i.e. 'strong' vegetation – e.g. mangrove). Conversely, a low NDVI means a small red-edge (i.e. 'weak' vegetation – e.g. grass). It is apparent that there is a dramatic change in NDVI simply by traversing across a flight line boundary (i.e. the boundary between adjacent flight lines), which makes no physical sense. Field work conducted at a later date showed that dense mangroves exist in the regions defined by both the yellow and green coloured regions, while sparse vegetation exists in the red region.

Spectrally examining several pixels in both the green and yellow regions provides some answers as to the reason of negative NDVI values. Figure 63 displays two such spectra.

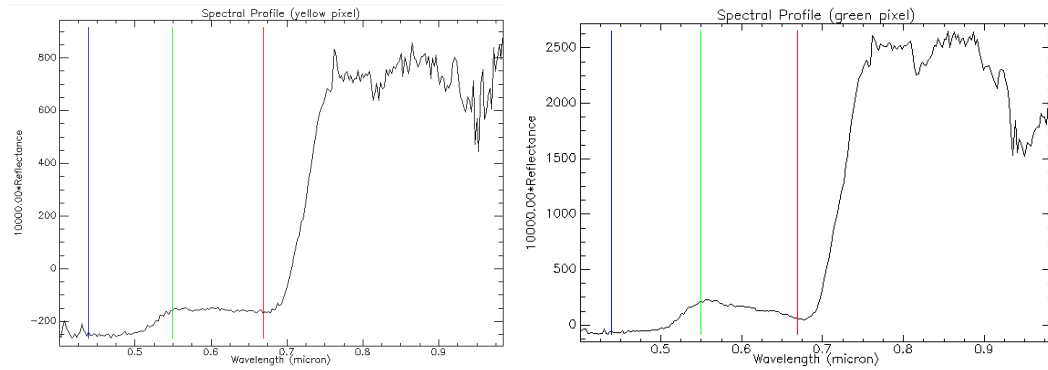


Figure 63: Sample spectra for two pixels; one each in the yellow (left) and green (right) regions of Figure 62. Note the difference in brightness (the vertical scales) in the yellow-region spectrum compared to the green-region spectrum. (Each spectrum is scaled by 10,000).

The blue, green and red vertical lines are superimposed onto each plot by default when plotting spectra in ENVI. They relate to the RGB wavelengths used to display an image. The RGB wavelengths in this case are contained in the blue, green and red spectral regions; the image displayed in ENVI is a true colour RGB image. When examining spectra of pixels, a true colour image was indeed displayed. Spectra were then exported and plotted. Hence the RGB colours are superimposed onto the spectral plots.

The spectra in the yellow coloured region (of Figure 62) tends to be darker in the RGB region of the spectrum compared to the green region. They also tend to be negative, and is mathematically explained by referring back to the definition of the NDVI:

$$NDVI = \frac{NIR - R}{NIR + R} \quad \text{(Equation (2.6.2.1.1) of Section 2.6.2.1)}$$

Actually NIR and R are functions; $R(NIR)$ and $R(R)$, where NIR and R are wavelengths corresponding to the (reflectance (R)) functions $R(NIR)$ and $R(R)$. In the case for

Figure 63 (left), $R(\text{NIR}) \approx 730$ and $R(\text{R}) \approx -165$ units of reflectance (scaled by 10,000) as the R and NIR wavelengths are 670 nm and 800 nm, respectively.¹⁵

Therefore, $\text{NDVI} = \frac{895}{565} \approx 1.58$.

Clearly, the negative reflectance in the red spectral region causes the numerator to be larger than the denominator; i.e.:

$$(\text{NIR} - \text{R}) > (\text{NIR} + \text{R}) \text{ for } \text{R} < 0; \therefore \text{NDVI} > +1$$

The existence of negative reflectances, should not occur; by definition, reflectances are defined between 0 and 1 and suggests the existence of bad data.

In the worst-case scenario, $\text{R} = -\text{NIR}$ so the denominator is zero (or equivalently $\text{NIR} = -\text{R}$). The NDVI thereby takes on an infinite result. Considering negative reflectances (i.e. out of bounds values), this result is entirely possible.

More details concerning 'weak' and 'strong' vegetation is withheld until Section 4.5.2, but the point is that extreme values are possible, even for an infinite result (in theory).

Over the region of Finucane Island (i.e. Figure 61), some 18% of unmasked pixels are out of range NDVI values (i.e. $\text{VI} > +1$ or $\text{VI} < -1$). Over the whole PHPA_Ref image, the largest positive value encountered was 971,505. Another dozen values are in excess of 100,000, but overall, only 3% of all (unmasked) pixels are out of bounds. The fact that so many occur over Finucane Island is explained by the analysis of Section 4.5.3.3, where negative reflectances are found mostly in the northern regions of the whole Port Hedland image.

¹⁵ Remember that the exact wavelengths require interpolation from the discrete measured wavelengths; the values given in the numerical example are approximations using the values in the graphed spectrum rather than a rigorous mathematical approach.

4.5.2 Image Classification using a Mean Gradient

To eliminate out-of-bound NDVI values, caused by negative reflectances (Section 4.5.1), it was decided to investigate the feasibility of using a straight forward gradient positioned on the red-edge.

In the most basic purely mathematical form, the gradient (m) is defined by the slope between Cartesian coordinate points (x_2, y_2) and (x_1, y_1) where $x_1 < x_2$:

$$m = \frac{\Delta y}{\Delta x} = \frac{y_2 - y_1}{x_2 - x_1}$$

In remote sensing, the gradient takes the form:

$$m = \frac{R(\lambda_2) - R(\lambda_1)}{\lambda_2 - \lambda_1} \quad (4.5.1)$$

with the reflectance at wavelengths λ_1 and λ_2 will be denoted by $R(\lambda_1)$ and $R(\lambda_2)$, respectively. The equation is, essentially identical in form to that of Equation (2.6.2.1) of Section 2.6.2).

As the NDVI offers the flexibility to be used on reflectance or radiance data (Section 2.6.2.1), this gradient must therefore offer the same flexibility as it is conceptually very similar to the NDVI.

As detailed in Section 2.6.2.1, for multispectral data, the NDVI utilised reflectances in two bands. Therefore, the ratio is defined using two points. This has not changed with hyperspectral data. Instead, two specific wavelengths are targeted (e.g. Equations (2.6.2.1.2) or (2.6.2.1.3) of Section 2.6.2.1).

As the PHPA data is hyperspectral, it is constructive to extend the gradient defined above (Equation 4.5.1) to allow it to utilise more wavelengths. If four wavelengths were selected, then averages for two pairs of wavelengths and reflectances still allow a gradient to be calculated. In this case:

$$\overline{R}_{12} = \frac{1}{2} [R(\lambda_1) + R(\lambda_2)] \text{ and } \overline{R}_{34} = \frac{1}{2} [R(\lambda_3) + R(\lambda_4)]$$

Note that the wavelengths are arranged in ascending order i.e. $\lambda_1 < \lambda_2 < \lambda_3 < \lambda_4$.

Figure 64 clarifies concept.

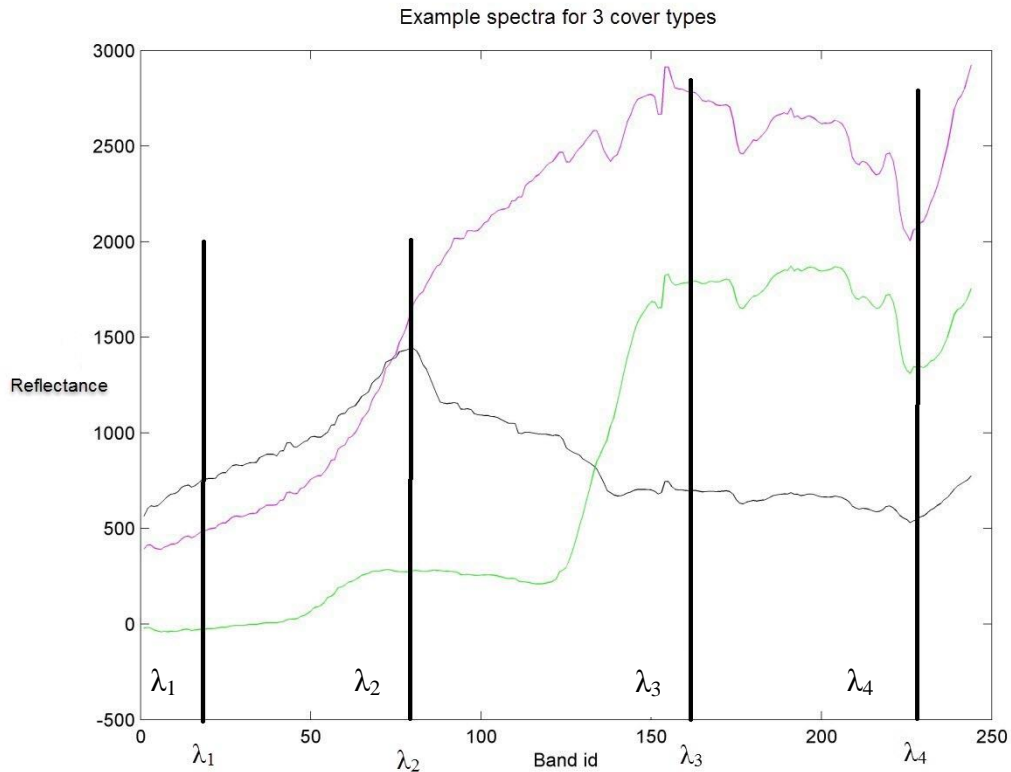


Figure 64: Examples of three mean cover types spectra; water (black), soil (magenta) and vegetation (green).

Note the reflectance unit has been scaled by 10,000 and the use of band numbers rather than wavelengths on the horizontal axis.

Figure 64 shows spectral corresponding to 3 cover types; vegetation, water, soil.

The spectra were taken from the PHPA_Ref image (specifically, the Utah region) and smoothed using a median 3 point moving average to reduce noise.

Effectively, the use of 4 wavelengths define 2 intervals for which the gradient is calculated. The mean reflectance in the first interval defines \overline{R}_{12} , while \overline{R}_{34} defines the mean reflectance in the second interval. Similarly, the mean wavelengths for the first interval $\overline{\lambda}_{12}$ and second interval $\overline{\lambda}_{34}$ are:

$$\overline{\lambda}_{12} = \frac{1}{2}[\lambda_1 + \lambda_2] \text{ and } \overline{\lambda}_{34} = \frac{1}{2}[\lambda_3 + \lambda_4]$$

The gradient takes the form:

$$\overline{R}_{\beta\alpha} = \frac{\overline{R}_{34} - \overline{R}_{12}}{\overline{\lambda}_{34} - \overline{\lambda}_{12}} \quad (4.5.2)$$

and shall hereforth be referred to as the mean-gradient (abbreviated to MG). The Greek letters α and β refer to the first and second intervals, respectively. These two Greek letters allow many wavelengths to be defined in each interval. More details are given in Appendix H.

In the case of Equation 4.5.2, the 4 spectral reflectances effectively reduce down to 2 mean spectral reflectances (and similarly for the wavelengths) from which the gradient is calculated. It should be noted either reflectance or radiance-based data may in fact be used to define R.

As the hyperspectral data contains many more points, the concept above is extended. A second (slightly different) approach is also considered to calculate the MG. The details are given in Appendix H, and for an equal number of wavelengths in each interval, the two approaches match. For this reason, an even number of points is considered in each interval on the red-edge.

The benefit of this MG based method is that noisy airborne data (on the red-edge) is smoothed due to calculating a mean reflectance (or radiance). This translates to a reduced sensitivity to spectral noise. Furthermore, a zero valued denominator is impossible to obtain and therefore avoids infinities. Note that, unlike the NDVI, which is scaled so that $-1 \leq \text{NDVI} \leq 1$, the MG is not scaled. Instead, the mean gradient is unbounded. In addition, although the NDVI is unitless, the MG is not and units are expressed in (reflectance or radiance)/wavelength.

The following red-edge definitions were found to be effective for classifying vegetation.

$$\lambda_1 = 0.6854 \quad \lambda_2 = 0.7164 \quad [\text{interval 1}]$$

$$\lambda_3 = 0.7188 \quad \lambda_4 = 0.7498 \quad [\text{interval 2}]$$

Table 19: Defined red-edge wavelengths for each of the two intervals.

Note that these wavelengths define the endpoints for each interval. This means that λ_1 and λ_2 respectively define the beginning and end wavelengths in the first interval ($\lambda_1 < \lambda_2$). In reality, more wavelengths were used within this interval, with 14 in each of the first and second interval (inclusive of the endpoints λ_1 , λ_2 , λ_3 and λ_4).

The effectiveness of the MG method was assessed using data from the Utah region. In a similar manner to the NDVI (i.e. Figure 61, p. 191), a pixel by pixel MG map is shown in Figure 65 (left image).

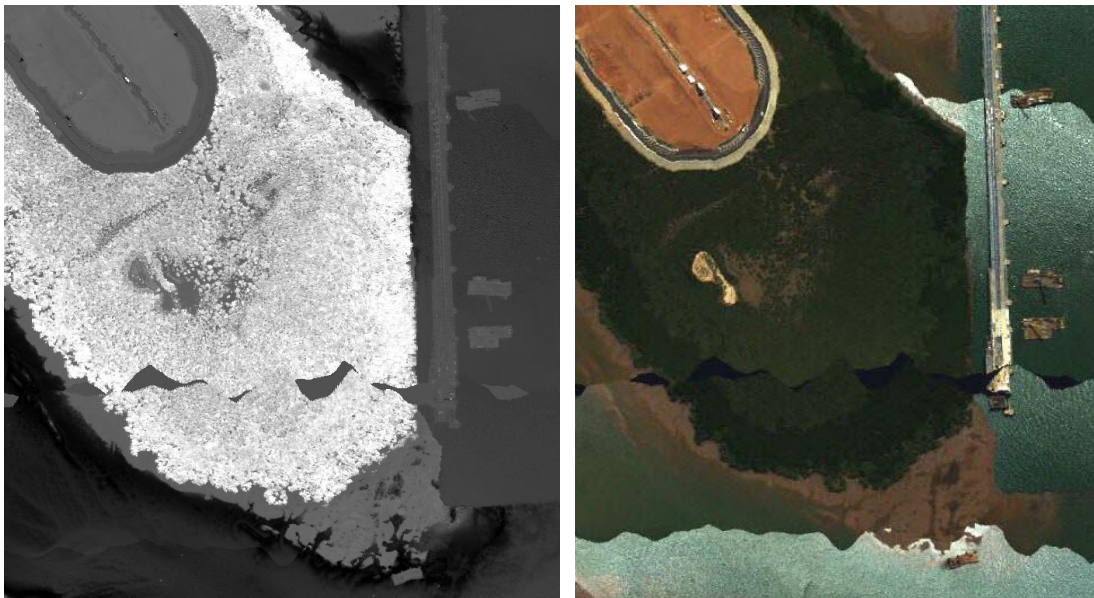


Figure 65: Mean-gradient map (left) and the associated true colour image (right). Higher gradient values are associated with very bright (white) regions and indicate dense vegetation. Very dark shades represent deep water.

As for the NDVI results of Section 4.5.1, bright white pixels represent strong vegetation (i.e. those containing a large red-edge), while darker shades relate to soil or water.

To examine all of the gradients in more detail, it is useful to construct a frequency histogram. The result is shown in Figure 66.

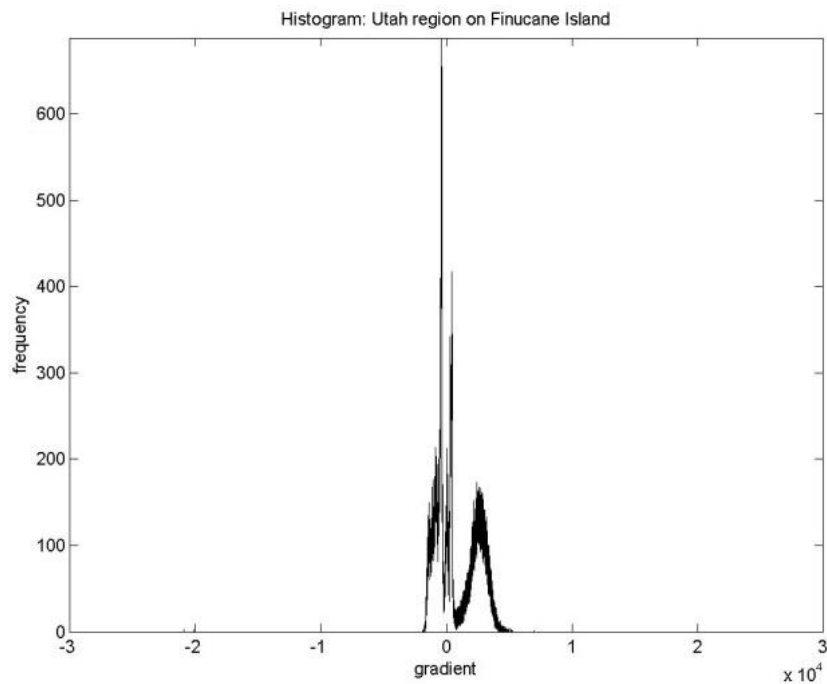


Figure 66: Frequency histogram for all mean gradients in the Utah region. Note that the gradients are multiplied by 10,000 (as shown on the horizontal axis). Also, the number of pixels containing the particular gradient is displayed on the vertical axis.

While some extreme gradients do exist, they are too small in frequency to be discernible in the figure. It is clear that most gradients are located between -2000 and 5000. With a change of axis, the histogram reveals more structure (see Figure 67). The gradient values relate to cover types and may be used to produce a classification map. From left to right in the histogram, the three cover types are water, followed by soil and finally vegetation. Recall that the frequency relates to the number of pixels. The histogram shows that the number of pixels decreases showing one cover type before and moving onto another type. However, the lack discernible gaps between gradients indicates that categorisation into three basic cover types is not possible in reality. In an ideal situation, the gradient values would form distinct bands, with water to the left, soil in the middle and vegetation on the right (as in Figure 68).

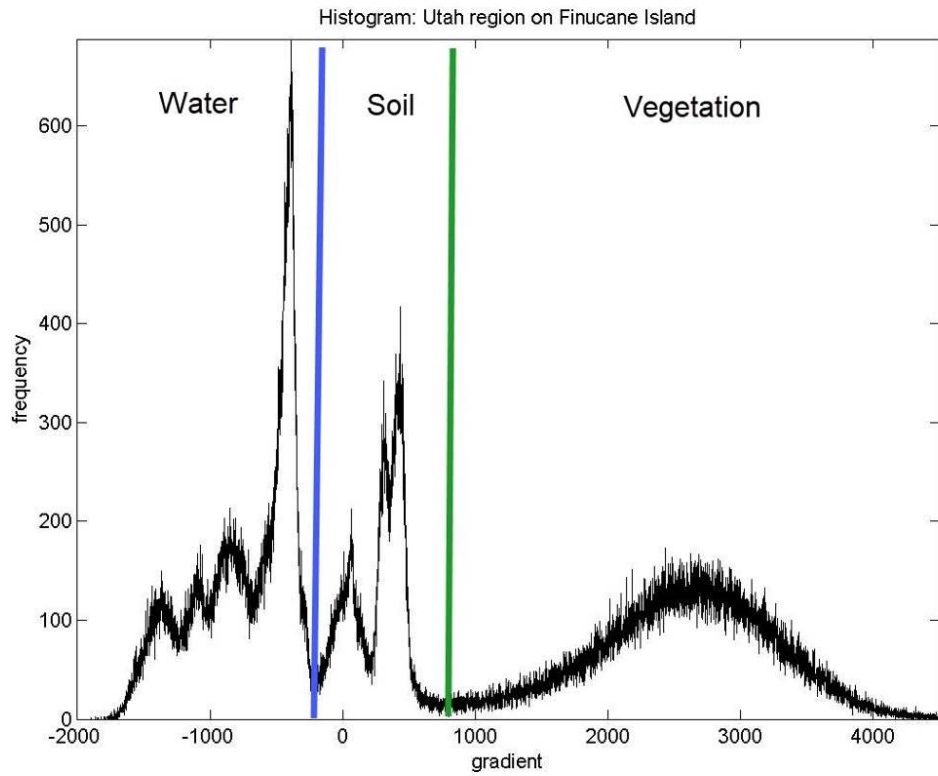


Figure 67: Frequency histogram for the MG over the Utah region on Finucane Island. Finer structural details are discernible due rescaling of Figure 66.

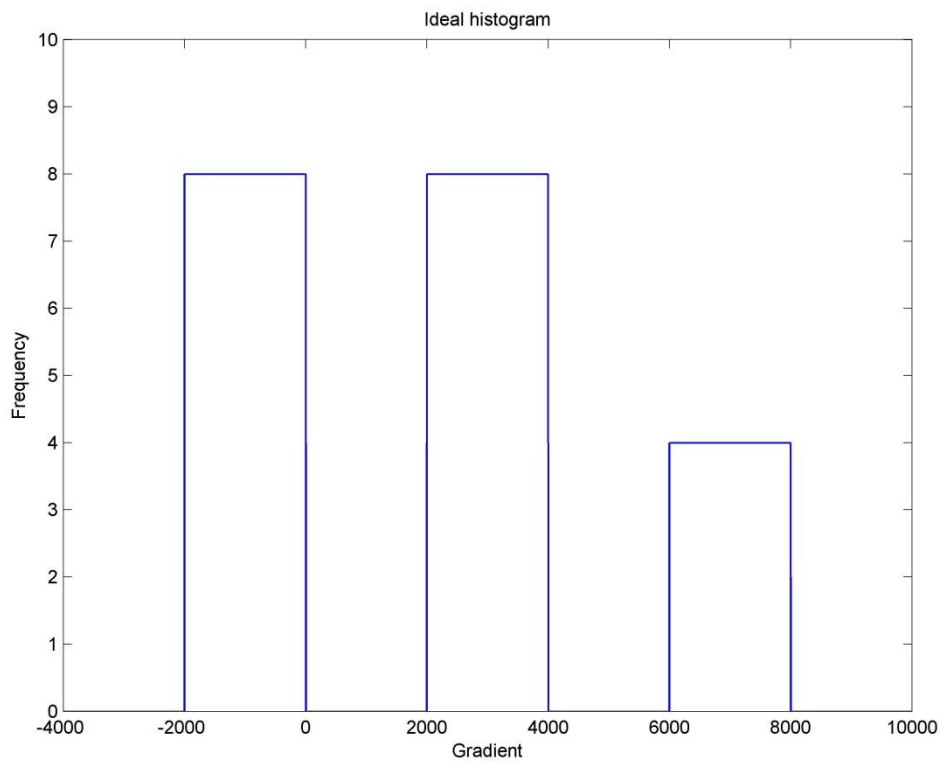


Figure 68: In the ideal situation, the cover types are separated with no overlap.

In Figure 68, water and soil appear in equal proportions with half as much vegetation. The frequency represents a direct count of pixels being classified according to the gradient.

The lack of gaps between the bands in Figure 67 is due to proportions of mixtures between the cover types. Water consists of dark (deep) water in addition to shallow water where physically the spectrum contains a mixture of water and soil (mud). Therefore, gradients range from large negative values for deep water to small negative values for mud. Soil exists in a state from mud (small negative gradients) to dry soil, to mixtures of soil and vegetation (e.g. low lying grass or sparsely populated small vegetation). Vegetation starts from mixtures containing soil (small positive gradients) to pure vegetation, reminiscent of dense mangrove forests (large positive gradients).

The question of selecting threshold gradient values to form categories depends on the number of defined categories. For example, broad gradient values may be selected to categorise water, soil and vegetation. However, more thresholds are then required for finer detail – e.g. water, water and soil, soil, soil and vegetation and finally vegetation. Even vegetation may be broken down into sparse low-density vegetation to dense vegetation. Therefore, the selection of exact boundaries are not clear-cut and depend on the detail required.

Interestingly, the minimum locations of the histogram curve correspond to important gradient boundaries separating each of the land cover types. The MATLAB (Matrix Laboratory by MathWorks¹⁶) package was used to assist in determining these minima in an effective manner. However, the histogram required a large moving average to smooth out the rapid changes (a 51 point moving average was particularly effective). Figure 69 shows the result.

The blue and green vertical lines are positioned at a MG of -214 and 756, respectively. Although the gradients were retrieved using MATLAB, individual pixel spectra were physically inspected using ENVI to attach physical meaning to the calculated values. Using these two threshold values (-214 and 756) allows three broad cover types to be defined (i.e. water, soil and vegetation).

¹⁶ Homepage: <https://au.mathworks.com/>

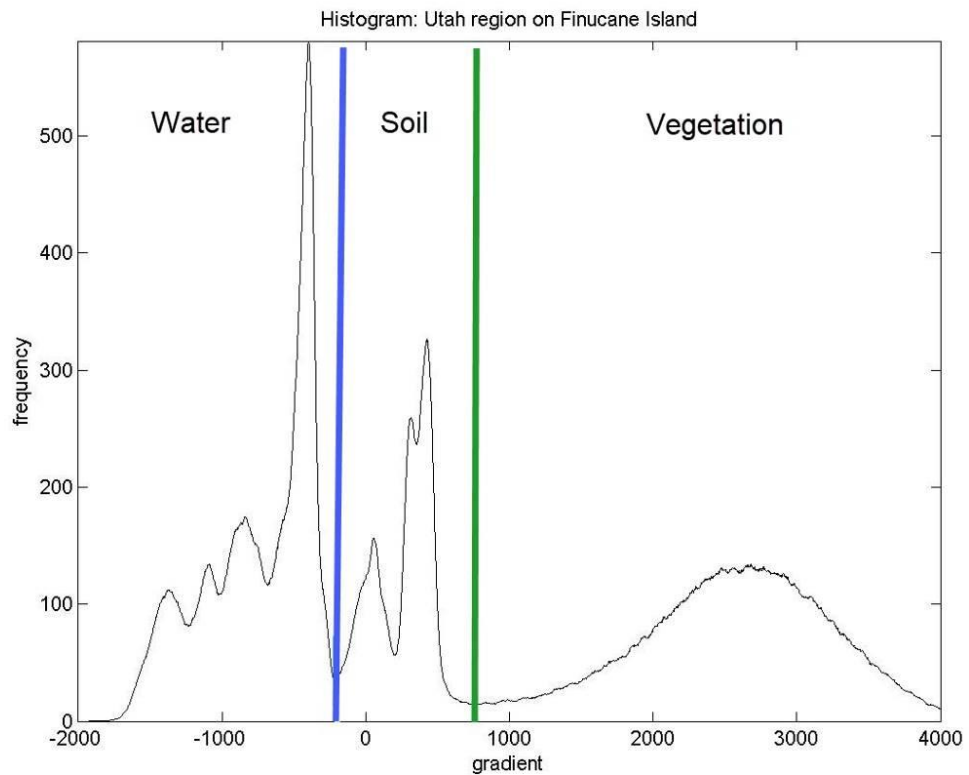


Figure 69: The result of smoothing the gradient of Figure 67 by a 51-point moving average. Negative gradients relate to water spectra, while soil ranged from small negative to moderate gradients. Vegetative gradients are all positive, being larger in value than soil.

The effectiveness of using appropriate gradient threshold ranges to define three broad cover types (i.e. water, soil and vegetation) is shown in Figure 69. Figure 70 shows the three classes; the red class defines $MG \leq -214$ and physically corresponds to water (deep and shallow). The green class relate to $MG > -214$ but $MG < 756$ which defines soil (mud to dry soil). The blue class represents vegetation, where $MG \geq 756$. The black region are missing data between adjacent flight lines.

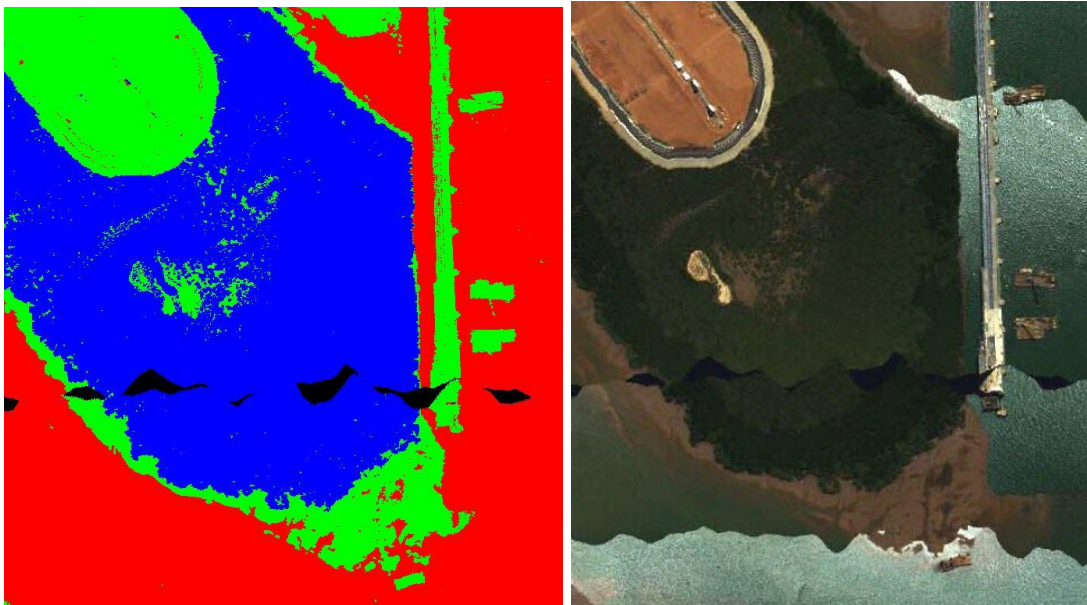


Figure 70: The left image shows the classification result for 3 classes using the MG. The true colour image for the same region is shown on the right.
 (For the left image, the colours represent: blue = vegetation, red = water, green = soil; black = missing data (therefore unclassified)).

From Figure 70, it is possible to calculate the (pixel) areas covered by each of the 3 cover types:

Class colour	Cover type	Area % (by pixels)
Blue	Vegetation	40.30
Red	Water	39.70
Green	Soil	20.00

Table 20: Areas corresponding to each of the three cover types.

The masked (black) pixels represent missing flight line data, accounting for 1.14 % of the image but were not included in the area calculations (i.e. the areas for each cover type are expressed in terms of the total number of pixels containing data).

The question naturally arose as to what those other minima/maxima gradient values represent in the histogram (Figure 69). Again, the use of MATLAB allowed the values to be accurately determined, with the selections shown in the following table.

class colour	Minimum	maximum
Red	-30000	-1224
Green	-1223	-1026
Blue	-1025	-679
Yellow	-678	-214
Aqua	-213	207
Magenta	208	756
Red-Purple	757	30000

Table 21: Effective red-edge gradients for 7 classes.
(actually, class 8 relates to unclassified pixels; they appear as black)

With the classes defined according to the ranges specified in Table 21, more classification detail results (see Figure 71, left image).

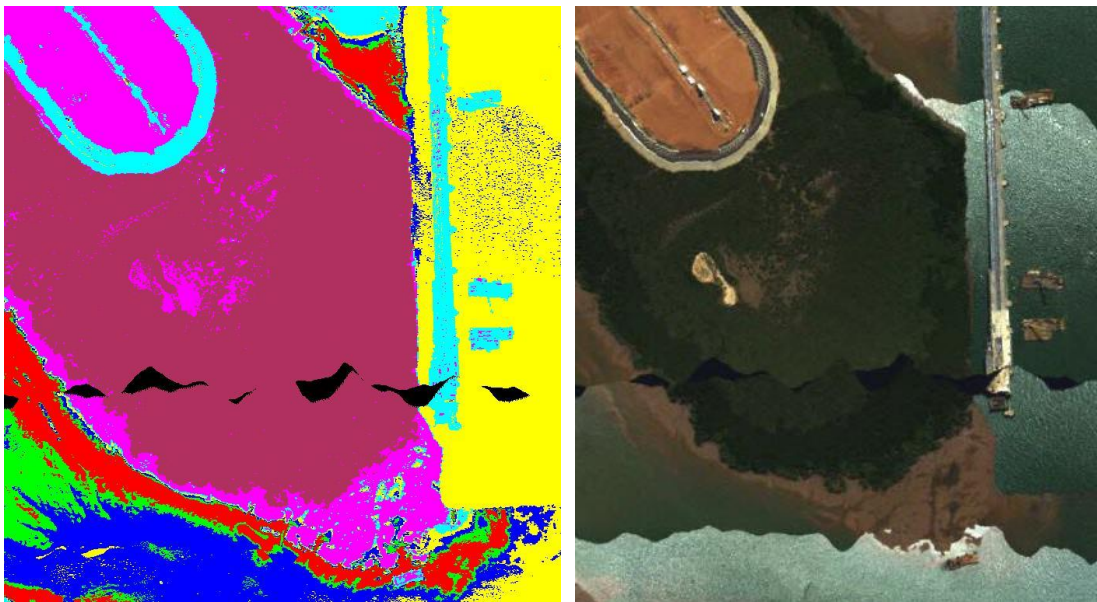


Figure 71: Classification result for 7 classes (left image). The true colour image is shown on the right to help identify the cover types.

Spectrally examining several pixels of Figure 65 (left) shows that the very bright (white) pixels (representing vegetation) typically returned MG values in excess of 4000. The dark water pixels are the most negative, returning MG values such as -1500 (corresponding to the red region in Figure 71 (left)).

Pixel areas for each class (i.e. threshold interval) are given in Table 22.

Class colour	Cover type	Area % (by pixels)
Red-Purple	Vegetation	40.29
Magenta	Soil	12.90
Aqua	Soil	7.09
Yellow	Water	20.27
Blue	Water	9.28
Red	Water	6.07
Green	Water	4.09

Table 22: Areas corresponding to each of the seven cover types.

As for the areas quoted in Figure 70 (left image), the black pixels for Figure 71 (left image) were not counted; i.e. the percentages are expressed in terms of pixels containing data.

When the areas are added together for each subdivided class (e.g. water) in Table 22, they match to that of the broader definition in Table 20. For example, adding together all the areas for water in Table 22 gives the same result as that in Table 20. The same applies to soil. As vegetation was not subdivided, the areas between both tables are the same (subject to rounding off errors).

The ore stockpiles at Utah (see Figure 60, p. 190 for a true colour map) is defined by one class in Figure 70 (left image) but by dividing the interval into two, finer structure is revealed Figure 71 (left). For instance, the road around the stockpiles is now clearly discernible. Water also appears more detailed; mud (i.e. water and soil) now indicated by the red class, while the blue class shows deeper water.

An important detail has so far been omitted concerning the MG calculation for the Utah dataset. A C++ program was written to track the MG values for the construction of a frequency histogram. Initially, the task of tracking the wide range of gradients were too numerous and led to program crashes. As a result, gradients were scaled by a factor of 1/10 and suitably binned. However, as the further need to plot histograms were no longer required, all mean-gradients were left unscaled

in all work to follow. The results and conclusions that have been made thus far remain valid.

Encouraged by the results thus far, the MG approach was applied to the whole PHPA_Ref image. Unlike that for the Utah spectral dataset, each pixel was not median filtered in this case; the spectral (reflectance) data were used directly to calculate mean gradient values. In similar vein as before, the C++ program calculated a MG for each pixel and stored the data as a MG map (see Figure 72 – note that the right section of the image has been removed as it is dominated by salt ponds (see Figure 36 (right image), p. 131 of Section 3.2)).

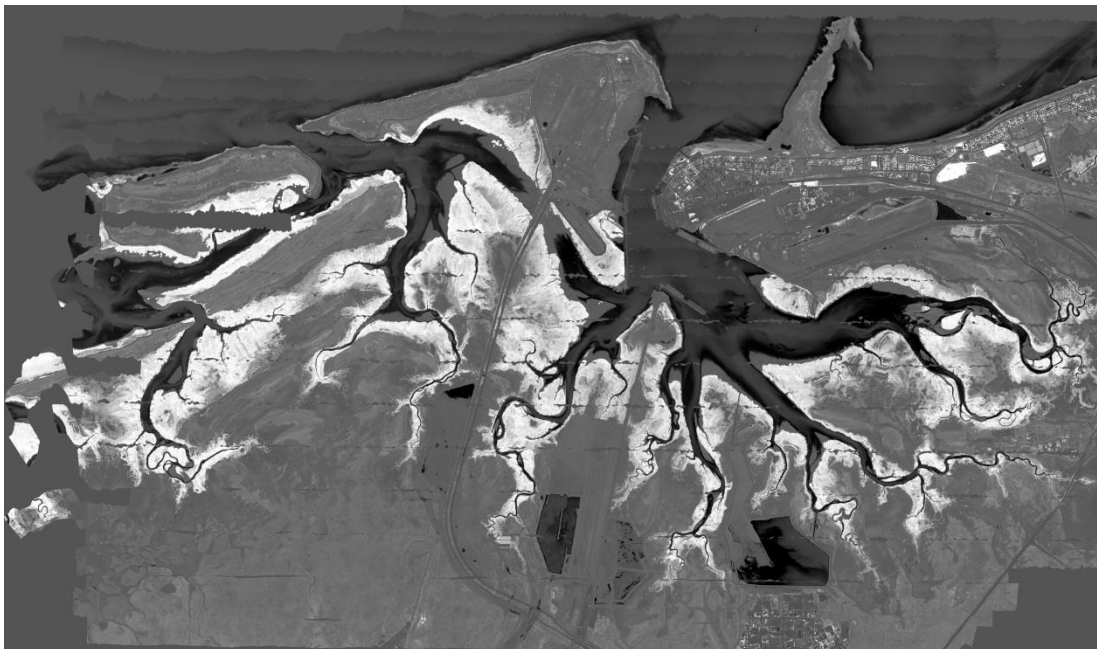


Figure 72: Mean-gradient map result showing bright regions containing vegetation.

Comparing the MG image with a true colour image (Figure 42, p. 141 of Section 3.3) the brighter (i.e. 'whiter') pixels again dominate over the dense mangrove forested regions. Over Finucane Island, the result is similar to Figure 61 (p. 191 of Section 4.5.1) which used the NDVI instead of the MG. Similarly, the greater the red-edge gradient, the 'stronger' the vegetation. The greyer pixels relate to lower density vegetation, e.g. scrubland. As the pixels become darker, the low-density vegetation turns to soil and finally water (being particularly black). These findings are in agreement with earlier results for Utah.

Later on in this thesis, there is an interest to mask out all pixels but those for 'strong' vegetation. Therefore, different threshold values need to be examined to find an acceptable value. As the histogram for Utah made clear (Figure 69, p. 202), there is no one value.

Figure 73 shows the result where all MG values $< 5,000$ are eliminated from the MG image (i.e. Figure 72).



Figure 73: The effect of removing all MG values less than 5000 in Figure 72.

The black regions contain MG values less than 5000 (in addition to masked pixels – i.e. those containing no data). As expected, as the MG for water are all negative, the water regions have been masked (i.e. black). Numerous soil pixels also fall into the same category.

Overlapping the gradients $\geq 5,000$ onto the original image (i.e. non-masked) reveals the full effect (shown in Figure 74).

For the sparse vegetation in the southern extent of the region, spectral analysis suggests the presence of 'weak' vegetation (e.g. small grasses) – later confirmed by field work data. The same is true for Finucane Island, where regions of grassland have been 'captured'. As our primary interest lies NOT in classifying different types of grasses but rather the dense luscious mangrove forested regions, the threshold must be increased to capture 'stronger' vegetation. Several other MG thresholds, in

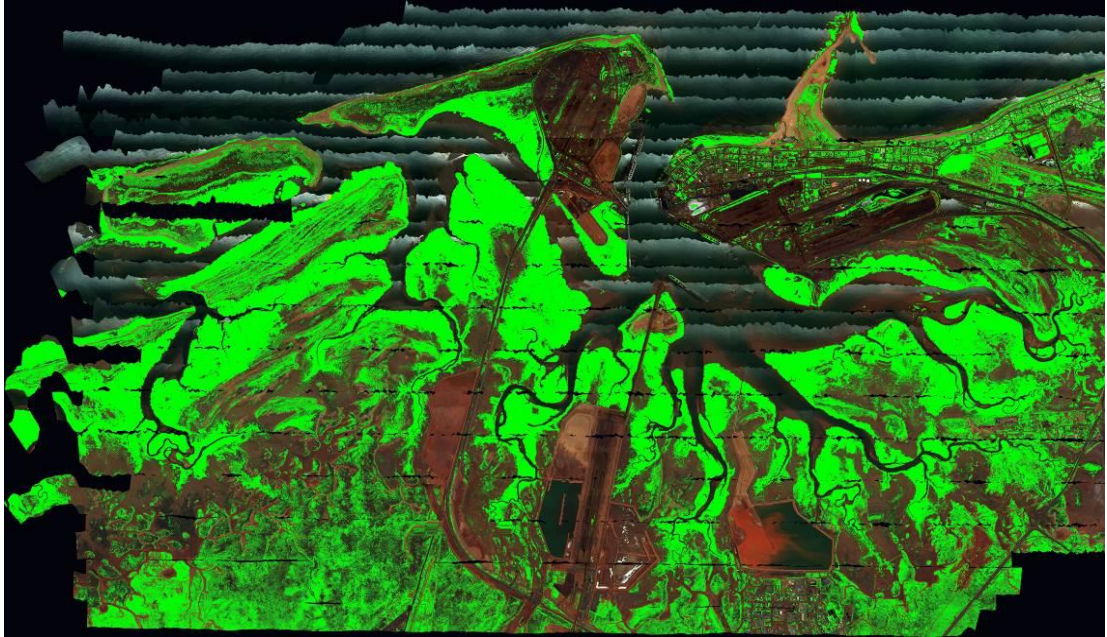


Figure 74: The green colour represents vegetation, with a MG threshold of at least 5,000 superimposed onto the original true colour image.

the range from 5,000 – 15,000, were spectrally examined on a pixel-by-pixel basis to examine the effect on mapping vegetative density. From this work, a threshold of 10,000 appeared as an acceptable vegetative result with particular emphasis on the dense mangrove forests (as shown in Figure 75).



Figure 75: Vegetation map using a MG threshold of at least 10,000.

The 10,000 MG threshold captures mangroves very strongly (although it also captures the densely packed green grassed-oval regions in the north-eastern urban residential areas). The dense green-grassed regions contain a sharp red-edge, for which the method is unable to distinguish from mangroves. The task of the MG method is to find vegetative pixels, rather than classifying vegetative types. For that, advanced classification techniques are required which analyse whole spectral regions rather than a limited set of values located on the red-edge (i.e. 14 in each of the two intervals).

Superimposing the MG gradient map onto the original true colour image shows the effectiveness in locating dominant mangrove forests (in particular). The result is shown in Figure 76.

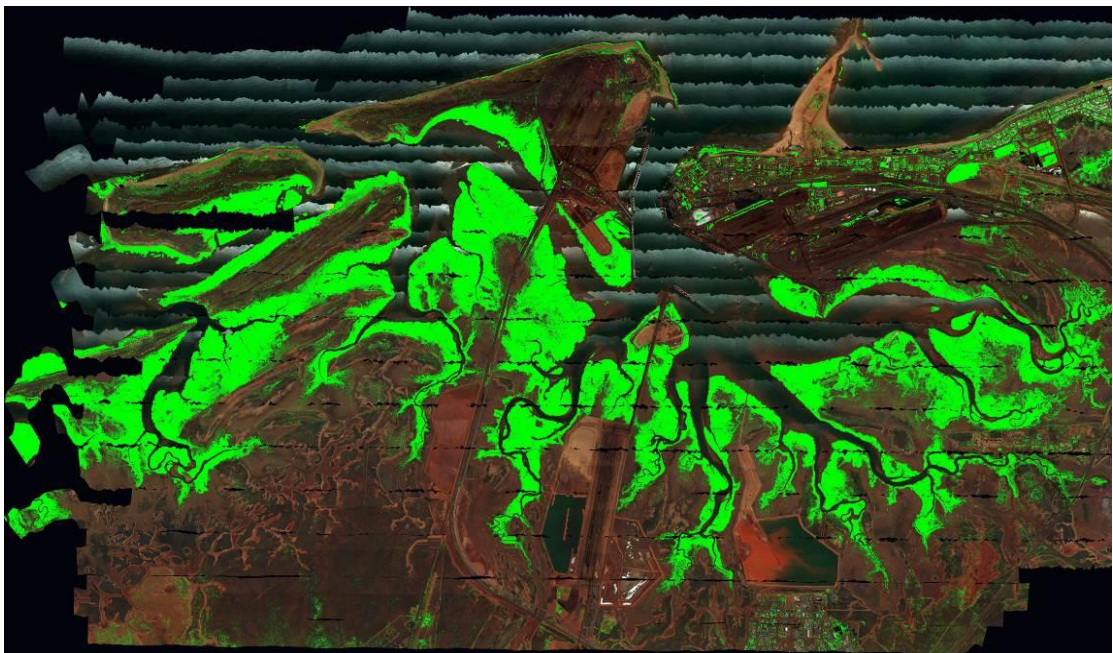


Figure 76: Vegetative regions are shown in green, using a MG threshold of at least 10,000 representing 'strong' vegetation. The result is superimposed onto the original true colour image.

A threshold of 30,000 (Figure 77) is clearly an overkill, as mangroves on Finucane island (including Utah) and other regions are eliminated.

The superimposed image (Figure 78) clearly identifies regions of mangroves now being excluded. This is not desired, although the map does show where the

'strongest' (i.e. most probable locations) 'densest' mangroves appear (excluding the green ovals in the urban residential region to the northeast).

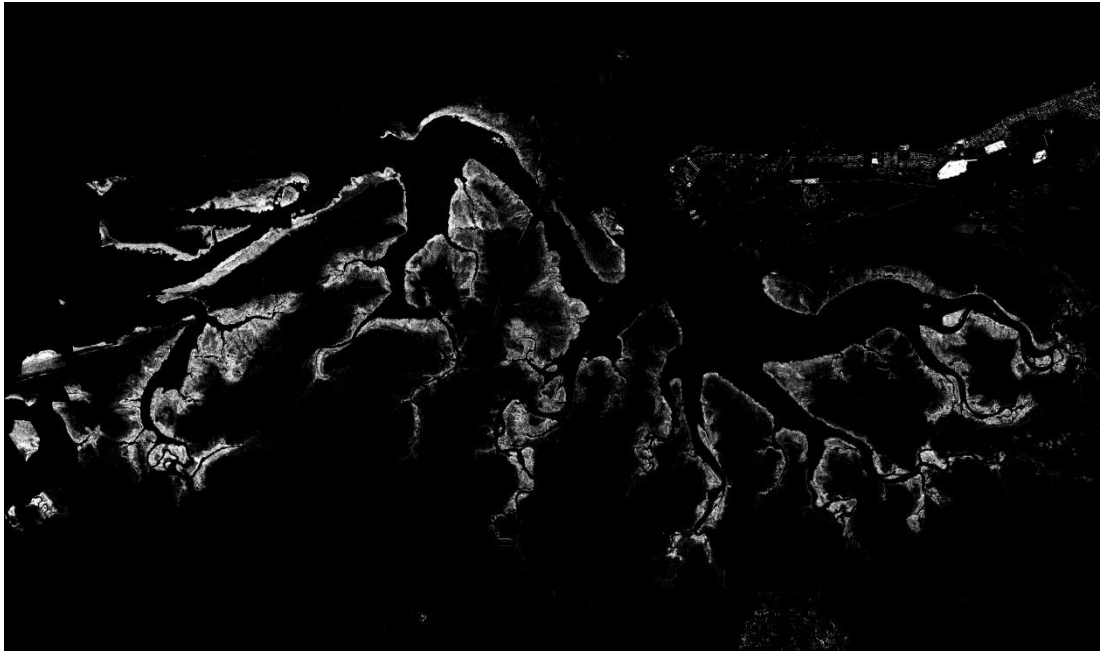


Figure 77: The MG map for a threshold of at least 30,000.

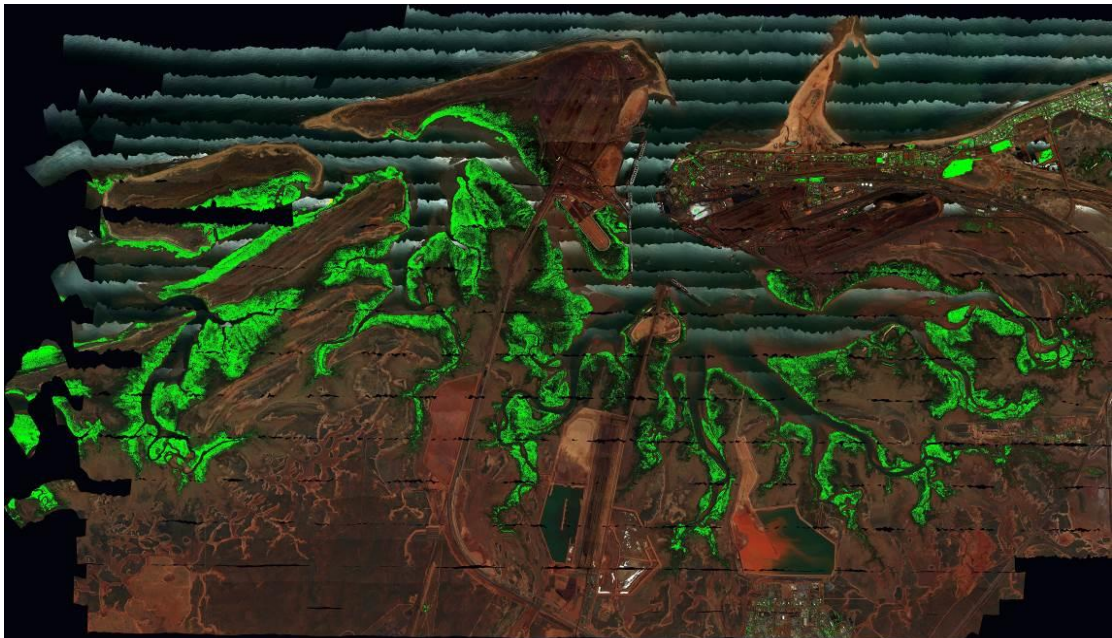


Figure 78: Vegetation shown in green, using a MG threshold of at least 30,000. This represents very 'strong' vegetation. The result is superimposed onto the original true colour image. Some regions of mangroves are clearly excluded by choosing such a large threshold.

Further threshold values were examined and their impact on masking out vegetation. These ranged from 2,000 to 15,000 in units of 1,000 and included 20,000 and 30,000. Although it is clear that 30,000 is too large (as it excludes large regions of mangrove forests), a MG threshold of 5,000 is too small as it includes too much low-density vegetation (e.g. grassland or mixed pixels containing vegetation and soil). In the end, a sound value for a threshold of 10,000 allowed for 'strong' vegetation (e.g. mangrove forests) but removing 'weak' vegetation. As the MG map was produced in ENVI format, individual pixels were examined for both MG values alongside spectra. A threshold of 10,000 is also easier to remember, compared to (say) 9,827 – another reason for the 10,000 threshold! In reality, how much is gained between 10,001 and 9,990? The exact value for a suitable threshold is somewhat arbitrary but only within a limit. A value of 12,000 was deemed a little too high, while 8,000 or 9,000 was too low – again concluded by individually examining spectra of dozens of pixels alongside their MG.

The selection of a suitable threshold is also plagued by a number of factors. During the course of the thesis work, it became apparent that the PHPA_Ref image is not spectrally consistent. Due to spectral changes over the scene and within a particular flight line, gradients will change depending on pixel location. As a result, individual vegetative pixels were closely examined (spectrally) at various locations on the map. Overall though, the threshold single value of 10,000 remained an acceptable trade-off.

It should be remarked that the resolution of the 'green' vegetation images (i.e. Figure 74, Figure 76 and Figure 78) are limited when displayed in full. For example, the dense green class on Finucane Island appears very dense but may not necessarily be so, leading to a false impression of the true situation. An example of such a situation is depicted in Figure 79 (in blue).

The region covered by the red box of Figure 79 (left) is magnified in Figure 79 (right), which shows the blue class to be significantly less dense under higher resolution. These were considerations in determining a suitable threshold for vegetation.

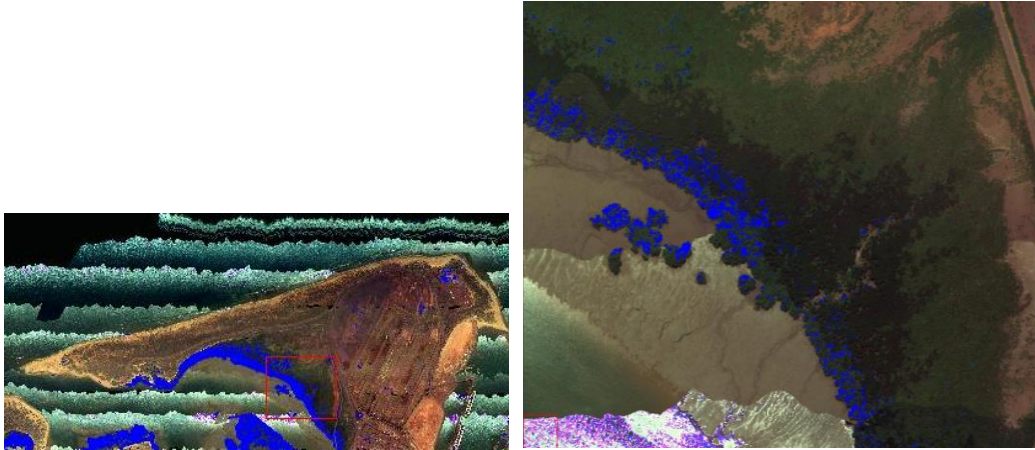


Figure 79: A region that appears to be densely vegetated as indicated by the blue overlay (left) but may not necessarily be so (right).

In general, the following observations appeared to hold roughly true:

Mean-gradient thresholds greater (and equal to) than:

- 5000: captures grassland/bushes
- 8000: captures small trees and shrub
- 10000: medium sized trees (more clearly than 8000)
- 20000: Mangroves

(these values are approximate, but laboriously obtained nevertheless!)

A map can be produced using different ranges of thresholds. Figure 80 shows the result whereby vegetation is categorised into two classes, while soil and water and soil are broadly categorised using one class each.

The threshold values defined are:

- 7000 & 10000 (indicated in light green, indicating low-density (weak) vegetation).
- 10000 – 27000 (indicated in dark green, indicating ‘strong’ (or high probability) vegetation).
- 0 – 7000 (brown, indicating non-vegetation).

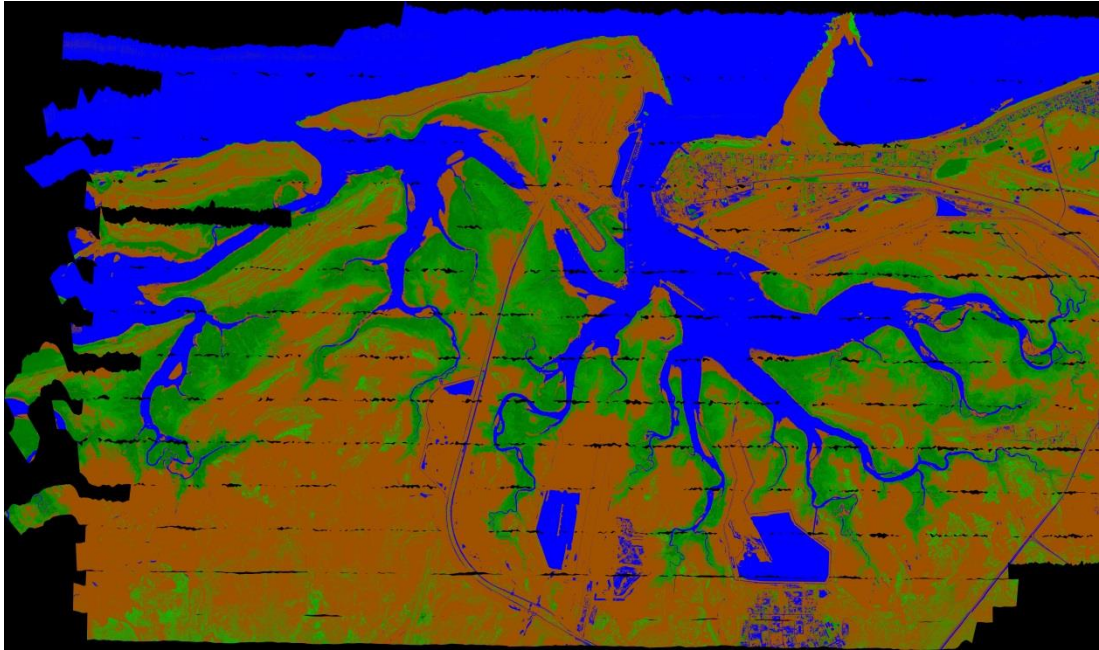


Figure 80: Vegetation map for 3 cover types (in an analogous manner to Figure 70).

It should be remarked that the MG map was derived using the MG formula, which utilises the red-edge (only!). As such, Figure 80 shows that buildings appear as water. Although the purist may state the map is inaccurate, it is in fact correct as far as vegetation is concerned. The work in this thesis is not concerned with distinguishing buildings from water, but rather vegetation from non-vegetation. Non-vegetation is defined as “not vegetation” and includes soil, water, buildings, and roads.

The results of this section clearly demonstrate the ability to separate vegetation from non-vegetation. This work is used in Section 4.5.6 to develop a vegetative mask, which is a filter to remove all non-vegetative pixels from the classification process.

4.5.3 Image and Spectral Issues

The behaviour of the NDVI over Finucane Island revealed spectral changes between adjacent flight line boundaries (i.e. due to obvious flight line boundaries in Figure 62, p. 191 of Section 4.5.1). This is disturbing, highlighting issues even at the simple VI level for vegetation versus non-vegetation classification. For even higher levels of

classification, the confidence in the results decreases further. It is vital for the PHPA_Ref image to be as spectrally consistent as possible prior to higher level classifications. This section examines more closely the PHPA_Ref image, revealing a number of issues; some serious and others that may be ignored in the context of vegetative classification.

4.5.3.1 Missing Data

Data not recorded during the airborne survey display as black pixels in the PHPA_Ref image (Figure 42, p. 141 of Section 3.3). There are whole regions of unrecorded data (probably deliberate). For example, there is no recorded data in the north-east and south-eastern ‘corners’ of the map. Unfortunately smaller regions also exist, mostly between flight lines, some which contain mangrove forests. A vegetative classification map is therefore incomplete.

The few million pixels (not captured) do not change the estimated percentage of missing data in any significant manner, as they amount to ≈ 3.4 million pixels out of ≈ 153 million (i.e. some 2% of the total image).

In practice, missing data between flight lines may be reconstructed by interpolation from neighbouring pixels (P. M. Mather, and Koch, M. (2011), p. 89). However, in our case, this is not feasible as the gap between flight lines is often too wide.

4.5.3.2 Spectral Changes across Flight Lines

The brightness changes for flight lines containing water, as evident from Figure 42 (p. 141 of Section 3.3). A magnified view over a small section of Finucane Island is shown in Figure 81 for closer scrutiny. The position of the small region is more readily identified from Figure 60 (p. 190 of Section 4.5.1,).

Figure 81 shows a series of 6 complete flight lines along with two partial ones (the northern-most and southern-most flight lines).



Figure 81: True colour image showing water brightness changes within individual flight lines.

Each flight line runs in a west-east direction (left-right in the image). Toward the northern end of each flight line, the water is particularly bright (due to sunglint). Traversing from north to south within each flight line, the water brightness becomes darker. This raises a question as to whether the brightness over land is actually uniform within a flight line; the change in reflectance over water is dramatic and very clear. If only the brightness changed, then the SA remains unchanged – i.e. there is no real change in spectrum. However, it is clear that the spectral shape does change, as it influences classification results (e.g. Figure 62, p. 191 of Section 4.5.1 and Figure 97 (left image), p. 241 of Section 4.5.7)).

4.5.3.3 Spectral Artefacts

There are several regions in the PHPA_Ref image where spectra are shaped unnaturally (termed spectral artefacts). Figure 82 contains an example for a yellow-coloured artefact.

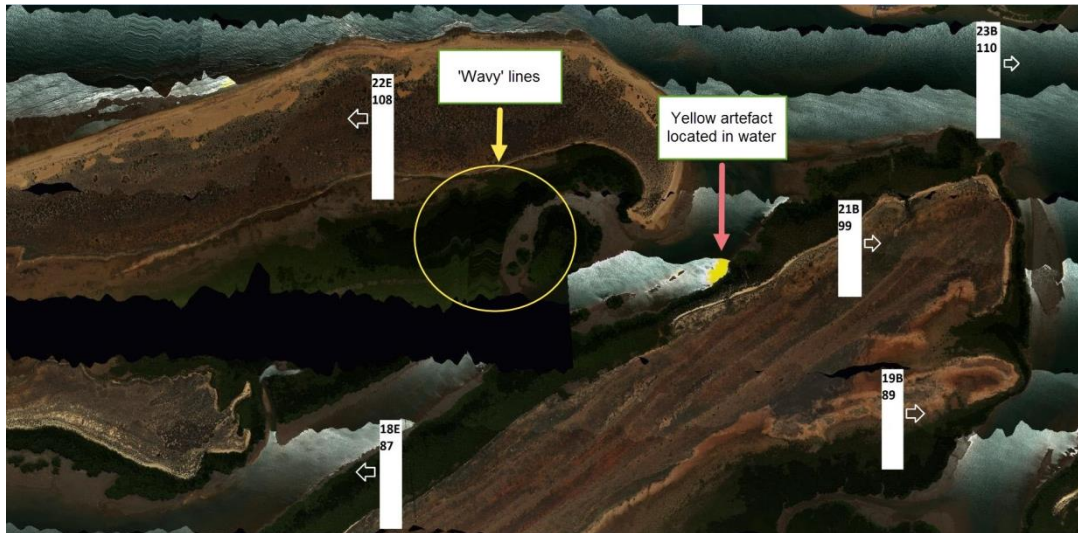


Figure 82: Spectra in the yellow region are distorted. The ‘wavy’ lines are navigational distortions rather than spectral.

To understand the nature of the artefact, Figure 83 shows a spectrum for a pixel located in the yellow region.

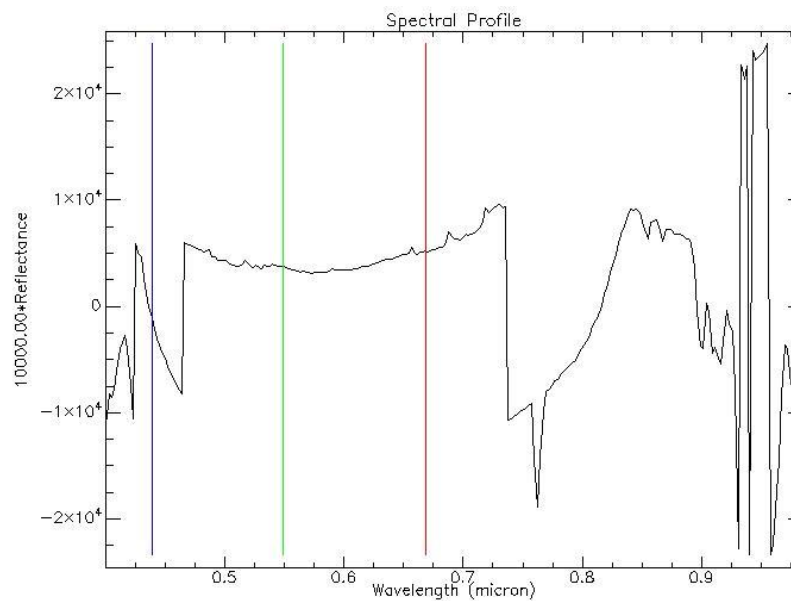


Figure 83: A pixel spectrum located in the yellow artefact region.

Numerous negative reflectances are clearly present and not just in the blue end of the spectrum. The image in Figure 82 is constructed using just the three spectral bands indicated by vertical coloured lines in Figure 83. The spectrum at the green and red bands appear to have ‘reasonable’ (positive) reflectances, however several wavelengths in the blue spectral region are clearly distorted and show numerous

negative reflectances. These yellow regions of pixels tend to be located where the water pixels are particularly bright. It is therefore likely that sunglint is overloading the sensor with the Tafkaa atmospheric model being unable to correct for this situation. The sunglint-affected water spectrum (Figure 83) appears very different to a 'pure' water spectrum (e.g. Figure 64, p. 196 of Section 4.5.2) (seawater being referred to here as water).

Figure 82 also shows a region containing "wavy" lines (magnified in Figure 84), which occurs throughout several locations in the PHPA_Ref image.

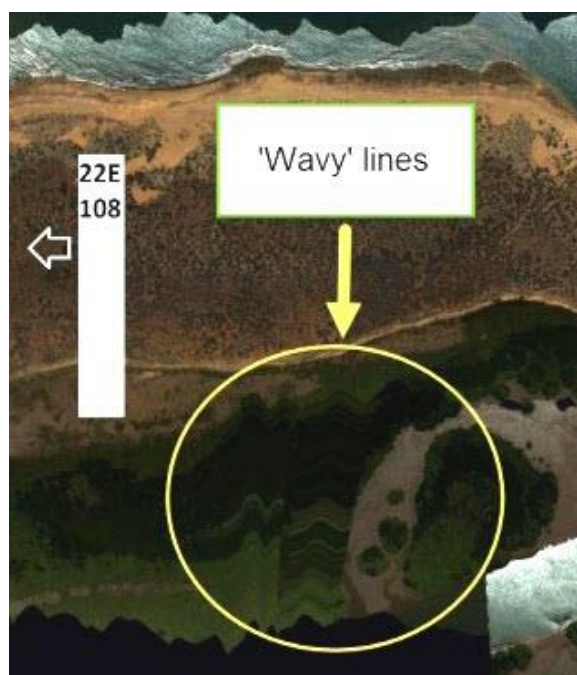


Figure 84: A magnified view of the 'Wavy' line region of Figure 82. Both brightness and contrast are adjusted in the image for visual enhancement.

These "wavy" lines are caused by errors in the navigation information and do not relate directly to spectral issues (Richards, 2013, p. 50).

Further spectral issues were first apparent in Section 4.5.1, where negative spectra affected NDVI consistency between adjacent flight lines. This work is extended by examining spectra in five ROI's for numerous vegetative spectra over Finucane Island. Figure 85 shows these five ROI's for which spectral means were calculated. Although the image is a true-colour image for the region, only vegetative pixels were used to calculate a single mean spectrum for each of the five ROI's. The

vegetative-mask of Section 4.5.2 was used to select the pixels (using a threshold of 10,000 – i.e. effectively the vegetative-mask of Section 4.5.6). These mean spectra are displayed in Figure 86.

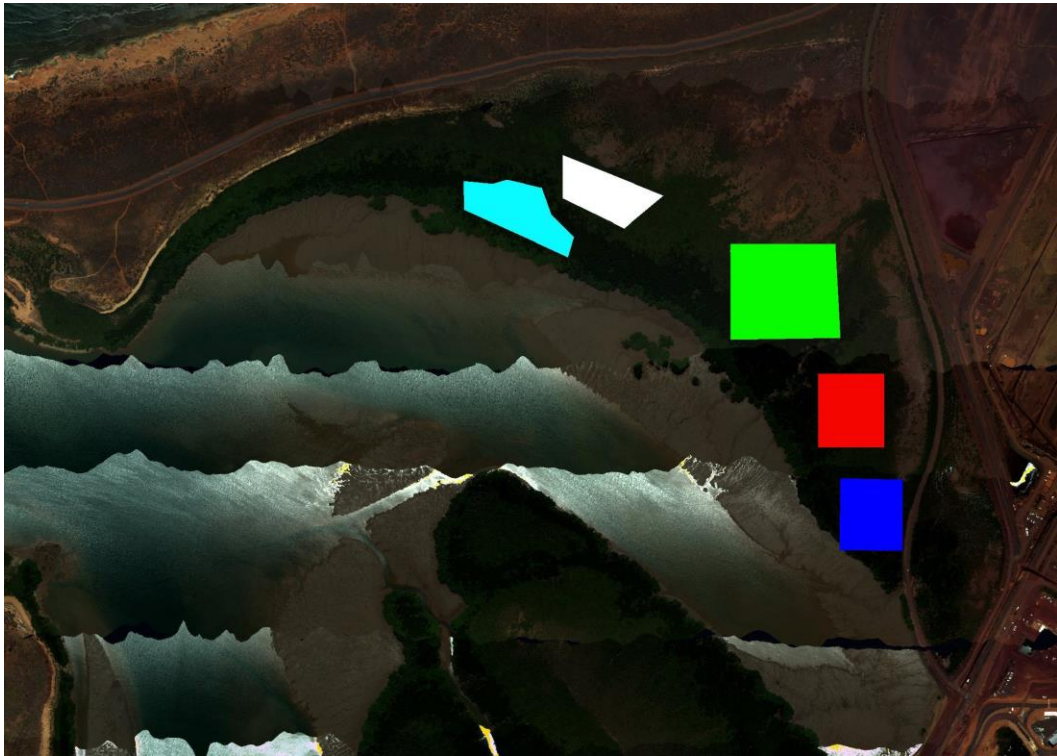


Figure 85: Vegetative spectral means were calculated for each of the five ROI's over Finucane Island in the PHPA_Ref image.

The mean vegetative spectrum for each ROI is plotted in Figure 86. Each line-colour in the plot corresponds to the ROI-colour in Figure 85 with the exception of the white ROI, for which the mean vegetation spectrum is represented by a black spectrum in the plot.

Disturbingly, most mean vegetation spectra contain negative reflectances, not only in the blue region but other visible bands. Pixels affected by negative reflectances appear dark. It is therefore possible to examine grey scale single band images (e.g. band 1) to examine the extent of the problem. However, it is possible that all other bands exhibit positive reflectances, so a misleading picture is presented to the analyst. Although we are limited to a three band image, it is better to plot a wider range of the blue bands. Experience has shown that blue-end wavelengths are more numerous in having negative reflectances, compared to other wavelengths. Therefore, it is unlikely that a region of red bands exhibits

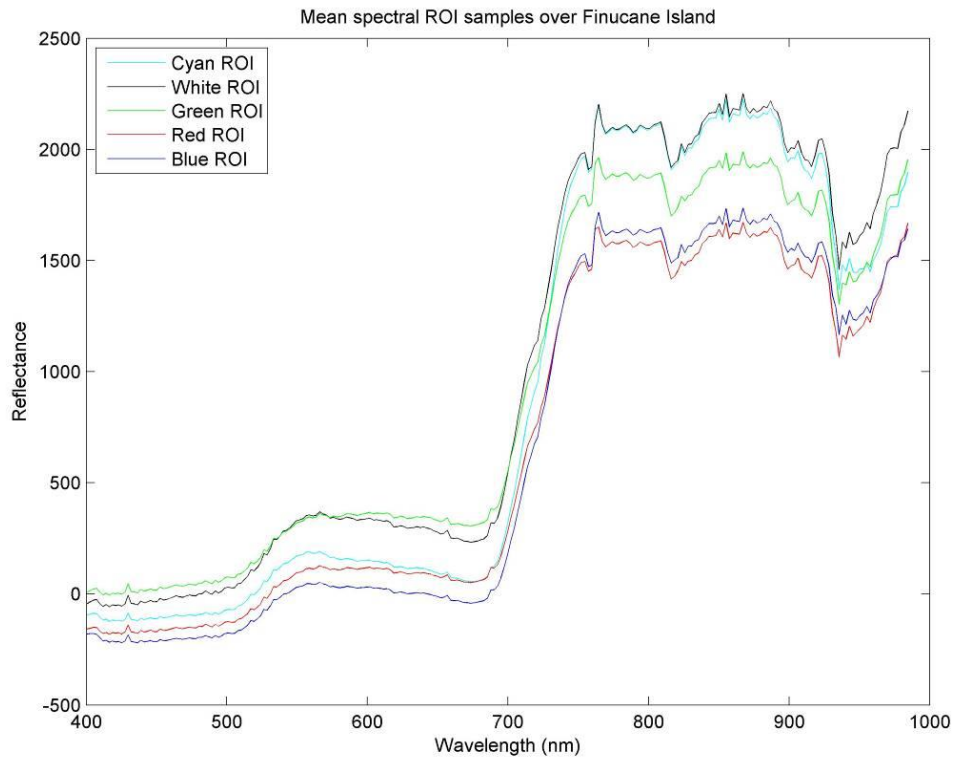


Figure 86: Vegetative spectral means corresponding to each of the five ROI's over Finucane Island using the PHPA_Ref image. The five ROI's are shown in Figure 85. Note: the reflectances are scaled by 10,000.

negative reflectances while the blue bands contain positive values. The converse is not true; red bands may exhibit positive reflectances but not necessarily over the blue bands. With these points in mind, the image formed in Figure 87 uses band 1 (400.7 nm) for blue, band 22 (448.0 nm) for green and band 44 (498.7 nm) for red to form the RGB image. Dark regions correspond to negative reflectances. A blue region means that it contains a higher intensity for band 1 than the other two bands. The image has been contrast enhanced using histogram linear 2% stretching (Harris Geospatial Solutions, 2019g).

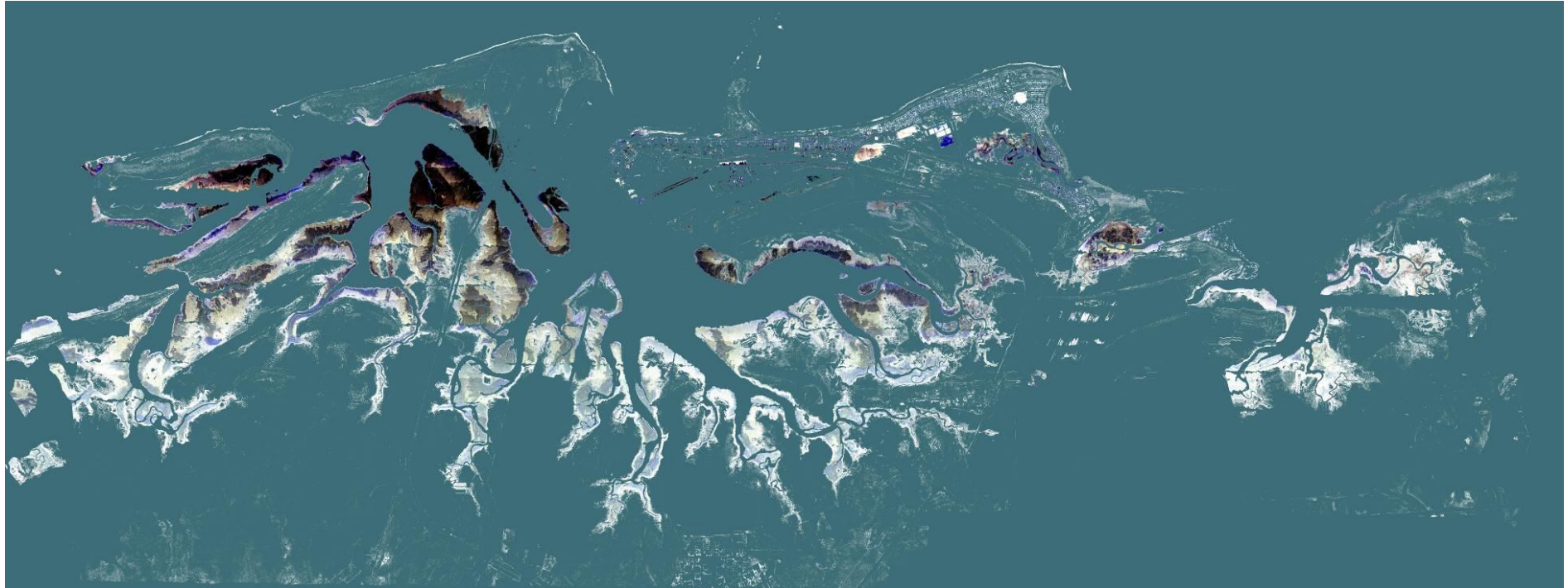


Figure 87: RGB (true colour) image using band 1 (400.7 nm) as blue, band 22 (448.0 nm) as green and band 44 (498.7 nm) as red using the vegetative-masked PHPA_Ref image. Dark regions correspond to negative reflectance spectra. The image has been contrast enhanced using histogram linear 2% stretching.

According to the dark regions displayed in Figure 87, negative reflectance spectra are predominantly located in the northern-half of the image.

Using Figure 87 as a baseline, other regions over the PHPA_Ref image were examined to study the extend of the negative reflectances. An additional four ROI's were defined for which mean vegetative spectra were calculated. Although Figure 88 shows a true-colour image, the vegetative spectra were extracted from the PHPA_Ref image that has been vegetatively-masked (i.e. using the same procedure as for the Finucane Island region earlier).



Figure 88: Vegetative spectral means were calculated for each four ROI's of using the PHPA_Ref image.

In a similar manner to that earlier for Figure 86, the colours depicted in the plot (Figure 89) correspond to the ROI colours of Figure 88 with the exception of three. The plotted mean vegetation spectrum for the white ROI is represented in black. In addition, the spectra represented in blue and magenta correspond to two single pixel spectra contained within the green and red ROI, respectively.

Although the mean vegetative spectrum corresponding to the Green ROI contains no negative reflectances in the blue (or other) wavelengths, numerous individual spectra containing negative reflectances in the blue wavelength region do exist. A single spectral sample contained within the green ROI is represented in blue in Figure 89. The same comments apply to the red ROI, where the mean vegetative spectrum all contain positive reflectances, despite numerous individual spectra containing negative reflectances. A single spectral example contained within the red ROI is displayed in magenta, where negative reflectances extend over virtually all blue bands. Despite there being a number of negative spectra, the mean vegetative

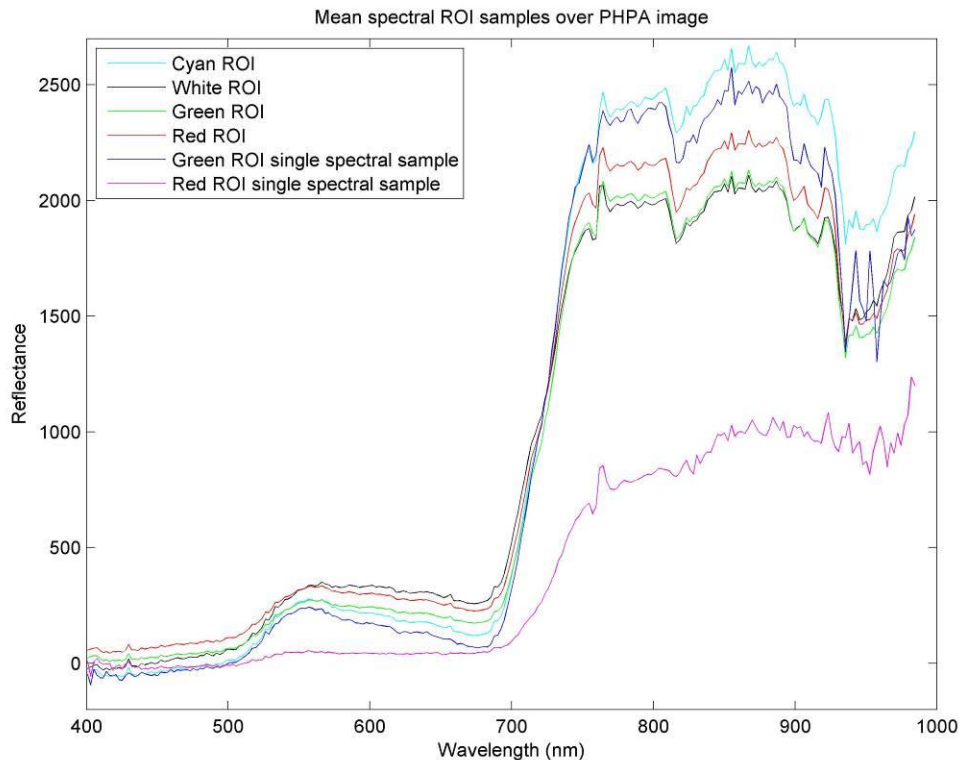


Figure 89: Vegetative spectral means corresponding to each of the four ROI's in the PHPA_Ref image. The four ROI's are shown in Figure 88. Two single pixel spectra are also shown in this plot.

spectrum for both the green and red ROI's contain positive reflectances extending over all the wavelengths, which is due to there being a larger number of pixels containing positive rather than negative reflectance spectra. This is not the case for the mean spectra in the cyan or white ROI's.

All plotted spectral are noisy, not only over the NIR range but also in the blue spectral end (near 430 nm). Considering that the spectra are reflectance spectra, the result produced by radiometric correction is somewhat disappointing.

Over Finucane Island, a relationship between the location of the ROI (Figure 85) and the mean reflectance spectra (Figure 86) is unclear. However, on a larger scale (i.e. the whole PHPA region - Figure 88), there appears to be a pattern. The mean vegetative spectra for the cyan ROI is lower (i.e. less negative) than those corresponding to the white ROI (the black spectrum in Figure 89). Further south, the mean vegetative spectra corresponding to the green ROI is more positive, while the red ROI contains the most positive of all mean vegetative spectra. Although there

are different patterns within Finucane Island, taken as a whole, the spectra on Finucane Island are more negative (Figure 86) than those in Figure 89. Therefore, overall, spectra in the north of the PHPA region tend to exhibit more negative reflectances (particularly in the blue spectral region) than those further to the south. In a direction from north to south, negative spectra becomes more positive. The negative reflectances occur mostly (but not exclusively) in the blue end of the spectrum. A trend indeed exists; Figure 109 (p. 266 of Section 4.5.9.1) shows this clearly, when vegetative spectra are analysed over the image. A fuller discussion is withheld until Section 4.5.9.1.

The poor spectral behaviour may be due to a number of causes. One could be due to canopy shadowing, which causes vegetative spectra to be bluer and darker (as discussed in Section 2.3.2). Apart from canopy shadowing effects, the poor behaviour for the blue spectra are also likely to be due to deficiencies in the atmospheric correction process. According to the Tafkaa User's Guide (Montes et al., 2004), negative reflectances may be due to overcorrection by Tafkaa but more likely are related to instrument calibration problems. Interestingly, Yang et al. (2009) actually removed the first 16 bands prior to mangrove classification (as discussed in Section 2.8.1), involving the airborne AISA+ hyperspectral sensor (the AISA EAGLE sensor recorded the PHPA data).

4.5.4 Summary and Discussion

The NDVI is a vegetative index, which exploits the red-edge of a vegetative spectra to derive a value. For an image, the NDVI is calculated for each pixel spectrum, with those containing positive values indicative of vegetation. The larger the number (up to +1), the 'stronger' (i.e. higher probability) the vegetation, as was demonstrated for an image over Finucane Island in Section 4.5.1.

Several regions on Finucane Island contain negative reflectances, frequently covering the blue spectral region and sometimes even beyond. These negative reflectances cause the NDVI to be saturated, a concern as the NDVI lies outside acceptable limits (-1 to +1). The NDVI values also massively overflow at a number of pixels, reaching well into the thousands.

The NDVI utilises only two reflectance (or radiance) values at two wavelengths (on either side of the red-edge). For multispectral data, this restriction may be sufficient but for hyperspectral data there are many more bands to utilise, thereby allowing for a mean red-edge gradient. Effectively, this helps smooth noisy airborne data and is a feature of the mean-gradient (MG) approach. First introduced in Section 4.5.2, the MG also eliminates out-of-bound values as divide by zero calculations are no longer possible. The disadvantage is that, unlike the NDVI, the MG method is not unitless as the concept is based on a mathematical definition of a gradient.

In a similar manner to the NDVI, the MG method is also able to distinguish between different cover types (e.g. water, soil and vegetation). In particular, Section 4.5.2 introduced the gradient histogram plot, to assist in selecting suitable MG threshold values for the production of thematic-based maps. The larger the MG value, the more confidence that the cover type is vegetation. This allowed for the production of a range of different vegetative maps based on different thresholds. The vegetative map with a threshold of 10,000 is extensively used in latter sections, as the threshold is particularly suitable in eliminating non-significant vegetative types (e.g. dry grass) but retaining mangrove forests.

Section 4.5.3 identified several spectral inconsistencies with the airborne reflectance image (i.e. PHPA_Ref). The change in class membership across a flight line boundary has been demonstrated in Section 4.5.1 (Figure 62). This has serious repercussions in the classification work, as shall be discussed later (Section 4.5.7).

The key points are:

- Large vegetative regions in the PHPA_Ref image contain negative reflectances in pixel spectra, particularly in the northern region of the image, resulting in out-of-bound NDVI values.
- The MG method overcomes problems associated with negative reflectances and noisy spectra in the red-edge position.
- The MG method produces similar results to the NDVI in identifying different cover types, especially vegetation.

- Classification using the NDVI causes classes to change across flight line boundaries.
- Inconsistent classification (using the NDVI) is caused by changes in spectral shapes between flight lines.

The key finding of this work is that of spectral changes, both between and within flight lines, thereby affecting classification. This is a serious problem and first identified over Finucane Island (Section 4.5.3.2). A large-scale study and correction mechanism is proposed, forming the bulk of Section 4.5.9.

This point will be returned to soon. First, it is necessary to classify PHPA_Ref hyperspectral image by developing a classification paradigm.

4.5.5 Classification Paradigm

This section begins with a discussion before outlining a paradigm for classifying a hyperspectral image.

Discussion

The preceding sections highlighted the difficulties encountered for supervised classification (i.e. SAM), when using the PHPA hyperspectral library for training. Due to the noisy nature of airborne spectra and the high spectral (ASD) similarities between mangroves, SAM classification of mangroves at species level is not possible using the techniques described.

In remote sensing, it is common (and necessary) to reduce the size of images using feature reduction. For hyperspectral data, it is particularly beneficial as the datasets tend to be very large. Apart from obvious computational benefits – smaller storage requirements and faster processing speed – there are other stronger reasons why hyperspectral data is reduced. The Hughes effect (Section 2.5.2) showed that greater classification accuracy is attained by feature reduction. Practical examples are found in the literature; for example, PC transforming CASI data (using 8 spectral bands at 1 m spatial resolution) prior to classification

produced the highest levels of accuracy (E. P. Green, C. D. Clark, et al., 1998). The same arguments apply to classifying mangroves (e.g. Tanumi Kumar et al. (2013) – as discussed in detail in Section 2.8.1).

Two rather common transforms applied by researchers are both the PC and MNF. The characteristics of both have been discussed in the literature review (see Sections 2.5.3 and 2.5.4 as well as Section 2.9). Appendix F contains a detailed numerical example of PCA.

Both the PC and MNF transforms (discussed below) were applied to the PHPA_Ref_VI image (formed by vegetatively masking the PHPA_Ref image). To clarify, the desire is to perform classification of vegetation - there is no interest in classifying non-vegetative structures (the development of this mask forms the basis of Section 4.5.6). After the transformation, the image is left with transformed bands. Feature reduction is concerned with selecting a subset of these bands. Various approaches are found in the literature, each with advantages and disadvantages (as discussed in Section 2.5.3). With due consideration, it was decided to use the 99% cumulative variance method.

Classification is performed on the actual transform-reduced image, using k-means and/or ISODATA unsupervised classification. There are cases made in favour of using the MNF transform instead of the PC transform. According to A. A. Green et al. (1988) (Section 2.5.4), the MNF transform is particularly well suited for airborne hyperspectral images. Such is the case here, as the PHPA survey recorded image data using an aerial hyperspectral (AISA EAGLE) sensor. Furthermore, MNF based classification images result in higher accuracies (according to Mundt et al. (2005) (Section 2.5.4)). In practice, when MNF transforms were applied to several hyperspectral images, the cumulative variance (%) decreased only gradually, leading to the retention of some 240 MNF bands out of 246 in total (for a 99% threshold). This is an unacceptable outcome for two reasons. Firstly, there is hardly any reduction in the number of bands; the Hughes effect is not expected to be minimised in this situation (therefore, it is questionable if classification accuracy would be increased). Moreover, from a computational viewpoint the retention of

240/246 bands means the total file size (of the transformed data) is $98 \text{ GB} \times 2 \times 240/246 = 191 \text{ GB}$.¹⁷ The time taken to classify such a file would run into days (possibly more than a week). The second reason is that often 245 MNF bands are required when following the Kaiser-Guttman rule (where eigenvalues > 1.0 are retained Section 2.5.3). This method is therefore also unacceptable (Appendix S.2 provides further detail).

Instead, the cumulative variance approach using the PC transform consistently resulted in a much more rapid decay. Typically, a retention of 8 - 15 PC bands for a 99% cumulative variance threshold (in most cases). This led to a file size of around 6 – 12 GB. Computationally, unsupervised classification of such a file takes (roughly) 6 hours for the 12 GB file. In view of these results and factors, PCA is used (instead of MNF) as the method of choice in this thesis; PCA both decorrelates and is commonly used in feature reducing images in remote sensing. It is “the method technique of choice for dimension reduction” (Kaewpijit et al., 2003).

The last step in the classification process assesses the spectral separability of the classes in a thematic map. The step is a post-classification exercise. The thematic map contains a number of classes, some of which may not be sufficiently spectrally separable. For example, specifying 50 classes for k-means classification means that small spectral differences are distinguished and represented as different classes. However, in practice the spectral differences may be due to noise, vegetative condition and so on. A number of these 50 classes are not necessary spectrally different, thereby requiring merging with other classes. The JM separability distance is ideal in determining whether classes require merging, as its properties are well defined and understood (the details were outlined in Section 2.5.5). It is a statistical measure and relates to the probability of having spectrally separable classes.

Paradigm

The production of a thematic map from a hyperspectral image are summarised into the following steps:

¹⁷ *In C++, a float data type requires twice as much memory as an integer, leading to a doubling in the original file size.*

1. Using a vegetative-mask to eliminate all non-vegetative pixels from the image.
2. PC transform of the hyperspectral image.
3. Selecting a subset of PC bands to retain (using the 99% cumulative threshold approach).
4. Unsupervised classification using k-means or ISODATA on the PC reduced image.
5. Assessing the separability of classes using JM distance (to allow class merging – if required).

Step 1 removes all non-vegetation spectra from the image. Steps 2 and 3 define feature reduction, whereas classification (step 4) results in a thematic map. Step 5 answers how spectrally different the classes are and whether any of them require merging to further increase the level of confidence that particular classes do in fact belong to the same cover type (e.g. grass). If all classes are found to be separable, then the number of classes specified to the classifier needs increasing prior to carrying out step 5 again.

Comments:

The PC transform is performed on the hyperspectral image using a vegetative mask (i.e. developed in Section 4.5.6). The mask represents ‘strong’ vegetation, in particular capturing the mangrove forests. Classification is therefore applied only to ‘strong’ vegetation.

JM distances are calculated with the assistance of ENVI, whose results are interpreted as the spectral separability between class pairs. These results are used as a basis to decide the particular classes which need to be merged, a process employed by other researchers in the classification of remote sensing data (e.g. Thomas et al. (2003)).

Instead of merging, classes may instead require increased separation. Consider a k-means classification result for 2 defined classes. It is likely that these are spectrally highly separable, resulting in a high JM distance. For this particular scenario, it is

clear that a higher number of classes are required to extract more classes. The JM distance therefore provides a clue as to the number of classes to specify to the classifier.

Elaboration of step 1:

Images are filtered using a vegetative mask, resulting in a new image containing 'strong' vegetation. The 10,000 MG threshold of Section 4.5.2 is used.

Elaboration of step 2:

The PhD candidate used the ENVI software package to perform the actual PC transformation. It should be noted that ENVI actually uses a shift in origin to ensure that brightness values remain positive. This is further elaborated in Section 6.3.3 in Richards (2013) (p. 173). Appendix F contains a calculation to prove this assertion, in addition to a detailed example of the PCA process.

As previously stated, from a computational viewpoint, the original hyperspectral file stores integer values but the act of either a PCA or MNF transformation results in a file with floating-point data. The effect is a doubling in file size to store the transformed band data. Therefore, computationally if the band reduction is not at least 50%, then there is unlikely to be a performance gain in further processing.

Elaboration of step 3:

The methods available for PC transform band selection were discussed in Section 2.5.3. By experience, the scree test method was found inappropriate due to the difficulty in finding a 'break'. In addition, the method of retaining eigenvalues > 1.0 is also inappropriate, as it led to the retention of too many bands. In fact, in most practical situations, all eigenvalues were found to be > 1.0 . This means all PCA bands would need to be retained!

The 95% and 99% cumulative variance choices were the most satisfactory for the PCA transform but not for the MNF transform where it often meant losing just one

band from the 246 bands. As a result, the MNF was dropped in favour of PCA for feature reduction.

Elaboration of step 4:

Although the unsupervised ISODATA classifier allows for a range of classes to be specified, k-means requires a specific number of classes. This is useful as it provides a higher degree of control for separability analysis.

For a supervised classifier, Section 4.4.5 raised a number of concerns in using a hyperspectral library for training, limiting its effectiveness. Another approach uses pixel spectra itself for training. However, there is another complication, which adds further uncertainty. A direct match in location between a single pixel and the associated field trip location relies on an accurate position as given by the GPS. If the exact location of the ASD cover type can be identified in the image itself, then the image spectra could be used for training. The identification of the cover type is known, due to the field-sampled ASD location. However, in practice there are uncertainties associated with the location. Not only is there an uncertainty associated with the location of the ASD (see Appendix I.2) but when translated to a pixel location, ENVI does not always identify the exact pixel intended (see Appendix I.1). The natural variability in vegetation cover types is often too extreme to take the approach of “near enough is good enough”. Although some mangrove trees were sufficiently well isolated (e.g. Figure 221, p. 541 of Appendix I.2) to eliminate positional doubt, in reality this was a rare occurrence (e.g. Figure 90), where a 1 or 2 m change in location means encountering a different mangrove species. Field trip data showed several site locations where mangrove species were highly variable (see Section 4.6.3). In fact, it is well known that wetlands, which includes mangroves, are heterogeneous ecosystems containing highly mixed species (Lu & He, 2018).

If the species were distributed like crops in a typical agricultural field, then the cover types would likely be uniformly distributed and a small change in position can be catered for. Grouping individual pixels having like spectra for training is also not a safe option. For one, differences between several mangrove species are minute



Figure 90: The photo (on Finucane Island) shows different species (different green tones) of mangrove separated by 1 – 2 m. The spatial pixel resolution is 1 m.

(as shown visually in Figure 57, p. 175 and quantitatively in Appendix G.3). In addition, the decision made by the human analyst may be in error. Two identical species may also appear spectrally different according to many factors (e.g. stress, phenology, etc.). Then there is the question of the number and location (ideally random) of spectra which need to be taken (Appendix D.1) and even whether the samples represent pure or mixed spectra.

Pixel size is another factor, as smaller pixels require higher locational precision. Field work identified regions where mangrove species change over just a few metres. Photographic evidence is presented in Section 4.6.3 (e.g. Figure 148, p. 341). This introduces questions such as; where exactly the pixel boundary is located (in relation to the photograph). What portion of the mangrove is located in the actual pixel? This introduces mixed-pixels - unsuitable for training a classifier. The uncertainty of the GPS is estimated at 4 – 8 m, as estimated using the approaches discussed in Appendix I.2.

There is yet another complication, involving the selection of pixel spectra for training a supervised classifier. As discussed in Section 4.4.5, image spectra change

according to location. Therefore, even if the identity and exact position of a cover type were known, spectra collected at different locations are expected to differ. Normalisation improves the consistency, but makes them less ASD like. Therefore, the ASD hyperspectral library can not be used, even with a normalised reflectance image. This is especially true for a normalised radiance image, which (as seen later) produced the best unsupervised classification result.

Taken together, it was decided that unsupervised classification was the best way forward, as it is unbiased in finding spectral patterns. It also does not rely on training pixels. The unsupervised classification algorithm of ENVI was used to perform the actual classification task.

Elaboration of step 5:

The JM distance measure is used to assess class separability, instead of the transformed divergence, as the JM distance gives improved results and has similar distance interpretation (Section 2.5.5).

An attempt is made to produce three separate thematic maps for each of the following three JM distances (representing three levels of confidence):

$$JM \geq 1.7$$

$$JM \geq 1.8$$

$$JM \geq 1.9$$

As the JM distance increases, the class separabilities increase. This translates to higher confidence (i.e. probability) that the classes are spectrally separable. JM distances ≥ 1.9 in particular are highly separable. This allows classification results to be ranked according to classification confidence; a map where classes are separable to $JM \geq 1.9$ represents a highly confident (synonymous with high probability) thematic map where all classes are highly separable.

In practice, the production of the three thematic maps was influenced by the separability statistics after class pair merging. For example, merging classes for a

map containing classes of low separability (e.g. $JM \geq 1.7$) may result in a new map where the separability increases directly to $JM \geq 1.9$. As a result, the production of a map where classes are separable to $JM \geq 1.8$ is not necessarily possible (as the results show in Sections 4.5.7, 4.5.9 and Appendix O).

The ENVI software package was used to calculate JM distances between class pairs and for the actual process of class merging. By default, ENVI also orders the class separability statistics, in ascending order. Unfortunately, ENVI does not provide an optimised manner by which JM distances can be calculated. In practical terms, ROI's had to be created for each class prior to the JM distance calculation between class pairs. After class merging, new distances had to be calculated due to class membership changes (of the merged classes). This involved creating new ROI's for each class whose membership changed and recalculating new JM distances. Overall, the process is iterative but rather tedious.

The significance of step 5 is that classes are separable based on statistically valid arguments, leading to a series of thematic maps, whereby the existence of classes is based on various degrees of confidence. The class merging concept is also in line with the 10 classification criteria for land cover classification by J. B. Anderson (1971) (Section 2.6).

4.5.6 Development of a Vegetation-Mask

This section develops a vegetation-mask using the results of Section 4.5.2.

In particular interest is the MG threshold of 10,000. While the MG map of Figure 75 (p. 208 of Section 4.5.2) contains actual MG values (for each pixel), a vegetative mask contains just two values. A value of 1 signifies that a specific pixel contains vegetation (of threshold $\geq 10,000$) while a value of 0 signifies otherwise (e.g. 'weak' vegetation, soil, water). The result is a black and white image as depicted in Figure 91.

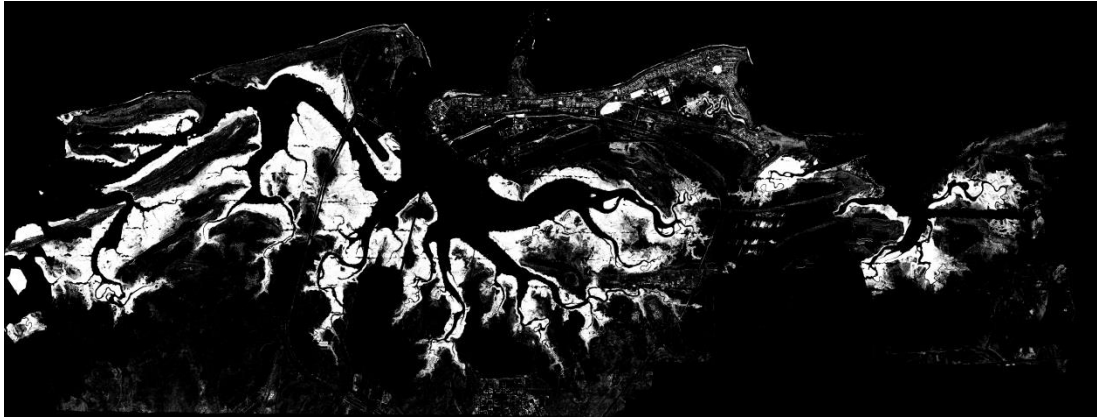


Figure 91: Mask file for 'strong' vegetation (represented by white pixels).

The advantages of such a file are many. Firstly, it is a small file (only 204 MB) which is read together with an image file. For example, a pixel read from the PHPA_Ref image (containing the full spectrum) is checked against the corresponding pixel value of the mask file. A mask value of 1 (white) means the pixel is retained, otherwise the whole spectrum is set to 0. Another advantage is that images may be masked for different thresholds, without any change in computer code, simply by adopting the corresponding mask; creating the set of masks is a simple process.

There are yet further advantages. The preceding section (Section 4.5.5) mentioned both the PC transform and the classification process itself would be performed with the aid of ENVI. It turns out that the mask file must indeed be specified together with the PHPA_Ref image to ensure that background pixels (i.e. the black pixels, containing zero valued spectra for all bands) are not included in the calculations. Testing (refer to Appendices W.2 & W.3) showed that classification results to indeed differ in the absence of specifying these masks.

Comparing the two images of Figure 92 highlights the effectiveness of the vegetative mask.



Figure 92: Original image for a small region of suburban Port Hedland (left) and the corresponding vegetative-mask (right).

The result of Figure 92 shows the presence of (strong) vegetation. Absent are man-made structures, such as buildings and roads.

4.5.7 Classification of the PHPA_Ref_VI image

The first step of the classification paradigm (Section 4.5.5) involves using the vegetative-mask (Figure 91) to the PHPA_Ref image (Figure 42, p. 141), resulting in a new image PHPA_Ref_VI (Figure 93). The new image uses the same name as the original image but carries the “_VI” suffix to indicate that it is vegetatively masked.

Thesis Standard: When an image is masked using the vegetation-mask of Section 4.5.6, a new image is created with the same name but carrying the _VI suffix.

Note that Figure 93 is a contrast-enhanced image of the original image, which is shown in Figure 336 (p. 724, of Appendix U). ENVI displays images using 256 DN values (8 bits). For 16 bit images (as is the case here), the number of DN values exceeds the display capability, so ENVI uses a histogram to remap DN values. The

effect of negative reflectances cause a rescale of masked (zero pixels) to positive values. Instead of displaying as black, masked pixels now appear blueish (see Figure 336 p. 724 of Appendix U). The undesired effect is overcome by manually manipulating the histogram. Further details are given in Appendix U.

The PHPA_Ref_VI image clearly displays (horizontal) striping across the whole region. These artefacts are analysed in much further detail in Section 4.5.9.1.

For step 2 of the classification paradigm, the PHPA_Ref_VI is PC transformed with the assistance of ENVI. Figure 94 shows the (desired) rapid decay in eigenvalues.

The number of PC bands to retain relies on the 99% (threshold) cumulative variance threshold. Due to the rapid eigenvalue decay, the cumulative variance instead rapidly grows, as shown in Figure 95.

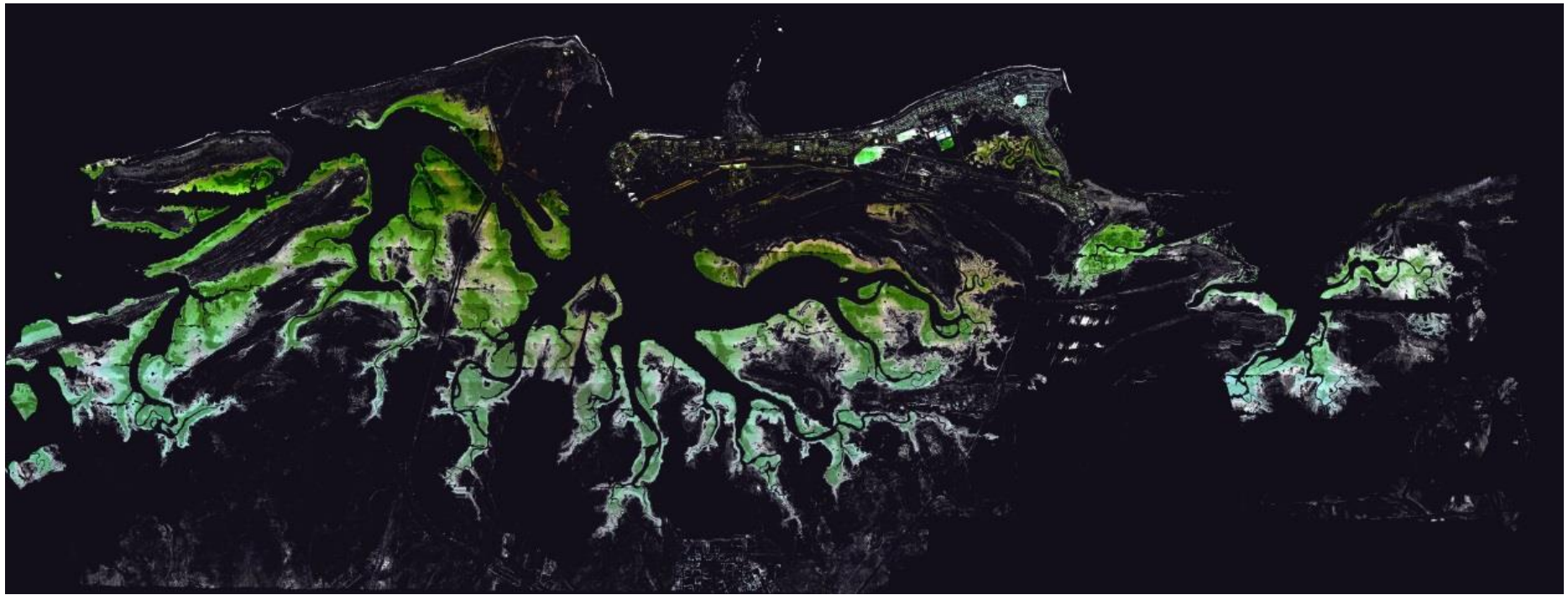


Figure 93: A true colour (contrast enhanced) image for the result of applying the vegetation-mask (i.e. Figure 91 of Section 4.5.6) to the PHPA_Ref image. The result is an PHPA_Ref_VI image, containing 'strong' vegetation (i.e. $\geq 10,000$ gradient threshold).

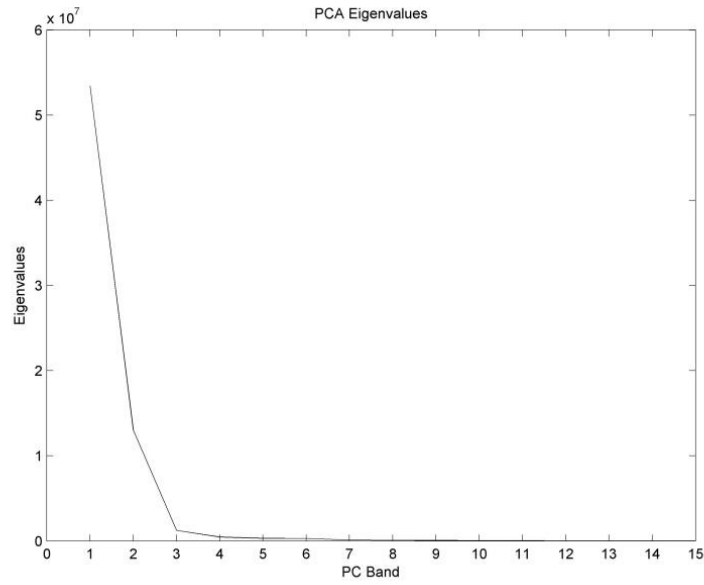


Figure 94: Rapid drop-off in eigenvalues for the PC transform of PHPA_Ref_VI.
(only the first 15 PC bands are shown).

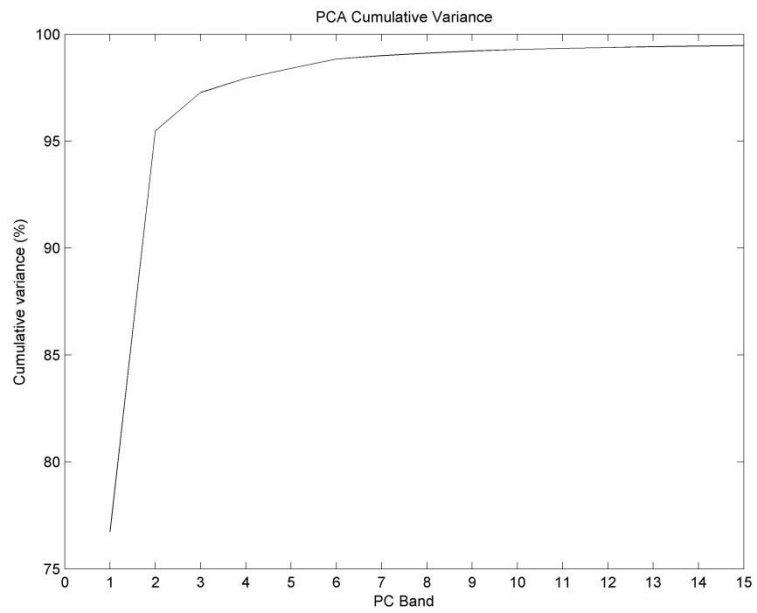


Figure 95: Rapid growth for the cumulative variance (%) of the PC transformed PHPA_Ref_VI data.
(only the first 15 PC bands are shown).

A threshold of 99% for the cumulative variance is reached (indicated in bold font) after only 9 PC bands. Table 24 contains the actual values.

PC band	Cumulative variance (%)	PC band	Cumulative variance (%)
1	76.41	6	98.58
2	95.04	7	98.77
3	97.00	8	98.91
4	97.78	9	99.04
5	98.33	10	99.13

Table 23: Cumulative variance (in % and rounded to 2 d.p.) for the PC transform of the PHPA_Ref_VI image.

The first 9 PC bands account for 99% of the total variance. Therefore, 9 PC bands are retained for classification purposes (Note: only the first 10 PC bands are shown in this table). The order of PC bands are given in ascending order by increasing cumulative variance.

The table shows that 76% of the total variance is contained in the first PC band. Using 99% as a basis for the cut-off in our selection process, the first 9 PC bands need to be retained. Recall the need for feature reduction is to obtain a higher classification accuracy – a consequence of the Hughes effect. In some ways, this may be viewed as a positive as it leads to smaller datasets. Computationally, the 9 PC bands result in a file that is $196 \text{ GB} / 246 \times 9 \approx 7.2 \text{ GB}$ in size. Compared to the original PHPA_Ref dataset (98.0 GB), the drastically smaller file leads to a vast increase in computational processing speed for subsequent classification work.

Step 4 of the classification paradigm uses the 9 PC band transformed dataset for k-means unsupervised classification. In general, a maximum of 50 iterations were deemed sufficient to obtaining a satisfactory result (see Appendix V). The results for a 10 class k-means classification is shown in Figure 96.

Just as for the PHPA_Ref_VI image (Figure 93), the classification map also exhibits horizontal striping. In fact, the artefact affects the classification negatively, as is portrayed in Figure 97 (left image). There is an obvious class boundary associated with the flight line boundary.

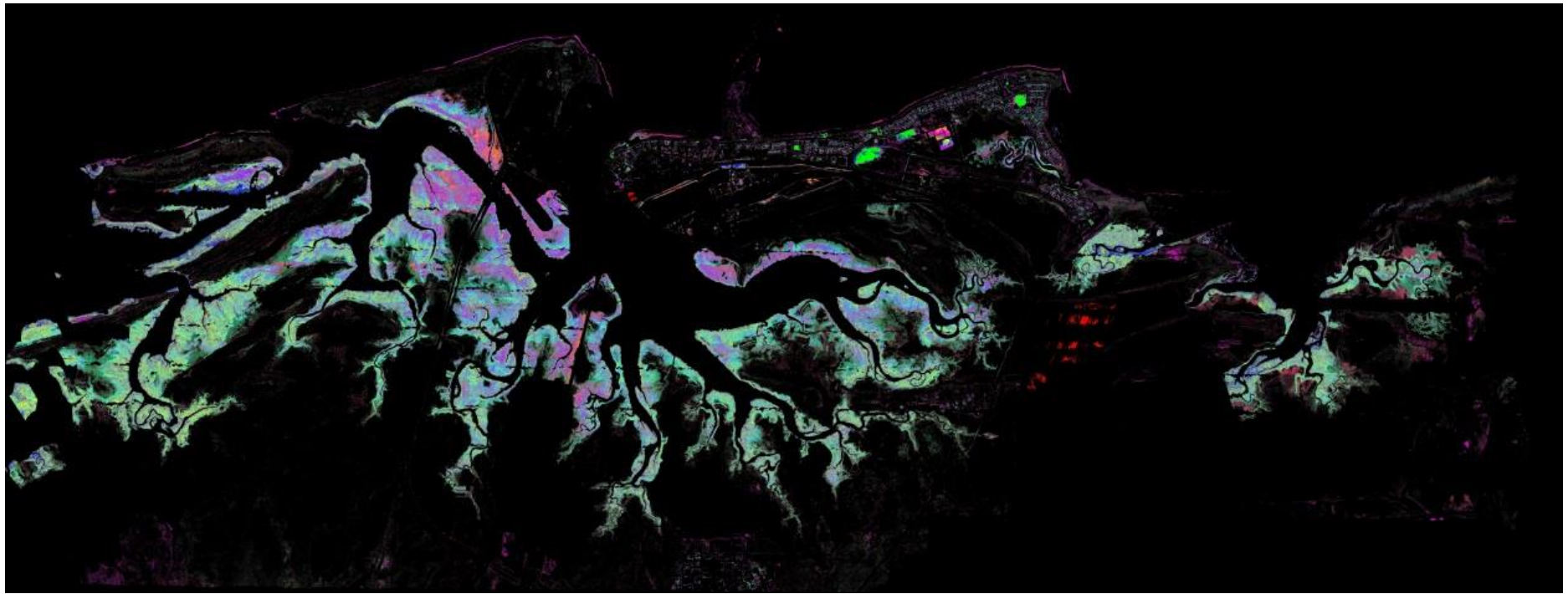


Figure 96: The thematic map from k-means classifying a 9 PC band PHPA_Ref_VI dataset using 10 clusters and 50 iterations.

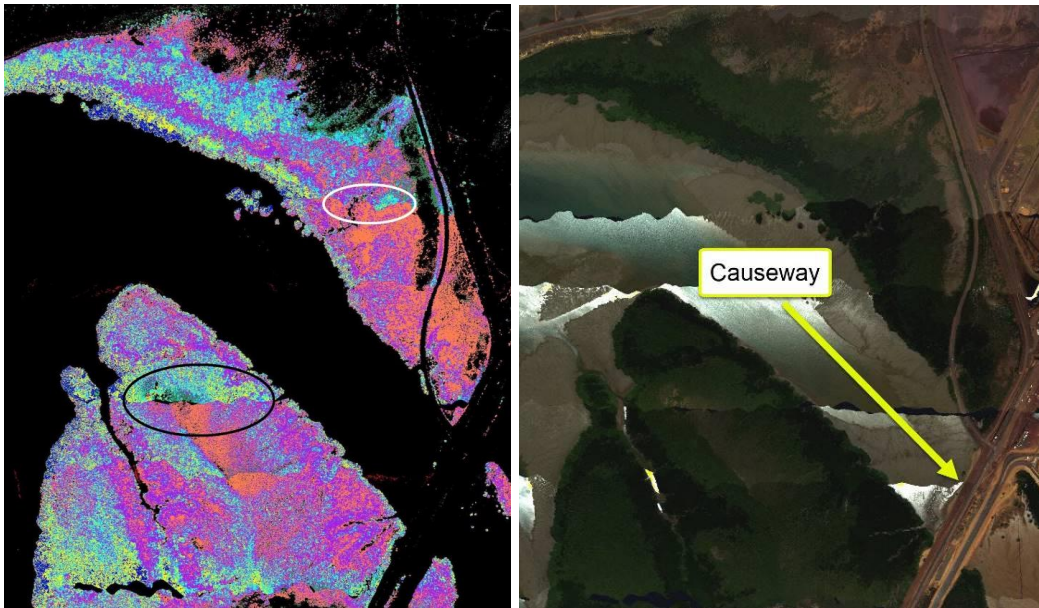


Figure 97: The effect of horizontal striping causing class membership changes across flight lines (left image). The corresponding PHPA_Ref true colour image is shown on the right.

According to the classification result (Figure 97, left image), classes change when traversing flight line boundaries. This characteristic was also observed for the simple NDVI classification result (Figure 62, p. 191 of Section 4.5.1). Adjacent pixels near a flight line edge but located within the same flight line, appear to be unchanged. However, by traversing just a single row of pixels (i.e. to enter an adjacent flight line), the class membership changes. The result is very disconcerting and very unlikely to correspond to physical reality – why would a mangrove forest suddenly change in composition, depending on where the airborne sensor is located? The result does not make sense. The integrity of the thematic map is therefore under question as spatially the results appear unsound. The distribution within a flight line itself may appear to be coherent but definitely not between flight lines.

Ignoring the undesired spatial effects for the moment and treating this purely as a mathematical exercise, the class pair separabilities (i.e. distinguishability) were calculated using JM distances for each class pair. This defines the final step of the classification paradigm (step 5). With the aid of ENVI, the separability statistics were calculated for all 10 classes and are as shown in Table 24. Only JM distances less than 1.92 are given (relevant for class-pairs which require merging). Note that the

identity of each class (e.g. class 4) is not made in relation to the class colour displayed in Figure 96.

class 4 & class 5: 1.5032
class 3 & class 4: 1.5089
class 5 & class 9: 1.5182
class 7 & class 8: 1.5505
class 9 & class 10: 1.5742
class 8 & class 10: 1.5860
class 8 & class 9: 1.7463
class 5 & class 8: 1.8564
class 6 & class 7: 1.8974
class 5 & class 7: 1.9196

Table 24: Separability report for the k-means 10 class (50 iterations) classifier of the 9 PC band N_Ref_VI_VI dataset.

Note: 1) only values for JM < 1.92 are shown, 2) the relationship between individual class numbers and class colours (for Figure 96) are omitted, 3) JM distances are given in order of increasing JM distances, 4) JM distances are rounded to 4 d.p..

The table is arranged in ascending order according to JM distances between class pairs. For example, the first row shows that the JM distance between classes 4 & 5 is 1.5032. As stated in Section 2.5.5, distances < 1.7 are poorly separated.

Therefore, there is a high probability that classes 4 & 5 are spectrally very similar and require merging into one class. JM distances over 1.8 are moderately well separable, while JM distances over 1.9 (e.g. classes 5 & 7 – the last entry in the table) are highly separable. Therefore, there is a high probability that class-pair (i.e. 5 & 7) are spectrally dissimilar; these classes do not require merging.

It is important to note that, although Table 24 shows the JM calculation for 10 class pairs, the calculation is based on class-pair combinations for 10 classes. The 10 classes represent all the 10 classes resulting from the thematic map (as specified into the k-means classifier). Therefore, 10 classes (1 to 10) are still considered as no merging has occurred; the wording in the table caption may be misinterpreted as a list of 10 JM distance class-pairs rather than a total of 10 classes being considered. This will become clearer later on.

As a JM distance of 1.7 is the minimum desired separability (as it represents a low probability of class distinguishability), several class pairs need merging (as evident from the table). However, care must be taken in combining them;

combining classes 4 & 5 and 3 & 4 simultaneously would be incorrect as they're not mutually exclusive. Suppose that 4 → 5 (i.e. class 4 is now merged with class 5 and relabelled as class 5), thereby generating a new (larger) region for class 5; the number of pixels for the merged region being equivalent to the pixel sum of both class 4 & 5. The JM distance between classes 3 & 5 will therefore be changed (due to membership change of class 5). Hence, 4 → 5 and 3 → 4 cannot be performed in one operation. The approach is to merge the classes with the lowest JM distance then recalculate the JM distances. The approach is repeated until all class pairs form satisfactory minimum JM distance (e.g. 1.7).

It is worth noting that the operation 4 → 5 changes the merged population. The population of class 4 remains unchanged and is no longer used; nor is the pre-merged class 5 population. They are both insignificant in this context. What is significant is the merged population (i.e. class 4 plus class 5). For convenience, the overwriting of class 5 was easier than creating a new class. It is unclear beforehand what to label the merged class as, if a consecutive order is maintained. For instance, should the merging of class 4 and class 5 be labelled as class 20? What if this is merged at a later time? What happens to class 4 and class 5, which are no longer used? Should all classes be renamed to be ordered consecutively? In the end, overwriting class 5 was done for convenience and has no effect, as the historical class 4 and class 5 (i.e. pre-merged) populations are no longer required. The tracking is also easier (e.g. which classes were merged to form class 20?). By eliminating class 4 from an ENVI ROI but using the merged class 5 population, it is clear that class 5 is a merged class using class 4 (as merged classes are numbered up – i.e. class 4 → class 5 and not class 5 → class 4).

With these factors in mind, the separability statistics for the result where class 4 is merged into class 5 are shown in Table 25. The effect is a reduction in the total number of classes on the thematic map.

As class 4 no longer exists, only 9 classes exist (i.e. 1 to 3 and 5 to 10). The table shows classes 3 and 5 to 10; classes 1 and 2 are not shown as JM distances > 1.92 are excluded from the table but still exist on the thematic map.

class 5 & class 9: 1.4663
class 7 & class 8: 1.5505
class 9 & class 10: 1.5742
class 8 & class 10: 1.5860
class 3 & class 5: 1.6572
class 8 & class 9: 1.7463
class 5 & class 8: 1.8539
class 6 & class 7: 1.8974
class 5 & class 7: 1.9157

Table 25: Separability report for the k-means 10 class (50 iterations) classifier of the 9 PC band N_Ref_VI_VI dataset after class 4 is merged into class 5 (leaving 9 separable classes).

Note: 1) only values for JM < 1.92 are shown, 2) the relationship between individual class numbers and class colours (for Figure 96) are omitted, 3) JM distances are given in order of increasing JM distances, 4) JM distances are rounded to 4 d.p..

Next, class 5 is merged into class 9. After merging, the new JM distances are calculated (results shown in Table 26).

class 7 & class 8: 1.5505
class 8 & class 10: 1.5860
class 3 & class 9: 1.6632
class 9 & class 10: 1.6692
class 8 & class 9: 1.7776
class 6 & class 7: 1.8974

Table 26: Separability report for the k-means 10 class (50 iterations) classifier of the 9 PC band N_Ref_VI_VI dataset after class 5 is merged into class 9 (leaving 8 separable classes).

Note: 1) only values for JM < 1.92 are shown, 2) the relationship between individual class numbers and class colours (for Figure 96) are omitted, 3) JM distances are given in order of increasing JM distances, 4) JM distances are rounded to 4 d.p..

At this point both class 7 can be merged into class 8 and class 3 merged into class 9 in one step, with the new JM results shown in Table 27. Continuing the process, class 8 is merged into class 10 (Table 28), leaving 5 separate classes (i.e. 1, 2, 6, 9, 10) with JM distances of ≥ 1.7 .

The resulting thematic map for JM ≥ 1.7 is shown in Figure 98. The threshold of 1.7 is considered to represent poorly separable classes. Indeed, it could be argued that the JM distance between classes 9 & 10 is < 1.7 (i.e. a value of 1.6948). However, to one decimal place it is equivalent; the accepted thresholds of Section 2.5.5 are stated to one decimal place.

class 8 & class 10: 1.5564
class 9 & class 10: 1.5966
class 8 & class 9: 1.7861
class 2 & class 6: 1.9418

Table 27: Separability report for the k-means 10 class (50 iterations) classifier of the 9 PC band N_Ref_VI_VI dataset after class 7 is merged into class 8 and class 3 into class 9 (leaving 6 separable classes).

Note: 1) only values for JM < 1.95 are shown, 2) the relationship between individual class numbers and class colours (for Figure 96) are omitted, 3) JM distances are given in order of increasing JM distances, 4) JM distances are rounded to 4 d.p..

class 9 & class 10: 1.6948
class 2 & class 6: 1.9418
class 6 & class 10: 1.9598
class 2 & class 9: 1.9965
class 6 & class 9: 1.9974
class 2 & class 10: 1.9994
class 1 & class 6: 2.0000
class 1 & class 2: 2.0000
class 1 & class 10: 2.0000
class 1 & class 9: 2.0000

Table 28: Complete separability report for the k-means 10 class (50 iterations) classifier of the 9 PC band N_Ref_VI_VI dataset after class 8 is merged into class 10 (leaving 5 separable classes).

Note: 1) all JM distance values are shown, 2) the relationship between individual class numbers and class colours (for Figure 96) are omitted, 3) JM distances are given in order of increasing JM distances, 4) JM distances are rounded to 4 d.p..

Interestingly, a well-defined class structure now appears on Finucane Island amongst the mangrove forests.¹⁸ The region of interest is highlighted by a yellow circle in Figure 99 (top image) and will be discussed further in Section 4.5.11.1.

¹⁸ The class structure only appears on the JM ≥ 1.7 map. There is no ≥ 1.8 map, and the structure is absent in the JM ≥ 1.9 map.

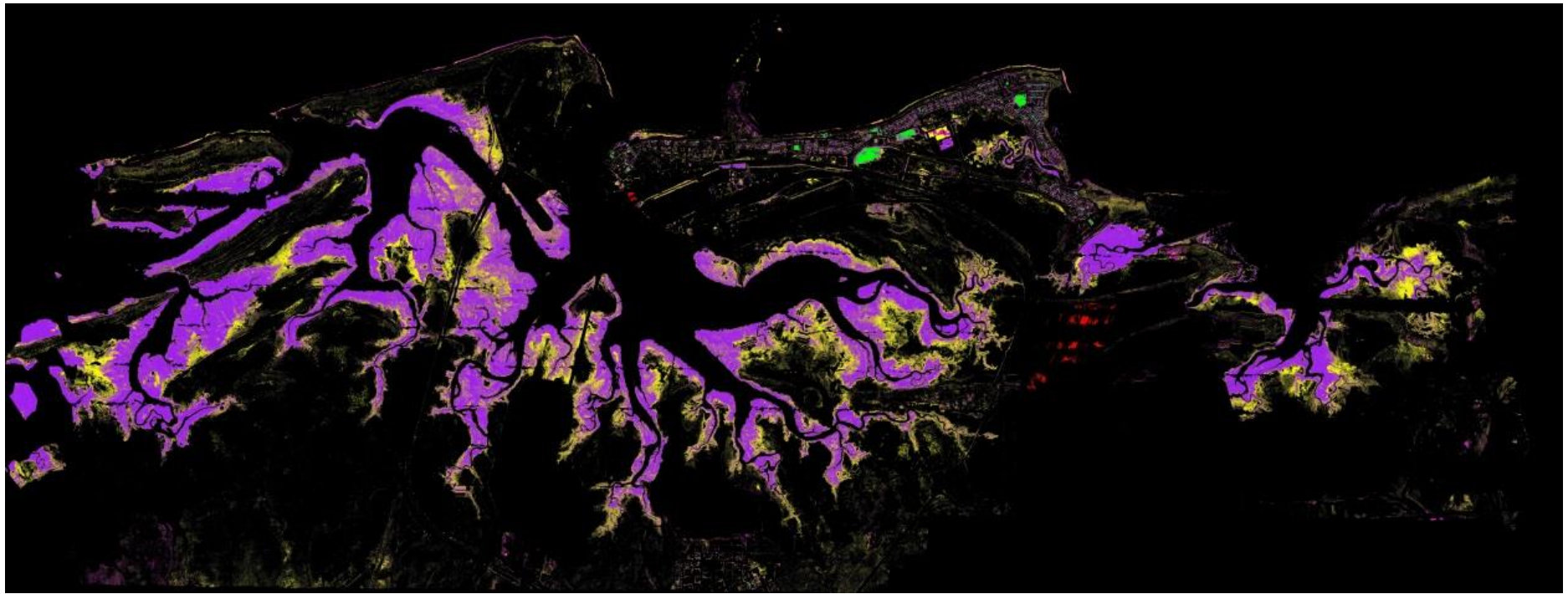


Figure 98: Thematic map as obtained by merging classes from the 10 class k-means classified map, leaving a total of 5 classes separable at $JM \geq 1.7$.

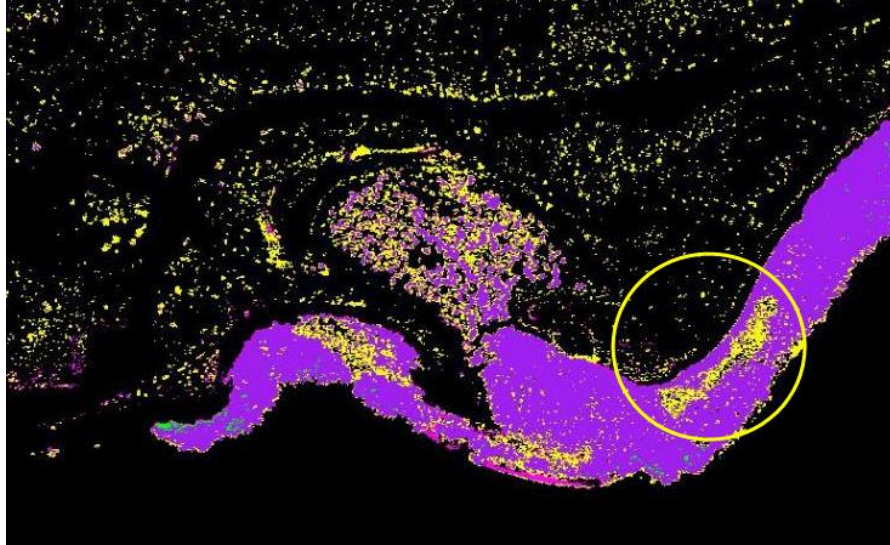


Figure 99: Magnified view of Figure 98 over Finucane Island.

At $JM \geq 1.7$ there appears to be a well-defined class structure amongst the mangrove forest (top image). The bottom image shows the location for the class structure (of the top image) as a true colour image in addition to a magnified view.

Increased class separability confidence is gained by continuing the class merging process. However, there is no result for a $JM \geq 1.8$ - hence the lack of an actual image. The reason is found by referring back to Table 28, which shows that classes 9 & 10 produce the least amount of separation ($JM = 1.6948$). However, by merging

class 9 into class 10 immediately produces a JM = 1.9418, as shown in Table 29; there is no unique result for a threshold of 1.8. The results of this Table 29 are appropriate for a JM threshold of 1.9.

class 2 & class 6: 1.9418
class 6 & class 10: 1.9826
class 2 & class 10: 1.9940
class 1 & class 6: 2.0000
class 1 & class 2: 2.0000
class 1 & class 10: 2.0000

Table 29: Separability report leaving 4 highly separable classes at JM \geq 1.9.
Note: 1) all class-pair separability JM distances are shown, 2) the relationship between individual class numbers and class colours (for Figure 96) are omitted, 3) JM distances are given in order of increasing JM distances, 4) JM distances are rounded to 4 d.p..

Hence, class pair merging does not always allow for three separate images of increasing class pair separability (i.e. JM \geq 1.7, JM \geq 1.8 and JM \geq 1.9), which was one aim as described in Section 4.5.5. In fact, subsequent work (later in this thesis), shows that production of these three distinct thematic maps is rarely possible.

The results shown in Table 29 leads to the image displayed in Figure 100, where just 4 classes are left for JM \geq 1.9

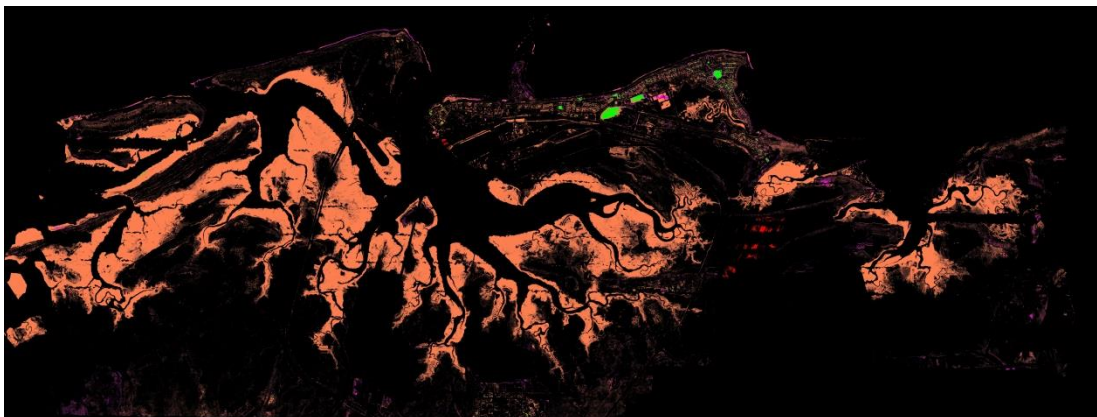


Figure 100: Thematic map as obtained by merging classes from the 10 class k-means classified map, leaving a total of 4 classes at JM \geq 1.9.

The main difference, by comparing Figure 98 with Figure 100, is the lack of differentiability between classes in the mangrove regions. Figure 98 shows spatial structures consisting of purple and yellow classes, while as the class separability confidence increases, Figure 100 leaves just one brown coloured class dominating

the majority of the scene. Both images contain separate classes at the same locations in the suburban regions, of no interest to mangrove classification.

The information content of Figure 100 is considered poor, compared to the detail desired; one class dominating the mangrove forested region!

The $JM \geq 1.9$ leads to highly separable classes but leaves a map similar to a simple vegetative map (i.e. like Figure 75, p. 208, of Section 4.5.2). Although there is less confidence in class separability with the $JM \geq 1.7$ map (i.e. Figure 98), there is more confidence that all spatial structures are vegetation.

Unsupervised classification was also performed using ISODATA, to examine any thematic differences. Using default settings in ENVI, a range of 5 to 10 classes were specified (for 50 iterations), with the resultant thematic map shown in Figure 101.

As might be expected, the horizontal 'striping' effect is once again apparent just as for the k-means result (Figure 96).

Spectral inconsistencies between flight lines are causing both methods of unsupervised classification to consider the spectra to be different, thereby forming separate clusters. There are clearly spectral issues with the PHPA_Ref hyperspectral image, which were uncovered in Section 4.5.3.2 and manifesting themselves in the results here.

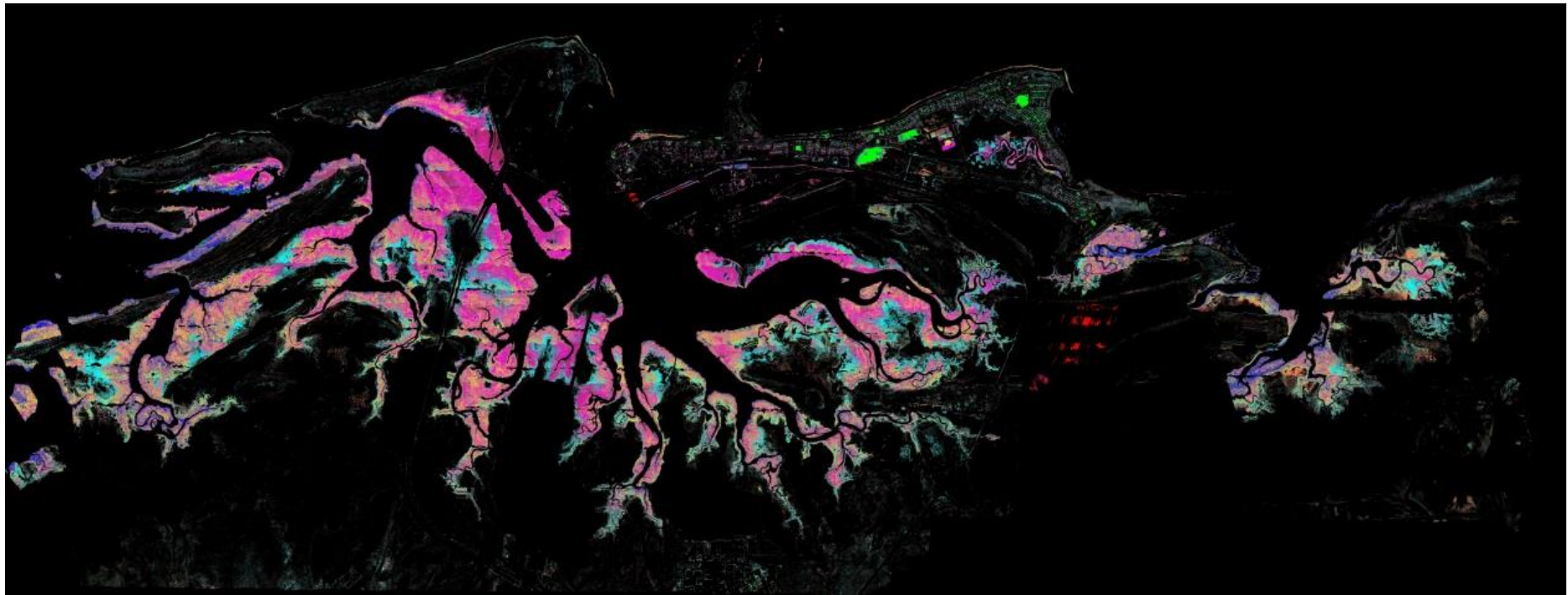


Figure 101: The thematic map resulting from a 9 PC band PHPA_Ref_VI dataset using ISODATA unsupervised classification. A range of 5 to 10 clusters with 50 iterations resulted in 10 classes.

4.5.8 Atmospheric Correction Analysis

As detailed in the literature review (Section 2.4.2 in particular), atmospheric correction converts a radiance-based image to a reflectance type, which is devoid of differences due to illumination and viewing geometry effects. As this thesis utilised the Tafkaa model for atmospheric correction, it is important to understand how Tafkaa converts airborne measured radiance to a surface reflectance. Although the mathematical treatment is left to Appendix 0, the mathematical functions rely on several parameters. For example, the atmospheric transmittance depends on absorption and scattering due to gasses and aerosols. Tafkaa models these parameters based on gas content of the atmosphere (e.g. H₂O, O₃, CO₂, and so on) and takes in account the underlying scattering physics (i.e. Mie, Rayleigh and aerosol scattering).

Parameters which specify the sensor view angle, sensor altitude, time of day, position (longitude and latitude) and are passed to the model using a Tafkaa header file. An example for the file format is shown in Table 30.

```
samples = 1
lines = 1
image_center_date = {
  2010, 9, 17}
image_center_time = {
  4, 10, 21.000}
image_center_lat = {
  20, 18, 31.000}
image_center_lat_hem = S
image_center_long = {
  118, 33, 16.000}
image_center_long_hem = E

  < *** centre part remains the same *** >

image_center_zenith_ang = {
  0., 0., 0.000}
image_center_azimuth_ang = {
  0., 0., 0.000}
sensor_altitude = 0.598265
tafkaa_ground_elevation = 0.000
```

Table 30: A list of significant parameters required by Tafkaa. This sample was obtained from the header file from flight line segment 23b (but modified to store a single spectrum).

The “<*** centre part remains the same ***>” entry (near the centre of each file) signifies the existence of a block of information which is common between all Tafkaa header files.

Other parameters crucial to Tafkaa include; ozone concentration, humidity and water vapour, aerosol model. These are specified in the Tafkaa .input file rather than the header file, one for each data file. Table 31 shows an example of the Tafkaa parameters defined in such an input file.

tafkaa_input_image_name	= f:\tafkaa_data\phLO01a_Rad_sb_R.bip
tafkaa_data_directory	= f:\tafkaa\LSF\
tafkaa_atmo_model	= mid latitude summer
tafkaa_atmo_clmwvap	= 0.9
tafkaa_atmo_gasses	= {H2O, O3, N2O, O2}
tafkaa_atmo_ozone	= 0.3
tafkaa_use_prev_atmo_trans	= 0
tafkaa_aerosol_method	= -1
tafkaa_aerosol_model	= coastal
tafkaa_aerosol_rh	= 50%
tafkaa_aerosol_tau550	= 0.05
tafkaa_atmo_no2_scale	= 1.0
tafkaa_exclude_aerosol_models	= { urban }
tafkaa_aerosol_weights	= {0.,0.,0.,0.,0.,0.,0.,0.,0.,1.,1.,1.,1.,1.}
tafkaa_wind_speed	= 2
tafkaa_interp_sensor_altitude	= true
tafkaa_geometry	= 0
tafkaa_use_which_masks	= {none}
tafkaa_output_scale_factor	= 10000
tafkaa_output_type	= refl
tafkaa_output_root_name	= f:\tafkaa\fl01\out0\phLO01a_Rad_sb_R

Table 31: Example for the contents of a Tafkaa input file.

It was previously mentioned that the IMO_Ref reflectance image was supplied to the PhD candidate (Section 3.3). Fortunately, this included both the airborne radiance data and the Tafkaa input files. The input data files contain the Tafkaa parameters and there is one such file for each flight line segment. The PhD candidate was able to produce an identically stitched image to the IMO_Ref image by using the same input files. The PhD candidate’s image is termed PHPA_Ref in this thesis. After gaining confidence in understanding the mechanics behind producing such an image, the parameters were investigated more closely to examine if any of them could be improved, to better cater for the atmospheric conditions

experienced at Port Hedland on the day of the airborne survey. For example, the relative humidity on the day of acquisition varied between 38% to 51% (using the meteorological data acquired from <http://www.bom.gov.au>). The Tafkaa input file shows 50% by means of the “tafkaa_aerosol_rh” parameter (which is the minimum setting that can be specified). Other type of parameters were also investigated, for example, the sun-sensor geometry. The angles for the Tafkaa-determined solar zenith and solar azimuth angles were examined manually against a NOAA Solar Calculator (2016). The differences between Tafkaa and the NOAA Solar Calculator (2016) are well below 1%. These angles (along with other parameters) are displayed in Table 134 (p. 710 of Appendix Q.2) for each flight line segment.

In fact, all input parameters specified in all flight line segment files for both the Tafkaa input files and header files, all appeared reasonable with respect to the documentation outlined in the Tafkaa User's Guide (Montes et al., 2004). Therefore, the reflectance PHPA_Ref image appears sound with respect to the supplied parameters. However, it is known that there are spectral brightness inconsistencies in the image (Section 4.5.3). Because of this, another approach was adopted to produce a more spectrally consistent image. The method is termed normalisation. Two approaches were taken; the radiance set of images did not use Tafkaa in any way, while the normalised reflectance-based images did. This work forms the basis of the next section and is the main theme of the thesis.

The Tafkaa User's Guide (Montes et al., 2004) states that negative reflectances in the spectral blue-end region is possibly caused by calibration issues with the airborne sensor, which describes the situation reminiscent of the work found under Section 4.5.3.3. However, even this does not explain the negative spectra brightness trend, being particularly bad in the northern regions compared to the south-based regions of the PHPA_Ref image (Section 4.5.3.3).

After a detailed investigation into the Tafkaa parameter settings, no unreasonable values were found. This study is therefore unable to explain the spectral brightness peculiarities discussed in Section 4.5.3. For these reasons, a different approach is taken with the aim of producing a spectrally consistent image – a normalised image. The mechanics behind producing these normalised images are discussed in the next section (Section 4.5.9), and lead to two main categories of

image-types; radiance-based and reflectance-based. The normalisation process which produced radiance-based images do not use a radiometric correction model at all, unlike the reflectance-based images.

4.5.9 Image Normalisation

This section outlines the motivation behind improving the consistency of spectra in the PHPA_Ref image.

Several issues were apparent by the preceding work:

- Spectral changes in brightness were clearly evident both within and between adjacent flight lines (Section 4.5.3.2). Large regions of the PHPA image, particularly in the northern extent, contain negative reflectances in the blue-end of the spectrum (Section 4.5.3.3).
- Class inconsistencies across flight line boundaries in thematic map (Section 4.5.7).

The minor spectral changes as a result of Tafkaa parameter adjustment (Section 4.5.8) were unable to cater for the spectral inconsistencies in the PHPA_Ref image (Section 4.5.3). As a result, a different approach is adopted to improve the overall image spectral consistency.

This section begins by examining the PHPA_Ref pixel spectra over the whole image, and reveals spectral inconsistencies on a much larger scale to that discovered thus far (Section 4.5.9.1).

Spectral consistency is improved using a correction method termed normalisation; the steps are explained in Section 4.5.9.2. It allows for the construction of improved spectral image data termed **normalised**, as normalising may be defined as “to *bring or return to a normal or standard condition or state*” (Lexico, 2019). Here, the term correction implies the generation of a spectrally more consistent image over the scene. Correction does not imply the ability to determine

the 'true' ground truth spectrum for each pixel - the method only aims to improve image spectral consistency.

The reason why Section 4.5.9.2 specifically provides details about the construction of one normalised image (i.e. N_Rad_VI) is because the classification of this particular image results in best thematic map (classification falls under Section 4.5.11).

A simple RGB image comparison in Section 4.5.9.3 shows the result of improved spectral brightness for the N_Rad_VI image in relation to PHPA_Ref, due to normalisation. Section 4.5.9.4 explains the difficulties in comparing both images from a spectral viewpoint.

The normalised approach also led to the construction of several other images, whose reasons are outlined in Section 4.5.9.5.

Section 4.5.9.6 spectrally assesses image spectra with ASD field samples using SAs.

A summary and discussion in Section 4.5.10 concludes the image normalising section, before proceeding to classifying the N_Rad_VI image (Section 4.5.11).

4.5.9.1 Line-averaging Process and Spectral Effects

The limited flight line brightness study for Finucane Island (Section 4.5.3.2) is now extended to cover the whole Port Hedland region.

The process of line-averaging calculates a single mean reflectance, for each wavelength independently and extends over each horizontal row of pixels. Figure 102 helps to explain the concept.

Figure 102 shows four flight lines – 27 & 26 (the two northern-most flight lines) and 2 & 1 (the two southern-most flight lines). As detailed in Section 3.3, the flight numbers from north to south are sequentially: 27, 26, 24, 29, 25, 28, 23 and then proceed in descending sequential order, ending at flight line 1 at the southern-most extent of the scene.

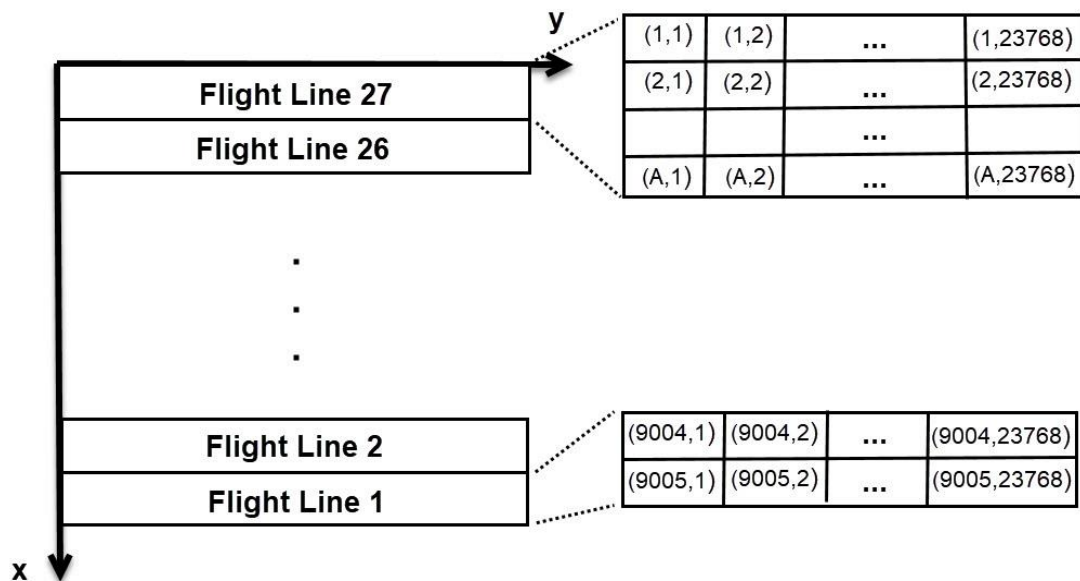


Figure 102: Pixel orientation in relation to flight line number.

The pixel coordinate system shown in Figure 102 defines (1,1) as the very first pixel, which is located in the northern-most and western-most corner of the image. The next pixel along the first row (row 1) is labelled (1, 2) and ends at (1, 23768). All of these pixels belong to flight line 27. The left-most pixel for row 1 is labelled (1, 1), while the very last pixel is labelled (A, 23768), implying that the 'width' of the flight line is 'A' pixels wide. However, this is not exactly correct. The stitched image (Figure 42, p. 141 of Section 3.3) clearly shows that the flight line boundaries (between adjacent flight lines) appear roughly sinusoidal in nature. Therefore, the 'width' of flights lines vary. The ramification of this is that it is not possible to directly relate a line-average value (e.g. 23,000) in an image with an associated flight line in a flight line segment, as it may belong to the existing flight line or the adjacent one (this will become clearer below). Line-averages near flight line boundaries may actually be located 'above' or 'below' (e.g. flight line 27 or 26) a flight line.

The very last row is 9005 and therefore the left-most pixel in flight line 1 is labelled (9005, 1). ENVI shows the dimensions of the stitched image by specifying 9005 lines and 23768 samples in the associated image header file. The line-

averaging terminology stems from averaging all 23768 pixels in each of the 9005 lines.

The line-averaging process ignores masked pixels (i.e. black pixels in an image, as these contain no spectral data). Therefore, if the first 1000 column-pixels in line 1 were masked pixels, then line-averaging ignores those pixels and the mean spectrum (for each band) is calculated based on $23768 - 1000 = 22768$ unmasked pixels. As there are 246 bands, line-averaging results in 246 mean values corresponding to each line of pixels.

Clearly, a line-averaged plot for all spectra (consisting of all 246 wavelengths) would overwhelm the analyst. Instead, for practical analytical purposes, four wavelengths are selected to cover a broad range of the spectrum and in each colour region (e.g. 448 nm lies in the blue spectral region). The four wavelengths selected are in the (B,G,R,IR):

- Blue (448.0 nm)
- Green (549.4 nm)
- Red (649.7 nm)
- IR (718.8 nm)

Note: All line-averaged plots (e.g. Figure 103 to Figure 111) from this point on display four colours (Blue, Green, Red and Black), representing these four wavelengths.

The IR band is graphically displayed using a black colour and is included due to its significance to vegetative analysis (detection and analysis). The other wavelengths are represented using their 'proper' colours (e.g. blue wavelength as blue in the plot). Figure 103 shows four curves, one for each of these four wavelengths. Each curve shows the average reflectance (scaled by 10,000) over the whole image – all 9005 lines.

Graphically, line 1 corresponds to the northern-most line of the PHPA image (i.e. Figure 42, p. 141 of Section 3.3), while line 9005 corresponds to the southern-most line of the image.

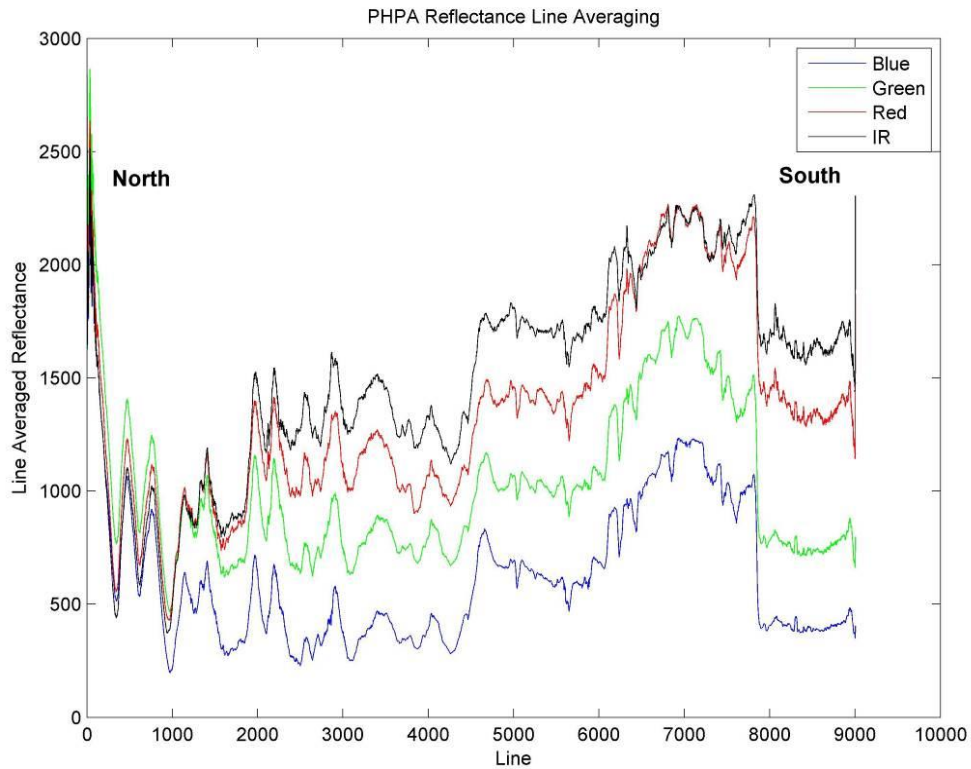


Figure 103: Line-averaged reflectance plot for the PHPA_Ref image (unmasked). The result is obtained by averaging the spectrum for each line of pixels. The averages for only 4 bands are shown. (Note: the reflectance is scaled by 10,000).

The general characteristics for regions defined in the PHPA image (Figure 42, p. 141 of Section 3.3) may be approximately described in terms of pixel line location. Regions consisting of mostly open water are generally located around lines 1 to 1000, corresponding to open sea (with little land). The northern lines from 1 to 3000 are dominated by ocean but also contain land. Sun glint is the main culprit behind the large reflectance mean values, which ‘overload’ the mean reflectance, thereby causing a bias away from low reflectance land cover types. Lines 1500 to 7000 are generally mangrove forests and soil, while salt ponds exist between lines 4500 and 7800. Both water and salt ponds contribute greatly to the line-averaging result (as demonstrated in Appendix L.3, where water and salt-pond pixels (but not land pixels) are removed from PHPA_Ref prior to line-averaging).

The shortfall of the preceding plot concerns the transitions between individual flight lines, which are not particularly evident as the plot reflects the stitched image consisting of all 29 flight lines. To examine brightness patterns both within and between individual flight lines more clearly, it is necessary to line-average each flight line image individually.

As detailed earlier, there are 29 flight lines which are further composed of 137 flight line segments. For example, flight line 1 is composed of flight line segments 1a, 1b and 1c while flight line 2 is composed of flight line segments 2a and 2b.

Figure 104 shows this diagrammatically.

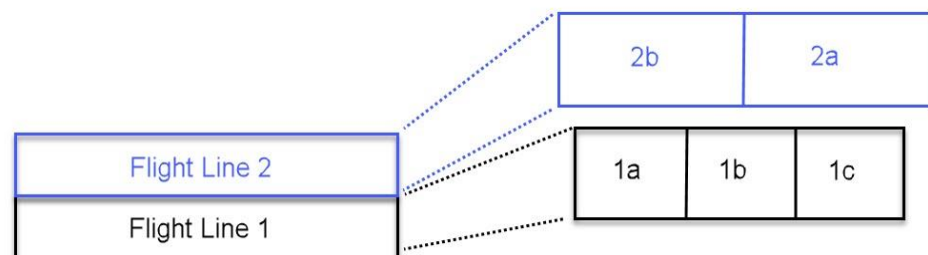


Figure 104: The complete flight lines 1 and 2 are composed of flight line segments.

The number of flight line segments to form a complete flight line was given in Table 11 (p. 142, Section 3.3) and varies from 2 (to form a complete flight line 2) to 6. Stitching flight line segments together forms a “complete” flight line. For example, stitching together the three flight line segments (1a, 1b, 1c) results in the complete flight line 1.

As mentioned previously, the stitched image removes overlap between flight line segments; each flight line thereby varies in ‘width’ (i.e. number of lines of pixels). However, prior to stitching, each individual flight line segment is exactly 965 pixels ‘wide’. It is insignificant in this context that the ‘length’ of a flight line segment varies - from approximately 2500 to 3100, with 3000 being particularly common. This description fails to consider other complications when calculating a line-average, but the key points remain true and may be omitted here (further technical details are found in Appendix K.4).

Whereas the flight line ‘width’ was unknown in Figure 102, it is now exactly 965 in Figure 105 - Figure 105 uses the same pixel coordinate system as Figure 102.

Note that Figure 102 describes the system for a stitched image, while Figure 105 specifically describes the system with respect to individual flight lines, rather than the stitched image. Although the flight line 'length' was previously known (23768 pixels), it is now unknown (although usually 3000 per flight line segment). The value of 'B' in Figure 105 is the sum of the all the individual lengths of all individual flight line 27 segments. This varies for different flight lines. So, flight line 1 has a total length of 'C' pixels. As detailed in Figure 104, flight line 1 is composed of flight line segments 1a, 1b and 1c. The sum of their lengths is equal to the total length of flight line 1 (i.e. the value for 'C').

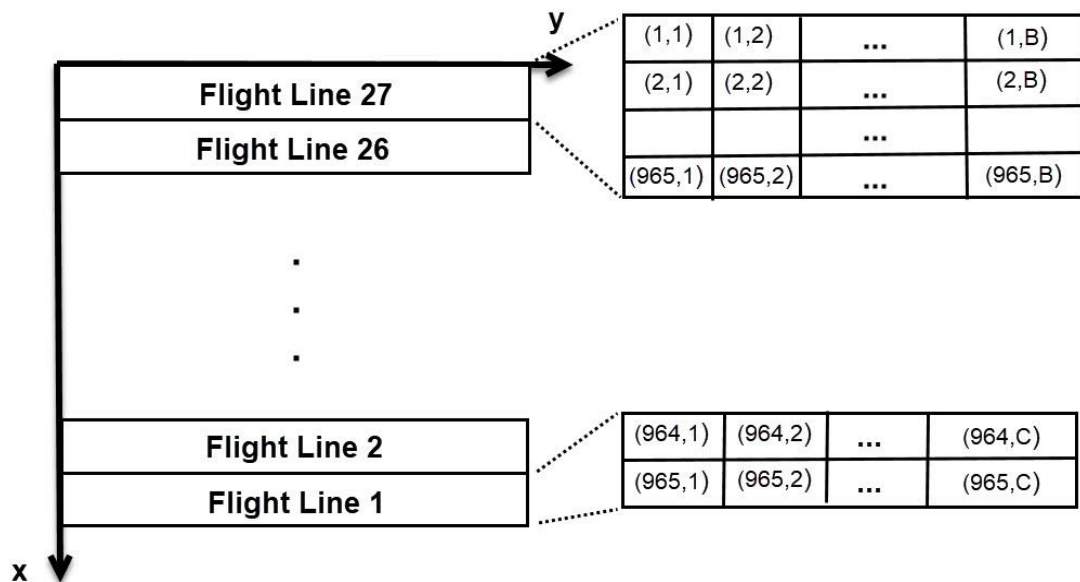
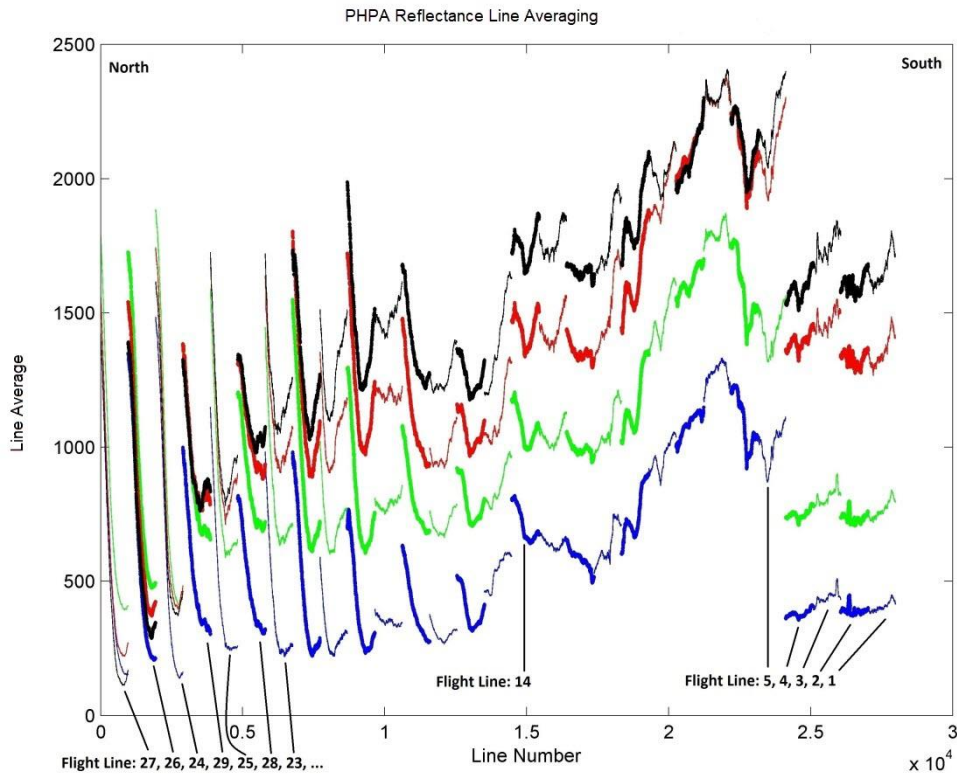


Figure 105: Flight line and pixel orientation in relation to flight line number.
Each flight line contains exactly 965 pixels (termed the 'width' of the flight line).

In terms of forming a complete image, there are $29 \times 965 = 27985$ lines, although the final stitched image only contains 9005 lines. After georectification, a lot of flight line overlap leads to a relatively small stitched image. In computing terms, a total of 166 GB of flight line segment files reduce to 98 GB in the final stitched image. These points were touched on in Section 3.3, in particular Figure 43 (page 143), where the 'width' of each label (e.g. 4C and 5B) were related back to the individual flight line segments.

Figure 106 shows the line-averages corresponding to the individual flight line reflectance data instead of the stitched image (i.e. PHPA_Ref image). The plot colours use the same wavelength definitions as for Figure 103.



**Figure 106: Line-averaging plot, showing the mean result over each flight line for the PHPA reflectance image.
Note: the reflectance is scaled by 10,000.**

Note that technically, line-averages are obtained flight line by flight line (by joining up the necessary flight line segments). As a result, the stitched PHPA_Ref image cannot be used to directly compare individual line numbers in this plot.

Compared to Figure 103, individual flight lines are emphasised by the use of 'heavy' and 'light' ('wavy') lines in the plot (Figure 106).

The flight line order from north (left hand side of plot) to south (right hand side of plot) is: 27, 26, 24, 29, 25, 28, 23. The flight lines then proceed in descending sequential order, ending at flight line 1 at the southern extent of the scene (right hand side of plot).

Flight line 27 contains mainly water. The NIR reflectance (black curve) is low, as expected due to high NIR absorption of the water layer. Red wavelengths are also highly absorbed by water. Wavelengths between 450 and 550 nm are less absorbed

by water. Therefore, the reflectances for NIR should be low, followed by red with blue and green absorbed less. This general pattern is exhibited in Figure 106. The NIR for vegetation is high over land, as expected.

Referring back to Figure 103 and Figure 106, both plots clearly show brightness changes within individual flight lines) in addition to sudden brightness jumps between adjacent flight lines. The flight lines should form a continuous set, with no breaks between them. The difference in brightness between the northern and southern end of an individual flight line is unexpected. The brightness variability is systemic and related to the position within a flight line rather than correlated with cover types in the scene.

The brightness bias inherent in the image should have been eliminated by atmospheric correction. Therefore, it is of interest to analyse the line-averaging result in the original airborne radiance data to examine the brightness behaviour across the 137 flight line segments. The result is displayed in Figure 107, with the image named PHPA_Rad (to signify that it is based on the original radiance airborne data).

Comparing the radiance plot (Figure 107) with the reflectance plot (Figure 106) reveals a number of notable similarities (note the difference in scale and units between the two figures). These include:

- The general shape of each flight line (for each band).
- The northern flight lines being affected by sunglint.
- The sharp transition between flight lines 4 and 5 (where the salt ponds are located).

The salt ponds (see Figure 42, p. 141 or Section 3.3) are located at flight lines 5 to 15, inclusive).

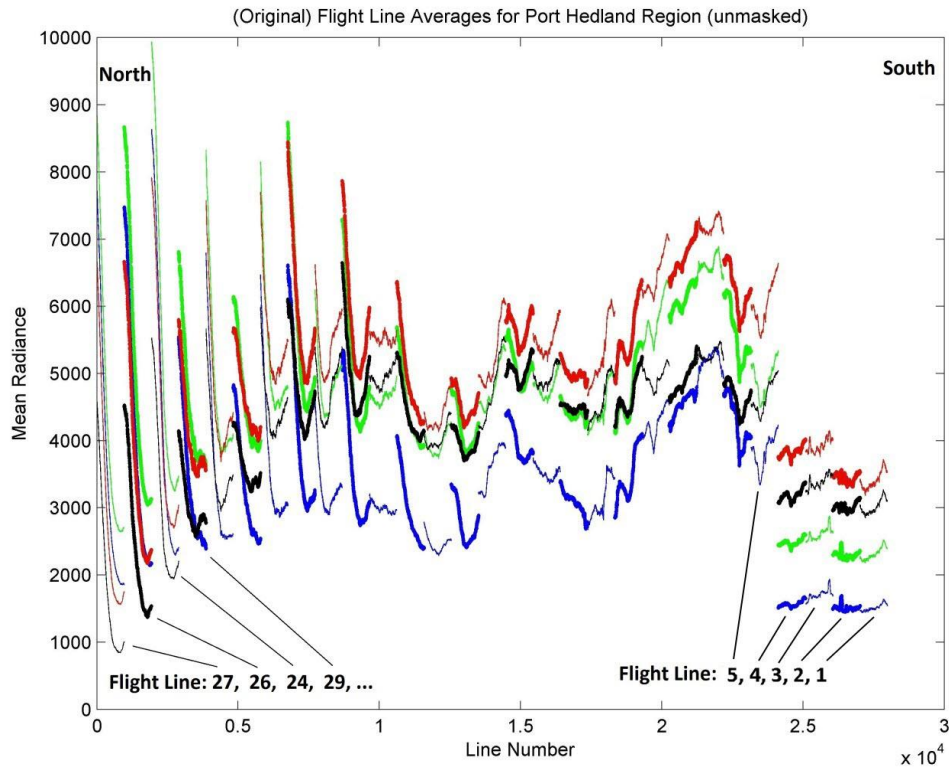


**Figure 107: Line-averaging plot, showing the mean result over each flight line of the radiance image (i.e. PHPA_Rad).
Note: the radiance is scaled by 90 in units of $W \cdot m^{-2} \mu m^{-1} sr^{-1}$.**

As concerns previously for the reflectance plot, the radiance plot is also affected by the bright water (i.e. sunglint) and salt pond regions. Therefore, it is of interest to examine the radiance line-averaging plot in the absence of these regions. Furthermore, as our interest lies in classifying vegetation, the vegetative-mask of Section 4.5.6 (with a threshold over 10,000) needs to be applied to the PHPA_Rad image, leaving 'strong' vegetative pixels. However, in practice there is a major complication. The line-averaging process is by flight line (Figure 107) rather than one whole stitched image. The vegetative-mask of Section 4.5.6 masks one complete image; it does not cater for individual flight lines. Therefore, each of the 137 flight line segments must be vegetatively masked. The techniques of Section 4.5.6 remain valid. The end result is having 137 vegetatively-masked flight line segments, all not georectified (further details are given in Appendix L.4).

The vegetatively-masked image is referred to as PHPA_Rad_VI, indicating that the image was formed by applying the vegetative-mask to the PHPA_Rad image. In

strict terms, an image has not been constructed at this stage; instead each flight line segment has been masked, leaving the line-averaged result as shown in Figure 108.

By line-averaging just vegetation, a number of main characteristics are apparent. Firstly, there are still brightness changes within flight lines, at times quite abrupt (e.g. around line number 1500). The southern-end of many individual flight lines are also generally brighter than the northern-end (e.g. flight lines 3 to 9, 15 to 24). Also, there are still gaps between flight line boundaries, although generally the gaps between southern flight line edges are not as pronounced as those for the north.

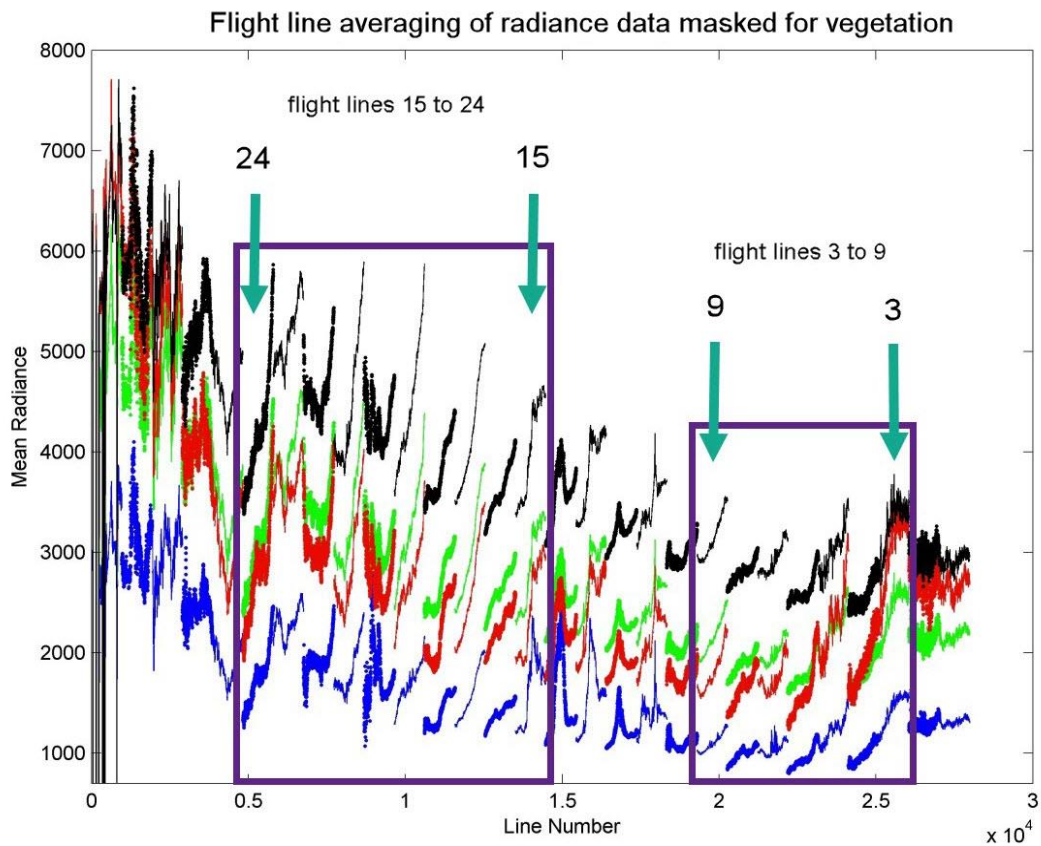


Figure 108: Mean flight line radiances obtained from the masked-vegetative (individual) radiance flight lines (with gradient over 10,000).

This means line-averages were obtained on pixels containing 'strong' vegetation, only. The flight lines contained in the purple boxes show individual flight lines that are brighter in the south compared to the north.

Note: A suitable scale emphasises the characteristics of each flight line-average. The radiance is scaled by 90 in units of $W \cdot m^{-2} \mu m^{-1} sr^{-1}$.

The gap between flight line 4 and 5 is significantly reduced by removing the salt ponds regions (located at flight lines 5 to 15, inclusive).¹⁹ The last point concerns the general trend over each of the (four) bands; an overall decreasing trend in brightness from north to south.

These observations are cause for concern, as the ‘strong’ vegetation (with many regions being composed of primarily mangrove forests²⁰) is expected to be fairly uniform in brightness within a flight line as well as over the whole scene. In addition, the brightness changes between adjacent flight lines are also non-physical. A correction process is detailed in Section 4.5.9.2 which addresses these concerns.

Although the atmospheric correction by Tafkaa did not produce a consistent reflectance image (i.e. Figure 106) in terms of brightness, it did alleviate the global brightness trend found in the radiance data. Figure 109 shows the line-averaging result for reflectance files, using the same vegetative mask as for Figure 108. This image is referred to as PHPA_Ref_VI.

It should be noted that the reflectance plot (Figure 109) contains fewer flight lines than the radiance plot (i.e. with Figure 108). This is due to the vegetative-mask not finding any pixels in the reflectance image for flight lines 27 & 26 (i.e. the two northern-most ones). The left-most flight line is therefore 24 followed by 29 and so on. This is not the case for the radiance image; further details are provided in Appendix L.5.

While Tafkaa reduced the general brightness trend, as evident in the reflectance plot (Figure 109 compared to Figure 108), many characteristics remain similar to the radiance plot; the brightness being more pronounced in the southern region within a flight line in addition to the ‘gaps’ between adjacent flight lines. Negative reflectance values are also evident in the blue band, particularly at flight lines 20, 21, 22 (situated the southern side of Finucane Island). The infrared band sits above the red band (i.e. is brighter), just as for the radiance data (Figure 108), which makes sense as vegetation reflects NIR more strongly than R. The reversal of these two bands in the absence of the water and salt pond regions but with the presence

¹⁹ *The gap is also not as pronounced when soil is left in the scene (See Appendix L.6). Therefore, the gap is caused by the salt ponds only.*

²⁰ *Evidence: field work showed the existence of mangrove forests.*

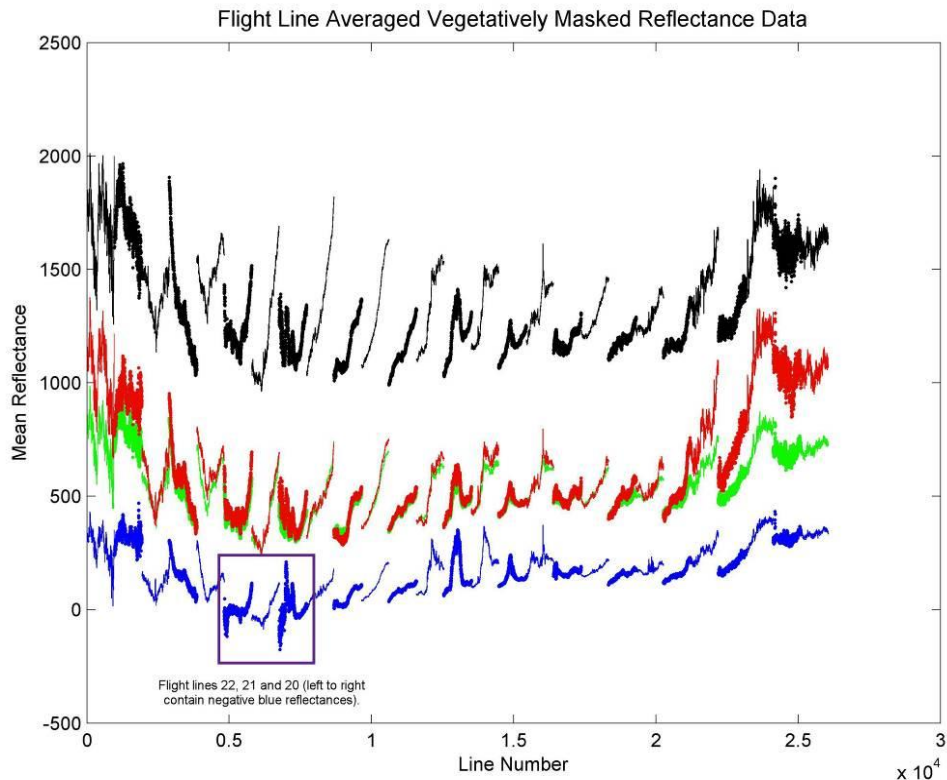


Figure 109: Line-averaged reflectances after applying the vegetative mask to individual reflectance flight lines (the reflectance is scaled by 10,000). The purple box highlights that blue wavelengths for flight lines 20, 21 and 22 are affected by negative reflectances.

of soil in the image, is due to the red soil dominant over the whole scene (as seen in Figure 273 of Appendix L.6, p. 606).

Comparing the PHPA_Ref (Figure 106) with PHPA_Ref_VI (Figure 109) reveals similar observations as for the radiance data. Again, the southern-end of individual flight lines tend to be brighter than the northern-end. Gaps are also still apparent between flight lines. However, the extreme bright line-averages in the northern end of the image (i.e. line numbers 0 to 10,000) are drastically reduced. In addition, salt-pond regions (flight lines 5 to 15) has dramatically reduced the brightness so that the flight line edges match up much more closely (e.g. flight line 4 and flight line 5).

The next section introduces a method to eliminate three brightness inconsistencies. The steps are: removing brightness differences within flight lines, detrending the overall brightness across the scene (north to south) and joining up flight line edges. The process is termed normalisation. However, care must be taken to preserve the spectral and spatial characteristics already present.

4.5.9.2 Normalisation Process

Normalisation is concerned with improving the spectral consistency of an image.

Three separate processes are required:

1. Rotation of individual flight lines (to eliminate brightness trends within a flight line).
2. Removing the general brightness trend over the whole image.
3. Removing jumps in brightness between adjacent flight lines.

Note that the steps are repeated for each band independently; therefore, the whole spectrum is adjusted wavelength by wavelength. Also the normalisation steps in this section are somewhat generalised. There are more factors involved; explicit technical steps, including computational details, are elaborated upon in Appendix K but not required here for conceptual understanding.

This section describes the normalisation process for the N_Rad_VI image (i.e. Figure 108). In strict terms, the N_Rad_VI image has not been formed at this point. Rather, it is the vegetatively-masked flight line segments that are normalised prior to stitching to form one image.

Instead of using Tafkaa to eliminate brightness changes in the scene (which produced an unsatisfactory result), the normalisation process will replace the radiometric model by using an empirical approach instead. The process applies to all uncorrected georectified radiance flight line segments.

The first step corrects local (i.e. individual) flight lines (i.e. rotation). To smooth out each end of a particular flight line, a single mean is taken over the first five points (lines 1 to 5 in the flight line). The same applies to the other end, taking another single mean of the last five points (lines 961 to 965). A straight line is constructed between these two points, and rotated about the centre (line 483). The final result is shown graphically in Figure 110. By rotating each flight line about the centre, the brightness difference between both ends is evened out. The term 'each end' refers to the northern and southern sides of each flight line.

Note that, technically, the unit is no longer radiance in Figure 110. For the fully normalised process (where all three steps are performed), the unit is termed normalised radiance. During the first two steps, the unit for the intermediate process falls between radiance and normalised radiance.

The effect of rotating each flight line (about the centre) is evident by comparing Figure 110 with Figure 108. For example, the highly varying change in brightness for flight line 3 (in Figure 108) is now 'flattened out' – the north-south trend within the flight line is drastically reduced. Within the flight line, a certain degree of

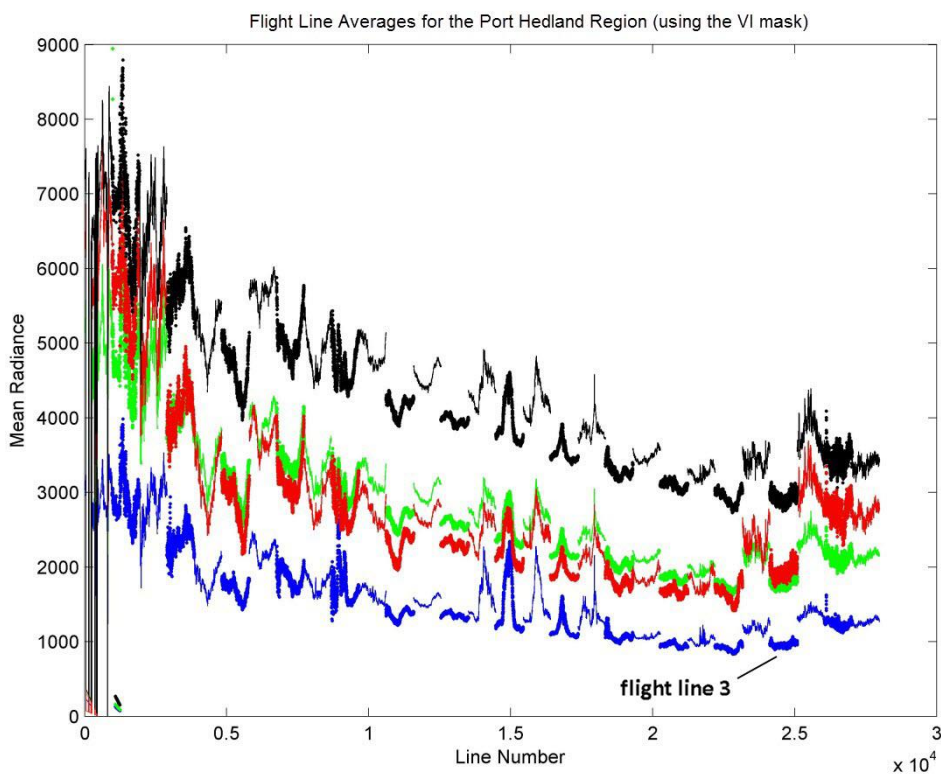


Figure 110: Plot showing the result of rotating each individual flight line of Figure 108. Note: Each radiance is scaled by 90.

'stretching' will occur for each band, depending on the extent of the north-south brightness trend. For instance, by rotating flight line 3 about the centre (in a clockwise direction) the brightness decreases in the southern-end of the flight line, while increasing in the northern-end. Significantly, the underlying fine structure of the flight line is preserved by the rotation. Although the change is made to the line-averaged radiance (for each band), each individual each spectrum will be changed

when reconstructing the full normalised image. Therefore, the normalisation process is incapable of spectrally correcting each pixel spectrum to match the 'correct' spectrum in the scene but it will produce more consistent spectra on a larger scale. The term 'correct' is taken to mean the ASD recorded ground-truth under ideal conditions.

Further correcting (i.e. step 2) involves brightness detrending on a global scale followed by the joining up of each flight line segment (step 3). The global detrending process consists of calculating the mean of all line-averaged values (radiance in this case) for each of four flight lines in the south and north. For example, one mean spectral value for flight line 1 using all 965 lines. This process is repeated for flight lines 2 to 4 - thereby covering the southern 4 flight lines. In a similar manner, one mean spectral value is calculated using the 4 northern-most flight lines – i.e. flight lines 27, 26, 24 and 29. One global mean is then calculated from the 4 southern-most individual flight line values (i.e. from flight lines 1 to 4). This defines the first global mean value (at the southern end). Likewise, the second global mean is obtained using the mean of the 4 northern-most local (i.e. individual) flight lines. These two global means then define two points for the global line, which smooths the large local light line variations particularly in the north. A global linear line is then constructed using these two global means. To equalise the brightness trend, the line is rotated about the centre; termed detrending the global line. Local flight line centres are consequently shifted to lie on this global detrended line. Since the amount of shift is known (i.e. using the centre of each local flight line), the rest of the local flight line-averaged values are also moved to the new position. Practically, the process is repeated individually for each of the 246 bands to form the complete spectrum. Further explicit details are given in Appendix K.3, which may be referred to in order to enhance the understanding of key steps.

To remove any gaps between adjacent flight lines (step 3 of the normalisation process), individual flight lines are moved up or down (i.e. brighter or darker) with respect to the flight line to the right (i.e. right in the plot, corresponding to the south geographically). For example, the local flight line 2 is moved so that the southern-most edge is positioned at the same brightness as that for the northern-most edge of flight line 1. The process is then repeated by comparing flight line 3

with flight line 2, and so on, in an iterative manner, until all flight line edges are been lined up. Practically, a complete spectrum is formed by lining up each of the adjacent flight lines for each of the 246 bands (Further explicit details are given in Appendix K.3).

The final normalised result, with global detrending and the joining of adjacent flight lines is shown in Figure 111.

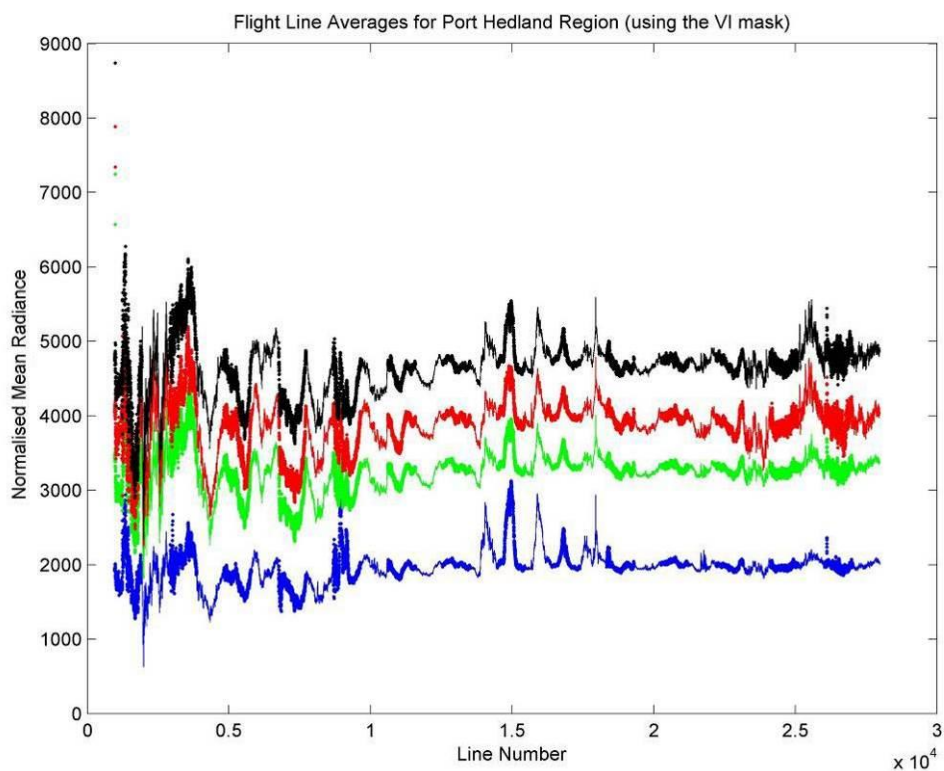


Figure 111: Using the result of Figure 110 (where each individual flight lines is rotated about the centre), this final plot shows the effect of joining adjacent flight line edges after global linear detrending. Note: Each radiance is scaled by 90.

Note in Figure 111 that, as the full normalisation process is complete, the brightness values (vertical axis) are now in terms of normalised mean radiance, as the mean radiance was normalised. Furthermore, instead of the unit being radiance, it is now normalised radiance.

The preceding two steps (global detrending and joining of adjacent flight lines) flatten the flight line for each band – i.e. they essentially lie in a straight line. Detrending on the global level is expected to result in an image where spectra are more consistent in brightness along the north-south direction. Figure 111 clearly

shows that all flight line edges join up, eliminating gaps between adjacent flight lines.

It is important to emphasise that the normalisation processes described (i.e. flight line rotation, global linear de-trending and flight line edge alignment) are all performed separately for each band.

To form the new image (termed the normalised image), each spectrum is constructed based on the difference in brightness between the line-averaged results of Figure 111 and Figure 108.

Figure 112 shows the final stitched image where each pixel spectrum is adjusted in the PHPA_Rad image through the normalisation process. In strictly terms, each of the 137 flight line segments corresponding to the PHPA radiance images (PHPA_Rad_VI) requires spectral adjustment forming 137 normalised radiance (N_Rad_VI) flight line segments (i.e. 137 vegetatively-masked flight line segments). The image of Figure 112 is the result of stitching all 137 N_Rad_VI flight line segments to form one complete image. The image is referred to as **N_Rad_VI** (N for normalised, Rad for radiance-based and VI to indicate the PHPA_Rad image was masked for vegetation prior to line-averaging).

Although normalisation only corrected vegetative spectra in the N_Rad_VI image, a complete image can be formed (i.e. containing non-vegetation as well). There are a few caveats to note. As the line-averages were calculated based on the N_Rad_VI image (i.e. the unstitched image), only vegetation have been normalised 'correctly' (in particular those with a gradient threshold of $> 10,000$). To form a complete image, every pixel spectrum for every cover type has been normalised instead. As a result, the normalised image (i.e. Figure 112) reveals spectral inconsistencies over the salt ponds regions when displaying the image using RGB bands (further details are given in Appendix M). For our purpose, these non-vegetative spectral inconsistencies are inconsequential; the aim of the thesis is only to classify vegetation. However, it is useful for the analyst to view the complete image for geographical purposes (for instance, compare Figure 112 against Figure 113).

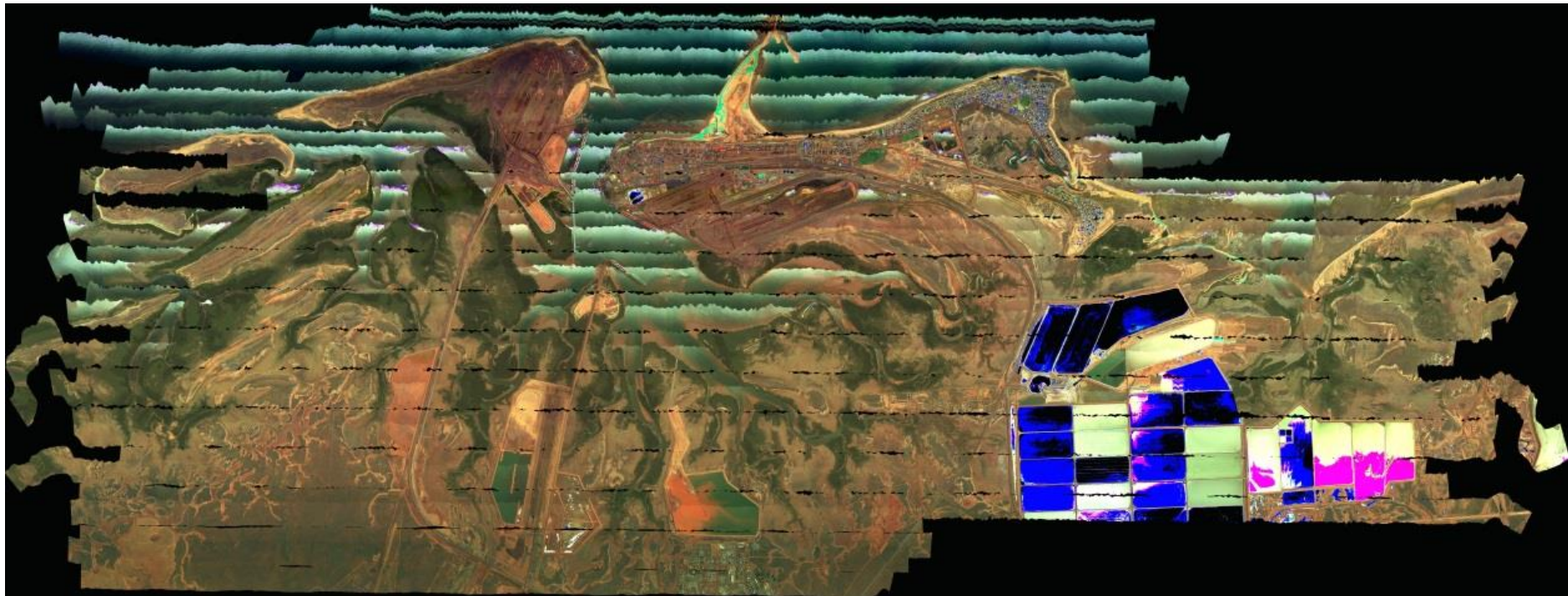


Figure 112: The N_Rad_VI image (true colour) obtained by normalising the vegetatively-masked PHPA_Rad image. The spectral artefacts (e.g. over the salt pond regions) they are false spectra due to spectral reconstruction based on vegetative line-averaging. Only vegetative spectra are normalised correctly in this image. The non-vegetative cover types allow for a full image reconstruction.

Each pixel spectrum has changed as a result of the normalisation process, which is more consistent in brightness overall. Because of the spectral changes, spectral ratios (e.g. NDVI, mean-gradient) are affected. These spectral changes are apparent due to changes in the relative spacing between the spectral curves in Figure 110 and Figure 111 compared to Figure 108. The improved spectral consistency lead to improved unsupervised classification (see later), as the similarity of clusters in feature space is expected to increase. However, due to the change in spectral shape, an individual pixel spectrum for a specific cover type is not expected to resemble any corresponding spectrum in the hyperspectral library, thereby making the SAM classifier (or indeed, any supervised classifier) unsuitable for classification.

The N_Rad_VI image indicates that a normalised radiance image was constructed from vegetatively-masked flight lines, thereby eliminating non-vegetation from Figure 112. N_Rad_VI is a complete image (i.e. it also includes non-vegetative pixels). The act of applying the same vegetative-mask again to N_Rad_VI adds another suffix “_VI”, leaving just vegetation. The image N_Rad_VI_VI is used for classification (see Figure 113).²¹

In summary, the key steps for generating a normalised (either reflectance or radiance) image are:

1. Line-averaging of each of the individual 29 flight lines.
2. Rotating each of the individual 29 flight lines.
3. De-trending the overall global linear ‘line’.
4. Joining up adjacent flight line edges.
5. Comparing the results from steps 2 to 4 with the original (i.e. unmodified) flight line segment files to modify each pixel spectrum and generate a new set of flight line segment files (now normalised).
6. Georectifying each of the 137 flight line segments.
7. Stitching the 137 flight line segments together to form a new (complete) image; the normalised hyperspectral reflectance/radiance image.

²¹ *In the strictest sense, the reconstructed N_Rad_VI_VI image could be constructed without the intermediate N_Rad_VI image, by masking out non-vegetative pixels in the PHPA_Rad image. However, it is useful to form a complete geographic-type image, allowing for timely visual identification of regions in the Port Hedland coastal region.*

Although this section outlined the key steps and processes in generating a normalised image, there are further technical considerations, which are given in Appendix K. These additional details are not required to understand the rest of the work that follows.

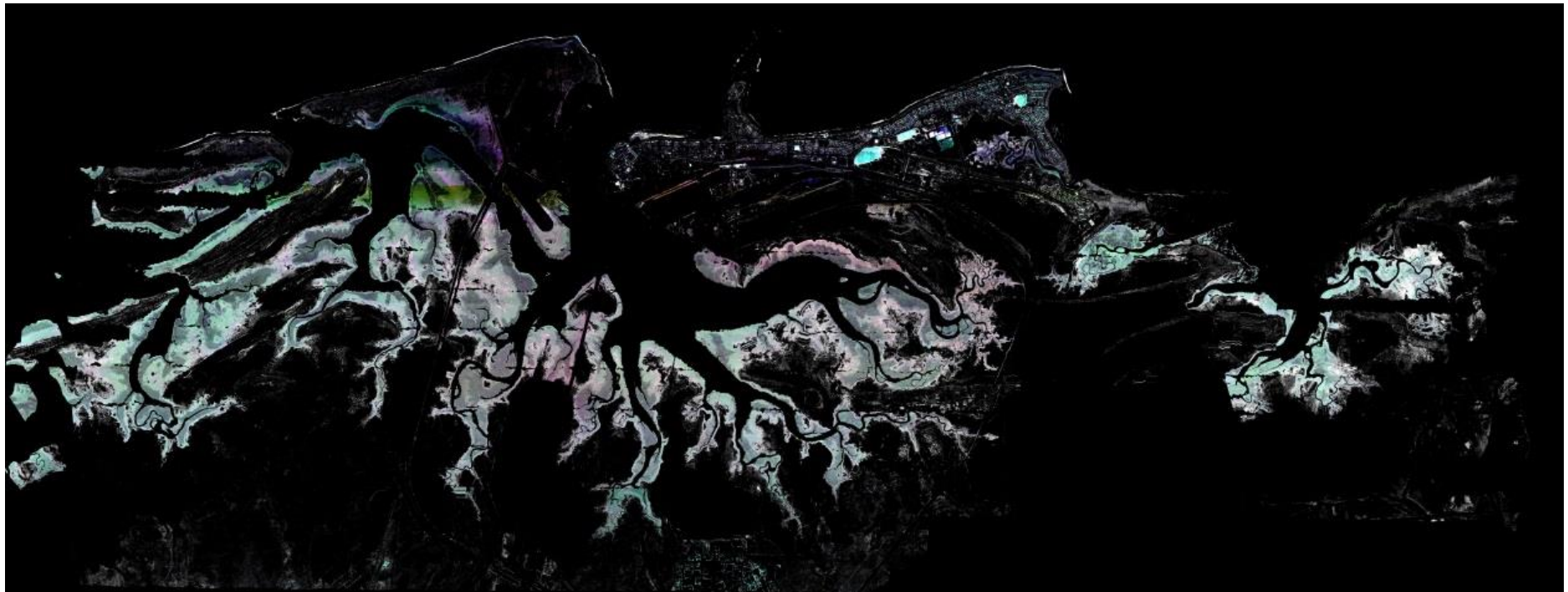


Figure 113: The N_Rad_VI_VI image as obtained by vegetative masking of the N_Rad_VI image (Figure 112).

4.5.9.3 Image Comparisons

The normalisation process aims to remove spectral brightness inconsistencies. This section restricts comparisons to RGB images. Evidently, the RGB N_Rad_VI image (Figure 112, p. 272) appears brighter overall compared to the RGB PHPA_Ref image (Figure 41, p. 140).

Although it is difficult to visually assert any improvement within a particular flight line, the large brightness changes between adjacent flight lines are smaller in the N_Rad_VI images, as shown below.

To highlight these differences, four regions are selected (see Figure 114). It needs to be emphasised that the N_Rad_VI corrects spectral brightnesses for vegetation. Therefore, only vegetative pixels are of interest in the comparisons in this section. Although the complete image shows both vegetative and non-vegetative pixels, the normalised correction process only corrects vegetation brightnesses. To form the complete image, non-vegetative spectra were also corrected based on the normalisation of vegetative spectra. The caveat is for some non-vegetative spectra to appear as spectral artefacts in true colour image (see Section 4.5.3.3).

The original PHPA_Ref (Figure 41, p. 140 of Section 3.3) appears very dull. The images from Figure 115 to Figure 118 are contrast enhanced and brighter to aid in comparisons with the PHPA_Rad images.

In Figure 115 to Figure 118, the PHPA_Ref images appear on the left while the N_Rad_VI images appear on the right. The N_Rad_VI images appear brighter overall compared to the PHPA_Ref image in these figures. Figure 115 was selected in particular for comparison, due to spectral issues encountered in that region (Section 4.5.3). The N_Rad_VI (i.e. right image) shows flight line boundaries that are certainly no worse than the PHPA_Ref (left image). Although the flight line boundaries are still apparent in circled regions B and D, they are very difficult to discern in circled regions A and C. In fact, by eye the boundaries at A and C appear to have been eliminated.

In regions further to the south (i.e. compared to Figure 115), spectra are more consistent. The flight line boundaries for the N_Rad_VI images are diminished in effect and at times, even unnoticeable at several locations in Figure 116. For

example, the brightness change across the flight line boundary in the white circled region is still discernible, but not in the yellow coloured circles (particularly for the lighter coloured vegetation). Similar observations pertain to Figure 117, where the flight line boundary is greatly reduced, particularly for the yellow circled regions. The brightness of vegetation across flight line boundaries in Figure 118 is particularly uniform. This region is located further to the south in the Port Hedland image, corresponding to flight lines at 9 to 12, where line-averaged brightness differences (between flight lines) are smaller compared to regions further north as can be seen from Figure 119. For example, the pink coloured arrow shows the difference in IR mean radiance between flight lines 18 and 19 – right on the boundary. Compared to flight lines further to the south (e.g. between 8 & 9), the gap between adjacent flight lines is much larger. The NIR spectral region is vital for vegetative spectra, as the red-edge is located there. Variability within a flight line is also more extreme in the north. This is evident by examining the ‘length’ of the IR mean curve within flight line 19. Recall that it is vegetation which is corrected, so comparing the flight line boundary between flight lines 11 and 12 for water is incorrect. Again, for light coloured vegetation, the flight line boundary is particularly difficult to discern in the N_Rad_VI image compared to the PHPA_Ref image (e.g. between flight lines 9 & 10).

Overall, the true colour images shows improved RGB spectral consistency in the normalised N_Rad_VI image over all flight line boundaries, despite PHPA_Ref having been atmospherically corrected using Tafkaa, which should have resulted in improved brightness consistency.

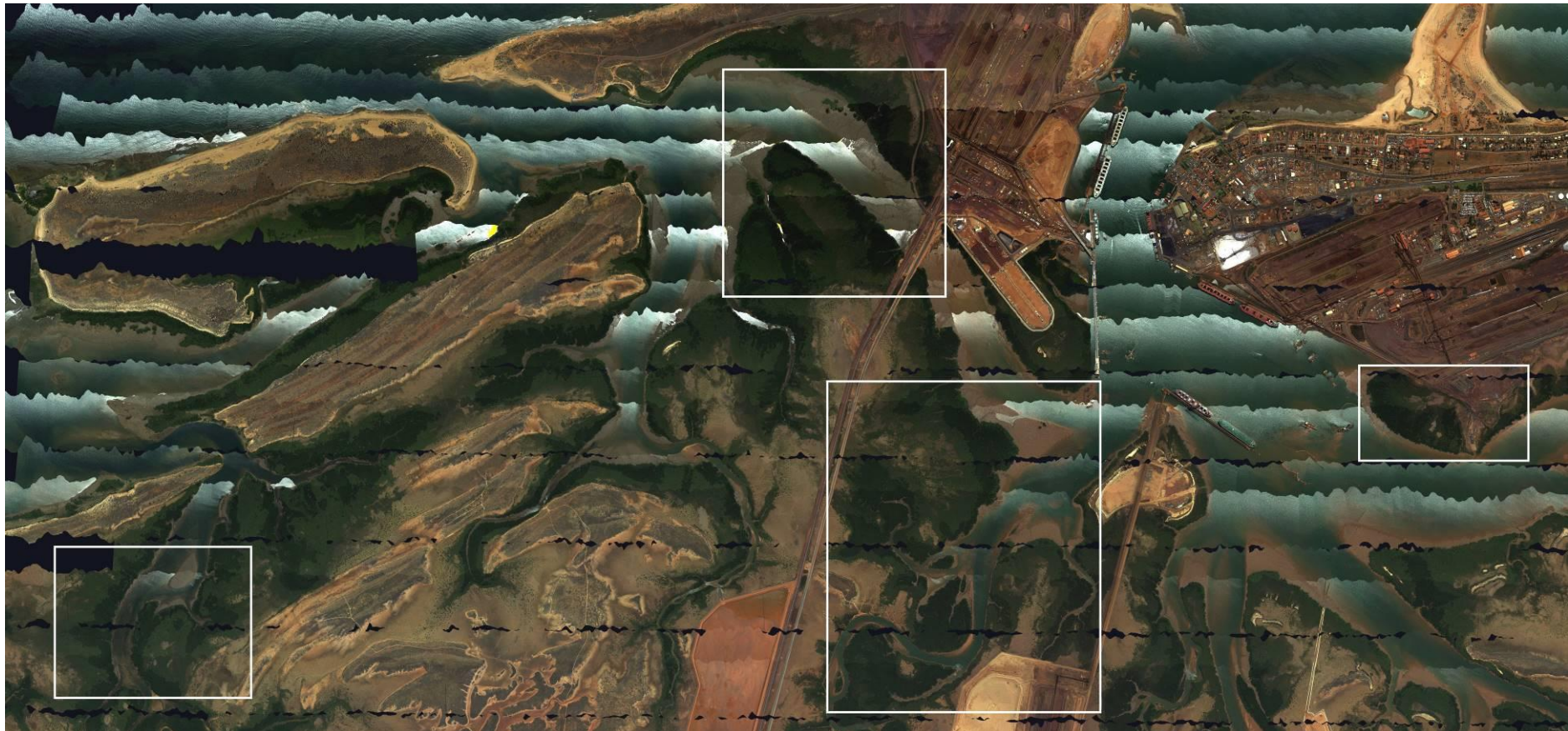


Figure 114: The white boxed regions indicate the magnified locations for Figure 115 to Figure 118.
These regions are used to illustrate the difference in brightness quality between the PHPA_Ref and N_Rad_VI images.

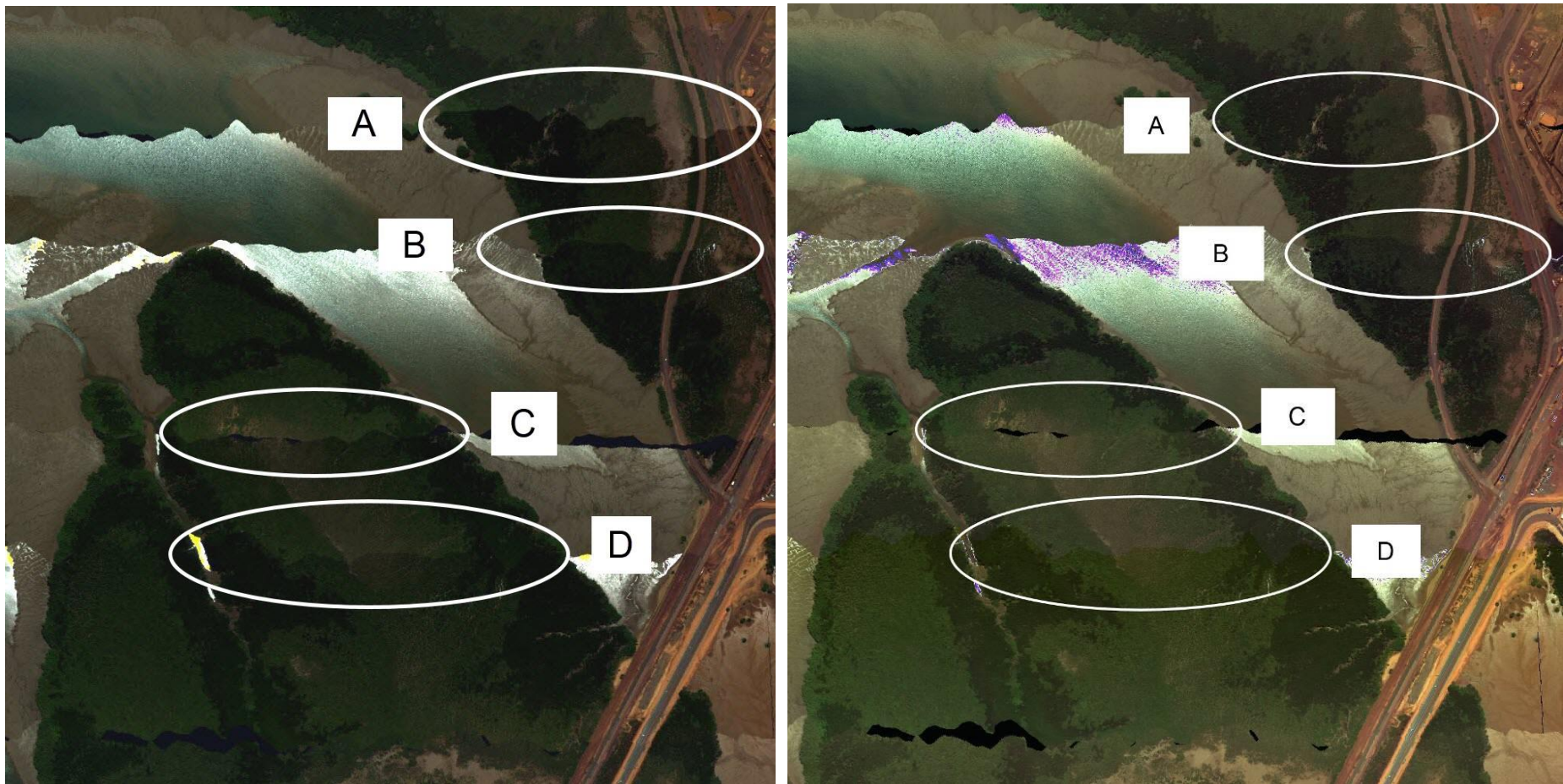


Figure 115: Magnified view of the northernmost region of Figure 114.

It shows shows improved brightness consistencies between adjacent flight line boundaries for the N_Rad_VI image (right image) compared to PHPA_Ref (left image). Region A marks the intersection between flight lines 28 and 23; B between 23 and 22; C between 22 and 21, and D between 21 and 20.

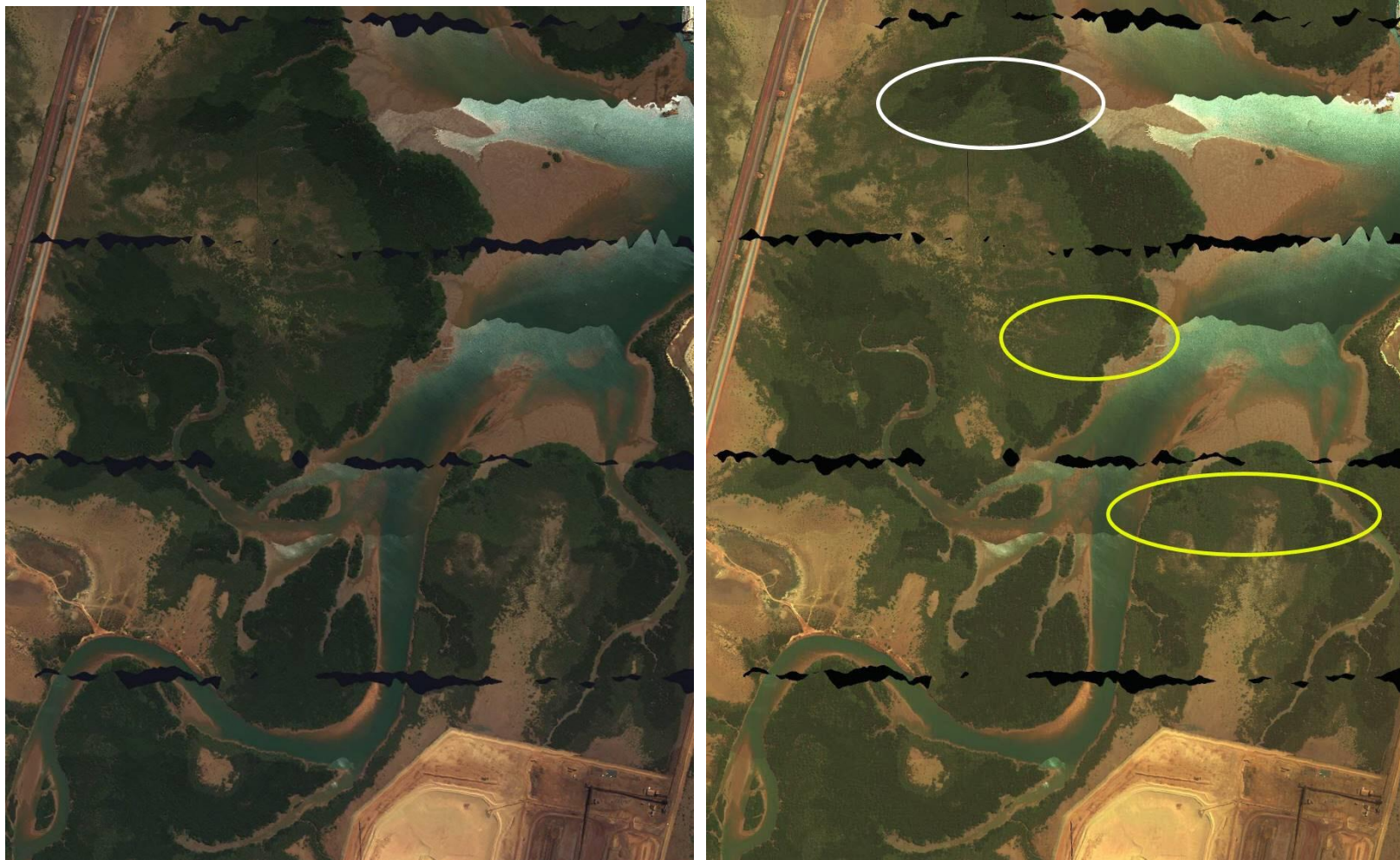


Figure 116: Magnified view of the centre region of Figure 114.
The flight line boundaries apparent in the PHPA_Ref (left) image are diminished in the N_Rad_VI (right) image.



Figure 117: Magnified view of the eastern region of Figure 114.
The flight line boundary in the centre of both images is dramatically reduced in the N_Rad_VI (right) image compared to the PHPA_Ref (left) image.

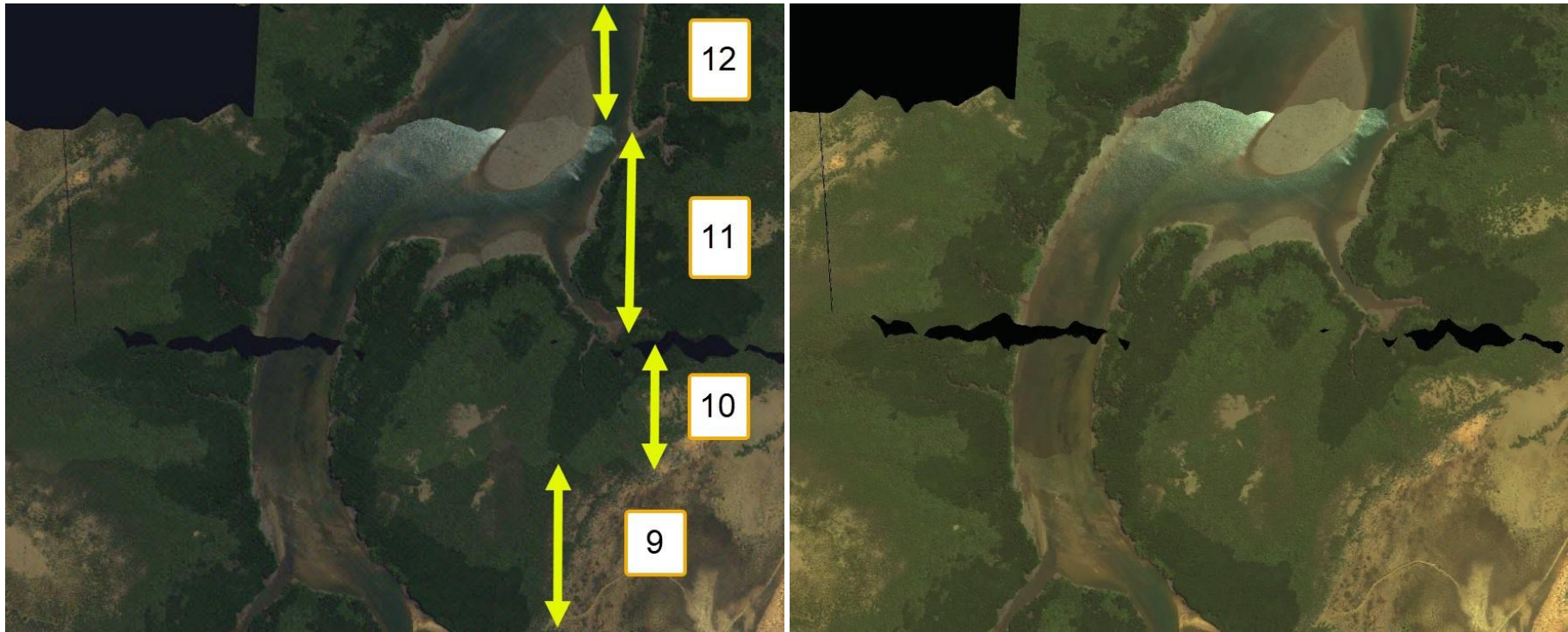


Figure 118: Magnified view of the western region of Figure 114.

The flight line edges are particularly hard to discern in the N_Rad_VI image (right), compared to the PHPA_Ref image (left). The numbers on the left image indicate the flight number, starting at 9 and ending at 12.

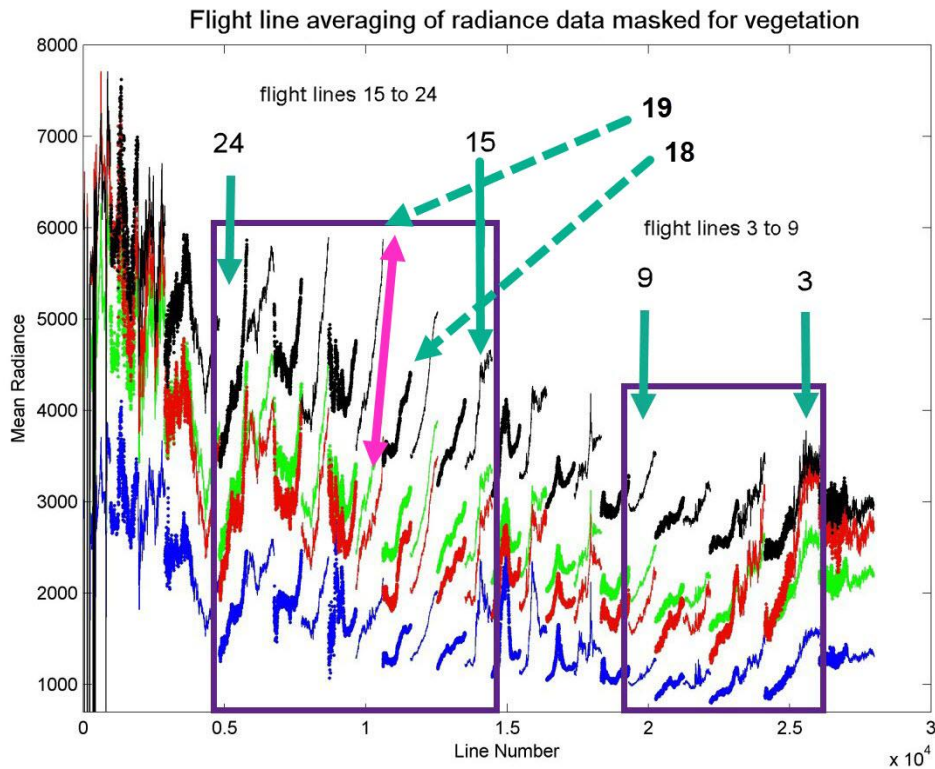


Figure 119: The pink coloured arrow shows the large difference in NIR between adjacent flight line edges 18 and 19. In general, adjacent flight line differences between southern flight lines (e.g. flight lines 3 to 9) are smaller in comparison to those further north (e.g. flight lines 15 to 24). This image is an edited form of the line-averaged N_Rad_VI image plot (Figure 108 (p. 264 of Section 4.5.9.1)).

4.5.9.4 Normalisation Mean Spectral Effect on Images

The normalised images appear not only brighter but also more consistent in RGB colours across flight line boundaries, as shown in the preceding section.

To extend the analysis, a wider range of wavelengths need to be examined. However, so as not to be overwhelmed, sample brightnesses are taken at the four key wavelengths as used in previous plots (Section 4.5.9.1). Although only consisting of four wavelengths, they span a wide range of the spectrum.

Using the coordinate system introduced in Section 4.5.9.1, a plot is produced whereby each point represents one of the four wavelengths from a pixel spectrum, starting at pixel (1, Y) and extending vertically downwards (i.e. in the direction from north to south in the image) to pixel (9005, Y). The “Y” coordinate defines the

transect (i.e. vertical row of pixels) plotted. Figure 120 illustrates the location for the values where Y is equal to 6500 and 7000 (represented by the yellow and blue coloured vertical lines, respectively).

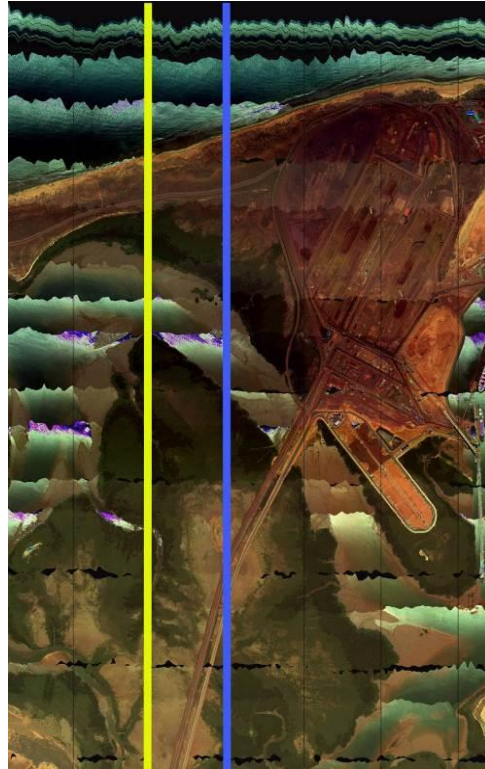


Figure 120: The yellow and blue transects represent a vertical line of pixels located at rows 6500 and 7000, respectively.

Note: The vertical lines in Figure 120 are not shown in their full extent.

Note that the vertical lines in Figure 120 are only intended to illustrate the position of transects 6500 and 7000 and actually extend over all 9005 pixels in the vertical direction (Figure 120 only shows a small section of the image).

A transect for row 6500 is shown in Figure 121 corresponding to the N_Rad_VI_VI image. Gaps in the data (e.g. from line number 7000 to 8000) represent the absence of vegetation. The colour definitions in the plot follows those of Section 4.5.9.1; the blue colour is the normalised mean radiance at a blue wavelength of 448.0 nm, green at 549.4 nm, red at 649.7 nm and black (representing infra-red) at 718.8 nm.

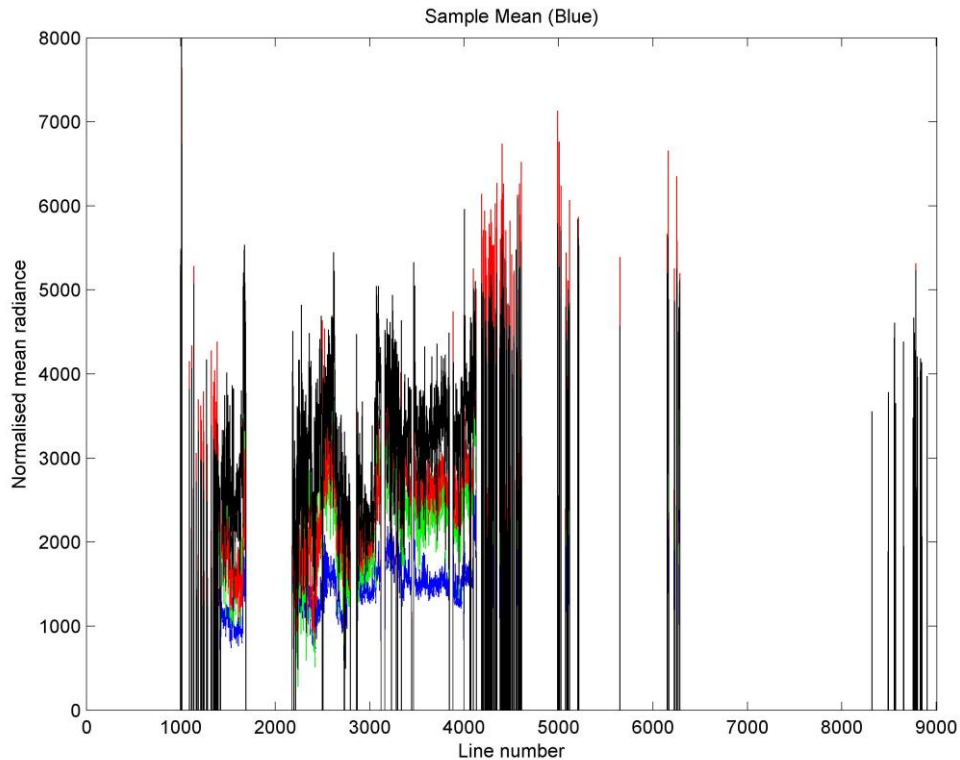
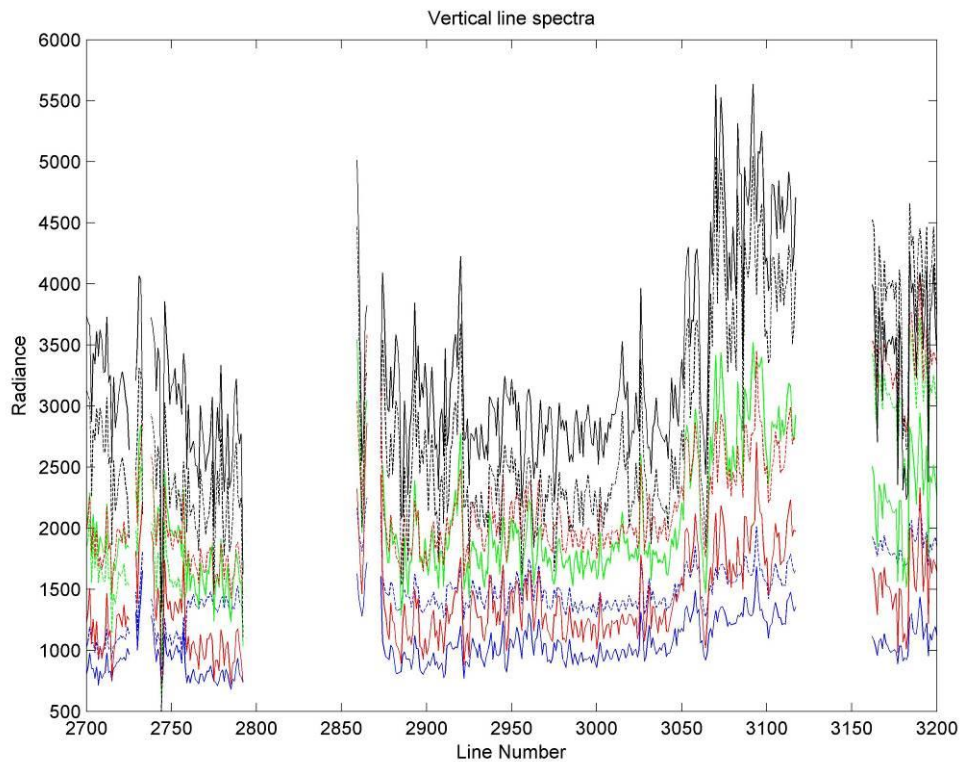


Figure 121: N_Rad_VI_VI image transect at pixel row 6500 (the blue vertical line displayed in Figure 120).

Figure 122 shows a comparison between two images, covering pixels 2700 to 3200 at row 6500 (i.e. (2700, 6500) to (3200, 6500)). The colour definitions remain the same (i.e. the blue plot colour represents the mean brightness at 448.0 nm, and so on) but the dashed and solid lines represent two different images. The solid and dashed lines correspond to the PHPA_Rad_VI and N_Rad_VI_VI images, respectively. However, the two images represent different data. The PHPA_Rad_VI image has units of radiance, while the N_Rad_VI_VI has units of normalised radiance. The plot data shows line-averaged radiance and normalised line-averaged radiance, corresponding to the PHPA_Rad_VI and N_Rad_VI_VI data, respectively. Therein lies a problem. How can they be compared? Which one is better, as there is no data to compare against. Another question concerns data consistency across a flight line boundary, which is not easy to identify in the image. Which data is the more consistent one is difficult to judge. They are mean values after all – the mean of all spectra of vegetation pixels across the whole horizontal line of pixels in the image.



**Figure 122: The four solid lines relate to the PHPA_Rad_VI image, while the dashed lines relate to the N_Rad_VI_VI image.
 Note: The units for the vertical axis are both radiance (for the full lines) and normalised reflectance (for the dashed lines).**

For flight line segments, each file is 965 pixels wide. Flight line boundaries exist at locations defined by multiples of 965. These values are: 965, 1930, 2895, 3860, 4825, 5790, 6755, 7720, 8685 and 9650. However, the image consists of 9005 lines. Therefore, pixels are eliminated due to overlap. For the flight line boundary located at line 2895 in Figure 122, data in that vicinity exists ranging from 2873 to 3117. It is unclear where the data from line 2895, from a flight line segment, coincides in the stitched image.

Comparing reflectance-based images presents a further issue. The N_Ref_VI_VI image only has 8577 vertical lines of pixels instead of 9005 (see Appendix L.5). To plot a comparison between these images, the 428 difference must be taken into account to line the data up correctly. Figure 123 shows the result but for a transect at row 7000.

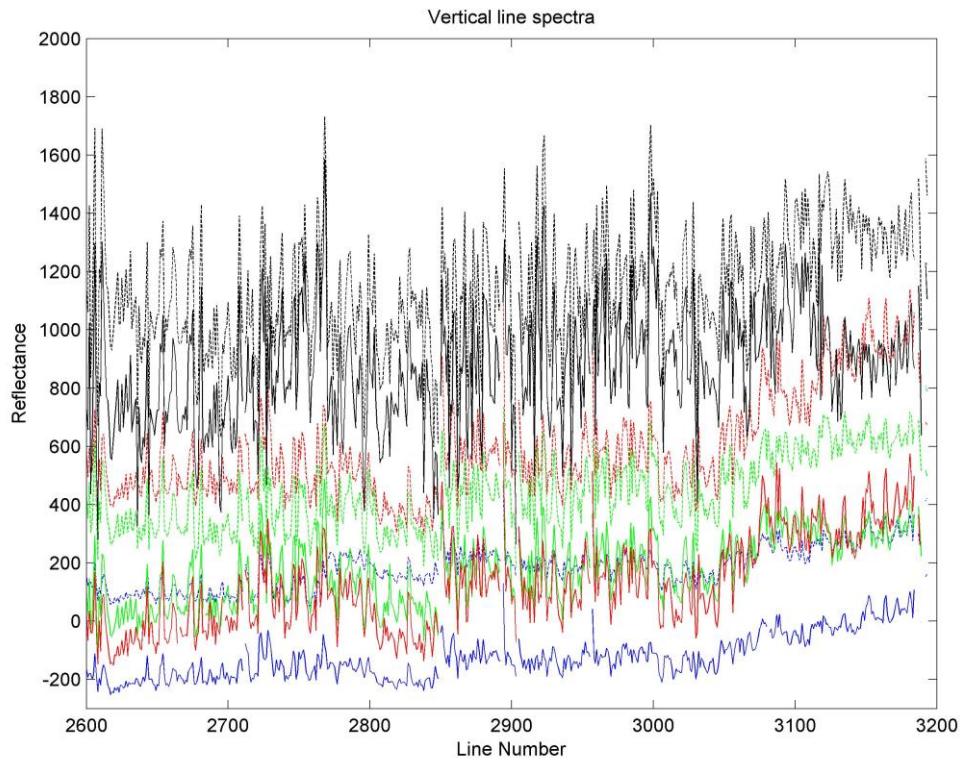


Figure 123: The full lines relate to data obtained from the PHPA_Ref_VI image, while the dashed lines represent data from the N_Ref_VI_VI image. Line numbering is with respect to the PHPA_Ref_VI image.

Note: The units for the vertical axis are both reflectance (for the full lines) and normalised reflectance (for the dashed lines).

Again, like Figure 122, it is not clear from Figure 123 which data is better. In the immediate vicinity of line 2895 (where the flight boundary should exist), only lines 2849, 2893, 2904, 2956 are missing.²² Other attempts to identify the boundaries from either spectral data or the plots were also unclear.

The results of this section raises concerns about how best to compare normalised spectral data to those contained in the original image. Not only do the units differ but there is no data available to identify the better image using these plots. In addition, the plot data are line-averaged data, not individual spectra. Therefore, comparison with ASD field data is not feasible, even when other complications are put aside (e.g. locational uncertainties, ASD data recorded at different time compared to image data, spectral quality due to noise, and so on). The plots also do not contribute toward identifying the effect of data consistency

²² The resolution of the plot is limited, with individual pixel data having been examined instead.

near flight line boundaries, as the location of these boundaries are uncertain in the stitched image in relation to the individual flight line segment images.

However, images may be compared using other means. One such study is presented in Section 4.5.9.6, where ASD spectra are compared to image spectra, while a much larger study is given in Appendix N, using image spectral means extending over carefully selected regions of pixels. The work argues that the N_Rad_VI is, spectrally, the most consistent normalised image.

As for the mean line brightness effect near flight line boundaries, Appendix O contains such a study but where flight line segments were used, as boundary locations are incompatible to the stitched image. It shows that dramatic spectral jumps can occur in individual pixel spectra, as a result of rapid spectral mean changes. A solution is also demonstrated to minimise these effects in normalised spectra.

4.5.9.5 Normalised Images Nomenclature

In Section 4.5.9.1, both reflectance (PHPA_Ref) and radiance (PHPA_Rad) images were line-averaged revealing brightness changes on a local flight line and global level. However, by first vegetatively masking the image (reflectance or radiance), the line-averaged plots increased in spectral brightness consistency.

As the N_Rad_VI image produced the 'best' classification result; the steps in Section 4.5.9.2 were explained in relation for that particular image. The word 'best' relates to it producing the highest quality thematic map, based on the highest number of statistically separable classes and (visually) their defined spatial structures.

Instead of using a vegetative-mask to remove 'weak' vegetation, other masks allowed for a different set of normalised images. For instance, line-averaging using a land-mask removes water spectra from the image prior to normalising and has the additional effect of removing salt pond regions. All land (including soil and vegetation) pixels were left unchanged. The mask is termed "**_Land**", whose development is described in Appendix L.2.

One further mask removes residential areas in the north-eastern region of the Port Hedland townsite. The dense mangrove forests on Finucane Island are located at the same latitudinal position as the residential areas, so the effect of removing residential regions was investigated on the classification result. This mask is termed “**_Res**” (further details are given in Appendix L.7).

After applying either the land or residential mask, the normalisation process (either for reflectance or radiance-based images) led to a new normalised image. This new image was then vegetatively-masked (Section 4.5.6) prior to classification.

The nomenclature for all images in this thesis follows a systematic naming process. There are two fundamental image data types available: reflectance and radiance. Therefore, an image containing the word “**_Ref**” indicates that reflectance data were used to generate the new image. Similarly, “**_Rad**” describes that radiance data were used as the source. An image constructed using the normalised process (i.e. using the steps from Section 4.5.9.2) is indicated by the prefix “**N**”. The type of mask applied prior to normalising is indicated by “**_Land**”, “**_VI**” or “**_Res**”. One additional image was also constructed, whereby no mask at all was used; “**_NoMask**”. For example, a “PHPA_Rad_VI” image indicates that the original radiance data (i.e. PHPA_Rad) was masked using the vegetative-mask, leaving just vegetation pixels. The “N_Ref_Land” image was produced by using a land-mask on reflectance data (i.e. PHPA_Ref), thereby eliminating all water and salt pond regions, then normalised. Prior to classification, the image was masked using the vegetative-mask, as we are only interested in classifying vegetation. Therefore, “N_Ref_Land” becomes “N_Ref_Land_VI”; the **_VI** indicating that the image was masked for vegetation. The image where no mask was applied, used the PHPA_Ref image (i.e. reflectance data) and then normalised prior to vegetative-masking. The intent was to investigate the normalisation process on the original reflectance image i.e. in the absence of using any mask (leaving all pixels in the image prior to normalisation, including water pixels, salt pond, soil and urban areas). The image formed is the “N_Ref_NoMask” image. The corresponding image used for classification is N_Ref_NoMask_VI.

Figure 124 summarises the processes used to produce various types of reflectance-based images, along with their nomenclature. Adjacent to each

description are numbers and letters surrounded in brackets. These are thesis sections where further details concerning the images and their classification are found. In the figure, N/A indicates that no mask was constructed (as no pixels were masked).

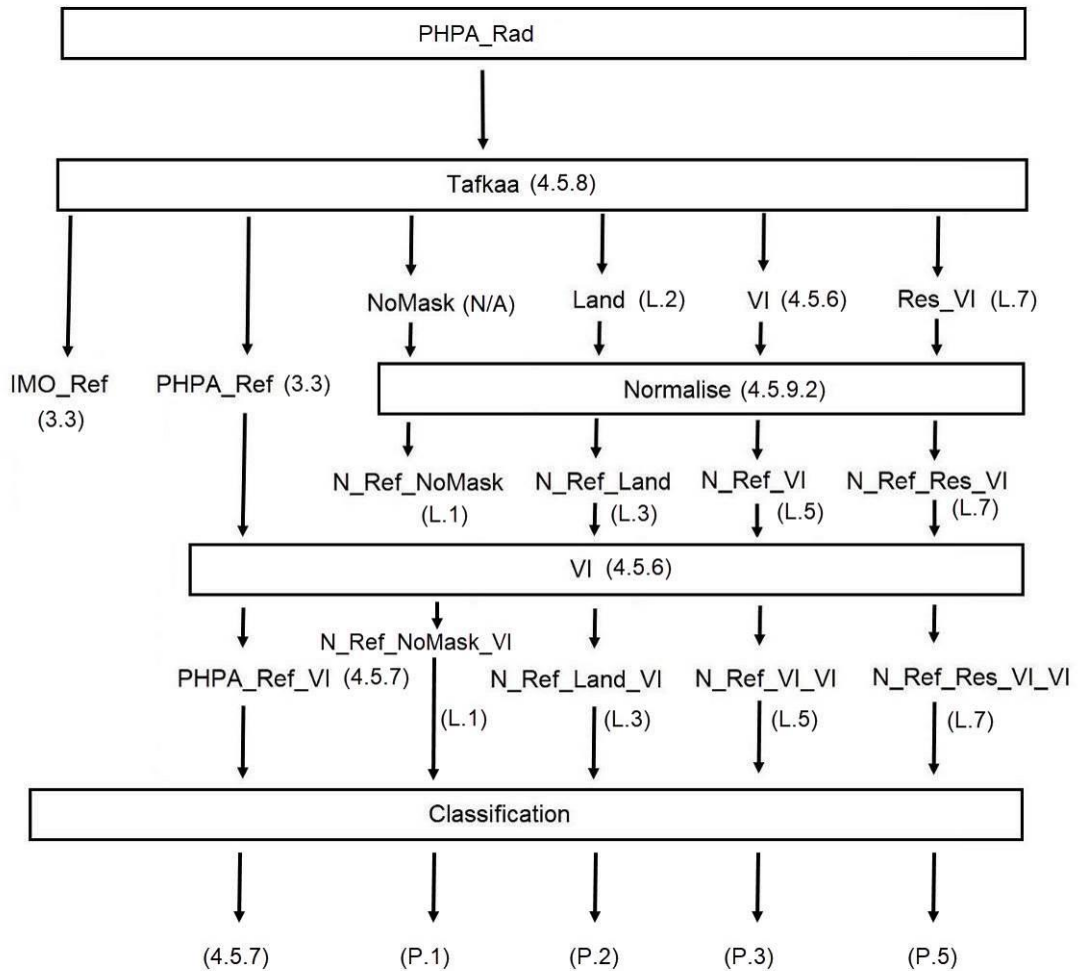


Figure 124: Overview of the processes used to generate stitched reflectance-based images.

As an example of how Figure 124 is interpreted, consider the N_Ref_Land image. Initially, the airborne radiance data (PHPA_Rad) is atmospherically corrected (using Tafkaa) leaving reflectance data. A land-mask was then applied to the reflectance data, thereby removing all water (including salt pond regions) from the scene. That result is line-averaged and normalised. The reconstructed image (after normalisation) is N_Ref_Land and includes the water pixels and so on. Prior to the

classification, the vegetative-mask (VI) is applied, leaving ('strong') vegetation over the scene. This image is the N_Ref_Land_VI.

Still referring to the N_Ref_Land image and using Figure 124, details concerning Tafkaa is found in Section 4.5.8, while Appendix L.2 describes the mechanics behind the land-mask. The normalisation process is described in Section 4.5.9.2. The N_Ref_Land image is shown in Appendix L.3, which uses the vegetative mask (of Section 4.5.6) to produce a N_Ref_Land_VI image, which is also presented in Appendix L.3. Classification of this image is performed in Appendix P.2, where the results are discussed.

In an analogous manner to Figure 124, Figure 125 relates to radiance-based images.

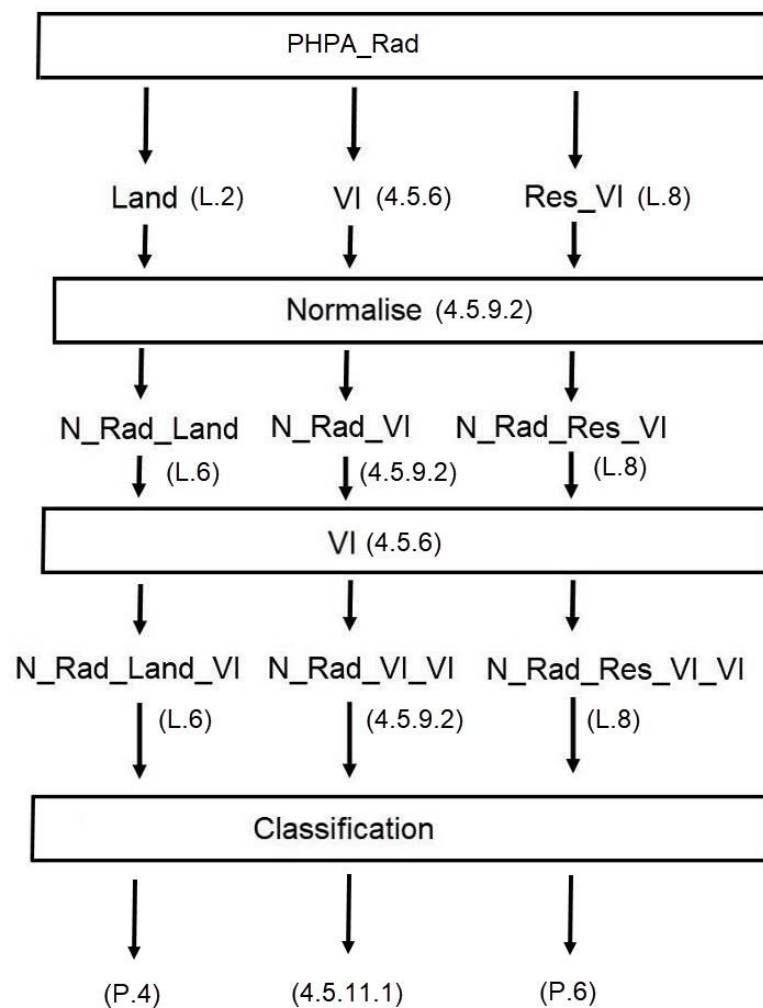


Figure 125: Overview of the processes used to generate stitched radiance-based images.

Figure 125 shows that, unlike Figure 124, there is no corresponding radiance version of N_Ref_NoMask; i.e. N_Rad_NoMask was not constructed. The reason is that, in the absence of masking, the quality of the N_Ref_NoMask image is poor. The N_Ref_NoMask image relies on normalising the large-valued brightnesses (caused by water and the salt pond regions) – i.e. normalising Figure 106 (p. 261 of Section 4.5.9.1). Appendix L.1 is dedicated toward the construction of N_Ref_NoMask. Due to the similarities exhibited in Figure 106 (for reflectance data) and Figure 107 (for radiance data), in terms of overwhelming brightnesses caused by water and the salt pond regions, it is reasonable to expect a similarly poor product for the N_Rad_NoMask as for the N_Ref_NoMask. For this reason, the N_Rad_NoMask was not constructed for analysis.

Note that not all images were used for classification. For example, PHPA_Rad_VI was not classified, as the spectral brightness inconsistencies exhibit similar extreme ranges of values (for each band) to those in the PHPA_Ref_VI (i.e. the general characteristics for the features in Figure 106 and Figure 107 are similar). As the classification for PHPA_Ref_VI was unsatisfactory (Section 4.5.7), the PHPA_Rad_VI image is also expected to produce unsatisfactory results.

4.5.9.6 Spectral Comparison between ASD and Hyperspectral Datasets

To examine the effect on vegetative spectra by the normalisation process, it is useful to plot several image spectra together to examine the differences between them. The comparisons are made with respect to ASD spectra, which contain reflectance spectra. Comparisons of ASD spectra with radiance-based images are not appropriate, as they are different units.

The comparison requires accurate matching between the ASD spectra geographical position with the image pixel position. Even though ASD measurements were accompanied with GPS positional data, the uncertainty of those positions impacts the ability to accurately locate the corresponding pixel location in the image. Field work showed that the location of mangrove species may vary in distances less than the GPS uncertainty. For example, Figure 90 (p. 231 of Section 4.5.5) shows that mangrove species vary within distances of a few metres.

The GPS uncertainty is estimated at 4 m to 8 m (from Appendix I.2), thereby making it possible for the position to represent a different species of mangrove to the one intended. In addition, the dimensions of each pixel is one by one metre. It is possible that a pixel may consist of two different species mangrove, so the pixel contains a spectral portion of each species (i.e. the pixel contains mixed spectra).

Due to these difficulties, the precise positional correspondence between ASD sampling positions with the airborne-sensed pixel data are known for just two locations. In particular, two well-distinct trees are located on Finucane Island in isolation and surrounded by grassland, making the image position identifiable. Appendix I.2 contains a discussion (with photographs), demonstrating position certainty for these two species.

The first species to be compared is the mangrove [FR] *Avicennia marina*. The ASD reflectance spectrum is displayed in Figure 126, with image-based mean reflectance spectra overlaid from several images (using identical pixels in all plotted reflectance-based images - the technical details behind calculating a mean spectrum is covered in Appendix W.4 and involves several steps). The tree covers a small number of pixels but as the position is easily identified in the image, there is no doubt that the average spectrum of these pixels relate to the same tree in all images.

In the 400 to 440 nm range and beyond 750 nm, all image spectra are particularly noisy compared to the ASD spectrum. In the 400 – 440 nm range, the noise is amplified in the normalised images compared to the original reflectance image (i.e. PHPA_Ref_VI). An explanation and remedy to the noise amplification is offered in Appendix O. For wavelengths, over 750 nm, the noise appears in all images.

The plot corresponding to the PHPA_Ref_VI image shows an overall negative gradient in the 550 – 680 nm range, which matches the ASD spectrum more closely than the normalised images.

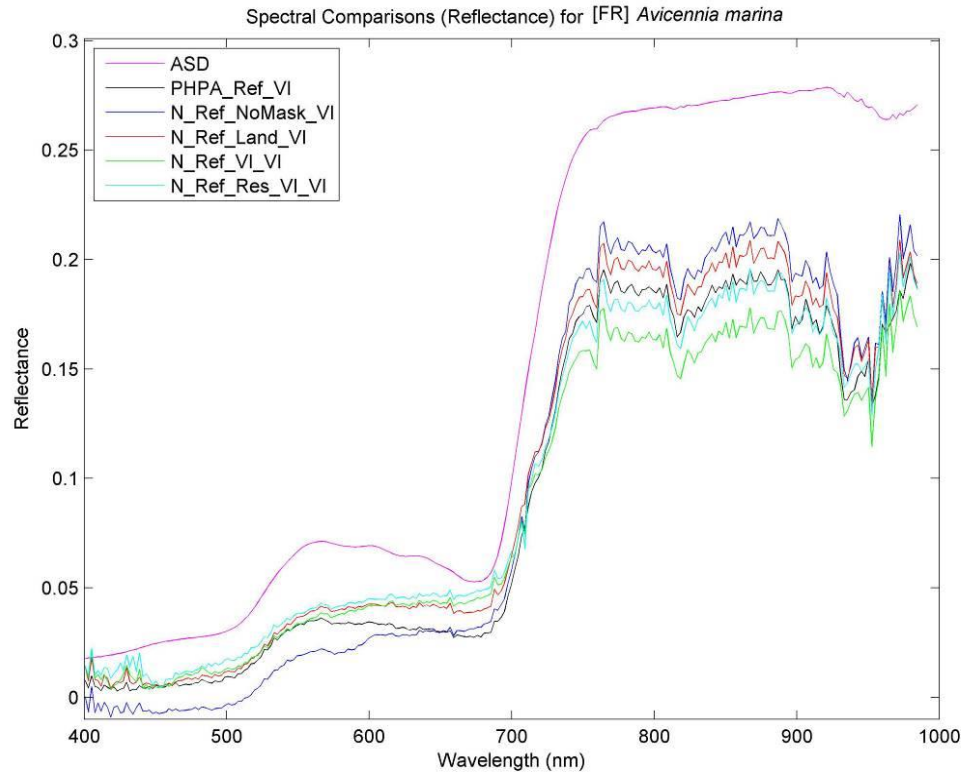


Figure 126: Spectral reflectance of [FR] *Avicennia marina* collected in-situ with the ASD, and spectra derived from the PHPA_Ref_VI image and the four normalised Reflectance-based images.

Note that both the ASD and PHPA_Ref_VI have units of reflectance, all normalised images are in units of normalised reflectance.

Although the reflectances for the ASD spectrum appears higher compared to the image-based spectra, this is not necessarily the case; it is easy to imagine a downward shift (by a constant factor), to allow the reflectance of both ASD and image spectra coincide more closely (although the slopes will still remain identical). As demonstrated in Appendix E.3, the SA remains unchanged when one spectrum is scaled by a constant factor. Equivalently, all image spectra could be scaled upwards.

The use of SAs allows for a quantitative assessment between the spectra in the plot (Figure 126). The results are summarised in Table 32.

[FR] <i>Avicennia marina</i>	ASD	PHPA_Ref_VI	N_Ref_ NoMask_VI	N_Ref_ Land_VI	N_Ref_ VI_VI	N_Ref_ Res_VI_VI
ASD	-	0.11	0.15	0.09	0.09	0.09
PHPA_Ref_VI		-	0.07	0.04	0.08	0.08
N_Ref_NoMask_VI			-	0.09	0.12	0.12
N_Ref_Land_VI				-	0.05	0.05
N_Ref_VI_VI					-	0.02

Table 32: Spectral angles between reflectance-based image pairs for [FR] *Avicennia marina*.

The SA between the ASD spectrum and the original reflectance image (PHPA_Ref_VI) is 0.11 rad. With the exception of the N_Ref_NoMask_VI image, whose spectral quality is questionable (as argued in Appendix N), this exceeds the 0.09 rad for all normalised images. This suggests that the normalised images are spectrally more alike to the ASD spectra than the PHPA_Ref image. Although the SAs of 0.09 and 0.11 rad represent a high degree of similarity (according to Section 4.4.1), it is encouraging that normalised images have not produced a worse result than the original reflectance image (PHPA_Ref_VI). This is an important point, as the characteristic features of spectra must be preserved for classification.

The second tree species examined is the [FR] *Acarica sp.*, which is actually not a mangrove. Interestingly, this species is spectrally very similar to [LP] *Avicennia marina*, and [FU] *Aegiceras corniculatum*1. The SAs between [FR] *Acarica sp.* and [LP] *Avicennia marina* is only 0.02 ± 0.03 rad, and 0.03 ± 0.03 rad between [FR] *Acarica sp.* and [FU] *Aegiceras corniculatum*1 (from Table 75, p. 504 of Appendix G.3).

The plot presented in Figure 127 is identical to Figure 126, except that the spectra now represent [FR] *Acarica sp.*. Table 33 gives a quantitative assessment of their differences based on SA.

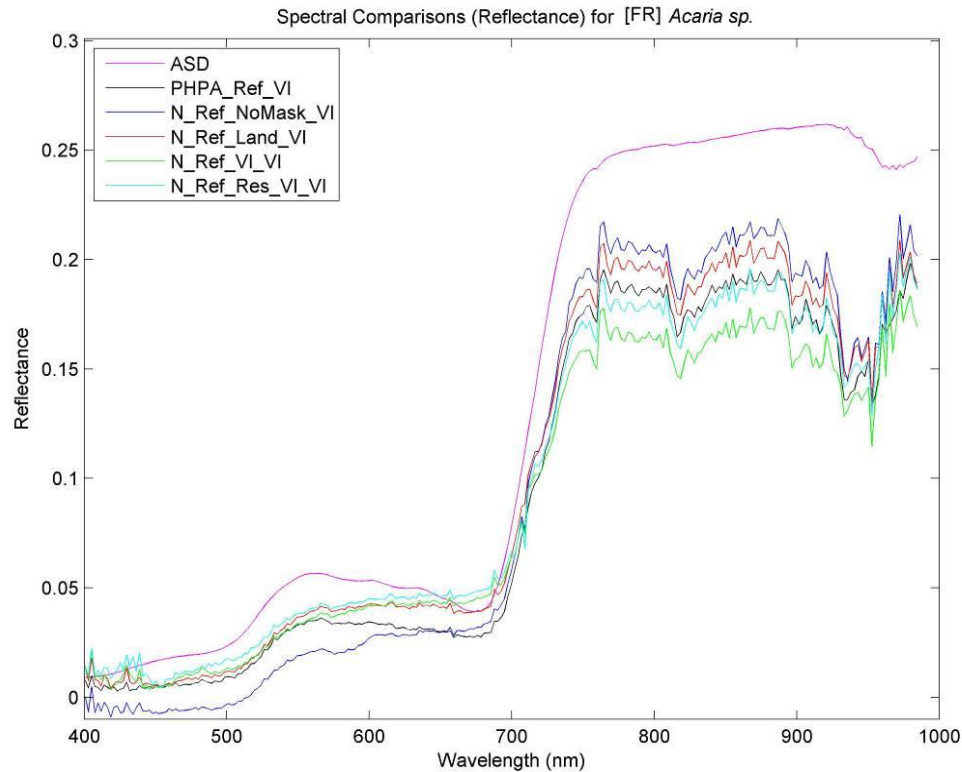


Figure 127: Spectral reflectance of [FR] *Acaria sp.* collected in-situ with the ASD, and spectra derived from the PHPA_Ref_VI image and the four normalised Reflectance-based images.

Note that both the ASD and PHPA_Ref_VI have units of reflectance, all normalised images are in units of normalised reflectance.

The spectral characteristics in Figure 127 are similar to those identified for Figure 126 (i.e. noise and gradient behaviour). Again, the three N_Ref_Land_VI, N_Ref_VI_VI and N_Ref_Res_VI_VI produce consistent spectra, which are no worse than the original reflectance image (PHPA_Ref_VI); all SAs are 0.11 rad with the ASD spectrum (except the N_Ref_NoMask_VI which is a poor image).

Based on the given results, the normalised spectra are no worse (and sometimes better) in matching up ASD ground spectra with image spectra than the original reflectance data. However, making a generalised statement based on comparing just two ASD spectral samples with the images is not justifiable. Also, the number of pixels compared is small in relation to the total number contained in the whole image. Another complication concerns the behaviour of normalisation itself, which may introduce undesired spectral features in certain circumstances. A detailed discussion for a radiance-based spectrum is found in Appendix O and is also

applicable to reflectance-based spectra as the methodology behind normalisation is identical.

[FR] <i>Acaria sp.</i>	ASD	PHPA_Ref_VI	N_Ref_NoMask_VI	N_Ref_Land_VI	N_Ref_VI_VI	N_Ref_Res_VI_VI
ASD	-	0.11	0.20	0.11	0.11	0.11
PHPA_Ref_VI		-	0.14	0.05	0.07	0.07
N_Ref_NoMask_VI			-	0.16	0.17	0.18
N_Ref_Land_VI				-	0.03	0.04
N_Ref_VI_VI					-	0.03

Table 33: Spectral angles between reflectance-based dataset pairs for [FR] *Acaria sp.*

Evidently, this section showed that normalisation does not ‘fix’ spectra to make them more ASD-like. Instead, normalisation has the effect of improving spectral brightness consistencies in an image.

4.5.10 Summary and Discussion

Spectral inconsistencies in the PHPA_Ref image were documented in Section 4.5.3. Of particular concern are the brightness inconsistencies both within and across flight line boundaries. In addition, negative reflectances are particularly evident in the northern extend of the PHPA_Ref image, affecting mainly the blue-end of the spectrum. Those Tafkaa parameters expected to cause most change, were adjusted to examine real differences in output reflectances (Section 4.5.8). However, the lack of very little (if any) change suggested that the inherent image spectral problems could not be resolved using Tafkaa alone. It is known that the lack of instrument calibration (Montes et al., 2004), reduces the model’s ability to effectively correct the hyperspectral data (Miller, Del Castillo, & Mckee, 2005, p. 57).

In view of these brightness issues, an attempt was made to classify the PHPA_Ref image to examine what extent the underlying issues have on the final thematic map. Section 4.5.5 outlined a current paradigm to classify hyperspectral datasets,

whereby the image is vegetatively masked (Section 4.5.6), prior to the decreasing the large number of highly correlated bands (typical of hyperspectral data) using a PC transform. These identify features in the data, which are ranked in terms of variance. A (typically) small selection of these transformed bands contain 99% of the data variance, thereby increasing classification accuracy (due to the Hughes effect). Another benefit is the increase in computational processing speed for any subsequent processes (e.g. classification). The resulting thematic map contains classes, which must be spectrally assessed using JM distance separability statistics. Those spectral classes falling below a threshold distance must be merged to increase confidence in class separability; this means the classes are well defined with confidence.

For the PHPA_Ref image, PCA left a 9 PC band image for k-mean unsupervised classification, leaving a 10 class thematic map but with questionable results, as classes differed on opposite sides of an adjacent flight line boundary. This means that a shift in flight boundary location would result in a positional change in classes. The result, being clearly non-physical in nature, means that the vegetative composition changes, depending on the location of the airborne sensor recording the data. Being utter nonsense, this non-physical result lends further strength that the brightness changes in the image are leading to real problems in classification work, and cannot be ignored. This led to a detailed study of image spectra over the whole scene, forming the basis for the work under Section 4.5.9.

The technical details behind the line-averaging process are outlined in Section 4.5.9.1. Brightness inconsistencies are particularly evident over water-based regions (i.e. including salt pond regions). Figure 106 shows that individual flight line edges do not line up and occurs over the scale of the whole image. This means there is a brightness change by traversing a flight line. Even within individual flight lines, there is variability, particularly in the geographic northern end of the map. The same holds true for radiance-based data (Figure 107). As the atmospheric correction (i.e. Tafkaa) did not eliminate the spectral inconsistencies, this means there is a deeper inconsistency. It demonstrates that it is unable to 'correct' radiance data to produce consistent reflectance data. The Tafkaa model is one widely used in the remote sensing community and reputable. One possibility is to fix

reflectance brightness inconsistencies, while another is to bypass the atmospheric correction routine altogether (since the spectra are inconsistent anyway), and correct radiance data instead. Both approaches were adopted in this thesis. However, as the N_Rad_VI data produced the best spectral quality, that image was retained in the main discussion while all other images were placed in Appendix L. The differences between all the normalised images, as produced in this thesis, are explained in Section 4.5.9.5.

After generating new images, it is of interest to examine how they compare to each other. A rather simple true-colour image comparison in Section 4.5.9.2 shows that the flight line boundaries are more consistent in brightness for the image N_Rad_VI image compared to the original PHPA_Ref image. To be clear, note that the brightness is more consistent across flight line boundaries. In actual fact, as normalisation adjusts the brightness of each wavelengths independently, the whole spectral shape is adjusted. If all wavelengths were changed in the same way, then the spectrum remains the same; the SA would be zero (as it is independent of brightness). Such is not the case here.

A spectral-based argument is presented in Appendix N, where spectral means over key regions are compared for each image. The evidence suggests that the N_Rad_VI image is spectrally the most consistent.

Actual spectral comparisons, involving ASD and reflectance-based images, were found in Section 4.5.9.6. It highlights that normalised spectral data is not more ASD-like compared to original (i.e. un-normalised) data. The normalisation process improves spectral consistency in an image. It does not, nor can it (nor is it intended) correct image spectra to ASD-like spectra (nor a reduced-resolution of it).

The key points are:

- The atmospheric model (Tafkaa) does not adequately remove spectral inconsistencies in image data.
- Without normalisation, classification leads to inconsistent spatial class distributions.

- Normalisation adjusts spectra based on a three step process, whereby spectra are made more consistent within and between individual flight lines. It also removes individual (i.e. for each wavelength independently) brightness trends across the whole image.
- Normalisation leads to more consistent spectra on a large scale. It does not correct existing pixel spectra to make them more ASD-like.
- Feature reduction is performed on an image that is vegetatively masked, which is then classified.

4.5.11 Thematic Maps

The thematic map for the PHPA_Ref_VI image has already been produced in Section 4.5.7. This followed the classification paradigm developed in Section 4.5.5. This section and the rest of the thesis (i.e. the Appendices) follows the same paradigm.

With the N_Rad_VI_VI map derived in Section 4.5.9.2, it is classified in Section 4.5.11.1. Class spectra are analysed in Section 4.5.11.2, while a summary and discussion follows in Section 4.5.11.3.

Note that only the N_Rad_VI_VI map is considered under this section (i.e. Section 4.5.11). All other normalised-derived maps are found in Appendix L and classified in Appendix P (using the same classification paradigm of Section 4.5.5). The N_Rad_VI image produced the best result. Therefore, only this image is considered for detailed study in this Section (4.5.11) and the resulting thematic map compared in the next Section 4.6.

The PC plots are not given (as little is gained from them), although the relevant tabular values for the percentage cumulative variances are provided to support the results of the classification process and to aid discussion.

4.5.11.1 Classifying the N_Rad_VI_VI image

As the classification process has been explained explicitly in Section 4.5.7, this section limits any explanations in favour of presenting the results.

Using the 99% cumulative variance threshold method, a total of 15 PC bands needed retaining after PC transforming the N_Rad_VI_VI (see Table 34). This is the highest number for PC band retention of all images considered in this thesis (further discussion is withheld until Section 4.5.11.3).

PC band	Cumulative variance (%)	PC band	Cumulative variance (%)
1	56.69	9	98.54
2	87.85	10	98.65
3	95.46	11	98.76
4	96.62	12	98.84
5	97.39	13	98.91
6	97.83	14	98.98
7	98.13	15	99.04
8	98.36	16	99.09

Table 34: Cumulative variance (in % rounded to 2 d.p.) of the PC transform for the N_Rad_VI_VI image.

The first 15 PCA bands account for 99% of the total variance. Therefore, 15 PC bands are retained for classification purposes (Note: only the first 16 PC bands are shown in this table). The order of PC bands are given in ascending order by increasing cumulative variance.

Classifying the 15 PC band image using a 10 class k-means classifier (shown in Figure 128) produced 10 separable classes. Encouragingly, all 10 classes were immediately separable to $JM \geq 1.7$ (using JM separability statistics), with JM distances between class-pairs less than 1.97 shown in Table 35. Note that the identity of each class (e.g. class 6) is not made in relation to the class colour displayed in Figure 128. No other dataset (refer to Section 4.5.7 and Appendix O) produced this immediate level of class separability as for the 15 PC transformed N_Rad_VI_VI dataset.

class 6 & class 7: 1.7071
class 7 & class 8: 1.7188
class 4 & class 8: 1.7498
class 3 & class 4: 1.7522
class 5 & class 8: 1.7784
class 4 & class 5: 1.8117
class 3 & class 5: 1.8204
class 5 & class 7: 1.9125
class 8 & class 9: 1.9685

Table 35: Separability report for the k-means 10 class (50 iterations) classifier of the 15 PC band N_Rad_VI_VI dataset.

Note: 1) only values for JM < 1.97 are shown, 2) the relationship between individual class numbers and class colours (for Figure 128) are omitted, 3) JM distances are given in order of increasing JM distances, 4) JM distances are rounded to 4 d.p..

The 10 classes displayed in the thematic map of Figure 128 are therefore spectrally separable to a low degree of confidence (i.e. where $JM \geq 1.7$). To examine the effect of increasing the level of confidence to a moderate level (where $JM \geq 1.8$), classes were merged where class-pairs have separabilities less than 1.8. The resulting thematic map is shown in Figure 129 with 6 classes left after merging. The highest confidence map is shown in Figure 130 for $JM \geq 1.9$, leaving just 5 classes. Clearly, as the level of confidence for class-pair spectral separabilities increase, the number of classes retained decreases. Figure 129 contains more class detail (the yellow region) than Figure 130. Therefore, it is highly likely that the vast dull-green regions of Figure 130 represents vegetation, while the yellow class structure in Figure 129 represents (to a moderate probability) a different cover type (possibly a different type of vegetation). It is worth noting that the class colours were manually adjusted in Figure 129 and Figure 130 to aid visual comparisons between the two images. The colours in Figure 128 use default ENVI colour codes.

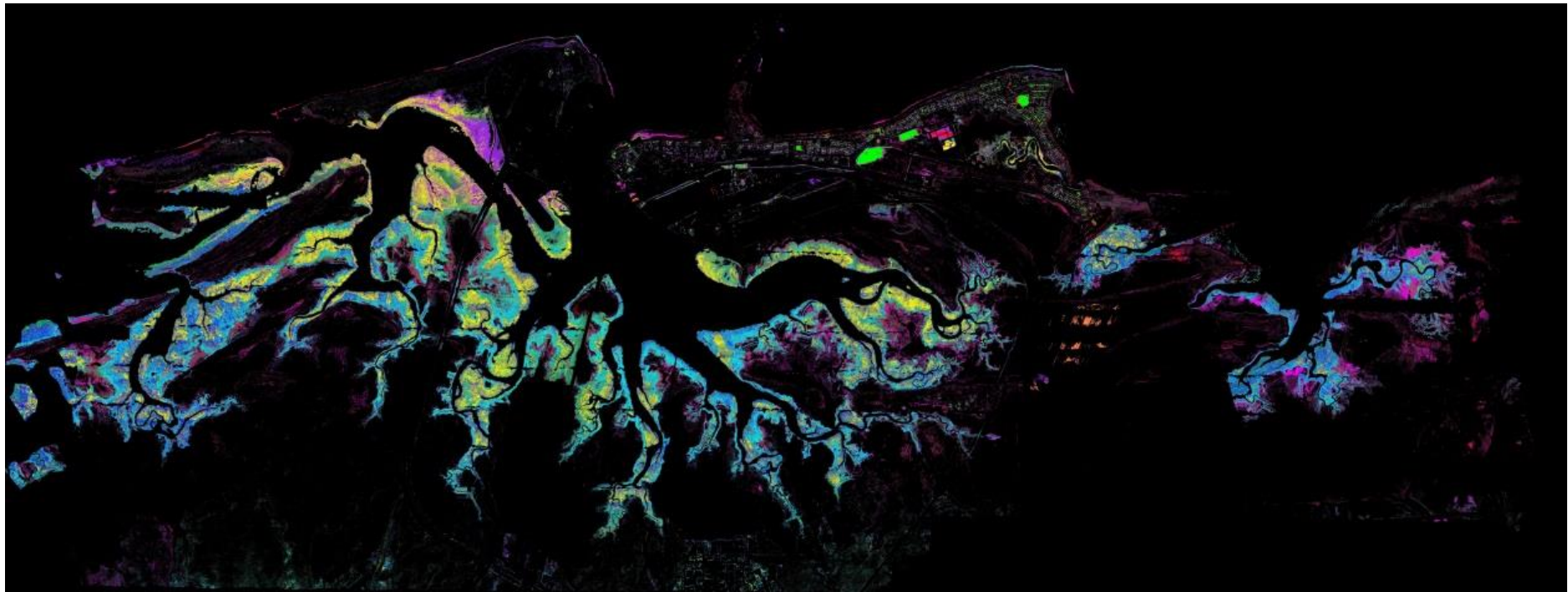


Figure 128: Thematic map using 50 iterations for a 10 class k-means classifier of the 15 PC band N_Rad_VI_VI dataset.
All 10 classes were immediately separable at $JM \geq 1.7$.

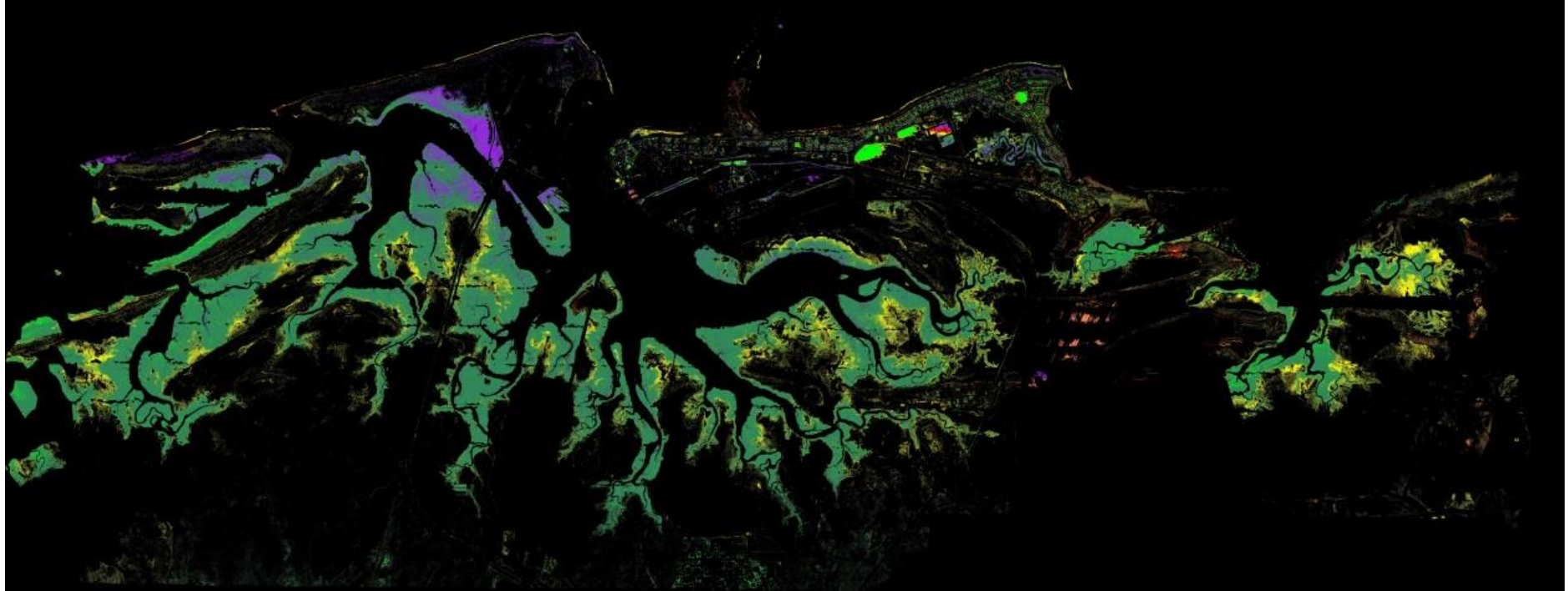


Figure 129: Thematic map by merging classes from the 10 class k-means classifier of the 15 PC band N_Rad_VI_VI dataset.
A total of 6 classes remain moderately separable to $JM \geq 1.8$.

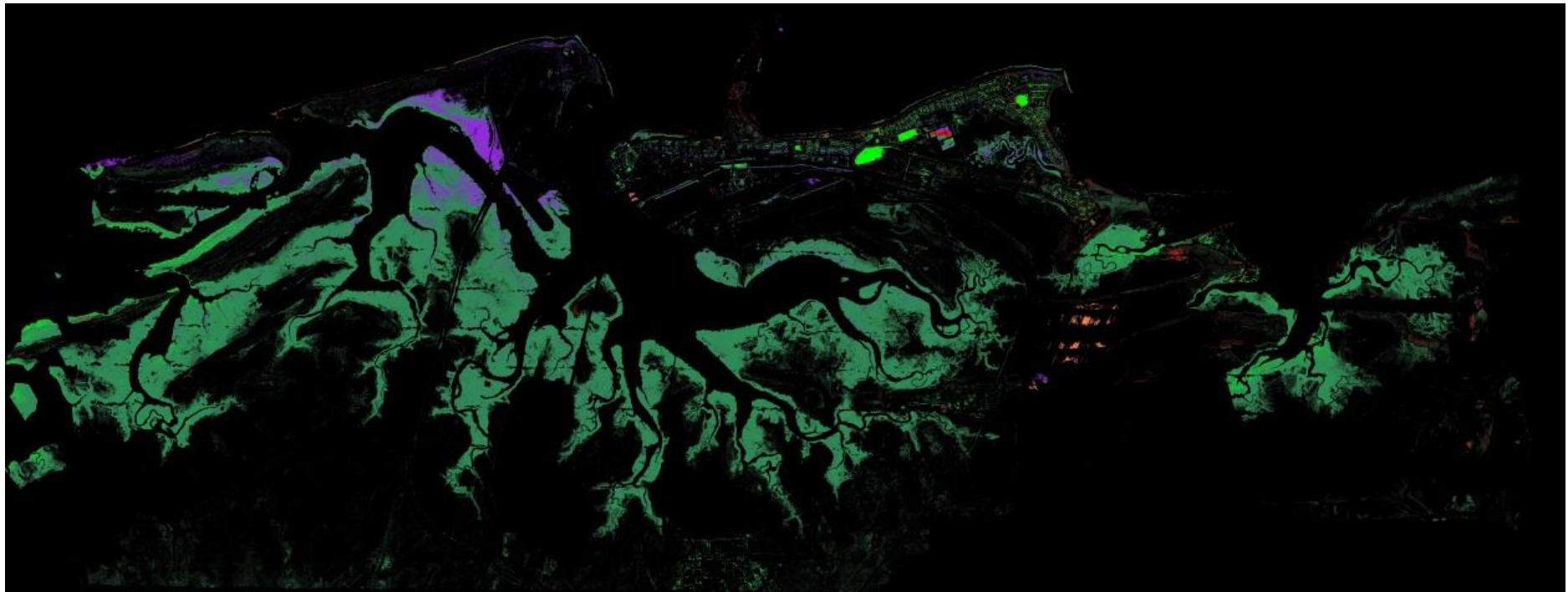


Figure 130: Thematic map by merging classes from the 10 class k-means classifier of the 15 PC band N_Rad_VI_VI dataset.
A total of 5 classes remain highly separable to $JM \geq 1.9$.

Given that the 10 classes were immediately separable for the 10-cluster k-means classification, it is of interest to examine the results for a 15 cluster specification corresponding to the current 15 PC band N_Rad_VI_VI dataset. The additional clusters may reveal more detailed vegetative structures by allowing the classifier to define additional classes containing smaller distances between cluster centres. By calculating the separability statistics for a larger number of clusters, it is possible that some (or all) of these additional classes require merging to meet a JM distance limit of 1.7. The result cannot be known *a priori*, but ideally some (or all) of the new classes will be separable, thereby allowing the additional classes to capture finer spectral differences.

The k-means 15 class classification result (for 50 iterations) is presented in Figure 131 with the separability statistics for class-pairs given in Table 36.

class 4 & class 5: 1.4874
class 6 & class 10: 1.5495
class 8 & class 11: 1.5624
class 12 & class 13: 1.5792
class 5 & class 6: 1.6004
class 13 & class 14: 1.6307
class 5 & class 7: 1.6315
class 7 & class 12: 1.6567
class 8 & class 9: 1.6879

Table 36: Separability report for the k-means 10 class (50 iterations) classifier where JM \geq 1.7 of the 15 PC band N_Rad_VI_VI dataset.

Note: 1) only values for JM < 1.70 are shown, 2) the relationship between individual class numbers and class colours (for Figure 131) are omitted, 3) JM distances are given in order of increasing JM distances, 4) JM distances are rounded to 4 d.p..

Table 36 shows that class 4 (represented in dark green of Figure 131) and class 5 (in aqua colour) are the least separable with a JM distance of 1.4874. Therefore, spectrally there is a very high probability that these two classes are spectrally inseparable, thereby requiring class merging. Both classes 4 and 5 appear in roughly equal proportions in the image; 6.23% and 9.67% of the class pixels respectively.²³

²³ Note: To clarify, the percentages are expressed in terms of total class pixels. The masked (i.e. black) pixels are not included in the statistic. Therefore, a value of 50% represents half of all displayed class pixels, rather than half of the total image (which includes the black (masked) pixels). This comment holds true for all such statistics in this section.

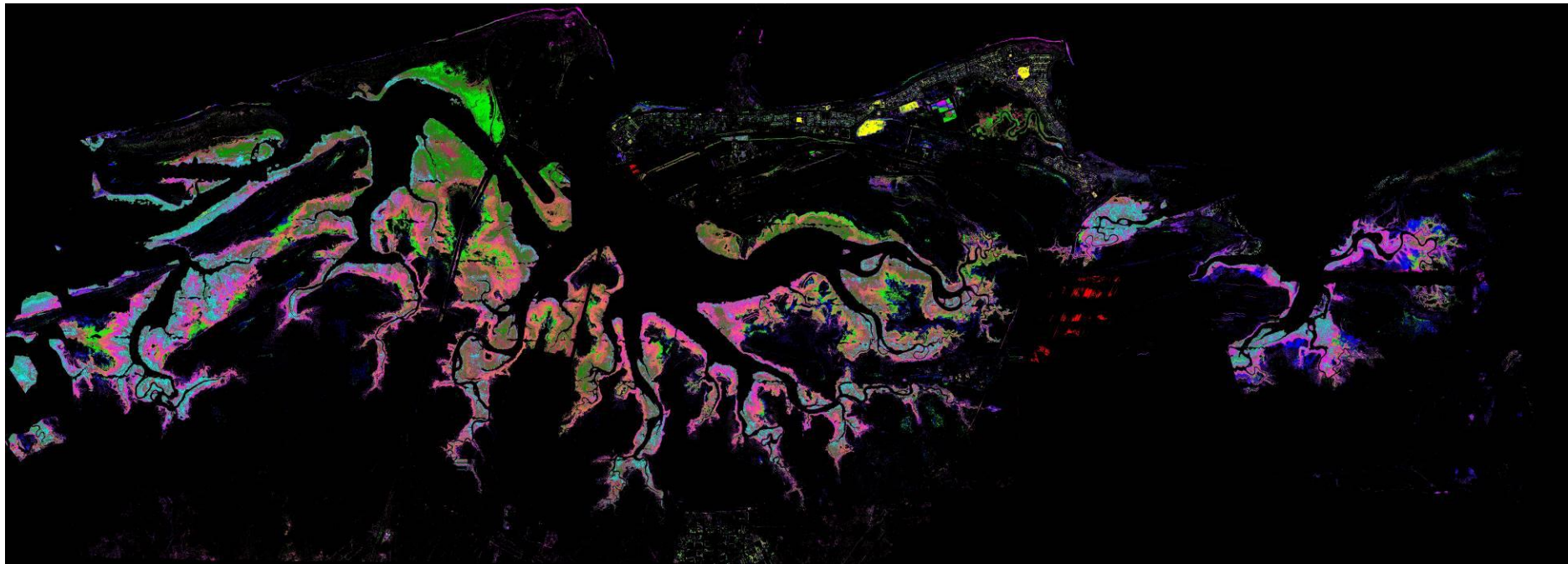


Figure 131: Thematic map using 50 iterations for a 15 class k-means classifier of the 15 PC band N_Rad_VI_VI dataset.

To produce a thematic map whereby classes are separated to a low degree of confidence (i.e. $JM \geq 1.7$), a total of 5 of the 15 classes needed merging, producing the map displayed in Figure 132. The corresponding separability statistics (from $1.7 \leq JM < 1.96$) are given in Table 37.

class 12 & class 11: 1.7160
class 3 & class 4: 1.7565
class 4 & class 12: 1.8328
class 11 & class 13: 1.8504
class 3 & class 11: 1.8528
class 4 & class 11: 1.9595

Table 37: Separability report for the k-means 15 class (50 iterations) classifier where $JM \geq 1.7$ for the 15 PC band N_Rad_VI_VI dataset.

Note: 1) only values for $JM < 1.96$ are shown, 2) the relationship between individual class numbers and class colours (for Figure 128) are omitted, 3) JM distances are given in order of increasing JM distances, 4) JM distances are rounded to 4 d.p..

To further increase class separability confidence, class-pairs were merged to reach a $JM \geq 1.8$ threshold, resulting in the image shown in Figure 133. A total of 8 moderately separable classes (from the initial 15 classes) remained to meet $JM \geq 1.8$, while a total of 6 highly separable classes remained at $JM \geq 1.9$ (Figure 134).

Note that a median filter (3x3) has been used in thematic maps Figure 132 to Figure 134 to smooth local variations and to emphasise the gross structure. The use of a post-classification median filter is not uncommon in remote sensing; a 3x3 median filter was used by E. P. Green, Mumby, Edwards, Clark, and Ellis (1998), while both J. Gao (1999) and Held et al. (2003) are two examples where a 5x5 median filter was applied in their work.

An attempt was also made to define the same class colours in Figure 132 to Figure 134, with particular emphasis using different shades of green to represent vegetation. Therefore, while the vegetation in Figure 131 contains different class colours between Finucane Island (mostly green) and Pretty Pool (mostly aqua), both regions are covered using a green colour.

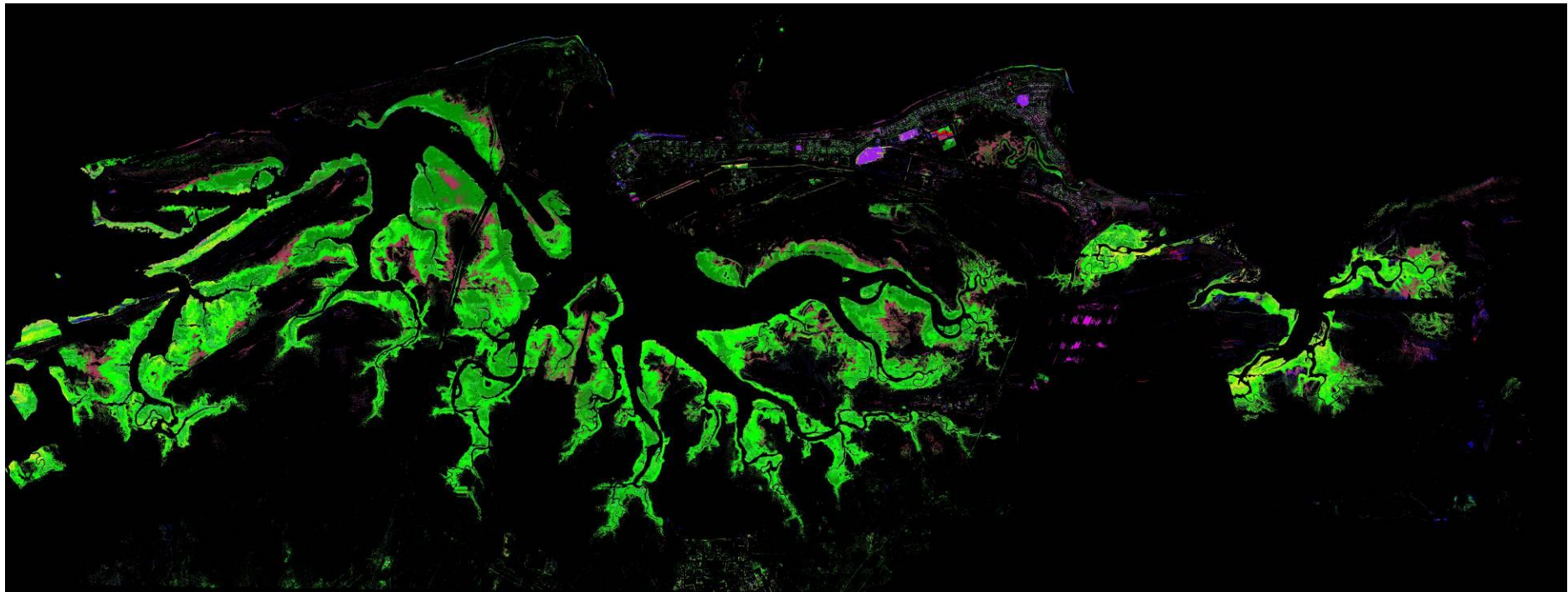


Figure 132: Thematic map as obtained by merging classes from the 15 class k-means classifier of the 15 PC band N_Rad_VI_VI dataset. A total of 10 classes remain separable to low confidence at $JM \geq 1.7$. A post-classification median filter (3x3) smoothed out local variations.

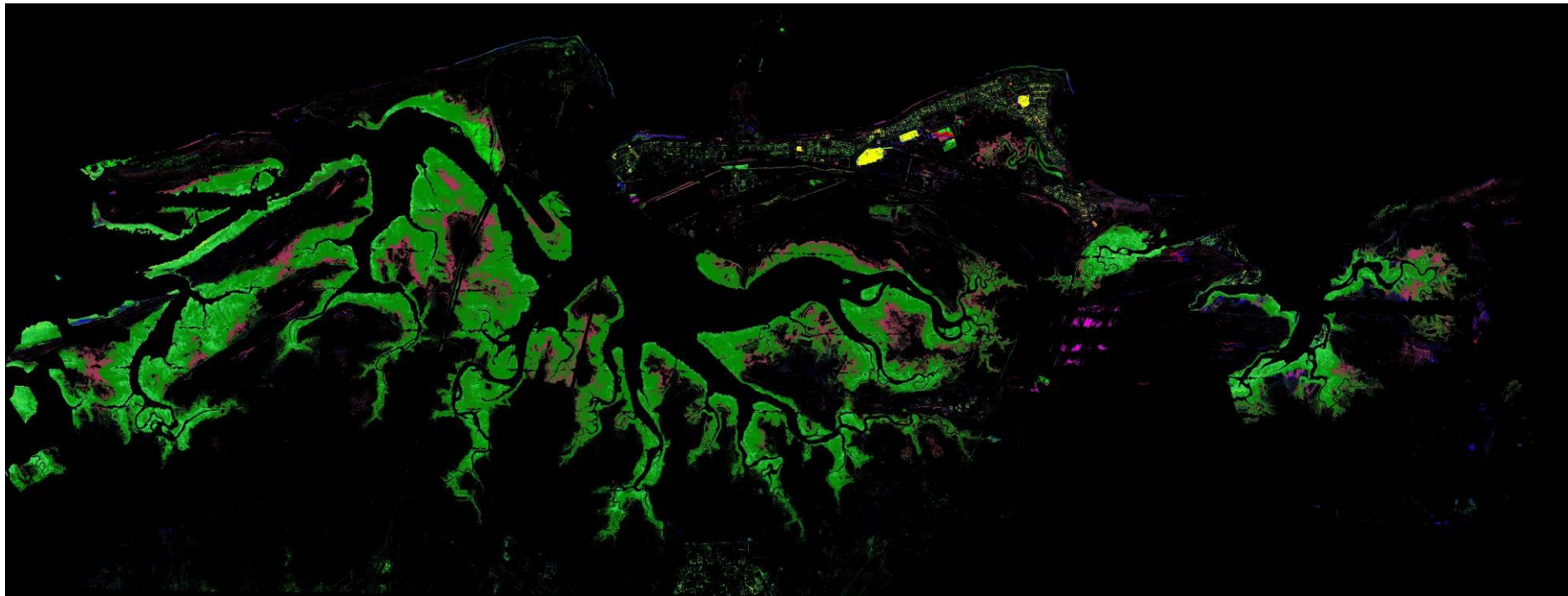


Figure 133: Thematic map as obtained by merging classes from the 15 class k-means classifier of the 15 PC band N_Rad_VI_VI dataset. A total of 8 classes remain moderately separable to $JM \geq 1.8$. A post-classification median filter (3x3) smoothed out local variations.

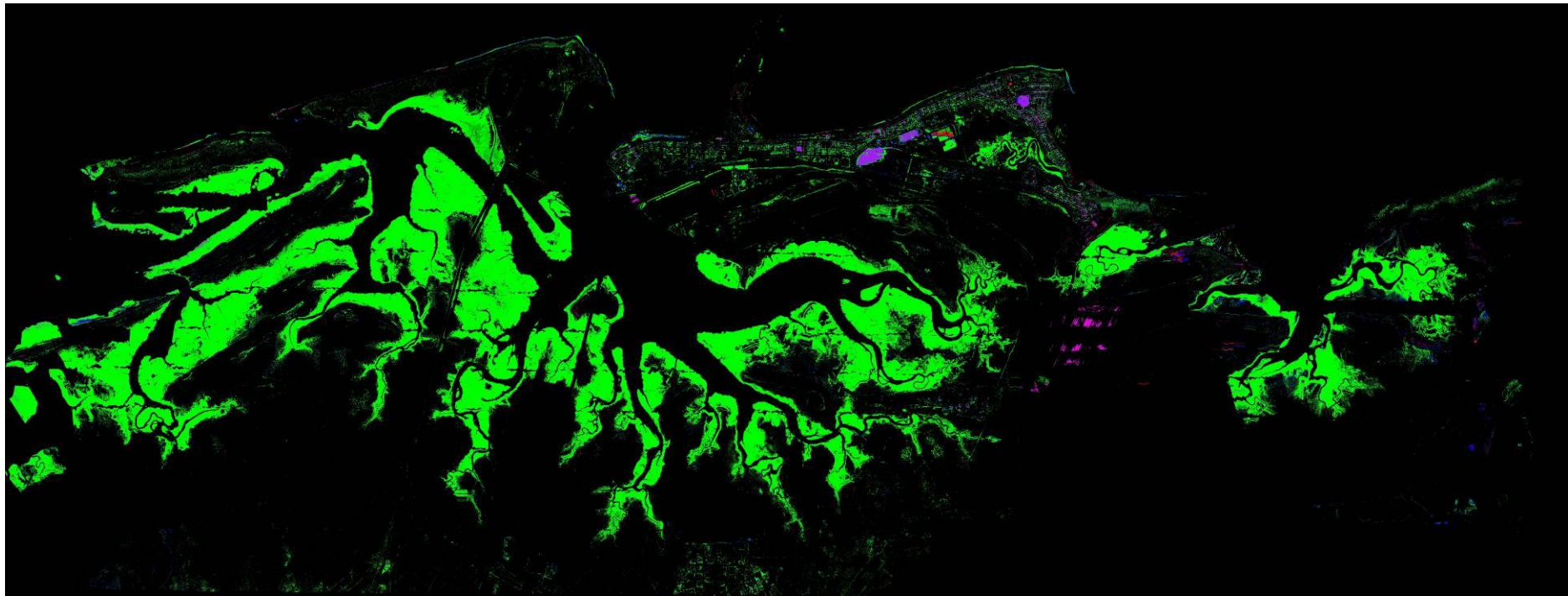


Figure 134: Thematic map as obtained by merging classes from the 15 class k-means classifier of the 15 PC band N_Rad_VI_VI dataset. A total of 6 classes remain highly separable to $JM \geq 1.9$. A post-classification median filter (3x3) smoothed out local variations.

Finally, any statistics presented in this section relate to the unfiltered thematic map. Therefore, the class-pair separability JM distance tables (Table 36 to Table 39) and class population statistics (Table 40) were calculated using the unfiltered thematic maps rather than the median filtered ones as displayed in Figure 132 to Figure 134.

The separability statistics corresponding to the $JM \geq 1.8$ and $JM \geq 1.9$ images are given in Table 38 and Table 39 respectively.

class 4 & class 12: 1.8252
class 13 & class 12: 1.8421
class 8 & class 13: 1.9642
class 1 & class 8: 1.9845
class 14 & class 13: 1.9846

Table 38: Separability report for the k-means 15 class (50 iterations) classifier where $JM \geq 1.8$ for the 15 PC band N_Rad_VI_VI dataset.

Note: 1) only values of $JM < 1.99$ are shown, 2) the relationship between individual class numbers and class colours (for Figure 133) are omitted, 3) JM distances are given in order of increasing JM distances, 4) JM distances are rounded to 4 d.p..

Note that Table 38 only displays JM distances between class pairs being less than 1.99. The most spectrally similar classes (4 & 12) has a JM distance of 1.8252. These correspond to the large dark green region (occupying 54% - from Table 40 for JM 1.8) and the blueish green colour (occupying 15% of the image in Table 40 for JM 1.8). These two regions and the maroon coloured region (class 13 - occupying 24% of the image) are merged to form the light green coloured class in the $JM \geq 1.9$ image (Figure 134) and represents 93% of the image (class 13 in Table 40 for JM 1.9). Therefore, there is a high degree of confidence that the light green coloured class in Figure 134 (for $JM \geq 1.9$) represents vegetation (recall that the N_Rad_VI_VI data is the N_Rad_VI image but masked for vegetation).

As the level of spectral similarity decreases (e.g. vegetation of different cover types, such as mangrove and grass), the confidence of spectral separability increases (e.g. $JM \geq 1.8$). Conversely, the level of spectral detail increases with a corresponding decrease in level of confidence. The probability of spectral separation thereby decreases. Consequently, Figure 133 (for $JM \geq 1.8$) shows a finer degree of structure for (possibly) vegetation than Figure 134 but at a lower level of

confidence. Figure 132 (for $JM \geq 1.7$) reveals even more classes, thereby defined by a finer structure of features; possibly the addition of mixed spectra containing vegetation and soil - mixing soil spectra with vegetation reduces the length of the red-edge (but the red-edge is still present). The thematic map for 15 classes (Figure 131) appears to contain finer class structures. However, separability statistics (Table 36) suggests otherwise - a number of those classes are spectrally too similar (or identical within JM distance bounds). There is, therefore a very low confidence attached to the additional information content associated with these extra classes (i.e. 15 classes versus 10 classes for the $JM \geq 1.7$ image), as they are mathematically too spectrally similar to exhibit a physically well-defined structure (e.g. a vegetative type).

The separability statistics of the $JM \geq 1.9$ image is given in Table 39, where the minimum distance (between the class 8 blue and class 13 light green regions) are highly separable at $JM = 1.9783$. However, the blue class only accounts for 2.83% of pixels. A small number of pixels (e.g. red, yellow, blue, dark green and magenta) occur in between the dominating large light green coloured region.

class 8 & class 13: 1.9783
class 1 & class 8: 1.9845

Table 39: Separability report for the k-means 15 class (50 iterations) classifier where $JM \geq 1.9$ for the 15 PC band N_Rad_VI_VI dataset.

Note: 1) only values for $JM < 1.99$ are shown, 2) the relationship between individual class numbers and class colours (for Figure 134) are omitted, 3) JM distances are given in order of increasing JM distances, 4) JM distances are rounded to 4 d.p..

Table 40 shows the proportion (in %) of class pixels occupied by each class for each of the thematic maps from Figure 132 to Figure 134.

The $JM \geq 1.7$ table (defined in Table 40) shows that class 3 (6.97%) was merged with class 4 (7.73%) and renamed to class 4 (6.97% + 7.73% = 14.70% corresponding to the class 4 entry in the $JM \geq 1.8$ table). An attempt was made to define a consistent class colour scheme. In the preceding example, for the $JM \geq 1.7$ table, class 3 is coloured yellow and class 4 as blueish green. The merging of these two

JM 1.7

class	Npts	% of class total	class colour
1	193191	0.75	red
2	415718	1.61	purple
3	1798472	6.97	yellow
4	1995096	7.73	blueish green
8	730991	2.83	blue
11	9176824	35.55	green
12	4830232	18.71	dark green
13	6126043	23.73	maroon
14	475990	1.84	light green ²⁴
15	71694	0.28	magenta

JM 1.8

class	Npts	% of class total	class colour
1	193191	0.75	red ²⁵
2	415718	1.61	yellow ²⁵
4	3793568	14.70	blueish green
8	730991	2.83	blue ²⁵
12	14007056	54.26	dark green
13	6126043	23.73	maroon
14	475990	1.84	light green
15	71694	0.28	magenta ²⁵ (red on Figure 163)

JM 1.9

class	Npts	% of class total	class colour
1	193191	0.75	red
2	415718	1.61	yellow
8	730991	2.83	blue
13	23926667	92.69	light green
14	475990	1.84	dark green
15	71694	0.28	magenta

Table 40: Proportions of each class (in %) occupying the final thematic maps of Figure 132 (for JM \geq 1.7), Figure 133 (for JM \geq 1.8) and Figure 134 (for JM \geq 1.9). The class colours were defined using ENVI.

classes results in a class 4 blueish green colour in the JM \geq 1.8 table (in Table 40).

Therefore, it is possible to follow through (to a certain degree) the merging of

²⁴ Class 14 is coloured thistle in Figure 162 (right image), p.362 of Section 4.6.4.

²⁵ Classes 1, 2, 8 & 15 are all coloured red in Figure 161 (right image, p. 361) and Figure 163 (right image, p. 363) of Section 4.6.4. The reasons are made clear in Section 4.5.11.2.

classes between one thematic map and another (in the direction of increasing JM distance; from $JM \geq 1.7$ to $JM \geq 1.8$ to $JM \geq 1.9$).

Although difficult to assert from Figure 132 and Figure 133, a well-defined coherent class structure on Finucane Island is located amongst the mangrove forests, as shown more clearly in Figure 135. The structure exists at low to moderate probabilities but is absent at $JM \geq 1.9$, indicating the structure is not present to a high degree of confidence. This reaffirms that the level of class detail decreases as the probability of class-pair separability increases, as expected.

This particular spatial structure (on Finucane Island) was also present in the thematic map for the PHPA_Ref_VI image (see Figure 99, p. 247 of Section 4.5.7) but only at $JM \geq 1.7$. Although the N_Rad_VI_VI image still retains the structure at $JM \geq 1.8$ (i.e. at a higher level of probability), no such structure exists on the PHPA_Ref_VI thematic map as there is no such map. Further discussion concerning the class structure is found in Appendix P.4.

While the classification above used the whole N_Rad_VI_VI spectral range (400.7 - 984.5 nm), many of these are particularly noisy as detailed in Section 4.5.9.6. Appendix P.7 shows the classification for the N_Rad_VI_VI_subset image, where wavelengths span the range 400.7 – 733.1 nm. The differences between these two images are summarised in Table 41.

	N_Rad_VI_VI	N_Rad_VI_VI_subset
PC Bands ²⁶	15	6
$JM \geq 1.7$	10	6
$JM \geq 1.8$	6	4
$JM \geq 1.9$	5	3

Table 41: Comparison between N_Rad_VI_VI and N_Rad_VI_VI_subset

For example, for the N_Rad_VI_VI image, the number of PC bands (after PCA) is 15, of which 10 were separable to a JM distance of (at least) 1.7. Overall, Appendix P.7

²⁶ The “PC Bands” entry is the result when using the 99% cumulative variance threshold method. The table also shows the number of classes corresponding to the JM distances separabilities. For example, 6 classes for N_Rad_VI_VI_subset at $JM \geq 1.7$.

shows the N_Rad_VI_VI_subset thematic map as being inferior to that as produced using the full spectral range (i.e. N_Rad_VI_VI).

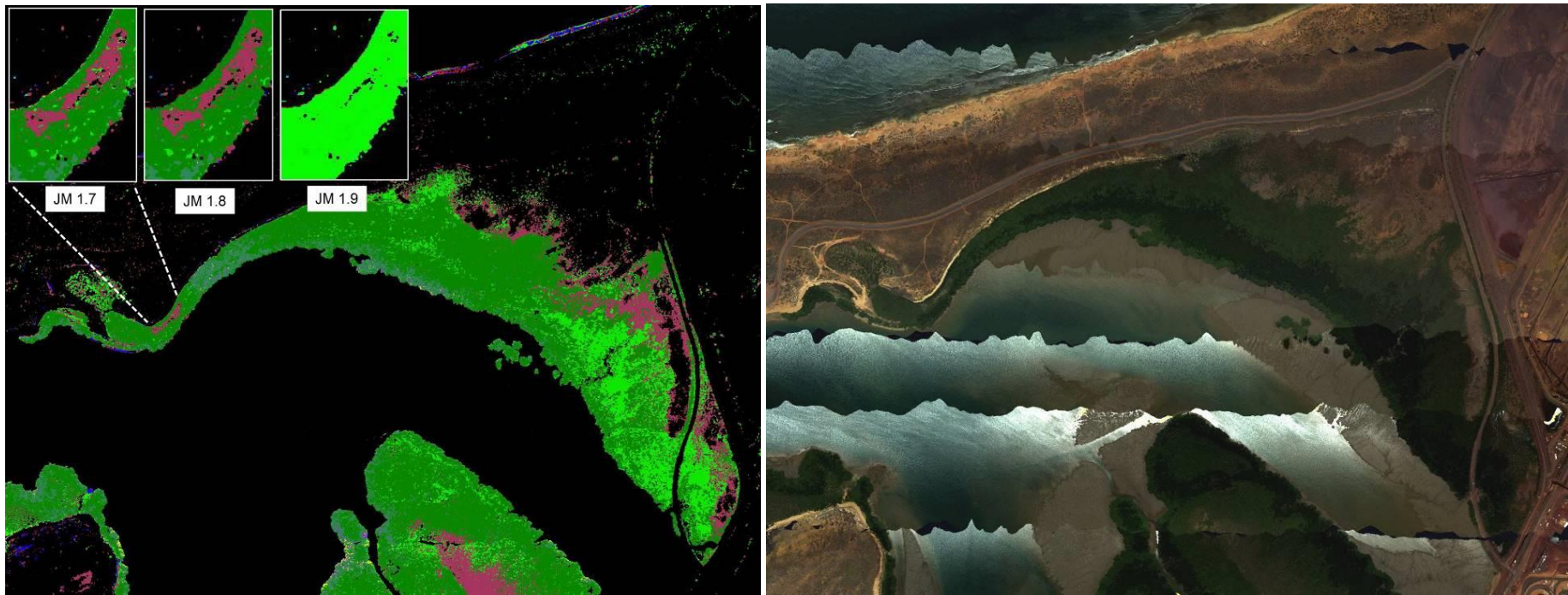


Figure 135: The left image shows the existence of a distinct class amongst the mangrove forests over Finucane Island, to a moderate degree of confidence ($JM \geq 1.8$). The top left corner of the left image shows a magnified view of this region. The class does not appear at the $JM \geq 1.9$ distance. The right image shows the true colour image corresponding to the left image. The left image used a post-classification median filter (3x3) to smooth out local variations.

4.5.11.2 Analysis of Thematic Map

It is of interest to examine the spectral differences between the classes in the $JM \geq 1.8$ N_Rad_VI_VI thematic map (i.e. Figure 133, p. 310 of Section 4.5.11.1). This map is hereforth also referred to as the JM18 map. Similarly, the JM17 map refers to the $JM \geq 1.7$ N_Rad_VI_VI thematic map - Figure 132, p. 309 of of Section 4.5.11.1). Note that this whole section is dedicated toward analysing the JM18 map. Statistically, the classes are spectrally separable to moderate degree of confidence. This map was therefore selected as the basis to identify the physical composition of vegetation during a second field trip (Section 4.6.1).

Table 40 (the JM 1.8 table) shows only small proportions for four of the classes: class 1 (< 1% of class total), class 2 (2%), class 8 (3%) and class 15 (< 1%). Figure 136 displays the normalised radiance mean spectra for each of these four classes.

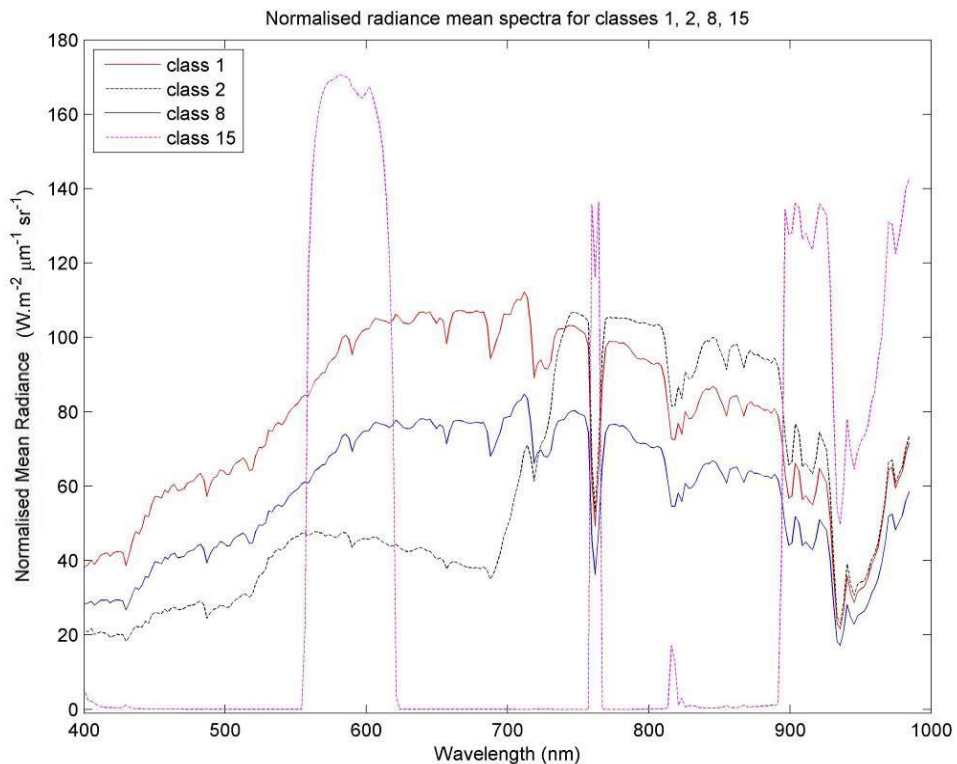


Figure 136: Normalised radiance mean spectra for classes 1, 2, 8 and 15 (corresponding to the $JM \geq 1.8$ N_Rad_VI_VI thematic map of Figure 133, p. 310).

Figure 136 shows that class 2 exhibits a strong red-edge indicative of vegetation, while the red-edge is weak for classes 1 and 8. Moreover, the spectra for both classes 1 and 8 are similar but with class 1 being brighter than class 8.

Although the spectrum has units of normalised radiance, the data is fundamentally derived from a radiance-based image. The contention is whether the red-edge is observable in a radiance spectrum, as the literature defines the red-edge in terms of reflectance data. However, the NDVI exploits the red-edge property of vegetation and may use either reflectance or radiance units (as highlighted by Jackson and Huete (1991) and discussed in Section 2.6.2.1). However, there is another caveat. The radiance unit relies on calibration coefficients to convert from raw data, which are wavelength dependent (due to atmospheric scattering – see Section 2.3.3 and Appendix 0). Therefore, if the calibration coefficients are equal for the wavelengths defined in the NDVI, the ratio will be equal to that as used by the reflectance. In practice, these calibration coefficients are rarely equal (Jackson & Huete, 1991). However, the supposition made here is that, although the individual radiances over the red-edge are likely to be incorrect (due to atmospheric absorption), the overall red-edge is still an observable characteristic in a radiance spectrum despite atmospheric absorption at 760 nm (due to oxygen). Figure 137 clearly shows the red-edge in the reflectance spectrum, which is also clearly observable in the radiance spectrum of Figure 138.

The normalised radiance mean spectrum for class 15 is clearly non-vegetative. Unfortunately, the spike at around the 750 nm has ‘tricked’ the mean-gradient algorithm into passing it of as a vegetation spectrum (Section 4.5.2). As a consequence, these spectral regions form part of the vegetative-mask (Figure 91, p. 234 of Section 4.5.6). The location of class 15 pixels places it directly amongst the salt ponds, as depicted in Figure 139. These non-vegetative pixels are of no interest to the thesis objectives. Therefore, class 15 is dismissed from any further work.

Figure 140 shows an example for the location of class 1 (in red colour), class 2 (in yellow) and class 8 (in blue).

The yellow coloured class regions occur over grassed areas, such as ovals and residential lawns. The red coloured class may represent a dried state of grass (i.e.

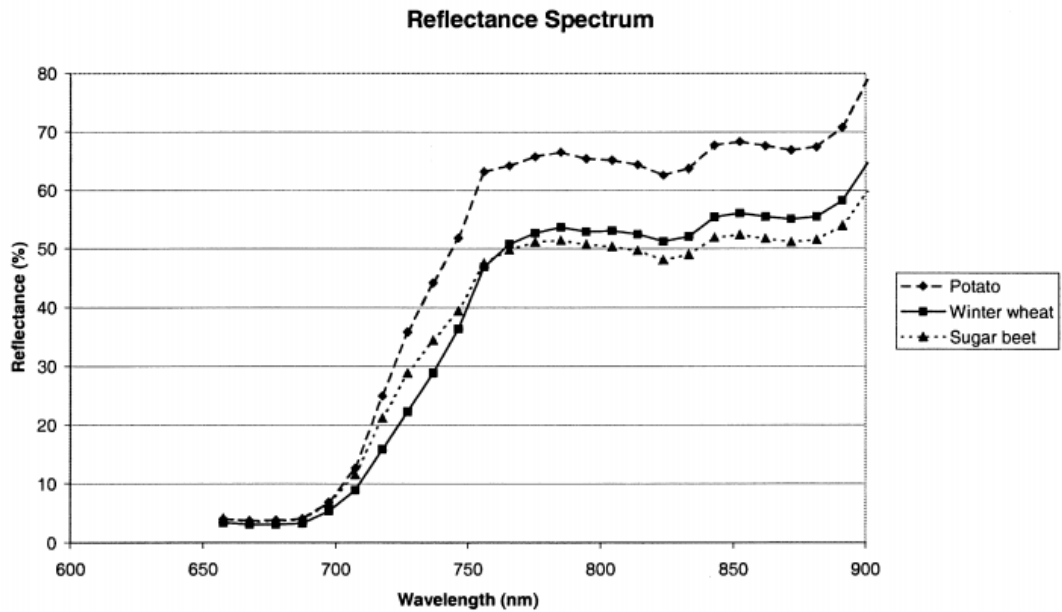


Figure 137: The red-edge is clearly evident in the reflectance spectrum. (figure taken from F. D. Van Der Meer, De Jong, S. M. (2001), figure 23 p. 192).

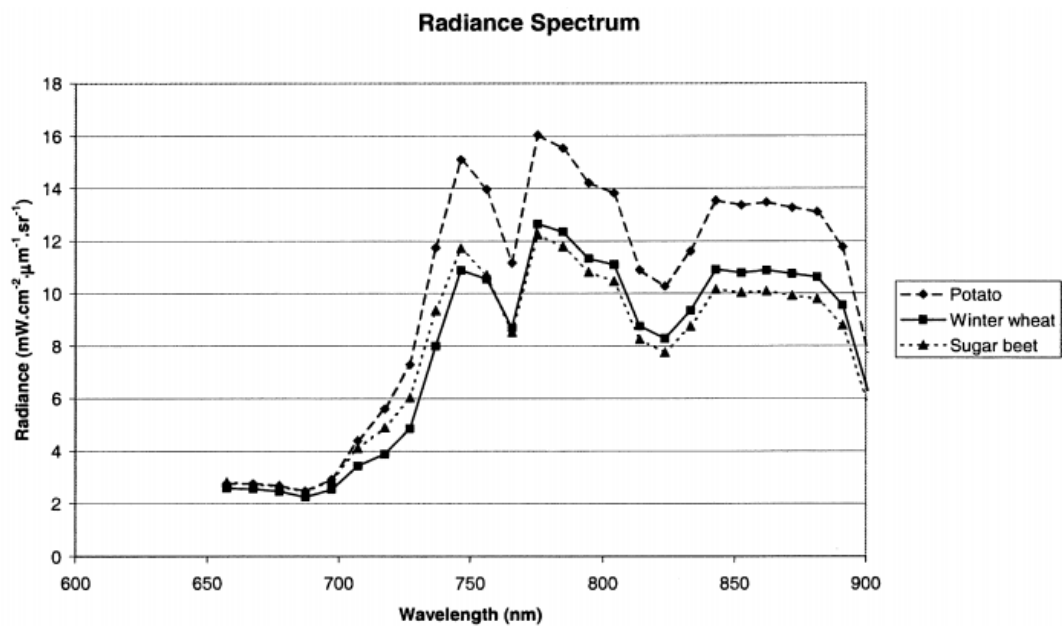


Figure 138: The red-edge is also well defined in the radiance spectrum corresponding to Figure 137. (figure taken from F. D. Van Der Meer, De Jong, S. M. (2001), figure 22 p. 191).

turning brown) or grass surrounded by soil (i.e. mixed pixels of vegetation and soil spectra). The blue coloured class appears even more affected by soil and is less-

bright than the vegetation for class 1 (consistent with observations from Figure 136).

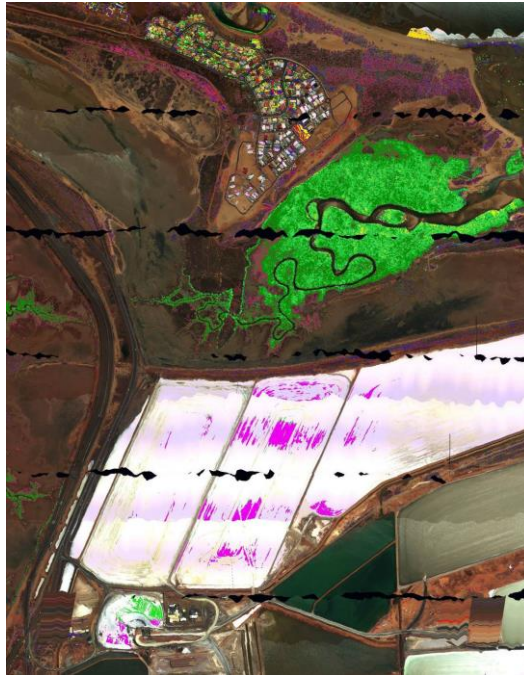


Figure 139: Location of class 15 (represented in magenta colour) pixels lie amongst the salt pond regions (to the south of Pretty Pool).



Figure 140: The left image shows classes 1 (red), 2 (yellow) and 8 (blue) (from Figure 133, p. 310 - where $JM \geq 1.8$) superimposed onto a true colour image of Port Hedland. The right image shows the same region but without the superimposed classes.

It should be noted that not all the red class areas represent grass. One such area is depicted in Figure 141 (left image), geographically located (roughly) toward the

centre (horizontally) of the Port Hedland urban settlement. The plot displayed in Figure 141 (right figure) shows an example spectrum corresponding to the red coloured class of Figure 141 (left image).

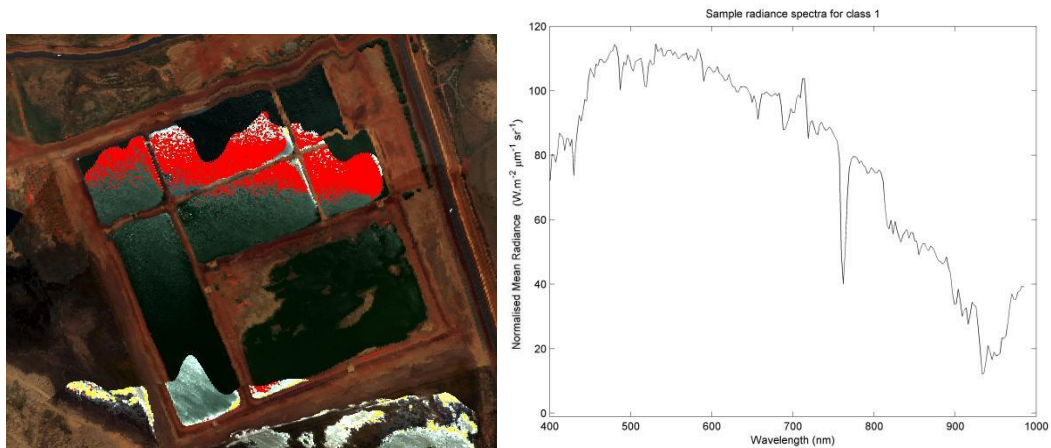


Figure 141: Class 1 (red colour) also occurs in water (left image). The spectrum is not reminiscent of vegetation, as shown in the right figure.

The four classes (i.e. 1, 2, 8 and 15) are clearly not mangroves and not of interest to the objectives of this thesis. In fact, the four classes are combined into one red superclass, as given in the final JM18 map; Figure 161 (right image) and Figure 163 (right image) of Section 4.6.4. These four classes are also separable at $JM \geq 1.7$ and are identical to those at $JM \geq 1.8$ (see Table 40). Therefore, this red superclass also exists in the JM17 map displayed in Figure 174, p. 381 of Section 4.6.6. These four classes comprise a total of about 5% of pixels.

That leaves classes 4, 12, 13 and 14, which appear vegetative in nature (see Figure 142).

The JM distance between classes 4 & 12 is lowest at 1.8252 (from Table 38 (p. 312 of Section 4.5.11.1) and duplicated in Table 42) while classes 13 & 14 have a JM distance of 1.9846. The SAs are 0.12 rad and 0.16 rad, respectively between the class pairs (as shown in Table 42). Both JM distances and SAs show a low degree of similarity between classes 13 & 14. The highest proportion of classes belong to class 12 (with 54%) and class 13 (with 24%). The JM distance between classes 13 & 14 shows they are spectrally well separated (1.8421) with a SA of 0.22 rad. It should be noted that the JM distance is a higher order statistic and incorporates the spread

of data, while the SA does not as it is a first order statistic. Therefore, a low JM distance between a pair of classes does not necessarily mean the SA is lower than that for high JM distance. This situation is observed from Table 42.

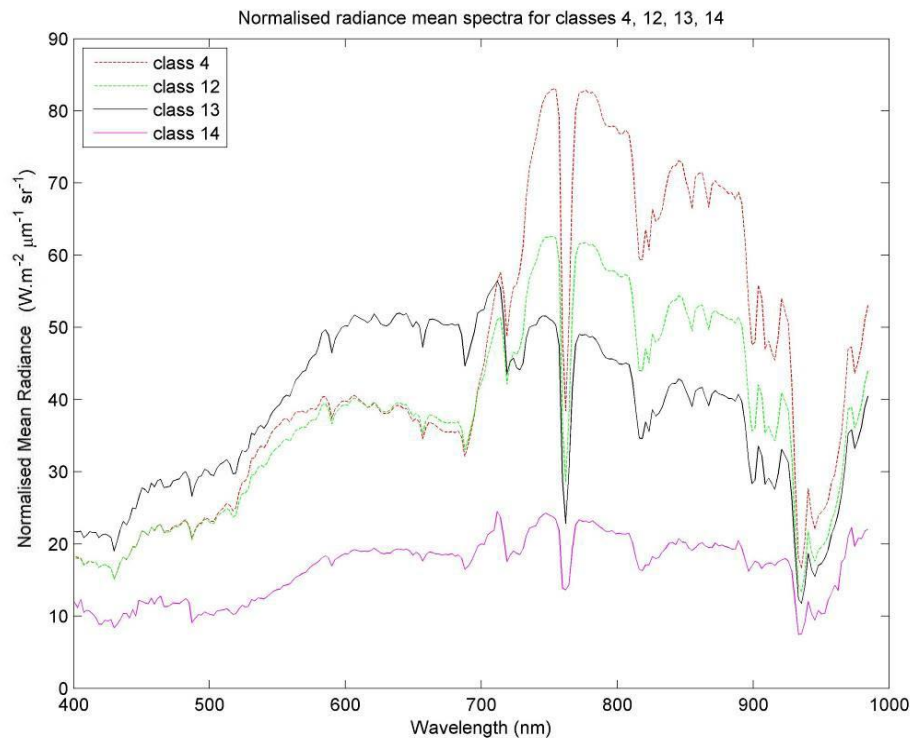


Figure 142: Normalised radiance mean spectra for classes 4, 12, 13 and 14 (corresponding to the $JM \geq 1.8$ N_Rad_VI_VI thematic map of Figure 133, p. 310).

class pairs	SAM (rad)	JM
4 & 12	0.12	1.8252
13 & 12	0.22	1.8421
8 & 13	0.03	1.9642
1 & 8	0.04	1.9845
14 & 13	0.16	1.9846

Table 42: Both JM and spectral angles are given between class pairs corresponding to the $JM \geq 1.8$ N_Rad_VI_VI thematic map of Figure 133 (p. 310 of Section 4.5.11.1). Note the ascending order for the JM distance, starting with the smallest value for the top entry. The corresponding SA column does not follow an increasing angle with a corresponding increase in JM distance. Note: only JM distances < 1.99 are displayed in this table.

Table 43 shows all possible SAs between the vegetative classes corresponding to Figure 142.

class	4	12	13	14
4	-	0.12	0.35	0.24
12		-	0.22	0.14
13			-	0.16
14				-

Table 43: All SA pairs are shown for classes 4, 12, 13 and 14. All angles are in radians.

The key point is that the smallest SA is 0.12 rad between classes 4 & 12, which is larger than the majority of angles between mangrove species (see Table 68, p. 497, Appendix G.3). The largest SA is 0.13 ± 0.04 rad, between *Osbornia octodonta* and *Ceriops australis*, as detailed in Section 4.4.2.²⁷ The smallest SA of 0.12 rad falls within the limits of the largest SA of 0.13 ± 0.04 rad, showing that the thematic classes are not able to represent mangroves at species level.

These SAs were derived from ASD reflectance data (at ground level). The thematic map discussed in this section was derived from normalised radiance-based data (i.e. N_Rad_VI_VI). The assumption is that SAs between ASD and the airborne image are compatible. So, the SA of 0.13 ± 0.04 rad, between *Osbornia octodonta* and *Ceriops australis* is assumed to be the same regardless of the data source.

Atmospheric correction attempts to produce an ‘ideal’ spectrum, so spectra are able to be compared, independent of the recorded source. In reality, even the ASD recorded spectra are subject to uncertainty (e.g. atmospheric, adjacency effects, instrumental noise due to temperature), even by ignoring natural variability in the target (e.g. vegetation). The situation is even worse when SAs are compared to radiance data, especially normalised radiance which incorporates a spectral brightness shift in addition to the atmospheric effects already in place for radiance data. The wavelength dependence for the BRDF means different changes made to a particular spectrum based on wavelength. This changes the SA – the SA is invariant with respect to brightness only if the whole spectrum is shifted (not just

²⁷ Note: The SAs in Table 68 cover all mangroves. The ‘non-typical’ vegetative spectral samples are excluded in this section, with reasons briefly provided in Section 4.4.2 and more fully in Appendix G.3).

brightnesses at particular wavelengths). Further details are given in Appendix Q regarding atmospheric effects.

The point is that the SAs between class types are possibly larger than those implied for the normalised image. So, the smallest SA of 0.12 rad between classes 4 & 12 is likely to be larger in a relative manner. That is, it is even more likely that the classes do not represent mangroves at species level.

A particular class may indeed represent a group of spectrally similar mangroves. Indeed this is rather expected, as the vegetative-mask eliminated 'weak' vegetation. However, as the SAs between the mangrove species are too small, the classifier is unable to differentiate between them, thereby placing several species into broader categories.

The physical interpretation to these 4 key classes (4, 12, 13, 14) are left until Section 4.6.3, which relies on data collected during the second field trip.

4.5.11.3 Summary and Discussion

Classification aimed to produce thematic maps at three levels of confidence; low, medium and high, using JM distance thresholds of 1.7, 1.8 and 1.9, respectively. For the N_Rad_VI_VI image, the lowest confidence map (at $JM \geq 1.7$) contains 10 classes. At medium confidence ($JM \geq 1.8$), 8 classes exist in the thematic map, while at high confidence, only 6 distinct classes exist dominated by one occupying 93% of the image.

The thematic map (Figure 128) corresponding to the N_Rad_VI_VI image contains spatially consistent class structures, which the PHPA_Ref_VI thematic map did not have (Figure 96, p. 240 of Section 4.5.7). The normalisation process has removed class spectral inconsistencies, which were particularly evident previously.

As outlined in Section 4.5.9.5, a total of seven normalised images were created (four reflectance-based and three radiance-based). The details behind constructing those images are provided in Appendix L.

Table 45 (displayed at the end of this section) contains a summary for the classification outcome for each image classified. It shows the image used in the classification process, along with the section/appendix which contains the details.

Furthermore, the Table 45 presents the number of PC bands that were retained to meet the 99% cumulative variance threshold, the unsupervised classification method used and the number of spectrally distinct classes, based on JM distances. The headings describe the classification scheme used, with JM distances directly below. For instance, the numbers beneath JM1.7 indicate the number of classes separable with at minimum JM distance of 1.7. As an example, consider the classification details for the PHPA_Ref_VI image. Directly beside the image name is the section/appendix location – in this case “Section 4.5.7”. All the technical details and result related to classification for this image, is located there. The PC column indicates that PCA produced a 9 PC band image for classification, using a cumulative variance of 99%. For the k-means classifier, 5 classes were spectrally separable at a JM distance of at least 1.7. For the ISODATA unsupervised classifier with 10 classes, just 6 were separable with $JM \geq 1.7$. There is no result in the JM1.8 column, as the merging of the lowest two classes resulted in all remaining five classes being separable to at least $JM = 1.9$.

It is interesting to compare the amount of spatial classification detail with the number of PC bands (in Table 45), as the retaining of more PC bands produced higher quality thematic maps. This means that the maps contained additional useful information content. However, the PHPA_Ref_VI_VI image contains inconsistent data and although PCA required 10 PC bands, it produced poor results. This shows that PCA is dependent on the consistency of data. However, overall, the more PC bands, the higher the useful information content in the thematic map. As an example of poor spatial information content, the thematic map for N_Rad_Land_VI where $JM \geq 1.9$ (i.e. Figure 329, p. 688 of Appendix P.4) displays limited class structures over mangrove forested regions, but used 11 PC bands. The N_Rad_VI_VI retained the highest number of PC bands out of all databases examined – a total of 15 PC bands. The resulting thematic maps are rich in detail, particularly Figure 132 (where classes are separable to at least JM 1.7), compared to other maps. This is not be altogether surprising, as having more PC bands captures more spectral variance in the image. Therefore, there is less correlation (i.e. more variability) between the bands in the N_Rad_VI_VI image compared to the others; a spectrally deeper structure is therefore contained in the image. It is not difficult to imagine

the effect of classifying a very highly correlated dataset, leaving just one PC band, where little useful information is expected to be extracted in the data mining process. Spectral analysis (Appendix N) predicted that the N_Rad_VI_VI image would produce the best thematic mapping results, based on the consistency of spectral sample regions.

It was remarked in Appendix L.6 that the R & IR bands for the N_Rad_Land image were highly correlated (see Figure 276). The normalised plot based on the vegetative-mask (i.e. N_Ref_VI (Figure 270, Appendix L.5) and N_Rad_VI (Figure 111, p. 270 of Section 4.5.9.2)) exhibits less correlation, and is expected to impact the PC transform and ultimately classification results. Table 45 shows that the number of PC bands retained is higher for images based on the vegetative-based mask compared to the land-mask; for example, 9 PC bands for the N_Ref_Land_VI compared to 10 for N_Ref_VI_VI. The difference is more pronounced between N_Rad_Land_VI and N_Rad_VI_VI, where the number of PC bands are 11 and 15, respectively. Also, radiance-based images generally led to more PC bands than corresponding reflectance-based images (e.g. N_Rad_Land_VI compared to N_Ref_Land_VI); the only exception being the N_Ref_Res_VI_VI image compared to N_Rad_Res_VI_VI. For highly correlated data, the number of PC components retained is less than for lowly-correlated data. The results are as expected.

Although it appears as though the thematic map reveals more structure with an increase in the number of PC bands, this is true up to a point. Due to the Hughes effect, there is in fact an optimal number of PC bands to give the highest classification accuracy. Beyond this optimal number (either lower or higher), classification accuracy actually drops (Ma, Gong, Hu, Meng, & Xu, 2013).

Table 45 also shows a colour scheme, where cells are coloured green yellow or pink. This is used to categorise the visual appearance/quality of the map. For example, for a highly confident map, mangroves tend to fall under one class ($JM \geq 1.9$). However, the information content is low, as it is a map that simply states where vegetation is located. For a lower confident product (e.g. $JM \geq 1.7$), the classes are less separable, but their smaller spectral differences define new regions. These may reveal new spatial structures amongst the mangrove forests. A three level colour scheme was used to summarise the level of detail apparent in the

thematic maps (green, yellow or pink). Those exhibiting a higher class structural content were considered excellent (a green colour). In practical terms, Figure 100 (p. 248 of Section 4.5.7) shows a lack in detail, and is therefore considered 'poor', as virtually the whole map contains just one class structure. The associated cell in Table 45 is therefore shaded pink. However, limited class structures exist amongst the mangrove forests in Figure 98 (p. 246 of Section 4.5.7), so it is considered 'good'. An excellent map is found in Figure 132 (p. 309 of Section 4.5.11.1), defining multiple and highly detailed class structures over the mangrove forests. Note that, even if the 10 classes of Figure 96, p. 240 (of Section 4.5.7) were separable (to at least $JM = 1.7$), the map would be rated as 'poor', as the class structures are not consistent. Table 45 shows the radiance-based normalised images produced the most detailed thematic maps.

The blank entries in Table 45 indicate the absence of classification. For example, for the PHPA_Ref_VI image, no attempt was made to produce a thematic map based on a k-means 15 class classifier. The reason for this, is that no improved thematic map was expected over that as produced by the k-means 10 class map. Already for the 10 class map, several classes had to be merged to form a low confidence map (i.e. 5 classes were left from the 10 for a minimum JM distance of 1.7). Maps produced by ISODATA classification, were also, generally, very similar to those produced through k-means. Therefore, only a select few ISODATA thematic maps were produced.

Although not having been discussed thus far, a subsetted form of the PHPA_Rad_VI_VI image was also generated, on the basis of removing noisy spectral regions; wavelengths outside the 501 nm – 733.1 nm range were removed (further details appear in Appendix P.7). The PC transform resulted in a 6 PC band image for the subsetted PHPA_Rad_VI_VI_subset image, compared to 15 PC bands when using the full spectral range. A 15 class k-means classification produced a 7 class thematic map, having spectral separability at $JM \geq 1.7$. The gross spatial class structures over the mangrove forested regions more closely resemble those in the JM18 map (i.e. N_Rad_VI_VI using the full spectral range), although major differences exist over Finucane Island. In addition, the additional class structures from the JM17 map (N_Rad_VI_VI using the full spectral range) are absent.

Therefore, subsetting the data results in a thematic map where classes are less separated and with less spatial structures. The use of the full spectral data leads to a more confident product (i.e. higher class separability) containing more spatial structures.

Image	PCA	Unsupervised classification using k-means with 10 classes		
	PC bands 99%	JM1.7	JM1.8	JM1.9
PHPA_Ref_VI (Section 4.5.7)	9	5		4
N_Ref_NoMask_VI (Appendix P.1)	8			3
N_Ref_Land_VI (Appendix P.2)	9		5	4
N_Ref_VI_VI (Appendix P.3)	10	5		4
N_Rad_Land_VI (Appendix P.4)	11			6
N_Rad_VI_VI (Section 4.5.11.1)	15	10	6	5
N_Ref_Res_VI_VI (Appendix P.5)	9	5		4
N_Rad_Res_VI_VI (Appendix P.6)	7			3

Image	PCA	Unsupervised classification using k-means with 15 classes		
	PC bands 99%	JM1.7	JM1.8	JM1.9
PHPA_Ref_VI (Section 4.5.7)	9			
N_Ref_NoMask_VI (Appendix P.1)	8			
N_Ref_Land_VI (Appendix P.1)	9			
N_Ref_VI_VI (Appendix P.3)	10		7	5
N_Rad_Land_VI (Appendix P.4)	11	7		6
N_Rad_VI_VI (Section 4.5.11.1)	15	10	8	6
N_Ref_Res_VI_VI (Appendix P.5)	9	6	5	4
N_Rad_Res_VI_VI (Appendix P.6)	7		4	3

Table 44: Summary table characterising all k-means classification results.

Note: Results for the N_Rad_VI_VI subset are not shown but discussed in this section. Blank entries indicate that no classification was performed for that image.

Image	PCA	Unsupervised classification using ISODATA with 10 classes		
	PC bands 99%	JM1.7	JM1.8	JM1.9
PHPA_Ref_VI (Section 4.5.7)	9	6		5
N_Ref_NoMask_VI (Appendix P.1)	8			
N_Ref_Land_VI (Appendix P.1)	9			
N_Ref_VI_VI (Appendix P.3)	10			5
N_Rad_Land_VI (Appendix P.4)	11	6		5
N_Rad_VI_VI (Section 4.5.11.1)	15	8		6
N_Ref_Res_VI_VI (Appendix P.5)	9	6		5
N_Rad_Res_VI_VI (Appendix P.6)	7			3

Image	PCA	Unsupervised classification using ISODATA with 15 classes		
	PC bands 99%	JM1.7	JM1.8	JM1.9
PHPA_Ref_VI (Section 4.5.7)	9			
N_Ref_NoMask_VI (Appendix P.1)	8			
N_Ref_Land_VI (Appendix P.1)	9		6	5
N_Ref_VI_VI (Appendix P.3)	10	7		6
N_Rad_Land_VI (Appendix P.4)	11		7	6
N_Rad_VI_VI (Section 4.5.11.1)	15	11	8	7
N_Ref_Res_VI_VI (Appendix P.5)	9			
N_Rad_Res_VI_VI (Appendix P.6)	7			4

Table 45: Summary table characterising all ISODATA classification results.

Note: Results for the N_Rad_VI_VI subset are not shown but discussed in this section. Blank entries indicate that no classification was performed for that image.

4.6 Objective 3b: Thematic Map Interpretation and Validity

This Objective 3b is concerned with interpretation of the thematic map and comparing the results against known third party products.

Classification of the N_Rad_VI_VI image led to a thematic map (Figure 133, p. 310 of Section 4.5.11.1), having 8 separable classes with well-defined spatially coherent structures.

This Objective 3b interprets the classes defined in the thematic map of Figure 133, based on data obtained during a second field trip. Sections 4.6.1 to 4.6.3 is concerned with planning and interpreting the classes found on the thematic map.

In addition, Objective 3b is concerned with validating the integrity of the thematic map. The thematic map is compared to image products as produced previously by other sources (Section 4.6.4). Confidence in the integrity of the thematic map is gained if the gross structural spatial characteristics are in agreement with maps from the other sources (i.e. the between the thematic map of Section 4.5.11.1 and the literature).

4.6.1 Field Trip Planning

The unsupervised classification process has produced separable classes based on sound mathematical practices for the N_Rad_VI_VI thematic map. However, the interpretation of those classes requires field data. As such, it is necessary to examine the vegetative composition for each class. Access to sites were even more restrictive for the second field trip compared to the first. A plan was devised and sent to PHPA (in particular Nicole Wylie) for approval.

The planning stage had to take into account site accessibility, time and prioritisation for 'more important' vegetative cover types to be examined (some classes being more important to identify than others).

A total of 35 sites were deemed appropriate for closer inspection in the time available, which covered the period from the 21st - 24th September 2015. In

practice, some time was lost during the first and last days due to flights and accommodation arrangements.

At each site, the type of vegetation was recorded including estimates of the density and approximate height of vegetation. Density refers to the proximity of vegetation to each other and their height. For instance, the density is high for vegetation in close proximity with no gaps in-between (when viewed from above). In terms of pixels, the vegetation would form a continuum. Low density relates to dispersed shrubs, consisting of patches of soil in between individual shrubs. It should be noted that both density and vegetation heights were approximated, as no actual measurements were taken in a biological sense. The term density as applied here is expected to differ to that as defined in an ecological study.

It is important to consider the particular ground cover structure with respect to pixels. For example, consider nine pixels. Suppose one single pixel is filled exactly with a single shrub (i.e. a perfectly square-shaped shrub), while the remaining eight pixels each consists of soil. Each pixel thereby contains either vegetation or a soil spectrum – a binary outcome. In reality, this binary outcome is unlikely to occur. For instance, consider a group of four single pixels as shown in Figure 143. Suppose a single shrub lies in the centre of this group (indicated by the green colour), while the rest is comprised of soil (indicated by the yellow colour).

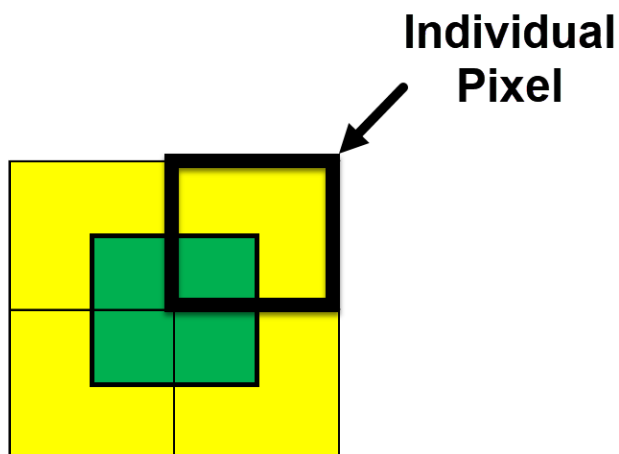


Figure 143: Mixed pixels

Each of the individual pixels is then comprised of a proportion of one quarter vegetation and three quarters soil. The spectrum of each individual pixel (shown in

a black outline) is thereby mixed, containing vegetation and soil. The soil spectrum reduces the red-edge of the vegetation, thereby making it appear less defined. Due to this factor, the density of vegetation must be recorded in field work.

Any visible signs of stress were also noted but it must be highlighted that no scientific instrumental data were recorded to quantify vegetative stress in any manner. Nor were biologists present to assist in making this assessment. From a spectral viewpoint, the visible appearance of salt on leaves causes a shift in the red-edge position. However, it does not mean the vegetation is under stress in a biological sense. For mangroves, these salt deposits are part of a natural process (American Museum of Natural History, n.d.).

Digital photographs were also recorded at each site, for future reference. Each photograph also stored the GPS location (i.e. the location is stored in each photo) of the shot location.

The following maps (Figure 144 to Figure 147) identify the chosen field sites and obtained by overlaying the thematic map onto the Port Hedland true colour image. The $JM \geq 1.8$ thematic map (Figure 133, p. 310 of Section 4.5.11.1) was selected for the planning stage, as the classes exist to a moderate degree of confidence. Physical and legal accessibility in addition to health and safety regulations were factored into the planning stage prior to approval by Nicole Wylie.

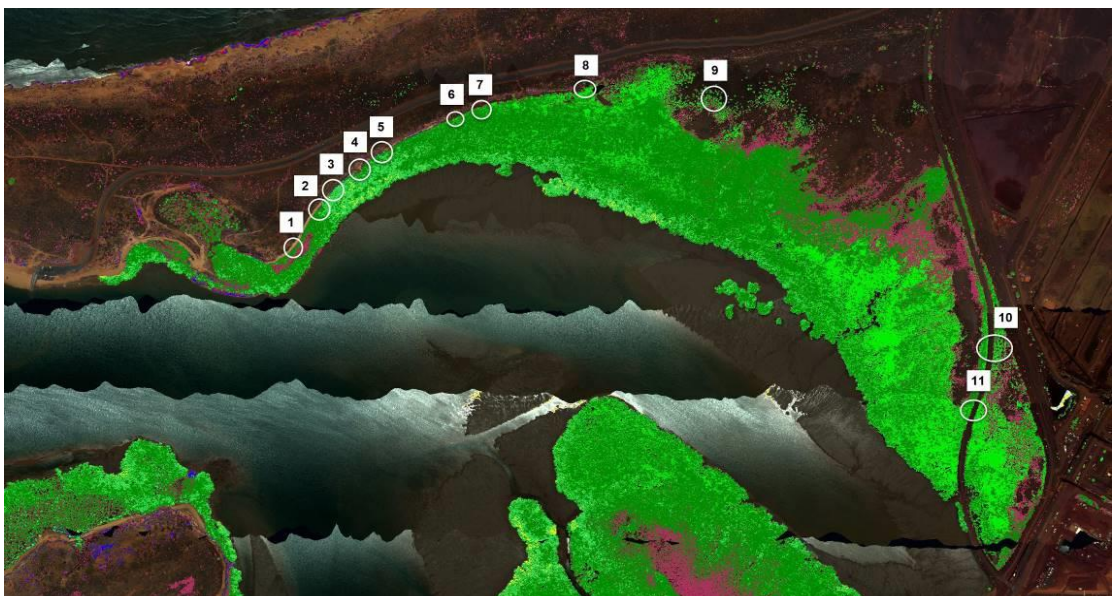


Figure 144: Field sites selected on Finucane Island using the $JM \geq 1.8$ thematic map (Figure 133, p. 310 of Section 4.5.11.1).

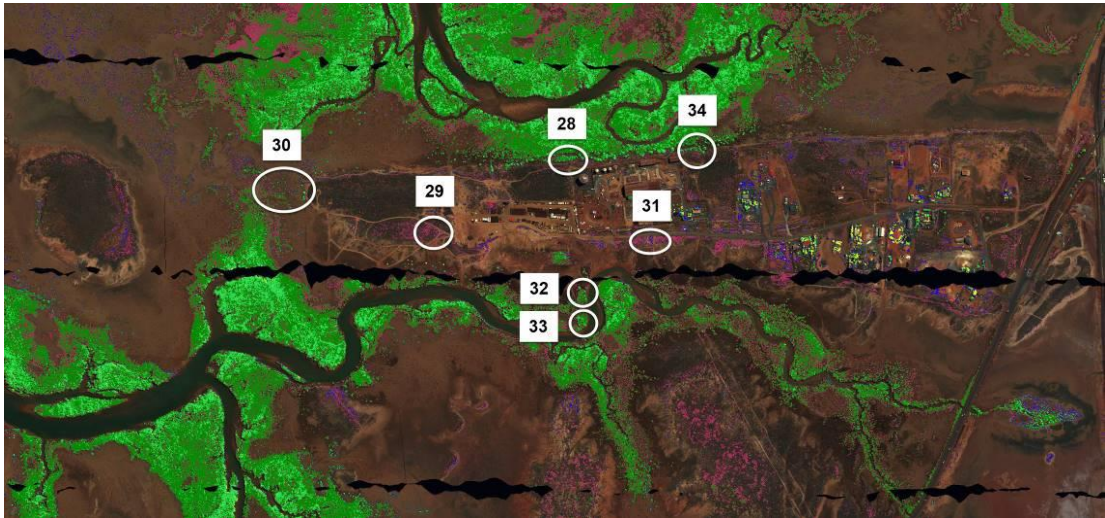


Figure 145: Field sites selected at Redbank using the $JM \geq 1.8$ thematic map (Figure 133, p. 310 of Section 4.5.11.1).

The planning phase also incorporated GPS coordinates for each planned site, in order to minimise the locational uncertainty between thematic class location and field location during the ground work. The use of a handheld GPS measuring device assisted in correctly locating (within uncertainty) a field site for data collection.



Figure 146: Carefully identifying and spectrally recording a mangrove. The tablet contains the thematic map, allowing for careful in-situ comparison with ground vegetation. The clipboard contains the GPS coordinates for each site and log sheets to record the results.

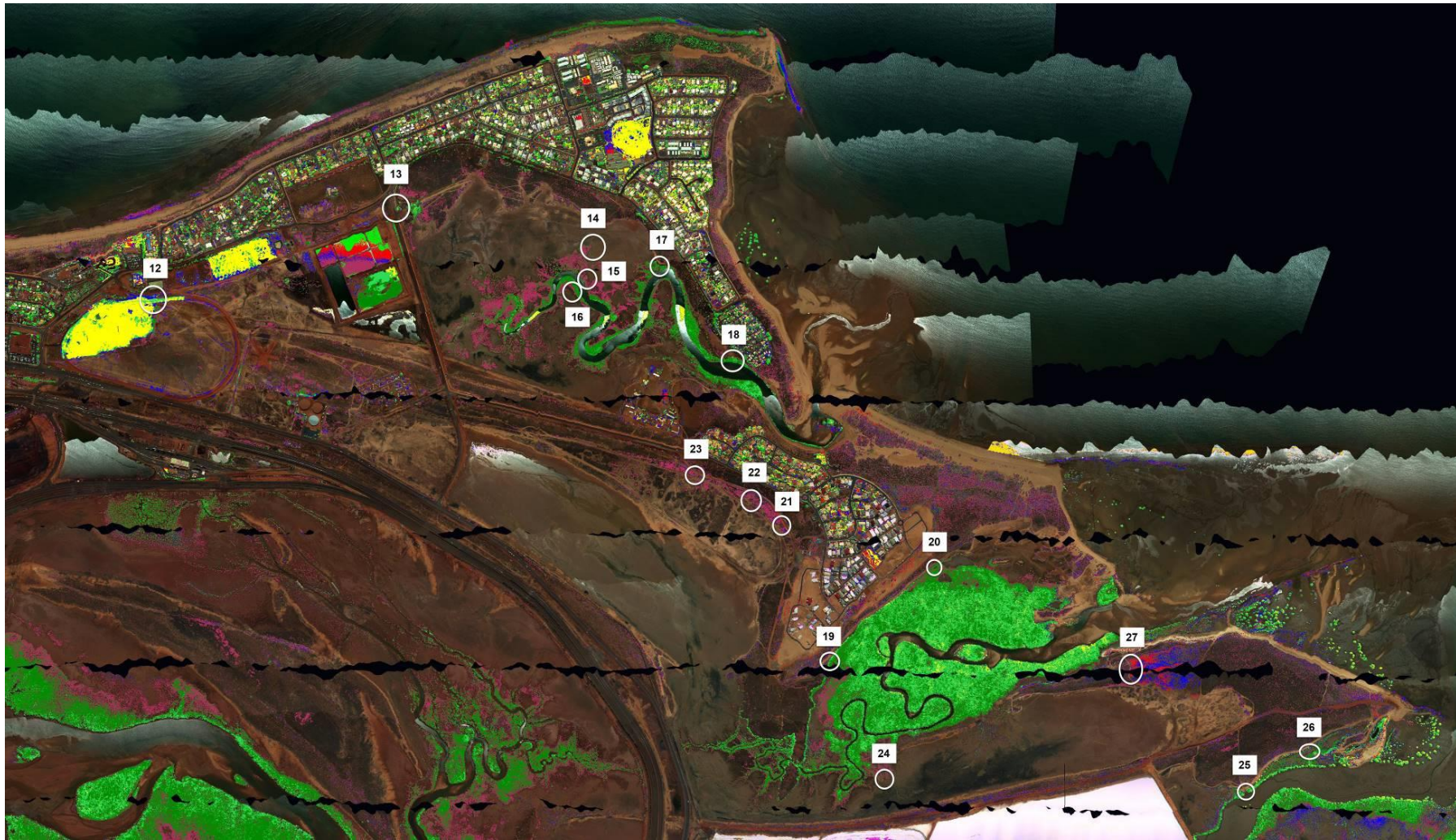


Figure 147: Field sites selected in the Port Hedland coastal region using the $JM \geq 1.8$ thematic map (Figure 133, p. 310 of Section 4.5.11.1).

As far as the field trip was concerned, the major factors influencing vegetative spectra include:

- density of vegetation (e.g. tightly or loosely packed)
- visual assessment of vegetative height (e.g. tall or short).
- visual assessment of dust and/or salt on the leaves
- presence of flowering
- water content (e.g. dried out leaves or luscious green leaves)

These details were carefully recorded to assist with the deciphering of information conveyed in the thematic classes.

4.6.2 Field Work Results

Rather than having to record the full name for each mangrove, the following abbreviations were used in the field.

Abbreviation	Mangrove species
AM	<i>Avicennia marina</i>
CA	<i>Ceriops australis</i>
RS	<i>Rhizophora stylosa</i>
BE	<i>Bruguiera exaristata</i>
OO	<i>Osbornia octodonta</i>
AA	<i>Aegialitis annulata</i>
AC	<i>Aegiceras corniculatum</i>

Table 46: Mangrove abbreviations used in-field.

Numerous sites, with particular emphasis on the ones labelled in Figure 144 to Figure 145 were visited and photographed. No spectral samples were taken (which was done in the first field trip). Visual assessment for each site was noted, as illustrated in Table 47.

Consider two examples having the descriptions given in Table 47. Site 3 states “CA & AM on edge with AM further in”. Therefore CA (*Ceriops australis*) and AM (*Avicennia marina*) were found on the outer edge of the mangrove forest with AM (mostly) further in (i.e. away from the immediate edge). A photo is supplied in Figure 148. The edge marks the transition ‘boundary’ between mangrove forests and grassland (i.e. where the PhD candidate is standing)

At another location (site 34), the description is “mixed ~60% AM, 40% CA” describes a region consisting of a mixed population of mangroves, having roughly 60% AM and 40% CA. A photo is shown in Figure 153.

Estimates of populations were performed visually and are rough estimates.

class location	photo id	vegetation present
1	571-576	CA & AM mixture (~50% each).
2	577-586	50% CA & AM on edge with AM further in
3	587-598	15% CA & AM on edge with AM further in
4	599-605	15% CA & AM on edge with AM further in
5	606-608	CA & AM on edge with AM further in
6	609-613	25% CA & AM on edge with AM further in
7	614-617	15% CA & AM on edge with AM further in
8	618-624	15% CA & AM on edge with AM further in
8	625-626	AM single tree
9	627-637	Odd CA. Mostly AM. Brown grass. Sand.
10	638-645	AM
11	646-649	AM
12	650-651	green grass
13	652-657	Oleander tree
14	658-666	small shrubs of AM
15	667-671	area contains ~40% CA ~60% AM with sand between
16	672-675	area contains ~40% CA ~50% AM ~10% RS
17	676-682	small shrubs of ~95% AM (odd CA between).
17		RS on water's edge opposite bank
18	683-694	area contains ~10% CA ~90% AM mixed small shrub of mangroves
18		10% CA 80% AM 10% RS small shrubs of mangroves
19	695-705	100% AM (brown grass at edge)
20	706-711	100% AM
21	712-716	brown grass
22	717-719	brown grass
23	720-724	brown grass
24	725-743	100% AM less dense small shrubs. Sand between.
25	744-765	mixed 15% CA 85% AM
26	766-775	100% AM less dense small shrubs. Sand between.
27	776-790	dense greyish small shrubs
27		small dense shrub patches?
27		small green shrubs
28	794-803	~70% AM with ~30% CA mostly mixed.
29	804-813	brown grass
30	814-828	sparse small 100% AM. Sand between.
31	829-839	brown grass
32	848	mixed ~55% AM, 45% CA.
33	870	100% CA colony and 100% AM colony further 'down'
34	853-862	mixed ~60% AM, 40% CA.
35	863-869	brown grass

Table 47: Example of recording field trip results.

4.6.3 Field Interpretation of Thematic Classes

The results of the field trip were analysed systematically to provide a meaningful interpretation to the classes displayed in the thematic map (i.e. Figure 133 for $JM \geq 1.8$ (p. 310 of Section 4.5.11.1)), with particular emphasis to classes 4, 12, 13, 14 identified in Section 4.5.11.2.

After careful and detailed analysis of the field data with the thematic map, the conclusions are summarised in Table 48.

class	% of class total	Map colour	Interpretation
4	15	blueish green	High density tall (over 3 m) mangroves.
12	54	dark green	High density medium height (1 m to 3 m) mangroves.
13	24	maroon	Medium density low height (around 1 m) mangrove shrub and low density dwarf mangrove shrub (around 0.25 m). Mostly <i>Avicennia marina</i> .
14	2	light green ²⁸	High density mangroves (probably <i>Rhizophora Stylosa</i>).

Table 48: Summary of interpretation for the classes of the $JM \geq 1.8$ N_Rad_VI_VI thematic map (i.e. Figure 133, p. 310 of Section 4.5.11.1).

In this table, the “map colour” column refers to the map colour in Figure 133 (p. 310 of Section 4.5.11.1), while the “% of class total” column describes the total population occupied by the particular class in the map; this total does not include masked (i.e. black) pixels.

The rest of this section discusses the evidence for the class interpretations presented in Table 48.

²⁸ The colour is “thistle” on the JM17 map (Figure 162, p. 362 (right image)).

Class 4: High density tall (over 3 m) mangroves (map colour: blueish green)

The photographs illustrated in Figure 148 and Figure 149 are located at sites 3 and 4 respectively (the sites are labelled on Figure 144 (p. 334 of Section 4.6.1) and are located on Finucane Island). The thematic map shows class 4 at site 3, and class 12 at site 4.



Figure 148: Site 3 contains *Ceriops australis* near the edge (the darker mangrove) while *Avicennia marina* is found (mostly) further in (the lighter mangrove). The thematic map defines class 4 at this site, consisting of tall mangroves.

Interestingly, classes 4 and 12 are spectrally the most similar of all thematic classes with a JM distance of 1.8252 (Table 42, p. 323 of Section 4.5.11.2). Moreover, the mean spectra are also similar between classes 4 and 12 in the 400 – 700 nm range (Figure 142, p. 323 of Section 4.5.11.2). However, major differences occur in the NIR region, where class 4 (located at site 3) is much brighter than class 12 (at site 4). The result is also observed through the examination of individual vegetative pixel spectra in the image. To the human eye, the NIR lies beyond our senses. Therefore, the human eye perceives similar mangroves (except the different RGB shades - lighter and darker mangroves at carefully selected wavelengths (e.g. especially



Figure 149: Site 4 is similar to site 3 (Figure 148), containing *Ceriops australis* near the edge (the darker mangrove) while *Avicennia marina* is found (mostly) further in (the lighter mangrove). The thematic map defines class 12 at this site. The mangroves located here are shorter compared to those shown in Figure 148.

near 550 nm – i.e. perceived as green)). The spectrum shows a much larger brightness difference in the NIR, beyond the small differences in shades in the RGB wavelengths (as perceived by the eye). It is important to realise that Figure 142 shows mean normalised radiance spectra for the whole class. Therefore, these mean spectra incorporate the different mangroves which exist, including those having different RGB brightnesses.

The major focus here is to account for the difference in brightness in the NIR spectral region between class 4 and class 12; the difference in normalised radiance extending over the rest of the spectrum (RGB) is relatively small.

One possibility is to interpret the difference in terms of nutrient levels of the mangroves. Section 2.3.2 showed that reflectances in the NIR are generally higher for nutrient-deficient wheat (Ayala-Silva & Beyl, 2005). However, as detailed in Section 2.3.2, a reference spectrum is required in order to make spectral comparisons. In this case, no such spectrum exists. If it is supposed that class 12 spectra represent reference spectra of healthy mangroves, then class 4 mangroves

(having higher NIR normalised radiances) could represent nutrient-deficient mangrove spectra. As nutrient deficient wheat results in stunted growth (Ayala-Silva & Beyl, 2005), the same is expected for mangroves due to chlorosis. However, field work shows the mangroves to be particularly tall in the region defined by class 4, thereby being contradictory.

Another interpretation relates to the age of the mangrove leaves. If both classes 4 and 12 represent the same mangrove species, then they could represent different stages of development. In Section 2.3.2, Figure 9 (p. 34 of Section 2.3.2) and Figure 10 (p. 34) showed different reflectances depending on the senescence stage of wheat, while Figure 11 (p. 35) shows the age effect of maize leaves. There is also ASD field evidence (Figure 180, p. 464 of Appendix G.2), where the NIR reflectance is higher for [FM] *Avicennia marina* 3 (a young mangrove) compared to [FM] *Avicennia marina* 2 (mature). This interpretation suggests that for class 4 is composed of younger mangroves, which are taller than older (mature) mangroves. Although it may appear as another contradictory result, when viewed from an airborne platform, younger leaves may indeed be expected at the top of canopies. However, the spatial distribution of class 4 mangroves suggests that the younger leaved vegetation are located (mostly) along estuaries. Spectrally, these young leaves must be in sufficient quantities to overcome the mixed spectra from older leaves in the canopy. This suggests some kind of growth spurt over the whole Port Hedland coastal region, all along the estuaries and coincidentally, near the time of the Port Hedland airborne survey. However, the mangrove forests are very well established and any such growth spurts are unlikely. It seems inherently unlikely for the leaf age to be a reasonable interpretation to account for the high NIR reflectance.

It is also possible to base the interpretation on water content. Class 12, having the lower normalised radiance in the NIR region, must contain less water than class 4 mangroves (according to the interpretation of Figure 12 (p. 36)). However, although, on the whole class 4 mangroves are located predominantly along estuaries, this is not always the case. There are exceptions in local regions. For example, at Pretty Pool, both classes 4 and 12 are distributed in clusters, both inland and along estuaries. There are also regions where class 4 resides on one side

of an estuary while class 12 lies directly opposite, making it difficult to justify why the water content of class 12 mangroves is less than class 4. Also, there are class 4 mangroves further inland. Again, it is difficult to justify why class 4 mangroves contain a higher water content compared to class 12 lying directly along the water's edge. Overall, the difference in NIR normalised radiance is not explained satisfactorily in terms of water content.

Mixed pixels surrounded by non-vegetation decreases the red-edge length (Figure 143, p. 333 of Section 4.6.1). Figure 6 (p. 29 of Section 2.3.2) shows that the NIR reflectance is increased greatly by the addition of leaf layers, while leaving the RGB reflectance relatively unchanged – a situation reminiscent of the class 4 normalised mean spectrum. The NDVI is therefore (by design) related to vegetative density, which includes canopies consisting of many leaf layers – more leaves increase the vegetative density by increasing the NIR reflectance. The spatial location of class 4 mangroves appear mostly along estuaries, although a region does exist further inland on Finucane Island. Evidence from field work showed the existence of numerous very tall mangrove trees on Finucane Island in particular. ASD reflectance spectra in the NIR shows *Rhizophora stylosa* as a dark mangrove, while *Avicennia marina* is particularly bright - see Figure 57 (p. 175 of Section 4.4.2). Both these species are the tallest mangroves found in the Port Hedland coastal region (see Appendix T). It is important to highlight that ASD reflectances were recorded from a limited number of leaf layers, while the airborne sensor records canopies in areas of 1m². Therefore, the airborne sensor is expected to record higher NIR reflectances for dense canopies.

Another factor relates to the possibility that class 4 mangroves represents a higher proportion of spectra being composed of *Avicennia marina* (which is high in NIR) compared to *Rhizophora stylosa* (having dark NIR), thereby increasing the NIR reflectances. If *Avicennia marina* is taller than *Rhizophora stylosa*, then higher NIR reflectances are expected (when viewed from above), especially if the darker NIR reflectances of *Rhizophora stylosa* are masked by the taller *Avicennia marina*. Conversely, taller *Rhizophora stylosa* (i.e. compared to *Avicennia marina*) would decrease the NIR reflectances, even when consisting of multiple leaf (canopy) layers – the extent of NIR reflectance depends on the mangrove height and number of leaf

layers. These suppositions need field evidence, although appear reasonable. Field work revealed *Avicennia marina* interspersed with *Ceriops australis*. The SA between these two species is 0.13 ± 0.04 rad but forms one class on the thematic map (Table 16, p. 177 of Section 4.4.2). Consequently, the map class (class 4) is labelled as mangroves, as it could (theoretically) consist of any mangrove species. The high NIR normalised radiance suggests dense vegetation, and the mangroves situated there appear healthy due to the lack of observed chlorosis. Therefore, overall the class 4 consists of tall healthy dense canopy mangrove forests, thereby consisting of many leaf layers. There is field evidence to support this interpretation (although no formal tree height measurements were taken). Figure 150 shows particularly tall mangroves (approximately 4 m) located at site 2 (labelled in Figure 144, p. 334 of Section 4.6.1), especially further in from the edge. At site 2, class 4 mangroves appear a little in from this edge. Class 4 also exists at site 3, where the tall mangroves are evident from Figure 151 and although there is no scale reference, it is known from field work that the mangroves are reminiscent in height to those displayed in Figure 150. However, class 4 does not appear at site 4, where the mangroves are shorter, as evident from Figure 152.

A probability argument extends the class interpretation to tall healthy dense canopy *Avicennia marina*, as it was observed to be the most common mangrove. With this interpretation, it is understood that there is an associated uncertainty, as a proportion of mangroves are different species. No formal population statistics were conducted to estimate this uncertainty, but the field evidence suggests an order of around 15%.



Figure 150: Tall mangroves at site 2, especially further in from the edge. Class 4 mangroves appear a little in from this edge



Figure 151: Tall mangroves at site 3, especially further in from the edge, defined by class 4 on the thematic map.



Figure 152: Mangroves at site 4 are shorter in height, defining class 12 on the thematic map.

Class 12: High density medium height mangroves (1 – 3 m) (map colour: dark green)

Figure 149 (defining class 12) and Figure 148 (defining class 4) shows similar mangroves, even though the NIR is much brighter in Figure 148. An interpretation was offered above in relation to tree canopy height on the basis of number of leaf layers and the result given in Figure 6 (p. 29 of Section 2.3.2). Again, *Avicennia marina* was the dominant species in population. The mangroves are of high density (i.e. closely packed) and of medium height (approximately 1 m to 3 m).

At site 34 (Figure 153), the mangrove density is also high but individual mangroves are lower in height – around 1 to 2 m. The proportions of each mangrove also differs – roughly 40% *Ceriops australis* and 60% *Avicennia marina*.

The classifier is unable to spectrally distinguish between *Ceriops australis* and *Avicennia marina* owing to the spectral similarity, thereby placing both mangroves into one class in the thematic map. The SA between these species is 0.13 ± 0.04 rad (Table 16, p. 177 of Section 4.4.2) – equal largest in the table.²⁹ Figure 53 (p. 171 of Section 4.4.1) shows that 0.13 rad indicates a high degree of spectral similarity. Therefore, class 12 incorporates all mangroves, as the SA between other mangroves are less than 0.13 rad. However, on the argument of probability (i.e. through field

²⁹ Although there are larger SAs in Table 69, p. 498 of Appendix G.3 (where all ASD spectral samples are displayed), the uncertainties encompass the SA of 0.13 rad.

work observations), a mixture consisting of both *Ceriops australis* and *Avicennia marina* is reasonably expected.

Overall, field work evidence suggests the following interpretations for class 12 corresponding to the thematic map of Figure 133 for $JM \geq 1.8$:

- High density (i.e. tightly packed) mangroves of at least 1 metre in height (but less than 3 m). Mostly consisting of mixtures of *Ceriops australis* and *Avicennia marina* species but mostly *Avicennia marina*.



Figure 153: Site 34 consists of roughly 40% *Ceriops australis* (the darker mangrove) and 60% *Avicennia marina* (the lighter mangrove). The thematic map defines class 12 at this site.

Class 13: Medium density low height (around 1 m) mangrove shrub (mostly *Avicennia marina*) and low density dwarf shrub (around 0.25 m) mangroves (mostly *Avicennia marina*). (map colour: maroon).

At sites 14 and 24 (both labelled in Figure 147 (p. 336 of Section 4.6.1), small shrubs of *Avicennia marina* exist with medium density, with photographic evidence presented in Figure 154 and Figure 155, corresponding to each respective site.



Figure 154: Medium dense small shrubs of (mostly) *Avicennia marina* exist at site 14 (of Figure 147).



Figure 155: Medium dense small shrubs of (mostly) *Avicennia marina* exist at site 24 (of Figure 147).

The height of the mangroves shrub are approximately 1 m. The causeway that joins Finucane Island to the mainland also contains the maroon coloured class (see Figure 156), a portion which is shown in Figure 157. Again, *Avicennia marina* exist at that location, but at very sparse density. These shrubs are referred to as dwarf shrubs (a few are circled in yellow in Figure 157), as they are only about 25 cm in height.³⁰

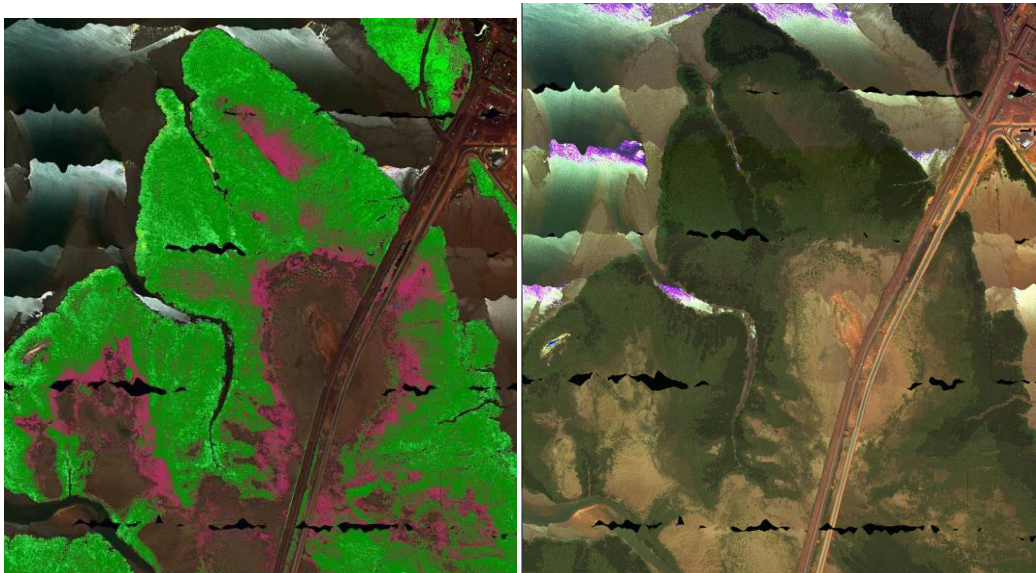


Figure 156: Comparison between thematic map, superimposed onto the true colour image (left image) and the true colour RGB image (right image). Sparse shrubs of *Avicennia marina* are contained in the maroon coloured class, as evident in the colour photograph of Figure 157.



Figure 157: Photographic evidence of sparsely populated dwarf shrubs of *Avicennia marina* (circled in yellow). The photographed region corresponds to the maroon coloured class 13 on the thematic map.

³⁰ The relationship between shrubs and their heights may vary in definition. The United States Department of Agriculture - Natural Resources Conservation Service (n.d.) defines a subshrub as being under 0.5 m, but never over 1 m (it is also called a dwarf-shrub), while the spruce (2018) defines a subshrub as under 0.25 m in height.

However, not all sites covered in maroon colour were mangroves. For example, site 21 (Figure 158) was dominated by dry (brown) grass instead of *Avicennia marina*.

Spectrally, the result is not altogether surprising. For medium-dense mangroves, the soil spectral signature will mix with that for mangrove, reducing the length of the red-edge. Recall that the airborne sensor records spectra in areas of 1 m by 1 m (this was explained in Section 4.6.1 with reference to Figure 143, p. 333). The canopy height is also limited, unable to completely mask the underneath soil, resulting in mixed spectra. Notice also that the NIR normalised radiance is also lower (on average) for class 13 compared to classes 4 & 12 (in Figure 142). More canopy means more leaf layers, resulting in higher NIR reflectance (Figure 6, p. 29 of Section 2.3.2). There are different explanations available to account for the spectral signature of the low-lying brown grass (Figure 158). Firstly, it is possible that there is a mixture of grass and soil spectra, all the more likely on windy days when soil particles intersperse amongst the grass (the PHPA airborne survey was conducted on a windy day – see Section 3.2). However, by appearance, the grass appeared dry – the reduced water content decreasing the length of the red-edge, thereby making it appear ‘less vegetative’. Figure 12 (p. 36 of Section 2.3.2) shows that at a low RWC (e.g. RWC = 0.10), the spectral signature of peace lily appears less-vegetative in nature than a well-watered water lily. In reality, both these factors may account for the observed spectral signature of class 13.

The characteristic pencil-like roots (a unique characteristic of *Avicennia marina* – see Appendix T) were easily discernible amongst the soil in the region photographed in Figure 157. The mangroves are low in height and density – termed dwarf shrub mangroves.

Although the material presented for class 13 contains evidence for *Avicennia marina*, the high spectral similarity between mangroves suggests that this class 13 encompasses more species of mangroves than just *Avicennia marina* (Table 68 to Table 89 of Appendix G.3). It is known that *Avicennia marina* is the most abundant mangrove in the Port Hedland coastal region, making up approximately 66% of the total mangrove population (E. Paling, Humphreys, & McCardle, 2003), with *Rhizophora Stylosa* the second most abundant at 18% (see Table 50, p. 374 of



Figure 158: A photograph at site 21 (of Figure 147) shows mostly dry brown grass. The region corresponds to the maroon coloured class 13 in the thematic map.

Section 4.6.4). The maroon coloured class 13 regions, are located away from direct contact with water estuaries; it is known that *Avicennia marina* is found further inland than *Rhizophora Stylosa* (Semeniuk, 1983). Putting these facts together, it is likely that, if class 13 describes a sparsely populated mangrove, then that mangrove is likely to be *Avicennia marina*. However, this is not a definite; dry brown grassed regions also produce the same spectral signature (i.e. within the limit for the class), due to the mixed spectral nature of soil and vegetation, but is probably located even further inland than *Avicennia marina*.

A comment is needed to elaborate on the word “density”. Figure 150 to Figure 152 shows mangroves which are packed tightly together, where canopy leaves overlap. Figure 154 shows a lower vegetative content, having a much lower density of leaves. Due to the size of the mangrove trees in Figure 150 to Figure 152, the actual trees are further apart. Therefore, the distance between tree trunks are further apart compared to the stems in Figure 154, although no actual physical measurement was taken. Therefore, the word “density” refers to vegetative density, not spatial density of vegetation. If it were, then grass would be extremely high in density! It is the vegetative density which affects the red-edge length, upon which classification is based. Therefore, Figure 154 (having lower vegetative

content) is considered as being of medium density compared to the high density mangroves in Figure 150 to Figure 152.

Overall, field work evidence suggests the following interpretations for class 13 (in maroon) for the thematic map of Figure 133 for $JM \geq 1.8$:

- Medium density low height (around 1 m) mangrove shrub mostly (*Avicennia marina*).
- Low density dwarf shrub (around 0.25 m) mangroves (mostly *Avicennia marina*).
- A possibility of finding dry brown grass (but probably further inland).

Class 14: High density *Rhizophora Stylosa* mangroves (map colour: light green)

While only occupying 2% of the total number of class pixels, class 14 is located predominantly on Finucane Island; a mangrove-rich environment. Therefore, the interpretation of class 14 may hold some useful information.

Spectrally, the JM distance between classes 13 (the region coloured in maroon) and 14 (coloured in light green) is very high (at 1.9846 - Table 42, p. 323 of Section 4.5.11.2), suggesting class 13 and 14 spectra are vastly different. Class 12 (in dark green) and class 14 (in light green) are even more spectrally separable, as the JM distance is 1.9989.

The mangroves at field work site 11 (Figure 144, p. 334 of Section 4.6.1) are only about 2 m tall. *Avicennia marina* were observed during field work (along the edge), but the class appears further in, and not directly accessible.

Class 14 mean spectra are very dark compared to both class 13 and class 12, and over all wavelengths - i.e. including the NIR which cannot be observed visually (Figure 142, p. 323 of Section 4.5.11.2). Therefore, the vegetation must be dark and very dissimilar to other mangroves. The mean ASD spectra for the seven mangrove species plot (Figure 57, p. 175 of Section 4.4.2) shows that both *Aegiceras corniculatum* and *Rhizophora Stylosa* are dark mangroves, particularly in the NIR spectral region (compared to other mangroves). However, as *Rhizophora Stylosa* is the second most abundant mangrove (18%) species (after *Avicennia marina*) in the

Port Hedland coastal region (E. Paling et al., 2003), it is more likely that class 14 represents *Rhizophora Stylosa*.

There is, however, a troubling aspect to this interpretation. Figure 57 (p. 175 of Section 4.4.2) shows the NIR region being much brighter than the RGB region of the spectrum. Figure 142 is a radiance spectrum (with units of normalised radiance) but shows a similar (low) brightness extending over the RGB and NIR regions for class 14 – the spectrum is basically ‘flat’. The spectrum appears virtually non-vegetative in nature, but the strong vegetative mask passed it as vegetation. It should be noted that the vegetative mask was developed from reflectance-based data, where the length of the red-edge is not affected by atmospheric absorption. Atmospheric absorption is not expected to account for such a decrease in the NIR, as evident by comparing the reflectance (Figure 137, p. 320 of Section 4.5.11.2) and radiance (Figure 138, p. 320 of Section 4.5.11.2) spectra in the NIR. The surrounding region on Finucane Island is particularly dense in mangroves. Maps, as produced from other sources (Section 4.6.4) also show dense mangrove populations in the region occupied by class 14. There is no clear explanation offered when examining the spectra in Section 2.3.2, in terms of phenology, stress, canopy density and so on, in relation to the ‘flat’ spectrum. As the spectrum appears virtually non-vegetative, perhaps there is a mixture of non-vegetative spectra. Phenological evidence from field work, for *Avicennia marina*, also does not account for the spectral pattern - Figure 180 (p. 464 of Appendix G.2) shows too little difference between the left (a mature mangrove) and the right plots (a young mangrove). Iron oxide dust effects are also unlikely to account for the observed class 14 spectral characteristics. Comparing Figure 180 with Figure 192 (left image, p. 476 of Appendix G.2) shows that iron dust decreases the red-edge length, but the NIR region is still particularly bright – it does not explain the spectral pattern for class 14. However, comparing a healthy *Avicennia marina* spectrum (Figure 180, p. of 464 Appendix G.2) with one where the leaves are particularly noticeable in having salt crust (Figure 184, right image, p. 468 of Appendix G.2), shows that salt does indeed reduce the brightness in both the RGB and the NIR regions (more so than iron-oxide). In particular, the brightness in the NIR region is affected more than the RGB region, so the NIR region is closer in brightness to that in the RGB region. The extent is not as drastic as that

in Figure 142, but it could be that the mangroves are more seriously affected by salt crust than that observed in-field, and/or due to a combination of factors (e.g. high salt content and a particularly low water content reducing the NIR as shown in Figure 12, p. 36 of Section 2.3.2). While the plot of Figure 142 shows mean spectra, it is possible that some regions (fewer in number) contain a higher NIR brightness while a larger number of mangroves contain a lower brightness.

Interestingly, the true colour RGB image, as presented in Figure 159 (left), appears to show regions of class 14 as darker-shaded mangroves (at least on Finucane Island). The corresponding thematic map (i.e. Figure 133 for $JM \geq 1.8$) is placed on the right hand side of Figure 159. The right image shows the light green regions (of class 4) present over the eastern section of Finucane Island but absent in the western half, while the RGB image still shows dark regions. However, there is a danger of correlating the spatial class structures with the dark shaded mangrove regions in an RGB image, as the RGB image is produced from just three bands (the choice of RGB bands were defined in Section 3.3). The pattern described by the light green coloured class may in fact be describing another feature instead, as the whole hyperspectral spectrum (246 bands) is used in the classification process. This argument is strengthened as the RGB darker regions directly to the south of Finucane Island (as indicated in Figure 159) are not included into this class 14.

Overall, class 14 is well defined but rather dark over the whole spectrum (i.e. RGB and NIR). *Rhizophora Stylosa* is a dark mangrove (in the RGB) and particularly dark in the NIR compared to other mangroves (except *Aegiceras corniculatum*). Incorporating the probability argument, where *Rhizophora Stylosa* is the second most abundant mangrove, class 14 is most likely to represent *Rhizophora Stylosa*.

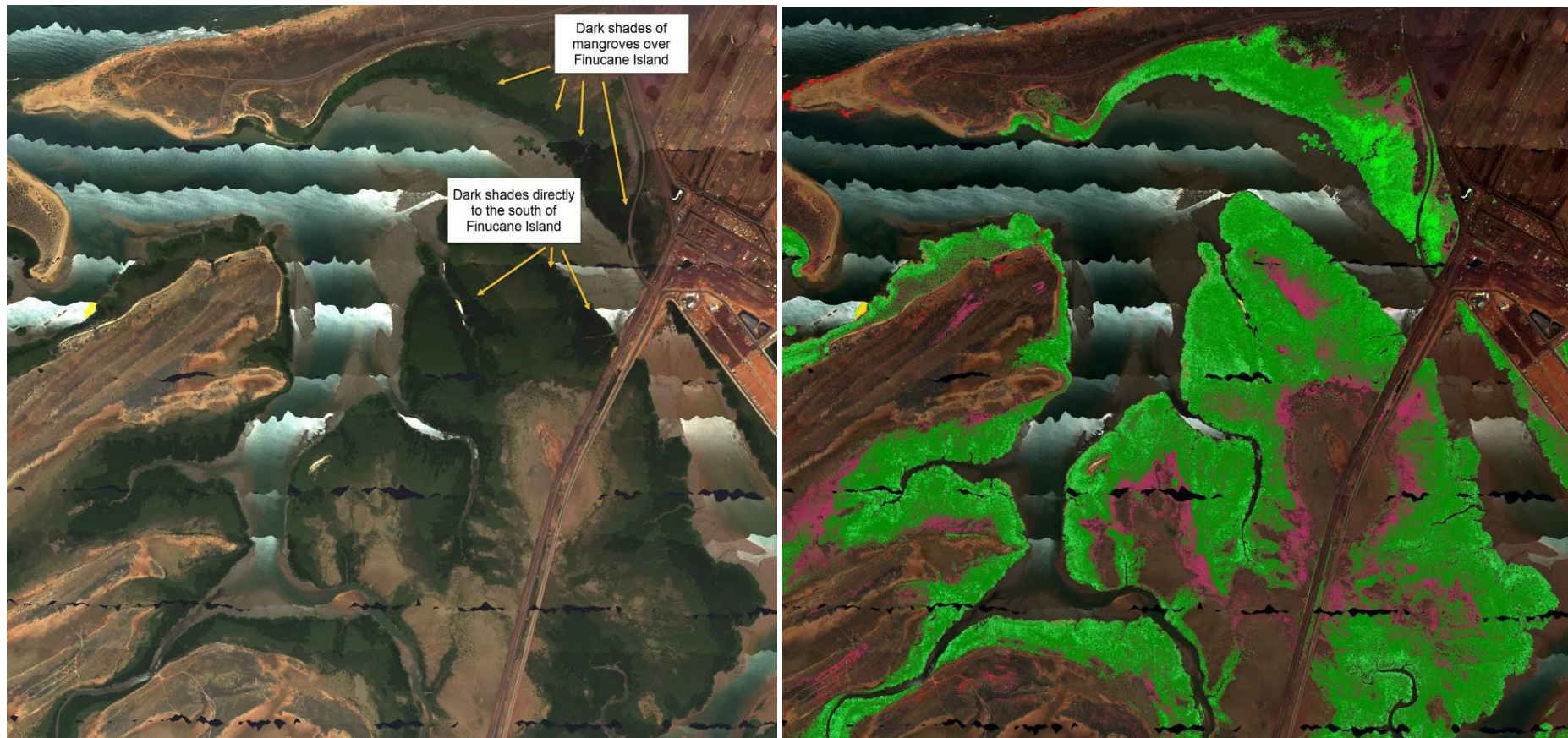


Figure 159: The dark shades of mangroves discernible on the left true colour image (RGB) also appear present over Finucane Island on the thematic map (Figure 133 for $JM \geq 1.8$) but absent elsewhere. (Both the contrast and brightness were enhanced in the left image).

4.6.4 Validation with Published Maps and Discussion

WorleyParsons (<http://www.worleyparsons.com>) is an international professional organisation offering consultancy and advisory services who have undertaken various projects for the Port Hedland Port Authority. One such project monitored the impact to mangrove communities as a result of the Port Hedland harbour expansion (Pilbara Ports Authority, 2016, p. 4).

In April 2012, WorleyParsons (hereforth abbreviated to WP) used high resolution aerial photography, field work data, sonar mapping and a video drop camera to map aquatic coastal vegetation (e.g. coral, algae). Although this was their primary interest, they also mapped mangrove species, with some identified by species name (see Figure 160). This WP map is found on page 9 of the “Lumsden Point General Cargo Facility – Benthic Habitat Survey” report (WorleyParsons, 2013).

Two species of mangroves are included in the WP map; *Avicennia marina* and *Rhizophora stylosa* as they are the easiest to distinguish using the combined aerial photography and associated on-ground validation. They are also the most abundant species of mangrove. This map suggests that both species are homogenously distributed. In reality, it is more heterogeneous, according to Nicole Wylie who has carried out numerous on ground surveys in the region (personal communication). This conclusion is also evident based on our own field work.

The WP map (Figure 160), and both thematic maps Figure 132 (p. 309 of Section 4.5.11.1) and Figure 133 (p. 310 of Section 4.5.11.1) - referred to as JM17 and JM18 maps, respectively - were vertically split in half to aid the current discussion.

The WP map in Figure 160 shows a greenish-yellow coloured box in the legend followed by the description “A. marina scattered”, which implies low density *Avicennia marina*. Encouragingly, the maroon coloured regions on both Figure 161 and Figure 162 are spatially highly correlated to these greenish-yellow coloured regions on the WP map. These figures are shown a few pages down, beginning at page 361. The interpretation offered in Section 4.6.3 was: “medium density low height (around to 1 m) mangrove shrub and low density dwarf mangrove shrub (around 0.25 m). Mostly *Avicennia marina*”. There is also the possibility of finding

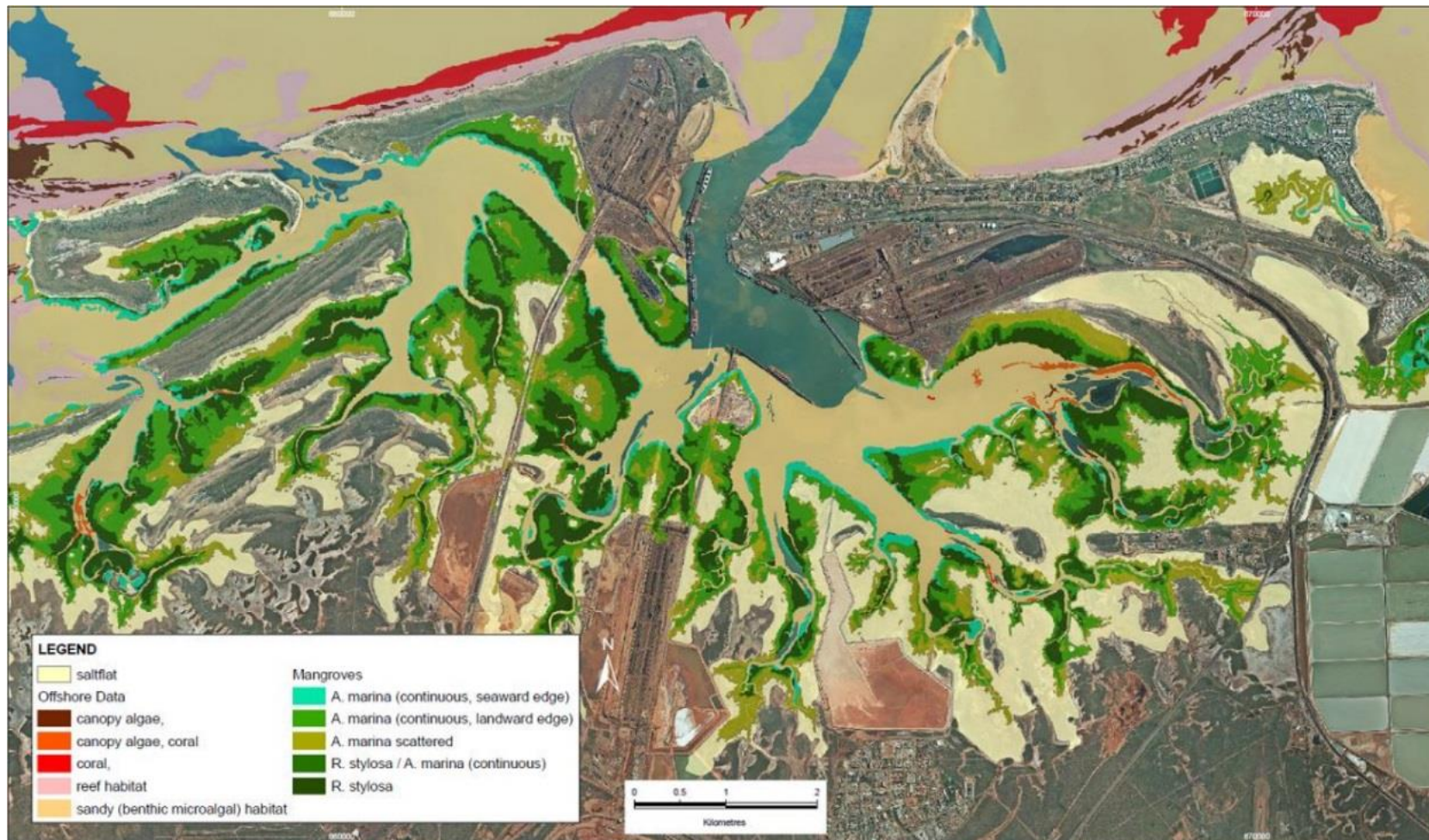


Figure 160: Vegetative classification map as produced by WorleyParsons (i.e. WP map) (supplied to the PhD candidate by Nicole Wylie but is part of a formal report in WorleyParsons (2013)).

dry brown grass. Due to the multiple interpretations offered to the maroon coloured region, it is impossible to know in advance which interpretation is correct. That is, a maroon-coloured class in one region could represent dry brown grass, while another region contains medium density *Avicennia marina*. An expert may offer the correct interpretation based on habitat knowledge of vegetation. For instance, for regions further away from estuaries, the less water availability results in lower density and smaller (in size and height) mangroves. For distances exceeding a threshold, where mangroves are unable to grow, the lack of water makes brown grass more likely.

Both the JM18 and JM17 maps (both Figure 161 and Figure 162, right images) include a region with well-defined classes on Finucane Island (represented in light green in the JM18 map but thistle on the JM17 map). This region is circled on Figure 162, right image. The colour change was adopted to improve differentiability between the various green coloured shades in the JM17 image. Class 14 is the region in question on both JM17 and JM18 maps, and are highly distinct (spectrally) on both maps. No such region is defined on the WP map; the class interpretation suggests a dark mangrove - Section 4.6.3 suggests high density *Rhizophora Stylosa*.

With reference to Figure 161, the JM18 map is dominated by dark green regions in, defining mangrove species in general – i.e. they represent all mangrove species, as they are spectrally inseparable. Section 4.6.3 interprets these dark green regions as “high density medium height (1 m to 3 m) mangroves”. However, as *Avicennia marina* is the most abundant mangrove, the interpretation could be extended based on probability: “likely to be *Avicennia marina*” or “mostly *Avicennia marina*”. Incorporating the knowledge that *Rhizophora stylosa* is the second most abundant mangrove, the interpretation could be adjusted to “*Avicennia marina* or *Rhizophora stylosa*” (covering most bases). WP states: *Rhizophora stylosa* and *Avicennia marina* in this region. The same comments apply to Figure 163.

The dark green class (class 12) in the JM18 map (Figure 161 (right image)) is defined by two classes (class 11 (in light green³¹) and 12 (in dark green)) in the JM17

³¹ Specifically, Table 40 (p. 314 of Section 4.5.11.1) gives class 14 as “light green” and class 11 as “green” (i.e. a darker green compared to class 14). To aid the discussion presented hereforth, class 11 is now referred to as “light green”. The population of pixels for class 11 is about 36% while class 14 is under 2% (and ignored in this discussion).

map (Figure 162 (right image)). This is made clear by comparing the circled region below Finucane Island in Figure 162 (right image – i.e. about half way down the image) to Figure 161 (right image – it is not circled here). Mathematically, these light green and dark green coloured classes (11 and 12) form the lowest degree of separability (JM distance of 1.7160) in the JM17 map. For this reason, they are merged in the JM18 map (into class 12) to increase the spectral separability, thereby increasing the confidence of having distinct class features. Despite the low spectral separability, the spatial structures followed by the dark green (class 12) relate particularly well to the dark green regions in the WP map. The same applies to the light green class (of the JM17 map), reminiscing the light green coloured regions in the WP map. WP interprets the dark and light green regions as *Rhizophora stylosa* and *Avicennia marina*, respectively. Spatial similarities between the green (light and dark) classes are also found with Figure 164.

The dark and light green coloured regions defined on the WP map closely follow the dark and light shaded mangrove forested regions, as illustrated in Figure 165. Considering the close spatial relationship between the similar shades of mangrove forests in the RGB true colour image to those regions defined in the WP map, it is likely that WP used photointerpretation to classify those regions. This is not surprising, as photointerpretation is the most common form of classification. A knowledgeable analyst, who is familiar with the characteristics of mangrove forests, could interpret these regions to a certain degree of confidence. Mangroves have preferential sites for habitation and certain species are limited to specific areas (e.g. close to the water's edge, or further inland) (Duke, 1952). In fact, *Rhizophora stylosa* tends to locate on sandy shores or even in open seawater (International Union for Conservation of Nature and Natural Resources (2019) and Queensland Government Department of Agriculture and Fisheries (2013)). Therefore, an expert may conclude that the dark green class on the JM17 map represents *Rhizophora stylosa*.

Figure 166 shows the normalised mean radiance spectra for five classes of the JM17 map. As stated above, the JM17 map (e.g. Figure 162 (right image) and Figure 164 (right image) contains light green (class 11) regions and dark green (class 12) regions. The light green regions have a higher RGB brightness than the dark green



Figure 161: The left image shows the left half of the WorleyParsons image (Figure 160). The corresponding region for the JM18 (i.e. Figure 133 for $JM \geq 1.8$) thematic map is shown to the right and superimposed onto the true colour image.



Figure 162: The left image shows the left half of the WorleyParsons image (Figure 160). The corresponding region for the JM17 (i.e. Figure 132 for $JM \geq 1.7$) thematic map is shown to the right and superimposed onto the true colour image.

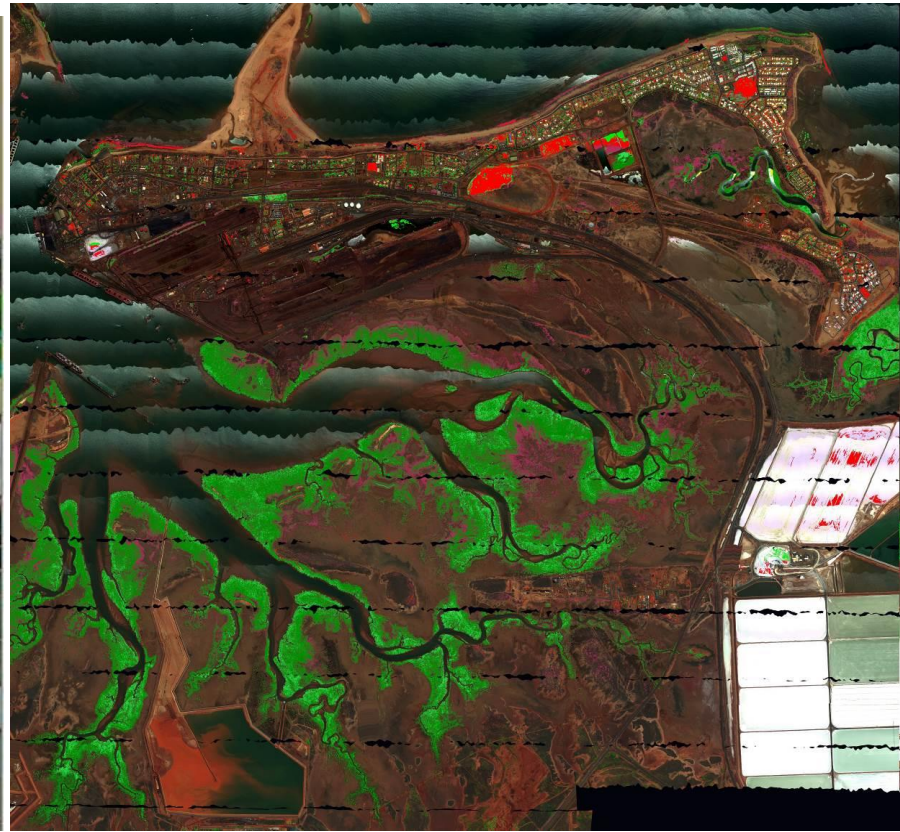


Figure 163: The left image shows the right half of the WorleyParsons image (Figure 160). The corresponding region for the JM18 (i.e. Figure 133 for $JM \geq 1.8$) thematic map is shown to the right and superimposed onto the true colour image.

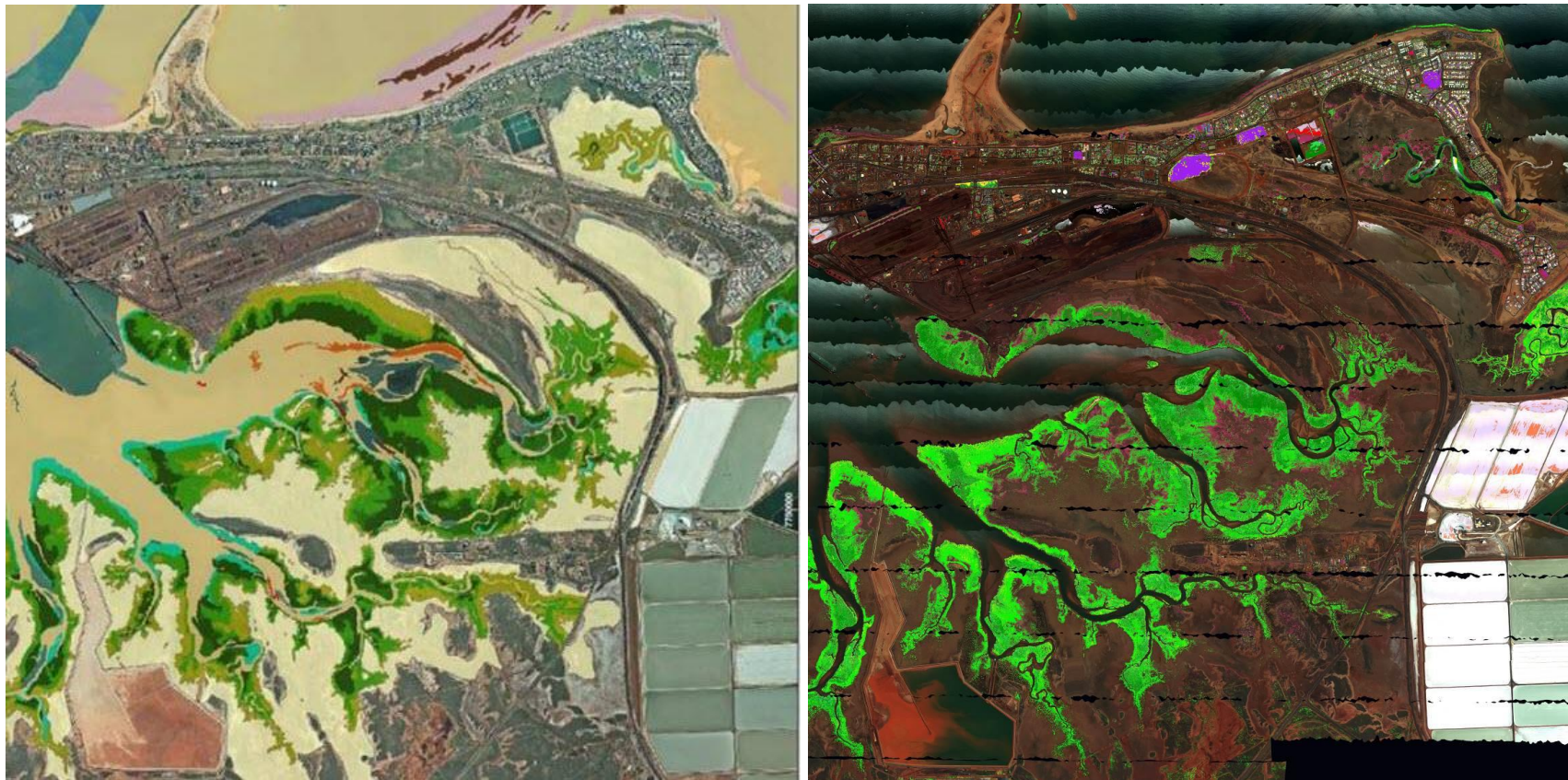


Figure 164: The left image shows the right half of the WorleyParsons image (Figure 160). The corresponding region for the JM17 (i.e. Figure 132 for $JM \geq 1.7$) thematic map is shown to the right and superimposed onto the true colour image.



Figure 165: The left image shows a region near Finucane Island in true colour. The corresponding WP map is shown to the right.

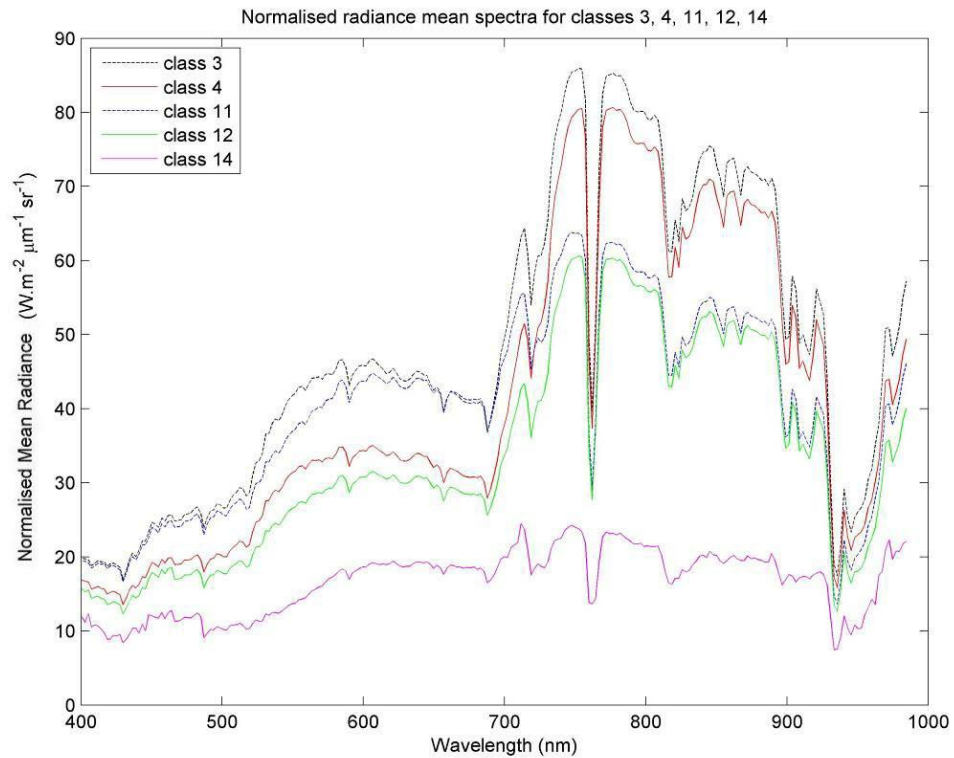


Figure 166: Normalised mean radiance spectra for classes 3, 4, 11, 12 and 14 of the JM17 map.

regions, although the brightness in the NIR are similar. This may be seen by comparing Figure 162 (right image) with Figure 165. The similar NIR brightness but different RGB brightnesses are opposite to the spectral signature expected for canopy height (i.e. number of leaf layers – discussed in full in Section 4.6.3). However, visually, the light green region (class 11) appears lighter than the dark green region (class 12). This explains the similarity to photointerpretation based on RGB shades. Physically, the lighter and darker green regions in the JM17 map are expected to be *Avicennia marina* and *Rhizophora stylosa*, respectively, as *Avicennia marina* is visually brighter than the characteristically dark *Rhizophora stylosa* (Figure 57, p. 175 of Section 4.4.2); these two species are also the most common mangroves.

Since the lowest spectral separability, corresponding to classes 11 and 12 (with a JM of 1.7160) provides physically meaningful spatial results, the question naturally arises is whether the second lowest JM distance (i.e. in excess of 1.70) also represents physically meaningful features. These next two lowest classes

correspond to classes 3 and 4, with a JM distance of only 1.7565. Mathematically, this means that there is a low probability that classes 3 and 4 are well defined (i.e. spectrally separable). For this reason, these two classes were combined (into class 4) for the JM18 map. However, classes 3 and 4 are more distinct than classes 11 and 12, according to the JM distance.

A region over Pretty Pool having different shades of mangrove-based pixels is shown in Figure 167. The red rectangular region in Figure 167 is magnified and displayed in Figure 168; the left image is the true colour image (contrast and brightness enhanced), while the right image shows the corresponding region from the N_Rad_VI_VI image, upon which the JM17 map is classified – i.e. it is not the classification of JM17 superimposed onto a true colour image. Indeed, the shading in this right image (i.e. right image of Figure 168) offers more contrast than the true colour image of Figure 168 (i.e. left image, already having been enhanced). With referral to Figure 166, the normalised mean radiance spectra corresponding to class 3 is much brighter in the RGB than class 4 and similar in the NIR.



Figure 167: True colour image (contrast and brightness enhanced) over Pretty Pool. Both dark and lightly shaded mangroves are clearly visible in the image. The squared red region is magnified in the left image of Figure 168.

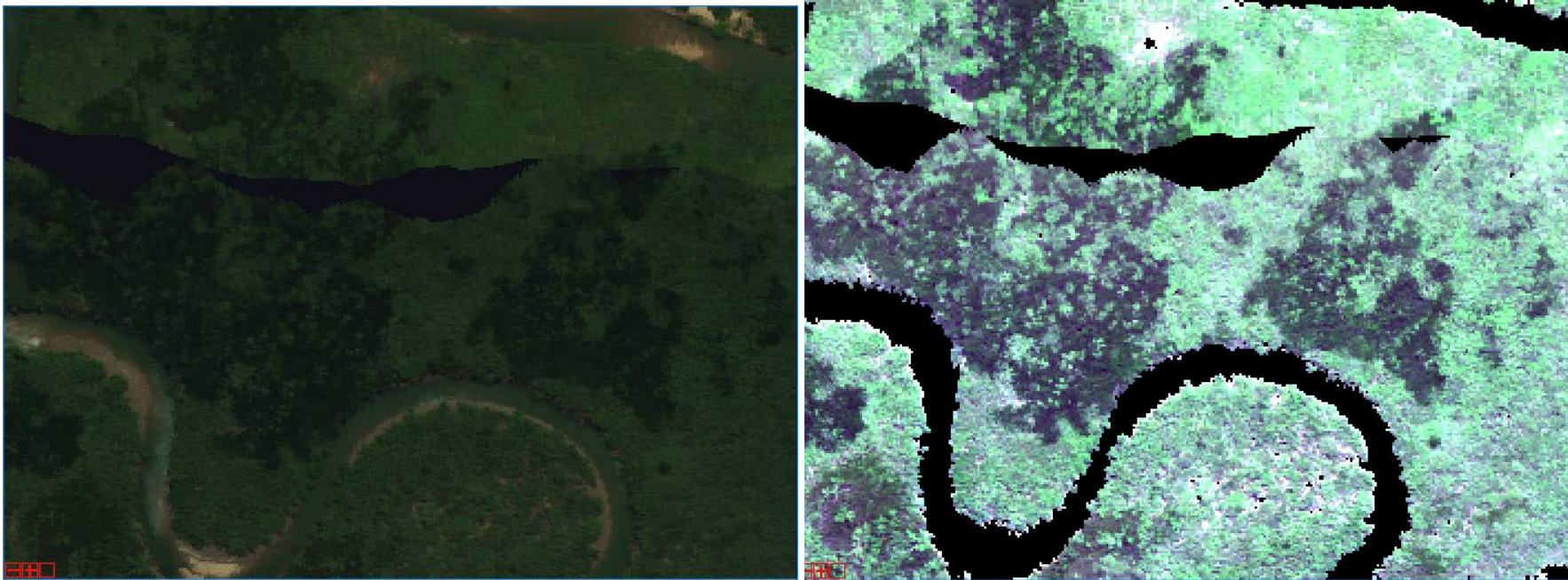


Figure 168: The left image shows the true colour image (contrast and brightness enhanced) for the red squared boxed region of Figure 167. The region exists in Pretty Pool, where dark and lightly shaded mangroves are apparent. The N_Rad_VI_VI image, is displayed on the right (no enhancements made). The various levels of pixel shades in the right image are more discernable.

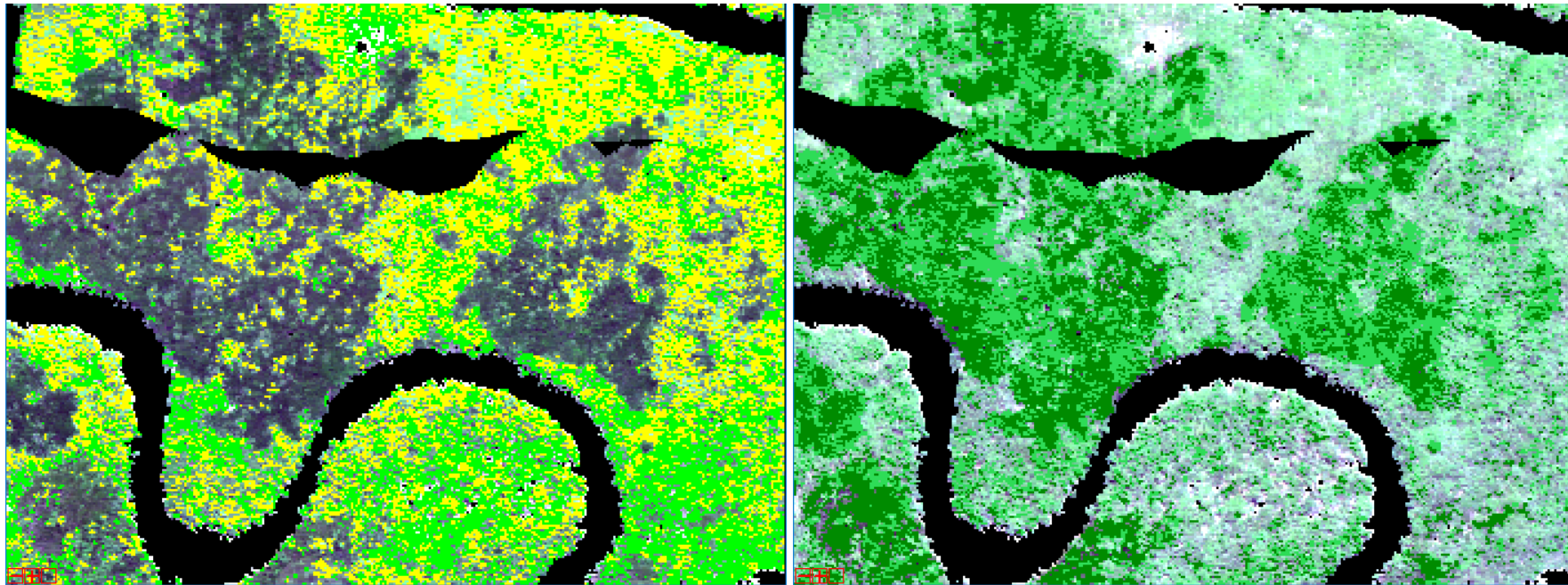


Figure 169: The left image shows classes 3 and 11 (group 1), while the right image shows classes 4 and 12 (group 2). Both class groups are superimposed onto the N_Rad_VI_VI image. Group 1 classes relate to RGB lightly shaded mangrove trees, while group 2 classes relate to the RGB dark shades.

The left image of Figure 169 displays classes 3 (in yellow) and 11 (in light green), both superimposed onto the N_Rad_VI_VI image. Both classes are defined over lightly shaded mangrove regions, with the yellow coloured class in particular corresponding to the lighter of the two shaded regions. The right image (of Figure 169) shows a blueish green and dark green class (classes 4 and 12, respectively). Although the blueish green region (class 4) represents the lighter of the two shades (i.e. with class 12 in the RGB spectrum of Figure 166), the NIR normalised mean radiance is much higher (i.e. brighter) than that for class 12 (dark green). If both classes 4 and 12 represent a dark mangrove, then the blueish green coloured region (i.e. class 4) could represent taller dark mangroves compared to those found in the dark green coloured region (i.e. class 12) - an interpretation based on an earlier discussion found under class 4 in Section 4.6.3. If the spectrum for class 14 (in Figure 166) represents *Rhizophora stylosa* (being the darkest mangrove), then both class 4 and 12 could represent *Ceriops australis* (being brighter than *Rhizophora stylosa* and the third most abundant mangrove according to WorleyParsons (2011, p. 1)). These mangroves defined in the blueish green (class 4) regions may be taller than those of in the dark green regions (class 12).

However, while *Ceriops australis* can grow to being a tall mangrove (about 10 m in height – see Appendix T), the abundance is significantly lower compared to *Rhizophora stylosa* according to Table 50 (p. 374). Despite the spectrum being brighter, on the argument of probability and being a dark mangrove, it is more likely that both classes 4 and 12 represent *Rhizophora stylosa* (taller and shorter, respectively).

A similar interpretation extends to the yellow shaded regions of Figure 169 (i.e. class 3), as the brightness in the NIR is much higher than for light green coloured region (i.e. class 11). Therefore, both class 3 and 11 could represent *Avicennia marina* but those in regions defined by class 3 may be taller than those of class 11. Note that both these interpretations take into account the probability of occurrence, as both these mangroves are the most common species. The interpretations for these findings were unable to be confirmed due to lack of physical data; during field work, these locations were inaccessible due to the dense mangroves and estuaries (which may be populated with crocodiles). A remote

camera, mounted on a UAV, would be particularly useful in the field to gather more data for interpretative purposes.

Spectrally, there is a high degree of confidence for the existence of both regions defined by classes 4 and 12, given their JM distance of 1.8328. Interestingly, class 3 and 11, which define the lighter shaded mangroves, exists with even more confidence (JM distance of 1.8528). However, the probability for the existence of class pairs 3 and 4 is low (JM of 1.7565) and more so for class pairs 11 and 12 (JM of 1.7160). These statistics are summarised in Table 49, along with class interpretation. AM refers to *Avicennia marina*, while RS refers to *Rhizophora stylosa*. The words “tall” and “short” refers to tall and short mangroves and are relative to each other; but without more data, it is not possible to provide actual heights.

RGB shading	Class, map colour and interpretation	Class, map colour and interpretation	JM distance
Light mangrove	3, yellow, Tall AM	11, light green ³² , Short AM	1.8528
Dark mangrove	4, blueish green, Tall RS	12, dark green, Short RS	1.8328
JM distance	1.7565	1.7160	

Table 49: A two way JM distance table for classes of 3, 4, 11 and 12 in the JM17 map. Classes 3 and 11 are defined in the RGB light shaded mangrove regions, while 4 and 12 are located in the RGB dark mangrove regions.

Table 49 shows that there is less confidence for both short and tall mangroves being distinguishable with each other (e.g. tall AM and tall RS), while a higher degree of confidence exists distinguishing between short and tall mangroves (e.g. tall AM and short AM). This is rather interesting, as different species (AM and RS) were merged into one class in the JM18 map (e.g. classes 3 and 4 from JM17 into class 4 for the JM18 map, and similarly for classes 11 and 12). However, classes 3 and 11 (both AM) were not merged, nor classes 4 and 12, both RS. Therefore, classes were

³² In this section class 11 (in comparison to class 12) is the lighter of the greens, while in Table 40 it is green (as it darker than class 14). Class 14 only occupies 1.8% of pixels, while class 11 is 35.6%, so to aid discussion, class 11 is referred to as light green in this section.

merged according to the height of the mangrove rather than the species, as they were spectrally less separable.

It is possible to make an assumption about the actual heights, thereby providing an interpretation for the “short” and “tall” mangroves. The JM17 classes 3 and 4 (both “tall”) were merged into class 4 on the JM18 map, which was visually observed to contain high density mangroves over 3 m. The field trip showed mangroves also being particularly high in density, and tall at Pretty Pool. Therefore, “tall” may also refer to mangroves over 3 m. The “short” mangroves from class 12 on the JM18 map were 1 to 3 m in height; classes 11 and 12 from the JM17 map were merged into class 12 on the JM18 map. However, some caution is advised, as there is no field data at Pretty Pool to support either of these claims. Worse still, on a wider scale, there is no field evidence even for the JM18 class 12 to be 1 to 3 m in height across the whole Port Hedland coastal region (and class 4 to be over 3 m tall). Despite this, the spectra are similar in pattern over wide regions (e.g. class 4) as classification is based on the examination (mathematically) of spectral patterns and grouping them. The separability statistics provides confidence in spectrally distinct classes. As the spectral patterns are similar across wide regions, a physical interpretation at one site is expected to produce a similar interpretation elsewhere.

A much earlier study was also undertaken by E. Paling et al. (2003), concerning the effects on mangroves due to harbour development. This map from February 1993 is shown in Figure 170 (on the next page). Unfortunately, the resolution of the map is low but it does show regions containing rarer mangrove species (e.g. *Aegiceras corniculatum*) situated in the harbour region and alongside estuaries. The absence of classes defined in these regions on either the JM17 or JM18 thematic maps, shows that the classifier was not able to spectrally distinguish between the common and rarer mangroves – a result expected due to the high spectral similarity between mangroves (discussed in Section 4.4.2). It should be remarked that the 1993 map was obtained using an aerial colour photograph and verified using data from several sources; a helicopter, a 4WD and a boat - so these rarer mangroves exist to a high degree of confidence. A problem in using this 1993 map is that the population may have changed, as the thematic map was produced based on an airborne hyperspectral survey some 20 years later. Despite this, there is certainly a

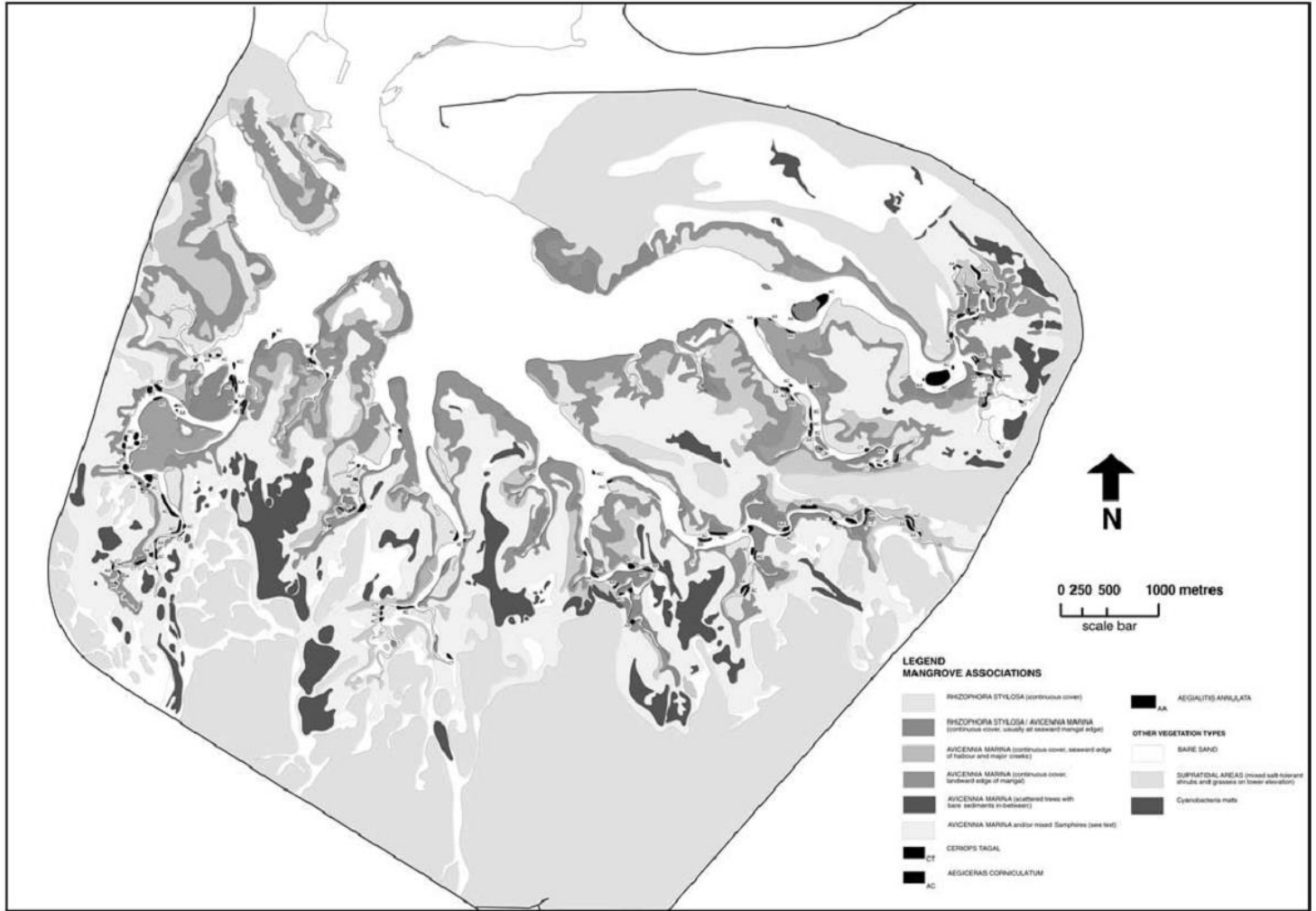


Figure 170: Species of mangroves present in 1993 (taken from figure 2 by E. Paling et al. (2003))

degree of spatial correlation between the regions defined in the published map (i.e. by E. Paling et al. (2003)) and the thematic map, especially for the JM17 map. Again, this is an encouraging result and increases the level of confidence in the class spatial patterns displayed on the thematic map.

According to E. Paling et al. (2003), *Rhizophora stylosa* and *Avicennia marina* make up the majority of the mangrove populations. Interestingly, E. Paling et al. (2003) have also defined the same mixed community (*R. stylosa/Avicennia marina*) as WorleyParsons (Figure 160). A summary of community populations are shown in Table 50.

Community	(ha)	(%)	(%) JM17 map
<i>Rhizophora stylosa</i>	203	18.3	18.7 (12)
<i>R. stylosa/Avicennia marina</i>	152	13.7	9.6 (4+14)
<i>A. marina</i> (seaward fringe)	37	3.3	
<i>A. marina</i> (behind <i>R. stylosa</i>)	451	40.7	42.5 (11+3)
<i>A. marina</i> (scattered trees)	241	21.8	23.7 (13)
<i>Ceriops tagal</i>	3	0.3	
<i>Aegiceras corniculatum</i>	10	0.9	
<i>Aegialitis annulata</i>	11	1.0	
Samphires	758		
Cyanobacterial mats	207		

Table 50: Mangrove communities and their populations.

The first three columns were copied from Table 2 of E. Paling et al. (2003). The far right column is labelled (%) JM17 map, and represents the populated pixels (%) belonging to the classes listed in brackets.

For the JM17 map, the dark green region (class 12) defines 18.7% of the region (see Table 40, p. 314 of Section 4.5.11.1). It is a dark mangrove (possibly *Rhizophora stylosa*), which matches the 18.3% statistic very closely in Table 50. The light green region (class 11) is possibly *Avicennia marina*, defining 35.6% of the thematic map (see Table 40). This result is comparable to that in Table 50 which shows 40.7%. If the yellow region (class 3) is also added to class 11, the result gives 42.5%. This

leaves the blueish green region (class 4), which is also a dark mangrove (similar to class 12 over the RGB spectral range). Some 7.7% make up these regions on the thematic map, which might be incorporated into the 13.7% total for the mixed community of *R. stylosa/Avicennia marina* of Table 50. If the thistle region (class 14) is added to the blueish green region (class 4), then 1.84% added to 7.73% is 9.6%. Both classes 4 and 14 were interpreted as *Rhizophora stylosa*, but in reality might be a mixed community of predominant *R. stylosa/Avicennia marina* (as defined by E. Paling et al. (2003)). The maroon coloured region (class 13) also compares favourably; 23.7% (on the thematic map) with 21.8% as *A. marina* (scattered trees).

Although the JM17 map aimed to interpret mangroves by species, the approach taken by both WP and E. Paling et al. (2003) differs in defining mixtures of mangroves (e.g. *R. stylosa/Avicennia marina*), in addition to specifying their placement (e.g. “seaward fringe”). Another difference lies in the extent of the maps. The region covered by the JM17 map covers vast regions of the Port Hedland coastal region (similar in extent to the WP map, but a little larger), while E. Paling et al. (2003) (Figure 170) appears mainly concerned with the immediate harbour region. Nevertheless, the population proportions (Table 50) agree to within about 5%, which is an encouraging result.

Overall, the final thematic map (i.e. Figure 132 and Figure 133) appears to be a solid product both quantitatively and qualitatively. The classes are not placed in questionable locations, such as those positioned by classifying the PHPA_Ref_VI image (i.e. Figure 96, p. 240 of Section 4.5.7). The normalised process has produced a thematic product having well-defined spatially coherent structures, with structures reminiscent of broad structures of other map products (e.g. WP (Figure 160) and E. Paling et al. (2003) (Figure 170)) as obtained through in-depth field work and expert analysts.

4.6.5 Summary and Discussion

The spectral inconsistencies in the PHPA_Rad_VI image was made consistent using normalisation, thereby resulting in the N_Rad_VI_VI image. Standard hyperspectral

remote sensing classification techniques led to a thematic map exhibiting highly consistent spatial patterns reminiscent of third party maps.

Overall, the 'best' thematic map (i.e. JM18 map - Figure 133, p. 310 of Section 4.5.11.1) is deemed to be a solid product both quantitatively and qualitatively. The spectral classes are well defined and spectrally well separable. Spatially, the spatial class structures follow third party products (e.g. Figure 160, p. 358 of Section 4.6.4) on a gross scale. Section 4.6.3 provided details as to the interpretation of the four classes defined for the mangrove forested regions, and relate to mangrove density and height.

The JM17 map (Figure 132, p. 309 of Section 4.5.11.1) defines two new regions (over the JM18 map), although they are spectrally less separable and therefore are defined to a lower degree of confidence. However, comparisons with the WP map presents strong evidence that the classes do represent physical cover types and must be taken seriously. This is observed by comparing the WP map (Figure 161 (left image) with both the JM18 map (i.e. Figure 161, right image)) and JM17 map (i.e. Figure 162, right image). For this reason, the JM17 map is also included in Section 4.6.6, which presents the final maps along with a legend. Spectral evidence suggests that the additional two classes in the JM17 map (compared to the JM18 map) relate to mangrove heights.

Class interpretations and populations are also reminiscent of the third party products; within 5% for the map by E. Paling et al. (2003) (Figure 170). Although the thematic patterns define different density mangroves, they mostly cover just two species: *Avicennia marina* and *Rhizophora stylosa*, with *Avicennia marina* being particularly dominant across the Port Hedland coastal region. Furthermore, there is spectral evidence that the additional classes in the JM17 map (compared to the JM18 map) relate to mangrove heights.

4.6.6 Mangrove Distribution Maps for the Port Hedland Coastal Region

This section presents are the best maps as derived from normalisation and classification. The first two maps correspond to the JM18 map (i.e. Figure 133 for $JM \geq 1.8$ (p. 310 of Section 4.5.11.1)), where classes are confidently defined as

separable classes. The last two maps were derived from the JM17 map (i.e. Figure 132 (p. 309 of Section 4.5.11.1)), which contains two additional classes, although mathematically, at a lower degree of confidence. Physically, the JM17 map is the best product, as there is evidence from the WP map that the low probability classes do exist.

The higher probability JM18 map contains the broad category “mangroves”, as (spectrally) any mangrove may be present there. However, field work suggests that *Avicennia marina* makes up the majority of these mangroves.

The lower probability JM17 map attempts to be more precise in categorising mangrove species, although at a cost of introducing a higher degree of uncertainty. The classes describe *Avicennia marina* and *Rhizophora stylosa*, mostly consisting of high density canopies and/or high density distributions spatially. The classes also describe both tall (over 3 m) and short mangroves (1 m to 3 m).

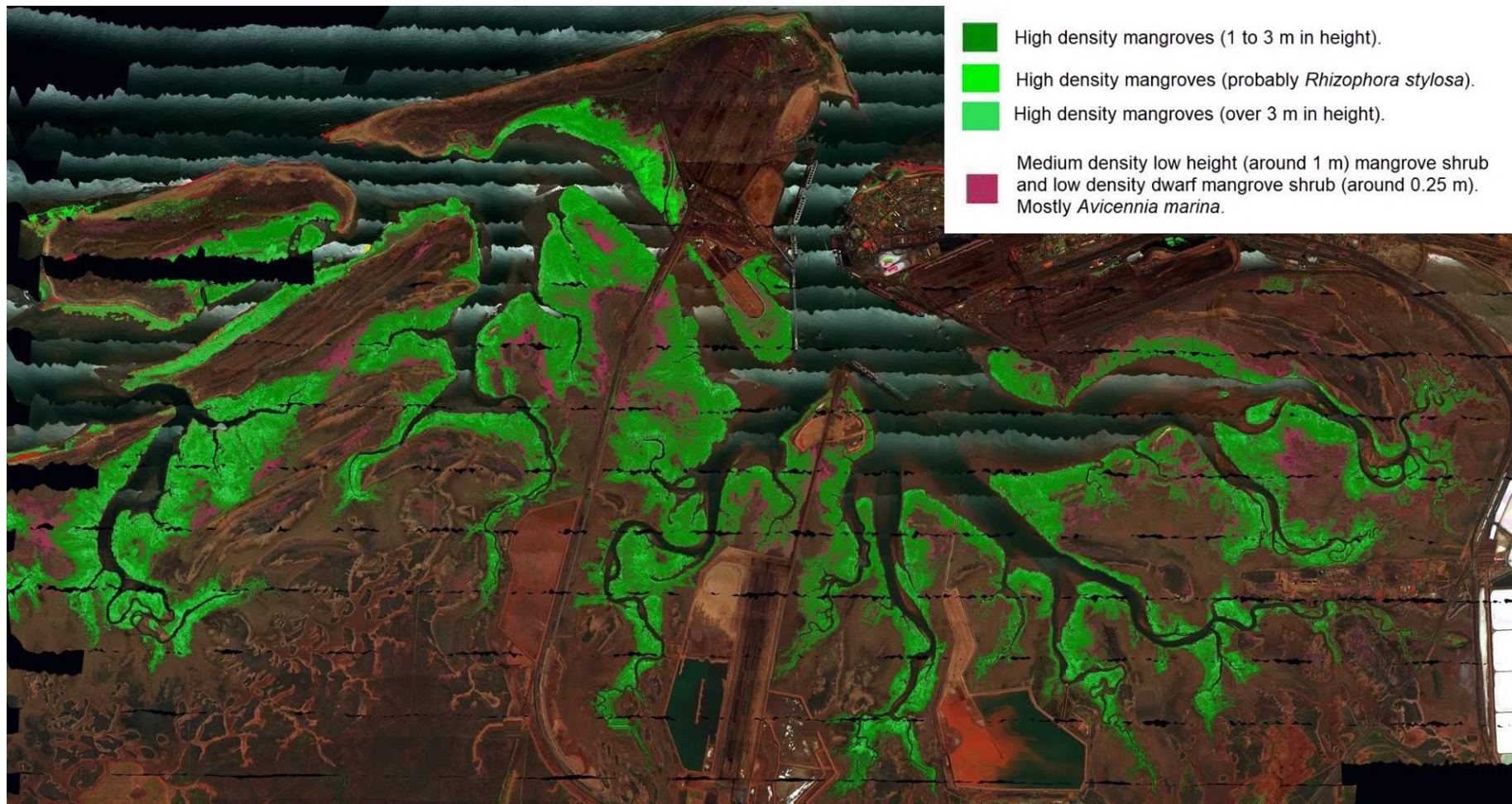


Figure 171: Left side of the JM18 map with a legend.

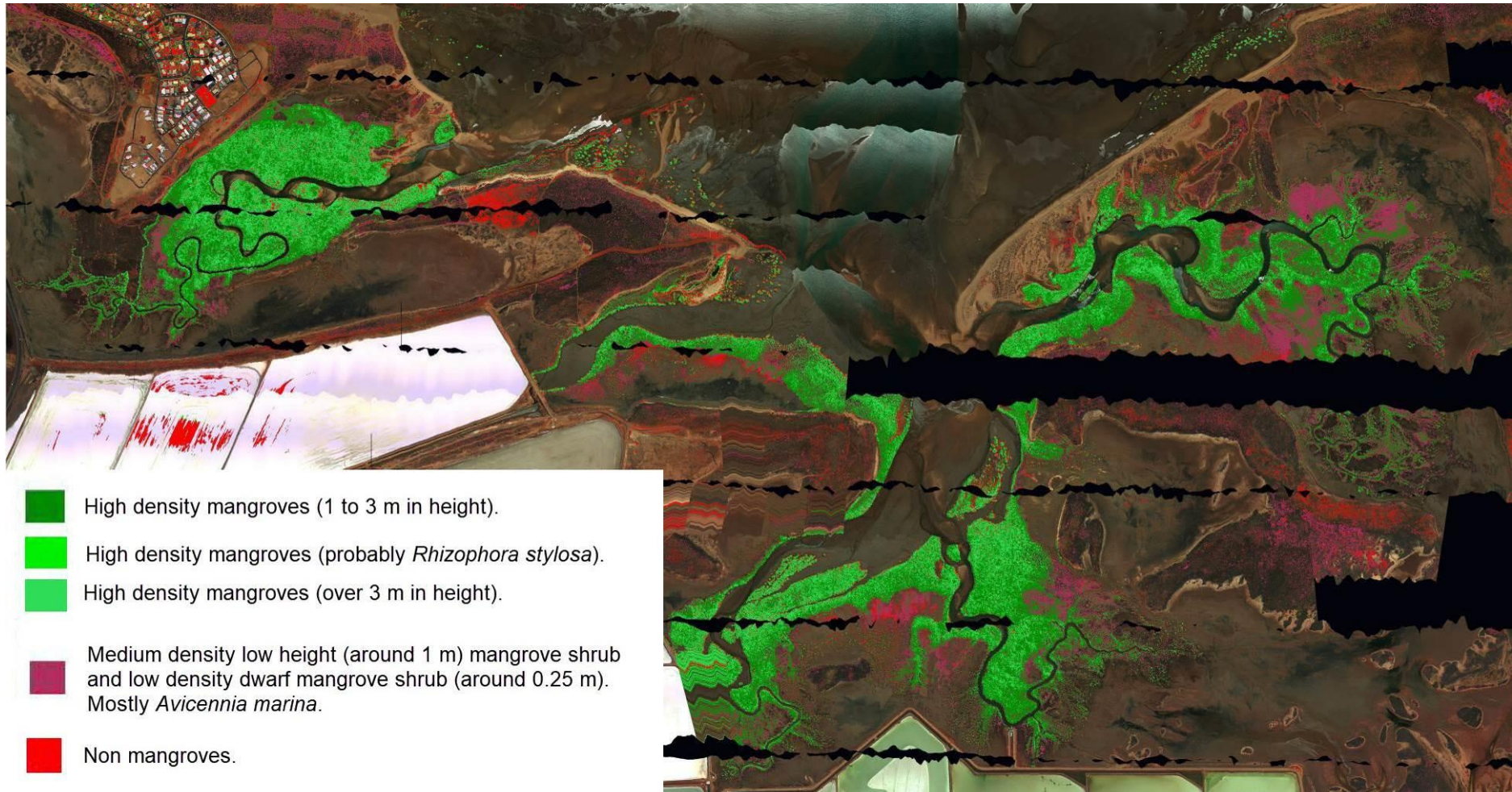


Figure 172: Right side of the JM18 map with a legend.

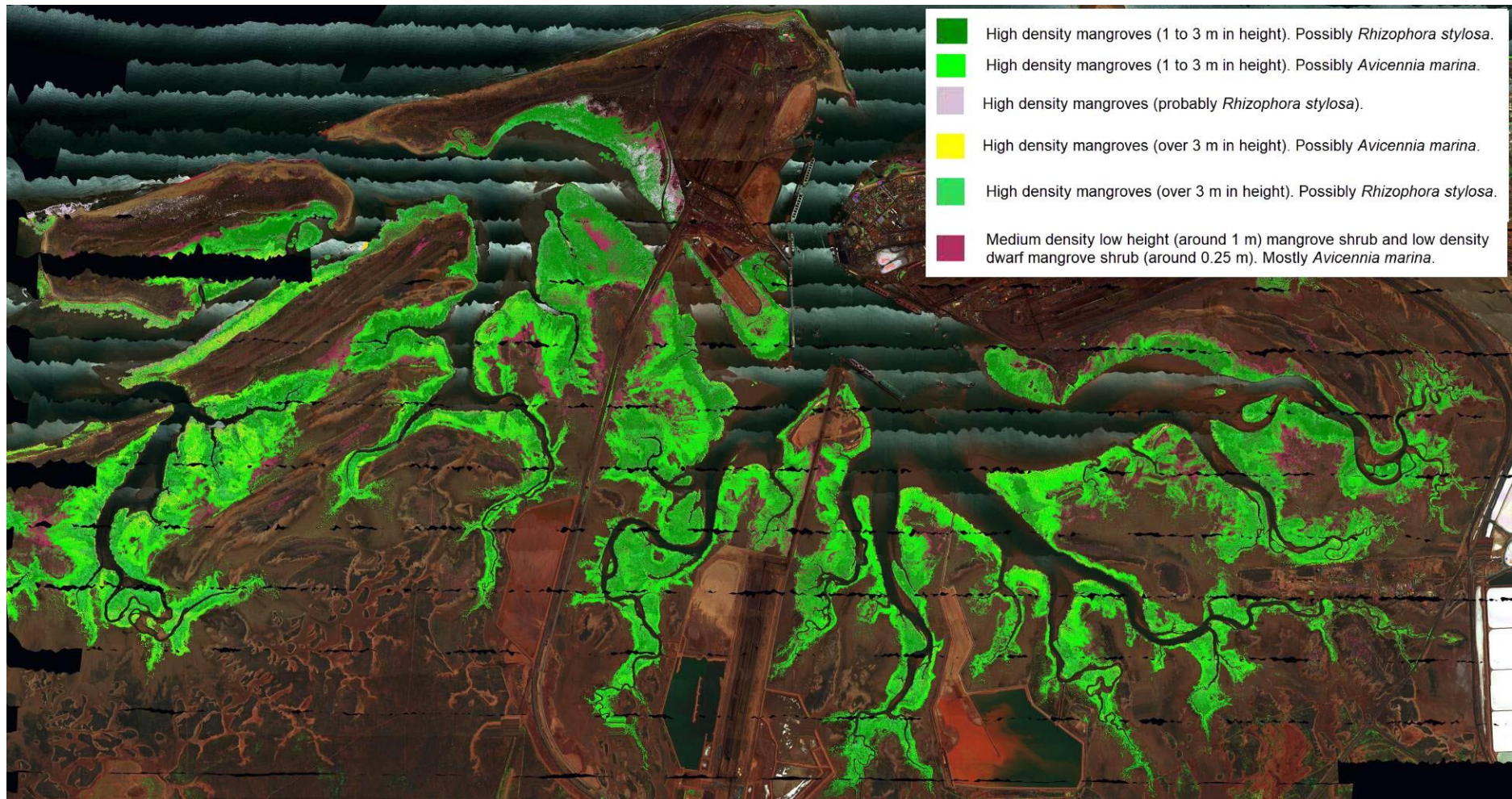


Figure 173: Left side of the JM17 map with a legend.

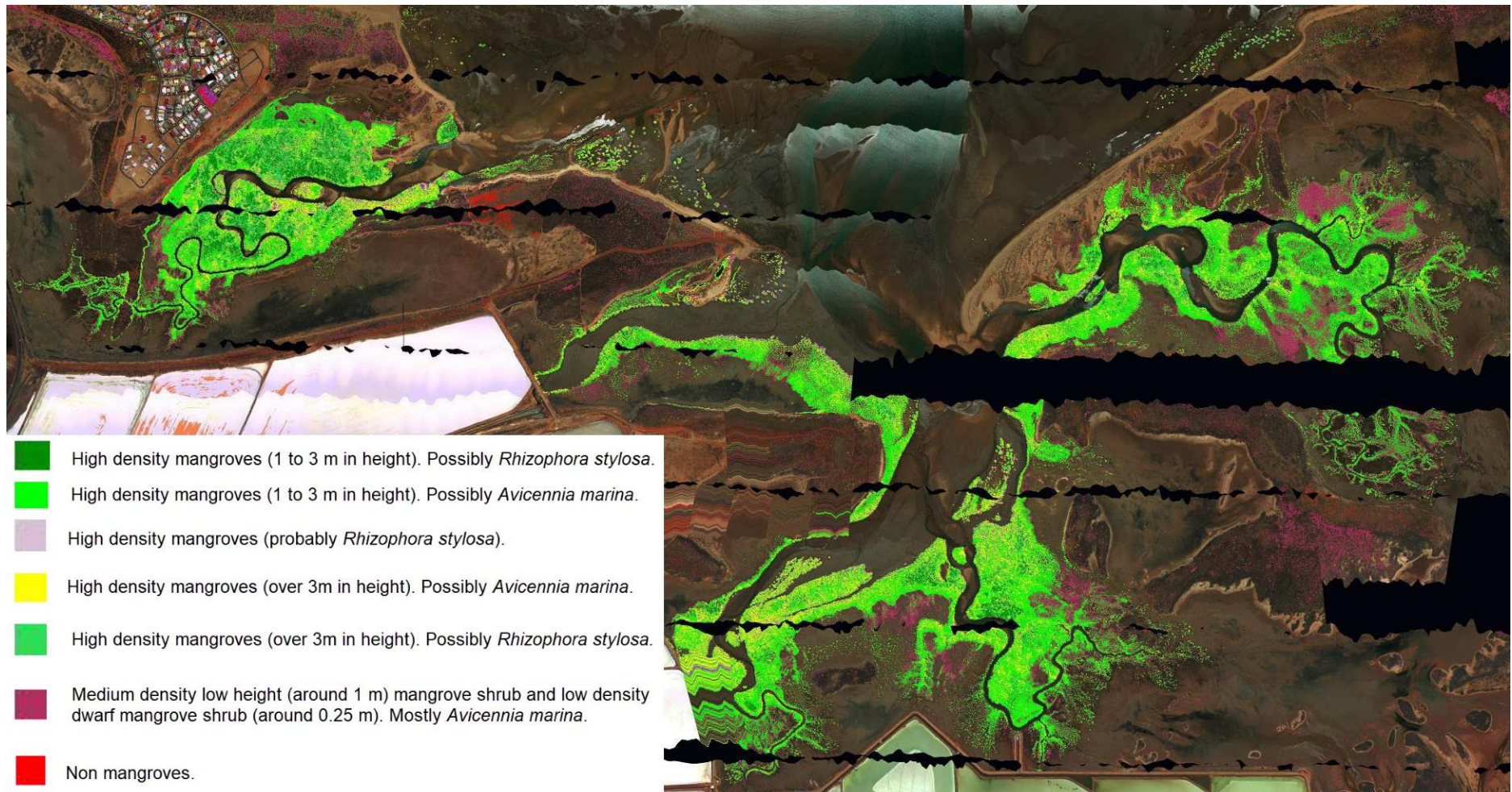


Figure 174: Right side of the JM17 map with a legend

5 Conclusion and Recommendations

The research in this thesis demonstrates that hyperspectral images having spectral brightness inconsistencies may be improved using the normalisation approach developed in this work. The technique adjusts individual pixel spectra to be more consistent within-class over an image but not designed to adjust individual spectra with reference to “true” spectra, such as the ASD ground spectra. The work demonstrated that normalised radiance-based images proved superior in classification to reflectance-based images, as the classes were more numerous and displayed statistically greater separability. The normalisation technique is an image-based empirical approach and is applicable to any hyperspectral image.

The objectives were defined in Section 1.3. These are elaborated upon to demonstrate how they were successfully addressed in the thesis, along with a brief conclusion.

Objective 1:

Development of a hyperspectral library of vegetative species for the Port Hedland coastal region.

The objective was addressed under Section 4.3, whereby an ASD field spectrometer recorded spectral samples of vegetation in the Port Hedland coastal region. For each cover type, mean spectra and their uncertainties were calculated and graphed.

Objective 2:

To investigate the ability to discriminate between and classify different types of vegetative matter, with particular emphasis on mangroves.

This objective was addressed under Section 4.4. Spectral angles were calculated between each pair of cover types and their relative magnitudes interpreted. The high degree of ASD spectral similarities between the seven mangrove species at

Finucane Island demonstrates the high spectral fidelity required to distinguish between them.

A quantitative technique introduced in Section 4.4.3 examined the extent of spectral similarity between mangrove species using a tally-based system. On average, and compared to all other mangroves, *Osbornia octodonta* is the most dissimilar, while *Bruguiera exaristata* is spectrally the most similar (followed closely by *Rhizophora stylosa* and *Aegialitis annulata*). This means that, on average, it is easiest to distinguish *Osbornia octodonta* from all other mangroves, while *Bruguiera exaristata* is especially difficult to distinguish from other mangroves.

Objective 3:

To produce and interpret a vegetation map and assess its validity to those produced by other parties.

The first part of the objective, concerning the production of a vegetation map, is found under Section 4.5. The largest spectral angle between pairs of mangroves using ASD data is 0.13 ± 0.04 rad, while the spectral angle between the ASD and image reflectance spectra is 0.11 rad for *Avicennia marina*. This demonstrates that by using ASD spectra in training a spectral angle supervised classifier, the noisy image spectral data is incapable of distinguishing between different species of mangroves.

At the simplest level, a vegetation map simply shows the location of vegetation using image spectra. The NDVI is a particularly simple and common method to produce such a map. In this thesis, the mean-gradient is functionally similar to the NDVI but incorporates additional wavelengths, thereby smoothing the noisy airborne data. A vegetation-mask was developed from the mean-gradient method, where different threshold values relate to the density of vegetation in a map. Fundamentally, this meets the objective stated above, although the PHPA hyperspectral data would be underutilised in this case. The vast data volume contained in hyperspectral data allows it to potentially produce a much more detailed vegetation map than a simple NDVI map, as many more wavelengths can

be incorporated. However, more advanced data mining techniques must be used to extract the useful information.

It was demonstrated that only when the spectral brightnesses in the PHPA image were made consistent, did it lead to consistent classes in the thematic map. As a result, the bulk of the thesis was directed toward producing spectrally consistent image spectra, using a process termed normalisation.

Our interest lies in classifying vegetation, particularly mangroves. Consequently, all non-vegetation was first removed from the normalised image, prior to adopting standard hyperspectral remote sensing techniques, such as PCA feature reduction followed by unsupervised classification. The separability of each pair of thematic classes was assessed statistically using JM distances. Three thematic maps were produced from the best normalised image (i.e. N_Rad_VI_VI). These maps considered thematic classes at increasing JM distance thresholds and subsequently increasing levels of class confidence. The production of the JM18 map was the main focus of the thesis, whereby classes exist to a moderate degree of confidence and is a compromise between poor (JM17) and high (JM19) degrees of class separability. The JM19 thematic map contains thematic classes separable to a JM distance of at least 1.9. The classes represent vegetation to a high degree of confidence but their class numbers are low (just two of the six classes specifically relate to mangroves). For the JM18 map, eight classes exist to a moderate degree of confidence, although only four relate to mangroves. This map is shown in Section 4.6.6 with a legend interpreting the spatial features in ecological terms. However, further investigative work found that the JM17 map, whereby classes are separable to low probability, was subsequently found to contain physically meaningful interpretations. Out of the ten separable classes, six relate to mangroves. This map is also presented in Section 4.6.6 with a legend.

The interpretation for each thematic class was based on field trip data in addition to analysing class mean spectral data. Field work evidence showed regions consisting of highly similar mangrove communities but composed of distinct classes on the thematic map. Field work showed these communities having different canopy heights, while spectrally mean class spectral brightness differences occurred in the NIR region. These were attributed to vegetative densities (spatial and/or

canopy). Although canopy heights were not formally measured, field work showed differences at approximately 3 m. Field evidence for other classes revealed very short mangroves and dwarf mangrove shrubs. Although the classes in the JM18 map have generic interpretations for mangroves, the JM17 map is a lower confidence map and as such, an attempt was made to name actual mangrove species (based on probability arguments). Field work showed the majority of the mangroves to be *Avicennia marina*, while *Rhizophora Stylosa* and *Ceriops australis* were found in lower proportions. Based on analysing both mean class spectra, in addition to the probability of occurrence of particular mangrove species, the mangroves defined in the classes in the JM17 map were subsequently identified as *Avicennia marina*, and *Rhizophora Stylosa*.

A commercially produced mangrove map (WorleyParsons, 2013) for the same region was produced using a combination of airborne photography and field surveys, and useful for comparison and validation with the results of the thesis (although the airborne map is not to be assumed as “correct”). Encouragingly, the classes contained in the thematic maps, as produced using normalised images, were more consistent compared to the map as produced using the original (unnormalised) hyperspectral image (i.e. PHPA_Ref_VI). As the data mining techniques remained the same, this demonstrated that normalisation improved the consistency of classes in classification maps. Furthermore, using reasonable assumptions, the total population of each mangrove community was found to be within 5% when comparing the map by E. Paling et al. (2003) to the JM17 map in this thesis. The map comparison work thereby fulfils thesis objective 3.

Based on the work in this thesis, a number of recommendations are subsequently outlined.

Wetlands, which includes mangroves, are heterogeneous ecosystems containing highly mixed species (Lu & He, 2018). At lower resolutions, different species are not able to be resolved. However, UAV's attain ultrahigh spatial resolutions, as high as 2 cm (Cao et al., 2018), thereby offering the possibility to capture much finer spatial detail. Under laboratory conditions, both Wang et al. (2004) and Vaiphasa et al. (2005) demonstrated the effectiveness of using a handful of wavelengths to distinguish between mangrove species. It would be interesting to explore the

possibility of using similar feature selection approaches with the PHPA hyperspectral library, to identify key wavelengths that distinguish the mangroves located in the Port Hedland coastal region. These key selection wavelengths could be programmed into a UAV-based sensor. Currently, hyperspectral sensors record data over hundreds of bands. Much of this data is highly correlated at specific wavelengths, requiring removal through feature reduction techniques. The selection of a few key bands has the additional benefit of reducing processing time and storage requirements. These key wavelengths may be tailored to the remote sensing product desired. For example, the classification of mangrove against non-mangroves, classifying different species of mangrove, or monitoring mangrove leaf water content. The UAV based sensor can also be programmed with a different set of key wavelengths to monitor (for example) nutrient levels in mangroves. These techniques are also applicable to different fields, e.g. in agriculture, where agricultural crops nutrition can be monitored.

The high spatial resolution of UAVs allows for a higher chance of discerning particularly small mangroves or other vegetation.

A similar approach to Zarco-Tejada et al. (2014) or Stefanik et al. (2011) (based on UAV stereo-vision) can be used to extract DEM information. However, the significant overlap in flight track recording will limit the spatial region being covered. Therefore, it is suggested that a small region, consisting of highly mixed mangrove communities, be remotely sensed at high spatial resolution. Classification accuracy is then assessed using various spatial resolutions, in a similar manner to those in other studies (e.g. Lu and He (2018), Cao et al. (2018)), with an appropriate resolution selected to cover a wider region in a timely manner.

There are also benefits in using mangrove height data for mangrove classification, as demonstrated by other studies incorporating LiDAR data with hyperspectral data (e.g. Lijuan, Yong, Wenyi, Zengyuan, and Mingze (2011), Moses Azong Cho et al. (2012)). Tall mangrove species, such as the mature *Rhizophora sp.* can be distinguished from the shorter *Avicennia sp.* using LiDAR data, as *Rhizophora sp.* grow taller than *Avicennia sp.* (see Appendix T). As PHPA LiDAR data is available, it is recommended that it be processed and fused with the existing classification product. It would be interesting to compare LiDAR-based height information to

UAV-derived DEM data (like Zarco-Tejada et al. (2014)) and to compare the LiDAR-incorporated classification results with earlier thesis results. Perhaps the data recorded by a LiDAR sensor is able to be sufficiently replaced by DEM data for classification purposes.

It would also be interesting to analyse the benefits of OBIA to pixel-based classification, as some studies suggest improved classification accuracies (e.g. Kamal and Phinn (2011)), although a claim disputed by Duro et al. (2012).

Field work was made more difficult due to the density of mangrove forests, often too dense to traverse comfortably and without inflicting damage to the tree. Health and safety regulations also severely limited access to field sites. The PHPA vegetation map contains an interpretation in relation to mangrove canopy height. However, many of the taller mangroves are found along estuaries, away from direct visual observation on the ground. A UAV, carrying two cameras would allow for the recording of stereoscopic images, from which tree heights may be calculated and considered an alternative approach to deriving DEM data from flight overlaps.

It is also recommended to conduct field work simultaneously with an airborne-based survey, to minimise spectral differences between the two approaches based on phenology and senescence in particular. It might be worthwhile targeting the flowering season of mangroves, to identify rare mangroves in the region. For instance, during the period of September, only two mangroves could possibly flower (according to Duke (1952)). These are *Aegialitis annulata*, which flowers from June – Sept and *Bruguiera exaristata*, which flowers from Sept – Oct. A field trip could be conducted by biologists to examine when flowers are in bloom for these species at known sites. A remote sensing survey during these periods could assist in identifying particular species, as phenological changes in reflectances are observable features (Carvalho, Schlerf, van der Putten, & Skidmore, 2013).

Studies have shown the importance of utilising hyperspectral wavelengths beyond 990 nm in mangrove species differentiability. The PHPA airborne survey only recorded radiance data over wavelengths in the range 400.7 - 984.5 nm. However, Wang and Sousa (2009) showed that six wavelengths were important in mangrove discrimination, of which 3 exceeded the 1000 nm. Similarly, work by Vaiphasa et al. (2005) concluded that four key wavelengths discriminated their

mangroves, with three exceeding 1000 nm. Although both these conclusions were based on studying mangrove reflectances under laboratory conditions, it would be interesting to examine the effects of using a fuller hyperspectral range of wavelengths in airborne data for species discrimination.

As a final point, the lack of instrument calibration reduces the Tafkaa atmospheric model's ability to effectively correct hyperspectral data (Miller et al. (2005, p. 57) and Montes et al. (2004)). Therefore, it is recommended that in future, the hyperspectral instrument be calibrated prior to airborne remote sensing.

6 References

- A. Berk, G. P. A., L. S. Bernstein, P. K. Acharya, H. Dothe, M. W. Matthew, S. M. Adler-Golden, J. H. Chetwynd, Jr., S. C. Richtsmeier, B. Pukall, C. L. Allred, L. S. Jeong, and M. L. Hoke. (1999). MODTRAN4 Radiative Transfer Modeling for Atmospheric Correction. *SPIE Proceeding, Optical Spectroscopic Techniques and Instrumentation for Atmospheric and Space Research III*, 3756. Retrieved from <http://spectral.com/publications.shtml>.
- Airbus Defence & Space. (2015). Airbus Defence and Space Constellation. Retrieved from <http://www.intelligence-airbusds.com/en/147-spot-6-7-satellite-imagery>.
- Alongi, D. M. (2002). Present state and future of the world's mangrove forests. *Environmental Conservation*, 29(3), 331-349. Retrieved from <http://search.proquest.com/docview/203164725?accountid=10382>
http://link.library.curtin.edu.au/openurl?url_ver=Z39.88-2004&rft_val_fmt=info:ofi/fmt:kev:mtx:journal&genre=unknown&sid=ProQ:ProQ%3Aagriculturejournals&atitle=Present+state+and+future+of+the+world%27s+mangrove+forests&title=Environmental+Conservation&issn=03768929&date=2002-09-01&volume=29&issue=3&spage=331&au=Alongi%2C+Daniel+M&isbn=&jtitle=Environmental+Conservation&bttitle=&rft_id=info:eric/&rft_id=info:doi/.
- Alongi, D. M. (2008). Mangrove forests: Resilience, protection from tsunamis, and responses to global climate change. *Estuarine, Coastal and Shelf Science*, 76(1), 1-13. <https://doi.org/10.1016/j.ecss.2007.08.024>
- American Museum of Natural History. (n.d.). What's a Mangrove? And How Does It Work? Retrieved from <https://www.amnh.org/explore/videos/biodiversity/mangroves-the-roots-of-the-sea/what-s-a-mangrove-and-how-does-it-work>.
- Anderson, J. B. (1971). Land-use classification schemes. *Photogrammetric Engineering & Remote Sensing*, 37, 379-387. Retrieved from
- Anderson, J. R., Hardy, E. E., Roach, J. T., & Witmer, R. E. (1976). A Land Use And Land Cover Classification System For Use With Remote Sensor Data. *Geological Survey Circular 671, United States Government Printing Office, Washington*. Retrieved from
- Andrews, L. C. (1986). *Elementary partial differential equations*. Orlando, Florida: Academic Press.
- Asner, G. P., & Martin, R. E. (2009). Airborne Spectranomics: Mapping Canopy Chemical and Taxonomic Diversity in Tropical Forests. *Frontiers in Ecology and the Environment*, 7(5), 269-276. <https://doi.org/10.2307/25595147>
- Australian Institute of Marine Science. (n.d.). Mangrove is more than just a tree. Retrieved from: <http://www.aims.gov.au/docs/projectnet/mangroves-more-than.html>. Retrieved from <http://www.aims.gov.au/docs/projectnet/mangroves-more-than.html>.
- Ayala-Silva, T., & Beyl, C. A. (2005). Changes in spectral reflectance of wheat leaves in response to specific macronutrient deficiency. *Advances in Space Research*, 35(2), 305-317. <https://doi.org/https://doi.org/10.1016/j.asr.2004.09.008>
- Baloloy, A. B., Blanco, A. C., Sta. Ana, R. R. C., & Nadaoka, K. (2020). Development and application of a new mangrove vegetation index (MVI) for rapid and accurate mangrove mapping. *ISPRS Journal of Photogrammetry and Remote Sensing*, 166, 95-117. <https://doi.org/https://doi.org/10.1016/j.isprsjprs.2020.06.001>

- Bartholy, J., & Pongracz, R. (2005). Extremes of ground-based and satellite measurements in the vegetation period for the Carpathian Basin. *Physics and Chemistry of the Earth, Parts A/B/C*, 30(1–3), 81-89. <https://doi.org/http://dx.doi.org/10.1016/j.pce.2004.08.012>
- Basheer, M. A., El Kafrawy, S. B., & Mekawy, A. A. (2019). Identification of mangrove plant using hyperspectral remote sensing data along the red sea, Egypt. *Egyptian Journal of Aquatic Biology and Fisheries*, 23(1), 27-36. <https://doi.org/10.21608/ejabf.2019.25932>
- Bauer, M. E., Craig S. T. Daughtry, Larry L. Biehl, Edward T. Kanemasu, & Hall, F. G. (1986). Field Spectroscopy of Agricultural Crops. *IEEE Transactions on Geoscience and Remote Sensing*, GE-24(1), 65-75. Retrieved from
- Beh Boon Chun, Jafri, M. Z. M., & San, L. H. (2011). Reflectance Characteristic of Certain Mangrove Species at Matang Mangrove Forest Reserve, Malaysia. *Proceeding of the 2011 IEEE International Conference on Space Science and Communication (IconSpace) 12-13 July 2011, Penang, Malaysia*, 147-151. Retrieved from
- Belluco, E., Camuffo, M., Ferrari, S., Modenese, L., Silvestri, S., Marani, A., & Marani, M. (2006). Mapping salt-marsh vegetation by multispectral and hyperspectral remote sensing. *Remote Sensing of Environment*, 105(1), 54-67. <https://doi.org/http://dx.doi.org/10.1016/j.rse.2006.06.006>
- Ben-Dor, E. (2002). Quantitative remote sensing of soil properties *Advances in Agronomy* (Vol. Volume 75, pp. 173-243): Academic Press. [http://dx.doi.org/http://dx.doi.org/10.1016/S0065-2113\(02\)75005-0](http://dx.doi.org/http://dx.doi.org/10.1016/S0065-2113(02)75005-0)
- Ben-Dor, E., Chabrilat, S., Demattê, J. A. M., Taylor, G. R., Hill, J., Whiting, M. L., & Sommer, S. (2009). Using Imaging Spectroscopy to study soil properties. *Remote Sensing of Environment*, 113, Supplement 1(0), S38-S55. <https://doi.org/10.1016/j.rse.2008.09.019>
- Benediktsson, J. A., Sveinsson, J. R., & Amason, K. (1995). Classification and feature extraction of AVIRIS data. *Geoscience and Remote Sensing, IEEE Transactions on*, 33(5), 1194-1205. <https://doi.org/10.1109/36.469483>
- Bhattarai, B., & Giri, C. (2011). Assessment of mangrove forests in the Pacific region using Landsat imagery. *Journal of Applied Remote Sensing*, 5(1), 053509-053509. <https://doi.org/10.1117/1.3563584>
- Boccia, V. (2019). TM & ETM+. 26-08-19. Retrieved from <https://earth.esa.int/web/sppa/mission-performance/esa-3rd-party-missions/landsat-1-7/tm-etm/sensor-description>.
- Borgelt, C., Timm, H., & Kruse, R. (2000, 7-10 May 2000). *Using fuzzy clustering to improve naive Bayes classifiers and probabilistic networks*. Paper presented at the Fuzzy Systems, 2000. FUZZ IEEE 2000. The Ninth IEEE International Conference on. <https://doi.org/10.1109/FUZZY.2000.838633>
- Burden, R. L., & Faires, J. D. (1989). *Numerical Analysis* (4th ed.). Boston: PWS-Kent.
- Bureau of Meteorology. (2015). Tropical Cyclones Affecting Port Hedland. Retrieved from <http://www.bom.gov.au/cyclone/history/wa/ptthed.shtml>.
- Calculator, N. S. (2016). NOAA Solar Calculator. Retrieved from <http://www.esrl.noaa.gov/gmd/grad/solcalc/>.
- Campbell, J. B., & Wynne, R. H. (2011). *Introduction to Remote Sensing* (Fifth Edition ed.): The Guilford Press.

- Canty, M. J. (2009). *Image Analysis, Classification, and Change Detection in Remote Sensing: With Algorithms for ENVI/IDL* (2nd ed.): CRC Press.
- Cao, J., Leng, W., Liu, K., Liu, L., He, Z., & Zhu, Y. (2018). Object-Based Mangrove Species Classification Using Unmanned Aerial Vehicle Hyperspectral Images and Digital Surface Models. *Remote Sensing*, *10*, 89. <https://doi.org/10.3390/rs10010089>
- Carlson, T. N., & Ripley, D. A. (1997). On the relation between NDVI, fractional vegetation cover, and leaf area index. *Remote Sensing of Environment*, *62*(3), 241-252. [https://doi.org/http://dx.doi.org/10.1016/S0034-4257\(97\)00104-1](https://doi.org/http://dx.doi.org/10.1016/S0034-4257(97)00104-1)
- Carvalho, S., Schlerf, M., van der Putten, W. H., & Skidmore, A. K. (2013). Hyperspectral reflectance of leaves and flowers of an outbreak species discriminates season and successional stage of vegetation. *International Journal of Applied Earth Observation and Geoinformation*, *24*(Supplement C), 32-41. <https://doi.org/https://doi.org/10.1016/j.jag.2013.01.005>
- Cashion, B. (2013). Mangrove forest cover fading fast. *Environmental Development*, *8*(0), 105-112. <https://doi.org/http://dx.doi.org/10.1016/j.envdev.2013.09.001>
- CASI. (n.d.). Compact Airborne Spectrographic Imager (CASI). Retrieved from http://geo.arc.nasa.gov/sge/jskills/top-down/OTTER/OTTER_docs/CASI.html.
- Cattell, R. B. (1966). The Scree Test For The Number Of Factors. *Multivariate Behavioral Research*, *1*(2), 245-276. https://doi.org/10.1207/s15327906mbr0102_10
- Center for Coastal Physical Oceanography. (n.d.). Spectral Vegetation Indices (SVIs). Retrieved from http://www.ccpo.odu.edu/SEES/veget/class/Chap_4/4_5.htm.
- Chandelier, L., & Martinoty, G. (2009). A Radiometric Aerial Triangulation for the Equalization of Digital Aerial Images and Orthoimages. *Photogrammetric Engineering & Remote Sensing*, *75*(2), 193-200. Retrieved from
- Chang, S.-H., & Collins, W. (1983). Confirmation of the airborne biogeophysical mineral exploration technique using laboratory methods. *Economic Geology*, *78*(4), 723-736. <https://doi.org/10.2113/gsecongeo.78.4.723>
- Chavez, P. S. J. (1988). An improved dark-object subtraction technique for atmospheric scattering correction of multispectral data. *Remote Sensing of Environment*, *24*(3), 459-479. [https://doi.org/10.1016/0034-4257\(88\)90019-3](https://doi.org/10.1016/0034-4257(88)90019-3)
- Cho, M. A., Debba, P., Mathieu, R., Naidoo, L., van Aardt, J., & Asner, G. P. (2010). Improving Discrimination of Savanna Tree Species Through a Multiple-Endmember Spectral Angle Mapper Approach: Canopy-Level Analysis. *Geoscience and Remote Sensing, IEEE Transactions on*, *48*(11), 4133-4142. <https://doi.org/10.1109/tgrs.2010.2058579>
- Cho, M. A., Mathieu, R., Asner, G. P., Naidoo, L., van Aardt, J., Ramoelo, A., . . . Erasmus, B. (2012). Mapping tree species composition in South African savannas using an integrated airborne spectral and LiDAR system. *Remote Sensing of Environment*, *125*(0), 214-226. <https://doi.org/10.1016/j.rse.2012.07.010>
- Cho, M. A., & Skidmore, A. K. (2006). A new technique for extracting the red edge position from hyperspectral data: The linear extrapolation method. *Remote Sensing of Environment*, *101*(2), 181-193. <https://doi.org/10.1016/j.rse.2005.12.011>
- Chulhee, L., & Landgrebe, D. A. (1993). Analyzing high-dimensional multispectral data. *Geoscience and Remote Sensing, IEEE Transactions on*, *31*(4), 792-800. <https://doi.org/10.1109/36.239901>

- Clark, C. D., Ripley, H. T., Green, E. P., Edwards, A. J., & Mumby, P. J. (1997). Cover Mapping and measurement of tropical coastal environments with hyperspectral and high spatial resolution data. *International Journal of Remote Sensing*, 18(2), 237-242. <https://doi.org/10.1080/014311697219033>
- Cohen, W. B., & Goward, S. N. (2004). Landsat's Role in Ecological Applications of Remote Sensing. *BioScience*, 54(6), 535-545. [https://doi.org/10.1641/0006-3568\(2004\)054\[0535:lrieao\]2.0.co;2](https://doi.org/10.1641/0006-3568(2004)054[0535:lrieao]2.0.co;2)
- Coleman, T. L., Gudapati, L., & Derrington, J. (1990). Monitoring forest plantations using Landsat Thematic Mapper data. *Remote Sensing of Environment*, 33(3), 211-221. [https://doi.org/http://dx.doi.org/10.1016/0034-4257\(90\)90032-H](https://doi.org/http://dx.doi.org/10.1016/0034-4257(90)90032-H)
- Collins, W. (1978). Remote sensing of crop type and maturity. *Photogramm. Eng. Remote Sens.*, 44, 43-55. Retrieved from https://www.asprs.org/wp-content/uploads/pers/1978journal/jan/1978_jan_43-55.pdf.
- Conese, C., & Maselli, F. (1992). Use of error matrices to improve area estimates with maximum likelihood classification procedures. *Remote Sensing of Environment*, 40(2), 113-124. [https://doi.org/10.1016/0034-4257\(92\)90009-9](https://doi.org/10.1016/0034-4257(92)90009-9)
- Congalton, R. G. (1988a). A comparison of sampling schemes used in generating error matrices for assessing the accuracy of maps generated from remotely sensed data. *Photogrammetric Engineering and Remote Sensing*, 54(5), 593-600. Retrieved from
- Congalton, R. G. (1988b). Using spatial autocorrelation analysis to explore the errors in maps generated from remotely sensed data. *Photogrammetric Engineering and Remote Sensing*, 54(5), 587-592. Retrieved from
- Congalton, R. G. (1991). A review of assessing the accuracy of classifications of remotely sensed data. *Remote Sensing of Environment*, 37, 35-46. Retrieved from
- Congalton, R. G., & Green, K. (1999). *Assessing the Accuracy of Remotely Sensed Data: Principles and Practices*. Boca Raton, FL: Lewis Publishers.
- Costello, A. B., & Osborne, J. W. (2005). Best practices in exploratory factor analysis: four recommendations for getting the most from your analysis. *Practical Assessment, Research & Evaluation*, 10(7), 1-9. Retrieved from
- Cutler, J. C. (2014). Mangrove ecology. Retrieved from [http://editors.eol.org/eoearth/wiki/Mangrove_\(Mangrove_ecology\)](http://editors.eol.org/eoearth/wiki/Mangrove_(Mangrove_ecology)).
- D'Iorio, M., Jupiter, S. D., Cochran, S. A., & Potts, D. C. (2007). Optimizing Remote Sensing and GIS Tools for Mapping and Managing the Distribution of an Invasive Mangrove (*Rhizophora mangle*) on South Molokai, Hawaii. *Marine Geodesy*, 30(1-2), 125-144. <https://doi.org/10.1080/01490410701296663>
- Dalponte, M., Bruzzone, L., & Gianelle, D. (2012). Tree species classification in the Southern Alps based on the fusion of very high geometrical resolution multispectral/hyperspectral images and LiDAR data. *Remote Sensing of Environment*, 123(0), 258-270. <https://doi.org/10.1016/j.rse.2012.03.013>
- Dalponte, M., Bruzzone, L., Vescovo, L., & Gianelle, D. (2009). The role of spectral resolution and classifier complexity in the analysis of hyperspectral images of forest areas. *Remote Sensing of Environment*, 113(11), 2345-2355. <https://doi.org/10.1016/j.rse.2009.06.013>

- Das, S., Ghose, M. (1996). Anatomy of leaves of some mangroves and their associates of Sundarbans, West Bengal. *Phytomorphology: An International Journal of Plant Morphology*, 46(2), 139-150. Retrieved from
- Dinuls, R., Erins, G., Lorencs, A., Mednieks, I., & Sinica-Sinavskis, J. (2012). Tree Species Identification in Mixed Baltic Forest Using LiDAR and Multispectral Data. *Selected Topics in Applied Earth Observations and Remote Sensing, IEEE Journal of*, 5(2), 594-603.
<https://doi.org/10.1109/jstars.2012.2196978>
- Dougherty, G. (2012). *Pattern Recognition and Classification: An Introduction*. New York: Springer.
- Duke, N. (1952). *Australia's Mangroves: The Authoritative Guide to Australia's Mangrove Plants*: Brisbane : University of Queensland and Norman C. Duke.
- Duro, D. C., Franklin, S. E., & Dubé, M. G. (2012). A comparison of pixel-based and object-based image analysis with selected machine learning algorithms for the classification of agricultural landscapes using SPOT-5 HRG imagery. *Remote Sensing of Environment*, 118, 259-272. <https://doi.org/https://doi.org/10.1016/j.rse.2011.11.020>
- Edwards Jr, T. C., Moisen, G. G., & Cutler, D. R. (1998). Assessing Map Accuracy in a Remotely Sensed, Ecoregion-Scale Cover Map. *Remote Sensing of Environment*, 63(1), 73-83.
[https://doi.org/http://dx.doi.org/10.1016/S0034-4257\(96\)00246-5](https://doi.org/http://dx.doi.org/10.1016/S0034-4257(96)00246-5)
- Eismann, M. (2012). *Hyperspectral Remote Sensing*. Bellingham, Washington: SPIE Press.
- Emery, C. (2009). Mangroves Reduced Storm Death Toll. *Frontiers in Ecology and the Environment*, 7(5), 237. <https://doi.org/10.2307/25595135>
- Epiphanio, J. N., & Huete, A. R. (1995). Dependence of NDVI and SAVI on sun/sensor geometry and its effect on fAPAR relationships in Alfalfa. *Remote Sensing of Environment*, 51(3), 351-360.
[https://doi.org/10.1016/0034-4257\(94\)00110-9](https://doi.org/10.1016/0034-4257(94)00110-9)
- ESA. (2019). PRISMA (Hyperspectral Precursor and Application Mission). 2019. Retrieved from <https://directory.eoportal.org/web/eoportal/satellite-missions/p/prisma-hyperspectral>.
- Escobar, D. E., Everitt, J. H., Noriega, J. R., Cavazos, I., & Davis, M. R. (1998). A Twelve-Band Airborne Digital Video Imaging System (ADVIS). *Remote Sensing of Environment*, 66(2), 122-128.
[https://doi.org/http://dx.doi.org/10.1016/S0034-4257\(98\)00053-4](https://doi.org/http://dx.doi.org/10.1016/S0034-4257(98)00053-4)
- European Space Agency. (2020). Sentinel-2 Spatial and Spectral Resolutions. Retrieved from <https://sentinel.esa.int/web/sentinel/missions/sentinel-2/instrument-payload/resolution-and-swath>.
- Foody, G. M. (2008). Harshness in image classification accuracy assessment. *International Journal of Remote Sensing*, 29(11), 3137-3158. <https://doi.org/10.1080/01431160701442120>
- Foody, G. M. (2008). RVM - based multi - class classification of remotely sensed data. *International Journal of Remote Sensing*, 29(6), 1817-1823. <https://doi.org/10.1080/01431160701822115>
- Foody, G. M. (2009). Sample size determination for image classification accuracy assessment and comparison. *International Journal of Remote Sensing*, 30(20), 5273-5291.
<https://doi.org/10.1080/01431160903130937>
- Foody, G. M., & Mathur, A. (2004). A relative evaluation of multiclass image classification by support vector machines. *IEEE Transactions on Geoscience and Remote Sensing*, 42(6), 1335-1343.
<https://doi.org/10.1109/TGRS.2004.827257>

- Fu, K. S., Landgrebe, D. A., & Phillips, T. L. (1969). Information processing of remotely sensed agricultural data. *Proceedings of the IEEE*, 57(4), 639-653.
<https://doi.org/10.1109/PROC.1969.7019>
- Galvão, L. S., Roberts, D. A., Formaggio, A. R., Numata, I., & Breunig, F. M. (2009). View angle effects on the discrimination of soybean varieties and on the relationships between vegetation indices and yield using off-nadir Hyperion data. *Remote Sensing of Environment*, 113(4), 846-856. <https://doi.org/10.1016/j.rse.2008.12.010>
- Gao, B.-C., & Goetz, A. F. H. (1990). Column Atmospheric Water Vapor and Vegetation Liquid Water Retrievals From Airborne Imaging Spectrometer Data. *J. Geophys. Res.*, 95(D4), 3549-3564.
<https://doi.org/10.1029/JD095iD04p03549>
- Gao, B.-C., Heidebrecht, K. B., & Goetz, A. F. H. (1993). Derivation of scaled surface reflectances from AVIRIS data. *Remote Sensing of Environment*, 44(2-3), 165-178.
[https://doi.org/10.1016/0034-4257\(93\)90014-o](https://doi.org/10.1016/0034-4257(93)90014-o)
- Gao, B.-C., Montes, M. J., Ahmad, Z., & Davis, C. O. (2000). Atmospheric Correction Algorithm for Hyperspectral Remote Sensing of Ocean Color from Space. *Appl. Opt.*, 39(6), 887-896. Retrieved from <http://ao.osa.org/abstract.cfm?URI=ao-39-6-887>.
- Gao, B.-C., Montes, M. J., Davis, C. O., & Goetz, A. F. H. (2009). Atmospheric correction algorithms for hyperspectral remote sensing data of land and ocean. *Remote Sensing of Environment*, 113, Supplement 1(0), S17-S24. <https://doi.org/10.1016/j.rse.2007.12.015>
- Gao, J. (1998). A hybrid method toward accurate mapping of mangroves in a marginal habitat from SPOT multispectral data. *International Journal of Remote Sensing*, 19(10), 1887-1899.
<https://doi.org/10.1080/014311698215045>
- Gao, J. (1999). A comparative study on spatial and spectral resolutions of satellite data in mapping mangrove forests. *International Journal of Remote Sensing*, 20(14), 2823-2833.
<https://doi.org/10.1080/014311699211813>
- Ghiyamat, A., & Shafri, H. Z. M. (2010). A review on hyperspectral remote sensing for homogeneous and heterogeneous forest biodiversity assessment. *International Journal of Remote Sensing*, 31(7), 1837-1856. <https://doi.org/10.1080/01431160902926681>
- Gilbert, M. A., González-Piqueras, J., García-Haro, F. J., & Meliá, J. (2002). A generalized soil-adjusted vegetation index. *Remote Sensing of Environment*, 82(2-3), 303-310.
[https://doi.org/http://dx.doi.org/10.1016/S0034-4257\(02\)00048-2](https://doi.org/http://dx.doi.org/10.1016/S0034-4257(02)00048-2)
- Goetz, A. F. H. (2009). Three decades of hyperspectral remote sensing of the Earth: A personal view. *Remote Sensing of Environment*, 113, Supplement 1(0), S5-S16.
<https://doi.org/10.1016/j.rse.2007.12.014>
- Goetz, A. F. H., Kindel, B. C., Ferri, M., & Zheng, Q. (2003). HATCH: results from simulated radiances, AVIRIS and Hyperion. *Geoscience and Remote Sensing, IEEE Transactions on*, 41(6), 1215-1222. <https://doi.org/10.1109/tgrs.2003.812905>
- Gonzalez, R. C., & Woods, R. E. (2008). *Digital Image Processing* (3rd ed.): Pearson Prentice Hall.
- Gonzalez, R. C., Woods, R. E., & Eddins, S. L. (2009). *Digital Image Processing Using MATLAB*: Gatesmark Publishing.
- Goodenough, D. G., Dyk, A., Niemann, K. O., Pearlman, J. S., Hao, C., Han, T., . . . West, C. (2003). Processing Hyperion and ALI for forest classification. *Geoscience and Remote Sensing, IEEE Transactions on*, 41(6), 1321-1331. <https://doi.org/10.1109/tgrs.2003.813214>

- Goodenough, D. G., Hao, C., Gordon, P., Niemann, K. O., & Quinn, G. (2012, 22-27 July 2012). *Forest applications with hyperspectral imaging*. Paper presented at the Geoscience and Remote Sensing Symposium (IGARSS), 2012 IEEE International. <https://doi.org/10.1109/igarss.2012.6351973>
- Goodenough, D. G., Li, J. Y., Asner, G. P., Schaepman, M. E., Ustin, S. L., & Dyk, A. (2006, July 31 2006-Aug. 4 2006). *Combining Hyperspectral Remote Sensing and Physical Modeling for Applications in Land Ecosystems*. Paper presented at the Geoscience and Remote Sensing Symposium, 2006. IGARSS 2006. IEEE International Conference on. <https://doi.org/10.1109/igarss.2006.518>
- Goodenough, D. G., Pearlman, J., Hao, C., Dyk, A., Tian, H., Jingyang, L., . . . Olaf Niemann, K. (2004, 20-24 Sept. 2004). *Forest information from hyperspectral sensing*. Paper presented at the Geoscience and Remote Sensing Symposium, 2004. IGARSS '04. Proceedings. 2004 IEEE International. <https://doi.org/10.1109/igarss.2004.1369826>
- Granek, E., & Ruttenberg, B. I. (2008). Changes in biotic and abiotic processes following mangrove clearing. *Estuarine, Coastal and Shelf Science*, 80(4), 555-562. <https://doi.org/10.1016/j.ecss.2008.09.012>
- Green, A. A., Berman, M., Switzer, P., & Craig, M. D. (1988). A transformation for ordering multispectral data in terms of image quality with implications for noise removal. *Geoscience and Remote Sensing, IEEE Transactions on*, 26(1), 65-74. <https://doi.org/10.1109/36.3001>
- Green, E. P., Clark, C. D., Mumby, P. J., Edwards, A. J., & Ellis, A. C. (1998). Remote sensing techniques for mangrove mapping. *International Journal of Remote Sensing*, 19(5), 935-956. <https://doi.org/10.1080/014311698215801>
- Green, E. P., Mumby, P. J., Edwards, A. J., Clark, C. D., & Ellis, A. C. (1998). The Assessment of Mangrove Areas Using High Resolution Multispectral Airborne Imagery. *Journal of Coastal Research*, 14(2), 433-443. <https://doi.org/10.2307/4298797>
- Green, R. O., Eastwood, M. L., Sarture, C. M., Chrien, T. G., Aronsson, M., Chippendale, B. J., . . . Williams, O. (1998). Imaging Spectroscopy and the Airborne Visible/Infrared Imaging Spectrometer (AVIRIS). *Remote Sensing of Environment*, 65(3), 227-248. [https://doi.org/10.1016/s0034-4257\(98\)00064-9](https://doi.org/10.1016/s0034-4257(98)00064-9)
- Haboudane, D., Miller, J. R., Pattey, E., Zarco-Tejada, P. J., & Strachan, I. B. (2004). Hyperspectral vegetation indices and novel algorithms for predicting green LAI of crop canopies: Modeling and validation in the context of precision agriculture. *Remote Sensing of Environment*, 90(3), 337-352. <https://doi.org/10.1016/j.rse.2003.12.013>
- Han, T., Goodenough, D. G., Dyk, A., & Chen, H. (2004, 20-24 Sept. 2004). *Hyperspectral feature selection for forest classification*. Paper presented at the Geoscience and Remote Sensing Symposium, 2004. IGARSS '04. Proceedings. 2004 IEEE International. <https://doi.org/10.1109/igarss.2004.1368698>
- Hardin, P. J., & Jensen, R. R. (2011). Small-Scale Unmanned Aerial Vehicles in Environmental Remote Sensing: Challenges and Opportunities. *GIScience & Remote Sensing*, 48(1), 99-111. <https://doi.org/10.2747/1548-1603.48.1.99>
- Harris Geospatial Solutions. (2019a). Display Tools. Retrieved from <http://www.harrisgeospatial.com/docs/DisplayTools.html#StretchTypes>.
- Harris Geospatial Solutions. (2019b). ENVI Header Files. Retrieved from <http://www.harrisgeospatial.com/docs/ENVIHeaderFiles.html>.

- Harris Geospatial Solutions. (2019c). Minimum Noise Fraction Transform. Retrieved from <http://www.harrisgeospatial.com/docs/minimumnoisefractiontransform.html>.
- Harris Geospatial Solutions. (2019d). Principal Components Analysis. Retrieved from <http://www.harrisgeospatial.com/docs/PrincipalComponentAnalysis.html>.
- Harris Geospatial Solutions. (2019e). Spectral Angle Mapper. Retrieved from <https://www.harrisgeospatial.com/docs/spectralanglemapper.html>.
- Harris Geospatial Solutions. (2019f). Stretch Types Background. Retrieved from <https://www.harrisgeospatial.com/docs/BackgroundStretchTypes.html>.
- Harris Geospatial Solutions. (2019g). Stretch Types Background. Retrieved from <http://www.harrisgeospatial.com/docs/BackgroundStretchTypes.html>.
- Hartigan, J. A. (1975). *Clustering Algorithms*: John Wiley & Sons Inc.
- Hastie, T., Tibshirani, R., & Friedman, J. (2009). *The Elements of Statistical Learning: Data Mining, Inference, and Prediction* (2nd ed.): Springer.
- Hay, A. M. (1979). Sampling Designs to Test Land-Use Map Accuracy. *Photogrammetric Engineering & Remote Sensing*, 45, 529-533. Retrieved from
- Held, A., Ticehurst, C., Lymburner, L., & Williams, N. (2003). High resolution mapping of tropical mangrove ecosystems using hyperspectral and radar remote sensing. *International Journal of Remote Sensing*, 24(13), 2739-2759. <https://doi.org/10.1080/0143116031000066323>
- Hexagon. (2019). ERDAS IMAGINE. Retrieved from <https://www.hexagongeospatial.com/products/power-portfolio/erdas-Imagine>.
- Hirano, A., Madden, M., & Welch, R. (2003). Hyperspectral image data for mapping wetland vegetation. *Wetlands*, 23(2), 436-448. <https://doi.org/10.1672/18-20>
- Hoffer, R. M., & Johannsen, C. J. (1968). Ecological potentials in spectral signature analysis. *Agricultural Equipment Station Journal No. 3479. Purdue University*. Retrieved from
- Holmes, O. (2012). High Resolution Digital Aerial Imagery vs High Resolution Satellite Imagery – Part 1. 2012. Retrieved from <http://aerometrex.com.au/blog/?p=217>.
- Horler, D. N. H., Dockray, M., & Barber, J. (1983). The red edge of plant leaf reflectance. *International Journal of Remote Sensing*, 4(2), 273-288. <https://doi.org/10.1080/01431168308948546>
- Hruska, R., Mitchell, J., Anderson, M., & Glenn, N. F. (2012). Radiometric and Geometric Analysis of Hyperspectral Imagery Acquired from an Unmanned Aerial Vehicle. *Remote Sensing*, 4(9), 2736-2752. Retrieved from <https://www.mdpi.com/2072-4292/4/9/2736>.
- Hu, B., Lucht, W., Li, X., & H. Strahler, A. (1997). Validation of kernel-driven semiempirical models for the surface bidirectional reflectance distribution function of land surfaces. *Remote Sensing of Environment*, 62(3), 201-214. [https://doi.org/http://dx.doi.org/10.1016/S0034-4257\(97\)00082-5](https://doi.org/http://dx.doi.org/10.1016/S0034-4257(97)00082-5)
- Hubert-Moy, L., Cotonnec, A., Le Du, L., Chardin, A., & Perez, P. (2001). A Comparison of Parametric Classification Procedures of Remotely Sensed Data Applied on Different Landscape Units. *Remote Sensing of Environment*, 75(2), 174-187. [https://doi.org/http://dx.doi.org/10.1016/S0034-4257\(00\)00165-6](https://doi.org/http://dx.doi.org/10.1016/S0034-4257(00)00165-6)

- Huete, A. R. (1988). A soil-adjusted vegetation index (SAVI). *Remote Sensing of Environment*, 25(3), 295-309. [https://doi.org/10.1016/0034-4257\(88\)90106-x](https://doi.org/10.1016/0034-4257(88)90106-x)
- Huete, A. R., Jackson, R. D., & Post, D. F. (1985). Spectral response of a plant canopy with different soil backgrounds. *Remote Sensing of Environment*, 17(1), 37-53. [https://doi.org/http://dx.doi.org/10.1016/0034-4257\(85\)90111-7](https://doi.org/http://dx.doi.org/10.1016/0034-4257(85)90111-7)
- Hughes, G. (1968). On the mean accuracy of statistical pattern recognizers. *Information Theory, IEEE Transactions on*, 14(1), 55-63. <https://doi.org/10.1109/TIT.1968.1054102>
- Imani, M., & Ghassemian, H. (2015). Feature space discriminant analysis for hyperspectral data feature reduction. *ISPRS Journal of Photogrammetry and Remote Sensing*, 102(0), 1-13. <https://doi.org/http://dx.doi.org/10.1016/j.isprsjprs.2014.12.024>
- International Union for Conservation of Nature and Natural Resources. (2019). *Rhizophora stylosa*. Retrieved from <https://www.iucnredlist.org/species/178850/7626520>.
- Irons, J. R., Campbell, G. S., Norman, J. M., Graham, D. W., & Kovalick, W. M. (1992). Prediction and measurement of soil bidirectional reflectance. *IEEE Transactions on Geoscience and Remote Sensing*, 30, 249-260. Retrieved from
- Jackson, R. D., Clarke, T. R., & Susan Moran, M. (1992). Bidirectional calibration results for 11 spectralon and 16 BaSO4 reference reflectance panels. *Remote Sensing of Environment*, 40(3), 231-239. [https://doi.org/http://dx.doi.org/10.1016/0034-4257\(92\)90005-5](https://doi.org/http://dx.doi.org/10.1016/0034-4257(92)90005-5)
- Jackson, R. D., & Huete, A. R. (1991). Interpreting vegetation indices. *Preventive Veterinary Medicine*, 11(3-4), 185-200. [https://doi.org/http://dx.doi.org/10.1016/S0167-5877\(05\)80004-2](https://doi.org/http://dx.doi.org/10.1016/S0167-5877(05)80004-2)
- Jean-Baptiste, N., & Jensen, J. R. (2006). Measurement of Mangrove Biophysical Characteristics in the Bocozele Ecosystem in Haiti Using ASTER Multispectral Data. *Geocarto International*, 21(4), 3-8. <https://doi.org/10.1080/10106040608542397>
- Jensen, J. R. (1996). *Introductory digital image processing: a remote sensing perspective*. Upper Saddle River, N.J.: Prentice Hall.
- Jensen, J. R., Lin, H., Yang, X., Ramsey, E., Davis, B. A., & Thoemke, C. W. (1991). The measurement of mangrove characteristics in southwest Florida using SPOT multi-spectral data. *Geocarto International*, 2, 13-21. <https://doi.org/10.1080/10106049109354302>
- Jensen, R., Mausel, P., Dias, N., Gonser, R., Yang, C., Everitt, J., & Fletcher, R. (2007). Spectral analysis of coastal vegetation and land cover using AISA+ hyperspectral data. *Geocarto International*, 22(1), 17-28. <https://doi.org/10.1080/10106040701204354>
- Jia, G. J., Burke, I. C., Kaufmann, M. R., Goetz, A. F. H., Kindel, B. C., & Pu, Y. (2006). Estimates of forest canopy fuel attributes using hyperspectral data. *Forest Ecology and Management*, 229(1-3), 27-38. <https://doi.org/10.1016/j.foreco.2006.03.021>
- Jones, H. G., and Vaughan, R. A. (2010). *Remote Sensing of Vegetation* (first ed.): Oxford University Press, USA.
- Kaewpijit, S., Le Moigne, J., & El-Ghazawi, T. (2002, 2002). *A wavelet-based PCA reduction for hyperspectral imagery*. Paper presented at the Geoscience and Remote Sensing Symposium, 2002. IGARSS '02. 2002 IEEE International. <https://doi.org/10.1109/igarss.2002.1026707>
- Kaewpijit, S., Le Moigne, J., & El-Ghazawi, T. (2003). Automatic reduction of hyperspectral imagery using wavelet spectral analysis. *Geoscience and Remote Sensing, IEEE Transactions on*, 41(4), 863-871. <https://doi.org/10.1109/tgrs.2003.810712>

- Kailath, T. (1967). The Divergence and Bhattacharyya Distance Measures in Signal Selection. *Communication Technology, IEEE Transactions on*, 15(1), 52-60. <https://doi.org/10.1109/TCOM.1967.1089532>
- Kaiser, H. F. (1960). The application of electronic computers to factor analysis. *Educational and Psychological Measurement*(April), 141-151. Retrieved from
- Kaiser, H. F. (1986). The application of electronic computers to factor analysis. *Current Contents*, 40(cc/Number 40), 18. Retrieved from
- Kaiser, H. F. (1991). Coefficient alpha for a principal component and the Kaiser-Guttman rule. *Psychological Reports*, 68(3), 855-858. <https://doi.org/10.2466/pr0.1991.68.3.855>
- Kamal, M., & Phinn, S. (2011). Hyperspectral Data for Mangrove Species Mapping: A Comparison of Pixel-Based and Object-Based Approach. *Remote Sensing*, 3(10), 2222-2242. Retrieved from <https://www.mdpi.com/2072-4292/3/10/2222>.
- Kamaruzaman, J., & Kasawani, I. (2007). Imaging Spectrometry on Mangrove Species Identification and Mapping in Malaysia. *WSEAS TRANSACTIONS on BIOLOGY and BIOMEDICINE*, 4(8), 118. Retrieved from
- Kaufman, Y. J., & Tanre, D. (1992). Atmospherically resistant vegetation index (ARVI) for EOS-MODIS. *Geoscience and Remote Sensing, IEEE Transactions on*, 30(2), 261-270. <https://doi.org/10.1109/36.134076>
- Kendall, M. G. (1961). *A Course in the Geometry of n-Dimensions*: Hafner Publishing.
- Kharuk, V. I., Ranson, K. J., Kozuhovskaya, A. G., Kondakov, Y. P., & Pestunov, I. A. (2004). NOAA/AVHRR satellite detection of Siberian silkmoth outbreaks in eastern Siberia. *International Journal of Remote Sensing*, 25(24), 5543-5556. <https://doi.org/10.1080/01431160410001719858>
- Kimes, D. S. (1983). Dynamics of directional reflectance factor distributions for vegetation canopies. *Appl. Opt.*, 22(9), 1364-1372. Retrieved from <http://ao.osa.org/abstract.cfm?URI=ao-22-9-1364>.
- Koedsin, W., & Vaiphasa, C. (2013). Discrimination of tropical mangroves at the species level with EO-1 hyperion data. *Remote Sensing*, 5(7), 3562-3582. Retrieved from <http://www.scopus.com/inward/record.url?eid=2-s2.0-84881532079&partnerID=40&md5=2d12a40c3e2b2698f80af2699bc80891>.
- Kotchenova, S. Y., & Vermote, E. F. (2007). Validation of a vector version of the 6S radiative transfer code for atmospheric correction of satellite data. Part II. Homogeneous Lambertian and anisotropic surfaces. *Appl. Opt.*, 46(20), 4455-4464. Retrieved from <http://ao.osa.org/abstract.cfm?URI=ao-46-20-4455>.
- Kotchenova, S. Y., Vermote, E. F., Matarrese, R., & Klemm, J. F. J. (2006). Validation of a vector version of the 6S radiative transfer code for atmospheric correction of satellite data. Part I: Path radiance. *Appl. Opt.*, 45(26), 6762-6774. Retrieved from <http://ao.osa.org/abstract.cfm?URI=ao-45-26-6762>.
- Kovacs, J. M., Flores-Verdugo, F., Wang, J., & Aspden, L. P. (2004). Estimating leaf area index of a degraded mangrove forest using high spatial resolution satellite data. *Aquatic Botany*, 80, 13-22. Retrieved from
- Kramer, H. J. (2002a). AVIRIS. Retrieved from <https://directory.eoportal.org/web/eoportal/airborne-sensors/aviris>.

- Kramer, H. J. (2002b). Landsat-7. Retrieved from <https://directory.eoportal.org/web/eoportal/satellite-missions/l/landsat-7>.
- Kruse, F. A. (2004). Comparison of ATREM, ACORN, and FLAASH Atmospheric Corrections using Low-Altitude AVIRIS Data of Boulder, Colorado. In *proceedings 13th JPL Airborne Geoscience Workshop, Jet Propulsion Laboratory, 31 March – 2 April 2004, Pasadena, CA, JPL Publication 05-3*(ftp://popo.jpl.nasa.gov/pub/docs/workshops/04_docs/Kruse-JPL2004_ATM_Compare.pdf). Retrieved from http://hgimaging.com/FAK_Pubs.htm.
- Kumar, L., Skidmore, A. K., & Mutanga, O. (2010). Leaf level experiments to discriminate between eucalyptus species using high spectral resolution reflectance data: use of derivatives, ratios and vegetation indices. *Geocarto International*, 25(4), 327-344. <https://doi.org/10.1080/10106040903505996>
- Kumar, T., Mandal, A., Dutta, D., Nagaraja, R., & Dadhwal, V. K. (2019). Discrimination and classification of mangrove forests using EO-1 Hyperion data: a case study of Indian Sundarbans. *Geocarto International*, 34(4), 415-442. <https://doi.org/10.1080/10106049.2017.1408699>
- Kumar, T., Panigrahy, S., Kumar, P., & Parihar, J. (2013). Classification of floristic composition of mangrove forests using hyperspectral data: case study of Bhitarkanika National Park, India. *Journal of Coastal Conservation*, 17(1), 121-132. <https://doi.org/10.1007/s11852-012-0223-2>
- Laba, M., Gregory, S. K., Braden, J., Ogurcak, D., Hill, E., Fegraus, E., . . . DeGloria, S. D. (2002). Conventional and fuzzy accuracy assessment of the New York Gap Analysis Project land cover map. *Remote Sensing of Environment*, 81(2–3), 443-455. [https://doi.org/http://dx.doi.org/10.1016/S0034-4257\(02\)00020-2](https://doi.org/http://dx.doi.org/10.1016/S0034-4257(02)00020-2)
- Laliberte, A. S., Goforth, M. A., Steele, C. M., & Rango, A. (2011). Multispectral Remote Sensing from Unmanned Aircraft: Image Processing Workflows and Applications for Rangeland Environments. *Remote Sensing*, 3(11), 2529-2551. Retrieved from <https://www.mdpi.com/2072-4292/3/11/2529>.
- Landgrebe, D. A. (2003). *Signal Theory Methods in Multispectral Remote Sensing*. Hoboken, New Jersey: Wiley-Interscience.
- Lechner, A. M., Langford, W. T., Bekessy, S. A., & Jones, S. D. (2012). Are landscape ecologists addressing uncertainty in their remote sensing data? *Landscape Ecology*, 27(9), 1249-1261. <https://doi.org/http://dx.doi.org/10.1007/s10980-012-9791-7>
- Ledesma, R. D., Valero-Mora, P., & Macbeth, G. (2015). The Scree Test and the Number of Factors: a Dynamic Graphics Approach. *The Spanish Journal of Psychology*, 18, null-null. Retrieved from
- Lee, C., Theiss, H. J., Bethel, J. S., & Mikhail, E. M. (2000). Rigorous Mathematical Modeling of Airborne Pushbroom Imaging Systems. *Photogrammetric Engineering & Remote Sensing*, 66(4), 385-392. Retrieved from
- Leifer, I., Lehr, W. J., Simecek-Beatty, D., Bradley, E., Clark, R., Dennison, P., . . . Wozencraft, J. (2012). State of the art satellite and airborne marine oil spill remote sensing: Application to the BP Deepwater Horizon oil spill. *Remote Sensing of Environment*, 124(0), 185-209. <https://doi.org/10.1016/j.rse.2012.03.024>
- Lenot, X., Achard, V., & Poutier, L. (2009). SIERRA: A new approach to atmospheric and topographic corrections for hyperspectral imagery. *Remote Sensing of Environment*, 113(8), 1664-1677. <https://doi.org/10.1016/j.rse.2009.03.016>

- Lexico. (2019). Normalize. Retrieved from <https://www.lexico.com/en/definition/normalize>.
- Li, L., Ustin, S. L., & Lay, M. (2005). Application of AVIRIS data in detection of oil-induced vegetation stress and cover change at Jornada, New Mexico. *Remote Sensing of Environment*, 94(1), 1-16. <https://doi.org/http://dx.doi.org/10.1016/j.rse.2004.08.010>
- Li, Q. S., Wong, F. K. K., & Fung, T. (2017). ASSESSING THE UTILITY OF UAV-BORNE HYPERSPECTRAL IMAGE AND PHOTOGRAMMETRY DERIVED 3D DATA FOR WETLAND SPECIES DISTRIBUTION QUICK MAPPING. *Int. Arch. Photogramm. Remote Sens. Spatial Inf. Sci.*, XLII-2/W6, 209-215. <https://doi.org/10.5194/isprs-archives-XLII-2-W6-209-2017>
- Li, Y., Viña, A., Yang, W., Chen, X., Zhang, J., Ouyang, Z., . . . Liu, J. (2013). Effects of conservation policies on forest cover change in giant panda habitat regions, China. *Land Use Policy*, 33(0), 42-53. <https://doi.org/http://dx.doi.org/10.1016/j.landusepol.2012.12.003>
- Lijuan, L., Yong, P., Wenyi, F., Zengyuan, L., & Mingze, L. (2011, 24-26 June 2011). *Fusion of airborne hyperspectral and LiDAR data for tree species classification in the temperate forest of northeast China*. Paper presented at the Geoinformatics, 2011 19th International Conference on. <https://doi.org/10.1109/Geoinformatics.2011.5981118>
- Lillesand, T., Kiefer, R. W., and Chipman, J. W. (2008). *Remote Sensing and Image Interpretation* (6th ed.): Wiley.
- Lu, B., & He, Y. (2018). Optimal spatial resolution of Unmanned Aerial Vehicle (UAV)-acquired imagery for species classification in a heterogeneous grassland ecosystem. *GIScience & Remote Sensing*, 55(2), 205-220. <https://doi.org/10.1080/15481603.2017.1408930>
- Ma, W., Gong, C., Hu, Y., Meng, P., & Xu, F. (2013). *The Hughes phenomenon in hyperspectral classification based on the ground spectrum of grasslands in the region around Qinghai Lake*. Retrieved from <http://dx.doi.org/10.1117/12.2034457>.
- Mahdavi, S., Salehi, B., Granger, J., Amani, M., Brisco, B., & Huang, W. (2018). Remote sensing for wetland classification: a comprehensive review. *GIScience & Remote Sensing*, 55(5), 623-658. <https://doi.org/10.1080/15481603.2017.1419602>
- Manna, S., & Raychaudhuri, B. (2018). Mapping distribution of Sundarban mangroves using Sentinel-2 data and new spectral metric for detecting their health condition. *Geocarto International*. <https://doi.org/10.1080/10106049.2018.1520923>
- Manson, F. J., Loneragan, N. R., Harch, B. D., Skilleter, G. A., & Williams, L. (2005). A broad-scale analysis of links between coastal fisheries production and mangrove extent: A case-study for northeastern Australia. *Fisheries Research*, 74(1-3), 69-85. <https://doi.org/10.1016/j.fishres.2005.04.001>
- Martin, M. E., Newman, S. D., Aber, J. D., & Congalton, R. G. (1998). Determining Forest Species Composition Using High Spectral Resolution Remote Sensing Data. *Remote Sensing of Environment*, 65(3), 249-254. [https://doi.org/http://dx.doi.org/10.1016/S0034-4257\(98\)00035-2](https://doi.org/http://dx.doi.org/10.1016/S0034-4257(98)00035-2)
- Mather, P., and Brandt, T. (2009). *Classification Methods for Remotely Sensed Data* (2nd ed.): CRC Press.
- Mather, P. M., and Koch, M. (2011). *Computer Processing of Remotely-Sensed Images* (4th ed.): Wiley-Blackwell.
- Matthew, M. W., Adler-Golden, S. M., Berk, A., Felde, G. W., Anderson, G. P., Gorodetzky, D., . . . Shippert, M. (2003). Atmospheric correction of spectral imagery: evaluation of the FLAASH

- algorithm with AVIRIS data. *SPIE Proceeding, Algorithms and Technologies for Multispectral, Hyperspectral, and Ultraspectral Imagery IX*, 5093, 474-482.
<https://doi.org/10.1117/12.499604>
- Mausel, P. W., Kramber, W. J., & Lee, J. K. (1990). Optimum band selection for supervised classification of multispectral data. *Photogrammetric Engineering and Remote Sensing*, 56, 55-60. Retrieved from
- McCoy, R. M. (2005). *Field Methods in Remote Sensing*. New York: The Guilford Press.
- Meroni, M., Rossini, M., Guanter, L., Alonso, L., Rascher, U., Colombo, R., & Moreno, J. (2009). Remote sensing of solar-induced chlorophyll fluorescence: Review of methods and applications. *Remote Sensing of Environment*, 113(10), 2037-2051.
<https://doi.org/10.1016/j.rse.2009.05.003>
- Miller, R. L., Del Castillo, C. E., & Mckee, B. A. (2005). *Remote Sensing of Coastal Aquatic Environments : Technologies, Techniques and Applications* (Vol. 7): Dordrecht : Springer Netherlands.
- Milovich, J. A., Frulla, L. A., & Gaguardini, D. A. (1995). Environment contribution to the atmospheric correction for Landsat-MSS images. *International Journal of Remote Sensing*, 16(14), 2515-2537. <https://doi.org/10.1080/01431169508954574>
- Monserud, R. A., & Leemans, R. (1992). Comparing global vegetation maps with the Kappa statistic. *Ecological Modelling*, 62(4), 275-293. [https://doi.org/http://dx.doi.org/10.1016/0304-3800\(92\)90003-W](https://doi.org/http://dx.doi.org/10.1016/0304-3800(92)90003-W)
- Montes, M. J., Gao, B.-C., & Davis, C. O. (2004). Tafkaa User's Guide. Retrieved from http://torpedo.nrl.navy.mil/tu/ps/pdf/pdf_loader?dsn=3002538.
- Mundt, J. T., Glenn, N. F., Weber, K. T., Prather, T. S., Lass, L. W., & Pettingill, J. (2005). Discrimination of hoary cress and determination of its detection limits via hyperspectral image processing and accuracy assessment techniques. *Remote Sensing of Environment*, 96(3-4), 509-517.
<https://doi.org/http://dx.doi.org/10.1016/j.rse.2005.04.004>
- Myers, V. I. (1970). *Soil, water and plant relations*. Washington, DC.: National Academy of Sciences.
- Myneni, R. B., & Asrar, G. (1994). Atmospheric effects and spectral vegetation indices. *Remote Sensing of Environment*, 47(3), 390-402. [https://doi.org/10.1016/0034-4257\(94\)90106-6](https://doi.org/10.1016/0034-4257(94)90106-6)
- NASA Landsat Science. (2019a). Landsat-9. Retrieved from <https://landsat.gsfc.nasa.gov/landsat-9/>.
- NASA Landsat Science. (2019b). Landsat 8. Retrieved from <https://landsat.gsfc.nasa.gov/landsat-data-continuity-mission/>.
- NASA Landsat Science. (2019c). Landsat 9 Instruments. Retrieved from <https://landsat.gsfc.nasa.gov/landsat-9/instruments/>.
- NASA Landsat Science. (2019d). Landsat History. Retrieved from <https://landsat.gsfc.nasa.gov/about/history/>.
- NASA Landsat Science. (2019e). Spectral Characterization. Retrieved from <https://landsat.gsfc.nasa.gov/spectral-characterization/>.
- Newton, A. C., Hill, R. A., Echeverría, C., Golicher, D., Rey Benayas, J. M., Cayuela, L., & Hinsley, S. A. (2009). Remote sensing and the future of landscape ecology. *Progress in Physical Geography*, 33(4), 528-546. <https://doi.org/http://dx.doi.org/10.1177/0309133309346882>

- Pal, M., & Foody, G. M. (2010). Feature Selection for Classification of Hyperspectral Data by SVM. *Geoscience and Remote Sensing, IEEE Transactions on*, 48(5), 2297-2307. <https://doi.org/10.1109/TGRS.2009.2039484>
- Pal, M., & Mather, P. M. (2006). Some issues in the classification of DAIS hyperspectral data. *International Journal of Remote Sensing*, 27(14), 2895-2916. <https://doi.org/10.1080/01431160500185227>
- Paling, E., Humphreys, G., & McCardle, I. (2003). The effect of a harbour development on mangroves in northwestern Australia. *Wetlands Ecology and Management*, 11(5), 281-290. <https://doi.org/http://dx.doi.org/10.1023/B:WETL.0000005538.74513.de>
- Paling, E., Humphreys, G., McCardle, I., & Thomson, G. (2001). The effects of iron ore dust on mangroves in Western Australia: Lack of evidence for stomatal damage. *Wetlands Ecology and Management*, 9(5), 363-370. <https://doi.org/http://dx.doi.org/10.1023/A:1012008705347>
- Paling, E. I., Kobryn, H. T., & Humphreys, G. (2008). Assessing the extent of mangrove change caused by Cyclone Vance in the eastern Exmouth Gulf, northwestern Australia. *Estuarine, Coastal and Shelf Science*, 77(4), 603-613. <https://doi.org/10.1016/j.ecss.2007.10.019>
- Perkins, T., Adler-Golden, S., Matthew, M. W., Berk, A., Bernstein, L. S., Lee, J., & Fox, M. (2012). Speed and accuracy improvements in FLAASH atmospheric correction of hyperspectral imagery. *Optical Engineering*, 51(11), 111707-111701. <https://doi.org/10.1117/1.oe.51.11.111707>
- Piironen, R., Heiskanen, J., Möttöus, M., & Pellikka, P. (2015). Classification of crops across heterogeneous agricultural landscape in Kenya using AisaEAGLE imaging spectroscopy data. *International Journal of Applied Earth Observation and Geoinformation*, 39(0), 1-8. <https://doi.org/http://dx.doi.org/10.1016/j.jag.2015.02.005>
- Pilbara Ports Authority. (2016). South West Creek Dredging and Reclamation Project. Retrieved from https://www.pilbaraports.com.au/PilbaraPortsAuthority/media/Documents/PORT%20HEDLAND/ENVIRONMENT%20AND%20HERITAGE/Monitoring%20and%20Reporting%20Programs/2016-Post-Dredge-Mangrove-Health-Monitoring-Report_Rev1-24month-A408457.pdf.
- Pilbara Ports Authority. (2019). Port of Port Hedland. Retrieved from <https://pilbaraports.com.au/Port-of-Port-Hedland>
- Pilbara Ports Authority. (n.d.). Dust Management Leading Practice Guidelines. Retrieved from <https://www.pilbaraports.com.au/PilbaraPortsAuthority/media/documents/PORT%20HEDLAND/ENVIRONMENT%20AND%20HERITAGE/Monitoring%20and%20Reporting%20Programs/Dust-Management-Leading-Practice-Guidelines.pdf>.
- Port Hedland Port Authority. (2011). South West Creek Dredging and Reclamation Proposal. Retrieved from <https://www.pilbaraports.com.au/getmedia/fdbd9023-b09b-46bb-94c0-93fb23eca677/EPAReportandRecommendations.pdf.aspx>.
- Port Hedland Port Authority. (n.d.). PHPA Development Plan. Retrieved from https://www.pilbaraports.com.au/PilbaraPortsAuthority/media/Documents/PORT%20HEDLAND/Planning%20and%20Development/PHPA-Development-Plan-Book_LowRes.pdf.
- Prasad, K. A., & Gnanappazham, L. (2014). *Discrimination of mangrove species of Rhizophoraceae using laboratory spectral signatures*. Paper presented at the International Geoscience and Remote Sensing Symposium (IGARSS). Retrieved from <http://www.scopus.com/inward/record.url?eid=2-s2.0-84911426402&partnerID=40&md5=4af3c6d7f4eb58cc5afb394450351674>.

- Press, W. H., Flannery, B. P., Teukolsky, S. A., & Vetterling, W. T. (1992). *Numerical Recipes in C: The Art of Scientific Computing*, (2nd ed.): Cambridge University Press.
- Price, J. C. (1994). How unique are spectral signatures? *Remote Sensing of Environment*, 49(3), 181-186. [https://doi.org/http://dx.doi.org/10.1016/0034-4257\(94\)90013-2](https://doi.org/http://dx.doi.org/10.1016/0034-4257(94)90013-2)
- Queensland Government Department of Agriculture and Fisheries. (2013). Red mangrove. 17 Oct 2013. Retrieved from <https://www.daf.qld.gov.au/business-priorities/fisheries/habitats/marine-plants-including-mangroves/common-mangroves/red-mangrove>.
- Ramsey, E. W., & Jensen, J. R. (1996). Remote Sensing of Mangrove Wetlands: Relating Canopy Spectra to Site-Specific Data. *Photogrammetric Engineering and Remote Sensing*, 62(8), 939-948. Retrieved from
- RealAustraliaTravel. (2014). Western Australia Map. Retrieved from <http://www.realaustraliatravel.com/western-australia-map.html>.
- ReSe Applications. (n.d.). ATCOR - 2/3/4 Atmospheric & Topographic Correction. Retrieved from https://www.rese-apps.com/pdf/Atcor_Flyer.pdf.
- Richards, J. A. (2013). *Remote Sensing Digital Image Analysis* (5th ed.). Berlin: Springer-Verlag.
- Richter, R., Bachmann, M., Dorigo, W., & Muller, A. (2006). Influence of the Adjacency Effect on Ground Reflectance Measurements. *Geoscience and Remote Sensing Letters, IEEE*, 3(4), 565-569. <https://doi.org/10.1109/lgrs.2006.882146>
- Roberts, D. A., Green, R. O., & Adams, J. B. (1997). Temporal and spatial patterns in vegetation and atmospheric properties from AVIRIS. *Remote Sensing of Environment*, 62(3), 223-240. [https://doi.org/http://dx.doi.org/10.1016/S0034-4257\(97\)00092-8](https://doi.org/http://dx.doi.org/10.1016/S0034-4257(97)00092-8)
- Robertson, A. I., & Blaber, S. J. M. (1992). *Plankton, epibenthos and fish communities. In: Tropical Mangrove Ecosystems*. Washington DC, USA, American Geophysical Union.: A.I. Roberson & D.M. Alongi.
- Rosenfield, G. H., Fitzpatrick-Lins, K., & Ling, H. S. (1982). Sampling for Thematic Map Accuracy Testing. *Photogrammetric Engineering and Remote Sensing*, 48, 131-137. Retrieved from
- Royal Meteorological Society. (2018). The Beaufort Scale. Retrieved from <https://www.rmets.org/resource/beaufort-scale>.
- S.M. Adler-Golden, M. W. M., L.S. Bernstein, R.Y. Levine, A. Berk, S.C. Richtsmeier, P.K. Acharya, G.P. Anderson, G. Felde, J. Gardner, M. Hoke, L.S. Jeong, B. Pukall, J. Mello, A. Ratkowski, and H.-H. Burke. (1999). Atmospheric Correction for Short-wave Spectral Imagery based on MODTRAN4. *SPIE Proceeding, Imaging Spectrometry V*, 3753. Retrieved from <http://spectral.com/publications.shtml>.
- Sandau, R. (2010). *Digital Airborne Camera : Introduction and Technology*. Dordrecht, Netherlands: Springer Netherlands.
- Sandmeier, S., Müller, C., Hosgood, B., & Andreoli, G. (1998). Physical Mechanisms in Hyperspectral BRDF Data of Grass and Watercress. *Remote Sensing of Environment*, 66(2), 222-233. [https://doi.org/http://dx.doi.org/10.1016/S0034-4257\(98\)00060-1](https://doi.org/http://dx.doi.org/10.1016/S0034-4257(98)00060-1)
- Satyanarayana, B., Mohamad, K. A., Idris, I. F., Mohd-Lokman, H., & Dahdouh-Geubas, F. (2011). Assessment of mangrove vegetation based on remote sensing and ground-truth

- measurements at Tumpat, Kelantan Delta, East Coast of Peninsular Malaysia. *International Journal of Remote Sensing*, 32(6), 1635-1650. <https://doi.org/10.1080/01431160903586781>
- Schmidt, K. S., & Skidmore, A. K. (2003). Spectral discrimination of vegetation types in a coastal wetland. *Remote Sensing of Environment*, 85(1), 92-108. [https://doi.org/10.1016/S0034-4257\(02\)00196-7](https://doi.org/10.1016/S0034-4257(02)00196-7)
- Schowengerdt, R. A. (2007). *Remote Sensing: Models and Methods for Image Processing* (3rd ed.): Academic Press.
- Scottish Environment Protection Agency. (n.d.). Nitrogen oxides, NO and NO₂ as NO₂. Retrieved from <http://apps.sepa.org.uk/spripa/Pages/SubstanceInformation.aspx?pid=122>.
- Seelig, H. D., Hoehn, A., Stodieck, L. S., Klaus, D. M., Adams Iii, W. W., & Emery, W. J. (2008). The assessment of leaf water content using leaf reflectance ratios in the visible, near - , and short - wave - infrared. *International Journal of Remote Sensing*, 29(13), 3701-3713. <https://doi.org/10.1080/01431160701772500>
- Semeniuk, V. (1983). Mangrove distribution in Northwestern Australia in relationship to regional and local freshwater seepage. *Vegetation*, 53(1), 11-31. <https://doi.org/10.1007/bf00039767>
- Siljestrom, P. A., Moreno, A., Vikgren, K., & Caceres, L. M. (1997). Technical note The application of selective principal components analysis (SPCA) to a Thematic Mapper (TM) image for the recognition of geomorphologic features configuration. *International Journal of Remote Sensing*, 18(18), 3843-3852. <https://doi.org/10.1080/014311697216658>
- Silleos, N. G., Alexandridis, T. K., Gitas, I. Z., & Perakis, K. (2006). Vegetation Indices: Advances Made in Biomass Estimation and Vegetation Monitoring in the Last 30 Years. *Geocarto International*, 21(4), 21-28. <https://doi.org/10.1080/10106040608542399>
- Smith, T. J., III, Robblee, M. B., Wanless, H. R., & Doyle, T. W. (1994). Mangroves, hurricanes, and lightning strikes. *Bioscience*, 44(4), 256. Retrieved from <http://search.proquest.com/docview/216358820?accountid=10382>
http://link.library.curtin.edu.au/openurl?url_ver=Z39.88-2004&rft_val_fmt=info:ofi/fmt:kev:mtx:journal&genre=article&sid=ProQ:ProQ%3Abiologyjournals&atitle=Mangroves%2C+hurricanes%2C+and+lightning+strikes&title=Bioscience&issn=00063568&date=1994-04-01&volume=44&issue=4&spage=256&au=Smith%2C+Thomas+J%2C+III%3BRobblee%2C+Michael+B%3BWanless%2C+Harold+R%3BDoyle%2C+Thomas+W&isbn=&jtitle=Bioscience&btile=&rft_id=info:eric/&rft_id=info:doi/
- Specim, S. I. L. (2012). Aisa EAGLE hyperspectral sensor. <http://www.specim.fi/index.php/products/airborne/aisaeagle/>. Retrieved from <http://www.specim.fi/index.php/products/airborne/aisaeagle/>.
- Spectral Sciences Inc. (2016a). About MODTRAN. Retrieved from http://modtran.spectral.com/modtran_about.
- Spectral Sciences Inc. (2016b). Top Questions about MODTRAN. Retrieved from http://modtran.spectral.com/modtran_faq.
- SPOT Image. (2010). Spot satellite technical data. *Spot image*. Retrieved from http://www.intelligence-airbusds.com/files/pmedia/public/r329_9_spotsatellitetechnicaldata_en_sept2010.pdf.

- Stefanik, K. V., Gassaway, J. C., Kochersberger, K., & Abbott, A. L. (2011). UAV-Based Stereo Vision for Rapid Aerial Terrain Mapping. *GIScience & Remote Sensing*, 48(1), 24-49.
<https://doi.org/10.2747/1548-1603.48.1.24>
- Stehman, S. V. (2001). Statistical rigor and practical utility in thematic map accuracy assessment. *Photogrammetric Engineering & Remote Sensing*, 67(6), 727-734. Retrieved from
- Strang, G. (1988). *Linear Algebra and Its Applications* (3rd ed.): Harcourt Brace Jovanovich.
- Swain, P. H., A.G. Wacker. (1971). Comparison Of The Divergence And B-Distance In Feature Selection, Information Note 020871. *Laboratory for Applications of Remote Sensing, Purdue University, West Lafayette, IN*. Retrieved from
- Swain, P. H., R.C. King. (1973). Two Effective Feature Selection Criteria For Multispectral Remote Sensing. *Proc. Intl. Joint Conf. On Pattern Recognition, Washington, DC, Nov. 1973. LARS Technical Note 042673*. Retrieved from
- Thampanya, U., Vermaat, J. E., Sinsakul, S., & Panapitukkul, N. (2006). Coastal erosion and mangrove progradation of Southern Thailand. *Estuarine, Coastal and Shelf Science*, 68(1-2), 75-85.
<https://doi.org/10.1016/j.ecss.2006.01.011>
- The Editors of Encyclopaedia Britannica. (2019). Inertial guidance system. 01-08-2015 and 12-09-19. Retrieved from <http://www.britannica.com/technology/inertial-guidance-system>.
- the spruce. (2018). The Definition of a Subshrub. 25 Jul 2018. Retrieved from
<https://www.thespruce.com/what-is-a-subshrub-3269808>.
- Thenkabail, P. S., Enclona, E. A., Ashton, M. S., & Van Der Meer, B. (2004). Accuracy assessments of hyperspectral waveband performance for vegetation analysis applications. *Remote Sensing of Environment*, 91(3-4), 354-376. <https://doi.org/10.1016/j.rse.2004.03.013>
- Thenkabail, P. S., Lyon, J. G., and Huete, A. (2011). *Hyperspectral Remote Sensing of Vegetation* (first ed.): CRC Press.
- Thenkabail, P. S., Smith, R. B., & De Pauw, E. (2000). Hyperspectral Vegetation Indices and Their Relationships with Agricultural Crop Characteristics. *Remote Sensing of Environment*, 71(2), 158-182. [https://doi.org/10.1016/S0034-4257\(99\)00067-X](https://doi.org/10.1016/S0034-4257(99)00067-X)
- Thomas, V., Treitz, P., Jelinski, D., Miller, J., Lafleur, P., & McCaughey, J. H. (2003). Image classification of a northern peatland complex using spectral and plant community data. *Remote Sensing of Environment*, 84(1), 83-99.
[https://doi.org/http://dx.doi.org/10.1016/S0034-4257\(02\)00099-8](https://doi.org/http://dx.doi.org/10.1016/S0034-4257(02)00099-8)
- Thomlinson, J. R., Bolstad, P. V., & Cohen, W. B. (1999). Coordinating Methodologies for Scaling Landcover Classifications from Site-Specific to Global: Steps toward Validating Global Map Products. *Remote Sensing of Environment*, 70(1), 16-28.
[https://doi.org/http://dx.doi.org/10.1016/S0034-4257\(99\)00055-3](https://doi.org/http://dx.doi.org/10.1016/S0034-4257(99)00055-3)
- Tian, X. Z. Q. (2013). A mangrove recognition index for remote sensing of mangrove forest from space. *Current Science* 105(8), 1149-1155. Retrieved from
- Tomlinson, P. B. (2016). *The Botany of Mangroves* (2 ed.). Cambridge: Cambridge University Press.
- Toussaint, G. (1972). Comments on "The Divergence and Bhattacharyya Distance Measures in Signal Selection". *Communications, IEEE Transactions on*, 20(3), 485-485.
<https://doi.org/10.1109/TCOM.1972.1091157>

- Treitz, P., & Howarth, P. (1999). Hyperspectral remote sensing for estimating biophysical parameters of forest ecosystems. *Progress in Physical Geography*, 23(3), 359-390. Retrieved from <http://search.proquest.com/docview/231200466?accountid=10382>.
- Treitz, P., & Howarth, P. (2000). Integrating Spectral, Spatial, and Terrain Variables for Forest Ecosystem Classification. *Photogrammetric Engineering & Remote Sensing*, 66(3), 305-317. Retrieved from
- United States Department of Agriculture - Natural Resources Conservation Service. (n.d.). Growth Habits Codes and Definitions. Retrieved from https://plants.usda.gov/growth_habits_def.html.
- Ustin, S. L., Roberts, D. A., Gamon, J. A., Asner, G. P., & Green, R. O. (2004). Using Imaging Spectroscopy to Study Ecosystem Processes and Properties. *BioScience*, 54(6), 523-534. [https://doi.org/10.1641/0006-3568\(2004\)054\[0523:uistse\]2.0.co;2](https://doi.org/10.1641/0006-3568(2004)054[0523:uistse]2.0.co;2)
- Vaiphasa, C. (2006). Consideration of smoothing techniques for hyperspectral remote sensing. *ISPRS Journal of Photogrammetry and Remote Sensing*, 60(2), 91-99. <https://doi.org/http://dx.doi.org/10.1016/j.isprsjprs.2005.11.002>
- Vaiphasa, C., Ongsomwang, S., Vaiphasa, T., & Skidmore, A. K. (2005). Tropical mangrove species discrimination using hyperspectral data: A laboratory study. *Estuarine, Coastal and Shelf Science*, 65(1-2), 371-379. <https://doi.org/10.1016/j.ecss.2005.06.014>
- Van Der Meer, F. D., De Jong, S. M. (2001). *Imaging Spectrometry: Basic Principles and Prospective Applications*: Springer.
- Van der Meer, F. D., van der Werff, H. M. A., van Ruitenbeek, F. J. A., Hecker, C. A., Bakker, W. H., Noomen, M. F., . . . Woldai, T. (2012). Multi- and hyperspectral geologic remote sensing: A review. *International Journal of Applied Earth Observation and Geoinformation*, 14(1), 112-128. <https://doi.org/10.1016/j.jag.2011.08.002>
- Varshney, P. K., & Arora, M. K. (2004). *Advanced Image Processing Techniques for Remotely Sensed Hyperspectral Data* (1st ed.). Heidelberg: Springer.
- Velicer, W. F., & Jackson, D. N. (1990). Component Analysis versus Common Factor Analysis: Some Further Observations. *Multivariate Behavioral Research*, 25(1), 97-114. https://doi.org/10.1207/s15327906mbr2501_12
- Wang, L., Silván-Cárdenas, J. L., & Sousa, W. P. (2008). Neural Network Classification of Mangrove Species from Multi-seasonal Ikonos Imagery. *Photogrammetric Engineering & Remote Sensing*, 74(7), 921-927. Retrieved from
- Wang, L., & Sousa, W. P. (2009). Distinguishing mangrove species with laboratory measurements of hyperspectral leaf reflectance. *International Journal of Remote Sensing*, 30(5). Retrieved from
- Wang, L., Sousa, W. P., & Gong, P. (2004). Integration of object-based and pixel-based classification for mapping mangroves with IKONOS imagery. *International Journal of Remote Sensing*, 25(24), 5655-5668. <https://doi.org/10.1080/014311602331291215>
- Weatherzone. (2017). Port Hedland Ap Climate. Retrieved from <http://www.weatherzone.com.au/climate/station.jsp?lt=site&lc=4032>
- Wilkie, M. L., & Fortuna, S. (2003). Status and trends in mangrove area extent worldwide. *Rorest Resources Assessment Working Paper 63*. Rome: Forest Resources Division, Food and Agriculture Organization of the United Nations (FAO). Retrieved from

- Williams, D. R. (2019). Earth Fact Sheet. 22 April 2019. Retrieved from <http://nssdc.gsfc.nasa.gov/planetary/factsheet/earthfact.html>.
- Wilson, P., & Cooper, C. (2008). Finding the magic number. *the psychologist*, 21(october), 886-867. Retrieved from
- Winarso, G., Purwanto, A.D., Yuwono, D.M. (2014). New mangrove index as degradation health indicator using remote sensing data: Segara Anakan and Alas Purwo case study. *12th Biennial Conference of Pan Ocean Remote Sensing Conference (PORSEC 2014)*, 309-316. Retrieved from
- Winter, E. M. (2003). Detection of mines using hyperspectral remote sensors and detection algorithms. 625-630. <https://doi.org/10.1117/12.484922>
- Wong, F. K. K., & Fung, T. (2014). Combining EO-1 Hyperion and Envisat ASAR data for mangrove species classification in Mai Po Ramsar Site, Hong Kong. *International Journal of Remote Sensing*, 35(23), 7828-7856. Retrieved from <http://www.scopus.com/inward/record.url?eid=2-s2.0-84912046388&partnerID=40&md5=f9166c6d8d81bdabe6c5dae036135ea2>.
- WorleyParsons. (2011). Mangrove health monitoring report. Retrieved from https://www.pilbarareports.com.au/getmedia/b631b86e-b0eb-4414-972c-b82777126636/Mangrove_Health_Monitoring_Report_1.pdf.aspx.
- WorleyParsons. (2013). Lumsden Point General Cargo Facility - Benthic Habitat Survey. 30. Retrieved from http://www.epa.wa.gov.au/sites/default/files/Referral_Documentation/1987-RSD_Appendix%203_Benthic%20Habitat%20Survey_FINAL.pdf.
- Wulder, M. A., Franklin, S. E., White, J. C., Linke, J., & Magnussen, S. (2006). An accuracy assessment framework for large - area land cover classification products derived from medium - resolution satellite data. *International Journal of Remote Sensing*, 27(4), 663-683. <https://doi.org/10.1080/01431160500185284>
- Wulder, M. A., Hall, R. J., Coops, N. C., & Franklin, S. E. (2004). High Spatial Resolution Remotely Sensed Data for Ecosystem Characterization. *BioScience*, 54(6), 511-521. [https://doi.org/10.1641/0006-3568\(2004\)054\[0511:hsrrsd\]2.0.co;2](https://doi.org/10.1641/0006-3568(2004)054[0511:hsrrsd]2.0.co;2)
- Xiaoping, W., Ni, G., Jing, W., Jie, Z., & Jingsong, W. (2008, 7-11 July 2008). *Monitoring Growth Status of Spring Wheat in Rainfed Agriculture Area in Loess Plateau with Hyperspectral Reflectance Data at Canopy and Leaf Level*. Paper presented at the Geoscience and Remote Sensing Symposium, 2008. IGARSS 2008. IEEE International. <https://doi.org/10.1109/IGARSS.2008.4779449>
- Xiuping, J., Bor-Chen, K., & Crawford, M. M. (2013). Feature Mining for Hyperspectral Image Classification. *Proceedings of the IEEE*, 101(3), 676-697. <https://doi.org/10.1109/JPROC.2012.2229082>
- Yang, C., Everitt, J. H., Fletcher, R. S., Jensen, R. R., & Mausel, P. W. (2009). Evaluating AISA + Hyperspectral Imagery for Mapping Black Mangrove along the South Texas Gulf Coast. *Photogrammetric Engineering & Remote Sensing*, 75(4), 425-435. Retrieved from
- Yelena M. Gambarova, A. Y. G., Rustam B. Rustamov, Maral H. Zeynalova (2010). Remote Sensing and GIS as an Advance Space Technologies for Rare Vegetation Monitoring in Gobustan State National Park, Azerbaijan. *Journal of Geographic Information System*, 2(2), 7. <https://doi.org/10.4236/jgis.2010.22014>

- Zarco-Tejada, P. J., Diaz-Varela, R., Angileri, V., & Loudjani, P. (2014). Tree height quantification using very high resolution imagery acquired from an unmanned aerial vehicle (UAV) and automatic 3D photo-reconstruction methods. *European Journal of Agronomy*, 55, 89-99. <https://doi.org/https://doi.org/10.1016/j.eja.2014.01.004>
- Zarco-Tejada, P. J., Miller, J. R., Noland, T. L., Mohammed, G. H., & Sampson, P. H. (2001). Scaling-up and model inversion methods with narrowband optical indices for chlorophyll content estimation in closed forest canopies with hyperspectral data. *Geoscience and Remote Sensing, IEEE Transactions on*, 39(7), 1491-1507. <https://doi.org/10.1109/36.934080>
- Zhang, C., Kovacs, J. M., Wachowiak, M. P., & Flores-Verdugo, F. (2013). Relationship between hyperspectral measurements and mangrove leaf nitrogen concentrations. *Remote Sensing*, 5(2), 891-908. <https://doi.org/10.3390/rs5020891>
- Zhang, K., Liu, H., Li, Y., Xu, H., Shen, J., Rhome, J., & Smith Iii, T. J. (2012). The role of mangroves in attenuating storm surges. *Estuarine, Coastal and Shelf Science*, 102–103(0), 11-23. <https://doi.org/10.1016/j.ecss.2012.02.021>
- Zheng, Q., Kindel, B. C., & Goetz, A. F. H. (2003). The High Accuracy Atmospheric Correction for Hyperspectral Data (HATCH) model. *Geoscience and Remote Sensing, IEEE Transactions on*, 41(6), 1223-1231. <https://doi.org/10.1109/tgrs.2003.813125>

“Every reasonable effort has been made to acknowledge the owners of copyright material. I would be pleased to hear from any copyright owner who has been omitted or incorrectly acknowledged”

APPENDICES

Appendix A Vegetation Indices

The NDVI (Section 2.6.2.1) is based on the simpler RVI (Relative Vegetation Index), and although the NDVI is the most popular VI in remote sensing, it has shortcomings that led to the development of other VI's; one such VI is the SAVI. Both the RVI and SAVI are discussed in Appendices A.1 and A.2, respectively.

A.1 Relative Vegetation Index (RVI)

The RVI is simply defined as:

$$RVI = \frac{NIR}{R}$$

(Huete et al., 1985)

It is also known as a Simple Ratio vegetation index (SR) (Center for Coastal Physical Oceanography, n.d.).

The value of the RVI tends to be quite large for small values of R, and is also sensitive to sparse vegetation densities, although less so to high vegetation densities. The NDVI is functionally equivalent to the RVI and overcomes shortcomings of the RVI by being less sensitive to sparse vegetation densities and more sensitive to high vegetation densities. The values given by the NDVI is an improved index compared to the RVI (Jackson & Huete, 1991). According to Lillesand (2008, p. 466), the NDVI also helps to compensate for changing different illumination conditions, surface slope and aspect.

A.2 Soil Adjusted Vegetation Index (SAVI)

Under certain conditions, the soil-reflected spectral response may appear indistinguishable from vegetation (Huete, 1988). A significant amount of NIR flux is transmitted by the vegetation canopy, which is transmitted back toward the sensor. However, the sensor records a limited amount of red light as it is strongly absorbed

by the upper leaf layers in the canopy. As a result, both the RVI (Appendix A.1) and NDVI (Section 2.6.2.1) were found to be higher with darker soil substrates. The type and state (wet or dry) of the soil in addition to variability in soil brightness, influences the value obtained by the NDVI (Huete et al., 1985). This has implications for canopy structures, as open canopies (e.g. savannah's) reveals more soil and dead leaf matter (organic matter) than closed canopies (e.g. dense rainforests).

It is worth noting that the work during the 1980's (e.g. Huete) predates the spectral quality exhibited by hyperspectral sensing. Many VI's are expressed in terms of two values (usually reflectance) at two wavelengths (R and NIR). Therefore, the changes in both R and NIR stated above due to soil and vegetative canopy behaviour will affect the NDVI. However, by recording a more complete spectrum (e.g. as taken by a hyperspectral sensor), issues such as soil and vegetation appearing indistinguishable, is expected to diminish as a red-edge is more prominent.

For the production of a vegetative map (against non-vegetation), the shortcomings of the NDVI must be factored into the analysis. Huete (1988) attempted to reduce the effect of soil on the NDVI by deriving a new type of index - the SAVI:

$$SAVI = \frac{(NIR - R)}{(NIR + R + L)}(1 + L) \quad (A.1.1)$$

Compared to the NDVI, this equation introduces a new parameter, L, which is termed the "correction factor".

Huete (1988) analysed the effect of SAVI on broad-leaf cotton (having a planophile canopy) and narrow-leaf grass (having an erectophile canopy) and found that a single value of $L = 0.5$ successfully minimised soil noise in both these different canopies. It was further suggested that it should be able to model soil-vegetation spectral behaviour ranging from sparse to dense canopies. As evident from Equation (A.1.1), a value of $L = 0$ reduces the SAVI back to the NDVI. The correction factor L ranges from 0 to ∞ . Several soil types, ranging from bright to dark, were tested against LAI and it was found that for $LAI = 0.5$ (intermediate

vegetation density), the NDVI varied from 0.24 - 0.60 whereas SAVI ranged from 0.21 - 0.24. This demonstrates that SAVI is much less affected by soil brightness compared to the NDVI. For a LAI = 1 (very low vegetation density), NDVI varied from 0.44 to 0.74 while SAVI ranged from 0.38 - 0.40 (a LAI > 4 represents a closed and dense forest canopy (Zarco-Tejada et al., 2001)). Clearly, the SAVI will not saturate nearly as fast as the NDVI, as is evident from Figure 4 in Huete (1988). The SAVI behaves especially well for light soil (where the NDVI reaches saturation at LAI = 3).

Mathematically, the SAVI greatly improves upon the non-linearity of the NDVI (especially) with the LAI, being more linear. However, it has been found to be "*more sensitive to changes in view angle than the NDVI, and that this difference was more pronounced for antisolar (i.e. sun positioned behind the sensor) viewing directions*" (Epiphanio and Huete (1995)).

More recently, Haboudane et al. (2004) have defined a narrowband version of SAVI, suited for use with hyperspectral data:

$$SAVI = \frac{(R_{800} - R_{670})}{(R_{800} + R_{670} + L)}(1 + L)$$

A.3 Mangrove Specific Vegetation Indices

A.3.1 The Mangrove Recognition Index (MRI)

The MRI was introduced qualitatively in Section 2.3.2. Mathematically, it is defined by Tian (2013):

$$MRI = |GVI_L - GVI_H| \times GVI_L \times (WI_L + WI_H)$$

In this equation, the vegetation characteristics are described by the Greenness Vegetation Index (GVI), while the Wetness Index (WI) characterises canopy water information.

The expression $|GVI_L - GVI_H|$ denotes the change in vegetation between low-tide and high-tidal levels. This change is large for mangroves due to the tidal inundation, and very small otherwise. The sum $(WI_L + WI_H)$ is very high for mangroves and low otherwise. Therefore, in calculating the MRI for each pixel, those with larger values are indicative of pixels belonging to mangrove forests.

A.3.2 The Mangrove Vegetation Index (MVI)

A clear disadvantage of the preceding MRI is that it requires both high and low tidal data. The Mangrove Vegetation Index (MVI), developed by Baloloy et al. (2020) overcomes this problem, and is defined by:

$$MVI = \frac{(NIR - Green)}{(SWIR1 - Green)}$$

The NIR, Green and SWIR1 bands correspond to reflectances in bands 8 (842 nm), 3 (560 nm) and 11 (1610 nm), respectively, of the Sentinel-2 satellite.

The expression $|NIR - Green|$ enhances the greenness difference between mangroves and non-mangroves, while the distinct moisture content of mangroves are captured by $|SWIR1 - Green|$. The probability of finding a mangrove at a pixel is directly proportional to the value of the MVI.

A.4 Other Vegetation Indices

Several other (broadband) VI's have been developed. An excellent review of numerous other VI's are outlined in Silleos et al. (2006), while Haboudane et al. (2004) defines several VI's using narrowband equivalents.

Appendix B Atmospheric Models – a basic review

There are broadly two main methods by which remotely sensed data is corrected; those based on models and those on empirical approaches. This appendix provides a brief overview of both approaches.

MODTRAN

The MODTRAN model is maintained by Spectral Sciences Incorporated (<http://www.spectral.com>).

MODTRAN 4 (A. Berk 1999) is an atmospheric model written in FORTRAN and caters for sky and path irradiance (Richards, 2013). There are 6 model atmospheres to select from (e.g. mid-latitude summer) (Spectral Sciences Inc., 2016b), each catering for different atmospheric temperature and gas profiles.

The latest version is MODTRAN 6 (<http://modtran.spectral.com/>), which improves upon version 4 by increasing the spectral resolution to ultra-spectral range, upgrading code to modern standards (C/C++), increasing algorithmic performance and incorporating a graphical interface.

MODTRAN *"solves the radiative transfer equation including the effects of molecular and particulate absorption/emission and scattering, surface reflections and emission, solar/lunar illumination, and spherical refraction."* (Spectral Sciences Inc., 2016a).

6S

The acronym 6S stands for "Second Simulation of a Satellite Signal in the Solar Spectrum".

Unlike MODTRAN, 6S incorporates a BRDF model in addition to a vegetative canopy model (Eismann, 2012, p. 209).

The 6S code was released in July 1997. The home site for the 6S code is located at: <http://6s.ltdri.org/> with technical documentation located at: <http://6s.ltdri.org/pages/manual.html>.

The acronym 6SV stands for “Second Simulation of a Satellite Signal in the Solar Spectrum Vector” and is an extension to 6S by accounting for radiation polarization.

At the time of writing, 6SV2.1 is the most current code version (<http://6s.ltdri.org/pages/downloads.html>), released in June 2015.

6SV has the following characteristics:

“The 6S code is a basic RT code used for calculation of lookup tables in the MODIS atmospheric correction algorithm. It enables accurate simulations of satellite and plane observation, accounting for elevated targets, use of anisotropic and Lambertian surfaces and calculation of gaseous absorption. The code is based on the method of successive orders of scatterings approximations and its first vector version (6SV1), capable of accounting for radiation polarization”.

(source: <http://6s.ltdri.org/>)

Technical papers by Kotchenova, Vermote, Matarrese, and Klemm (2006) and Kotchenova and Vermote (2007) evaluate the performance of 6SV1 against several models, including MODTRAN.

ATREM (Atmospheric Removal Algorithm)

A radiative transfer approach to atmospheric correction initially led to the development of ATREM. This model covers the 0.4 - 2.5 μm region and caters for scattering and aerosols by incorporating the 5S code; however all surfaces were considered to be horizontal with Lambertian reflectances and it does not take into account bi-directional effects. The 5S code has other shortcomings, among them the inability to correct for hazy conditions and it also did not incorporate methane bands which contains a significant absorption peak of around 20% near 2.35 μm (B.-C. Gao et al., 1993).

According to Kruse (2004), 6S radiative transfer code is used to model atmospheric scattering. This implies an upgrade to the original ATREM model to improve scattering accuracies.

As a result of the recently discovered effects of NO₂ on vegetation, the ATREM model has been upgraded by incorporating newly-developed 6S code containing a module to incorporate NO₂ absorption effects (B.-C. Gao et al., 2009). The scale on which vegetation is affected by NO₂ depends on the vegetative type but generally includes chlorosis (yellowing of leaves). Acid rain forms in the presence of NO₂ with water which has an adverse effect on vegetation (Scottish Environment Protection Agency, n.d.).

Shortcomings of the ATREM model include the inability to correct for topographic and adjacency effects (B.-C. Gao et al., 2009). When ATREM was applied to vegetative areas, it was found to overestimate water vapour content (Goetz et al., 2003).

Despite these shortcomings, ATREM has been widely used in the hyperspectral remote sensing community (Zheng et al., 2003) before alternative models became available. This was mainly made possible due to improvements in computer technology, allowing more sophisticated models to be developed.

Some of these alternative models are considered next.

HATCH (High-Accuracy Atmospheric Correction for Hyperspectral data)

As with ATREM, this model was also developed primarily for use in correcting hyperspectral data, but has similar shortcomings; namely, its inability to correct for adjacency effects (Matthew et al., 2003) and it assumes a Lambertian surface for targets. Aerosols are also considered homogenous throughout a scene (Zheng et al., 2003).

Despite these shortcomings, the HATCH model more accurately models the transmittance where multiple gases absorb strongly (e.g. H₂O and CO₂ at 2.0 μm). It incorporates a technique called the "smoothness test" for more accurate water vapour column retrieval (Zheng et al., 2003).

As with ATREM, HATCH focuses on the 0.4 - 2.5 μm region and has been found to be accurate at 5 - 10 % of the signal for most wavelengths (when compared to MODTRAN-4) (Goetz et al., 2003).

The difficulty ATREM had with retrieving water content from vegetation is mainly overcome with HATCH, provided that the 0.94 μm band is used. It still has problems with the 1.14 μm band and is a shortcoming of the model (Goetz et al., 2003).

Another version called HATCH-2d was developed to compensate for the "smile-effect", as a result of calibration errors in the Hyperion sensor with favourable results (Goetz et al., 2003).

The code is available from the University of Colorado in Boulder, Colorado through a license agreement (B.-C. Gao et al., 2009).

ATCOR 4 (Atmospheric and Topographic Correction)

This is a commercial product and is available from <https://www.rese-apps.com/software/download/index.html>

The ATCOR4 flyer (ReSe Applications, n.d.) lists the following characteristics (but not limited to):

- support for hyperspectral sensors (including airborne)
- aerosol retrieval
- water vapour retrieval (including the 0.94 and 1.13 μm bands)
- removal of haze, cloud shadows.
- correction for the spectral smile effect.

ATCOR is based on MODTRAN-5 code. According to the ATCOR - Code Comparison webpage <http://www.rese.ch/products/atcor/compare.html>, it takes into account terrain height (DEM) and both DEM and BRDF illumination effects.

ACORN (Atmospheric CORrection Now)

As with ATCOR 4, this is also a commercial product but uses MODTRAN 4 code (and hence caters for atmospheric molecular and aerosol scatter as well as gas absorption).

It does not incorporate any correction module for the adjacency effect (Matthew et al., 2003). As Kruse (2004) points out, a key feature of ACORN is in its ability "to

solve for the overlap of absorptions between water vapour and liquid water in surface vegetation".

The latest version is ACORN6lx and is maintained by ImSpec LLC (Advanced Imaging and Spectroscopy) (<http://imspecco.ipower.com/>).

FLAASH (Fast Line-of-Sight Atmospheric Analysis of Spectral Hypercubes)

FLAASH is maintained by Spectral Sciences Inc (<https://www.spectral.com/how-we-deliver/licensed-software/>). Under license, it is available from Harris Geospatial Solutions an add-on to the ENVI package.

FLAASH uses the MODTRAN 4 radiative transfer correction code (Matthew et al., 2003). It is a commercial product and may be purchased as an add-in module to ENVI (ENvironment for Visualizing Images). The product accounts for adjacency effects (unlike most other models), an effect which becomes significant for small surfaces in moderate to high aerosol levels (S.M. Adler-Golden, 1999). Using AVIRIS data, differences in spectra due to adjacency effect were highlighted for an extremely hazy region (visibility of ~ 7km) over a rural region in North Carolina. Although this region was dominated by vegetation, patches of bare soil and small water bodies exists. Correction for the adjacency effect eliminated residual chlorophyll-like reflectances caused by vegetative scattering (Matthew et al., 2003). The model has the ability to derive surface reflectances from hyperspectral data in moderate aerosol/haze conditions.

Compared to ATREM or ACORN, FLAASH produces large temporary files - about 5 times the size of the data file to be processed. Further comparisons are found in Kruse (2004).

Perkins et al. (2012) replaced the MODTRAN execution code with a new radiative transfer look-up table option and achieved high computational speeds at ~10 s per image per computer processor. With these kinds of speeds, real-time processing of atmospheric correction to hyperspectral images is within reach.

SIERRA (Spectral reflectance Image Extraction from Radiance with Relief and Atmospheric correction)

This model is designed for hyperspectral imagery over mountainous regions. It uses the environmental function from the 6S code to evaluate contributions from the surroundings to the upwelled diffuse radiance. MODTRAN 4 code is used for the radiative transfer calculations. BRDF effects are also modelled. The adjacency component is modelled using the same model as ATCOR 4. Under clear atmospheric conditions, both SIERRA and ATCOR 4 produce very similar results with differences becoming apparent under less favourable conditions (such as sharper relief and lower aerosol visibility) (Lenot, Achard, & Poutier, 2009).

The above models are all radiative transfer models, based on the physical processes that occur due to the atmosphere. Empirical approaches use the image data itself to form a correction. The Dark Object Subtraction (DOS) method is particularly popular for multispectral images (Jones, 2010, p. 139).

DOS (Dark Object Subtraction)

The dark-object subtraction technique removes the scattering effect of light (called haze), which is an additive effect. A dark object is identified in the NIR spectrum of the image (e.g. water, shadows) and the DN's for each band are identified from a histogram. Because these DN values represent zero reflectance, they are subtracted from each pixel value throughout the band. However, the atmospheric effects vary across a ROI (region of interest), leading to the "Improved Dark-Object Subtraction" technique. Here, Chavez (1988) considers five atmospheric conditions for defining the scattering model (from very clear to very hazy) and uses relative scattering methods based on these definitions. For instance, for clear conditions, the relative scattering follows more of a $\sim\lambda^{-2}$ to $\sim\lambda^{-0.7}$ relationship, rather than a Rayleigh or Mie relationship. Although improved results were apparent, overcorrection still occurred for certain bands.

Appendix C Feature Reduction – mathematical details

C.1 Characteristics of Hyperspace

A pixel spectrum is represented by a vector, the components of which contain the spectral values corresponding to a set of wavelengths. For hyperspectral data, there are hundreds of components for each pixel-vector. The behaviour of mathematics in such high space needs to be understood in order to develop algorithms for data mining.

To examine the peculiar effects of high dimensional space, first consider a fraction of space occupied by a hypersphere inside a hypercube. In one dimensional space, the fraction is clearly 1. In two dimensional space, this equates to the fraction occupied by a circle inside a square:

$$\frac{\pi r^2}{(2r)^2} = \frac{\pi}{4} \approx 0.7854$$

For three dimensional space, it is the fraction occupied by a sphere inside a cube:

$$\frac{\frac{4}{3}\pi r^3}{(2r)^3} = \frac{\pi}{6} \approx 0.5236 \quad (\text{C.1.1})$$

The treatment to follow in this section was mostly obtained from Landgrebe (2003) (chapter 5).

Extending the above calculation to higher dimensional space is not a trivial task. Fortunately, equations can be found in Kendall (1961) (or even through a quick google search).

In d-dimensional space, the volume of a hypersphere (radius r) is given by:

$$V_s(r) = \frac{2r^d \pi^{\frac{d}{2}}}{d\Gamma(\frac{d}{2})}$$

(where Γ is the gamma function)

The volume of a hypercube in $[-r, r]^d$ is:

$$V_c(r) = (2r)^d$$

The fraction of space (as calculated earlier) is easily shown to be:

$$\frac{V_s(r)}{V_c(r)} = \frac{\pi^{\frac{d}{2}}}{d 2^{d-1} \Gamma(\frac{d}{2})} \quad (\text{C.1.2})$$

Together with the following identities (Andrews, 1986, p. 399):

$$\Gamma(x) = (x-1)!$$

$$\Gamma\left(\frac{1}{2}\right) = \sqrt{\pi} \quad (\text{C.1.3})$$

$$\Gamma(x+1) = x\Gamma(x) \quad (\text{C.1.4})$$

it is easy to show that in 3D space, Equation (C.1.1) can be obtained from Equation (C.1.2). We note that for 3D space ($d = 3$):

$$\frac{\pi^{\frac{3}{2}}}{3 \times 2^2 \Gamma(\frac{3}{2})} = \frac{\pi}{6}$$

where $\Gamma(\frac{3}{2}) = \Gamma(\frac{1}{2} + 1) = \frac{1}{2} \Gamma(\frac{1}{2}) = \frac{1}{2} \sqrt{\pi}$ (obtained by using the identities shown in Equations (C.1.3) and (C.1.4)).

An interesting observation becomes clear when considering the results the first few dimensions (up to $d = 7$, as Landgrebe (2003) did); this is enough to make a number of important observations.

d	$\frac{V_s(r)}{V_c(r)}$
1	1
2	0.7854
3	0.5236
4	0.3084
5	0.1645
6	0.0807
7	0.0369
...	...
d	$\frac{\pi^{\frac{d}{2}}}{d 2^{d-1} \Gamma(\frac{d}{2})}$

Figure 175: Fractional volume of a hypersphere inscribed in a hypercube (correct to 4 d.p.).

The non-linear relationship between the number of dimensions and fractional volume becomes clear when illustrated graphically, as in Figure 176.

Interestingly:

$$\lim_{d \rightarrow \infty} \frac{V_s(r)}{V_c(r)} = 0.$$

These results show that in high dimensional space, the fractional volume decreases for increasing dimension. This implies that most of hyperspace is empty, becoming emptier as the dimension increases.

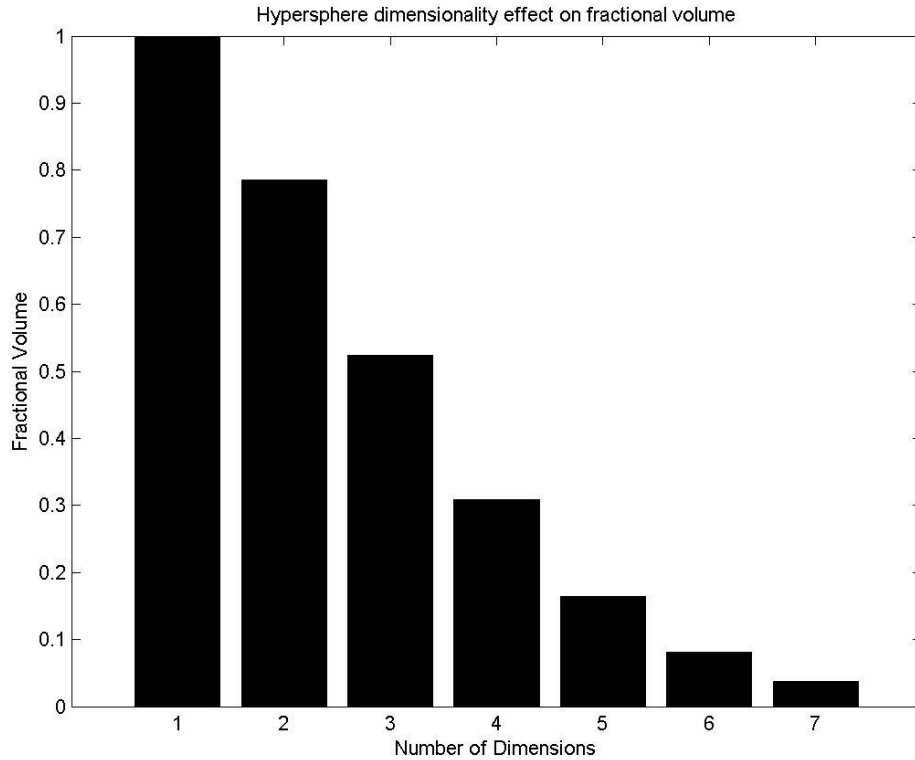


Figure 176: Fractional volume decreases (non-linearly) with increasing number of dimensions.

Another property of high dimensional data is concerns the distribution of data in hyperspace. The mathematical argument given next leads to the conclusion where most of the data tends to be located toward the edges in hyperspace.

Consider N uniformly distributed data points in a hypersphere (centred at the origin). The median distance from the origin to the closest data point is given by:

$$d(p, N) = \left(1 - \left(\frac{1}{2} \right)^{\frac{1}{N}} \right)^{\frac{1}{p}}$$

(Hastie et al., 2009, p. 23)

Consider $N = 1000$ (i.e. 1000 sample points) and $p = 246$ (i.e. 246 hyperspectral bands), then $d(246, 1000) \approx 0.7909$. For a low dimensional problem (e.g. $p = 5$) the result is: $d(5, 1000) \approx 0.2334$. The median distance for 246 dimensions is much

greater than for 5 dimensions. Therefore, most data points occur further from the origin which shows that most data occupies the corners of hyperspace.

This behaviour is also true for normally distributed data (Landgrebe (2003) chapter 5.4); in fact, both the mean and standard deviation are dependent on the number of dimensions.

C.2 Principal Component Analysis (PCA)

Before detailing the transformation process, it is worthwhile recapping the expression for a pixel vector \mathbf{x} . This was given by Equation (2.5.3.1) of Section 2.5.3:

$$\mathbf{x} = \begin{bmatrix} x_1 \\ x_2 \\ \vdots \\ x_N \end{bmatrix} \quad (\text{C.2.1})$$

for N bands.

The theoretical background is developed and clearly explained in Richards (2013), whose process we will follow (mostly) here. However, some symbols have been changed between various references to standardise the formulae in this section obtained from other sources.

A principal component transformation is a linear transformation where the transformation matrix (\mathbf{G}) maps pixel vector \mathbf{x} onto a new vector \mathbf{y} . It is described mathematically by:

$$\mathbf{y} = \mathbf{G}\mathbf{x}$$

It can be shown that (Richards, 2013, p. 168):

$$\mathbf{C}_y = \mathbf{G}\mathbf{C}_x\mathbf{G}^T \quad (\text{C.2.2})$$

where \mathbf{C}_y is the covariance matrix in the rotated space. In this form, matrix \mathbf{G} contain orthonormal eigenvectors and \mathbf{C}_x the eigenvalues along the diagonal (Strang, 1988, p. 296). Furthermore, as \mathbf{G} is an orthogonal matrix (because the covariance matrix is symmetric i.e. $\mathbf{C}_x = \mathbf{C}_x^{-1}$), $\mathbf{G}^T = \mathbf{G}^{-1}$ (Strang, 1988, p. 167).

Multiplying (C.2.2) on the left by \mathbf{G}^{-1} :

$$\mathbf{G}^{-1}\mathbf{C}_y = \mathbf{G}^{-1}\mathbf{G}\mathbf{C}_x\mathbf{G}^{-1}$$

$$\mathbf{G}^{-1}\mathbf{C}_y = \mathbf{C}_x\mathbf{G}^{-1}$$

and multiply by \mathbf{G} on the right:

$$\mathbf{G}^{-1}\mathbf{C}_y\mathbf{G} = \mathbf{C}_x\mathbf{G}^{-1}\mathbf{G}$$

$$\mathbf{G}^{-1}\mathbf{C}_y\mathbf{G} = \mathbf{C}_x$$

i.e. $\mathbf{C}_x = \mathbf{G}^{-1}\mathbf{C}_y\mathbf{G}$. This shows that matrices \mathbf{C}_x and \mathbf{C}_y are similar (Strang, 1988, p. 304) which means that the eigenvalues for both \mathbf{C}_x and \mathbf{C}_y are equal.

The elements in the \mathbf{C}_x matrix:

$$\mathbf{C}_x = \begin{bmatrix} \lambda_1 & & \mathbf{0} \\ & \ddots & \\ \mathbf{0} & & \lambda_N \end{bmatrix}$$

are arranged such that $\lambda_1 > \lambda_2 > \dots > \lambda_N$ (for convenience).

C.3 Separability Measures

The argument for Equation (2.5.5.7) (of Section 2.5.5) is given next.

The probability of correct classification (P_c) is given by Richards (2013, p. 352) as:

$$P_c < 1 - \frac{1}{8} \left[1 - \frac{1}{2} d_{ij}^T \right]^4 \quad (\text{C.3.1})$$

However, the PhD candidate believes this should in fact be:

$$P_c < 1 - \frac{1}{4} \left[1 - \frac{1}{2} d_{ij}^T \right]^4 \quad (\text{C.3.2})$$

The reason for this statement concerns equation (52) from Kailath (1967), which was corrected by Toussaint (1972). Equation (52) by Kailath (1967) states:

$$P_E > \frac{1}{8} e^{-d_{ij}/2}$$

(and used by Richards (2013, p. 352)) was corrected (by Toussaint (1972)) to:

$$P_E \geq \frac{1}{4} e^{-d_{ij}/2}$$

Therefore,

$$P_c < 1 - \frac{1}{4} e^{-d_{ij}/2} \quad (\text{C.3.3})$$

Now, by using Equation (2.5.5.4) (copied here for convenience)

$$d_{ij}^T = 2 \left(1 - e^{-d_{ij}/8} \right)$$

we have

$$e^{-d_{ij}/8} = \left(1 - \frac{d_{ij}^T}{2}\right)$$

$$\therefore d_{ij} = -8 \ln \left[1 - \frac{1}{2} d_{ij}^T\right]$$

Now, using this result for d_{ij} :

$$e^{-\frac{d_{ij}}{2}} = e^{4 \ln \left(1 - \frac{1}{2} d_{ij}^T\right)}$$

Substituting this result into (C.3.3) gives the desired result:

$$P_c < 1 - \frac{1}{4} \left[1 - \frac{1}{2} d_{ij}^T\right]^4 \quad (\text{C.3.4})$$

Appendix D Error Matrices and Accuracy Assessment

Appendix D.1 provides more detail concerning the error matrix than Section 2.7. Calculations are demonstrated by considering an example. The number of suitable training samples required for supervised classifiers are also discussed in the context of hyperspectral data.

A detailed discussion of the Khat statistic follows in Appendix D.2.

D.1 Error Matrix

The error matrix is also called a contingency table (Conese & Maselli, 1992), a confusion matrix (Kaewpijit et al. (2002); Dalponte, Bruzzone, and Gianelle (2012)) or indeed even an agreement matrix (Lechner et al., 2012). It is the most widely used approach in remote sensing to assess classification accuracies in relation to field data (Giles M. Foody, 2008).

To illustrate how the error matrix relates to assessing classification accuracy, it is useful to consider an example of the process involved. However, it is first necessary to define the tabular entries in mathematical terms, as given by Table 51.

To keep the example simple, the entries in Table 51 cover just three classes – A, B and C. In practice, class A may represent a particular species of mangrove, class B water cover, while class C might be a type of soil. The elements of the error matrix have been denoted by e_{11} etc. The representation for a total of three classes (in this example) means that $n = 3$. The sums for each row are indicated by subscript r ; for example, the sum of each of the elements in row 2 is represented by s_{2r} . For the columns, the sum of all the row elements in column 1 is given by s_{c1} (subscript c indicating a column summation).

		Reference data classes			
		A	B	C	Total
Thematic map classes	A	e_{11}	e_{12}	e_{13}	$s_{1r} = \sum_{c=1}^n e_{1c}$
	B	e_{21}	e_{22}	e_{23}	$s_{2r} = \sum_{c=1}^n e_{2c}$
	C	e_{31}	e_{32}	e_{33}	$s_{3r} = \sum_{c=1}^n e_{3c}$
	Total	$s_{c1} = \sum_{r=1}^n e_{r1}$	$s_{c2} = \sum_{r=1}^n e_{r2}$	$s_{c3} = \sum_{r=1}^n e_{r3}$	$s_{cr} = \sum_{i=1}^n s_{ir}$

Table 51: Example for the structure of a simple error matrix.

Note that:

$$s_{cr} = \sum_{i=1}^n s_{ir} = \sum_{i=1}^n s_{ci}$$

i.e. the sum of all row totals equals the sum of all column totals. It is also evident that the matrix will always be square. Training data is entered along the diagonal elements – i.e. $e_{ii} : i=1 \dots n$.

A detailed example is provided in Campbell and Wynne (2011, p. 417) to illustrate how the matrix is populated in practice. Drawing inspiration from this simple example, a new extended example is given in Table 52 to aid the discussion of further concepts. In this case, 20 pixels have been selected for accuracy assessment. In practice, classes for each of these 20 pixels are obtained using ground truth data (i.e. training data) and assessed against the same 20 pixels in the thematic map.

Pixel id	Thematic	Training
1	A	A
2	A	A
3	A	A
4	A	A
5	C	A
6	B	B
7	B	B
8	B	B
9	B	B
10	B	B

Pixel id	Thematic	Training
11	D	B
12	D	B
13	C	C
14	C	C
15	C	C
16	C	D
17	D	D
18	D	D
19	D	D
20	D	D

Table 52: Example of an accuracy assessment table.

This table uses 4 classes; A, B, C and D. The resulting error matrix is shown in Table 53 (using the information from Table 52).

		Reference data classes				
		A	B	C	D	Total
Thematic map classes	A	4	0	0	0	4
	B	0	5	0	0	5
	C	1	0	3	1	5
	D	0	2	0	4	6
	Total	5	7	3	5	20

Table 53: Corresponding error matrix using the data from Table 52.

There are two different types of errors defined in this work. Both Richards (2013) (p. 397 - 398) and Lillesand (2008) (p. 585 - 586) have been sourced in the definitions of these error types.

An omission error occurs when a pixel is misclassified in the thematic map. In the example provided (Table 53), the thematic map contains two pixels of class D

(labelled by pixel id's 11 and 12 in Table 52) but according to the ground truth data they should belong to class B. With respect to ground truthing, these two pixels have been omitted (hence the term omission error). The column entries in the error matrix represent errors of omission.

An error of commission is due to a classification error on the thematic map (caused by the classifier). Referring to Table 53, in addition to 3 pixels of class C (i.e. correctly identified classification – pixel id's 13, 14 and 15 in Table 52), the thematic map included real (i.e. training) classes A & D (one pixel of each – i.e. at pixel id's 5 and 16 in Table 52). These pixels have been included as class C and make up the row entries in the error matrix. The classifier has committed an error (hence the term commission error) by classifying both classes A & D as class C.

The matrix may be viewed from two viewpoints – either the producer (i.e. analyst) or the user (Campbell & Wynne, 2011, p. 417). The producer (i.e. the analyst who produced the thematic map) is interested in understanding how accurate the map is. In this case, for class D this amounts to $\frac{4}{5} = 80\%$ i.e. 80% of pixels are correctly classified. Note that the total "5" in the denominator is obtained from the column total for class D. On the other hand, the user (i.e. the person using the map) is interested in knowing how well the map is able to predict classes on the ground. Quantitatively, for class D, this amounts to $\frac{4}{6} = 67\%$ i.e. 67% of pixels of class D represents class D on the ground. Note that the total "6" in the denominator is obtained from the row total for class D.

In general (and using the notation previously defined in Table 51), the producer's and user's accuracy for each class is given by:

Class	Producer's Accuracy	User's Accuracy
A	$\frac{e_{11}}{s_{c1}} = \frac{4}{5} = 80\%$	$\frac{e_{11}}{s_{1r}} = \frac{4}{4} = 100\%$
B	$\frac{e_{22}}{s_{c2}} = \frac{5}{7} = 71\%$	$\frac{e_{22}}{s_{2r}} = \frac{5}{5} = 100\%$
C	$\frac{e_{33}}{s_{c3}} = \frac{3}{3} = 100\%$	$\frac{e_{33}}{s_{3r}} = \frac{3}{5} = 60\%$
D	$\frac{e_{44}}{s_{c4}} = \frac{4}{5} = 80\%$	$\frac{e_{44}}{s_{4r}} = \frac{4}{6} = 67\%$

Table 54: The Producer's and User's accuracy as calculated using the data in Table 53.

In the literature, both the producer's and user's accuracy are commonly expressed as a percentage rather than a fraction.

In general, for a particular class i , the producer accuracy is given by:

$$\frac{e_{ii}}{s_{ci}} \text{ where: } s_{ci} = \sum_{r=1}^n e_{ri}$$

where:

$$\left. \begin{array}{l} i \\ n \end{array} \right\} = \begin{array}{l} \text{class number (e.g. } i = 1 \text{ represents class A, } i = 2 \text{ is class B, etc.)} \\ \text{total number of classes} \end{array}$$

The user's accuracy may be similarly expressed for the i 'th class:

$$\frac{e_{ii}}{s_{ir}} \text{ where: } s_{ir} = \sum_{c=1}^n e_{ic}$$

It is common to define an overall accuracy, given by:

$$\frac{\sum_{i=1}^n e_{ii}}{s_{cr}}$$

To complete the example (i.e. for Table 53), the overall accuracy is:

$$\frac{\sum_{i=1}^n e_{ii}}{s_{cr}} = \frac{4+5+3+4}{20} = \frac{16}{20} = 80\%$$

In the ideal case, the error matrix will only contain diagonal elements, which will give all accuracies (i.e. producer, user and overall) a value of 100%.

As the error matrix relies on accurate training data, some questions arise:

- what sample size of training data is required?
- how do we determine the sample size for each different class which exists in the image?
- what is the distribution for the training data?

There are no simple answers to these questions. The Hughes effect is particularly significant for hyperspectral data and is expected to play a part in answering some of these questions, as an increase in the number of samples does not imply an increase in classification accuracy. It appears that most papers do not relate their analysis to the Hughes effect – although, it is briefly mentioned by P. M. Mather, and Koch, M. (2011, p. 282).

There needs to be a compromise between the sample size and the accuracy; it is neither practical nor logical to sample every pixel and question the very purpose to carry out remote sensing!

The question regarding the training sample size has no universally accepted answer. In fact, in a review by Giles M. Foody (2009), finds that the sample size may range from tens to tens of thousands or even more. A clearer answer is summarised

in a table by Richards (2013), using a 95% confidence level for accuracy and with an error of $\pm 4\%$. Table 55 shows those results.

Thematic map accuracy (%)	Number of testing pixels required
70	525
75	469
80	400
85	319
90	225
95	119

Table 55: Number of training pixels required to produce a thematic map of accuracy 95% with error $\pm 4\%$. (This table was sourced from Richards (2013, p. 410)).

Interestingly, the number of pixels required decreases with increasing accuracy which might be expected in view of the Hughes effect (but not discussed by Richards (2013)).

In remote sensing, it appears to be common practice to aim for an accuracy of overall 85% (Giles M. Foody (2008); Giles M. Foody (2009); Wulder, Franklin, White, Linke, and Magnussen (2006)) but no class being less than 70% (Thomlinson, Bolstad, & Cohen, 1999) and is the recommended minimum requirements for interpretative use. The origin of the so-universally accepted figure of 85% may in many cases be traced back to J. B. Anderson (1971) and J. R. Anderson et al. (1976) (Giles M. Foody, 2008). It should be remarked that J. B. Anderson (1971) provided a framework for orbital (high altitude) imagery to evaluate land-use classification schemes. Giles M. Foody (2008) questions whether this is applicable to the finer mapping scales found in more recent maps and argues that the 85% accuracy figure would nowadays be viewed as a producer's accuracy.

It is worthwhile considering a practical case to link together the various theoretical components so far. For example, G. M. Foody (2008) selected a training set comprising 100 randomly selected pixels for each class. In this case, six classes were defined to match six agricultural crop types. Furthermore, a second

independent training set was acquired comprising 320 randomly located pixels. The 320 figure is remarkably similar to the 319 pixels of Table 55, and suggests that the accuracy target was set to 85%. In fact, an overall accuracy of 91.25% was achieved using a relevance vector machine (which is based on the SVM).

So far, little consideration has been made concerning the distribution of the training pixels. In general, a selection of 319 pixels could be taken anywhere, even for one class located in one small region. This clearly is not desired nor intended. The solution lies in stratified random sampling, where random sampling is performed for each class (Lillesand (2008, p. 588); Hay (1979)). Indeed, this is exactly the approach adopted by G. M. Foody (2008) in the practical example given above. The effect of random sampling increases the classification accuracy (Mahesh Pal & Mather, 2006), as discussed in Section 2.6.4.1. In practice, limitations may arise due to regions being inaccessible. For example, in Port-Hedland accessibility to some land regions require special access as it falls under a mining lease and subject to health and safety regulations. Apart from requesting formal access, an induction is often required before access is granted. The whole exercise adds to the time and cost of field work cost, with potentially little gain in return. Furthermore, many areas are inaccessible as there are no roads in the vicinity. Driving over mangroves is not an option. The dense mangrove forests make accessibility near-impossible even by foot. Some areas were even designated with crocodile warning signs; we were not equipped to deal with such dangers.

In practice therefore, random sampling may be difficult or virtually impossible to conduct. Congalton and Green (1999) found that only about 50% of their randomly selected sample locations could be visited in the field. The statistics (i.e. error matrix accuracies) strictly rely on the randomness of the samples. Inappropriate selection of samples may well result in the introduction of bias into the error matrix thereby leading to an over or under estimation of the true accuracy (Congalton, 1991). A detailed discussion is found in Stehman (2001) outlining acceptable trade-offs between location accessibility and randomness.

Complications aside, the question that must be asked is how many samples are required for each class?

A mathematically based argument based on a 95% confidence level suggests a minimum of 50 samples per class; in fact, 50 – 100 is recommended (Hay, 1979). As a result, ~ 50 randomly selected samples (per class) appears to be a popular choice (Giles M. Foody, 2009) and also endorsed by Lillesand (2008, p. 588). With particular emphasis on the ML classifier, Mahesh Pal and Mather (2006) suggests 30 samples per class.

Alternative guidelines exist; Table 56 comes from Rosenfield, Fitzpatrick-Lins, and Ling (1982) who (like Hay (1979)) used a purely mathematically based argument based on binomial probability to derive their conclusions – there is no regard made for the Hughes effect, which is understandable in the pre-hyperspectral image era.

Thematic class accuracy (%)	Number of testing pixels required
50	60
55	57
60	60
65	52
70	45
75	40
80	30
85	19

Table 56: Number of testing pixels required for a single class category with 95% confidence and 10% error (the table was taken from Rosenfield et al. (1982) and adopted to the form of Richards (2013, p. 410), Table 11.6).

Congalton and Green (1999) suggests 75 or even 100 samples per category if there are more than 12 categories. These numbers are in line with the recommendation of 50 – 100 by (Hay, 1979). Combining the two recommendations, it is perhaps reasonable to randomly select 50 samples per class up to 12 classes and increase that number to 75 or 100 samples for regions containing more than 12 classes. Some classes may also be more important than others; for less important classes, a

smaller sample size preserves the accuracy for the more important classes (Stehman, 2001).

Other forms of sampling exist; in all, there are five commonly used in remote sensing (Congalton, 1988a). For the issue concerning physical accessibility, cluster sampling holds some promise. A cluster (i.e. groups of pixels) is used as one sampling unit. The clusters should be 10 pixels in size; larger units may be used but no more than 25 pixels (Congalton, 1988a). An example of cluster sampling in practice is found in Edwards Jr, Moisen, and Cutler (1998). Compared to other sampling schemes, the information per unit sample within a cluster is lower and that classification errors are clustered spatially (Stehman, 2001).

With the important questions now answered, we now turn to other issues which need to be considered; such as the timing of the sampling for the training data itself. Obtaining training classes at different times relative to the survey may result in classes on the thematic map that were there at the time but no longer present. Seasonal impacts are also a factor with vegetation – ground truthed spectra may appear different to those recorded by the remote sensor. The error matrix does not take any of these timing events into account (Hay, 1979). In addition, the error matrix is only as good as the quality of the training data itself.

When analysing thematic maps on a pixel by pixel basis, there is the assumption that ground truth data may be matched up with the exact pixel. In practice, this is often not the case; thereby disagreements are entered into the error matrix and subsequently recorded as errors in the thematic map (Giles M. Foody, 2008) – i.e. the error matrix does not cater for locational effects (Hay, 1979). A bias is therefore introduced, leading to a decrease in classification accuracy. The error matrix further assumes that pixels are unmixed and that classes are spectrally separable (Giles M. Foody, 2008).

Giles M. Foody (2008) argues that accuracy targets should be defined with the application in mind and that the target is a function of the “... *data set used (e.g. spatial and spectral resolution), the classes defined (e.g. number and detail of classes) and user needs (e.g. tolerance to error and impacts of variation in error severity)*”. This means that the universal target of 85% is meaningless and that the level accuracy is defined according to the application for which the thematic map is

to be used (Giles M. Foody, 2008). Laba et al. (2002) argues that 85% should not be used as a target. In fact, irrespective of the methodologies and taxonomical detail used, in a review of several mapping projects, the producer's and user's accuracy lie in the 50 - 70% range. Furthermore, Laba et al. (2002) believe that map accuracies may approach 80% through the use of sensors consisting of higher spectral, spatial and temporal resolutions.

An accuracy assessment framework for large area land cover products (i.e. 145 km × 111 km per map sheet, using satellite data) is considered by Wulder et al. (2006), detailing numerous factors to consider in the planning and assessment stages. Many of these factors also appear to be appropriate on smaller levels.

As a final point, a pixel influences adjacent pixel values (termed autocorrelation), which has an effect on not only the classification process but also in accuracy assessment of maps (Congalton, 1988b). The effects of autocorrelation increase as the spatial resolution increases (Congalton, 1988b).

Clearly, more research is needed to improve the accuracy in assessing thematic maps without introducing biases, which are not necessarily real errors (but recorded as such).

D.2 Khat Statistic

The k (KHAT) statistic (or Kappa) gives *“the percentage of correct values of an error matrix due to “true” agreement versus “chance” agreement”* (Lillesand, 2008, p. 590). It is defined as:

$$\hat{k} = \frac{\text{observed accuracy} - \text{chance agreement}}{1 - \text{chance agreement}}$$

and computed by:

$$\hat{k} = \frac{N \sum_{i=1}^r x_{ii} - \sum_{i=1}^r (x_{i+} \cdot x_{+i})}{N^2 - \sum_{i=1}^r (x_{i+} \cdot x_{+i})} \quad (\text{D.2.1})$$

where:

r = number of rows in the error matrix

x_{ii} = number of observations in row i and column i (on the major diagonal)

x_{i+} = total of observations in row i (shown as marginal total to right of the matrix).

x_{+i} = total of observations in column i (shown as marginal total at bottom of the matrix).

N = total number of observations included in matrix.

(Lillesand, 2008, p. 590).

A value of one (ideal case) indicates true agreement, while zero represents a chance agreement in the error matrix. For example, a value of 0.90 means there is a 90% chance that the observed classification is better than one resulting purely by chance. Negative values indicate very poor classification performance. A comprehensive discussion on the interpretation of these values is found in Monserud and Leemans (1992).

To illustrate a practical evaluation for k (using Equation (D.2.1)), the values given in Table 53 will be used.

$$\sum_{i=1}^r x_{ii} = 4 + 5 + 3 + 4 = 16$$

$$\sum_{i=1}^r (x_{i+} \cdot x_{+i}) = 4 \times 5 + 5 \times 7 + 5 \times 3 + 6 \times 5 = 100$$

Note that $\sum_{i=1}^r (x_{i+} \cdot x_{+i}) = \sum_{i=1}^r (x_{+i} \cdot x_{i+})$ and that $N = 20$ (the number of training pixels).

$$\text{Hence, } \hat{k} = \frac{20 \times 16 - 100}{20^2 - 100} = \frac{220}{300} = 0.73$$

Unlike the three accuracies used for the error matrix (i.e. the producer's, user's and overall accuracy) the Kappa coefficient tends to be expressed as a fraction to 2 decimal places rather than a percentage value.

Kappa values relate to classification agreement; those used by Monserud and Leemans (1992) are shown in the following table:

Kappa bounds	Degree of agreement
< 0.05	No
0.05 – 0.20	Very poor
0.20 – 0.40	Poor
0.40 – 0.55	Fair
0.55 – 0.70	Good
0.70 – 0.85	Very good
0.85 – 0.99	Excellent
0.99 – 1.00	Perfect

Table 57: Numeric interpretation of the Kappa coefficient in relation to the degree of classification agreement.

Despite the proponents for the Kappa coefficient, opponents point to shortcomings whereby (for example) the classification accuracy may in fact be lower due to an overestimation in the degree of chance agreement (Giles M. Foody, 2008).

Appendix E Supervised Classification

The mathematical details behind two particularly common supervised classifiers are outlined for the maximum likelihood (ML) (Appendix E.1) and the support vector machine (SVM) (Appendix E.2). The final section (Appendix E.3) contains a proof to show the invariance of SAM for spectra under different illumination conditions.

E.1 Maximum Likelihood (ML)

Equation Chapter 5 Section 1

An ML decision rule is mathematically decided by:

$$\mathbf{x} \in \omega_i \text{ if } p(\omega_i | \mathbf{x}) > p(\omega_j | \mathbf{x}) \text{ for all } j \neq i \quad (\text{E.1.1})$$

(Richards, 2013, p. 250)

Here $p(\omega_i | \mathbf{x})$ is the probability that vector \mathbf{x} belongs to class ω_i . This rule simply states that the probability that \mathbf{x} belongs to a class must be greater than the probability that it belongs to another class.

Bayes theorem is then applied:

$$p(\omega_i | \mathbf{x}) = \frac{p(\mathbf{x} | \omega_i) p(\omega_i)}{p(\mathbf{x})}$$

where $p(\mathbf{x} | \omega_i)$ is called the posterior probability, which can be determined from the training pixels for the class. It can be shown that by using the discriminant function:

$$g_i(\mathbf{x}) = \ln p(\mathbf{x} | \omega_i) + \ln p(\omega_i)$$

the decision rule given by Equation (E.1.1) reduces to:

$$\mathbf{x} \in \omega_i \text{ if } g_i(\mathbf{x}) > g_j(\mathbf{x}) \text{ for all } j \neq i$$

Now, the Gaussian distribution function is used for $p(\mathbf{x} | \omega_i)$. A multidimensional version, suitable for hyperspace (Section 2.5.1) leads to:

$$p(\mathbf{x} | \omega_i) = (2\pi)^{-N/2} |\mathbf{C}_i|^{-1/2} \exp\left\{-\frac{1}{2}(\mathbf{x} - \mathbf{m}_i)^T \mathbf{C}_i^{-1} (\mathbf{x} - \mathbf{m}_i)\right\} \quad (\text{E.1.2})$$

(Richards, 2013, p. 252)

Note the inclusion of the covariance matrix and vector forms for the variables, the number N spectral dimensions, and the change in the constant (2π) compared to the lower dimensional Gaussian:

$$p(x | \omega_i) = (2\pi)^{-1/2} \sigma_i^{-1} \exp\left\{-\frac{1}{2}(x - m_i)^2 / \sigma_i^2\right\} \quad (\text{E.1.3})$$

(Richards, 2013, p. 481)

(σ_i is the standard deviation of class i).

As a consequence, the discriminant function becomes:

$$g_i(\mathbf{x}) = -\ln |\mathbf{C}_i| - (\mathbf{x} - \mathbf{m}_i)^T \mathbf{C}_i^{-1} (\mathbf{x} - \mathbf{m}_i) \quad (\text{E.1.4})$$

This then, is the maximum likelihood classifier.

As the Gaussian function has a tail that is infinite in length, classes far from the centre may still contribute to the class label. This is undesirable, so in practice a threshold value is used to constraint the distribution. Additionally, we note that the Mahalanobis distance (Equation 2.5.1.2 of Section 2.5.1) is once again part of Equation (E.1.2). Furthermore, the term:

$$(\mathbf{x} - \mathbf{m}_i)^T C_i^{-1} (\mathbf{x} - \mathbf{m}_i)$$

actually allows the ML classifier to take on a quadratic surface (as it is a quadratic function of \mathbf{x}) instead of a linear surface. This improvement allows straight lines to be replaced by curves in the forms of parabolas, ellipses and circles (in 2D space). In hyperspace these surfaces become hyperparaboloids, hyperellipsoids and hyperspheres, respectively.

E.2 Support Vector Machine (SVM)

The SVM was introduced in Section 2.6.4.2 but avoided the mathematical details, which are outlined below.

Figure 31 (p. 101 of Section 2.6.4.2) showed two classes separated by a boundary. The boundary for this 2D situation takes the form of a line:

$w_1x_1 + w_2x_2 + w_3 = 0$. In N dimensional space, this takes the vector form:

$\mathbf{w}^T \mathbf{x} + w_{N+1} = 0$. The column vectors \mathbf{x} are the usual pixel vectors but here we have also introduced weight vectors \mathbf{w} .

This enables us to write conditions describing the location for each of the two classes (as defined in Figure 31):

$$\mathbf{x} \in \text{class 1 if } \mathbf{w}^T \mathbf{x} + w_{N+1} \geq 0$$

$$\mathbf{x} \in \text{class 2 if } \mathbf{w}^T \mathbf{x} + w_{N+1} < 0$$

The next step introduces two marginal hyperplanes but with an optimal hyperplane between them. These are scaled to unity, so in all we write:

$$\left. \begin{array}{l} \mathbf{x} \in \text{class 1 if } \mathbf{w}^T \mathbf{x} + w_{N+1} \geq +1 \\ \mathbf{x} \in \text{class 2 if } \mathbf{w}^T \mathbf{x} + w_{N+1} \leq -1 \end{array} \right\} \quad (\text{E.2.1})$$

This allows us to introduce a new constraint by controlling the maximum distance between the surfaces and allows for some degree of misclassification of classes.

Although not all the mathematical details are presented here, effectively we desire to solve the following equation:

$$\alpha_i \{y_i (\mathbf{w}^T \mathbf{x} + w_{N+1}) - 1\} = 0$$

The α_i coefficients are Lagrange multipliers (which “effectively weigh each training vector according to its importance in determining the decision surface” Eismann (2012, p. 591); Dalponte et al. (2009) effectively makes the same statement). The y_i functions simply control the class labelling scheme, where $y_i = +1$ for class 1 pixels and $y_i = -1$ for class 2 pixels (compare to Equation (E.2.1)).

A significant outcome of this work is that only training samples that fall close to the hyperplane (called support vectors) are required as they determine the marginal hyperplanes. This drastically reduces the need for large training samples, which is a major advantage over the ML classifier.

Using these results, we finally have a test condition for class membership:

$$\text{sgn} \{ \mathbf{w}^T \mathbf{x} + w_{N+1} \} = \text{sgn} \left\{ \sum_{i \in S} \alpha_i y_i \mathbf{x}_i^T \mathbf{x} + w_{N+1} \right\} \quad (\text{E.2.2})$$

(the symbol S refers to the sum being over the support vectors only).

The signum (or sign) function sgn is defined as:

$$\text{sgn}(x) = \begin{cases} -1 & \text{if } x < 0 \\ 0 & \text{if } x = 0 \\ +1 & \text{if } x > 0 \end{cases}$$

For example, if $\mathbf{w}^T \mathbf{x} + w_{N+1} < 0$ then we obtain -1 (i.e. class 2).

Notice that we have defined the SVM classification in terms of $\mathbf{x}^T \mathbf{x}$, which is linear (i.e. gives a hyperplane). Another strength of the SVM method is that this does not have to be the case. Instead, we could define a function $\phi(\mathbf{x})$ and write Equation (E.2.2) accordingly:

$$\text{sgn}\left\{\phi(\mathbf{w})^T \phi(\mathbf{x}) + w_{N+1}\right\} = \text{sgn}\left\{\sum_{i \in S} \alpha_i y_i \phi(\mathbf{x}_i)^T \phi(\mathbf{x}) + w_{N+1}\right\}$$

A kernel function is defined by writing:

$$k(\mathbf{x}_i, \mathbf{x}) = \phi(\mathbf{x}_i)^T \phi(\mathbf{x})$$

The kernel function describes the shape of the decision boundary as shown in Figure 31 of Section 2.6.4.2.

E.3 Spectral Angle Mapper (SAM)

The spectral angle formula was originally defined in Section 2.6.4.3, but is copied here for convenience.

$$\theta = \cos^{-1} \left(\frac{\sum_{i=1}^n r_i t_i}{\left[\sum_{i=1}^n r_i^2 \right]^{1/2} \left[\sum_{i=1}^n t_i^2 \right]^{1/2}} \right) \quad (\text{E.3.1})$$

Here, r_i is the reference pixel vector and t_i the target (image) pixel vector. The summation extends over all n bands.

Multiplying all reference spectra by a constant, means $r_i \rightarrow C r_i$ where C is a constant. It is important to realise that r_i is not replaced by $c_i r_i$ where c_i takes on different values. Spectrally, this means that the reflectance (or radiance) at each wavelength must be multiplied by one constant (or individual equal constants),

rather than different individual constants. Changing individual wavelengths by a multiplication factor has the effect of changing the whole spectrum (e.g. making it brighter) but the spectral angle with another cover type will remain unchanged.

Mathematically, putting $r_i \rightarrow Cr_i$ and with referral to Equation (E.3.1):

$$\sum_{i=1}^n r_i t_i \rightarrow \sum_{i=1}^n Cr_i t_i$$

The numerator therefore becomes:

$$\sum_{i=1}^n Cr_i t_i = C \sum_{i=1}^n r_i t_i$$

For the denominator:

$$\left[\sum_{i=1}^n r_i^2 \right]^{1/2} \rightarrow \left[\sum_{i=1}^n Cr_i^2 \right]^{1/2}$$

and finally,

$$\left[\sum_{i=1}^n (Cr_i)^2 \right]^{1/2} = C \left[\sum_{i=1}^n r_i^2 \right]^{1/2}$$

The final operation, for Equation (E.3.1), involves dividing the numerator expression by the denominator. As the C 's cancel, the significance is realised - θ remains invariant. A similar result applies to changing the whole target spectrum ($t_i \rightarrow Ct_i$). The simultaneous modification to both spectra also results in an unchanged spectral angle.

Suppose C_1 and C_2 are different constants (although they do not need to be).

Substituting $r_i \rightarrow C_1 r_i$ and $t_i \rightarrow C_2 t_i$ in the numerator gives

$$\sum_{i=1}^n r_i t_i \rightarrow \sum_{i=1}^n C_1 r_i C_2 t_i$$

The numerator therefore becomes:

$$\sum_{i=1}^n C_1 r_i C_2 t_i = C_1 C_2 \sum_{i=1}^n r_i t_i$$

For the denominator:

$$\left[\sum_{i=1}^n r_i^2 \right]^{1/2} \rightarrow \left[\sum_{i=1}^n (C_1 r_i)^2 \right]^{1/2} \quad \text{and} \quad \left[\sum_{i=1}^n t_i^2 \right]^{1/2} \rightarrow \left[\sum_{i=1}^n (C_2 t_i)^2 \right]^{1/2}$$

Therefore,

$$\left[\sum_{i=1}^n (C_1 r_i)^2 \right]^{1/2} = C_1 \left[\sum_{i=1}^n r_i^2 \right]^{1/2} \quad \text{and} \quad \left[\sum_{i=1}^n (C_2 t_i)^2 \right]^{1/2} = C_2 \left[\sum_{i=1}^n t_i^2 \right]^{1/2}$$

The final operation, for Equation (E.3.1), involves dividing the numerator expression by the denominator. As the product $C_1 C_2$ cancel out, the spectral angle θ remains unchanged. This means that any spectrum may be changed by a constant, resulting in an identical spectral angle. Note that each wavelength needs to be multiplied by that constant, otherwise the spectral shape has changed which therefore represents a different spectrum (i.e. that of a different cover type). A corollary of the mathematics shows that two spectra are identical if the first is different to the second by a multiplicative factor. This result helps in understanding the nature of spectra angles in relation to spectra (examples were given in Section 4.4.1).

Appendix F PCA – A Detailed Numerical Example

This section provides a detailed example of a PCA calculation. It also provides for an understanding of exactly what is displayed by an ENVI PC transformed image.

We shall follow the example provided in Sections 6.3.1 and 6.3.2 as found in Richards (2013). In particular, Richards (2013, p. 172) defined the following pixel vectors:

$$\mathbf{x} = \begin{bmatrix} 2 \\ 2 \end{bmatrix}, \begin{bmatrix} 4 \\ 3 \end{bmatrix}, \begin{bmatrix} 5 \\ 4 \end{bmatrix}, \begin{bmatrix} 5 \\ 5 \end{bmatrix}, \begin{bmatrix} 3 \\ 4 \end{bmatrix}, \begin{bmatrix} 2 \\ 3 \end{bmatrix} \quad (\text{F.0})$$

The principal component transformation matrix is explained sufficiently well by Richards (2013, p. 171), and therefore will not be derived here. The result is:

$$\mathbf{G} = \begin{pmatrix} 0.82 & 0.57 \\ -0.57 & 0.82 \end{pmatrix} \quad (\text{F.1})$$

The pixel vectors in the PC space are:

$$\mathbf{y} = \begin{bmatrix} 2.78 \\ 0.50 \end{bmatrix}, \begin{bmatrix} 4.99 \\ 0.18 \end{bmatrix}, \begin{bmatrix} 6.38 \\ 0.43 \end{bmatrix}, \begin{bmatrix} 6.95 \\ 1.25 \end{bmatrix}, \begin{bmatrix} 4.74 \\ 1.57 \end{bmatrix}, \begin{bmatrix} 3.35 \\ 1.32 \end{bmatrix} \quad (\text{F.2})$$

as obtained by calculating $\mathbf{y} = \mathbf{G}\mathbf{x}$. The columns of \mathbf{G} correspond to eigenvectors.

In a more practical sense, the pixel vectors are in the form of:

$$\begin{bmatrix} \text{band1} \\ \text{band2} \end{bmatrix}$$

An ENVI image file was created for the 6 pixels as given by Vector (F.0) and the “PC Forward Rotation” calculated.

The results ENVI returned were as follows:

$$\mathbf{H} = \begin{pmatrix} 0.819067 & 0.573697 \\ -0.573697 & 0.819067 \end{pmatrix} \quad (\text{F.3})$$

$$\mathbf{r} = \begin{bmatrix} -2.089147 \\ -0.368055 \end{bmatrix}, \begin{bmatrix} 0.122685 \\ -0.696382 \end{bmatrix}, \begin{bmatrix} 1.515450 \\ -0.451012 \end{bmatrix}, \begin{bmatrix} 2.089147 \\ 0.368055 \end{bmatrix}, \begin{bmatrix} -0.122685 \\ 0.696382 \end{bmatrix}, \\ \begin{bmatrix} -1.515450 \\ 0.451012 \end{bmatrix} \quad (\text{F.4})$$

In this case, \mathbf{H} and \mathbf{r} refer (respectively) to the principal component transformation matrix and pixel vectors in PC space as obtained by ENVI.

To make the link to ENVI abundantly clear, the band 1 values in the ENVI PC image contain the values -2.089147, 0.122685, etc., while for band 2 the values are: -0.368055, -0.696382, etc.

Comparing the principal component transformation matrix (i.e. Matrix (F.3) with Matrix (F.1)), the only difference is that Matrix (F.1) has been rounded to 2 decimal places. So, these two matrices are identical (i.e. $\mathbf{G} = \mathbf{H}$). However, the pixel coordinates in the PC transformed space are different (i.e. Vector (F.4) is different to Vector (F.2)).

The difference is explained through a shift in origin. This method is outlined in section 6.3.3 of Richards (2013, p. 173), which shifts the origin of the principal components space to make the brightness values positive. The covariance matrix remains the same.

In this case, only the first two pixel values (in transformed and shifted-origin space) are calculated below for this demonstration, therefore vector \mathbf{r} becomes:

$$\mathbf{r} = \begin{bmatrix} -2.089147 \\ -0.368055 \end{bmatrix}, \begin{bmatrix} 0.122685 \\ -0.696382 \end{bmatrix}$$

and

$$\mathbf{x} \text{ reduces to } \begin{bmatrix} 2 \\ 2 \end{bmatrix}, \begin{bmatrix} 4 \\ 3 \end{bmatrix}.$$

By shifting the origin and using matrix \mathbf{H} from ENVI (Matrix (F.3)), we find the coordinates identical to the values contained in the ENVI PC image. The equation is:

$$\mathbf{r} = \mathbf{H}(\mathbf{x} - \mathbf{m}),$$

where \mathbf{m} is the mean vector of \mathbf{x} (using all bands - i.e. Vector (F.0))

having values:

$$\mathbf{m} = \begin{bmatrix} 3.50 \\ 3.50 \end{bmatrix}$$

An interesting property is that the sum of all band 1 components equals zero. The same applies to band 2. In fact, the origin shift gives a mean for all bands to equal zero (as is evident from Vector (F.4)).

For reference, the ENVI PCA statistics file contents are included (Table 58) to clarify the link between theory and practice. A MATLAB program was written for this demonstration and included as Table 59, along with the output of the program in Table 60.

Basic Stats	Min	Max	Mean	Stdev	Num	Eigenvalue
Band 1	2	5	3.500000	1.378405	1	2.670470
Band 2	2	5	3.500000	1.048809	2	0.329530

Covariance	Band 1	Band 2
Band 1	1.900000	1.100000
Band 2	1.100000	1.100000

Table 58: ENVI PCA statistics file content (converted into formatted tabular form).

(continued over the page)

Correlation	Band 1	Band 2
Band 1	1.000000	0.760886
Band 2	0.760886	1.000000

Eigenvector	Band 1	Band 2
Band 1	0.819067	0.573697
Band 2	-0.573697	0.819067

Table 58: ENVI PCA statistics file content (converted into formatted tabular form).

The eigenvector data corresponds to the principal component transformation matrix (see Equation (F.1)). The results may be duplicated using a MATLAB program.

```
% Richards p172
p1 = [2 2]; % pixel 1
p2 = [4 3]; % pixel 2

% Principal components transformation matrix
G = [ 0.82 0.57 ; -0.57 0.82 ];

% PC coords
disp( 'PC coords for Richards' );
disp( G*p1 );
disp( G*p2 );

% envi.
% Shift the origin (p 173 Richards) is given by p1-m (for pixel 1).
% Principal components transformation matrix (using eigenvector
% components as given by envi PCA stats).
Ge = [ 0.819067 0.573697 ; -0.573697 0.819067 ];

m = [3.5 3.5];

% PC components of matrix G, but Ge are the eigenvectors in the image.
disp( 'PC coords for envi' );
disp( Ge*(p1-m) );
disp( Ge*(p2-m) );
```

Table 59: MATLAB program used to link ENVI's PC coordinates with that obtained by theory.

PC coords for Richards

2.7800
0.5000

4.9900
0.1800

PC coords for ENVI

-2.0891
-0.3681

0.1227
-0.6964

Table 60: Program output for the MATLAB program listed in Table 59.

The PC coords for Richards agree with to those of Vector (F.2), while the PC coords for ENVI agree with Vector (F.4). Note that only two components were calculated by the MATLAB program.

Referring back to Table 58, the following matrices were defined:

$$\mathbf{C}_x = \begin{bmatrix} 1.90 & 1.10 \\ 1.10 & 1.10 \end{bmatrix} \quad \mathbf{C}_y = \begin{bmatrix} 2.67 & 0 \\ 0 & 0.33 \end{bmatrix} \quad \mathbf{R}_x = \begin{bmatrix} 1.00 & 0.76 \\ 0.76 & 1.00 \end{bmatrix}$$

where, \mathbf{C}_x is the covariance matrix in the original space, \mathbf{C}_y is the covariance matrix in the principal component space and \mathbf{R}_x is the correlation matrix.

If the elements of \mathbf{C}_x are defined according to:

$$\mathbf{C}_x = \begin{bmatrix} C_{11} & C_{12} \\ C_{21} & C_{22} \end{bmatrix}$$

then C_{12} (and C_{21}) gives the degree of correlation between bands 1 and 2 (Gonzalez & Woods, 2008, p. 843). In this case, bands 1 and 2 are positively correlated, as is also evident from the correlation matrix.

The diagonal components of \mathbf{C}_y are the eigenvalues.

$$\mathbf{C}_y = \begin{bmatrix} \lambda_1 & 0 \\ 0 & \lambda_2 \end{bmatrix}$$

The diagonal components also represent the variance of the principal components. This has a direct significance for an image as $\lambda_1 > \lambda_2 > \dots > \lambda_N$ (N bands). When referring back to the PC transformed image from ENVI, the first band contains the highest variation, the second band the next highest, all the way down to the Nth band.

Visually, band 1 contains the highest contrast while band N contains little contrast; little information can be obtained from band N and the image appears featureless. Explicit examples of images are found in Gonzalez, Woods, and Eddins (2009, p. 668).

Often in dimensionality reduction operations, 95% or 99% of the cumulative variance is retained. The total cumulative contribution of each band is calculated using the means shown next. Using the above eigenvalues as defined in matrix \mathbf{C}_y , the calculation is as follows:

$$\text{The sum of all eigenvalues} = 2.67 + 0.33 = 3.$$

The percent variance of:

$$\text{Band 1} = (2.67 / 3) \times 100 = 89\%$$

$$\text{Band 2} = (0.33 / 3) \times 100 = 11\% \text{ (cumulative variance} = 89\% + 11\% = 100\%).$$

Therefore, by retaining only the first band, we account for 89% of the variance in the data.

This limited example illustrates the process involved.

Consider a real-world example, where the following numbers were obtained:

		eigenvalue	cumulative variance	cumulative variance (%)
Band	1	17753.85	17753.85	91.93
Band	2	911.92	18665.77	96.66
Band	3	240.11	18905.88	97.90
Band	4	115.86	19021.75	98.50
Band	5	86.88	19108.63	98.95
Band	6	69.61	19178.24	99.31
Band	7	44.86	19223.10	99.54
Band	8	37.03	19260.13	99.73
Band	9	27.47	19287.60	99.88
Band	10	23.79	19311.39	100.00
	Total	19311.39	189716.35	100.00

**Table 61: Example of retaining the first p bands, depending on the threshold value set for the total cumulative variance (%).
In this case, p = 2 or 6 PC bands would be selected for a 95% or 99% threshold, respectively.**

Explicitly:

For band 2:

$$\text{Cumulative variance} = 17753.85 + 911.92 = 18665.77$$

$$\text{Cumulative variance (\%)} = (18665.77 / 19311.39) \times 100 = 96.66 \%$$

For band 3:

$$\text{Cumulative variance} = 18665.77 + 240.11 = 18905.88$$

$$\text{Cumulative variance (\%)} = (18905.88 / 19311.39) \times 100 = 97.90 \%$$

etc.

In practice, the statistics from ENVI were exported to a (text) file, and a written MATLAB program was used to calculate these cumulative variances (%).

Appendix G Field Trip 1 Results

This Appendix presents the results of the first field trip, conducted in September 2013 in the Port Hedland coastal region.

G.1 Field Trip Logs

The full day-to-day logs of the first field trip are given below.

Spectral samples were also taken for different trees but of the same species. They are differentiated from each other by the inclusion of a numbered suffix attached to the species name.

Locational codes (e.g. [FM]) are explained in Table 67 of Appendix G.2. Further details concerning the nomenclature was covered in Section 4.3.3.

Date:	02-09-2013	
Conditions:	Excellent. Cloud free. No wind for the majority of the period, with slight intermittent breeze during the latter period. Temperature: 35°C.	
Location:	Finucane Island	
	Cover type sampled	Notes
[FM]	<i>Osbornia octodonta</i>	
[FM]	<i>Ceriops australis</i>	
[FM]	<i>Avicennia marina 1</i>	old tree
[FM]	<i>Avicennia marina 2</i>	mature tree
[FM]	<i>Avicennia marina 3</i>	young tree
[FM]	<i>Bruguiera exaristata 1</i>	
[FM]	<i>Bruguiera exaristata 2</i>	
[FM]	<i>Rhizophora stylosa</i>	
[FM]	<i>Aegialitis annulata 1</i>	green leaves
[FM]	<i>Aegialitis annulata 2</i>	green leaves
[FM]	<i>Aegialitis annulata 3</i>	yellow leaves

Table 62: Log of mangrove samples taken at Finucane Island.

Location:	Utah on Finucane Island	
	Cover type sampled	Notes
[FU]	<i>Avicennia marina</i>	dusty leaves (thick red dust)
[FU]	<i>Aegiceras corniculatum 1</i>	clean leaves
[FU]	<i>Aegiceras corniculatum 2</i>	dusty leaves (thick red dust)
[FU]	Red soil	Located around <i>Salsola kali</i> (below)
[FU]	<i>Salsola kali</i>	

Table 63: Log of samples taken at Utah.

The notes field shows that *Aegialitis annulata* 3 contained a number of yellow leaves, in contrast to *Aegialitis annulata* 1 & 2. Spectral differences are therefore expected.

[FM] *Avicennia marina* 1 was a particularly old mangrove, whereas [FM] *Avicennia marina* 2 was considered to be a representative well-matured mangrove. A particularly young mangrove was [FM] *Avicennia marina* 3. Variability in spectral measurements for [FM] *Avicennia marina* 3 were higher than for [FM] *Avicennia marina* 1 (Figure 179) & *Avicennia marina* 2 (Figure 180), possibly due to enhanced background soil interference (being a smaller, young mangrove).

The effect of the yellow leaves for [FM] *Aegialitis annulata* 3 (Figure 179) with [FM] *Aegialitis annulata* 1 (or 2) (Figure 178), is to cause a blue-shift and shortening of the red-edge.

At Utah (i.e. [FU] location), some of the species sampled contained a thick layer of iron-oxide (likely) dust (presumably from the nearby stockpiles), thereby affecting shortening the red-edge with an accompanying blue-shift. Evidence may be taken by comparing [FM] *Avicennia marina* 1 (Figure 179) with [FU] *Avicennia marina* (Figure 192) or [FU] *Aegiceras corniculatum* 1 (Figure 191) with [FU] *Aegiceras corniculatum* 2 (Figure 191).

Date:	03-09-2013	
Conditions:	Excellent. Cloud free. No wind for the majority of the period, with slight intermittent breeze during the latter period. Temperature: 38°C.	
Location:	Finucane Island (grassland)	
[FR]	Cover type sampled	Notes
[FR]	<i>Trianthena turgidifolia</i>	
[FR]	<i>Triodia pungens</i>	
[FR]	<i>Frankenia (ambita)</i>	
[FR]	Sandy salty crusty soil	
[FR]	<i>Tecticornia sp. 1</i>	big plant, near mangrove
[FR]	<i>Tecticornia sp. 2</i>	plant in better condition1
[FR]	<i>Tecticornia sp. 3</i>	plant in better condition2
[FR]	<i>Tecticornia sp. 4</i>	deadish (lots of crusty salty leaves)
[FR]	<i>Sporobolus virginicus 1</i>	
Location:	Finucane Island (near the road)	
[FR]	Cover type sampled	Notes
[FR]	<i>Sporobolus virginicus 2</i>	
[FR]	<i>Avicennia marina</i>	salt crust on quite a few leaves
[FR]	<i>Acaria sp.</i>	

Table 64: Log of samples taken at Finucane Island.

Note: The common name for *Sporobolus virginicus* is marine couch, while *Triodia pungens* is referred to as spinifex.

Date:	04-09-2013	
Conditions:	Scattered thin cirrus clouds. Light wind. Temperature: 39°C.	
Location:	Redbank	
	Cover type sampled	Notes
[RB]	Dry soil	Soil spectral sample near mangroves
[RB]	Wet soil	Soil spectral sample taken in the water near mangroves
[RB]	Shallow water soil	
[RB]	<i>Ceriops australis</i>	
[RB]	<i>Avicennia marina</i>	
[RB]	<i>Rhizophora stylosa</i>	
[RB]	<i>Bruguiera exaristata</i>	
Location:	Lumsden Point	
	Cover type sampled	Notes
[LP]	Salty reddish crust	Typical red soil but containing a layer of crusty salt.
[LP]	<i>Tecticornia sp.</i>	
[LP]	<i>Limonium</i>	
[LP]	<i>Avicennia marina</i>	
[LP]	Hard packed dirt road	
[LP]	Dredge dam on top	
[LP]	Dredge dam road	Road contains fine red sand

Date:	05-09-2013	
Conditions:	Excellent. Cloud free. Light wind. Temperature: ~35°C	
Notes:	No ASD samples were taken today; the ASD Notebook crashed. The opportunity was taken to photograph large vegetative structures in sparse areas. They are valuable, as they're easily identifiable in airborne images.	

Table 65: Log of samples taken at Redbank and Lumsden Point.

Date:	06-09-2013	
Conditions:	Excellent. Cloud free. No wind for the majority of the period, with an occasional breeze during the latter period. Temperature: 37°C.	
Location:	Pretty Pool	
	Cover type sampled	Notes
[PP]	Road (sandy hard packed)	
[PP]	<i>Trianthema turgidifolia</i>	
[PP]	<i>Tecticornia sp. 1</i>	
[PP]	<i>Triodia pungens</i>	
[PP]	* <i>Aerva javanica</i>	
[PP]	<i>Corchorus parviflorus</i>	
[PP]	<i>Acacia translucens</i>	
[PP]	Shell laden sand	(sand is located between bushes and contains many shells)
[PP]	* <i>Cenchrus ciliaris</i>	
[PP]	Old bitumen	Leftover bitumen road
[PP]	<i>Tecticornia sp. 2</i>	
[PP]	Interstitial salt crusted sand	
[PP]	Salt flat plain	

Table 66: Log of samples taken at Pretty Pool. The "*" symbol denotes Weeds.

Note:

Multiple digital photographs were taken for each cover-type sampled. In the actual field log, the photo identity (a number) and their numerical range was recorded corresponding to each spectral sample. This data, along with the individual photographs have been omitted from the thesis.

G.2 ASD Spectral Plots

This section contains the full set of ASD spectral plots which have been collected during the first field trip. The details behind their construction were discussed in Section 4.3.1.

A special code defines the physical location for each ASD spectral sample. The date column tracks when samples were taken at each particular location.

Location	Code	Date
Finucane Island (mangrove region)	FM	02-09-2013
Finucane Island (Utah)	FU	02-09-2013
Finucane Island (road region)	FR	03-09-2013
Redbank	RB	04-09-2013
Lumsden Point	LP	04-09-2013
Pretty Pool	PP	06-09-2013

Table 67: Region codes identifies the physical location where ASD spectral samples were collected.

Figure 35 (p. 131, of Section 3.2) identified the key field site collection regions, while Figure 177 shows a breakdown of the locations specific to Finucane Island (as defined above in Table 67).



Figure 177: The three field regions on Finucane Island as defined in Table 67. FM corresponds to the dense mangrove region, FR defines sites along the road (and grassland further in) and FU for the Utah region.

Each plot given below represents the ASD spectrum of one cover type (individual plant species or soil type). Each mean spectrum is represented by a black solid line, while a dashed magenta line represents the spectral uncertainty, as calculated by the SD (standard deviation). More details were provided in Section 4.3.3, including the nomenclature for each title.

The vertical axis in all plots covers the same range – from -0.05 to 1.05. These values cater for all reflectance values, where the largest and smallest (mean \pm SD) values are \approx 1.05 and -0.05, respectively. Using identical scales for all axes allows plots to be readily compared.

Region: Finucane Island (mangrove) [FM]

Vegetative Spectra

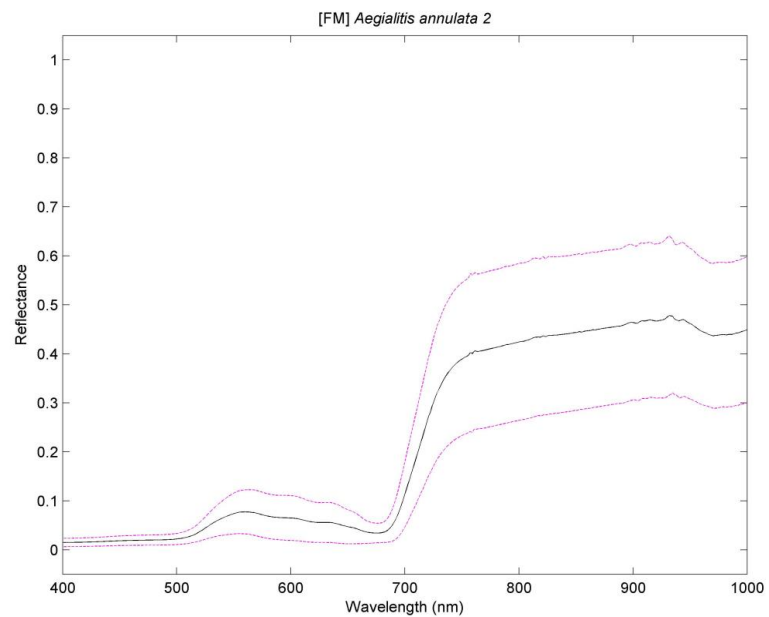
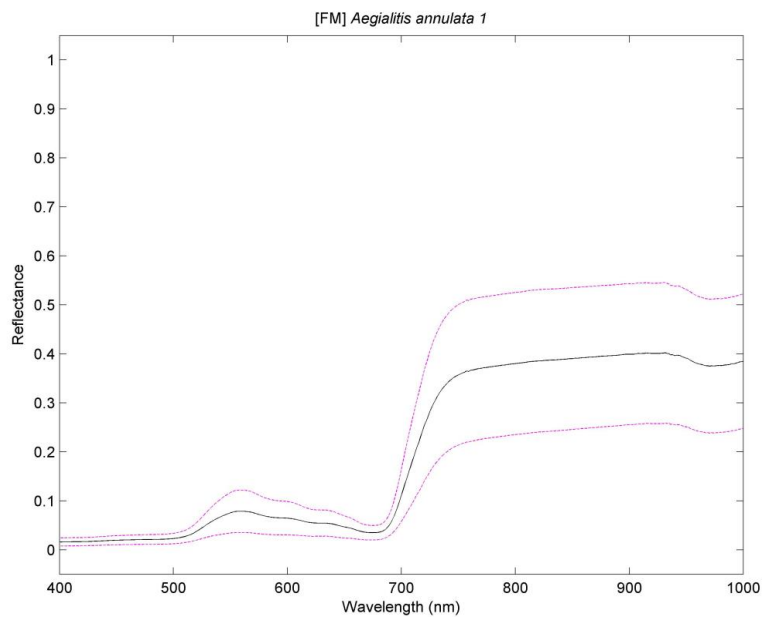


Figure 178: *Aegialitis annulata* spectra sampled from different trees (1 & 2). [FM]

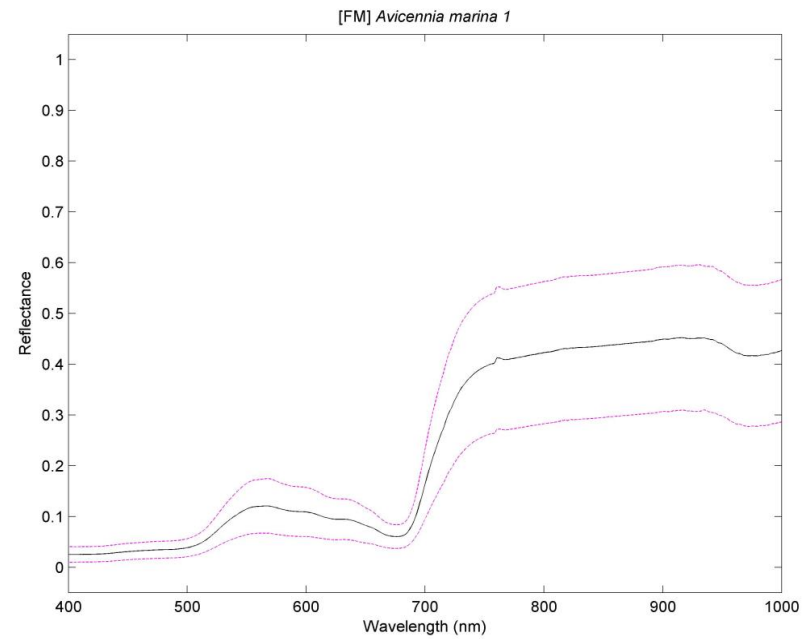
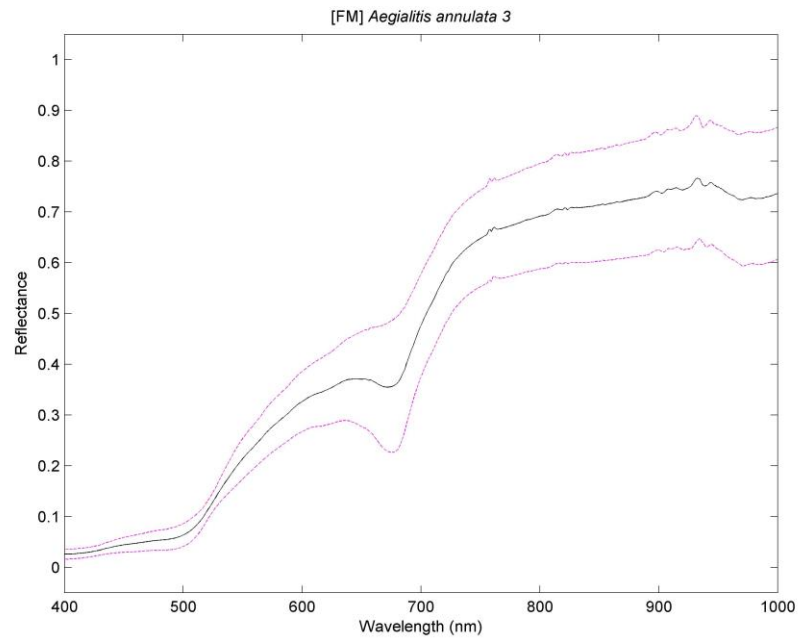


Figure 179: *Aegialitis annulata* 3 (left) and *Avicennia marina* 1 (right). [FM]

Notes: *Aegialitis annulata* 1 & 2 & 3 all contained numerous green leaves. *Aegialitis annulata* 3 additionally contained yellow leaves, which were included in the ASD spectral samples. *Avicennia marina* 1 spectra were sampled from a mature (old) plant.

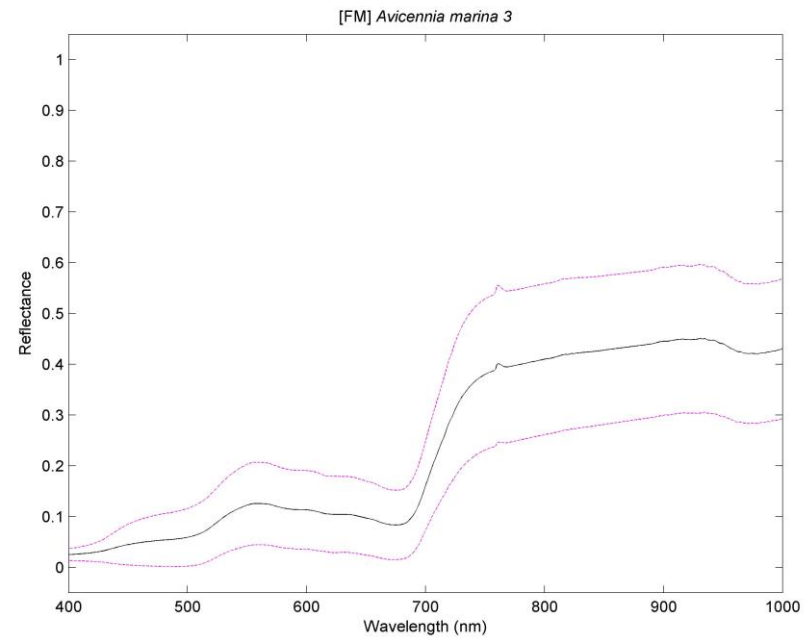
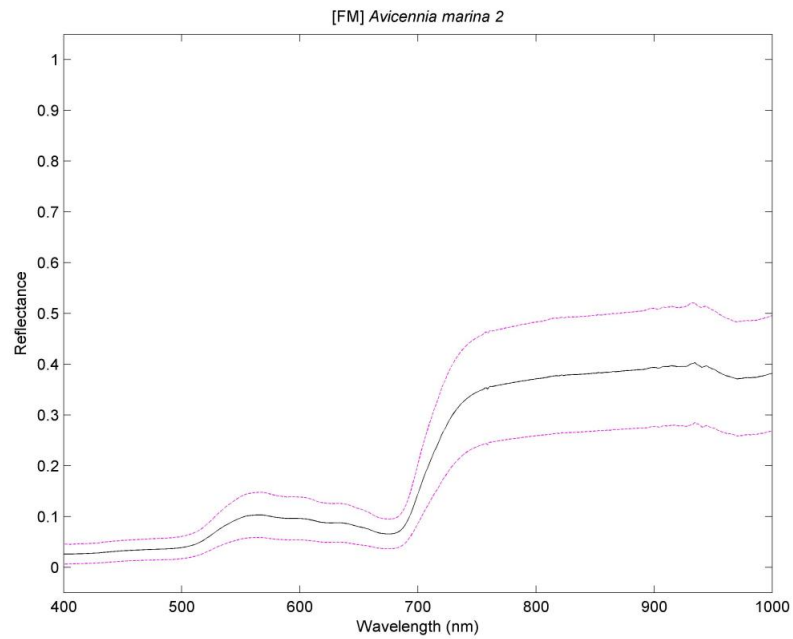


Figure 180: *Avicennia marina* 2 & 3 (left and right image, respectively). [FM]

Note: Both spectral samples for *Avicennia marina* 1 & 2 were taken from a mature mangrove, while *Avicennia marina* 3 was obtained from a young mangrove.

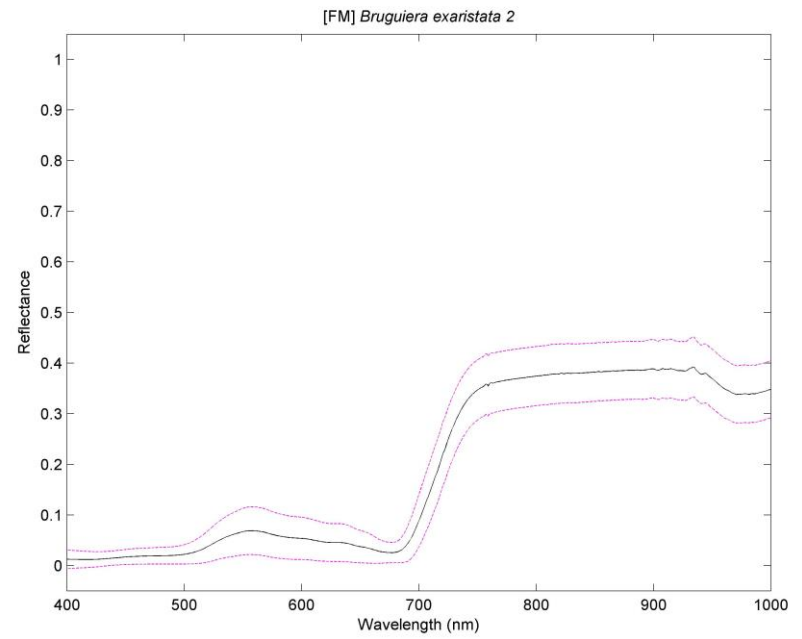
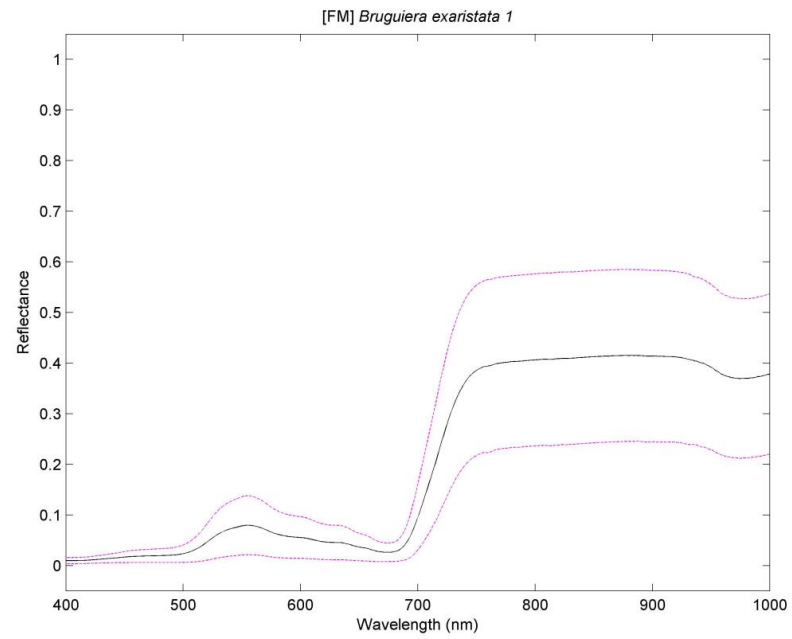


Figure 181: *Bruguiera exaristata* 1 & 2 (left and right image, respectively). [FM]

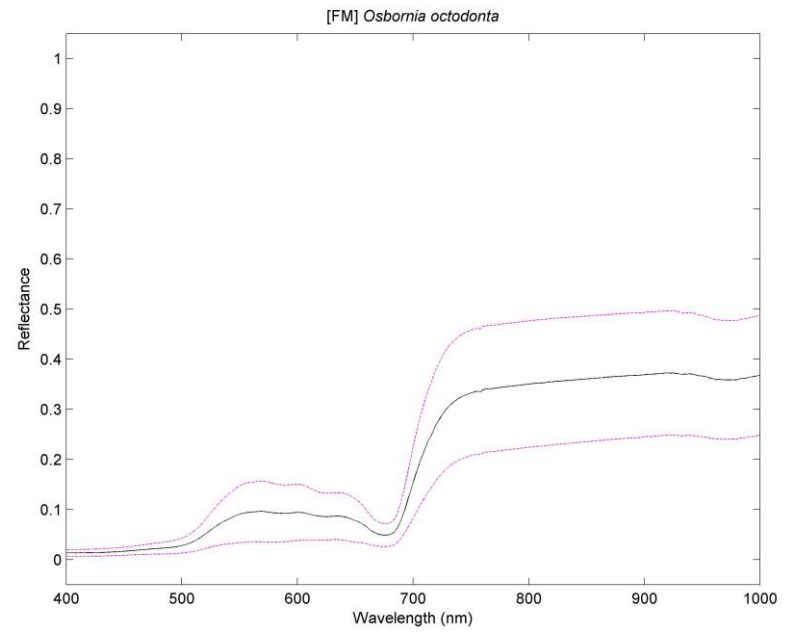
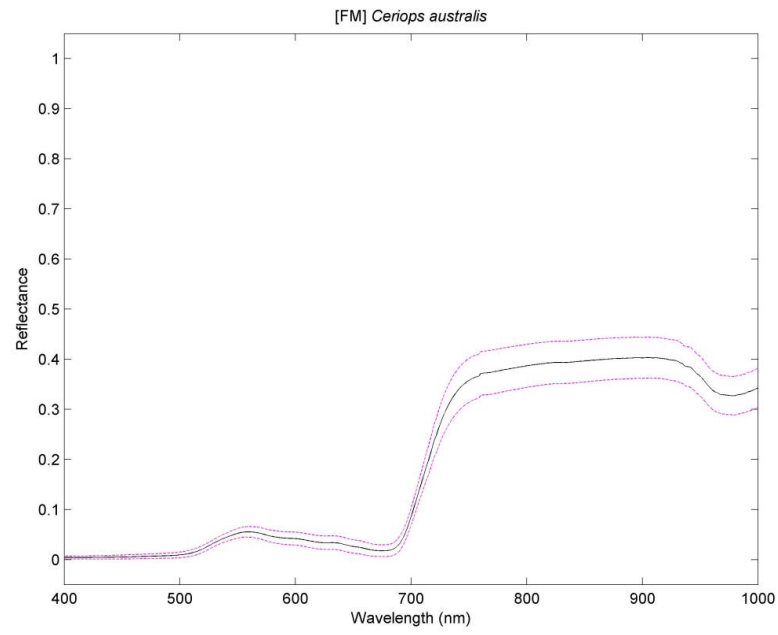


Figure 182: *Ceriops australis* (left) & *Osbornia octodonta* (right). [FM]

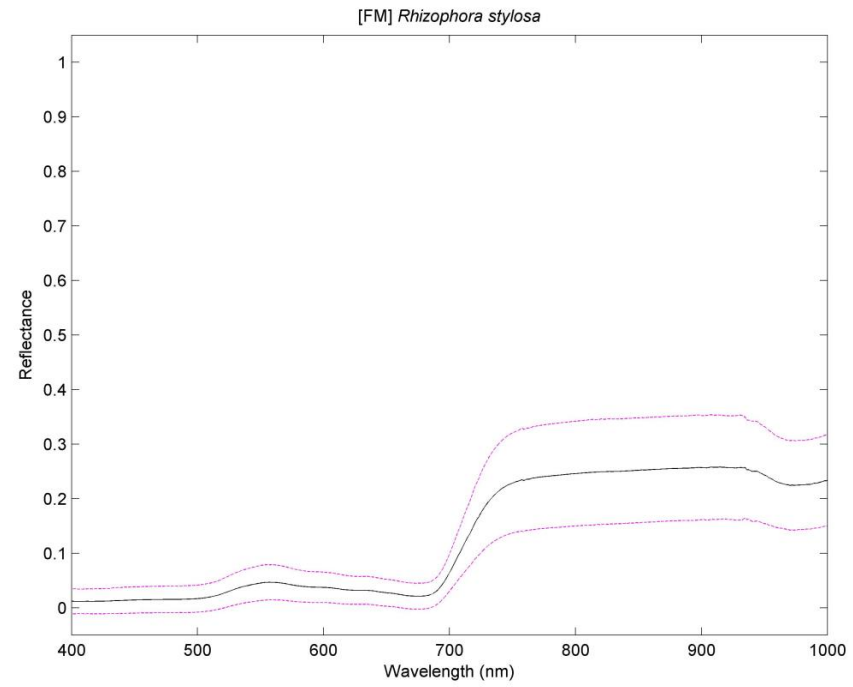


Figure 183: *Rhizophora stylosa*. [FM]

Region: Finucane Island (road) [FR]

Vegetative Spectra

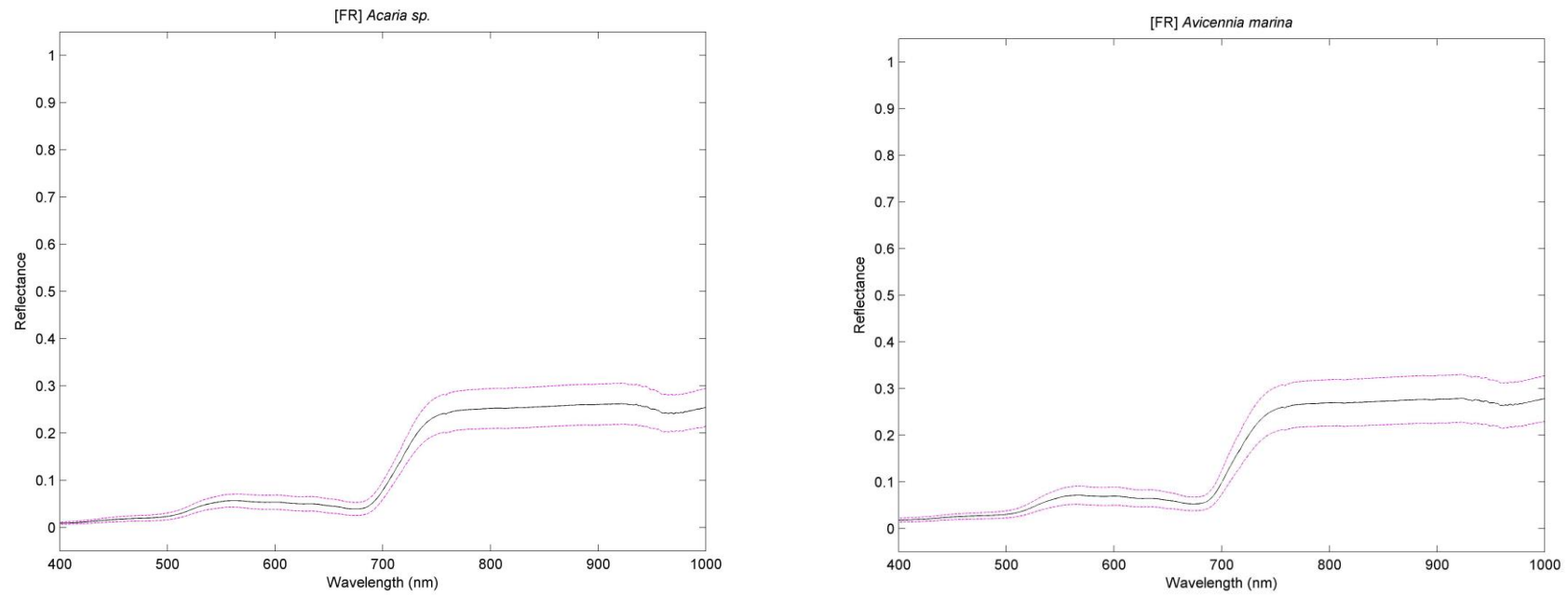


Figure 184: *Acaria sp.* (left) & *Avicennia marina* (right). [FR]

Note: This *Avicennia marina* contained numerous leaves comprising salt crust deposits.

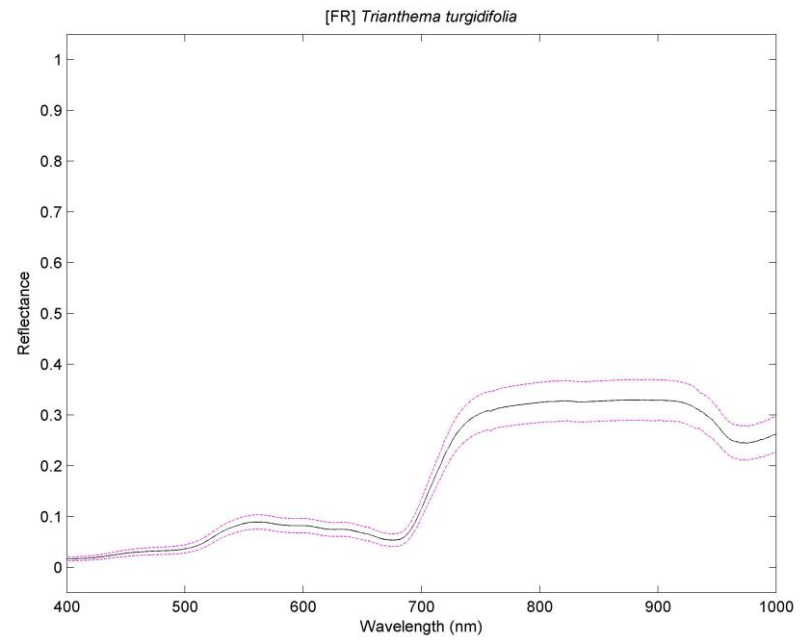
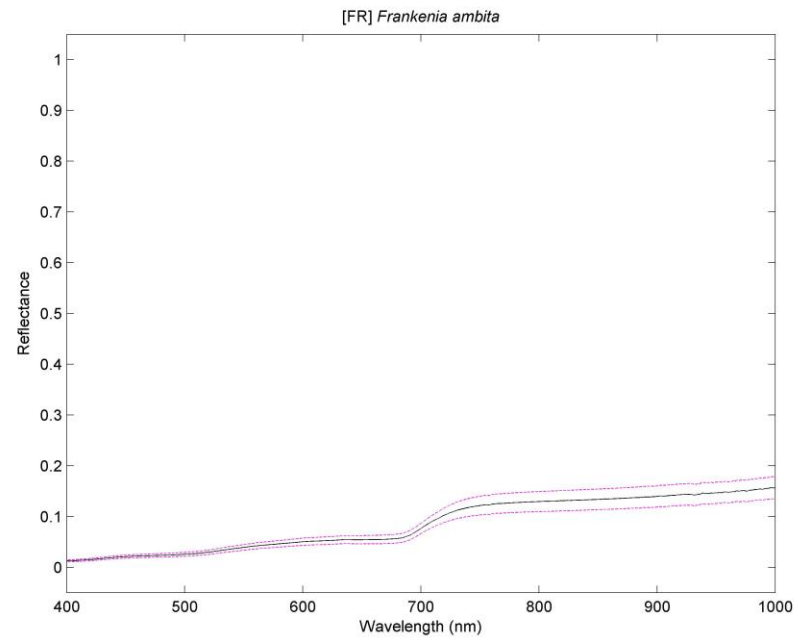


Figure 185: *Frankenia ambita* (left) & *Trianthena turgidifolia* (right). [FR]

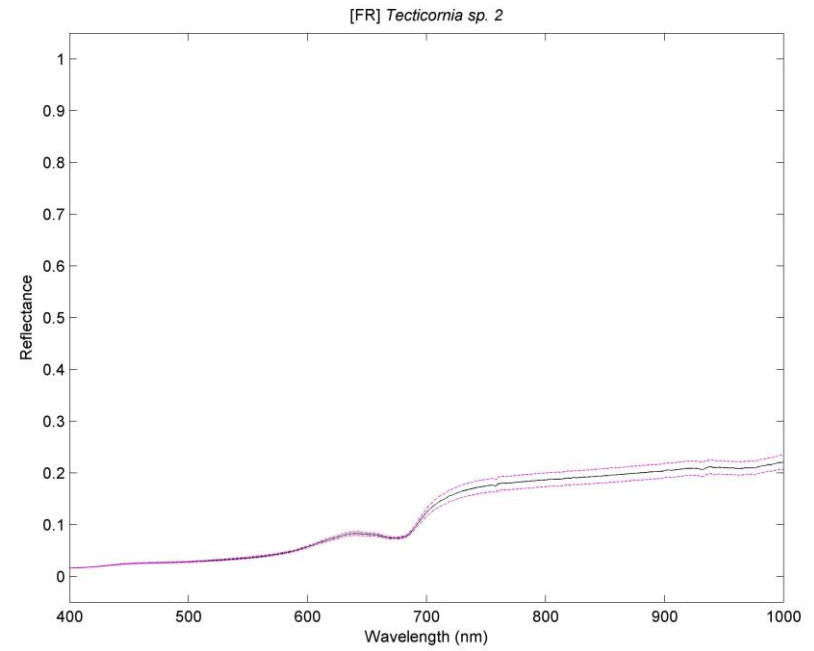
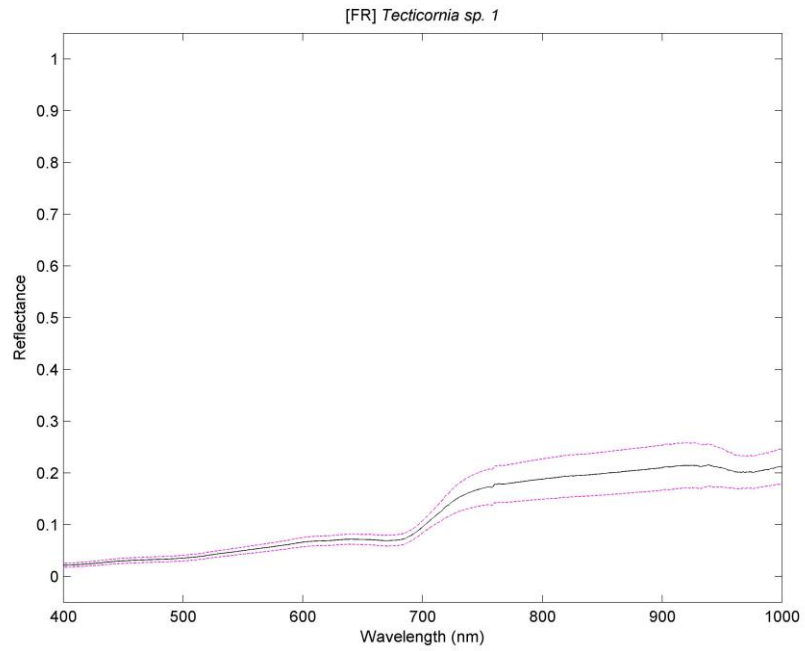


Figure 186: *Tecticornia sp. 1* (left) & *Tecticornia sp. 2* (right). [FR]

Note: *Tecticornia sp. 2* appeared to be in better condition than *Tecticornia sp. 1*, which appeared very dry and unhealthy.

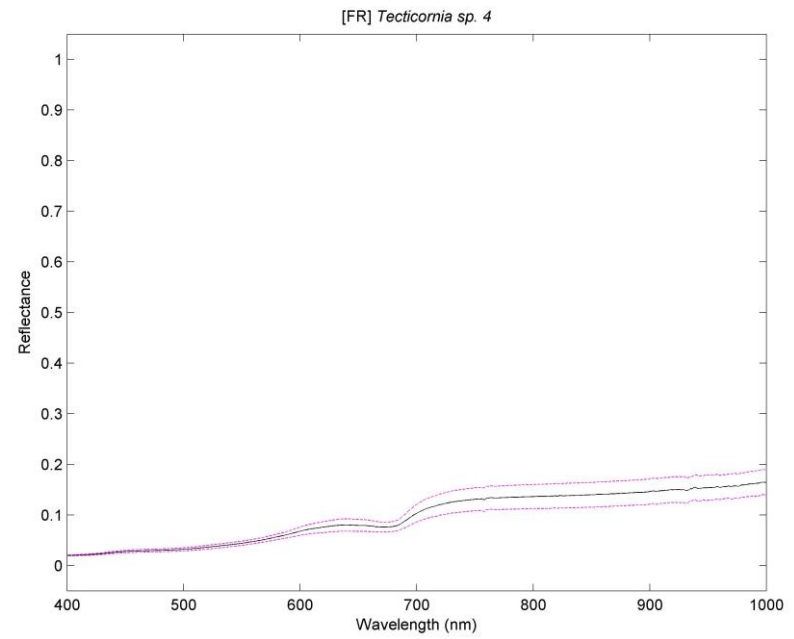
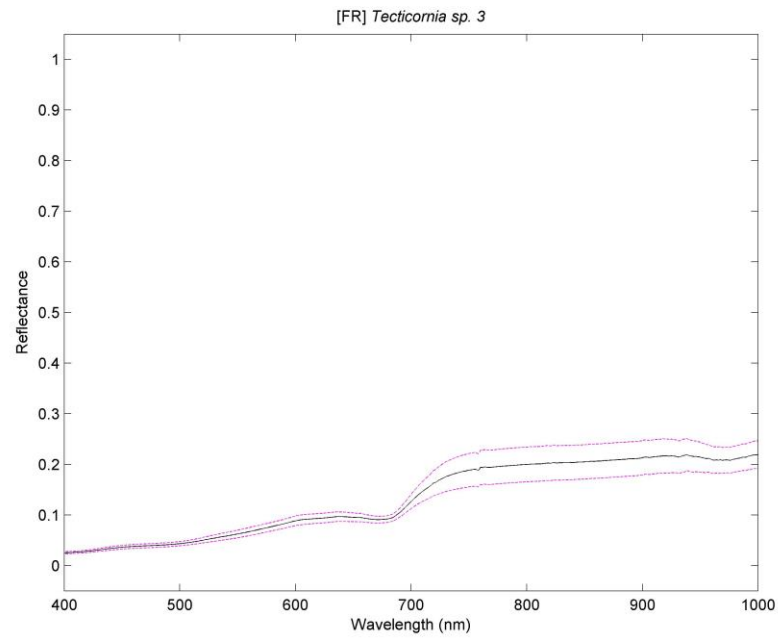


Figure 187: *Tecticornia sp. 3* (left) & *Tecticornia sp. 4* (right). [FR]

Note: *Tecticornia sp. 4* contained many crusty salty leaves, in comparison to *Tecticornia sp. 1, 2 & 3*.

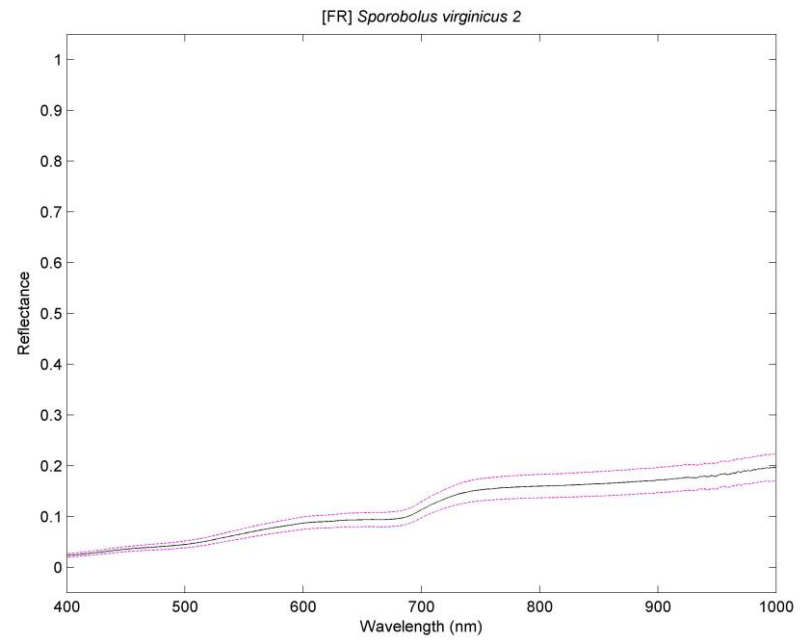
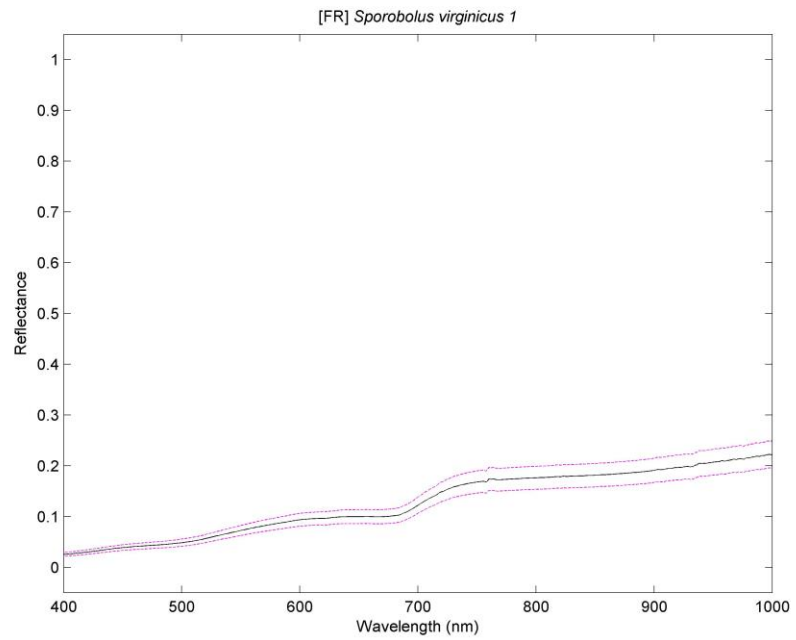


Figure 188: *Sporobolus virginicus* 1 (left) & *Sporobolus virginicus* 2 (right). [FR]

Note: *Sporobolus virginicus* is synonymous with Marine couch.

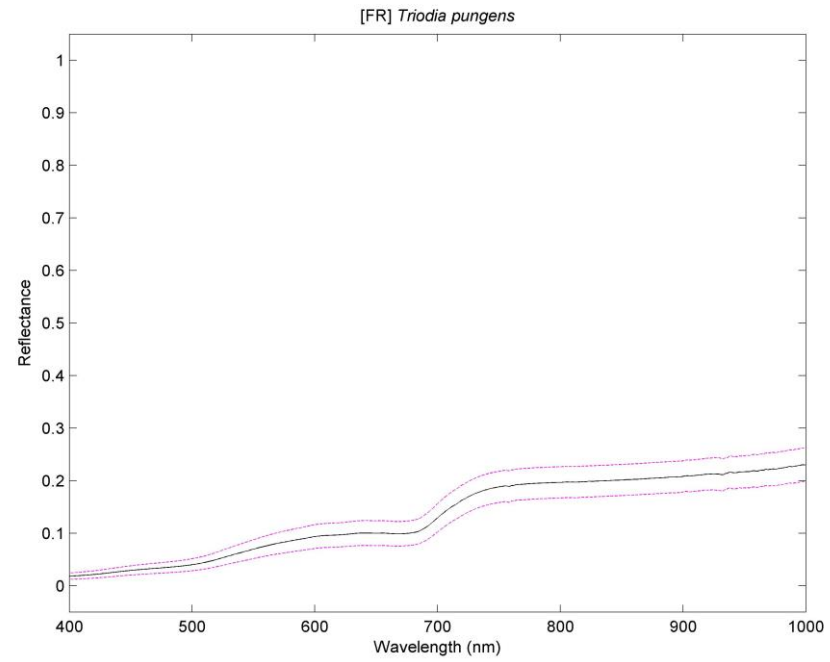


Figure 189: *Triodia pungens*. [FR]

Note: *Triodia pungens* is synonymous with spinifex.

Non-vegetative Spectra

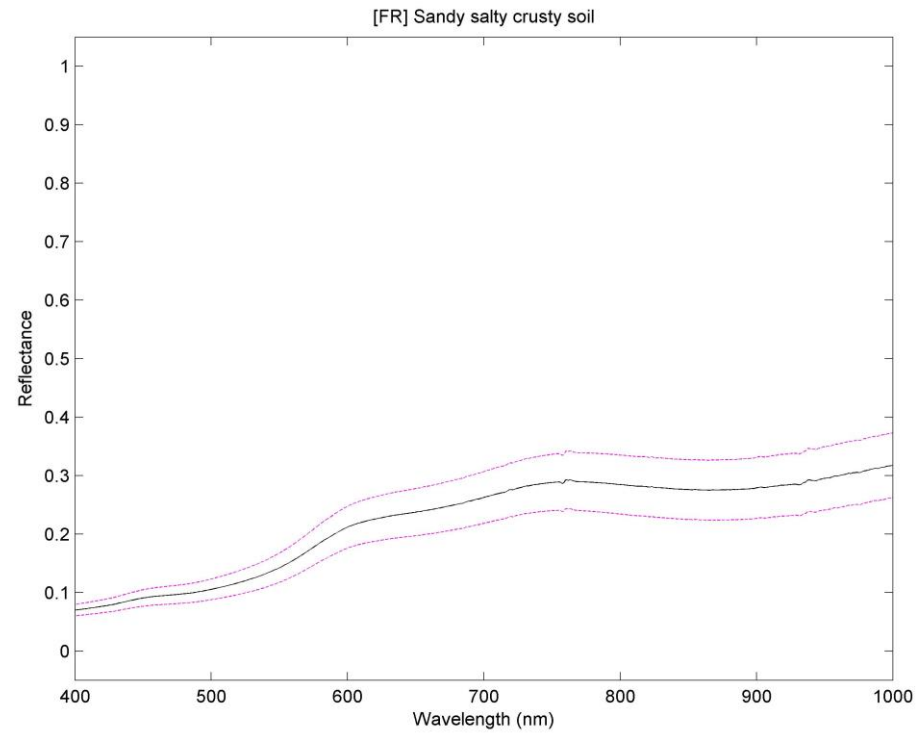


Figure 190: Sandy salty crusty soil. [FR]

Region: Finucane Island (Utah) [FU]

Vegetative Spectra

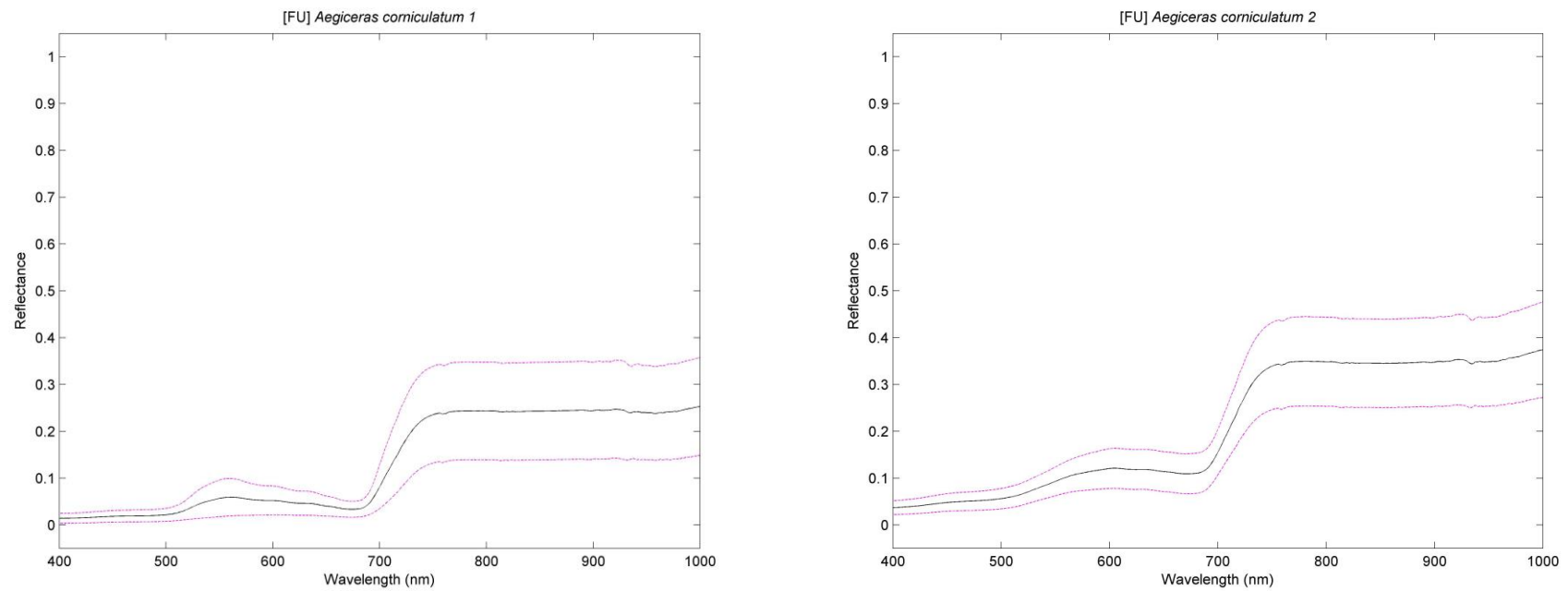


Figure 191: *Aegiceras corniculatum 1* (left) & *Aegiceras corniculatum 2* (right). [FU]

Note: The leaves for *Aegiceras corniculatum 1* were in a clean state, while that for *Aegiceras corniculatum 2* contained numerous leaves coated in a thick red dust (presumed to be iron oxide dust from the nearby stockpiles).

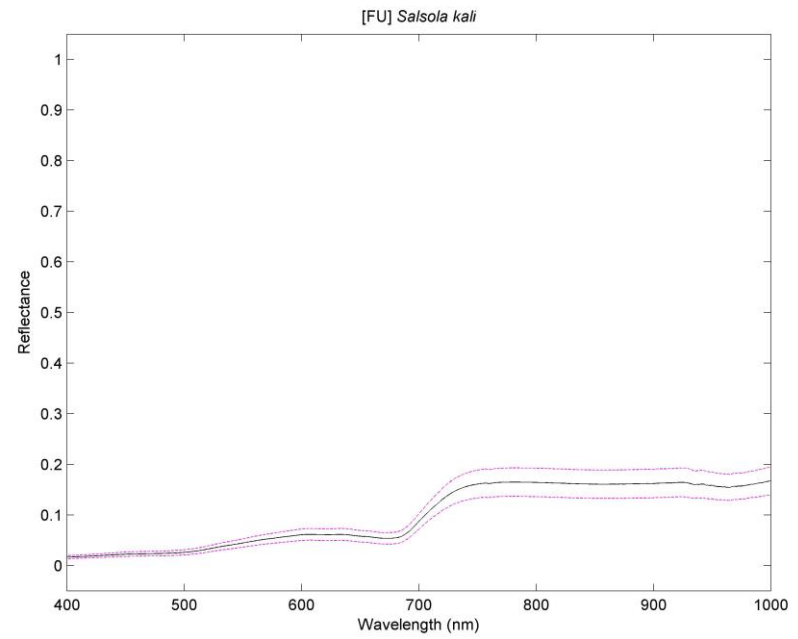
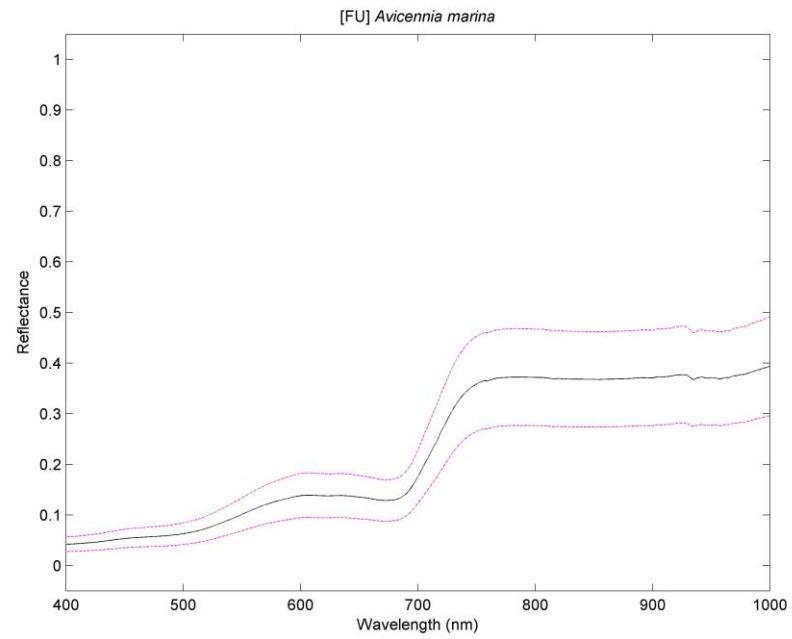


Figure 192: *Avicennia marina* (left) & *Salsola kali* (right). [FU]

Note: *Avicennia marina* contained numerous leaves coated in a thick red dust (presumed to be iron oxide dust from the nearby stockpiles).

Non-vegetative Spectra

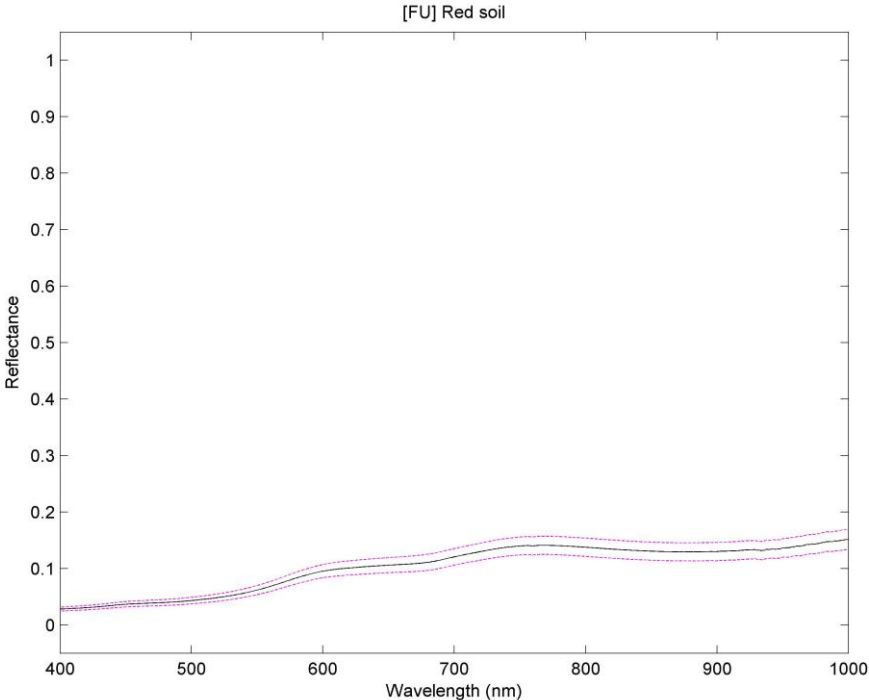


Figure 193: Red soil. [FU]

Region: Redbank [RB]

Vegetative Spectra

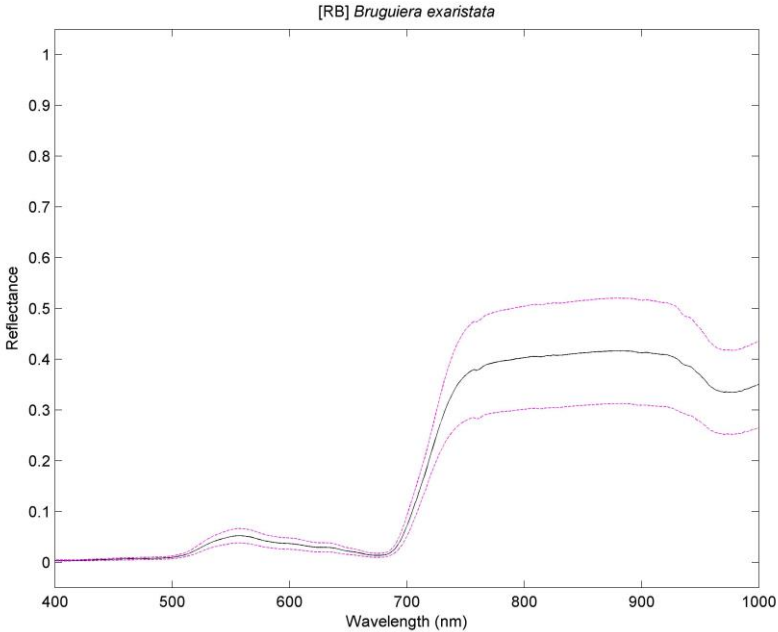
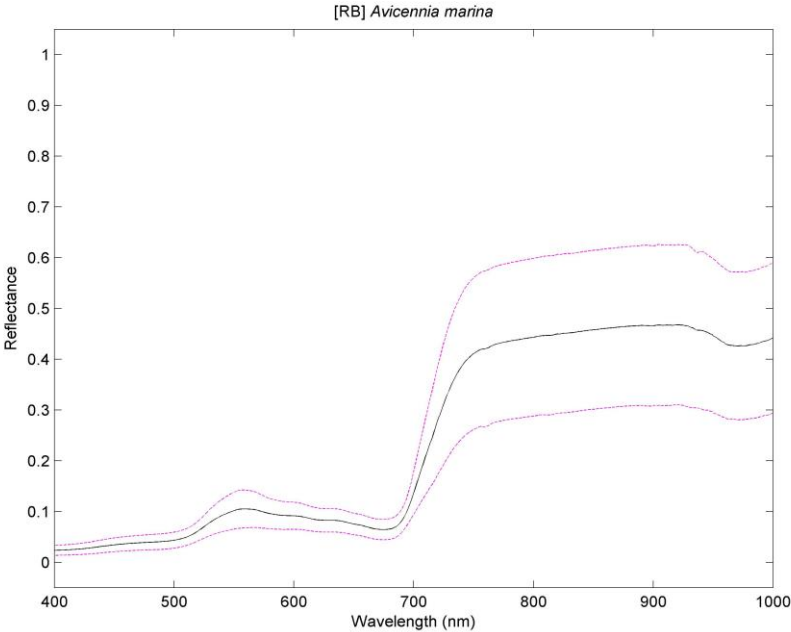


Figure 194: *Avicennia marina* (left) & *Bruguiera exaristata* (right). [RB]

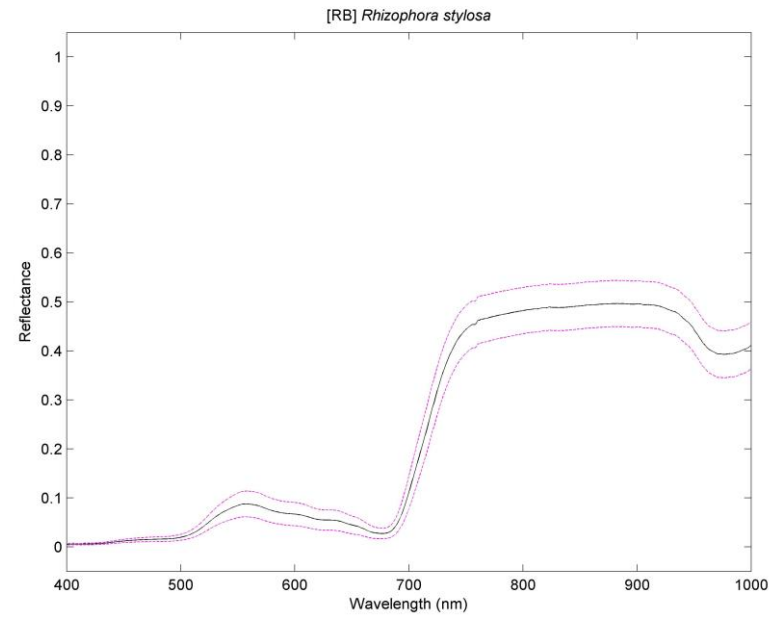
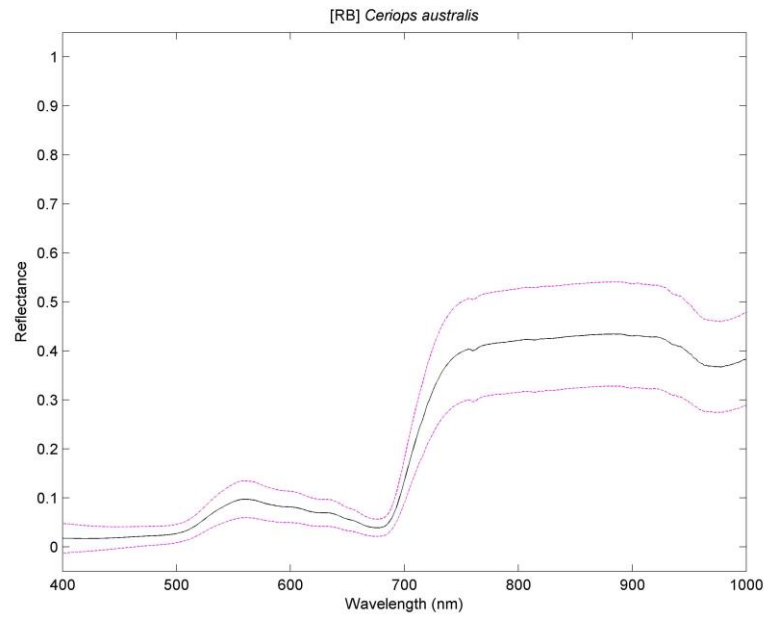


Figure 195: *Ceriops australis* (left) & *Rhizophora stylosa* (right). [RB]

Non-vegetative Spectra

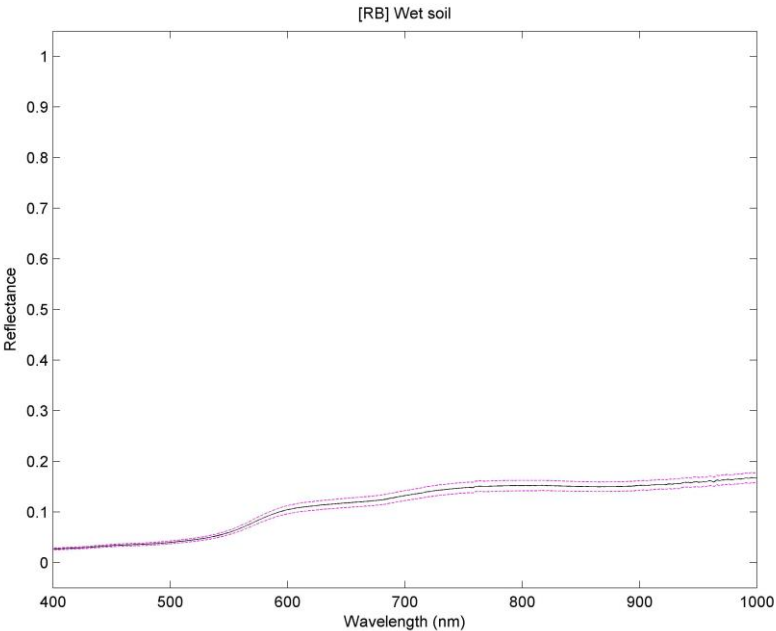
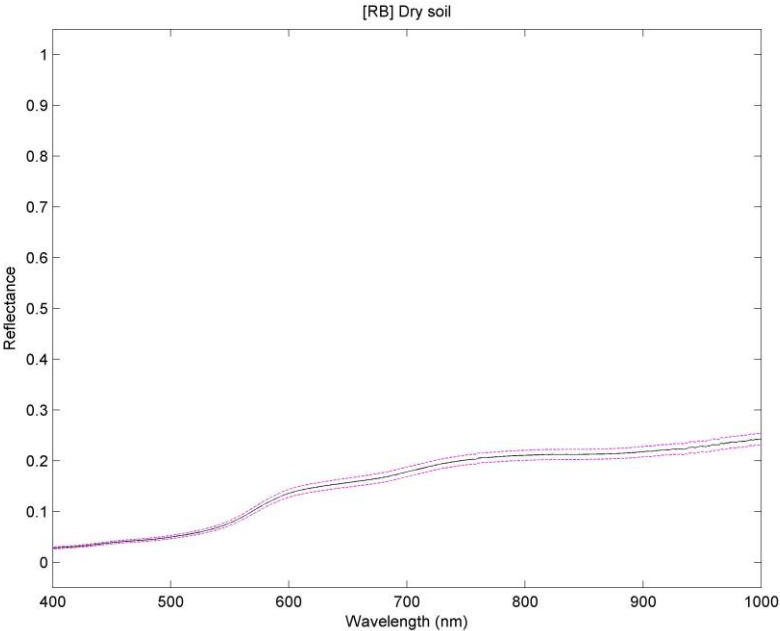


Figure 196: Dry soil (left) & Wet soil (right). [RB]

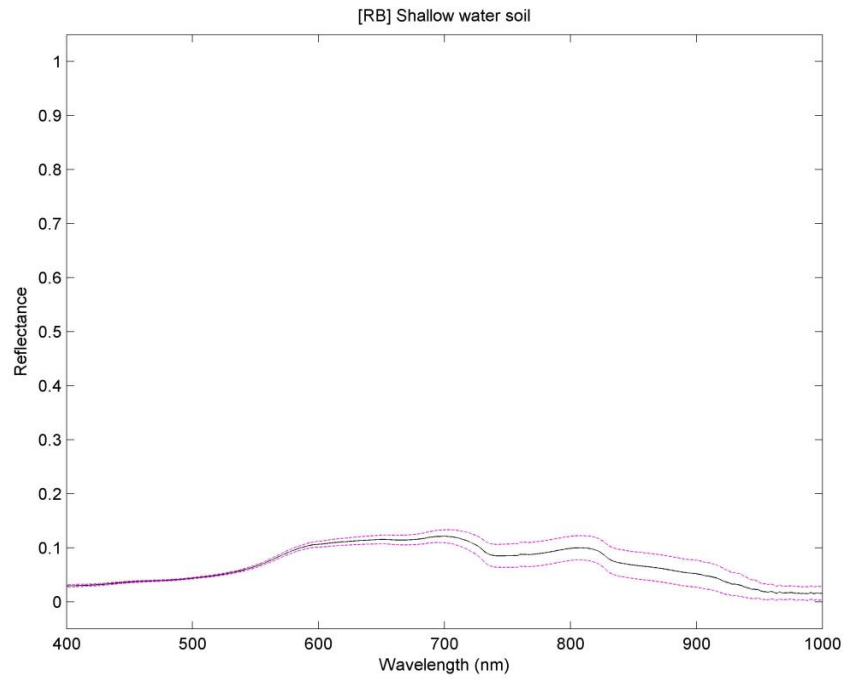


Figure 197: Shallow water soil. [RB]

Region: Lumsden Point [LP]

Vegetative Spectra

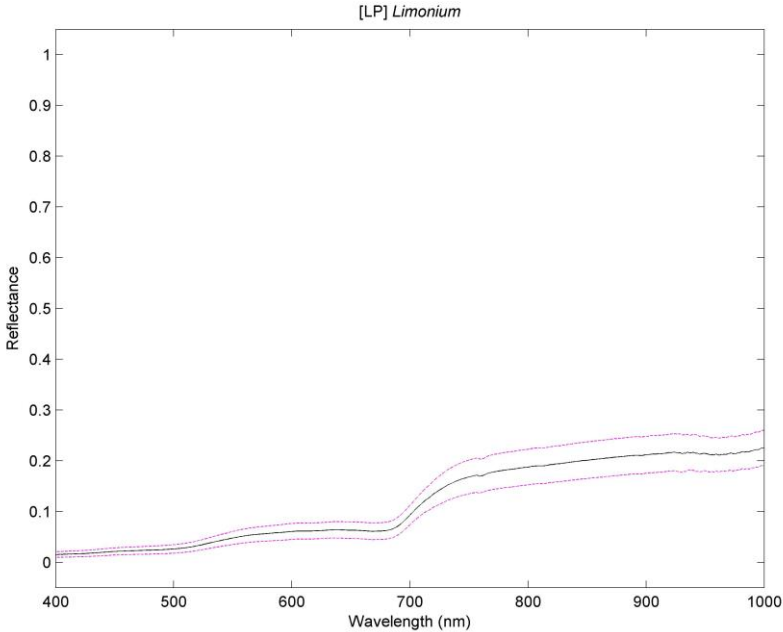
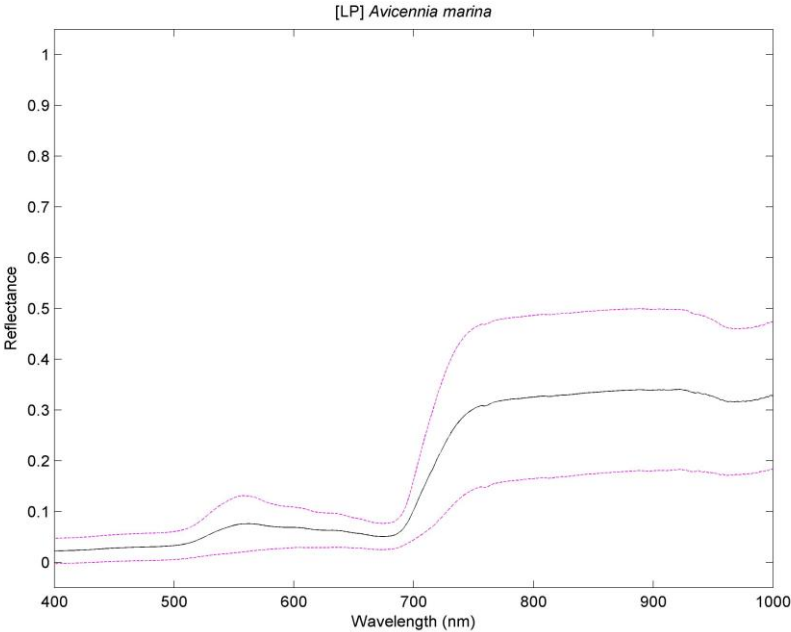


Figure 198: *Avicennia marina* (left) & *Limonium* (right). [LP]

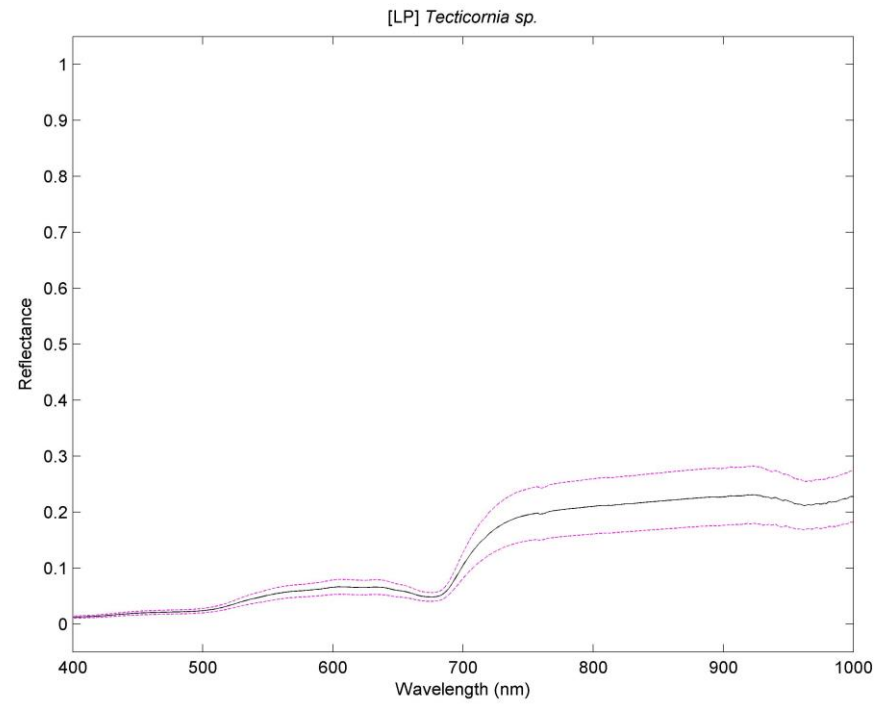


Figure 199: *Tecticornia sp.* (left). [LP]

Non-vegetative Spectra

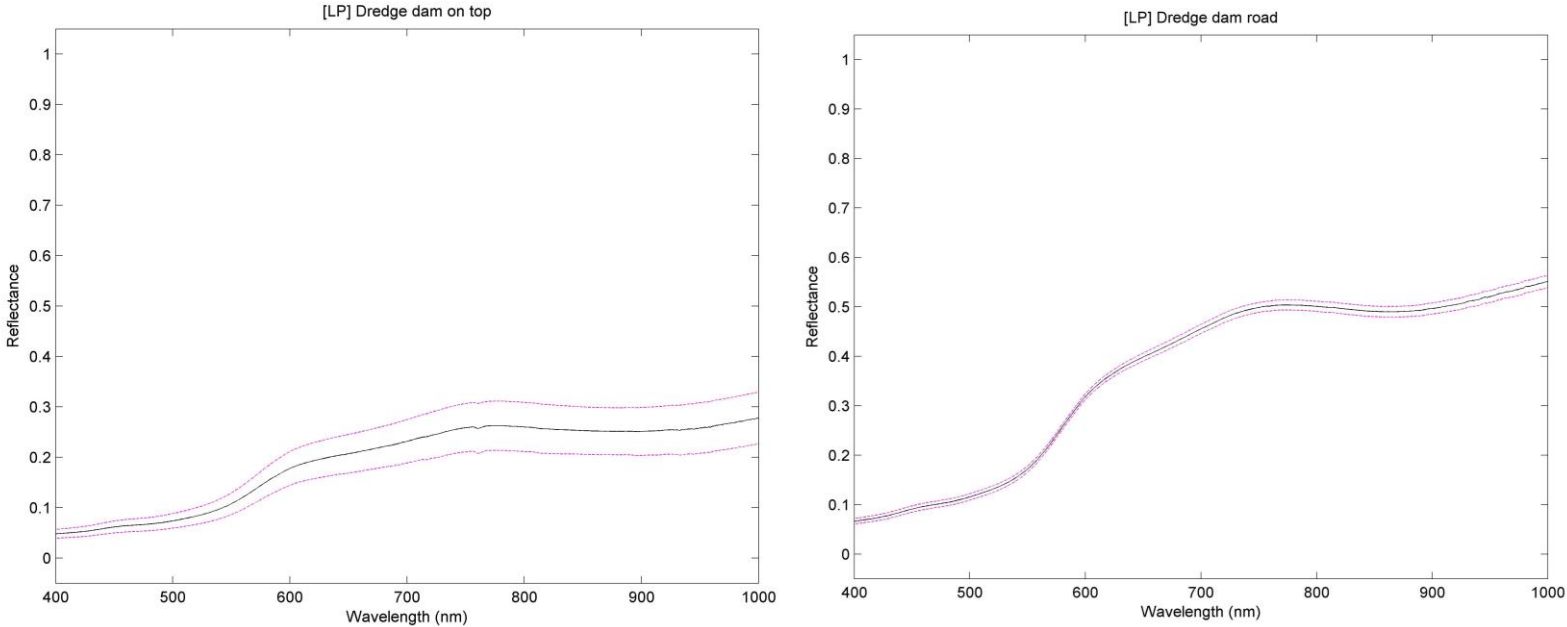


Figure 200: Dredge dam on top (left) & Dredge dam road (right). [LP]

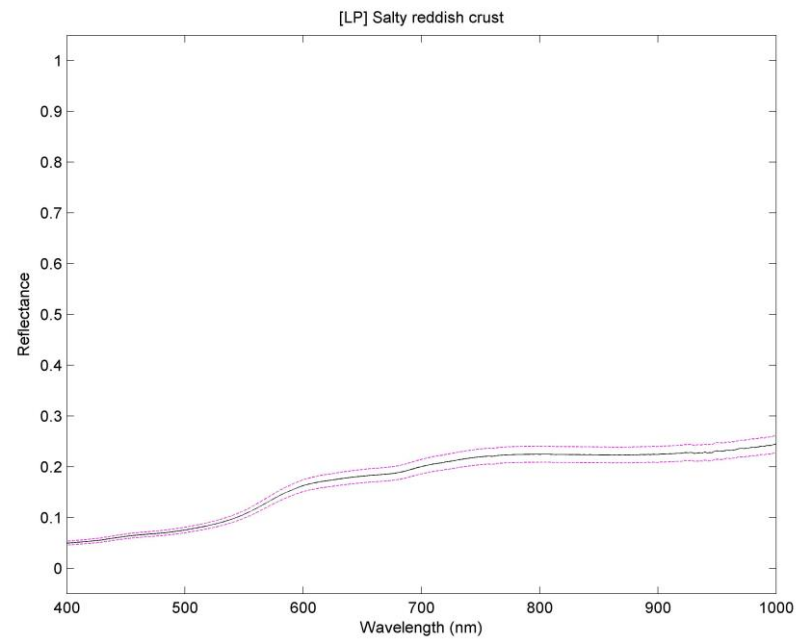
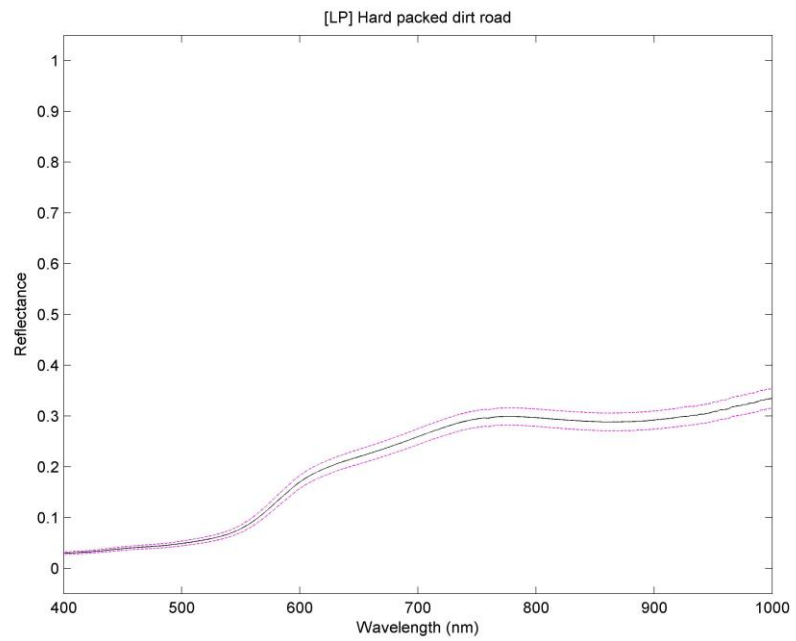


Figure 201: Hard packed dirt road (left) & Salty reddish crust (right). [LP]

Region: Pretty Pool [PP]

Vegetative Spectra

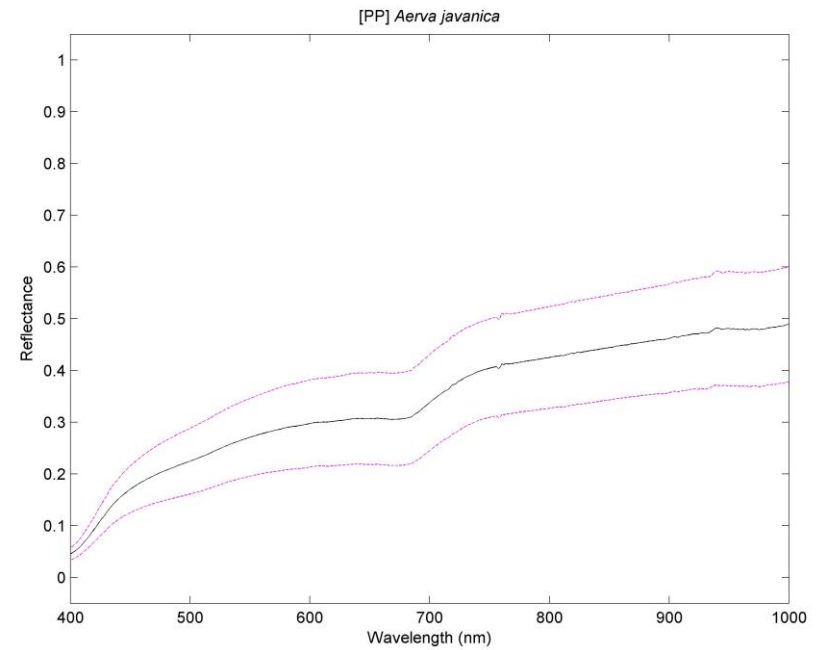
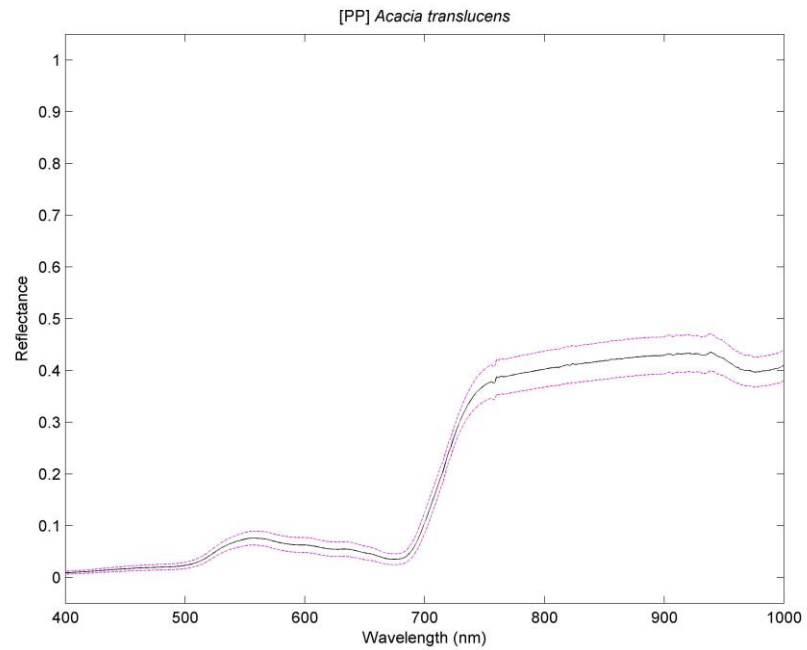


Figure 202: *Acacia translucens* (left) & *Aerva javanica* (right). [PP]

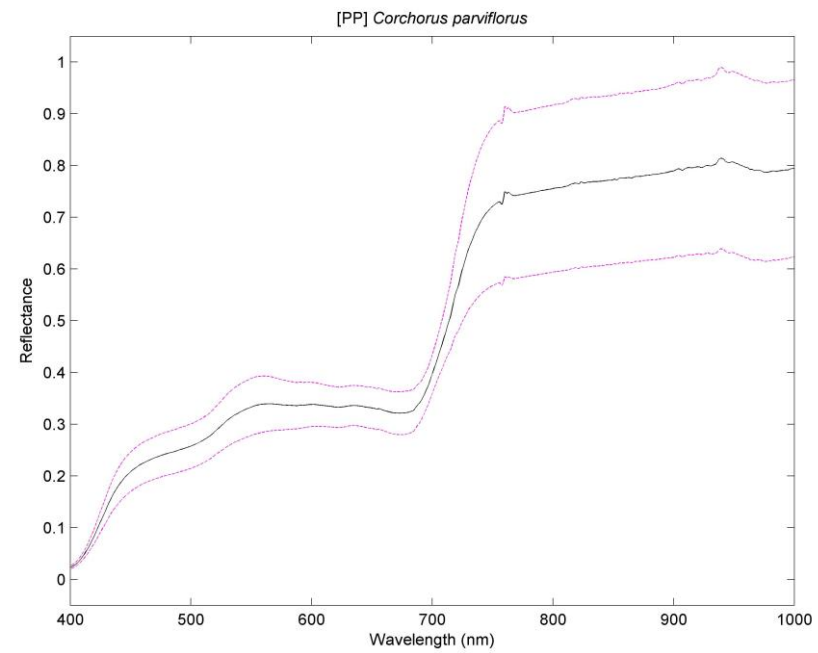
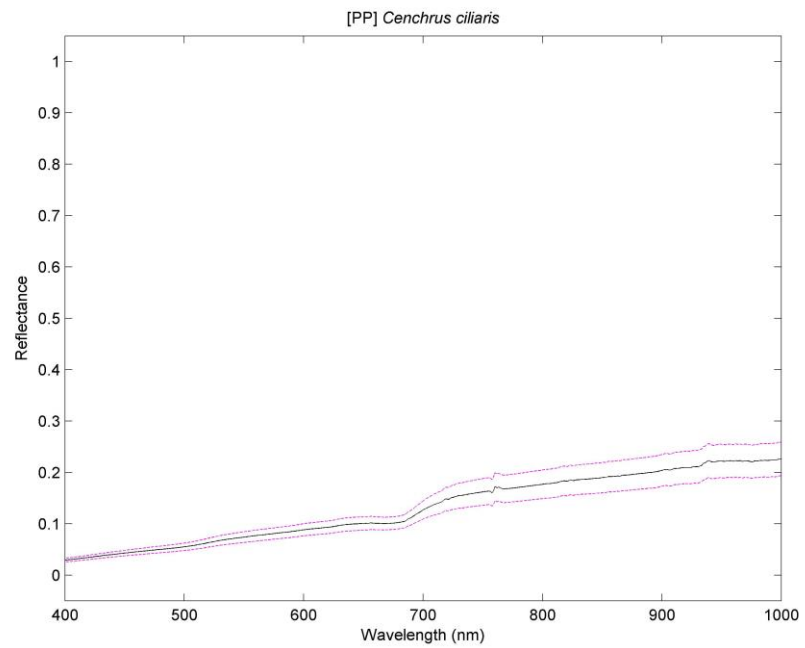


Figure 203: *Cenchrus ciliaris* (left) & *Corchorus parviflorus* (right). [PP]

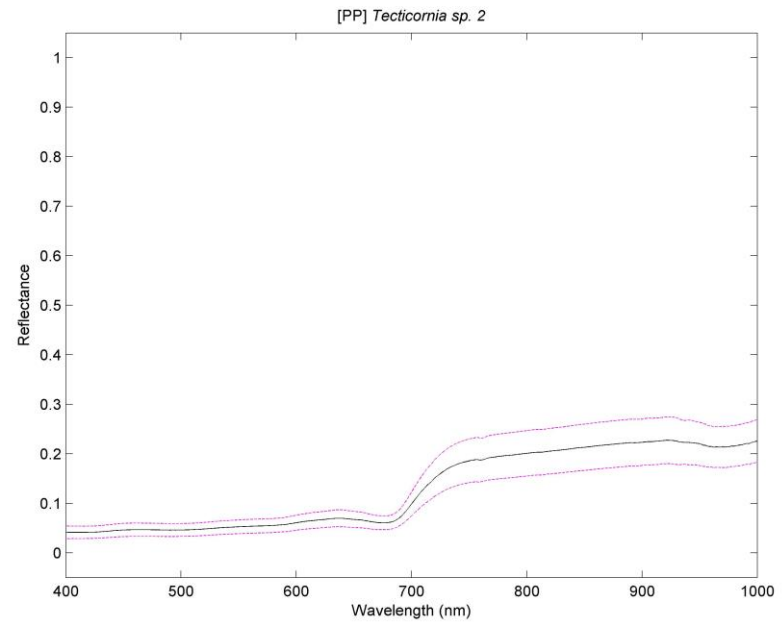
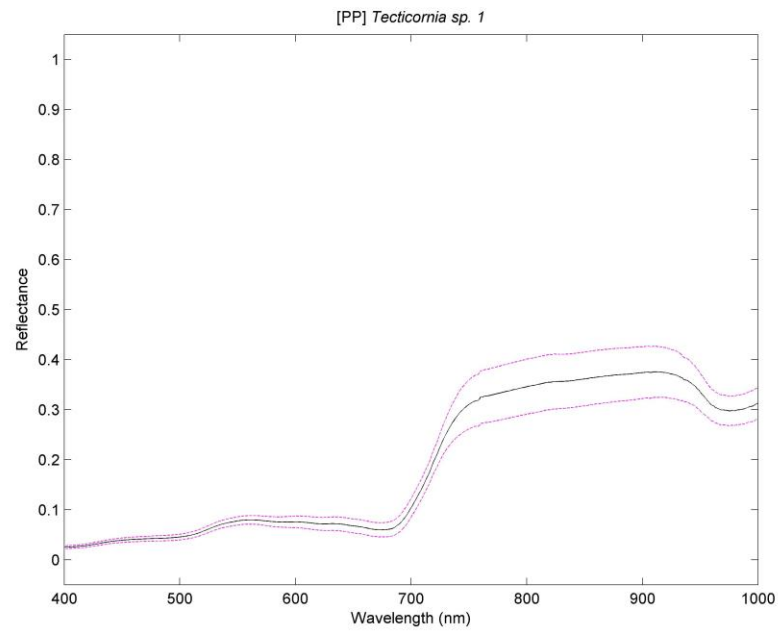


Figure 204: *Tecticornia sp. 1* (left) & *Tecticornia sp. 2* (right). [PP]

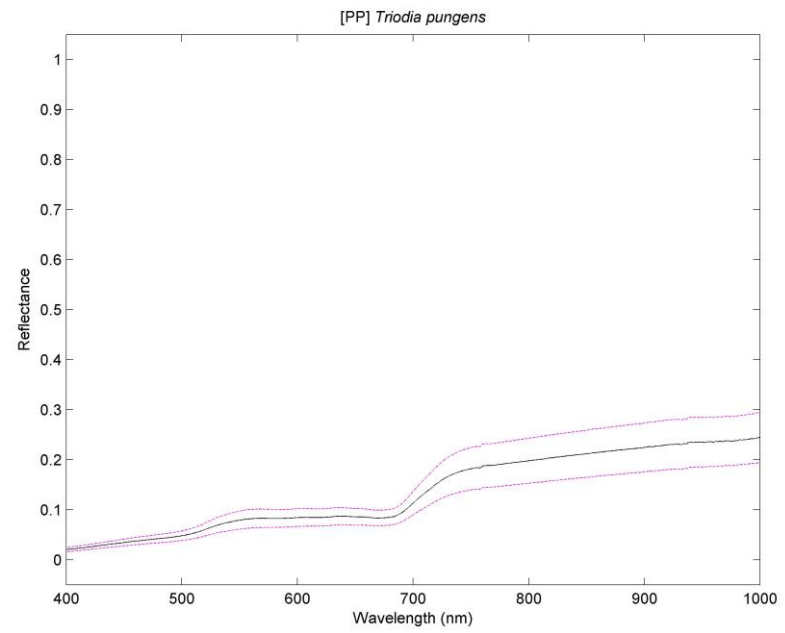
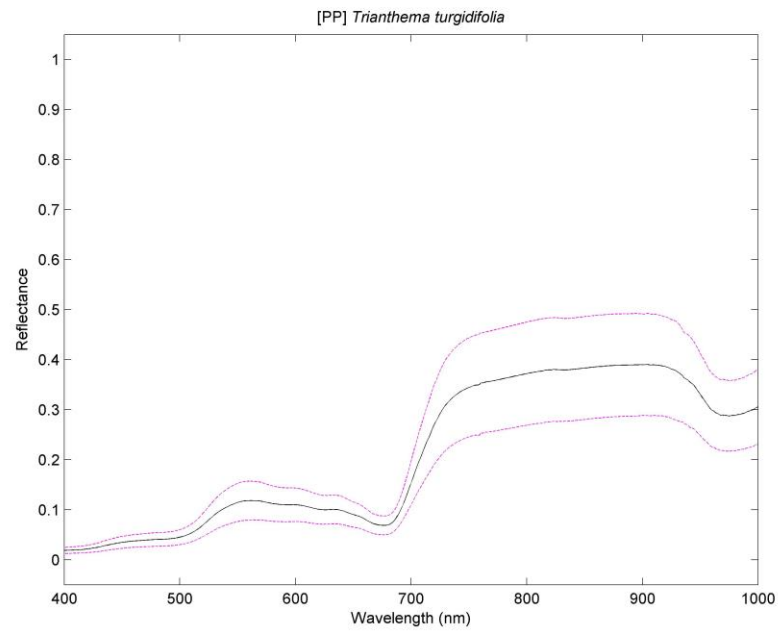


Figure 205: *Trianthesma turgidifolia* (left) & *Triodia pungens* (right). [PP]

Note: *Triodia pungens* is synonymous with spinifex.

Non-vegetative Spectra

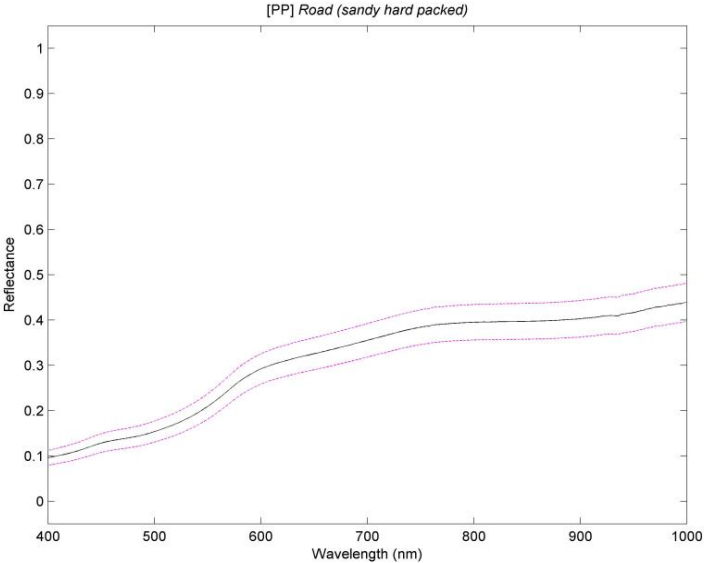
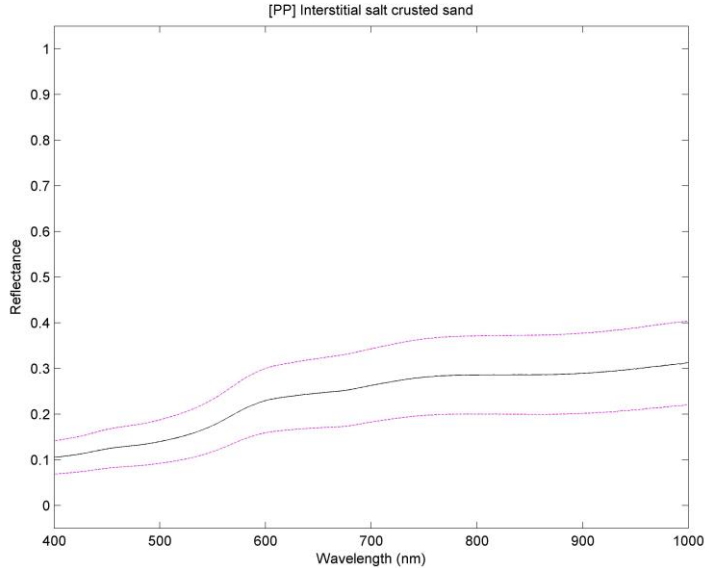


Figure 206: Interstitial salt crusted sand (left) & Road (sandy hard packed) (right). [PP]

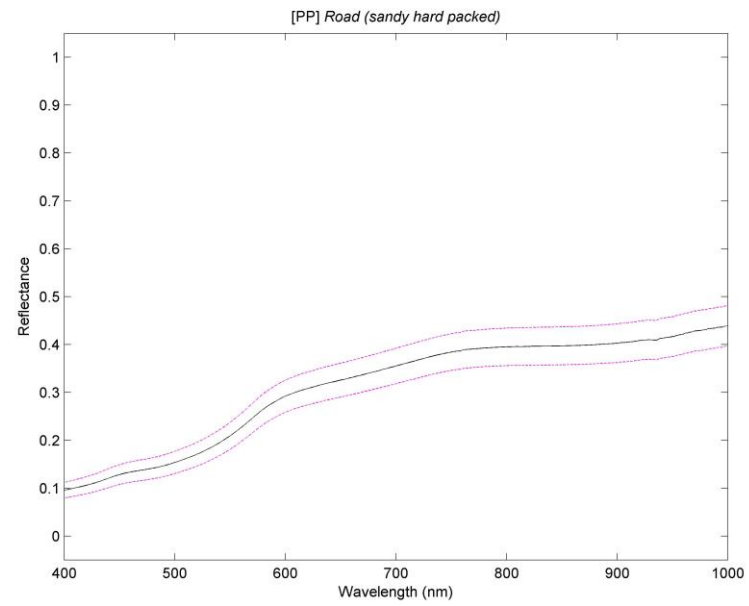
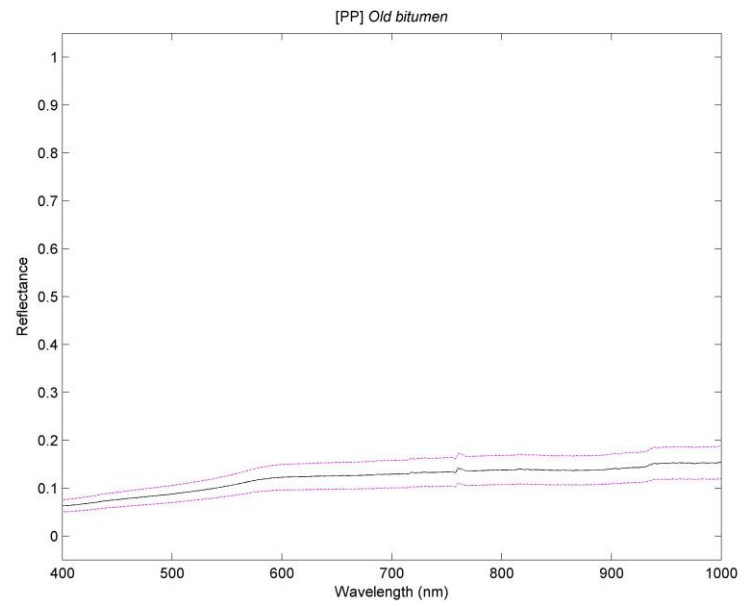


Figure 207: Old bitumen (left) & Salt flat plain (right). [PP]

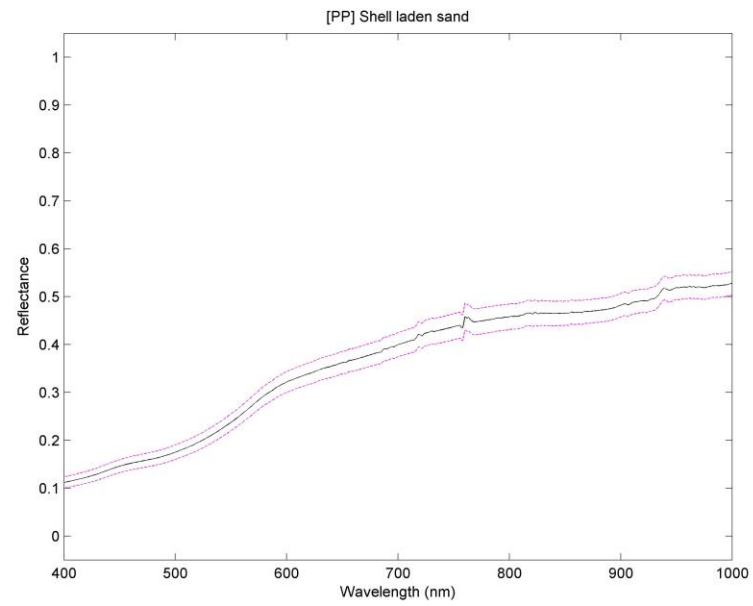


Figure 208: Shell laden sand. [PP]

G.3 Spectral Angles between Spectra

The tables given in this appendix, contain SA (in radians) between the mean spectra of every cover type in addition to an error estimate (in terms of one standard deviation). The calculation made use of Equation (2.6.4.3.1) of Section 2.6.4.3, which (for convenience) is copied here:

$$\theta = \cos^{-1} \left(\frac{\sum_{i=1}^n r_i t_i}{\left[\sum_{i=1}^n r_i^2 \right]^{1/2} \left[\sum_{i=1}^n t_i^2 \right]^{1/2}} \right) \quad (\text{G.3.1})$$

In practice, a single cover type consists of several ASD measurements. Therefore, there is no 'single' \mathbf{r} vector corresponding to the reference cover type and no 'single' \mathbf{t} vector for the target cover type.

Instead, each cover type consists of (typically) 15 ASD measurements. Therefore, to obtain a single \mathbf{r} (reference) vector and a single \mathbf{t} (target) vector, it is necessary to calculate the mean of each set of measurements corresponding to each cover type. This mean spectrum was obtained through the following process. Each ASD spectral measurement is stored into a file and numbered sequentially (00000, 00001, ... , 00015). Each file contains the reflectance corresponding to each wavelength covering the range from 350 – 2500 nm. To obtain the mean spectral measurement for a cover type, an average is taken for each band (individually) over all files. The process can be described mathematically using the following definitions.

Let \mathbf{S}_{cn} denote a vector containing n bands, where c represents a specific cover type. For example, for cover type α with 15 spectral measurements as recorded by the ASD:

$$\mathbf{S}_{\alpha 1} = \begin{bmatrix} b_1 \\ \vdots \\ b_n \end{bmatrix}, \mathbf{S}_{\alpha 2} = \begin{bmatrix} b_1 \\ \vdots \\ b_n \end{bmatrix}, \dots, \mathbf{S}_{\alpha 15} = \begin{bmatrix} b_1 \\ \vdots \\ b_n \end{bmatrix}$$

For the ASD, there $n = 2500 \text{ nm} - 350 \text{ nm} + 1 = 2,151$.

Therefore, for cover type α , the p spectral measurements forms the set $\mathbf{S}_\alpha = \{\mathbf{S}_{\alpha 1}, \mathbf{S}_{\alpha 2}, \dots, \mathbf{S}_{\alpha p}\}$ while for cover type β the set of q measurements is denoted by $\mathbf{S}_\beta = \{\mathbf{S}_{\beta 1}, \mathbf{S}_{\beta 2}, \dots, \mathbf{S}_{\beta q}\}$. Typically, $p = q = 15$ as 15 spectral ASD samples were (usually) recorded in practice during the field work conducted in this thesis.

The mean spectral angle θ (from Equation (G.3.1)) uses the mean measurement representative for each cover type:

$$\overline{\mathbf{S}}_\alpha = \frac{\sum_{m=1}^p \mathbf{S}_{\alpha m}}{p} \quad \text{and} \quad \overline{\mathbf{S}}_\beta = \frac{\sum_{n=1}^q \mathbf{S}_{\beta n}}{q}$$

Individual measurements are denoted by m and n for vectors $\overline{\mathbf{S}}_\alpha$ and $\overline{\mathbf{S}}_\beta$, respectively. For example, $\mathbf{S}_{\alpha 3}$ denotes the third measurement for cover type α .

By considering $\overline{\mathbf{S}}_\alpha$ to be the reference vector \mathbf{r} and $\overline{\mathbf{S}}_\beta$ to be the target vector \mathbf{t} (the order is actually insignificant as is clear from Equation (G.3.1)), the mean spectral angle $\bar{\theta}_{\alpha\beta}$ can be calculated.

The uncertainty between the two cover types involves calculating a spectral angle for each of the possible combinations of measurements between cover types. A standard deviation is then calculated for each combination but instead uses $\bar{\theta}_{\alpha\beta}$ as the mean. Although the process is somewhat difficult to describe qualitatively, the mathematical definitions thus far defined aids in describing the process quantitatively.

Consider the two sets of measurements; $\{\mathbf{S}_{\alpha 1}, \mathbf{S}_{\alpha 2}, \dots, \mathbf{S}_{\alpha p}\}$ and $\{\mathbf{S}_{\beta 1}, \mathbf{S}_{\beta 2}, \dots, \mathbf{S}_{\beta q}\}$. For the first measurement of cover type α i.e. $\mathbf{S}_{\alpha 1}$, it is possible to calculate the spectral angle θ between $\mathbf{S}_{\alpha 1}$ and each and every member of $\{\mathbf{S}_{\beta 1}, \mathbf{S}_{\beta 2}, \dots, \mathbf{S}_{\beta q}\}$. Now, θ can be calculated between $\mathbf{S}_{\alpha 1}$ & $\mathbf{S}_{\beta 1}$ (denoted by

$\theta_{\alpha_1\beta_1}$) and again between \mathbf{S}_{α_1} & \mathbf{S}_{β_2} (i.e. $\theta_{\alpha_1\beta_2}$) and so on, until the last pair \mathbf{S}_{α_1} & \mathbf{S}_{β_q} ($\theta_{\alpha_1\beta_q}$) is reached. As the full set of q measurements belonging to cover type β is used, it is possible to abbreviate the spectral angle between the first measurement of cover type α with all measurements of cover type β as $\theta_{\alpha\beta}$. To extend this treatment to include all p measurements belonging to cover type α , the total set of spectral angles is written as $\theta_{\alpha\beta} \equiv \{\theta_{\alpha_1\beta}, \theta_{\alpha_2\beta}, \dots, \theta_{\alpha_p\beta}\}$, where the number of spectral angles is equal to $p \times q$ quantities.

The standard deviation is usually expressed in the form:

$$SD = \sqrt{\frac{\sum_{i=1}^N (x_i - \bar{x})^2}{N-1}}$$

Using the definitions expressed above, the expression becomes:

$$\tilde{\theta}_{\alpha\beta} = \sqrt{\frac{\sum_{i=1}^p \sum_{j=1}^q (\theta_{\alpha_i\beta_j} - \bar{\theta}_{\alpha\beta})^2}{p \times q - 1}}$$

which represents the uncertainty $\tilde{\theta}_{\alpha\beta}$.

The full equation for the spectral angle between cover types α and β is written as: $\hat{\theta}_{\alpha\beta} \equiv \bar{\theta}_{\alpha\beta} \pm \tilde{\theta}_{\alpha\beta}$.

The tables displayed over the next few pages contain expressions for $\hat{\theta}_{\alpha\beta}$ and have been arranged firstly by site, then vegetative type and concluding with non-vegetation (e.g. soil) – all alphabetically ordered. The SAs (spectral angles) were calculated over the 400 – 990 nm wavelength range, to match that of the airborne sensed hyperspectral data.

There are a few caveats which require explaining. When comparing SAs between mangrove species, some species samples were excluded. This was briefly mentioned in Section 4.4.2 for *Aegialitis annulata*³, which contains yellow leaves

while the two other samples belonging to the same species, did not (i.e. they were green). Therefore *Aegialitis annulata*3 is omitted when comparing spectral similarities between mangrove species. These vegetative types are referred to as 'non-typical'. The full daily field logs, as given in Appendix G, provides further details concerning the 'state' of vegetation sampled, although the 'state' was not scientifically assessed. For example, the leaves on some mangroves were covered in dust. The dust thickness was not measured but visually and physically assessed (by rubbing particular leaves between finger tips). The tables given in Appendix G show a number of 'non-typical' vegetation samples; these include [FU] *Avicennia marina*, [FU] *Aegiceras corniculatum*2, [FU] *Aegialitis annulata*3, [FR] *Tecticornia sp.4*, and [FR] *Avicennia marina*.

Note: In the tables presented below, species such as [FU] *Aegiceras corniculatum* 2 and [FU] *Aegiceras corniculatum*2 represent the same sample; the absence of a space between species name and their sample number does not change the actual sample, as first commented on in Section 4.3.3. Some minor inconsistencies exist in this thesis. For example, Figure 57 (p. 175 of Section 4.4.2) does not contain a space between the sample number and the species name, while the plots in Appendix G.4 do.

	Region	FM	FM	FM	FM	FM	FM	FM	FM
Region	Cover Type	<i>Aegialitis annulata1</i>	<i>Aegialitis annulata2</i>	<i>Aegialitis annulata3</i>	<i>Avicennia marina1</i>	<i>Avicennia marina2</i>	<i>Avicennia marina3</i>	<i>Bruguiera exaristata1</i>	<i>Bruguiera exaristata2</i>
FM	<i>Aegialitis annulata1</i>		0.03 ± 0.05	0.25 ± 0.03	0.06 ± 0.03	0.07 ± 0.04	0.09 ± 0.08	0.04 ± 0.04	0.04 ± 0.05
FM	<i>Aegialitis annulata2</i>			0.26 ± 0.05	0.09 ± 0.04	0.09 ± 0.04	0.11 ± 0.08	0.05 ± 0.05	0.04 ± 0.06
FM	<i>Aegialitis annulata3</i>				0.19 ± 0.03	0.18 ± 0.03	0.17 ± 0.05	0.27 ± 0.04	0.27 ± 0.05
FM	<i>Avicennia marina1</i>					0.02 ± 0.04	0.04 ± 0.07	0.09 ± 0.04	0.09 ± 0.05
FM	<i>Avicennia marina2</i>						0.03 ± 0.07	0.10 ± 0.04	0.10 ± 0.05
FM	<i>Avicennia marina3</i>							0.12 ± 0.08	0.12 ± 0.08
FM	<i>Bruguiera exaristata1</i>								0.02 ± 0.07
FM	<i>Bruguiera exaristata2</i>								
FM	<i>Ceriops australis</i>								
FM	<i>Osbornia octodonta</i>								
FM	<i>Rhizophora stylosa</i>								

Table 68: Spectral angles (in radians) of FM with other FM land cover types.

	Region	FM	FM	FM	FR	FR	FR	FR	FR
Region	Cover Type	<i>Ceriops australis</i>	<i>Osbornia octodonta</i>	<i>Rhizophora stylosa</i>	<i>Acaria Sp</i>	<i>Avicennia marina</i>	<i>Frankenia ambita</i>	<i>Tecticornia sp1</i>	<i>Tecticornia sp2</i>
FM	<i>Aegialitis annulata1</i>	0.07 ± 0.02	0.08 ± 0.04	0.03 ± 0.06	0.04 ± 0.03	0.08 ± 0.04	0.20 ± 0.04	0.17 ± 0.06	0.18 ± 0.02
FM	<i>Aegialitis annulata2</i>	0.07 ± 0.04	0.10 ± 0.05	0.04 ± 0.07	0.07 ± 0.04	0.10 ± 0.05	0.21 ± 0.05	0.18 ± 0.06	0.20 ± 0.04
FM	<i>Aegialitis annulata3</i>	0.30 ± 0.03	0.18 ± 0.03	0.26 ± 0.04	0.21 ± 0.03	0.18 ± 0.04	0.09 ± 0.02	0.12 ± 0.03	0.10 ± 0.02
FM	<i>Avicennia marina1</i>	0.12 ± 0.04	0.03 ± 0.04	0.08 ± 0.04	0.04 ± 0.03	0.03 ± 0.03	0.15 ± 0.04	0.12 ± 0.05	0.14 ± 0.02
FM	<i>Avicennia marina2</i>	0.13 ± 0.04	0.03 ± 0.03	0.08 ± 0.04	0.04 ± 0.03	0.02 ± 0.04	0.13 ± 0.04	0.10 ± 0.05	0.13 ± 0.02
FM	<i>Avicennia marina3</i>	0.15 ± 0.08	0.05 ± 0.07	0.10 ± 0.08	0.06 ± 0.07	0.04 ± 0.07	0.12 ± 0.06	0.08 ± 0.07	0.12 ± 0.04
FM	<i>Bruguiera exaristata1</i>	0.04 ± 0.03	0.11 ± 0.04	0.02 ± 0.07	0.06 ± 0.04	0.10 ± 0.05	0.23 ± 0.05	0.19 ± 0.06	0.21 ± 0.03
FM	<i>Bruguiera exaristata2</i>	0.04 ± 0.05	0.11 ± 0.04	0.02 ± 0.08	0.06 ± 0.04	0.10 ± 0.05	0.23 ± 0.06	0.19 ± 0.07	0.21 ± 0.04
FM	<i>Ceriops australis</i>		0.13 ± 0.04	0.05 ± 0.06	0.10 ± 0.03	0.13 ± 0.04	0.26 ± 0.04	0.22 ± 0.06	0.24 ± 0.03
FM	<i>Osbornia octodonta</i>			0.09 ± 0.04	0.06 ± 0.03	0.04 ± 0.03	0.14 ± 0.04	0.12 ± 0.05	0.13 ± 0.02
FM	<i>Rhizophora stylosa</i>				0.05 ± 0.05	0.09 ± 0.05	0.21 ± 0.05	0.18 ± 0.07	0.20 ± 0.03

Table 69: Spectral angles (in radians) of FM with other FM and FR land cover types.

	Region	FR	FR	FR	FR	FR	FR	FR	FU
Region	Cover Type	<i>Tecticornia sp3</i>	<i>Tecticornia sp4</i>	<i>Sporobolus virginicus1</i>	<i>Sporobolus virginicus2</i>	<i>Trianthema turgidifolia</i>	<i>Triodia pungens</i>	Sandy-salty crusty soil	<i>Aegiceras corniculatum1</i>
FM	<i>Aegialitis annulata1</i>	0.23 ± 0.04	0.28 ± 0.03	0.29 ± 0.03	0.30 ± 0.04	0.11 ± 0.03	0.25 ± 0.05	0.45 ± 0.03	0.05 ± 0.04
FM	<i>Aegialitis annulata2</i>	0.25 ± 0.05	0.30 ± 0.04	0.30 ± 0.04	0.32 ± 0.05	0.14 ± 0.04	0.26 ± 0.06	0.47 ± 0.04	0.08 ± 0.05
FM	<i>Aegialitis annulata3</i>	0.08 ± 0.02	0.09 ± 0.02	0.11 ± 0.02	0.11 ± 0.02	0.20 ± 0.03	0.06 ± 0.03	0.23 ± 0.02	0.21 ± 0.04
FM	<i>Avicennia marina1</i>	0.17 ± 0.04	0.23 ± 0.03	0.23 ± 0.03	0.24 ± 0.04	0.08 ± 0.02	0.19 ± 0.04	0.39 ± 0.03	0.04 ± 0.04
FM	<i>Avicennia marina2</i>	0.16 ± 0.04	0.21 ± 0.03	0.22 ± 0.03	0.23 ± 0.05	0.09 ± 0.02	0.18 ± 0.05	0.38 ± 0.03	0.04 ± 0.04
FM	<i>Avicennia marina3</i>	0.15 ± 0.06	0.20 ± 0.06	0.20 ± 0.07	0.21 ± 0.08	0.09 ± 0.05	0.17 ± 0.06	0.36 ± 0.08	0.06 ± 0.07
FM	<i>Bruguiera exaristata1</i>	0.26 ± 0.05	0.31 ± 0.04	0.31 ± 0.04	0.33 ± 0.05	0.11 ± 0.04	0.27 ± 0.05	0.47 ± 0.04	0.07 ± 0.05
FM	<i>Bruguiera exaristata2</i>	0.25 ± 0.06	0.31 ± 0.05	0.31 ± 0.05	0.32 ± 0.06	0.12 ± 0.04	0.27 ± 0.06	0.47 ± 0.06	0.08 ± 0.05
FM	<i>Ceriops australis</i>	0.29 ± 0.04	0.34 ± 0.03	0.35 ± 0.03	0.36 ± 0.04	0.13 ± 0.03	0.30 ± 0.05	0.50 ± 0.03	0.11 ± 0.03
FM	<i>Osbornia octodonta</i>	0.17 ± 0.04	0.22 ± 0.03	0.22 ± 0.03	0.24 ± 0.04	0.09 ± 0.02	0.18 ± 0.04	0.38 ± 0.03	0.05 ± 0.04
FM	<i>Rhizophora stylosa</i>	0.24 ± 0.05	0.29 ± 0.05	0.30 ± 0.05	0.31 ± 0.06	0.10 ± 0.04	0.26 ± 0.06	0.46 ± 0.06	0.06 ± 0.05

Table 70: Spectral angles (in radians) of FM with FR and FU land cover types.

	Region	FU	FU	FU	FU	RB	RB	RB	RB
Region	Cover Type	<i>Aegiceras corniculatum</i> 2	<i>Avicennia marina</i>	<i>Salsola kali</i>	Red soil	<i>Avicennia marina</i>	<i>Bruguiera exaristata</i>	<i>Ceriops australis</i>	<i>Rhizophora stylosa</i>
FM	<i>Aegialitis annulata</i> 1	0.15 ± 0.04	0.17 ± 0.04	0.18 ± 0.04	0.42 ± 0.03	0.04 ± 0.04	0.09 ± 0.03	0.05 ± 0.05	0.06 ± 0.02
FM	<i>Aegialitis annulata</i> 2	0.17 ± 0.05	0.19 ± 0.05	0.20 ± 0.05	0.44 ± 0.04	0.06 ± 0.05	0.09 ± 0.04	0.08 ± 0.06	0.07 ± 0.04
FM	<i>Aegialitis annulata</i> 3	0.13 ± 0.03	0.11 ± 0.03	0.11 ± 0.03	0.20 ± 0.02	0.22 ± 0.04	0.31 ± 0.03	0.23 ± 0.04	0.28 ± 0.03
FM	<i>Avicennia marina</i> 1	0.10 ± 0.04	0.12 ± 0.04	0.12 ± 0.04	0.36 ± 0.03	0.04 ± 0.03	0.14 ± 0.04	0.06 ± 0.05	0.11 ± 0.04
FM	<i>Avicennia marina</i> 2	0.09 ± 0.04	0.10 ± 0.04	0.11 ± 0.04	0.35 ± 0.03	0.04 ± 0.03	0.15 ± 0.04	0.07 ± 0.04	0.12 ± 0.04
FM	<i>Avicennia marina</i> 3	0.08 ± 0.06	0.09 ± 0.05	0.11 ± 0.06	0.34 ± 0.07	0.06 ± 0.07	0.17 ± 0.08	0.09 ± 0.07	0.14 ± 0.07
FM	<i>Bruguiera exaristata</i> 1	0.17 ± 0.05	0.19 ± 0.05	0.20 ± 0.06	0.44 ± 0.04	0.06 ± 0.05	0.06 ± 0.03	0.05 ± 0.07	0.04 ± 0.04
FM	<i>Bruguiera exaristata</i> 2	0.17 ± 0.06	0.19 ± 0.06	0.20 ± 0.06	0.44 ± 0.05	0.06 ± 0.06	0.06 ± 0.05	0.05 ± 0.07	0.03 ± 0.05
FM	<i>Ceriops australis</i>	0.21 ± 0.04	0.23 ± 0.04	0.23 ± 0.04	0.47 ± 0.03	0.10 ± 0.05	0.03 ± 0.03	0.07 ± 0.06	0.03 ± 0.03
FM	<i>Osbornia octodonta</i>	0.10 ± 0.04	0.11 ± 0.03	0.11 ± 0.04	0.35 ± 0.03	0.06 ± 0.03	0.16 ± 0.04	0.07 ± 0.04	0.12 ± 0.03
FM	<i>Rhizophora stylosa</i>	0.16 ± 0.05	0.18 ± 0.05	0.19 ± 0.05	0.43 ± 0.05	0.05 ± 0.06	0.07 ± 0.06	0.04 ± 0.08	0.04 ± 0.06

Table 71: Spectral angles (in radians) of FM with FU and RB land cover types.

	Region	RB	RB	RB	LP	LP	LP	LP	LP
Region	Cover Type	Dry soil	Shallow water soil	Wet soil	<i>Avicennia marina</i>	<i>Tecticornia sp</i>	<i>Limonium</i>	Dredge dam on top	Dredge dam road
FM	<i>Aegialitis annulata1</i>	0.37 ± 0.03	0.85 ± 0.11	0.40 ± 0.03	0.05 ± 0.03	0.11 ± 0.04	0.14 ± 0.06	0.42 ± 0.03	0.40 ± 0.03
FM	<i>Aegialitis annulata2</i>	0.39 ± 0.04	0.88 ± 0.11	0.42 ± 0.04	0.07 ± 0.04	0.13 ± 0.05	0.15 ± 0.06	0.44 ± 0.04	0.41 ± 0.04
FM	<i>Aegialitis annulata3</i>	0.14 ± 0.02	0.64 ± 0.10	0.17 ± 0.02	0.21 ± 0.03	0.14 ± 0.03	0.13 ± 0.04	0.19 ± 0.02	0.16 ± 0.02
FM	<i>Avicennia marina1</i>	0.31 ± 0.03	0.79 ± 0.11	0.34 ± 0.03	0.04 ± 0.03	0.06 ± 0.04	0.09 ± 0.05	0.36 ± 0.03	0.34 ± 0.03
FM	<i>Avicennia marina2</i>	0.30 ± 0.03	0.79 ± 0.11	0.33 ± 0.03	0.04 ± 0.03	0.05 ± 0.04	0.08 ± 0.05	0.35 ± 0.03	0.33 ± 0.03
FM	<i>Avicennia marina3</i>	0.29 ± 0.07	0.78 ± 0.13	0.32 ± 0.07	0.06 ± 0.07	0.05 ± 0.06	0.07 ± 0.07	0.34 ± 0.07	0.32 ± 0.06
FM	<i>Bruguiera exaristata1</i>	0.39 ± 0.04	0.86 ± 0.12	0.42 ± 0.04	0.07 ± 0.04	0.14 ± 0.05	0.17 ± 0.06	0.44 ± 0.04	0.42 ± 0.04
FM	<i>Bruguiera exaristata2</i>	0.39 ± 0.05	0.86 ± 0.12	0.42 ± 0.05	0.07 ± 0.04	0.14 ± 0.05	0.17 ± 0.06	0.44 ± 0.05	0.42 ± 0.05
FM	<i>Ceriops australis</i>	0.42 ± 0.03	0.89 ± 0.11	0.45 ± 0.03	0.10 ± 0.03	0.17 ± 0.04	0.20 ± 0.06	0.47 ± 0.03	0.45 ± 0.03
FM	<i>Osbornia octodonta</i>	0.30 ± 0.03	0.79 ± 0.11	0.33 ± 0.03	0.06 ± 0.03	0.05 ± 0.04	0.09 ± 0.05	0.35 ± 0.03	0.33 ± 0.03
FM	<i>Rhizophora stylosa</i>	0.38 ± 0.05	0.85 ± 0.12	0.41 ± 0.05	0.05 ± 0.05	0.12 ± 0.04	0.15 ± 0.06	0.43 ± 0.05	0.41 ± 0.05

Table 72: Spectral angles (in radians) of FM with RB and LP land cover types.

	Region	LP	LP	PP	PP	PP	PP	PP	PP
Region	Cover Type	Hard packed dirt road	Salty reddish crust	<i>Acacia translucens</i>	<i>Aerva javanica</i>	<i>Cenchrus ciliaris</i>	<i>Corchorus parviflorus</i>	<i>Trianthema turgidifolia</i>	<i>Tecticornia sp. 1</i>
FM	<i>Aegialitis annulata1</i>	0.36 ± 0.03	0.43 ± 0.03	0.03 ± 0.03	0.42 ± 0.04	0.28 ± 0.03	0.25 ± 0.05	0.13 ± 0.03	0.08 ± 0.03
FM	<i>Aegialitis annulata2</i>	0.38 ± 0.04	0.45 ± 0.04	0.02 ± 0.06	0.43 ± 0.05	0.30 ± 0.04	0.27 ± 0.06	0.16 ± 0.04	0.10 ± 0.04
FM	<i>Aegialitis annulata3</i>	0.13 ± 0.03	0.21 ± 0.02	0.26 ± 0.04	0.24 ± 0.02	0.13 ± 0.02	0.15 ± 0.02	0.18 ± 0.03	0.22 ± 0.04
FM	<i>Avicennia marina1</i>	0.31 ± 0.03	0.37 ± 0.03	0.08 ± 0.04	0.36 ± 0.04	0.23 ± 0.03	0.20 ± 0.05	0.08 ± 0.02	0.07 ± 0.03
FM	<i>Avicennia marina2</i>	0.30 ± 0.03	0.36 ± 0.03	0.09 ± 0.04	0.35 ± 0.04	0.22 ± 0.04	0.19 ± 0.05	0.09 ± 0.02	0.07 ± 0.03
FM	<i>Avicennia marina3</i>	0.29 ± 0.06	0.34 ± 0.08	0.10 ± 0.08	0.33 ± 0.09	0.20 ± 0.07	0.17 ± 0.08	0.09 ± 0.05	0.07 ± 0.06
FM	<i>Bruguiera exaristata1</i>	0.39 ± 0.04	0.45 ± 0.04	0.04 ± 0.04	0.44 ± 0.05	0.31 ± 0.04	0.27 ± 0.06	0.14 ± 0.05	0.09 ± 0.04
FM	<i>Bruguiera exaristata2</i>	0.39 ± 0.05	0.45 ± 0.05	0.03 ± 0.06	0.44 ± 0.06	0.31 ± 0.05	0.27 ± 0.07	0.14 ± 0.05	0.08 ± 0.05
FM	<i>Ceriops australis</i>	0.41 ± 0.03	0.48 ± 0.03	0.06 ± 0.03	0.47 ± 0.04	0.34 ± 0.03	0.31 ± 0.05	0.16 ± 0.03	0.11 ± 0.04
FM	<i>Osbornia octodonta</i>	0.30 ± 0.03	0.36 ± 0.03	0.09 ± 0.04	0.36 ± 0.04	0.23 ± 0.03	0.20 ± 0.05	0.09 ± 0.02	0.09 ± 0.03
FM	<i>Rhizophora stylosa</i>	0.38 ± 0.04	0.44 ± 0.05	0.03 ± 0.06	0.43 ± 0.06	0.30 ± 0.05	0.26 ± 0.07	0.13 ± 0.04	0.07 ± 0.05

Table 73: Spectral angles (in radians) of FM with LP and PP land cover types.

	Region	PP	PP	PP	PP	PP	PP	PP
Region	Cover Type	<i>Tecticornia sp. 2</i>	<i>Triodia pungens</i>	Interstitial salt crusted sand	Old bitumen	Road (sandy hard packed)	Salt flat plain	Shell laden sand
FM	<i>Aegialitis annulata1</i>	0.16 ± 0.03	0.22 ± 0.04	0.49 ± 0.03	0.54 ± 0.04	0.44 ± 0.03	0.43 ± 0.03	0.42 ± 0.03
FM	<i>Aegialitis annulata2</i>	0.18 ± 0.04	0.23 ± 0.05	0.50 ± 0.04	0.56 ± 0.05	0.46 ± 0.04	0.45 ± 0.04	0.43 ± 0.04
FM	<i>Aegialitis annulata3</i>	0.16 ± 0.02	0.11 ± 0.02	0.29 ± 0.02	0.36 ± 0.04	0.23 ± 0.02	0.22 ± 0.02	0.21 ± 0.02
FM	<i>Avicennia marina1</i>	0.12 ± 0.03	0.16 ± 0.04	0.43 ± 0.03	0.48 ± 0.04	0.38 ± 0.03	0.37 ± 0.03	0.36 ± 0.03
FM	<i>Avicennia marina2</i>	0.10 ± 0.03	0.15 ± 0.04	0.42 ± 0.03	0.47 ± 0.04	0.37 ± 0.03	0.36 ± 0.03	0.35 ± 0.03
FM	<i>Avicennia marina3</i>	0.09 ± 0.05	0.13 ± 0.06	0.40 ± 0.08	0.45 ± 0.09	0.35 ± 0.08	0.34 ± 0.08	0.33 ± 0.08
FM	<i>Bruguiera exaristata1</i>	0.19 ± 0.04	0.24 ± 0.05	0.51 ± 0.04	0.56 ± 0.05	0.46 ± 0.04	0.45 ± 0.04	0.44 ± 0.04
FM	<i>Bruguiera exaristata2</i>	0.18 ± 0.05	0.24 ± 0.06	0.51 ± 0.06	0.56 ± 0.06	0.46 ± 0.05	0.45 ± 0.06	0.44 ± 0.05
FM	<i>Ceriops australis</i>	0.22 ± 0.03	0.28 ± 0.04	0.54 ± 0.03	0.59 ± 0.04	0.49 ± 0.03	0.48 ± 0.03	0.47 ± 0.03
FM	<i>Osbornia octodonta</i>	0.12 ± 0.03	0.16 ± 0.04	0.42 ± 0.03	0.48 ± 0.04	0.38 ± 0.03	0.36 ± 0.03	0.35 ± 0.03
FM	<i>Rhizophora stylosa</i>	0.17 ± 0.05	0.23 ± 0.05	0.49 ± 0.06	0.55 ± 0.06	0.45 ± 0.05	0.44 ± 0.06	0.43 ± 0.05

Table 74: Spectral angles (in radians) of FM with PP land cover types.

	Region	FR	FR	FR	FR	FR	FR	FR	FR
Region	Cover Type	<i>Acaria Sp</i>	<i>Avicennia marina</i>	<i>Frankenia ambita</i>	<i>Tecticornia sp1</i>	<i>Tecticornia sp2</i>	<i>Tecticornia sp3</i>	<i>Tecticornia sp4</i>	<i>Sporobolus virginicus1</i>
FR	<i>Acaria Sp</i>		0.04 ± 0.03	0.17 ± 0.04	0.13 ± 0.06	0.16 ± 0.02	0.19 ± 0.04	0.25 ± 0.03	0.25 ± 0.03
FR	<i>Avicennia marina</i>			0.13 ± 0.04	0.10 ± 0.05	0.13 ± 0.02	0.16 ± 0.04	0.21 ± 0.03	0.22 ± 0.04
FR	<i>Frankenia ambita</i>				0.05 ± 0.04	0.06 ± 0.02	0.05 ± 0.03	0.09 ± 0.03	0.09 ± 0.04
FR	<i>Tecticornia sp1</i>					0.07 ± 0.02	0.08 ± 0.04	0.13 ± 0.05	0.13 ± 0.06
FR	<i>Tecticornia sp2</i>						0.09 ± 0.02	0.12 ± 0.02	0.14 ± 0.02
FR	<i>Tecticornia sp3</i>							0.06 ± 0.03	0.07 ± 0.03
FR	<i>Tecticornia sp4</i>								0.05 ± 0.01
FR	<i>Sporobolus virginicus1</i>								
FR	<i>Sporobolus virginicus2</i>								
FR	<i>Trianthema turgidifolia</i>								
FR	<i>Triodia pungens</i>								
FR	Sandy-salty crusty soil								

Table 75: Spectral angles (in radians) of FR with other FR land cover types.

	Region	FR	FR	FR	FR	FU	FU	FU	FU
Region	Cover Type	<i>Sporobolus virginicus</i> 2	<i>Trianthema turgidifolia</i>	<i>Triodia pungens</i>	Sandy-salty crusty soil	<i>Aegiceras corniculatum</i> 1	<i>Aegiceras corniculatum</i> 2	<i>Avicennia marina</i>	<i>Salsola kali</i>
FR	<i>Acaria Sp</i>	0.26 ± 0.04	0.09 ± 0.02	0.21 ± 0.05	0.41 ± 0.03	0.03 ± 0.03	0.11 ± 0.05	0.13 ± 0.04	0.14 ± 0.04
FR	<i>Avicennia marina</i>	0.23 ± 0.05	0.08 ± 0.02	0.18 ± 0.05	0.37 ± 0.04	0.04 ± 0.04	0.08 ± 0.04	0.10 ± 0.04	0.10 ± 0.04
FR	<i>Frankenia ambita</i>	0.11 ± 0.04	0.18 ± 0.03	0.06 ± 0.04	0.26 ± 0.04	0.16 ± 0.05	0.07 ± 0.03	0.06 ± 0.03	0.08 ± 0.02
FR	<i>Tecticornia sp1</i>	0.14 ± 0.06	0.14 ± 0.05	0.10 ± 0.05	0.30 ± 0.05	0.14 ± 0.06	0.06 ± 0.04	0.06 ± 0.03	0.08 ± 0.03
FR	<i>Tecticornia sp2</i>	0.15 ± 0.03	0.17 ± 0.02	0.10 ± 0.03	0.29 ± 0.02	0.16 ± 0.03	0.09 ± 0.01	0.09 ± 0.01	0.09 ± 0.01
FR	<i>Tecticornia sp3</i>	0.08 ± 0.04	0.18 ± 0.04	0.04 ± 0.03	0.22 ± 0.03	0.19 ± 0.05	0.09 ± 0.04	0.07 ± 0.04	0.07 ± 0.04
FR	<i>Tecticornia sp4</i>	0.05 ± 0.02	0.24 ± 0.03	0.05 ± 0.03	0.18 ± 0.02	0.24 ± 0.04	0.14 ± 0.04	0.12 ± 0.03	0.13 ± 0.03
FR	<i>Sporobolus virginicus</i> 1	0.02 ± 0.03	0.25 ± 0.03	0.05 ± 0.03	0.18 ± 0.02	0.25 ± 0.04	0.15 ± 0.04	0.13 ± 0.03	0.14 ± 0.03
FR	<i>Sporobolus virginicus</i> 2		0.25 ± 0.04	0.06 ± 0.04	0.16 ± 0.03	0.26 ± 0.05	0.16 ± 0.05	0.14 ± 0.04	0.14 ± 0.04
FR	<i>Trianthema turgidifolia</i>			0.21 ± 0.04	0.38 ± 0.03	0.09 ± 0.03	0.12 ± 0.03	0.13 ± 0.03	0.12 ± 0.04
FR	<i>Triodia pungens</i>				0.21 ± 0.04	0.21 ± 0.05	0.11 ± 0.04	0.09 ± 0.04	0.09 ± 0.03
FR	Sandy-salty crusty soil					0.41 ± 0.04	0.30 ± 0.04	0.28 ± 0.04	0.28 ± 0.04

Table 76: Spectral angles (in radians) of FR with other FR and FU land cover types.

	Region	FU	RB	RB	RB	RB	RB	RB	RB
Region	Cover Type	Red soil	<i>Avicennia marina</i>	<i>Bruguiera exaristata</i>	<i>Ceriops australis</i>	<i>Rhizophora stylosa</i>	Dry soil	Shallow water soil	Wet soil
FR	<i>Acaria Sp</i>	0.38 ± 0.03	0.02 ± 0.05	0.11 ± 0.03	0.05 ± 0.05	0.08 ± 0.03	0.33 ± 0.03	0.81 ± 0.11	0.36 ± 0.03
FR	<i>Avicennia marina</i>	0.35 ± 0.03	0.04 ± 0.03	0.15 ± 0.04	0.07 ± 0.04	0.12 ± 0.04	0.30 ± 0.03	0.78 ± 0.11	0.32 ± 0.03
FR	<i>Frankenia ambita</i>	0.23 ± 0.03	0.17 ± 0.05	0.28 ± 0.04	0.20 ± 0.05	0.24 ± 0.04	0.18 ± 0.03	0.69 ± 0.10	0.21 ± 0.03
FR	<i>Tecticornia sp1</i>	0.27 ± 0.05	0.13 ± 0.06	0.24 ± 0.06	0.16 ± 0.06	0.21 ± 0.06	0.22 ± 0.05	0.72 ± 0.11	0.25 ± 0.05
FR	<i>Tecticornia sp2</i>	0.26 ± 0.01	0.16 ± 0.03	0.26 ± 0.02	0.18 ± 0.03	0.23 ± 0.03	0.20 ± 0.01	0.72 ± 0.10	0.24 ± 0.01
FR	<i>Tecticornia sp3</i>	0.20 ± 0.03	0.20 ± 0.05	0.30 ± 0.04	0.22 ± 0.05	0.27 ± 0.04	0.15 ± 0.03	0.65 ± 0.10	0.17 ± 0.03
FR	<i>Tecticornia sp4</i>	0.15 ± 0.01	0.25 ± 0.04	0.36 ± 0.03	0.27 ± 0.04	0.32 ± 0.03	0.10 ± 0.01	0.62 ± 0.10	0.13 ± 0.01
FR	<i>Sporobolus virginicus1</i>	0.16 ± 0.01	0.26 ± 0.04	0.36 ± 0.03	0.28 ± 0.05	0.33 ± 0.03	0.11 ± 0.01	0.62 ± 0.10	0.13 ± 0.01
FR	<i>Sporobolus virginicus2</i>	0.14 ± 0.03	0.27 ± 0.05	0.37 ± 0.04	0.29 ± 0.06	0.34 ± 0.04	0.10 ± 0.02	0.60 ± 0.10	0.12 ± 0.03
FR	<i>Trianthema turgidifolia</i>	0.36 ± 0.02	0.08 ± 0.02	0.15 ± 0.03	0.07 ± 0.04	0.11 ± 0.03	0.32 ± 0.02	0.76 ± 0.11	0.34 ± 0.02
FR	<i>Triodia pungens</i>	0.18 ± 0.04	0.22 ± 0.05	0.32 ± 0.04	0.24 ± 0.05	0.29 ± 0.05	0.13 ± 0.04	0.64 ± 0.11	0.16 ± 0.04
FR	Sandy-salty crusty soil	0.04 ± 0.02	0.42 ± 0.04	0.52 ± 0.03	0.43 ± 0.05	0.48 ± 0.03	0.11 ± 0.02	0.46 ± 0.09	0.07 ± 0.02

Table 77: Spectral angles (in radians) of FR with FU and RB land cover types.

	Region	LP	LP	LP	LP	LP	LP	LP	PP
Region	Cover Type	<i>Avicennia marina</i>	<i>Tecticornia sp</i>	<i>Limonium</i>	Dredge dam on top	Dredge dam road	Hard packed dirt road	Salty reddish crust	<i>Acacia translucens</i>
FR	<i>Acaria Sp</i>	0.02 ± 0.03	0.08 ± 0.04	0.11 ± 0.05	0.38 ± 0.03	0.36 ± 0.03	0.33 ± 0.03	0.39 ± 0.03	0.05 ± 0.03
FR	<i>Avicennia marina</i>	0.04 ± 0.03	0.05 ± 0.03	0.08 ± 0.05	0.34 ± 0.03	0.33 ± 0.03	0.30 ± 0.03	0.35 ± 0.03	0.09 ± 0.04
FR	<i>Frankenia ambita</i>	0.16 ± 0.04	0.10 ± 0.04	0.07 ± 0.05	0.23 ± 0.03	0.21 ± 0.03	0.19 ± 0.03	0.24 ± 0.03	0.21 ± 0.05
FR	<i>Tecticornia sp1</i>	0.13 ± 0.06	0.07 ± 0.04	0.04 ± 0.06	0.27 ± 0.05	0.25 ± 0.05	0.22 ± 0.04	0.27 ± 0.05	0.18 ± 0.06
FR	<i>Tecticornia sp2</i>	0.15 ± 0.02	0.09 ± 0.02	0.07 ± 0.03	0.26 ± 0.01	0.23 ± 0.01	0.20 ± 0.01	0.27 ± 0.01	0.20 ± 0.03
FR	<i>Tecticornia sp3</i>	0.19 ± 0.03	0.12 ± 0.04	0.11 ± 0.05	0.19 ± 0.03	0.18 ± 0.02	0.16 ± 0.02	0.20 ± 0.03	0.24 ± 0.04
FR	<i>Tecticornia sp4</i>	0.24 ± 0.02	0.17 ± 0.03	0.16 ± 0.05	0.15 ± 0.01	0.13 ± 0.01	0.12 ± 0.01	0.16 ± 0.01	0.30 ± 0.04
FR	<i>Sporobolus virginicus1</i>	0.25 ± 0.02	0.18 ± 0.03	0.16 ± 0.06	0.16 ± 0.01	0.15 ± 0.01	0.14 ± 0.01	0.16 ± 0.01	0.30 ± 0.04
FR	<i>Sporobolus virginicus2</i>	0.26 ± 0.04	0.19 ± 0.04	0.17 ± 0.06	0.14 ± 0.03	0.13 ± 0.02	0.13 ± 0.01	0.14 ± 0.03	0.31 ± 0.05
FR	<i>Trianthema turgidifolia</i>	0.09 ± 0.02	0.10 ± 0.03	0.14 ± 0.04	0.35 ± 0.02	0.34 ± 0.02	0.31 ± 0.02	0.36 ± 0.02	0.13 ± 0.03
FR	<i>Triodia pungens</i>	0.21 ± 0.04	0.14 ± 0.05	0.12 ± 0.06	0.18 ± 0.04	0.16 ± 0.03	0.14 ± 0.03	0.19 ± 0.04	0.26 ± 0.05
FR	Sandy-salty crusty soil	0.41 ± 0.03	0.34 ± 0.03	0.33 ± 0.06	0.05 ± 0.02	0.10 ± 0.02	0.15 ± 0.02	0.03 ± 0.02	0.46 ± 0.04

Table 78: Spectral angles (in radians) of FR with LP and PP land cover types.

	Region	PP	PP	PP	PP	PP	PP	PP	PP
Region	Cover Type	<i>Aerva javanica</i>	<i>Cenchrus ciliaris</i>	<i>Corchorus parviflorus</i>	<i>Trianthema turgidifolia</i>	<i>Tecticornia sp. 1</i>	<i>Tecticornia sp. 2</i>	<i>Triodia pungens</i>	Interstitial salt crusted sand
FR	<i>Acaria Sp</i>	0.38 ± 0.04	0.25 ± 0.04	0.22 ± 0.05	0.10 ± 0.03	0.06 ± 0.03	0.13 ± 0.03	0.18 ± 0.04	0.45 ± 0.03
FR	<i>Avicennia marina</i>	0.34 ± 0.04	0.22 ± 0.04	0.18 ± 0.05	0.09 ± 0.02	0.07 ± 0.03	0.10 ± 0.03	0.15 ± 0.04	0.41 ± 0.03
FR	<i>Frankenia ambita</i>	0.24 ± 0.04	0.09 ± 0.04	0.10 ± 0.03	0.16 ± 0.03	0.17 ± 0.05	0.08 ± 0.02	0.05 ± 0.03	0.30 ± 0.04
FR	<i>Tecticornia sp1</i>	0.27 ± 0.06	0.13 ± 0.06	0.12 ± 0.05	0.13 ± 0.04	0.13 ± 0.07	0.05 ± 0.04	0.07 ± 0.04	0.33 ± 0.05
FR	<i>Tecticornia sp2</i>	0.28 ± 0.03	0.14 ± 0.02	0.15 ± 0.03	0.16 ± 0.02	0.17 ± 0.04	0.09 ± 0.01	0.10 ± 0.02	0.34 ± 0.02
FR	<i>Tecticornia sp3</i>	0.21 ± 0.03	0.08 ± 0.03	0.09 ± 0.02	0.16 ± 0.04	0.19 ± 0.05	0.10 ± 0.02	0.07 ± 0.02	0.26 ± 0.03
FR	<i>Tecticornia sp4</i>	0.18 ± 0.03	0.07 ± 0.01	0.12 ± 0.02	0.22 ± 0.03	0.25 ± 0.04	0.15 ± 0.02	0.10 ± 0.02	0.23 ± 0.02
FR	<i>Sporobolus virginicus1</i>	0.16 ± 0.03	0.04 ± 0.01	0.09 ± 0.02	0.22 ± 0.03	0.25 ± 0.05	0.15 ± 0.02	0.08 ± 0.03	0.21 ± 0.02
FR	<i>Sporobolus virginicus2</i>	0.14 ± 0.03	0.05 ± 0.02	0.10 ± 0.03	0.23 ± 0.04	0.26 ± 0.05	0.16 ± 0.04	0.10 ± 0.04	0.20 ± 0.03
FR	<i>Trianthema turgidifolia</i>	0.36 ± 0.03	0.25 ± 0.03	0.20 ± 0.04	0.03 ± 0.03	0.07 ± 0.03	0.14 ± 0.02	0.19 ± 0.03	0.42 ± 0.03
FR	<i>Triodia pungens</i>	0.20 ± 0.04	0.07 ± 0.03	0.10 ± 0.03	0.18 ± 0.04	0.22 ± 0.05	0.13 ± 0.03	0.07 ± 0.02	0.25 ± 0.04
FR	Sandy-salty crusty soil	0.12 ± 0.01	0.20 ± 0.02	0.22 ± 0.05	0.36 ± 0.03	0.41 ± 0.04	0.31 ± 0.03	0.26 ± 0.03	0.07 ± 0.02

Table 79: Spectral angles (in radians) of FR with PP land cover types.

	Region	PP	PP	PP	PP
Region	Cover Type	Old bitumen	Road (sandy hard packed)	Salt flat plain	Shell laden sand
FR	<i>Acaria Sp</i>	0.50 ± 0.04	0.40 ± 0.03	0.39 ± 0.03	0.38 ± 0.03
FR	<i>Avicennia marina</i>	0.47 ± 0.04	0.37 ± 0.03	0.35 ± 0.04	0.34 ± 0.03
FR	<i>Frankenia ambita</i>	0.36 ± 0.04	0.25 ± 0.03	0.24 ± 0.04	0.22 ± 0.03
FR	<i>Tecticornia sp1</i>	0.39 ± 0.06	0.29 ± 0.05	0.27 ± 0.06	0.26 ± 0.06
FR	<i>Tecticornia sp2</i>	0.40 ± 0.03	0.29 ± 0.01	0.28 ± 0.02	0.26 ± 0.01
FR	<i>Tecticornia sp3</i>	0.32 ± 0.04	0.21 ± 0.03	0.20 ± 0.03	0.19 ± 0.03
FR	<i>Tecticornia sp4</i>	0.29 ± 0.03	0.17 ± 0.02	0.16 ± 0.02	0.15 ± 0.02
FR	<i>Sporobolus virginicus1</i>	0.27 ± 0.03	0.17 ± 0.02	0.15 ± 0.02	0.14 ± 0.02
FR	<i>Sporobolus virginicus2</i>	0.26 ± 0.04	0.15 ± 0.03	0.14 ± 0.03	0.12 ± 0.03
FR	<i>Trianthema turgidifolia</i>	0.47 ± 0.03	0.38 ± 0.02	0.37 ± 0.03	0.36 ± 0.02
FR	<i>Triodia pungens</i>	0.32 ± 0.05	0.20 ± 0.04	0.19 ± 0.04	0.17 ± 0.04
FR	Sandy-salty crusty soil	0.15 ± 0.04	0.03 ± 0.01	0.06 ± 0.02	0.05 ± 0.02

Table 80: Spectral angles (in radians) of FR with PP land cover types.

	Region	FU	FU	FU	FU	FU	RB	RB	RB
Region	Cover Type	<i>Aegiceras corniculatum1</i>	<i>Aegiceras corniculatum2</i>	<i>Avicennia marina</i>	<i>Salsola kali</i>	Red soil	<i>Avicennia marina</i>	<i>Bruguiera exaristata</i>	<i>Ceriops australis</i>
FU	<i>Aegiceras corniculatum1</i>		0.11 ± 0.05	0.13 ± 0.05	0.13 ± 0.05	0.38 ± 0.04	0.04 ± 0.04	0.13 ± 0.04	0.05 ± 0.05
FU	<i>Aegiceras corniculatum2</i>			0.02 ± 0.04	0.04 ± 0.04	0.27 ± 0.04	0.12 ± 0.05	0.22 ± 0.04	0.14 ± 0.05
FU	<i>Avicennia marina</i>				0.03 ± 0.03	0.25 ± 0.03	0.14 ± 0.04	0.24 ± 0.04	0.16 ± 0.04
FU	<i>Salsola kali</i>					0.25 ± 0.04	0.15 ± 0.05	0.25 ± 0.04	0.16 ± 0.05
FU	Red soil						0.39 ± 0.04	0.49 ± 0.03	0.40 ± 0.05
RB	<i>Avicennia marina</i>							0.11 ± 0.04	0.05 ± 0.06
RB	<i>Bruguiera exaristata</i>								0.09 ± 0.06
RB	<i>Ceriops australis</i>								
RB	<i>Rhizophora stylosa</i>								
RB	Dry soil								
RB	Shallow water soil								
RB	Wet soil								

Table 81: Spectral angles (in radians) of FU and RB with other FU and RB land cover types.

	Region	RB	RB	RB	RB	LP	LP	LP	LP
Region	Cover Type	<i>Rhizophora stylosa</i>	Dry soil	Shallow water soil	Wet soil	<i>Avicennia marina</i>	<i>Tecticornia sp</i>	<i>Limonium</i>	Dredge dam on top
FU	<i>Aegiceras corniculatum1</i>	0.10 ± 0.03	0.33 ± 0.04	0.81 ± 0.11	0.36 ± 0.04	0.03 ± 0.04	0.08 ± 0.04	0.12 ± 0.05	0.38 ± 0.04
FU	<i>Aegiceras corniculatum2</i>	0.19 ± 0.04	0.23 ± 0.04	0.71 ± 0.11	0.25 ± 0.04	0.11 ± 0.04	0.07 ± 0.03	0.08 ± 0.04	0.27 ± 0.04
FU	<i>Avicennia marina</i>	0.21 ± 0.04	0.21 ± 0.03	0.69 ± 0.11	0.23 ± 0.03	0.13 ± 0.04	0.08 ± 0.03	0.08 ± 0.04	0.25 ± 0.03
FU	<i>Salsola kali</i>	0.21 ± 0.05	0.21 ± 0.04	0.68 ± 0.11	0.23 ± 0.04	0.14 ± 0.04	0.08 ± 0.03	0.10 ± 0.04	0.25 ± 0.04
FU	Red soil	0.45 ± 0.03	0.08 ± 0.01	0.47 ± 0.09	0.05 ± 0.01	0.38 ± 0.02	0.31 ± 0.03	0.30 ± 0.05	0.03 ± 0.01
RB	<i>Avicennia marina</i>	0.08 ± 0.04	0.34 ± 0.04	0.82 ± 0.11	0.37 ± 0.04	0.01 ± 0.05	0.09 ± 0.04	0.11 ± 0.05	0.39 ± 0.04
RB	<i>Bruguiera exaristata</i>	0.04 ± 0.03	0.44 ± 0.02	0.90 ± 0.11	0.47 ± 0.02	0.12 ± 0.02	0.19 ± 0.04	0.22 ± 0.06	0.49 ± 0.02
RB	<i>Ceriops australis</i>	0.06 ± 0.06	0.36 ± 0.04	0.82 ± 0.12	0.38 ± 0.04	0.05 ± 0.05	0.11 ± 0.05	0.15 ± 0.06	0.40 ± 0.05
RB	<i>Rhizophora stylosa</i>		0.40 ± 0.03	0.86 ± 0.11	0.43 ± 0.03	0.09 ± 0.02	0.15 ± 0.04	0.19 ± 0.06	0.45 ± 0.03
RB	Dry soil			0.54 ± 0.10	0.04 ± 0.01	0.33 ± 0.02	0.26 ± 0.03	0.24 ± 0.05	0.07 ± 0.01
RB	Shallow water soil				0.50 ± 0.09	0.81 ± 0.11	0.75 ± 0.11	0.75 ± 0.11	0.47 ± 0.09
RB	Wet soil					0.36 ± 0.02	0.29 ± 0.03	0.28 ± 0.05	0.03 ± 0.01

Table 82: Spectral angles (in radians) of FU and RB with other RB and LP land cover types.

	Region	LP	LP	LP	PP	PP	PP	PP	PP
Region	Cover Type	Dredge dam road	Hard packed dirt road	Salty reddish crust	<i>Acacia translucens</i>	<i>Aerva javanica</i>	<i>Cenchrus ciliaris</i>	<i>Corchorus parviflorus</i>	<i>Trianthema turgidifolia</i>
FU	<i>Aegiceras corniculatum1</i>	0.36 ± 0.04	0.33 ± 0.04	0.39 ± 0.04	0.07 ± 0.04	0.38 ± 0.05	0.25 ± 0.04	0.21 ± 0.06	0.10 ± 0.03
FU	<i>Aegiceras corniculatum2</i>	0.25 ± 0.04	0.23 ± 0.03	0.28 ± 0.04	0.17 ± 0.05	0.28 ± 0.04	0.15 ± 0.04	0.12 ± 0.05	0.11 ± 0.03
FU	<i>Avicennia marina</i>	0.23 ± 0.03	0.21 ± 0.03	0.26 ± 0.03	0.18 ± 0.04	0.26 ± 0.04	0.14 ± 0.03	0.11 ± 0.04	0.12 ± 0.03
FU	<i>Salsola kali</i>	0.23 ± 0.04	0.21 ± 0.03	0.26 ± 0.04	0.19 ± 0.05	0.26 ± 0.04	0.15 ± 0.03	0.12 ± 0.03	0.11 ± 0.03
FU	Red soil	0.07 ± 0.01	0.12 ± 0.01	0.03 ± 0.01	0.43 ± 0.03	0.13 ± 0.01	0.18 ± 0.02	0.21 ± 0.04	0.33 ± 0.03
RB	<i>Avicennia marina</i>	0.37 ± 0.04	0.34 ± 0.04	0.39 ± 0.04	0.05 ± 0.04	0.38 ± 0.05	0.25 ± 0.05	0.22 ± 0.06	0.10 ± 0.02
RB	<i>Bruguiera exaristata</i>	0.46 ± 0.02	0.43 ± 0.02	0.50 ± 0.02	0.08 ± 0.03	0.49 ± 0.03	0.36 ± 0.03	0.32 ± 0.05	0.18 ± 0.04
RB	<i>Ceriops australis</i>	0.38 ± 0.04	0.35 ± 0.04	0.41 ± 0.05	0.06 ± 0.05	0.41 ± 0.06	0.28 ± 0.05	0.24 ± 0.06	0.09 ± 0.04
RB	<i>Rhizophora stylosa</i>	0.43 ± 0.03	0.40 ± 0.03	0.46 ± 0.03	0.06 ± 0.03	0.45 ± 0.04	0.33 ± 0.03	0.29 ± 0.05	0.14 ± 0.04
RB	Dry soil	0.04 ± 0.01	0.06 ± 0.01	0.08 ± 0.01	0.38 ± 0.03	0.16 ± 0.01	0.13 ± 0.01	0.18 ± 0.03	0.29 ± 0.03
RB	Shallow water soil	0.51 ± 0.10	0.55 ± 0.10	0.47 ± 0.09	0.87 ± 0.11	0.52 ± 0.09	0.64 ± 0.10	0.64 ± 0.11	0.74 ± 0.11
RB	Wet soil	0.04 ± 0.01	0.08 ± 0.01	0.05 ± 0.01	0.41 ± 0.03	0.15 ± 0.01	0.16 ± 0.02	0.20 ± 0.04	0.31 ± 0.03

Table 83: Spectral angles (in radians) of FU and RB with LP and PP land cover types.

	Region	PP	PP	PP	PP	PP	PP	PP	PP
Region	Cover Type	<i>Tecticornia sp. 1</i>	<i>Tecticornia sp. 2</i>	<i>Triodia pungens</i>	Interstitial salt crusted sand	Old bitumen	Road (sandy hard packed)	Salt flat plain	Shell laden sand
FU	<i>Aegiceras corniculatum1</i>	0.08 ± 0.03	0.13 ± 0.03	0.18 ± 0.04	0.44 ± 0.04	0.50 ± 0.05	0.40 ± 0.04	0.39 ± 0.04	0.38 ± 0.04
FU	<i>Aegiceras corniculatum2</i>	0.13 ± 0.04	0.08 ± 0.02	0.10 ± 0.03	0.34 ± 0.04	0.40 ± 0.05	0.29 ± 0.04	0.28 ± 0.04	0.27 ± 0.04
FU	<i>Avicennia marina</i>	0.14 ± 0.04	0.08 ± 0.02	0.09 ± 0.03	0.32 ± 0.03	0.38 ± 0.04	0.27 ± 0.03	0.26 ± 0.03	0.25 ± 0.03
FU	<i>Salsola kali</i>	0.15 ± 0.04	0.09 ± 0.02	0.11 ± 0.02	0.32 ± 0.04	0.38 ± 0.04	0.27 ± 0.04	0.26 ± 0.04	0.25 ± 0.04
FU	Red soil	0.38 ± 0.04	0.29 ± 0.02	0.23 ± 0.03	0.11 ± 0.02	0.18 ± 0.03	0.05 ± 0.01	0.07 ± 0.01	0.06 ± 0.01
RB	<i>Avicennia marina</i>	0.05 ± 0.04	0.13 ± 0.04	0.18 ± 0.05	0.45 ± 0.04	0.50 ± 0.05	0.41 ± 0.04	0.39 ± 0.04	0.38 ± 0.04
RB	<i>Bruguiera exaristata</i>	0.12 ± 0.04	0.23 ± 0.03	0.29 ± 0.04	0.55 ± 0.03	0.61 ± 0.03	0.51 ± 0.03	0.50 ± 0.03	0.49 ± 0.02
RB	<i>Ceriops australis</i>	0.07 ± 0.05	0.16 ± 0.04	0.21 ± 0.05	0.47 ± 0.05	0.53 ± 0.06	0.43 ± 0.05	0.41 ± 0.05	0.40 ± 0.05
RB	<i>Rhizophora stylosa</i>	0.09 ± 0.04	0.20 ± 0.03	0.26 ± 0.04	0.52 ± 0.03	0.57 ± 0.04	0.47 ± 0.03	0.46 ± 0.03	0.45 ± 0.03
RB	Dry soil	0.33 ± 0.04	0.24 ± 0.02	0.18 ± 0.02	0.17 ± 0.02	0.24 ± 0.03	0.10 ± 0.02	0.11 ± 0.01	0.09 ± 0.01
RB	Shallow water soil	0.80 ± 0.11	0.73 ± 0.10	0.69 ± 0.10	0.44 ± 0.08	0.43 ± 0.07	0.47 ± 0.09	0.49 ± 0.09	0.50 ± 0.09
RB	Wet soil	0.36 ± 0.04	0.27 ± 0.02	0.21 ± 0.03	0.14 ± 0.02	0.21 ± 0.03	0.08 ± 0.01	0.09 ± 0.01	0.07 ± 0.01

Table 84: Spectral angles (in radians) of FU and RB with PP land cover types.

	Region	LP	LP	LP	LP	LP	LP	LP	PP
Region	Cover Type	<i>Avicennia marina</i>	<i>Tecticornia sp</i>	<i>Limonium</i>	Dredge dam on top	Dredge dam road	Hard packed dirt road	Salty reddish crust	<i>Acacia translucens</i>
LP	<i>Avicennia marina</i>		0.08 ± 0.03	0.11 ± 0.05	0.38 ± 0.02	0.36 ± 0.02	0.33 ± 0.02	0.39 ± 0.02	0.06 ± 0.03
LP	<i>Tecticornia sp</i>			0.06 ± 0.04	0.31 ± 0.03	0.29 ± 0.03	0.26 ± 0.03	0.32 ± 0.03	0.13 ± 0.04
LP	<i>Limonium</i>				0.30 ± 0.05	0.28 ± 0.05	0.25 ± 0.05	0.31 ± 0.05	0.15 ± 0.06
LP	Dredge dam on top					0.05 ± 0.01	0.10 ± 0.02	0.04 ± 0.01	0.43 ± 0.03
LP	Dredge dam road						0.05 ± 0.01	0.08 ± 0.01	0.41 ± 0.03
LP	Hard packed dirt road							0.13 ± 0.01	0.38 ± 0.03
LP	Salty reddish crust								0.44 ± 0.03

Table 85: Spectral angles (in radians) of LP with other LP and PP land cover types.

	Region	PP	PP	PP	PP	PP	PP	PP	PP
Region	Cover Type	<i>Aerva javanica</i>	<i>Cenchrus ciliaris</i>	<i>Corchorus parviflorus</i>	<i>Trianthema turgidifolia</i>	<i>Tecticornia sp. 1</i>	<i>Tecticornia sp. 2</i>	<i>Triodia pungens</i>	Interstitial salt crusted sand
LP	<i>Avicennia marina</i>	0.38 ± 0.03	0.25 ± 0.03	0.21 ± 0.05	0.10 ± 0.03	0.05 ± 0.03	0.12 ± 0.03	0.18 ± 0.04	0.44 ± 0.03
LP	<i>Tecticornia sp</i>	0.32 ± 0.04	0.18 ± 0.04	0.16 ± 0.04	0.09 ± 0.02	0.10 ± 0.04	0.09 ± 0.02	0.12 ± 0.04	0.38 ± 0.03
LP	<i>Limonium</i>	0.30 ± 0.06	0.15 ± 0.06	0.15 ± 0.05	0.13 ± 0.03	0.12 ± 0.05	0.07 ± 0.03	0.09 ± 0.05	0.37 ± 0.06
LP	Dredge dam on top	0.15 ± 0.01	0.18 ± 0.01	0.21 ± 0.04	0.33 ± 0.03	0.38 ± 0.04	0.29 ± 0.02	0.24 ± 0.02	0.12 ± 0.02
LP	Dredge dam road	0.18 ± 0.01	0.17 ± 0.01	0.21 ± 0.03	0.32 ± 0.02	0.36 ± 0.04	0.27 ± 0.02	0.22 ± 0.02	0.17 ± 0.02
LP	Hard packed dirt road	0.21 ± 0.01	0.17 ± 0.01	0.21 ± 0.03	0.29 ± 0.02	0.33 ± 0.04	0.25 ± 0.02	0.21 ± 0.02	0.22 ± 0.02
LP	Salty reddish crust	0.12 ± 0.01	0.18 ± 0.02	0.21 ± 0.04	0.34 ± 0.03	0.38 ± 0.04	0.29 ± 0.02	0.24 ± 0.03	0.09 ± 0.02

Table 86: Spectral angles (in radians) of LP with PP land cover types.

	Region	PP	PP	PP	PP
Region	Cover Type	Old bitumen	Road (sandy hard packed)	Salt flat plain	Shell laden sand
LP	<i>Avicennia marina</i>	0.50 ± 0.04	0.40 ± 0.02	0.39 ± 0.03	0.38 ± 0.02
LP	<i>Tecticornia sp</i>	0.44 ± 0.04	0.34 ± 0.03	0.32 ± 0.03	0.31 ± 0.03
LP	<i>Limonium</i>	0.42 ± 0.06	0.32 ± 0.06	0.30 ± 0.06	0.29 ± 0.06
LP	Dredge dam on top	0.20 ± 0.03	0.06 ± 0.02	0.08 ± 0.01	0.07 ± 0.01
LP	Dredge dam road	0.24 ± 0.03	0.11 ± 0.02	0.12 ± 0.01	0.10 ± 0.01
LP	Hard packed dirt road	0.29 ± 0.03	0.15 ± 0.02	0.16 ± 0.01	0.14 ± 0.01
LP	Salty reddish crust	0.17 ± 0.03	0.03 ± 0.01	0.05 ± 0.01	0.05 ± 0.01

Table 87: Spectral angles (in radians) of LP with PP land cover types.

	Region	PP	PP	PP	PP	PP	PP	PP	PP
Region	Cover Type	<i>Acacia translucens</i>	<i>Aerva javanica</i>	<i>Cenchrus ciliaris</i>	<i>Corchorus parviflorus</i>	<i>Trianthema turgidifolia</i>	<i>Tecticornia sp. 1</i>	<i>Tecticornia sp. 2</i>	<i>Triodia pungens</i>
PP	<i>Acacia translucens</i>		0.43 ± 0.04	0.30 ± 0.04	0.27 ± 0.06	0.14 ± 0.03	0.08 ± 0.03	0.17 ± 0.04	0.23 ± 0.04
PP	<i>Aerva javanica</i>			0.16 ± 0.03	0.17 ± 0.05	0.33 ± 0.04	0.37 ± 0.05	0.27 ± 0.04	0.22 ± 0.04
PP	<i>Cenchrus ciliaris</i>				0.10 ± 0.02	0.23 ± 0.03	0.25 ± 0.05	0.14 ± 0.03	0.07 ± 0.03
PP	<i>Corchorus parviflorus</i>					0.18 ± 0.04	0.21 ± 0.06	0.13 ± 0.04	0.08 ± 0.03
PP	<i>Trianthema turgidifolia</i>						0.09 ± 0.03	0.13 ± 0.02	0.17 ± 0.03
PP	<i>Tecticornia sp. 1</i>							0.12 ± 0.04	0.18 ± 0.05
PP	<i>Tecticornia sp. 2</i>								0.09 ± 0.02
PP	<i>Triodia pungens</i>								
PP	Interstitial salt crusted sand								
PP	Old bitumen								
PP	Road (sandy hard packed)								
PP	Salt flat plain								
PP	Shell laden sand								

Table 88: Spectral angles (in radians) of PP with other PP land cover types.

	Region	PP	PP	PP	PP	PP
Region	Cover Type	Interstitial salt crusted sand	Old bitumen	Road (sandy hard packed)	Salt flat plain	Shell laden sand
PP	<i>Acacia translucens</i>	0.50 ± 0.04	0.55 ± 0.04	0.45 ± 0.04	0.44 ± 0.04	0.43 ± 0.03
PP	<i>Aerva javanica</i>	0.10 ± 0.02	0.14 ± 0.04	0.10 ± 0.01	0.08 ± 0.01	0.09 ± 0.01
PP	<i>Cenchrus ciliaris</i>	0.23 ± 0.03	0.28 ± 0.04	0.18 ± 0.02	0.16 ± 0.03	0.15 ± 0.02
PP	<i>Corchorus parviflorus</i>	0.25 ± 0.05	0.30 ± 0.05	0.21 ± 0.05	0.19 ± 0.05	0.19 ± 0.04
PP	<i>Trianthema turgidifolia</i>	0.39 ± 0.03	0.45 ± 0.04	0.35 ± 0.03	0.34 ± 0.03	0.33 ± 0.03
PP	<i>Tecticornia sp. 1</i>	0.44 ± 0.04	0.49 ± 0.05	0.40 ± 0.04	0.38 ± 0.04	0.37 ± 0.04
PP	<i>Tecticornia sp. 2</i>	0.34 ± 0.03	0.39 ± 0.04	0.30 ± 0.02	0.29 ± 0.03	0.27 ± 0.02
PP	<i>Triodia pungens</i>	0.29 ± 0.03	0.34 ± 0.04	0.24 ± 0.03	0.23 ± 0.03	0.21 ± 0.03
PP	Interstitial salt crusted sand		0.08 ± 0.03	0.07 ± 0.02	0.07 ± 0.02	0.09 ± 0.02
PP	Old bitumen			0.14 ± 0.04	0.14 ± 0.03	0.15 ± 0.04
PP	Road (sandy hard packed)				0.03 ± 0.02	0.03 ± 0.01
PP	Salt flat plain					0.03 ± 0.01
PP	Shell laden sand					

Table 89: Spectral angles (in radians) of PP with other PP land cover types.

G.4 Full Spectral plots and Spectral Angles

The preceding two sections (Appendix G.2 & G.3) were concerned with the reflectance covering a limited wavelength range; 400 – 990 nm, which corresponds closely to the sensed range of the airborne AISA EAGLE hyperspectral sensor.

This section plots the spectral angles extending from 400 – 2500 nm. In reality, atmospheric absorption affects specific wavelength ranges, as outlined in Section 4.3.1. Following the treatment of P. S. Thenkabail et al. (2004), the following atmospheric windows were excluded from the plots: 1350-1440, 1790-1990 and 2360-2500 nm.

Rather than reproducing all the plots and tables of Appendix G.2 & G.3, the seven mangrove species shown in Figure 57 (p. 175, of Section 4.4.2) are considered instead. The main point highlights that the spectral angles (SAs) are – with few exceptions - larger between pairs of cover types extending over the full spectral range (400 – 2500 nm), compared to the airborne spectral range (400 – 990 nm). Larger SAs indicate larger spectral dissimilarity and therefore suggests that a larger spectral range discriminates more effectively between mangrove species.

	Region	FM	FM	FM	FM	FM	FM	FR	FU
Region	Cover Type	<i>Aegialitis annulata</i> ¹	<i>Avicennia marina</i> ¹	<i>Bruguiera exaristata</i> ¹	<i>Ceriops australis</i>	<i>Osbornia octodonta</i>	<i>Rhizophora stylosa</i>	<i>Avicennia marina</i>	<i>Aegiceras corniculatum</i> ¹
FM	<i>Aegialitis annulata</i> ¹		0.07 ± 0.05	0.07 ± 0.07	0.20 ± 0.05	0.07 ± 0.06	0.10 ± 0.06	0.10 ± 0.05	0.09 ± 0.05
FM	<i>Avicennia marina</i> ¹			0.07 ± 0.06	0.17 ± 0.05	0.09 ± 0.06	0.08 ± 0.07	0.13 ± 0.05	0.14 ± 0.05
FM	<i>Bruguiera exaristata</i> ¹				0.14 ± 0.05	0.12 ± 0.07	0.05 ± 0.09	0.15 ± 0.07	0.15 ± 0.07
FM	<i>Ceriops australis</i>					0.25 ± 0.06	0.10 ± 0.09	0.28 ± 0.06	0.29 ± 0.05
FM	<i>Osbornia octodonta</i>						0.15 ± 0.07	0.06 ± 0.05	0.06 ± 0.05
FM	<i>Rhizophora stylosa</i>							0.18 ± 0.07	0.19 ± 0.07
FR	<i>Avicennia marina</i>								0.06 ± 0.05
FU	<i>Aegiceras corniculatum</i> ¹								

Table 90: Full spectral angles (in radians) of selected mangrove species on Finucane Island.

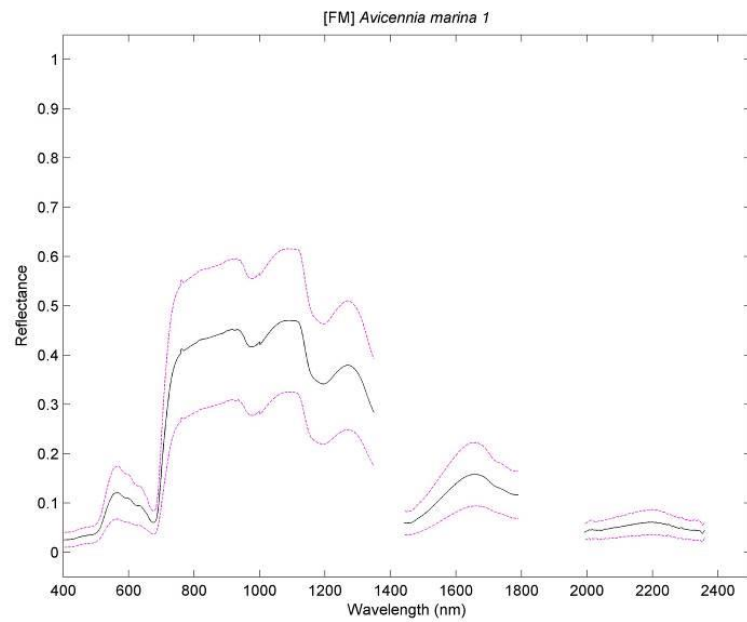
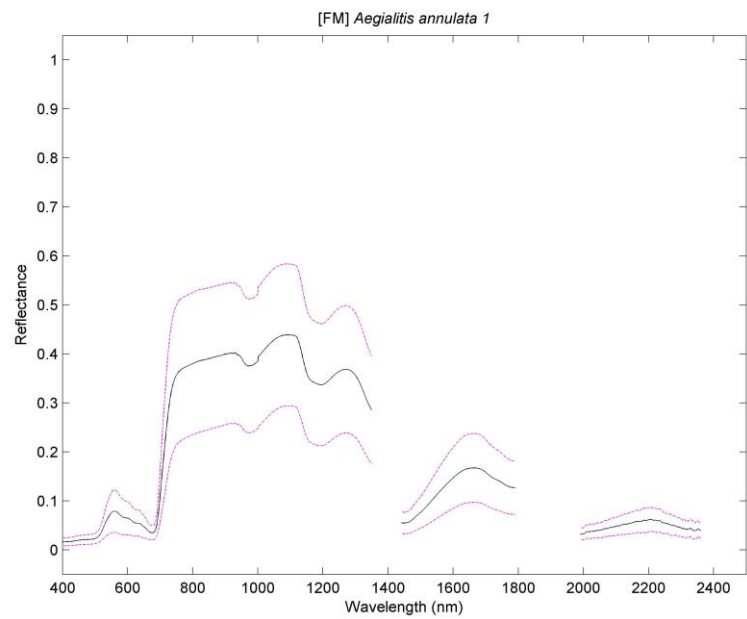


Figure 209: Full spectral plots for *Aegialitis annulata 1* (left) and *Avicennia marina 1* (right). [FM]

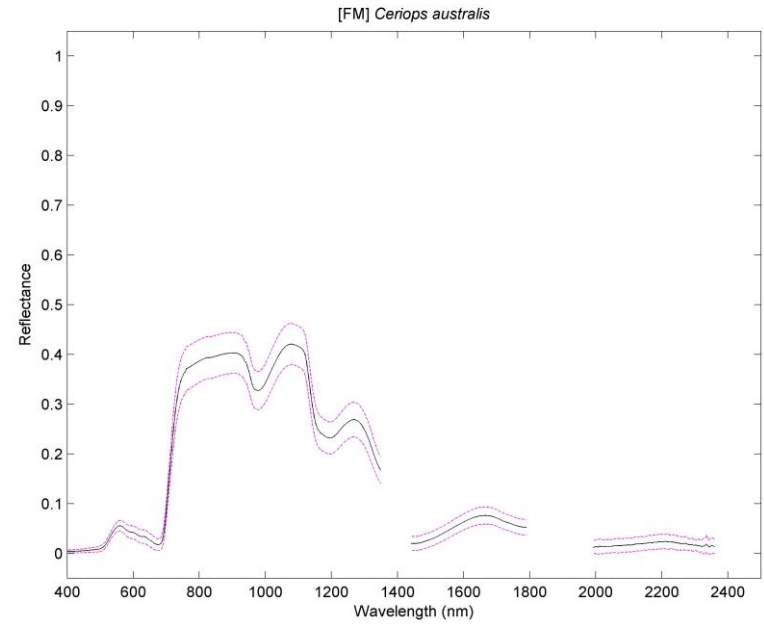
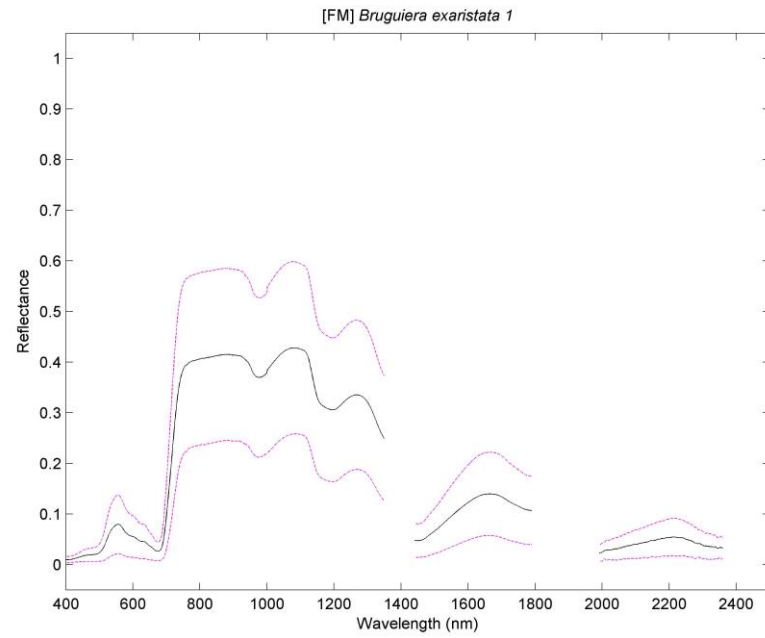


Figure 210: Full spectral plots for *Bruguiera exaristata 1* (left) and *Ceriops australis* (right). [FM]

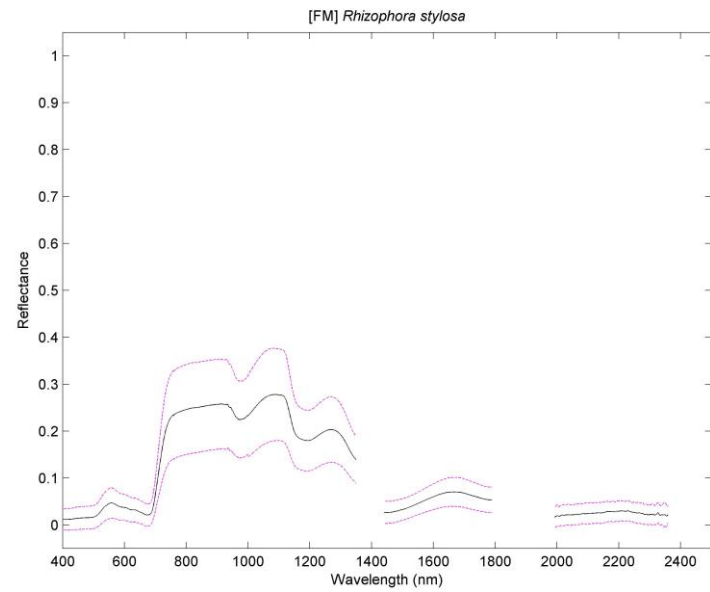
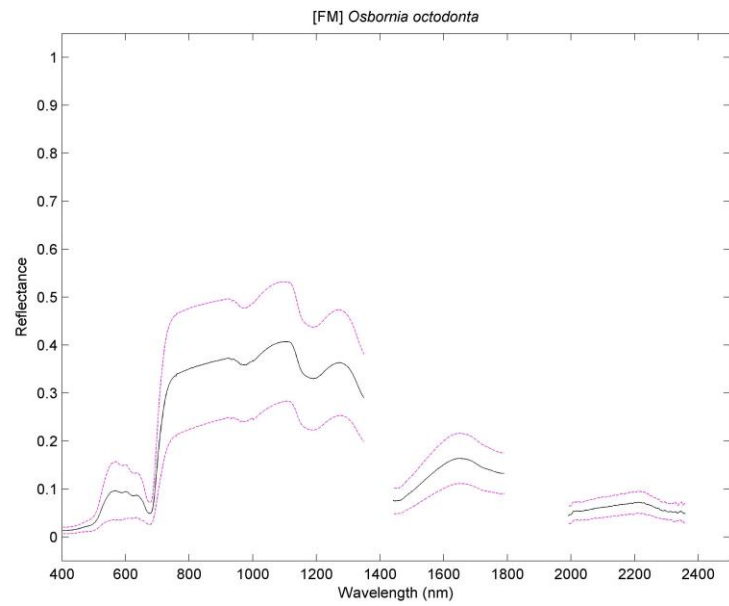


Figure 211: Full spectral plots for *Osbornia octodonta* (left) and *Rhizophora stylosa* (right). [FM]

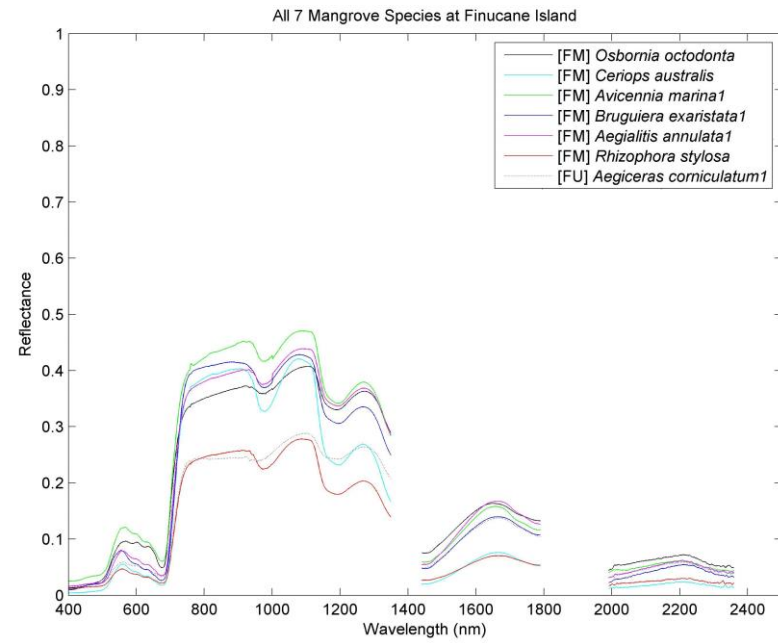
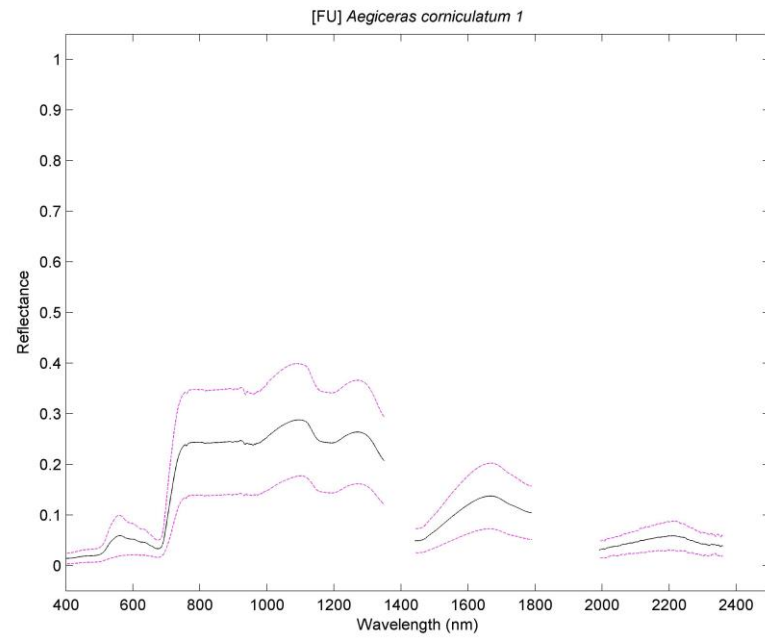


Figure 212: Full spectral plots for *Aegiceras corniculatum* 1 [FU] (left) and the 7 mangrove species found at Finucane Island.
Note: The right plot extends from 0 to 1 and contains only the mean spectral reflectance values (i.e. no uncertainties are displayed).

Appendix H Gradient Red-Edge Method

H.1 Method 1

Section 4.5.2 described one method of defining the mean gradient along the red-edge. As stated in that section, the full derivation will be shown here.

To aid this discussion, referral is made to Figure 64 (p. 196 of Section 4.5.2), where wavelengths λ_1 to λ_2 were defined for interval 1 while λ_3 to λ_4 defined interval 2. These four wavelengths define the starting and ending positions of each interval. Practically, four wavelengths are defined from which the mean gradient is calculated. However, behind the scenes, we need to average over many more wavelengths.

Therefore, consider breaking down the wavelengths in interval 1 into m values of $\alpha : \alpha_1, \alpha_2, \dots, \alpha_m$ and interval 2 into n values of $\beta : \beta_1, \beta_2, \dots, \beta_n$. This effectively means that $\lambda_1 = \alpha_1$, $\lambda_2 = \alpha_m$, $\lambda_3 = \beta_1$, and $\lambda_4 = \beta_n$ when related back to Figure 64.

When extended to cover more wavelengths, the mean gradient for the reflectance (or radiance) in interval 1 and 2 become (respectively):

$$\overline{R_\alpha} = \sum_{i=1}^m \frac{R(\alpha_i)}{m} \qquad \overline{R_\beta} = \sum_{j=1}^n \frac{R(\beta_j)}{n}$$

Similarly, the mean wavelengths for interval 1 and interval 2 are (respectively):

$$\overline{\alpha} = \sum_{i=1}^m \frac{\alpha_i}{m} \qquad \overline{\beta} = \sum_{j=1}^n \frac{\beta_j}{n}$$

The mean gradient for the reflectance (or radiance), denoted by $\overline{R_{\beta\alpha}}$ is:

$$\overline{R_{\beta\alpha}} = \frac{\overline{R_\beta} - \overline{R_\alpha}}{\beta - \alpha}$$

(the above is of similar form to Equation 4.5.2 of Section 4.5.2 but more generalised).

Or, in full:

$$\overline{R_{\beta\alpha}} = \frac{\sum_{j=1}^n \frac{R(\beta_j)}{n} - \sum_{i=1}^m \frac{R(\alpha_i)}{m}}{\sum_{j=1}^n \frac{\beta_j}{n} - \sum_{i=1}^m \frac{\alpha_i}{m}} \quad \text{H.1.0}$$

H.1.1 Special Case on Method 1

As a special condition, consider having an equal number of wavelengths defined in each interval. This means that $m = n$. Substituting this into Equation H.1.0 gives:

$$\overline{R_{\beta\alpha}} = \frac{\sum_{i=1}^n (R(\beta_i) - R(\alpha_i))}{\sum_{i=1}^n (\beta_i - \alpha_i)}$$

Having $m = n$ has another effect (assuming all wavelengths are equally spaced):

$$\beta_1 - \alpha_1 = \beta_2 - \alpha_2 = \dots = \beta_n - \alpha_n$$

There are n members in total, instead of m in interval 1 and n in interval 2.

Hence,

$$\sum_{i=1}^n (\beta_i - \alpha_i) = (\beta_1 - \alpha_1) + (\beta_2 - \alpha_2) + \dots + (\beta_n - \alpha_n) = n(\beta_n - \alpha_n)$$

This gives our final result for the special case when $m = n$ (i.e. equal number of wavelengths in each interval):

$$\overline{R}_{\beta\alpha} = \frac{\sum_{i=1}^n (R(\beta_i) - R(\alpha_i))}{n(\beta_n - \alpha_n)} \quad (\text{H.1.1.1})$$

The significance of this result will become clear after we examine an alternative method for calculating the mean gradient.

H.2 Method 2

Instead of calculating the mean for each R in each interval, the mean may be calculated between pairs of R values that exist in each interval. These mean values are then be averaged.

It is clear that in this case the condition $m = n$ must be met (due to necessary pairing between the intervals). This means that this method is more restrictive, as the number of wavelengths in each interval must be equal. However, it is interesting to explore and compare the result to the first method (above).

Calculating the first gradient (between β_1 and α_1) gives:

$$R_{\beta_1\alpha_1} = \frac{R(\beta_1) - R(\alpha_1)}{\beta_1 - \alpha_1}$$

and similarly for other gradients.

In general, the mean gradient is given by:

$$\overline{R}_{\beta\alpha} = \frac{R_{\beta_1\alpha_1} + R_{\beta_2\alpha_2} + \dots + R_{\beta_n\alpha_n}}{n} = \sum_{i=1}^n \frac{R_{\beta_i\alpha_i}}{n}$$

or more explicitly,

$$\overline{R}_{\beta\alpha} = \frac{1}{n} \left(\frac{R(\beta_1) - R(\alpha_1)}{\beta_1 - \alpha_1} + \frac{R(\beta_2) - R(\alpha_2)}{\beta_2 - \alpha_2} + \dots + \frac{R(\beta_n) - R(\alpha_n)}{\beta_n - \alpha_n} \right)$$

However, $\beta_1 - \alpha_1 = \beta_2 - \alpha_2 = \dots = \beta_n - \alpha_n$ (for equally spaced wavelengths).

Hence,

$$\overline{R}_{\beta\alpha} = \frac{\sum_{i=1}^n (R(\beta_i) - R(\alpha_i))}{n(\beta_n - \alpha_n)} \quad (\text{H.2.1})$$

This shows that Equation (H.2.1) and Equation (H.1.1.1) are equal. Hence, the two methods above produce the same the mean gradient but only when $m = n$, a condition of the second method. The wavelengths must also be equally spaced.

In practical terms, the first method was adopted and a program written for implementation. The method is more flexible as any two wavelengths can be selected (for each interval) without concern for an equal number of wavelengths (in each interval).

Appendix I GPS Locational Uncertainties

I.1 GPS Coordinates and ENVI Pixel Space

An investigation was undertaken to explain the behaviour of ENVI pixel coordinates, which was found to be inconsistent when the cursor was moved by one pixel.

A rather arbitrary location was selected for study, with the pixel position as shown in. The ENVI zoom box (Figure 213 (right)) displays the pixel location in the image.

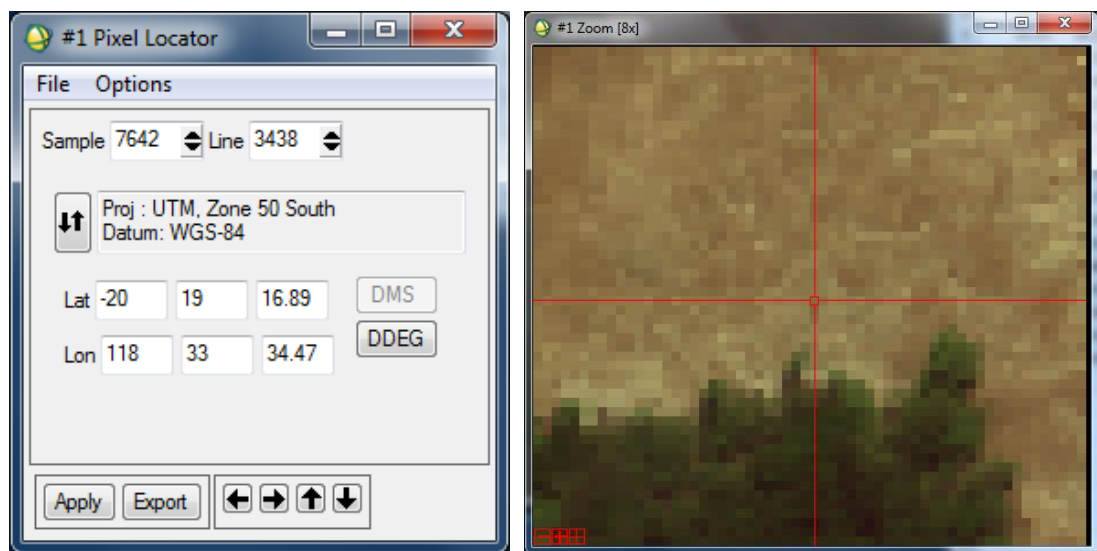


Figure 213: ENVI's Pixel Locator tool (left) and the pixel location as displayed on the true colour image (right).

By moving the cursor left or right, the pixel's longitudinal position is recorded (this investigation is restricted to the longitudinal position). The results are summarised in Table 91, but only for the degrees in seconds.

pixel 1	pixel 2	pixel 3	pixel 4	pixel 5	pixel 6	pixel 7
34.41	34.44	34.47	34.51	34.54	34.58	34.61
34.42	34.45	34.48	34.52	34.55	34.59	etc.
34.43	34.46	34.49	34.53	34.56	34.60	
		34.50		34.57		

Table 91: Pixel values (in seconds) as displayed by the Pixel Locator tool.

The bold numbers represent the values returned by the Pixel Locator tool. For example, the left-most pixel (pixel 1) displayed coordinates of 34.41 seconds. By moving the cursor one position to the right (the adjacent pixel - pixel 2), the coordinates were displayed as 34.44 seconds. The next pixel was, 34.47, etc. The values underneath each bold number represent the values that belong to that pixel. For example, in addition to 34.51 (the bold value), 34.52 and 34.53 still belong to pixel 4, as pixel 3 ends with 34.50 and pixel 5 begins with 34.54.

When actual values are entered into the Pixel Locator tool, ENVI does not always place the cursor in the pixel corresponding to the entered result. For example, by entering 34.42, ENVI displays 34.41 in the Pixel Locator tool (referencing pixel 1). For pixel 4, entering 34.52, 34.53, 34.54 actually relates to pixel 4 (located at 34.51). The results are summarised in Table 92. Interestingly, 34.54 should belong to pixel 5 (according to Table 91), but when manually entered, the cursor remains at the position of pixel 4. Instead, 34.55 now belongs to pixel 5.

Manually entering values into the Pixel Locator tool gave the following results:

pixel 1	pixel 2	pixel 3	pixel 4	pixel 5	pixel 6	pixel 7
34.41	34.44	34.48	34.51	34.55	34.58	34.62
34.42	34.45	34.49	34.52	34.56	34.59	etc.
34.43	34.46	34.50	34.53	34.57	34.60	
	34.47		34.54		34.61	

Table 92: Pixel values (in seconds) as entered into the Pixel Locator tool.

These values differ to those displayed in Table 91. To be clear, Table 91 shows the coordinates (in seconds) belonging to the pixels as indicated (e.g. 34.41, 34.42 and 34.43 all belong to pixel 1). In Table 92, entering the values as shown in the table, into the Pixel Locator tool, positions the cursor onto the pixels shown. For example, entering 34.48 places the cursor onto pixel 3.

An explanation is found by first considering the distance covered by 1 second of latitude. The Earth's radius has a volumetric mean radius as 6371.0 km (Williams, 2019).

Therefore, the distance represented by 1 second at the latitude of 20°20' (south) is:

$$\text{Distance} = \frac{\left(\frac{1}{3600}\right)}{360} \times 2\pi \times 6371 \times \cos\left(20 + \frac{20}{60}\right) \approx 28.9628 \text{ m}$$

Both tables (Table 91 and Table 92) show that multiple coordinates occupy the same pixels (e.g. pixel 1 has three). There is a 0.01 s difference between these locations, which equates to 0.29 m (as 1 s is calculated as 28.9628 m).

Now, the spatial resolution is 1 m in the image. As 1 second represents 28.9628 m, 1 metre represents:

$$\frac{1}{28.9628} \approx 0.0345 \text{ s}$$

If we started at 34.41 seconds for pixel 1, then the next pixel should start at 34.41 + 0.0345 = 34.4445 seconds. However, the Pixel Locator in ENVI only caters for 2 decimal places, so this becomes 34.44 seconds. Comparing this result with Table 91, we do indeed have pixel 2 starting at 34.44 seconds. But what if we entered 34.47 into the Pixel Locator? According to Table 91, this should fit into pixel 3 but according to Table 92, ENVI places this into pixel 2. Performing the calculation manually gives: 34.47 + 0.0345 = 34.5045, which ENVI rounds to 34.50. The value of 34.5045 should belong to pixel 4, but instead this value is truncated to 34.50, thereby placing it into pixel 3. The following table avoids making these calculations by hand.

The values to the right of Table 93 are obtained by adding 0.0345 to each of the corresponding values on the left. The pixel id corresponds to that as given in the corresponding table. The values under the heading of Table 91 are the same as those under Table 91 but written vertically. It shows a value of 34.41 for pixel 1. Adding 0.0345 to this value produces 34.4445, the value directly to the right. This relates to pixel 2 in Table 92. These values (to 4 d.p.) are actually truncated to 2 d.p.

and match the values in Table 92. So, 34.4445 belongs to pixel 2 in Table 92, where it is written as 34.44.

Pixel id in Table 91		Pixel id in Table 92	
pixel 1	34.41	34.4445	pixel 2
	34.42	34.4545	
	34.43	34.4645	
pixel 2	34.44	34.4745	
	34.45	34.4845	pixel 3
	34.46	34.4945	
pixel 3	34.47	34.5045	
	34.48	34.5145	pixel 4
	34.49	34.5245	
	34.50	34.5345	
pixel 4	34.51	34.5445	
	34.52	34.5545	pixel 5
	34.53	34.5645	
pixel 5	34.54	34.5745	
	34.55	34.5845	pixel 6
	34.56	34.5945	
	34.57	34.6045	
pixel 6	34.58	34.6145	
	34.59	34.6245	pixel 7
	34.60	34.6345	
pixel 7	34.61	34.6445	
	etc.	etc.	

Table 93: Comparing actual Pixel values (in seconds) (Table 91) to those entered into the Pixel Locator tool (Table 92).

It can therefore be considered that 0.0345 s is an angular limit imposed by the spatial resolution of the image. The maximum angular error is therefore 0.0345 s, as the pixel does not change actual position. This needs to be considered when calculating pixel locations using GPS coordinates.

I.2 Integrity of GPS Coordinates in ASD Measurements

During the first PHPA field trip during September 2013, each ASD measurement was accompanied by a handheld GPS reading. In addition the digital camera also had its

own GPS system (through an attachment), so GPS coordinates were stored into the each photo taken. In this section, it is of interest to compare the GPS coordinates recorded by these two devices.

However, it is first necessary to explain how to convert between ASD GPS coordinates and image coordinates.

The ASD field spectrometer is attached by a notebook (as shown in Figure 45, p. 153 of Section 4.3.1). The notebook contains ViewSpec Pro software which writes recorded spectral samples to log files. Although each spectrum is recorded to one individual file, the GPS coordinates are stored into one file. Table 94 shows is an excerpt from one of these log files.

```
4/4/2013 9:24:39 AM,c:\asd_data\redbank00000.asd,GPGGA,012439,2020.8088,S,11837.0723,E,1,11,1.3,10.2,M,-0.1,M,,*7D
4/4/2013 9:24:46 AM,c:\asd_data\redbank00001.asd,GPGGA,012445,2020.8088,S,11837.0720,E,1,11,1.1,9.9,M,-0.1,M,,*44
4/4/2013 9:24:51 AM,c:\asd_data\redbank00002.asd,GPGGA,012451,2020.8085,S,11837.0722,E,1,11,1.3,10.1,M,-0.1,M,,*7C
4/4/2013 9:24:58 AM,c:\asd_data\redbank00003.asd,GPGGA,012459,2020.8085,S,11837.0721,E,1,10,1.1,9.9,M,-0.1,M,,*44
4/4/2013 9:25:05 AM,c:\asd_data\redbank00004.asd,GPGGA,012505,2020.8095,S,11837.0725,E,1,11,1.3,9.9,M,-0.1,M,,*4A
4/4/2013 9:25:12 AM,c:\asd_data\redbank00005.asd,GPGGA,012511,2020.8094,S,11837.0723,E,1,11,1.3,9.7,M,-0.1,M,,*46
```

Table 94: A small excerpt from the GPS log file entries. Each entry represents one ASD measurement. In total, 6 measurements are displayed in this table.

The first entry shows that a single ASD measurement was recorded into file “redbank0000.asd”. It is a binary file, which requires conversion to ASCII format using the file conversion routine built into the ViewSpec Pro software. This file contains the spectrum of a single measurement. By recording another spectral sample, the software package automatically increments the file number to “0001”, as shown in the second file entry in Table 94.

The first entry also contains recorded GPS coordinates:

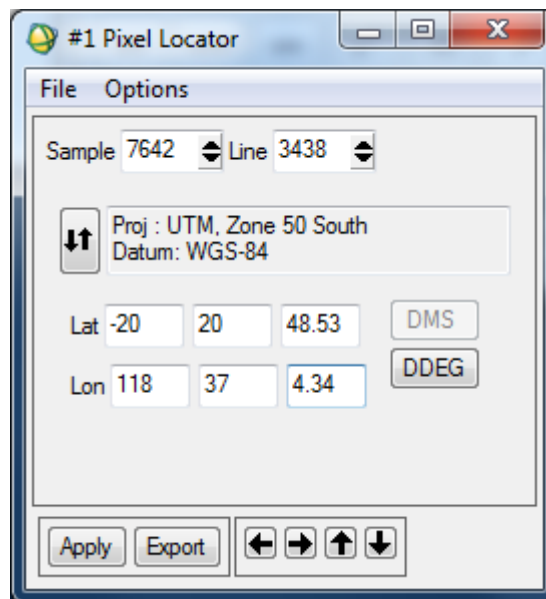
2020.8088,S,11837.0723,E

This is clearly in (latitude, longitude) format.

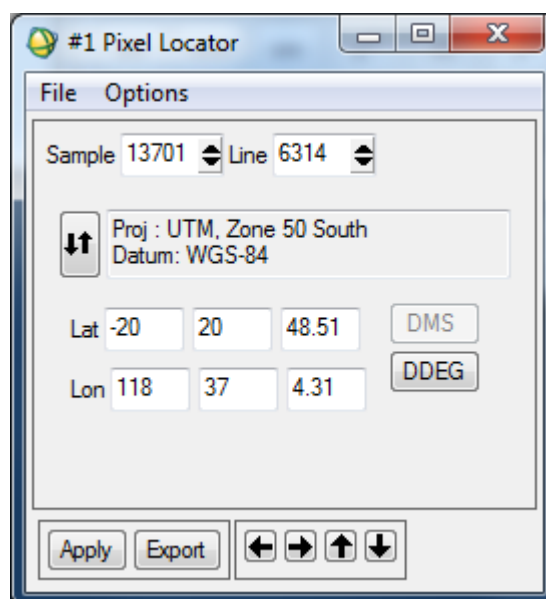
It is useful to convert this into a suitable format for use with ENVI’s Pixel Locator tool. The first four numbers (i.e. “2020”) means: 20°20’. The “S” indicates that the location is recorded in the southern hemisphere. By convention, the latitude for the northern hemisphere is positive, while the southern hemisphere is negative.

Effectively this means that the first 4 numbers is: $-20^{\circ}20'$. To convert the .8088 to seconds, we multiply by 60 giving $48.528''$. In all the result is: $-20^{\circ}20'48.528''$. Using the same approach, the longitudinal coordinates are: $118^{\circ}37'4.338''$.

In the ENVI Pixel Locator tool (where numbers must be rounded to 2 decimal places), the number is as shown:



As explained in Appendix I.1, there is a maximum error of 0.0345 s and ENVI actually returns the coordinates shown:



The coordinates stored in a photographed image are somewhat easier to convert. A photo was made in the vicinity of the ASD measurement, so an exact coordinate match is not expected (measurement uncertainty aside). The coordinates of a photo's property tab reveals the GPS coordinates. An example is provided in Figure 214.

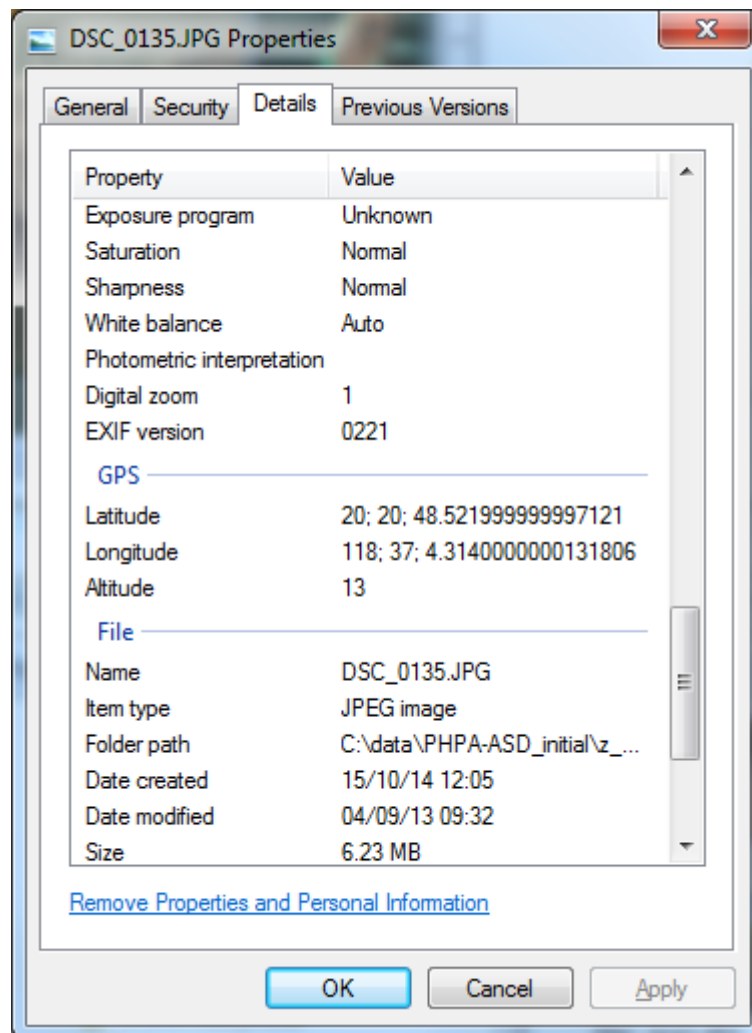


Figure 214: The GPS coordinates are stored in the photographed image file.

The coordinates here are clearly: (-20°20'48.522", 118°37'4.314").

These locations compare favourably and relate to an ASD measurement of [RB] dry soil at a site at Redbank.

Comparison between ASD and photo GPS coordinates with geographic coordinates (from the image) attempted to quantify any locational uncertainty.

The position for two easily-identifiable cover types on Finucane Island were used in this investigation. The first being the *Acaria sp.* [FR], which formed a distinct and large feature that is easily recognised on both the ground and in the airborne image. Figure 215 shows why it is easily identifiable, as it is located in the open. Figure 216 shows a closer view of the tree.



Figure 215: [FR] *Acaria sp.* on Finucane Island. This is easily identifiable in the hyperspectral image, as it is a large feature located in an isolated spot against grassland.



Figure 216: Close-up photo taken of the [FR] *Acaria sp.* from Figure 215.

The photo's GPS coordinates for the location shown in Figure 216 is: $20^{\circ}18'5.076''S$ and $118^{\circ}33'21.828''E$. The location returned by ENVI (i.e. using the Pixel Locator tool) is: $20^{\circ}18'5.06''S$ and $118^{\circ}33'21.83''E$, showing a difference in latitude of $0.016''$; however, this falls within the 0.0345 s limit, as discussed in Appendix I.1. Therefore, the position should be placed in the correct pixel (see Figure 217).

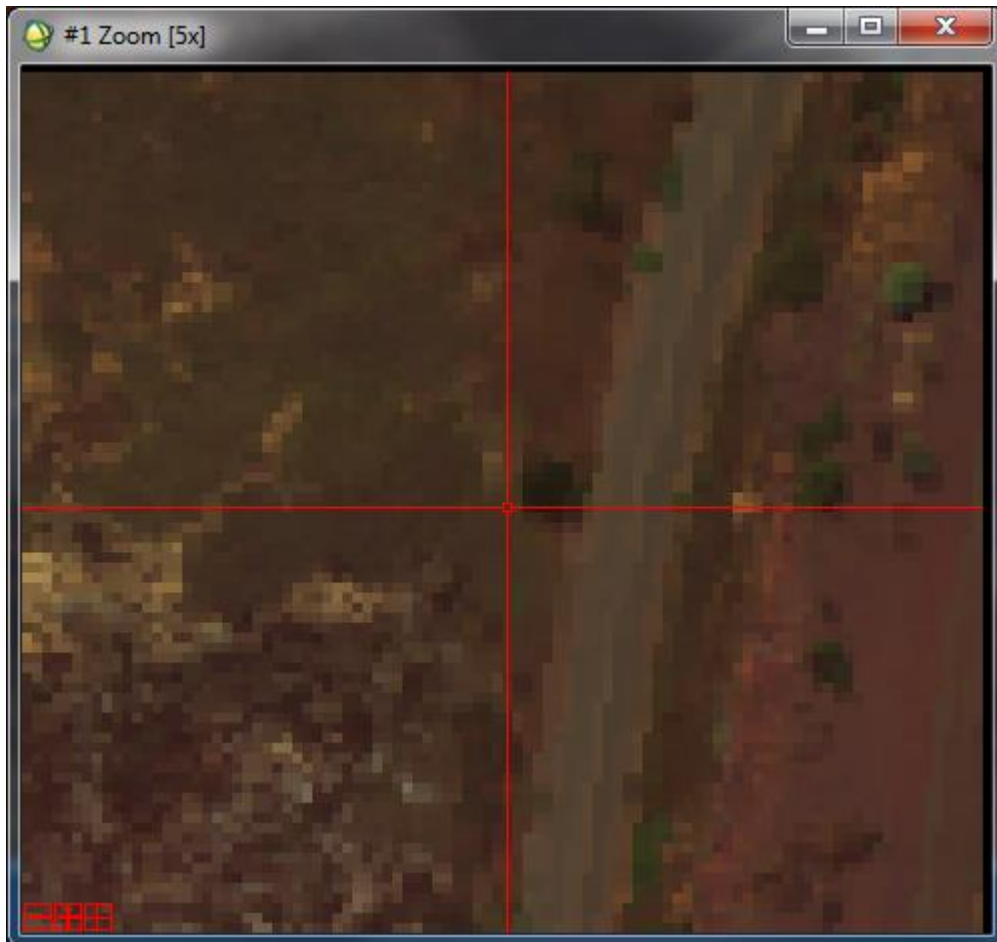


Figure 217: Photograph's GPS location for [FR] *Acaria Sp.* shown in image.

If the tree's growth remained constant over the 3 year period, then the photo's coordinates could be in error by about 1 m. However, inspection of the photo's shot angle with the image as displayed, shows the ENVI coordinates to match the photograph remarkably well and within error ($0.0345s$).

As for the ASD measurements, using $2018.0843,S,11833.3611,E$ as a typical coordinate for this feature (i.e. $20^{\circ}18'5.06''S$ and $118^{\circ}33'21.67''E$), the selected pixel is as shown in Figure 218.

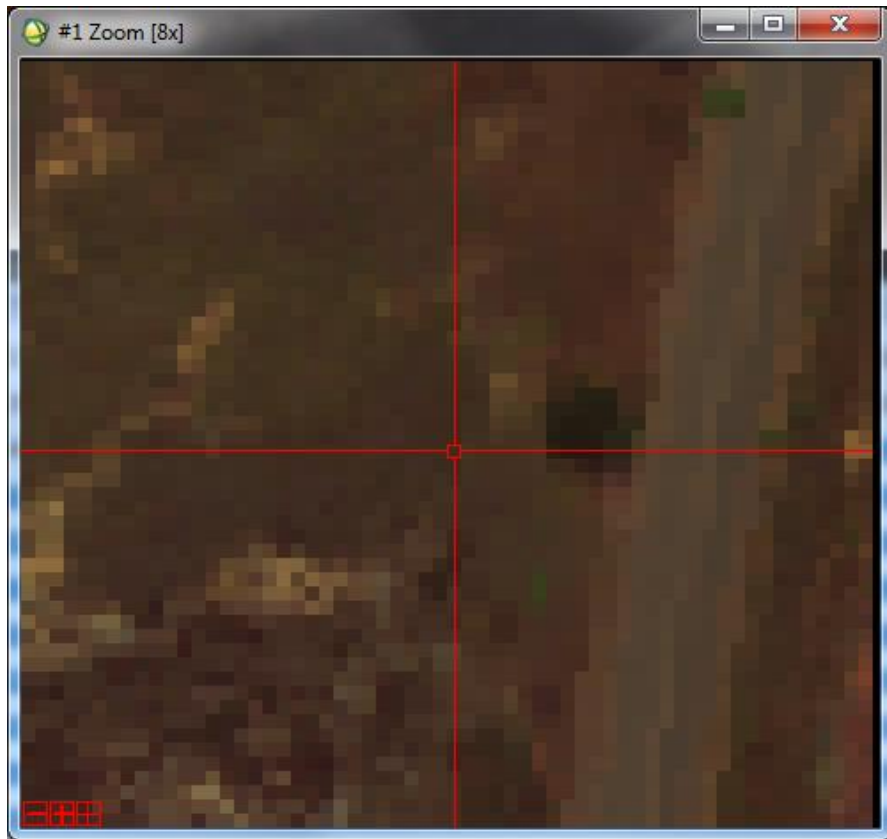
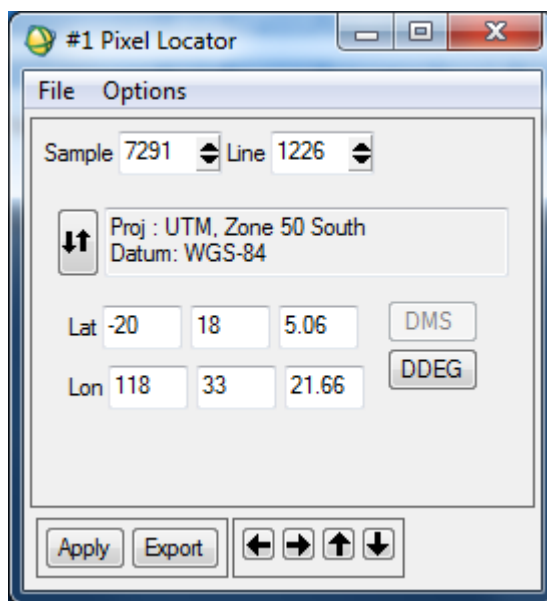


Figure 218: ASD GPS location for [FR] *Acaria sp.*

By typical coordinate, it means that one a typical result was taken from the 15-odd measurements for each cover type (Table 94 shows 6 measurements in total). The corresponding position, as given by the ENVI Pixel Locator is as shown:



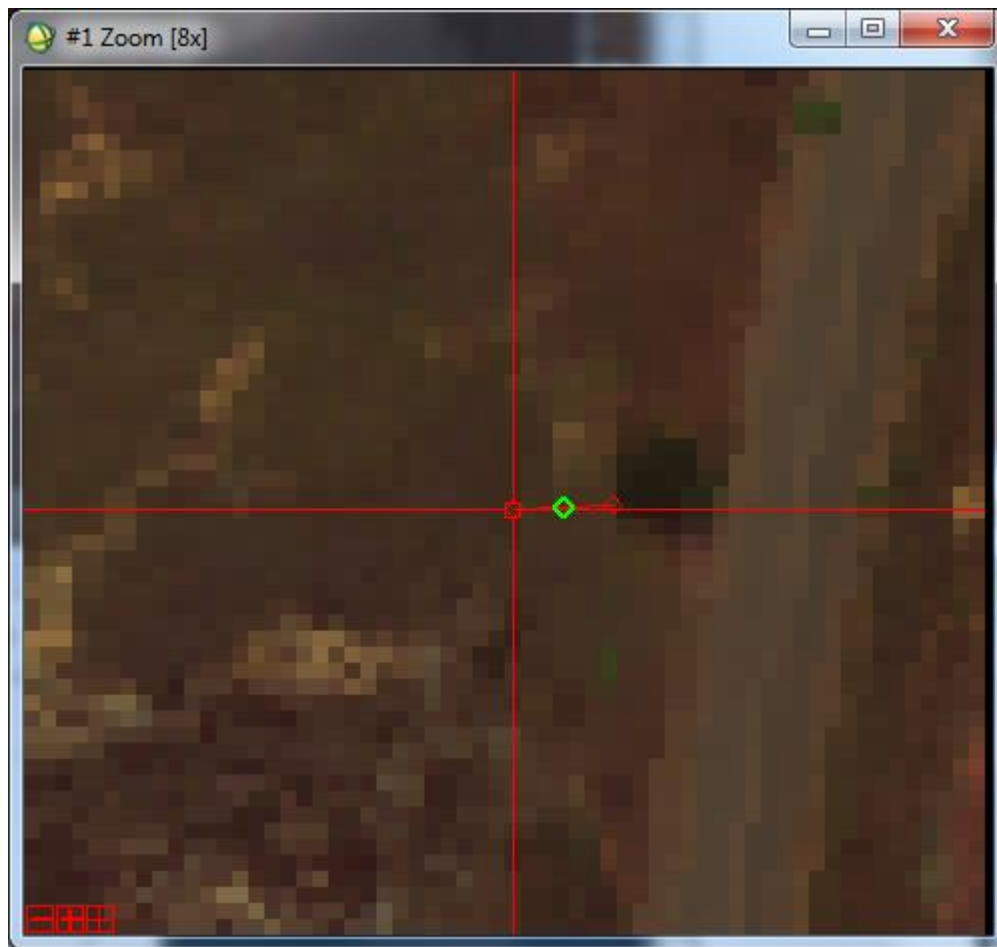


Figure 219: Measuring the distance from the ASD GPS coordinates for [FR] *Acaria sp.* to the edge of the feature (i.e. minimum distance).

Using the ENVI measurement tool, the coordinates appear to be in error by about 5–6 m. The distance is the length between the position as indicated in Figure 217 (for the photograph) and Figure 218 (for the ASD).

There is one additional, really distinct feature that was sampled on Finucane Island. In fact, it is located near the previous location for [FR] *Acaria sp.*.

A photo (Figure 220) for [FR] *Avicennia marina* shows this distinct feature, in the open grassland.



Figure 220: [FR] *Avicennia marina* on Finucane Island.

The coordinates for the photo was: $20^{\circ}18'6.516''S$ and $118^{\circ}33'18.258''E$, corresponding to the location as shown in the Figure 221. The position of the shot agrees to a high degree with the position in the image, although the photo is known to have been taken further east, as indicated in the image given in Figure 222.

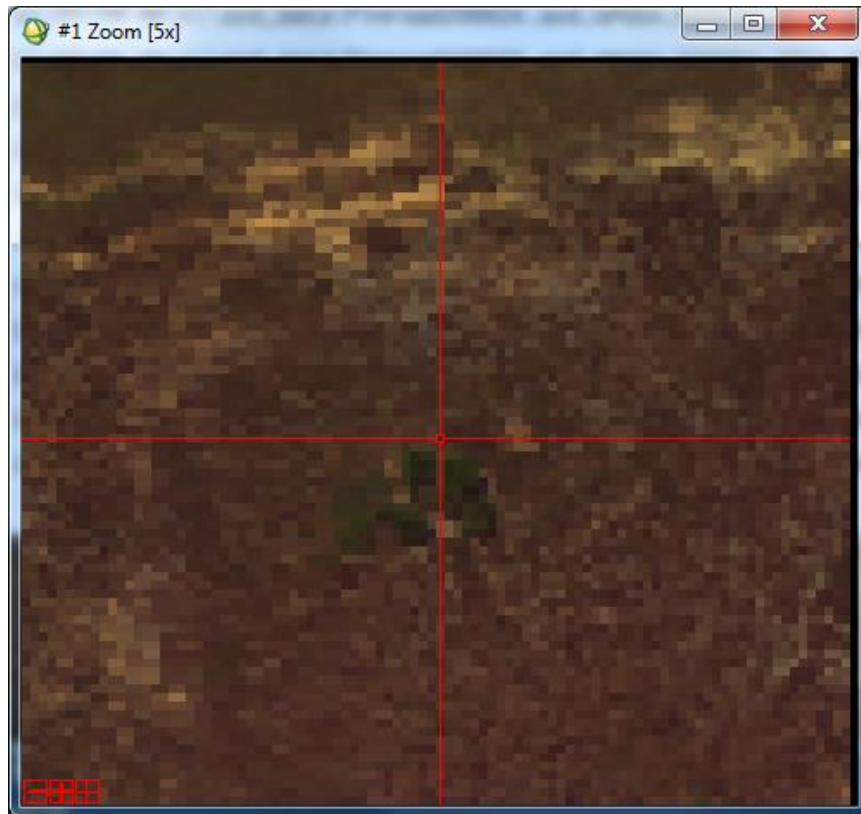


Figure 221: Photographic GPS location for [FR] *Avicennia marina* on Finucane Island.

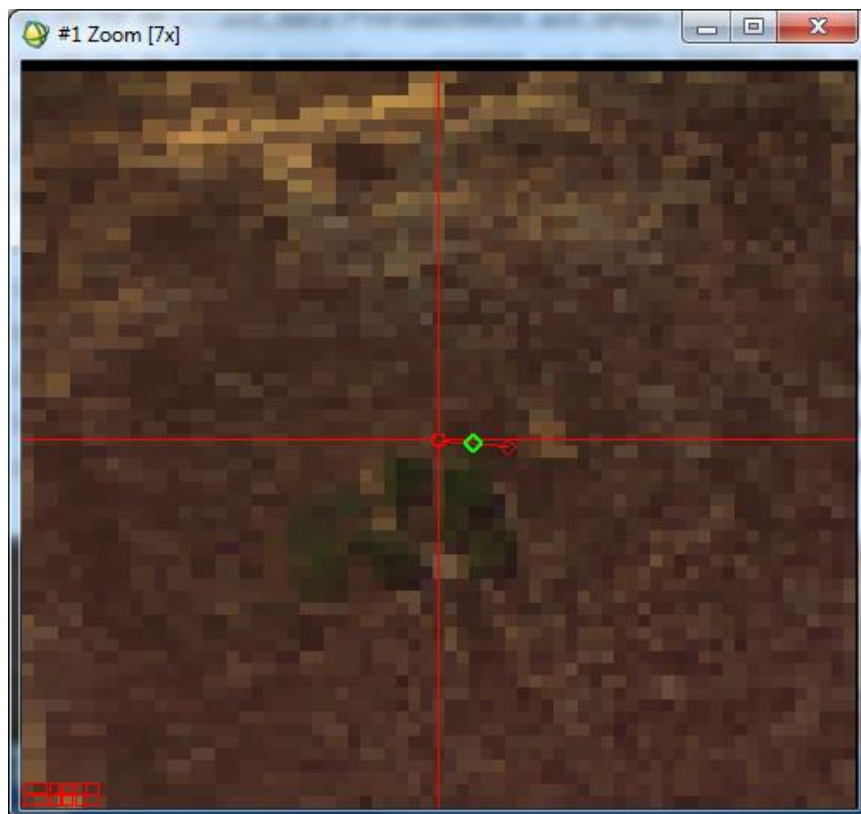


Figure 222: Probable correct photo location for [FR] *Avicennia marina*.

ASD measurements also places the field technician closer to the tree. According to the ENVI's Display Measurement Tool, the distance between the red circle and red square amounts to approximately 5.9 m. Again, it is unknown to what extent (if any) the tree has grown in the 3 year period between the PHPA airborne and the field surveys.

Similar approaches compared ASD and photographic GPS positions, using shot angles and static features (large trees, distinct shrubs, man-made structures), leading to an estimated discrepancy of about 6 m. The GPS unit itself (attached to the ASD) frequently recorded an uncertainty in the range of 4 - 8 m. Although the GPS unit attached to the digital camera will also be in error, it appears from the findings presented in this appendix that a 4 - 8 m measurement uncertainty is not unreasonable.

The limited pixel spatial resolution also determines the extent of placing an ASD measured cover type with the image. For instance, multiple GPS positions with an accuracy to the nearest 0.1 m is able to be placed confidently into a 1 m x 1 m pixel. However, the same is not true if the GPS accuracy is 10 m; such measurements will be located at different pixels. Appendix I.1 showed that multiple positions occupies the same pixel and is a result of rounding numbers.

It would be interesting for future field work, to "walk around" the edge of a distinct feature in a (say) clockwise direction (starting from the north) and taking measurements every 45° in a full circle. Furthermore, the process could be repeated several times (at various time intervals). This would assist in determining if there are any random or systematic errors in the GPS coordinates.

The work in this appendix shows that the GPS coordinates of the ASD do not exactly match up to those in an image, even when taking into account the spatial resolution of pixels. This means that ASD spectral samples for specific cover types are unlikely to be precisely matched on the actual airborne image. Cover types between ASD and the image therefore need to be carefully selected for direct spectral comparisons.

Appendix J Supervised SAM Classification

The work outlined in this section examines the effectiveness of the SAM classifier using ASD spectra from the PHPA hyperspectral library (Appendix J.1) and using image pixels themselves (Appendix J.2).

J.1 Image SAM Classification using ASD Spectra

Using the PHPA_Ref image, a spectral angle (SA) is calculated between a mean reference spectrum (for a particular cover type - as stored in the hyperspectral library) and each image pixel spectrum. The result is stored as a new image, whereby each pixel contains just the SA. A similar approach was taken for the NDVI (Figure 61).

Due to the mismatch in wavelengths between the image and ASD spectra, each image-based spectrum was interpolated to match the ASD wavelengths (and therefore reflectance values) (further details are given in Appendix R).

Ideally, the SA is zero representing a positive match for the pixel with the cover type reference spectrum. However, in practice, spectral uncertainties in reference spectra requires a compromise; a SA range from 0 to 0.1 rad was regarded as a match between reference and target spectra.

In both Figure 223 and Figure 224, regions covered in green indicate high spectral similarity (0 – 0.1 rad). The orange coloured region contains SAs from 0.1 – 0.2 rad, while magenta indicates regions over 0.2 rad. Therefore, SAs over 0.2 rad are deemed spectrally dissimilar to the extent that they deny positive cover type identification.

Classification using [FM] *Ceriops australis* as the reference cover type led to the map shown in Figure 223 (left), while that for [FM] *Rhizophora stylosa* is shown in Figure 223 (right). Spectral angles less than 0.1 rad are indicated in green, indicating high spectral similarity. For [FM] *Ceriops australis*, a total of 83585 green pixels were identified while for [FM] *Rhizophora stylosa* the total is 45859. Unfortunately, there is significant overlap in pixels between the two species; a total of 35962 green

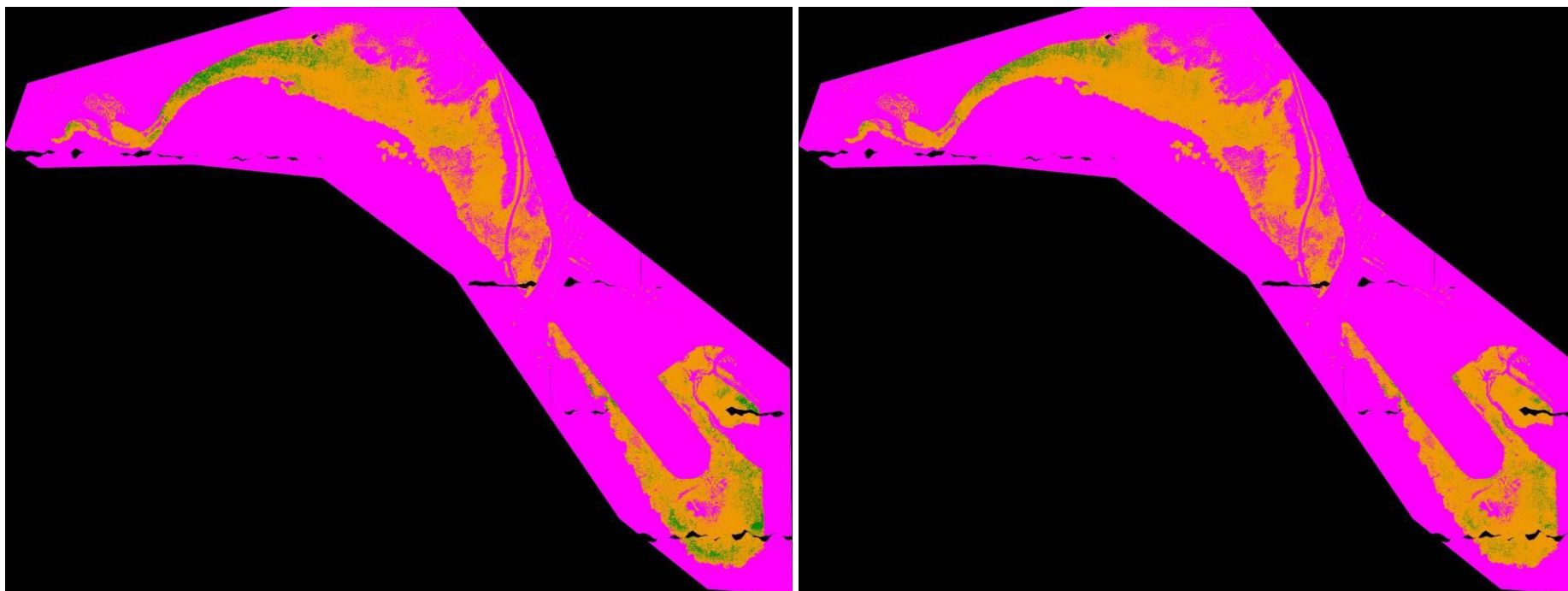


Figure 223: SAM classification map for [FM] *Ceriops australis* (left) and [FM] *Rhizophora stylosa* (right).

The green colour indicates a small SA of 0.1 rad suggesting a high likelihood of occurrence of that cover type. Orange indicates a SA of between 0.1 and 0.2 rad – a small chance of cover type occurrence. Magenta contains SA over 0.2 rad (very low likelihood of cover type occurrence).

(Note: The [FM] code system refers to the ASD sampling location, as explained in Section 4.3.3 and Appendix G.2, page 460).

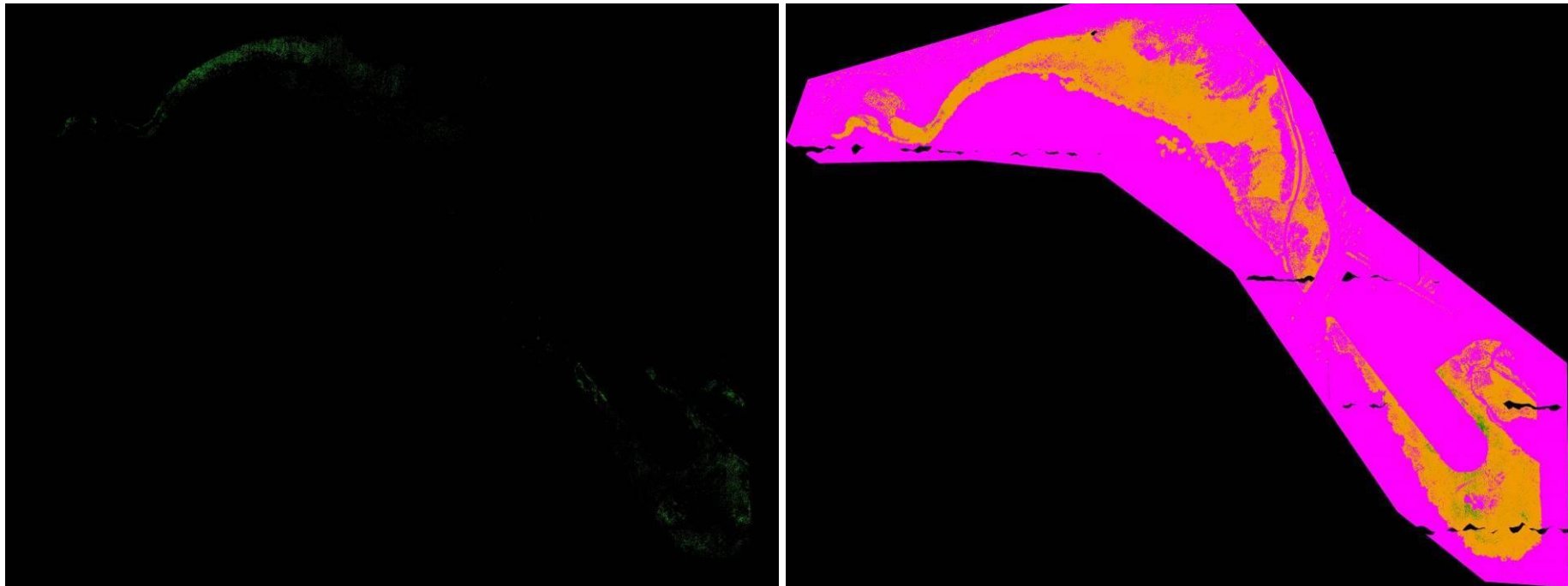


Figure 224: Equal occurrence between [FM] *Ceriops australis* and [FM] *Rhizophora stylosa* is shown in green and represent the pixels in common between Figure 223 (left and right). The right image shows the SAM classification map for [FM] *Avicennia marina 1*. The green colour indicates a small SA of 0.1 rad suggesting a high likelihood of occurrence of that cover type. Orange indicates a SA of between 0.1 and 0.2 rad – a small chance of cover type occurrence. Magenta contains SA over 0.2 rad (very low likelihood of cover type occurrence).

(Note: The [FM] code system refers to the ASD sampling location, as explained in Section 4.3.3 and Appendix G.2, page 460).

pixels belong to both species. Therefore, most of the [FM] *Rhizophora stylosa* species (78%) could be also classified as [FM] *Ceriops australis* or 43% of [FM] *Ceriops australis* as [FM] *Rhizophora stylosa*. The extent of overlapping pixels are shown in Figure 224 (left). This means that the species are not separable to a SA of 0.1 rad. In fact, the ASD spectral data shows that both species are spectrally similar with a SA of just 0.05 ± 0.06 (from Table 69, p. 497, Appendix G.3).

Although in Figure 223 the location of [FM] *Ceriops australis* appears sound (based on field work studies), it is not for [FM] *Rhizophora stylosa* species, which tends to be located on sandy shores or even in open seawater (International Union for Conservation of Nature and Natural Resources (2019) and Queensland Government Department of Agriculture and Fisheries (2013)). The region displayed in Figure 223 (right) appears far inland. One solution is to select a smaller SA, to increase the spectral similarity between reference [FM] *Rhizophora stylosa* and the image spectra. However, this results in even more uncertainty (see below).

Further concerns were uncovered for the SAM classification of [FR] *Avicennia marina*. Using a relatively large SA of 0.1 rad, the lack of green regions in Figure 224 (right) suggests a small population for the species. However, field work shows this species as the most abundant mangrove of all species (E. Paling et al. (2003) - in particular; Table 50, p. 374 of Section 4.6.4).

The reasons for the poor spectral matching between image and ASD spectra were briefly discussed using Figure 59 (p. 180 of Section 4.4.2). For convenience, the figure is copied here to Figure 225, which shows a large difference in spectral quality between airborne and ASD reflectance spectra; with the airborne spectrum being particularly noisy. In fact, the SA between the airborne (PHPA_Ref) and [FR] ASD *Avicennia marina* spectra is 0.11 rad.

The large SA between airborne and ASD spectra highlights the difficulty in matching up pixel spectra with a specific cover type. The same difficulty extends to other cover types, for example, [FR] *Acaria sp.* (not a mangrove) where the SA is 0.11 rad and suggests that the green class region (where SA is less than 0.10 rad) is meaningless when incorporating the spectral uncertainty. Both airborne and ASD spectra are shown in Figure 226.

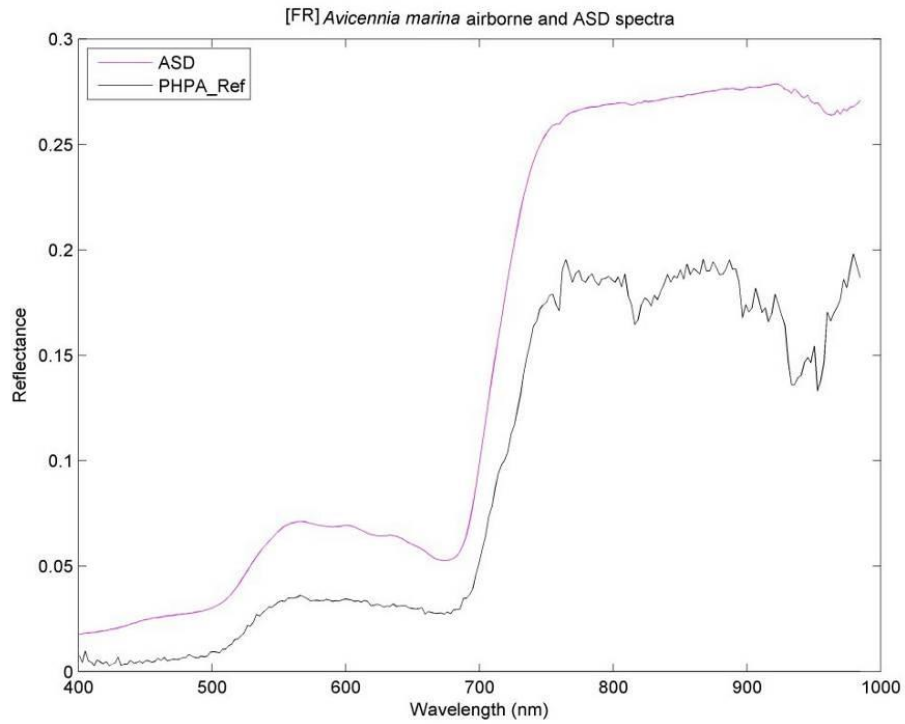


Figure 225: Plot showing ASD and airborne (PHPA_Ref data) spectra for [FR] *Avicennia marina* on Finucane Island. The SA between ASD and the airborne spectra is 0.09 rad.

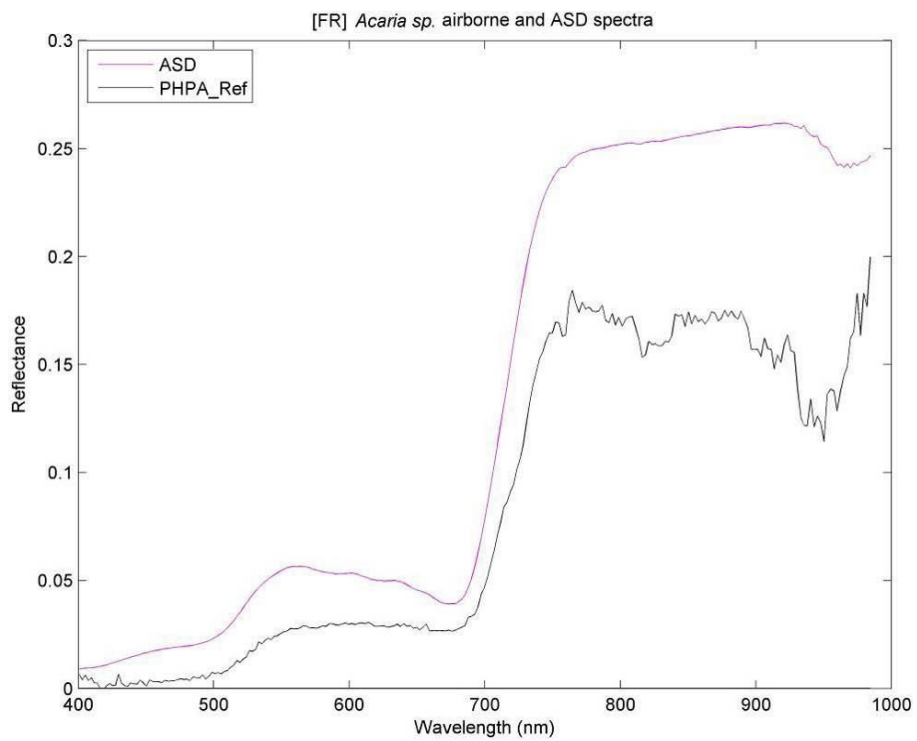


Figure 226: Plot showing ASD and airborne (PHPA_Ref data) spectra for [FR] *Acaria sp.* on Finucane Island. The SA between ASD and the airborne spectra is 0.11 rad.

Note that the position of the airborne spectra is known and matched with the corresponding ASD spectral sample. Further details are found in Section 4.5.9.6.

The large SA difference between pixel and ASD spectra poses a significant problem in classification, particularly as the SA between several mangrove species are smaller. This means that classification to species level leads to highly ambiguous results. For instance, the SA between AIR and ASD for [FR] *Avicennia marina* is 0.11 rad which is larger than the SA between [FR] *Avicennia marina* and all other mangrove species (when incorporating the uncertainty). Therefore, using the [FR] *Avicennia marina* reference spectrum to calculate a SA pixel-by-pixel is ambiguous as it actually matches up all other species of mangroves. Therefore, SAM is unable to confidently classify mangroves at species level.

In theory, it is possible to use pixel spectra themselves for training. However, locational uncertainties in matching pixel and field location persists. These factors were discussed in Section 4.5.5.

There are additional factors to complicate the identification of cover types with pixels, as discussed earlier in Section 4.4.2 (e.g. spectral changes due to the time delay between the recording of airborne and ASD spectra).

As SAM is insensitive to spectral brightness differences, the difference in brightness between airborne and ASD cannot be an issue. However, brightness changes in spectra (causing mismatch between the two) will cause SA changes. This erodes further confidence in using SAM for mangrove species classification.

J.2 SAM using Image Reference Data

This section investigates the ability of a SAM supervised classifier in removing all cover types except vegetation, from an image using only pixel spectra. A small test image is selected from the PHPA_Ref image and used for classification. The number of bands is left untouched – i.e. the test image contains 246 bands. It consists of a region consisting of vegetation, water and a beach. Actual classification is performed using a C++ program, although the visual environment and selection of training pixels is performed using ENVI.

The following steps outline the approach undertaken.

Steps:

1. Using ENVI, select training (pixel) samples of similar spectra for each cover type from the hyperspectral image. For example, collect (at random) five spectra of deep water.
2. A mean spectrum for the five spectra is calculated. A SA between each spectrum and the mean spectrum is calculated, with the maximum SA difference (i.e. maximum deviation from the mean) recorded. The process is repeated for each cover type.
3. Each pixel spectrum is compared to the maximum angle (of step 2) for each cover type separately. Therefore, classification proceeds on the same image for each cover type separately using the maximum angle and the particular cover type's mean spectrum for training.
4. Classification results are stored in binary ENVI .BIP file format, where classified pixels are either black or white. The black regions are superimposed onto grey or true colour images, while white pixels are used on a black background and shows, more clearly, where the classified pixels are located.

A written C++ program classifies an ENVI .BIP file type. The advantage of the .BIP file is that pixel spectra are read and therefore processed sequentially one after another. There are dramatic increases in performance using this format. In fact, for the (400 m by 400 m) test region, displayed in Figure 227, classification for the three cover types was achieved in only 20 seconds using the ENVI .BIP type file (having file size of 75 Mb). The processing was performed on a on a Microsoft Windows 7 64bit Intel Quad Core-2 Q9550 2.83GHz processor. The C++ 64-bit executable program was generated using Intel Composer XE 2013 under MS Visual Studio 2010.

Three regions are identified, as indicated by the red, yellow and black regions in Figure 227. Initially, five spectra were randomly located within each cover type. The three regions are; 1) deep water (shown by the red region), 2) shallow water (yellow) (containing a mixed proportion of water and sand), and 3) beach (black)

(i.e. sand). These samples were recorded using ENVI and a library built for each cover, then exported to three separate text files. Each of the text files contained the location of the sampled spectra, the wavelength and the five sampled spectra in columns. These files were then separately used (i.e. one cover type at a time) into the C++ classification program.



Figure 227: The three regions used in this preliminary study (400 m × 400 m) superimposed onto a true colour image.

The black coloured pixel areas (about a quarter the way up in in Figure 227) contain no data and lie between two adjacent flight lines. Notice that the vegetation at the bottom flight line (in the south east) appears darker than the flight line above. This characteristic was identified early on in the thesis research, although the extent was unknown until a formal investigation was conducted, ultimately leading to the normalisation work.

Figure 228 shows three spectra, each one corresponding to each of the three regions defined in Figure 227. The extent of noise in all three airborne spectra are evident. The deep water spectrum (in red) is generally darker (up to $0.75 \mu\text{m}$) than the shallow water spectrum (in yellow) due to absorption, while the beach spectrum is particularly bright in the NIR.

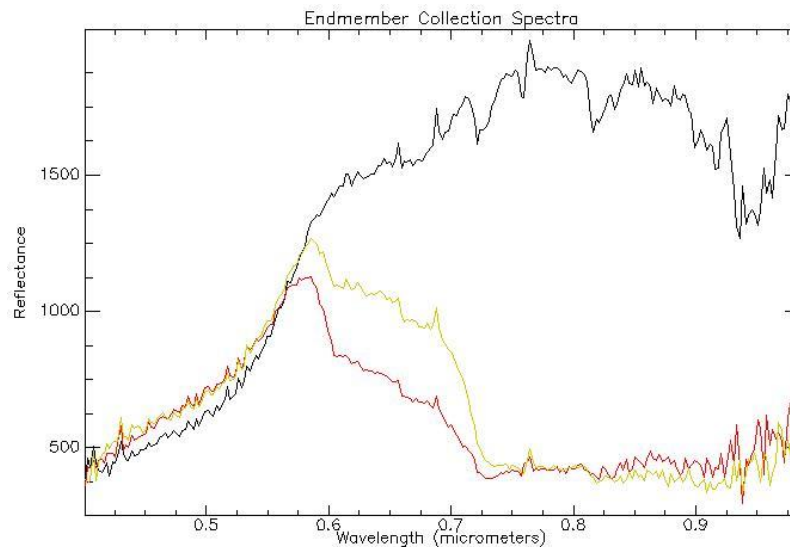


Figure 228: Example pixel spectra collected for training.
The red spectrum corresponds to a spectral sample in deep water, the yellow spectrum for a pixel located in shallow water and black for a pixel in the black (beach) region as indicated in Figure 227. Note that these spectra are not mean spectra but individual pixel spectra instead. The reflectance is scaled by 10,000.

Let ϑ_{DW} , ϑ_{SW} , and ϑ_B , denote the SAs (in radians) for deep water, shallow water and beach, respectively. These angles are those used in the classifier. The default angles (i.e. maximum angle between mean spectra of a cover type and their five training spectra) are: $\vartheta_{DW} = 0.11$ rad, $\vartheta_{SW} = 0.13$ rad, $\vartheta_B = 0.02$ rad. Figure 229 shows the classification result using these default mean SAs. The black regions (showing classified pixels) are superimposed onto the true colour image Figure 227. In the discussion hereforth, the missing data pixels between the adjacent flight lines are ignored; referral to black pixels only relate to classified pixels, not missing data. In Figure 230 each pixel in the grey-image actually has stored the magnitude of the SA, reminiscent to the concept introduced for the NDVI image of Figure 61 (p. 191 of Section 4.5.1) but now instead storing SA sizes. The left image of Figure 230 shows the classification result, where black pixels represent the deep water cover type as classified pixels, using only deep water training pixels. Similarly for the right image of Figure 230, but where the pixels represent shallow and deep water classified pixels (in black). It appears that deep water is distinct from shallow water, as deep water is located in the north-east region with shallow water further toward the beach area. Figure 231 shows just the classified pixels but in white colour (not

superimposed onto an image). This time, the left and right images (of Figure 231) show only the classification results for deep water (left image) and shallow water (right image). Clearly, there is overlap, where shallow water pixels are located in deep water regions, and vice versa. The union of both left and right images of Figure 231 gives the result displayed in the right image of Figure 230. The classification result using only the beach cover type is shown in Figure 232 – the white pixels. The union of Figure 231 (both) and Figure 232 gives rise to the classification pattern displayed in Figure 229.



Figure 229: Classification result using default spectral angles.
The black regions represent individual classified pixels (with the exception of omitted data between the adjacent flight lines).

By increasing the SA, more pixels are included by the classifier. The shallow water and deep water cover types become inseparable. It is important to note that if the angles are made too large, then the whole region is classified for that particular cover type. Therefore, pixel regions need to be inspected each time SAs are adjusted to find a suitable trade-off. Figure 233 shows the classification result when $\vartheta_{DW} = 0.5$ rad (left image) and $\vartheta_B = 0.5$ rad (right image), leaving only about 3% of the image unclassified. Note that the white pixels represent classified pixels. The result clearly shows that all water is accounted for, while the beach result is over-represented and encompasses the vegetative regions.

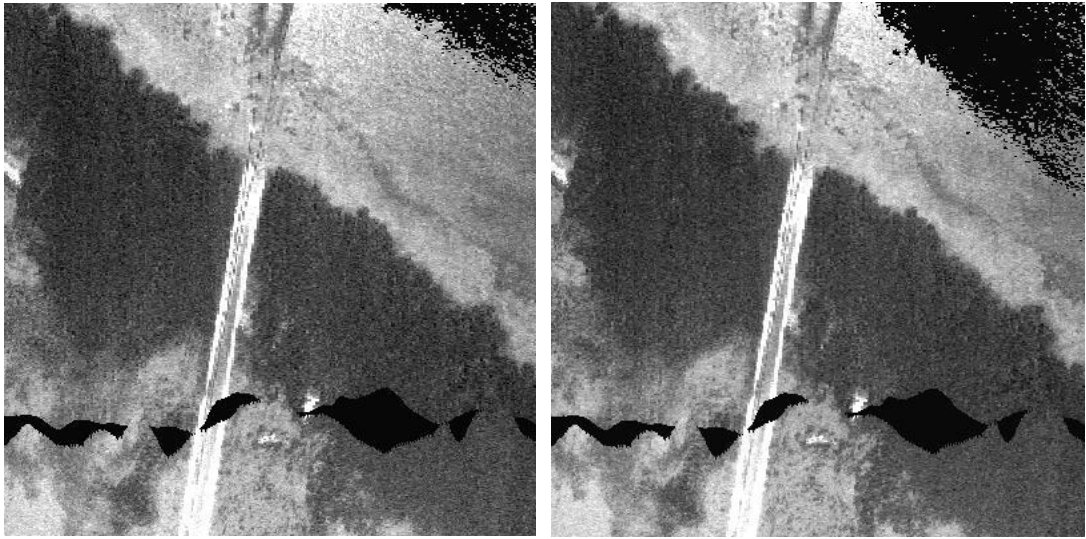


Figure 230: Classification result using the default angle for deep water (left). The image on the right shows overlap between shallow water and deep water classification.

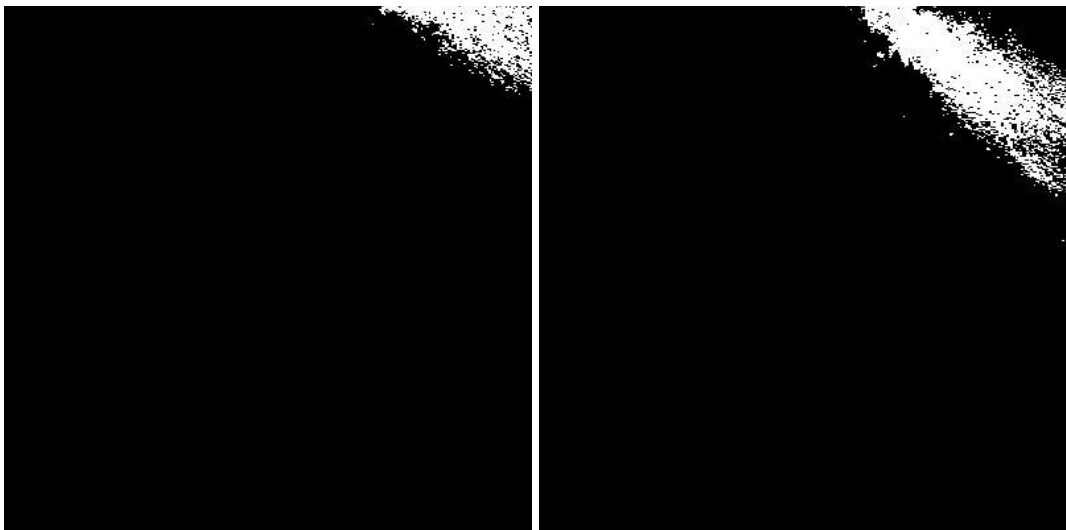


Figure 231: Classification result using the default angle for deep water (left) and shallow water (right). There is a significant amount of overlap between the two cover types.

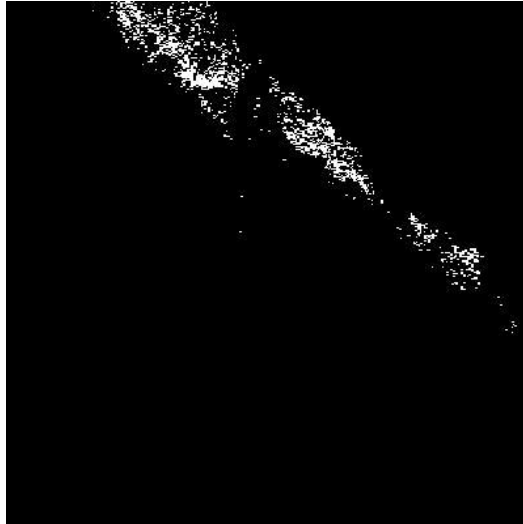


Figure 232: Classification result using the default angle for the beach only.

Decreasing the SA for the beach is clearly required. The default SA $\vartheta_B = 0.02$ rad is too small, as it only classifies a portion of the beach (Figure 229 and Figure 232), while $\vartheta_B = 0.5$ rad is clearly far too large (Figure 233, right image). A good result was produced when using $\vartheta_B = 0.2$ rad, as shown in Figure 234 (left image), leaving vegetation intact and removing sand and water cover types. However, the white pixels along the beach region were left unclassified. A satisfactory result Figure 234 (right image) was obtained by increasing ϑ_{DW} to 0.6 rad but leaving ϑ_B as 0.2 rad.



Figure 233: Classification result using a SA of 0.5 rad. The left image shows that water is classified, while the right image corresponds to the beach result. Note that the white pixels represent classified pixels. There are no overlapping classification pixels in this result.

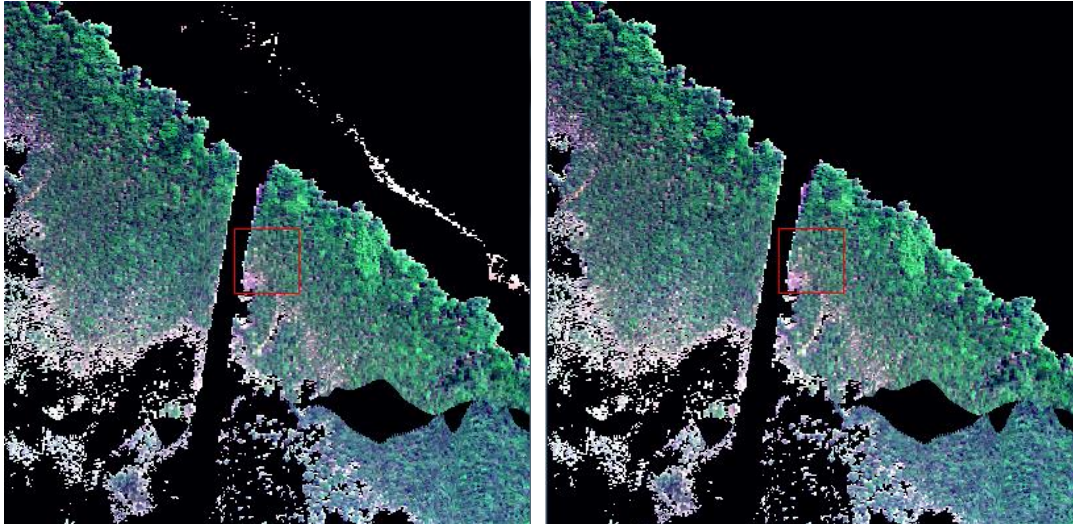


Figure 234: Classified results where: $\vartheta_{DW} = 0.5$, $\vartheta_{SW} = 0$, and $\vartheta_B = 0.2$ (left image) and $\vartheta_{DW} = 0.6$, $\vartheta_{SW} = 0$, and $\vartheta_B = 0.2$ (right image).

The work of this section demonstrates that by using just a handful of pixel spectra for training, with appropriate SAs, the SAM supervised classifier produces satisfactory results. Of course, in this case, vegetation spectra could be identified using vegetative spectral samples or the NDVI. Although not tested, small SAs are expected to distinguish vegetative pixels from non-vegetative pixels due to the large difference in spectra between vegetation and non-vegetation, mainly due to the red-edge. The black spectrum in Figure 228 (corresponding to the beach) exhibits some similarities to vegetative spectra; the high NIR reflectances. However, although there is an 'edge' near 550 nm, it is not the characteristic vegetative red-edge, which is located near 700 nm. Therefore, overall, a small SA should distinguish vegetation from other cover types in the scene. The work in this appendix 'did things the other way around' just to prove that the supervised method works.

Appendix K Technical details behind Normalisation

This appendix elaborates on the technical details behind generating a normalised image. Both computational and technical details are described.

K.1 Steps

The basic normalising steps may be summarised as follows:

1. Application of an appropriate mask (vegetation (Section 4.5.6) or land (Appendix L.2)) to each radiance/reflectance image flight line segment file (i.e. all 137 files).
2. Line-averaging each Radiance/reflectance masked flight line segment, over each band. The mean line-averages results are written to files; image data of odd numbered flight lines were inverted.
3. Flattening of local (i.e. individual) flight lines by rotating the mean (i.e. line-averaged) result (for each band) about the centre.
4. Detrending the global line.
5. Lining up adjacent local flight line edges.
6. Spectrally correcting the image flight line segments to generate a new set of normalised flight line segments.
7. Georectification of each normalised flight line segment.
8. Stitching each normalised flight line segment to form one complete image.

These steps are further elaborated in Appendix K.3.

K.2 Further Background

Flight lines were processed starting at flight line 1 (south), then proceeding to flight line 2 (next line north) etc. The flight line order was discussed in detail in Section 3.3. To recapitulate, the sequential order is (from south to north):

1, 2, 3, ... , 23, 28, 25, 29, 24, 26, 27.

(i.e. the first 23 flight lines are in sequential ascending order and flight line 27 is the northern-most flight line).

Computationally, the PHPA_Ref file is read from west to east and north to south. Therefore, line 1 actually represents the northern-most line of pixels (in a west-east direction) and is part of flight line 27. Therefore, graphically, all line-averaged plots begin with line 1, so the left-most region of a plot represents the northern-most region in an image.

As each odd-numbered flight line is inverted with respect to even-numbered flight lines, this presents an issue - without inversion, the last line (sample 965) of flight line 27 will appear as line 1 on the graph. We take as 'standard' the even-numbered flight lines, so all odd-numbered flight lines must be inverted. Further clarification details are given in Appendix K.4.

K.3 Technical Elaboration of Steps

The steps to produce a normalised image were outlined in Appendix K.1. This section provides more explicit detail for each step.

Step 1 (masking):

With the exception of one image (i.e. N_Ref_NoMask), all images were masked prior to normalisation (refer to Figure 124 and Figure 125 of Section 4.5.9.4). More specifically, it is each flight line segment that was masked and normalised.

Three masks were developed in this thesis – vegetation (Section 4.5.6), land (outlined in Appendix L.2) and res (details are provided in Appendix L.7 - although this mask was initially discussed briefly in Section 4.5.9.4).

There are 137 flight line segment files in all. Masking each of these files led to 137 masked flight line segment files (i.e. new files). Each individual masked flight line took about 3 - 5 mins to produce – note that flight lines consist of flight line segments. For example, flight line 1 consists of flight line segments 1a, 1b and 1c. Therefore, the whole of flight line 1 took approximately 3 - 5 mins to produce.

The radiance/reflectance flight line segment files were stored in .BSQ format, and although .BIP gives enhanced performance, a file conversion to type .BIP was not required for this first step. Each file segment is 965 samples in size (with line size generally around 3000), amounting to 1.5 GB for each flight segment. This easily fits into computer memory (total RAM was 16 GB). Each .BSQ file was converted to .BIP format in memory, then masked and directly saved into .BIP file format. In the end, 137 file segment files were in .BIP format, ready for the next step. The .BIP files process much faster than .BSQ files, hence the conversion.

The whole normalisation process was coded in C++, as it brings major performance enhancements compared to script based languages (e.g. Python or MATLAB). However, all normalisation plots were produced using MATLAB, reading in formatted text (.txt) data files as produced by the C++ programs.

Step 2 (line-averaging):

Each spectrum line had to be averaged, meaning each line of pixels (in an west to east direction) for the stitched image (PHPA_Ref), but in a north to south direction for individual flight line segments (discussed later in Appendix K.4). For flight line 1, this meant calculating a mean over each individual file (e.g. 1a, 1b, 1c), for all 965 lines (i.e. lines of pixels) and for each individual band (except masked 'black' pixels, which do not contain spectral data). For odd-numbered flight lines, the mean results were written in reverse order to 29 .txt (text) files (one .txt file per flight line) due to image inversion. Writing each odd-numbered flight line in this manner eliminates an additional step of having to invert each odd-numbered flight line (segments) file, thereby increasing computational efficiency. Computationally, it took approximately 2.5 hours to produce these .txt files (29 in all - one for each flight line).

These .txt files contain stored line-averaged radiance/reflectance data (for each band) and for each pixel line (965 in total). A MATLAB program extracted the four B,G,R and IR bands for plotting, to facilitate further analysis (e.g. Figure 106, p. 261 of Section 4.5.9.1).

Step 3 (local flight line rotation):

This step marks the first step in the normalisation process, graphically amounting to rotating each 'wavy' line for each flight line (for each band) about the centre. An example plot was given in Figure 106 (p. 261 of Section 4.5.9.1). Figure 235 gives a simplified schematic representation, where the 'wavy' flight lines are straightened. Note that there are 246 bands in total but just one band is considered in the examples given in this section (i.e. Figure 235 to Figure 239).

Just 15 discrete points are displayed in Figure 235 and in a magnified view of the (continuous) 965 point flight line. The blue 'dot' represents the centre of the flight line, which is diagrammatically located at line number 8, but in reality is located at line 483. If these points lie in a line containing a negative/positive slope, then the direction of rotation (about the flight line centre) is anti-clockwise/clockwise. The effect of rotation de-trends the brightness change in the north-south direction within an individual flight line.

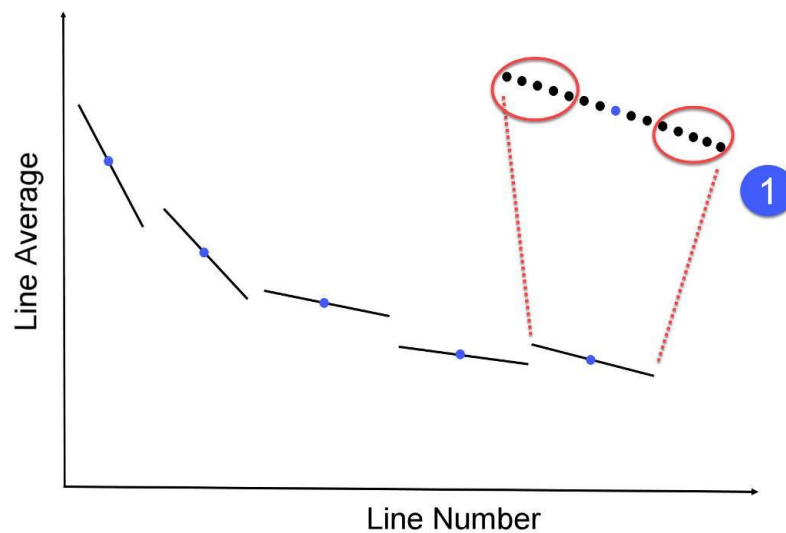


**Figure 235: Simplistic representation of the first step of normalisation.
Only one band is considered in this example.**

In the first step of the normalisation process, flight lines are rotated by calculating two single mean values, each from a group of 5 values at each end of each line (as circled in red in Figure 235). A linear line is then constructed between these two mean values, which is then rotated to form a 'flat' (i.e. horizontal) line of zero gradient. All other line-averaged values are adjusted accordingly and their values stored in data files in plain text ASCII format (.txt files). For all the 5 flight lines displayed in Figure 235, the rotation about the centre point (the blue dot) is in the anti-clockwise direction, as all gradients are negative. Computer data processing itself was very fast, taking only about a minute to calculate all 29 flight lines.

Figure 236 shows the final result simplistic representation of rotating each flight line of Figure 235.

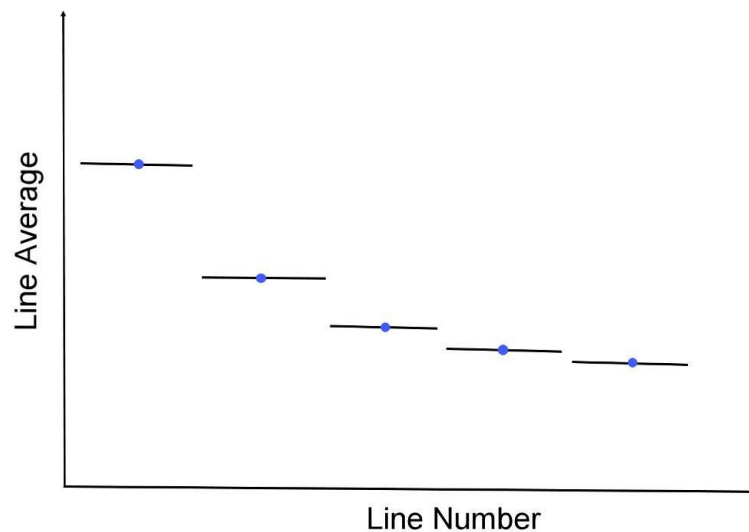


Figure 236: Simplistic representation for the effect of rotating all flight lines. Only one band is considered in this example.

Step 4 (detrending global line):

Although the brightness trends within each flight line are now eliminated, as depicted in Figure 236, there is still an overall trend between individual flight lines.

Step 2 of the normalisation process is very similar to step 1 but instead of rotating about a single flight line, the rotation is now performed over the whole scene. Again, a linear line is constructed with the centre of rotation at flight line 15. A single mean point is calculated for each of the 29 flight lines (one for each band).

In Figure 236, the blue points represent these single point means, as the flight lines are 'flat' in this simplistic representation. Next, a single point mean is calculated from the first group of these means (i.e. the blue dots in the plot) and another single point from the last group of means. These groups are 4 points in size. Relating this back to the PHPA_Ref image, this means using the average band values from flight lines 1 to 4 (the southern end) and calculating a single mean (for each band). The process is then repeated for the northern end i.e. using flight lines 27, 26, 24 and 29.

A linear line is then constructed between these two means. Figure 237 helps to explain the concept, although only 5 mean points are shown (the blue points) and only for one band; there are a total of 246 linear lines in practice (one for each band). The dashed line marks the approximate position of the linear line, while the "X" marks the position of the centre of this line.

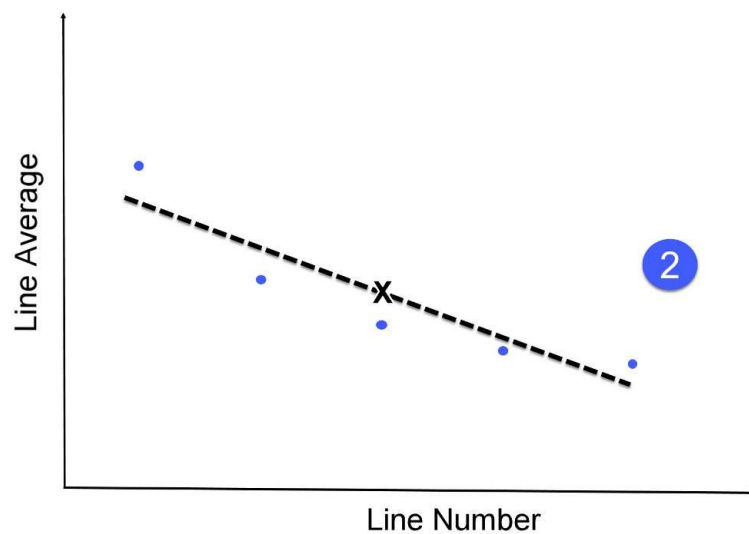
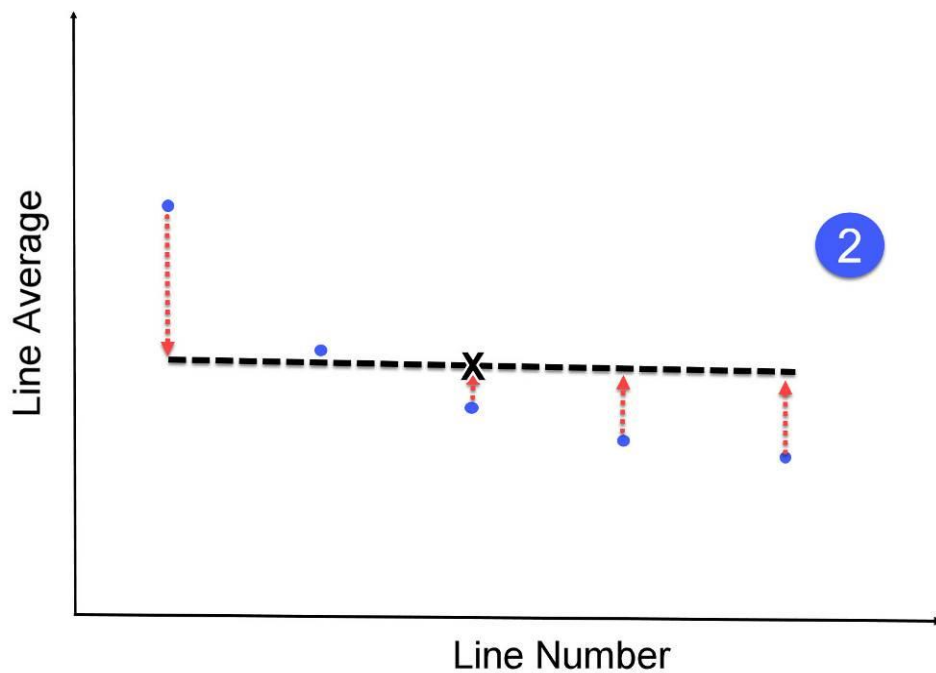


Figure 237: Simplistic representation of the second step of normalisation. Only one band is considered in this example.

Whereas each linear line in Figure 236 is local (i.e. applied to each flight line independently), this linear line is global as it extends over all flight lines. The rotation is also on a global scale (whereas previously it was local); the effect which is shown in Figure 238.



**Figure 238: Simplistic representation for the effect of rotating the global linear line
Only one band is considered in this example.**

As for step 1 previously, each line-average is now adjusted by moving line-averages accordingly. Also, new .txt files store the adjusted line-averages, with the whole processing completed in a minute.

The process of global detrending is now complete, defining step 2 of the normalisation process. It has the effect of eliminating the overall brightness bias over the whole scene (from flight line 1 in the south to flight line 27 in the north).

Step 5 (joining flight line edges):

This normalisation step removes the gaps between adjacent flight lines by calculating the difference between the adjacent edges. Figure 239 helps explain the concept.

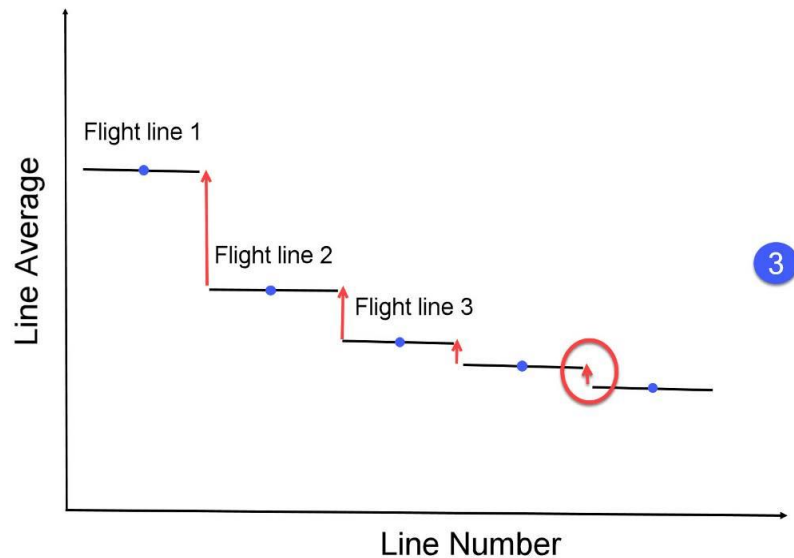


Figure 239: A simplistic representation of the third (and last) step of normalisation. Only one band is considered in this example.

Note that, this figure does not follow from Figure 238 as it now shows an global trend. The gaps between the adjacent flight line edges (marked by a red circle) are exaggerated to help illustrate the concept.

After local (i.e. normalisation step 1) and global (i.e. normalisation step 2) corrections, the gaps (or 'jumps') between adjacent flight line edges need lining up. The first flight line (i.e. the one on the left) is left unchanged. The edge of the second flight line is adjusted to line up with the first. Then the third flight line is adjusted to the second, and so on. The process is recursive and applied to each band separately.

Relating this back to earlier work, Figure 106 (p.261 of Section 4.5.9.1) clearly shows these jumps in brightness between flight line edges – it makes no physical sense why changing the line of pixels by one (in a west-east direction) should affect

the brightness to such a large extent (e.g. the jump between the southern-most line number for flight line 3 and the northern-most line number for flight line 2). Therefore, step 3 of normalisation lines these edges up, by moving the whole flight line 'up' or 'down' (as represented graphically). All flight lines were moved with respect to the flight line 27 (the northern-most) – i.e. flight line 27 is left unchanged, flight line 26 (the next one) is adjusted to line up the northern-most edge with the southern-most edge of flight line 27. Then, flight line 24 is lined up to flight line 26, and so on, in a recursive manner.

Since flight line 27 contains no negative spectra, it leaves all normalised spectra positive as all adjustments are made with respect to this flight line.

Computationally, the 29 flight line-averaged .txt files obtained from the normalised step 2 process were thereby modified to line up any flight line gaps between adjacent flight lines. Overall, all 29 flight line .txt files now contain the final normalised line-averages. From this, it is possible to adjust the original image spectra to form new normalised (more consistent) spectra, as described next.

Step 6 (creating normalised flight line segments):

Using the original (i.e. as produced from the un-normalised image e.g. PHPA_Ref_VI) mean data files (from step 2) and the normalised mean data files (from step 5 above), all pixel spectra in each line and each band is adjusted; thereby leading to the normalised image. There is the possibility that the brightness adjustment results in an integer overflow; this was also catered for by setting large brightness values to zero.

The process of normalising each spectrum shifts each radiance (or reflectance) value in a positive or negative direction (as a result of rotation – e.g. an individual flight line or the global line), thereby potentially generating values that are too large. The ENVI .BSQ file allows, by default, integer values of up to 32767 (short int limit) as the binary data is stored as 2 bytes per value. This means that the normalising process may result in overflow values. As the code was written in C++, an overflow may result in a circular definition where values appear as valid but are actually invalid. For example, in C++ $32767 + 1$ may result in a negative number (e.g.

-32768 but it is likely to also depend on the compiler). This issue can be overcome by defining each data value as a 4-byte entry; however, that doubles the actual file size. Given that the 137 files (which defines the 29 flight lines) require some 166 GB of data, any size increase not only increases storage requirements, but also processing and memory requirements (as each file is read into memory for processing). An individual file is around 1.5 GB and there may be up to 6 per flight line. This amounts to 9 GB of memory to line-average a flight line. Doubling this means using all available memory (18 GB). Given that the computer used in this thesis has a limit of 16 GB, some serious hard drive thrashing would occur, dramatically slowing down processing speed.

In view of these problems, and given that we are primarily interested in vegetation anyway, the super-bright regions were therefore deleted by using a threshold. This means that spectral band values exceeding the threshold were set to zero. This threshold was defined by examining several spectra using ENVI's regions of interest tool. The threshold was selected to ensure that the chances of excluding any band in a vegetative spectrum would not be excluded.

Computationally, it took about 4 - 7 mins to produce each new flight line (i.e. with all segments; e.g. flight line 2 contains only 2 segments and took 3.5 mins, while flight line 5 contains 6 segments and took 8 mins).

Care had to be taken with the mean data files, as they are written in reverse order with respect to odd-numbered flight line files; otherwise, the data is stored in the wrong order. In effect, the inverted files had to be inverted again prior to actual normalising the input flight line segment files. In addition, twice inverting the file allows the direction to remain intact with respect to the original input files. This is important as the original of the inverted files thereby retains the 'correct' direction with respect to the .GLT (georectification) files – these are in the order as recorded by the flight.

From a processing viewpoint, the new radiance (or reflectance) files were produced to point in the same direction as the original (supplied) radiance (or reflectance) files.

The output format for the new radiance/reflectance files was .BSQ, as the georectification process 'prefers' this format for efficient processing (see next step).

Step 7 (georectification of normalised flight line segments):

Although most processing favours the .BIP format, this is not true for georectification. A significant speedup factor is achieved using .BSQ files instead of .BIP files prior to applying the .GLT files for georectification.

During the course of the thesis, ENVI .BSQ files had to be converted to .BIP and vice-versa many times. A C++ program was written to eliminate the monotonous task of clicking several times in ENVI for each of the conversion process. In fact, while ENVI took around 10 mins to convert a flight line segment file (e.g. 1a), the C++ program only took 1.5 mins. Considering that 137 files need converting, this amounted to about 19.5 hour saving (23 hours down to 3.5 hours).

The .GLT files were applied to each of the 137 .BSQ reflectance files by using an IDL script, thus greatly facilitating the process. This has the effect of correcting the geometry of the image. The ENVI help file states that a .GLT file contains “map locations for every pixel”. A projection is also selected to place geographic coordinates onto each pixel (longitude, latitude). The selected projection is: UTM, Zone 50 South.

The georectification process took around 30 seconds per file if the image (i.e. each flight line) format was of type .BSQ (versus 4 mins for a .BIP formatted file). Furthermore, experimentation revealed that if the flight line files were of type .BSQ and georectified, then the output files were .BSQ. However, if the input flight line segment files were of type .BSQ but the .GLT files were converted to .BIP format and used for georectification, the flight line files were of type .BIP. The GLT files were supplied (to the PhD candidate) in .BIL format.

Step 8 (stitching normalised flight line segments to form a complete image):

To form our final 98 GB normalised image, the individual 137 (1.5 GB maximum file size) normalised flight line segments were stitched together using the ENVI Classic application. Each file segment was converted from .BSQ to .BIP format, as it was desired to have the final (stitched) file in .BIP format (which is much faster from a processing viewpoint).

If the individual .BSQ files were retained, the final stitched image of 98 GB took 18.5 hours to convert to .BIP format. As the normalised flight lines segments were already stored as .BIP format, no conversion is necessary. However, if they were in .BSQ format, it is much faster to convert file segments (e.g. fl01a, fl01b, ...) to .BIP prior to the stitching process. This conversion takes around 2.5 - 3 hours (using the developed C++ program) and saves a lot of time overall in the end.

Using ENVI Classic, stitching was performed using: Map -> Mosaicking -> Georeferenced. Crucially, the “**Data Value to Ignore**” must be set to 0 (zero), or flight lines will exhibit large gaps between them (see Figure 240). Flight lines with missing data (zero) will otherwise overwrite overlapped flight lines containing valid data. Setting this to zero allows those (i.e. zero) flight lines to become transparent, thereby displaying non-zero values from other flight lines.

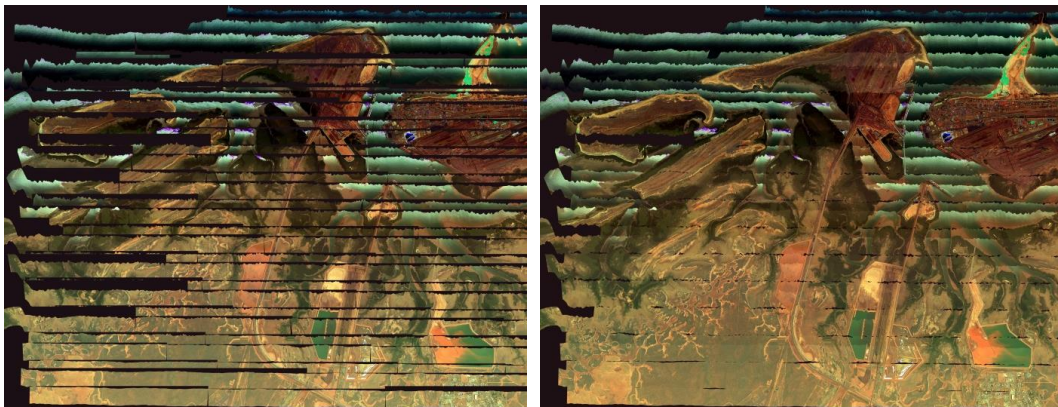


Figure 240: a) Incorrectly stitching an image and b) the right way (true colour images).

As several normalised images were produced using the same settings, an ENVI template file was created. This template file would then be modified easily using a “search and replace” function for subsequent flight line segment files.

K.4 Flight Line Behaviour and Georectification

As previously mentioned, the stitched image (Figure 42, p. 141 of Section 3.3) is comprised of 137 flight line segments. In that image, each flight line segment consists of exactly 965 horizontal pixels (called samples). The number of vertical pixels (called lines) vary from 2500 to 3100 but 3000 lines is particularly common for flight line segments.

Figure 241 shows an image for flight line segment 1b (i.e. the second segment of flight line 1). Notice that the image orientation is 'vertical' rather than 'horizontal' as in the stitched image. The spectral data is stored in ENVI .BSQ file format and a file size of 1.5 GB (typically). As the values are read one-by-one, they form the numbers starting in the northwestern-most pixel followed by the next pixel value to the right and so on. Overall, the order is left to right and top to bottom (of the image).

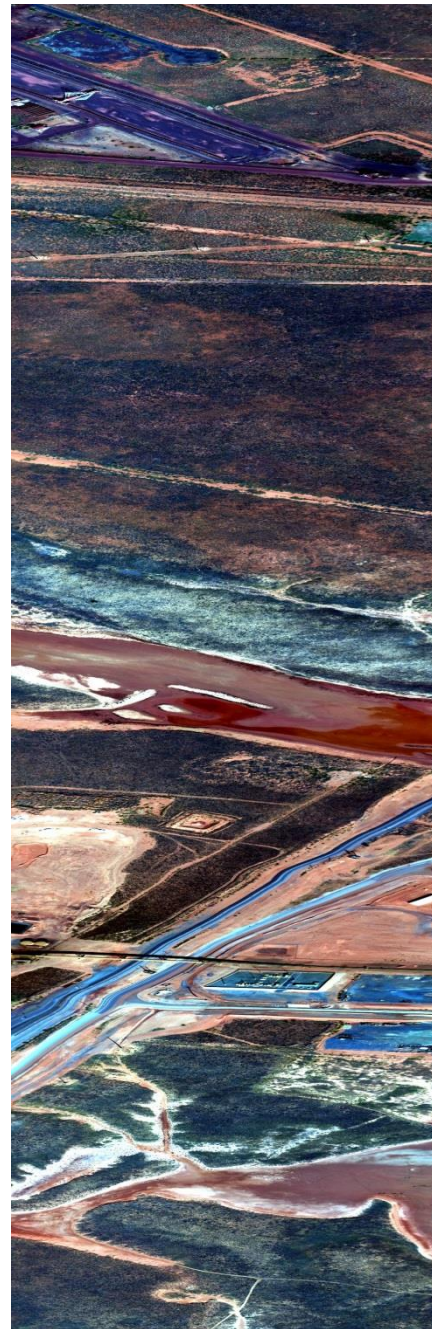


Figure 241: True colour image of an uncorrected georectified PHPA_Rad flight line segment 1b.

Notice that the geometry in these flight line segments are distorted. This is apparent when considering the vertical lines in the lower half of the image, representing straight roads. The distortion is caused by the pitch and roll of the aircraft (Campbell & Wynne, 2011, p. 21).

By default, none of the flight line segments are georectified. Note that each pixel spectrum is unaffected by the geometric distortion.

The associated georectified image is shown in Figure 242 for flight line segment 1b. Notice how the image orientation is now anti-clockwise. This time, the roads in Figure 241 appear straight due to georectification.



Figure 242: True colour image for the georectified PHPA_Rad flight line segment 1b.

Next, consider the uncorrected georectified PHPA_Rad flight line segment 2a, as displayed in Figure 243. The corresponding georectified image is given in Figure 244.

Previously, for flight line segment 1b, the georeferenced image (Figure 242) is obtained by rotating the PHPA_Rad image (Figure 241) anti-clockwise. However, this time (for flight line segment 2a) the PHPA_Rad image (Figure 243) is rotated clockwise in the georectified image (Figure 244).

In terms of data processing, the direction must be taken into account so that data is processed in the same consistent manner across all flight lines (e.g. when line-averaging in Section 4.5.9.1).

The direction of rotation of a flight line segment relies on the order in which data were recorded during the airborne flight. A georectified image for flight line 2 must be rotated in a clockwise direction. This is due to the airborne flight moving from east to west, so that the sensor records data in the opposite order compared to that before (i.e. flight line 1). Effectively, this amounts to a reordering of pixels in terms of flight line numbering. If this were not accounted for, the line-averaging result would be wrong. Therefore, prior to line-averaging, each odd numbered flight line segment had to be inverted to comply with the 'standard' direction as defined in the PHPA_Ref image (Figure 42, p. 141 of Section 3.3). All C++ code written had to factor this in, adding in a layer of complexity.



Figure 243: True colour image of an uncorrected georectified PHPA_Rad flight line segment 2a.



Figure 244: True colour image for the georectified PHPA_Rad flight line segment 2a.

Practically, to maintain the correct ordering of pixel data being read by the program, flight line segments must be inverted. This consists of exchanging the northwestern-most pixel with the southeastern-most pixel and so on. The result is illustrated in Figure 245.

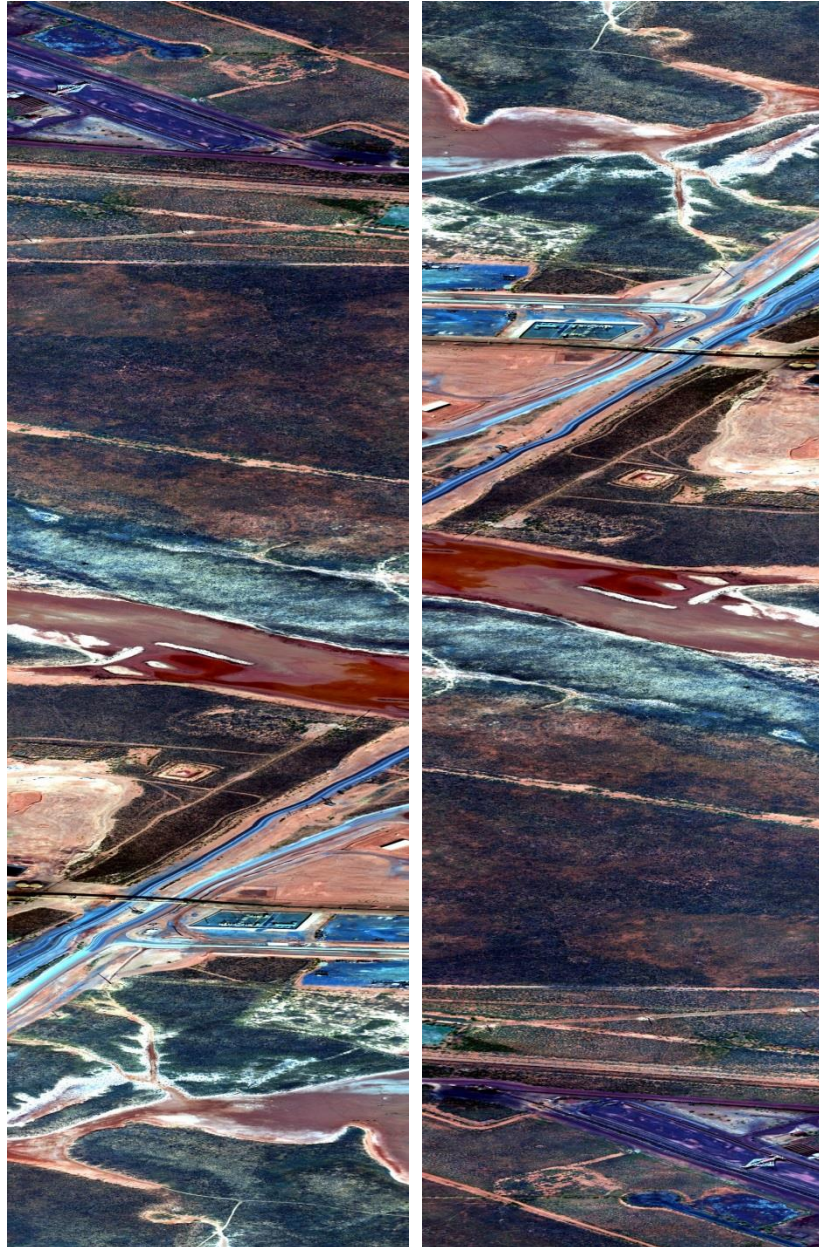


Figure 245: PHPA_Rad image for flight line segment 1b. The left image shows the default orientation, while the right image shows the inverted image.

Computationally, data is now read correctly by starting from the northwestern-most pixel and moving right to the end before proceeding to the next line down and repeating the process. Unfortunately, this has the effect of swapping line-averaged lines; line 1 is now line 965, and so on. This must be rectified to ensure the ordering is correct for each inverted line-averaged result (including plots). A quick fix is to write the lines in reverse order to line-averaged data files.

In theory, it is possible to apply the geographic lookup table files (.GLT) to the inverted image. However, that leaves the coordinates all wrong. Therefore, after

processing, inverted files were inverted back again prior to being georectified; effectively, a twice inverted image generates the same image direction as prior to the inversion (i.e. the original image). This consideration forms part of step 6 (Appendix K.3) of the normalisation process.

The way georectification works is explained in the notes supplied with ENVI Classic Help; pixels are relocated to their exact positions (if an exact match is found) or by using a nearest-neighbour pixel. Although this minimises geometrical 'warping', the disadvantage of this approach is that a spectrum for an adjacent row would therefore affect the spectrum in the current row. Since all spectra are modified equally by row, but differently to another row, this means that the corrections made to each row now overlap and "pollute" the neighbours.

The rotation of flight line segments raises a dilemma with line-averaging terminology. Referring back to Figure 102 (p. 256, Section 4.5.9.1), the PHPA_Ref image has 9005 lines (vertical pixels) and 23768 samples (horizontal pixels). Each of the sample pixels were averaged across (horizontally) for each of the 9005 lines – termed 'line-averaging'. Figure 241 now shows 965 samples and 3000 lines. The 'line-average' is now actually taken over each sample now instead of lines (i.e. averaging vertical pixels for each sample). So, line-averaging is not always over lines of pixels! However, in the georectified image of Figure 242, this is the other way around, due to the image rotation. The stitched image is actually composed of these 'rotated' images. Nevertheless, it is understood that line-averaging for a flight line segment refers to an average taken over each of the 965 samples – effectively, pretending that the image has been rotated.

Appendix L Additional Normalised Hyperspectral Images

In addition to the constructed N_Rad_VI image (Section 4.5.9.2), several other approaches were made to obtain spectrally consistent images. It turns out that the N_Rad_VI image led to the best thematic map, which is why the earlier discussion (i.e. under Section 4.5.9) relates to that image.

This appendix discusses the different approaches taken in order to construct normalised images (i.e. in addition to the N_Rad_VI image outlined in Section 4.5.9.2). The line-averaging process is identical to that covered in Section 4.5.9.1, in addition the normalisation steps detailed in Section 4.5.9.2. Also, the plots use the same colour definitions as previously.

Due to the high similarities to previous work, detailed explanations are restricted. The focus here is to show the different approaches taken to obtain normalised images.

L.1 N_Ref_NoMask image construction

The normalisation process, outlined in Section 4.5.9.2, used radiance flight segments and a vegetation-mask to construct a normalised image.

This section uses no mask at all and constructs a normalised image based on using all available image data. The line-averaged result is given in Figure 246.

Note that this figure is identical to Figure 106 (Section 4.5.9.2, p. 261).

The first step in the normalisation process (outlined in Section 4.5.9.2) rotates each flight line of Figure 246 about the centre, with the result shown in Figure 247.

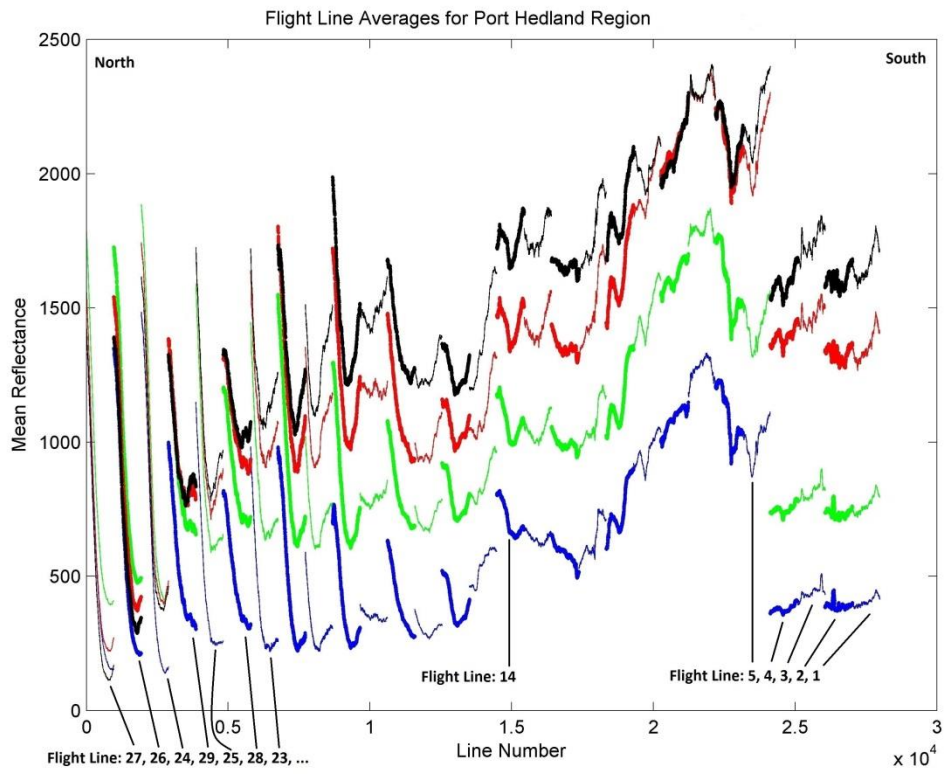


**Figure 246: Line-averaging plot, showing the mean result over each flight line for the reflectance image (PHPA_Ref).
Note: the reflectance is scaled by 10,000.**

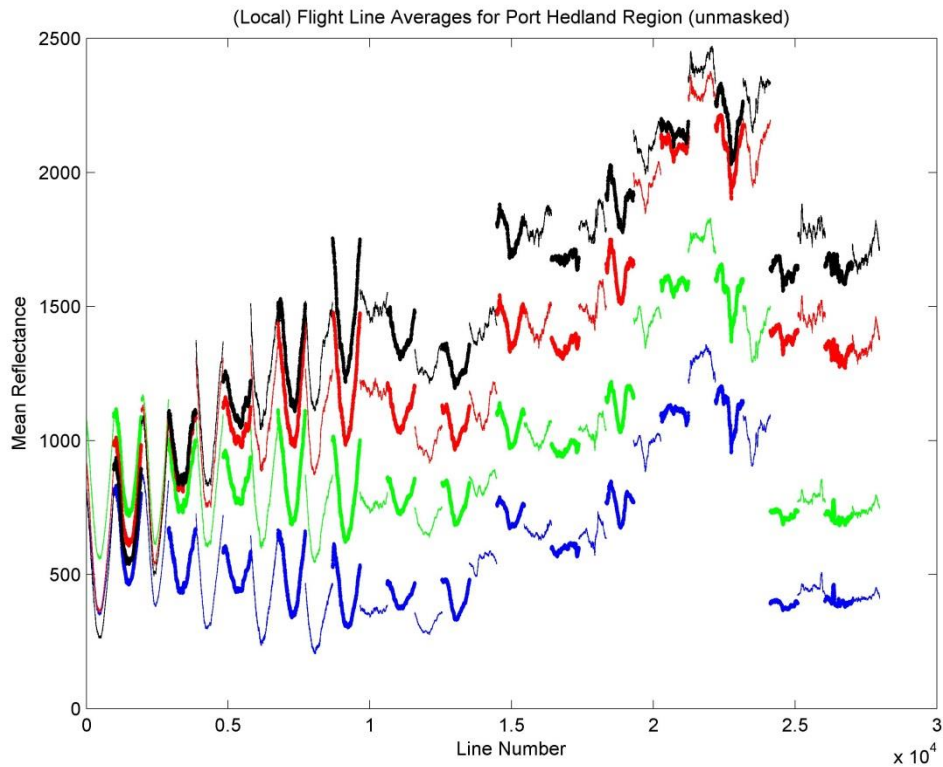


Figure 247: Mean reflectance (scaled by 10,000) of four spectral bands for the 29 flight lines of Figure 246 but with each individual flight line rotated about its centre.

Note: The unit on the vertical axis is left as reflectance. In actual fact, during this intermediate normalisation step, it falls between a normalised reflectance and the pure reflectance unit.

The rotation of individual flight lines greatly improves the brightness-consistency, particularly for the southern-based flight lines (e.g. flight line 1 to 4). The effect of rotation on the northern-based flight lines creates parabolic-like shapes for each individual wavelength. However, there are still discontinuities between adjacent flight lines. The aim is to equalise the brightness both within and between flight lines. Originally, the line-averaged reflectance for the northern-end of each northern-based flight line (e.g. flight lines 27, 26, 24, 29, 25, 28, 23) was exceptionally high. This is caused by sunglint (see Figure 106, p. 261 of Section 4.5.9.1). After rotation, both the northern and southern ends of flight lines are now equal in brightness.

With each of the individual flight lines having been rotated about the centre, there remains two final steps in the normalisation process - global detrending and joining up of individual adjacent flight lines. The final result is depicted in Figure 248.

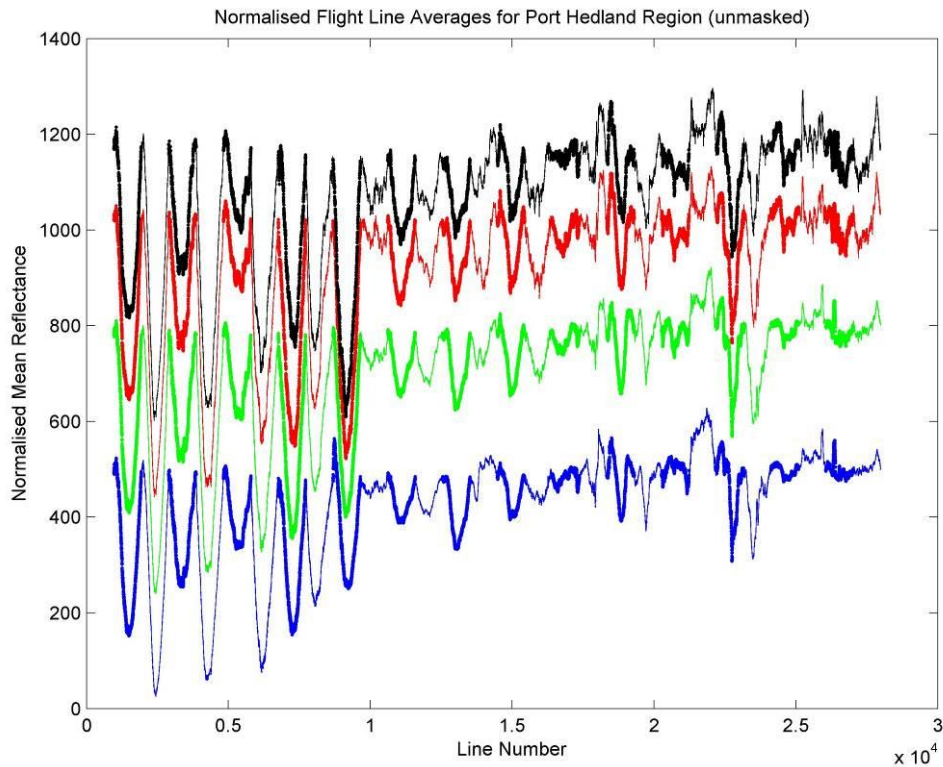


Figure 248: Using the result of Figure 247, where each individual flight line is rotated about the centre, this final plot shows the effect of global linear detrending in addition to the joining up of adjacent flight line edges. Note: the reflectance is scaled by 10,000.

Note that the vertical axis now has units of normalised reflectance instead of reflectance. Each brightness value (vertical axis) is no longer a mean reflectance but rather a normalised mean reflectance, as the mean reflectance was normalised.

It is also appropriate to emphasise that the mathematical processes described (i.e. flight line rotation, global linear de-trending and flight line edge alignment) were all performed separately for each band, although only four spectral bands are displayed in Figure 246 to Figure 248 - the red, green, blue and NIR bands. The corrections applied to each spectral band are independent.

The normalised image is termed the N_Ref_NoMask image (Figure 249). For comparison purposes, the PHPA_Ref image has been copied to Figure 250.

Comparing Figure 249 with that of Figure 250 shows Figure 249 having distinct dark 'stripes' or 'bands' corresponding to the salt pond locations. The mean line-average from each band in the image is the same, however with the high reflectance of the salt ponds the reflectance of the land is decreased to compensate. Comparing the plots of Figure 249 with Figure 250 shows the normalising process as having decreased the brightness over the salt pond regions. In addition, both the northern flight lines (e.g. 29, 28, 25) and the southern flight lines (i.e. 1, 2, 3) are brighter in the normalised image. It should be noted that the bands selected for displaying images differ slightly to those in the plots, so the RGB image bands (defined in Section 3.3) do not have a one to one correspondence to that in the plot (RGB,IR) (defined in Section 4.5.9.1). The ENVI RGB default bands to display an image were given in Section 3.3; (B) 438.8 nm (G) 549.4 nm (G) and (R) 668.7 nm. However, as the B wavelengths range from 400 – 500 nm, a centre wavelength of 448.0 nm was selected (450 nm does not exist). For similar reasons, centre wavelengths were selected for G and R also. In all, plots were standardised to (B) 448.0 nm, (G) 549.4 nm, (R) 649.7 nm. The IR was selected to be close to the red-edge inflection point, with 718.8 nm selected.

In the case of the N_Ref_NoMask image (Figure 249), the normalisation process left a number of flight lines darker than the others. This is not surprising as the global linear detrending step is unable to cater for the non-linear trend apparent in Figure 246. As a result, the normalisation method is not very successful when applied to the complete image. The use of masks allows trends to be identified more readily and are more (globally) linear (particularly for radiance data); these observations stem from the work in the rest of the sections of this appendix.

The derivation of the N_Ref_NoMask_VI image (i.e. Figure 249) from the N_Ref_NoMask image (i.e. Figure 251) follows the same vegetative masking method as outlined in Section 4.5.7). Again, the _VI suffix indicates that a vegetation-mask (Section 4.5.6) has been applied to derive an image containing only vegetation.

Note that Figure 251 has been contrast enhanced to stretch the RGB colours over a suitable range. Further details are given in Appendix U.

The N_Ref_NoMask_VI image (Figure 251) is classified in Appendix P.1.

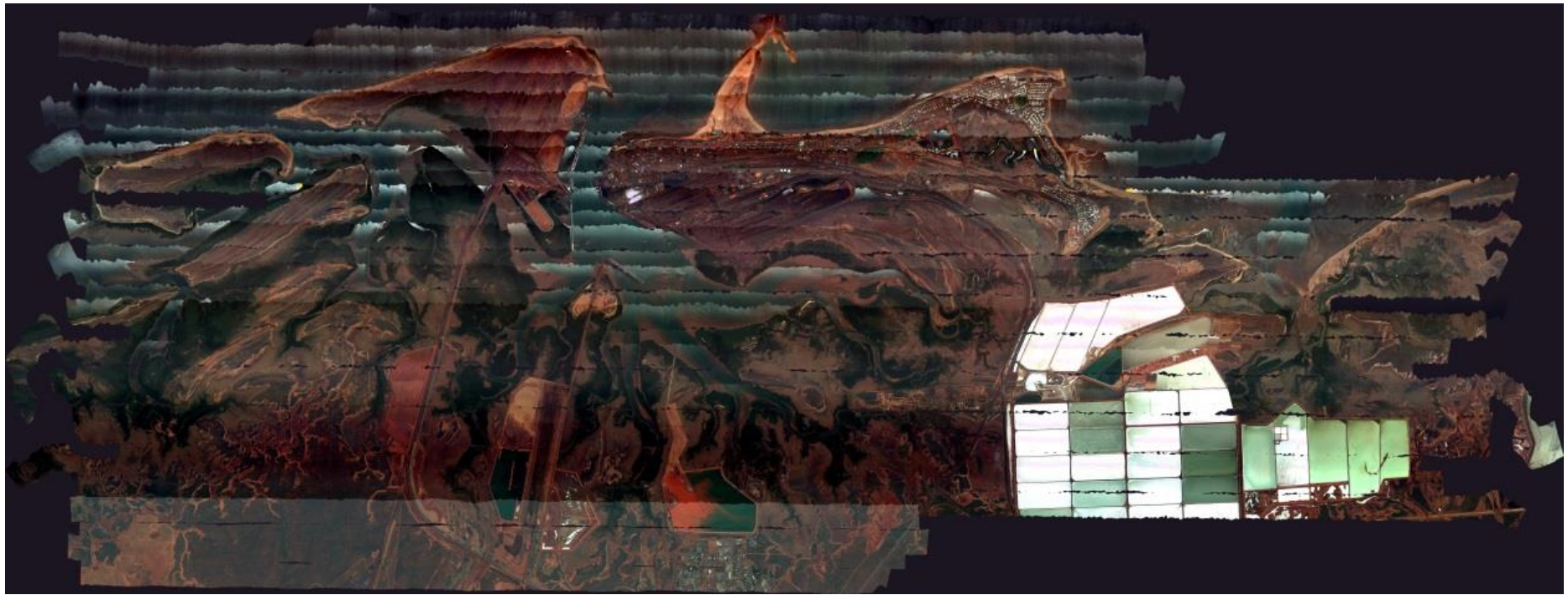


Figure 249: This true colour image shows the N_Ref_NoMask as constructed using the normalisation process. No mask was applied to the reflectance image, leading to poor brightness consistencies across multiple flight lines.

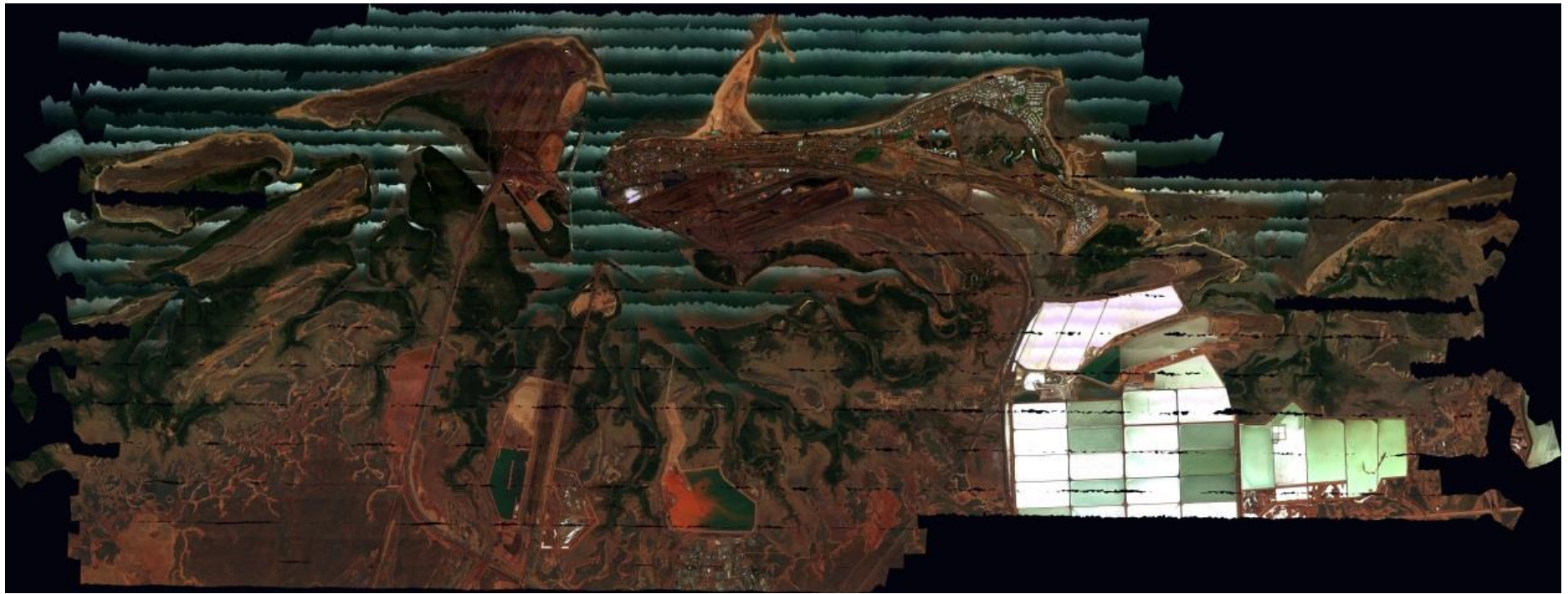


Figure 250: The true colour image of PHPA_Ref, as stitched from the PHPA airborne reflectance data.



Figure 251: The N_Ref_NoMask image of Figure 249 has been masked with the vegetation-mask of Section 4.5.6 and is referred to as the N_Ref_NoMask_VI. This image is ready for classification (results given in Appendix P.1). This image has been contrast enhanced to more 'accurately' display the true colours (using the process described in Appendix U). This image shows 'stripes' or 'bands' of varying brightness, as a result of the linear normalisation process.

L.2 Development of a Land-mask

The N_Ref_NoMask image (Figure 249, p. 578 of Appendix L.1) shows that the overwhelming brightness of the salt pond regions clearly overwhelms the line-averaged mean reflectance, thereby reducing the effectiveness of normalisation.

As demonstrated in Section 4.5.9.1, a global linear trend is more apparent when an image is masked for vegetation (i.e. by eliminating all non-vegetative pixel spectra). Other masks were also attempted. This section outlines a land-mask, which removes water from an image, and has the additional effect of removing salt pond regions but leaving soil, vegetation and urban structures (e.g. roads and buildings) intact.

During the thesis work, as the brightness issues of the PHPA_Ref image became apparent – thought possibly due to atmospheric correction issues - the radiance data were favoured for the development of a more consistent land-mask. The assumption was made that it was less affected by brightness problems, leading to a more consistent definition for a land-mask. Consequently, the land-mask developed in this section (and also the vegetative-mask of Appendix L.4) was developed using radiance data as opposed to reflectance data.

The process is actually a recursive situation, as the land-mask is required prior to obtaining an improved image, from which another (improved) land-mask can be derived. A compromise must be reached at some point in the process. As it turns out, the land-mask developed in this section proved highly satisfactory.

A mask, similar to that of Section 4.5.6 (using zeros and ones) but for each flight line segment instead, can be used to mask either radiance or reflectance-based data. The process is fast, as each radiance/reflectance image pixel is compared to the masked pixel. The purpose of the mask is to either accept a pixel or ignore it. A mask value of zero indicates that the spectrum must be eliminated (e.g. water), while a value of one indicates land where the spectrum is retained in a (new) land-masked flight segment. The cover types in both the radiance and reflectance datasets are (in reality) identical by pixel location anyway; only the actual spectral band values differ between the images.

The initial approach at developing a land-mask attempted to exploit the full set of hyperspectral bands to eliminate water from each of the flight line segment images. Both the unsupervised classification schemes k-means and ISODATA were utilised with the aim of creating a map containing water versus land regions (i.e. non-water). The merging (if required) of classes allows distinct land versus water regions to be defined, from which a mask is generated.

In practice, many flight line file segments contain water, in one form or another (sea, river, salt ponds, dredge ponds). Some flight lines do not contain any water, as found by spectrally examining the PHPA_Ref image (Figure 42, p. 141 of Section 3.3). Therefore, a small number of flight lines do not require classification; for instance, the following flight lines segments contain only water:

27: a,c,d

26: a

24: d

These flight lines segments are therefore completely masked, thereby eliminating any processing required. Further work categorised the remaining flight line segments in an attempt to identify those which require masking. Table 95 shows the flight line segments which contain a mixture of land and water (i.e. both) pixels or just land (i.e. no water). However, the results were not always clear, so round and square brackets were introduced to highlight uncertain results. Flight line segments surrounded by round brackets (e.g. “25: (e)”) suggests that the whole flight line segment contains water, but not with absolute certainty. Those surrounded by square brackets (e.g. “19: [d]”) indicates that the whole flight line segment contains only land, but again, not with complete certainty. In practice, it was not always clear from the image itself whether a pixel did indeed contain water, even when individual pixel spectra were examined.

Unfortunately, the analysis did not drastically reduce the workload, as still over 100 individual files had to be processed for the development of a mask.

Flight line segment	Flight line segment	Flight line segment
29: a,b,c,d	19: a,b,c,[d],e	09: a,b,c,d,e,f
28: a,b,c,d	18: a,[b],c,d,e	08: a,b,c,d,e
27: b	17: a,b,c,d,e,f	07: b,c,d,e
26: b,c	16: a,b,c,d,e	06: a,b,c,e
25: a,b,c,d,(e)	15: a,b,c,d,e	05: b,c,d,e,[f]
24: a,b,c	14: a,b,c,d,e	04: a,b
23: a,b,c,d,(e)	13: a,b,c,d	03: [b],c
22: b,c,d,e	12: a,b,c,d,e	02: [a]
21: a,b,c,d,e,f	11: a,b,c,d,e,[f]	
20: a,b,c,d	10: a,b,c,d,e	

Table 95: A list of flight line segments containing land and water.
Flight line 01: a, b, c consists of only land, so there is no entry in the table.

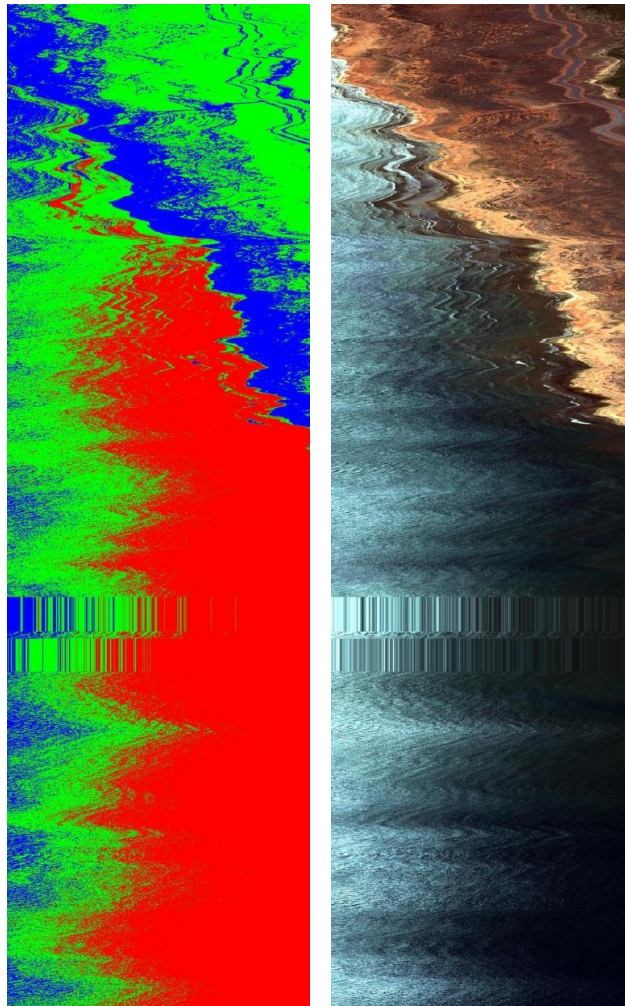


Figure 252: k-means classification result using three classes (left image) for flight line segment 29a (right image – in true colour).
The true colour image is inverted and not georectified.

To test the feasibility of using hyperspectral unsupervised classification (i.e. k-means and ISODATA) in distinguishing between land (which includes vegetation) and water cover types, a suitable test region was selected for further investigation. Flight line segment 29a was initially selected, as it contains the three main cover types of interest; a large body of water, land and a region of dense vegetation. Using the k-means classifier, this flight line was initially classified using three classes (aiming to represent water, land and vegetation). The result is shown in Figure 252. The result is clearly unsatisfactory; the green and blue coloured classes are found on both land and water. Even the road is classified as water! (or conversely, water classified as land!). Only the red coloured class shows a satisfactory result - that corresponding to the physical water cover type.

Classification using ISODATA also produced unsatisfactory results, despite defining various ranges for classes. It was anticipated that by increasing the number of classes, a separate class would form to define the road. Classes would then be merged to form the final mask (land and water). However, in practice, the results were unfavourable.

These unsupervised methods were further applied to several other flight segment files. Although there were few successful results, most were unsatisfactory in being able to distinguish between land and water. Another factor in this work concerns the amount of processing time for each flight segment - around 10 - 15 mins, despite using the .BIP file format (shown to be around 30% faster than .BSQ files for classification). To process the required set of flight line segments, some 22 hours is needed - if each file takes 10 mins to process (not to mention the time to set up each job in ENVI).

A second approach used the "Classification Workflow" tool of the ENVI 5 product. Using the Region of Interest Tool, appropriate training areas were selected from the image itself and categorised into land or water classes. The Maximum Likelihood classifier was then used to classify the untrained regions of the image. This classifier has a reputation of producing sound results with good performance. A similar approach had shown promising results for the SAM classifier (see Appendix J.2).

Compared to unsupervised classification (k-means and ISODATA), selecting suitable training data adds yet another step to the process; a tedious process when having to be repeated for all the files listed in Table 95.

In practice, selecting training data proved difficult at times, especially near the boundary between water and sand (i.e. the beach). It was difficult to determine (initially by eye and then spectrally) if those pixels contains water or if the coast just appears dark. In addition, there is the question of how muddy a beach needs to be in order to be considered (dry) sand. Further difficulties concerned working with geometrically distorted radiance images, where wavy shorelines tend to be almost unrecognisable - pixels ordinarily located on beaches were often difficult to discern in the geometrically distorted images. These factors clearly affect the ability of selecting sound training regions. Furthermore, the considerable amount of time spent selecting (appropriate) training regions was yet another issue.

In the end, the results were (like the unsupervised results) mixed for the several flight line segments tested. At times, there were clear issues with the end product, where regions of water were classified as land and vice-versa. Experiments were performed whereby training areas were small but numerous and compared against large training areas (less numerous - where the user basically classified the whole image by hand). This situation is not ideal with potential negative ramifications due to biased human-analyst decision-making, based on a limited selection of bands (i.e. the image itself is displayed using only three bands upon which the human analyst makes judgements).

Other experiments were conducted by selecting common regions as one class (e.g. water), and other regions as land or unknown. These classes were then merged together in the end product, requiring (manual) input by the human analyst (a monotonous task).

The approaches considered thus far made use of ENVI and the full set of hyperspectral bands for classification; but produced mostly unsatisfactory results. Clearly, another approach had to be developed – one that is automated by requiring minimal user input. Ideally, the approach would also produce the desired results in a timelier manner.

Consequently, the investigation went back to basics, by examining spectral differences between the three cover types. In particular, water, land and vegetative (pixel) spectra were examined in an attempt to determine a means of spectral separation based on radiance values at particular wavelengths. A program could then be written to automate the process, all with minimum user intervention. The disadvantage with this approach is that it only uses a limited set of carefully selected wavelengths.

Figure 253 shows several spectral samples (plotted using several colours) for different 'types' of water (i.e. deep dark water, shallow water, sunglint water), collected from flight line segment 29a radiance data. The spectrum containing the high radiance values correspond to sunglint water (displayed in aqua colour on the plot), while the low radiance values clearly represent dark water (e.g. the magenta plotted spectrum).

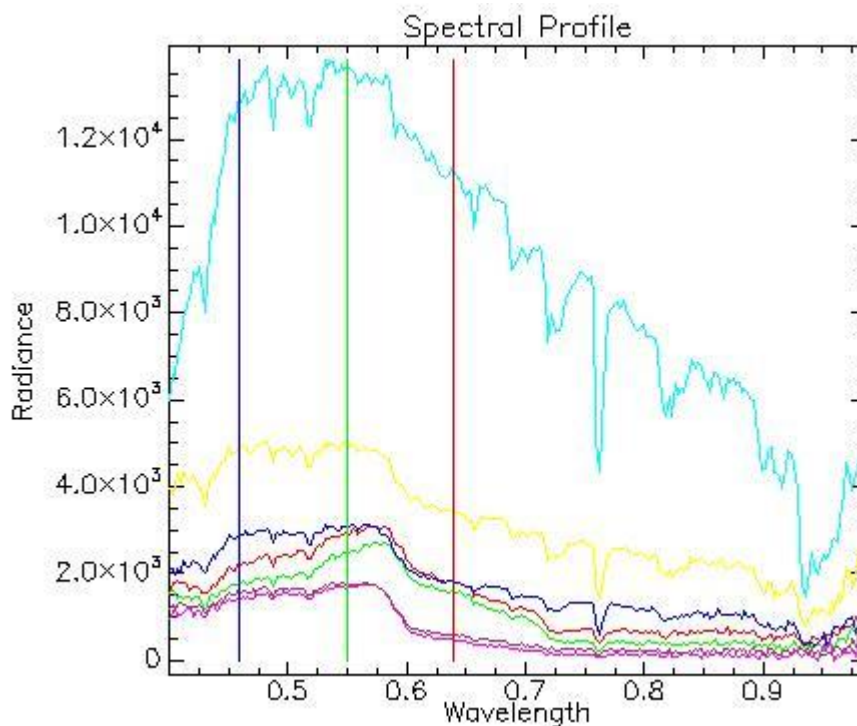


Figure 253: Sample spectra collected from flight line segment 29a for water (dark water as well as sunglint areas).
Note: The vertical scale are in units of radiance (scaled by 90) while the wavelength (horizontal scale) are in units of μm .

Although the spectral samples show a range of brightnesses, the overall gradient for water is negative between 0.5 μm and 0.8 μm (i.e. by drawing a line between the

radiance values corresponding to these two wavelengths). The same is true between 0.58 μm and 0.60 μm , but as that range is rather small, it is possible that further samples invalidates the negative gradient result over this small range. A noisy spike in the signal could also hamper this effect. A broader range allows for a broader-based gradient and subsequently 0.8 μm was selected.

In a similar manner, spectral samples for soil (Figure 254) and vegetation (Figure 255) are also plotted.

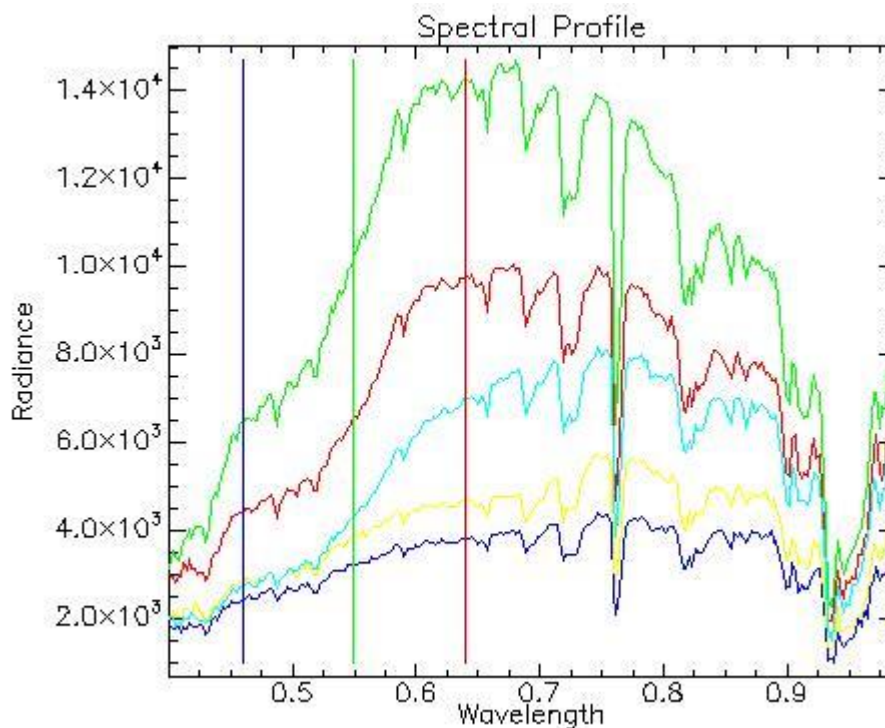


Figure 254: Spectral samples for soil from flight line segment 29a.
The italic notes beneath Figure 253 (p. 586) also apply to this plot.

As the vertical axis scales differ between the plots in Figure 253 to Figure 255, Figure 256 shows a single plot of spectral samples covering all cover types (i.e. soil, water (dark and sunglint) and vegetation) on one set of axes. This helps to identify spectral patterns between the spectral cover types.

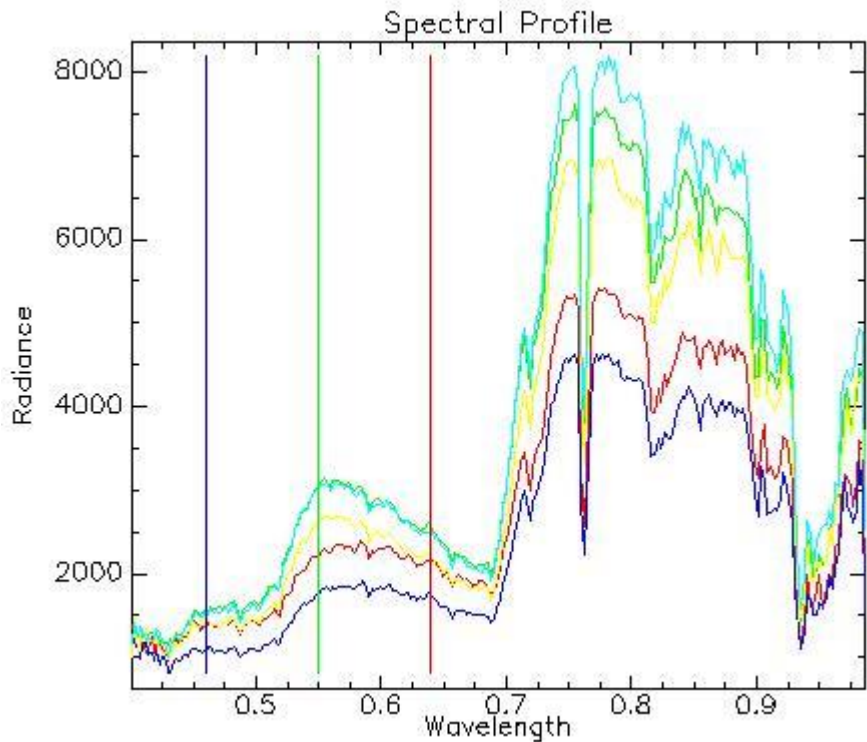


Figure 255: Spectral samples for vegetation from flight line segment 29a.
The italic notes beneath Figure 253 (p. 586) also apply to this plot.

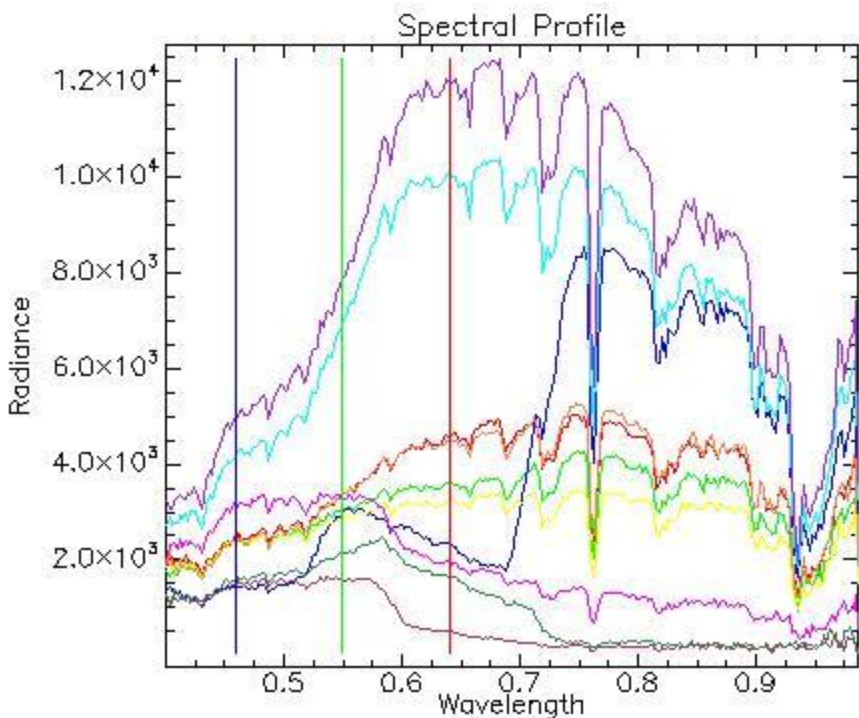


Figure 256: Spectral samples for soil, water and vegetation displayed on the same vertical scale for comparison.
The italic notes beneath Figure 253 (p. 586) also apply to this plot.

As discussed above, the gradient for water spectra is negative between 0.5 μm and 0.8 μm . The 0.7 μm was not selected as it defines the characteristic vegetative spectral region (i.e. the red-edge) and it was presumed that it is possible for some vegetation (not included in the sample) to contain similar radiances to that at 0.5 μm , thereby giving vegetation a near-zero gradient (reminiscent of soil). To minimise these kinds of possibilities, it was decided to use the higher radiance value at 0.8 μm to differentiate between the three cover types (water, soil and vegetation). Over this range, the gradient of water appears mostly negative, soil appears mostly flat (with small positive gradients), whereas vegetation is strongly positive.

To develop a land-mask, two methods were defined to spectrally distinguish between the cover types:

1. An average (in a similar manner to the mean-gradient method for vegetation of Section 4.5.2) using wavelengths 0.4825 to 0.5125 for interval 1 and 0.7743 to 0.8062 for interval 2. A mean gradient was then derived based on these intervals.
2. $\text{gradient} = \frac{R(0.8062) - R(0.5125)}{0.8062 - 0.5125}$, where $R(0.8062)$ is the radiance value at 0.8062 μm , etc.

The advantage of method 1 is that it is an average-based approach, so individual points are less sensitive to noise, while method 2 uses just two single points.

The gradient maps appear to show some promise in distinguishing water from land. The bright-white regions represent large positive gradient values.

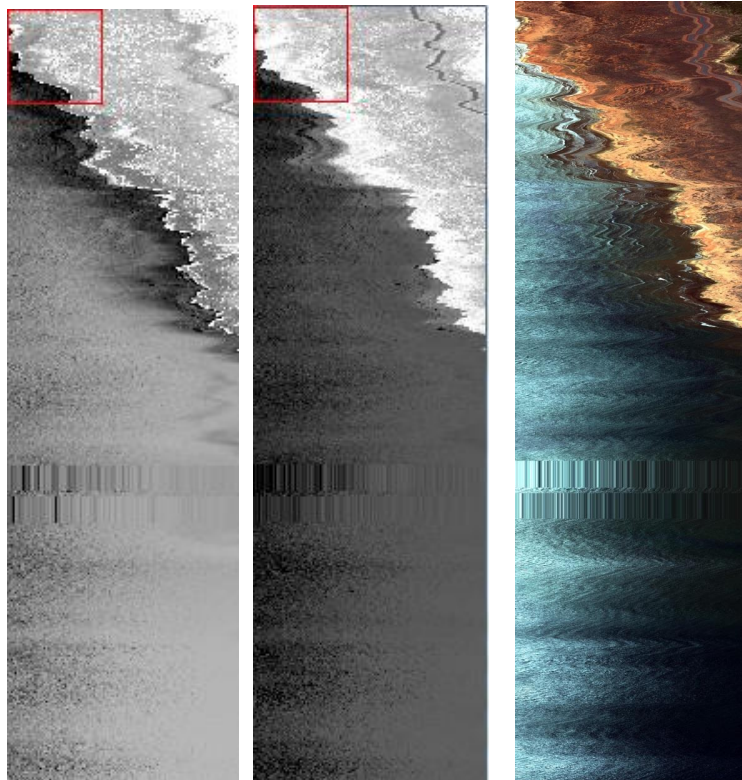
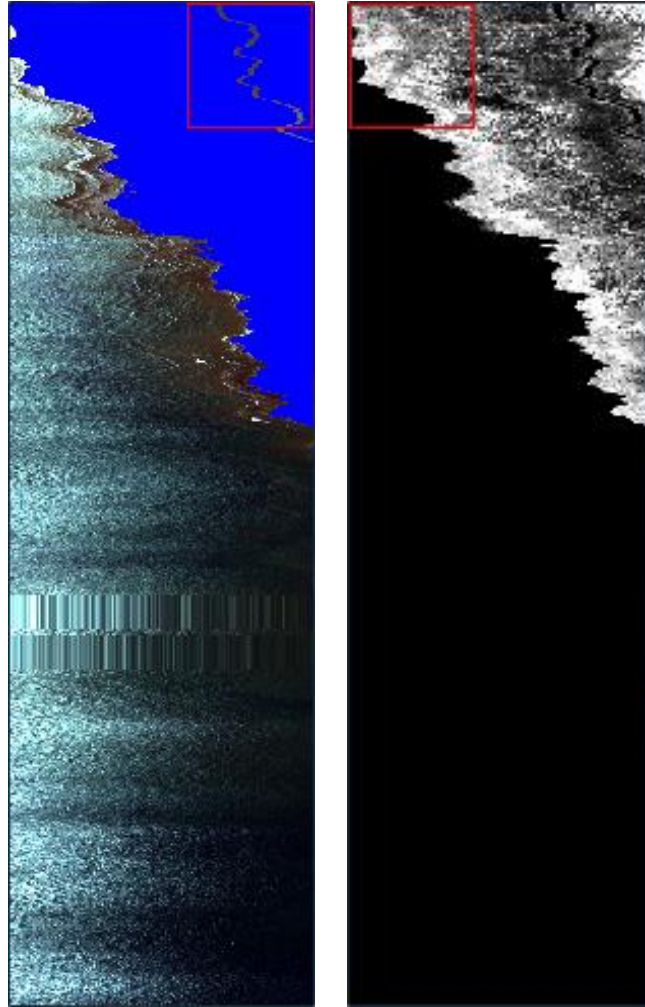


Figure 257: Gradient maps for a) method 1 (left), b) method 2 (middle). The image on the far right shows flight line segment 29a in true colour (which is the same as the right image of Figure 252).

The first method is a failure (shown in Figure 257a) as there are overlapping gradients between water and land (as shown by the similar shades of grey in water and land in Figure 257a – confirmed in practice by examining individual pixel values). Method 2 shows a particularly bright region (top right in Figure 257b) where gradients are positive. This is an encouraging result as it corresponds to a region of vegetation.

A clearer picture of the situation arises when a blue ROI is superimposed onto the true colour image (Figure 257c) containing only positive gradients. As method 1 was considered a failure, the result is not shown in Figure 258.



**Figure 258: Gradient threshold map for method 2 (left).
Blue regions contain positive gradients. The right figure (b) shows all
water masked out (in black), leaving only land and part of the road.**

The blue region for Method 2 clearly distinguishes water from land (Figure 258a). Figure 258b shows the result of removing all gradients less than zero. Interestingly, the road also contains negative gradients, thereby considered to be part of the water cover type (or indeed vice-versa). A land-mask containing roads would have little effect to line-averaging (prior to normalisation) due to their small number of pixels in relation to land pixels. After normalisation, a vegetation-mask eliminates all non-vegetation (i.e. including roads) prior to classification. The inclusion of a few road pixels is an acceptable trade-off in a land-mask which masks flight line segments in an efficient manner, both computationally and with no user intervention.

Encouraged by the result of Method 2, it was tested for numerous other radiance-based flight line segments. Of particular interest concerned the gradient behaviour over the salt-pool regions in flight line segment 5e. Ideally, method 2 removes these regions. The results are shown in Figure 259, where water is removed.

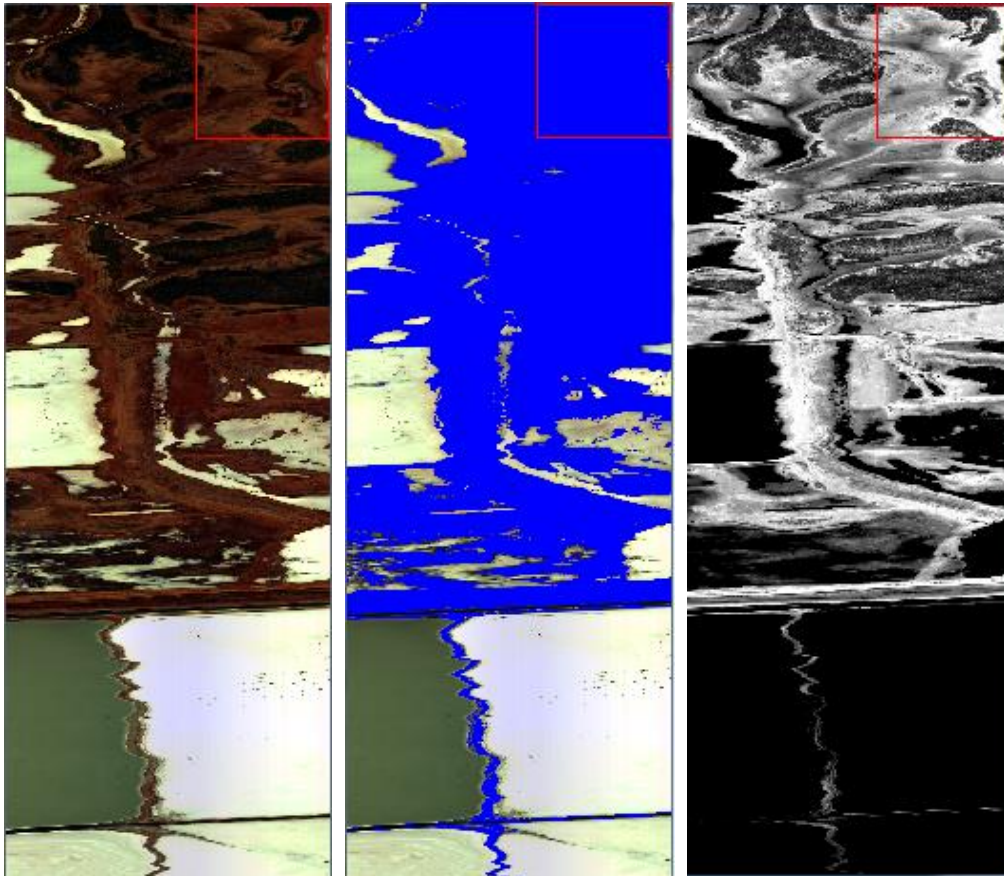


Figure 259: a) True colour image for flight line segment 5e (left, although an inverted image); b) blue region shows pixels that are retained (i.e. gradient > 0) (centre); c) gradient map, showing black regions that are masked out as a result of the gradient threshold (i.e. gradient < 0).

The behaviour of other flight lines were also investigated. The results for flight line segment 6b is given in Figure 260.

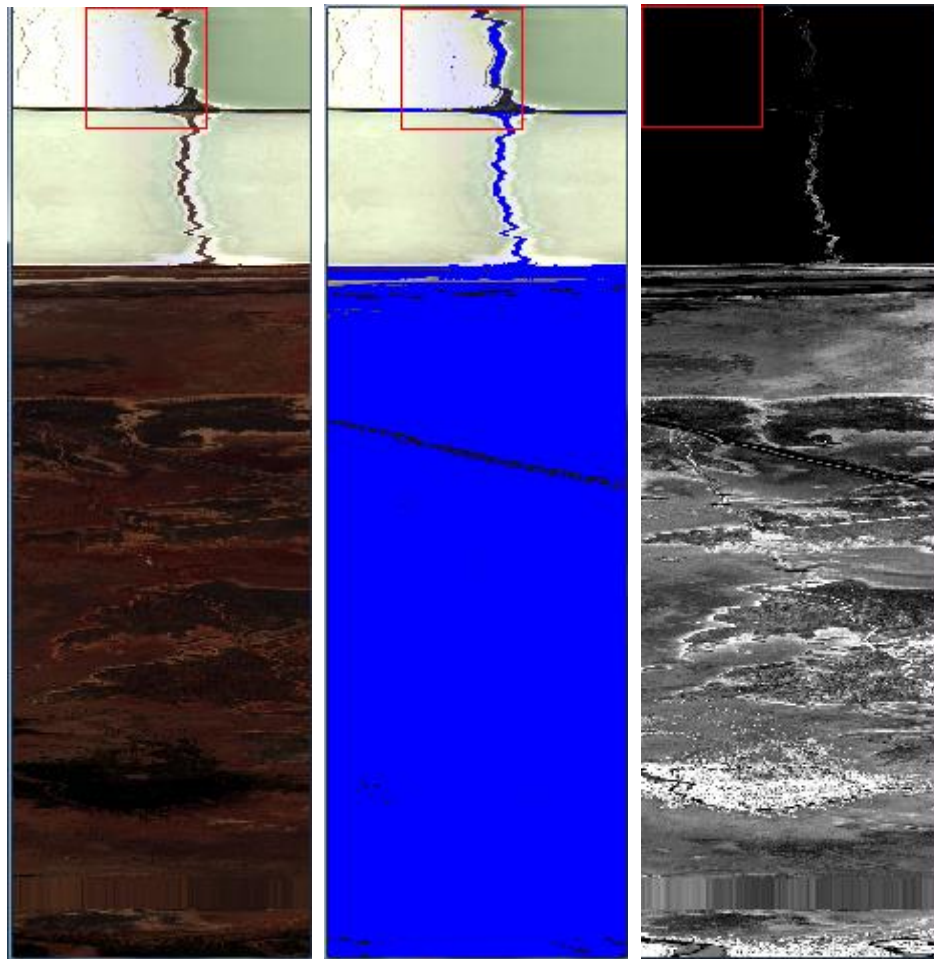


Figure 260: a) Original true colour image for flight line segment 6b (left); b) blue region shows pixels that are retained (i.e. gradient > 0) (centre); c) gradient map, showing masked out pixels in black.

The results are not perfect; a few pixels in the red 'boxed' region (of Figure 260) are inconsistently classified as water and non-water (as represented by the blue colour and shown in Figure 261). It is possible that some dust covers these regions, thereby 'mudding' the 'pure' water spectra. Encouragingly they amount to only a few pixels. It is possible that the erroneous pixels are eliminated using a different threshold. This was not investigated. The development of a 100% effective land-mask is also beyond the scope of the thesis objectives. The small number of erroneous pixels are not expected to cause a great effect in the mean line-averaging result, as they are outnumbered by a vastly greater number of 'correctly-masked' pixels.

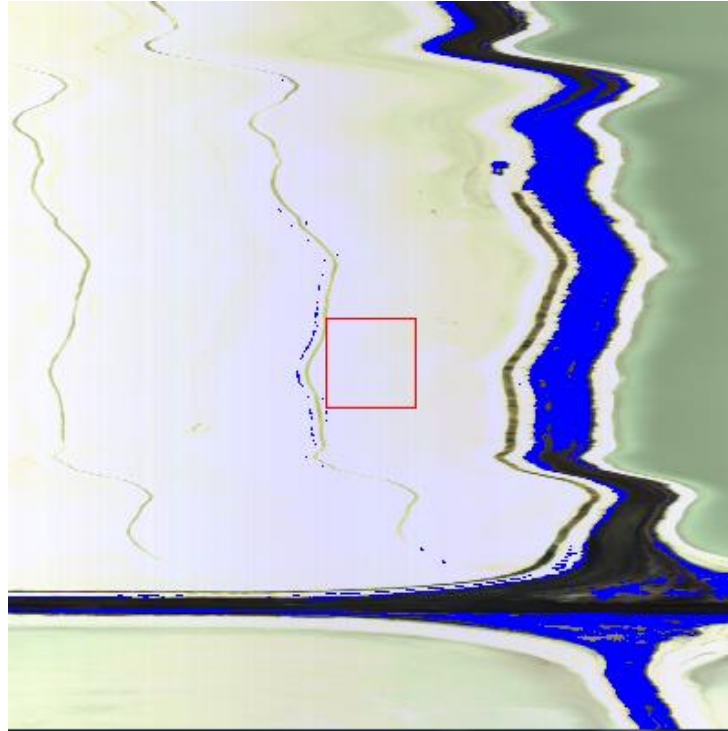


Figure 261: A magnified view of the red 'boxed' region of Figure 260b. Ideally, the thin-blue paths (on the left-half of the image) should not be present (remember that the blue pixels represent pixels that are retained – i.e. they do not contain water). The thick blue line on the right-half of the image represents a road. The non-blue pixels (on the road) do appear to contain water (spectrally), which encouragingly are removed. Perhaps wind sprayed some water onto different parts of the road, considering it was windy during the airborne survey (see Section 3.2).

As mentioned in the caption for Figure 261 above, the road was considered to be a water cover type in Figure 257. The road is a bitumen type of road on Finucane Island (as observed from field work). The regions between the salt ponds appear to be dirt roads. The windy conditions may have sprayed salt and water onto parts of the road, thereby accounting for the classification result.

In the big picture scheme, the thesis objective is to ultimately separate vegetation from land and water; a perfect land-mask is not required. It is, however, more important to have a sound vegetative mask, which is offered by the mean-gradient approach of Section 4.5.2.

Closer examination over urban residential areas reveals that the mask also removes buildings but not roads.

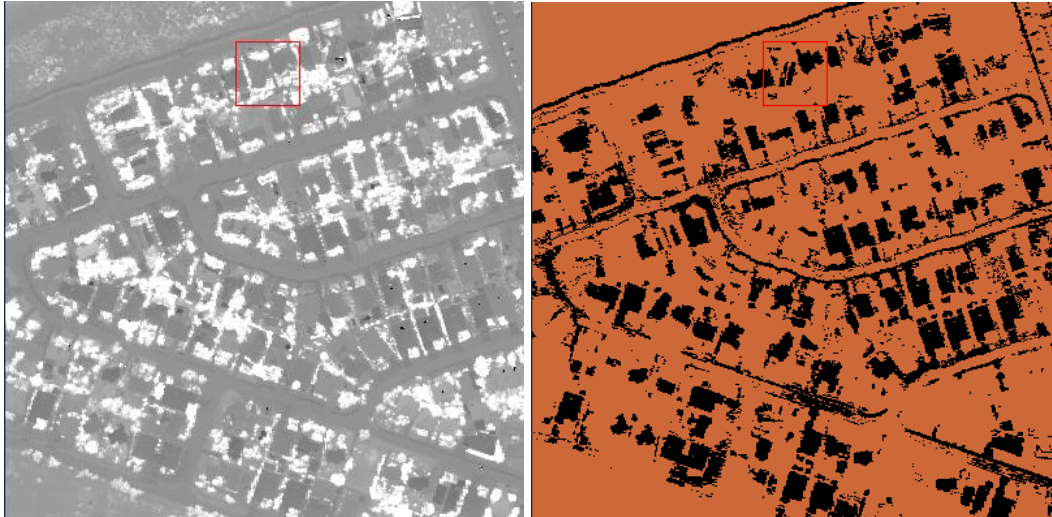


Figure 262: Buildings exhibited negative gradients (therefore masked which shows up as black pixels in the right image). However, residential vegetation (shown as bright white in the left image) such as lawns in backyards have not been masked out, nor have roads (i.e. corresponding to the sienna colour in the right image).

Further tests were conducted on other flight line segments (the results are not shown here) leading to the same encouraging results.

In the line-averaging process, the number of pixels in each horizontal line representing man-made cover types (e.g. roads) amount to a ‘small’ portion of the total number of pixels. In addition, the included soil (which appears to be of the same type and widespread) are expected to smooth out line-averages caused by spectral deviations from other cover types.

Overall, method 2 allows for an automated and quick approach to mask out water for each of the 137 flight line segments. Advantages offered by this approach include 1) the production of very sound results, 2) the use of no human analyst input – i.e. an automatic approach, 3) rapid processing due to the simplistic algorithm, 4) ease of integration into existing C++ code for batch processing.

L.3 N_Ref_Land image construction

Using the land-mask of Appendix L.2, each of the 137 reflectance-based flight line segments had their water pixels removed (this includes the salt pond regions).

Following through the same process as outlined in Section 4.5.9.1, the line-averages are re-evaluated for each land-masked flight line. The result is shown in Figure 263.

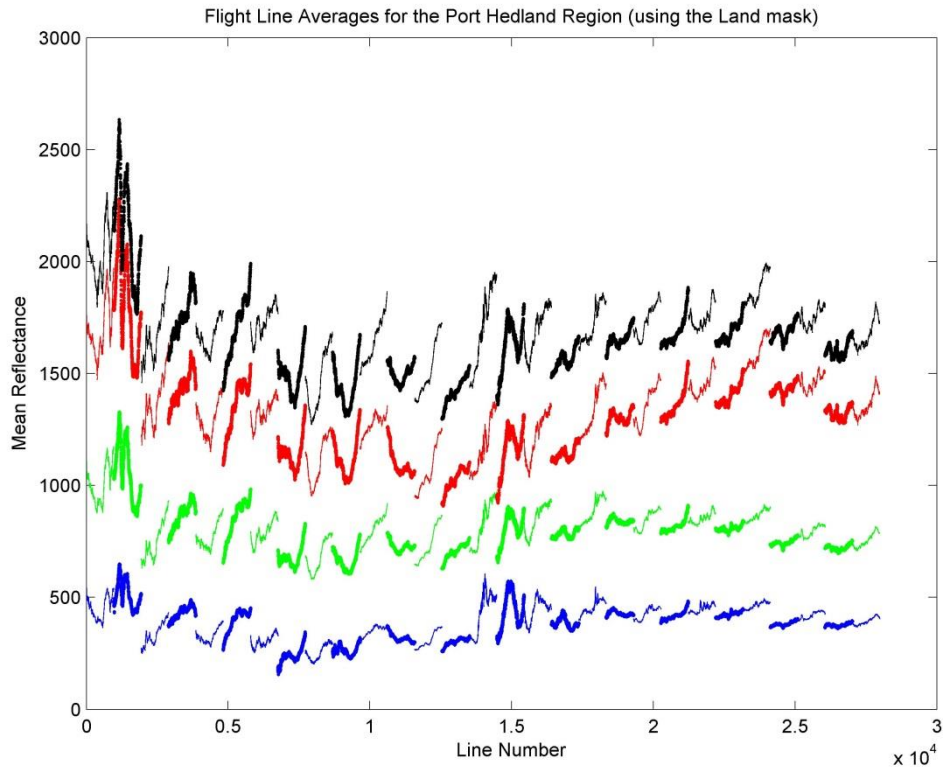


Figure 263: Line-averaging plot for land-masked individual reflectance flight line segments.

Note: the reflectance is scaled by 10,000.

The very abrupt brightness change between flight lines 4 and 5 are clearly absent in the land-masked line-averaging result (Figure 263) compared to the unmasked result (i.e. Figure 106, p. 261 of Section 4.5.9.1). Likewise, the bright sunglint water regions on the northern-side of northern flight lines are also absent (e.g. flight lines 27, 26, 24, etc.). The land-masked result makes it easier discern the behaviour of brightnesses on both a global scale and the local scale. For instance, many flight lines appear brighter on the southern side of a flight line (than the northern side). The northern-most flight line (i.e. 27) also appears brighter than the rest of the flight lines, at least for the four bands under consideration. Further comparisons between the land-masked and unmasked results show that the flight line-averages are relatively unchanged for the southern flight lines; some minor changes are evident in (for example) flight lines 1 and 2, owing to a few man-made pools of

water. However, the relatively smooth lines for flight lines 1 to 6 indicate a fairly uniform (in brightness) set of features. Compared to Figure 106 (p. 261 of Section 4.5.9.1), the spectral nature for land-based features in the northern flight lines are now very clear; previously, the bright water regions masked out any discernible characteristics in Figure 106 (p. 261 of Section 4.5.9.1).

Furthermore, other major characteristics are:

- Flight lines where vegetation begins to dominate (left $\frac{2}{3}$ of Figure 263 i.e. line numbers 0 to $\approx 17,000$) appear to have significant features. The mean reflectances of lines for the right $\frac{1}{3}$ of the figure appear less rich in features (flatter, more uniform in brightness).
- Spectral brightness values increase with increasing wavelength (e.g. red is brighter than blue).

The last point is particularly true for flight line 26, where the unmasked line-averaged result (Figure 106) for both red and blue wavelengths are fairly similar, whereas the red is much brighter than the blue wavelength in the land-masked result (Figure 263).

To generate a new image, the normalising process firstly rotates each individual flight line (about the centre). The details were described in Section 4.5.9.2 and to avoid unnecessary repetition, only the resulting plots will be presented along with an appropriate discussion.

The effect of rotating each flight line is shown in Figure 264. It was observed (and discussed) that for Figure 247 (p. 575, Appendix L.1), the effect of rotation resulted in several northern flight lines being (equally) bright in both the northern and southern ends of a particular flight line but rather dim in the middle. Figure 264 shows a more desirable result, where the brightness is more consistent over a whole flight line. However, some of the undesirable behaviours are still present. For example, flight line 27 still exhibits the parabolic-like behaviour where both the

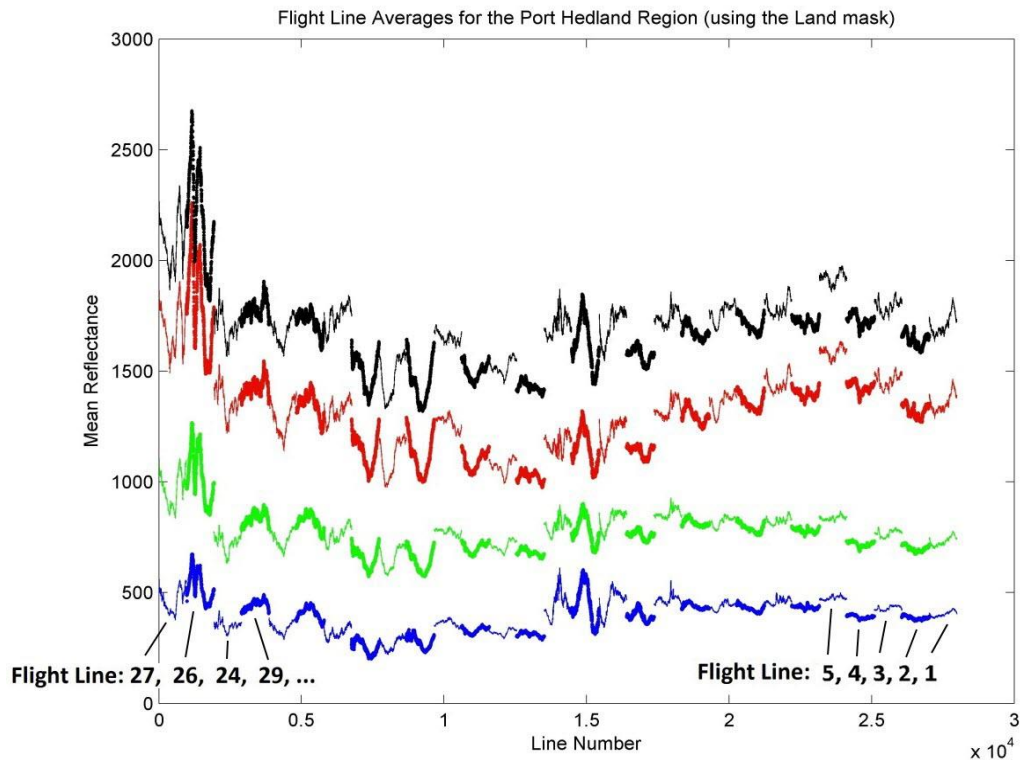
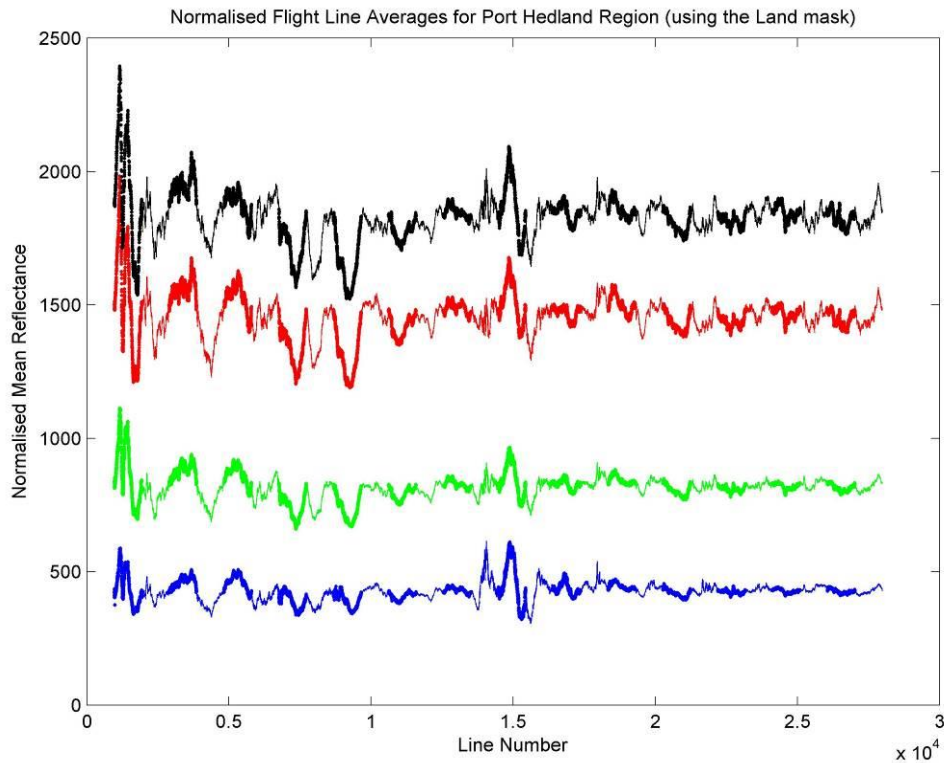


Figure 264: Plot showing the effect of rotating each individual flight line of Figure 263 (the land-masked line-averaged plot) about its centre.
Note: the reflectance is scaled by 10,000.
The italic notes beneath Figure 247 also apply to this plot.

northern and southern sides of the flight line are brighter than the middle region but it is clear that flight line 27 consists of mostly water (which has been removed). Referring back to Figure 42 (p. 141 of Section 3.3), the observed effect must be due to soil, as the flight line contains no vegetation (further evidence is presented in Figure 268 of Appendix L.5, where no vegetation exists when the vegetation-mask is applied). Other flight lines (e.g. flight line 29) contain the opposite shape – reminiscent of an inverted parabola. Again referring to Figure 42 (p. 141 of Section 3.3), it appears the dark stockpile in the centre of the flight line decreases the averaging result.

The next two normalisation steps involve global detrending and the joining of flight line edges; the result is shown next in Figure 265.



**Figure 265: Using the result of Figure 264 (where each individual flight lines were rotated about its centre), this final plot shows the effect of global linear detrending and the joining of adjacent flight line edges.
Note: the reflectance is scaled by 10,000.**

As before, pixel spectra are ‘corrected’ (i.e. made more consistent) in the PHPA_Ref image via the normalisation process, resulting in a stitched **N_Ref_Land** hyperspectral image as shown in Figure 266. Note that the nomenclature was introduced earlier in Section 4.5.9.4; **N** stands for normalised - due to the normalising process; **_Ref** as the data is of reflectance type and **_Land** to indicate it was land-masked (using the 137 flight line segments) prior to normalisation. Note that even though both the water and salt pond regions were masked out, they were placed back to form a complete image (i.e. Figure 266). In reality, these water-based pixels (water and salt pond regions) have also been modified according to the normalised process (Section 4.5.9.2 also produced details but related to the N_Rad_VI image). The intention is to form an easily recognisable image; this is particularly the case in an upcoming section (Appendix L.5) and further comments will be refrained until then. Although the water-based pixels have been placed back to form a complete image, for classification purposes this makes no difference.

They are removed prior to vegetative classification, in addition to land-based non-vegetative pixels. As the water-based pixels have been modified, they may introduce artefacts (see Appendix L.2).

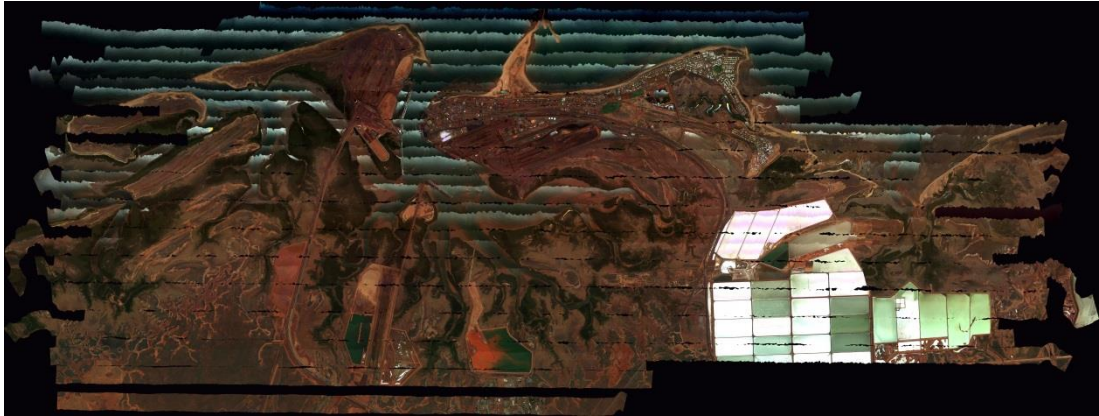


Figure 266: The true colour N_Ref_Land stitched image.
Note: The thick black missing flight line data (flight line 2) due to human programming error.

Note: Human error resulted in a stitched image containing a ‘thick black band’ near flight line 2. An omitted programming step to automate the stitching process led to the omission of data. Rather than constructing a new image (which is a very time consuming process!), the re-work was deemed unnecessary due to the lack of mangrove vegetation in the ‘thick black banded’ region.

With the complete image formed (i.e. Figure 266), the **N_Ref_Land_VI** image is formed (Figure 267) using the same vegetative-mask as outlined in Section 4.5.6.

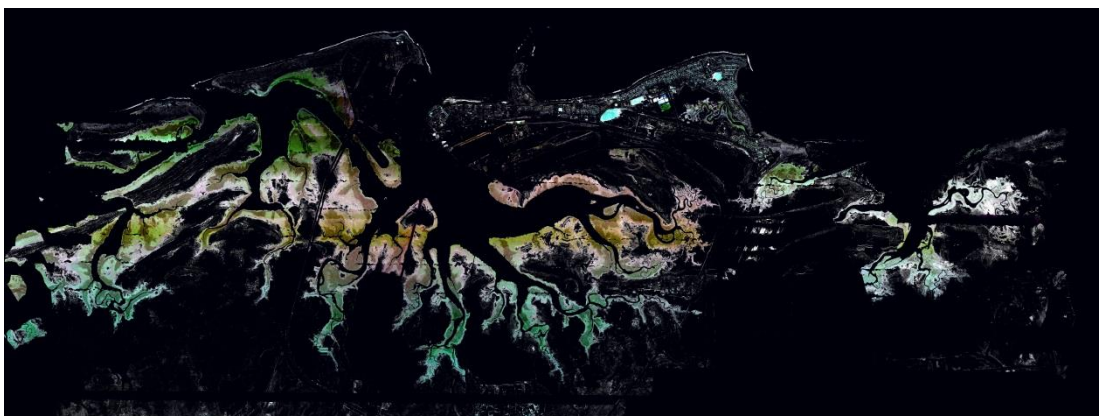


Figure 267: The true colour N_Ref_Land_VI image formed by applying the vegetation-mask (i.e. Figure 91 of Section 4.5.6) to the N_Ref_Land image.
The result contains ‘strong’ vegetation (i.e. > 10,000 gradient threshold).

The actual classification details are left for Appendix P.1.

The line-averaging result after applying a land-mask to the PHPA_Ref image highlighted clear patterns (Figure 263) which were previously hidden (Figure 106) (e.g. an overall global brightness trend). The land-mask removes water prior to line-averaging.

L.4 Development of a vegetation-mask

The mask developed in Section 4.5.6 only applies to the stitched (georectified) image. New vegetative masks had to be developed for each of the 137 flight line segments. Although the land-mask of Appendix L.2 is based on radiance data, the vegetation-masks were derived from the 137 flight line segments using reflectance data (the stitched image which corresponds to PHPA_Ref). Again, the mean-gradient method (as in Section 4.5.6) were used in deriving the masks. These 137 flight line segment files were (again) not georectified, so they could be applied directly to the raw data flight line segment files. Again, a gradient threshold over 10,000 (as in Section 4.5.6) was used to retain 'strong' vegetation. Therefore, effectively, the stitched image produced from the 137 vegetatively-masked flight line segments is identical to the fully stitched PHPA_Ref image, having been masked using the one large vegetative mask from Section 4.5.6.

L.5 N_Ref_VI image construction

The process of forming the N_Ref_VI image is identical to the N_Ref_Land image (Appendix L.3), except for the mask applied prior to line-averaging. Instead of the land-mask, the vegetation-mask Appendix L.4 is used to remove 'weak' vegetation from each PHPA_Ref flight line segment. The line-averaged plot (based on 'strong' vegetation) is as shown in Figure 268.

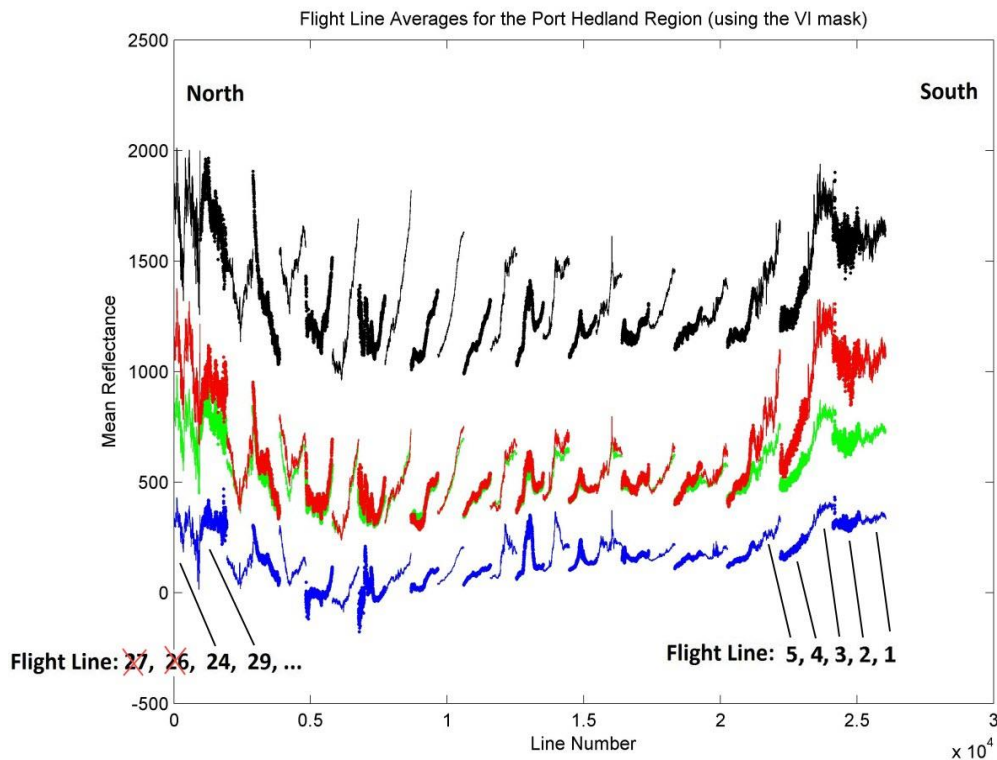


Figure 268: Line-averaging plot for vegetatively-masked individual reflectance flight lines.
 As the northern-most flight lines (i.e. 27 and 26) contains no 'strong' vegetation, this plot has only 27 flight lines, thereby making the northern-most flight line 24 (i.e. the left hand flight line in the plot).
 Note: the reflectance is scaled by 10,000.

As the vegetative-mask did not 'detect' any 'strong' vegetative-pixels in the two northern-most flight lines – i.e. 27 and 26, these two flight lines were removed.

To maintain compatibility with the rest of the plots (for comparison reasons), the two flight lines were artificially generated containing a mean of zero. Therefore, there are still $29 \times 965 = 27,965$ lines of pixels.

The result for the local flight line correction (i.e. rotation of individual flight lines) is shown in the following 'complete' plot (Figure 269) which contains 29 flight lines.

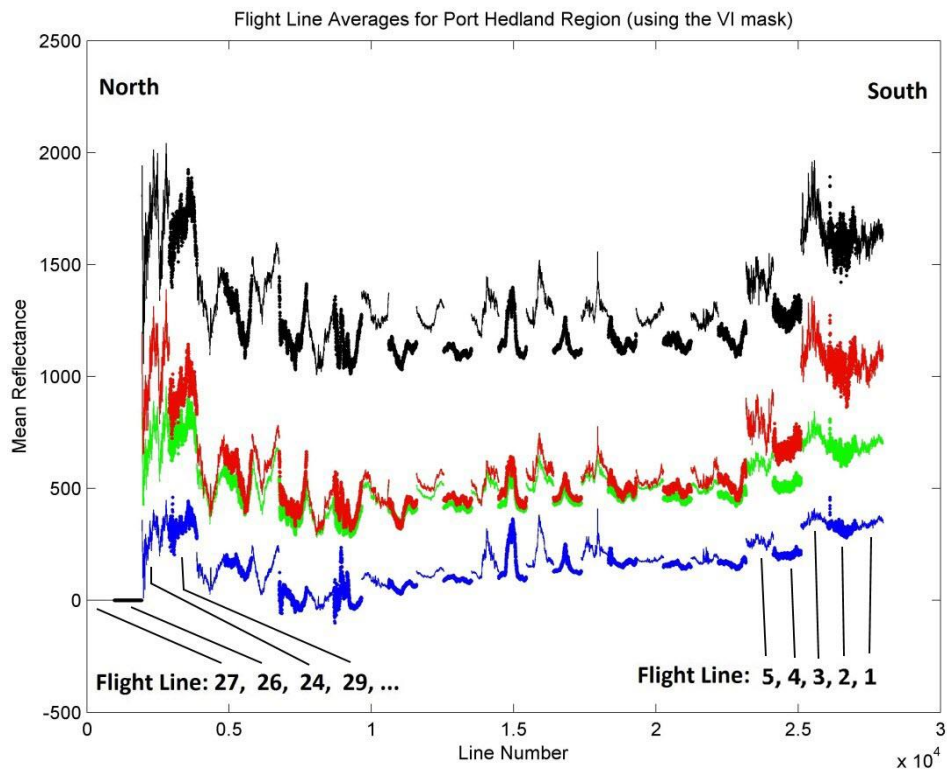


Figure 269: The plot shows the effect of rotating each individual flight line of Figure 268 (the vegetatively-masked line-averaged plot). Note: the reflectance is scaled by 10,000. *The italic notes beneath Figure 247 (p.575) also apply to this plot.*

Again, following the same process as previously, the result for the fully normalised flight lines – i.e. global detrending and the joining up of local flight lines edges – is shown in Figure 270.

It needs to be noted that the global detrending ignored the zero-mean reflectances for flight lines 27 and 26. They are only placed in the plots to keep the same line number position as all the other line-averaged plots. The data were ignored in the normalisation algorithm.

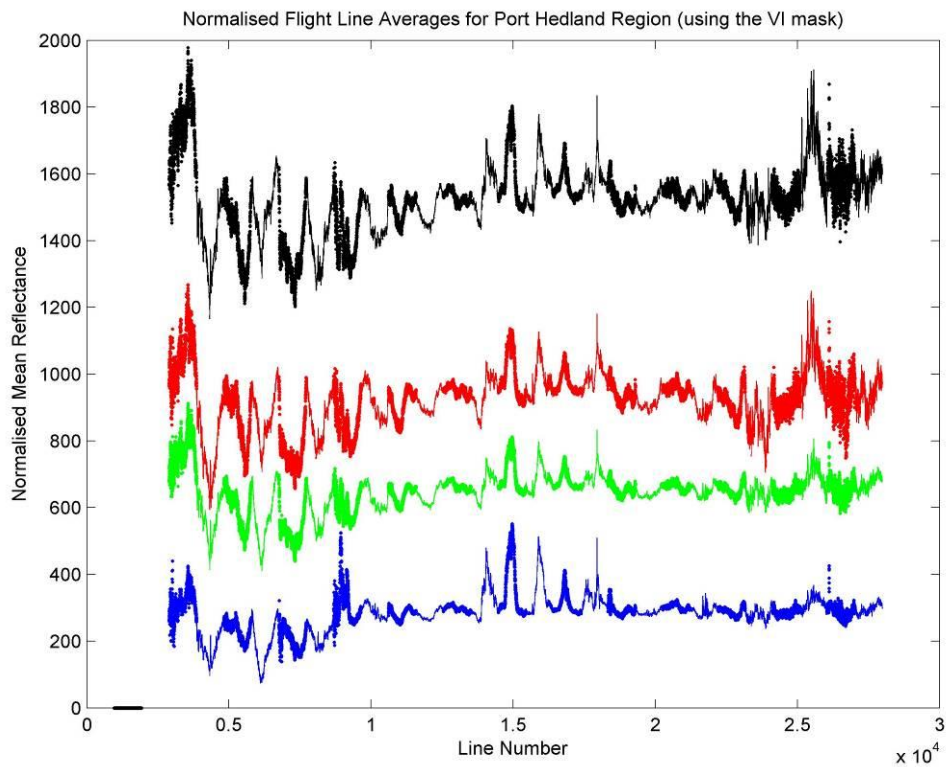


Figure 270: Using the result of Figure 269, where each individual flight line is rotated about its centre, this final plot shows the effect of global linear detrending in addition to the joining up of adjacent flight line edges. Note: the reflectance is scaled by 10,000.

The result of correcting each pixel spectrum (including non-vegetative pixels) is displayed in Figure 271 – the **N_Ref_VI** image.

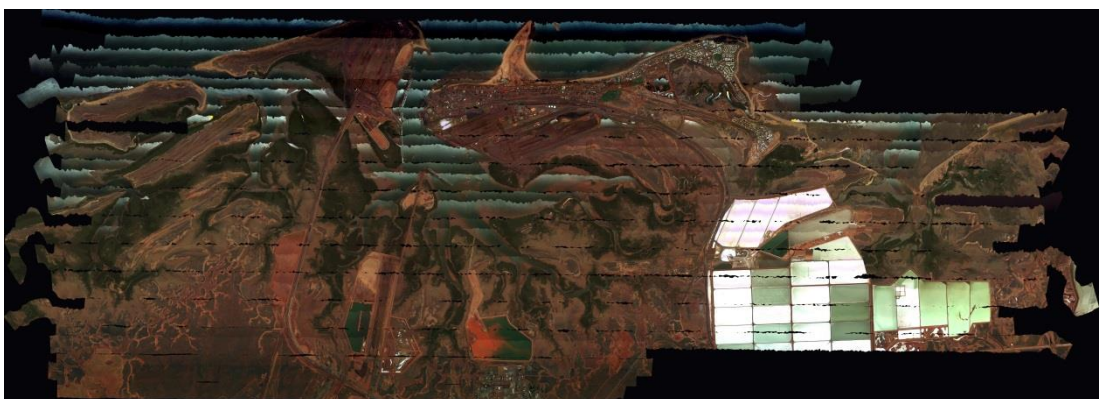


Figure 271: The true colour **N_Ref_VI** stitched image.

The **N_Ref_VI_VI** image (Figure 272) is classified in Appendix P.3.



Figure 272: The result of applying the vegetative-mask (i.e. Figure 91 of Section 4.5.6) to the **N_Ref_VI** image. The result is an **N_Ref_VI_VI** image, containing 'strong' vegetation (i.e. > 10,000 gradient threshold).

The image is smaller than all other vegetative-masked images considered thus far (e.g. Figure 93 (p. 237 of Section 4.5.7) and Figure 267), due to the elimination of the two northern-most flight lines. As a result, the vegetative-only mask of Section 4.5.6 had to be suitably resized (to apply to the smaller stitched image). The resulting 'smaller' vegetative-only mask had to remain identical to that developed before, to place all vegetative-masked images on equal footing with each other when comparing classification results. This means that pixel-by-pixel, the mask content would remain identical but requires the removal of the two northern-most flight lines. A simple solution was found by treating the mask as a 'standard' image and resizing it appropriately with the aid of ENVI, thereby allowing Figure 272 to be generated from Figure 271.

L.6 N_Rad_Land image construction

Using our previously developed land-mask (Appendix L.2) but applied to each radiance-based flight line segments (i.e. instead of reflectance), a new line-average plot was produced. The result is displayed in Figure 273.

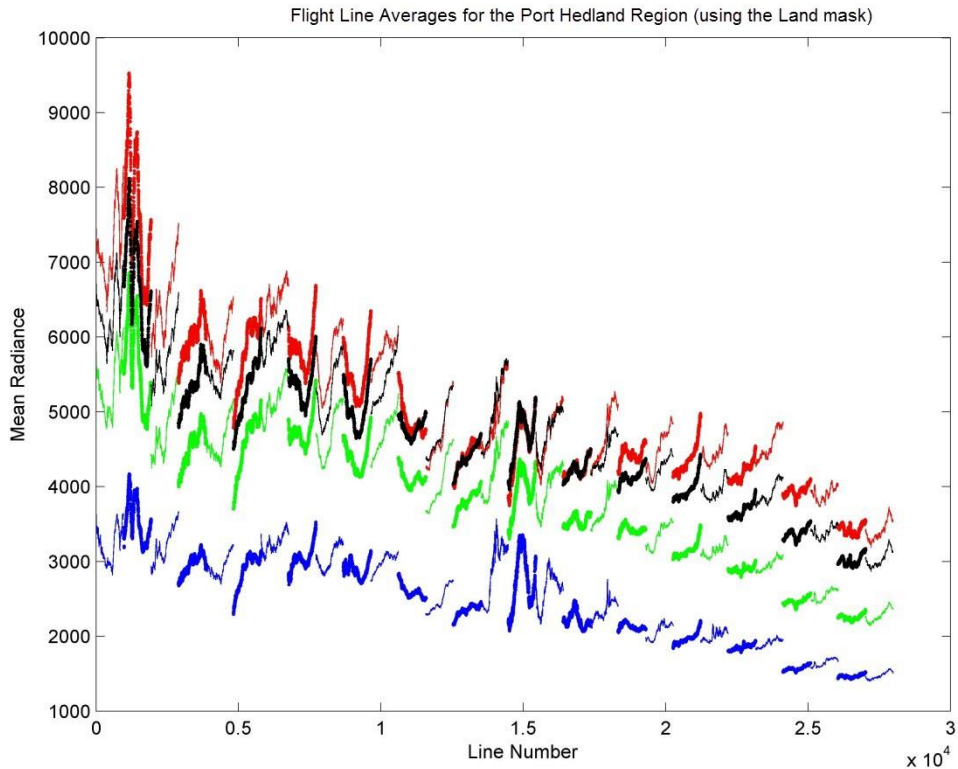


Figure 273: Line-averaging result after land-masking the individual radiance flight lines. The radiance is scaled by 90 in units of $W \cdot m^{-2} \mu m^{-1} sr^{-1}$.

One major difference in comparing Figure 273 with Figure 263 (Appendix L.3) is the clear downward global trend in brightness (from left to right) for each band. This characteristic motivated the normalisation step for detrending the overall brightness.

The normalisation process rotates each individual flight line, with the result shown in Figure 274.

Following through the steps described in Section 4.5.9.2, the removal of the global trend leads to the line-averaged result shown in Figure 275.

Removal of the general linear trend ‘flattens’ the brightnesses for each band over the whole scene.

The final step connects each adjacent flight line edge. The final plot covering all three normalisation steps is given in Figure 276.

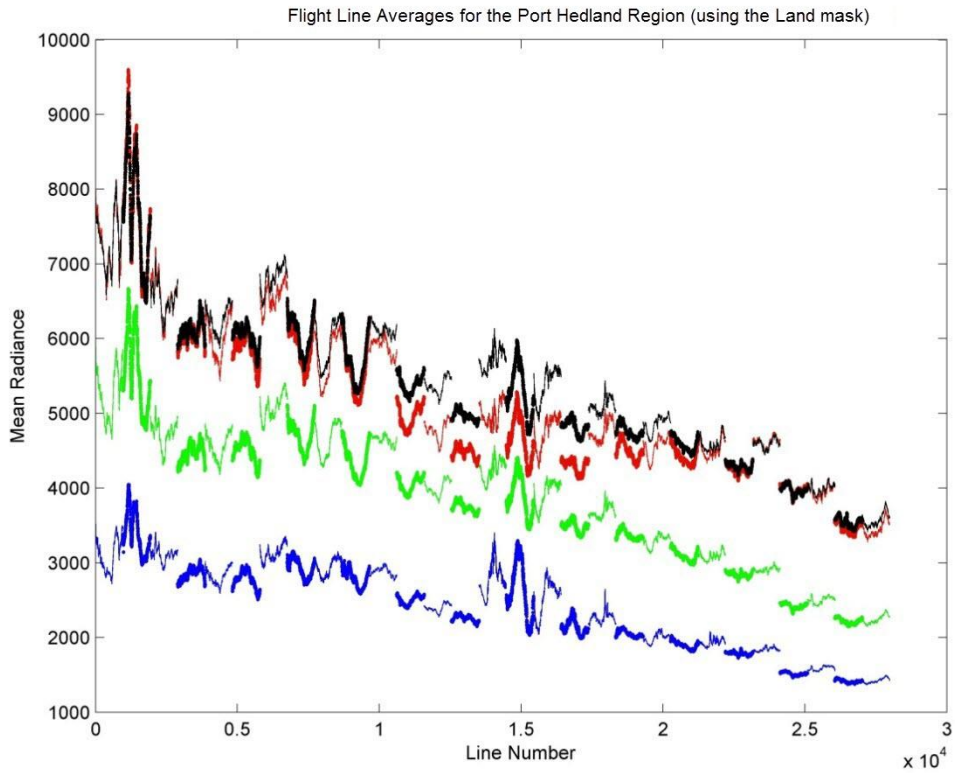


Figure 274: The plot shows the effect of rotating each individual flight line of Figure 273 (the land-masked line-averaged plot).

Note: The unit on the vertical axis is left as radiance. In actual fact, during this intermediate normalisation step, it falls between a normalised radiance and the pure radiance unit. The radiance is also scaled by 90 in units of $W \cdot m^{-2} \mu m^{-1} sr^{-1}$.

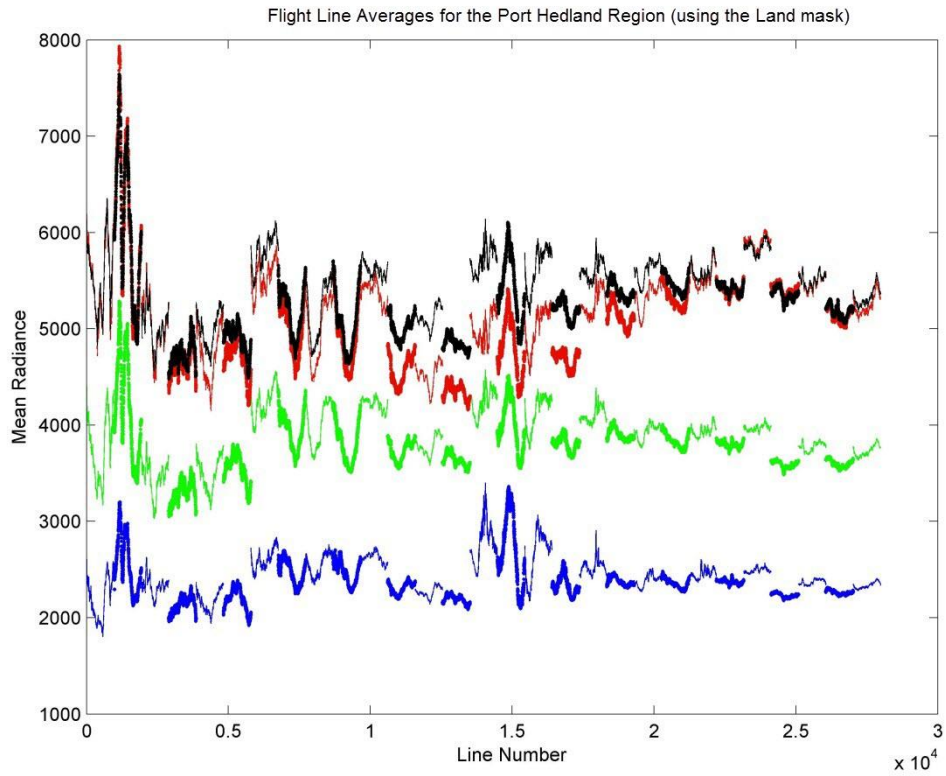


Figure 275: Using the result of Figure 274 (where each individual flight lines is rotated about its centre), this final plot shows the effect of global linear brightness detrending, which removes the overall brightness trend in the north-south direction.
The italic notes beneath Figure 274 also apply to this plot.

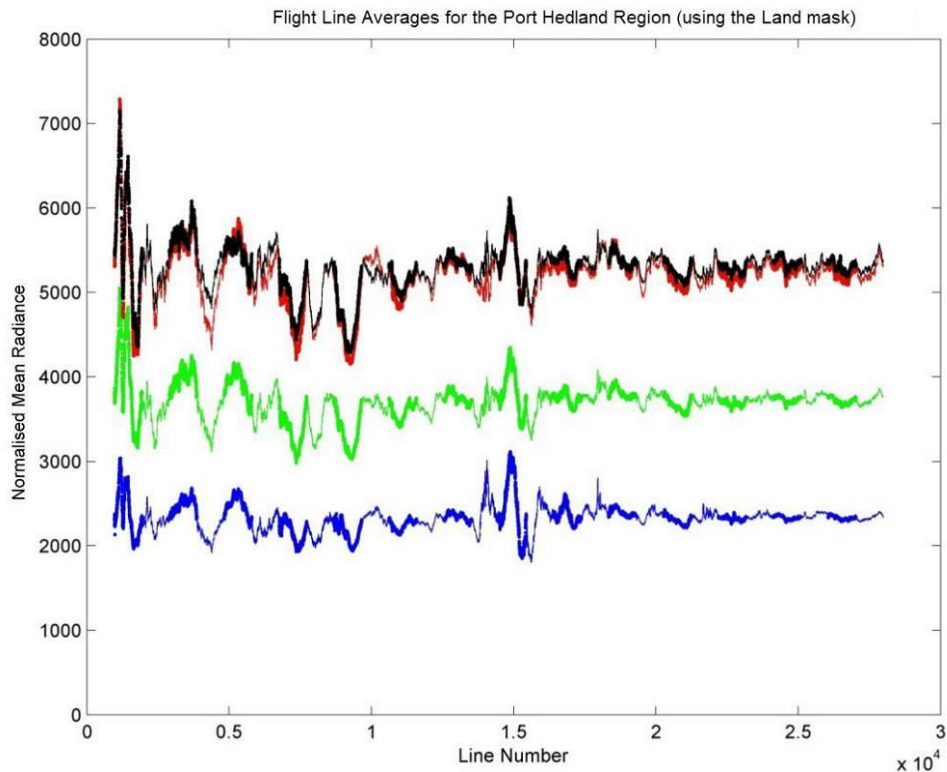


Figure 276: The plot shows the result of connecting the adjacent flight line edges of Figure 275 (where each individual flight lines is rotated about its centre in addition to global linear detrending).

The plot in Figure 276 (using radiance data) resembles that of Figure 265 (using reflectance data), except that the R and NIR bands now appear to be highly correlated. In fact, it is the final step of normalisation, whereby adjacent flight line edges are lined up, that has increased the R and NIR correlation (compare Figure 276 with Figure 275). The less separation in R and NIR bands may affect classification negatively, as the red-edge is a significant characteristic in vegetative classification. The retention of a higher number of PC bands for N_Rad_VI_VI of 15 compared to 11 (for N_Rad_Land_VI from Table 45, p. 331 of Section 4.5.11.3) does suggest more correlation between bands for the land-masked data than the vegetatively-masked data (i.e. N_Rad_Land versus N_Rad_VI). It should be noted that the normalisation plots (e.g. Figure 276) only display 4 bands. It is possible that by displaying more R and NIR bands, the correlation decreases (this was not investigated visually in this thesis). The PC transform applies to all bands, so the results of Table 45 (p. 331 of Section 4.5.11.3) overcomes these (4 band) display shortcomings.

Continuing with the normalisation process, a new stitched image (i.e. **N_Rad_Land**) was produced, as shown in Figure 277. The nomenclature was explained in Section 4.5.9.4.

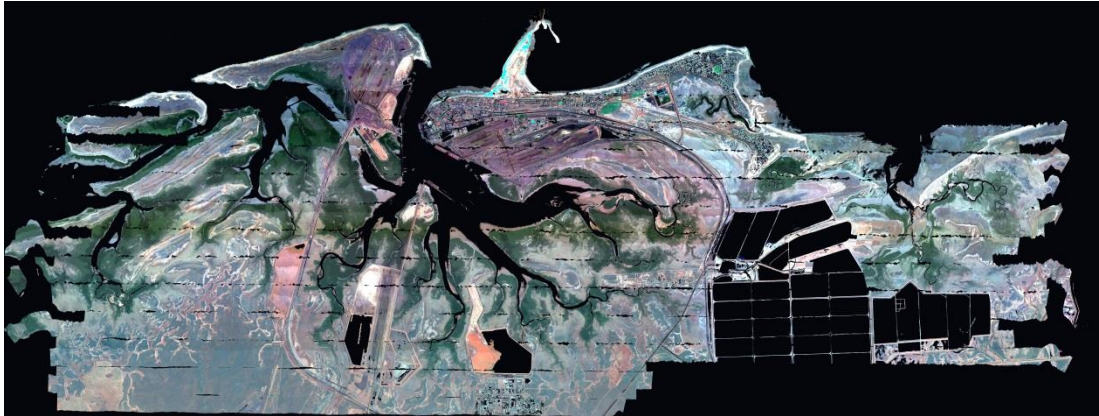


Figure 277: The N_Rad_Land true colour image, showing the absence of water and salt pond regions, in addition to urban settlement (e.g. buildings).

Note that, unlike Figure 266, this image is complete; the missing flight lines in the south (of Figure 266) is now present and correctly constructed, as the data is present in Figure 276 (i.e. only the stitched image of Figure 266 missed the data due to human error). For illustrative purposes, Figure 277 clearly shows the removal of all water-based pixels.

Finally, the **N_Rad_Land_VI** image is shown in Figure 278, ready for classification (which is performed in Appendix P.4).

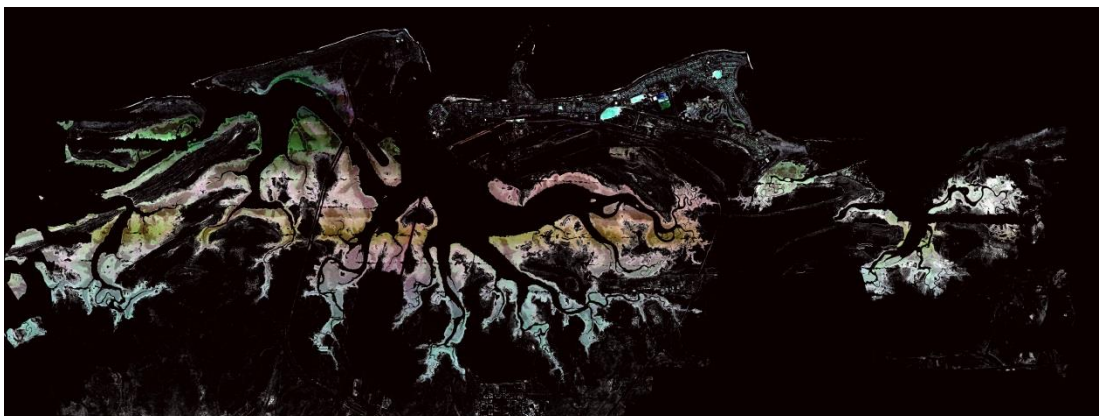


Figure 278: The true-colour result of applying the vegetation-mask (i.e. Figure 91 of Section 4.5.6) to the N_Rad_Land image. The outcome is the N_Rad_Land_VI image, containing 'strong' vegetation (i.e. based on the > 10,000 gradient threshold).

L.7 N_Ref_Res_VI image construction

Figure 272 (p. 605) contains urban grassed ovals and lawns appearing in large regions of the northern section of the PHPA image (which defines the town of Port Hedland). Their inclusion of these cover types have an effect on the line-averaging of mangrove spectra in pixels on the same horizontal pixel-line (with respect to a stitched image).³³ As a result, the urban residential areas were removed to allow comparisons to be made with the N_Ref_VI result.

The process of masking was achieved by writing a C++ program to remove pixels from (uncorrected georectified) flight line segments between two horizontal rows of pixels.

Using ENVI, reasonable horizontal pixel positions were defined marking the start and ending pixels. All pixels between these positions were masked out. A simple horizontal line approach was adopted, although more complicated shapes may be easily programmed. An example of such a result is shown in Figure 279.

The line-averaged result is shown in Figure 280. Note the similarity of Figure 280 to Figure 269 (p. 603, Appendix L.5), where zero-mean line-averages are once again artificially inserted for the two northern-most flight lines. As only the northern-residential flight lines have been modified, all other averaging values are identical to Figure 269 (i.e. N_Ref_VI).

Figure 281 shows the effect of rotating each local flight line about the individual flight line centre.

³³ Note: To clarify, the direction is horizontal with respect to an uncorrected (georectified) stitched image (e.g. Figure 241, p. 568 of Appendix K.4), or a vertical direction with respect to a flight line segment in a stitched image (e.g. Figure 42, p.141 of Section 3.3), or a fully georectified flight line segment (e.g. Figure 242, p. 569 of Appendix K.4). The differences in terminology was outlined in Appendix K.4.

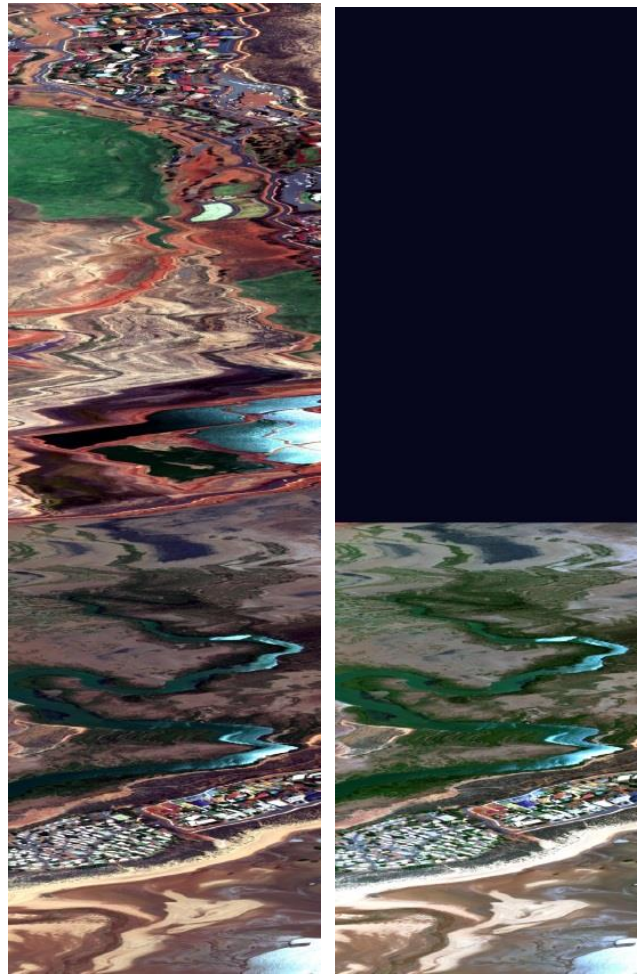


Figure 279: The left image shows the original flight line segment 23d (not georectified). The right image shows the removed urban residential regions. Both images are true colour and neither are enhanced (see Appendix U for more details).

Note that some urban residential regions were left in this particular image, to preserve the mangroves present for both normalising and classification (i.e. both mangrove and urban residential pixels both lie on horizontal rows of pixels and are not separable simply by deleting rows of pixels).

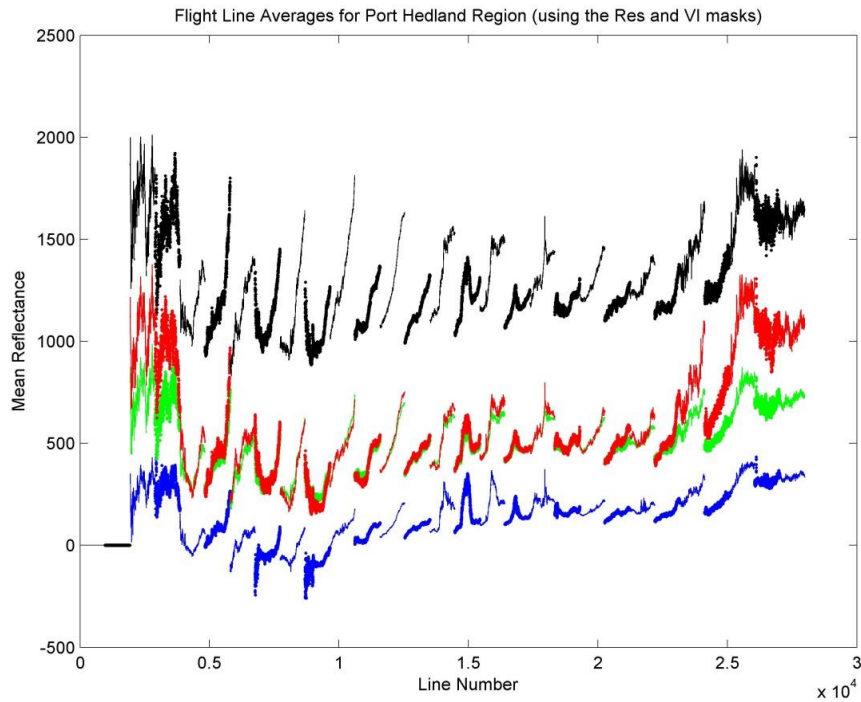


Figure 280: The line-averaging plot when the VI mask is applied to the individual reflectance files, with urban residential areas removed from the northern flight lines.
Note: the reflectance is scaled by 10,000.

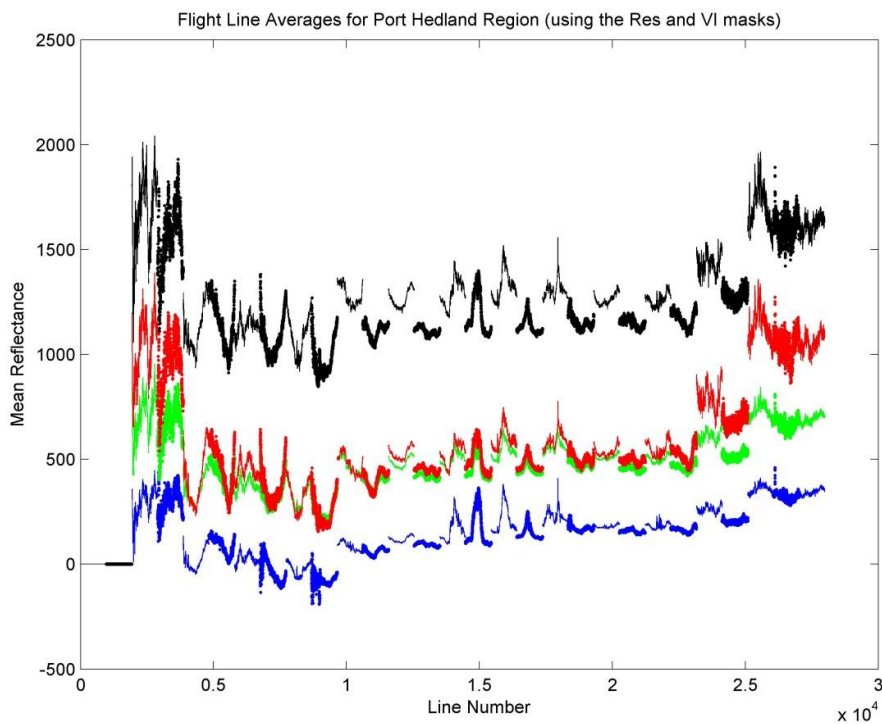


Figure 281: The plot shows the effect of rotating each individual flight line of Figure 280 (the vegetatively-masked and Residential-masked line-averaged plot).
Note: the reflectance is scaled by 10,000.
 The italic notes beneath Figure 247 (p. 575) also apply to this plot.

Apart for the northern-residential flight lines (beginning with flight line 19 and extending further northwards), the line-averaged reflectances remain identical to N_Ref_VI (Figure 269, p. 603 of Appendix L.5). This is due to the same process as the N_Ref_VI image being applied to construct the N_Ref_Res_VI image, except for the flight line segment containing northern residential regions (i.e. for flight line 19 and further northwards). Therefore, all flight line-averages to the south of flight line 19 remain unchanged. A programming trick eliminated duplicate calculations, by copying the flight line-averaged reflectances from the N_Ref_VI computer files to N_Ref_Res_VI computer files (for flight lines south of flight line 19).

Figure 282 shows the final normalised plot; the result of the three normalisation steps (outlined in Section 4.5.9.2) applied to Figure 280.

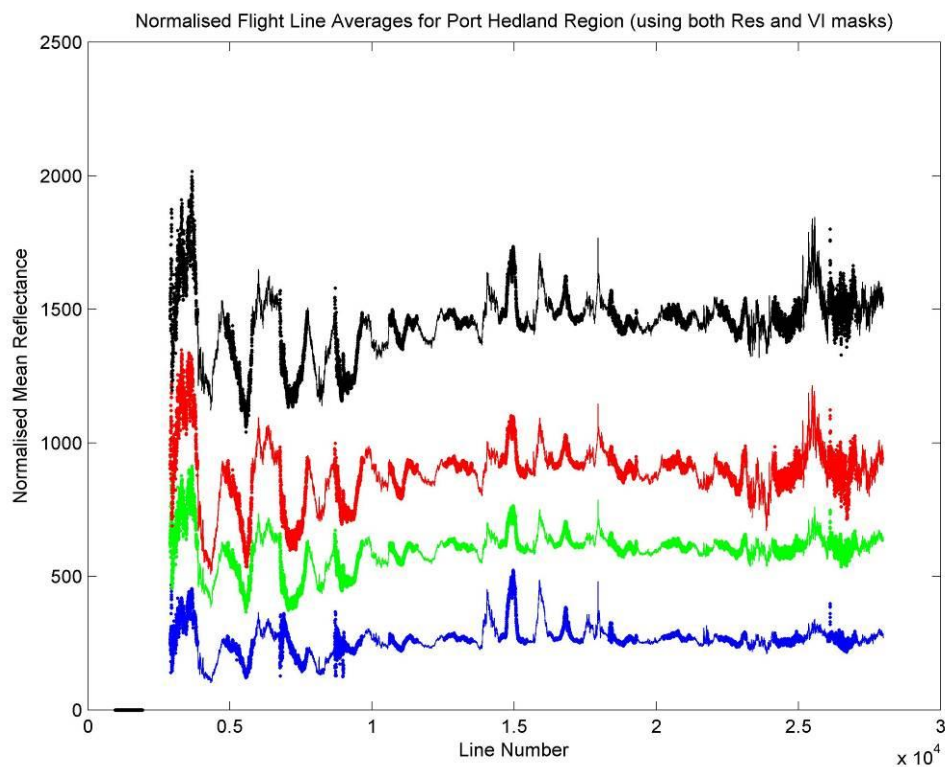


Figure 282: Using the result of Figure 281 (where each individual flight line is rotated about its flight line centre), this final plot shows the effect of global linear detrending and joining adjacent flight line edges.
Note: the reflectance is scaled by 10,000.

As the line-averaged reflectances for the northern-residential flight lines are different (compared to Figure 270, p. 604), the coordinates where the global linear line exists is also different to that of the N_Ref_VI. Hence, global linear detrending results in all line-averages being different (i.e. all flight lines) to Figure 270. It should be noted that the detrending process ignored the manually added zero-mean reflectances for flight lines 27 and 26.

After modifying each pixel spectrum, the newly formed stitched image is shown in Figure 283. This normalised image termed **N_Ref_Res_VI** (_Res stands for residential – i.e. residential regions were removed).



Figure 283: A true-colour representation of the N_Ref_Res_VI image.

In this case, the modified vegetative-mask developed in Appendix L.5 cannot be directly applied to this N_Ref_Res_VI image, due to the removal of urban regions. It appears that yet another new vegetative-mask had to be developed to omit the vegetative pixels in the urban residential areas. However, with a little thought, a workaround was quickly developed using a simple trick. The previous mask (containing 0 and 1 values) developed for the N_Ref_VI_VI is identical in size (i.e. both N_Ref_VI_VI & N_Ref_Res_VI have flight lines 26 & 27 missing). The only change concerns the location of the newly masked pixels in the N_Ref_Res_VI image. Therefore, using the mask for the N_Ref_VI_VI and the N_Ref_Res_VI image (containing the newly masked pixels), the N_Ref_Res_VI_VI image was formed by copying pixels from N_Ref_Res_VI for non-zero valued pixels (i.e. not the black regions) but only if the vegetation-mask (based on N_Ref_VI_VI) has a value of one (indicating strong presence of vegetation). Otherwise, the pixel spectrum was set to

zero. This ensured that vegetation detected in the now-masked residential region was not copied to the new N_Ref_Res_VI_VI image. A C++ program was written to perform this task in a timely manner. The resulting N_Ref_Res_VI_VI image is displayed in Figure 284, ready for classification in Appendix P.5.

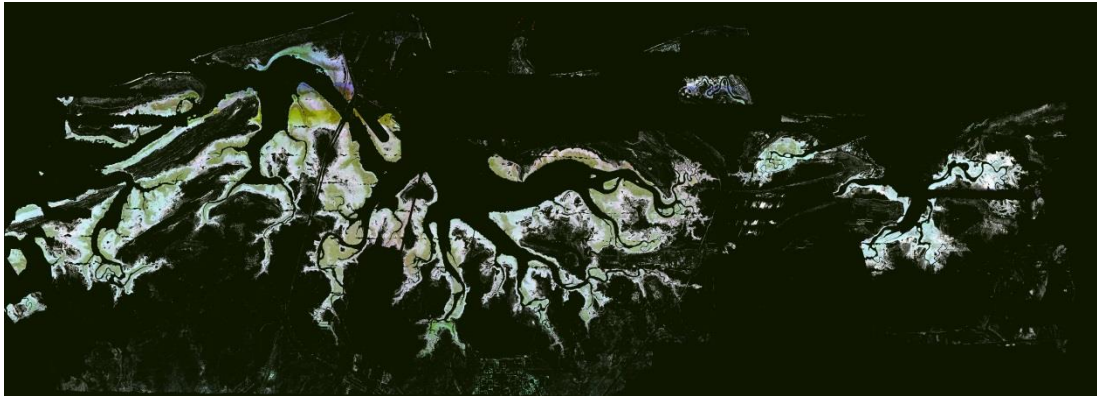


Figure 284: The true colour N_Ref_Res_VI_VI image, whereby residential green regions (e.g. grass) have been removed.

L.8 N_Rad_Res_VI image construction

In a very similar manner to Appendix L.7 above, instead of forming an N_Ref_Res_VI image based on reflectance data, this section forms the N_Rad_Res_VI (i.e. based on the radiance data). However, unlike that for the reflectance data, the two northern-most flight lines (26 & 27) are not eliminated for the radiance data (i.e. a few water-based vegetative pixels are retained).

This result is identical to Figure 108 (p. 264 of Section 4.5.9.1), except for the northern flight lines (due to the removal of residential areas – the details were provided in Appendix L.7).

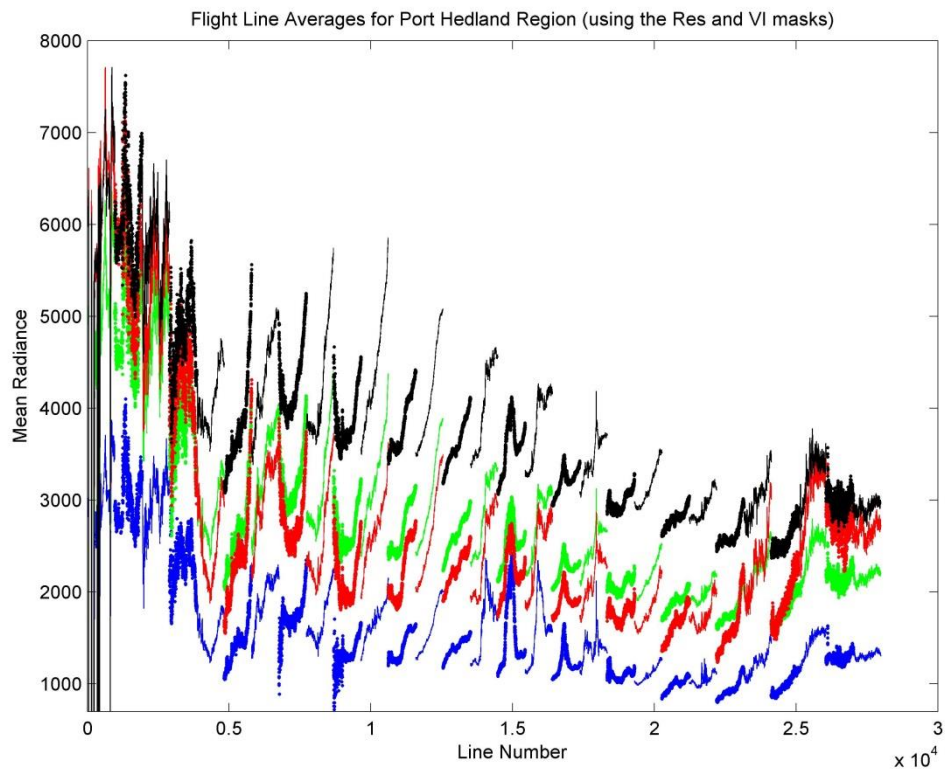


Figure 285: Mean flight line radiances for the masked-vegetative (individual) radiance images (gradient > 10,000), with urban residential areas removed from the northern flight lines.
Note: The radiance is scaled by 90 in units of $W \cdot m^{-2} \mu m^{-1} sr^{-1}$.

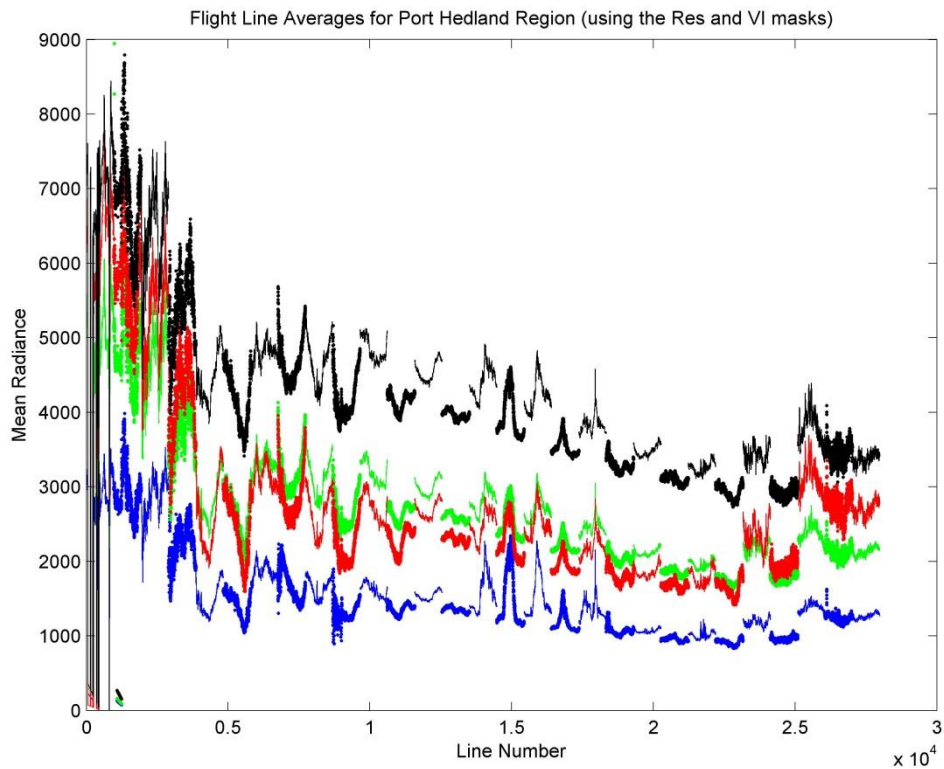


Figure 286: The plot shows the result of rotating each individual flight line of Figure 285 (the vegetatively-masked and Residential-masked line-averaged plot) about its centre.
The italic notes beneath Figure 274 also apply to this plot.

The plot for the full normalised correction is shown next in Figure 287.

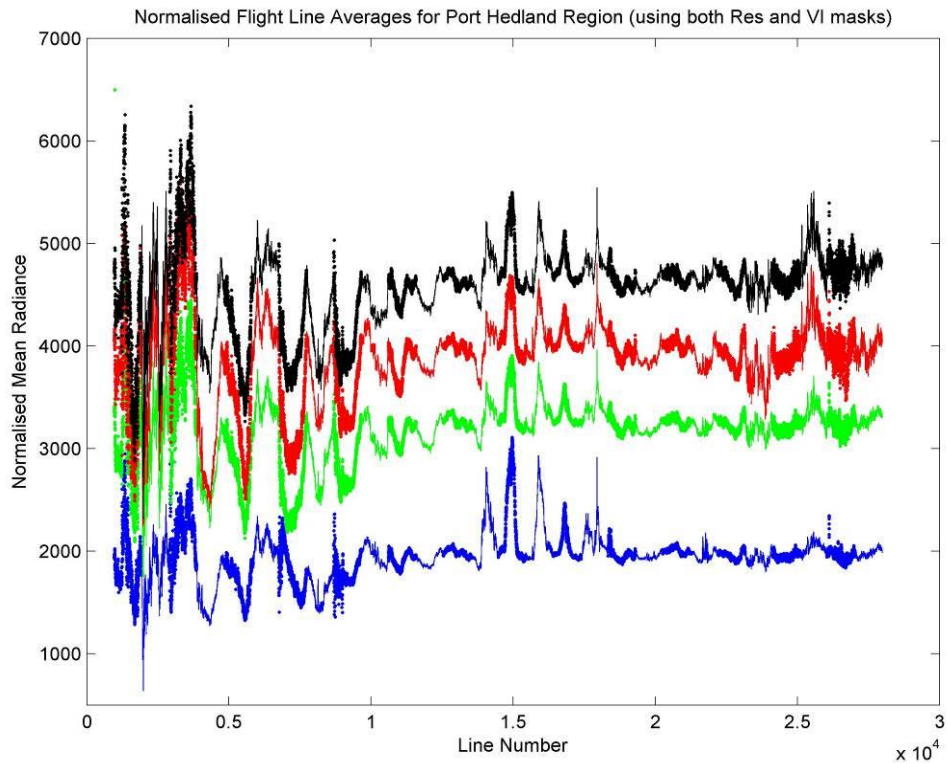


Figure 287: The fully normalised plot, using the result of Figure 286 (where each individual flight lines is rotated about its flight line centre), this final plot shows the effect global linear brightness detrending and the joining up of adjacent flight line edges.

Note: The radiance is scaled by 90 in units of $W \cdot m^{-2} \mu m^{-1} sr^{-1}$.

As for the N_Ref_Res_VI image, the global trend line changes all averages. Also, prior to global detrending, only the non-residential (masked) regions have identical line-averaged values to the N_Rad_VI result. Both these points were explained in Appendix L.7.

The final **N_Rad_Res_VI** image is shown in Figure 288.

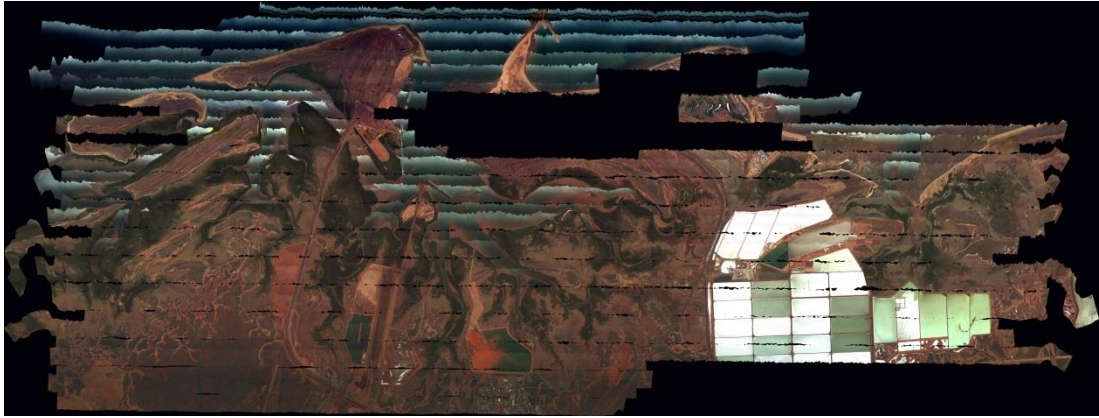


Figure 288: The true colour N_Rad_Res_VI image.

Also in a similar manner to that for the N_Ref_Res_VI image, a new mask had to be developed. The vegetative mask and vegetative gradient file (i.e. where the gradient > 10,000) both had to be modified to incorporate the new masked urban residential regions. The same programming approach was taken to construct these masks (the details were provided in Appendix L.7).

The N_Rad_Res_VI_VI image (below) is used in Appendix P.6 for classification.

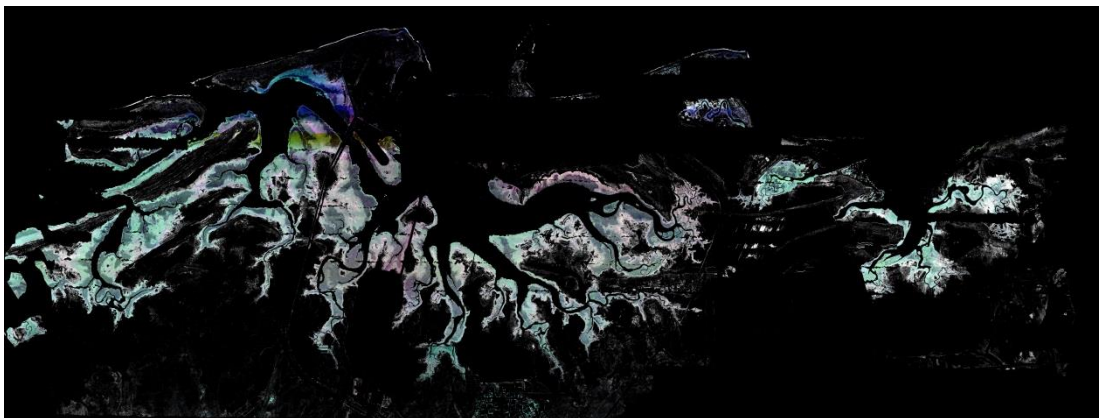


Figure 289: The resulting N_Rad_Res_VI_VI image

Appendix M Artificial Spectral Artefacts

Pixels over excessively bright regions in the N_Rad_VI image (Figure 112, p. 272 of Section 4.5.9.2) contains spectral artefacts. These artefacts are also present in the PHPA_Ref image, as discussed in Section 4.5.3.3.

The reconstructed N_Rad_VI image contains the whole image, not just vegetation (even though normalisation was based on vegetative spectra). As all pixels were included, some existing bright pixels (e.g. salt pond regions) are added to in brightness as part of the normalisation process. This can cause those spectra to become distorted. The effect is caused by overflow errors, thereby introducing artificial artefacts (i.e. the effect is not physical). Note that although this section discusses the N_Rad_VI image in specific detail, the same technical details relate to any normalised image (radiance or reflectance).

The storage format of numbers in a binary image affects the maximum value which can be stored. Each value (intensity) is recorded as an integer type of 4 bytes in size (by default). In this thesis, these values describe reflectance/radiance or normalised reflectance/radiance.

For reflectance data, the small values are not stored in float formatted type (which would double the file size compared to the integer storage format), but rather, the numbers are multiplied by a scale factor and stored as an integer (which effectively truncates the number). The larger the scale factor, the more accurate the representation of the number. For example, 0.51 scaled by 10 leads to 5 (and the 0.1 number left is lost). But scaled by 100 leaves the number intact. However, there is a limit of 32767. So, an appropriate scale factor must be selected carefully. For reflectances, the scale factor is specified in the ENVI header file (parameter: `image_scale_factor`). The Tafkaa .input file specifies parameters to convert radiance data to reflectance data. The scale factor is controlled through parameter: `tafkaa_output_scale_factor` (example: Table 31, p. 252 of Section 4.5.8). The ENVI header file uses a scale factor of 10,000 for reflectance data and 90 for radiance data files (in the data used for this thesis).

As the normalising process modifies the radiance/reflectance values, it can lead to existing values (with respect to the values as stored in the pre-normalisation

flight line segment files) being added to (potentially exceeding the maximum integer number) or subtracted from (potentially leading to more negative spectra).

Since the maximum integer number that can be stored is 32767, it was decided that spectral values > 32767 (overflow) be put to zero³⁴. Note that single band values were set to zero, not the whole spectrum.

While these large numbers can be catered for by doubling the byte size per file entry (such as a float type), it has the effect of doubling the image size (100 GB becoming 200 GB) - as each float type is double the byte size of an integer. It is not possible to mix data types within a single file – e.g. short int for numbers < 32767 and long int otherwise. The file doubling effect has a dramatic effect from a computational viewpoint as processing time vastly increases as well as file storage requirements.

Analysis showed that the regions affected by overflow, were the already bright water and salt pond regions. Since this has no effect on vegetative classification, the artificially produced spectral artefacts were left in the final complete image and removed prior to classification.

An example of an overflow spectrum for the N_Rad_VI image, is shown Figure 290 (right), corresponding to a pixel in the pink region of Figure 112 (p. 272 of Section 4.5.9.2). Physically, the pixel is located in the salt pond region. The pink region has been magnified in Figure 290 (left). It is not difficult to determine the location of this region in relation to Figure 112 (p. 272 of Section 4.5.9.2), due to the position of the missing flight line data (Figure 290).

³⁴ *Computationally, spectral values were generated as a long int type. If the spectral value exceeded that of a short int type (in C++), it was set to zero. This way, all data were still stored as a short int type.*

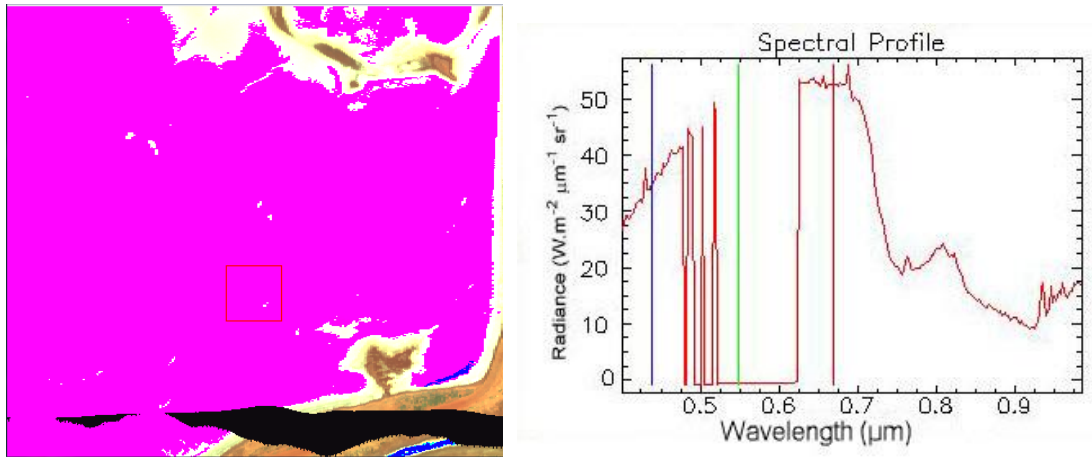


**Figure 290: An example of a spectrum (right image) corresponding to a pixel in the pink coloured region of the true colour image map. The location occurs in the salt pond region.
Note: The vertical scale are in units of normalised radiance (scaled by 90).**

Note the numerous normalised radiances set to zero; particularly between 0.52 and 0.62 μm . Note that single overflow values were set to zero, rather than the whole spectrum.

The displayed image relies on the ‘standard’ RGB combinations defined in this thesis - i.e. bands 18 (B), 66 (G) and 116 (R), corresponding to 0.4388, 0.5494 and 0.6687 μm respectively – as outlined in Section 3.3). These bands are indicated by the blue, green and red vertical lines on the spectral plot above (right image of Figure 290). The normalised radiance located at the green coloured band (i.e. the vertical line at 0.5494 μm) is zero. However, there is a blue normalised radiance value of ~ 3500 and a higher red value (~ 5200), a combination which produces the pink coloured pixel observed.

Similar explanations apply to both the light blue coloured pixels (Figure 291) and the blue regions (Figure 292).

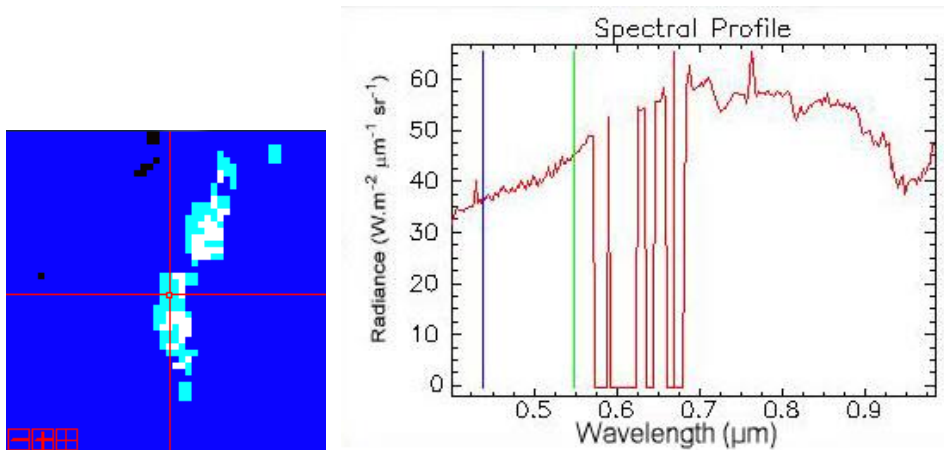


Figure 291: An example spectrum (right image) corresponding to a pixel in the light blue region of Figure 112.
Note: The vertical scale are in units of normalised radiance (scaled by 90).

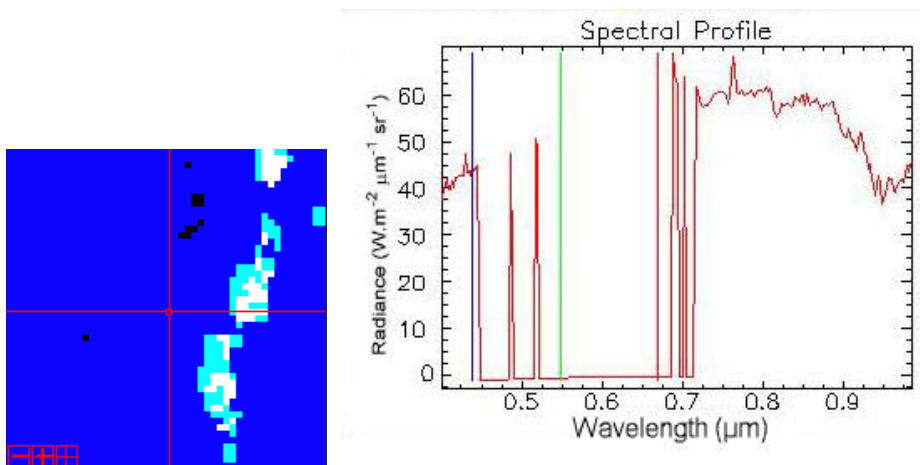


Figure 292: An example spectrum (right image) corresponding to a pixel in the blue region of Figure 112.
Note: The vertical scale are in units of normalised radiance (scaled by 90).

Very clearly, the normalised radiance for both the red and green bands are zero leaving just the contribution in the blue band (for Figure 292, right image). This explains the blue coloured pixels. Selecting different combinations of RGB bands would cause a different result in displayed pixel colour. For example, the selection of a slightly larger blue band (say 0.45 μm) in an RGB image would result in a zero normalised radiance value, thereby causing the whole pixel to appear black (leaving the green and red wavelengths unchanged).

Appendix N Spectral Analysis of Normalised images

N.1 Image ROI Selection Strategy

Section 4.5.9.6 compared ASD spectra for two vegetation cover types against image pixel spectra using both reflectance and radiance-based images.

In this section, it is of interest to compare image vegetation mean spectra between the normalised images. Mean spectra are also compared to PHPA_Ref_VI and PHPA_Rad_VI images. The comparisons include analysing the effectiveness of the normalisation steps in a spectral sense. The steps for the normalising process were described by 1) rotation of each flight line, 2) de-trending a global trend and 3) joining up of flight line edges (as described in Section 4.5.9.2).

The mean spectra are calculated for several regions over the image using the ENVI ROI tool. Unfortunately, ENVI also counts masked pixels in the calculation (more on this later in this section). Using the same ROI between several images allows plotted mean spectra to be compared. Unlike the comparisons conducted in Section 4.5.9.6, any comparison involving the ASD is now out of the question, as the investigation is not confined to examining the spectral differences of a single particular cover type. In addition, it is not possible to directly compare radiance spectra with ASD reflectance spectra. Instead, the ROI spectral regions are now expected to contain several different cover types.

The choice of defining each ROI is based on the understanding of the mechanics behind the normalisation process and named according to their location in the image. For example, ROI 2b defines a ROI in flight line segment 2b; ROI 22d N defines a ROI in flight line segment 22d but the northern end. There is also a ROI 22d S for the southern end. Both ROI NW and ROI SW relate to the northwestern and southwestern region (respectively) of the PHPA_Ref image (Figure 42, p. 141 of Section 3.3).

The earlier flight line-averaging results in Section 4.5.9.1 (e.g. Figure 106, p. 261) or the plots in Appendix L (e.g. Figure 246, Figure 263, Figure 268, Figure 273, Figure 280, Figure 285) show a jump in flight line brightness between flight lines 2 & 3. The flight line-averages do not dramatically change as much in this southern-end based

region, compared to regions further north. In addition, the line-averages do not vary widely within each flight line. This line-average behaviour applies to both reflectance and radiance plots. Hence, ROI 2b and ROI 3a were defined to investigate the extent of improved spectral consistency for normalised mean vegetative spectra, in relation to each other, especially compared to the original PHPA_Ref (for reflectance-based images) and the PHPA_Rad_VI image (for radiance-based normalised images). The normalisation process removes these gaps.

A sharp flight line boundary is apparent in the PHPA_Ref image (i.e. Figure 42, p. 141 of Section 3.3) between ROI 22d and ROI 23b, so it is of interest to examine the spectral behaviour at those locations. ROI 22d is situated on Finucane Island where spectra over the flight line is highly varying (in particular the brightness of the IR band, as is evident from Figure 106, p. 261 of Section 4.5.9.1). The choice of ROI 22d allows for a closer examination of the practical consequence of flight line rotation, as each end (north and south of the flight line) are vastly different in brightness. Flight line segment 28c covers the highest population of mangroves on Finucane Island hence spectral behaviour for ROI 28c are of particular interest.

Normalisation also has the effect of detrending brightnesses over a global scale. Both ROI NW and ROI SW examines the effect of global detrending, as both regions are located on opposite sides of the rotation centre for the global detrending line in the normalising process. Therefore, there is an expectation that both brightnesses are roughly similar to each other (although not identical, as there is no reason to suspect that vegetation will be identical under identical conditions as defined by both regions).

All ROI's defined above are displayed in Figure 293 to Figure 295. The process of obtaining mean spectra for each ROI appears simple. The ENVI statistics tool appears to be able to conveniently calculate the mean of all the spectra, which encompasses the defined pixels within a ROI. However, in practice, the process is more complicated in order to obtain the results presented below. The technical points are outlined in Appendix W.4; basically, the masked pixels are counted toward the mean calculation. Therefore, if a ROI defined in the north is compared to the south with identical pixels, the results may differ if the number of masked pixels between the two ROI's differs. The mean results may therefore not



Figure 293: ROI defined on Finucane Island: ROI 28c (blue) and ROI 23b (green). The position of the flight line boundary lies between the two regions (and shown previously in Figure 60, p. 190 of Section 4.5.1). A gamma correction of 1.5 has also been applied to the image to emphasise the location of flight boundaries.



Figure 294: ROI defined on Finucane Island: ROI 22d N (yellow) and ROI 22d S (red). Note the flight line segment 22d in this image is located directly below flight line segment 23b, as indicated in green in Figure 293.

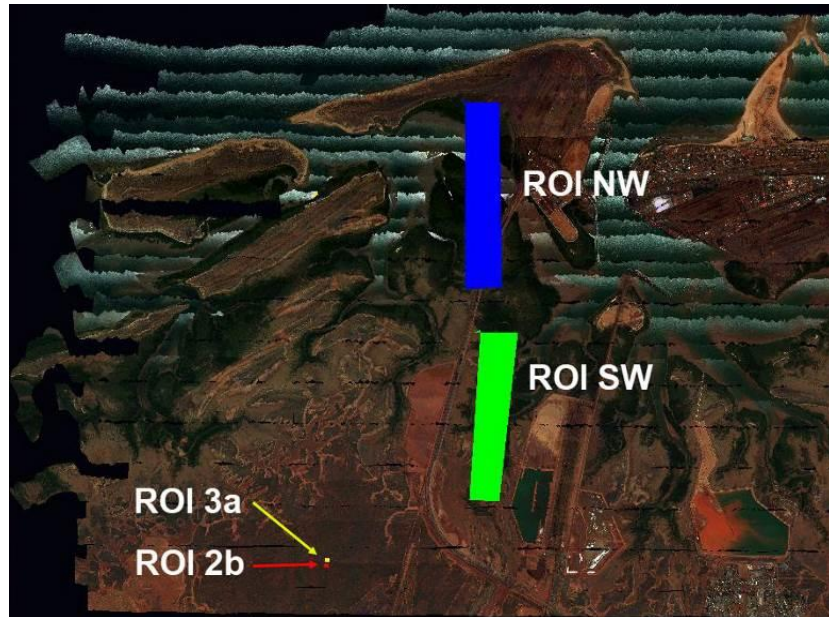


Figure 295: The location for the large ROI's NW (blue) and ROI SW (green) in relation to the image. To the southwest, there are two small ROI's: ROI 2b (red) and ROI 3a (yellow).

be compared to each other for a particular image. Between images, the number of masked pixels defined within a ROI will be the same (as the same vegetative-mask was applied to each image). In this situation, the mean corresponding to a particular ROI may be directly compared between each image (although the mean is incorrect unless there are zero masked pixels).

Mean reflectance spectra corresponding to each ROI are shown in Figure 296 to Figure 304 (beginning on page 631) with corresponding spectral angles (SAs) between the mean spectra given in Table 98 to Table 107. The comparisons involving mean radiance spectra will commence after reflection spectra. Note that the vertical scale changes between plots and that all reflectances are scaled by 10,000.

For consistency, the colour definitions used in both reflection-based and radiance-based plots are equivalent for the same image type (e.g. N_Ref_Land_VI and N_Rad_Land_VI – i.e. Land_VI represents the same image type). The definitions for reflectance-based images are shown in Table 96.

The reasons for selecting these colours is that black 'stands out' (on the plot) and represents the original (i.e. unprocessed image). The blue represents water (as water spectra were processed in this image), red for soil (as soil spectra were

processed but not water), green for vegetation (the image is vegetation based). Cyan was selected for the _Res_ based images as the plot is very similar (in most cases) to the green plot. Both colours – green and cyan – are still well represented on the plot without one dominating the other too much (thereby allowing for easy visual comparisons).

Reflectance-based image	Plot colour	Colour reason
PHPA_Ref_VI	black	Colours are used for plots derived from normalised images (black is not a colour)
N_Ref_NoMask_VI	blue	Using no mask leaves water prior to normalisation
N_Ref_Land_VI	red	Soil (reddish) is left in prior to normalisation
N_Ref_VI_VI	green	Vegetation is left in prior to normalisation
N_Ref_Res_VI_VI	cyan	

Table 96: Plot colours associated with reflectance-based images.
Reasons for colour selection are also given, making it easier to recall the associated colour with the image.

Similarly, for radiance-based plots the colour definitions are self-evident (see Table 97).

Radiance-based image	Plot colour	Colour reason
PHPA_Rad_VI	black	Colours are used for plots derived from normalised images (black is not a colour)
N_Rad_Land_VI	red	Soil (reddish) is left in prior to normalisation
N_Rad_VI_VI	green	Vegetation is left in prior to normalisation
N_Rad_Res_VI_VI	cyan	

Table 97: Plot colours associated with radiance-based images.
Reasons for colour selection are also given, making it easier to recall the associated colour with the image.

It is important to emphasise that, as each image has been vegetatively masked (i.e. all image names contain the suffix `_VI`), the sampled pixels contained within a particular ROI contains only vegetative spectra. This applies to both reflectance and radiance-based images.

In this appendix, the term reflectance is used to describe the brightness in all spectra, even though, for normalised images, the reflectances are actually normalised reflectances. The same comment applies to radiances, which are also used in normalised radiance-based images.

This appendix is subdivided into three parts. The first part studies spectra for reflectance-based images, while the second part relates to radiance-based images. A conclusion is presented as the final section.

N.2 Reflectance-based images

For ROI 2b, the spectral comparison plot is shown in Figure 296. Each plotted image spectrum (e.g. `PHPA_Ref_VI`) is a mean of all vegetative spectra contained in ROI 2b. Any masked pixels contained within the ROI are excluded from the mean calculation.

Figure 296 shows the `N_Ref_NoMask_VI` spectrum to be quite dark beyond the 600 nm spectral region and particularly in the NIR region. This is understandable, given that the bright water pixels were not removed prior to normalisation (water strongly absorbs NIR). The `N_Ref_Land_VI` reflectances in the plot is brighter in the green and red spectral regions than the other images. Although Figure 296 shows the final spectral result of the normalisation process, its origins can be understood by referring to both Figure 263 (p. 596 of Appendix L.3) and Figure 265 (p. 599 of Appendix L.3). On those plots, recall that flight line 2 corresponds to the second ‘wavy’ line in from the right (see Figure 106, p. 261 of Section 4.5.9.1). ROI 2b actually represents a subset of that ‘wavy’ line, as the whole ‘wavy’ line represents the whole of flight line 2 – i.e. comprised of all segments 2a, 2b and 2c.

Comparing the normalised line-average of Figure 265 to the land-masked line-average in Figure 263, the red coloured ‘wavy’ line has increased in brightness reflectance. Although a single red wavelength is represented, the whole spectrum

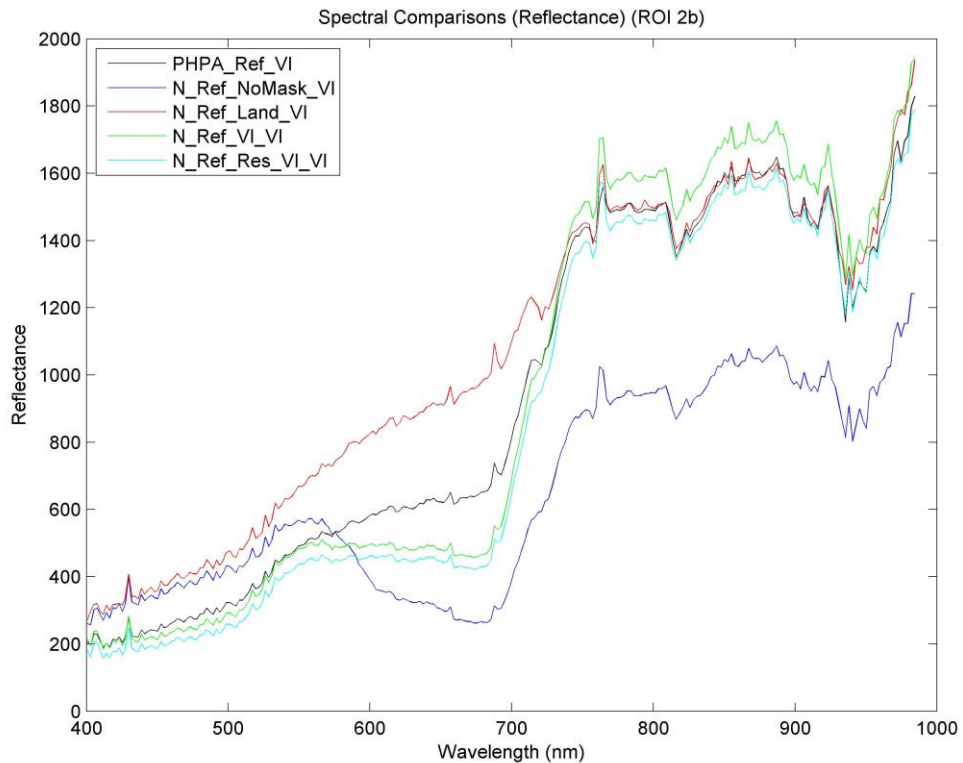


Figure 296: Mean spectra for the five reflectance-based images, corresponding to ROI 2b. (Note: the reflectance is scaled by 10,000)

of Figure 296 shows a corresponding increase. The results of whole spectra are explained by referring back to the line-averaging results. Clearly, by leaving soil spectra intact in the image, the normalised image (N_Ref_Land) increases the red spectra (the soil over Port Hedland appears reddish).

Moreover, there are spectral differences predominantly between $\approx 550 - 700$ nm, where the slope is mostly positive for PHPA_Ref_VI (and N_Ref_Land_VI) but negative for all other images. The large negative slope factor contributes to the large SA difference by N_Ref_NoMask_VI compared to PHPA_Ref_VI, as shown in Table 98.

The SAs in Table 98 shows that, for example, N_Ref_VI_VI is more similar to PHPA_Ref_VI (at 0.08 rad) than N_Ref_Land_VI (at 0.20 rad).

Another consequence of the normalisation process is that the red-edge has increased in length, a concept first introduced in Section 4.5.1, for both the N_Ref_Res_VI_VI and N_Ref_VI_VI compared to PHPA_Ref_VI. The NIR band has been extended at the base while retaining a similar reflectance value at the apex.

ROI 2b	PHPA_Ref_VI	N_Ref_NoMask_VI	N_Ref_Land_VI	N_Ref_VI_VI	N_Ref_Res_VI_VI
PHPA_Ref_VI	-	0.18	0.13	0.08	0.08
N_Ref_NoMask_VI		-	0.20	0.19	0.20
N_Ref_Land_VI			-	0.20	0.20
N_Ref_VI_VI				-	0.07

Table 98: Spectral angles (in radians) between the image mean ROI spectra corresponding to Figure 296.

The same is not true for the N_Ref_Land_VI image, where the red-edge has decreased substantially in length. The N_Ref_NoMask_VI spectrum appears to be a poorer result, where the red-edge takes on a less pronounced slope and is less bright. Given the rather ‘weak’ gradient vegetation present in ROI 2b (based on field knowledge and spectral analysis of the PHPA_Ref image), the lengthening of the red-edge by both the N_Ref_Res_VI_VI and N_Ref_VI_VI images with respect to the PHPA_Ref_VI image would have the effect of creating ‘stronger’ vegetation. The small-red-edge in the N_Ref_Land_VI is due to the inclusion of soil being in the normalisation process. The vegetation in this region is ‘weak’ (e.g. grasses and shrub) while soil pixels are numerous. To the naked eye, the soil is a reddish colour; therefore, the reflectance in the red spectral region is high, leading to a small red-edge. This effect may be significant for classification as the intensity of the NIR reflectance has been used to differentiate deciduous trees (maple) from coniferous trees (pine) (Lillesand (2008), p. 15 and Section 2.6.2.1). The red-edge is clearly more pronounced for the N_Ref_VI_VI compared to the N_Ref_Land_VI, as the former does not contain line-averaged soil spectra. The absence of the red soil clearly exposes the red-edge more clearly. It is important to note that the length of the red-edge is relative to the spectra within the image itself. For instance, although the N_Ref_Land_VI has a small red-edge compared to the N_Ref_VI_VI, it will produce a larger red-edge for ‘stronger’ vegetation. The key is that spectral consistency is required within an image rather than between image.

The plot shown in Figure 296 shows similar spectral patterns for the N_Ref_VI_VI and N_Ref_Res_VI_VI, as expected. Only the northern flight lines have been

modified by removing the urban residential areas for N_Ref_Res_VI_VI; the rest of the data remains the same. The only difference is due to the global trend line being slightly modified due to the changed northern flight line data. The detrending has a minor effect on the whole scene. Therefore, it is reasonable for both N_Ref_VI_VI and N_Ref_Res_VI_VI spectra to be very similar to each other in most of the ROI analysis undertaken in this section.

The preceding ROI 2b spectral samples were taken in the northern-end of flight line 2; in particular, flight line segment 2b. Figure 297 shows the spectral mean result for the southern-end of the adjacent flight – i.e. flight line segment 3a. The plot shows the single means, each corresponding to the reflectance-based images for ROI 3a (excluding masked pixels).

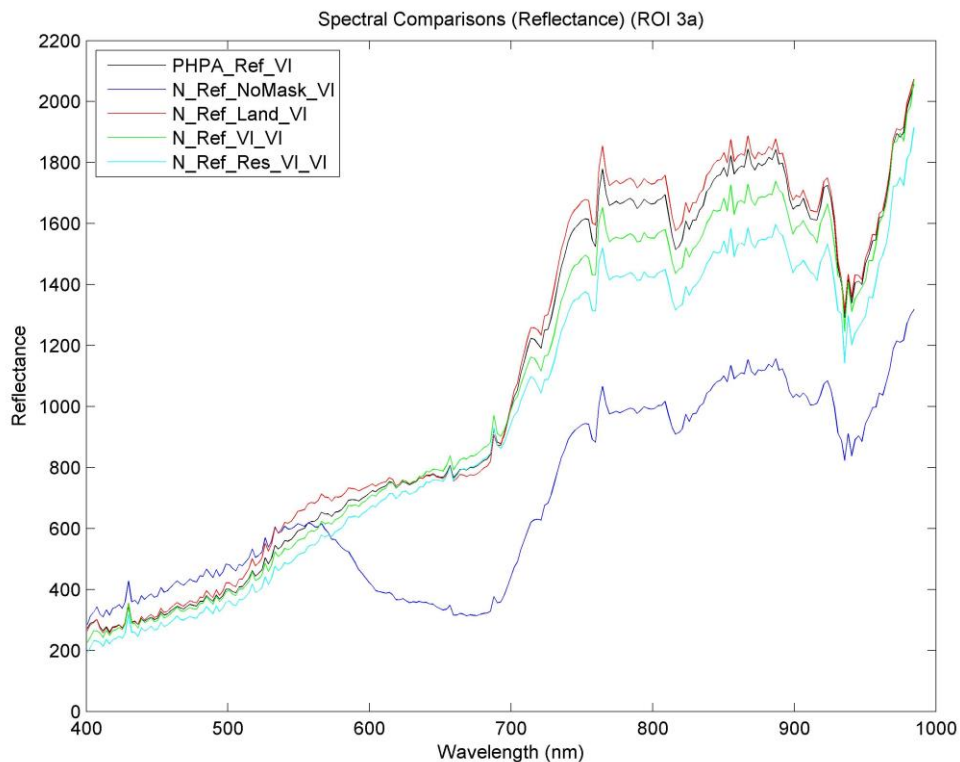


Figure 297: Mean reflectance spectra for ROI 3a.
(Note: the reflectance is scaled by 10,000)

As previously mentioned, one objective of the normalising process is to decrease the reflectance of spectra in the northern section of a flight line with respect to the southern section. Comparing the mean reflectance results for ROI 2b (i.e. Figure 296) with those for ROI 3a, it is indeed observed that mean spectra for the

N_Ref_VI_VI are generally lower for the ROI 2b than for the ROI 3b, especially for wavelengths less than ≈ 700 nm.

With the exception of the N_Ref_NoMask_VI spectra, all spectra follow a well-defined pattern over the full spectral range. This result is reflected by the small SA values given in Table 99. Furthermore, the ‘weak’ vegetation remains ‘weak’ as portrayed by the small red-edge between the spectra.

ROI 3a	PHPA_Ref_VI	N_Ref_NoMask_VI	N_Ref_Land_VI	N_Ref_VI_VI	N_Ref_Res_VI_VI
PHPA_Ref_VI	-	0.18	0.02	0.03	0.04
N_Ref_NoMask_VI		-	0.18	0.19	0.20
N_Ref_Land_VI			-	0.04	0.05
N_Ref_VI_VI				-	0.01

Table 99: Spectral angles (in radians) between the image mean ROI spectra corresponding to Figure 297.

Flight line segment 22d lies on Finucane Island and contains a very distinct boundary with flight line segment 23b. Mean spectra were collected for both a northern and southern region within this (i.e. 22d) flight line segment. The aim is to compare spectra at both ends of the flight line. Figure 294 shows the two ROI’s defined. The normalisation process should have made the brightnesses more consistent over the whole flight line segment; although in practice there are complications as the final stitched image contains overlapping flight line regions (more will be mentioned about this a little later).

The mean spectra for the northern and southern ends of flight line segment 22d takes the form shown in Figure 298 (left) and Figure 298 (right), respectively. In Figure 298, the left plot in particular, reveals the rather disturbing negative reflectances found over a wide range of wavelengths for the PHPA_Ref_VI image right up to the red-edge. The effect is even more pronounced in the N_Ref_NoMask_VI spectra. Negative spectra were previously identified and discussed in Section 4.5.3.3. With the exception of the N_Ref_NoMask_VI image, a much larger number of reflectances have been made positive. This is an

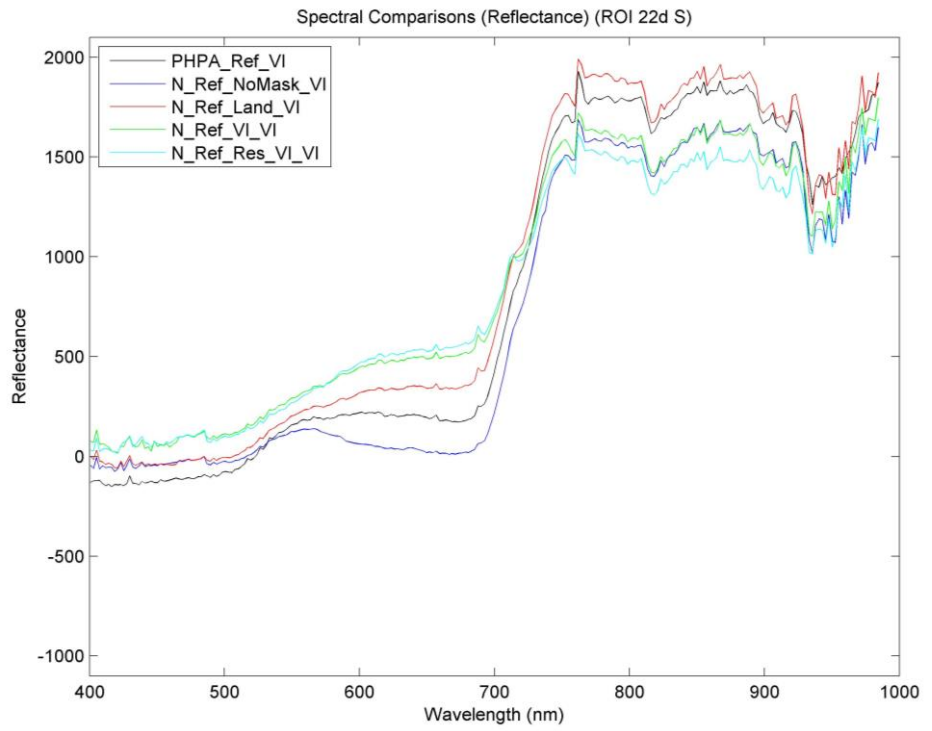
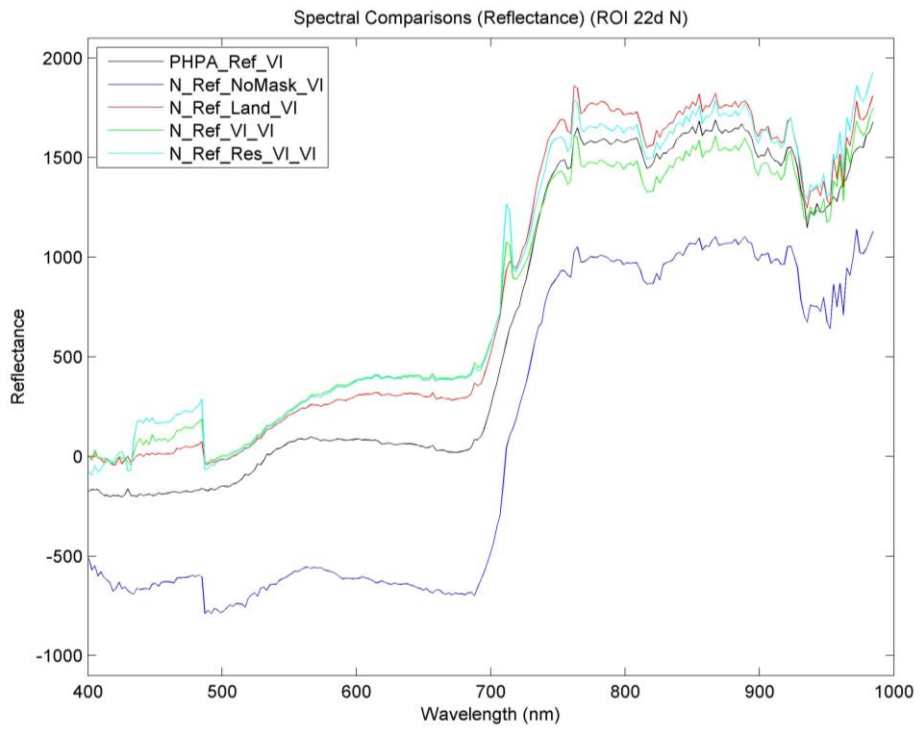


**Figure 298: Mean reflectance spectra for ROI 22d N (left) and ROI 22d S (right).
(Note: the vertical scales are identical and the reflectance is scaled by 10,000).**

encouraging result and indeed expected as an outcome of the normalisation process.

Unfortunately, the presence of the rather sharp bump near the 700 nm wavelength, present in three of the normalised images - a discouraging result. It is evident that PHPA_Ref spectra are noisy (e.g. Figure 59, p. 180 of Section 4.4.2) - the spectra are certainly not smooth functions. Abrupt signal changes are amplified in the normalisation process, as demonstrated in Appendix O in relation to the 'square wave'-like pattern which appears in the blue spectral region. A remedy is also offered in Appendix O, decreasing the sensitivity due to noise.

A SA table has been included for completeness and again shows the largest differences exist between the N_Ref_NoMask_VI image and other images.

ROI 22d N	PHPA_Ref_VI	N_Ref_NoMask_VI	N_Ref_Land_VI	N_Ref_VI_VI	N_Ref_Res_VI_VI
PHPA_Ref_VI	-	0.63	0.14	0.21	0.02
N_Ref_NoMask_VI		-	0.77	0.83	0.82
N_Ref_Land_VI			-	0.08	0.08
N_Ref_VI_VI				-	0.04

Table 100: Spectral angles (in radians) between the mean spectra corresponding to Figure 298 (left image).

ROI 22d S	PHPA_Ref_VI	N_Ref_NoMask_VI	N_Ref_Land_VI	N_Ref_VI_VI	N_Ref_Res_VI_VI
PHPA_Ref_VI	-	0.08	0.07	0.17	0.20
N_Ref_NoMask_VI		-	0.13	0.22	0.26
N_Ref_Land_VI			-	0.11	0.14
N_Ref_VI_VI				-	0.04

Table 101: Spectral angles (in radians) between the mean spectra corresponding to Figure 298 (right image).

The spectral plots for both ROI 22b N and ROI 22b S have the same vertical scale (Figure 298), to aid our discussion. The reflectances over the NIR wavelengths are

highest for the N_Ref_Land, as the line-averaging plot for the N_Ref_Land (Figure 263, p. 596) shows in comparison with the N_Ref_VI (Figure 268, p. 602). The reddish background soil increases the red to NIR reflectances in the spectrum resulting in a larger line-averaging results, thus increasing each adjusted spectrum for the N_Ref_Land.

From Figure 298, for wavelengths less than 700 nm, the reflectances of spectra contained in the normalised images are higher than those in the PHPA_Ref_VI image (the N_Ref_NoMask_VI is now omitted from any further discussion due to the poor spectral quality). Both the N_Ref_Land_VI & N_Ref_VI_VI plots show a higher degree of similarity in reflectance values compared to the PHPA_Ref_VI, possibly an encouraging result.

Figure 299 shows the flight line boundary at point B to be less discernible for the N_Ref_VI than PHPA_Ref. This edge is defined by the intersection of flight line segments 22d (to the south) and 23b (to the north). As a result, spectral samples are now analysed to provide further insight into the reasons for the apparent improvement. The word apparent signifies caution, as Figure 299 was constructed using only 3 bands without regard to the other 243 bands. A spectrum provides a complete picture of the real situation, but cannot be fully represented in a true colour image.

Between the flight boundaries, indicated by A and B, lies flight line segment 23b. Directly to the north of the boundary at A lies flight line segment 28c while directly south of the boundary at B is flight line segment 22d. The gamma of both images has been adjusted to 1.5 to help emphasise the flight boundaries.

Overall, the PHPA_Ref image (Figure 299, left), is darker than the N_Ref_VI image (Figure 299, right). Comparing the mean spectra for ROI 22d N (Figure 298, left) with ROI 22d S (Figure 298, right) shows that the normalised images are brighter than the original PHPA_Ref image (recall that the N_Ref_NoMask_VI is omitted from the discussion for reasons provided earlier). Indeed, there are far fewer negative reflectances, particularly in the ROI 22d N plot for wavelengths less than 700 nm. Similar comments apply to the mean spectra plot for ROI 23b (shown in Figure 300).

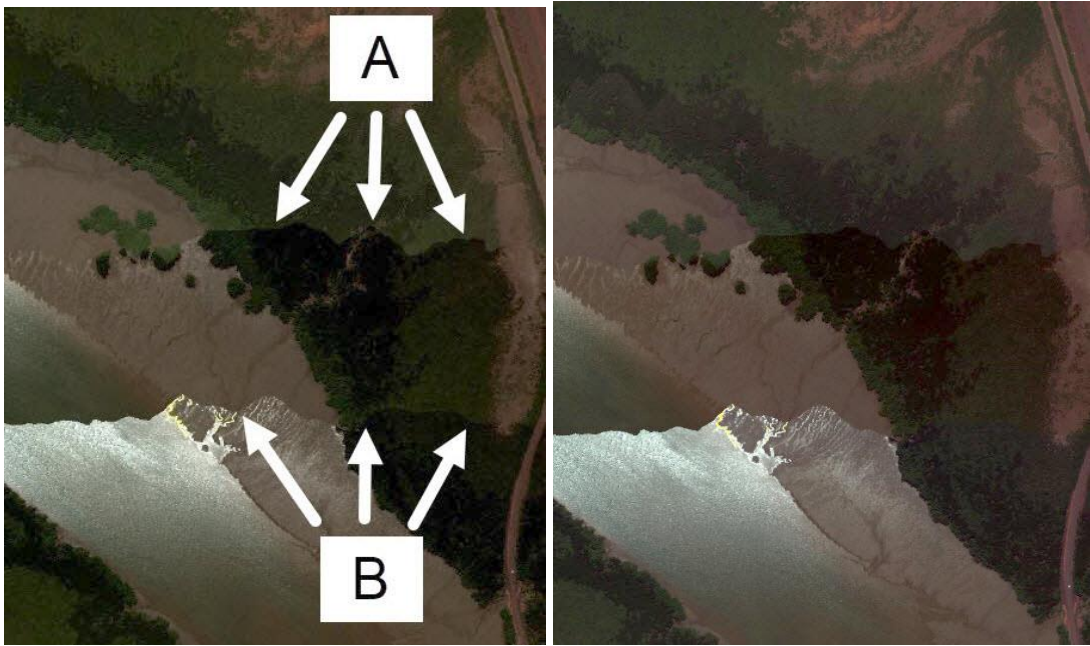
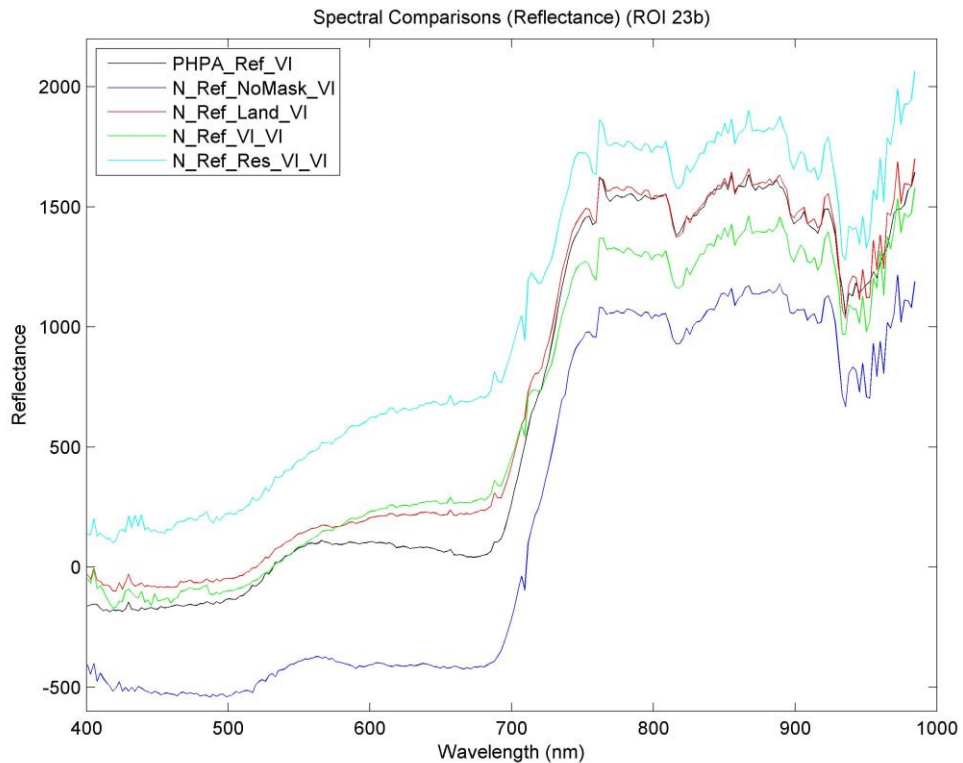


Figure 299: True colour image of flight line edges for the PHPA_Ref (left) and the N_Ref_VI (right) image. The regions are located on Finucane Island.

The flight line boundary located at B (in Figure 299, right) appears less pronounced for N_Ref_VI than PHPA_Ref (Figure 299, left). To the southern side of the boundary lies ROI 22d N while ROI 23b lies just to the south of the boundary at A. Spectrally, it is expected that the brightness difference between them is more pronounced for the PHPA_Ref data than the N_Ref_VI (which is spectrally more uniform). This amounts to comparing Figure 298 (left, for ROI 22d N) with Figure 300 (for ROI 23b). Spectrally, the reflectances corresponding to ROI 23b (i.e. Figure 300) appear darker than for ROI 22d N (i.e. Figure 298). The brightness difference between the two plots for the N_Ref_VI_VI appears larger than for the PHPA_Ref_VI. There are a few considerations. Firstly, the true colour image of Figure 299 for N_Ref_VI was reconstructed from N_Ref_VI_VI. That is, the reflectance-segmented files were vegetatively masked prior to the normalisation process. Therefore, vegetation spectra have been normalised and made more consistent. However, based on the line-averages as calculated for vegetation (because of the vegetative mask), a true colour image was reconstructed. Therefore, all non-vegetative spectra have also been adjusted (falsely – further details were given in Section 4.5.9.2 and Appendix M). The second point is that Figure 299 may be a false representation of the true situation. The 3 band image has been constructed using the default RGB bands, as



**Figure 300: Mean reflectance spectra for ROI 23b (shown in Figure 293).
(Note: the reflectance is scaled by 10,000)**

defined in Section 3.3 – i.e. Band 18 (B): 0.4388 μm , Band 66 (G): 0.5494 μm and Band 116 (R): 0.6687 μm . It is possible that the 3 band image is giving an incomplete picture in this case; although the image appears ‘better’, spectrally the differences appear somewhat less pronounced. It is interesting to compare the actual reflectance values for both images at these wavelengths. These have been summarised in Table 102.

Clearly, the differences for the N_Ref_VI_VI exceed those of the PHPA_Ref_VI at each of these display RGB wavelengths. For example, between ROI 22d N and ROI 23b at the green wavelength, the difference between them is 10 units of reflectance (i.e. 80 – 70) for the PHPA_Ref_VI image.

A re-examination of the ROI’s reveals that ROI 23b incorporates darker vegetation than ROI 22d N. Instead, spectra must be sampled closer to boundary B (of Figure 299, left). These two ROI’s are displayed in Figure 301 – the red and green ROI’s located to the north and south of the boundary, respectively. Note that in this case, both images are not exactly the same file size. This is due to the vegetative

PHPA_Ref_VI	B (0.4388 μm)	G (0.5494 μm)	R (0.6687 μm)
ROI 22d N	-188	70	22
ROI 23b	-169	80	43

N_Ref_VI_VI	B (0.4388 μm)	G (0.5494 μm)	R (0.6687 μm)
ROI 22d N	90	231	391
ROI 23b	-101	84	269

Table 102: Reflectance values (scaled by 10,000) corresponding to default RGB wavelengths as used in this thesis. The reflectances correspond to the plots in Figure 300 (for ROI 23b) and Figure 298 (for ROI 22d N) for the PHPA_Ref_VI and N_Ref_VI_VI images.

mask eliminating the northern-most two flight lines in N_Ref_VI_VI. Extensive reasons were given in Appendix L.5. However, a suitable transformation allows the ROI to be defined at identical locations in both images, using the techniques outlined in Appendix W.4. The ROI average plots are shown in Figure 302.

The plots in Figure 302 show that the reflectances of the N_Ref_VI_VI image are more closely matched than those for the PHPA_Ref_VI image (with a few exceptions; e.g. between $\approx 430 - 490$ nm). The reflectances at the default RGB wavelengths (used in this thesis) are given in Table 103, which tells the same story. Therefore, the N_Ref_VI_VI data is more consistent than the PHPA_Ref_VI, as it produces more similar spectral data between adjacent flight boundaries. Some spectral differences are expected, as there is no reason to suggest that both north and south ROI's contain identical vegetative matter.

One interesting aspect shown in Figure 300 concerns the effect of removing the urban residential areas along with the large ponds of water (flight line segment 23D of Figure 42, p. 141 with the full region removal displayed in Figure 283, p. 615). All reflectances in the N_Ref_Res_VI spectrum have increased, especially over the RGB wavelengths (i.e. less than 700 nm). These are indicated by the large SAs in Table 104.

There are other sharp boundaries present in the PHPA_Ref image (Figure 42, p. 141 of Section 3.3). For example, one lies between flight line segment 28c (to the north) and 23b (to the south), corresponding to flight line boundary A in Figure 299.

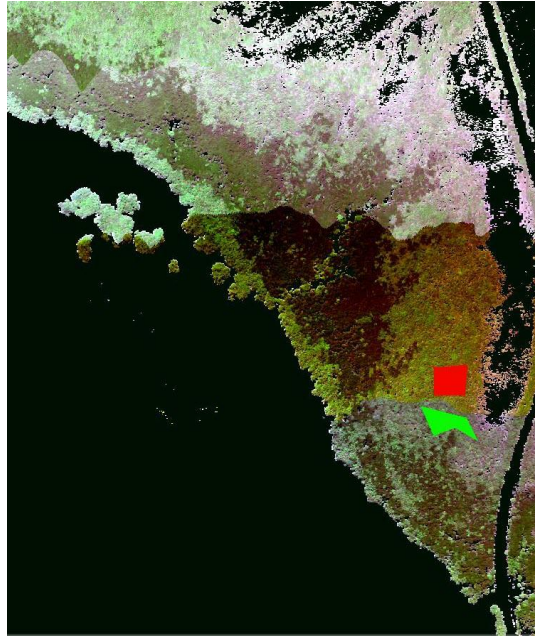


Figure 301: This image shows the defined ROI's superimposed onto the N_Ref_VI_VI image. The ROI's surround the flight line boundary as represented by position "B" in Figure 299 (left image). The image is contrast enhanced using linear 2% stretch.

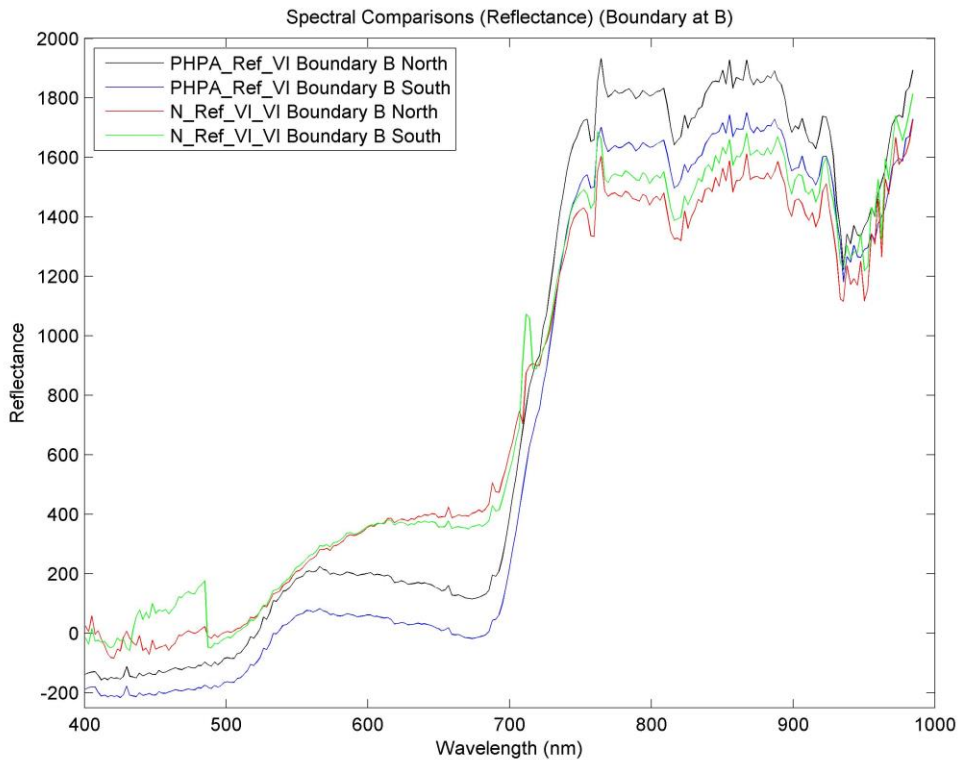


Figure 302: ROI averages for PHPA_Ref_VI and N_Ref_VI_VI to the north (the red ROI in Figure 301) and south (the green ROI in Figure 301) of the flight line boundary "B" (represented by "B" in Figure 299 (left image)). (Note: the reflectance is scaled by 10,000).

PHPA_Ref_VI	B (0.4388 μm)	G (0.5494 μm)	R (0.6687 μm)
North	-134	184	119
South	-200	60	-15

N_Ref_VI_VI	B (0.4388 μm)	G (0.5494 μm)	R (0.6687 μm)
North	-8	208	396
South	79	221	355

Table 103: Reflectance values (scaled by 10,000) corresponding to default RGB wavelengths as used in this thesis. The reflectances correspond to the plots in Figure 302.

ROI 23b	PHPA_Ref_VI	N_Ref_NoMask_VI	N_Ref_Land_VI	N_Ref_VI_VI	N_Ref_Res_VI_VI
PHPA_Ref_VI	-	0.45	0.09	0.12	0.30
N_Ref_NoMask_VI		-	0.53	0.54	0.74
N_Ref_Land_VI			-	0.06	0.21
N_Ref_VI_VI				-	0.20

Table 104: Spectral angles (in radians) between the image mean ROI spectra corresponding to Figure 300.

Comparing ROI 23b (Figure 300) with ROI 28c (Figure 303) we note that the reflectances for ROI 28c tend to be higher compared to ROI 23b (with the exception of N_Ref_Res_VI_VI). The result is borne out in the N_Ref_VI image of Figure 293, where pixels in ROI 23b (shown in green in Figure 293) are dark compared to those in ROI 28c (the blue region in Figure 293). The result is a clearly identifiable flight line boundary.

Spectrally, the N_Ref_Land_VI spectrum bares a good resemblance to the PHPA_Ref_VI image (where the SA is 0.05 rad – see Table 105 over the page). As previously discussed, the effect is caused by line-averaging included soil pixels. Removal of soil clearly has the effect of decreasing the height of the red-edge in addition to decreasing the gradient.

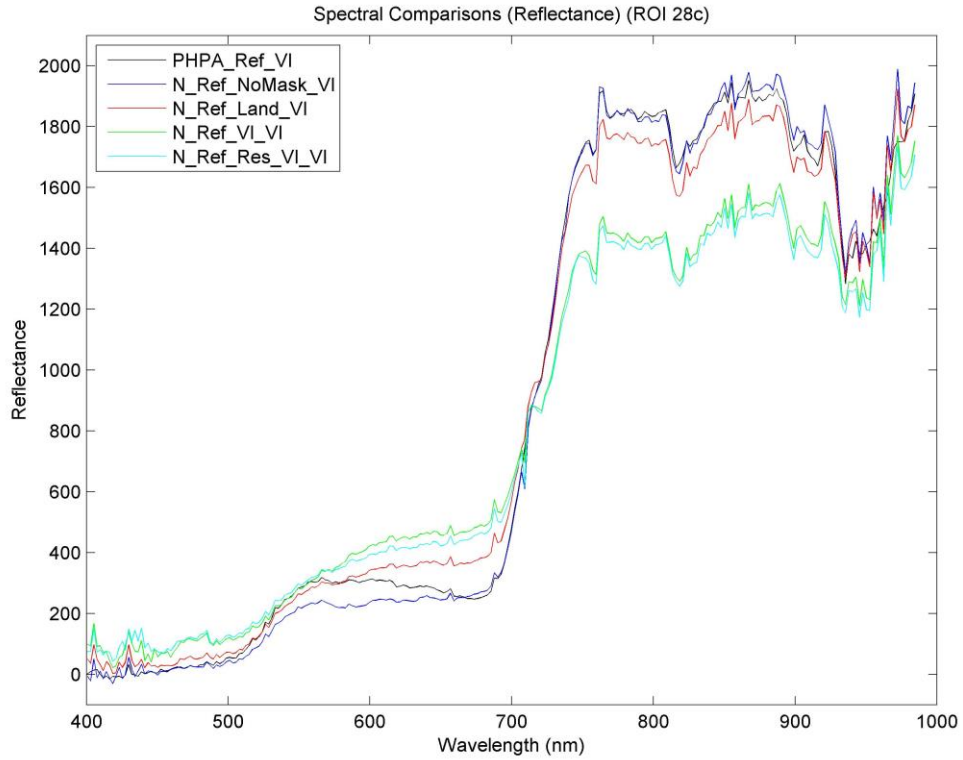


Figure 303: Mean reflectance spectra for ROI 28c.
(Note: the reflectance is scaled by 10,000)

Spectral angles corresponding to the studied images are provided in Table 105.

ROI 28c	PHPA_Ref_VI	N_Ref_NoMask_VI	N_Ref_Land_VI	N_Ref_VI_VI	N_Ref_Res_VI_VI
PHPA_Ref_VI	-	0.04	0.05	0.13	0.13
N_Ref_NoMask_VI		-	0.06	0.14	0.13
N_Ref_Land_VI			-	0.09	0.08
N_Ref_VI_VI				-	0.02

Table 105: Spectral angles (in radians) between the image mean ROI spectra corresponding to Figure 303.

The final comparison, for reflectance-based images, is concerned with the effect of the global trend linear line. On opposite sides near the centre of the pivot (i.e. centre of the trend line), it is expected that the brightness would appear more equal, as the reflectances have been normalised. Both ROI NW and ROI SW were defined to examine this in detail. The defined ROI's were displayed in Figure 295,

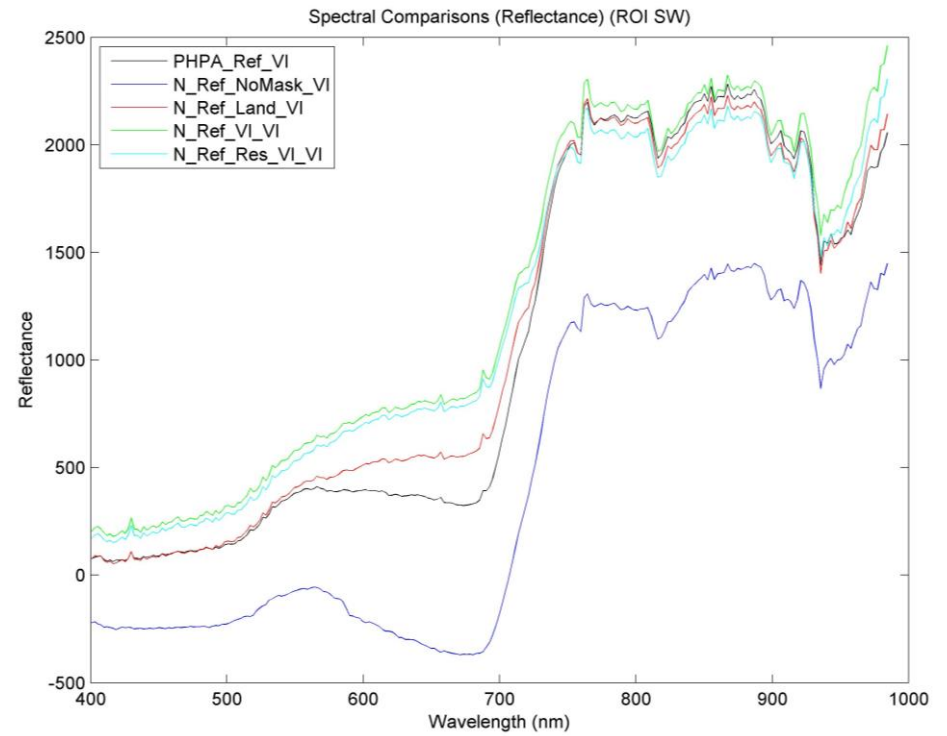
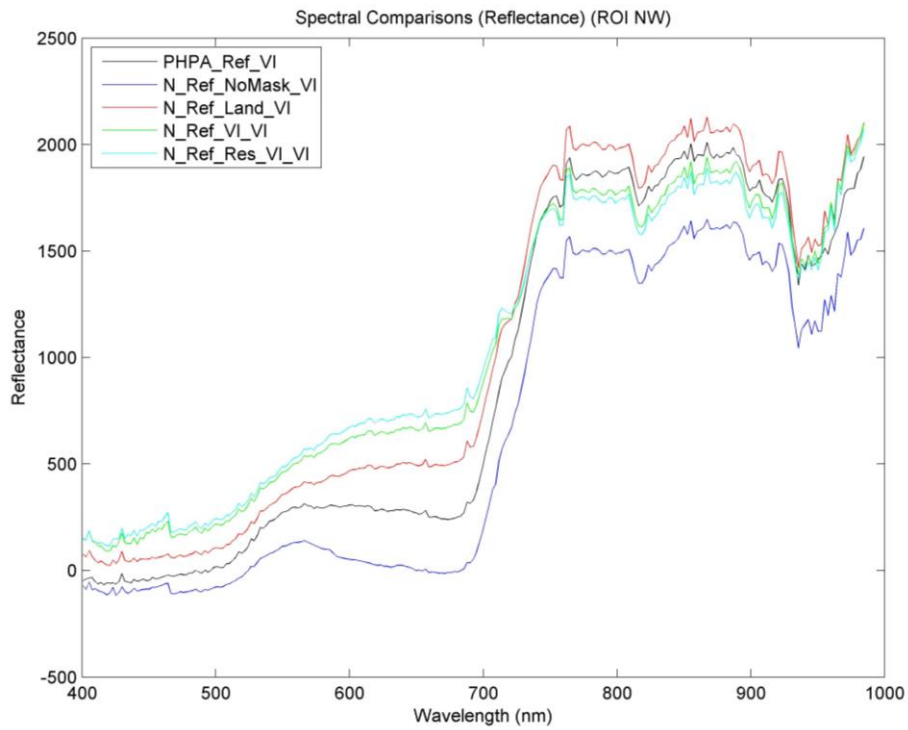


**Figure 304: Mean reflectance spectra for ROI NW (left) and ROI SW (right).
 (Note: the vertical scales are identical and the reflectance is scaled by 10,000).**

while the mean plots are given in Figure 304. Naturally, it is unreasonable to expect identical spectral reflectances for both ROI's, as there is no reason to suppose the vegetation to be identical in both ROI's.

The encouraging fact to take away from this is that the spectral brightnesses are similar to each other between both plots over wavelengths up to ≈ 700 nm, especially for the N_Ref_VI_VI. This does not apply to the PHPA_Ref_VI spectra, as there is a larger reflectance for ROI SW compared to ROI NW in the RGB region. The NIR region tells a different story and could be related to the different vegetation present between the two regions.

The SAs for both the ROI NW and ROI SW regions are shown in Table 106 & Table 107.

ROI NW	PHPA_Ref_VI	N_Ref_NoMask_VI	N_Ref_Land_VI	N_Ref_VI_VI	N_Ref_Res_VI_VI
PHPA_Ref_VI	-	0.12	0.09	0.18	0.21
N_Ref_NoMask_VI		-	0.20	0.29	0.32
N_Ref_Land_VI			-	0.10	0.13
N_Ref_VI_VI				-	0.03

Table 106: Spectral angles (in radians) between the image mean ROI spectra corresponding to Figure 304 (left).

ROI SW	PHPA_Ref_VI	N_Ref_NoMask_VI	N_Ref_Land_VI	N_Ref_VI_VI	N_Ref_Res_VI_VI
PHPA_Ref_VI	-	0.38	0.07	0.16	0.16
N_Ref_NoMask_VI		-	0.43	0.52	0.52
N_Ref_Land_VI			-	0.09	0.09
N_Ref_VI_VI				-	0.01

Table 107: Spectral angles (in radians) between the image mean ROI spectra corresponding to Figure 304 (right).

Both of these tables once again show the close spectral similarity between N_Ref_VI_VI and N_Ref_Res_VI_VI. The small SA of 0.01 rad (indicating very high spectral similarity) between these two images for ROI SW is expected, as the major

change between the two images involved the removal of the (mainly) vegetative pixels in the urban residential areas (as shown in Figure 283, p. 615), which corresponds to the northern region. The northern region (ROI NW) shows a larger SA (i.e. 0.03 rad), as expected due to larger effects on line-averaging thereby affecting normalised spectra.

N.3 Radiance-based images

Besides normalised reflectance-based images, normalised radiance-based images were also generated. A similar study now follows using identical pixels for each ROI, as defined in Appendix N.1.

As for the reflectance plots, the radiance vertical scale changes between plots. Furthermore, the radiances are scaled by 90. Although all radiance-based plots are displayed on the same graph, the units are not all based on radiance; normalised images are in units of normalised radiance.

Beginning with ROI 2b (Figure 305) the close relationship between N_Rad_VI_VI and N_Rad_Res_VI_VI is once again evident. In addition, all normalised spectra are brighter than the PHPA_Rad_VI, just like they were in reflectance-based spectra (Figure 296).

Some of the most striking features present in the radiance plots (Figure 305) are the atmospheric absorption lines. The two main lines are located at 760 nm and 940 nm and caused by oxygen and water vapour absorption, respectively (as evident from the work in Section 2.3.3). All radiance plots are expected to contain these atmospheric absorption lines, as the plots have not been atmospherically corrected using a radiometric model (e.g. Tafkaa).

Comparisons between the mean radiance plots, corresponding to ROI 2b (Figure 305) and ROI 3a (Figure 306), shows the radiance brightnesses to be better matched compared to those from reflectance-based images (i.e. Figure 296 and Figure 297). For example, the N_Rad_Land_VI radiance at 400 nm is $\approx 19 \text{ W}\cdot\text{m}^{-2} \mu\text{m}^{-1} \text{ sr}^{-1}$, written here as $\text{Rad}(400 \text{ nm}) \approx 19$, while $\text{Rad}(600 \text{ nm}) \approx 40$.

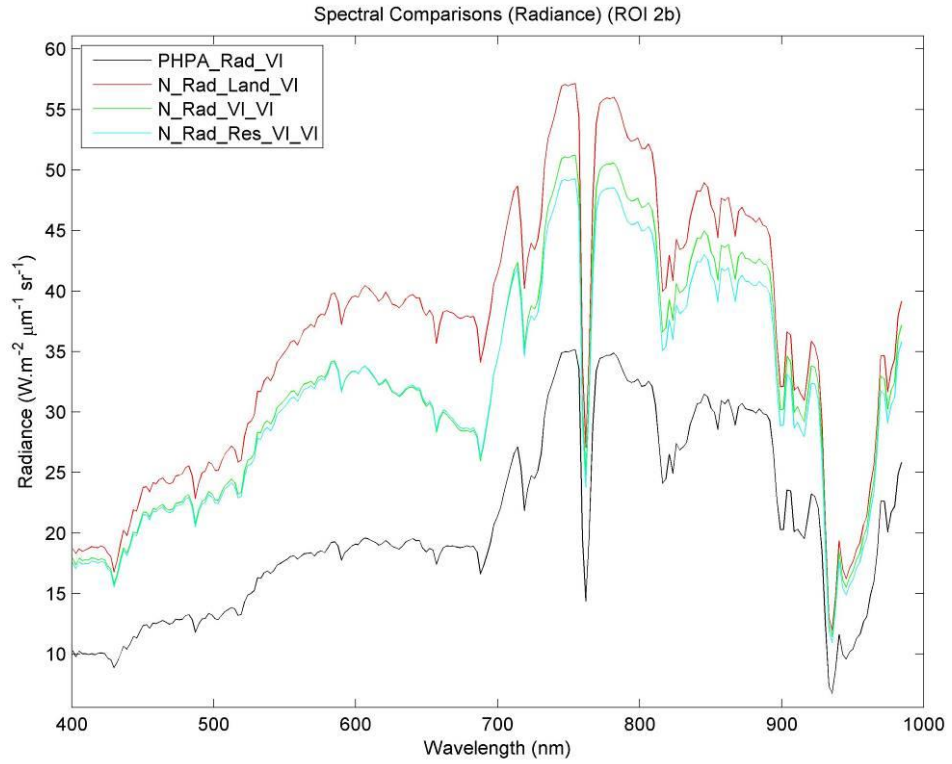


Figure 305: Mean spectra corresponding to the four radiance-based images for ROI 2b.

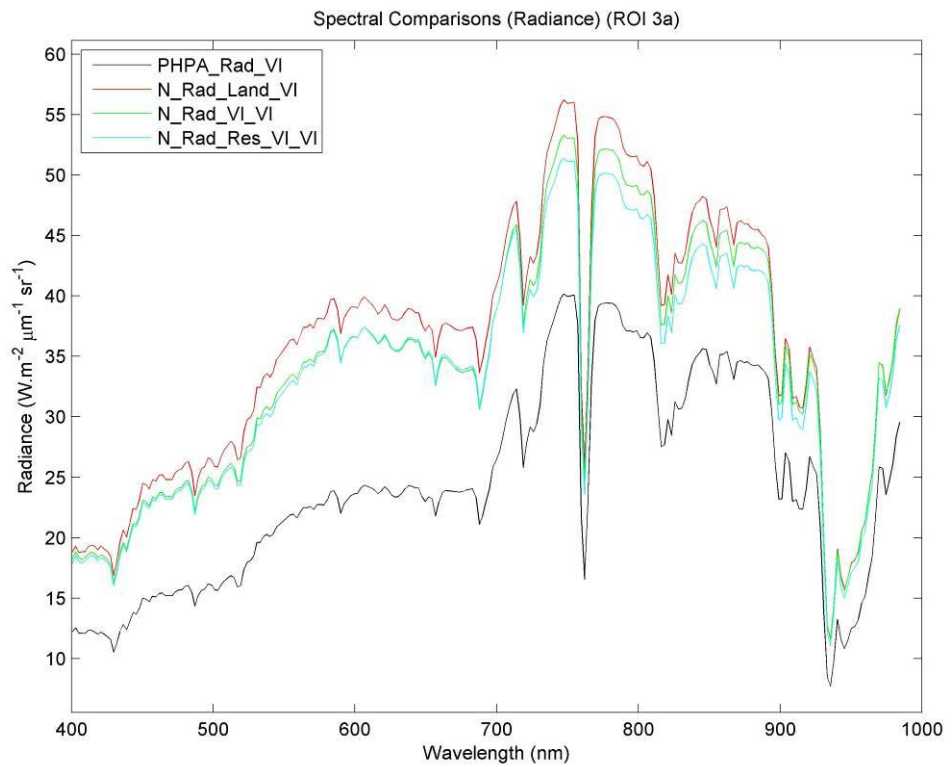


Figure 306: Mean spectra corresponding to the four radiance-based images for ROI 3a.

Overall, similar radiance values (along with curve characteristics such as gradients) exist between both ROI 2b and ROI 3a plots for the normalised images. The radiance values vary for the PHPA_Rad_VI. For instance, from the ROI 2b plot (Figure 305); $\text{Rad}(400 \text{ nm}) \approx 10$, $\text{Rad}(600 \text{ nm}) \approx 17$ while from the ROI 3a plot the results are $\text{Rad}(400 \text{ nm}) \approx 13$ and $\text{Rad}(600 \text{ nm}) \approx 22$. The normalised (radiance) images are more consistent between the flight lines and brighter. For example, $\text{Rad}(400 \text{ nm}) \approx 18$ for all images and for both ROI 2b and ROI 3a.

The length of the red-edge for the reflectance plot (i.e. ROI 3a - Figure 297) appears to be generally unchanged but not so for ROI 2b (Figure 296). However, for the corresponding radiance plots the only change appears an increase in brightness – both the shape and length are well preserved compared to the PHPA_Rad_VI images. In fact, the red-edge is relatively short in both radiance plots. This could be viewed as a positive result, as the vegetation is ‘weak’ at both ROI locations and likely encompasses similar vegetative types (and similar state). Similar brightnesses indicate that the brightness bias in traversing across a flight line has been decreased. This is what the normalising process aims to achieve.

The SAs between the images corresponding to the same ROI are given Table 108 and Table 109. The maximum SA of 0.09 rad indicate a high degree of similarity between spectra (SA magnitudes were discussed in Section 4.4.1).

ROI 2b	PHPA_Rad_VI	N_Rad_Land_VI	N_Rad_VI_VI	N_Rad_Res_VI_VI
PHPA_Rad_VI	-	0.11	0.08	0.09
N_Rad_Land_VI		-	0.05	0.04
N_Rad_VI_VI			-	0.02

Table 108: Spectral angles (in radians) between the image mean ROI spectra corresponding to Figure 305.

Again, both the plots and the SA calculations suggest that similar spectra exist between the images on a large scale for both ROI's (i.e. ROI 2b & ROI 3a).

ROI 3a	PHPA_Rad_VI	N_Rad_Land_VI	N_Rad_VI_VI	N_Rad_Res_VI_VI
PHPA_Rad_VI	-	0.08	0.07	0.08
N_Rad_Land_VI		-	0.02	0.02
N_Rad_VI_VI			-	0.02

Table 109: Spectral angles (in radians) between the image mean ROI spectra corresponding to Figure 306.

In comparing the ROI 22d N reflectance (Figure 298) with the radiance plot (Figure 307, left), we find the ‘bump’ feature at ≈ 700 nm even more pronounced for radiance data. The PHPA_Rad_VI plot contains a ‘small’ bump whereas the PHPA_Ref_VI plot does not (although under close scrutiny, a minor change in gradient is just evident). The fact that neither of these images have been normalised suggests that Tafkaa has all but removed the bump. The bump is less pronounced for the N_Ref_Land_VI based plot (compared to other N_Ref_x images – i.e. x is VI_VI, Ref_VI or Res_VI) and although the bump is quite pronounced for the N_Rad_Land_VI, it appears less so than the other N_Rad_y images (where y is VI_VI, Res_VI). This suggests that soil is smoothing out the differences in both reflectances and radiances around the 700 nm wavelengths.

The PHPA_Ref image also contains soil but unlike the N_Ref_Land_VI image, it also contains water. Both the red and IR wavelength regions for the N_Rad_Land_VI image appear to be well correlated with similar radiances (as shown in Figure 276 (p. 609)).³⁵ Therefore, soil has the effect of removing the sharp change between mean flight line-averages. It is possible that, with soil spectra present, smaller differences exist between flight line segment 22d and 23b. When larger differences exist, the final stitched image may have removed troublesome pixels (e.g. those containing large deviations in spectra between flight lines) to give a smooth transition for images such as the N_Ref_VI_VI (or N_Rad_VI_VI).

It is also worth noting that these ‘bumps’ (at ≈ 700 nm) are larger for both the N_Ref_Res_VI_VI and N_Rad_Res_VI_VI (i.e. Figure 298 & Figure 307) compared to

³⁵ The word “appear” signifies that only one wavelength for each of red and infra-red are plotted and that the conclusion was based on this. A formal correlation analysis was not performed and beyond the scope of the thesis objectives.

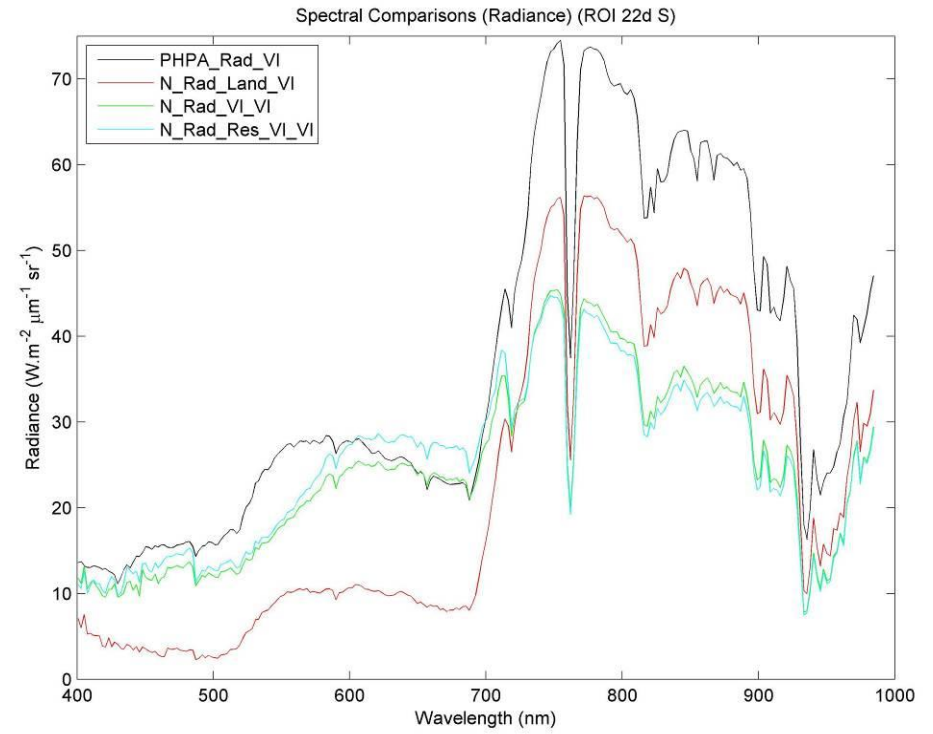
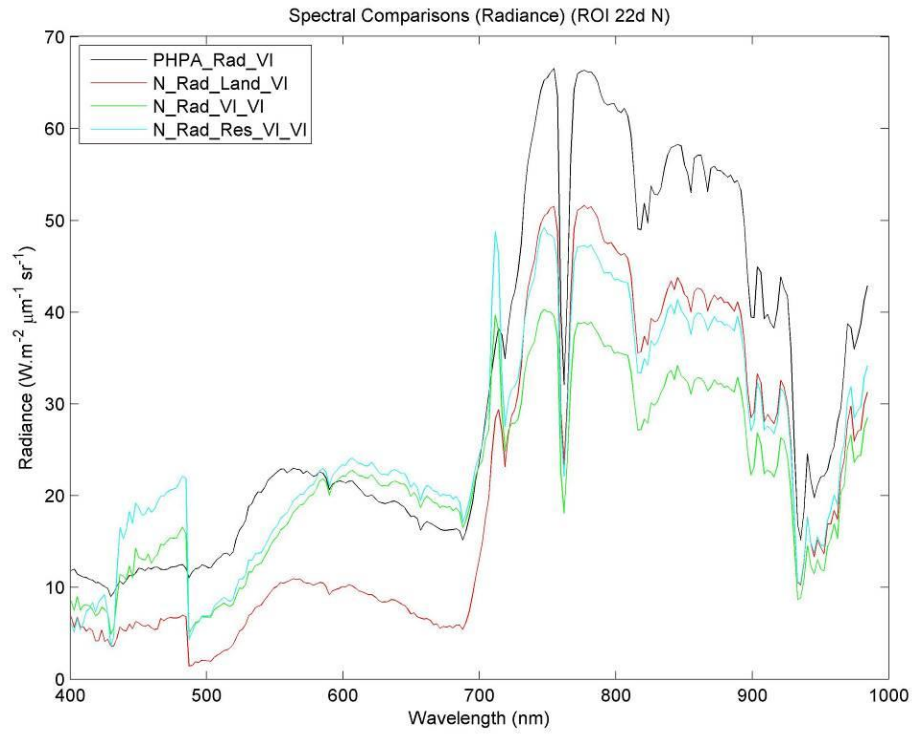


Figure 307: Mean radiance spectra for ROI 22d N (left plot) and ROI 22d S (right plot).

the N_Ref_VI_VI and N_Rad_VI_VI plots. The removal of the 'weak' residential grassed spectra increases the bump height. The 'strong' vegetative mangroves along the flight line have been made weaker due to the 'weaker' vegetation (i.e. urban-based grassed regions) in line-averaging. The spectral change is more pronounced for the N_Ref_Res_VI and N_Rad_Res_VI_VI images.

The length of the red-edge, for all reflectance-based images in ROI 22d N and ROI 22d S (Figure 298), are similar to that of the PHPA_Ref_VI plot. However, for the corresponding radiance-based images (Figure 307), this is no longer the case. Interestingly, it is the vegetation-based normalised images, which have been affected - i.e. the N_Rad_VI_VI and N_Rad_Res_VI_VI (but not the N_Rad_Land_VI). Both the N_Rad_VI_VI and N_Res_VI_VI experience a substantial decrease in the red-edge length compared to the original (i.e. unprocessed PHPA_Rad_VI) plot. The vegetative spectra are mainly for mangrove forests, containing a particularly strong NDVI index (and large gradient). This could give rise to concern, as a decrease in red-edge will lead to an NDVI value relating to 'weaker' vegetation (e.g. grass). However, as the normalisation process is consistent, all spectra in N_Rad_VI_VI would be modified consistently across the whole image. Therefore, weak vegetation would contain an even smaller red-edge; spectra are relative to each other in a particular image meaning that comparisons between images are irrelevant. Interestingly, the N_Rad_Land_VI red-edge appears similar in length to PHPA_Rad_VI but with a decrease in brightness.

Interestingly, between 500 – 600 nm, the radiances between a) N_Rad_VI_VI and N_Rad_Res_VI_VI are similar in shape, as are those between b) N_Rad_Land_VI and PHPA_Rad_VI. However, between a) and b) the shape changes. The spectral shapes between reflectance plots (Figure 304) are fairly similar, especially between the normalised images, although there is a gradient difference between the PHPA_Ref_VI and the normalised images.

For ROI 22d N, the 'square' function appears in both reflectance and radiance plots, while being absent in both plots for ROI 22d S. The origin of this 'square function' appears to be due to the original image but amplified by the Normalisation process. For instance, the 'square' function appears at $\approx 430 - 480$ nm in ROI 23 d (Figure 308) and even in ROI 22d S (Figure 307, right plot).

The earlier reflectance spectral comparison between ROI 22d N (Figure 298) and ROI 23b (Figure 300) found that normalised spectra were brighter (except the N_Ref_Res_VI). For the radiance data, this is not the case. Recall that the aim was to reduce the brightness of the northern-end of a particular flight line and to line them up with the next (adjacent) flight line. This observation holds well for wavelengths over 600 nm (in Figure 307) when considering the N_Rad_VI_VI and N_Rad_Res_VI for ROI 22d N. However, for ROI 23b, only the N_Rad_VI_VI brightnesses appear sound – i.e. for wavelengths over 600 nm, both the spectral shape and radiance values appear to be similar between ROI 22d N and ROI 23b (Figure 307 and Figure 308) compared to corresponding reflectance plots (Figure 298 and Figure 300). Once again, it is worth noting that the spectra are unlikely to be identical due to the different vegetation (and their possibly their states) sampled at each ROI.

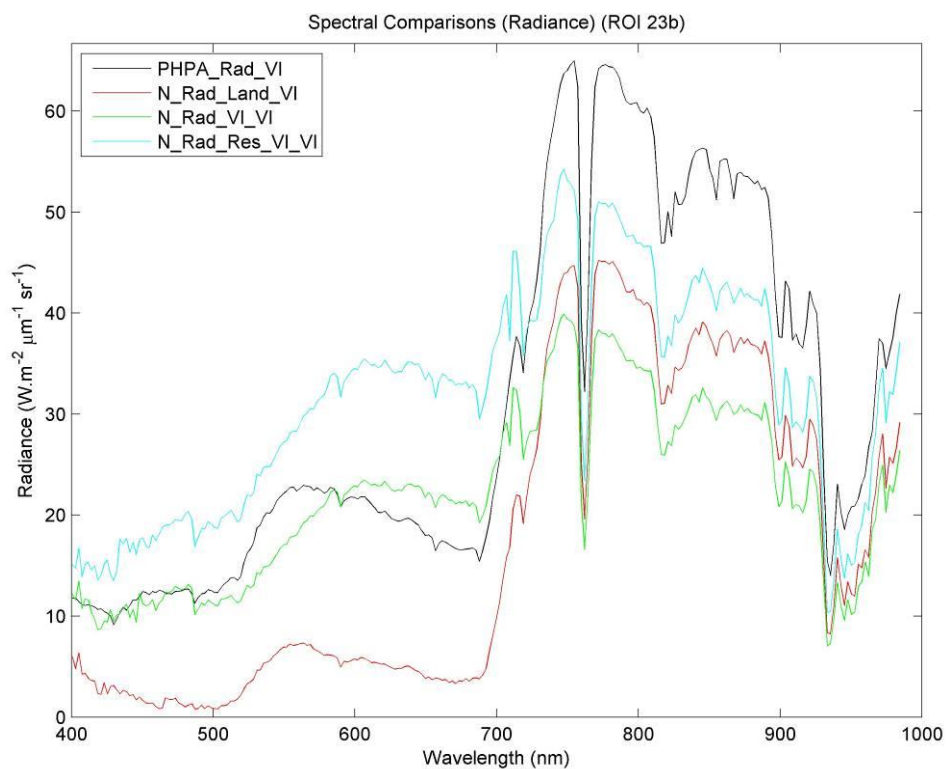


Figure 308: Mean radiance spectra for ROI 23b.

The following tables (Table 110 to Table 112) contain SAs between the radiance-based images for ROI 23b, ROI 22d N and ROI 22d S. These show the large SAs

between the PHPA_Rad_VI image and normalised data, indicating that significant changes have occurred due to normalisation.

ROI 23b	PHPA_Rad_VI	N_Rad_Land_VI	N_Rad_VI_VI	N_Rad_Res_VI_VI
PHPA_Rad_VI	-	0.23	0.24	0.29
N_Rad_Land_VI		-	0.46	0.51
N_Rad_VI_VI			-	0.06

Table 110: Spectral angles (in radians) between the image mean ROI spectra corresponding to Figure 308.

ROI 22d N	PHPA_Rad_VI	N_Rad_Land_VI	N_Rad_VI_VI	N_Rad_Res_VI_VI
PHPA_Rad_VI	-	0.15	0.22	0.19
N_Rad_Land_VI		-	0.34	0.30
N_Rad_VI_VI			-	0.07

Table 111: Spectral angles (in radians) between the image mean ROI spectra corresponding to Figure 307.

ROI 22d S	PHPA_Rad_VI	N_Rad_Land_VI	N_Rad_VI_VI	N_Rad_Res_VI_VI
PHPA_Rad_VI	-	0.21	0.18	0.25
N_Rad_Land_VI		-	0.37	0.43
N_Rad_VI_VI			-	0.07

Table 112: Spectral angles (in radians) between the image mean ROI spectra corresponding to Figure 307.

In a similar manner to that for reflectance, for the flight line boundary indicated at point B (of Figure 299, left), a mean spectrum was calculated for each of the two ROI's shown in Figure 301. Because the N_Rad_VI image is identical in size to the PHPA_Rad image, exactly the same ROI's were used on both images. Recall that the N_Ref_VI image is smaller than the PHPA_Ref (reasons were given in Appendix L.4), leading to unequal sizes. The spectral plots are given Figure 309.

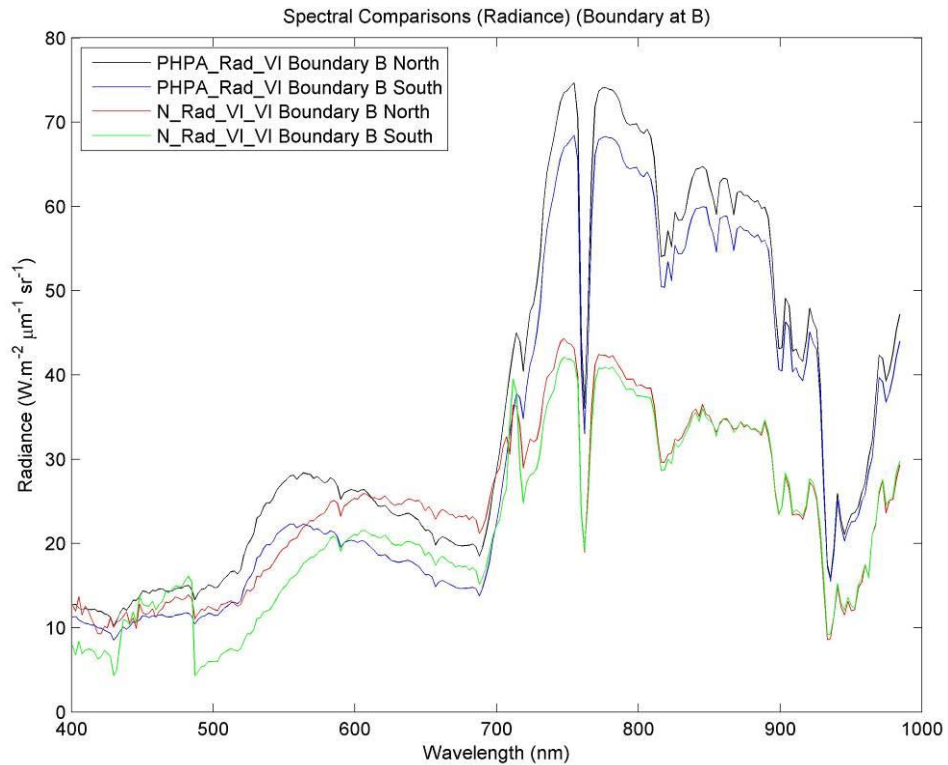


Figure 309: ROI averages for PHPA_Rad_VI and N_Rad_VI_VI to the north (the red ROI in Figure 301) and south (the green ROI in Figure 301) of the flight line boundary “B” (represented by “B” in Figure 299 (left image)).

The brightness of the southern ROI is darker for both images compared to the north. However, the difference in brightness between these two ROI’s is fairly constant from ≈ 480 to 700 nm for both images. The ‘square’ waveform is evident in the N_Rad_VI_VI in the southern ROI in the blue spectral region. Interestingly, the radiances in the NIR region (over 700 nm) exhibit a higher degree of similarity between the ROI’s for the N_Rad_VI_VI image. This suggests the NIR spectra are similar on both sides of the boundary, possibly leading to increased spectral consistency. However, the length of the red-edge is much smaller than the PHPA_Rad_VI image. The length is a relative measure – if ‘weak’ vegetation in all regions of the image contain a smaller red-edge but spectra are more consistent over all flight boundaries, then cluster formation (in the classification process) is expected to yield more consistent results. Spectra appear to be more consistent for the N_Rad_VI_VI between ROI 23b (south of the flight line boundary “A” in Figure 299, left) and ROI 28c (north of flight line boundary “A”) than for the N_Ref_VI_VI;

both the spectral shape and intensities appear similar. The plot for ROI 28c is shown in Figure 310.

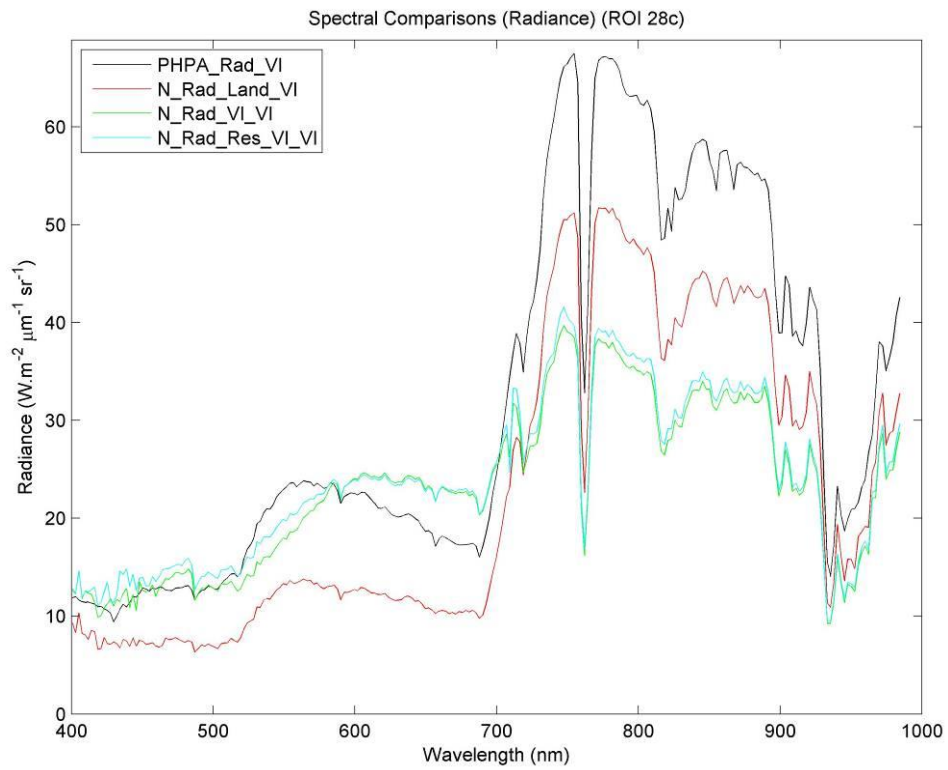


Figure 310: Mean radiance spectra for ROI 28c.

For completeness, the SA table for ROI 28c (Table 113) demonstrates large spectral changes for the vegetative-masked images (i.e. N_Rad_VI_VI and N_Rad_Res_VI_VI). However, the N_Rad_VI_VI spectra appear dark (for both ROI 23b (Figure 308) and ROI 28c) compared to the others, although there is a higher degree of similarity to the PHPA_Rad_VI with a SA of 0.09 rad.

ROI 28c	PHPA_Rad_VI	N_Rad_Land_VI	N_Rad_VI_VI	N_Rad_Res_VI_VI
PHPA_Rad_VI	-	0.09	0.25	0.25
N_Rad_Land_VI		-	0.32	0.32
N_Rad_VI_VI			-	0.03

Table 113: Spectral angles (in radians) between the image mean ROI spectra corresponding to Figure 310.

Global detrending (of line-averaging) suggests that ROI NW (Figure 295) and ROI SW (Figure 295) should have somewhat similar radiance spectra over all wavelengths, although some variation is expected due to natural variability in vegetation defined in each ROI.

The purpose of global detrending is to equalise brightness trends across the whole image (in a north-south direction). Figure 311 shows that ROI NW contains brighter spectra for the original data (PHPA_Rad_VI) compared to ROI SW. This brightness trend should reduce in normalised images. Indeed, the N_Rad_VI_VI spectra for ROI SW are generally brighter than the original PHPA_Rad_VI image up to ≈ 700 nm and similar in the NIR region. While spectra in the south should become brighter, those in the north should darken. This is the case in the NIR region for N_Rad_VI_VI. As expected, similar observations pertain to the N_Rad_Res_VI_VI image (being almost identical to N_Rad_VI_VI). To equalise brightnesses over the region, the radiances up to ≈ 700 nm for the N_Rad_VI_VI image are fairly similar in magnitude in both ROI NW and ROI SW – an encouraging result. Variations in vegetation spectra contained in each ROI could explain the spectral differences. The red soil clearly affects the brightnesses in the N_Rad_Land_VI image. Although the radiances in the NIR region appear more consistent between the two ROI's (i.e. similar magnitudes), the brightnesses up to ≈ 700 nm differ rather significantly; those in the ROI NW region have actually decreased.

Spectral angles show N_Rad_VI_VI to exhibit large spectral differences to PHPA_Rad_VI (e.g. 0.24 and 0.31 rad) but are highly similar to N_Rad_Res_VI_VI (0.04 and 0.02 rad), suggesting little change for N_Rad_Res_VI_VI. The red soil present in the N_Rad_Land_VI image places it closer (spectrally) to the PHPA_Rad_VI image (0.08 and 0.12 rad) than to the N_Rad_VI_VI image (0.31 and 0.19 rad).

Overall, it is expected that N_Rad_VI_VI (and possibly N_Rad_Res_VI_VI) are spectrally the most consistent images for classification purposes.

ROI NW	PHPA_Rad_VI	N_Rad_Land_VI	N_Rad_VI_VI	N_Rad_Res_VI_VI
PHPA_Rad_VI	-	0.08	0.24	0.28
N_Rad_Land_VI		-	0.31	0.35
N_Rad_VI_VI			-	0.04

Table 114: Spectral angles (in radians) between the mean spectra corresponding to Figure 311 (left plot).

ROI SW	PHPA_Rad_VI	N_Rad_Land_VI	N_Rad_VI_VI	N_Rad_Res_VI_VI
PHPA_Rad_VI	-	0.12	0.31	0.32
N_Rad_Land_VI		-	0.19	0.20
N_Rad_VI_VI			-	0.02

Table 115: Spectral angles (in radians) between the mean spectra corresponding to Figure 311 (right plot).

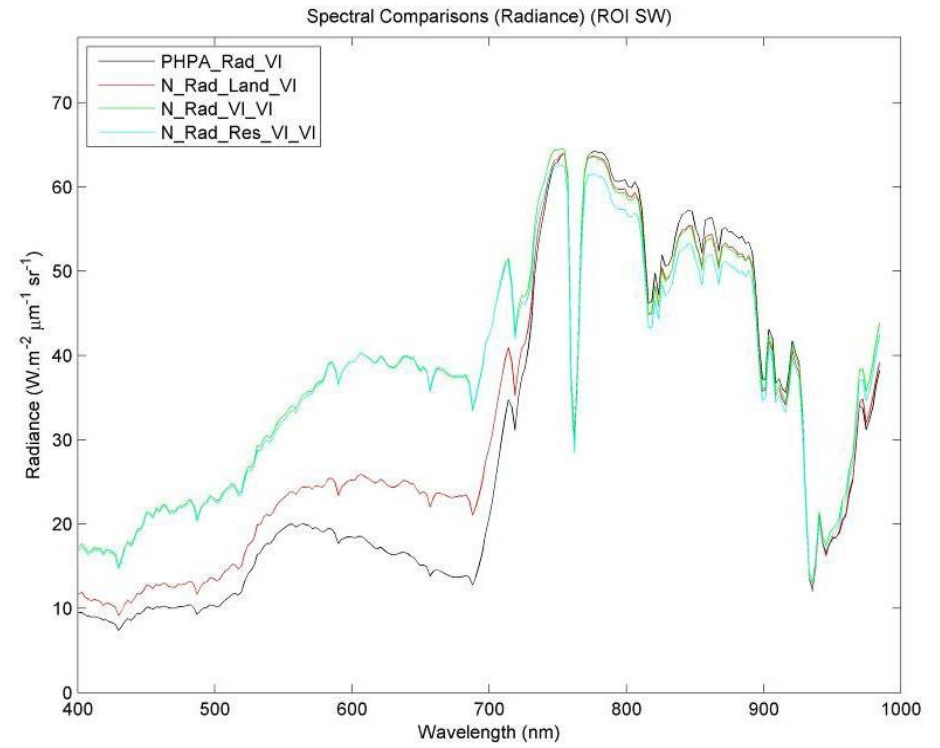
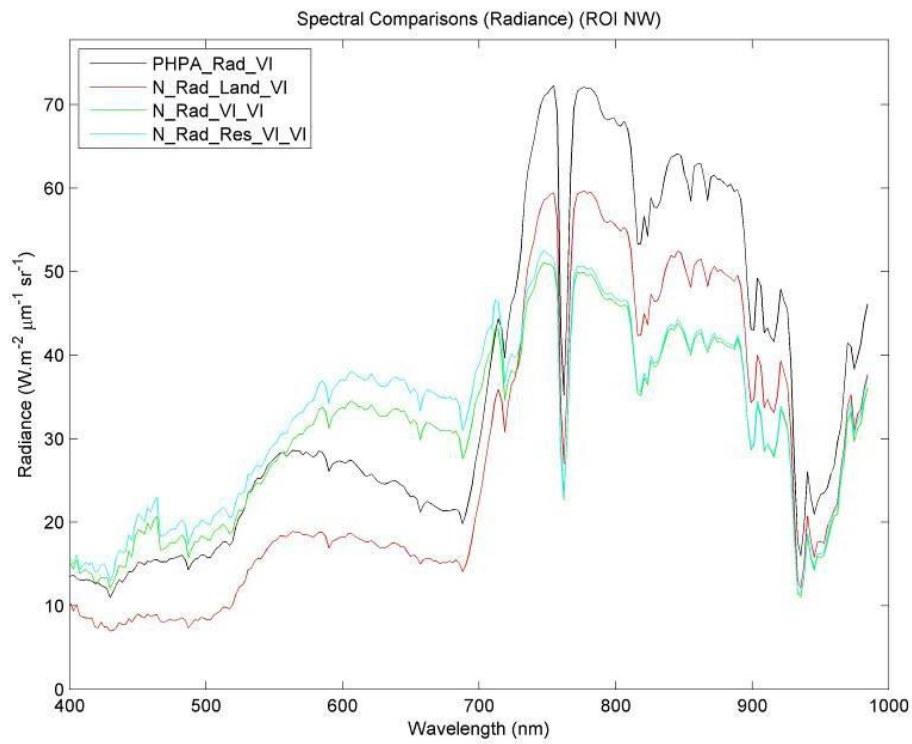


**Figure 311: Mean radiance spectra for ROI NW (left plot) and ROI SW (right plot).
(Note: the vertical scales are identical).**

N.4 Conclusion

For the reflectance-based images, the N_Ref_NoMask_VI plot deviates significantly from other plots (e.g. for ROI 2b (Figure 296), ROI 3a (Figure 297)) and tends to be darker, especially for ROI 23b (Figure 300) where negative reflectances are particularly large. The N_Ref_Res_VI is bright for ROI 23b (Figure 300), perhaps too much due to the large difference between plots; the image was constructed through the removal of urban residential regions in the north. For the most part, the N_Ref_Res_VI is spectrally very similar to N_Ref_VI_VI. Whether the change is an improvement remains to be seen in the classification process; however, compared to ROI 28c, the brightnesses appear too extreme and therefore the integrity of the N_Ref_Res_VI remains under question. The spectral consistency (shape and intensities) appears sound for the N_Ref_VI_VI image. Spectral changes between regions (Figure 302) are to be smaller overall for N_Ref_VI_VI compared to the PHPA_Ref_VI. Based on the arguments presented, the N_Ref_VI_VI might indeed be the most promising image, in terms of what the normalisation process attempts to achieve.

The normalisation process has the desired effect of placing the brightness on similar terms between individual flight line boundaries (Figure 302). Similar to the reflectance-based images, the N_Rad_Res_VI appears too bright at ROI 23b (from Figure 300 and Figure 308) compared to ROI 28c (from Figure 303 and Figure 310). The N_Rad_Land_VI holds promise but most of the spectra appears too dark (e.g., ROI 28c (Figure 310), ROI NW (Figure 311, left)). The radiance values over the RGB range differ more than for the N_Rad_VI_VI image, when comparing ROI NW and ROI SW. At ROI 2b (Figure 305), the spectrum is particularly bright for the N_Rad_Land_VI, leading to the conclusion that it may be somewhat inconsistent. Overall, the N_Rad_VI_VI appears to offer the most spectrally consistent result, even at ROI 23b (Figure 300) and ROI 28c (Figure 310), where there are small brightness changes between flight line boundaries.

The evidence suggests that the radiance-based images are spectrally more sound (due to the normalisation process) than the reflectance-based images. The true test lies in the performance of a classifier in producing a consistent thematic map.

A comment needs to be made regarding the particular characteristic of normalised spectra. Individually, a (pixel) spectrum will be different to that of the PHPA_Ref image. This has already been discussed in Section 4.5.9.6. In fact, when comparisons were made with ASD spectra, the normalised spectra were observed to deviate more in relation to PHPA_Ref spectra. Although this appears to be a bad result, the normalisation process is consistently applied to all spectra. As a result, spectra might individually deviate somewhat from 'true' spectra (e.g. ASD-type quality) but the spectra are more consistent. A land cover type at a particular location in the image is therefore expected to exhibit a similar spectrum of the same type but situated at a different location (e.g. a northern-based pixel with a southern-based pixel in the image). The spectra are therefore consistent with each other although inconsistent against the ASD. Even PHPA_Ref image spectra exhibit inconsistency of this nature - although the inconsistencies are due to other effects; e.g. limitations in atmospheric correction, instrumental limitations, etc.. For spectra in the PHPA_Ref image, a pixel spectrum to the south and north of an immediate flight line boundary are different and even results in different classifications for the same land cover type (as demonstrated in Section 4.5.7). The individual spectrum might bare closer resemblance to an ASD spectrum, but the consistency is not there in each pixel across the whole image.

As a result, the normalised images (particularly those exhibiting a higher degree of spectral consistency; especially the N_Rad_VI_VI) are expected to produce more consistent (spatially) thematic maps.

Appendix O Normalisation Spectral Artefacts

Spectra adjusted by normalisation may introduce undesired spectral artefacts. In certain situations, features in original spectra may be magnified or apparently introduced.³⁶

A discussion follows in this section for one particular case and introduces a technique to help alleviate the issue.

One rather disturbing spectral artefact introduced by normalisation is evident from Figure 307 (p. 650 of Appendix N), where large radiance ‘jumps’ occur in the blue-end of the spectrum (near 450 nm and 480 nm). Even the reflectance-based plots are not immune from this effect (Figure 298, p. 635 of Appendix N). The spectral samples for these two plots were obtained using ROI’s in flight line 22d (Figure 294, p. 627 of Appendix N).

This section investigates the cause for the radiance ‘jump’ in Figure 307 with respect to the N_Rad_VI_VI image (the green line), as it is considered the ‘best’ image, in terms of spectral consistency. It also produced the most accurate classification map.

To appreciate why these spectral ‘jumps’ are introduced into the normalised spectra, it is necessary to refer to the flight line-averaged result. However, the previous plots used throughout this thesis (e.g. Section 4.5.9.2 and Appendix N) are now of little value, as the selected wavelengths (defined in Section 4.5.9.1) do not cover the blue spectral end. Instead, the four wavelengths (applicable to this section only) are now restricted to the blue (B) region:

B1 (420.8 nm)

B2 (450.3 nm)

B3 (480.2 nm)

B4 (501.0 nm)

³⁶ The term “Apparently” is used, because the flight line rotational effect is biased toward large brightness values. It depends on the original data, so it appears to be introduced – not introduced ‘out of nowhere’.

These four blue (B) wavelengths are defined according to their location on 'either side' of the 'jumps', as indicated in Figure 312.

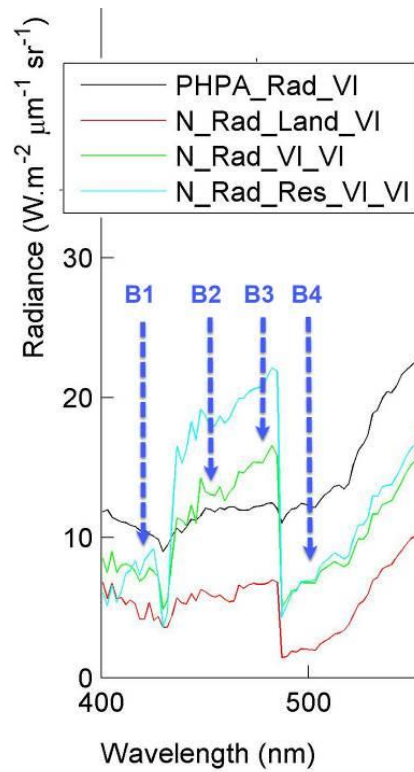


Figure 312: Magnified view over the blue spectral region of ROI 22d N (Figure 307).

A new flight line-averaging plot is displayed in Figure 313, covering these four blue wavelengths. Note that the units for radiance are actual values, not scaled (for most of this thesis, radiances were scaled by a factor of 90).

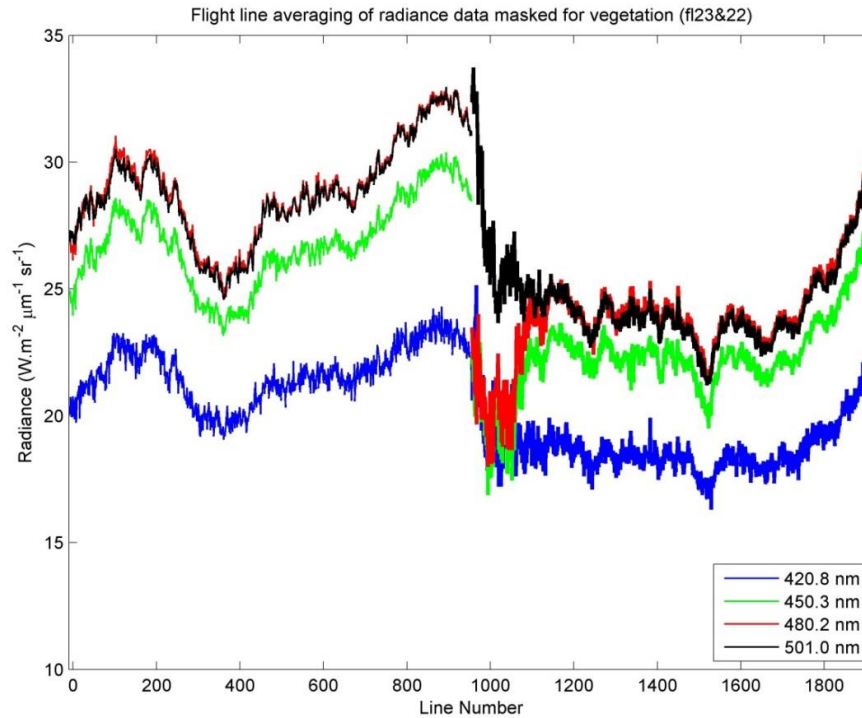


Figure 313: Flight line-average plot for flight lines 23 (left) and 22 (right) for the PHPA_Rad_VI image.

To re-iterate, these flight line-averages cover the whole flight line; not an individual flight line segment. In addition, all four ‘lines’ (coloured in blue, green, red and black) now represent four wavelengths in just the blue spectral region, whereas previously in this thesis, they represented a wavelength in each spectral region (blue, green, red and infra-red).

Note that the line number (the x-axis in the Cartesian coordinate system) in Figure 313 is deliberately made to span two multiples of 965 rows. The rest of this appendix follows this convention, as it helps to identify where one flight line ends and the next one starts (each flight line being 965 rows long). In Figure 313, line numbers 1 to 965 covers the line-average for flight line 23, while line numbers 966 to 1930 (i.e. 2 x 965) covers the line-averaging for flight line 22. The true line numbers are actually 6755 to 7720 and 7720 to 8685 for flight line segments 22 and 21, respectively.

Figure 313 shows a strong correlation between each of the four wavelengths in flight line 23, as the curves are virtually non-intersecting and deviate mostly parallel to each other. Although not shown here, the four curves for most of the other flight

line-averaged plots also behave in this manner. However, the red and green coloured lines (covering 480.2 nm and 450.3 nm, respectively) behave very differently near the beginning of flight line 22 (between line numbers 966 and 1150). The brightness for both these wavelengths increase rather sharply, with dramatic consequences for the normalisation process. It is interesting to contrast Figure 313 with that of the normalised result, given in Figure 314.

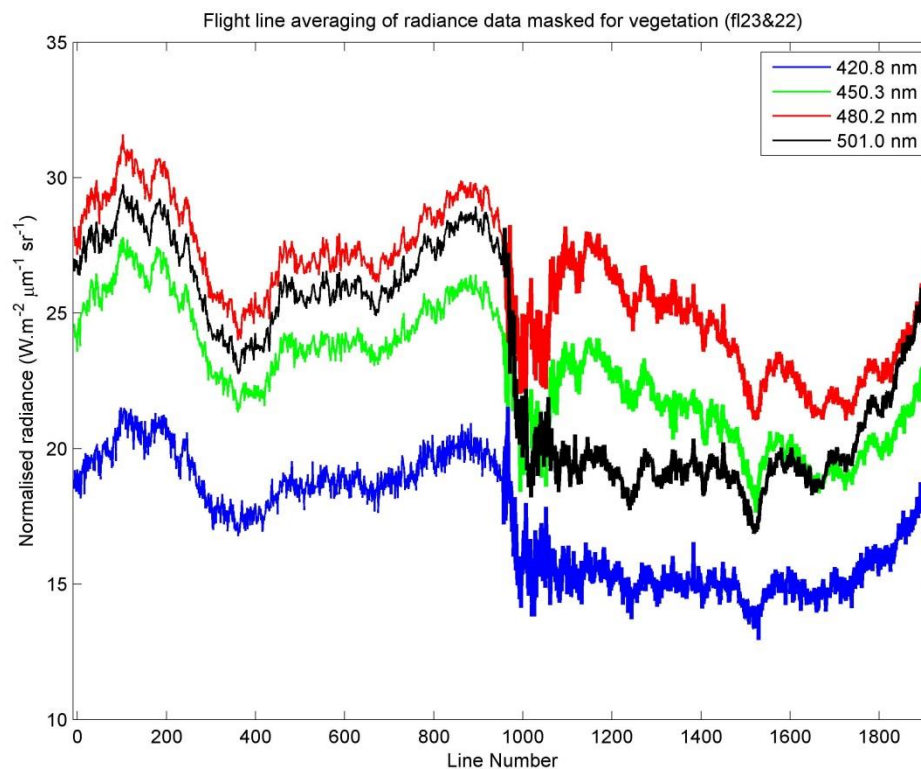


Figure 314: N_Rad_VI_VI line-averaged result for flight lines 23 (left) and 22 (right). Note the units are unsealed and are now normalised radiance.

Note that while the line-averages cover the whole flight line (e.g. 22) the spectrum given in Figure 312 applies to a particular ROI defined in the northern region of flight line segment 22d. This ROI was defined in the fully stitched image as represented by Figure 294, p. 627 of Appendix N. As there is no direct correspondence between the line numbers in the stitched image and the individual flight line segment images, it is not directly possible to relate the lines to each other. In fact, referring back to whole PHPA image of Figure 42 (p. 141 of Section 3.3), flight line 22d appears narrower than (say) flight line segment 29c, as

not all 965 lines were used in the stitching process (Figure 43, p. 143 of Section 3.3 shows a more extreme example). Despite this, the ROI is defined in the northern region of flight line segment 22d and relates to line numbers (approximately) 1100 to 1200.

To appreciate the relationship between both Figure 313 and Figure 314 with the actual spectrum displayed in Figure 312, it is helpful to break the analysis into steps. Figure 313 (for the PHPA_Rad_VI data) shows the green, red and black coloured curves to be of similar brightness between lines numbers 1100 to 1200. These wavelengths correspond to the positions marked by B2, B3 and B4 (respectively) in Figure 312, and show similar brightnesses at these positions (i.e. for the PHPA_Rad_VI data). However, in Figure 314 (for the N_Rad_VI_VI data) the red curve is the brightest overall, followed by green, then black (the blue is ignored as it contributes little to this discussion). Again, these relate to the positions at B2, B3 and B4 of Figure 312, but this time the N_Rad_VI_VI curve is of interest rather than the PHPA_Rad_VI. Indeed, the highest brightness is at position B3 (red curve), followed by B2 (green curve) and B4 (black curve).

Overall, by comparing Figure 313 and Figure 314, the line-average curves for flight line 23 are similar, resulting in 'cleaner' spectra - i.e. very little 'jumps' in brightness (see Figure 300, p. 639 of Appendix N). But, for ROI 22d N, spectra contain 'jumps'. Toward the southern section of flight line 22 (lines 1800 onwards), the curves are more alike. This results also in 'clean' spectra, as displayed in the right hand plot of Figure 307 (p. 650 of Appendix N). Therefore, 'jumps' in normalisation spectra occur due to non-parallel curves in line-average plots. Evidence that these spectral brightness 'jumps' are caused by the rotation of individual flight lines (one for each band) – defining step 1 in the normalisation process – is illustrated in Figure 315. Note that the plot shows only the effect for the first step of the full normalisation process. The units are therefore not normalised radiance. However, nor are they strictly radiance as the raw (i.e. original) radiances have been modified. As only one step was performed from the three, the radiance unit is more appropriate than normalised radiance but it must be noted that the unit is not strictly correct.

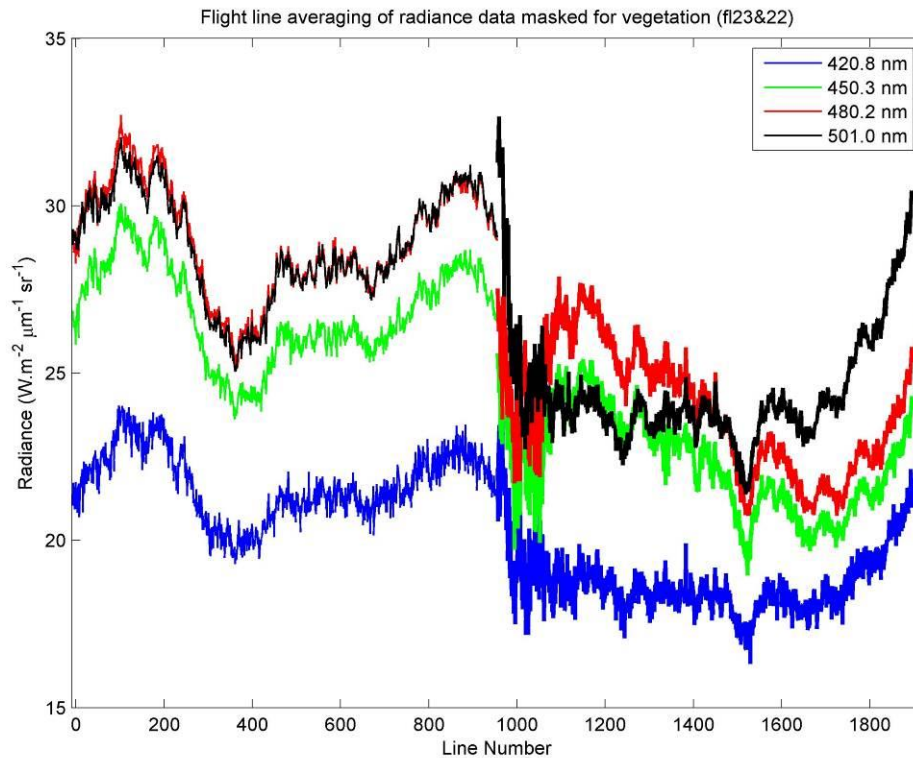


Figure 315: The effect of flight line rotation for PHPA_Rad_VI (step 1 of the normalisation process).

The first step of normalisation rotates the flight line (for each band) about the centre. This has a dramatic effect on the red curve for flight line 22 in Figure 313, as evident from Figure 315. Whereas the radiances for line numbers 1100 onwards are very similar to the black curve in Figure 313, this is no longer the case in Figure 315. It is clear that the rotation of the flight line has a dramatic effect, with consequences for constructing normalised spectral images. It is the shape of the red curve in Figure 313 that has led to this effect. As the rotation of flight lines are dependent on the mean of the first and last five brightness values of a flight line (described in detail in step 3 of Appendix I), one extreme value is able to affect the whole process dramatically, greatly affecting the mean.

One way to reduce the effect of extreme brightness values is to delete lines of affected pixels. If \bar{x} denotes the mean of the brightnesses for a particular band in the flight line and SD the standard deviation for this band, then the condition $\bar{x} \pm 3SD$ is used to reject or accept the line-average for that line. This 3SD condition is checked for each band independently. If a particular line-average value lies

outside of this condition, then all the line-averages for the whole line is rejected. This rejection is applied to each of the 246 bands (i.e. all bands are deleted).

For flight line 23, this criterion led to the rejection of 5 line numbers, while 59 were rejected for flight line 22 (i.e. 6% of lines). In both situations, most of the rejections occurred toward the beginning and end of the flight line, where the extreme line-average brightness values exist. The resulting plot is shown in Figure 316 and should be compared to Figure 313. The spaces in Figure 313 correspond to the deleted lines. Notice that the sharp peak in Figure 313 for the black line near line number 965 has been reduced. The rotation of this black line is not as dramatically influenced by the extreme brightness values.

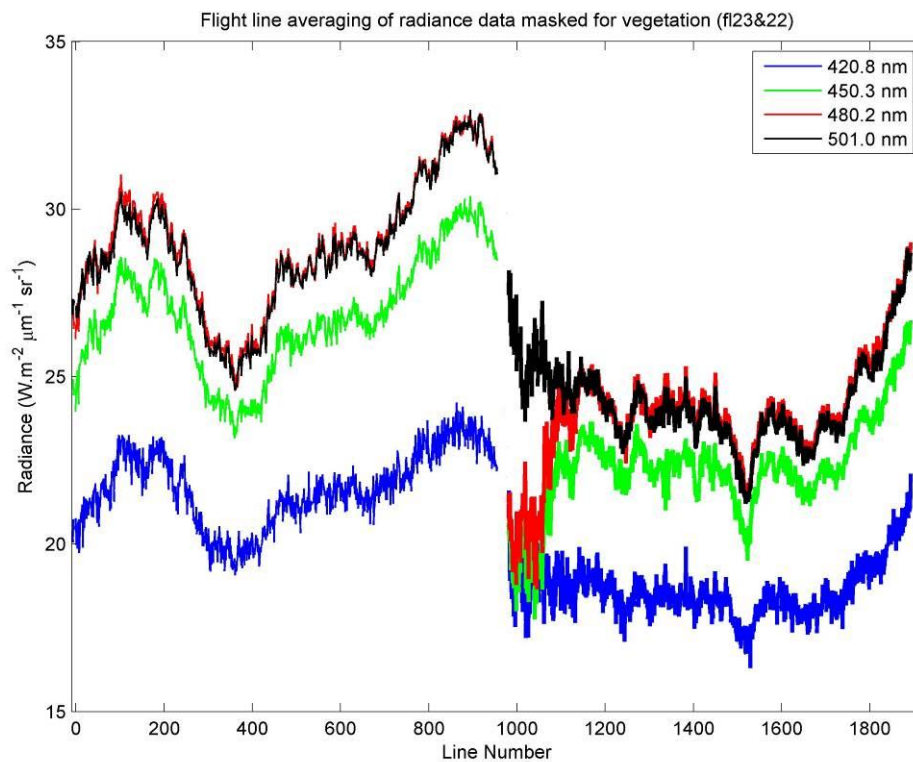


Figure 316: The blank spaces indicate the removal of lines due to excessively large radiances in the PHPA_Rad_VI image.

The fully normalised plot is shown in Figure 317.

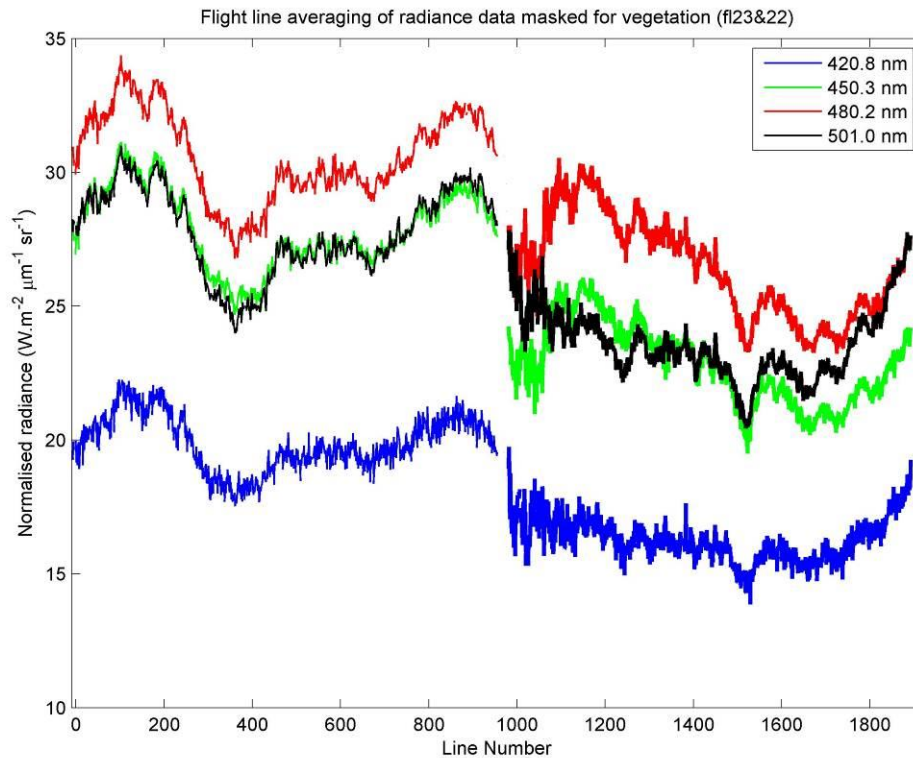


Figure 317: Fully normalised line-average result after the removal of extreme radiances.

For flight line 22 (between line numbers 966 and 1930), the green curve now lies closer to the black curve. This is more reminiscent of Figure 313, the line-average result of PHPA_Rad_VI - prior to any normalisation.

There are practical considerations to applying this condition in practice. When line-numbers are deleted, this could potentially affect the steps of the normalisation process. For example, deleting the first 10 lines of a flight line changes the algorithm for flight line rotation, as it relies on calculating the mean of the first 5 line numbers. Instead, the algorithm is modified to search for the first 5 consecutive line numbers, allowing a mean to be calculated. In addition, this mean must exist before the midpoint of the rotation (i.e. at a location less than line number 483). A similar consideration applies to calculating a mean for the last 5 line-numbers (they must exist after line number 483). For the global line rotation, the same problem (and solution) exists but for 4 line-numbers. In the last step of normalisation - the joining of flight line edges - these edges may not necessarily exist (as they have been deleted). For this, the first and last non-deleted line-numbers were actually used. For example, if line numbers 960 to 965 were deleted,

then the value at line number 959 is used. Previously, line number 965 would be used (but no longer exists). The justification is that the brightness change within a flight line is smaller than those between flight lines. For example, in Figure 108 (p. 264 of Section 4.5.9.1), the difference in brightness for the blue curve between flight line 3 adjacent to flight line 4 is much larger than the difference in brightness in the first and (say) 10th line number in flight line 3 (there are 965 in all).

Mean spectra were again calculated using a similar north and south ROI to those previously defined for flight line segment 22d. The result is given in Figure 318.

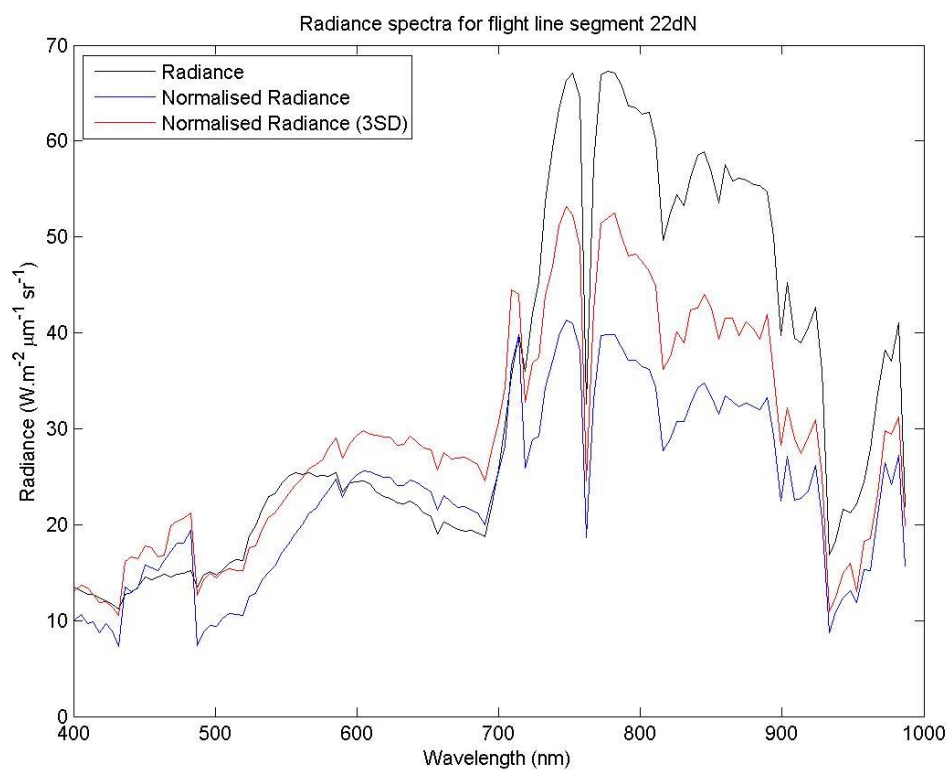


Figure 318: Mean spectra over a group of pixels of flight line 22d in the northern region for the full normalisation process.

Note: units are radiance for the black line and normalised radiance otherwise.

The black line shows the mean spectrum for PHPA_Rad_VI (in units of radiance), while the red and magenta lines relate to the normalised N_Rad_VI_VI images (in units of normalised radiance). The “Normalised Radiance (3SD)” legend refers to mean spectra where line-averages exceed the 3SD criterion defined earlier in this section. The ‘jumps’ in the blue-spectral end is smaller for the red line than the

magenta line, demonstrating the positive effect of eliminating 'extreme' radiance values but at the cost of deleting pixel lines.

The process was repeated for the southern ROI in flight line segment 22d, with the mean spectral plot displayed in Figure 319.

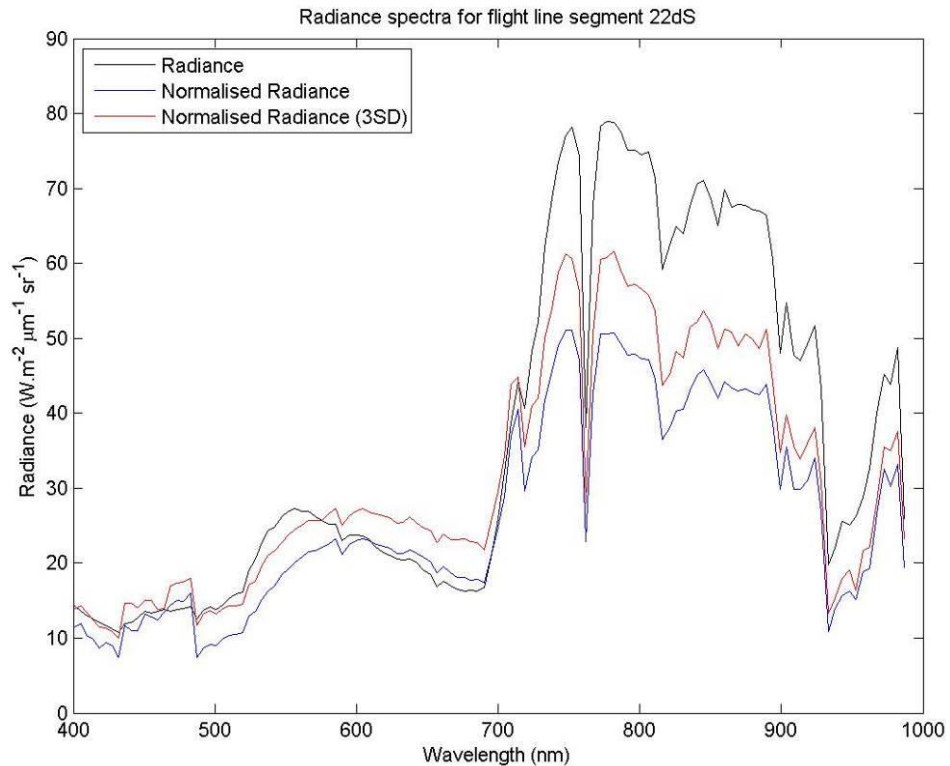


Figure 319: Mean spectra over a group of pixels of flight line 22d in the southern region for the full normalisation process.

Note: units are radiance for the black line and normalised radiance otherwise.

The comments made above for Figure 318 concerning the radiance units for these three lines apply here also. The magenta line appears to be missing but the data is actually identical to that of the red line. The normalised radiance (in magenta) is decreased when 'extreme' radiance values are eliminated (i.e. exceeding the 3SD criterion), which is shown in red.

Considering that most plots, of the type like Figure 313 did not show intersecting line-averaged curved (e.g. the red and green coloured curves). This is particularly evident for flight line 22 between line numbers 966 and (roughly) 1100. It is

questionable whether there is some negative influence in the data recording process, which the normalisation process is unable to cater for.

As part of normalisation, the rotational effect of flight lines caused these spectral 'jumps' (local). Eliminating outlier brightnesses based on three standard-deviations from the mean reduces the extreme 'jumps' in normalised spectra. Nonetheless, there is a cost whereby lines of pixels were deleted – 6% for flight line 22. However, this may not be a bad effect for questionable data quality.

Other strategies have not been tested. Taking a mean over an extended range of flight line end-points will remove outlier-brightnesses through smoothing. Another method is to rotate flight lines based not on a linear-line but a curved function although the rotational centre point position becomes less trivial.

Appendix P Thematic Maps

With the exception of the N_Rad_VI_VI and PHPA_Ref_VI images, all other classification results are given in this appendix. This includes the images produced in Appendix L. The N_Rad_VI_VI image produced the best thematic map, therefore retained in the main body of the thesis and discussed in detail (Section 4.5.11.1). The term 'best' describes the highest number of classes with the highest spectral separability overall. The PHPA_Ref_VI image was classified in Section 4.5.7.

The paradigm given in Section 4.5.5 is used in all classification with the process illustrated in Section 4.5.7 for the PHPA_Ref image; this involves using PCA for feature reduction prior to unsupervised classification. For this reason, the results and discussions in this appendix are kept brief, to avoid constant repetition of the same steps.

P.1 Classification based on the N_Ref_NoMask_VI image

After PC transforming the N_Ref_NoMask_VI image, a cumulative variance threshold of 99% determines the number of PC bands to retain. Originally having 246 PC bands, the now-reduced PC dataset (comprising of 8 PC bands) is classified.

Table 116 shows the first 10 PC bands only. A cumulative variance threshold of 99% is reached after only 8 PC bands.

The k-means and ISODATA classification results are shown in Figure 320 and Figure 321, respectively. Both thematic maps use default ENVI class colours.

Band striping effects clearly still represents an undesired effect in both these thematic maps, as it did previously for the PHPA_Ref_VI thematic map (Figure 96, p. 240 of Section 4.5.7). In addition, classes appear to be influenced by the salt pond regions, as spectra on those horizontal flight lines are classified differently to those outside of these regions. Classification using k-means, restricted to either 5 and 15 classes showed similar effects, as did the ISODATA results using two separate ranges; 5 (minimum number of classes specified) to 10 (maximum number of classes specified) and 5 to 15 classes. The result for 5 to 10 classes is shown in Figure 321; other results are not shown here.

PC band	Cumulative variance (%)	PC band	Cumulative variance (%)
1	76.73	6	98.84
2	95.47	7	98.99
3	97.27	8	99.11
4	97.94	9	99.21
5	98.40	10	99.28

Table 116: Cumulative variance (in % rounded to 2 d.p.) for the PC transform of the N_Ref_NoMask_VI image.

The first 8 PCA bands account for 99% of the total variance. Therefore, 8 PC bands are retained for classification purposes (Note: only the first 10 PC bands are shown in this table). Note the order of PC bands are given in ascending order by increasing cumulative variance.

As the band striping effect is present in both ISODATA and k-means maps, the integrity of the thematic map result is questionable. Hence, class separabilities (using JM distances) were examined only for the k-means thematic map.

For the k-means classifier, many of the 10 classes are inseparable, as the JM distances for class-pairs indicate (see Table 117).

class 9 & class 10: 1.3894
class 3 & class 6: 1.4793
class 7 & class 8: 1.4957
class 6 & class 7: 1.5275
class 8 & class 10: 1.5404
class 5 & class 8: 1.5789
class 4 & class 5: 1.6048
class 7 & class 9: 1.6864
class 5 & class 7: 1.6933
class 5 & class 6: 1.7167
class 3 & class 4: 1.7290
class 4 & class 6: 1.7931
class 7 & class 10: 1.7934
class 6 & class 9: 1.8655
class 8 & class 9: 1.9254

Table 117: Separability report for the k-means 10 class (50 iterations) classifier of the 8 PC band N_Ref_NoMask_VI dataset.

Note: 1) only values for JM < 1.93 are shown, 2) the relationship between individual class numbers and class colours (for Figure 320) are omitted, 3) JM distances are given in order of increasing JM distances, 4) JM distances are rounded to 4 d.p..

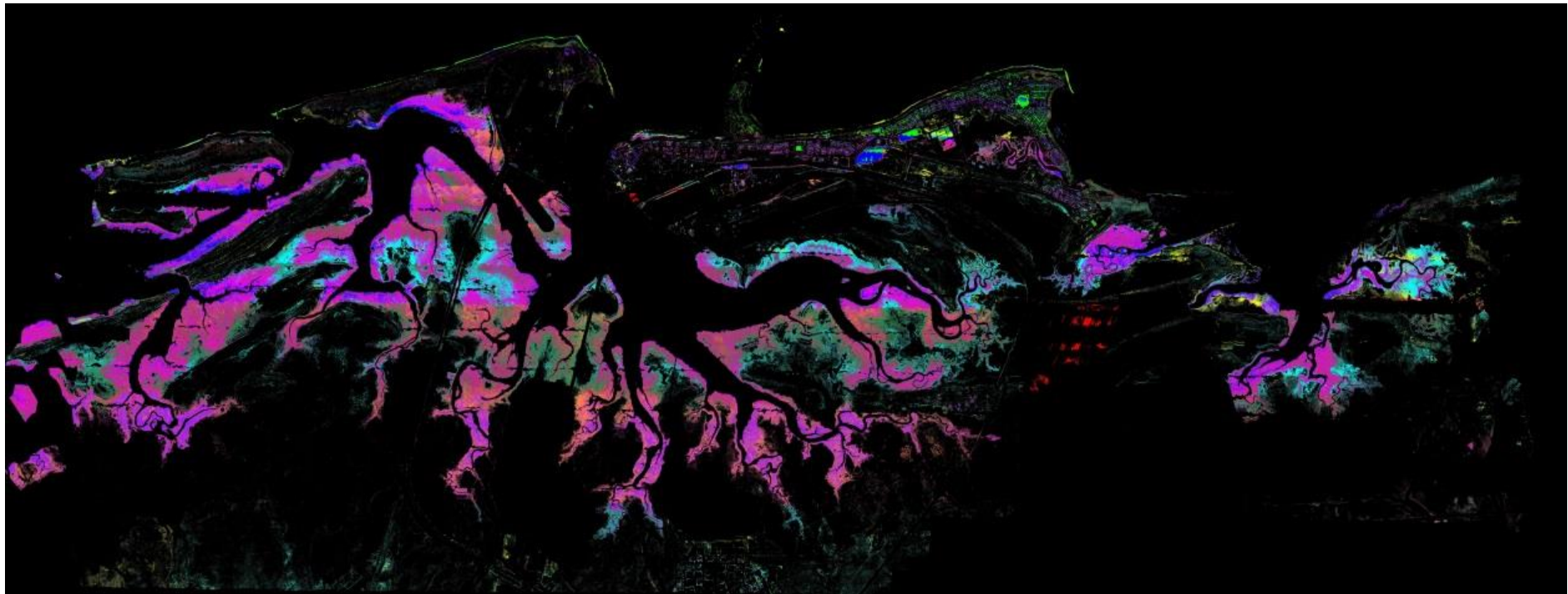


Figure 320: Thematic map as obtained using 50 iterations for a 10 class k-means classifier of the 8 PC band N_Ref_NoMask_VI dataset.

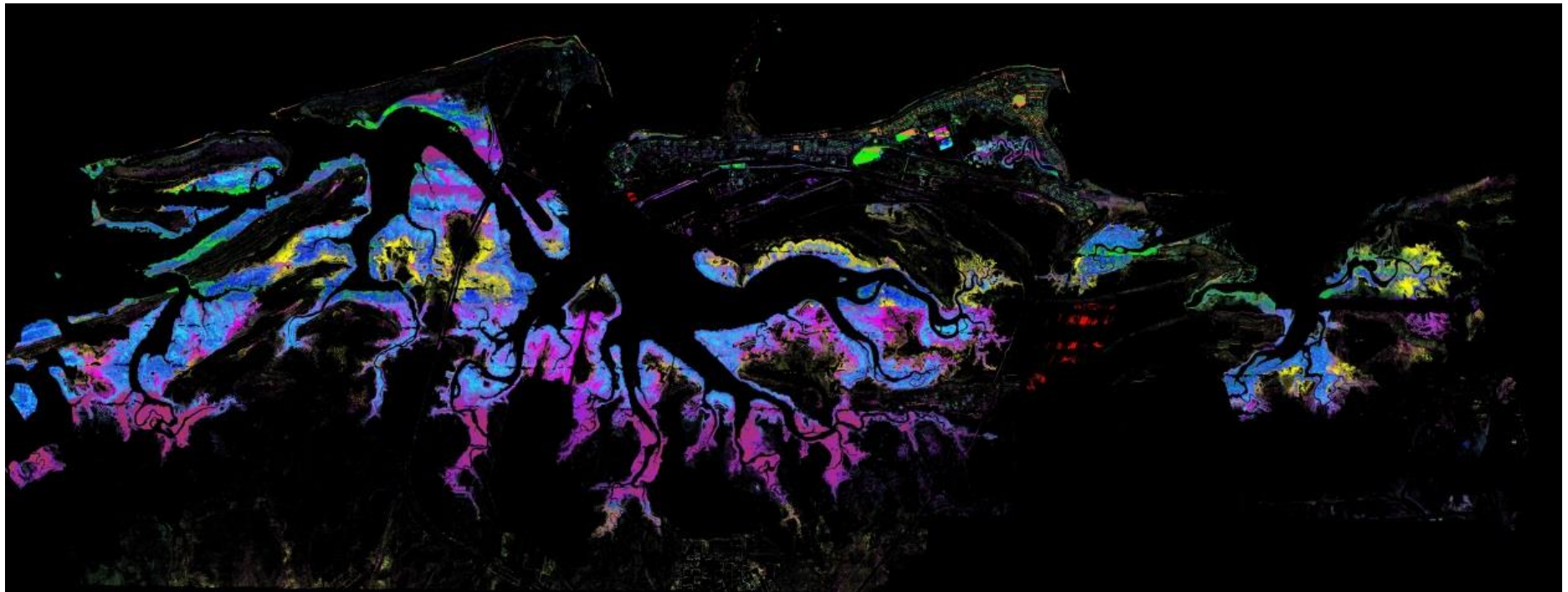


Figure 321: Thematic map as obtained using 50 iterations for an ISODATA classifier (5 to 10 class range) of the 8 PC band N_Ref_NoMask_VI dataset.

In general, more class-pairs became inseparable with increasing number of clusters defined in the classifier. The result is expected, as the classifier attempts to spectrally discriminate at lower cluster distances (thereby decreasing class separability) in order to match the user-defined specification for the number of classes. The question is what constitutes a reasonable number of classes. The small separabilities between classes indicate that even 10 classes were too many.

To increase class separation confidence, class pairs were merged. Only three distinct classes were separable for a highly confident (where $JM \geq 1.9$) thematic map - as shown in Figure 322. From a practical viewpoint, this is not ideal as there is a lack of detail, as all mangrove forests are defined by just one class.

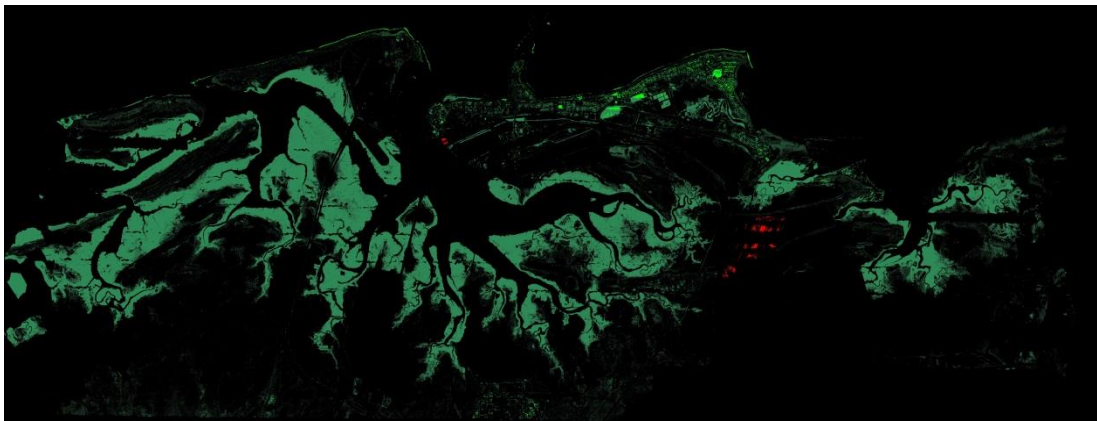


Figure 322: Thematic map as obtained by merging classes from the 10 class k-means classifier of the 8 PC band N_Ref_NoMask_VI dataset. A total of 3 classes remain highly separable at $JM \geq 1.9$.

The JM distances for the three surviving classes for which $JM \geq 1.9$, is shown in Table 118.

class 2 & class 8: 1.9847
class 1 & class 2: 2.0000
class 1 & class 8: 2.0000

Table 118: Separability report for the k-means 10 class (50 iterations) classifier where $JM \geq 1.9$ of the 8 PC band N_Ref_NoMask_VI dataset.

Note: 1) all class-pair separability JM distances are shown, 2) the relationship between individual class numbers and class colours (for Figure 322) are omitted, 3) JM distances are given in order of increasing JM distances, 4) JM distances are rounded to 4 d.p..

It was not possible to produce a thematic map where class pairs have a $JM \geq 1.8$, as explained using Table 119. The following table shows the separabilities just prior to the leading to Figure 322.

class 4 & class 8: 1.6164
class 2 & class 4: 1.9262
class 2 & class 8: 1.9904
class 1 & class 2: 2.0000
class 1 & class 4: 2.0000
class 1 & class 8: 2.0000

Table 119: Separability report for the k-means 10 class (50 iterations) classifier where $JM \geq 1.8$ of the 8 PC band N_Ref_NoMask_VI dataset.

Note: 1) all class-pair separability JM distances are shown, 2) the relationship between individual class numbers and class colours (for Figure 322) are omitted, 3) JM distances are given in order of increasing JM distances.

Combining classes 4 & 8 in Table 119 resulted in the JM distances given in Table 118. As the JM distance between classes 4 & 8 are < 1.7 (i.e. 1.6164), no class image could be formed for class-pairs having $JM \geq 1.7$. The effect of combining classes 4 & 8 gave immediate rise to $JM > 1.9$ (resulting in Figure 322).

The thematic maps Figure 320 and Figure 321 exhibit striping effects, demonstrating that the bright water and salt pond regions clearly have an effect on the class distribution outcome. This result led to the examination of flight line-averaged reflectances in the absence of these regions, which subsequently led to the development of a land-mask and the production of the N_Ref_Land_VI image.

P.2 Classification based on the N_Ref_Land_VI image

The PC transformation of the N_Ref_Land_VI image leaves 9 PC bands for a cumulative variance threshold of 99%, as shown in Table 120.

The thematic map is shown in Figure 323, obtained by k-means classification of 10 classes. The spatial distribution and consistency of the classes in Figure 323 are more consistent than previous thematic maps; Figure 96 (p. 240 of Section 4.5.7), Figure 320 and Figure 321 - the horizontal flight line striping are no longer apparent.

PC band	Cumulative variance (%)	PC band	Cumulative variance (%)
1	76.65	6	98.65
2	95.18	7	98.83
3	97.12	8	98.97
4	97.89	9	99.08
5	98.41	10	99.16

Table 120: Cumulative variance (in % rounded to 2 d.p.) for the PC transform of the N_Ref_Land_VI image.

The first 9 PCA bands account for 99% of the total variance. Therefore, 9 PC bands are retained for classification purposes (Note: only the first 10 PC bands are shown in this table). Note the order of PC bands are given in ascending order by increasing cumulative variance.

The ISODATA classification (using a range of 5 to 10 classes) thematic map appears similar that as produced by k-means previously (i.e. Figure 323). The ISODATA result is portrayed in Figure 324. Both images use ENVI default class colour definitions.

Pair class separability calculations, using the JM distance for the k-means (10 class) classification result, are shown in Table 121.

class 5 & class 9: 1.4675
class 3 & class 4: 1.4685
class 4 & class 6: 1.5039
class 8 & class 9: 1.5307
class 5 & class 6: 1.5684
class 4 & class 5: 1.5711
class 3 & class 6: 1.6755
class 6 & class 8: 1.6850
class 5 & class 8: 1.6881
class 7 & class 8: 1.7565
class 6 & class 7: 1.8884
class 2 & class 7: 1.9099

Table 121: Separability report for the k-means 10 class (50 iterations) classifier of the 9 PC band N_Ref_Land_VI dataset.

Note: 1) only values for JM < 1.91 are shown, 2) the relationship between individual class numbers and class colours (for Figure 323) are omitted, 3) JM distances are given in order of increasing JM distances, 4) JM distances are rounded to 4 d.p..

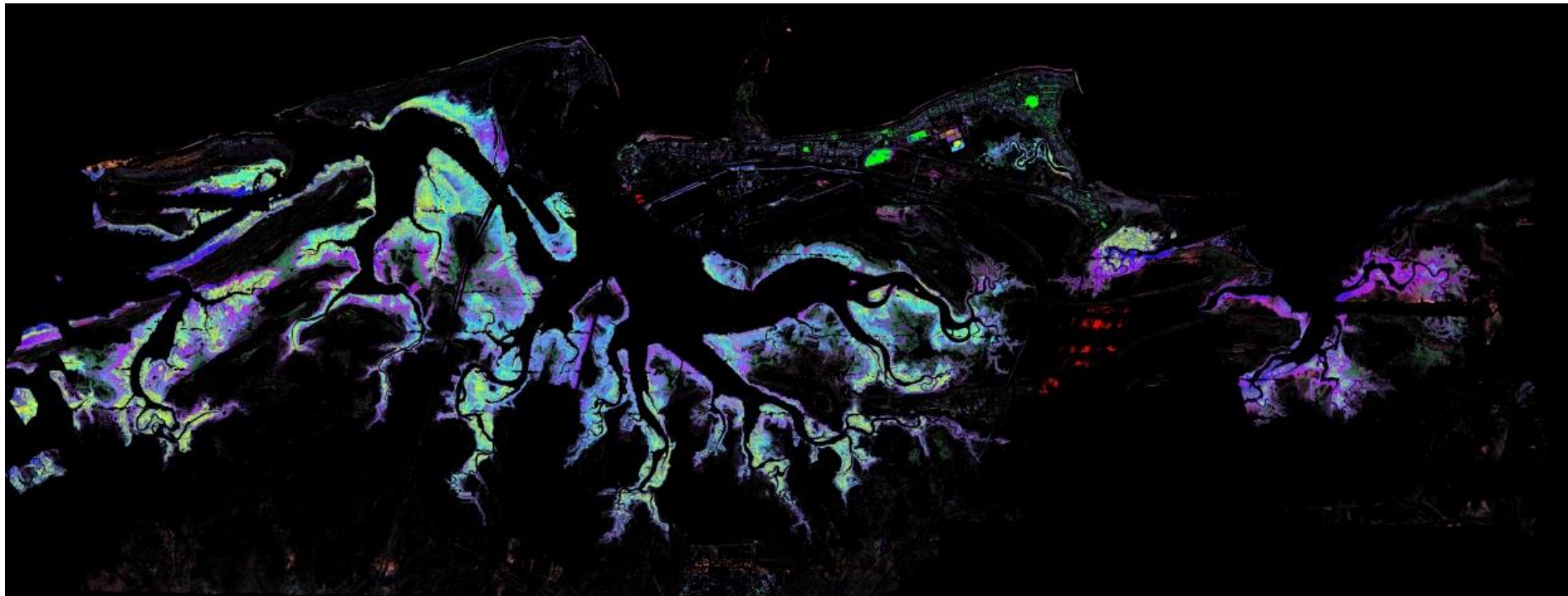


Figure 323: The thematic map for the 9 PC band PHPA_Ref_Land_VI dataset using k-means unsupervised classification with 10 clusters and 50 iterations.

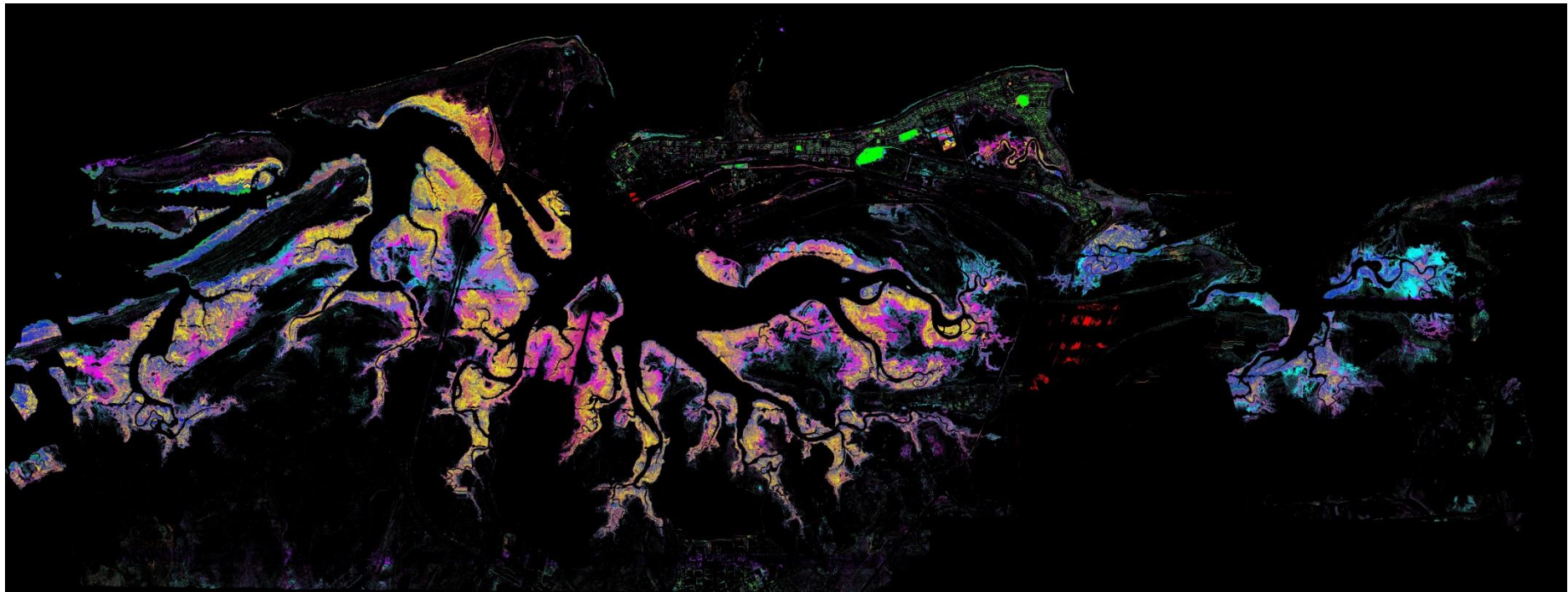


Figure 324: The thematic map for the 9 PC band PHPA_Ref_Land_VI dataset using ISODATA unsupervised classification for a range of 5 to 10 clusters with 50 iterations.

Several classes were merged to increase the class separability to $JM \geq 1.8$. Figure 325 shows the result, where just 5 of the 10 classes remain moderately separable.

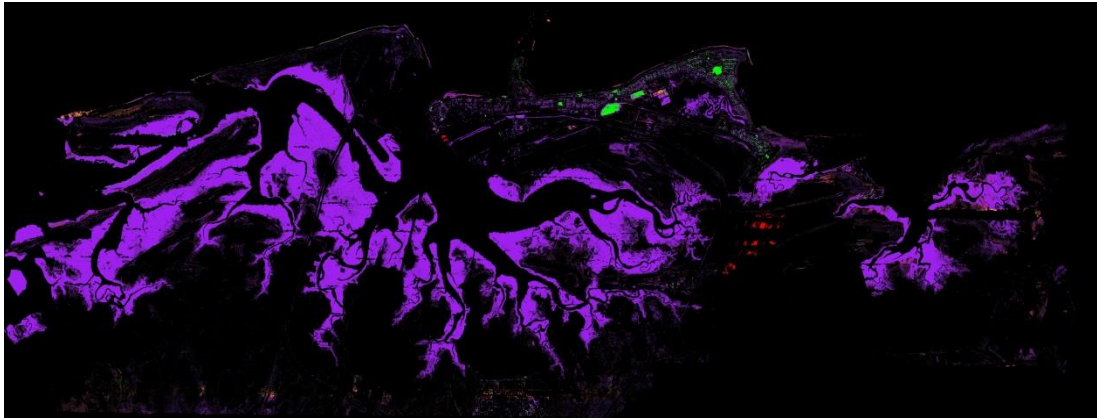


Figure 325: Thematic map as obtained by merging classes from the 10 class k-means classifier of the 9 PC band N_Ref_Land_VI dataset. A total of 5 classes remain moderately separable to $JM \geq 1.8$.

The separability statistics corresponding to Figure 325 are shown in Table 122.

class 7 & class 9: 1.8293
class 2 & class 7: 1.9099
class 2 & class 9: 1.9944
class 9 & class 10: 1.9997
class 7 & class 10: 2.0000
class 1 & class 2: 2.0000
class 2 & class 10: 2.0000
class 1 & class 7: 2.0000
class 1 & class 9: 2.0000
class 1 & class 10: 2.0000

Table 122: Separability report for the k-means 10 class (50 iterations) classifier of the 9 PC band N_Ref_Land_VI dataset. Evidently, 5 classes are moderately separable.

Note: 1) only values for $JM > 1.8$ are shown, 2) the relationship between individual class numbers and class colours (for Figure 323) are omitted, 3) JM distances are given in order of increasing JM distances, 4) JM distances are rounded to 4 d.p..

To achieve a higher separability, i.e. $JM > 1.9$, the merging of classes leaves just 4 classes, as class 7 is merged with class 9. The relatively few number of pixels for class 7 (< 5 % of the whole image) does not provide any (visually) significant change to that of Figure 325. Therefore, the class maps for $JM \geq 1.8$ and $JM \geq 1.9$ are (practically) the same.

Separability statistics (using JM distances) were also performed for the k-means 15 class map and ISODATA (both 5 - 10 & 10 - 15 classes). The findings have been briefly summarised in Table 45 (p. 331 of Section 4.5.11.3), although the analysis is not shown in this section; the process is identical to the k-means separability statistics process described above.

P.3 Classification based on the N_Ref_VI_VI image

The PC transformation of the N_Ref_VI_VI image leaves 10 PC bands for a cumulative variance threshold of 99%, as shown in Table 123.

PC band	Cumulative variance (%)	PC band	Cumulative variance (%)
1	77.50	6	98.49
2	95.09	7	98.67
3	96.97	8	98.83
4	97.76	9	98.95
5	98.28	10	99.04

Table 123: Cumulative variance (% rounded to 2 d.p.) of the PC transform for the N_Ref_NoMask_VI image. The first 10 PCA bands account for 99% of the total variance.

Therefore, 10 PC bands were retained for classification purposes (Note: only the first 10 PC bands are shown in this table). Note the order of PC bands are given in ascending order by increasing cumulative variance.

Classification using k-means with 10 classes results in a thematic map as shown in Figure 326. Class merging using separability statistics in this section is only considered for the 10 class k-means result. In practice, 15 classes were also investigated along with 5 - 10 and 10 - 15 class ranges for ISODATA. All these results are briefly summarised in Table 45 (p. 331 of Section 4.5.11.3).

It is apparent from Figure 326 that the horizontal flight line striping is absent and the classes are spatially coherent (unlike those in Appendix P.1). These aspects were also observed for the k-means 10 class classification thematic map N_Ref_Land_VI (Figure 323). It is encouraging that normalisation using either land (i.e.

N_Ref_Land_VI) or vegetative (i.e. N_Ref_VI_VI) based masks improve the thematic class consistency.

The JM distances for the 10 class k-means classification thematic map (Figure 326) is shown in Table 124.

class 4 & class 5: 1.4762
class 6 & class 7: 1.5305
class 5 & class 8: 1.5673
class 8 & class 9: 1.6131
class 7 & class 8: 1.6736
class 3 & class 4: 1.6744
class 7 & class 9: 1.7165
class 5 & class 7: 1.8663
class 5 & class 6: 1.9070

Table 124: Separability report for the k-means 10 class (50 iterations) classifier of the 10 PC band N_Ref_VI_VI dataset.

Note: 1) only values for JM < 1.92 are shown, 2) the relationship between individual class numbers and class colours (for Figure 326) are omitted, 3) JM distances are given in order of increasing JM distances, 4) JM distances are rounded to 4 d.p..

To produce a JM ≥ 1.7 map, classes were combined leaving just 5 in total. The resulting thematic map lacks definition for the majority of the vegetative region (Figure 327).

Continuing the class merging process leads directly to a JM ≥ 1.97 map containing just 4 classes (i.e. there is no JM ≥ 1.8 map). The result is not shown here.

An attempt was also made using the k-means classifier with 15 classes, which resulted in more classes having to be merged. It left 7 classes for JM ≥ 1.78 but again not amounting to an increase in definition over the mangrove forested regions.

Other classification results were also attempted but are not shown here; a brief summary is found in Table 45 (p. 331 of Section 4.5.11.3).

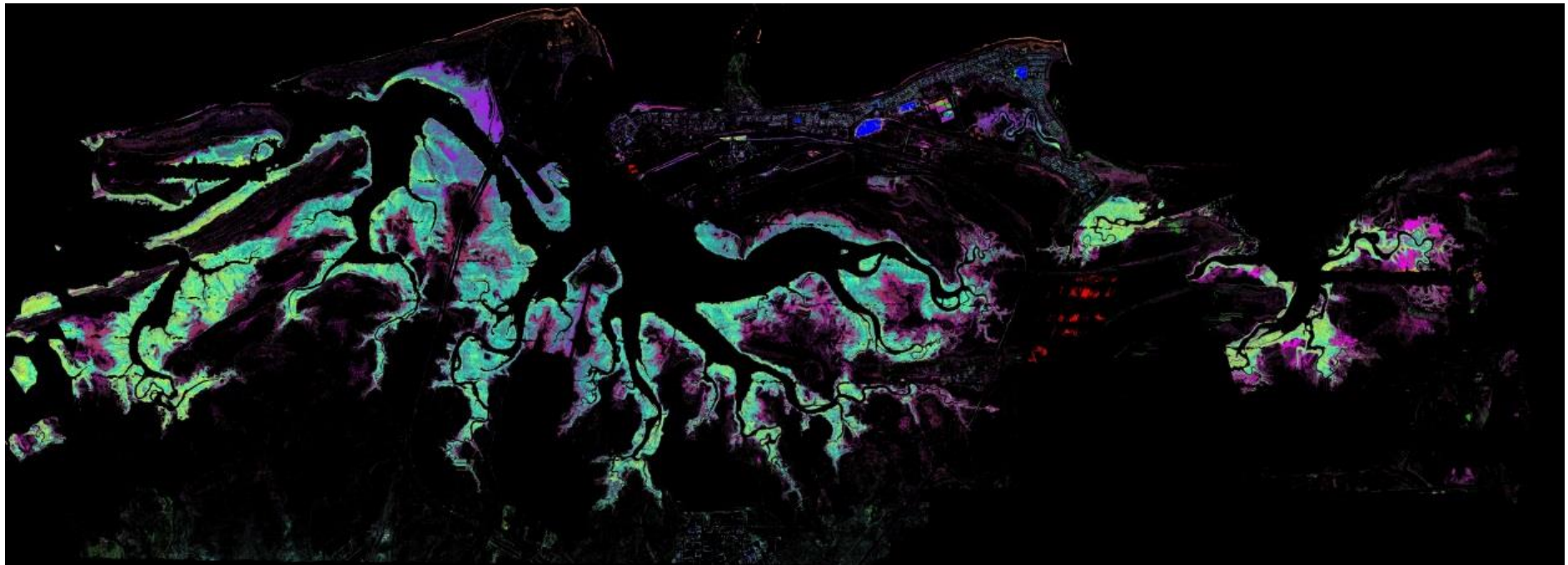


Figure 326: The thematic map resulting from a 10 PC band N_Ref_VI_VI dataset using k-means unsupervised classification with 10 clusters and 50 iterations.

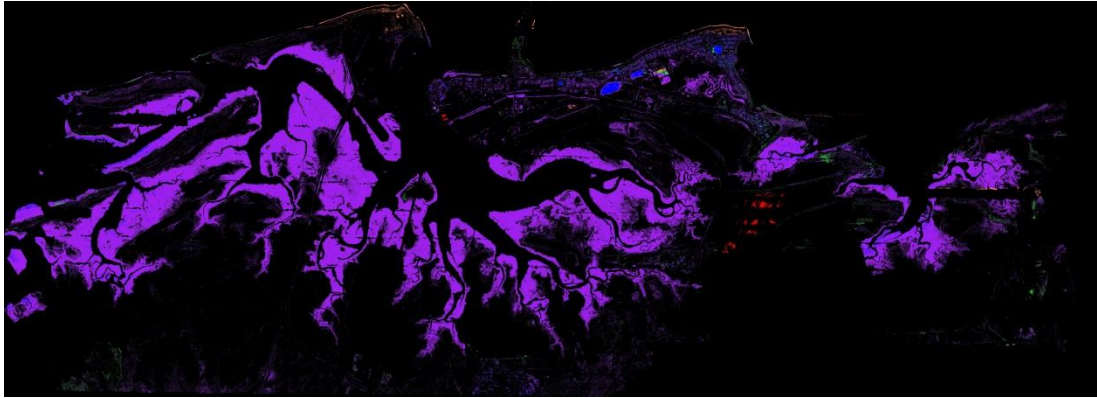


Figure 327: Thematic map as obtained by merging classes from the 10 class k-means classifier of the 10 PC band N_Ref_VI_VI dataset. A total of 5 classes remain separable to $JM \geq 1.7$.

P.4 Classification based on the N_Rad_Land_VI image

Note that the classification in this section applies to radiance-based data.

The PC transformation of the N_Rad_Land_VI image leaves 11 PC bands for a cumulative variance threshold of 99%, as shown in Table 125.

PC band	Cumulative variance (%)	PC band	Cumulative variance (%)
1	55.56	7	98.58
2	89.20	8	98.73
3	95.85	9	98.87
4	97.13	10	98.97
5	97.85	11	99.06
6	98.28	12	99.13

Table 125: Cumulative variance (in % and rounded to 2 d.p.) of the PC transform for the N_Rad_Land_VI image.

The first 12 PCA bands account for 99% of the total variance. Therefore, 11 PC bands were retained for classification purposes (Note: only the first 12 PC bands are shown in this table). Note the order of PC bands are given in ascending order by increasing cumulative variance.

For the 10 class k-means classification thematic map (Figure 328), the JM distances (in Table 126) suggest that 10 classes are too many in definition in the context of this dataset.

class 2 & class 7: 1.4394
class 3 & class 6: 1.5429
class 2 & class 3: 1.6110
class 7 & class 8: 1.6162
class 6 & class 7: 1.6212
class 2 & class 6: 1.6556
class 6 & class 8: 1.7300
class 5 & class 8: 1.9257

Table 126: Separability report for the k-means 10 class (50 iterations) classifier of the 11 PC band N_Rad_Land_VI dataset.

Note: 1) only values for JM < 1.93 are shown, 2) the relationship between individual class numbers and class colours (for Figure 328) are omitted, 3) JM distances are given in order of increasing JM distances, 4) JM distances are rounded to 4 d.p..

Class merging did not result in a thematic map for $JM \geq 1.7$ or $JM \geq 1.8$. Instead, the 10 class k-means result was reduced to 6 classes at a $JM \geq 1.91$. However, as is evident from Figure 329, the separability statistics have resulted in classes which are distinguishable to a high degree of confidence amongst the mangrove forests. There certainly appears to be a spatially coherent class structure.

A closer examination of Figure 328 over Finucane Island reveals a spatial structure reminiscent to that found earlier in Figure 99 (p. 247 of Section 4.5.7 – the thematic map for PHPA_Ref_VI) and Figure 135 (p. 317 of Section 4.5.11.1 – the thematic map for N_Rad_VI_VI). The difference to Figure 99 is that the confidence of class separability is now very high (i.e. $JM \geq 1.9$ for N_Rad_Land_VI), whereas previously the probability of class separability is low ($JM \geq 1.7$ for PHPA_Ref_VI). A similar result exists for the N_Rad_VI_VI dataset, where Figure 135 shows the structure at low and moderate probabilities (i.e. at $JM \geq 1.7$ and $JM \geq 1.8$). Interestingly, only the N_Rad_Land_VI produces the result at $JM \geq 1.9$. Nevertheless, all these results suggest the spatial structure to exist. Therefore, the structure is more pronounced in radiance-based images compared to reflectance-based images. For the reflectance-based images, the PHPA_Ref_VI image defines the region at $JM \geq 1.7$, while it is not as well defined in the other reflectances-based images (N_Ref_VI_VI and PHPA_Ref_Res_VI) for the same JM distance.

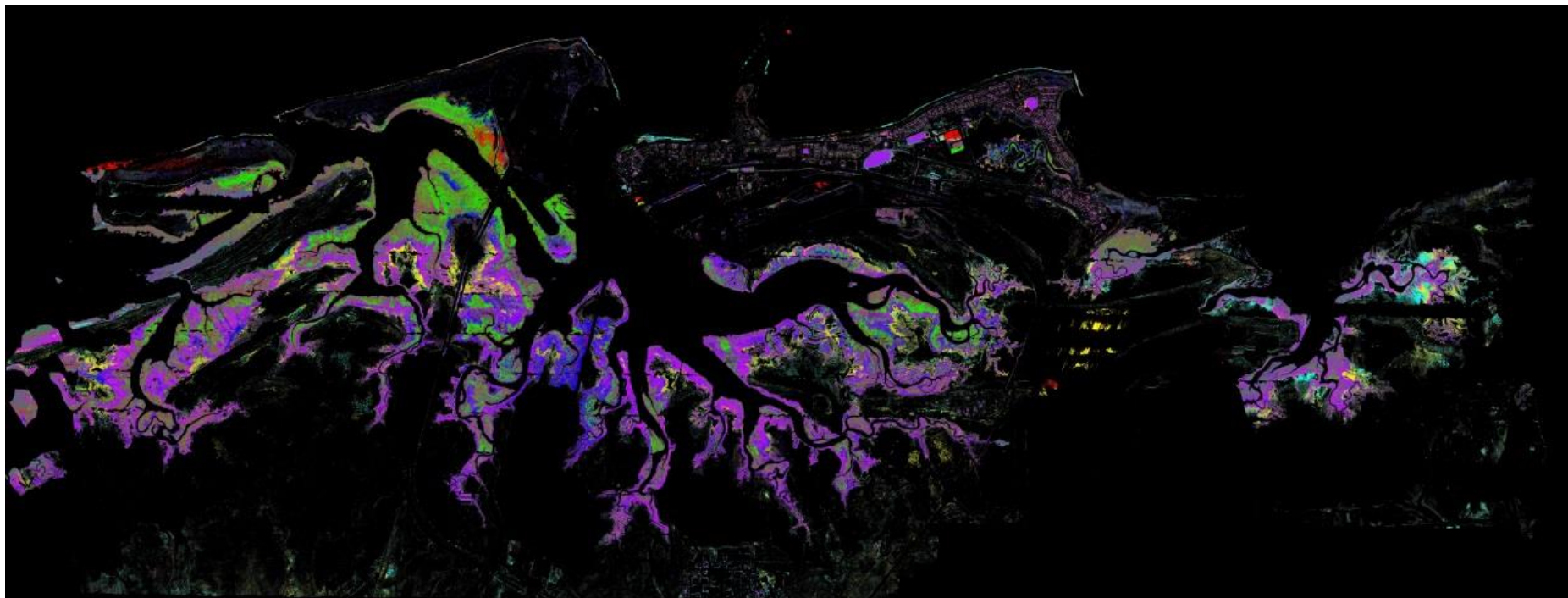


Figure 328: Thematic map as obtained by using 50 iterations for a 10 class k-means classifier of the 11 PC band N_Rad_Land_VI dataset.

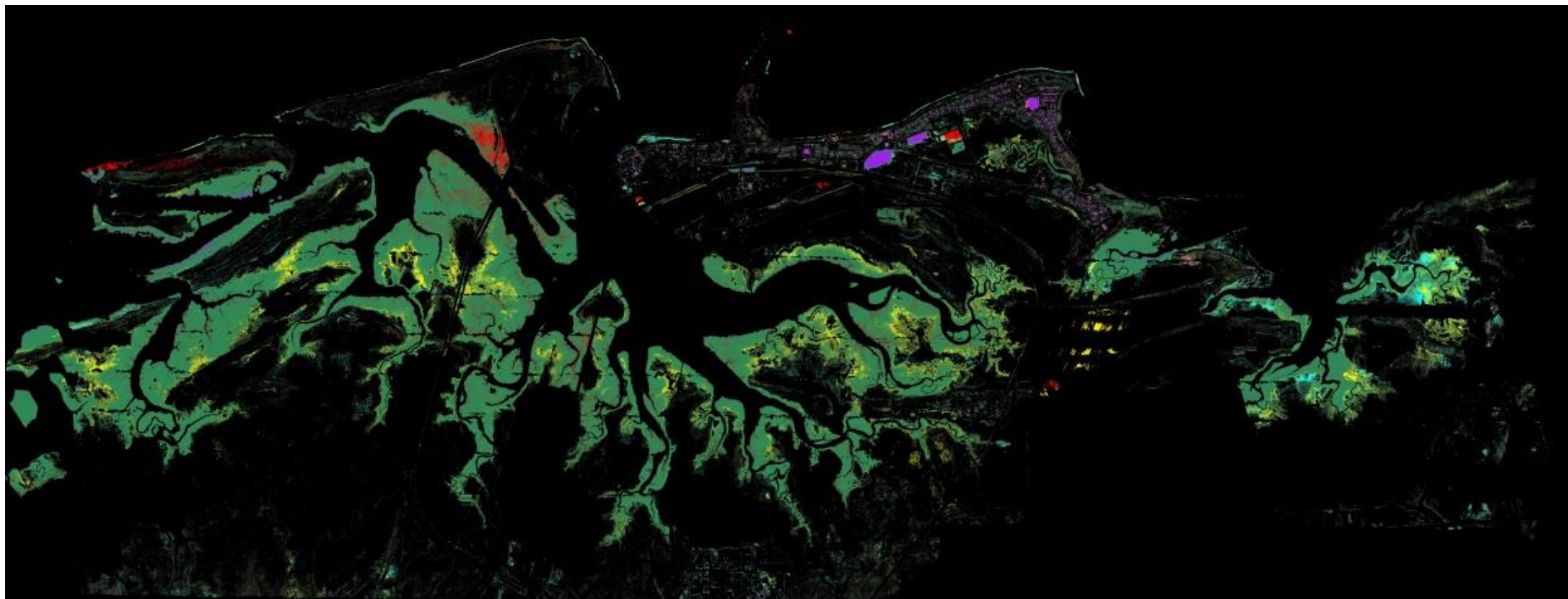


Figure 329: Thematic map as obtained by merging classes from the 10 class k-means classifier of the 11 PC band N_Rad_Land_VI dataset. A total of 6 classes remain highly separable at $JM \geq 1.9$. Note the presence of coherent class structures among the mangrove forested regions.

Practical data is required to determine what is actually located in the region of interest (i.e. the yellow circle indicated in Figure 330). However, it is encouraging that these characteristics are common between the PHPA_Ref_VI and N_Rad_Land_VI and N_Rad_VI_VI images.

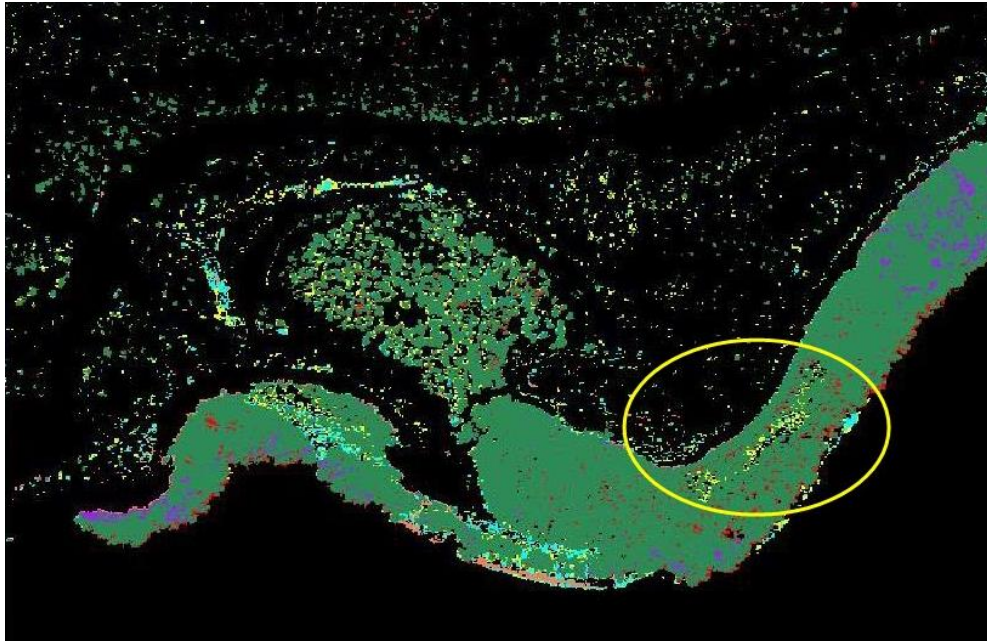


Figure 330: The yellow class structure is absent in most classification attempts except for the PHPA_Ref_VI (Figure 99 (p. 247 of Section 4.5.7)) and N_Rad_VI_VI (Figure 135 (p. 317 of Section 4.5.11.1)) thematic maps. The advantage of the above result is that the region is now defined with higher probability to any previous thematic map.

The final 6 class pairs are spectrally separated to a high degree of confidence, as shown in Table 127 (corresponding to $JM \geq 1.9$ of Figure 329).

The thematic map corresponding to the k-means classifier was also examined using 15 clusters. To reach a class separability at $JM \geq 1.7$ (actually ≥ 1.6989), 7 classes remained. The map also contains the class structure indicated by yellow circle in Figure 330 (the result is not shown here). In addition, the map contains spatial structures among the mangrove forests, reminiscent of the yellow and green regions as in Figure 329. However, surprisingly at $JM \geq 1.9$, both structures were no longer present (leaving only 6 classes).

The ISODATA classification results for 5 - 10 classes behaved very similar to k-means, where for $JM \geq 1.7$ a total of 6 classes were left and for $JM \geq 1.9$ leaving just

class 5 & class 8: 1.9157
class 9 & class 10: 1.9549
class 5 & class 10: 1.9571
class 4 & class 5: 1.9628
class 1 & class 8: 1.9876
class 1 & class 4: 1.9897
class 4 & class 8: 1.9923
class 8 & class 9: 1.9952
class 4 & class 10: 1.9975
class 5 & class 9: 1.9978
class 8 & class 10: 1.9991
class 1 & class 5: 1.9992
class 1 & class 10: 1.9997
class 1 & class 9: 1.9999
class 4 & class 9: 2.0000

Table 127: Separability report for the k-means 10 class (50 iterations) classifier where $JM \geq 1.9$ of the 11 PC band N_Rad_Land_VI dataset.

Note: 1) All class-pair values are shown in the table, 2) the relationship between individual class numbers and class colours (for Figure 329) are omitted, 3) JM distances are given in order of increasing JM distances, 4) JM distances are rounded to 4 d.p..

5 classes. Classification using 5 - 15 classes using ISODATA resulted in 7 classes at $JM \geq 1.8$ and 6 classes at $JM \geq 1.9$ with little differences between them. Overall, the behaviour for the classification results between k-means and ISODATA classifiers were very similar.

Again, the results are briefly summarised in Table 45 (p. 331 of Section 4.5.11.3) with ISODATA and k-means (15 classes) results not shown due to the lack of further useful class features present compared to what has been presented thus far.

P.5 Classification based on the N_Ref_Res_VI_VI image

This section examines the impact of removing the urban residential regions in the town of Port Hedland upon classification.

The PC transformation of the N_Ref_Res_VI_VI image leaves 9 PC bands for a cumulative variance threshold of 99%, as shown in Table 128.

Using the k-means classifier with 10 clusters (and 50 iterations) leaves just 5 classes (Figure 331) when class-pairs were merged to a distance of $JM \geq 1.65$ (Table 129).

PC band	Cumulative variance (%)	PC band	Cumulative variance (%)
1	76.94	6	98.68
2	95.50	7	98.83
3	97.39	8	98.96
4	98.00	9	99.07
5	98.51	10	99.15

Table 128: Cumulative variance (in % and rounded to 2 d.p.) of the PC transform for the N_Ref_Res_VI_VI image.

The first 9 PCA bands account for 99% of the total variance. Therefore, 9 PC bands were retained for classification purposes (Note: only the first 10 PC bands are shown in this table). The order of PC bands are given in ascending order by increasing cumulative variance.

The scene is dominated by the yellow colour (class 4), while limited structure is provided by the maroon (class 7). However, the separability between these two classes was limited ($JM = 1.6513$), as the results suggest in Table 129.

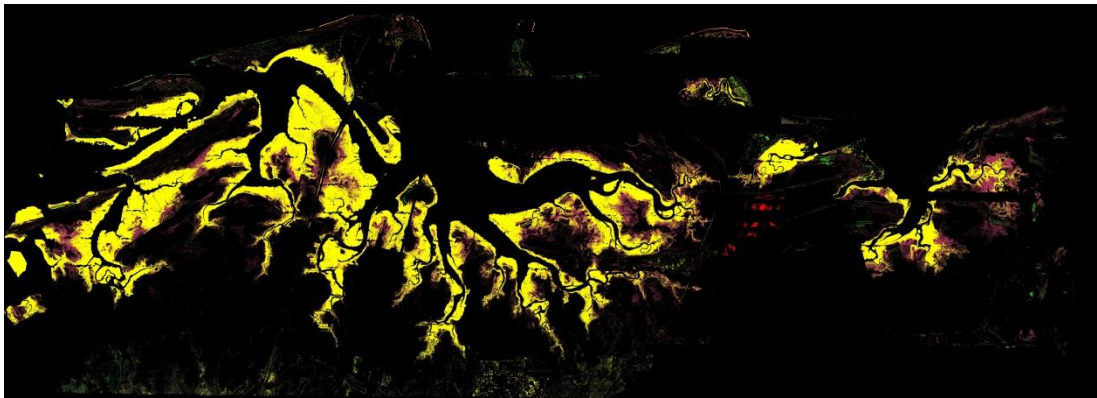


Figure 331: Thematic map as obtained by merging classes from the 10 class k-means classifier of the 9 PC band N_Ref_Res_VI_VI dataset. A total of 5 classes remain separable to $JM \geq 1.65$.

To increase the probability of class separation, the merging of both class 4 and class 7 immediately produced a minimum separability of $JM \geq 1.9$, as shown in Table 130.

A total of 4 classes remains after merging, with one class covering the whole mangrove region (similar to Figure 327).

class 7 & class 4: 1.6513
class 2 & class 7: 1.9604
class 2 & class 4: 1.9921
class 10 & class 4: 1.9936
class 10 & class 7: 1.9952
class 2 & class 10: 1.9999
class 1 & class 2: 2.0000
class 1 & class 4: 2.0000
class 1 & class 10: 2.0000
class 1 & class 7: 2.0000

Table 129: Separability report for the k-means 10 class (50 iterations) classifier where $JM \geq 1.65$ of the 9 PC band N_Ref_Res_VI_VI dataset.

Note: 1) all class-pair separability JM distances are shown, 2) the relationship between individual class numbers and class colours (for Figure 331) are omitted, 3) JM distances are given in order of increasing JM distances, 4) JM distances are rounded to 4 d.p..

class 2 & class 4: 1.9748
class 10 & class 4: 1.9908
class 2 & class 10: 1.9999
class 1 & class 2: 2.0000
class 1 & class 10: 2.0000
class 1 & class 4: 2.0000

Table 130: Separability report for the k-means 10 class (50 iterations) classifier where $JM \geq 1.9$ of the 9 PC band N_Ref_Res_VI_VI dataset.

Note: 1) all class-pair separability JM distances are shown, 2) the relationship between individual class numbers and class colours (for Figure 331) are omitted, 3) JM distances are given in order of increasing JM distances, 4) JM distances are rounded to 4 d.p..

Classification using ISODATA with 5 - 10 classes resulted in 6 classes for $JM \geq 1.7$, with a very similar class distribution to that of Figure 331. Interestingly, the two classes amongst the mangrove forests (i.e. like Figure 330) were found to have a $JM = 1.72$ compared to $JM = 1.65$ for the k-means result, suggesting a slightly higher probability for the existence of the spatial structure amongst the mangrove forest. Further merging of classes to reach $JM \geq 1.9$, resulted in a thematic map containing just 5 classes and very similar in appearance to that of Figure 327.

The lack of detail of mangrove forest structure is reminiscent of the results for the N_Ref_VI_VI thematic map (Figure 100, p. 248 of Section 4.5.7). The PC transform actually contained one less band than that for the N_Ref_VI_VI (Table 123) suggesting less spectral variability in the N_Ref_Res_VI dataset.

The removal of the urban residential region does not result in any real improvement compared to the earlier reflectance-based thematic maps.

P.6 Classification based on the N_Rad_Res_VI_VI image

As the N_Rad_VI_VI thematic map (Section 4.5.11.1 in particular Figure 133) is of particularly high quality, it is of interest to pursue the effect of removing the urban residential region.

However, in view of the limited improvement gained with the N_Ref_Res_VI thematic result of the previous section and considering the small number of PC bands in the feature-reduced image (just 7 PC bands from Table 131 compared to 15 PC bands of Table 34), the level of optimism for an improved classification product is low.

PC transforming the N_Rad_Res_VI_VI image leaves just 7 PC bands for a cumulative variance threshold of 99%, as shown in Table 131.

PC band	Cumulative variance (%)	PC band	Cumulative variance (%)
1	74.40	6	98.90
2	94.04	7	99.10
3	97.43	8	99.23
4	98.32	9	99.33
5	98.68	10	99.39

Table 131: Cumulative variance (in % and rounded to 2 d.p.) of the PC transform for the N_Rad_Res_VI_VI image.

The first 7 PCA bands account for 99% of the total variance. Therefore, 7 PC bands were retained for classification purposes (Note: only the first 10 PC bands are shown in this table). The order of PC bands are given in ascending order by increasing cumulative variance.

The classification results confirm this pessimistic view for a solid classification map. Low separability between classes (see Table 132) immediately resulted for a k-means classifier with 10 classes. This is very different to the result of Table 35 (p. 302 of Section 4.5.11.1) for the N_Rad_VI_VI where all classes were immediately separable to $JM \geq 1.7$.

class 7 & class 8: 1.4564
class 4 & class 6: 1.4583
class 3 & class 7: 1.5256
class 5 & class 8: 1.5514
class 1 & class 3: 1.5579
class 2 & class 3: 1.5694
class 2 & class 5: 1.5949
class 2 & class 4: 1.5995
class 1 & class 2: 1.6086
class 5 & class 7: 1.6499
class 3 & class 5: 1.7248
class 4 & class 5: 1.7944
class 5 & class 6: 1.9109

Table 132: Separability report for the k-means 10 class (50 iterations) classifier where $JM \geq 1.7$ of the 7 PC band N_Rad_Res_VI_VI dataset.

Note: 1) only values for $JM < 1.92$ are shown, 2) JM distances are given in order of increasing JM distances, 3) JM distances are rounded to 4 d.p..

The process of class merging directly resulted in a thematic map where $JM \geq 1.9$, containing just 3 classes (i.e. there is no result for $JM \geq 1.7$ and $JM \geq 1.8$).

class 9 & class 6: 1.9843
class 9 & class 10: 2.0000
class 10 & class 6: 2.0000

Table 133: Separability report for the k-means 10 class (50 iterations) classifier where $JM \geq 1.9$ of the 7 PC band N_Rad_Res_VI_VI dataset, leaving just 3 highly separable classes.

Note: 1) all class-pair separability JM distances are shown, 2) JM distances are given in order of increasing JM distances, 3) JM distances are rounded to 4 d.p..

The lack of detail was discouraging; the image is not shown here, as it contains just one class covering the whole mangrove region.

Similarly poor results were also obtained for both the k-means classifier (with 15 classes) and for ISODATA (5 - 10 and 10 - 15 classes).

The results are briefly summarised in Table 45 (p. 331 of Section 4.5.11.3).

P.7 Classification based on a spectral subset for N_Rad_VI_VI

Inconsistencies in reflectances over the blue-end spectral region, for the northern-end of the PHPA_Ref image, were highlighted previously in Section 4.5.3.3. For example, over Finucane Island, negative reflectances were observed in Figure 86 (p 219 of Section 4.5.3.3). The work of Appendix N (in particular, Figure 300 (p. 639)) showed that the negative reflectances are still present in normalised images. Moreover, the reflectance spectra are particularly noisy for wavelengths in excess of ≈ 710 nm.

Due to the undesired spectral effects at both ends of the spectrum, a range of wavelengths from the N_Rad_VI_VI image were removed. Note that the N_Rad_VI_VI image was targeted, as it produced the best thematic map, with the aim being to produce an even better classification product.

However, care must be taken not to remove too many wavelengths, in order to preserve the spectral features over the wavelengths needed to allow the classifier to categorise vegetation. Referring back to Figure 57 (p. 175 of Section 4.4.2), the ASD spectral means for the mangrove species shows a degree of differentiability between $\approx 500 - 700$ nm range. It was decided to eliminate wavelengths outside the 501 nm – 733.1 nm range (as the red-edge must be included; 710 – 720 nm – from Section 2.3.1); the ‘bump’ near 750 nm was intentionally eliminated (see Figure 307, p. 650 of Appendix N.3 for an example). The subsetted image thereby contains 106 bands with the image named **N_Rad_VI_VI_subset**.

A cumulative variance threshold of 99% was reached after only 6 PC bands (compared to 15 PC bands as shown in Table 34 (p. 301 of Section 4.5.11.1) for N_Rad_VI_VI). The k-means classifier for 10 classes (50 iterations) produced 6 classes separable at $JM > 1.68$ (see Figure 332), 4 classes at $JM > 1.82$ (whereby the yellow coloured class in Figure 332 merged with the purple coloured class) and 3 classes at $JM > 1.97$ (whereby all mangrove forest regions are described by just one class).

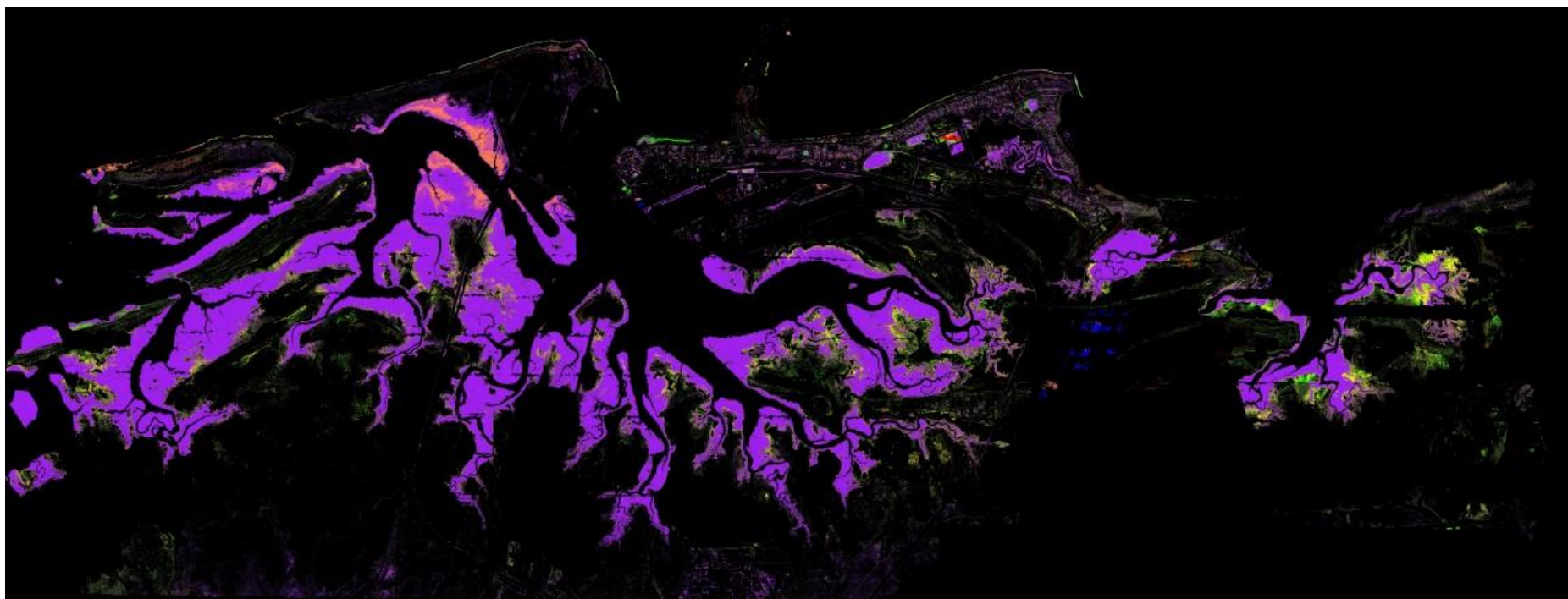


Figure 332: Thematic map as obtained by merging classes from the 10 class k-means classifier of the 6 PC band N_Rad_VI_VI_subset dataset. A total of 6 classes remain separable to $JM \geq 1.65$.

In previous work (Section 4.5.11.1), where the full spectrum for the N_Rad_VI_VI image was used, all 10 classes for the 10 class k-means classifier were immediately separable for at $JM > 1.7$ (Table 35, p. 302 of Section 4.5.11.1). The current work produced 6 classes separable at $JM > 1.68$, possibly due to the lower number of PC bands retained.

Like the full spectral N_Rad_VI_VI image, the subsetted N_Rad_VI_VI image was also classified using a 15 class k-means classifier; this time producing just 7 separable classes at $JM > 1.65$ - the result is displayed in Figure 333.

Increasing the confidence for class separation requires an increase in class separability. A total of 6 classes remain separable at $JM > 1.77$ with the loss of the aqua coloured class (in Figure 333) being integrated with the brown class. The loss of the urban residential grassed region (in particularly the rose-coloured oval) occurs at $JM > 1.83$, where brown coloured region now appears, leaving a total of 5 classes. At $JM > 1.89$, a total of 4 classes remains whereby all mangrove forests are placed into one class.

The gross spatial class structures in Figure 333 appear similar to the earlier result of Figure 133 (p. 310 of Section 4.5.11.1), with the major differences being located over Finucane Island. Figure 133 contains 8 classes separable to $JM \geq 1.8$, while Figure 333 has just 7 classes separable to $JM \geq 1.65$. Moreover, 10 classes remain separable to $JM \geq 1.7$ (Figure 132, p. 309 of Section 4.5.11.1) using the full spectrum (i.e. N_Rad_VI_VI) and contains even more structural detail than Figure 333 (and still at higher confidence - i.e. at $JM \geq 1.7$ instead of $JM \geq 1.65$).

Therefore, subsetting the N_Rad_VI_VI image results in a lower confidence map and possibly with less spectral variability, as the PC transform leaves just 6 PC bands (for the subset) compared to 15 PC bands for the full spectral range.

Although the results of this section were comparable to previous results, the work here has delivered an inferior thematic map, with reduced class separability.

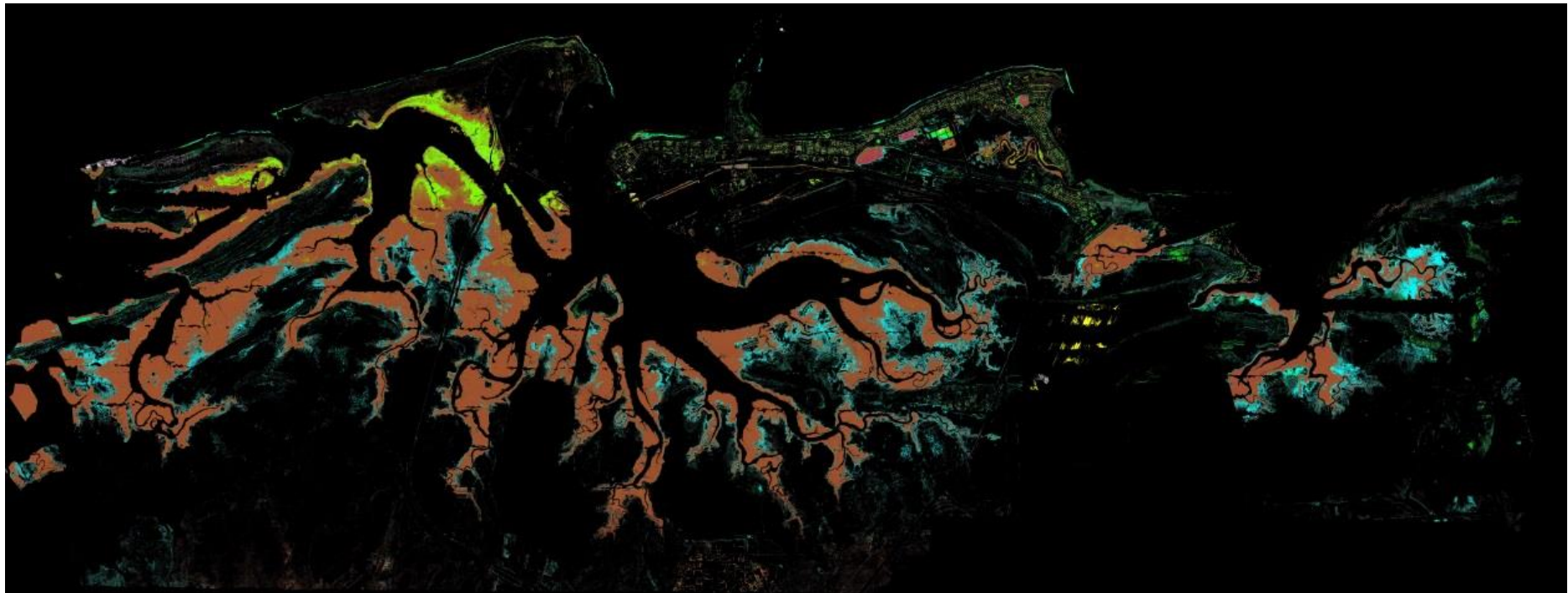


Figure 333: Thematic map as obtained by merging classes from the 15 class k-means classifier of the 6 PC band N_Rad_VI_VI_subset dataset. A total of 7 classes remain separable to $JM \geq 1.65$.

Appendix Q Tafkaa Model Details

Equation Chapter 17 Section 1 Target Surface Reflectance and the Tafkaa Model

This section provides a brief outline for relating the at sensor radiance to surface reflectance using the Tafkaa radiometric model.

The mathematical treatment in this section closely follows the work as outlined in the Tafkaa User's Guide (Montes et al., 2004). The terminology used in the following work were defined in Section 2.3.3.

The definitions listed below are used to derive an expression for the total radiance received at the sensor from a surface reflected pixel (over land):

L_t = total radiance measured at the airborne sensor

L_0 = path radiance

L_g = radiance reflected of from the target (i.e. the pixel).

For convenience, Figure 18 (Section 2.4.1) is copied below (to Figure 334) to assist with explaining the physics of atmospheric scattering.

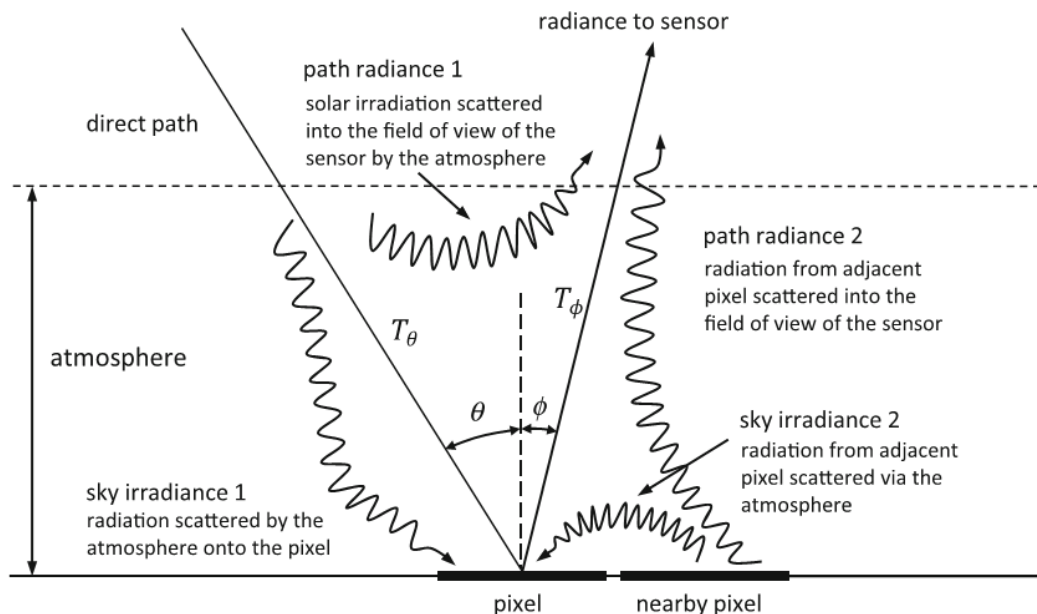


Figure 334: Atmospheric scattering effects on a pixel by solar radiation.
(Figure taken from Richards (2013, p. 34), Figure 2.5).

Consider the solar spectral irradiance at the top of the atmosphere, denoted by E_0 . The radiance arriving at the pixel (i.e. downwards) is reduced due to atmospheric scattering and absorption. The angle θ defines the zenith angle and accounts for the position of the sun with respect to the pixel. The altitude of the sun (from the pixel) is $90 - \theta$. The transmittance was first defined in Section 2.3.3 and describes the amount of radiation traversing through the atmosphere. A value of one indicates total transmission (zero absorption), while a value of zero removes any traversal of radiation (total absorption). The fraction of incoming solar irradiance from the top of the atmosphere arriving at the pixel is scaled by T_θ . The pixel is influenced by neighbouring pixels (the adjacency effect) and sky irradiance. The pixel radiance transmitted back up through the atmosphere is once again attenuated by T_ϕ . The path radiance (which is purely caused by the atmosphere - i.e. not ground pixel related) also affects the radiance detected at the sensor.

In the literature, it is common to relate the radiance detected at the sensor in terms of a downward and upward transmittance (e.g. Richards (2013) (Section 2.6) and Schowengerdt, 2007 (Section 2.2.2)). The Tafkaa User's Guide (Montes et al., 2004) is another culprit and writes the radiance detected at the sensor as:

$$L_t = L_0 + L_g t' \quad (\text{Q.1.1})$$

where t' is the transmission through the atmosphere of L_g . It should be remarked that the above equation is derived from the Tafkaa User's Guide (Montes et al., 2004) by setting the water radiance of direct and diffuse light specularly reflected off the sea surface to zero. Our interest concerns vegetation over land, thereby simplifying the equation in the Tafkaa User's Guide (Montes et al., 2004) to the form given by Equation (Q.1.1).

The radiances expressed in Equation (Q.1.1) are functions:

$$L_0 = L_0(\lambda; \theta, \phi; \theta_0, \phi_0; \tau_a; z_{sen}; z_{sur})$$

$$L_g = L_g(\lambda; \theta, \phi; \theta_0, \phi_0; W; \tau_a; z_{sur})$$

$$t' = t'(\lambda; \theta; \tau_a; z_{sen}; z_{sur})$$

Note that L_g is also a function of C in the Tafkaa User's Guide (Montes et al., 2004), where C is the set of parameters describing the air-water interface effects. As our interest lies in land-based pixels, the dependence on water allows the functional dependence of C to be ignored.

In these functions, it is useful to refer to Figure 335 for the definitions for the both the solar and viewing zenith and azimuth angles.

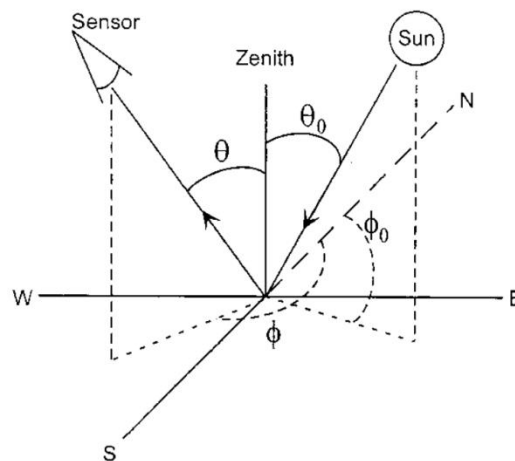


Figure 335: Sun-sensor geometry, showing the solar and viewing zenith and azimuth angles.
(Figure taken from Figure 2 of B.-C. Gao et al. (2000))

θ, ϕ = view zenith and azimuth angles of the line of sight at the sensor toward the Earth's surface.

θ_0, ϕ_0 = zenith and azimuth angles of the direct sunlight

τ_a = aerosol optical depth

z_{sen} = altitude of the sensor

z_{sur} = altitude of the ground pixel

W = wind speed

The aerosol optical depth is a measure of the amount of particles in the atmosphere (e.g. dust, smoke, pollution).

An assumption is made whereby the atmospheric transmission can be factored out into absorptive and scattered parts. Therefore T_g represents the total gaseous transmittance in the sun-surface-sensor path. Equation (Q.1.1) is thereby rewritten as:

$$L_t = T_g (L'_0 + L_g t'_u) \quad (\text{Q.1.2})$$

where $L'_0 = L_0 / T_g$ and t'_u is the effective upward transmission.

If the irradiance at the top of the atmosphere is $E_0 \mu_0$, then (in general) the reflectance ρ is obtained by $\rho(\lambda, \theta, \phi, \theta_0, \phi_0) = \pi L(\lambda, \theta, \phi, \theta_0, \phi_0) / E_0 \mu_0$.

Therefore, multiplying Equation (Q.1.2) by $\pi / E_0 \mu_0$ allows it to be expressed in terms of reflectances.

$$\frac{\pi L_t}{E_0 \mu_0} = T_g \left[\frac{\pi L'_0}{E_0 \mu_0} + \frac{\pi L_g t'_u t_d}{E_0 \mu_0 t_d} \right]$$

This allows for the following definitions of reflectances:³⁷

$$\rho_{obs}^* = \frac{\pi L_t}{E_0 \mu_0}$$

$$\rho_{atm}^* = \frac{\pi L'_0}{E_0 \mu_0}$$

$$\rho_g = \frac{\pi L_g}{E_0 \mu_0 t_d}$$

and

³⁷ Actually, the reflectances are scaled reflectances, which differ from the surface reflectances by a scale factor accounting for the slopes and aspects of the surface (B.-C. Gao et al., 1993).

$t_d = t_d(\lambda, \tau_a, \theta_0)$ and is the downward transmittance through the atmosphere to the target pixel.

Therefore:

$$\rho_{obs}^* = T_g \left[\rho_{atm}^* + \rho_g t_u t_d \right]$$

Solving for ρ_g gives the ground reflectance of the target pixel:

$$\rho_g = \frac{\frac{\rho_{obs}^*}{T_g} - \rho_{atm}^*}{t_u t_d} \quad (Q.1.3)$$

Equation (Q.1.3) expresses the ground reflectance ρ_g (the quantity of interest) in terms of the radiance measured at the sensor L_t as $\rho_{obs}^* = \pi L_t / E_0 \mu_0$. Tafkaa models the quantities ρ_{atm}^* , t_u , t_d and T_g .

Q.2 Flight Line Segment Parameters

Each flight line segment file (i.e. all 137 of them) contains an associated ENVI header file. These files contain valuable information, such as image size, spectral wavelengths used for the pixel spectra, and so on.

Parameters such as time of sensing, position (longitude and latitude) and altitude of the sensor are represented by flight line segment centre values. For instance, the stated position refers to the position of the centre of the flight line segment.

The table given below (Table 134) also displays the Tafkaa solar zenith angle and Tafkaa solar azimuth angles, both calculated by Tafkaa (through parameters “tafkaa_determined_solar_zenith_angle” and “tafkaa_determined_solar_azimuth_angle” in the header files). The columns for NOAA solar zenith angle and NOAA solar azimuth angle were calculated using the

NOAA Solar Calculator (2016), which required input data such as the position (longitude and latitude) and time (including date). Note that all angles are expressed in degrees.

The last two columns are “zenith difference” and “azimuth difference”. Both differences are calculated according to:

$$\text{zenith difference} = \text{Tafkaa zenith angle} - \text{NOAA zenith angle}$$

$$\text{azimuth difference} = \text{Tafkaa azimuth angle} - \text{NOAA azimuth angle}$$

The differences between the calculated Tafkaa and NOAA angles (using the NOAA Solar Calculator (2016) are all well below 1%. Therefore, the calculated solar-sensor geometry is sound as calculated by Tafkaa.

Table 134 starts on the following page and extends to page 710.

flight line segment id	flight line segment	time			tafkaa latitude			tafkaa longitude			Sensor altitude (km)	Tafkaa solar zenith angle	NOAA solar zenith angle	Tafkaa solar azimuth angle	NOAA solar azimuth	zenith difference	azimuth difference
		h	m	s	h	m	s	h	m	s							
1	01a	8	44	7	20	22	6.002	118	31	1.002	0.606	53.237	53.22	70.588	70.59	0.017	-0.002
2	01b	8	45	49	20	22	6.002	118	33	12.014	0.612	52.829	52.81	70.318	70.32	0.019	-0.002
3	01c	8	47	50	20	22	4.999	118	35	41.016	0.603	52.347	52.33	69.997	70.00	0.017	-0.003
4	02a	8	50	53	20	22	1.003	118	35	5.997	0.599	51.685	51.67	69.545	69.55	0.015	-0.005
5	02b	8	52	50	20	22	1.003	118	31	27.012	0.594	51.31	51.29	69.285	69.29	0.020	-0.005
6	03a	8	56	23	20	21	48.005	118	31	3.007	0.606	50.537	50.52	68.742	68.74	0.017	0.002
7	03b	8	57	43	20	21	48.005	118	33	17.012	0.601	50.213	50.19	68.509	68.51	0.023	-0.001
8	03c	8	59	14	20	21	48.005	118	35	13.000	0.600	49.854	49.84	68.248	68.25	0.014	-0.002
9	03d	9	0	18	20	21	48.005	118	36	36.991	0.602	49.601	49.58	68.061	68.06	0.021	0.001
10	04a	9	2	57	20	21	37.005	118	35	39.999	0.594	49.039	49.02	67.642	67.64	0.019	0.002
11	04b	9	4	39	20	21	37.005	118	32	53.996	0.598	48.71	48.69	67.392	67.39	0.020	0.002
12	04c	9	5	44	20	21	39.003	118	30	38.013	0.597	48.508	48.49	67.238	67.24	0.018	-0.002
13	05a	9	9	15	20	21	30.001	118	30	58.008	0.600	47.744	47.73	66.641	66.64	0.014	0.001
14	05b	9	11	12	20	21	31.003	118	33	18.001	0.600	47.29	47.27	66.278	66.28	0.020	-0.002
15	05c	9	12	37	20	21	30.001	118	36	4.993	0.598	46.947	46.93	65.998	66.00	0.017	-0.002
16	05d	9	14	22	20	21	30.001	118	38	21.004	0.593	46.54	46.52	65.661	65.66	0.020	0.001
17	05e	9	16	0	20	21	30.001	118	40	24.985	0.593	46.162	46.15	65.344	65.34	0.012	0.004
18	05f	9	17	15	20	21	30.001	118	41	54.990	0.590	45.874	45.86	65.099	65.10	0.014	-0.001
19	06a	9	19	52	20	21	19.001	118	40	18.997	0.596	45.34	45.32	64.639	64.64	0.020	-0.001
20	06b	9	21	16	20	21	19.001	118	37	17.997	0.598	45.087	45.07	64.415	64.42	0.017	-0.005
21	06c	9	22	54	20	21	19.001	118	34	34.988	0.594	44.779	44.76	64.142	64.14	0.019	0.002
22	06d	9	24	18	20	21	19.001	118	32	12.001	0.602	44.517	44.5	63.905	63.91	0.017	-0.005
23	06e	9	25	27	20	21	19.001	118	30	14.996	0.590	44.303	44.29	63.708	63.71	0.013	-0.002

24	07a	9	28	33	20	21	8.001	118	31	14.020	0.598	43.637	43.62	63.093	63.09	0.017	0.003
25	07b	9	30	31	20	21	8.001	118	33	40.001	0.597	43.193	43.18	62.668	62.67	0.013	-0.002
26	07c	9	31	52	20	21	8.001	118	36	16.996	0.599	42.876	42.86	62.358	62.36	0.016	-0.002
27	07d	9	33	35	20	21	8.001	118	38	29.985	0.598	42.488	42.47	61.977	61.98	0.018	-0.003
28	07e	9	35	16	20	21	9.003	118	40	35.999	0.593	42.112	42.1	61.596	61.60	0.012	-0.004
29	08a	9	38	26	20	21	2.000	118	40	43.991	0.592	41.458	41.44	60.921	60.92	0.018	0.001
30	08b	9	39	59	20	21	2.000	118	38	14.989	0.592	41.174	41.16	60.622	60.62	0.014	0.002
31	08c	9	41	49	20	21	2.000	118	35	14.017	0.595	40.841	40.83	60.263	60.26	0.011	0.003
32	08d	9	43	12	20	21	0.001	118	32	54.985	0.592	40.591	40.58	59.99	59.99	0.011	0.000
33	08e	9	44	27	20	21	0.001	118	30	48.999	0.597	40.365	40.35	59.742	59.74	0.015	0.002
34	09a	9	47	37	20	20	50.999	118	30	56.992	0.602	39.723	39.71	59.017	59.02	0.013	-0.003
35	09b	9	48	59	20	20	50.999	118	33	8.004	0.602	39.42	39.41	58.664	58.67	0.010	-0.006
36	09c	9	50	39	20	20	50.999	118	35	24.014	0.603	39.055	39.04	58.235	58.24	0.015	-0.005
37	09d	9	52	25	20	20	50.999	118	37	59.004	0.600	38.67	38.66	57.767	57.77	0.010	-0.003
38	09e	9	53	48	20	20	50.999	118	39	51.998	0.599	38.371	38.36	57.398	57.40	0.011	-0.002
39	09f	9	54	56	20	20	50.999	118	41	29.008	0.598	38.127	38.11	57.09	57.09	0.017	0.000
40	10a	9	57	14	20	20	38.001	118	40	38.004	0.594	37.683	37.67	56.531	56.53	0.013	0.001
41	10b	9	59	9	20	20	38.001	118	37	53.016	0.575	37.345	37.33	56.087	56.09	0.015	-0.003
42	10c	10	0	50	20	20	38.001	118	35	0.009	0.598	37.056	37.04	55.699	55.70	0.016	-0.001
43	10d	10	2	15	20	20	38.001	118	32	36.995	0.596	36.812	36.8	55.369	55.37	0.012	-0.001
44	10e	10	3	22	20	20	38.001	118	30	36.008	0.593	36.623	36.61	55.108	55.11	0.013	-0.002
45	11a	10	6	38	20	20	33.002	118	30	56.003	0.598	35.992	35.98	54.218	54.22	0.012	-0.002
46	11b	10	7	53	20	20	33.002	118	33	2.016	0.606	35.728	35.72	53.833	53.83	0.008	0.003
47	11c	10	9	47	20	20	33.002	118	35	22.009	0.600	35.34	35.33	53.253	53.25	0.010	0.003
48	11d	10	11	28	20	20	33.002	118	37	59.993	0.604	34.992	34.98	52.719	52.72	0.012	-0.001
49	11e	10	13	7	20	20	33.002	118	40	9.988	0.601	34.658	34.65	52.196	52.20	0.008	-0.004

50	11f	10	14	17	20	20	32.000	118	41	54.001	0.597	34.421	34.41	51.816	51.82	0.011	-0.004
51	12a	10	18	25	20	20	22.002	118	40	5.978	0.590	33.684	33.67	50.6	50.60	0.014	0.000
52	12b	10	20	17	20	20	22.002	118	36	58.991	0.593	33.385	33.38	50.082	50.08	0.005	0.002
53	12c	10	21	56	20	20	22.002	118	34	24.001	0.594	33.12	33.11	49.613	49.61	0.010	0.003
54	12d	10	23	47	20	20	22.002	118	31	22.013	0.598	32.826	32.82	49.083	49.08	0.006	0.003
55	12e	10	24	41	20	20	25.003	118	29	38.000	0.595	32.688	32.68	48.826	48.83	0.008	-0.004
56	13a	10	27	0	20	20	10.000	118	31	20.008	0.600	32.259	32.25	48.026	48.03	0.009	-0.004
57	13b	10	28	54	20	20	10.000	118	33	35.002	0.594	31.903	31.89	47.332	47.33	0.013	0.002
58	13c	10	30	35	20	20	10.000	118	36	14.002	0.599	31.583	31.57	46.691	46.69	0.013	0.001
59	13d	10	32	40	20	20	9.004	118	38	44.982	0.588	31.201	31.19	45.898	45.90	0.011	-0.002
60	13e	10	34	11	20	20	10.000	118	41	7.007	0.587	30.921	30.91	45.297	45.30	0.011	-0.003
61	14a	10	37	1	20	19	58.004	118	40	35.999	0.592	30.455	30.45	44.274	44.28	0.005	-0.006
62	14b	10	38	50	20	19	58.004	118	37	43.019	0.605	30.191	30.18	43.664	43.67	0.011	-0.006
63	14c	10	40	21	20	19	58.004	118	34	49.984	0.602	29.976	29.97	43.161	43.16	0.006	0.001
64	14d	10	41	49	20	19	59.000	118	32	21.998	0.612	29.768	29.76	42.659	42.66	0.008	-0.001
65	14e	10	43	0	20	20	1.005	118	30	24.994	0.609	29.602	29.59	42.247	42.25	0.012	-0.003
66	15a	10	48	1	20	19	53.005	118	30	58.008	0.598	28.818	28.81	40.218	40.22	0.008	-0.002
67	15b	10	49	40	20	19	54.001	118	33	4.021	0.599	28.55	28.54	39.474	39.48	0.010	-0.006
68	15c	10	51	37	20	19	54.001	118	35	7.013	0.602	28.24	28.23	38.591	38.59	0.010	0.001
69	15d	10	52	56	20	19	54.001	118	37	19.014	0.606	28.028	28.02	37.96	37.96	0.008	0.000
70	15e	10	54	32	20	19	53.005	118	39	26.016	0.610	27.778	27.77	37.198	37.20	0.008	-0.002
71	15f	10	55	45	20	19	53.005	118	41	26.014	0.597	27.588	27.58	36.599	36.60	0.008	-0.001
72	16a	10	58	18	20	19	41.003	118	40	35.999	0.607	27.24	27.23	35.475	35.48	0.010	-0.005
73	16b	11	0	10	20	19	41.003	118	37	46.013	0.606	27.014	27.01	34.701	34.70	0.004	0.001
74	16c	11	1	31	20	19	41.003	118	34	48.007	0.598	26.861	26.85	34.163	34.17	0.011	-0.007
75	16d	11	3	10	20	19	41.003	118	32	21.010	0.599	26.666	26.66	33.461	33.46	0.006	0.001

76	16e	11	4	23	20	19	41.003	118	30	21.011	0.609	26.527	26.52	32.942	32.94	0.007	0.002
77	17a	11	6	58	20	19	30.003	118	31	0.013	0.601	26.195	26.19	31.667	31.67	0.005	-0.003
78	17b	11	8	43	20	19	30.003	118	33	9.020	0.614	25.964	25.96	30.728	30.73	0.004	-0.002
79	17c	11	10	21	20	19	30.003	118	35	20.004	0.603	25.754	25.75	29.83	29.83	0.004	0.000
80	17d	11	11	47	20	19	30.003	118	37	30.000	0.615	25.572	25.56	29.023	29.03	0.012	-0.007
81	17e	11	13	29	20	19	31.005	118	39	27.004	0.611	25.367	25.36	28.073	28.08	0.007	-0.007
82	17f	11	14	57	20	19	31.005	118	41	17.994	0.609	25.193	25.19	27.236	27.24	0.003	-0.004
83	18a	11	17	19	20	19	24.001	118	40	33.994	0.610	24.947	24.94	25.998	26.00	0.007	-0.002
84	18b	11	19	11	20	19	24.001	118	37	48.018	0.603	24.777	24.77	25.084	25.09	0.007	-0.006
85	18c	11	20	26	20	19	24.001	118	34	53.005	0.597	24.672	24.67	24.505	24.51	0.002	-0.005
86	18d	11	22	18	20	19	23.006	118	32	24.992	0.615	24.509	24.5	23.561	23.56	0.009	0.001
87	18e	11	23	20	20	19	21.001	118	30	26.010	0.608	24.425	24.42	23.057	23.06	0.005	-0.003
88	19a	11	28	46	20	19	12.006	118	31	1.002	0.598	23.951	23.94	19.927	19.93	0.011	-0.003
89	19b	11	30	30	20	19	13.001	118	33	18.001	0.616	23.805	23.8	18.821	18.82	0.005	0.001
90	19c	11	32	16	20	19	13.001	118	35	59.995	0.609	23.66	23.65	17.666	17.67	0.010	-0.004
91	19d	11	34	9	20	19	13.001	118	38	21.004	0.604	23.52	23.51	16.442	16.44	0.010	0.002
92	19e	11	35	23	20	19	13.001	118	40	29.984	0.599	23.431	23.42	15.608	15.61	0.011	-0.002
93	19f	11	36	43	20	19	13.001	118	41	59.989	0.616	23.341	23.34	14.734	14.74	0.001	-0.006
94	20a	11	38	49	20	19	0.003	118	40	31.000	0.593	23.223	23.22	13.505	13.51	0.003	-0.005
95	20b	11	40	42	20	19	1.006	118	37	52.000	0.612	23.134	23.13	12.446	12.45	0.004	-0.004
96	20c	11	42	2	20	19	1.006	118	34	56.988	0.607	23.078	23.07	11.735	11.74	0.008	-0.005
97	20d	11	43	35	20	19	3.004	118	32	29.002	0.602	23.013	23.01	10.866	10.87	0.003	-0.004
98	21a	11	48	8	20	18	54.998	118	30	58.997	0.603	22.838	22.83	8.046	8.05	0.008	-0.004
99	21b	11	50	6	20	18	54.998	118	33	5.010	0.608	22.775	22.77	6.699	6.70	0.005	-0.001
100	21c	11	51	48	20	18	54.998	118	35	13.000	0.603	22.729	22.72	5.515	5.52	0.009	-0.005
101	21d	11	53	32	20	18	54.998	118	37	48.018	0.600	22.689	22.68	4.285	4.29	0.009	-0.005

102	21e	11	55	7	20	18	54.998	118	40	1.996	0.600	22.663	22.66	3.165	3.17	0.003	-0.005
103	21f	11	56	27	20	18	53.995	118	41	41.999	0.623	22.647	22.64	2.229	2.23	0.007	-0.001
104	22a	11	58	43	20	18	43.997	118	40	31.000	0.623	22.63	22.62	0.81	0.81	0.010	0.000
105	22b	12	0	36	20	18	43.997	118	37	54.005	0.600	22.627	22.62	359.699	359.70	0.007	-0.001
106	22c	12	2	15	20	18	43.997	118	35	2.014	0.611	22.631	22.62	358.752	358.76	0.011	-0.008
107	22d	12	4	9	20	18	43.997	118	32	31.007	0.609	22.644	22.64	357.629	357.63	0.004	-0.001
108	22e	12	5	12	20	18	43.997	118	30	17.990	0.610	22.653	22.65	357.043	357.05	0.003	-0.007
109	23a	12	8	32	20	18	30.999	118	31	7.017	0.592	22.705	22.7	354.852	354.85	0.005	0.002
110	23b	12	10	21	20	18	30.999	118	33	16.024	0.598	22.75	22.74	353.589	353.59	0.010	-0.001
111	23c	12	11	36	20	18	30.999	118	35	19.016	0.613	22.789	22.78	352.7	352.70	0.009	0.000
112	23d	12	13	30	20	18	30.999	118	37	32.005	0.620	22.855	22.85	351.392	351.40	0.005	-0.008
113	23e	12	14	46	20	18	34.996	118	39	10.992	0.602	22.907	22.9	350.518	350.52	0.007	-0.002
114	24a	12	18	22	20	17	51.998	118	37	56.010	0.597	23.046	23.04	348.294	348.30	0.006	-0.006
115	24b	12	19	59	20	17	51.998	118	34	58.004	0.623	23.116	23.11	347.408	347.41	0.006	-0.002
116	24c	12	21	42	20	17	51.998	118	32	21.998	0.614	23.196	23.19	346.448	346.45	0.006	-0.002
117	24d	12	22	59	20	17	51.998	118	30	24.994	0.588	23.261	23.25	345.737	345.74	0.011	-0.003
118	25a	12	25	16	20	18	15.000	118	31	3.007	0.594	23.408	23.4	344.318	344.32	0.008	-0.002
119	25b	12	26	31	20	18	15.996	118	33	18.001	0.614	23.499	23.49	343.469	343.47	0.009	-0.001
120	25c	12	28	26	20	18	15.996	118	35	22.998	0.624	23.64	23.63	342.234	342.24	0.010	-0.006
121	25d	12	30	0	20	18	15.996	118	37	39.009	0.617	23.766	23.76	341.214	341.22	0.006	-0.006
122	25e	12	30	57	20	18	13.998	118	38	53.002	0.604	23.845	23.84	340.605	340.61	0.005	-0.005
123	26a	12	32	58	20	17	45.001	118	37	52.000	0.611	23.992	23.99	339.459	339.46	0.002	-0.001
124	26b	12	34	52	20	17	45.001	118	34	53.005	0.624	24.135	24.13	338.478	338.48	0.005	-0.002
125	26c	12	36	8	20	17	43.998	118	32	34.990	0.624	24.232	24.22	337.842	337.84	0.012	0.002
126	27a	12	38	25	20	17	34.001	118	33	22.011	0.615	24.442	24.43	336.521	336.52	0.012	0.001
127	27b	12	40	19	20	17	34.001	118	35	39.999	0.623	24.637	24.63	335.378	335.38	0.007	-0.002

128	27c	12	41	22	20	17	34.001	118	37	22.996	0.618	24.752	24.74	334.738	334.74	0.012	-0.002
129	27d	12	42	21	20	17	34.001	118	38	38.994	0.608	24.86	24.85	334.157	334.16	0.010	-0.003
130	28a	12	47	52	20	18	26.001	118	38	0.981	0.624	25.46	25.45	331.265	331.27	0.010	-0.005
131	28b	12	49	47	20	18	20.995	118	35	5.008	0.617	25.655	25.65	330.375	330.38	0.005	-0.005
132	28c	12	51	15	20	18	21.997	118	32	46.992	0.614	25.809	25.8	329.708	329.71	0.009	-0.002
133	28d	12	52	36	20	18	21.997	118	30	39.001	0.617	25.953	25.94	329.101	329.10	0.013	0.001
134	29a	12	55	29	20	18	2.998	118	31	40.003	0.618	26.31	26.3	327.636	327.64	0.010	-0.004
135	29b	12	57	20	20	18	2.998	118	34	19.003	0.619	26.568	26.56	326.657	326.66	0.008	-0.003
136	29c	12	58	33	20	18	2.998	118	36	33.997	0.613	26.746	26.74	326.008	326.01	0.006	-0.002
137	29d	13	0	24	20	18	2.998	118	38	32.979	0.625	27.009	27	325.079	325.08	0.009	-0.001

Table 134: Time and navigation parameters for the central pixel in each flight line segment, obtained from each flight line segment header file.

Q.3 Tafkaa Computational Details

Tafkaa only works on radiance files that have not been georectified; therefore, georectification must occur after running the Tafkaa model.

Tafkaa relies on .input files (in ASCII text format), each of which defines relevant atmospheric parameters to the model (an example was given in Table 31, p. 252 of Section 4.5.8). In order to provide a non-biased comparison with the supplied IMO_Ref image (which is equivalent to the PHPA_Ref image – see Section 3.3), the same parameters were used to generate all reflectance-based images. Each of these parameters were investigated and found to be reasonable for the existing Port Hedland coastal region and therefore used in the existing correction. However, some parameters were adjusted to examine the effect of any change in reflectance - this was discussed in Section 4.5.8. Rather than modifying each file by hand, all Tafkaa .input files were fully generated using a C++ program, as modifying parameters in all 137 individual files is cumbersome and prone to user-based errors. Parameters within the .input files were also easily adjustable by the C++ program, thereby having the capability of producing new sets of .input files within seconds. Batch files were then written so that to each of the 137 .input files were automatically called by Tafkaa.

Relevant history (i.e. parameters and values used) are written by the Tafkaa program itself and appended (to the end) of ENVI .hdr files.

From a processing viewpoint, it is worthwhile converting ENVI .BSQ files to .BIP format. The conversion process itself only took about 1.5 minutes per file but the speed-up factor for running the Tafkaa model is truly astonishing; a 1.5GB .BSQ file took about 1 hour (sometimes more) to process, whereas the 1.5 GB .BIP file only took about 1 minute. In practice, the conversion between file formats was performed using a (user written) C++ program and yielding a performance increase of about 40% compared to ENVI's native file conversion tool.

It was also discovered that Tafkaa produces output files in the same format as input files; e.g. inputting a radiance .BIP file results in a reflectance .BIP file.

Appendix R SAM Interpolation Mathematical Details

This Appendix outlines in more detail the resampling process performed for the images of Section 4.5.1.

Unequal (wavelength) grids are formed as the ASD and airborne image spectral resolution were 1 nm and (approximately) 2.2 nm, respectively. Implementation of the spectral angle Equation (2.6.4.3.1) (Section 2.6.4.3) requires an equal number of points. As the ASD spectrum is the ‘finer’ of the two, reflectances in the 1 nm interval grid (i.e. ASD spectrum) was interpolated onto the coarser (2.2 nm interval) grid (airborne spectrum). The interpolation was performed using the routines from the well-known Numerical Recipes book (referred to as NR in this section) (by Press, Flannery, Teukolsky, and Vetterling (1992)). The spline routine obtains the second derivatives of the reflectance values in the original ASD spectrum. However, the routine requires second derivative end points. For this, equation 4-15 from Burden and Faires (1989, p. 150) was used for NR interpolation module splint and where it was stated that the 5 point forward derivative was particularly well suited to the cubic spline method. However, the backward formula was not given and had to be derived. As a result, the formulae used are as stated. For the forward derivate:

$$f'(x_0) = \frac{1}{12h} [-25f(x_0) + 48f(x_0 + h) - 36f(x_0 + 2h) + 16f(x_0 + 3h) - 3f(x_0 + 4h)]$$

A backward derivative (for the reverse direction) can be derived by replacing $h \rightarrow -h$ and rearranging the terms. This results in:

$$f'(x_0) = \frac{1}{12h} [3f(x_0 - 4h) - 16f(x_0 - 3h) + 36f(x_0 - 2h) - 48f(x_0 - h) + 25f(x_0)]$$

Owing to the age of the NR source code, these routines and several others had to be manually updated to meet new C++ standards for compilation. Both the Intel C++ Composer XE 2013 and Microsoft Visual Studio 2010 were used to develop the C++ source code early on in this thesis.

The development of a MATLAB program (using the spline routine) allowed for a comparison with the C++ interpolated values (for the same input data). A maximum difference in reflectance value was only 0.000001, which occurred in less than 2% of all wavelengths. As a result, the C++ program was used to calculate the SAM angles displayed in the tables (Section G.3). The program stored the spectral angles to a correctly-formatted text file ready for import by Microsoft Excel 2010.

Appendix S Classification Technicalities

S.1 JM Distance Pair Combinations

The JM distance is calculated between each class pair. As the number of class pairs increase, the number of possible pair combinations rapidly increases according to:

$${}^n C_k = \frac{n!}{k!(n-k)!}$$

where $k = 2$ in the current situation (i.e. the separability between class pairs (i.e. 2 classes)). In expanded form:

$$\text{Number of class pairs} = \frac{n!}{2(n-2)!} = \frac{n(n-1)}{2}$$

Where n is the number of number of classes. The number of class pair combinations grows rapidly; for 2 classes, there is only 1 possibility. For 3 classes, there are 3 combinations. For 4 classes, there are 6 combinations. For 10 classes, there are 45 while for 20 there are 190. It is not hard to see that for a 10 class classifier, keeping track of all JM distances between class pairs already presents a challenge. Although not required in the current thesis, a dendrogram is one method to help keep track of JM distances between large numbers of class pairs.

S.2 MNF Transform Band Selections

As an example of the inefficiency of the MNF transform (for the images in this thesis), consider the result for the N_Ref_NoMask image. Table 135 shows the cumulative variance for the last 27 MNF bands.

MNF band	Cumulative variance	MNF band	Cumulative variance
220	92.746670	234	96.914381
221	93.046941	235	97.207841
222	93.347069	236	97.499728
223	93.646919	237	97.790688
224	93.946673	238	98.080228
225	94.245202	239	98.367494
226	94.543668	240	98.649733
227	94.841258	241	98.927380
228	95.138793	242	99.200932
229	95.436131	243	99.471767
230	95.732662	244	99.720449
231	96.028464	245	99.958329
232	96.324026	246	100.000000
233	96.619449		

Table 135: The cumulative variance for each MNF transformed band for the N_Ref_NoMask image.

The results of Table 135 shows that a cumulative variance of 95% and 99% occurs at MNF bands 229 and 242, respectively. This is clearly not desired as the reduction amounts to only about 2% (for 99% threshold) and 7% (for a 95% threshold). As pointed out in Section 2.5.4, band selections based on the scree test or the Kaiser-Guttman rule (retaining eigenvalues > 1.0) were also inadequate. Computationally, the file size increased significantly, as a result of storing floating point formatted numbers as opposed to integers, thereby expecting to (at least) a doubling in calculation time.

The fact that the variance is not contained in the first few bands, suggests that the image is not particularly noisy. It is common for the MNF images to be non-noisy in the first few MNF bands, with latter images containing higher levels of noise. With reference to Section 2.5.4, researchers have used the MNF transform as a means to remove salt and pepper noise (in latter MNF images), then perform an inverse MNF transform resulting in an improved (i.e. less noise) image. The MNF transform was designed to minimise noise resulting in a series of images based on data quality, which was found to be particularly effective for airborne data (A. A. Green et al., 1988). However, A. A. Green et al. (1988) based their conclusion on

multispectral data (in particular, an airborne thematic mapper). The results of Table 135 might suggest that the PCA could be more effective for non-noisy hyperspectral images, hence the slow decay in the cumulative variance rather than a rapid decay – however, this assertion was not formally tested.

Interestingly, Mahesh Pal and Mather (2006) also had issues with the MNF transform. In particular, 13 MNF bands were selected from a 65 band DIAS (hyperspectral) dataset, for a region at La Mancha, Spain. It was found that the ML classifier led to poorer classification accuracy when the MNF bands were incorporated, compared to the original image. They suggested that the ineffectiveness in using the MNF transform for dimensionality reduction may have been due to the nature of their particular data. This implies that the performance of the MNF transform could be image dependent and explains the discrepancy between the poor performance of the PHPA hyperspectral-based datasets compared to the claim that MNF is particularly effective for airborne data (A. A. Green et al., 1988).

To summarise, the MNF is not particularly effective as a feature reduction method for reducing the PHPA hyperspectral data. The large number of bands to be retained is also computationally ineffective.

Appendix T Mangrove Botanic Classification

This section outlines key characteristics in identifying the seven species of mangrove found in the Port-Hedland coastal region. As the PHPA botanist Nicole Wylie was not available to assist with the second field trip (except the planning stage), it was up to the PhD candidate to correctly identify the mangrove species.

The book by Duke (1952) proved particularly useful as a resource in identifying key differences between mangrove species for botanic classification. The book is concise, thereby making it practical for use in the field. It also contains numerous colour images of important mangrove characteristics, such as flowers, bark, roots, leaves as well as the whole tree. Locational details where mangroves are found are also discussed; for example along the shoreline or further inland.

To aid in-field immediate classification, a rough type of flow chart was developed containing a summary of important distinguishing characteristics. The primary interest concerned the ability to distinguish just these seven mangrove types and hence the focus concerned examining key differences between just these seven. Where necessary, the book was consulted in the field to improve the level of confidence in having identified the correct species.

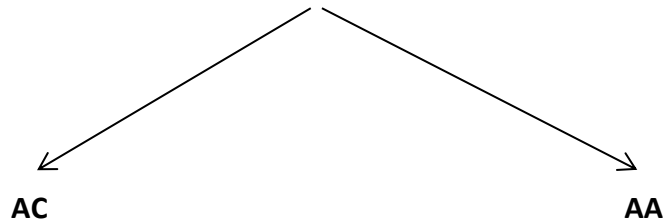
Of interest in the (second) field trip was the correct identification of the seven mangrove species as shown in the following table.

Abbreviation	Mangrove species
AM	<i>Avicennia marina</i>
CA	<i>Ceriops australis</i>
RS	<i>Rhizophora stylosa</i>
BE	<i>Bruguiera exaristata</i>
OO	<i>Osbornia octodonta</i>
AA	<i>Aegialitis annulata</i>
AC	<i>Aegiceras corniculatum</i>

Table 136: Abbreviations used to identify mangrove species during the field trip.

Using the two flow charts below, AM is easily identified by spotting the pencil-like roots (even from a distance!), while a particularly tall mangrove with stilt roots identify the RS mangrove. Another clue for RS is the rough red bark, which is another means of double checking the integrity of classification.

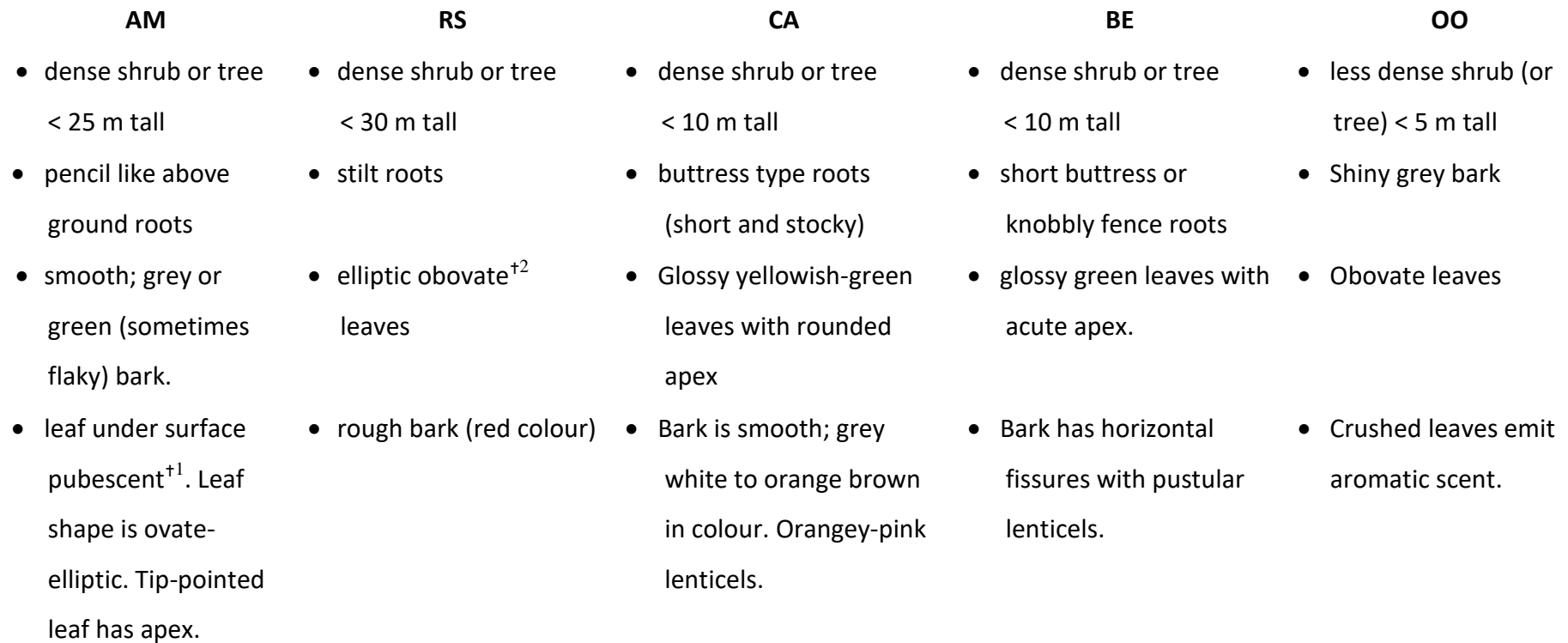
Alternate leaves



- dense shrub (or tree) < 5m tall
- isolated shrub
- salt on leaves (encrusted in patches)

- less dense shrub (or tree) < 2m tall
- fine salt along leaf surfaces
- flowering from June – Sept.

Opposite leaves



- Flowers Sept - Oct

- Roots (mostly occur) below ground.

⁺¹ pubescent means the leaf contains little hairs (e.g. AM).

⁺² obovate means the leaf is tear-shaped.

Appendix U Displaying image using ENVI

True colour images, presented in this thesis, contains a vast range of DN values. Representing such an image on screen (or as a printout) is not always possible, as explained in this section.

Image data may be stored using various data types, as shown in Table 137. Data stored in hyperspectral images (e.g. PHPA_Ref) use a type 2 data type (an integer), whereas PC transformed images are written using data type 4 (which allows for the storing of floating point numbers). Thematic maps contain whole numbers, thereby storing values in data type 1 format due to their limited range.

Image data representations:

- 1 = Byte: 8-bit unsigned integer
- 2 = Integer: 16-bit signed integer
- 3 = Long: 32-bit signed integer
- 4 = Floating-point: 32-bit single-precision
- 5 = Double-precision: 64-bit double-precision floating-point
- 6 = Complex: Real-imaginary pair of single-precision floating-point
- 9 = Double-precision complex: Real-imaginary pair of double precision floating-point
- 12 = Unsigned integer: 16-bit
- 13 = Unsigned long integer: 32-bit
- 14 = 64-bit long integer (signed)
- 15 = 64-bit unsigned long integer (unsigned)

Table 137: Image storage data types used by ENVI.

(Taken from: Harris Geospatial Solutions (2019b))

The following data types as used in this thesis are:

- 1 = Byte: used to create classification and mask files.
- 2 = Integer: used in all hyperspectral images (e.g. IMO_Ref, PHPA_Ref and all the normalised images).
- 4 = Floating-point: used to store spectral angle data, gradient data into images, PC (and MNF) transformed data files.

The smallest possible image results when data is written using data type 1. Suppose the file size of this file is 49 GB. Consider storing the data in this file in type 2 data format and leaving the number of pixels the same in number. As the number of bytes per entry doubles, the total file size doubles to 98 GB. The PHPA_Ref image has a file size of 98 GB. By PC transforming this image, all data needs to be stored as a floating point type. Therefore, the PC transformed PHPA_Ref image is 196 GB in size.

The relationship between the number of DN data values and the number of bits was discussed in Section 2.2.1. For data type 2 (i.e. 16 bits), there are $2^{16} = 65536$ possible DN values. Actually, the data type is signed, so it includes negative values. In effect, the range of possible values allowed is -32,768 to 32,767. Of course, negative image brightnesses are physically unrealistic.

ENVI displays an image using 256 DN values (i.e. it uses 8 bits). For an 8 bit image, there is no issue, as all DN values are displayed realistically. However, for a 16 bit image, the number of possible DN values exceeds the display capability; this presents a problem - a one to one correspondence between a DN and screen output does not exist. ENVI solves this problem by constructing a histogram based on the 16 bit image and remaps them (called contrast stretching) to cover the range from 0 to 255 (i.e. 256 DN numbers). The default conditions ENVI uses are documented in the notes from Harris Geospatial Solutions (2019a):

You can apply different contrast stretch types to enhance the appearance of an image. If the associated header file for an image specifies a default stretch, it is applied when you open the image. If the header file does not specify a stretch, then a stretch type is applied as follows:

- *No stretch is applied to 8-bit byte data.*
- *An optimized linear stretch is applied to 16-bit unsigned integer data.*
- *A linear 2% stretch is applied to all other data types.*

As mentioned above, an 8 bit image does not require stretching, so ENVI does not remap any DN values. The first condition states this explicitly. The second condition, for a 16-bit unsigned integer data, refers to data type 12 (see Table 137). This data type was not used in this thesis. Therefore, the last condition, regarding the 2% linear stretch applies to integer-based images (i.e. PHPA_Ref and all normalised images) in addition to PC transformed images. This last statement also implies that the 2% linear stretch is applied to data type 1 (e.g. thematic and mask images) images, although this does not seem necessary.

In reality, negative DN values (e.g. caused by negative reflectance values) are unable to be displayed. ENVI uses histogram stretching (automatically) to cater for these values instead. ENVI selects minimum and maximum values based on the rules described at Harris Geospatial Solutions (2019f) - the details are not repeated here. Consequently, scaling negative DN values into a positive range has the side-effect of also scaling the (prescaled) zero DN values (representing a masked black pixel), thereby turning them into positive (non-zero) values. Therefore, masked pixels, which should be zero and therefore appear black, may take on a blueish colour (as shown in Figure 336); the colour being dependent on the after-scaling value.

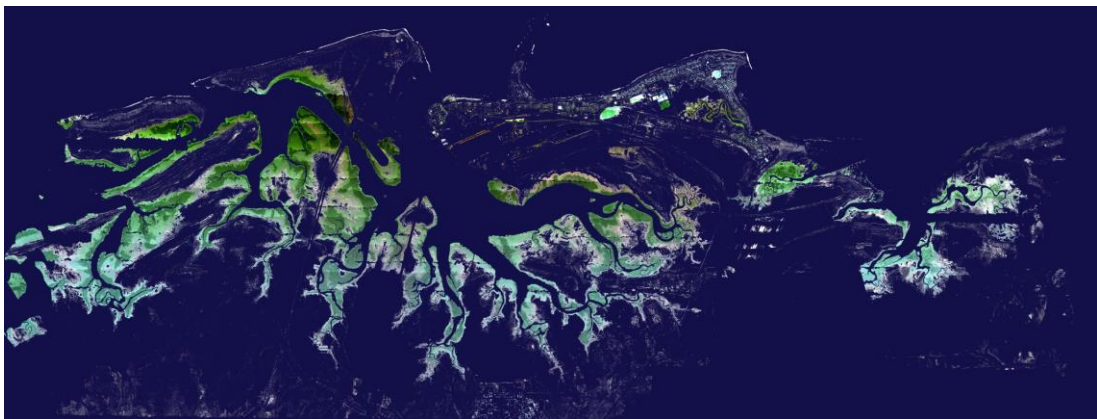


Figure 336: Automatic histogram stretching in ENVI changes black masked pixels to a dark-blueish colour.

Fortunately, ENVI allows the histogram to be manually manipulated by right clicking on the image and selecting interactive stretching. An example of an interactive histogram is shown in the following figure.

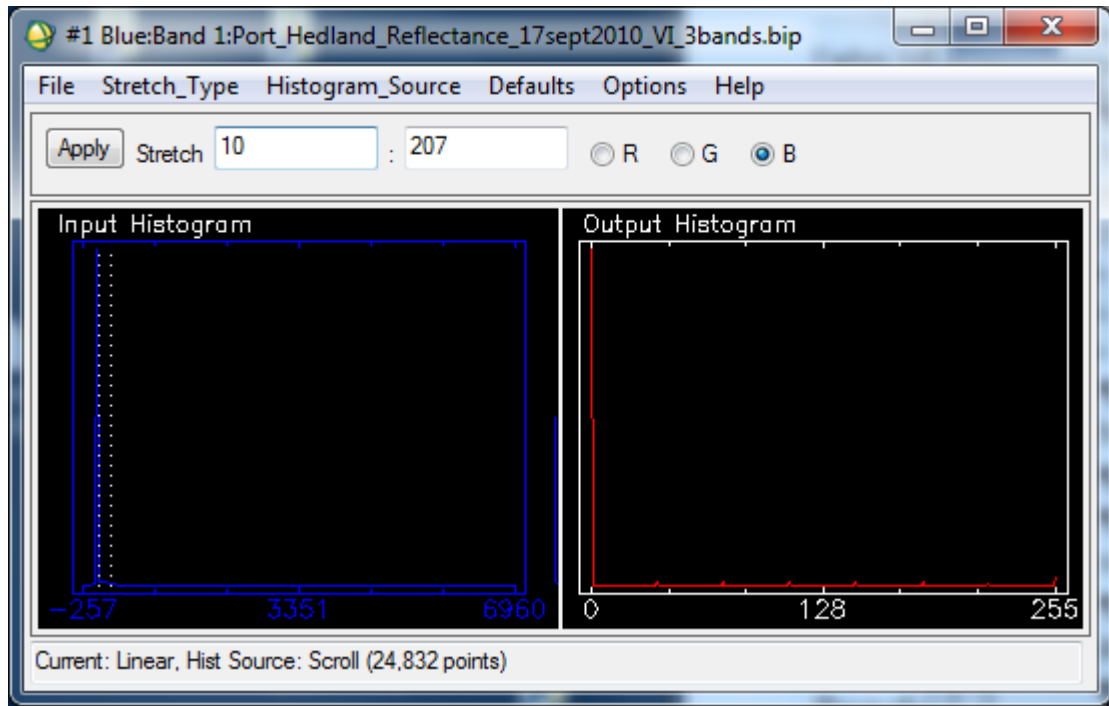


Figure 337: An example of interactively adjusting the histogram in ENVI.

The left histogram of Figure 337 shows the input histogram, while the right shows the output histogram (containing 256 DN values). For the input histogram, there are DN values that lie outside of the range defined by the two dotted white (vertical) lines. In the left histogram, moving the left white vertical dotted line further to the left allows the negative DN values to be situated between the two white dashed lines. When that range is then stretched, it causes some 'strange' colours to appear (as shown in Figure 336) – i.e. black masked pixels become dark blueish in colour.

By entering a minimum value of zero (for each of the RGB bands), the histogram stretches positive values only, leaving zero values as they are (corresponding to the black masked pixels). Some negative DN values are possibly excluded – although this was not explicitly checked. However, these negative DN values relate to negative reflectances, which appear in the northern-part of the image (as discussed in Section 4.5.3.3). They are limited in number in comparison to the DN positive

values. With the limited image resolution displayed in true colour images, a few missing pixels over (for example) Finucane Island (where most negative reflectances exist – see Section 4.5.3.3) is not noticeable. The final result is shown in Figure 338.

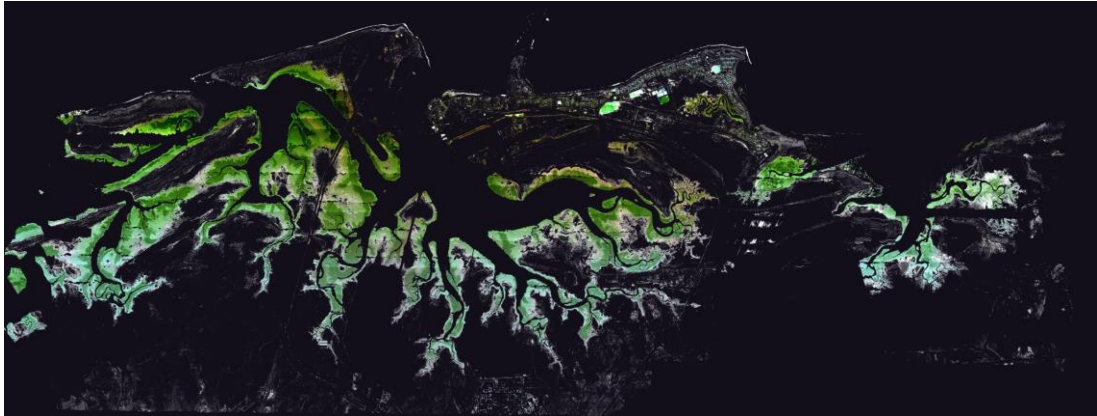


Figure 338: Manual adjustment of the histogram allows natural colours to appear – i.e. the black background is the way it should be, as they represent masked values (where all spectral values are equal to zero).

It should be noted that the histograms relate to the RGB bands selected for image display. As it is the blue bands that contains negative reflectances, the selection of the particular band impacts the histogram displayed. That is, by selecting a blue band having less negative reflectances, a smaller number of negative DN values will result in a smaller scaling change. So, instead of -257 being the negative most DN value (in Figure 337), selecting a nearby band may result in a larger number (e.g. -20).

Appendix V Unsupervised Classification in Practice

A question which arose during unsupervised classification work (for both k-means and ISODATA) concerned the number of 'acceptable' iterations for convergence. Specifying too few iterations results in a timely produced thematic map but at a cost of accuracy. The higher the number of iterations, the more 'stable' the thematic class populations but at a cost of increasing processing time. Stable refers to (ideally) unchanging class populations and distributions. This is expected to occur for very large numbers of iterations. For instance, for 10,000 iterations the classes are expected to be (almost) identical to 10,001 and even 11,000 iterations; although, this does depend on image dimensions and the number of bands. The larger the number of iterations, the smaller the changes with subsequently larger number of iterations, and the more stable the result. In testing small images, comparisons between thematic maps as produced for higher number of iterations (e.g. 20) against those with a very low number (e.g. 1 to 5), revealed major differences both visually and quantitatively for class populations. However, the results were not as discernible when comparisons were made between two higher numbered iterations (e.g. 20 & 25).

In the literature, D'Iorio et al. (2007) (Section 2.8.1) used 100 iterations and a maximum of 25 classes for ISODATA classification. P. M. Mather, and Koch, M. (2011, p. 236) suggests 35 iterations for ISODATA but for a desired number of 10 classes (and maximum of 50). From these sources, more iterations are used when classifying more classes. Therefore, in this thesis, a compromise was considered whereby 10 – 15 classes require between 35 and 50 iterations. In practice, classifying the large images in this thesis (i.e. vegetatively masked images such as PHPA_Ref_VI) using 100 iterations did not return a timely result, as actual processing extended over many days. Therefore a compromise of 50 iterations was decided upon, to return a sound result in two to three days per image.

The effect between 50 and 100 iterations on classification was investigated in a simple test. Using a 10 class k-means classifier, the only parameter that was changed was the number of iterations (i.e. 50 and 100). Previous results for the 50 iteration thematic maps were presented in Section 4.5.11.1 (for the PC transformed

N_Rad_VI_VI image); specifically, Figure 128 (for $JM \geq 1.7$, p. 303), Figure 129 (for $JM \geq 1.8$, p. 304) and Figure 130 (for $JM \geq 1.9$, p. 305).

Table 138 shows class populations at $JM \geq 1.7$ class pair separability for both 50 and 100 iterations on a 10 class k-means classifier.

JM17		
50 iterations	100 iterations	% change
9179328	9026720	0.59
6124597	6130623	-0.02
4835966	4890165	-0.21
1995498	2116033	-0.47
1797801	1855879	-0.22
725426	656386	0.27
476241	497914	-0.08
416201	397278	0.07
191638	171691	0.08
71694	71701	0.00

Table 138: k-means 50 and 100 iteration thematic map class populations, where classes are separable at $JM \geq 1.7$.

The largest class population corresponding to the 50 iteration thematic map is 9179328, while the 100 iteration thematic map produced 9026720. This represents the largest change in class population of 0.59% (highlighted in bold font).

In a similar manner to Table 138, Table 139 summarises the class populations for 50 & 100 iterations with class pair separabilities of $JM \geq 1.8$ and $JM \geq 1.9$.

JM18		
50 iterations	100 iterations	% change
14015294	13916885	0.38
6124597	6130623	-0.02
3793299	3971912	-0.69
725426	656386	0.27
476241	497914	-0.08
416201	397278	0.07
191638	171691	0.08
71694	71701	0.00

JM19		
50 iterations	100 iterations	% change
23933190	24019420	0.33
725426	656386	-0.27
476241	497914	0.08
416201	397278	-0.07
191638	171691	-0.08
71694	71701	0.00

Table 139: k-means 50 and 100 iteration thematic map class populations, where classes are separable to $JM \geq 1.8$ (left table) and $JM \geq 1.9$ (right table).

The largest change in class membership populations are 0.69% and 0.33%, corresponding to class separabilities $JM \geq 1.8$ and $JM \geq 1.9$, respectively. Overall, the maximum change in class population is only 0.69% while having a large impact on processing time (a few more days in fact!).

This investigation suggests that 50 iterations is an acceptable trade-off for classification accuracy in terms of performance; the percentage change in class membership population is small (below 1%) and not expected to cause any significant impact in real terms, while the computational performance gain is immense.

Appendix W Mask File Behaviour in ENVI

Mask files are paramount for ENVI to select the desired pixels for data processing, as the results in this appendix demonstrate.

The study was performed on a small image test region (displayed in Appendix W.1) to examine the effect of mask behaviour on both classification (Appendix W.2) and the PC transform (Appendix W.3). However, there are limitations to the application of masks when using ROI's, which is described in Appendix W.4 along with a remedy.

W.1 Mask building for a region in a test image

Although Section 4.5.6 briefly described how mask images were constructed, and their use, this section elaborates on their generation in computational terms.

An image defining a small region over Finucane Island was created from the full PHPA_Ref_VI image (i.e. Figure 93, p. 237 of Section 4.5.7 – which contains only vegetative pixels). This subset image consists of 400 x 400 pixels and is displayed in Figure 339 (left image). Each pixel contains 246 bands.

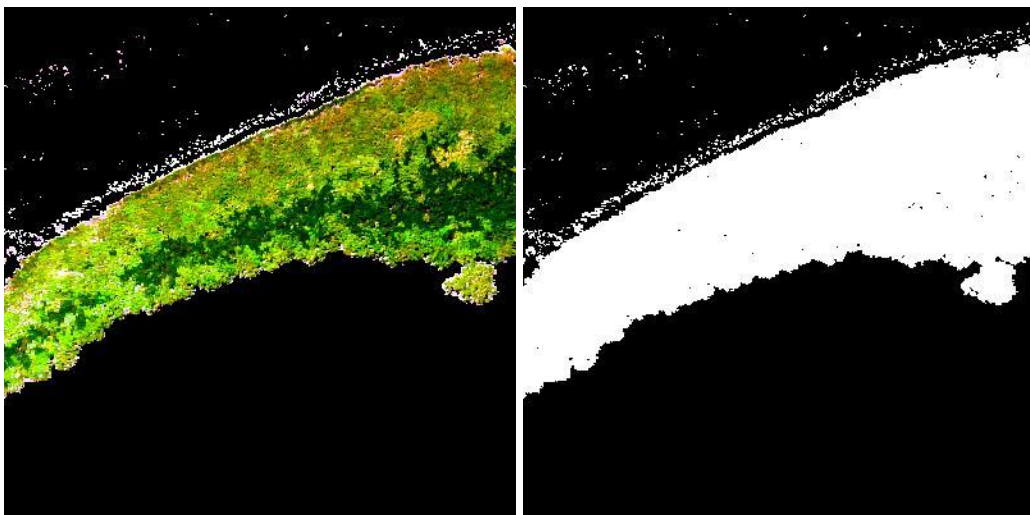


Figure 339: Region on Finucane Island used in this study (left image) and the associated mask (right image).

The corresponding mask to the image of Figure 339 (left image) is displayed in Figure 339 (right image), where values of 1 (represented in white colour) indicate that the pixel exists (i.e. contains vegetative data) in the left image, while a value of 0 (shown in black) signifies that the pixel contains no data (i.e. all spectral bands are zero – they contain no data of interest).

The mask was generated using a C++ program, which examined each pixel spectrally for the image (Figure 339, left). When a pixel contained even a single band having a non-zero reflectance value, is considered unmasked – i.e. it contains valid data. This corresponds to a pixel value of 1 in the mask file. Only if the reflectance for all bands corresponding to a pixel equals zero, the pixel in the mask is written as zero. This way, a mask file can be built very quickly for use in ENVI. The file format is required to be in binary, using a data type of 1 (see Appendix U for more information regarding data formats).

W.2 Unsupervised classification

In this study, a 10 class k-means classifier using 50 iterations classified the image test region shown in Figure 339 (left image).

ENVI allows a mask to be supplied when specifying parameters to the classifier prior to starting the actual image classification process. However, it is not mandatory. The left image of Figure 340 shows the classification result, but without the specification of a mask. In this case, every single pixel of the image was used in the classification process, including the undesired black regions in Figure 339 (left image), which contains no spectral data. Class pixel count statistics are shown in Table 140. The right image of Figure 340 shows a different result, when the mask of Figure 339 (right image) was specified to the classifier in ENVI.

The classification results are clearly different, with many more classes defined in the right image of Figure 340. Class statistics corresponding to each class outcome in Figure 340, are shown in Table 140 below.

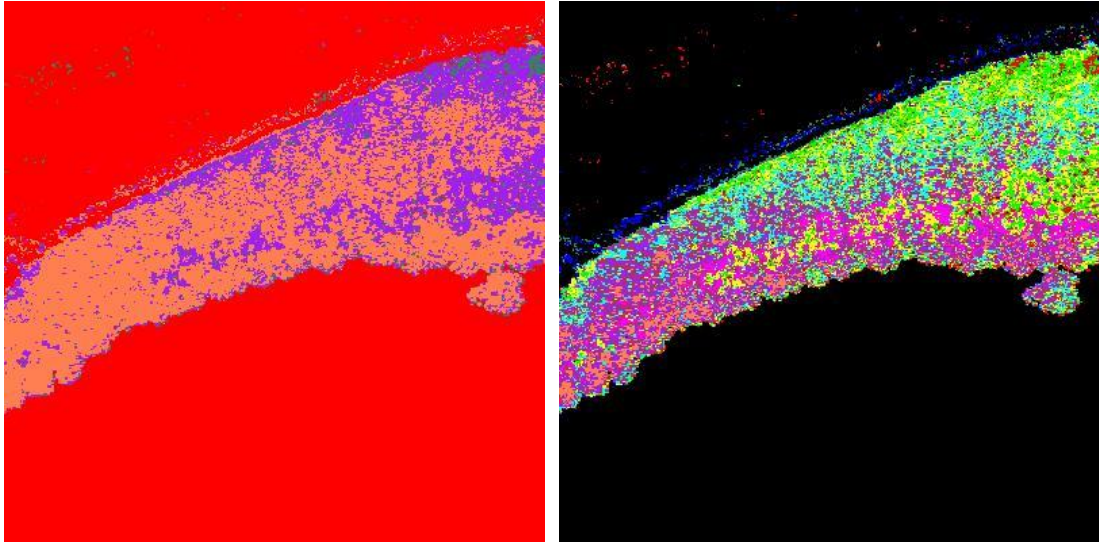


Figure 340: k-means classification result for the left image of Figure 339. The left image (of Figure 340) shows the result in the absence of specifying a mask, while the right image shows a different result when the mask in Figure 339 (right image) is used.

Class number	Number of pixels in Figure 340 (left) - no mask.	Number of pixels in Figure 340 (right) – with a mask.
0	No Entry	108880
1	108880	2031
2	0	6427
3	0	1187
4	0	9926
5	25	8335
6	126	4672
7	384	8916
8	1893	605
9	16351	6274
10	32341	2747

Table 140: Pixel counts for each class. The centre/right column shows the class populations corresponding to the left/right image of Figure 339.

Interestingly, when no mask is selected prior to classification, the classifier produces 10 classes (as specified by the user). However, class 1 consists of a large population of 108880 pixels, whereby the masked pixels (i.e. the black ones) in an image are categorised. As these are of no interest, only 9 classes are actually used from the 10. In effect, just 6 of the 10 classes (i.e. classes 5 to 10 in Table 140) produced 'meaningful' results according to the classifier. However, by using a mask file, the classifier correctly uses all of these 10 classes. The statistics table in ENVI actually contains an additional entry, that of class 0, which represents all the masked (black) pixels which were actually excluded from classification by the mask. Therefore, the results obtained by specifying a mask to the classifier produces the desired classification results.

It should be noted that the work here only demonstrates that, when classifying an image, a mask file must be specified along with any classifier parameters in ENVI, in order to classify the intended pixels. There is no interest here to assess class distance separabilities, as in JM distances (for instance). That topic was covered in Section 4.5.7.

W.3 PC Transform

A PC transform produced the eigenvalues, as shown in Table 141, for the test image of Figure 339 (left image).

The eigenvalues are dramatically different, when comparing the two columns in Table 141, depending on implementing the mask as shown in Figure 339 (right image). As the eigenvalues differ, it is no surprise that the PC band images also differ. Figure 341 shows the results for PC band 1 (no other PC bands are shown).

The results clearly demonstrates that ENVI requires a mask to process the right pixels in an image. Unfortunately, ENVI does not, by default, ignore black pixels (i.e. those where all spectral band values are zero). Although these black pixels signify to the analyst that these pixels are to be ignored and contain no useful data, ENVI treats these masked pixels as having useful data.

Although the results here apply to the PC transform, the same conclusion applies to MNF transforms of an image.

PC Band	Eigenvalues in the absence of a mask file.	Eigenvalues in the presence of a mask file.
1	127024606.06	19956721.17
2	981650.04	3033099.82
3	91896.73	159094.39
4	20874.39	63626.10
5	10316.50	25747.42
6	7476.36	14811.46
7	3011.57	8513.17
8	2654.06	8295.67
9	2499.11	7820.45
10	2440.59	7619.20

Table 141: The eigenvalues for the PC transform of Figure 339 (left image). The centre/right column shows the eigenvalues in the absence/presence of applying a mask. (Note: only the first 10 bands (in descending order) are displayed).

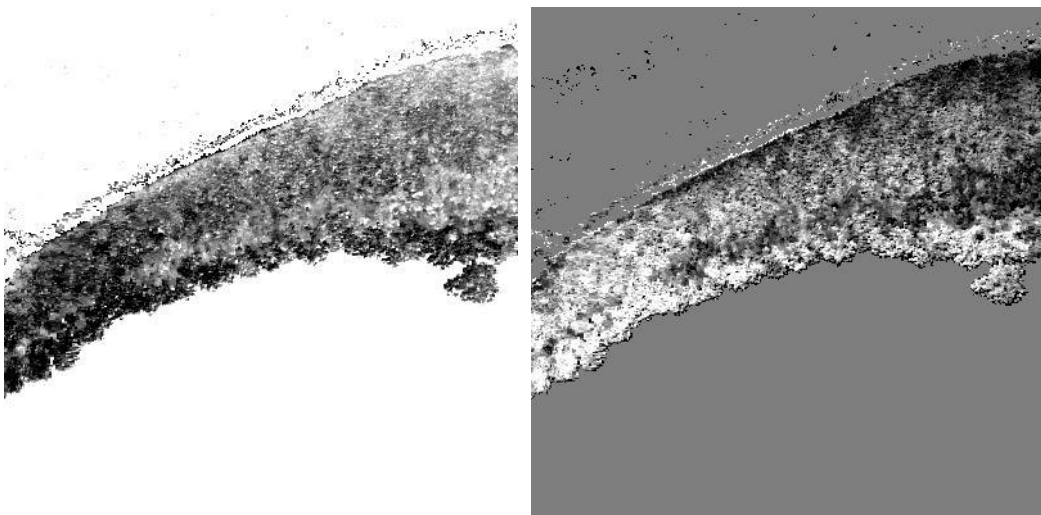


Figure 341: PC band 1 result in the absence (left image) and presence (right image) of applying the mask of Figure 339 (right image) to the test image (Figure 339, left image).

W.4 ROI Statistics Complications

This thesis contains numerous examples whereby mean spectra belonging to multiple images are displayed on a single plot (e.g. those displayed in Section 4.5.9.6 or Appendix N). These mean spectra were calculated using a single defined ROI but used on multiple images. Obtaining a mean spectrum for a particular ROI should be a simple task using the ENVI ROI Tool as depicted in Figure 342. The “Stats” button then calculates a mean spectrum covering over all the pixels defined for the ROI.

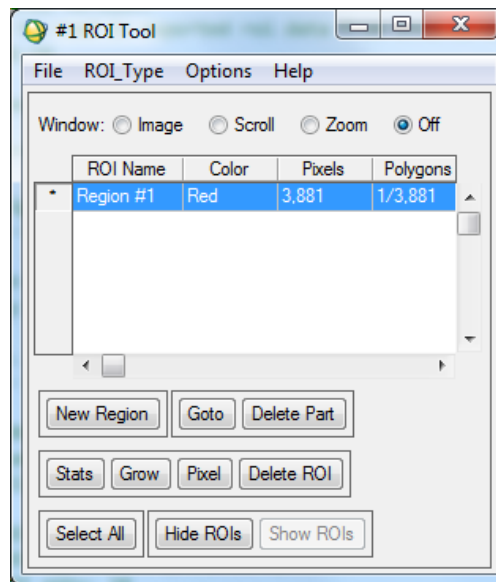


Figure 342: The ROI Tool in ENVI

However, in practice, ENVI behaves in a manner consistent to the findings described above in Appendices W.2 & W.3. This means that the statistics also include the (black) masked pixels in the calculation, which actually contains no spectral data. Therefore, the ROI mean result is actually a false result for the mean spectrum.

For proof, consider defining a small ROI over an isolated group of pixels whose purpose is to examine the effect of zero-based pixels on ROI statistics. These zero-based pixels contain no spectra. To simplify the analysis, the input image contains 3 bands rather than the full 246 bands.

A group of pixels was selected using the PHPA_Ref_VI image, with Figure 343 showing the extent of the test region.

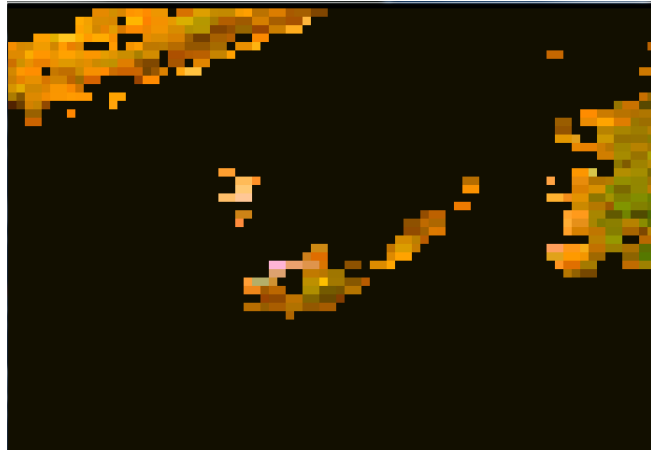


Figure 343: Test image used for the study in this section.

Figure 344 (below) shows the selection of a group of pixels in the above image (Figure 343), defining a small ROI (left image) and large ROI (right image).

Comparing Figure 343 with Figure 344 shows that the non-masked selected pixels are identical in both ROI's.

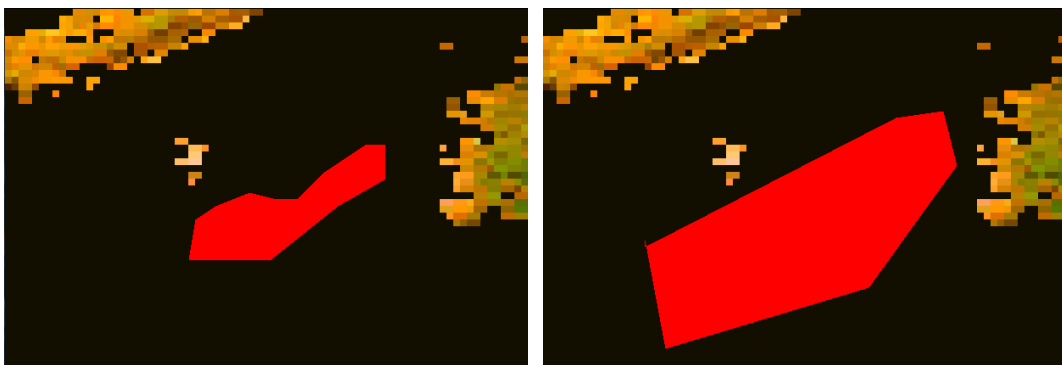


Figure 344: The left image shows a small ROI, while the ROI in the right image defines a larger group of pixels.

The small and large ROI contains 211 and 817 pixels, respectively. The larger ROI contains the same non-masked pixels as the smaller ROI; the large ROI contains an extra 606 (i.e. $817 - 211$) pixels compared to the number of pixels already defined in the small ROI.

As the small ROI already contains 111 masked pixels, there must be 100 non-masked pixels. The large ROI contains a total of $606 + 111 = 717$ masked pixels in total.

If ENVI ignores masked pixels, the statistics will be identical for both ROI's. The results returned by ENVI (using the ROI Tool) are summarised in Table 142 and Table 143, for the small and ROI, respectively.

Basic Stats	Min	Max	Mean
Band 1	-107	179	-6.421801
Band 2	0	448	123.639810
Band 3	0	855	249.663507

Table 142: Statistics as returned by the ENVI ROI Tool for the small ROI in Figure 344.

Basic Stats	Min	Max	Mean
Band 1	-107	179	-1.658507
Band 2	0	448	31.931457
Band 3	0	855	64.478580

Table 143: Statistics as returned by the ENVI ROI Tool for the large ROI in Figure 344.

As the statistics differ between Table 142 and Table 143, it shows that ENVI counts masked pixels toward the statistics. The negative reflectance mean for band 1 (located in the blue spectral region) is due to the image having negative reflectances (explained in Section 4.5.3.3).

The mean for the large ROI can be obtained directly from the mean of the small ROI. For example, for band 2 the mean for the large ROI is:

$$\frac{123.639810 \times 211}{817} = 31.931456$$

(the last decimal number differing by 0.000001 due to rounding error).

The inclusion of masked pixels by ENVI in data transformations and classifications are controlled using masks (as detailed in Appendices W.2 & W.3); ENVI has a mechanism allowing a mask to be specified prior to the calculation. However, it is a different matter when performing statistics on the image itself using ROI's. There

appears to be no way of excluding these masked (zero-spectra) pixels from the mean calculation for an ROI. Instead the statistics must be manually altered.

From Table 142 and Table 143, the “True mean” (i.e. excluding masked pixels) may be calculated using the following formula:

$$\text{True mean} = (\text{ENVI calculated mean}) \times (\text{number ROI of pixels}) / (\text{number of ROI pixels} - \text{number of zero-spectra pixels})$$

The “True mean” is the mean for the group of unmasked pixels defined in a ROI. For example, using the values from Table 142 for band 2:

$$\text{True mean} = 123.639810 \times 211 / (211 - 111) = 260.880000$$

Note that the mean in Table 142 is actually incorrect, as it includes the 111 masked pixels of the small ROI.

A “Scale factor” may be defined as:

$$\text{Scale factor} = (\text{number ROI of pixels}) / (\text{number of ROI pixels} - \text{number of zero-spectra pixels})$$

The “True mean” and the “Scale factor” are related by:

$$\text{True mean} = \text{False mean} \times \text{Scale factor}$$

where “False mean” is the mean obtained from the ROI (e.g. 123.639810 for band 2 in Table 142).

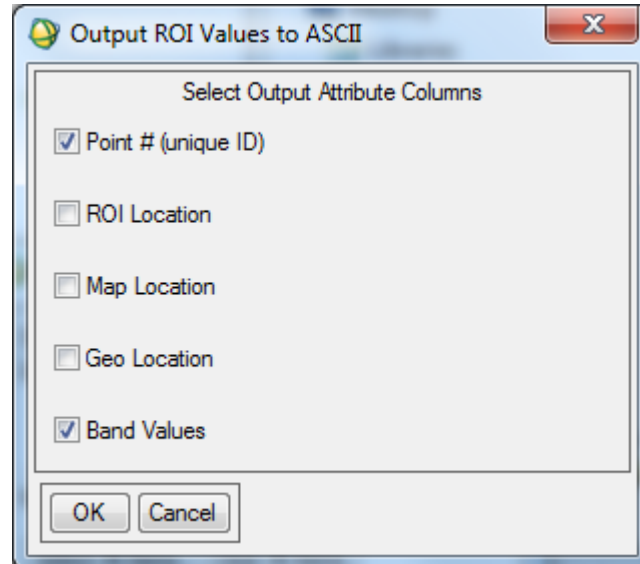
The “True mean” calculation would need to be calculated for every band, although the “Scale factor” remains a constant, even between images using the same ROI.

The “True mean” calculation can be ignored when comparing mean spectral distributions between images. Although the individual mean spectral values are incorrect, the spectral shape will be uniformly affected as each band is scaled

equally according to the “Scale factor”. As the same number of masked pixels are defined in each image (for the same ROI), the spectral shapes may be directly compared without consideration of the “True mean”.

Furthermore, the “True mean” calculation may also be ignored when defining a ROI from a classified result (i.e. thematic map) as the classes in the thematic map ignores these zero-pixels (recall also that a mask was applied prior to classification to exclude these zero-pixels). Hence, a ROI created on basis of a thematic class will not include the zero-pixels and therefore the “True mean” is already calculated. Other statistics (e.g. the standard deviation) are therefore also “True” in thematic maps.

The method adopted in this thesis to calculate the “True mean” of an ROI is to export each pixel spectrum to a (text) file. Only the band values are needed, although it is useful to include the Point number (as it numbers each pixel sequentially and thereby aids debugging). The image below shows the options to select in ENVI (i.e. the ‘ticked’ ones).



A C++ program was written to import the contents of this text file, which then counts the number of masked pixels (i.e. where all bands corresponding to pixel have a zero value). The corrected mean (“True mean”) result is then calculated, corresponding to the mean of all unmasked pixels contained in the ROI. It is this “True mean” data which was plotted in this thesis.

Another complication concerns the actual location of the ROI. Most image files were 100 GB, containing 23768 x 9005 pixels. However, both the N_Ref_VI_VI and N_Ref_Res_VI_VI files were each 98 GB in size, containing fewer flight lines (23768 x 8577 pixels). The details are found in Appendices L.5 and L.7. For an ROI placed on the 100 GB image, ENVI would not load the ROI onto a 98 GB image, despite both ROI's defining identical geographical coordinates in both images. Stranger still, the same pixels were displayed when both images (100 GB and 98 GB) were linked together in ENVI. This deepened the mystery in relation to ROI files. The binary format used in an ROI exported file remains unknown, despite exhaustive searches on the internet and even attempts at brute-force hacking. It is suspected that the coordinates are either stored by pixel number rather than geographically, given the experiences described above.

A solution was found by exporting the ROI location to a text file, then using a C++ program, modify the Y coordinates to reflect that of the smaller 98 GB file (as all ROI's were initially defined on the 100 GB file). In effect, a transformation in coordinates. The steps below describes the process:

Steps:

1. Open the image using just 3 bands, as derived from the 100 GB image (faster this way! – see comment below). Note that it is not possible to directly export the coordinates from a previously defined ROI into the ROI tool as ENVI needs an image first. Hence, we open a 3 band file instead.
2. Using the ROI tool, restore the ROI as defined originally from the 100 GB file.
3. Now, select: file -> output ROI's to ASCII (see Figure 345).
4. In the “edit output ASCII form ...”, we only need the ROI location, although exporting the Point # is also useful. A screen shot is shown below of this dialog box. The file is given an appropriate name - e.g. “ROI 2b from 100GB.txt”.

Step 1 needs clarification. Instead of opening the 100 GB file containing all 246 hyperspectral bands, we are only interested in a visual representation – i.e. the RGB bands. For this reason, a 3 band file was generated using the RGB

wavelengths defined throughout this thesis. The 3 band file is only about 1 GB as opposed to 100 GB, thereby loading much faster into memory. Nothing is gained by loading all the other bands for the purpose of defining ROI's!

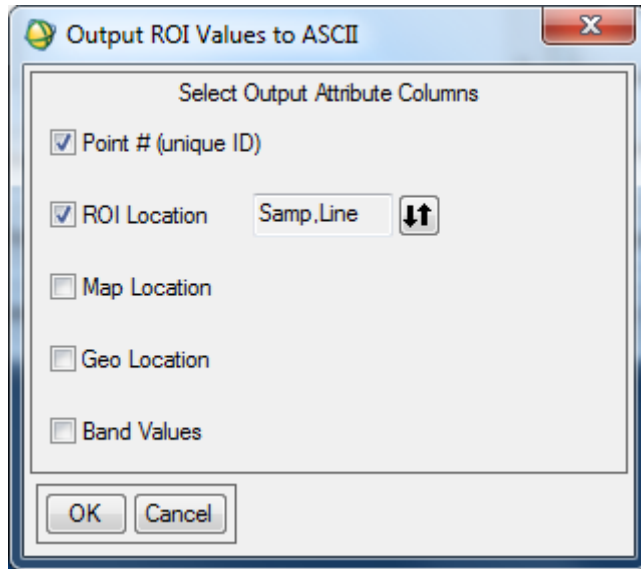


Figure 345: A screen capture of the ENVI “Output ROI Values to ASCII” dialog box.

An example of the exported data is shown below, for just the first three pixels, and actually corresponds to the ROI file of ROI2b (Figure 295, p. 628 of Appendix N).

```

; ENVI Output of ROIs (5.1) [Thu Jan 28 10:27:36 2016]
; Number of ROIs: 1
; File Dimension: 23768 x 9005
;
; ROI name: Region #1
; ROI rgb value: {255, 0, 0}Cashion, 2013
; ROI npts: 3881
; ID X Y
  1 4637 8179
  2 4636 8180
  3 4637 8180

```

Now, with respect to the smaller 98 GB file, the Y coords needs modifying. The 100 GB file has 9005 lines (i.e. rows of pixels), whereas the 98 GB file has 8577 lines instead (the number of samples (i.e. columns of pixels) remain the same). The difference is 428. So, each of the Y values need to be changed by

subtracting 428 from it. This then defines the new location for the ROI with respect to the 98 GB file. The result is:

```
; ENVI Output of ROIs (5.1) [Thu Jan 28 10:27:36 2016]
; Number of ROIs: 1
; File Dimension: 23768 x 8577
;
; ROI name: Region #1
; ROI rgb value: {255, 0, 0}
; ROI npts: 3881
; ID X Y
  1 4637 7751
  2 4636 7752
  3 4637 7752
```

A C++ program performed this conversion automatically. A further complication was discovered when there had to be at least one space preceding the numbers in the ID field. Without at least one space, ENVI wouldn't import the transformed (i.e. new) ROI text file for the 98 GB image.

5. Run the C++ program and give the output file an appropriate file name e.g. "ROI 2b from 98GB.txt".
6. Open the 3 band image version of the 98 GB image in ENVI.
7. Using the ROI tool for that image, import the new ROI text file. Change the settings to what is shown in Figure 346 below.
8. Save the ROI as an ENVI .roi file (in binary format - for convenience, so we don't have to go through the importing process again!).

Extensive testing showed that the ROI defined for the 100 GB file translates correctly to the 98 GB file. This allows for direct statistical comparisons to be made between the two differently sized images. Without this process, it is virtually impossible to select identical pixels between two differently sized images for direct plot comparisons (e.g. as in Section 4.5.9.6, Appendix N and elsewhere in this thesis).

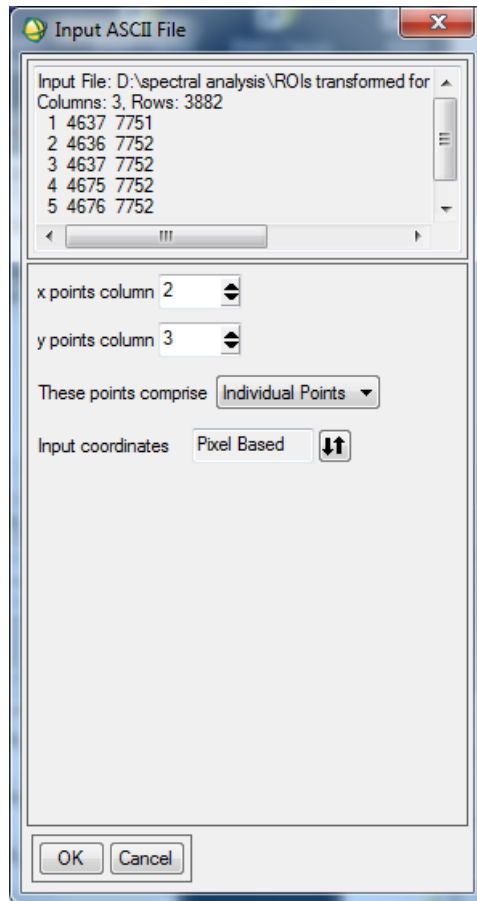


Figure 346: The ENVI dialog box used to import the a ROI text file.

Appendix X Meteorological Data

The data presented in this section is a summary of the full set of meteorological data purchased from the Bureau of Meteorology (<http://www.bom.gov.au>). The data covers the time period (17th September 2010) in the vicinity of the PHPA aerial hyperspectral survey. The meteorological data also included minute-by-minute data, which is not shown in this thesis.

Year	Month	Day	Precipitation in the 24 hours before 9am (local time) in mm	Maximum temperature in 24 hours after 9am (local time) in Degrees C	Minimum temperature in 24 hours before 9am (local time) in Degrees C	Speed of maximum wind gust in km/h	Direction of maximum wind gust in degrees	Time of maximum wind gust in HHMM 24 hour mode
2010	9	13	4	34.1	19.5	50	112	903
2010	9	14	0	25.3	20.6	40.7	143	1215
2010	9	15	4.6	21.4	16.2	31.3	105	701
2010	9	16	0	29.8	13.6	46.4	132	1146
2010	9	17	0	31.5	16.2	53.6	143	1429

Year	Month	Day	Relative humidity for observation at 00 hours Local Time in percentage %	Relative humidity for observation at 03 hours Local Time in percentage %	Relative humidity for observation at 06 hours Local Time in percentage %	Relative humidity for observation at 09 hours Local Time in percentage %	Relative humidity for observation at 12 hours Local Time in percentage %	Relative humidity for observation at 15 hours Local Time in percentage %	Relative humidity for observation at 18 hours Local Time in percentage %	Relative humidity for observation at 21 hours Local Time in percentage %
2010	9	13	90	85	69	22	24	22	43	40
2010	9	14	27	33	42	75	67	83	70	88
2010	9	15	93	94	87	86	92	84	81	89
2010	9	16	92	96	96	66	100	30	71	89
2010	9	17	96	98	78	51	38	55	86	78

Table 144: Meteorological data leading up to the day of the PHPA aerial survey (by day). The survey was conducted on the 17th September 2010.